ASME
SETTING THE STANDARD

Journal of Engineering for Gas Turbines and Power

Published Quarterly by ASME

VOLUME 129 • NUMBER 1 • JANUARY 2007

Transactions of the ASME, Journal of Engineering for Gas Turbines and Power (ISSN 0742-4795) is published quarterly (Jan., April, July, Oct.) by The American Society of Mechanical Engineers, Three Park Avenue, New York, NY 10016. Periodicals postage paid at New York, NY and additional mailing offices. POSTMASTER: Send address changes to Transactions of the ASME, Journal of Engineering for Gas Turbines and Power, c/o THE AMERICAN SOCIETY OF MECHANICAL ENGINEERS, 22 Law Drive, Box 2300, Fairfield, NJ 07007-2300.
CHANGES OF ADDRESS must be received at Society headquarters seven weeks before they are to be effective. Please send old label and new address.
STATEMENT from By-Laws. The Society shall not be responsible for statements or opinions advanced in papers or ... printed in its publications (B7.1, par. 3).

EDITORIAL

TECHNICAL PAPERS

Gas Turbines: Review Papers in Combustion & Fuels

Gas Turbines: Ceramics

Gas Turbines: Combustion and Fuels

Gas Turbines: Controls, Diagnostics, and Instrumentation

Gas Turbines: Cycle Innovations

(Contents continued on inside back cover)

This journal is printed on acid-free paper, which exceeds the ANSI Z39.48-1992 specification for permanence of paper and library materials. ♾™
♻ 85% recycled content, including 10% post-consumer fibers.

(Contents continued)

Journal of Engineering for Gas Turbines and Power JANUARY 2007

Volume 129, Number 1

Gas Turbines: Electric Power

Gas Turbines: Industrial and Cogeneration

Gas Turbines: Structures and Dynamics

Internal Combustion Engines

(Contents continued on facing page)

Journal of Engineering for Gas Turbines and Power **JANUARY 2007**

Volume 129, Number 1

The ASME Journal of Engineering for Gas Turbines and Power is abstracted and indexed in the following:

AESIS (Australia's Geoscience, Minerals, & Petroleum Database), Applied Science & Technology Index, Aquatic Sciences and Fisheries Abstracts, Civil Engineering Abstracts, Compendex (The electronic equivalent of Engineering Index), Computer & Information Systems Abstracts, Corrosion Abstracts, Current Contents, Engineered Materials Abstracts, Engineering Index, Enviroline (The electronic equivalent of Environment Abstracts), Environment Abstracts, Environmental Science and Pollution Management, Fluidex, INSPEC, Mechanical & Transportation Engineering Abstracts, Mechanical Engineering Abstracts, METADEX (The electronic equivalent of Metals Abstracts and Alloys Index), Pollution Abstracts, Referativnyi Zhurnal, Science Citation Index, SciSearch (The electronic equivalent of Science Citation Index), Shock and Vibration Digest

Journal of Engineering for Gas Turbines and Power

Editorial

Let me begin by wishing all of you a very happy and prosperous new year. I am proud to have been appointed editor of this journal, and I wish to take this opportunity to share with you my thoughts on the directions the journal is headed, issues to be resolved, and future challenges to be overcome—call it editorial rambling if you like.

This journal began 127 years ago as a collection of 17 papers on energy conversion technology in 1880 with Vol. 1 of Transactions of the ASME, and last year's Vol. 128 published around 110 papers in 956 pages. The high quality of published papers and diverse subject matter under the broad area of "Power and Energy" has sustained and enriched this journal for over a century. JEGTP is successful because it is a one-stop place to find authoritative research literature in gas turbines and power, and the "journal as a whole is greater than the sum of its parts." "Excellence is eternal" and this journal, like its parent ASME, *sets the standard*. Today, the journal has global outreach and a world-class stature and reputation—credit must surely go to its readers, authors, ASME staff, reviewers, associate editors, and past editors.

A succession of editors and the ASME have led the journal through changes that were essential to keeping up with the demands of the rapidly changing technical publication and production processes. For example, on July 1, 2004, the journal completely switched over to the use of the ASME Journal Tool for submission of papers.[1] Past editor Professor Lee Langston and editorial assistant Liz Langston aptly handled the challenge of transition to a completely electronic media, at the same time maintaining the quality and steady growth of the journal. Lee and Liz deserve our special appreciation for their volunteerism, leadership and hard work. Also, I express my deep gratitude to all the outgoing associate editors who persevered during the ongoing improvements in the journal tool.

JEGTP covers a wide range of topics such as Gas Turbine Technology, Power Generation, Nuclear Engineering, Internal Combustion Engines, Fuels and Combustion, and Advanced Energy Systems. The quality and mix of published papers is excellent. Thus, my goal is to build upon these strengths and expand the journal without sacrificing quality.

The future promises a rapid growth in all of the above areas embraced by JEGTP. Thus, my first challenge during 2006 was to secure ASME's approval for my nomination of six new outstanding individuals as associate editors. They are: Gas Turbine Combustion and Fuels, Dr. Nader Rizk (Rolls Royce Inc.) and Professor Thomas Sattelmayer (Technical University of Munich); Gas Turbine Structures and Dynamics, Dr. Jaroslaw Szwedowicz (ABB Turbo Systems Ltd.) and Dr. David Walls (Pratt & Whitney); and I.C. Engines, Professor Christopher Rutland (University of Wisconsin) and Dr. Thomas Ryan III (Southwest Research Institute). My congratulations to all these individuals for their selection, and I am looking forward to working with them.

All journal editors have a common goal of ensuring that the submitted papers are reviewed, selected, processed and published in a fair and expeditious manner. Its global outreach and world-class stature continues to grow JEGTP to the point that the journal is "bursting at its seams." This makes me proud, but at the same time concerned because an excessive publication backlog is unhealthy for any journal. During the past six months, I analyzed this situation and concluded that: all areas of JEGTP have experienced a steady growth over the last two decades; the journal has simply not kept pace with this growth; and finally, there appears to be no downturn, but only sustained future growth. I made my findings known to ASME and urged them to find a permanent solution. I am pleased to inform you that effective January 1, 2007, ASME has approved a permanent increase in journal pages by 350 or approximately 40 additional papers, thereby significantly reducing the backlog.

What great news to begin the new year. Now, your help is necessary in ensuring that JEGTP receives high-quality research papers to sustain its steady growth.

Dilip R. Ballal

[1] http://journaltool.asme.org

25 Years of BBC/ABB/Alstom Lean Premix Combustion Technologies

Klaus Döbbeling[1]
e-mail: klaus.doebbeling@power.alstom.com

Jaan Hellat

Alstom Power,
Brown Boveri Strasse 7,
CH-401 Baden,
Switzerland

Hans Koch[2]
ABB,
Raenkestrasse 23,
CH-8700 Kuesnacht ZH,
Switzerland

The paper will show the development of lean premix combustion technologies in BBC, ABB, and Alstom gas turbines. Different technologies have been developed and applied in Brown Boveri Company (BBC) before 1990. Considerable improvements with respect to NO_x *emissions as compared to gas turbines with a single combustor and a single diffusion burner for liquid and gaseous fuel have been achieved with burners with extended premixing sections and with multi-injection burners for annular combustors. Between 1990 and 2005, burners with short but effective premixing zones (EV burners: environmentally friendly V-shaped burners) have been implemented in all new gas turbines of the ABB (and later Alstom) fleet with* NO_x *levels well below 25 vppmd (@15%* O_2*). In addition to this, three variants of premix technologies have been successfully developed and deployed into Alstom GT engines: the sequential EV burners—a technology that allows premixing of natural gas and oil into a hot exhaust stream to reheat the exhaust gases of a first high-pressure turbine; the MBtu EV burners that are used to burn syngas in a premix flame with low* NO_x *emissions; and the advanced EV burners (AEV) that are capable to prevaporize and premix liquid fuel prior to combustion and burn it with very low* NO_x *emissions without water injection. The paper will give an overview of these technologies and their usage in Alstom gas turbines over the last* 25 years.
[DOI: 10.1115/1.2181183]

1 Introduction

In 1939, the first commercial stationary gas turbine was erected in Neuchatel, Switzerland by the former BBC. In the following decades, the gas turbine technology progressed with a series of important innovation steps; for example, the development of a recuperated, intercooled reheat gas turbine process for high gas turbine efficiency of 28% in the 1950s, the introduction of Ni and Co base alloys for higher turbine inlet temperatures in the 1960s, and the introduction of cooled turbine blading in the 1970s. In those times, combustion technology was not such a dominant delimiter for the whole gas turbine technology as it is today, and therefore the combustion targets were not as demanding as they are today. Nevertheless, the task for a gas turbine combustor development engineer was quite complex, since he had to provide a stable combustion with liquid and gaseous fuels over the whole load range with an acceptable hot gas profile, he had to ensure ignition and a sufficient burnout for increasing combustor loading, and he had to avoid coking and overheating. The fuels ranged from blast furnace gases to natural gases and LPG; for liquid fuels, heavy and crude oil were also possible. With regard to flue gas emissions, the only concern in those early times was the abatement of visible smoke.

In the 1970s, the emissions of CO, unburned hydrocarbons and especially the NO_x emissions started to attract attention; the first regulations for flue gas concentrations and emissions appeared, and the related measuring technologies made the step from lab to field applicability with an accuracy in the ppm range.

The gas turbine manufacturers started in an early phase to address low-NO_x technologies—in a very first step with the development of wet low-NO_x control techniques, which have been commercially available in the beginning of 1970. However, it also became clear, that wet NO_x control would not be a cost-effective path to reach very low NO_x emissions, and that instead, a quantum leap in the combustion technology was needed, to come up with a dry low-NO_x technology (Fig. 1).

In the former BBC, a first development strategy for dry low NO_x was formulated in the 1970s. Right from the beginning, it was concluded that the up-to-then combustor technology with a single diffusional burner and with a massive injection of secondary and mixing air into the combustor had no dry low-NO_x potential and that this technology must be completely left. The decision was taken to base the development strategy on two pillars. The one pillar was the development of a new lean premixed combustion and premix burner technology. The other pillar was the development for a reduction of the cooling and mixing air consumption in the combustor, leading finally to the annular combustor technology.

The principal idea of this approach was to reduce the NO_x generation in the reaction zones by avoiding high flame temperatures. The consequence of this approach was a generic change in the burner and combustor architecture and in the operation concept. The burners now were operating closer to extinction limits, and stabilizing with ignitable mixtures had to cope with new problem categories, with mixing quality, flashback sensitivity, lean extinction, and pulsation stability. The need to operate the combustor also at conditions below the lean extinction temperature of a single premix burner led to distributed multiburner systems with burner switching, staging, and piloting concepts. The combustor development, on the other hand, targeted to improve the liner wall cooling with new impingement, film, and convective cooling concepts. These technologies were first implemented in the single-burner combustors.

The race for higher gas turbine efficiency with increased firing temperatures led to a conflicting target with the simultaneous reduction of NO_x emissions. The consequence was to further reduce the amount of combustor cooling air and to redirect the air as

[1]Author to whom correspondence should be addressed.
[2]Retired.

Contributed by the International Gas Turbine Institute (IGTI) of ASME for publication in the JOURNAL OF ENGINEERING FOR GAS TURBINES AND POWER. Manuscript received August 25, 2005; final manuscript received September 28, 2005. IGTI Review Chair: K. C. Hall. Paper presented at the ASME Turbo Expo 2005: Land, Sea, and Air, Reno, NV, June 6–9, 2005, Paper No. GT2005-69269.

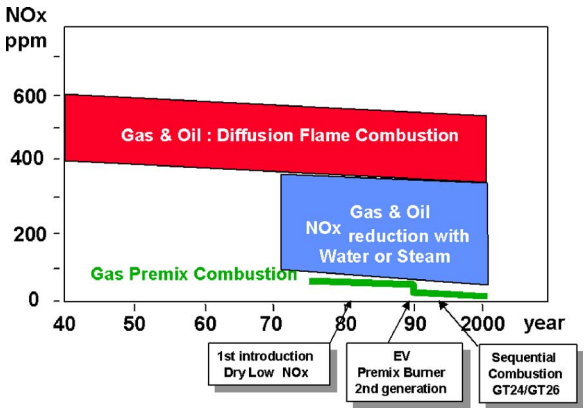

Fig. 1 NO_x reduction history

much as possible to the burner plane, in order to reduce the flame temperatures for a given hot gas temperature. The single combustor plus the hot gas distribution casing to the annulus of the turbine inlet was giving a constraint for the cooling air reduction due to the relative large hot gas surface. The solution to overcome this drawback was the development of the compact annular combustor with low cooling air consumption and a distributed annular multiburner arrangement (Fig. 2).

In retrospect, it must be stated that this two-track strategy decision of the BBC gasturbine development was a very wise anticipation of the future technology standard, which was at that time not at all obvious. Other technologies, which later turned out to be not sustainable, such as, for example, "rich burn quick quench," have also been on the market of dry low-NO_x ideas.

The very early start for a development of the dry low-NO_x technology with lean premix burners and a low-NO_x (annular) combustor led to the fact that the BBC (later ABB) engineers could achieve important technology milestones:

- 1984: the world's first commercial lean premixed combustion in gas turbines with 32 ppm NO_x in the GT13D Lausward
- 1988: the world's first annular multiburner combustor in a heavy duty gas turbine in the GT8 Purmerend
- 1995: the world's first reheat engine with a premixed sequential annular combustor system in the GT24 Gilbert

In the following, it will be shown how this evolutionary, step by step development process led to the actual low-NO_x performance and reliability of today's premixed combustion systems for gas turbines.

2 Lean Dry Low-NO_x Technology in Brown Boveri Gas Turbines: First Generation

Already in the 1970s, environmental aspects began to become a serious concern. In the U.S., the Clean Air Act of 1970, amended in 1977, was the primary federal environmental law applicable to power generation systems. The gas turbine New Source Performance Standards (NSPS) were issued in 1979. The NO_x emissions of gas turbines in utility use with more than 1×10^8 BTU/h were limited at that time to 75 ppm at 15% O_2. In California, more stringent regulations were already effective.

Water or steam injection into the flame was the normal practice to reduce the NO_x emissions. The single-combustion chamber with one burner only, which was a typical design feature of the former BBC gas turbine, was very favorable for this injection technique. The injected mass flow was in the order of the fuel flow—depending on the required NO_x values. As an advantage, the output of the gas turbine increases with increasing water mass flow. However, there were also significant disadvantages for the operator: the use of water affected adversely the cycle efficiency. In addition, water of demineralized quality and steam were in many cases not available. For these reasons, much pressure was put on the gas turbine industry to search for a dry low-NO_x solution.

2.1 Concept (see Fig. 3 and Ref. [1]). In 1978, a lean premix burning concept was developed realizing that because of the strong dependence of the thermal NO formation on the combustion temperature, a long step forwards towards low NO_x was only possible if the mixing process of fuel and air was separated from the combustion process itself, with the latter conducted under very lean conditions. Thus, the procedure was clear: First to create a mixture as lean and homogeneous as possible and then to burn it.

In a first step, the single combustion chamber concept was maintained, but the combustion chamber was equipped with a great number of vertical burner elements, each consisting of a premixing section and at their lower end of a swirler (flame holder), making the separation mentioned above. A common plenum for combustion guaranteed safe ignition and operation of the burners. For obtaining the greatest benefit for low NO_x, the burners were operated in a staged mode allowing a combustion relatively near the lean stability limit.

To meet the demand for the higher air flow of the burners, the

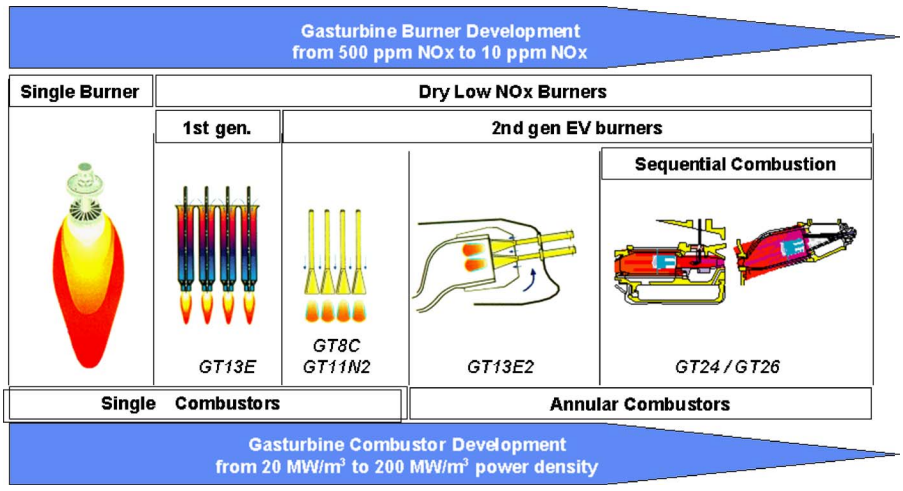

Fig. 2 Burner and combustor development roadmap

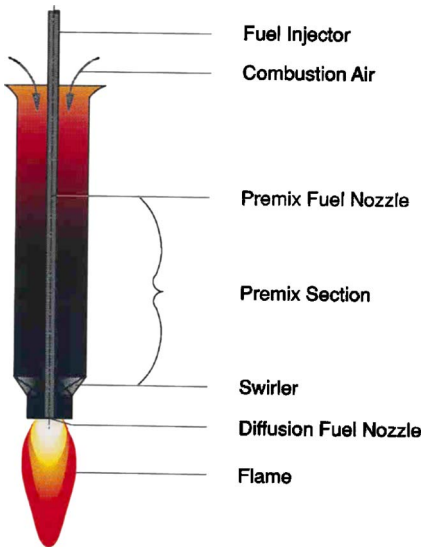

Fig. 3 First generation of dry low-NO_x burners

(a)

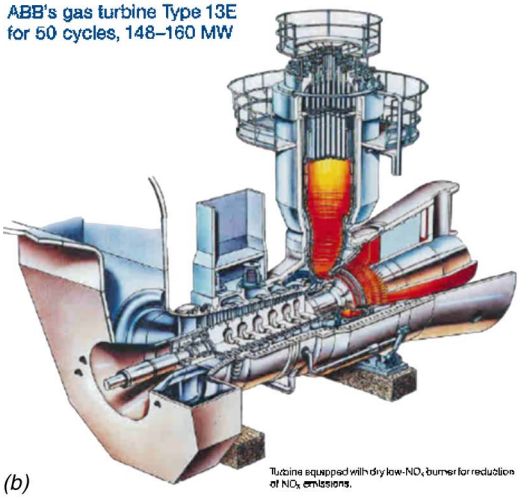

(b)

Fig. 4 (*a*) GT13 burners; (*b*) GT13 gas turbine

design of the cooling elements of the original flame tube was modified for reducing the cooling air adequate to the lower flame temperature. Furthermore, the secondary mixing air flow, which made up a significant portion in the former combustion chamber, was reduced.

Fuel specification and fuel injection: The most ambitious task besides the abatement of NO_x was the requirement to run the combustor not only with natural gas but also with oil no. 2. Therefore, the premixing section was also the vaporizer of the oil and its size was determined primarily by the demand of a high degree of vaporization.

Under load, gas and oil were injected at the entrance of the premixing section, and whenever necessary, a very small amount of fuel was added in the center of the swirler to improve the stability range. At the starting sequence of the engine, oil was injected at the swirler.

2.2 Laboratory Tests. It was clear from the beginning that full sized tests with one burner element were indispensable at engine conditions to obtain all the required information about questions such as:

- lean premix burning in general, stability limits, and ignition behavior
- NO, NO_2, UHC, and CO emissions
- flashback safety for different types of flame holder
- design specification of the best flame holder
- problems with auto-ignition (oil especially)
- degree of oil vaporization with different types of fuel injectors and under various load conditions
- degree of homogeneity that can be achieved in the premixing section with different types of fuel injectors and influence on NO_x
- design specification of the best fuel injectors
- design specification of the premixing/vaporizing element
- operating schedules of the engine combustion chamber as result of all these tests.

A detailed test program was worked out. Additional tests were also planned under atmospheric conditions with a small multielement test combustor for exercising burner staged operation. However, for the majority of tests, a high-pressure test facility was required, which at that time was not available in house. Therefore, all these development tests were performed by GASL in Westbury USA in an excellent cooperation so that in parallel to these tests, the design of the engine combustor could be made in the home office.

A few summarizing results of these laboratory tests are worth mentioning. As already mentioned, there were for oil and gas two injectors each, one in the premix section and one in the center of the swirler. For the oil, both injectors were air assist nozzles, the premix one operated in the reverse direction to the air. At full load condition, 85% of the oil was vaporized in the premix section at an entrance condition of 620 K and 11 bar. With regard to NO_x, approximately 10 ppm (15% O_2) were measured with 100% premix oil, and approximately 60 ppm (15% O_2) with 92% premix oil and 8% diffusion oil, demonstrating clearly the superiority of lean premix burning. For methane gas, results of the same order were obtained. Therefore, the NO_x requirements of that time were more than fulfilled.

The tests regarding auto-ignition and flashback were very difficult and the results often took a long time for correct interpretation. As an example: In the first period of the tests perforated plate flame holders were used. The pressure increase in the combustor at ignition was, in the beginning, sometimes high enough to produce a flow reversal into the premixing section, causing stable combustion at the upstream surface of the flame holder in the small areas between or outside the holes. These "burning nests,"

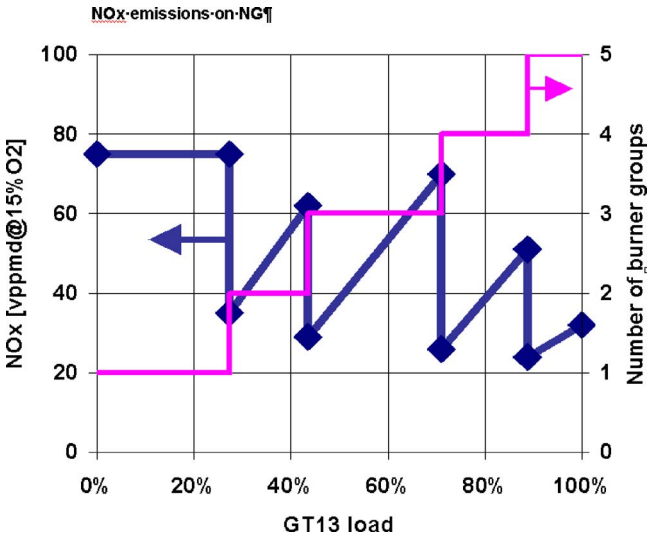

Fig. 5 NO_x data as function of GT13 engine load

which were not observed, could propagate slowly further into the mixer and, therefore, were discovered only after some time during the test by one of the thermocouples, when the whole volume flow became ignited. The phenomenon then appeared to be flashback or autoignition, but in fact neither was the case. The test procedure and installation was of course permanently improved and as a final result a swirl flame holder was evaluated with high resistance to flashback.

2.3 Engine Implementation (see Refs. [2,3]). The first engine combustor was installed in an already existing gas turbine of type 13 in the Stadtwerke Lausward in Düsseldorf, where the customer kindly agreed to perform tests on his engine. The combustor consisted of a package of 36 burners, which can be seen on Fig. 4 with the premixing elements and with the swirlers in their hexagonal configuration. The element in the center was the igniter. The injectors could be removed individually from outside. The fuel system, the control system, and the air assist compressor were also new. The burners were arranged normally in five groups for the staging schedule. Group 1, with the greatest number of burners, was more in the center and was always burning just from the starting. The remaining groups were added stepwise at higher load.

The commissioning of the new combustor went well; the flame was stable and ignited easily at the staging process, and there were no problems with auto-ignition or flashback.

2.4 Results: NO_x, Unburnt Hydrocarbons, and CO. For simplifying the operation, a small portion of "diffusion gas" respectively "diffusion oil" was normally added over the whole operation range. The full load data were the following with NO_x at 15% O_2:

Natural Gas.

- with some "diffusion gas" only on group 1: 32 ppm NO_x, 0 ppm UHC, 4 ppm CO
- with some "diffusion gas" on all burners: 53 ppm NO_x, 0 ppm UHC, 1 ppm CO

Oil No. 2.

- with some "diffusion oil" on all burners: 73 ppm NO_x, 1 ppm UHC, 1 ppm CO

In Fig. 5, NO_x data are given as an example for gas over the whole staging process.

Operation with fuel oil caused unexpected problems. After some time, the swirlers stained with oil deposits from the not-vaporized oil portion of the premixing elements, leading to damage of some swirlers during the following gas operation. This problem could not be solved, and therefore the operation with oil no. 2 was stopped.

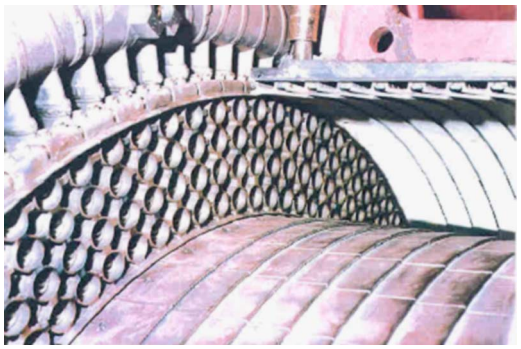

Fig. 6 Multi Injection Burner in the GT8 annular combustor

The first generation of the dry low-NO_x combustor was applied in six gas turbine units, of which two are still in operation. The lean premix combustion had proved to reduce the NO_x emissions significantly and to have the potential for further improvements. The whole system so far used, however, was too complex and was also susceptible to deterioration. For instance, it is interesting to note that after some time of operation, unclear problems appeared even with auto-ignition. The development of the second generation of lean premix burners had the target of overcoming these disadvantages.

3 Multi Injection Burner and Annular Combustor for GT8

Before continuing this report on the lean premixing line, another technical approach for a low-NO_x burner will briefly be discussed, which was developed at the same time to evaluate the best technical solution for low combustion pollutants and as a second target to combine this burner with a compact annular combustor. This was the first time that an annular combustor was used in a BBC gas turbine.

The burner was called "Multi Injection Burner." The idea was to use the complete cross section area of the annular combustor for a large number of small burners, minimizing thereby the flame length, the residence time, and thus the NO_x formation. The short flames as well as the regular flow pattern over the cross area—due to the many small burners—allowed the design of a relatively short combustor with reduced cooling air consumption, which again resulted in a higher air flow to the burners. The burners were designed for normal diffusion flames.

There were eight casted burner segments in the combustor annulus with a total number of 384 swirlers, each with a gas injector in the center (see Fig. 6). Ports for quenching air were arranged near the swirlers to reduce the high gas temperature immediately after burning. All burners were in operation over the whole load range of the gas turbine. The annular combustor was placed in straight line between the compressor and the turbine. The inner and outer walls consisted of cooling elements like tiles on a support carrier arranged in nine circumferential rows. In between, the cooling film was generated. The amount of cooling air was small.

Several gas turbines of type GT 8 with an output of 45 MW were equipped with this type of combustor, the first one in Purmerend (Holland) in 1988. The NO_x emission level at full load was approximately 70 ppm (15% O_2). This result showed that even with the high air flow in the burner the combustion took place at near stoichiometric conditions and furthermore that the short residence time did not compensate sufficiently the influence of the high temperature on the formation of NO_x.

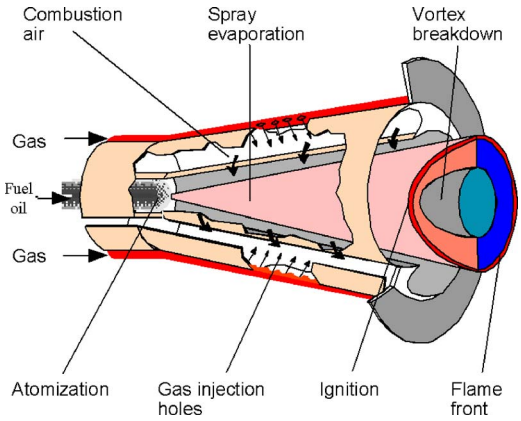

Fig. 7 EV burner principle

The result was clear: there was no way to get around the lean premix combustion for very low NO_x emissions. With the introduction of this combustion technology and with the realization of a compact annular combustor, an important development step had been achieved in the design of high-temperature gas turbines with low combustion pollutants.

The next paragraph will show the continuation of the development of the lean premix combustion technology at ABB.

4 The Second Generation: EV Premix Burner Technology (see Refs. [4–7])

The experience gained with the first generation dry low-NO_x technology led to an evolutionary further development of a new burner technology. The first generation premix burner had two main conceptional drawbacks. The length of the premix tube, providing an air settlement section and a premixing zone, which is needed to generate a homgeneous mixture, was much longer as compared to conventional diffusion burners. The other drawback was not to have an inherent protection against auto-ignition events. The flame stabilizer hardware was exposed to an ignitable mixture where rare events of auto-ignition or flame flashback from the reaction zone could occur under unusual conditions. Therefore, the first generation concept has been judged as being not suited for future more efficient gas turbines, since the higher air inlet pressure and temperature, and the higher flame temperature would increase the auto-ignition and the flashback sensitivity.

Fig. 9 EV burner cast body

The chosen approach of the second generation EV premix burner left the paradigm of existing design concepts for diffusional and premix burners. The main idea of the EV burner concept is derived from fundamental principles of vortical flows. It uses the vortex breakdown of a strongly swirling core flow as an aerodynamic control for the inner recirculation zone, which is needed to stabilize a premix flame, without the help of a swirler body or a center body, located in regions with ignitable mixture (Fig. 7).

The EV burner consists of two half-cone shells, which are displaced parallel to the axis, generating two tangential slots (see Figs. 7 and 8). The swirl strength of the flow entering through the tangential slots is increasing in axial direction and is adjusted such, that a vortex breakdown of the core flow occurs close to the burner exit. In the EV premix burner, no specific flame stabilizer hardware exists that is exposed—as in conventional premix burners—upstream to the ignitable mixture and downstream to the flame stabilization zone. As a result, the EV burner has an inherent safety against auto-ignition or flame flashback events.

Three aerodynamic features of the EV burner are important for the premix flame stabilization and generate the inherent flashback safety of this design (Fig. 9).

The aerodynamic features are:

- upstream of the vortex breakdown, the core flow is strongly accelerated, forming a natural flashback barrier
- downstream of the vortex breakdown, an inner recirculation is formed, ensuring the premix flame stabilization
- the aerodynamic fixation of the vortex breakdown in the free flow ensures a stable position of the flame root.

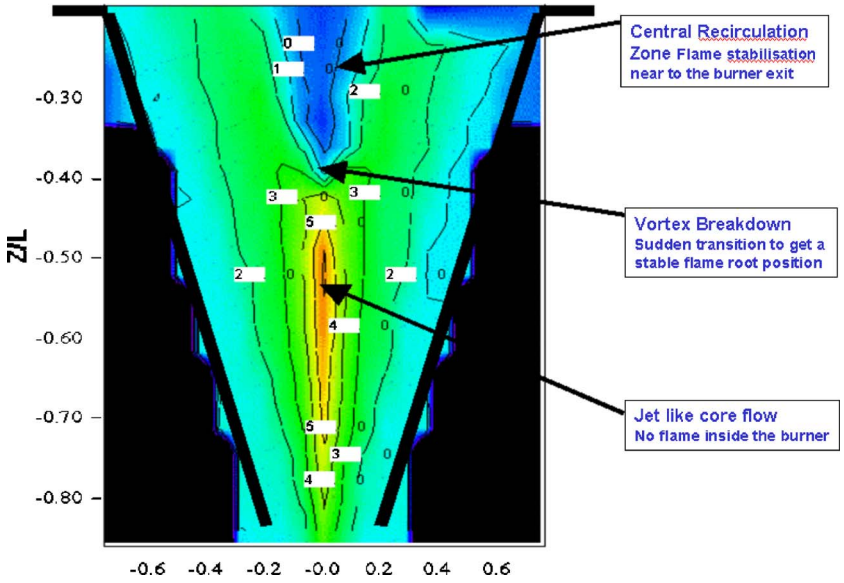

Fig. 8 EV burner axial flow field

The second important feature of the EV burner concerns the compact and effective generation of the fuel-air mixture. As shown in Fig. 7, the gaseous fuel is injected through a row of holes in a cross-flow direction into the air entering the tangential burner slots. Each gas injection jet has to penetrate only a small portion of the air and has to be mixed only with "its own" small portion of the incoming air. Since the air that enters the burner slots is equally distributed along the length of the slot, all little gas jets have to mix with the same portion of the air, which means that the mixing boundary conditions are equal and therefore the gas to air mixing performance is equally distributed in the whole flow field of the burner. The gas injection concept in the air slot stands for an inherent, equal predistribution of the fuel into the incoming air, and is therefore the precondition for the high mixing effectiveness, which leads to a homogeneous air to fuel mixture in spite of the extremely compact mixing section volume of the EV burner.

The relatively small volume in the cone is sufficient to generate a very homogeneous air-fuel mixture, which is a precondition for ultralow NO_x.

The liquid fuel is injected with a central plain jet nozzle in the cone head. The liquid plain jet disintegrates into small droplets within the burner leading cone. The swirling air flow distributes the droplets in the whole flow field, the flame stabilization occurs near to the burner outlet with the help of the inner recirculation zone.

For the annular combustor applications an additional pilot gas injection has been developed, in order to ensure the flame stabilization well below the premix extinction limits. The pilot lance is in the center of the burner cone and enriches the mixture of the core flow. Also in the pilot mode, the flame is stabilized with the inner recirculation zone.

4.1 Engine Implementation of the Second Generation EV Premix Burner. The first implementation of the EV burner was in the single combustor of a GT11 (Midland USA, 1993), where 36 burners plus a central ignition burner were arranged in a hexagonal three ring arrangement. The combustor was loaded by switching on and off single burners. The same principle of a hexagonal arrangement was later introduced into the single combustors of the GT13, GT9, GT8, and GT11N2. The first introduction of the EV burner with the described inner central pilot gas injection was in the annular combustor of the GT13E2 and GT10, and later into the GT8C2, GT24, and GT26. Today, the whole Alstom gas turbine fleet is available with a low-NO_x combustion system based on EV burners. During this comprehensive fleet implementation, the burner design has been continuously improved to reliability and long lifetime, and the manufacturing has been simplified from welded to casted design (Fig. 8). In the beginning, the EV burner was developed in different sizes. In the meantime the actual burner is a modular standard cast body design, which is introduced into the annular and single EV combustors of the different engines.

The adaption to the engine power is done with the number of burners. This standardization has the advantage that the burner development cycle could be simplified, since burner improvements with regard to design, reliability, stability, and combustion performance, have been realized and introduced uniformly into different engine and combustor types.

5 EV Premix Burner Technology for Syngas Combustion in the GT13E2MBTU (see Refs. [8–11])

An appropriate injection method for MBtu gases has to take the critical properties of these fuels into account. Injection of these MBtu fuels along the air inlet slots is no longer appropriate due to the high flame velocities of hydrogen containing fuels and the higher volume flux, which would distort the incoming air profile. A simple and effective injection design for the MBtu fuel has been developed. Instead of fuel injection along the slots, a number of circular holes close to the burner end inject fuel radially inward

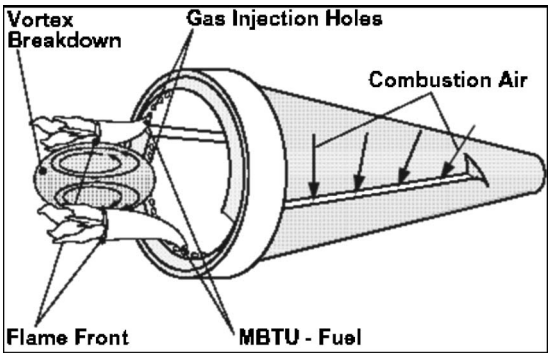

Fig. 10 EV burner adapted to syngas application

enabling inherently safe operation of the burner, even with high hydrogen content fuels (Fig. 10). No fuel is found inside the burner and care has been taken to keep the outer recirculation zone free from unmixed fuel. Due to the high velocity of the fuel injection, the flame stabilizes downstream of the burner. Here the fuel jets reach the hot recirculation zone. The air leaving the burner is entrained into the fuel jets, thus premixing the fuel and air. The standard EV burner has been shortened to increase the air velocity at the burner exit where the syngas injector holes are located. This acts to enhance mixing, thereby lowering NO_x emissions, and is an additional step to prevent flashback into the burner.

Due to these modifications, the combustion system is capable of burning undiluted syngas safely and fulfilling NO_x requirements with relatively small N_2 dilution to 7 MJ/kg heating value. This system is based on the proven EV burner and is also operable with oil no. 2.

The first ALSTOM application of a GT13E2 to hydrogen-based syngas fuel (API Energia, Falconara, Italy) was for residual oil gasification syngas. The NO_x performance of the GT13E2-MBtu is excellent and meets all guaranteed values. In the required syngas operation range between 50% and 100% load, measured NO_x values were below 25 vppmd @ 15% O_2 (Fig. 11). The measured CO values are also very low and stay below 3 vppmd @15% O_2.

6 ABB's SEV Burner Development and Application in the GT24/26 Engines (see Refs. [12,13])

Development of sequential combustion technology needed for reheat engines started in 1990 and was confirmed in engine tests with a GT24 at Gilbert (USA) power station in 1995. The advanced technology behind the GT24/GT26 is the sequential combustion system. With a pressure ratio of 30:1, the compressor delivers nearly double the pressure ratio of a conventional compressor. The compressed air is heated in a first combustion cham-

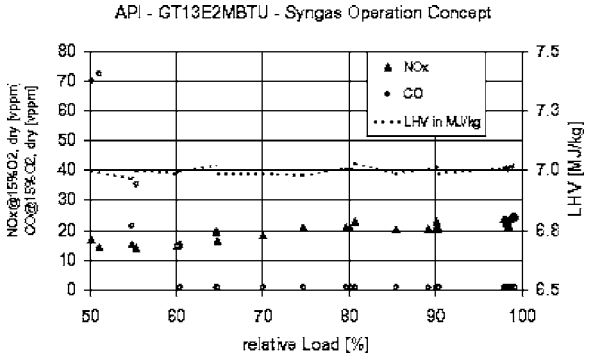

Fig. 11 GT13E2-MBtu syngas operation, NO_x emission as a function of GT load

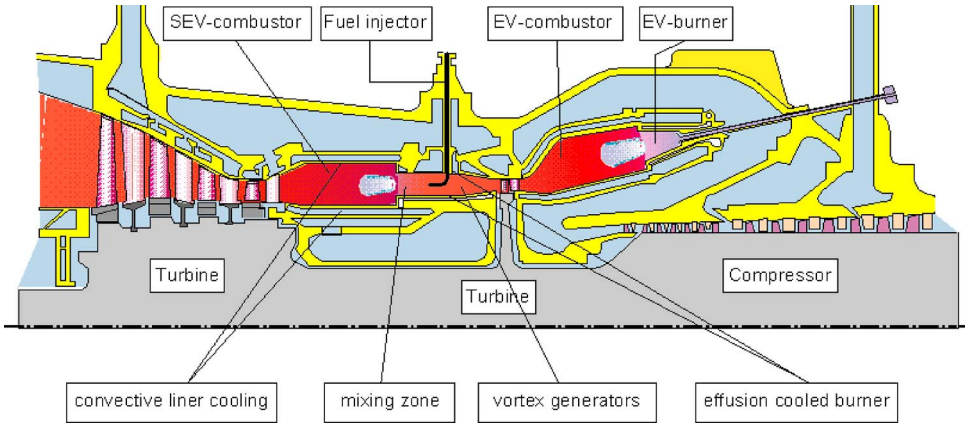

Fig. 12 GT24/26 sequential combustion gas turbine

ber (EV combustor). After the addition of about 60% of the fuel (at full load), the combustion gas expands through the first turbine stage. This one stage, high-pressure (HP) turbine lowers the pressure from 30 to approximately 15 bar. The remaining fuel is added in a second combustion chamber (SEV combustor), where the gas is again heated to the maximum turbine inlet temperature (Fig. 12). Final expansion in the four-stage, low-pressure turbine follows. Figure 13 shows the thermodynamic cycle of the sequential combustion process, while compares the cycle of the sequential combustion process with a conventional cycle. It is seen that for the same power output, a lower turbine inlet temperature is needed with the sequential combustion cycle.

Sequential combustion is not new in the history of power generation. During the 1950s and 1960s BBC delivered 24 plants with various combinations of intercooling in the compressor and two-stage combustion in the turbine. Nine of these plants are still in operation today.

In a conventional lean premix combustor (e.g., the EV combustion chamber) spontaneous ignition must be avoided, since it could lead to overheating of combustor components and to unacceptably high pollutant emissions. A reheat combustion system, such as the SEV (sequential EV) combustion chamber, can be designed to use the self-ignition effect for a simple and rugged construction. In order to achieve reliable spontaneous ignition with natural gas and to widen the stability range, combustor inlet temperatures higher than 1000°C over the whole operating range were selected for the GT24/GT26 SEV combustor. Successful operation of the SEV combustor requires that, in addition to ensuring self-ignition, emissions are kept low. For low NO_x emissions, the fuel and the hot HP turbine exit gas must be mixed well prior to ignition. If this is not the case burning will occur in fuel-enriched regions, where high flame temperatures result in high NO_x generation rates. An optimum relationship between the ignition delay and degree of premixing is therefore desirable, the former having to be kept short in order to ensure self-ignition and limit the size of the combustor. Furthermore, this optimum should be maintained over a wide range of fuel flow rates, which change with the combustor load and fuel compositions; e.g., as a result of different blends of natural gas.

6.1 Fuel Injection. In the SEV combustor of the GT24/GT26, the above optimum is reached through the use of carrier air, i.e., air that is bled from the compressor and injected into the SEV burner together with the fuel. The carrier air works both as a premixing enhancer, in that it maintains the momentum of the fuel jet (a factor critical to achieving high premixing quality), and as an ignition controller.

6.2 Aerodynamic and Fuel/Oxidant Mixing Within the Burner. As in the EV burner, fuel distribution and mixing within the SEV burner is achieved with the aid of vortical flow. The flame is anchored at the vortex breakdown position. The vortices are generated by delta wings, formed like ramps and located on the walls of the SEV burner (Fig. 14).

The requirements of low pressure drop and high safety against flame in the mixing zone led to delta-wing type vortex generators,

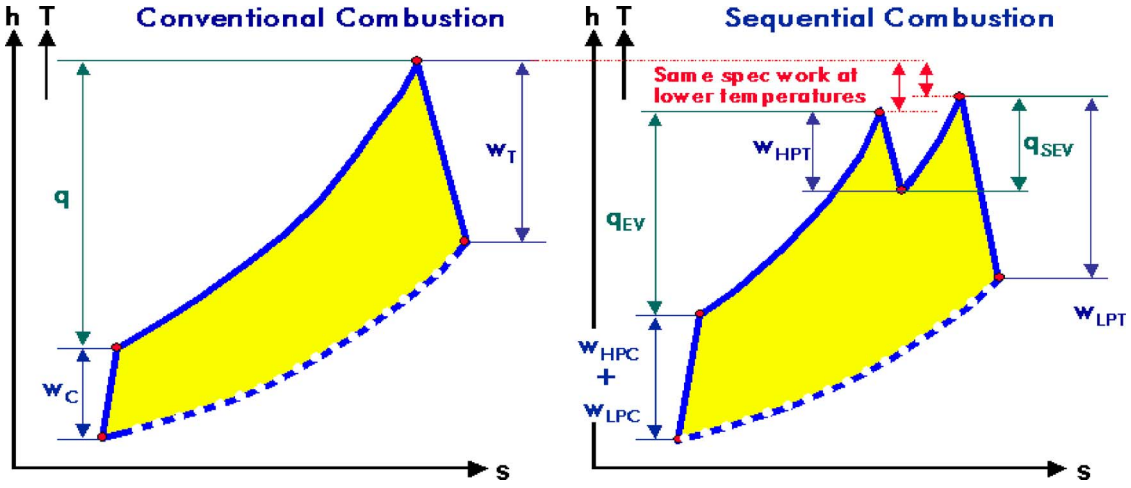

Fig. 13 GT24/26 reheat cycle

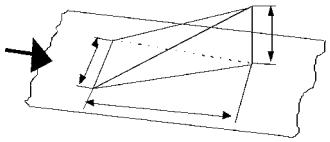

Fig. 14 Delta-wing vortex generators

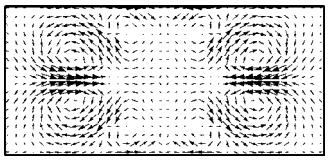

Fig. 16 Vortical flow pattern in the SEV burner

which can generate streamwise vortices without any recirculation zones. In order to satisfy other practical considerations such as mechanical integrity and cooling, a tetrahedral geometry, which consists of two half-delta-wing side surfaces and a full-delta-wing upper surface, has been chosen.

In Fig. 15 the arrangement of the vortex generators in the SEV burner together with the fuel lance is shown. The fuel is injected through four holes together with the carrier air from a fuel lance downstream of the vortex generators.

Figure 16 shows the vortical flow pattern downstream of the vortex generators. Four pairs of vortices are generated such that each fuel jet is injected in one of the vortices (see Figs. 15 and 17).

6.3 Engine Implementation and Results. After first implementation of the reheat combustion technology in the GT24 in Gilbert (USA, 1995), the 50 Hz version was launched in 1997 with a GT26 at ENBW Karlsruhe, Germany (see Fig. 18). Today, 75 GT24/26 engines are in commercial operation and have achieved more than 1.2×10^6 operating hours. The GT24/26 gas turbines are capable to run on NG and on oil with very low emissions, high availability, high part load efficiency, and low part load emissions. Figure 19 shows the NO_x emissions measured as a function of engine load.

7 ABB's AEV Burner Development and Application (see Ref. [14])

The AEV burner (advanced EV burner) was optimized with special emphasis on liquid fuel application. By using four instead of two inlet slots, the distribution of the radial inlet flow is more even, which makes the swirler completely safe against wall impingement of fuel droplets. The addition of a mixing tube allows for a longer evaporation time and for additional mixing in the gas phase (Fig. 20).

From the axial and tangential velocity profiles shown in Fig. 21 one can tell that a jetlike flow field with a distinct small body vortex core is rapidly formed within the conical swirl generator. At the exit of the swirler the maximum axial flow velocities on the centerline are in excess of two times the bulk velocity. This high velocity jet flow is maintained throughout the mixing tube, thus providing high flashback safety. Even close to the mixing tube

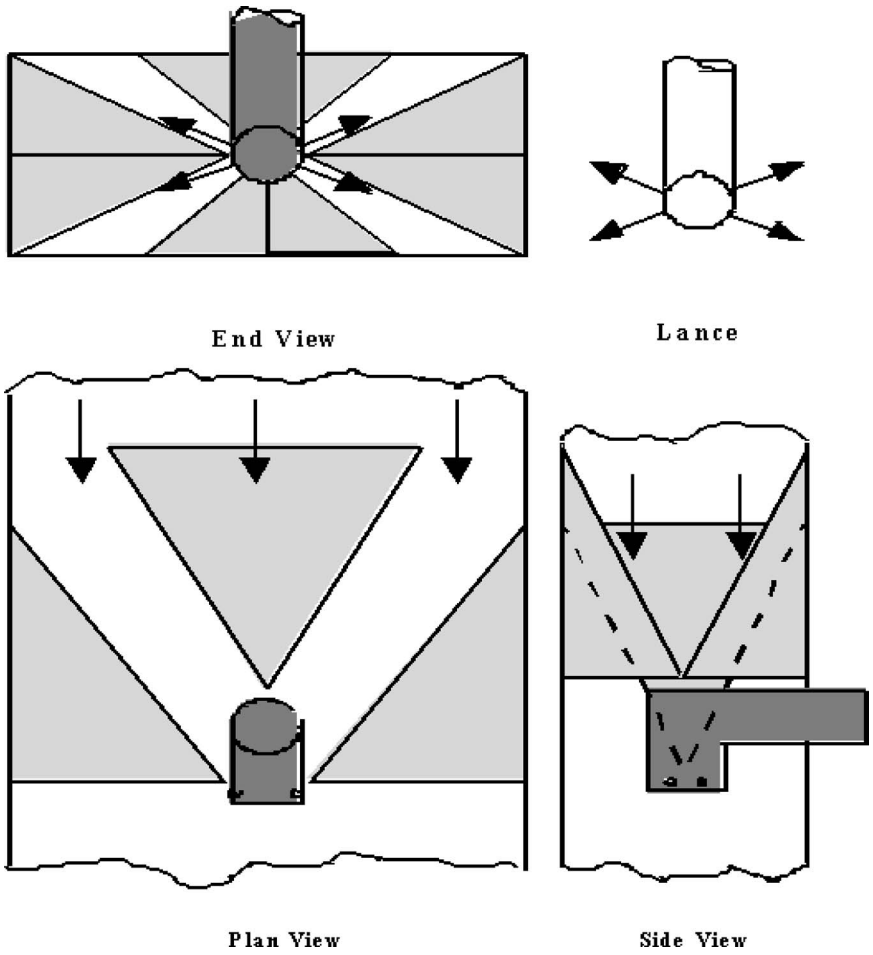

Fig. 15 Vortex generation and fuel injection in the SEV burner

Fig. 17 View from downstream into the SEV burner (fuel lance removed)

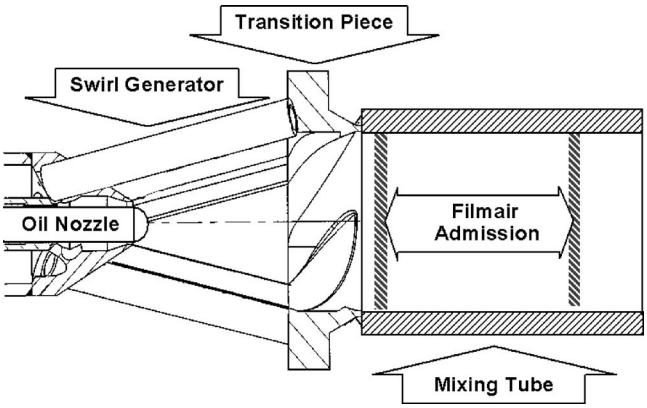

Fig. 20 Design features of the AEV burner

walls, high axial velocities can be achieved by proper admission of small amounts (<10% of total air flow) of additional air (Fig. 20). In combination with the dilution effect of this air addition flashback along the mixing tube walls can be suppressed very effectively.

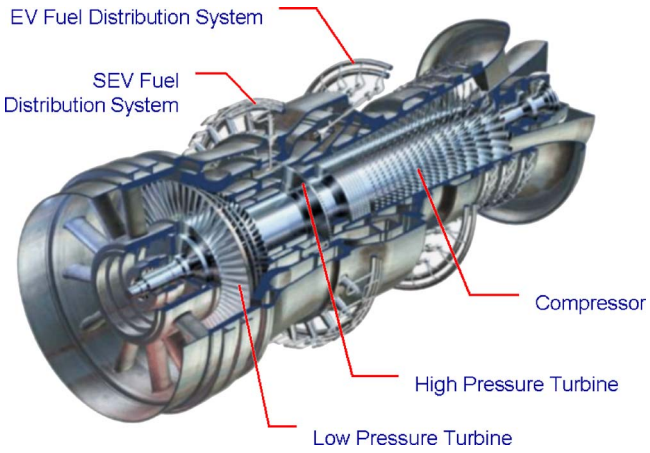

Fig. 18 GT24/26 main components

Since liquid fuel atomization, penetration, and evaporation are all heavily dependent on the surrounding atmosphere, it is difficult to find experimental techniques for investigations at real engine conditions. Numerical simulations are very helpful in this case, but due to the present state of models for two-phase flow (especially concerning droplet disintegration and the evaporation of multicomponent fuels), they cannot be used without experimental validation. For the AEV burner development, both numerical and experimental tools have been applied to study fuel/air mixture preparation.

The AEV burner was developed at the ABB research center in Dättwil, Switzerland and was extensively tested in atmospheric and full-pressure test rigs. The burner is integrated in the GTX100 and meets the emission targets on both oil (35 ppmv) and natural gas (15 ppmv) without water injection.

8 Annular Premix Combustor Development (see Ref. [8])

As a complement to the premix burner development the annular combustor development has been started at ALSTOM in an early phase. The low-NO_x performance of premix systems can be fully exploited when it is possible to redirect the combustor cooling air as much as possible to the premix burner inflow. This requirement gained increasing importance, due to the fact that the turbine entry temperatures have been raised in modern high efficiency gas turbines well above the extinction temperatures of premix flames.

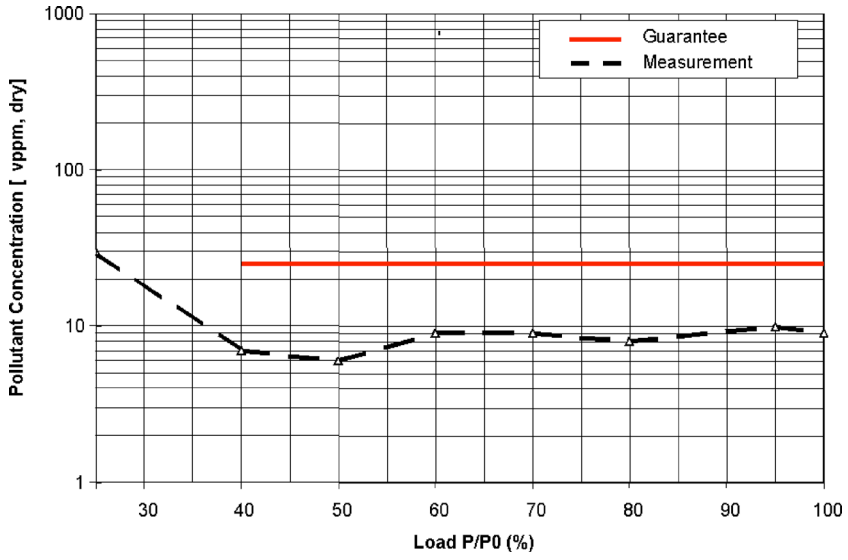

Fig. 19 GT24/26 NO_x [vppmd@15% O_2] emissions on natural gas

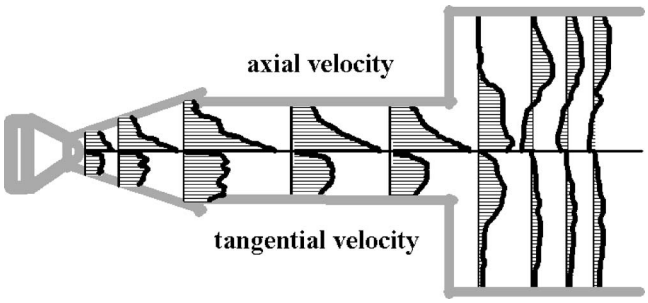

Fig. 21 Axial (top) and tangential (bottom) velocity profiles in the AEV burner

For these conditions air, which is entering the combustor downstream of the premix flame zone, contributes to an increase of the primary flame zone temperature and therefore causes excessive NO_x formation. The annular combustor principle has been chosen, in order to minimize the combustor surface, which is exposed to the hot gas, and by that to minimize the cooling air consumption. Furthermore, the annular design offers a compact and cost-effective design as compared to single combustors or can combustors.

The annular combustor design implies the distribution of a multitude of singular burners along the circumference. This requirement is completely inline with the generic premix combustor operation concept, which is based on a multiburner arrangement. The annular multiburner arrangement has several advantages, which all are based on the fact, that the individual burners are communicating with their neighbours in circumferential direction:

- cross-ignition from burner to burner is ensured without any cross-firing tubes;
- operation at part and full load with burner groups running at different flame temperatures or even with some burners switched off is possible. Those burners that are running below extinction are stabilized by their neighbors running above extinction, which leads to complete burnout at the combustor end and low NO_x emissions.
- the annular combustor generates a uniform hot gas temperature distribution at the turbine inlet, which is a precondition for long turbine lifetime in modern, highly efficient gas turbines.

The arrangement of the EV burners and of their swirl direction in the combustor has to take into account the induced tangential flows in the combustor annulus. With a smart arrangement of the burners and their swirl direction it is possible to substantially improve the crossignition, the part load stability, the mixing, and the turbine inlet temperature profile. This has been the main consideration for the arrangement of the 72 EV burners in the first annular premix combustor of the GT13E2 (see Fig. 22). The EV burners are equally distributed over the circumference in a staggered two- row arrangement.

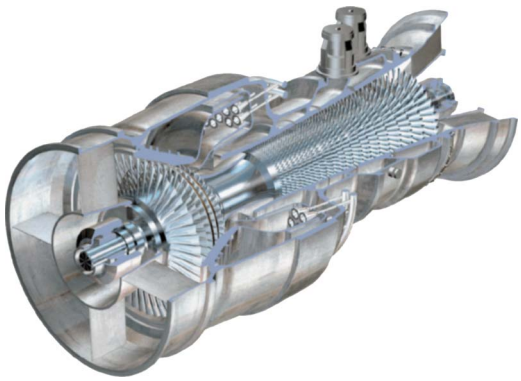

Fig. 22 GT13E2 with annular premix combustor

Fig. 23 View into the annular premix combustor of the GT26 (burners and igniter removed)

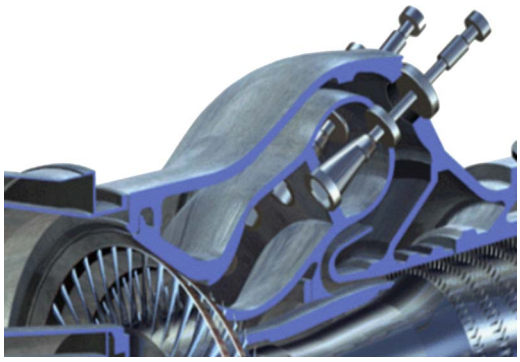

Fig. 24 Engine integration of the annular single row combustor in the GT8C2

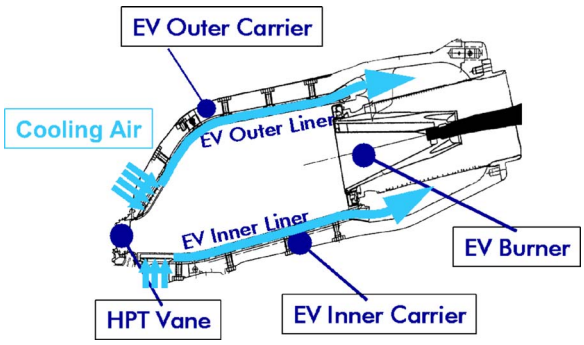

Fig. 25 Closed loop liner cooling system for annular premix combustors

In the following development steps the annular premix combustors of the GT24, GT26, and the GT8C2 have been realized with a simple, single-row burner arrangement (see Figs. 23 and 24).

The compactness of the annular combustor also enables the realization of a closed loop liner cooling system, where all liner cooling air is fed back to the air coming from the compressor. In order to achieve this closed loop liner cooling concept, the EV burners are separated from the combustor casing with an additional hood. (see Figs. 24 and 25). The closed loop cooling design requires a low burner pressure drop, as is the case with the EV burner, since the sum of the cooling pressure loss and the burner pressure loss contributes to the total combustor pressure loss.

9 Conclusions

The long development experience and a systematic step-by-step development strategy for premixed combustion systems is a prerequisite for the today's performance and achievements of low NO_x combustion. This development has been a key success factor for achieving very low emissions together with a high operational reliability and flexibility. The modular design of the annular premix combustor with EV and SEV burners has led to cost-efficient and reliable combustor systems for highly efficient gas turbines with a maximum benefit for the customer.

References

[1] Koch, H., Brühwiler, E., Strittmatter, W., and Sponholz, H. J., 1985, "The Development of a Dry Low NO_x Combustion Chamber and the Results Achieved," CIMAC, International Congress on Combustion Engines, Oslo, June.

[2] Marnet, Chr., Kassebohm, B., Koch, H., and Sponholz, H. J., 1984, "NO_x-Reduction in the Lausward Combined Cycle Gas Turbine Unit," VGB Conference "Power Plants 84" at the Hague, Oct.

[3] Koch, H., and Kassebohm, B., 1985, "Weitere Ergebnisse zur Stickoxidminderung am Kombiblock Lausward," VGB-Fachtagung "Gasturbinen und Gasturbinenbetrieb 1985," Essen, Novembere.

[4] Sattelmayer, T., Polifke, W., Winkler, D., and Döbbeling, K., 1996, "NO_x-Abatement Potential of Lean-Premixed GT-Combustors," ASME J. Eng. Gas Turbines Power, **120**, pp. 48–59.

[5] Sattelmayer, T., Felchlin, M. P., Haumann, J., Hellat, J., and Styner, D., 1992, "Second Generation Low-Emission Combustors for ABB Gas Turbines: Burner Development and Tests at Atmospheric Pressure," ASME J. Eng. Gas Turbines Power, **114**, pp. 118–125.

[6] Aigner, M., Mayer, A., Schiessel, P., and Strittmatter, W., 1990, "Second Generation Low-Emission Combustors for ABB Gas Turbines: Tests Under Full Engine Conditions," ASME Paper No. 90-GT-308.

[7] Aigner, M., and Müller, G., 1992, "Second Generation Low-Emission Combustors for ABB Gas Turbines: Field Measurements With GT11N-EV," ASME Paper No. 92-GT-322.

[8] Döbbeling, K., Knöpfel, H. P., Sattelmayer, Th., Müller, P., and Reyser, K., 1993, "ABB's Medium Btu EV Burner for Syngas Applications—Test Results and GCC Integration Concept," 12th EPRI Conference on Coal Gasification Power Plants, San Francisco, October 27–29.

[9] Scherer, V., Döbbeling, K., Reyser, K., and Viereck, D., 1994, "The ABB Type GT13E2 Gas Turbine and its Conversion to MBtu Syngas Firing Gasification Projects," 1st International Conference on Combined Cycle Power Generation, Calcutta, India, January 6–8.

[10] Döbbeling, K., Knöpfel, H. P., Polifke, W., Winkler, D., Steinbach, C. and Sattelmayer, T., 1996, "Low NO_x Premixed Combustion of MBtu Fuels Using the ABB Double Cone Burner (EV Burner)," J. Eng. Gas Turbines Power, **118**(4), pp. 765–772.

[11] Reiss, F., Griffin, T., and Reyser, K., 2002, "The ALSTOM GT13E2 Medium BTU Gas Turbine," ASME Paper No. GT-2002–30108.

[12] Döbbeling, K., Eroglu, A., Joos, F., and Hellat, J., 1999, "Novel Technologies for Natural Gas Combustion in Turbine Systems," Presented at Eurogas 99, Ruhr-Universität Bochum May 25-27.

[13] Ladwig, M., Philipson, St., Raza, M., and Suedland, M., 2004, "ALSTOM's GT24/GT26 Gas Turbine: Experience, Projects and Development," VDI Energietechnik Fachtagung: Gasturbines, Leverkusen, November.

[14] Jansohn, P., Ruck, T., Steinbach, C., Knöpfel, H.-P., Sattelmayer, T., and Troger, C., 1997, "Development of the Advanced EV (AEV) Burner for the ABB GTX 100 Gas Turbine," ASME Turbo Asia 97, Singapore.

[15] Senior, P., Lutum, E., Polifke, W., and Sattelmayer, T., 1993, "Combustion Technology of the ABB GT13E2 Annular Combustor," 20th International Congress on Combustion Engines (CIMAC), London, Paper No. G22.

Advancements in Gas Turbine Fuels From 1943 to 2005

Tim Edwards
AFRL/PRTG Building 490,
1790 Loop Road, North,
Wright-Patterson AFB, OH 45433-7103

The first provisional jet fuel specifications were published in 1943 in England (RDE/F/KER/210) and 1944 in the U.S. (AN-F-32a). Jet fuel has undergone many changes in subsequent years, with current specifications for JP-5 and JP-8 for the military in the U.S. and Jet A/Jet A-1 for commercial use worldwide. Jet fuel specifications are subject to constant tension between performance requirements and availability/cost considerations. In this paper we will discuss how jet fuels have evolved over the years from the first engines to current gas turbine engines. Jet fuels derived from nonpetroleum sources will also be discussed. [DOI: 10.1115/1.2364007]

Introduction

When the Wright Brothers needed fuel for their 1903 flight, they used "several cans of Standard Oil motor gasoline from a nearby boatyard" [1]. This casual fuel acquisition is in dramatic contrast to the industry needed to produce the 177 million gallons per day of jet fuel that are consumed worldwide [2]. In this paper the history of jet fuel development is traced from its origins with Whittle and Von Ohain in the late 1930s and early 1940s through the present day. This paper deliberately neglects the fascinating history of aviation gasoline, with its dramatic dependence of performance (octane number) on composition [3,4]. Gas turbines were expected to be much more fuel independent, with the continuous combustion process resembling that of boilers much more that of gasoline-powered engines. The dominance of gas turbine engines for aviation can be inferred from the trends in aviation gasoline and jet fuel production shown in Fig. 1 [2,5]. Once the commercial airline industry generally adopted the gas turbine engine in the late 1950s [6], the use of aviation gasoline was confined to the relatively small general aviation market. About 40% of world jet fuel consumption occurs in the U.S., with roughly 90% of U.S. consumption by commercial carriers. This paper is a distillation of more extensive reviews [3,7–10], and focuses on more recent developments.

A Brief Note on Terminology. Fuels based on petroleum distillates have incorporated a host of somewhat nebulous terms based on the terminology of the early refining industry. Early petroleum refineries were primarily distilleries, with products (fractions) differentiated by boiling point. Thus, a reader may come across unfamiliar terms such as kerosene, naphtha, gas oil, heavy or light fraction, sweet or sour crude, straight-run, hydrotreated, etc. Table 1 is an attempt to list the common terms for petroleum fractions [2,11–14]. There is considerable overlap between categories, as well as considerable disagreement about the definition of a particular generic category. For example, one reference gives a definition of kerosene as "a refined petroleum distillate that has a flash point of 25°C (77°F)" [12], in contrast to the boiling range definitions in Table 1. In general, as the boiling temperature increases, the molecular weight and density increase and the vapor pressure decreases. Thus, one might describe the upper boiling range of a fraction as the heavy or residual end of the fraction. Typical molecular weight distributions are shown in Fig. 2 for avgas and Jet A (equivalent to JP-8). Other specialty kerosene fuels with narrower boiling ranges also exist, such as JP-7 and RP-1 (Rocket Propellant-1), as shown in Fig. 2.

Aviation Gas Turbine Engine Fuels

The early pioneers in gas turbine development, Whittle in England, and Von Ohain in Germany, faced a wide variety of options in choosing a fuel for gas turbines. Whittle had considered diesel fuel, but ended up choosing illuminating kerosene because of an expected requirement for a lower freeze point than that available with diesel [9]. In contrast, Von Ohain originally demonstrated his turbine engine with hydrogen, but vehicle considerations led to a switch to liquid fuel [8,6,15]. The world's first turbojet-powered flight was made on 27 August 1939 in a Heinkel 178 aircraft burning avgas. The first flight of the Whittle engine occurred on 15 May 1941 in a Gloster Meteor aircraft using kerosene as the fuel. Despite their headstart in turbojet engine development, Germany did not decide until 1943 to produce jet-powered aircraft. One of the arguments for development at that time was Germany's shortage of high octane fuel and that the jet engine could run on diesel fuel [8]. Most of the jet engines developed before the end of World War II utilized conventional kerosene as a fuel. The first jet fuel specification was the Directorate of Engine Research and Development 2482 (DERD 2482), published in England in 1947.

As engines and specifications developed, it became apparent that several fuel properties were key to bounding the envelope of jet fuel characteristics. High-altitude operation meant fuel freeze point required attention. However, the lower the freeze point, the lower the fraction of crude oil that was suitable, so that the freeze point had to be balanced against availability. Higher fuel volatility/vapor pressure aided vaporization-controlled engine performance requirements such as altitude relight, which had to be traded against boil-off and entrainment losses from fuel tanks at altitude (as well as safety concerns from explosive mixtures in tank vapor spaces [16]). In the United States, JP-1 (see Fig. 3), JP-2, and JP-3 were ultimately unsuccessful attempts to balance the conflicting requirements of volatility, freeze point, and availability/cost [9]. Two fuels emerged in the late 1940s and early 1950s from this chaotic situation: a wide-cut naphtha/ kerosene mixture called JP-4 in the United States (MIL-F-5624 in 1950) and a kerosene fuel with a −50°C (−58°F) freeze point (DERD-2494 in England and Jet A-1 in ASTM D-1655 in the United States). This freeze point was arrived at through a significant research effort. ASTM D-1655 also specified Jet A with a −40°C (−40°F) freeze point. The Jet A-1 freeze point was changed from −50°C to −47°C in the late 1970s to increase the number of petroleum feedstocks that could be used to manufacture the fuel and thus increase availability and reduce the cost. The differences between the major aviation gas turbine fuels are summarized in Table 2. Civil aviation currently uses Jet A-1 (or its equivalent) throughout the world, except for domestic carriers in

Contributed by the International Gas Turbine Institute (IGTI) of ASME for publication in the JOURNAL OF ENGINEERING FOR GAS TURBINES AND POWER. Manuscript received October 1, 2005; final manuscript received February 1, 2006. Paper presented at the ASME Turbo Expo 2005: Land, Sea, and Air, Reno, NV, Paper No. GT2005-68171. IGTI Review Chair: K. C. Hall.

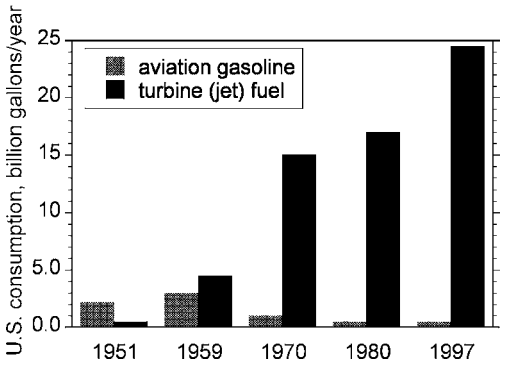

Fig. 1 Trends in U. S. aviation fuel consumption

the United States, who use Jet A to reduce the cost. The freeze point value in the specification is often the most difficult (and costly) for the refiner to meet. Military aircraft used JP-4 until converting to JP-8 in the 1980s (see Fig. 4). JP-8 (MIL-T-83133) is essentially Jet A-1 with three military-specified additives (as described later in conjunction with Fig. 5). The conversion to JP-8 occurred primarily to improve the safety of aircraft, although the "single fuel for the battlefield" concept (and the similarity of jet fuel to diesel fuel) is centered on the use of aviation kerosene in all U.S. Air Force and U.S. Army aircraft and ground vehicles. A similar process is occurring in the U.S. Navy, where the large variety of liquid fuels has shrunk down to just two, JP-5 for aircraft and F-76 diesel for all other liquid fuel requirements. Logistical considerations may drive commercial jet fuel to be the single battlefield fuel.

Table 1 Petroleum distillate terminology

Fractions	Approximate boiling range, °C	Typical average carbon number
Generic terms		
Gasoline	<200	
Naphtha	150–250	
Kerosene	200–300	
Fuel oil/Gas oil	>275	
Specific Products		
Aviation gasoline ("avgas")	45–145	C_7
Motor gasoline ("mogas")	30–200	C_7
Auto diesel	200–350	
Jet fuel	150–265	C_{11}

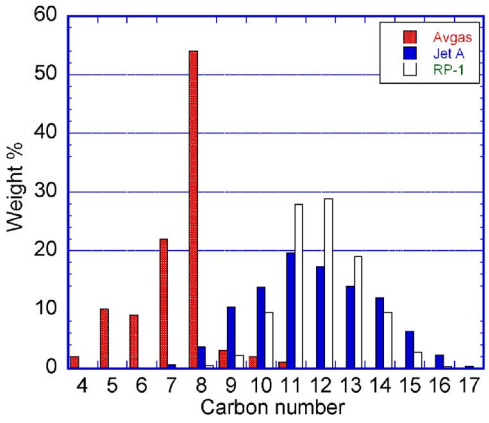

Fig. 2 Carbon number distribution for kerosene fuels and avgas

Fig. 3 Fuel requirements are often painted on aircraft. In this picture from the Nat'l Museum of the Air Force in Dayton, an early jet fighter (the P-80) specifies "JP-1."

The history of the evolution of conventional, widely available jet fuels from the late 1950s to the present is mainly the story of the evolution of test methods and fuel additives to maintain the integrity of the jet fuel supply and to improve safety and correct operational problems. Because of their importance, specifications/test methods and additives are discussed separately later. Specialty fuels were developed for various applications throughout the second half of the 20th century. In the early 1950s, JP-5 (included in MIL-F-5624) was developed. JP-5 is a high-flash-point (60°C/140°F) aviation kerosene used onboard U.S. Navy ships to enhance safety. The development of the higher Mach aircraft led to several specialty fuels. As the flight velocity increases, aerodynamic heating leads to larger amounts of heat being rejected to the fuel, both in the tanks and in the engine, leading to vapor pressure and thermal stability concerns. The cutoff point between the use of conventional Jet A-1/JP-8 fuels and specially produced fuels is between Mach 2.2 and 3. Thus, the Mach 2.2 Concorde uses Jet A-1, whereas the Mach 2-3 XB-70 and SR-71 used specialty fuels. JP-6 (MIL-F-25656) was a low-volatility kerosene developed for the Mach 2 XB-70 [17]. The Mach 3 SR-71 required JP-7 (MIL-T-38219), a low-volatility/high thermal stability, highly processed (low sulfur and aromatics) kerosene [9,16]. The U-2 high-altitude reconnaissance aircraft required both improved thermal stability and a lower freeze point in its fuel (JP-TS, MIL-T-25524) because of its high-altitude, long-duration cruise. These specialty fuels gave a higher performance than conventional aviation kerosenes, at the expense of higher fuel and logistical costs (JP-7 and JP-TS are roughly three times the cost of JP-8 and Jet A-1). The accepted operational temperature limits of these various fuels are approximately 163°C (325°F) for Jet A/Jet A-1/JP-8/JP-5, 219°C (425°F) for JP-TS, and 288°C (550°F) for JP-7 [18]. The accepted limit for gas turbine operation is approximately Mach 4.

Russian jet fuels underwent a parallel evolution throughout this period [19,20]. In most areas, current Russian fuels TS-1 and RT and Russian specifications (GOST 10227) are interchangeable with Jet A-1/JP-8. The main difference between fuels TS-1 and RT is in the area of thermal stability: TS-1 is a straight-run fuel, whereas RT is hydrotreated. By comparison with Jet A-1/JP-8, TS-1 and RT are lighter (have a lower initial boiling point and 10% recovery point in distillation) and have a correspondingly lower flash point and freeze point. Thus, worldwide there are three major specifications in civil use: ASTM D 1655, British Defence Standard (Def Stan) 91-91 (successor to DERD 2494), and Russian GOST 10227. International oil companies have created the "Joint Check List" to standardize jet fuel deliveries worldwide under Jet A-1/Def Stan 91-91 [2]. The International Air Transport Association has also issued guidance material for its members codifying the Jet A/Jet A-1/TS-1 specifications. Pustyrev [20] discusses two specialty Russian fuels specified in GOST 12308: T-8V, a higher density/higher flash-point kerosene and T-6, a high-density kerosene (specific gravity 0.84 vs 0.8 for Jet A-1/JP-8), which has no commercial or military counterpart in Europe or the United States. U.S. Air Force programs in the 1980s demonstrated

Table 2 Summary of major jet fuel characteristics (additive acronyms explained in the additive section below)

	JP-4	JP-5	JP-8	Jet A	Jet A-1
Base	Gasoline + Kerosene	Kerosene	Kerosene	Kerosene	Kerosene
Flash point (min), °C (°F)	n/a	60 (140)	38 (100)	38 (100)	38 (100)
Freeze point (max), °C (°F)	−58 (−72)	−46 (−51)	−47 (−53)	−40 (−40)	−47 (−53)
Additives (see Fig. 5)	AO, CI/LI, FSII, SDA	AO, CI/LI, FSII	AO, CI/LI, FSII, SDA	None	None

the production of fuels similar to T-6 [21,22], but no specification was published in the absence of user requirements.

Fuels Specification Requirements and Test Methods

Fuel specifications and testing have been an integral part of the development of aviation fuels. Fuel specifications are performance specifications in general and are written to allow any particular combination of hydrocarbons that meets the specified performance. Properties are allowed to vary to the extent that the variations will have no deleterious effect on the performance of the fuel in aircraft. The tighter (smaller variations in properties allowed) the specification is written, the higher is the cost of the fuel in general. The first U.S. Government specification was issued in 1907 for the purchase of gasoline (U.S. Navy specification 24 G.5), and required only that the fuel be of a certain specific gravity (density) and that it not be contaminated with materials that would leave a residue after fuel evaporation [8]. As fuel demand grew and problems in service became apparent, limitations on chemical composition and more performance requirements were added. By 1922 there were standard tests established for color (Saybolt number), corrosion and gums (copper dish test), and sulfur content (Doctor test), as well as others [9,23]. As described elsewhere [e.g., [8]], the octane number became an important specification requirement in 1930. Higher altitude operation led to a requirement for maximum freeze point. ASTM has been a key force in the development and standardization of test methods for fuel specification testing. Current aviation fuel specification requirements can be broken into three categories: chemical composition, physical properties, and miscellaneous requirements. Composition requirements include tests to determine the hydrocarbon types in the fuel, to evaluate the sulfur content, and to quantify the organic and inorganic acids in the fuel. Physical properties specified include density (or specific gravity), volatility, vapor pressure, flash point, viscosity, and freeze point. Miscellaneous requirements include the determination of heat of combustion, burning quality, corrosivity, cleanliness, particulates, thermal stability, color, existent gum, and electrical conductivity. The requirements table from the JP-8 specification is presented in Table 3. The Jet A/Jet A-1 specification (ASTM D1655, Def Stan 91-91) is very similar. Note the significant number of test methods employed in certifying JP-8, most driven by operational problems. More detailed discussions can be found in Martel [9] and the CRC Aviation Fuel Properties Handbook [23].

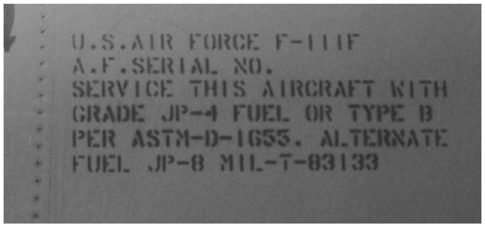

Fig. 4 The F-111F spanned the JP-4 to JP-8 conversion. ASTM-D-1655 Type B ("Jet B") is the commercial equivalent of JP-4.

Additives

Fuel additives are chemicals that are added to fuels to impart specific properties, or to counteract the effects of fuel contami-

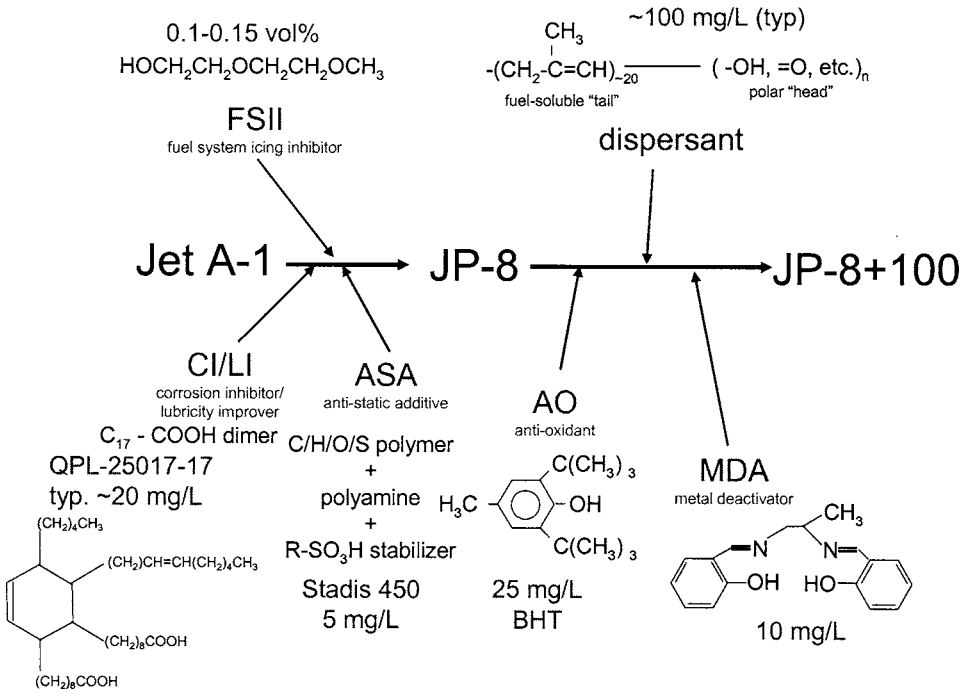

Fig. 5 Jet fuel additives. Antistatic additive is also called static dissipater additive (SDA).

Table 3 JP-8 specification chemical and physical requirements, MIL-DTL-83133E

Property	Min	Max	Test methods ASTM standards
Color, Saybolt		[a]	D156[b] or D6045
Total acid number, mg KOH/g		0.015	D3242
Aromatics, vol percent		25.0	D1319
Sulfur, total, mass percent		0.30	D129, D1266, D2622, D3120, D4294[b] or D5453
Sulfur mercaptan, mass percent OR		0.002	D3227
Doctor Test		negative	D4952
Distillation temperature, °C[c] (D2887 limits given in parentheses)			D86[b], D2887
Initial boiling point		[a]	
10% recovered		205 (186)	
20% recovered		[a]	
50% recovered		[a]	
90% recovered		[a]	
End point		300(330)	
Residue, vol percent		1.5	
Loss, vol percent		1.5	
Flash point, °C	38	[d]	D56, D93[b] or D3828[d]
Density or gravity			
Density, kg/L at 15°C OR	0.775	0.840	D1298 or D4052[b]
Gravity, API at 60°F	37.0	51.0	D1298
Freezing point, °C		−47	D2386[b], D 5901 or D5972
Viscosity, at −20°C, mm^2/s		8.0	D445
Net heat of combustion, MJ/kg	42.8		D3338[e] or D4809[b]
Hydrogen content, mass percent	13.4		D3701[b], D3343
Smoke point, mm, OR	25.0		D1322
Smoke point, mm, AND	19.0		D1322
Naphthalene, vol percent		3.0	D1840
Calculated Cetane Index		[a]	D976[f]
Copper strip corrosion, 2 hr at 100°C (212°F)		No. 1	D130
Thermal stability			D3241[a]
change in pressure drop, mm Hg		25	
heater tube deposit, visual rating		<3[l]	
Existent gum, mg/100 ml		7.0	D381
Particulate matter, mg/L		1.0	D2276[h] or D5452[b]
Filtration time, minutes		15	
Water reaction interface rating		1 b	D1094
Water separation index	[i]		D3948
Fuel system icing inhibitor, vol %	0.10[k]	0.15[k]	D5006[j]
Fuel electrical conductivity, ps/m			D2624

[a]To be reported—not limited.
[b]Referee test method.
[c]A condenser temperature of 0° to 4°C (32° to 40°F) shall be used for the distillation by ASTM D86.
[d]ASTM D56 may give results up to 1°C (2°F) below the ASTM D93 results. ASTM D3828 may give results up to 1.7°C (3°F) below the ASTM D93 results. Method IP170 is also permitted.
[e]When the fuel distillation test is performed using ASTM D2887, the average distillation temperature, for use in ASTM D3338, shall be calculated as follows: $V=(10\%+50\%+95\%)/3$.
[f]The mid-boiling temperature may be obtained by either ASTM D86 or ASTM D2887 to perform the cetane index calculation. ASTM D86 values should be corrected to standard barometric pressure.
[g]See 4.5.3 for ASTM D3241 test conditions and test limitations.
[h]A minimum sample size of 3.79 l.(1 gallon) shall be filtered. Filtration time will be determined in accordance with the procedure in Appendix A. This procedure may also be used for the determination of particulate matter as an alternate to ASTM D2276 or ASTM D5452.
[i]The minimum microseparometer rating using a microseparometer (MSEP) shall be as follows:

JP-8 additives	MSEP rating, min.
Antioxidant (AO)* , metal deactivator (MDA)*	90
AO*, MDA*, and fuel system icing inhibitor (FSII)	85
AO*, MDA*, and corrosion inhibitor/lubricity improver (CI/LI)	80
AO*, MDA*, FSII, and CI/LI	70

* Even though the presence or absence does not change these limits, samples submitted for specification conformance testing shall contain the same additives present in the refinery batch. Regardless of which minimum the refiner elects to meet, the refiner shall report the MSEP rating on a laboratory hand blend of the fuel with all additives required by the specification.
[j]The test shall be performed in accordance with ASTM D5006 using the DiEGME scale of the refractometer.
[k]The conductivity must be between 150 and 450 pS/m for F-34 (JP-8) and between 50 and 450 pS/m for F-35, at ambient temperature or 29.4 °C (85 °F), whichever is lower, unless otherwise directed by the procuring activity. In the case of JP-8 +100, JP-8 with the thermal stability improver additive (see 3.3.6), the conductivity limit must be between 150 to 700 pS/m at ambient temperature or 29.4 °C (85 °F), whichever is lower, unless otherwise directed by the procuring activity.
[l]Peacock or abnormal color deposits result in a failure.

nants that are not easily removed. The selection of additives is subject to many constraints. Additives intended to enhance performance of the fuel in one aspect can have deleterious effects on other fuel properties. A major concern is the compatibility of additives with the materials in the fuel system and in the engine hot section. A large number of fuel additives have been developed and

investigated over the years [9,23]. The following paragraphs contain brief discussions of the various additives currently in use. Many of these additives are shown in Fig. 5.

In 1954, the U.S. Government began using commercial pipelines to transport aircraft fuel to U.S. Air Force facilities. To combat the excessive corrosion in the ground fuel systems, and to reduce the carryover of corrosion products into aircraft fuel systems, corrosion inhibitor additive requirements were added to specifications for both avgas and turbine engine fuels. A specification (MIL-I-25017) was issued in 1954 for corrosion inhibitor additives. These additives also act to improve fuel lubricity (lubricating capability) and thus are often referred to as corrosion inhibitor/lubricity improver (CI/LI) additives. CI/LI additives are typically added at approximately 20 mg/L. CI/LI additives that are qualified for use in JP-8 are listed the Qualified Products List (QPL) associated with the current specification (MIL-PRF-25017G/QPL-25017-17). In an effort to streamline military specifications and bring them in line with commercial practice, most specifications have evolved into "performance" (MIL-PRF-xxxx) or "detailed" (MIL-DTL-xxxx) specifications.

Water contamination in aviation fuels has always been a serious problem. In liquid form, water can cause temporary flameout in the engine, but in solid form (ice), it can block filters and fuel lines and completely stop the flow of fuel to the engine. In the 1940s and 1950s, free, undissolved water in fuel was suspected as the cause of many in-flight incidents and accidents. A major research and development program was initiated to solve the water-in-fuel problem as a result of a B-52 crash in 1958. One objective was the development of a fuel system icing inhibitor (FSII). The FSII was to be added to the fuel, but would preferentially migrate to any free water present and act as an antifreeze. The current icing inhibitor used is diethylene glycol monomethyl ether at a maximum concentration of 0.15 vol.%. The FSII also acts to minimize the growth of micro-organisms in fuel, so it is sometimes referred to as a "biocide."

Because of their low electrical conductivity, aviation fuels can build up a static electrical charge, especially during fueling. Discharge of this built-up charge in areas where flammable fuel/air mixtures exist, for example, fuel tanks, has been a problem. A solution is use of static dissipator additives (SDA) in the fuel to increase the electrical conductivity of the fuel and increase the rate of charge dissipation. Octel Stadis 450 is the only currently approved SDA for turbine engine fuels [9]. Typical concentrations of 0.5–2.0 mg/L increase the fuel conductivity to between 200 and 600 pS/m (picoSiemens/m). As shown in Table 3, the minimum conductivity allowed in JP-8 is 150 pS/m. The main difference between commercial Jet A-1 fuel and military JP-8 fuel is the specified presence of a corrosion inhibitor, FSII, and SDA.

Antioxidant additives are added to turbine engine fuels and other petroleum products to prevent the formation of gums and peroxides during storage by reducing the formation of free radicals in the fuel. Peroxides are deleterious to thermal oxidative stability, being precursors to the formation of deposits. Peroxides also attack fuel tank polysulfide sealants and other fuel system elastomers. The most common antioxidants are hindered phenols, exemplified by 2,6 di-tert-butyl 4-methylphenol ("butylated hydroxytoluene" (BHT), also used in food). Normal antioxidant concentrations in turbine engine fuels range up to 14 mg/L (except as discussed below for JP-8+100).

Metal deactivator additives (MDAs) were initially added to gasolines that had been treated using the copper sweetening process (a method to convert mercaptan sulfur compounds to less noxious sulfur compounds). Copper is known to catalyze oxidation reactions that form gums, and so MDA was used to deactivate any traces of copper left in the fuel. MDAs function by forming a chelate with the metal. The chelate effectively isolates the metal from the fuel. Metal deactivators are optional additives in military turbine engine fuels, and are approved for use in military turbine engine fuels at concentrations up to 6 mg/L (unless added as part of JP-8+100 discussed later).

The JP-8+100 Program

Thermal stability [24] is another fuel property than can be improved by additives. Jet fuel picks up a significant amount of waste heat in aircraft fuel systems through the cooling of components and other fluids (such as engine oil). Thermal instability of the fuel results in deposit formation in fuel system passages, in controls, and on filters. Currently, the specification test device for thermal stability is the jet fuel thermal oxidation tester, as described in ASTM D3241. The JP-8+100 research program was initiated by the U.S. Air Force, in cooperation with other government agencies, industry, and universities, in 1989 [25,26]. The main goal of the program was to increase the heat sink capability of JP-8 fuel by 50%, by increasing the fuel operating temperature limit by 100°F (56°C), from 325°F to 425°F (163°C–219°C). This was to be accomplished by developing additives to blend with the fuel at a cost of one dollar or less per 1000 gallons (3.785 m^3) of fuel. It was felt that fuel additive development was the best compromise to balance the engine performance requirements (technology needs), fuel cost (economic factors), and fuel availability (strategic factors). JP-8+100 is designed to alleviate the need for the development of expensive specialty fuels such as JP-7 and JP-TS for future advanced aircraft and will decrease maintenance costs for current inventory aircraft. The JP-8+100 program led to a number of other advancements, including new test techniques, improved fuel/water separation technology, and a better understanding of fuel thermal-oxidative stability. The initial JP-8+100 additive package is based on a detergent/dispersant, packaged with an anti-oxidant and MDA (as shown in Fig. 5) at a total package (additives plus solvent) concentration of 256 mg/L. The JP-8+100 additive has been shown to produce 50%-95% reductions in deposits in more than 10 thermal stability test rigs with a wide variety of JP-8/Jet A fuels [26]. Several base-level trials have quantified significant reductions in fuel-related engine maintenance during use of the additive. Further discussion on the topic of thermal stability appears in the Future Trends section. Over 300 additive combinations have been screened in this program.

Nonpetroleum Fuels

The petroleum shortages of the 1970s led to the search for domestic sources of liquid transportation fuels. Large United States reserves of coal and oil shale (and Canadian reserves of tar sands) spurred the development of conversion processes to produce fuels from these nonpetroleum sources. In the 1980s, programs were initiated to demonstrate the suitability of fuel derived from shale [27–29], coal [30], and tar sands [31]. Engine testing and flight demonstrations of shale-derived JP-4 indicated no deleterious effects resulting from the use of shale-derived fuel. The success of this program indicated that the JP-4 specification was restrictive enough to provide adequate fuel, regardless of the hydrocarbon source. 2005 specification tests on the shale-derived JP-4 and JP-8 jet fuels showed that the fuel still met specification requirements after 20+ years in storage.

Jet fuels produced from synthesis gas ($CO+H_2$) via Fischer–Tropsch (F–T) technology are currently being studied for their suitability for aircraft [32,33]. The synthesis gas can be produced from coal, natural gas, or other carbon-containing materials. A mixture of petroleum-derived Jet A-1 and isoparaffinic kerosene derived from coal (with an upper limit of 50% sunthetic) is being delivered to aircraft in South Africa. A thorough study by Southwest Research Institute demonstrated that the 50/50 mixture properties fell well within the Jet A-1 specification range and should have no impact on engine operation [32,33]. The composition differences between the two fuels are shown in Figs. 6 and 7.

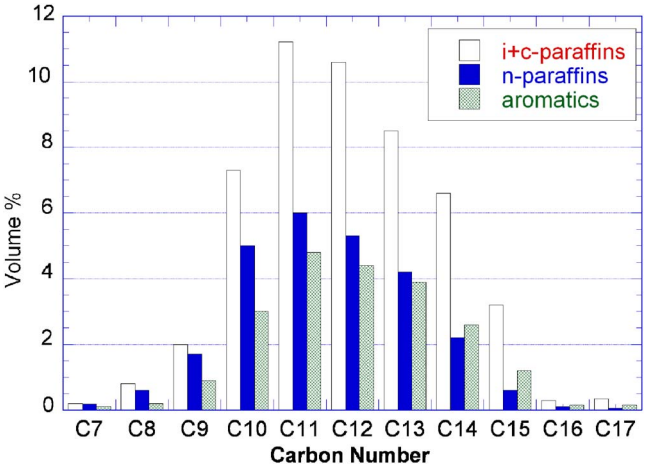

Fig. 6 Composition distribution for South African petroleum-derived Jet A-1 [31]

Lubricity and elastomer compatibility issues for use of the pure F–T fuel are currently being studied. The Propulsion Directorate has recently been investigating Fischer-Tropsch jet fuel supplied by DOE and Syntroleum (through an Army-led program) [34]. The pure "synthetic" fuel has excellent combustion and thermal stability properties.

Missile Fuels

Missiles impose quite different constraints from reusable aircraft on their fuels. Because of the expendable nature of missiles (and, thus, their relatively short life requirement and small fuel consumption), the cost of missile fuels is usually not a significant driver for missile system cost. Missiles are typically volume-limited, rather than weight limited, as are most aircraft, so that fuel volumetric energy is a key parameter. Storage stability is also key because missiles may be stored fueled for periods on the order of 10 years. Low-temperature and low-pressure performance are key drivers for air-launched missiles, which may be cold soaked at very low ambient temperatures. For example, the U.S. Air Force requires a −54°C (−65°F) freeze point for missile fuels, significantly lower than the freeze point of the fuel for the aircraft carrying the missile. Before the 1960s, the only fuels available for missiles were JP-4 and JP-5. RJ-4 was developed for the ramjet-powered Talos missile in the early 1960s [9,35]. RJ-4 is a mixture of the isomers of *exo*-tetrahydrodi(methyl cyclopentadiene), as

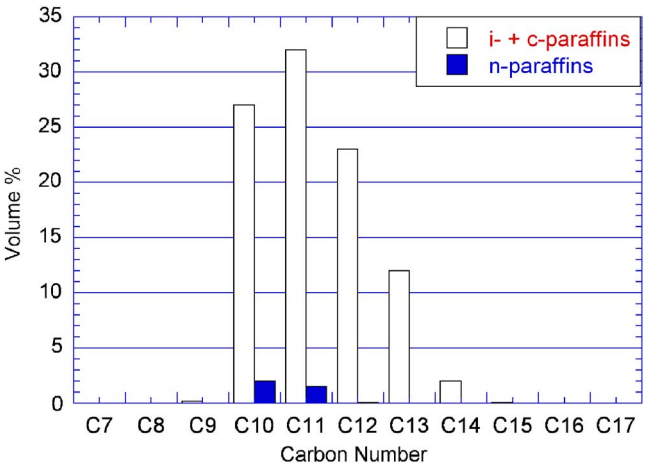

Fig. 7 Composition distribution for isoparaffinic kerosene produced from coal-derived synthesis gas by F-T process [31]

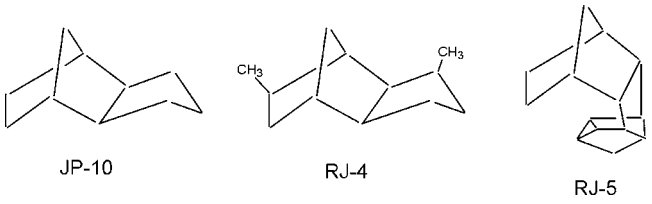

Fig. 8 Missile fuel structures

shown in Fig. 8, and was also known as TH dimer and H-MCPD. Joint U.S. Air Force/Navy research in higher density missile fuels for turbine-engine-powered cruise missiles culminated in the creation of JP-10 in the mid-1970s. JP-10 is *exo*-tetrahydrodicyclopentadiene (Fig. 8) and is the only airbreathing-missile fuel in operational use by the United States at the present time. JP-10 has the impressively low freeze point of −79°C (−110°F). Higher density missile fuels have been developed, for example, RJ-5, perhydrodi(norbornadiene), but cost and freeze-point limitations prevented field use. The potential for extending the range of missiles beyond what is possible with conventional high-density missile fuels prompted interest in slurry fuels that contain additives, such as boron, carbon, or aluminum in suspension in a gelled form. Such slurry fuels can provide a very high heating value per unit volume. The result of the many years of slurry fuel work demonstrated that formulation of stabilized slurry fuels is possible, but to make such fuels a viable option for turbine-engine-powered cruise missiles, a substantial amount of additional fuel system and propulsion engineering would be required.

Future Gas Turbine Fuels

It is difficult to predict the future (at least correctly), so perhaps the best way to end this paper is to pick a notional aircraft, and describe how its fuel would differ from JP-8/Jet A. Let's call it "JP-11," since JP-9 and JP-10 are taken. For example purposes, invent a Mach 4 SR-71 follow-on, designed to cruise at Mach 4 for long distances. This mission will place several very serious constraints on the fuel. First, at higher Mach numbers, the air surrounding the aircraft is a source of heating, not an available cooling resource. Thus, the fuel becomes the most useful cooling resource on-board the aircraft. The heat load rejected into the fuel for notional aircraft cooling increases rapidly with increasing Mach number. At Mach 4, a reasonable estimate might be 1400 kJ/kg (600 BTU/lb.) [36], which corresponds to a fuel temperature increase from ambient conditions to approximately 480°C (900°F). Thus, "JP-11" would need to have very high thermal stability, well beyond that of JP-8+100. Balanced against this apparent need for a "specialty" high-thermal-stability fuel (like JP-7) is the expectation that fuel cost and availability will still be one of the primary drivers for the aircraft operating cost in the future.

The Air Force Research Laboratory/Propulsion Directorate's High Heat Sink Fuel program has been pursuing a number of approaches to attaining this thermal stability in a JP-8/Jet A fuel. An initial step is "JP-8+225," a JP-8-based fuel that is stable to 288°C (550°F), equivalent to JP-7 [37]. Here 550°F is 225°F above the nominal temperature limit for JP-8/Jet A (325°F); hence the name JP-8+225, is irretrievably tied to the Fahrenheit temperature scale. The next step is a fuel stable to 900°F (480°C), which has been called "JP-900," inviting confusion by the change of terminology—it is not JP-8+900! It is estimated that 480°C (900°F) is the upper temperature limit for avoiding kerosene fuel thermal cracking/pyrolysis. Bulk fuel thermal reactions have the potential advantage of absorbing significant quantities of heat (hence "endothermic" fuels [36]), but lead to significant pyrolytic "coking" challenges [7]. The key challenge to achieving "JP-8+225" is thermal-oxidative deposition ("fouling,"

"coking"). Typical jet fuel critical temperatures are 370–400°C (700–750°F), so "JP-900" adds the additional challenges of operating in the supercritical phase and avoiding fuel pyrolytic degradation.

Multiple approaches to achieving thermal-oxidative stability [24] are being pursued, including advanced additives, fuel deoxygenation, and fuel system surface modifications. On-board fuel processing is being studied, including fuel deoxygenation by chemical [37–39] or physical [40] means. Note that deposition can depend upon dissolved oxygen levels in an obscure, nonlinear manner [41]. "Coke-tolerant" designs have also been studied [42], as have coke-resistant surfaces [43,44]. Advanced additives are being examined [45]. Enhanced models of thermal-oxidative fouling have developed [45–48]. A significant advance has been the replacement of fuel-dependent adjustable parameters by measurements of trace fuel species involved in the deposition process [49]. It has been demonstrated that fuel deoxygenation, alone or in combination with additives, can improve the thermal stability of JP-8/Jet A fuels to the level of JP-7 [40].

JP-11 could very well require a combination of all of these approaches, as well as a fuel system capable of handling "supercritical" vapor fuels [50]. The major difficulty in handling vapor fuels is the change of fuel phase and/or physical properties as the fuel heat load changes throughout a given mission. Coke removal from fuel systems to extend life is also being studied [51]. Fuel heat loads will also increase in the future through the use of cooled cooling air [52] or more integrated subsystems [53].

Recall from the discussion above that JP-7 is a "low-volatility" kerosene fuel. Why is that? The requirement for low volatility comes from the significant amount of heating of the wing fuel tanks that occurs during supersonic cruising. At Mach 3, the wing surface temperatures could exceed 260°C (500°F) [54]. Allowing for insulation and other factors, it would not be unreasonable to assume that the fuel in the wings could exceed 149°C (300°F) at Mach 3. At this temperature, JP-8 is very close to boiling, and the high vapor pressure of the fuel would cause serious boiloff losses, possible pump cavitation, and other problems—analogous to the problems encountered with high volatility jet fuels in the early years of turbine engine development. Thus, the JP-7 specification has a volatility limit at 149°C (300°F). At Mach 4, "JP-11" could see temperatures approaching 110°C (200°F) higher than at Mach 3, so "JP-11" would need to have even more stringent vapor pressure limits—or much better wing tank insulation or pressurized tanks. Alternatively, a strategy might be to use the fuel in the wing tanks first, so that the very hot wings at the end of the cruise leg are empty of fuel.

This low-volatility fuel does not come without a price, of course. Lower-volatility hydrocarbons have higher boiling points, but also have higher freeze points. The "freeze point" for a distillate hydrocarbon like a jet fuel is not the point at which the fuel becomes solid, but rather is the point at which the last of the solid disappears upon heating a fuel that has been frozen. Maximum freeze points of jet fuels range from −40°C (−40°F) for Jet A to −53°C (−63°F) for JP-TS. JP-7 has a specification maximum freeze point of −43.5°C (−46°F). It might be expected, then, that "JP-11" would have to allow a higher freeze point than JP-7. The higher freeze point might not be too important to the thermally challenged Mach 4 aircraft, but would prevent "JP-11" from being used in some other aircraft, and might cause concern during aerial refueling (or ground refueling in cold climates). It is also to be expected that this low-volatility fuel will be quite hard to ignite, which could be a serious concern for altitude relight. The SR-71 carried a pyrophoric ignition aid to help ensure altitude relight of JP-7.

Thus, "JP-11" will certainly be a challenging fuel to develop and use. Achieving Mach numbers greater than 4 will require non-gas-turbine propulsion and "endothermic" fuels, where deliberate fuel degradation reactions are allowed in the fuel system to absorb excess aircraft heat [16,36,55–57]. Achieving endothermic-fuel levels of heat sink while achieving gas-turbine levels of engine life (thousands of hours) is an enormous technical challenge.

Summary

This overview can only give a flavor of the extensive research that has accompanied the tremendous growth in aviation gas turbine fuels (and engines) since the first flight of a gas-turbine-powered aircraft more than 50 years ago.

References

[1] Crouch, T., 1989, *The Bishop's Boys*, Norton, New York.
[2] Bacha, J., Barnes, F., Franklin, M., Gibbs, L., Hemighaus, G., Hogue, N., Lesnini, D., Lind, J., Maybury, J., and Morris, J., "Aviation Fuels Technical Review," Chevron Products Company, 2000. (Also available at http://www.chevron.com/prodserv/fuels/bulletin/)
[3] Dukek, W. G., 1992, "Aviation and Other Gas Turbine Fuels," *Kirk-Othmer Encyclopedia of Chemical Technology*, 4th ed., Vol. 3, pp. 788–812.
[4] Ogston, A., 1981, "A Short History of Aviation Gasoline Development, 1903–1980," pp. 1–14 (SAE 810848), in *Trends in Aviation Fuels and Lubricants*, SP-492, SAE, Warrendale, PA.
[5] Gonzalez, C., 1989, "A Proposal for Fuel Specification Activities Relating to General Aviation Intermittent Combustion Engines," in *Future Fuels for General Aviation*, ASTM STP 1048, edited by K. H. Strauss and C. Gonzalez, American Society for Testing and Materials, Philadelphia, pp. 153–165.
[6] Davies, R. E. G., 2003, "The World's First Commercial Jets," Paper No. AIAA 2003-2882.
[7] Edwards, T., 2003, "Liquid Fuels and Propellants for Aerospace Propulsion: 1903–2003," J. Propul. Power, **19**, pp. 1089–1108.
[8] Dukek, W. G., and Winans, D. R., 1969, "Milestones in Aviation Fuels," Paper No. AIAA 69-779.
[9] Martel, C. R., 1987, "Military Jet Fuels, 1944–1987," Report No. AFWAL-TR-87-2062.
[10] Goodger, E., and Vere, R., 1985, *Aviation Fuels Technology*, Macmillan, London.
[11] Austin, G. T., 1984, *Shreve's Chemical Process Industries*, 5th ed., McGraw-Hill, New York.
[12] Speight, J. G., 1991, *The Chemistry and Technology of Petroleum*, 2nd ed., Marcel Dekker, Inc., New York.
[13] Streitweiser, A., and Heathcock, C., 1976, *Introduction to Organic Chemistry*, MacMillan, New York.
[14] Morrison, R. T., and Boyd, R. N., 1973, *Organic Chemistry*, 3rd ed., Allyn and Bacon, Inc., Boston.
[15] Prisell, E., 2003, "The Beginning of the Jet Age," Paper No. AIAA 2003-2721.
[16] Maurice, L. Q., Lander, H., Edwards, T., and Harrison, W. E., 2001a, "Advanced Aviation Fuels: A Look Ahead Via a Historical Perspective," Fuel, **80**, pp. 747–756, 2001.
[17] Freschl, E., and Steele, E. S., 1965, "Development of the XB-70A Propulsion System," AIAA Paper No. 65-571.
[18] Croswell, T. M., and Biddle, T. B., 1992, "High Temperature Fuel Requirements and Payoffs," *Aviation Fuel: Thermal Stability Requirements, ASTM STP 1138*, P. W. Kirklin and P. David, eds., American Society for Testing and Materials, Philadelphia.
[19] Ragozin, N. A., 1961, *Jet Propulsion Fuels*, Pergamon, New York.
[20] Pustyrev, O., 1993, "Aviation Fuel in the Russian Federation," *Proceedings of the 2nd International Symposium on Aviation Turbine Fuel Specifications*.
[21] Hanson, F. V., 1989, "Production of High Density Aviation Fuels via Novel Zeolite Catalyst Routes," Report No. WRDC-TR-89-2097.
[22] Smits, C. M., 1986, "High Density Jet Fuel Supply and Specifications," Report No. AFWAL-TR-86-2109.
[23] Coordinating Research Council, 1983, *Handbook of Aviation Fuel Properties*, CRC Report No. 530.
[24] Hazlett, R. N., 1991, *Thermal Oxidation Stability of Aviation Turbine Fuels*, ASTM Monograph 1, American Society for Testing and Materials, Philadelphia, PA.
[25] Heneghan, S. P., Zabarnick, S., Ballal, D. R., and Harrison, W. E., 1996, "JP-8+100: The Development of High Thermal Stability Jet Fuel," Paper No. AIAA 96-0403.
[26] Edwards, T., Harrison, B., Zabarnick, S., DeWitt, M., and Bentz, C. E., 2004, "Update on the Development of JP-8+100," Paper No. AIAA 2004-3886.
[27] Sikonia, J. G., Hilfman, L., Wilcox, J. R., Board, T. G., Gembicki, V. A., Yu, E., Gatsis, J. G., and Latos, E. J., 1982, "USAF Shale Oil to Fuels," Report No. AFWAL-TR-81-2116, Vol. II.
[28] Reif, H. E., Schwedock, J. P., and Schneider, A., 1982, "An Exploratory Research and Development Program leading to Specifications for Aviation Turbine Fuel From Whole Crude Shale Oil," Report No. AFWAL-TR-81-2087, Part V.
[29] Moore, H. R., Henton, L. M., Johnson, C. A., and Fabry, D. A., 1982, "Refining of Military Jet Fuels from Shale Oil," Report No. AFWAL-TR-81-2056.
[30] Smith, E. B., Guffey, F. D., and Nickerson, L. G., 1988, "Production of Jet Fuels from Coal Derived Liquids, Vol. III—Jet Fuels Potential of Liquid By-Products from the Great Plains Gasification Project," Report No. AFWAL-TR-87-2042, Vol. III.

[31] Talbot, A. F., Swesey, J. R., and Magill, L. G., 1987, "Turbine Fuels from Tar Sands Bitumen and Heavy Oil," Report No. AFWAL-TR-2043, Vol. II.
[32] Moses, C. A., Stavinoha, L. L., and Roets, P., 1997, "Qualification of Sasol Semi-Synthetic Jet A-1 as Commercial Jet Fuel," Paper No. SwRI-8531.
[33] Roets, P., Botha, J., Moses, C., and Stavinoha, L., 1998, "Stability and Handling of Sasol Semi-Synthetic Jet Fuel," *6th Int'l Conf. on Stability and Handling of Liquid Fuels*, Oct. 1997, DOE/CONF 971014 Vol. II, pp. 789–805.
[34] Edwards, T., Minus, D., Harrison, W., Corporan, E., DeWitt, M., Zabarnick, S., Balster, L., 2004, "Fischer-Tropsch Jet Fuels – Characterization for Advanced Aerospace Applications," Paper No. AIAA-2004-3885.
[35] Burdette, G. W., Lander, H. R., and McCoy, J. R., 1978, "High-Energy Fuels for Cruise Missiles," J. Energy, **2**, pp. 289–292.
[36] Lander, H., and Nixon, A. C., 1971, "Endothermic Fuels for Hypersonic Vehicles," J. Aircr., **8**, pp. 200–207.
[37] Beaver, B. D., Gao, L., Fedak, M. G., Coleman, M. M., and Sobkowiak, M., 2002, "Model Studies Examining the Use of Dicyclohexylphenylphosphine to Enhance the Oxidative and Thermal Stability of Future Jet Fuels," Energy Fuels, **16**, pp. 1134–1140.
[38] Edwards, T., 1998, "Prospects for JP-8+225, A Stepping Stone to JP-900," Paper No. AIAA 98-3532.
[39] Heneghan, S. P., Williams, T., Whitacre, S. D., and Ervin, J. S., 1996b, "The Effects of Oxygen Scavenging on Jet Fuel Thermal Stability," *ACS Petroleum Chemistry Division Preprints*, Vol. 41(2), pp. 469–473.
[40] Spadaccini, L. J., and Huang, H., 2002, "On-Line Fuel Deoxygenation for Coke Suppression," ASME J. Eng. Gas Turbines Power, **125**, pp. 686–692.
[41] Ervin, J. S., and Williams, T. F., 1996, "Dissolved Oxygen Concentration and Jet Fuel Deposition," Ind. Eng. Chem. Res., **35**, pp. 899–904.
[42] Spadaccini, L. J., Sobel, D. R., and Huang, H., 1999, "Deposit Formation and Mitigation in Aircraft Fuels," ASME Paper No. 99-GT-217.
[43] Jones, E., Balster, L., and Balster, W., 1996, "Autoxidation of Aviation Fuels in Heated Tubes: Surface Effects," Energy Fuels, **10**, pp. 831–836.
[44] Doungthip, T., Ervin, J., Ward, T., Williams, T., and Zabarnick, S., 2003, "Surface Deposition Within Treated and Untreated Stainless Steel Tubes Resulting from Thermal-Oxidative Degradation of Jet Fuel," Energy Fuels, **17**, pp. 577–586.
[45] DeWitt, M. J., and Zabarnick, S., 2002, "Development and Evaluation of Additives to Inhibit Oxidative Deposition of Jet Fuels," ACS Petroleum Chemistry Division Preprints, Vol. 47, pp. 183–186.
[46] Katta, V. R., Jones, E. G., and Roquemore, W. M., 1998, "Modeling of Deposition Process in Liquid Fuels," Combust. Sci. Technol., **139**, pp. 75–111.
[47] Zabarnick, S., 1998, "Pseudo-Detailed Chemical Kinetic Modeling of Antioxidant Chemistry for Jet Fuel Applications," Energy Fuels, **12**, pp. 547–553.
[48] Ervin, J. S., and Zabarnick, S., 1998, "Computational Fluid Dynamics Simulation of Jet Fuel Oxidation Incorporating Pseudo-Detailed Chemical Kinetics," Energy Fuels, **12**, pp. 344–352.
[49] Balster, L. M. T., Zabarnick, S., and Striebich, R. C., 2002, "Predicting the Fouling Tendency of a Thermally Stressed Jet Fuel by High Performance Liquid Chromatography (HPLC) Analysis," *ACS Petroleum Chemistry Division Preprints*, 2002, Vol. 47, pp. 161–164.
[50] Huang, H., Spadaccini, L. J., and Sobel, D. R., 2002, "Fuel-Cooled Thermal Management for Advanced Aero Engines," ASME Paper No. GT-2002-30070.
[51] Huang, H., and Spadaccini, L. J., 2001, "Coke Removal in Fuel-Cooled Thermal Management Systems," ASME Paper No. 2001-GT-0073.
[52] Bruening, G. B., and Chang, W. S., 1999, "Cooled Cooling Air Systems for Turbine Thermal Management," ASME Paper No. 99-GT-14.
[53] Chen, W-Z., Lin, T., Hill, B. P., Leamy, K., and Brown, J. R., 1998, "Integrated Airframe/Engine Thermal Management Systems," Paper No. IECEC-98-349.
[54] Schmidt, J. E., 1992, "Air Frame Considerations in Fuel Thermal Stability for Commercial Supersonic Flight," *Aviation Fuel: Thermal Stability Requirements, ASTM STP 1138*, P. W. Kirklin and P. David, eds., American Society for Testing and Materials, Philadelphia, pp. 34–56.
[55] Sobel, D. R., and Spadaccini, L. J., 1997, "Hydrocarbon Fuel Cooling Technologies for Advanced Propulsion," ASME J. Eng. Gas Turbines Power, **119**, pp. 344–351.
[56] Ianovski (Yanovskii), L. S., 1993, "Endothermic Fuels for Hypersonic Aviation," AGARD Conference on "Fuels and Combustion Technology for Advanced Aircraft Engines," AGARD CP-536, pp. 44–1 to 44–8.
[57] Maurice, L. Q., Edwards, T., and Griffiths, J., 2001, "Liquid Hydrocarbon Fuels for Hypersonic Propulsion," *Scramjet Propulsion* (AIAA Progress in Astronautics and Aeronautics Series, Vol. 189), E. T. Curran and S. N. B. Murthy, eds., pp. 757–822.

Ceramic Matrix Composite Combustor Liners: A Summary of Field Evaluations

Mark van Roode
Jeff Price
Josh Kimmel
Naren Miriyala
Don Leroux
Anthony Fahme
Kenneth Smith

Solar Turbines Incorporated,
P. O. Box 85376,
San Diego, CA 92186-5376

Solar Turbines Incorporated, under U.S. government sponsored programs, has been evaluating ceramic matrix composite combustor liners in test rigs and Solar's Centaur® 50S gas turbine engines since 1992. The objective is to evaluate and improve the performance and durability of CMCs as high-temperature materials for advanced low emissions combustors. Field testing of CMC combustor liners started in May of 1997 and by the end of 2004, over 67,000 operating hours had been accumulated on SiC/SiC and oxide/oxide CMC liners. NO_x *and CO emissions have been consistently* $<$15 ppmv *and* $<$10 ppmv*, respectively. Maximum test durations of* 15,144 h *and* 13,937 h *have been logged for SiC/SiC liners with protective environmental barrier coatings. An oxide/oxide CMC liner with a Friable Graded Insulation coating has been tested for* 12,582 h*. EBCs significantly improve SiC/SiC CMC liner life. The basic three-layer EBC consists of consecutive layers of Si, mullite, and BSAS. The durability of the baseline EBC can be improved by mixing BSAS with mullite in the intermediate coating layer. The efficacy of replacing BSAS with SAS has not been demonstrated yet. Heavy degradation was observed for two-layer Si/BSAS and Si/SAS EBCs, indicating that the elimination of the intermediate layer is detrimental to EBC durability. Equivalent performance was observed when the Hi-Nicalon fiber reinforcement was replaced with Tyranno ZM or ZMI fiber. Melt infiltrated SiC/SiC CMCs have improved durability compared to SiC/SiC CMCs fabricated by Chemical Vapor Infiltration of the matrix, in the absence of an EBC. However, the presence of an EBC results in roughly equivalent service life for MI and CVI CMCs. Results to date indicate that oxide/oxide CMCs with protective FGI show minor degradation under Centaur® 50S gas turbine engine operating conditions. The results of, and lessons learned from CMC combustor liner engine field testing, conducted through 2004, have been summarized.* [DOI: 10.1115/1.2181182]

Introduction

Today's industrial gas turbine development is driven by the demands of end users for improved performance, lower cost, high reliability, availability, maintainability, and durability, reduced emissions of NO_x and CO, and fuel flexibility. The contributing factors are rising fuel costs, the need to minimize operating and maintenance costs, and increasingly strict emissions regulations. However, the demand for higher efficiency and lower emissions makes it more challenging to provide adequate cooling of engine hot section components. Ceramic materials have the potential to provide the 30,000 h of trouble-free operation that industrial gas turbine operators expect, despite the more challenging environment of a high-performance turbine.

The interest in ceramics as structural materials for gas turbine hot section components (combustor liners, nozzles, blades, etc.) stemmed from their superior high-temperature durability compared to conventional metals, which enables higher component operating temperatures, and therefore, improved engine efficiency. Additionally, because of a reduced demand for hot section component cooling, air can be redirected to lean out the combustor primary zone and reduce NO_x emission. The reduction in cooling air also enables higher firing temperatures, which improves engine efficiency. Finally, the incorporation of a ceramic ("hot wall") combustor liner suppresses the formation of CO.

Since the early 1950s, programs have been conducted worldwide to incorporate ceramic hot section components in small gas turbines for transportation and cogeneration, medium-size engines for industrial power generation, and large engines for utility applications [1,2]. Through these programs, valuable lessons were learned. Design expertise was developed, material databases were established, and ceramic materials improved as fabrication processes matured.

Relatively recently, CMCs with continuous fiber reinforcement have been recognized as attractive structural ceramic materials for gas turbine hot section components. The higher fracture toughness of the best CMCs ($K_{1C} \geqslant 25$ MPa $m^{1/2}$) compared to that of the best commercially available silicon-based monolithic ceramics ($K_{1C} < 10$ MPa $m^{1/2}$) results in improved impact and slow crack growth resistance. Therefore, larger components with better durability can be fabricated from CMCs than from monolithics.

This paper summarizes the results and conclusions from the field tests to date with CMC combustor liners in Solar's *Centaur*® 50S gas turbine engines.

Development Overview

Solar® has successfully integrated and demonstrated CMCs for combustor liners for the *Centaur*® 50S gas turbine [3]. To date, over 67,000 h of field test experience has been accumulated with CMC liners over eight years of testing at two commercial sites. The work is being conducted with the support of the U.S. Dept. of Energy under the "Ceramic Stationary Gas Turbine" and "Advanced Materials for *Mercury*™ 50 Gas Turbine Combustion System" programs, and under the "Ceramic Matrix Composites for Advanced Engine Components" program, a collaborative effort of Siemens Westinghouse Power Corporation, ATK COI Ceramics, and *Solar*® under the umbrella of the U.S. National Institute of

Contributed by the International Gas Turbine Institute (IGTI) of ASME for publication in the JOURNAL OF ENGINEERING FOR GAS TURBINES AND POWER. Manuscript received October 1, 2004; final manuscript received March 1, 2005. IGTI Review Chair: K. C. Hall. Paper presented at the ASME Turbo Expo 2005: Land, Sea, and Air, Reno, NV, June 6–9, 2005, Paper No. GT2005-68420.

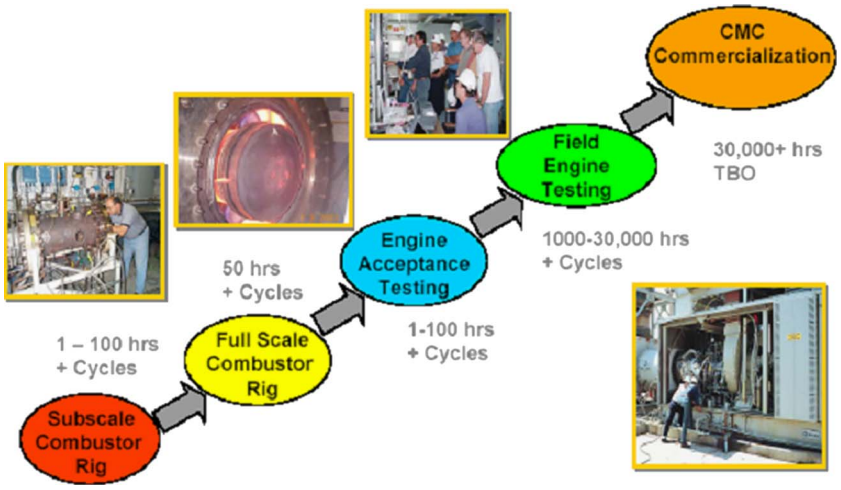

Fig. 1 Solar's ceramic combustor liner development strategy

Standards and Technology—Advanced Technology Program.

Figure 1 summarizes the steps in Solar's ceramic combustor liner development strategy, which involves sequential short term testing of promising ceramic materials and combustor designs. The test sequence includes: rig testing of subscale combustors, full scale liner tests in atmospheric and high pressure combustor rigs, and in-house and field testing in actual production engines. The rig and in-house engine tests are typically of short duration (1–100 h), and include steady state operation and thermal cycling. An in-house engine acceptance test is the final qualification for endurance testing at a field site. The ultimate field test goal is to achieve 30,000 h of operation, which is the typical time between overhaul for *Solar*® gas turbine engines.

Rig and engine testing at *Solar*® first qualified SiC/SiC CMC combustor liners for field testing in 1997. In 2003 an oxide/oxide CMC liner was qualified.

Engine Testing

Solar's *Centaur*® 50S gas turbines, which operate at a baseline TRIT of 1010°C (1850°F) and have an output power of ~4 MW, were used as the test engines for ceramic component development. These engines use the *Solar*® lean premix *SoLoNO*$_x$™ combustion technology system to limit emissions to less than 25 ppmv NO_x and 50 ppmv CO (15% O_2), respectively [4]. A schematic of the *Centaur*® 50S gas turbine engine and the hot section with combustor is shown in Fig. 2. Under the CSGT program the *SoLoNO*$_x$ combustor was redesigned to incorporate SiC/SiC CMC liners, which replaced the cylindrical, louver-cooled metallic liners in the primary zone (Fig. 2). The diameters of the outer and inner liner are 76 and 33 cm, respectively, and liner length is 20 cm (more recently, the length of the outer liner was shortened to 17.5 cm). The nominal wall thickness is in the 0.2–0.3 cm range for SiC/SiC CMCs [5,6] and 0.7 cm for oxide/oxide CMCs with FGI [7]. The liners are contained within a metallic housing that includes the upstream dome, the downstream conical sections, and metallic support cylinders. A layer of compliant insulation (Nextel) between the CMC liners and the metal cylinders mitigates radial contact stresses. Small axial gaps between the ends of the CMC cylinders and the metal housing prevent end loads. The CMC liners experience only thermal stresses from material temperature gradients. Stresses from mechanical loading have been eliminated in this design. A maximum local stress of ~76 MPa was predicted near the upstream edge of the cylinders, well within the stress limits of the SiC/SiC CMCs selected for this design [4].

In-house engine testing in the 1995–1997 time frame validated the CMC combustor liner design and short-term durability of the

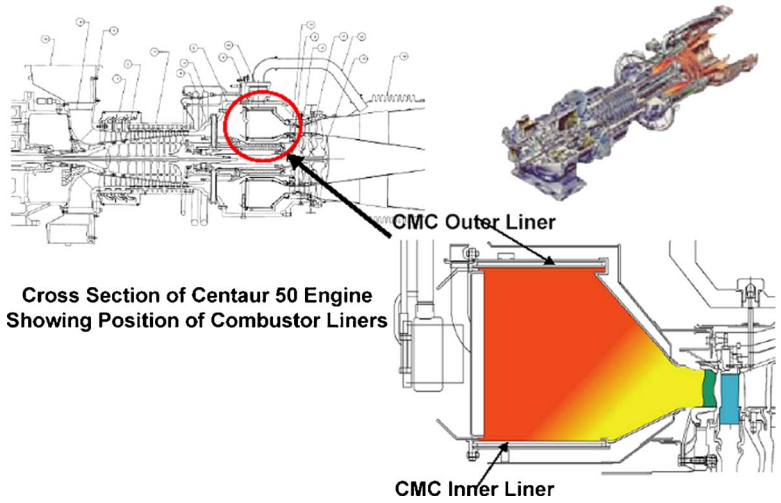

Fig. 2 Schematic of combustor with CMC liners in Solar's *Centaur*® 50S gas turbine

Fig. 3 The ChevronTexaco Bakersfield site with field test engine in package on the right

Fig. 5 CG Ni/PyC/E-SiC (CVI) liners before 100 h test

SiC/SiC CMC liners. Emissions measured during in-house testing were excellent with NO_x and CO levels typically below 15 ppmv and 10 ppmv, respectively [8].

Solar® started field testing of *Centaur*® 50S gas turbine engines with ceramic components in May 1997 at the oil exploration site of ARCO Western Energy in Bakersfield, California. Ownership of the site transferred to Texaco and subsequently to ChevronTexaco after the merger of Texaco with Chevron. Figure 3 shows the ChevronTexaco test site. For the field test the customer's *Centaur*® 50 gas turbine engine is replaced with a *Centaur*® 50S gas turbine engine fitted with CMC liners supplied by *Solar*®. The first two field tests also incorporated first-stage silicon nitride first-stage blades. A second test site, utilized from 1999 through 2003, was the Malden Mills textile factory in Lawrence, Massachusetts. The Malden Mills site has two *Centaur*® 50S gas turbine engines, both of which have been used for CMC liner testing (Fig. 4). At the Malden Mills site, the standard *SoLoNO*$_x$ combustors were replaced with pre-assembled combustors fitted with CMC liners [9,10].

The field testing of CMC liners at the two industrial end user sites through the end of 2004 is summarized in the Appendix (see Table 1). Included are also some key in-house tests at *Solar*® prior to field testing. The Appendix lists the composition of the CMC (fiber/interface coating/matrix) and of the EBCs or FGI used for protection of the CMCs in these tests, the duration of the tests, number of engine starts, and comments summarizing key lessons learned during the tests.

Engine Field Test CT-1

CMC liners with a CG-Nicalon fiber reinforcement and E-SiC CVI matrix and PyC interface coating (CG Ni/PyC/E-SiC–DLC) from a previous 100 h *Solar*® in-house test were used in the first field test at the Bakersfield site (Fig. 5) [9]. The test was halted after 948 h and 15 starts because of failure of the AS800 Si_3N_4 first-stage turbine blades, most likely resulting from impact damage by a dislodged combustor locating pin. While the liners were intact, early oxidation noted in the 100 h test by *Solar*® was much more severe after 948 h of field operation. Surface recession, evidenced by a heavy glassy deposit, was as much as 0.5 mm on the inner liner and <0.1 mm on the outer liner. Room temperature residual strength of the two liners was approximately 40–60% of the original material strength. Based on surface recession values, it was speculated that the inner liner operated at a temperature of 1260°C (2300°F) or higher. Emission levels, measured at 50–100% load operation, were <15 ppmv NO_x and <10 ppmv CO, respectively. Figure 6 shows the inner liner after the 948 h field test. Figure 7 shows representative microstructures of sections of the inner and outer liner [11].

The inner liner underwent post-test NDE (thermal diffusivity and air-coupled ultrasound) at ANL prior to destructive evaluation at ORNL. Interestingly, the degradation/recession was subsequently duplicated in simulated gas turbine environmental exposure testing at ORNL [12]. Therefore, the lower cost ORNL Keiser test rig testing can be used to cost-effectively screen candidate CMC liner systems. The environmental degradation is attributed to accelerated oxidation of SiC due to the presence of H_2O in the combustion environment [13].

Fig. 4 *Centaur*® 50S gas turbine engine at Malden Mills textile facility

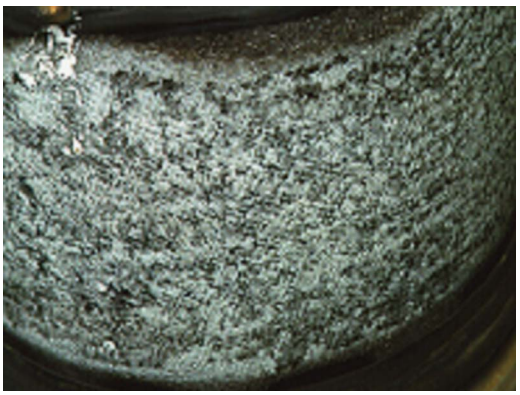

Fig. 6 CG Ni/PyC/E-SiC (CVI) inner liner after 948 h test (CT-1)

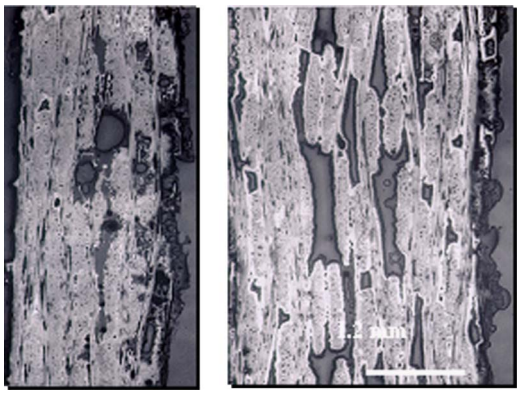

Fig. 7 Inner (left) and outer liner (right) sections after 948 h test (CT-1) [11]

Engine Field Tests CT-2 and CT-3

These two tests are discussed together since the same set of liners was used for both. Following the first field test at the Bakersfield site several changes were made to the CMC combustor liner system to reduce the oxidation of the SiC/SiC CMC liners. Design changes to the conduction path from the CMC liners to the metallic housings resulted in reduced wall temperatures for the CMC liners. Changes to the CMC liners themselves included using Hi-Nicalon fibers, which have improved strength and higher thermal conductivity, compared to the previously used CG-Nicalon fibers, increasing the CMC density, and increasing the thickness of the protective SiC CVD seal coat [5,9,14]. For CT-2 and CT-3, the inner and outer liner CMCs were HiNi/BN/E-SiC and HiNi/PyC/E-SiC (CVI matrix), respectively, supplied by DLC. The interfacial coatings were different: BN for the inner liner and PyC for the outer liner [6]. CT-2 ended after 352 h because of failure of the AS800 turbine blades. All further tests were conducted with metallic first-stage blades. The liners were re-inserted in the test engine for the subsequent CT-3 test, which was terminated after 1906 h to evaluate the oxidized versus unoxidized areas of the CMC liners. Both liners showed surface oxidation at the fuel injector impingement locations. The inner liner underwent post-test NDE (thermal diffusivity and air-coupled ultrasound) at ANL prior to destructive evaluation at ORNL. The maximum recession was approximately 0.2 mm, with a highest temperature recorded of 1175°C (2147°F). In the ORNL Keiser rig, recession of a SiC seal coat was measured as 0.05 mm/500 h. Again, as in CT-1, material degradation closely matched that encountered in simulated gas turbine environmental exposure testing at ORNL [6,11,12,14].

Engine Field Test CT-4

In this test, the HiNi SiC/PyC/E-SiC (CVI) outer liner of tests CT-2/3 was used with a new HiNi SiC/BN/SiC-Si MI liner from BFG. This was the first test with an MI inner liner. The test was conducted for a total of 2758 h with 26 starts. During an acceptance test at *Solar*®, a maximum temperature of 1260°C (2300°F) was recorded on both liners, but it was estimated that the liner temperatures during the field test were at least 20°C (36°F) lower. Following the completion of test CT-4, the outer liner had been field tested for a total of 5016 h (total exposure time including Solar's acceptance testing was 5028 h), and the inner liner had a field total of 2758 h (2762 h if the acceptance test is included) [6]. Digital photographs of the liner set following completion of the field test are shown in Fig. 8 [5,10,15].

The HiNi/BN/SiC-Si MI inner liner appeared in better condition than both the CVI inner and outer SiC/PyC, BN/SiC CMC liners after the completion of test CT-3. The outer liner was heavily degraded, having lost about 80% of its wall thickness in certain areas. The residual tensile strength of the liner was about 50% of the original material strength at room temperature and 1200°C (2192°F). Fiber pullout was still observed on specimen fracture surfaces, indicating composite behavior of the material, even after 5028 h of engine exposure [5,6,10,15]. Because of the unacceptable degradation, it appears that 5000 h is the approximate durability limit for HiNi/PyC/E-SiC CVI CMC liners in the *Centaur*® 50S gas turbine hot section. To increase life significantly, it was decided to apply protective environmental barrier coatings in subsequent engine field tests.

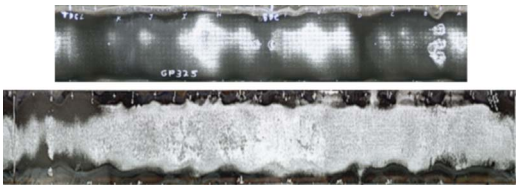

Fig. 8 Digital photographs of HiNi SiC/PyC/E-SiC (CVI) outer liner (top) and HiNi SiC/BN/SiC-Si (MI) inner liner (bottom) after 5016 field test hours (CT-4) [5,10,15]

Engine Field Test CT-5

A new set of liners was fabricated by ACI, which had acquired DLC in 1998, for the fifth field test at the Bakersfield site. The compositions were HiNi/BN/SiC-Si (MI) and HiNi/PyC/E-SiC (CVI), for the inner and outer liners, respectively. The CMC liners were protected with EBCs supplied by UTRC. The EBC, a three-layer coating system with composition Si/mullite+(BSAS)/BSAS, deposited by air plasma spray, was originally developed under the NASA Enabling Propulsion Materials (EPM) program, and optimized for the CSGT program [5,6,10,16]. Each coating layer is nominally 125 μm thick. The liner set prior to testing is shown in Fig. 9, and a micrograph of the basic EBC in Fig. 10 [17]. The EBC for the inner liner had the basic Si/mullite/BSAS composition. The outer liner EBC had a mixture of mullite and BSAS in the intermediate layer.

The field test was conducted between April 1999 and November 2000. Periodic borescope inspections showed degradation of the EBC and underlying substrate, but the liners remained functional until a borescope inspection at 13,937 h/61 starts revealed a breach of the inner liner CMC (see Fig. 11) [5,18,19]. The engine was subsequently shut down and sent to *Solar*® for teardown and inspection. Figures 12(*a*) and 12(*b*) are digital photographs of the inner and outer liners, respectively, after the engine test. There is heavy degradation of the EBC and of the underlying CMCs in areas where the EBC had debonded. Notwithstanding the degradation, it is evident that the EBC had provided signifi-

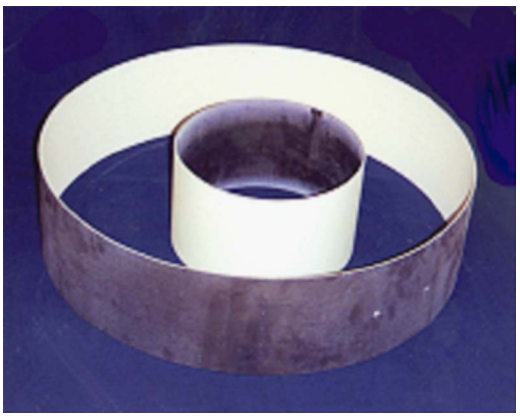

Fig. 9 CMC liner set with EBC for field test CT-5 [5,6,10,16]

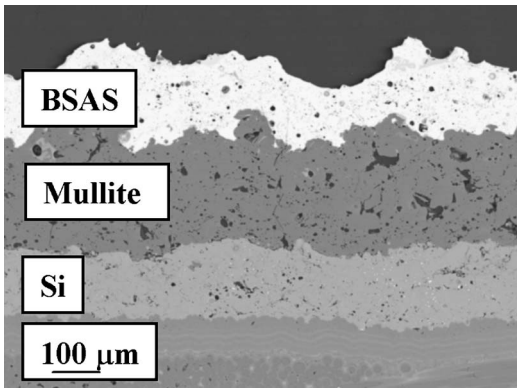

Fig. 10 Basic EBC microstructure [17]

cant protection to the CMCs with most of the surfaces fully intact, thereby extending their useful life by a factor of 2–3. Post-test evaluation showed the mixed layer EBC (mullite+BSAS intermediate layer) on the outer CMC liner to be more protective than the EBC with the single mullite intermediate layer on the inner CMC liner [17]. This observation correlated with the results of specimen testing in the ORNL Keiser rig under simulated gas turbine conditions that showed that the SiO_2 layer formed on Si was 5× thicker for Si/mullite/BSAS than that formed for Si/mullite +BSAS/BSAS [17]. The reduced rate of SiO_2 formation was attributed to the absence of excessive microcracking in the mixed-layer EBC, and therefore less oxygen ingress to the Si layer, compared to the Si/mullite/BSAS baseline.

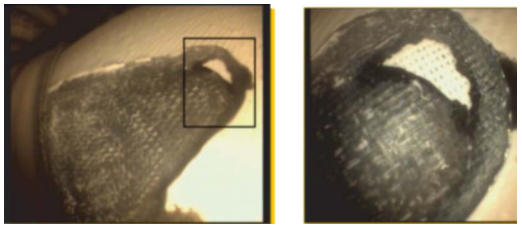

Fig. 11 Breach in HiNi SiC/BN/SiC-Si (MI) inner liner after 13,937 h test [5,18]

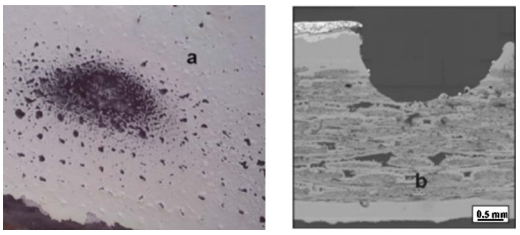

Fig. 13 Pitting on the HiNi SiC/PyC/E-SiC (CVI) outer liner (*a*) Area A in Fig. 12(*a*) [19], (*b*) pitting microstructure after 13,937 h test (CT-5) [17]

Extensive NDE was conducted on the liners as part of pre- and post-test materials evaluation. The purpose of the NDE is twofold: (1) detecting defects in the as-received liner CMC, before and after EBC application, prior to field testing, and (2) obtain information on liner CMC and EBC degradation upon completion of the field test, or after interim engine teardowns. Figure 12(*c*) is a thermal diffusivity NDE scan of the inner liner prior to the engine field test [5]. Note that there are low diffusivity areas that coincide with areas of degradation on the digital photographs (Fig. 12(*b*)). The NDE suggests possible defects at the inner liner EBC-CMC interface, which subsequently could have led to debonding of the EBC from the substrate.

Other modes of degradation with time included: (1) pitting near surface asperities from processing tooling marks (Figs. 13(*a*) and 13(*b*)), (2) surface recession of the BSAS topcoat (which was more severe for the highest temperature regions of the EBC, eventually resulting in localized removal of the BSAS), (3) phase separation of the mullite ($3Al_2O_3.2SiO_2$) intermediate layer into Al_2O_3 and SiO_2 upon exposure to the combustion environment following BSAS removal, and (4) oxidation of the EBC Si bond coat [17]. It was noted that EBC spallation tends to occur at the interface of the SiO_2 layer formed through oxidation of the Si, and the mullite intermediate layer [17]. It was observed that regions of the BSAS topcoat that were most heavily degraded were enriched in strontium aluminum silicate (SAS), suggesting that the Sr phases were more stable [17].

As was observed for the previous tests, there was significant loss of strength in the CMC/EBC system. Residual tensile strength at room temperature of specimens sectioned from the liner after

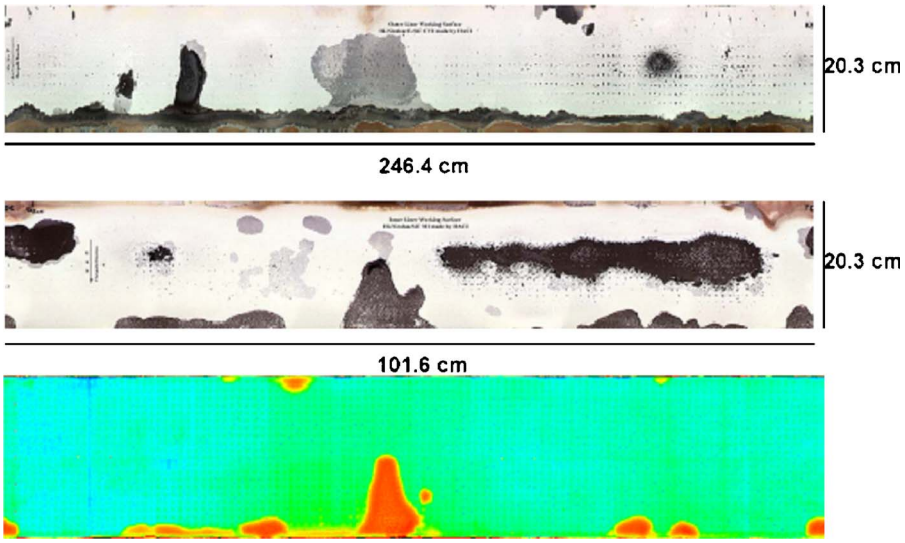

Fig. 12 Liners after 13,937 h test, (*a*) HiNi SiC/PyC/E-SiC (CVI) outer liner, (*b*) HiNi SiC/BN/SiC-Si (MI) inner liner, (*c*) thermal diffusivity scan of inner liner before test [5,6,18,19]

Fig. 14 Digital photographs of (*a*) HiNi/BN/SiC-Si (MI) inner liner and (*b*) HiNi/PyC/E-SiC (CVI) outer liner after 7238 h field test (MM-1) [5,18]

the 13,937 h test was 40–60% of the original material strength, depending on the extent of oxidation [19]. Interestingly, mechanical analysis at ORNL established that even sections of field tested liners for which the CMC and EBC appeared to be in good condition had significantly lower strength compared to the as-received component CMC, presumably because of oxidative degradation of the CMC constituents [20].

Engine Field Tests MM-1 and CT-6

The first test at the Malden Mills site was the second test in which the CMC liners were protected with EBCs. The outer liner CMC was a HiNi/PyC/E-SiC (CVI) from ACI and the inner liner CMC was a HiNi/BN/SiC-Si (MI) from BFG. The EBC was Si/mullite+BSAS/BSAS, similar to the EBC on the outer liner CMC in the CT-5 engine field test. This mixed-layer EBC was selected because it provided better protection than the baseline Si/mullite/BSAS EBC. The test was terminated in October 2000 after 7238 h and 159 starts due to an engine problem not associated with the CMC liners. Composite digital photographs of inner and outer liner are shown in Fig. 14 [5,18]. The outer liner had significantly more EBC spallation than the inner liner [18]. The CMCs were in relatively good condition since the EBCs had been largely protective, and a decision was made to strip the EBCs from the CMC liners, recoat the CMC liners with new EBCs, and resume liner testing [19,21]. The refurbished EBC for the outer liner was similar to that for the MM-1 test, but the inner liner had a Si/BSAS EBC, to evaluate if the mullite layer could be eliminated which would simplify the EBC application process.

The refurbished liners were field tested for an additional 5135 h at the Bakersfield site between September 2001 and May 2002, to give a cumulative total of 12,373 h and 202 starts. The liners in the combustor housing after teardown at *Solar*® are shown in Fig. 15. There was EBC degradation for both liners, but the localized degradation of the inner liner was more severe, possibly because of a eutectic reaction between the SiO_2 oxidation product from the Si bond coat and the BSAS layer at the higher temperature areas of the inner liner [22]. The presence of mullite in the intermediate layer prevents the eutectic reaction, and its incorporation into the EBC is therefore beneficial.

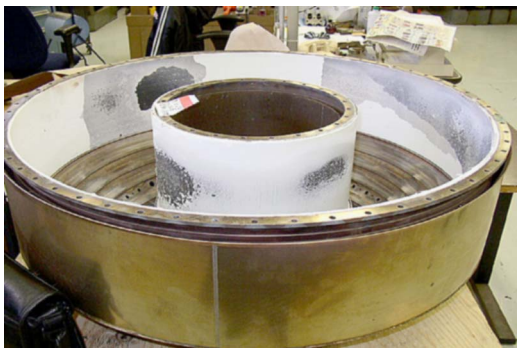

Fig. 15 Liners of MM-1 field test after additional 5135 h field test (CT-6); total test time: 12,373 h (CT-6)

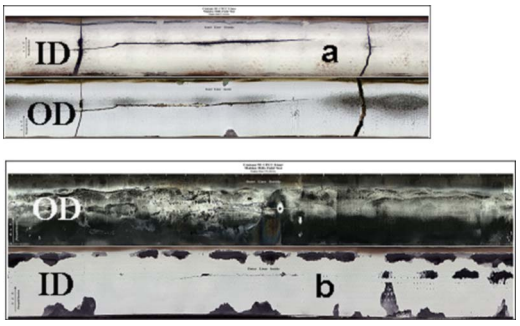

Fig. 16 Digital photographs of (*a*) TyZM/BN/SiC-Si (MI) inner liner and [23], (*b*) HiNi/PyC/SiC (CVI) outer liner after 15,144 h field test (MM-2); ID/OD: inner/outer diameter

Engine Field Test MM-2

This test, conducted between August 2000 and July 2002, was the longest to date with 15,144 h and 92 starts. The outer liner CMC was HiNi/PyC/E-SiC (CVI) from HACI (the successor to ACI in 1999 after the merger of AlliedSignal with Honeywell), while the inner liner was a TyZM/BN/SiC-Si (MI) liner from BFG. This was the first test in which the Hi-Nicalon fiber in the inner liner was replaced with the less expensive Tyranno ZM fiber. A SiC seal coat had been applied to both liners. The SiC seal coat is a dense surface coat that slows down ingress of oxidative species into the underlying more porous CMC. Both liners had the mixed-layer Si/mullite+BSAS/BSAS EBC [23].

The MM-2 field test was stopped because of circumferential and lateral cracks in the inner liner that had progressed through the CMC thickness (Fig. 16). While the EBC was still present on the majority of the liner surface, there was severe EBC degradation in the hottest areas, in close proximity to the fuel injectors. Aft edge spallation of the EBC observed in previous tests (e.g., Fig. 12, outer liner) was less, presumably because the EBC was also applied to the edges of the liners for this test. There was extensive oxidation and surface recession on the cold-side (ID) surfaces of the inner liner. The cracking of the inner liner matched areas of high thermal diffusivity in NDE scans. The high thermal diffusivity, which correlates with high thermal conductivity, and therefore higher temperatures, on the cold side of the liner, was attributed to CMC liner processing variations, localized higher density, lower thickness, or higher Si concentration. The higher temperature can be expected to accelerate the degradation on the cold side of the liner. Additionally, the circumferential cracking, which became apparent during borescoping early on in the test, could have resulted in the ingress of hot combustion gases into the liner, and subsequently accelerated degradation throughout the bulk and surfaces of the CMC. Microstructural evaluation clearly showed the presence of a SiO_2 oxidation layer at the (Si/mullite +BSAS) interface (Fig. 17). Surface recession of the BSAS layer and phase separation of mullite in the mixed intermediate layer was also observed. The Tyranno ZM fiber in the inner liner CMC showed no degradation in areas where the fiber was protected. This indicated that the less expensive Tyranno ZM fiber performed similarly to the Hi-Nicalon fiber under the conditions of the field test [23].

Engine Field Test MM-3

The most recent test, conducted between July 2002 and July 2003 at the Malden Mills site, was the first test in which both inner and outer liner CMC had been processed by melt infiltration. The TyZMI/BN/SiC-Si CMC incorporated the Tyranno ZMI fiber of Ube Industries, Ltd. Both liners had been fabricated by GE Power Systems Composites (PSC), which had acquired HACI in 2001. The details of this field test have been reported [24]. Degradation on the cold side of these liners was severe, presumably

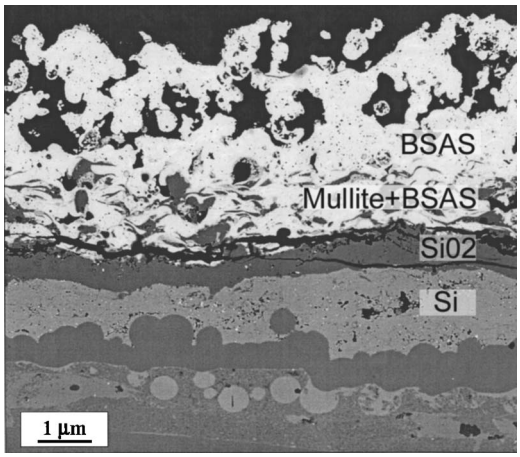

Fig. 17 SiO_2 layer on EBC at the (Si/Mulllite+BSAS) interface; inner liner after 15,144 h test [23]

because no SiC seal coat had been applied (potential cost saving from CMC processing simplification). The absence of a SiC seal coat exposes the porosity of the CMC, leading to significant oxidative degradation. The EBC had been modified from previous tests by replacing the BSAS with SAS, because steam rig testing at UTRC had shown SAS to degrade less than BSAS [24]. The EBC compositions used were Si/SAS for the inner liner and Si/mullite+SAS/SAS for the outer liner. Borescoping at the 3174 h mark indicated significant spallation of the SAS topcoat on the inner liner. The degradation of the Si/SAS liner EBC resulted in termination of the field test after 8368 h and 32 starts. The liner set after the test is shown in Fig. 18. It was concluded that the dual layer Si/SAS EBC was unstable. Interestingly, the low stability of the Si/SAS EBC parallels that of the dual-layer Si/BSAS EBC in the CT-6 field test. Visual inspection indicated the EBC on the outer liner to be in good condition. However, microscopy revealed significant degradation of the SAS topcoat and SiO_2 depletion in the mixed (mullite+SAS) interlayer of the outer liner EBC. The results of the MM-3 field test did not corroborate the favorable results of the steam rig testing at UTRC. Further optimization of the Si/mullite+SAS/SAS process will be required to take advantage of the lower surface recession of SAS compared to BSAS.

Engine Field Test CT-7

A field test was initiated in 2003 at the ChevronTexaco Bakersfield site to evaluate an oxide/oxide CMC outer liner that had been developed under an Advanced Technology Program project of the U.S. National Institute of Standards and Technology. The project was a collaboration among Siemens Westinghouse Power Corp., ATK COI Ceramics, and *Solar*®. Under this program, an outer liner had been fabricated based on a hybrid of an Al_2O_3/Al_2O_3 CMC with a thermally protective friable graded insulation surface coating. The FGI, which has an aluminosilicate composition and enables operation at high turbine inlet temperatures, can significantly lower the temperature of the underlying oxide/oxide CMC

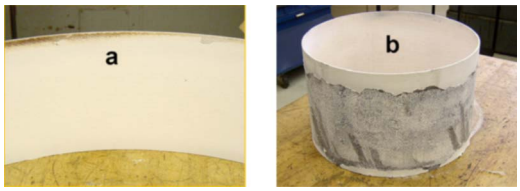

Fig. 18 TyZMI/BN/SiC-Si (MI) outer liner (*a*) and inner liner (*b*) after 8368 h field test (MM-3)

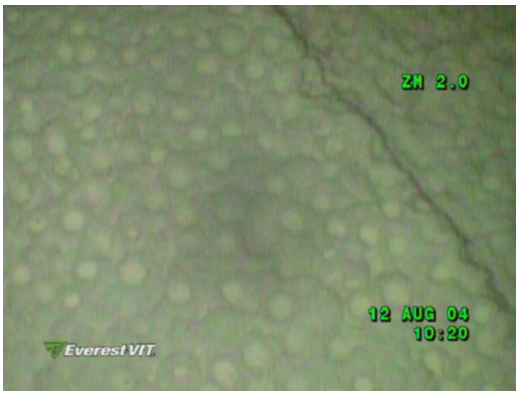

Fig. 19 Borescope image of oxide/oxide CMC outer liner with FGI after 10,667 h and 61 starts of engine test CT-7

substrate. In a high-pressure rig test at *Solar*® under the NIST ATP project the temperature gradient over the outer liner reached ~611°C (~1100°F). The maximum outer liner surface temperature was ~1149°C (~2100°F). The combustor primary zone temperature was ~1538°C (~2800°F). Actual liner temperatures were not measured during engine testing but a temperature gradient profile similar to that in the high-pressure rig test can be expected. The development of the hybrid CMC technology has been reported [7]. The inner liner in this test was a HiNi/BN/E-SiC (CVI) CMC, fabricated in the 1998–1999 time frame by DLC/ACI. An oxide/oxide CMC inner liner was not available at the time of the test.

In mid 2003, at the conclusion of the NIST ATP project, the liners had been tested for over 1000 h. Since borescoping showed the outer liner to be in excellent condition, the NIST program participants and the DOE agreed to continue the field testing under the DOE-sponsored Advanced Materials program. Figure 19 is a borescope image of the outer liner taken after 10,667 h/61 starts of engine operation showing the FGI surface. The diagonal line represents a step in the FGI thickness to accommodate the liner attachment. The inner liner showed significant EBC degradation at borescope inspections at 5885 h and 10,667 h, as expected from a CVI SiC/SiC CMC with an early vintage EBC.

A total of 12,582 h and 63 starts had accumulated when the test was halted in November 2004, for an intermediate engine teardown and visual and NDE inspection of the CMC liners. Inspection of the oxide/oxide outer liner after the 12,582 h field test showed minor localized damage: a few loose tows at the cold (OD) side, minor spallation of the FGI at the aft end of the liner, and some erosion of the FGI at the liner hot spots. ATK COI Ceramics repaired the outer liner by tying down the loose CMC tows, and applying FGI patches to the spalled area and one of the eroded hot spot areas. Figure 20 shows the oxide/oxide outer liner with FGI after repair ready for continued field testing. The dark areas near the liner edge are the result of contact with the metal housing. The field test is scheduled to resume in January. 2005. The inner liner is being replaced with a HiNi/BN/SiC-Si (prepreg MI) CMC liner with Si/mullite+BSAS/BSAS EBC fabricated by PSC and GRC.

Future Development

Continued field testing of CMC combustor liners is planned under the DOE Advanced Materials program. The objective is to achieve a significant increase in operating hours towards a goal of 30,000 h, the customary target time between overhaul (TBO) for *Solar*® industrial gas turbines. The field testing will enable an evaluation of improvements in SiC/SiC and oxide/oxide CMCs, and in EBCs and FGIs for surface protection.

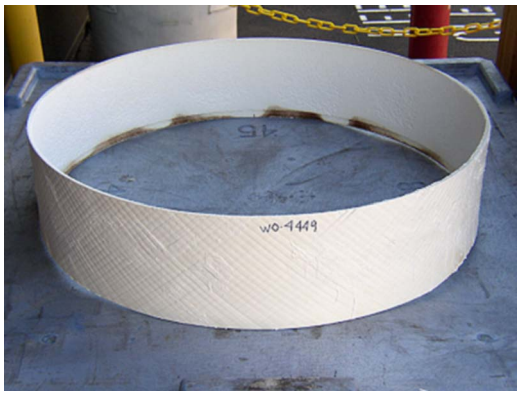

Fig. 20 Repaired oxide/oxide CMC liner with FGI prior to continuation of the field test

Summary

Over 67,000 h of operating experience have been acquired from field testing of CMC combustor liners since 1997 in Solar's *Centaur*® 50S gas turbine engines. Test durations of 15,144 and 13,937 h have been logged for SiC/SiC CMC liners with protective EBCs. An oxide/oxide CMC liner with FGI protective coating has been tested for 12,582 h. NO_x and CO emissions were <15 ppmv and <10 ppmv, respectively. In the absence of EBCs, MI SiC/SiC liners are more durable than CVI SiC/SiC liners. Ceramic oxide-based environmental barrier coatings improve SiC/SiC CMC liner life by a factor of 2–3. The durability of the baseline Si/mullite/BSAS is enhanced by mixing in BSAS with mullite in the intermediate coating layer. Microstructural analysis of tested liners indicated enhanced durability of a Sr-rich phase in the EBC topcoat, but the replacement of BSAS with SAS did not appear to have improved EBC durability. Heavy degradation of Si/BSAS and Si/SAS EBCs indicates that the elimination of the intermediate layer is detrimental to EBC durability. Equivalent CMC performance was observed when the Hi-Nicalon was replaced with Tyranno ZM or ZMI fibers. Melt infiltrated SiC/SiC CMCs have improved durability compared to SiC/SiC CMCs fabricated by Chemical Vapor Infiltration of the matrix, in the absence of an EBC. However, the presence of an EBC results in roughly equivalent service life for MI and CVI CMCs. An oxide/oxide CMC with protective FGI shows relatively minor degradation under *Centaur*® 50S engine operating conditions. EBC refurbishment for SiC/SiC CMCs, and FGI repair for oxide/oxide CMCs are being investigated to increase liner life. Continued field testing is planned to further evaluate CMCs, EBCs, and FGIs for improved combustor liner durability.

Acknowledgment

The work for this summary paper was conducted under DOE Contract No. DE-AC02-92CE40960, DOE cooperative agreement No. DE-FC26-00CH11049, and NIST cooperative agreement No. 70NANB9H3037. The authors gratefully acknowledge the guidance and support of staff from the DOE and NIST in the performance of the referenced government contracts. The authors also wish to express their appreciation to the suppliers of ceramic matrix composite liners, and to United Technologies Research Center, Oak Ridge National Laboratory, and Argonne National Laboratory with the development and evaluation of SiC/SiC CMCs and environmental barrier coatings, and to Siemens Westinghouse Power Corp., and ATK COI Ceramics with the development of oxide/oxide CMC liners with the FGI coating. The collaboration of the gas turbine end users: ChevronTexaco, Texaco, and ARCO, and Malden Mills Industries is also acknowledged.

Nomenclature

ACI	=	AlliedSignal Composites, Inc.
Al_2O_3	=	alumina
Al_2O_3/Al_2O_3	=	alumina/alumina CMC
ANL	=	Argonne National Laboratory
ARCO	=	Atlantic Richfield Corporation
AS800	=	silicon nitride from Honeywell Ceramic Components
ASME	=	American Society of Mechanical Engineers
ATP	=	Advanced Technology Program of NIST
BFG	=	BF Goodrich Aerospace (currently Goodrich Corp.)
BN	=	boron nitride fiber-matrix interface coating
BSAS	=	barium strontium aluminum silicate
Centaur® 50S	=	Solar's *Centaur*® 50 gas turbine with *SoLoNO$_x$* combustor
CG-Nicalon	=	ceramic grade Nicalon SiC fibers of Nippon Carbon Company
CMC	=	ceramic matrix composite
CO	=	carbon monoxide
COIC	=	ATK COI Ceramics
CSGT	=	Ceramic Stationary Gas Turbine
CT	=	field tests conducted at ARCO, Texaco, and ChevronTexaco, Bakersfield, California
CVD	=	chemical vapor deposition
CVI	=	chemical vapor infiltration
DLC	=	DuPont Lanxide Composites Inc.
DOE	=	U.S. Department of Energy
EBC	=	environmental barrier coating
E-SiC	=	enhanced-SiC CVI matrix in DLC CMCs
FGI	=	friable graded insulation
GE	=	General Electric Company
GRC	=	GE Global Research Center
HACI	=	Honeywell Advanced Composites, Inc.
H_2O	=	water
Hi-Nicalon, HiNi	=	Hi-Nicalon grade SiC fibers of Nippon Carbon Company
ID	=	inner diameter
Malden Mills	=	Malden Mills Industries, Lawrence, Massachusetts
K_{1C}	=	fracture toughness
MI	=	melt infiltration
MM	=	field tests conducted at Malden Mills
MPa	=	megapascal
MW	=	megawatt
NASA	=	National Aeronautics & Space Administration
NDE	=	nondestructive evaluation
NO_x	=	oxides of nitrogen
Nextel™	=	fibrous materials supplied by 3M™
NIST	=	National Institute of Standards and Technology
OD	=	outer diameter
ORNL	=	Oak Ridge National Laboratory
oxide/oxide	=	CMC with oxide fiber and oxide matrix
ppmv	=	parts per million by volume
PSC	=	GE Power Systems Composites
PyC	=	pyrolytic carbon fiber-matrix interface coating
SAS	=	strontium aluminum silicate
SCG	=	slow crack growth
Si	=	silicon
SiC	=	silicon carbide
SiC/SiC	=	CMC with SiC fiber reinforcement and SiC matrix

Table 1 Summary of combustor linear engine tests

Time (Refs.)	Site/Test	Hrs (Starts)	Liner CMCs, EBCs	Comments
10/95 [3,4]	*Solar*®	18 (10)	3D CG Ni SiC/PyC/SiC CVI (BFG)	First CMC liner engine test Validated design <15 ppmv NO_x (15% O_2)
4/97 [3,9]	*Solar*®	~100 (27)	CG Ni SiC/PyC/E–SiC CVI SiC seal coat (DLC)	Qualified CMC liners for field testing
5/97–7/97 [3,5,9,11–13]	CT-1	948 (15)	CG Ni SiC/PyC/E–SiC CVI SiC seal coat (DLC)	First CMC field test <15 ppmv NO_x, <10 ppmv CO CMC degradation/surface recession ORNL Keiser rig duplicates CMC degradation/surface recession in *Solar*® engine tests
2/98–3/98 [5,6,9,14]	CT-2	352 (31)	*Inner Liner*- HiNi SiC/BN/E–SiC CVI *Outer Liner*-HiNi SiC/PyC/E–SiC CVI SiC seal coat (DLC)	Improved (HiNi) fiber Improved conduction path
5/98–8/98 [6,11,12,14]	CT-3	1906(46)		5016 h on outer liner First test with MI inner liner
12/98–4/99 [5,6,10,15]	CT-4	2758 (26)	*Inner Liner*-HiNi SiC/BN/SiC–Si MI SiC seal coat (BFG) *Outer Liner*-HiNi/PyC/E–SiC CVI SiC seal coat (DLC)	MI CMCs degrade less than CVI CMCs
4/99–11/00 [5,6,10,16–19]	CT-5	13,937 (61)	*Inner Liner*-HiNi SiC/BN/SiC–Si MI SiC seal coat (ACI) Si/mullite/BSAS EBC (UTRC) *Outer Liner*-HiNi SiC/PyC/E–SiC CVI SiC seal coat (ACI) Si/mullite+BSAS/BSAS (mixed-layer) EBC (UTRC)	First test with EBCs 2–3× improved liner life NDE: EBC defects-correlate with inner liner degradation Degradation of outer liner EBC at surface asperities BSAS surface degradation Mullite phase separation Mixed-layer EBC superior
8/99–10/00 [18,19]	MM-1	7238 (159)	*Inner liner*-HiNi/BN/SiC–Si MI SiC seal coat (BFG) Si/mullite+BSAS/BSAS EBC (UTRC) *Outer liner*-HiNi/PyC/E–SiC CVI SiC seal coat (ACI) Si/mullite+BSAS/BSAS EBC (UTRC)	EBC in good condition following test EBC stripped and refurbished for CT-6 test
9/01–5/02 [19,21]	CT-6	5135 (43)	*Inner liner*-HiNi/BN/SiC–Si MI SiC seal coat (BFG) Si/BSAS EBC (UTRC) *Outer liner*-HiNi/PyC/E–SiC CVI SiC seal coat (ACI) Si/mullite+BSAS/BSAS EBC (UTRC)	Same liners as in MM-1 Test with refurbished EBC 12,373 h/202 starts total on CMCs Accelerated degradation of two-layer Si/SAS EBC
8/00–7/02 [23]	MM-2	15,144 (92)	*Inner liner*-TyZM/BN/SiC–Si MI SiC seal coat (BFG) Si/mullite+BSAS/BSAS EBC (UTRC) *Outer liner*-HiNi/PyC/E–SiC CVI SiC seal coat (HACI) Si/mullite+BSAS/BSAS EBC (UTRC)	Longest field test to date Use less expensive Tyranno ZM fiber EBC application on liner edges
7/02–7/03 [24]	MM-3	8368 (32)	*Inner liner*-TyZMI/BN/SiC–Si MI (HACI) Si/SAS EBC (UTRC) *Outer liner*-TyZMI/BN/SiC–Si MI (HACI) Si/mullite+SAS/SAS EBC (UTRC)	Less expensive Tyranno ZMI fiber First test with SAS EBC No CVD seal coat Two-layer Si/SAS EBC: heavy degradation Mixed layer EBC: good condition Heavy degradation on cold side liners
5/03–11/04 [7]	CT-7	12,582 (63)	*Inner liner*-HiNi/BN/E–SiC CVI SiC seal coat (ACI) Si/mullite/BSAS EBC (UTRC) *Outer liner*-Al_2O_3/Al_2O_3, Aluminosilicate FGI (COIC/SWPC)	First test on oxide/oxide CMC with FGI Oxide/oxide-CMC and FGI in relatively good condition Continued testing planned with new HiNi SiC/BN/SiC–Si MI inner liner

Note: Hours shown for field tests do not include engine acceptance testing at *Solar*®.

Si_3N_4 = silicon nitride
SiO_2 = silicon dioxide
Solar® = Solar Turbines Incorporated
SoLoNO$_x$™ = Solar's lean-premixed, dry, low NO_x combustion system
SWPC = Siemens Westinghouse Power Corporation
TRIT = turbine rotor inlet temperature
TyZM(I) = Tyranno ZM(I) SiC fibers of Ube Industries, Ltd.
UTRC = United Technologies Research Center

Appendix: Summary of Combustor Liner Engine Tests

See Table 1.

References

[1] 2002, "Ceramic Gas Turbine Design and Test Experience," *Progress in Ceramic Gas Turbine Development*, Vol. I, M. van Roode, M. K. Ferber, and D. W. Richerson, eds., ASME Press, New York.
[2] 2003, "Ceramic Gas Turbine Component Development and Characterization," *Progress in Ceramic Gas Turbine Development*, Vol. II, M. van Roode, M. K. Ferber, D. W. Richerson, eds., ASME Press, New York.
[3] Brentnall, W. D., van Roode, M., Norton, P. F., Gates, S., Price, J. R., Jimenez,

O., and Miriyala, O., 2002, "Ceramic Gas Turbine Development at Solar Turbines Incorporated," *Progress in Ceramic Gas Turbine Development*, Vol. I, M. van Roode, M. K. Ferber, and D. W. Richerson, eds., ASME Press, New York, Chap. 7, pp. 155–192.
[4] Smith, K., and Fahme, A., 1997, "Testing of a Full Scale, Low Emissions, Ceramic Gas Turbine Combustor," ASME Paper No. 97-GT-156.
[5] van Roode, M., and Price, J. R., 2000, "Ceramic Stationary Gas Turbine Program Overview," ATS Annual Program Review Meeting, Washington, D.C. December 4–6.
[6] Miriyala, N., Fahme, A., and van Roode, M., 2001, "Ceramic Stationary Gas Turbine Development—Ceramic Matrix Composite Component Development Summary," ASME Paper No. 2001-GT-0512.
[7] Szweda, A., Butner, S., Ruffoni, J., Bacalski, C., Layne, J., Morrison, J., Merrill, G., van Roode, M., Fahme, A., Leroux, D., and Miriyala, N., 2005, "Development and Evaluation of Hybrid Oxide/Oxide Ceramic Matrix Composite Combustor Liners," ASME Paper No. GT2005–68496.
[8] van Roode, M., Brentnall, W. D., Smith, K. O., Edwards, B. D., McClain, J., and Price, J. R., 1996, "Ceramic Stationary Gas Turbine Development Program—Fourth Annual Summary," ASME Paper No. 97-GT-317.
[9] Price, J. R., Jimenez, O., Faulder, L., Edwards, B., and Parthasarathy, V., 1999, "Ceramic Stationary Gas Turbine Development Program—Fifth Annual Summary," ASME J. Eng. Gas Turbines, Power, **121**(4), pp. 586–592.
[10] Price, J. R., Jimenez, O., Parthasarathy, V., Miriyala, N., and Leroux, D., 2000, "Ceramic Stationary Gas Turbine Development Program—Seventh Annual Summary," ASME Paper No. 2000-GT-0075.
[11] Miriyala, N., Simpson, J. F., Parthasarathy, V. M., and Brentnall, W. D., 1999, "The Evaluation of CFCC Liners After Field-Engine Testing in a Gas Turbine," ASME Paper No. 99-GT-395.
[12] More, K. L., Tortorelli, P. F., Ferber, M. K., Walker, R. L., Keiser, J. R., Brentnall, W. D., Miriyala, N., and Price, J. R., 1999, "Exposure of Ceramics and Ceramic Matrix Composites in Simulated and Actual Combustor Environments," ASME Paper No. 99-GT-292.
[13] Jacobson, N. S., 1993, "Corrosion of Silicon-Based Ceramics in Combustion Environments," J. Am. Ceram. Soc., **76**(1), pp. 3–28.
[14] Price, J. R., Jimenez, O., Parthasarathy, V., and Miriyala, N., 1999, "Ceramic Stationary Gas Turbine Development Program-Sixth Annual Summary," ASME Paper No. 99-GT-351.
[15] Miriyala, N., and Price, J. R., 2000, "The Evaluation of CFCC Liners After Field-Engine Testing in a Gas Turbine—II," ASME Paper No. 2000-GT-0648.
[16] Eaton, H., Linsey, G., More, K., Kimmel, J., Price, J., and Miriyala, N., 2000, "EBC Protection of SiC/SiC Composites in the Gas Turbine Combustion Environment," ASME Paper No. 2000-GT-0631.
[17] More, K. L., Tortorelli, P. F., Walker, L. R. W., Kimmel, J. B., Miriyala, N., Price, J. R., Eaton, H. E., Sun, E. Y., and Linsey, G. D., 2002, "Evaluating Environmental Barrier Coatings on Ceramic Matrix Composites after Engine and Laboratory Exposures," ASME Paper No. GT-2002-30630.
[18] Price, J., Jimenez, O., Miriyala, N., Kimmel, J. B., Leroux, D. R., and Fahme, T., 2001, "Ceramic Stationary Gas Turbine Development Program—Eighth Annual Summary," ASME Paper No. 2001-GT-517.
[19] Miriyala, N., Kimmel, J., Price, J., More, K., Tortorelli, P., Eaton, H., Linsey, G., and Sun, E., 2002, "The Evaluation of CFCC Liners After Field Testing in a Gas Turbine III," ASME Paper No. GT-2002-30585.
[20] More, K., and Lara-Curzio, E., ORNL, personal communications.
[21] Eaton, H. E., Linsey, G. D., Sun, E. Y., More, K. L., Kimmel, J. B., Price, J. R., and Miriyala, N., 2001, "EBC Protection of SiC/SiC Composites in the Gas Turbine Combustion Environment—Continuing Evaluation and Refurbishment Considerations," ASME Paper No. 2001-GT-0513.
[22] Lee, K. N., Fox, D. S., Eldridge, J. I., Zhu, D., Robinson, R. C., Bansal, N. P., and Miller, R. A., 2003, "Upper Temperature Limit of Environmental Barrier Coatings Based on Mullite and BSAS," J. Am. Ceram. Soc., **86**(8), pp. 1299–1306.
[23] Kimmel, J., Sun, E., Linsey, G. D., More, K., Tortorelli, P., and Price, J., 2003, "The Evaluation of CFCC Liners After Field Testing in a Gas Turbine IV," ASME Paper No. GT20-3-38920.
[24] Kimmel, J., Price, J., More, K., Tortorelli, P., Bhatia, T., and Linsey, G., 2005, "Evaluation of CFCC Liners With EBC in a Gas Turbine," ASME Paper No. GT2005-68961.

Combustion Instabilities and Control of a Multiswirl Atmospheric Combustor

Tongxun Yi

Ephraim J. Gutmark

Department of Aerospace Engineering and Engineering Mechanics, University of Cincinnati, Cincinnati, OH 45220-0070

Thermoacoustic instability and lean blowout (LBO) are investigated experimentally in an atmospheric swirl-stabilized combustor fueled with gaseous propane. Factors affecting combustion instability are identified. Sinusoidal or steady air forcing of either the swirling air shear layer or the fuel line, with less than 1.0% of combustion air, can reduce pressure oscillations amplitude by more than 20 dB. *Phase-shifted close-loop air forcing of the flame can reduce the pressure oscillations amplitude by* 13 dB. *For a constant air flow rate and air inlet temperature, initially smooth turbulent combustion exhibits relatively intense heat release oscillations with decreasing equivalence ratio, followed by a quiet state before blowout. High outer swirl intensity and a rich burning flame stabilization region can effectively extend the LBO limit.* [DOI: 10.1115/1.2181595]

1 Introduction

Increasingly strict emission regulations have a significant effect on the gas turbine combustion technology. Lean premixed (LP) combustion or direct injection of fuel into strong swirling flow generates very low emissions, including NO_x, CO, and unburned hydrocarbon (UHC), due to relatively low flame temperature. However, LP combustion is more susceptible to both dynamic and static instabilities than a diffusion flame. Dynamic instability refers to strong pressure pulsations due to positive coupling between pressure and heat release rate [1]. Historically, dynamic instability was first observed in rich burning devices, such as afterburners, rockets, and ramjets. In such devices, the flame is usually stabilized by backward-facing steps or bluff bodies. In recent years, considerable attention has been shifted to LP combustion in gas turbine engines where the flame is stabilized by the recirculating vortex breakdown. Compared to conventional gas turbine combustors, LP combustors do not have many cooling holes and much secondary air flow, so the acoustic damping is small. LP flames are also more likely to form large-scale uniform heat release responses to external disturbances such as velocity or pressure oscillations. To achieve the lowest possible NO_x generation, gas turbine engines may be required to operate just above the lean blowout limit. Thus, the engines are increasingly exposed to the danger of LBO, leading to the need of LBO extension.

Random oscillations of the heat release rate are among the typical features of turbulent combustion. Under certain conditions, well-organized self-sustained and internally coupled oscillations of pressure and heat release may occur, i.e., dynamic instability may develop. Time-lag mechanism [2], equivalence ratio variations [3], and shedding vortices [4,5] are among the common causes of dynamic instability. Both passive and active control strategies can be developed to stabilize combustion instability. Typical passive control strategies include dissipating acoustic energy using acoustic liners, modifying the combustor geometry, changing the fuel injection location or fuel atomization, and reducing the coherence of the shedding vortices [6,7]. Usually acoustic liners are effective in attenuating high-frequency acoustic oscillations, which is usually accomplished by converting acoustic energy into vorticity using a resonator or perforated plates attached to the combustor walls [8]. To achieve the maximum attenuation, the acoustic liners should be implemented nearby the pressure antinode where the acoustic oscillations are most intense. The size and depth of perforated holes should also be optimized. Passive strategies are usually effective for a limited range of operating conditions and may require major modifications to an existing combustor. As is known, it is usually difficult to predict the occurrence of combustion instability during the development stage of an engine. Compared with passive control strategies, the active ones are usually easier to implement and capable of working in a broader range. A typical active control approach is fuel modulation, introducing a secondary heat release perturbation to nullify the positive feedback between pressure and heat release rate
oscillations.

Sensors, actuators, and control algorithms are the main components of an active control system. The sensors should be able to work for a reasonably long period in harsh environments, i.e., high pressure and temperature environments. For control purposes, the sensors may not be required to provide an absolute measurement of quantities. Usually a relative measurement may suffice. Both pressure sensors and optical fibers can be used for this purpose. The locations and number of sensors required for a control system depend on the thermoacoustic characteristics of the combustion system. Usually the pressure sensors should be implemented nearby the pressure antinode. It seems that pressure sensors offer better control opportunities than optical fibers. Optical measurements usually require an optical access to a combustor and only provide line-of-sight heat release information instead of global information. Additionally, the optical fibers may be susceptible to carbon deposition, and their signal-to-noise ratio is usually not as good as that of a pressure sensor.

An active combustion control actuator should have high reliability, broad bandwidth (capable of working up to 1 kHz), and proportionality. For aeroengines, small size and weight are desirable. Currently, there is not a mature high-frequency actuator in the market. The active control systems may be classified as open loop or closed-loop, where the fuel actuator may work in a prescribed manner like monochromatic forcing or work according to a feedback law such as phase-shift, LQG/LTR, LMS, and adaptive control laws [9–12]. Some of the active control strategies also look at emission reduction for NO_x, CO, and UHC, combustion efficiency improvement, and flammability extension [13,14]. Most of the previous control works are for bluff-body-stabilized combustors or dump combustors instead of swirl-stabilized combustors. Swirling flows and associated breakdown have a profound effect on air/fuel mixing, flame structure, stability, combustion

Contributed by the Combustion and Fuels Division of the ASME for publication in the JOURNAL OF ENGINEERING FOR GAS TURBINES AND POWER. Manuscript received January 21, 2004; final manuscript received January 22, 2006. Review conducted by P. C. Malte.

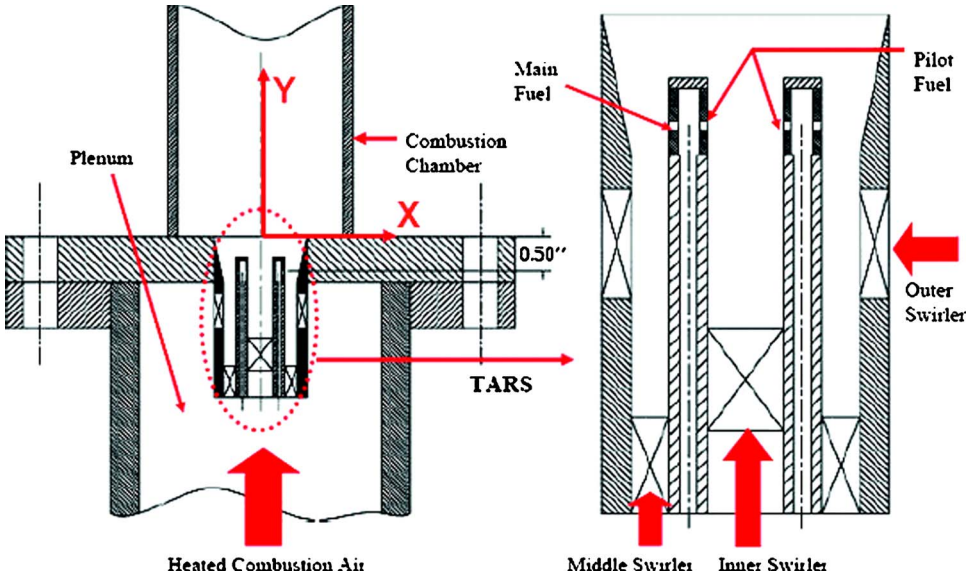

Fig. 1 Sketch of the atmospheric combustion rig

intensity, and pollutant formation [15,16]. Paschereit et al. [13] obtained planar or helical unstable modes by changing the blockage ratio of the combustion chamber exit. Using phase-shifted acoustic forcing, they achieved pressure attenuation and emission reduction simultaneously. The success of acoustic forcing is attributed to the reduced coherence of vortices.

Static instability or LBO usually occurs during transient periods, such as sudden power reduction. Combustion chemistry near the LBO is substantially different from that of normal combustion, which considerably complicates combustion modeling, analysis, and control. Gutmark et al. [17] extended the LBO limit of a premixed dump combustor by generating small-scale vortices using shear layer forcing. Sturgess and Heneghan [18] described the LBO sequence as intermittency in the shear flame, severe intermittency in the shear flame, and large scale axial movement of the flame region, and then lean blowout. They found that the LBO limit could be extended by exit blockage. Durbin and Ballal [19] noticed that the LBO limit could be extended by increasing the outer swirl intensity provided that the inner swirl is stronger than the outer swirl. Thiruchengode and Nair [20] denoted the local flame extinction and reignition preceding LBO as LBO precursors. Based on the detection of LBO precursors using thresholding, statistical, or frequency analysis, they extended the LBO limit by modifying the ratio of fuel injected to the flame stabilization zone.

In the present experimental study, influencing factors of dynamic instability for a multiswirl atmospheric combustor are identified. Dynamic instability is effectively attenuated by monochromatic or continuous air forcing of the swirling air shear layer, fuel line, and flame. By decreasing the fuel-air equivalence ratio while keeping the air flow rate and inlet air temperature constant, a series of structural changes are observed, namely dynamic instability, smooth turbulent combustion, relatively intense oscillations, quiet combustion, and LBO. The LBO limit is extended by increasing the outer swirl angle or by creating a rich burning flame stabilization region.

2 Experimental Setup

Gas turbine engines operate at high pressure, and the thermoacoustics are determined by the geometry of the whole system from the compressor exit, diffuser, combustor plenum, and combustor to the turbine inlet guide vanes. The excited acoustic modes and frequencies are determined by flame/acoustic interactions and the acoustic boundary conditions [21]. In some working conditions or engines, flow through the compressor last stage and the turbine inlet guide vanes can be treated as choked. The air fuel mixing, chemical heat release, and flame structure are affected by fuel, the fuel injector, air inlet velocity, the velocity profile at the swirler exit, and the combustor geometry.

An ideal simulator should have similar flow patterns and acoustic boundary conditions as a generic gas turbine engine. The simulator may operate at atmospheric pressure or elevated pressure. At high pressure, the laminar burning velocity is usually lower [22], and the buoyancy effect is less pronounced than at low pressure. Atmospheric rigs have been widely used in laboratory research. The flow pattern within a combustor is usually determined by the ratio of pressure drop across the swirler and the Reynolds number [23]. The choked flow at the plenum inlet and combustor exit can be conveniently achieved using converging nozzles or orifices. In this study, propane is used so that the complexities of fuel atomization can be neglected.

Figure 1 shows the atmospheric combustion rig and the Triple Annular Research Swirler (TARS) developed by Goodrich Aerospace. The combustion rig is vertically set up. Heated combustion air enters the combustion rig at the bottom. Air is supplied either from a 135 m^3 high-pressure tank (pressure 110 bar) or from a 67.5 m^3 low-pressure tank (pressure 12 bar). Air flow rate is measured using a thermal wire digital flow meter (EPI) with measurement error 0.1%. The combustion chamber is made of stainless steel or quartz, 0.66 m long with internal diameter 0.1 m. There is a series of instrumentation ports (interval 0.05 m) along the stainless steel chamber. A water-cooled Kistler dynamic pressure sensor 7061B, optical fibers, and a static pressure transducer (Drunk PMP4000) are implemented 0.08 m above the dump plane. Typical combustion instabilities in this rig roughly correspond to the quarter wave mode of the combustion chamber with pressure antinode at the dump plane. Beneath the combustion chamber is the extension section where the TARS is mounted. The TARS has three air swirlers, namely the inner (axial entry), middle (axial entry), and outer swirler (radial entry). For most tests in this paper, the swirl angles of the inner, middle, and outer swirlers are 30 deg (clockwise), 45 deg (counter clockwise), and 30 deg (clockwise), respectively. The air side pressure drop across the TARS is about 2% to 3% of the incoming air static pressure. The TARS has a main fuel line and a pilot fuel line. The combustor is fueled with gaseous propane which is directly injected into the strong swirling flows. The propane volume flow rate is measured using a digital gas flow meter (Alicat Scientific) with measurement error 1%.

Usually, the propane temperature is 283 K and pressure is about 60 psi. Beneath the extension rig is the air conditioning section featured with a wide angle diffuser, a coarse screen, a honeycomb, and several fine screens. The air-conditioning unit removes large vortices from the incoming air flow. Thermocouples and a static pressure transducer are installed at this section.

The data acquisition system includes a Dspace control desk, a Dspace board CP1104, Labview 7.0, and a NI DAQ board PCI-MIO-16XE-10. Typically the sampling frequency is 5000 Hz, and the data length is 10 s. A high-resolution (1024×1024 pixel) super blue ICCD camera from Roper Scientific is used for flame visualization. Usually, the OH^* optical fibers are used for line-of-sight heat release measurement. An F150 Precision Thermometer from $A\Sigma\Lambda$ and type B thermocouples with measurement uncertainty ±5 K are used for temperature measurements. The actuator is an automotive fuel injector PB2-1600 from RC Engineering. To check its dynamic response, axial velocity at the fuel injector exit is measured using a TSI hot film 1210-20 sensor. It is found that the fuel injector can only follow the open and close commands below 75 Hz. Above 100 Hz, the automotive valve cannot fully close, resulting in a dc shift in the air flow rate.

3 Characteristics of Dynamic Instability

Experiments show that with a small increase of equivalence ratio, combustion may experience stable, semi-stable, and unstable states. Combustion instability may exhibit a hysteresis phenomenon. That is, dynamic instability can be triggered by increasing the equivalence ratio up to a critical point while keeping the air flow rate and air inlet temperature constant. But decreasing the equivalence ratio from this critical point will not make unstable combustion disappear immediately.

For the present rig, unstable combustion may occur at high equivalence ratios (near or above stoichiometry) or low equivalence ratios (below stoichiometry). At low preheat temperature, unstable combustion usually occurs at equivalence ratios above one. Strong and persistent combustion oscillation is observed at equivalence ratio 1.22 and power 80 kW with unstable frequency of 250 Hz and pressure amplitude 9.64 kPa. The air inlet temperature is 298 K. Local heat release rate is measured using an OH^* optical fiber. The output voltage of the photomultiplier is assumed to be an increasing function of the local heat release rate [24]. The optical fiber is located 0.08 m above the dump plane and 0.03 m away from the quartz chamber. Dynamic pressure is measured 0.45 m below the dump plane. The pressure wave is originated from the combustion chamber and propagates downstream. Experiments with the stainless steel chamber show that the transportation delay is about 0.81 ms. The transportation time delay has been considered when interpreting the data. It is found that the phase difference between pressure signal and fiber output is about 45 deg, and that the amplitude of local heat release rate oscillations and its phase relationship with pressure do not change azimuthally but axially, which implies that the unstable mode is of planar wave mode. Temperature measurements along the combustion chamber show that the unstable acoustic mode and frequency correspond to the quarter wave mode of the combustion chamber.

Phase-locked ICCD images are taken to illustrate the instantaneous flame structure during one pressure cycle, and pressure is used as the trigger for the camera. Figure 2 shows the setup of the imaging system. The ICCD camera with an OH^* optical filter (bandwidth ~310 nm) is located 1.3 m away from the combustion rig. The imaging area extends from the dump plane to 0.12 m above where heat release is most intense. Sixteen images are taken for each pressure cycle with a phase interval about 22 deg. The intensifier gain is 128 and the gate width is 150 μs. The global heat release rate is assumed to be proportional to the sum of the pixel intensity. A trigger is generated when the filtered pressure (using a fourth-order Butterworth filter) crosses zero with positive slope. A bandpass filter is centered around the unstable

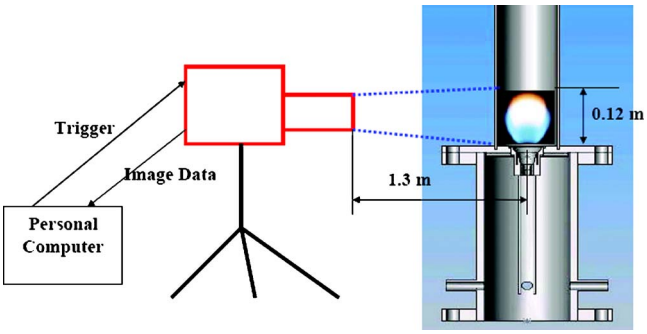

Fig. 2 Setup of the imaging system

frequency with bandwidth 20 Hz on both sides. The interval between two consecutive triggers can be varied within 24 ms.

Figure 3 shows the phase-locked ICCD images obtained by sweeping the trigger interval over one pressure cycle. It is clear that intense heat release occurs within the swirling shear layer, and the combustion zone and heat release rate vary within one pressure cycle. The strongest heat release occurs when pressure is at 48 deg, and the weakest heat release occurs when pressure is at 220 deg. The quasi-periodic oscillations of combustion zone and heat release might be associated with the swirling shear layer dynamics and precessing vortex core. It is reasonable to assume that the flame within the shear layer is tangential to the vortex breakdown region. When the vortex breakdown region moves upstream or downstream under the effects of pressure pulsations or acoustic velocity oscillations, the flame area and heat release may increase or decrease quasi-regularly. Air/fuel mixing and preignition might also be affected by the vortex breakdown motion. Under proper conditions, heat release oscillations might be positively coupled with pressure, leading to combustion instability. Equivalence ratio variations may be another potential instability mechanism. Pressure pulsations may introduce larger variations of air flow rate into the combustion chamber than the fuel flow rate, i.e., equivalence ratio variations. This is because the air side pressure drop across the TARS is 2 to 3% of the inlet static pressure while the propane pressure drop across the TARS is 60 psi. Figure 4 shows the average pixel intensity. It is clear that the phase difference between the pressure and global heat release rate is about 45 deg. The in-phase relationship implies the transfer of chemical heat release to the acoustic field.

4 Active Control of Dynamic Instability

4.1 Air Forcing of the Swirling Shear Layer. For NO_x reduction, it is beneficial to introduce well-premixed air/propane reactants into the combustion chamber instead of direct injection of propane into the swirling air flow. A simple approach is to implement an extension tube at the TARS exit, as shown in Fig. 5. This will ensure a better mixed air/propane reactant before combustion than direct fuel injection. However, combustion in this setup is more susceptible to unstable combustion since it is more like the LP combustion mode. As mentioned before, the TARS has three air swirlers, and it will become a radial-entry dump swirler by blocking the air passage through the inner and middle swirlers. The "blocked" TARS is shown in Fig. 5. It is worth noting that the "blocked" TARS will create a flame stabilization region burning rich at the TARS exit. As will be shown later in this paper, this may substantially extend the LBO limit, and thus reduce NO_x. For the quartz combustion chamber with "blocked" TARS and a mixing tube (0.025 m long with internal diameter 0.05 m), unstable combustion occurs at 260 Hz with pressure amplitude 6.5 kPa. The equivalence ratio is 0.78 and the power is 65 kW. The combustion air inlet temperature is 423 K.

Sinusoidal and steady air forcing of the swirling shear layer

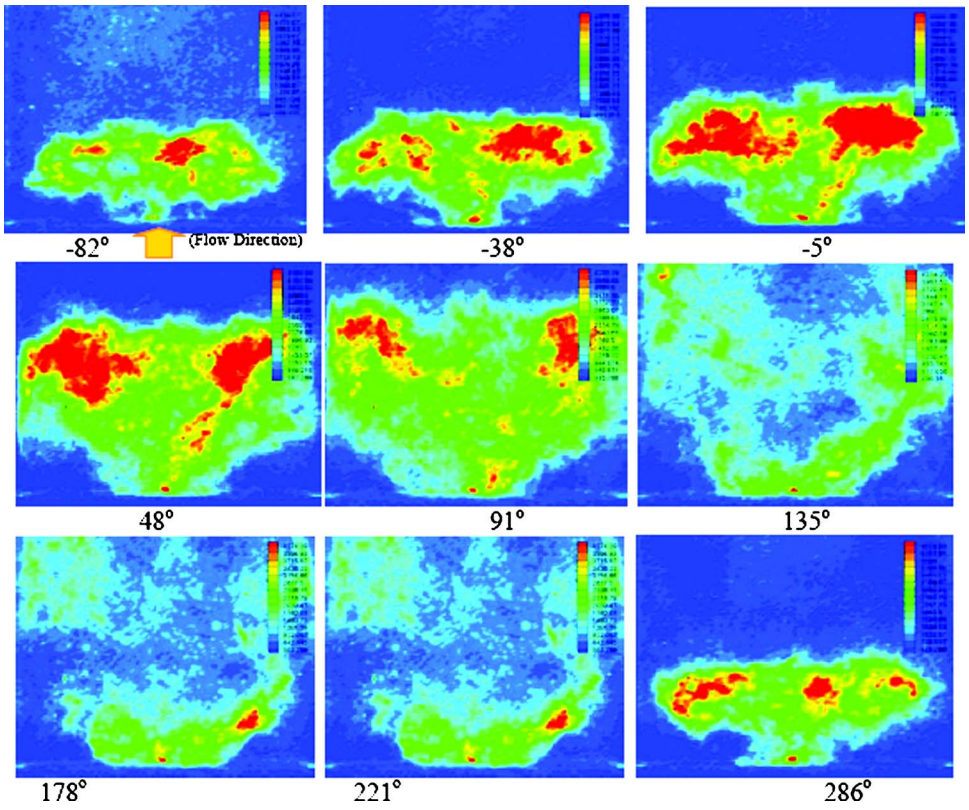

Fig. 3 Phase-locked ICCD images (fresh air/propane are introduced from the bottom of each picture)

effectively stabilize unstable combustion. The automotive fuel injector delivers forcing air to the swirling shear layer through a stainless tube with internal diameter of 1 mm. The forcing location is shown in Fig. 5. The forcing air pressure is 90 psi and the temperature is about 288 K. The forcing air flow rate is measured using an Alicat digital flow meter. Figure 6 shows that pressure oscillations are attenuated up to 36.5 dB within 350 ms with both steady air forcing and 100 Hz air forcing. For 100 Hz air forcing with 50% duty cycle, the amplitude of forcing air flow rate is about 1% of the combustion air flow rate. For steady air forcing, the forcing air flow rate is about 1% of the combustion air flow rate. By varying the forcing duty cycle, the forcing air flow rate can be changed. Not surprisingly, larger forcing air flow rate can achieve larger pressure amplitude reduction. However, no further reduction of pressure oscillations can be achieved when the forcing air flow rate is more than 2% of the combustion air flow rate. The attenuation of the combustion instability by the swirling shear layer forcing can be attributed to the enhanced generation of small-scale vortices via the Kelvin-Helmoltz instability mechanism. The improved air/fuel entrainment and mixing reduce trapping of large fresh fuel packets or unburned air/fuel mixture within large vortices, which leads to reduced instantaneous heat release oscillations after the vortices break up. As is known, combustion instability will be suppressed if the energy addition to the acoustic field is smaller than the acoustic energy dissipation across the boundaries.

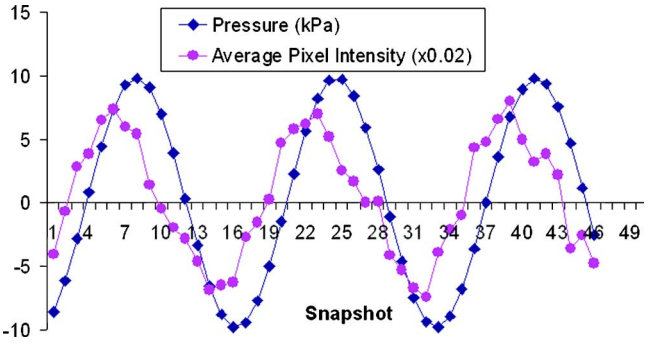

Fig. 4 Average pixel intensity and pressure

4.2 Air Forcing of the Fuel Line. For the stainless steel chamber with the "blocked" TARS and the mixing tube, unstable combustion occurs at 225 Hz with pressure amplitude of 1.38 kPa. The equivalence ratio is 0.83 and the power is 27 kW. The air inlet temperature is 423 K. Pressure pulsations can be effectively attenuated by introducing steady or sinusoidal air forcing to the fuel line. Figure 7 shows the conceptual scheme for fuel line forcing. Fuel and forcing air are ejected out of the TARS with the forcing air surrounded by propane.

Figure 8 shows that both sinusoidal air forcing and steady air forcing are effective in pressure attenuation. Pressure oscillations amplitude is reduced by 92% (23 dB) by sinusoidal air forcing at 240 Hz with 50% duty cycle. It is noticed that higher frequency forcing achieves larger pressure attenuation. Steady air forcing of the fuel line is not as effective as sinusoidal forcing. Fuel line forcing may reduce the pressure oscillations because of the enhanced momentum and penetration of fuel out of the TARS, which improve air/fuel mixing. The fuel line forcing may also help to generate small scale vortices within the swirling shear layer.

4.3 Air Forcing of Flame. Phase shift and sinusoidal air forcing of the flame are applied to suppress the pressure pulsations. The experimental setup is shown in Fig. 9. The stainless steel chamber with the "blocked" TARS and the mixing tube are used. Unstable combustion occurs at 225 Hz with pressure amplitude of

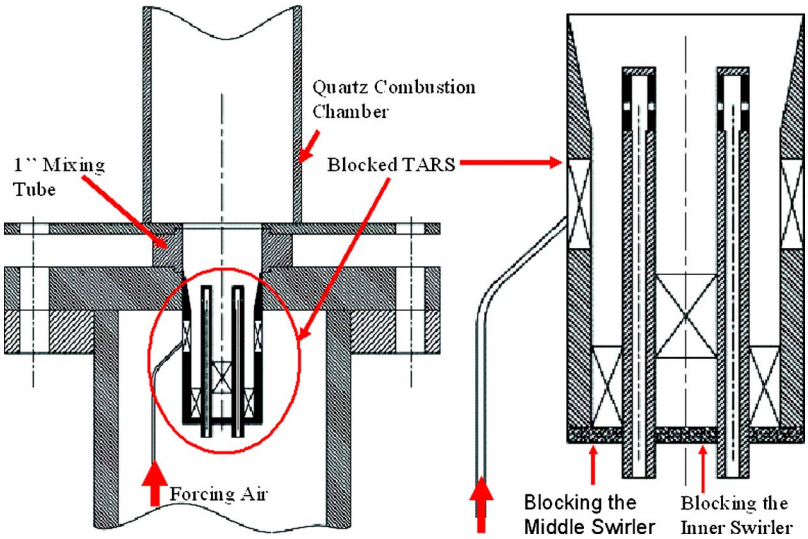

Fig. 5 Schematics of swirling shear layer forcing and "blocked" TARS detail (all main air enters through outer radial swirler)

1.38 kPa. The equivalence ratio is 0.83 and the power is 27 kW. The air inlet temperature is 423 K. Forcing air is introduced to the flame 0.08 m above the dump plane using an automotive fuel injector. The air forcing location is shown in Fig. 9. Forcing air pressure is about 90 psi. For sinusoidal forcing, the most effective forcing frequencies lie between 50 and 250 Hz. The maximum pressure reduction is 65% at 225 Hz. The amplitude of forcing air flow rate is about 1% of the combustion air flow rate. Steady air forcing of the flame is not effective in pressure attenuation.

Phase shift air forcing of the flame achieves more pressure attenuation than sinusoidal forcing. The pressure signal is measured 0.08 m above the dump plane and is filtered by a fourth-order Butterworth filter between 180 and 300 Hz; then it is delayed, amplified, and sent to the automotive injector for air forcing. The largest reduction of pressure oscillation is about 78% (13.2 dB), which is achieved at a control phase around 121.5 deg. Figure 10 shows pressure attenuation at control phase 121.5 deg. The control air flow rate is about 1% of the combustion air flow rate. Phase shift air forcing of the flame may achieve pressure attenuation because the air forcing modifies the instantaneous flame

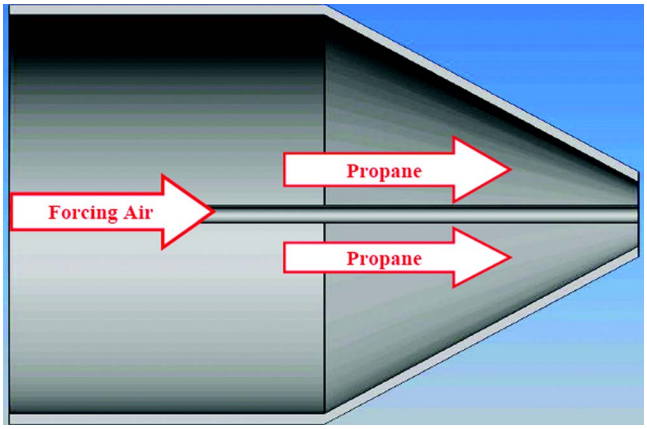

Fig. 7 Conceptual scheme for air forcing of fuel line

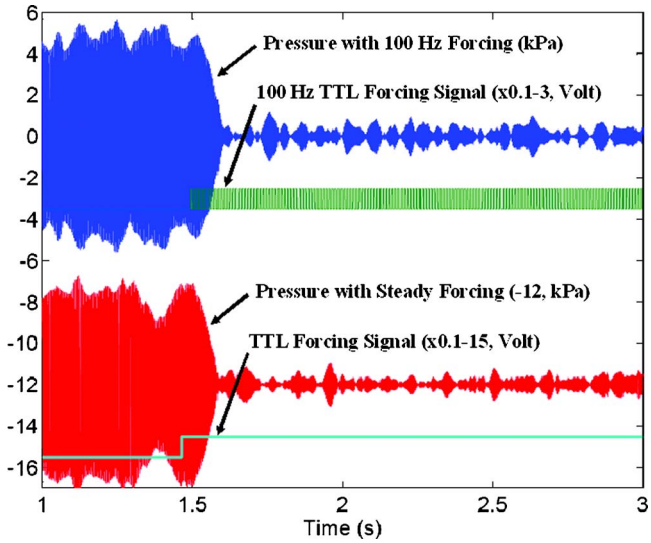

Fig. 6 Pressure attenuation using steady and 100 Hz air forcing of swirling shear layer

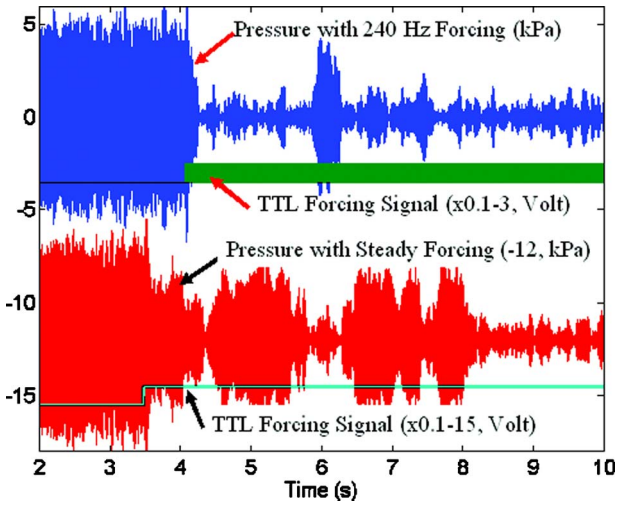

Fig. 8 Pressure attenuation by steady and sinusoidal air forcing of fuel line

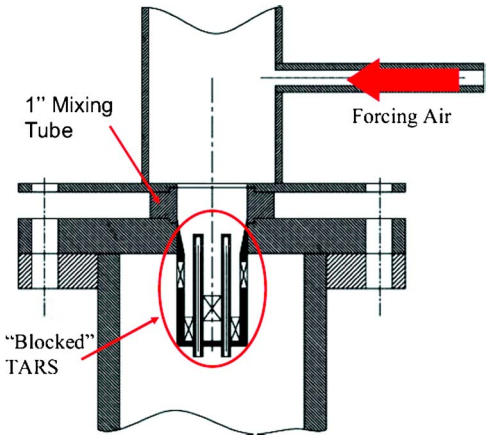

Fig. 9 Schematic of air forcing of flame

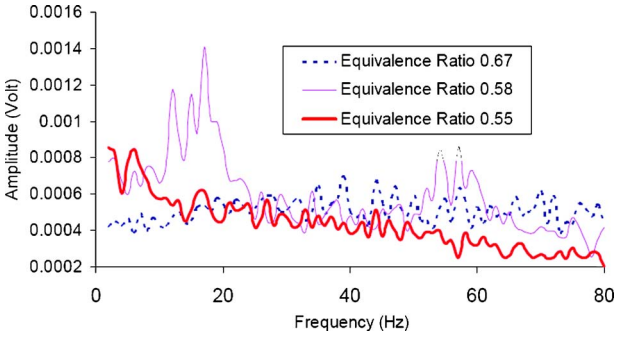

Fig. 11 OH* frequency spectrum at Re=41,000

structure, the flame area, and the instantaneous heat release rate. Under proper control phases, the forcing-induced heat release rate oscillations may counteract the intrinsic heat release rate oscillations, thus leading to pressure amplitude attenuation.

5 Characteristics and Control of Static Instability

LBO extension is important for LP combustion because engines are designed to operate very lean in order to achieve the lowest possible emissions. Combustors with good static stability are typically highly efficient, generating low CO, UHC, and NO_x. LBO may be affected by local strain rate, flame curvature, turbulent burning speed, turbulence intensity, combustor geometry, boundary conditions, and heat loss. The flame may extinguish at high stretch rates due to rapid cooling of the flame by fresh air/fuel or at low strain rates due to radiative heat loss. High strain rates may occur when a large vortex intrudes into the flame within swirling flows [25]. The flame response to unsteady strain rate is to a large extent determined by the time scales of the large turbulent structures, mass transfer, heat transfer, and chemical kinetics. Structural changes have been observed for combustion near the LBO [18,26].

In this study, LBO is approached by decreasing the fuel flow rate while keeping the air flow rate and air inlet temperature constant. The 0.66 m quartz tube and the mixing tube are used. Different from previous tests, the TARS is not blocked and the outer swirler angle is 55 deg (counterclockwise) instead of 30 deg (counterclockwise). The air inlet temperature is 288 K. ICCD images of OH* chemiluminescence show that the regions of high heat release rate oscillations overlap those of high mean heat release rate. The heat release rate oscillations near the LBO are 10% of the mean heat release rate, which is twice larger than that of the smooth combustion above the LBO. Faster reduction of the fuel rate leads to flame blowout at a higher equivalence ratio. With decreasing equivalence ratio, combustion exhibits a sequence of structure changes as shown in Fig. 11, where Re=41,000. The Reynolds number is defined as $\mathrm{Re}=UD/\nu$, where U is the average axial velocity at the TARS exit, D is the outer diameter of the TARS exit (0.05 m), and ν is the kinetic viscosity of air at 288 K. At equivalence ratio 0.67, the low-frequency components (below 100 Hz) of the OH* output are basically a random signal, typical of turbulent combustion. At an equivalence ratio 0.58, relatively intense combustion noise emerges, accompanied with a frequency peak cluster around 17 Hz in the OH* frequency spectrum, which may be associated with large scale flame extinctions and reignitions. At equivalence ratio 0.55, the relatively intense combustion noise disappears, resulting in a quiet state. The spectrum shows reduced amplitude with increasing frequency, a typical feature of a chaotic system which may result from successive bifurcations [26,27]. With a further reduction of equivalence ratio, the flame is lifted towards the chamber exit and anchors there, and extinguishesshortly thereafter. This process is accompanied by excessive CO formation.

Figure 12 shows that the LBO limit for swirling flows can be extended by increasing the outer swirl angle or creating a low-velocity and locally rich burning region at the center of the swirler exit. The latter is achieved by blocking the inner and middle swirls of the TARS. Note that the LBO limit refers to the equivalence ratio at which the LBO occurs. For the TARS, the LBO limit extends with higher Re. For swirling flows, the flame is mainly stabilized by the recirculating vortex breakdown at the TARS exit. At high Re or at high outer swirl angle, the tangential velocity is high, and consequently the negative radial pressure gradient is high, which favors the back flow of the hot products into the recirculating vortex breakdown region. For the "blocked" TARS, flame is still attached to the TARS exit near the LBO instead of being lifted.

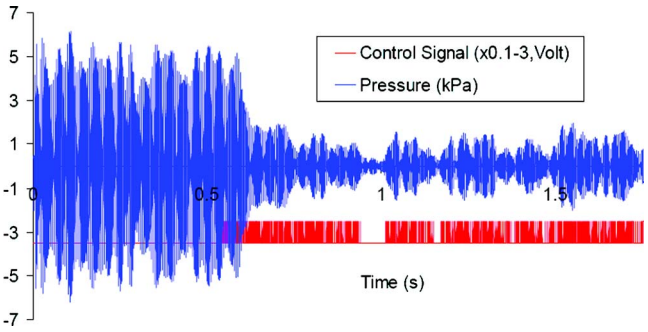

Fig. 10 Pressure dynamics with phase-shift air forcing

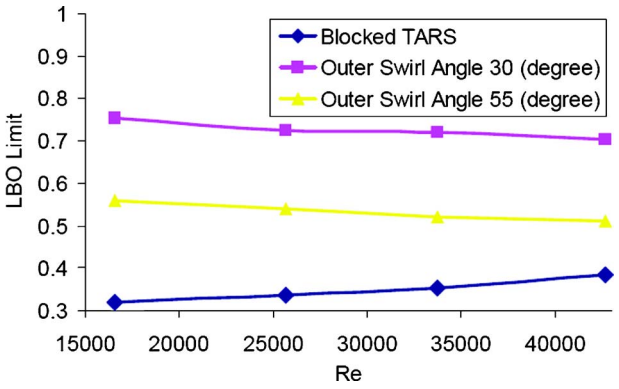

Fig. 12 LBO extension

6 Conclusions

Dynamic instability is affected by multiple factors, such as combustor geometry, inlet velocity profile, fuel, acoustic boundary conditions, and air inlet conditions. A subtle change of these parameters could affect the susceptibility of the rig to combustion instability and combustion oscillation intensity. For certain setups, sinusoidal or steady air forcing of the swirling shear layer using less than 1.0% of combustion air can attenuate pressure oscillations by more than 20 dB. Sinusoidal air forcing of the fuel line or phase shift forcing of the flame is also effective in pressure amplitude attenuation. With decreasing equivalence ratio while keeping air flow rate and inlet temperature constant, a series of structure changes are observed, namely dynamic instability, smooth turbulent combustion, intensified combustion oscillations, quiet combustion, and the LBO. The sequential changes of flame structures may provide a warning of the LBO. It is found that the LBO limit can be extended by increasing the outer swirl angle or creating a rich burning flame stabilization region.

References

[1] Rayleigh, J. W. S., 1945, *The Theory of Sound*, Dover Publications, New York.

[2] Crocoo, L., Grey, J., and Harrje, D. T., 1960, "Theory of Liquid Propellant Rocket Combustion Instability and Its Experiment Validation," ARS J., **30**(2), pp. 159–168.

[3] Chu, B. T., 1953, "On the Generation of Pressure Waves at a Plane Flame," *Fourth Int. Symp. on Comb.*, pp. 603–612.

[4] Gutmark, E. J., Parr, T. P., and Schadow, K. C., 1986, "Visualization of Vortex Dynamics in Flame Combustion," Bull. Am. Phys. Soc., **31**(10), p. 1681.

[5] Poinsot, T., Trouve, R. F., Veynante, D. P., Candel, S. M., and Esposito, E. J., 1987, "Vortex Driven Acoustically Coupled Combustion Instabilities," J. Fluid Mech., **177**, pp. 262–292.

[6] Schadow, K. C., and Gutmark, E. J., 1992, "Combustion Instability Related to Vortex Shedding in Dump Combustors and Their Passive Control," Prog. Energy Combust. Sci., **18**, pp. 117–132.

[7] Gutmark, E. J., and Grinstein, F., 1999, "Mixing in Non-Circular Jets," Annu. Rev. Fluid Mech., **31**, pp. 239–272.

[8] Dupere, I. J. D., and Dowling, A. P., 2002, "The Absorption of Axial Acoustic Wave by a Perforated Liner With Biased Flow," AIAA Paper No. 2002–2590.

[9] Schadow, K. C., Gutmark, E. J., and Parr, T. P., 1993, "Study of Combustion Dynamics for Passive and Active Control," Prog. Astronaut. Aeronaut., **151**, pp. 365–388.

[10] Annaswamy, A. M., EI-Rifai, O., Fleifilj, M., and Ghoniem, A. F., 1998, "A Model-Based Self-Tuning Controller for Thermoacoustic Instability," Combust. Sci. Technol., **135**, pp. 213–240.

[11] Riley, A. J., Park, S., Dowling, A. P., Evesque., S., and Annaswamy, A. M., 2003, "Adaptive Closed-Loop Control on an Atmospheric Gaseous Lean-Premixed Combustor," ASME Paper No. GT-2003-38418.

[12] Neumeier, Y., and Zinn, B. T., 1996, "Active Control of Combustion Instabilities with Real Time Operation of Unstable Combustor Modes," AIAA Paper No. 96-0758.

[13] Paschereit, C. O., Gutmark, F. J., and Weisenstein, W., 1999, "Coherent Structures in Swirling Flows and Their Role in Acoustic Combustion Control," Phys. Fluids, **11**(9), pp. 2667–2678.

[14] Gutmark, E. J., Parr, T. P., Wilson, K. J., Hanson-Parr, D. M., and Schadow, K. C., 1990, "Use of Chemiluminescence and Neural Networks in Active Combustion Control," *23rd Combustion Symposium* (International).

[15] Lilley, D. G., 1977, "Swirl Flows in Combustion: A Review," AIAA J., **15**(5), pp. 1063–1078.

[16] Froud, D. Y., Beale, A. J., O'Ooherty, T., and Syred, N., 1996, "Studies of Helmoltz Resonance in a Swirl Burner Furnace System," *26th Symposium on Combustion* (International), pp. 3355–3362.

[17] Gutmark, E. J., Parr, T. P., Wilson, K. J., et al., 1993, "Closed-Loop Control of a Flame and a Dump Combustor," IEEE Control Syst. Mag., **13**(2), pp. 74–78.

[18] Sturgess, G. J., and Heneghan, S. P., 1993, "Effects of Back-Pressure in a Lean Blowout Research Combustor," ASME J. Eng. Gas Turbines Power, **115**, pp. 486–498.

[19] Durbin, M. D., and Ballal, D. R., 1996, "Studies of Lean Blowout in a Step Swirl Combustor," ASME J. Eng. Gas Turbines Power **118**, pp. 72–77.

[20] Thiruchengode, M., and Nair, S., 2003, "An Active Control System for LBO Margin Reduction in Turbine Engines," AIAA Paper No. 2003-1008.

[21] Dowling, A. P., 1997, "Aeroacoustics and Active Noise Control," von Karman Institute for Fluid Dynamics, Lecture Series, July.

[22] Turns, S. R., 2000, *An Introduction to Combustion, Concepts and Applications*, McGraw-Hill, New York.

[23] Goginen, S., Shouse, D., Frayne, C., Stutrud, J., and Sturgess, G., 2002, "Combustion Air Jet Influence on Primary Zone Characteristics for Gas Turbine Combustors," J. Propul. Power, **18**(2), pp. 407–416.

[24] Roby, R. J., Hamer, A. J., Johnson, E. L., Tilstra, S. A., and Burt, T. J., 1995, "Improved Method for Flame Detection in Combustion Turbines," Trans. ASAE, **117**, pp. 332–340.

[25] Ju, Y., 1997, "On the Extinction Limit and Flammability Limit of Non-Adiabatic Stretched Methane-Air Premixed Flames," J. Fluid Mech., **342**, pp. 315–334.

[26] Bayliss, A., 1994, "From Traveling Waves to Chaos in Combustion," SIAM J. Appl. Math., **54**(1), pp. 147–174.

[27] Strogatz, S., 1994, *Nonlinear Dynamics and Chaos*, Addison-Wesley, Reading, MA.

Open-Loop Active Control of Combustion Dynamics on a Gas Turbine Engine

Geo. A. Richards

Jimmy D. Thornton

U.S. Department of Energy,
National Energy Technology Laboratory,
Morgantown, WV 26505

Edward H. Robey
U.S. Department of Energy,
Parsons Project Services,
Morgantown, WV 26505

Leonell Arellano
Solar Turbines, Inc.,
2200 Pacific Highway,
San Diego, CA 92101

Combustion dynamics is a prominent problem in the design and operation of low-emission gas turbine engines. Even modest changes in fuel composition or operating conditions can lead to damaging vibrations in a combustor that was otherwise stable. For this reason, active control has been sought to stabilize combustors that must accommodate fuel variability, new operating conditions, etc. Active control of combustion dynamics has been demonstrated in a number of laboratories, single-nozzle test combustors, and even on a fielded engine. In most of these tests, active control was implemented with closed-loop feedback between the observed pressure signal and the phase and gain of imposed fuel perturbations. In contrast, a number of recent papers have shown that open-loop fuel perturbations can disrupt the feedback between acoustics and heat release that drives the oscillation. Compared to the closed-loop case, this approach has some advantages because it may not require high-fidelity fuel actuators, and could be easier to implement. This paper reports experimental tests of open-loop fuel perturbations to control combustion dynamics in a complete gas turbine engine. Results demonstrate the technique was very successful on the test engine and had minimal effect on pollutant emissions. [DOI: 10.1115/1.2204978]

1 Introduction

Combustion instability has become a significant issue in the development and operation of low-emission stationary gas turbines. Compared to earlier diffusion flame combustors, stationary gas turbines now use premix combustion to reduce flame temperatures, thereby avoiding significant production of thermal NO_x. This approach to NO_x reduction is very effective, but the premixed flame is very prone to dynamic oscillations. Furthermore, the absence of combustion dilution holes in premixed systems provides little opportunity to dampen acoustic waves generated by the combustion. For these reasons, dynamics often hinder both the development and operation of premixed systems. Although premixed combustors have now been successfully commercialized in many instances, changes in fuel type, ambient conditions, or even engine wear can require adjustments to flow splits, power output, etc., to avoid dynamics. Thus, the operating margins for premixed systems are sometimes restrictive, and new techniques to stabilize premix combustion are needed. A recent review by Mongia et al. [1] provides more background.

Active control is a promising method to stabilize premixed combustion. As typically proposed, active control uses fuel modulation to adjust the dynamic response of the flame so that the feedback loop between heat release and acoustics is dynamically stable. The most common approach is to modulate the fuel at the frequency of any observed oscillations and control the phase to produce stability. This approach has been tested in various combustion test rigs [2–5]. This closed-loop approach has the advantage that the feedback can be adjusted to variable dynamic response with changes in operating conditions, fuel type, etc. A potential drawback is that the fuel needs to be modulated at the oscillating frequency and with adequate control of the modulation phase. Where oscillation frequency approaches 1 kHz, modulation places a significant mechanical demand on the fuel modulation valve and this has been the motive to develop subharmonic actuation [5]. Because stationary turbines will operate thousands of hours between maintenance, valve life is an issue for high-frequency control strategies. This issue is complicated by the requirement that valve modulation must produce fuel modulation at the point of premixing with desired phase and gain. This means that the fuel modulation valve should be located in the fuel injector, a hostile environment. Alternatively, the modulating valve can be located in a cooler location [6], but the connecting piping must have a specified acoustic impedance. This latter approach limits the actuating response at other frequencies. The tests in Sueme et al. [6] are the only prior tests carried out on a complete gas turbine engine.

Open-loop fuel modulation is an alternate approach to active control. By repeatedly modulating the fuel flow, oscillations can be dampened because the feedback loop is disrupted by the imposed modulation. Because the fuel modulation is not phased with the observed pressure oscillations, the fuel control valve requirements are simplified. Likewise, if modulation is successful at low frequencies, the cyclic life requirements of the valve are comparable to those in reciprocating gas engine fuel injectors. As an alternative to modulating the fuel flow, McManus et al. [7] showed that open-loop modulation of the shear layer in a step-stabilized flame could be used to control combustion dynamics. In a similar manner, Uhm and Acharya [8] investigated open-loop modulation of an air-jet aimed at the flame base in a laboratory swirl-combustor. The intermittent disruption at the base of flame controlled oscillations without compromising the flame-holding.

Richards et al. [9] demonstrate that it is possible to control oscillations with a low-frequency modulation of a pilot flame. The approach used a commercial valve to modulate the flow of fuel to a pilot flame and showed that natural oscillations could be significantly reduced by open-loop fuel modulation. A theoretical investigation by Prasanth et al. [10] and CFD analysis by Smith and Cannon [11] explained some of these results. Pashcereit et al. [12] showed that open-loop modulation of either the pilot or main fuel flow could suppress combustion dynamics in a premixed combustor.

Recently, researchers at Georgia Tech [13] have investigated open-loop fuel modulation as a method to control large amplitude combustion oscillations. Again, the idea for control was based on

Contributed by the Combustion and Fuels Division of ASME for publication in the JOURNAL OF ENGINEERING FOR GAS TURBINES AND POWER. Manuscript received by March 11, 2005; final manuscript received March 16, 2006. Review conducted by P. C. Malte.

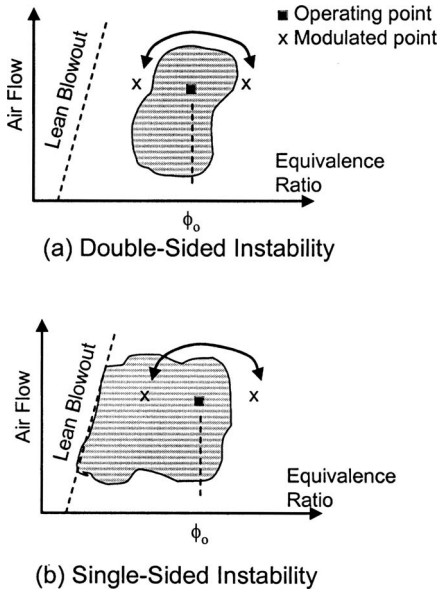

Fig. 1 Schematic of instability regions showing how fuel modulation can affect instability: (*a*) double-sided instability and (*b*) single-sided instability

the understanding that fuel modulation disrupts the feedback loop that drives oscillations. McManus et al. [14] report successful attenuation of premixed combustion oscillations using open-loop fuel modulation in a turbine combustor rig. As a side benefit, these authors showed that open-loop fuel modulation can extend the lean-blowout limit when compared to steady fuel injection.

Richards et al. [15] demonstrated oscillation control using open-loop modulation of the premix fuel flow. These authors showed that equivalence ratio modulation can successfully control oscillations when the stability map includes isolated islands of oscillations. The concept is shown in Fig. 1(*a*). The combustor behavior is plotted as a function of equivalence ratio and average air flow. As shown, oscillations may be confined to a specific region on this plot (shaded). If the desired operating point is inside this region, the combustor will oscillate. It is demonstrated [15] that fuel modulation can be used to alternate the combustor equivalence ratio between stable operating points which span the oscillating region. In this manner, the time average equivalence ratio is the desired operating point, but the instantaneous value is one of the stable operating conditions. Assuming that the imposed heat release modulations can be tolerated by downstream hardware, this technique can be used to stabilize combustion oscillations. Tests on a 30 kW laboratory combustor showed that a 300 Hz instability could be stabilized by modulating the fuel at frequencies of $<$20 Hz. The success of this technique depends on the time required for oscillations to develop during the transition between the left and right stable points, so that the results are specific to the combustor studied.

The instability shown in Fig. 1(*a*) is referred to in this paper as "double sided" because the oscillating region is bounded on both sides by stable conditions. For practical purposes, many instabilities are "single sided," meaning that the stability boundary divides stable from oscillating conditions, with no stable region on the opposite side of the stability boundary. In this case, modulating the equivalence ratio simply moves the combustor from stable to oscillating conditions; this has been demonstrated [15]. Thus, successful control using the fuel modulation concept would appear to be limited to double-sided instabilities. This limits the potential application to a small number of situations, since many practical dynamics problems are single sided.

To address this limitation, it is useful to recognize that turbine engine combustors usually use multiple fuel injectors. In these

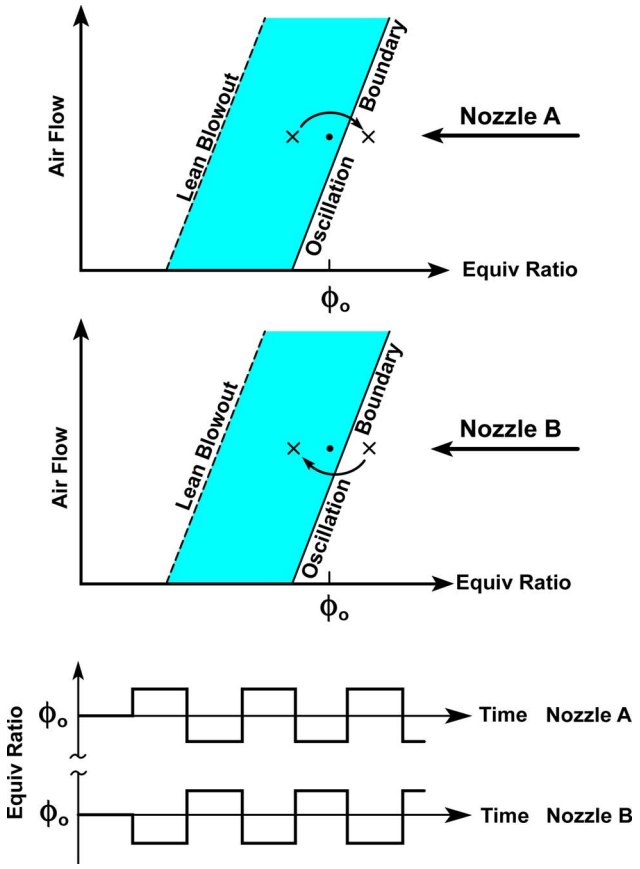

Fig. 2 Schematic of fuel modulation on two injectors, nozzles A and B

applications, it is conceivable that pairs of injectors can be modulated out of phase. The concept is shown in Fig. 2. Lean blowout is indicated by the dashed line on the left of the shaded oscillation region. The desired, time-average equivalence ratio ϕ_0 is shown inside the oscillation region. Referring to the time history of the equivalence ratio for injector A, the fuel is modulated to produce a square-wave history with an average value ϕ_0. Fuel modulation is also occurring on injector B, but the square wave is 180 deg out-of-phase with injector A. Thus, although injector A is operating with a stable equivalence ratio, injector B is operating at an unstable condition. The two injectors switch conditions at the modulation frequency, making B stable, while A is unstable. Using this approach to fuel modulation, at least one-half of the engine injectors are operating at stable conditions compared to the uncontrolled situation. Although this does not guarantee stability, it provides an excellent option for reducing the magnitude of combustion driving, and may warrant consideration on engine applications known to have single-sided instabilities. As will be shown, the frequency of fuel modulation can be relatively low for successful control, meaning that commercial fuel modulation valves can be used and located in the existing fuel piping. These concepts are explained further elsewhere [16] where the concept of periodic equivalence ratio modulation is given the acronym PERM.

To demonstrate the success of the PERM concept, it is necessary to test a combustor with multiple fuel injectors. For practical use, it is also necessary to evaluate the effect of PERM on pollutant emissions, and consider any collateral effects on the engine systems. This paper demonstrates the successful use of PERM on a gas turbine engine using 12 fuel injectors. The tests were carried out in a Cooperative Research and Development Agreement between Solar Turbines Inc. and the United States Department of Energy's National Energy Technology Laboratory. Results show

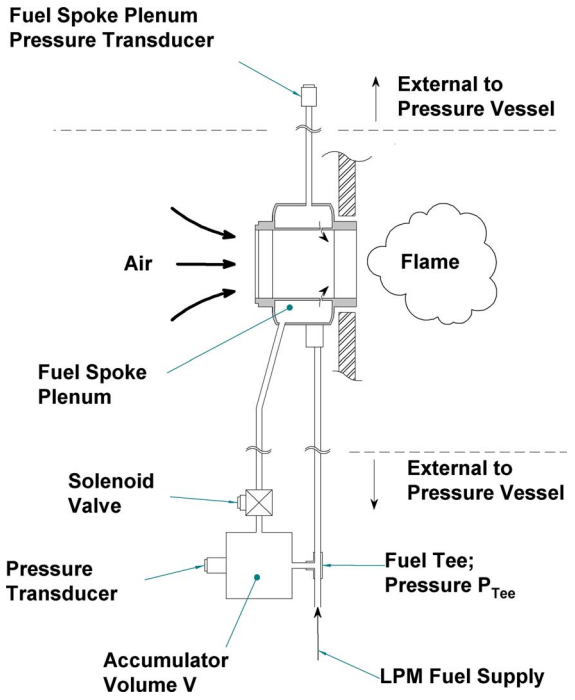

Fig. 3 Schematic of the fuel injector and hardware used to generate and quantify pulses in the single-injector combustion rig

that PERM was relatively easy to implement on a commercial engine platform, and demonstrated good control of combustion oscillations.

2 Single Fuel Injector Modulation Development

Before conducting complete engine tests, significant effort was made to develop and test the fuel modulation on a single fuel injector. Figure 3 shows a schematic of the fuel injector flow path with a solenoid and accumulator added to the baseline configuration. Note that when the solenoid is opened, there are two paths for fuel flow. Fuel flows from the accumulator into the premixer, momentarily increasing the fuel flow while the accumulator and supply pressure bleed down to new steady-state values. The two flow paths are set up with internal orifices so that the flow rate down each leg is established by the pressure drop along each path. If the solenoid is modulated, the pressure in the accumulator rises and falls with the fuel flow. As in Richards et al. [15], the variation in fuel flow can be calculated by measuring the accumulator pressure as follows. A control volume equation for mass conservation in the accumulator volume V is written as

$$\frac{d}{dt}(\rho V) = \dot{m}_{\text{in}} - \dot{m}_{\text{out}} \tag{1}$$

where the mass flow in and out of the accumulator are identified by the respective subscripts on the right, and the density is ρ. Assuming that the pressure P in the accumulator can be described by isentropic compression and expansion of the fuel with specific heat ratio γ, then $P\rho^{-\gamma}$=constant, and Eq. (1) can be rewritten

$$\frac{V}{c_0^2}\frac{dP}{dt} = \dot{m}_{\text{in}} - \dot{m}_{\text{out}} \tag{2}$$

where c_0 is the speed of sound in the fuel at the operating temperature. Ignoring the small volume of fuel stored in the connecting lines, Eq. (2) can be used to measure the variation in fuel flow by simply measuring the pressure in the accumulator. The terms on the right do not need to be individually determined. The difference between what is going in and out of the accumulator represents the fuel that is stored in the accumulator, and therefore not sent to the fuel injector. In this manner, Eq. (2) was used to calculate the size of fuel modulation from the slope of the accumulator pressure signal.

As shown in Fig. 3, an additional pressure transducer was added to the plenum that supplies the individual fuel jets that supply fuel to the premix air. Pressure measurements at this point can be used to further verify the size of pulses delivered to the premixing passage and provides a direct check on the pulse generation hardware. It was also possible to estimate the size of the fuel pulses by measuring the steady flow coefficients of the various flow paths with the solenoid open or closed, and then treat the problem as quasi-steady flow for the solenoid open, or closed. This approach compared within 10% of the measured accumulator pressure and showed that a quasi-steady model could be used to describe the flow modulation. This result is important for the actual engine installation (Sec. 4), where it was desired to avoid using an accumulator. The pulse hardware was designed to modulate the fuel flow by approximately ±12% of the average equivalence ratio. This value of modulation was selected based on initial testing (not described here) where the quantity of modulated fuel was studied, and it was shown that the target 12% produced adequate modulation of the flame for this fuel injector. Higher or lower modulation values could be studied (and, in some instances, were effective) by simply adjusting the orifices in the flow passages of Fig. 3.

The fuel solenoid was a commercial valve manufactured for natural gas injection in stationary reciprocating engines. The valve was rated to operate at modulation frequencies as high as 125 Hz, with a lifetime of several years in natural gas engine applications. The frequency response of the valve was tested by recording the pressure signals described in the preceding paragraph. It was found that the frequency response was essentially flat over the operating range. As noted above, the predicted and measured accumulator pressures agreed within 10% using a quasi-steady model for fuel flow, affirming the flat frequency response.

3 Experimental Combustion Tests Modulating a Single Fuel Injector

The fuel injector in Fig. 3 was installed in a single nozzle, can-type combustor at the National Energy Technology Laboratory. The combustor has been described elsewhere [17] and is shown in Fig. 4. Facilities at the National Energy Technology Laboratory can supply 1.4 kg/s, unvitiated air at temperatures up to 800 K, with maximum test pressures up to 30 atm. These capabilities allowed single fuel injector testing at temperatures, pressures, and flow rates which existed on the actual engine installation.

Referring to Fig. 4, air enters the inlet plenum at the left, and passes though the fuel nozzle where natural gas is premixed. Combustion is stabilized in the 19.8 cm (7.80 in) cylindrical combustion zone. The combustion zone walls are water cooled, and there are no dilution ports or cooling holes. The combustion products flow through a refractory plug that forms an exhaust neck (10.5 cm i.d., 22.9 cm length). This neck provides acoustic and flow boundaries that are representative of the actual engine installation. Baseline testing demonstrated that the combustor exhibited oscillations with frequencies comparable to those observed on the engine. An *exact* correspondence between oscillating conditions on the engine, and the test rig was not achieved, but the similarities were close enough to allow development. Cohen et al. [18] explain the complication of reproducing observed engine oscillations on a corresponding single-nozzle test rig. For these tests, there was no need to precisely duplicate oscillating behavior on the single-nozzle rig because subsequent testing was carried out in the complete engine (Sec. 4).

After leaving the exhaust neck, combustion products were quenched with a water spray to $<$475 K to minimize any postquenching reactions. The resulting products were sent to a

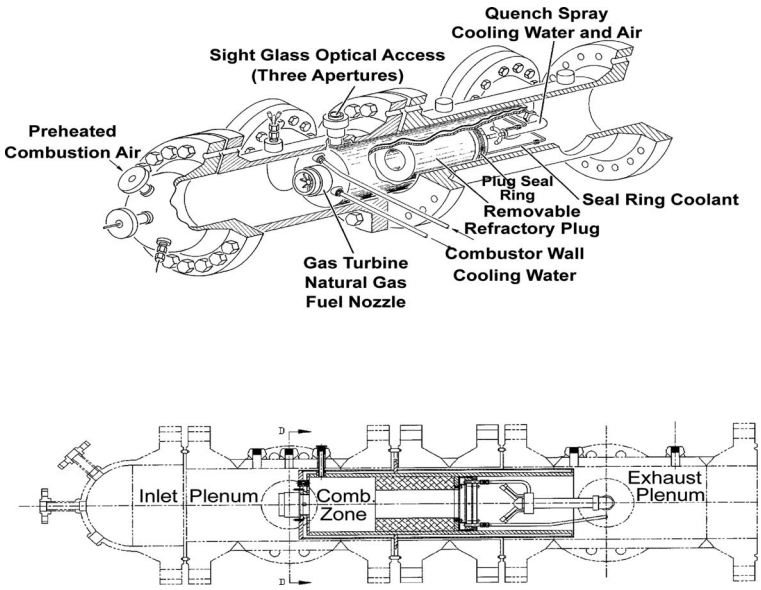

Fig. 4 Schematic of combustor used for single-injector test of fuel modulation

stack where a back-pressure control valve was used to establish the operating pressure. Pollutant emissions were measured in the exhaust stack downstream of the water spray.

The following instrumentation was used to record the test results. Dynamic pressures were recorded in the combustion zone using a Kistler model 206 dynamic pressure transducer, mounted outside the vessel on an infinite coil transmission line. Pressure in the fuel accumulator (Fig. 3) was also recorded with a Kistler model 206, mounted directly into the wall of the accumulator vessel. The combustion heat release perturbations were recorded with a fiberoptic probe, located 2.54 cm downstream of the combustion zone dump plane, viewing across the combustor centerline. The ultraviolet light generated by OH^* chemiluminescence (310 nm) can be used to monitor the variation in combustion heat release [19]. The light collected by the probe was passed through an optical interference filter, and focused on a photomultiplier to produce the heat release signal. The probe position did not provide a complete view of all the flame, but gave a qualitative picture of variations in the heat release as shown next.

The bulk air flow rate is defined by a reference velocity V_r, which is the mass flow divided by the inlet density and fuel nozzle cross-sectional area. Combustor testing was carried out at 7.8 atm pressure, two inlet air temperatures (533 K and 588 K), two reference velocities (V_r=59 m/s and 69 m/s), and a range of equivalence ratios ϕ. Results presented here are chosen as representative of the behavior observed during these tests. For reference, the operating conditions for the following figures are presented in Table 1, along with the NO_x and CO ratios discussed later.

Figure 5 presents the time history of various parameters at the test conditions indicated in Table 1. This is a baseline condition, without fuel modulation. The combustor pressure is shown on the top graph and indicates a strong oscillation at 240 Hz. The fuel manifold (spoke plenum, Fig. 3) pressure also oscillates, demonstrating the acoustics oscillations penetrate into the fuel delivery system, but are attenuated compared to the combustor pressure. Without fuel pulsing, the accumulator pressure is characterized by very low amplitude oscillations. The heat release signal from OH^* shows the oscillation in combustion that is driving the combustion dynamics. Finally, the lower graph shows the signal to the modulating solenoid, which is closed in this baseline condition.

Table 1 Test Conditions and Observed Emissions Ratios for Figs. 5–8.

Fig	V_r	ϕ	control action	CO ratio	NO_x ratio
5	69	0.55	baseline	1	1
6	69	0.55	10 Hz	~1	1.4
7	59	0.63	5 Hz	~1	1.16
8	59	0.56	5 Hz	42	2.15

When the fuel pulsing is activated, the oscillating history changes dramatically. Figure 6 shows the result of open-loop fuel pulsing at the same conditions as Fig. 5. Fuel pulsing was carried out at 10 Hz. At these conditions, the oscillating combustor pressure is dramatically modulated by the fuel pulsing. Noting the discussion concerning Eq. (2), the slope of the accumulator pressure indicates the fuel flow rate such that the equivalence ratio is higher when the accumulator empties and the pressure slope is negative. Thus, oscillations decline as the fuel flow from the accumulator increases the equivalence ratio, and the oscillations grow again as the solenoid closes. The OH^* signal shows that the oscillation in heat release is almost eliminated during a portion of the modulation cycle. These results are consistent with the description of single-sided combustion instability provided in Fig. 1, and demonstrate that this type of instability can only be turned on and off, but not eliminated by fuel modulation on a single fuel nozzle. However, actuation of multiple injectors in an engine may still produce control as shown in Sec. 4.

It is emphasized that the effect of fuel modulation on oscillations was very dependent on the operating conditions. In some instances, fuel modulation had very little effect on the observed oscillation. For example, Fig. 7 shows the effect of fuel modulation at different conditions than in Fig. 6. The fuel modulation produced little effect on the baseline oscillation. The baseline oscillation without control is not shown because it is very similar to that with control. Note that the lower limit of the OH^* signal rises and falls slightly with the fuel modulation, but the oscillation is almost unaffected. In this case, the fuel modulation is unsuccessful in moving the operating condition to a stable point as described in Fig. 1. As another example, Fig. 8 shows the effect of fuel pulsing at a lower average equivalence ratio than Fig. 7. At this condition, the oscillation is clearly interrupted by the control action. Note that the OH^* signal indicates that the flame is momentarily absent from the probe field of view—the flame is lifted

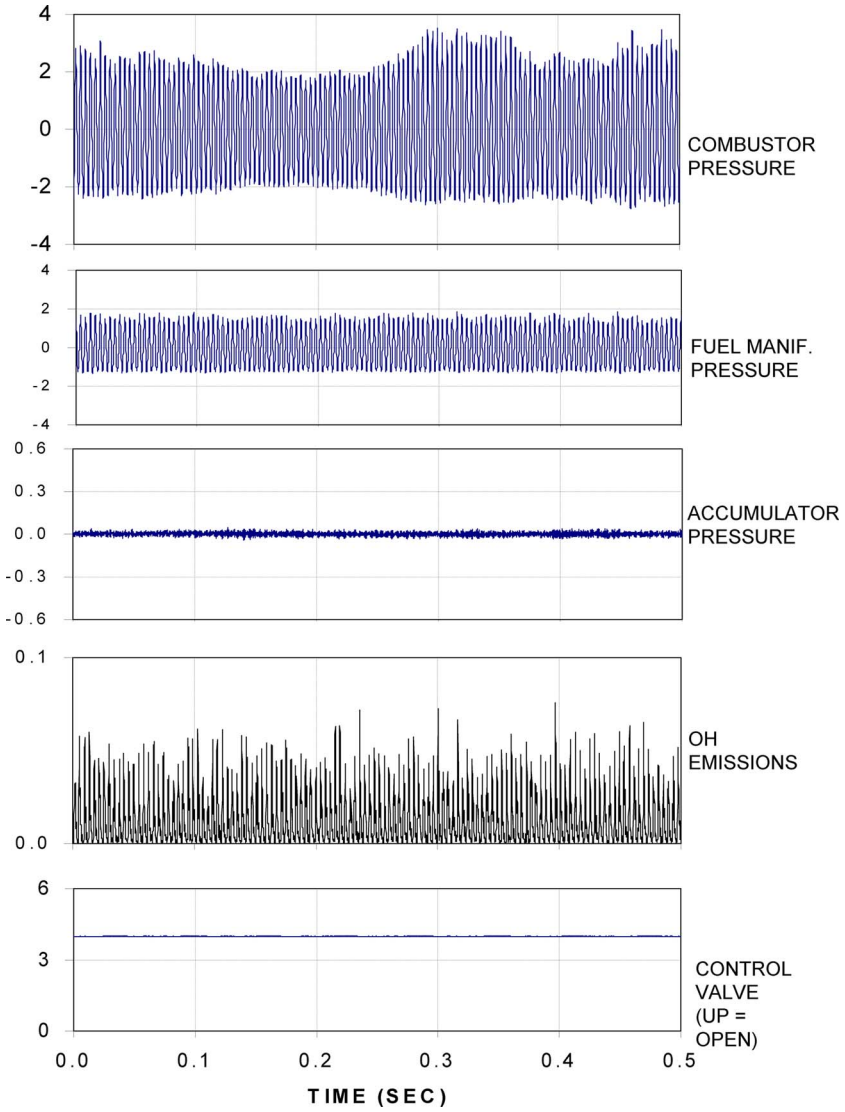

Fig. 5 History of various signals at conditions indicated in Table 1. This is the baseline, without fuel modulation (pressures in pounds per square inch).

as the equivalence ratio drops. Depending on the operating conditions, these results demonstrate that the PERM technique can significantly disrupt the flame anchoring. This may be a disadvantage because it could promote flame blowout, yet the flame was easily maintained in the present tests.

Pollutant emissions were recorded during the control cases described above. Table 1 reports the *ratio* of NO_x and CO emissions between the baseline and the modulated cases. In most cases, the effect of fuel modulation was an increase in the NO_x. The CO emissions were almost unaffected by the fuel modulation, except at the leanest operating condition, where the CO was dramatically increased. Noting the discussion of flame anchoring above, fuel modulation near the lean blowout may not be practical due to CO emissions and flame anchoring. These results are readily understandable. At higher equivalence ratios, the fuel modulation produces momentarily richer fuel pockets, which can produce hot transients that contribute to NO_x. As will be seen later, the emissions response in the engine application was quite different.

In summary, tests of the single fuel nozzle demonstrated that PERM could disrupt single-sided instabilities as described in Fig. 1. The effect on emissions was modest, except near the lean extinction, where problems in flame anchoring and high CO emissions may limit the application of this control technique.

4 Experimental Tests on a Gas Turbine Engine

Engine testing was carried out on an experimental test engine located at Solar Turbines. The combustor was an annular geometry, using 12 premix fuel nozzles. Figure 9 shows a cross-section of the combustor, identifying the fuel injectors and eight dynamic pressure transducers (PT-1 through PT-8). The open circles represent the position of the premixing passages supplying the combustor annulus. Two of the pressure transducers were mounted on the fuel supply lines to monitor the dynamic affects of the control pulses on the fuel manifold and the flow passage downstream of the modulating solenoid valve. These signals could be used to affirm the magnitude of the flow modulation. The remaining six pressure transducers (PT 1,2,4,5,7) were distributed around the perimeter of the combustor so that an root-mean-square (rms) pressure could be determined as an average of the six transducers. It was important to consider measurement of multiple transducers because tests without control showed that fixed acoustic nodes could be established in the annular geometry. Thus, a single-pressure measurement might provide a false picture of the amplitude of the oscillation.

As in the single-nozzle testing, a fiberoptic probe was used to record the OH chemiluminescence signal from a position 2.5 cm

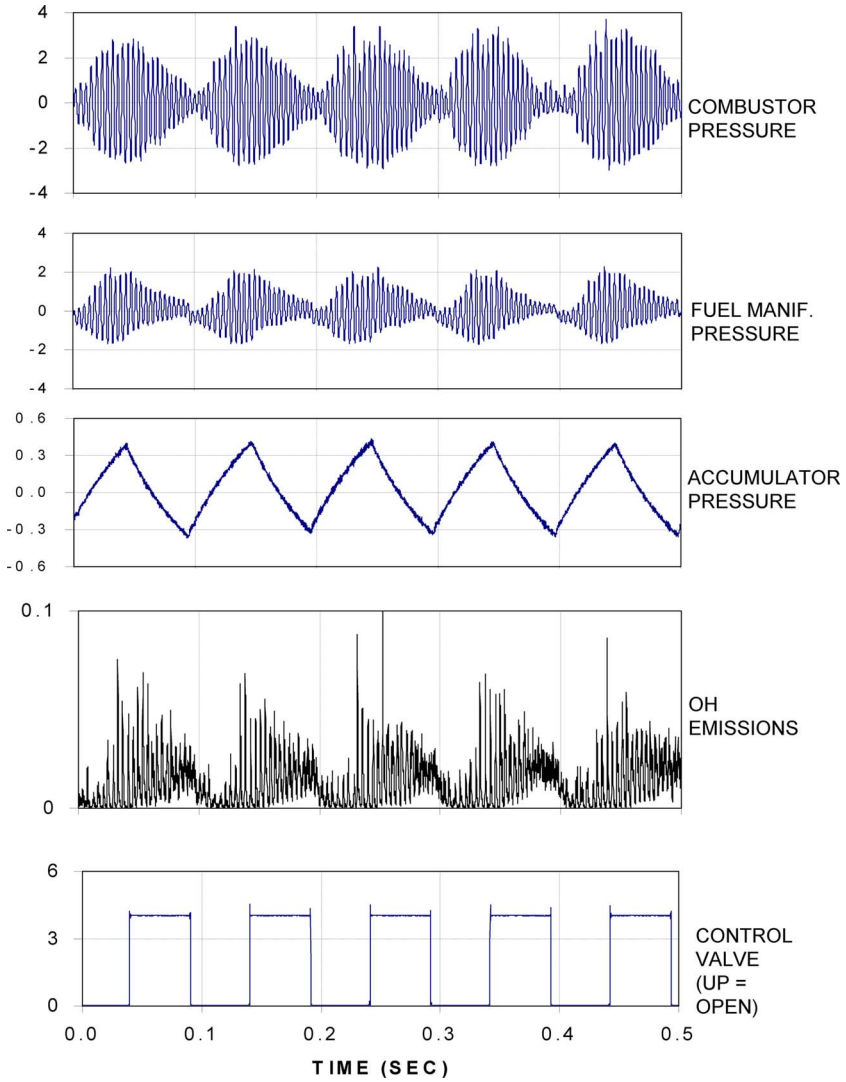

Fig. 6 History of various signals at conditions with fuel modulation. Same operating conditions as in Fig. 5, (pressures in pounds per square inch).

downstream of the injector face on fuel injector 2 (Fig. 9). This signal was used to verify the imposed heat release variations.

The fuel pulsing hardware was similar to that in Fig. 3, except that the fuel accumulator was absent. As explained in Sec. 3, testing with the fuel accumulator was used to quantify the unsteady flow rates produced by modulating one flow path but was not needed in the engine tests. All 12 injectors were outfitted with a solenoid and flow path similar to Fig. 3.

When PERM is activated, the open solenoids present added flow area for the gaseous fuel. If the throttle position were unchanged, this larger flow area would increase engine fuel flow. However, the engine control system still retains control of the fuel flow, so that the added flow area is readily compensated by a (slight) reduction in engine throttle position, so as to maintain the same engine power level before and after control is activated. During the transition between uncontrolled and controlled status, no problems were encountered with engine operation, flame out, or high turbine inlet temperatures.

Figure 10 is a schematic of the test cell instrumentation and control wiring. The solenoid valves were powered by a 12 V/48 amp power supply. Control signals activated the solenoid coils via a powered integrated circuit switch supplied by the solenoid. Control signals (TTL) were generated by the control computer software developed for this application. The control software was designed to allow rapid transition between various control modes and control parameters described below. The control computer also took an average of the six dynamic pressure transducers to calculate the rms pressures reported here. Also shown on Fig. 10, time-series data were recorded on a TEAC RD-145T digital audio tape recorder, using 16 channels with a sampling frequency of 6 kHz per channel. Pollutant emissions were recorded using standard infrared or chemiluminescent analyzers, following standard practices for engine emission measurements.

4.1 Control Modes. With 12 injectors, many different scenarios for fuel modulation exist. For example, referring to the numbering scheme on Fig. 9, modulation can increase the fuel flow on the even-numbered injectors, and then alternate with the odd-numbered injectors. Alternatively, one can increase the fuel flow on injectors 1–6, and then alternate with injectors 2–7, then 3–8, and so on. This latter scenario would produce a higher equivalence ratio in half of the combustor annulus, rotating at the modulation frequency. Compared to modulating odd-even, this would minimize the interaction between adjacent injectors, insuring that the high equivalence ratio on one injector was not impacted by leaner conditions from adjacent injectors.

In addition, scenarios are possible where a reduced number of

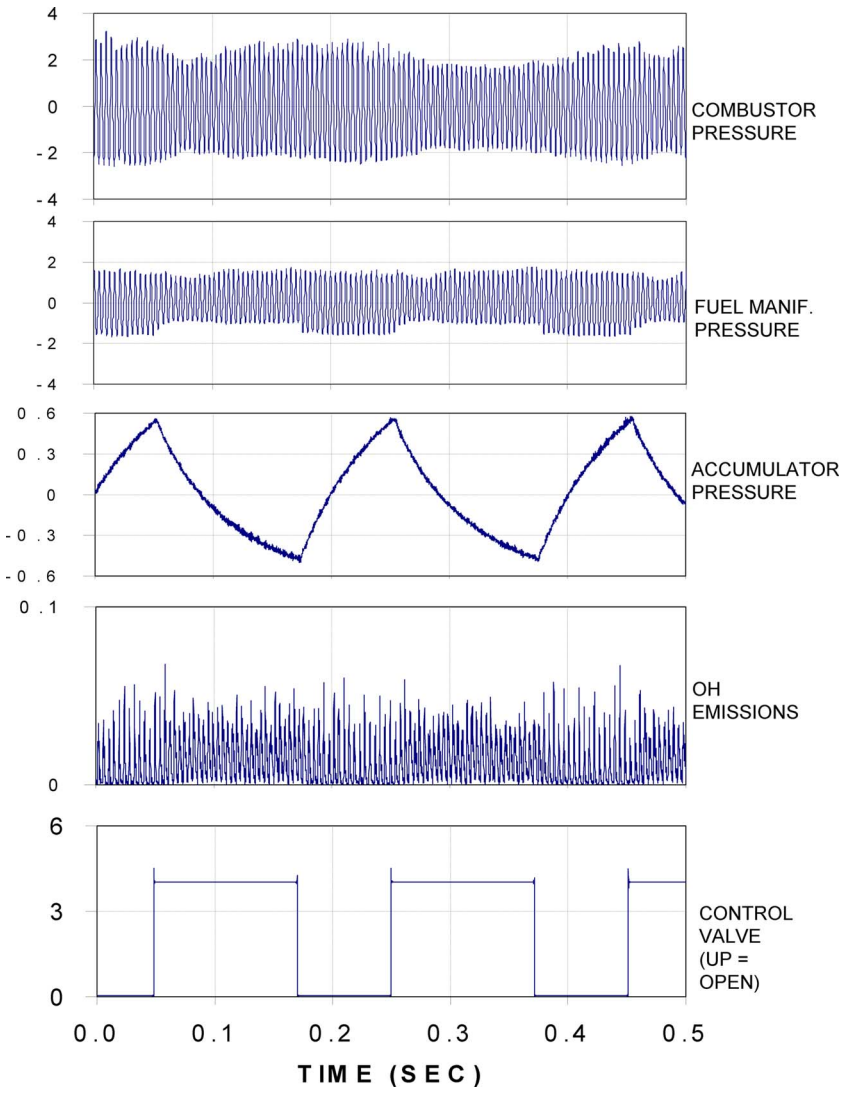

Fig. 7 History of signals at conditions (Table 1) where fuel modulation had little effect on the oscillation (pressures in pounds per square inch)

injectors are modulated. For reference, the term "overlap" will be used to describe the number of injectors where the solenoids are simultaneously open. The odd-even modulation describe above is therefore six-overlap because at any point in time, six solenoids are open.

As an example of four-overlap, one can modulate the fuel flow in just four injectors (1,4,7,10) and then switch to four more (2,5,8,11), and finally to the remaining (3,6,9,12). If control is successful modulating a reduced number of injectors, the impact on emissions may be reduced.

Thus, a case can be made for considering many different modulation scenarios. Testing on the engine was carried out with five different modulation scenarios, and overlap values of 1, 2, 4, and 6. Rather than describe all these different situations, this paper presents just a single-control scenario (odd-even). Testing other scenarios revealed that the control effects were qualitatively similar *as long as they used six-overlap modulation*. In other words, it was found that control of the baseline oscillation was only successful when six injectors were modulated together. Any arrangement of modulating the injectors with less than six-overlap was not able to produce control of the baseline oscillation.

4.2 Results of Engine Testing. The solenoids were modulated over a range of frequencies, using the odd-even scheme described above. Testing was conducted near full-load engine conditions, where dynamic oscillations were observed. Unlike the single-injector tests (Sec. 3) the engine testing was conducted with a small premixed pilot flame ($\sim$2% of the fuel) used to maintain flame anchoring. Figure 11 shows a graph of the RMS pressure, and the CO and NO_x emissions. As explained above, the rms was an average of the six combustor pressure transducers and was expressed as a percentage of the combustor operating pressure. The CO and NO_x emissions were normalized by the baseline value measured before the control action was activated. Figure 11 shows results at modulation frequencies ranging from 10 to 96 Hz. The 24 Hz, 48 Hz, and 96 Hz cases were tested because these frequencies were integral divisors of the main oscillation (288 Hz). It was desired to insure that the fuel modulation did not provide subharmonic driving of the combustor acoustic modes (which it did not).

Inspecting the graph, the effect of fuel modulation at any frequency is almost a threefold reduction in the rms pressure. The effect on NO_x is also very encouraging, demonstrating a modest *reduction* as control is actuated. However, the CO emissions rise unacceptably for modulation frequencies of $<$80 Hz, increasing by more than a factor of 4. At higher modulation frequencies, the CO is increased over the baseline by approximately a factor of 2,

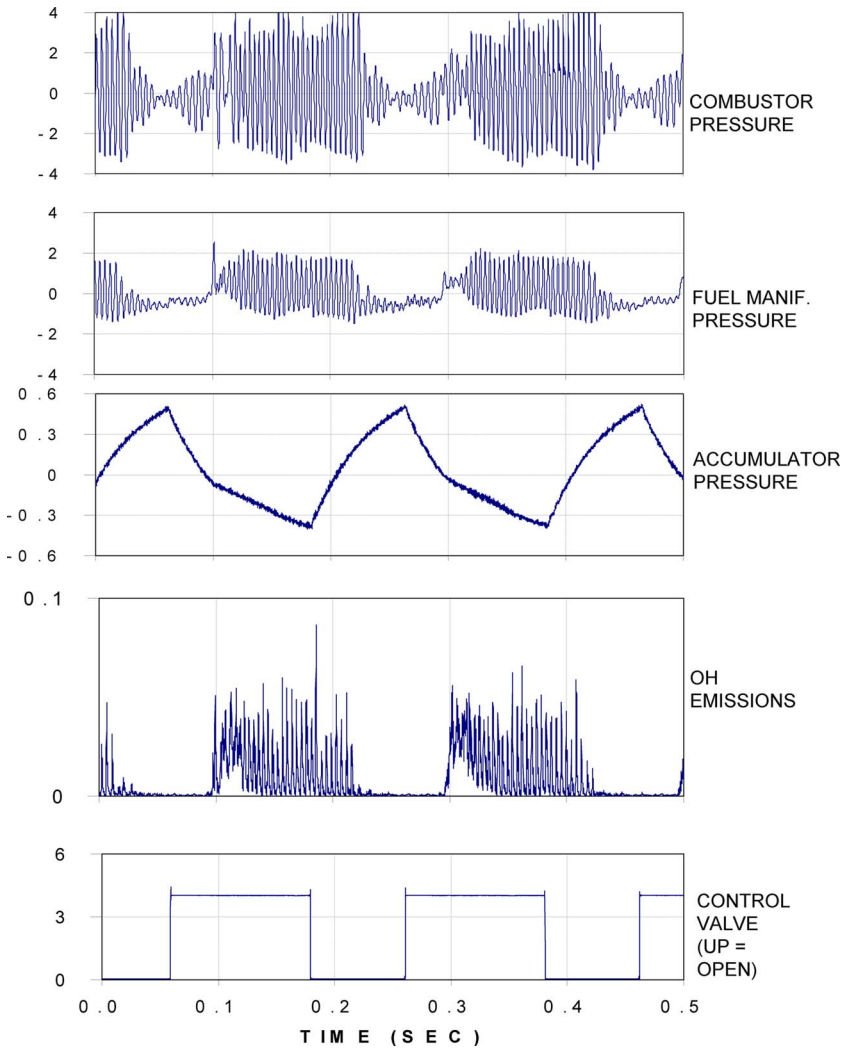

Fig. 8 History of signals at conditions (Table 1) where the flame anchoring was disrupted by the control action

while both the rms pressure and the NO_x levels remain lower than the baseline. The emissions behavior is discussed in more detail later, but it should be noted that both NO_x and CO emissions can depend on the presence or absence of oscillations. Thus, there is a compound effect on emissions from both the fuel modulation, and the control of the oscillation.

Tests with different modulation patterns discussed in Sec 4.1 showed comparable behavior. As long as the test used six-overlap (i.e., six solenoids open at any time), the combustor oscillation was controlled. During the controlled condition, the NO_x was comparable or less than the baseline, but the CO was always higher than the baseline. The CO level dropped with increasing modulation frequency, but was still at least a factor of two larger than the baseline. In addition, tests with duty cycles of $<50\%$ were also conducted, i.e., where the solenoids were opened for $<50\%$ of the period of modulation. As in lab scale tests described in [15], the reduced duty cycle was less effective at controlling the rms amplitude and is not reported here.

It is helpful to consider that time history of the oscillation. Figures 12(*a*) and 12(*b*) compare (i) the baseline condition in Fig. 11 with (ii) the fuel modulation at 40 Hz. Refer to Fig. 9 for the location of the various signals. In Fig. 12(*a*) the combustor pressure recorded from PT-1 and PT-2 show the baseline oscillation. Note that these pressures are located 60 deg apart on the liner (Fig. 9) and have different amplitudes because a fixed standing

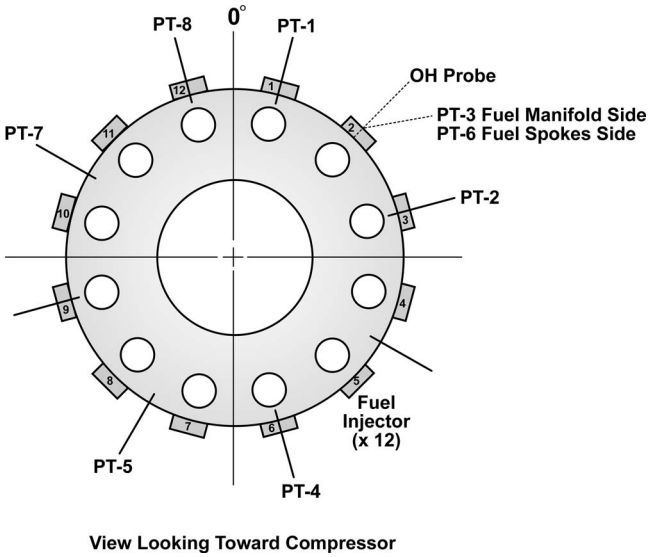

Fig. 9 Cross section of the engine combustor annulus. The fuel injector and pressure transducer (PT) numbering scheme is shown.

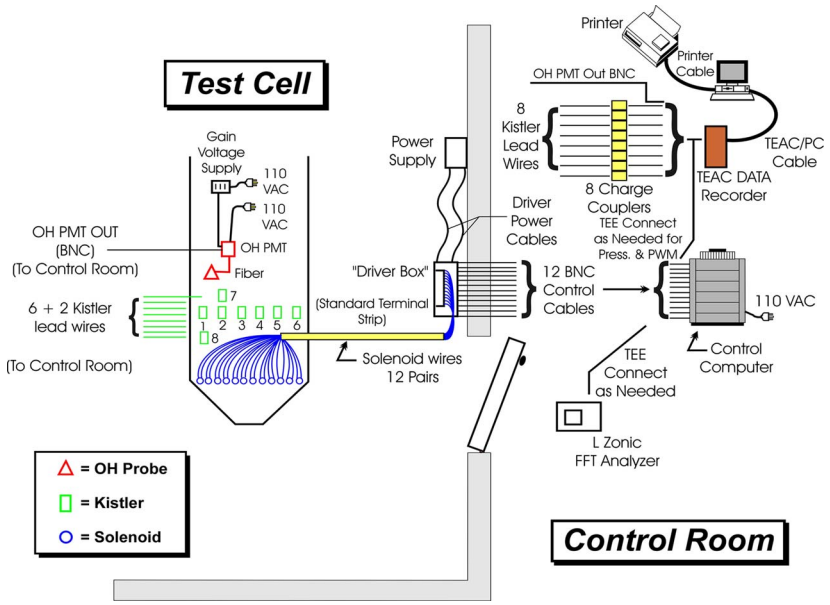

Fig. 10 Schematic of test cell and instrumentation layout

wave in the annulus of the combustor. The OH^* signal reflects the well-organized variation in heat release that drives the oscillating pressure. Considering Fig. 12(*b*) the solenoids are activated. For reference, the lower two traces show the odd-even actuation between injectors 2 and 3. Compared to Fig. 12(*a*) the oscillating pressure amplitudes are dramatically reduced, and the well-organized OH^* oscillation is appreciably disrupted. The large amplitude variation in heat release (measured at injector 1) is synchronized with the odd solenoid opening (injector 3 shown here). It should be noted that some organized oscillations persist in the combustor, but at much reduced amplitude. Compared to tests conducted in the single-nozzle experiments (Sec. 3), the OH^* signal does not indicate any problems with flame liftoff during the control event, but as noted, the CO emissions were undesirably high.

To further explore how control is achieved in this system, a separate test was conducted to evaluate what happens if the individual injectors were operating at constant, but different, equivalence ratios. This could be accomplished by simply opening the solenoids on the odd-numbered injectors (i.e., not modulating). In this manner, the odd-injectors would operate at the higher equivalence ratio, and the even-injectors would operate at the lower equivalence ratio. Referring again to Fig. 2, this could place nozzle A in a stable region, and nozzle B in an oscillating region.

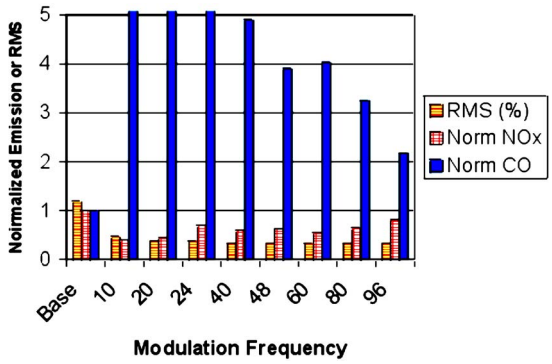

Fig. 11 Rms pressure (% of combustor pressure) and normalized emissions at the baseline condition, and with fuel modulation at various frequencies

Figure 13 shows the result of this test. The baseline rms and emissions are compared to what happens as the odd-numbered injector solenoids are progressively opened. Both the rms pressure and the CO emissions rise as the injectors are activated. As noted in Richards et al. [15], the PERM concept relies on modulating fast enough to avoid development of oscillations at any one operating condition. These data support the hypothesis that modulation is necessary to produce control, i.e., it is not adequate to simply operate the different fuel injectors at different values of ϕ. Figure 13 also shows the remarkable sensitivity of CO to changes in the fueling distribution. Activating even one solenoid produced a fourfold increase in CO, suggesting that some partial combustion products are being quenched downstream of the richer fuel injector. The drop, then rise, in CO as injectors 3 and 5 were activated was not spurious. Similar trends were observed when a comparable test was conducted activating injectors 1–6 in a sequential manner. In practical turbine combustion liners, it is widely recognized that CO emissions can be complicated by quenching in uncontrolled dilution air jets. Because this liner used a number of additional drilled holes for the optical OH probe, and pressure probes, air leaking around these ports may increase the CO levels.

It is important to note that the CO levels themselves depend on the presence of the oscillation. Thus, comparing the CO levels with and without modulation also compares the CO levels with and without the presence of strong oscillations. To show that the CO was not completely determined by the fuel modulation, a test was conducted with fuel modulation on an otherwise stable combustion condition. Figure 14 shows the result of fuel modulation at an engine condition where the baseline combustion is stable. Note that the rms pressure is not affected by the fuel modulation so that the increased CO is not attributed to the control of the oscillation. The fuel modulation at lower frequencies again produces an increase in CO emissions, but it is not as dramatic as in the cases where oscillations were eliminated by the control action. At the highest modulation frequency, the normalized CO was just 1.3 compared to the baseline. As in the control cases, the NO_x emissions actually decrease with the fuel modulation. This interesting effect on NO_x differs from studies in the lab combustor (Sec. 4), where fuel modulation almost always produced a modest increase in NO_x emissions. There are differences between the single-nozzle testing and the engine testing. The engine configuration has adjacent flames, liner cooling flows, and a stabilizing

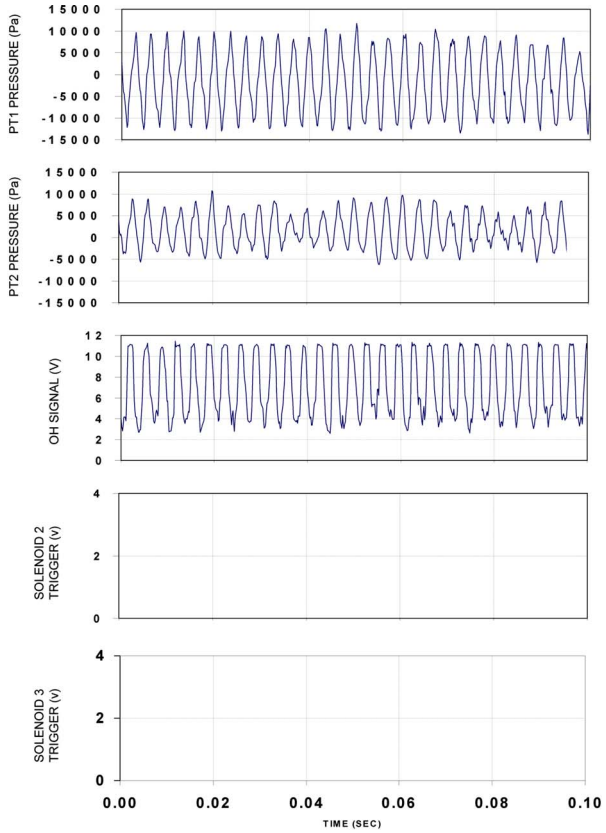

(*a*)

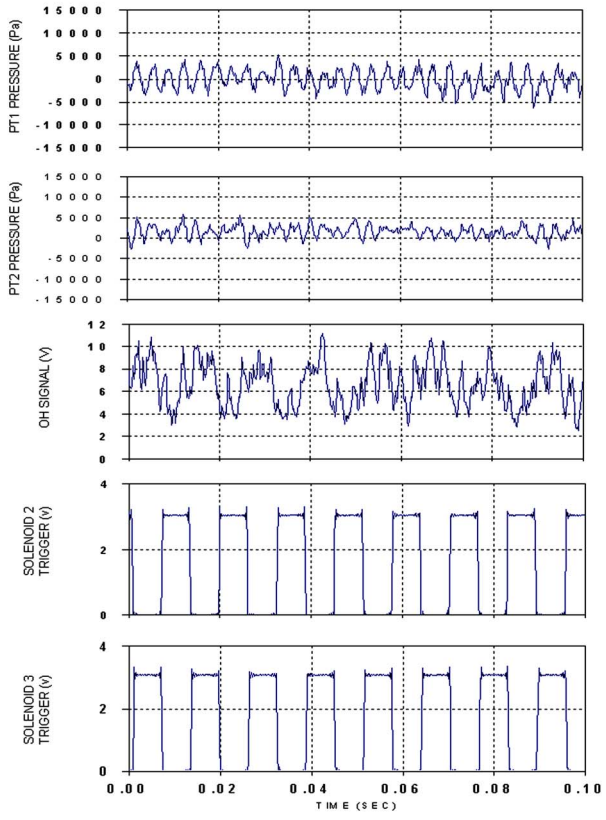

(*b*)

Fig. 12 (*a*) **Baseline dynamics at conditions of Fig. 11. Note the solenoid trigger signals are not active.** (*b*) **Observed dynamics with odd-even fuel modulation activated at 40 Hz. Note the odd-even activation of solenoid triggers 2 versus 3.**

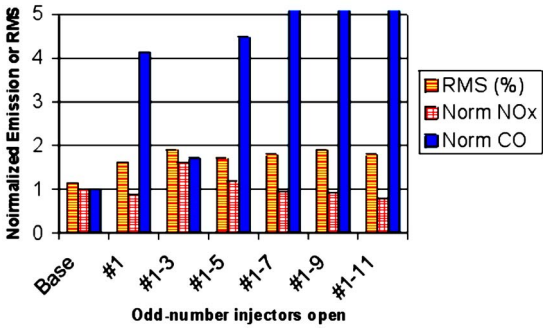

Fig. 13 Rms pressure and emissions for steady solenoid valve opening on odd-numbered injectors. The labels are inclusive (i.e.; injectors 1–7=1, 3, 5, 7, etc.).

pilot flame. However, these differences do not provide a clear explanation for the reduced NO_x observed during engine fuel modulation. As in the single-nozzle testing, it seems likely that momentary excursions to higherequivalence ratio should produce slightly more NO_x not less. More investigation is needed to understand this effect.

The promising control results presented here must be tempered by the recognition that PERM control cannot work at conditions where the baseline oscillation is not disrupted by an equivalence ratio shift. This was clear from single-nozzle testing presented in Fig. 7, where PERM had virtually no effect on oscillations. Just as Fig. 14 showed that PERM did not move the combustor to unstable conditions, other engine operating conditions demonstrated that PERM would not disrupt a stubborn oscillation and could even lead to oscillations. Additional testing of the PERM concept was conducted on a second engine application that did not have well defined stability boundaries. In that case, PERM modulation had little effect on the oscillation. These results can all be justified from the presence or lack of stability boundaries shown in Figs. 1 and 2. However, lacking detailed knowledge of the stability boundaries, no definitive prediction can be made about the success of PERM without testing. Fortunately, the hardware changes needed to conduct a test are modest and do not require any changes to the internal components of the engine. Development of both reduced and detailed models are planned to further explore the control effect, and the emissions data. The encouraging results presented here justify additional theoretical and experimental investigation of this approach.

5 Summary

A concept for open-loop active control of combustion dynamics was proposed, developed, and tested on a single fuel injector test rig and on a gas turbine engine. The control concept uses periodic

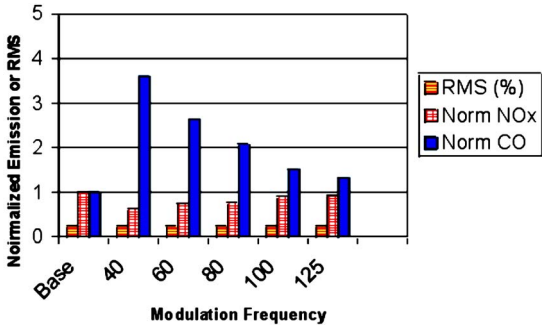

Fig. 14 Effect of fuel modulation on pollutant emissions when the engine conditions produce stable (nonoscillating) combustion

equivalence ratio modulation (PERM) to modulate the equivalence ratio on different fuel injectors so that at least one-half of the engine injectors are operating at stable conditions. Tests of this concept were developed on a single-injector test rig and showed that PERM could disrupt oscillations at many test conditions. Depending on test conditions, fuel modulation produced a modest increase in NO_x, and a widely variable effect on CO emissions, in the single-injector tests.

Tests on a gas turbine engine showed that PERM was relatively easy to install and operate using commercial fuel solenoids inserted in the fuel piping outside of the engine pressure casing. The fuel solenoids are designed for continuous cyclic service in reciprocating NG engines and are expected to have a lifetime of several years. No changes were made to the existing engine throttle control system. Tests demonstrated that control of oscillations required that the baseline oscillation exist near a stability boundary, such that equivalence ratio modulation could disrupt the oscillation. Engine testing showed that PERM could reduce oscillation amplitude by one-third, but with an increase in CO emissions, and a modest *decrease* in NO_x emissions. The reasons for the emissions response are not clear at this time, since single-injector testing showed that NO_x generally increased with fuel modulation. Additional modeling studies are suggested to fully explain both the control mechanism and the pollutant response.

Acknowledgment

Financial support from the U.S. Department of Energy is gratefully recognized. The technical staff at both NETL and Solar Turbines is acknowledged for helping plan and conduct this research. There are too many individual contributions to list here, but the authors wish to recognize the support of our co-workers.

References

[1] Mongia, H. C., Held, T. J., Hsiao, G. C., and Pandalai, R. P., 2003, "Challenges and Progress in Controlling Dynamics in Gas Turbine Combustors," J. Propul. Power, **19**(5), pp. 822–829.

[2] Cohen, J. H., Rey, N. M., Jacobson, C. A., and Anderson, T. J., 1999, "Active Control of Combustion Instabilities in a Liquid-Fueled Low-NO_x Combustor," ASME J. Eng. Gas Turbines Power, **121**(2), pp. 281–284.

[3] Sattinger, S. S., Neumeier, Y., Nabi, A., Zinn, B. T., Amos, D. J., and Darling, D. D., 1998, "Subscale Demonstration of the Active Feedback Control of Gas Turbine Combustion Instabilities," ASME Paper No. 98-GT-258.

[4] Johnson, C. E., Neumeier, Y., Zinn, B. T., Darling, D. D., and Sattinger, S. S., 2001, "Demonstration of Active Control of Combustion Instabilities on a Full-Scale Gas Turbine Combustor," ASME Paper No. 2001-GT-0519.

[5] Jones, C. M., Lee, J. G., and Santavicca, D. A., 1999, "Closed-Loop Active Control of Combustion Instabilities Using Subharmonic Secondary Fuel Injection," J. Propul. Power, **15**(2), pp. 1–7.

[6] Seume, J. R., Vortmeyer, N., Krause, W., Hermann, J., Hantschk, C.-C., Zangl, P., Gleis, S., Vortmeyer, D., and Orthmann, A., 1998, "Application of Active Combustion Instability Control to a Heavy Duty Gas Turbine," ASME J. Eng. Gas Turbines Power, **120**(4), pp. 721–726.

[7] McManus, K. R., Vandsburger, U., and Bowman, C. T., 1990, "Combustor Performance Enhancement Through Direct Shear Layer Excitation," Combust. Flame, **82**, pp. 75–92.

[8] Uhm, J. H., and Acharya, S., 2004, "Open Loop Control of Combustion Instability with a High-Momentum Air Jet," ASME Paper No. GT2004-53989.

[9] Richards, G. A., Yip, M. J., Robey, E., Cowell, L., and Rawlins, D., 1997, "Combustion Oscillation Control by Cyclic Fuel Injection," ASME J. Eng. Gas Turbines Power, **119**(2), pp. 340–343.

[10] Prasanth, R. K., Annaswamy, A. M., Hathout, J. P., and Ghoniem, A. F., 2002, "When Do Open Loop Strategies for Combustion Control Work?" J. Propul. Power, **18**(3), pp. 658–668.

[11] Smith, C. E., and Cannon, S. M., 1999, "CFD Assessment of Passive and Active Control Strategies for Lean, Premixed Combustors," AIAA Paper No. 99-0714.

[12] Pashcereit, C. O., Gutmark, E., and Weisenstein, W., 1999, "Control of Combustion Instabilities in a Premixed Combustor by Fuel Modulation," AIAA Paper No. 99-0711.

[13] Shcherbik, D., Neumeier, Y., Lubarsky, E., Zinn, B. T., McManus, K., Fric, T. F., and Srinivasan, W., 2003, "Suppression of Instabilities in Gaseous Fuel High-Pressure Combustor Using Non-Coherent Oscillatory Fuel Injection," ASME Paper No. GT2003-38103.

[14] McManus, K., Han, F., Dunstan, W., Barbu, C., and Shah, M., 2004, "Modeling and Control of Combustion Dynamics in Industrial Gas Turbines," ASME Paper No. GT2004-53872.

[15] Richards, G. A., Janus, M. C., and Robey, E. H., 1999, "Control of Flame Oscillations with Equivalence Ratio Modulations," J. Propul. Power, **15**(2), pp. 232–240.

[16] Richards, G. A., Janus, M. C., and Griffith, R. A., 2000, "Periodic Equivalence Ratio Modulation Method and Apparatus for Controlling Combustion Instability," U.S. Patent No. 6,059,560.

[17] Richards, G. A., and Janus, M. C., 1998, "Characterization of Oscillations During Premix Gas Turbine Combustion," ASME J. Eng. Gas Turbines Power, **120**(2), pp. 294–302.

[18] Cohen, J. M., Hibshman, J. R., Proscia, W., Rosjford, T. J., Wake, B. E., McVey, J. B., Lovett, J., Ondas, M., DeLaat, J., and Breisacher, K., 2000, "Experimental Replication of an Aeroengine Combustion Instability," ASME Paper No. 2000-GT-0093.

[19] Lee, J. G., and Santavicca, D. A., 2003, "Experimental Diagnostics for the Study of Combustion Dynamics in Lean Premixed Combustors," J. Propul. Power, **19**(5), pp. 735–750.

Catalytic Combustion Systems for Microscale Gas Turbine Engines

C. M. Spadaccini
Center for Micro and Nano Technology,
Lawrence Livermore National Laboratory,
Livermore, CA 94551

J. Peck

I. A. Waitz

Gas Turbine Laboratory,
Department of Aeronautics and Astronautics,
Massachusetts Institute of Technology,
Cambridge, MA 02139

As part of an ongoing effort to develop a microscale gas turbine engine for power generation and micropropulsion applications, this paper presents the design, modeling, and experimental assessment of a catalytic combustion system. Previous work has indicated that homogenous gas-phase microcombustors are severely limited by chemical reaction timescales. Storable hydrocarbon fuels, such as propane, have been shown to blow out well below the desired mass flow rate per unit volume. Heterogeneous catalytic combustion has been identified as a possible improvement. Surface catalysis can increase hydrocarbon-air reaction rates, improve ignition characteristics, and broaden stability limits. Several radial inflow combustors were micromachined from silicon wafers using deep reactive ion etching and aligned fusion wafer bonding. The 191 mm^3 *combustion chambers were filled with platinum-coated foam materials of various porosity and surface area. For near stoichiometric propane-air mixtures, exit gas temperatures of* 1100 K *were achieved at mass flow rates in excess of* 0.35 g/s. *This corresponds to a power density of* $\sim$1200 MW/m^3*; an 8.5-fold increase over the maximum power density achieved for gas-phase propane-air combustion in a similar geometry. Low-order models, including time-scale analyses and a one-dimensional steady-state plug-flow reactor model, were developed to elucidate the underlying physics and to identify important design parameters. High power density catalytic microcombustors were found to be limited by the diffusion of fuel species to the active surface, while substrate porosity and surface area-to-volume ratio were the dominant design variables.*
[DOI: 10.1115/1.2204980]

1 Introduction

Advances in silicon microfabrication techniques and microelectromechanical systems (MEMS) have led to the possibility of a new generation of micro heat engines for power generation and micro air-vehicle propulsion applications. Epstein et al. [1] and Groshenry [2] have reported the design for a silicon-based, micro gas turbine generator that may be capable of producing 10–50 W of power in a volume of <1 cm^3 while consuming 7 g of fuel per hour. Like their larger counterparts, an engine of the type shown in Fig. 1 requires a high-temperature combustion system to convert chemical energy into fluid thermal and kinetic energy.

Previous work in this area has shown that homogenous gas-phase microcombustors are limited by chemical reaction time scales [3–5]. Although hydrogen-air mixtures have been successfully burned in small volumes for micro gas turbine applications, storable hydrocarbon fuels, such as propane, will not combust at the desired mass flow rates within the desired combustor volumes [5]. As a result, heterogeneous catalytic processes have been pursued to increase reaction rates and improve stability.

This paper presents the results of work toward achieving high power density (high mass flow rate) operation of a microcombustion system with propane-air mixtures. These studies have resulted in the identification of critical design trades and recommendations for microcombustor design.

Section 2 discusses the challenges of combustion in a microscale environment and overviews previous work toward the development of silicon-based systems. The design, materials, and testing methodology for catalytic microcombustors are introduced in Sec. 3. In Sec. 4, results from testing of these devices are presented and Sec. 5 includes a low-order modeling effort to explain performance trends. Section 6 reviews design recommendations and trade-offs, and Sec. 7 summarizes the paper and presents areas of future work.

2 Microcombustion Challenges

The functional requirements of a microcombustor are similar to those of a conventional gas turbine combustor. These include the efficient conversion of chemical energy to fluid thermal and kinetic energy with low total pressure loss, reliable ignition, and wide flammability limits. However, the obstacles to satisfying these requirements are different for a microscale device. As first described by Waitz et al. [6], a microscale combustor is more highly constrained by inadequate residence time for complete combustion and high rates of heat transfer from the combustor. Microcombustor development also faces unique challenges due to material and thermodynamic cycle constraints. These constraints are reviewed in Secs. 2.1–2.4.

2.1 Time-Scale Constraints. For the energy conversion applications we are interested in, power density is the most important metric. As shown in Table 1, the high power density of a microcombustor directly results from high mass flow per unit volume. Since chemical reaction times do not scale with mass flow rate or combustor volume, the realization of this high power density is contingent upon completing the combustion process within a shorter combustor through-flow time.

For gas-phase combustors, this fundamental time constraint can be quantified in terms of a residence time-based Damköhler number; the ratio of the residence time to the characteristic chemical reaction time.

$$\mathrm{Da}_1 = \frac{\tau_{\mathrm{residence}}}{\tau_{\mathrm{reaction}}} \tag{1}$$

To ensure a Da_1 greater than unity (and complete combustion), a designer of a microcombustor can either increase the flow resi-

Contributed by the International Gas Turbine Institute (IGTI) of ASME for publication in the JOURNAL OF ENGINEERING FOR GAS TURBINES AND POWER. Paper presented at the ASME Turbo Expo 2005: Land, Sea, and Air, Reno, NV, June 6 – 9, 2005, Paper No. GT2005-68382. Manuscript August 25, 2005; final manuscript received September 28, 2005. IGTI Review Chair: K. C. Hall.

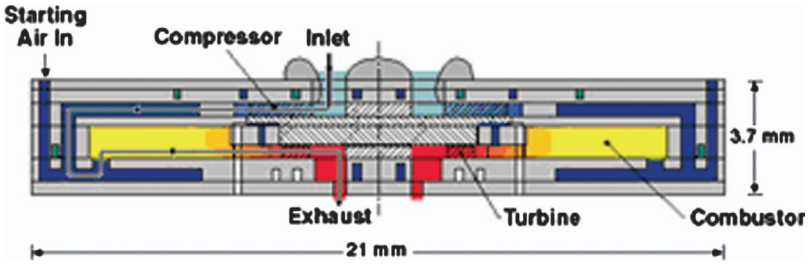

Fig. 1 Baseline engine schematic

dence time or decrease the chemical reaction time. The characteristic combustor residence time is given by the bulk flow through the combustor volume

$$\tau_{\text{residence}} \approx \frac{\text{volume}}{\text{volumetric flow rate}} = \frac{VP}{\dot{m}RT} \tag{2}$$

Residence time can be increased by increasing the size of the chamber, reducing the mass flow rate, or increasing the operating pressure. A chemical reaction time can be approximated by an Arrhenius-type expression.

$$\tau_{\text{reaction}} \approx \frac{[\text{fuel}]_0}{A[\text{fuel}]^a[\text{O}_2]^b e^{-E_a/RT_0}} \tag{3}$$

Reaction time is primarily a function of fuel properties and the mixture temperature and pressure.

Since high power density requirements mandate high mass flow rates through small chamber volumes, the mass flow rate per unit volume cannot be reduced without compromising device power density. Hence, there is a basic trade-off between power density and flow residence time

$$\text{Power density} \propto \frac{\dot{m}}{V} \propto \frac{\dot{m}_f LHV}{V} \propto \frac{\rho}{\tau_{\text{residence}}} \tag{4}$$

For a given operating pressure (and, thus, density), and assuming a fixed Da_I, reducing the chemical reaction time and thus required residence time, is the only means of ensuring complete combustion without compromising the high power density of the device.

One means of reducing this chemical reaction time-scale is to utilize heterogeneous surface catalysis. This oxidation process is fundamentally different from that occurring in a gas-phase combustion system. Typically, the reactions are significantly faster and there is no flame structure since the chemistry takes place on the catalyst surface. However, use of surface reactions introduces an additional time scale to consider when determining the rate-controlling process. The diffusion of the reactant species to the catalyst surface is often the controlling phenomenon. This diffusion time is related to the molecular diffusion coefficient for one species being transported through another and can be estimated using the Fuller correlation [7]

$$D_{AB} = \frac{1.013 \times 10^{-2} T^{1.75} \left(\frac{1}{M_A} + \frac{1}{M_B}\right)^{1/2}}{P[(\sum v_i)_A^{1/3} + (\sum v_i)_B^{1/3}]^2} \tag{5}$$

Noting that the diffusion time can be a critical factor in these systems, two additional nondimensional parameters become relevant. The diffusion-based Damköhler number can be written as the ratio of the diffusion time to the characteristic chemical reaction time

$$\text{Da}_2 = \frac{\tau_{\text{diffusion}}}{\tau_{\text{reaction}}} = \frac{(-R)d_h}{C_{b,s}D_{A,B}} \tag{6}$$

and indicates whether chemistry or mass transport are dominant. The Peclet number is defined as the ratio of the diffusion time to the residence time

$$\text{Pe} = \frac{\tau_{\text{diffusion}}}{\tau_{\text{residence}}} = \frac{v_b d_h}{D_{A,B}} \tag{7}$$

Peclet numbers larger than unity imply that significant quantities of reactants are being passed through the combustor without reaching the catalyst surface and reacting. For a high power density microcombustor with short through-flow times, this is the most fundamental limitation on power density.

Table 1 A comparison of the operating parameters and requirements for a microengine combustor to those estimated for a conventional GE90 combustor. (Note: residence times are calculated using inlet pressure and an average flow temperature of 1000 K.)

	Conventional combuster	Microcombustor
Length	0.2 m	0.001 m
Volume	0.073 m^3	6.6×10^{-8} m^3
Cross-sectional area	0.36 m^2	6×10^{-5} m^2
Inlet total pressure	37.5 atm	4 atm
Inlet total temperature	870 K	500 K
Mass flow rate	140 kg/s	1.8×10^{-4} kg/s
Residence time	~7 ms	~0.5 ms
Efficiency	>99%	>90%
Pressure ratio	>0.95	>0.95
Exit temperature	1800 K	1600 K
Power density	1960 MW/m^3	3000 MW/m^3

2.2 Heat Transfer Effects and Fluid-Structure Coupling. Energy loss due to heat transfer at the walls of the combustion chamber in a conventional gas turbine is typically neglected. However, for a microcombustor this is an important factor. The surface area-to-volume ratio for a microscale combustor is ~500 m^{-1}, or two orders of magnitude larger than that of a typical combustor.

Waitz et al. [6] have shown that the ratio of heat lost to that generated scales with the hydraulic diameter as follows:

$$\frac{E''}{\dot{E}} \propto \frac{1}{d_h^{1.2}} \tag{8}$$

The hydraulic diameter of a microcombustor is on the order of millimeters, hundreds of times smaller than that of a typical combustor. Therefore, the ratio of heat lost to that generated may be as much as two orders of magnitude greater than that of a large-scale combustor.

The effect of this large surface heat loss on homogeneous gas-phase combustion is twofold. First, large thermal losses have a direct impact on overall combustor efficiency. Therefore, typical large-scale combustor efficiencies of >99% are not feasible. Second, heat loss can increase kinetic times and narrow flammability limits through lowering reaction temperatures. This can exacerbate the constraints of short residence time.

In addition, the structures fabricated for these microcombustors

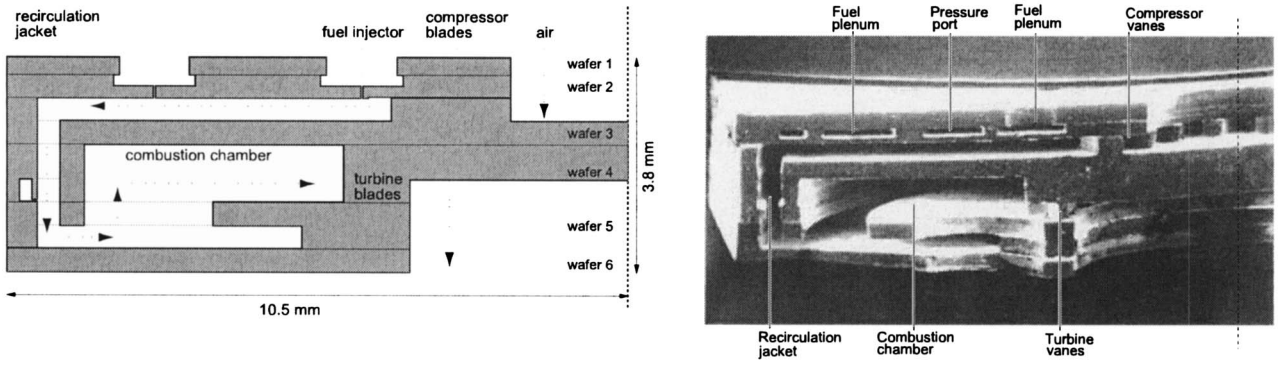

Fig. 2 Schematic (a) and SEM (b) of six-wafer microcombustor

are etched from silicon, which has a high thermal conductivity. This combined with the short heat conduction paths at the microscale lead to Biot numbers much less than unity (of order 0.01) and structures that tend to be isothermal. These heat transfer issues have a significant impact on catalytic systems where the heat is generated on a surface. The heat generated is more likely to be conducted away through the structure than transferred through a thermal boundary layer to the bulk flow. This can further reduce power density.

2.3 Material Constraints. There are also several material constraints imposed on a silicon microcombustion system. The most critical requirement is a wall temperature limit of $\lesssim$1300 K. At temperatures above this level, silicon begins to soften and lose its structural integrity. However, high surface heat transfer and the high thermal conductivity of silicon are beneficial in this case. Combustor wall temperatures can be kept below the 1300 K requirement by conduction of heat through the structure to the ambient. In addition, the rotating components of the microengine must maintain even lower wall temperatures, below 1000 K, due to creep considerations.

There are further material constraints imposed on the system when utilizing thin films of noble metal catalysts. Typically platinum based, these materials will begin to agglomerate when exposed to temperatures in excess of ~1200 K for significant periods of time. This will reduce the active surface area on which catalysis can occur.

2.4 Previous Work. Mehra and Waitz [8] were the first to develop a silicon, microfabricated combustor compatible with a realistic engine geometry. This combustor was 0.066 cm^3 in volume and was designed to operate using lean, premixed, hydrogen-air combustion. It was tested over a range of equivalence ratios spanning from 0.4 to 1.6 for a fixed mass flow rate of 0.045 g/s and atmospheric pressure. For premixed hydrogen-air operation, exit gas temperatures in excess of 1800 K were achieved with combustor efficiencies up to 70% and power densities near 1200 MW/m^3.

A more substantial six silicon wafer combustor, shown in Fig. 2, was also designed and tested by Mehra [3] and Mehra et al. [4]. This device consisted of a 191 mm^3 volume and a wraparound thermal isolation jacket. For gas phase hydrogen-air operation, exit gas temperatures in excess of 1800 K and efficiencies near 100% were achieved at mass flow rates of 0.12 g/s. This corresponds to a power density over 1100 MW/m^3. However, due to residence time constraints, this device did not achieve the target mass flow rate of 0.36 g/s resulting in flame blowout around 0.20 g/s.

Spadaccini et al. [5] and Spadaccini [9] improved on the gas-phase performance of the device by converting it to a dual-zone operating mode similar to that found in conventional-scale combustors. This consisted of a hot primary zone followed by a dilution zone. This was achieved by etching a series of holes through the upper wall of the combustion chamber splitting the flow in the thermal isolation jacket. Approximately half of the flow entered the combustor and burned near stoichiometric conditions in the primary zone while the other half entered through the top wall of the chamber to dilute and cool the flow to the appropriate exit temperature. The stable, hot primary zone increased reaction rates and improved performance, allowing operation above 0.22 g/s. However, this was still short of the design mass flow rate.

Spadaccini et al. [5] also tested several hydrocarbon fuels, including propane and ethylene in the six-wafer combustors. The ~5–20 times slower reaction rates of these fuels exacerbated the residence time constraints. This resulted in maximum mass flow rates of ~0.07 g/s and power densities less than 300 MW/m^3, well below the targets for micro gas turbine engine operation. Figure 3 highlights the performance difference between hydrogen and propane fuel. Furthermore, it has been the long-term goal of much of this work to achieve high power density operation of a microcombustor using storable hydrocarbon fuels. For this reason, propane-air combustors utilizing heterogeneous surface catalysis have been pursued and are the subject of the remainder of this paper.

There are several research groups pursuing microcombustors

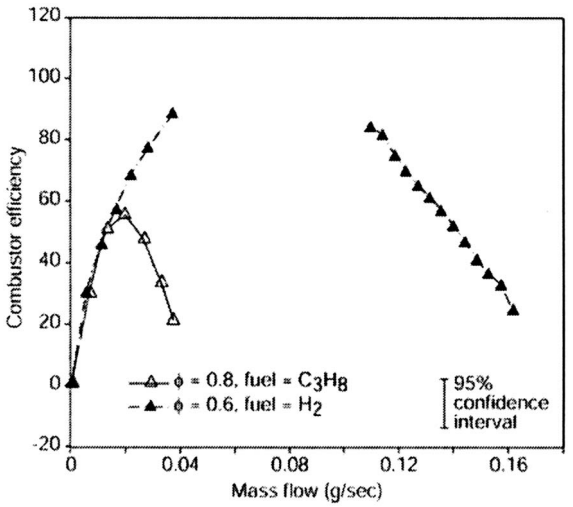

Fig. 3 Comparison of hydrogen and propane gas-phase performance

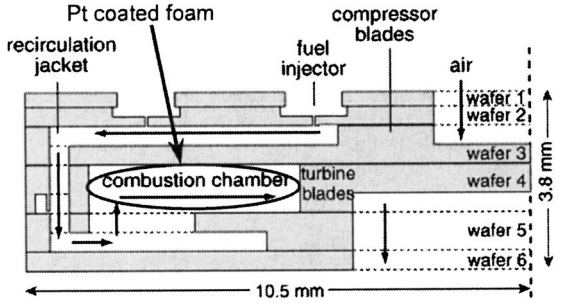

Fig. 4 Schematic of microcombustor showing location of catalyst material

for other types of small-scale power sources. Typically, these combustors run at significantly lower mass flow rates and power densities. This includes a silicon micromachined rotary engine being developed at the University of California, Berkeley, which involves combustion of gas-phase hydrogen-air mixtures ignited with a spark or glow plug [10]. Other catalytic microcombustor work has been conducted at MIT for suspended tube microreactors [11] and for thermoelectric generators [12]. A *swiss-roll* catalytic microcombustor has been developed at the University of Southern California for use as a thermoelectric generator with recuperation [13] while the smallest known combustor was fabricated and tested at the University of Oregon and burns propane catalytically over a platinum wire [14] in a volume of 0.050 mm^3.

3 Experimental Approach

To improve upon previous propane-air performance in the baseline six-wafer combustors, heterogeneous surface catalysis was implemented. For the experiments presented here, the baseline six-wafer device was used as the test device and platinum was chosen as the catalyst material.

3.1 Six-Wafer Catalytic Microcombustor. The baseline six-wafer device that had been used for previous experiments was fitted with platinum coated foam materials. Figure 4 indicates the location of the catalyst material inside the device. The silicon was etched using deep reactive ion etching (DRIE), and the wafers were aligned and fusion bonded together. The details of these microfabrication steps can be reviewed in Refs. [3,4]. The process of implanting the platinum-coated foam material into the devices during fabrication is discussed in [9,15]. The substrate materials and platinum deposition are presented in Secs. 3.2 and 3.3.

3.2 Catalyst Substrate Materials. Several catalyst substrate materials were used. This included a nickel foam material with a porosity of ~95%, a FeCrAlY foam with a porosity of 88.5%, and an Inconel-625 foam, which was 78% porous. Porosity is defined as the ratio of open volume to total volume of the material. This parameter will be referred to as α and can be written as

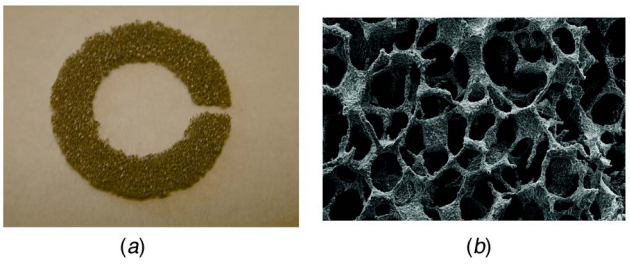

(*a*) (*b*)

Fig. 6 Photograph (a) and SEM (b) of 88.5% porous FeCrAlY foam substrate

$$\alpha = \frac{V_{\text{open}}}{V_{\text{total}}} \tag{9}$$

The foam substrate materials are shown in Figs. 5–7, where Figs. 5(*a*), 6(*a*), and 7(*a*) are photographs and Figs. 5(*b*), 6(*b*), and 7(*b*) are SEMs.

3.3 Catalyst Materials. After machining to the size and shape of the combustion chamber, the foam substrates required a platinum coating. Two methods were utilized to produce these layers. The first involved dipping the substrate in a chloroplatinic acid solution while the second consisted of using ionic plasma deposition. The first technique was performed on the 95% porous nickel substrate and the second technique on the FeCrAlY and Inconel-625.

Unsupported metal catalysts can be deposited onto a substrate using a solution of metal salt. In this procedure, the metal salt (H_2PtCl_6 in this case) is dissolved in deionized water. The substrate pieces are soaked in this solution then placed in a small tube furnace. The water is then evaporated followed by reacting the remaining compound with hydrogen at elevated temperature to remove the Cl in the form of HCl leaving only platinum on the surface. The nickel foam pieces were coated using this technique and typically increased in weight by approximately ~3–5 % creating layers approximately 2–3 μm thick. The procedure used is described in Ref. [9].

The FeCrAlY and Inconel-625 substrates were coated using ionic plasma deposition. This is a proprietary process developed by Ionic Fusion Corporation and involves propelling atoms of a given material by ionic acceleration and ballistically impregnating a substrate. It is a high-energy, low-temperature process that provides good penetration into porous substances [16]. The foam pieces were first coated with 2–3 μm of either Al_2O_3 or ZrO_2 followed by 2–3 μm of platinum. The FeCrAlY and Inconel-625 pieces increased in weight by approximately 4% and 2%, respectively. The ceramic interlayers acted as a diffusion barrier between the platinum and the metal substrates and are discussed in more detail in Ref. [9].

3.4 Experimental Setup and Diagnostics. Prior to testing, the microcombustors were packaged into a suitable test rig. In

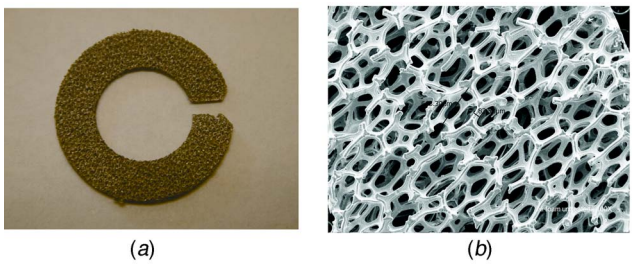

(*a*) (*b*)

Fig. 5 Photograph (a) and SEM (b) of 95% porous nickel foam substrate

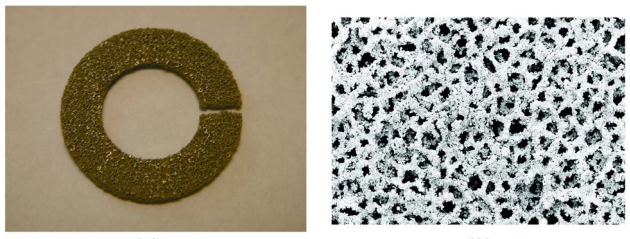

(*a*) (*b*)

Fig. 7 Photograph (a) and SEM (b) of 78% porous Inconel-625 foam substrate

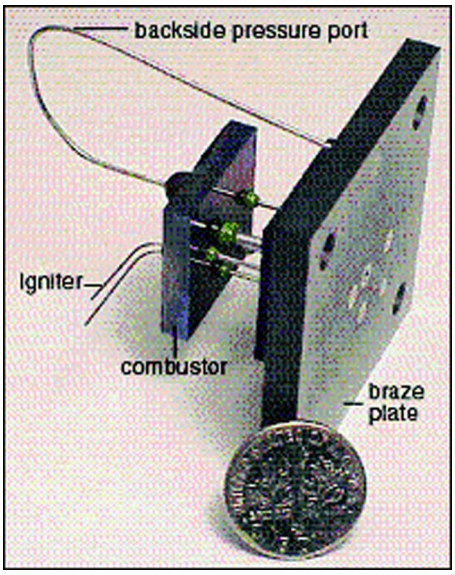

Fig. 8 Fully packaged microcombustor

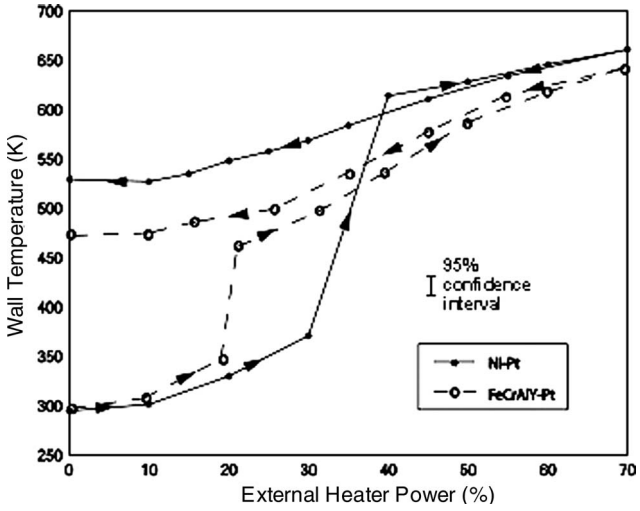

Fig. 9 Ignition characteristics for catalytic microcombustors

order to connect the device's microscale fluid channels to a macroscale feed system, a glass bead interconnect scheme was developed by Mehra [3]. Small Kovar tubing was hermetically sealed to the silicon with glass beads and brazed to a larger metal plate for connection to conventional fittings. A fully packaged device is shown in Fig. 8. A more detailed description of this process can be found in Refs. [3,17,18].

Because of the microscale of the devices, it is difficult to obtain nonintrusive measurements. Therefore, diagnostics were limited. Exit gas temperature was measured using a 0.0254 cm sheathed type K thermocouple. Because of the large temperature gradients along the length of the wire, an error analysis for the thermal conductivity, radiative emissivity, and calibration drifts predicted uncertainties up to ±130 K. A wall temperature measurement was also obtained with the same type thermocouple and an uncertainty of ±12 K. In addition to the temperature diagnostics, pressure was measured upstream in the cooling jacket and in the combustion chamber itself. A detailed uncertainty analysis can be found in Ref. [3].

4 Experimental Results

Overall combustor efficiency is defined as

$$\eta_c = \frac{(\dot{m}_a + \dot{m}_f)h_2 - \dot{m}_a h_1}{\dot{m}_f h_f} \tag{10}$$

where station (1) refers to the combustor inlet and station (2) is the combustor exit. The combustor efficiency can be written as the product of a *chemical efficiency*, and a *thermal efficiency*. These two efficiencies can be written as

$$\eta_{\text{chem}} = \frac{[(\dot{m}_a + \dot{m}_f)h_2 - \dot{m}_a h_1] + \dot{Q}_{\text{loss}}}{\dot{m}_f h_f} = \frac{\text{total enthalpy released}}{\text{maximum enthalpy release possible}} \tag{11}$$

$$\eta_{\text{therm}} = \frac{(\dot{m}_a + \dot{m}_f)h_2 - \dot{m}_a h_1}{[(\dot{m}_a + \dot{m}_f)h_2 - \dot{m}_a h_1] + Q_{\text{loss}}} = \frac{\text{enthalpy rise of fluid}}{\text{total enthalpy released}} \tag{12}$$

4.1 Ignition Characteristics. To ignite, the catalyst had to be heated using an external radiant heater to a suitable ignition temperature. Upon reaching this temperature, a hydrogen-air mixture was passed through the device and over the platinum catalyst. Initiation of the surface reaction ensued and both the wall and gas temperatures rose to a steady-state value. To accomplish this in the microcombustors, the entire chip was preheated with an external heater [19]. After achieving ignition, the heater was removed and the device continued to operate via autothermal combustion of the hydrogen-air mixture over platinum. Typically, a catalytic combustor will exhibit an ignition/extinction hysteresis similar to that shown by Williams et al. [20] and Goralski and Schmidt [21]. For the 95% porous nickel foam and the 88.5% porous FeCrAlY foam this is shown in Fig. 9. Wall temperature is plotted against heater power and ignition occurs at a heater power of approximately 20–30 % (around 80–100 °C). This figure is intended only to qualitatively show the ignition process and to illustrate the hysteresis. Although the catalytic microcombustors initially ignite with a hydrogen-air mixture, ultimately, the goal is to achieve autothermal combustion of propane-air mixtures over the platinum catalyst. To accomplish this, the device must be brought to a high-enough temperature to initiate propane-air catalytic reactions. This ignition temperature is significantly higher than that required for the hydrogen-air mixture and is on the order of 600 K [20]. This temperature was not attainable with the external heater. However, the heater can be used to ignite a hydrogen-air mixture that can further heat the catalyst to the required level for propane mixtures.

Propane is then added in small quantities until its ignition is observed via an additional temperature rise. At this point, the hydrogen concentration is lowered while propane is added to the mixture until there is only propane and air. More details of the ignition procedure and conversion to propane-air operation are contained in Ref. [9].

4.2 Performance Testing. Initial tests were performed on combustors that were fabricated without platinum on the substrate surface. This was done to isolate the effect of the foam structure itself inside the combustion chamber. Figure 10 shows the exit gas temperature for such a device with uncoated nickel foam material operating with propane-air combustion. The temperatures and flow rates are comparable to that reported in [3,5,9] for gas-phase devices and indicates that there is no catalytic activity and minimal effect from the foam itself.

In the case of the microcombustors with platinum catalyst coatings, significant performance improvement was achieved. Figures 11 and 12 show exit gas temperatures and overall combustor efficiency comparisons for the nickel foam (95% porous) and FeCrAlY foam (88.5% porous) devices both operating at a stoichiometric equivalence ratio. The lower porosity FeCrAlY com-

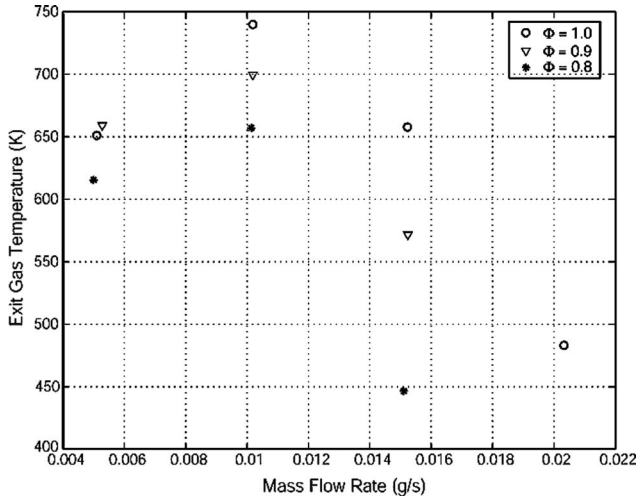

Fig. 10 Exit gas temperature for microcombustor with noncatalytic foam

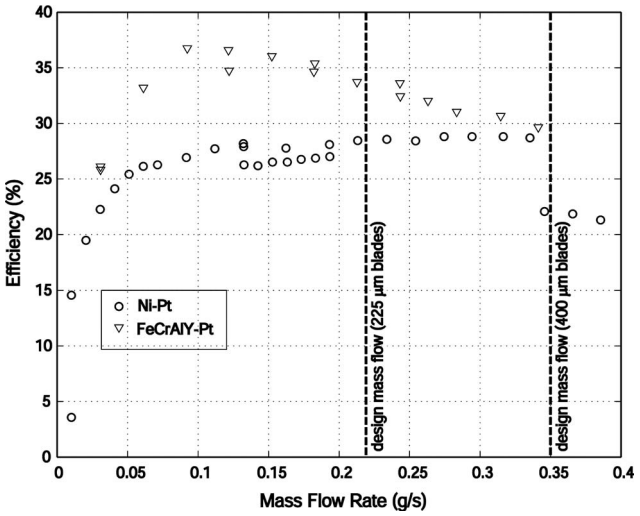

Fig. 12 Overall combustor efficiency plot comparing Ni-Pt and FeCrAlY-Pt devices for ϕ=1

bustor achieved exit gas temperatures over 150 K higher than the devices with the nickel substrate. This corresponds to an approximately 2–10 % higher efficiency over a range of mass flow rates. The sharp drop in performance at 0.35 g/s was a result of transients from the mass flow controllers that were operating at maximum flow levels. Although these temperatures and efficiencies are low, the mass flow rates achieved were in excess of 0.35 g/s, which satisfies the design mass flow rate for the microengine and exceeds that required for a lower flow rate engine design. These mass flow rates of interest are noted on the figures with vertical dashed lines. The maximum power density achieved for the platinum on nickel device was $\sim$1050 MW/m^3, which is a 7.5-fold increase over gas-phase propane-air power densities and about 95% of that for gas-phase hydrogen-air mixtures. For the less porous platinum on FeCrAlY combustor, the maximum power density was 1200 MW/m^3, which is approximately an 8.5-fold increase over gas-phase propane-air operation and about a 10% increase over that achieved by the gas-phase hydrogen-air device.

The overall combustor efficiency can be broken down into its thermal and chemical components. Wall temperature measurements combined with a one-dimensional (1D) heat transfer model [3] reveal that although heat loss is greater than in the gas-phase case, losses are dominated by chemical inefficiency. Figure 13 shows a breakdown of the efficiencies in the nickel-platinum device for a stoichiometric mixture ratio. The chemical efficiency at the mass flow rates of interest was $\sim$30%. Similar trends were observed in the FeCrAlY device although chemical efficiency was $\sim$40% between mass flow rates of 0.15–0.30 g/s.

Pressure drop through the combustor is also a critical parameter for the overall engine design. Because of thermodynamic cycle constraints for engine operation, total pressure loss must be limited to $<$5%. The pressure losses from the two devices are compared in Fig. 14 for operation at an equivalence ratio of unity. The lower porosity (higher density) FeCrAlY material exhibits higher pressure loss as expected. However, both devices are below the 5% total pressure loss constraint at mass flow rates of interest.

4.3 Failure Mechanisms. Testing of microcombustors with 78% porous Inconel-625 foam was not successful. Three devices were packaged and tested. None of these combustors would ignite with hydrogen-air or propane-air mixtures. The typical ignition procedures were attempted followed by higher heater settings and various flow rates and equivalence ratios. None of these variations on the startup procedure were successful. The inability to light

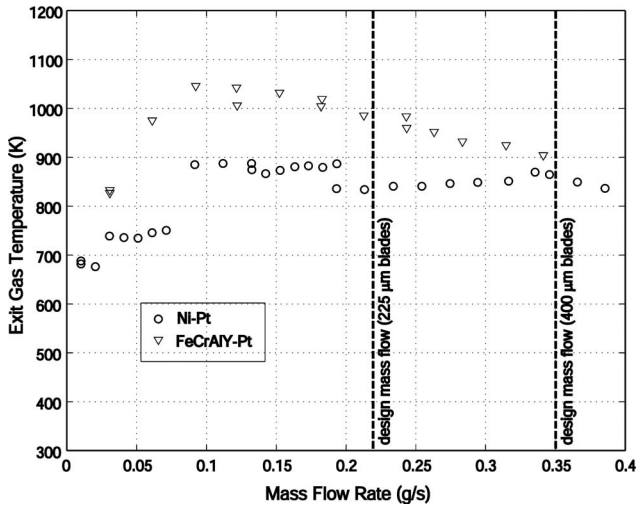

Fig. 11 Exit gas temperature plot comparing Ni-Pt and FeCrAlY-Pt devices for ϕ=1

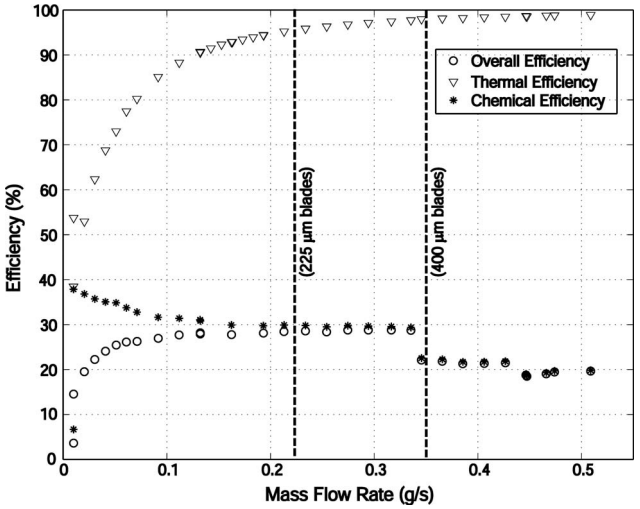

Fig. 13 Efficiency breakdown for catalytic microcombustor with Ni-Pt, ϕ=1.0

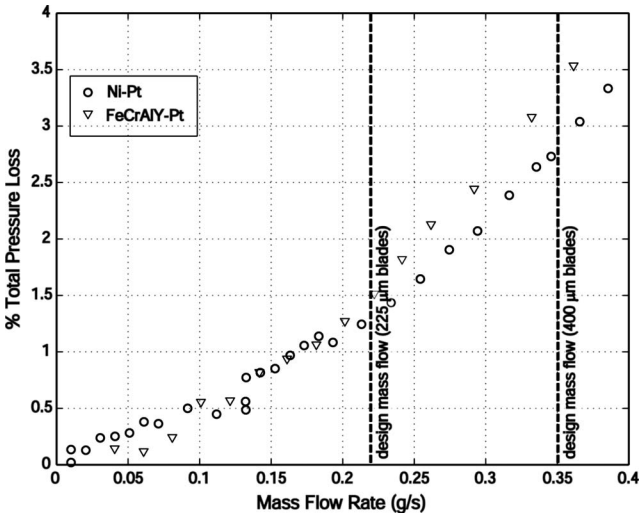

Fig. 14 Total pressure loss plot comparing Ni-Pt and FeCrAlY devices for ϕ=1

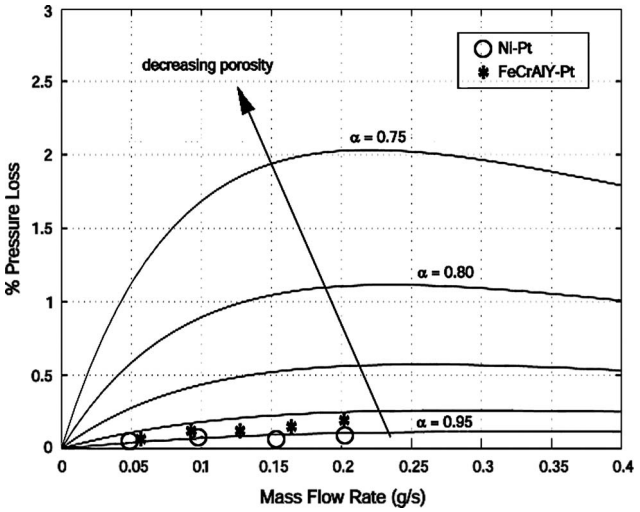

Fig. 15 Pressure loss versus mass flow rate for porous media, comparing estimates from Eq. (13) and experimental data

these combustors may have been due to the fuel-air mixture channeling around the foam rather than through it. Significant gaps may have been present around the foam due to the need to ensure that it easily fit into the combustion chamber for fabrication purposes. Other possible failure mechanisms include platinum agglomeration during high-temperature processing and inadequate platinum coverage inside the foam.

The nickel-platinum devices exhibited sporadic performance as well. Several devices ignited and operated only at lower temperatures. This was likely a result of platinum diffusion into the nickel substrate material. This was confirmed by a materials characterization analysis, which is summarized in Ref. [9]. As a result, the FeCrAlY-platinum devices were fabricated with a ceramic diffusion barrier layer. This prevented interdiffusion of the two metals during the high-temperature processing steps, but later led to some reduction of active surface area via agglomeration of the platinum layer [9,12].

5 Low-Order Modeling and Analysis

Several levels of modeling have been pursued to better understand the operation of a catalytic microcombustor and to develop design recommendations. A pressure loss correlation has been utilized to estimate the drop in stagnation pressure through a given catalyst substrate. Time-scale analyses have identified the limiting factors and important nondimensional parameters that govern high power density catalytic combustor performance. A one-dimensional isothermal plug flow reactor model was developed to further explore combustor performance over a range of conditions and catalyst geometries. This parametric study is synthesized in model-based operating maps.

5.1 Pressure Loss. Pressure loss through a porous substrate can be estimated from the Ergun equation for Reynolds numbers less than 300 (based on the thickness of a fiber or diameter of a catalyst particle) [7]

$$-\frac{dP}{dz} = \frac{v}{l}\frac{(1-\alpha)}{\alpha^3}\left[\frac{150\mu(1-\alpha)}{l} + 1.75\rho v\right] \tag{13}$$

where μ is the viscosity, v is velocity through the porous media, and l is a characteristic length scale, usually the width of a foam fiber or diameter of a particle in a packed bed. For the substrates of interest, Reynolds numbers are approximately 200–300.

Figure 15 shows an estimate of pressure loss through the nickel foam (95% porous) and the FeCrAlY foam (88.5% porous) used in the catalytic microcombustors. The thickness of a foam fiber was approximately 80–100 μm measured using a scanning electron microscope. The actual pressure vs. mass flow characteristic from the catalytic microcombustor experiments was used as input. The temperature was held constant at 1000 K. The pressure drop associated with this material is low according to the Ergun calculation while the measured pressure drop in the experiment was significantly higher, in the range of 1–3 %. However, the experiment measures the loss through the entire device not just the foam. If the measured pressure loss through the device without catalyst material is subtracted from that measured in this set of experiments, the loss attributable to the foam can be estimated. Total pressure loss from the original gas-phase device can be found in Ref. [3]. The data points in Fig. 15 are obtained by subtracting the total pressure loss of the gas-phase device from that of the catalytic microcombustor.

The additional curves shown on Fig. 15 indicate the estimated pressure loss (based on Eq. (13)) for lower porosity substrates (more dense foams). The same pressure versus mass flow characteristic, reactor temperature, and fiber thickness was used. The stagnation pressure loss through the foam increases as porosity decreases. However, the chart indicates that a significant decrease in porosity (and increase in catalytic material) can be introduced into the reactor without violating the maximum allowable combustor pressure loss of 5%. If the 1–3 % system pressure loss is included with this estimate of catalyst pressure loss, a substrate with a porosity of approximately 80–85 % could be used in the device.

5.2 Time-Scale Analysis. To determine which phenomena control the combustion process in a catalytic microcombustor, relevant physical time scales can be evaluated. These include reaction time, residence time, diffusion time of the fuel species, and diffusion time of the oxidizer. Residence time can be estimated from the volume, mass flow rate, pressure, and bulk gas temperature as in the gas-phase case (Eq. (2)). Reaction rate can be obtained from an Arrhenius-type rate expression. For a propane-air reaction on a platinum catalyst, the following mechanism can be used [7]

$$(-R_{C_3H_8}) = k_s[C_3H_8] \tag{14}$$

where the rate constant is

Table 2 Summary of non-dimensional parameters

Nondimensional parameter	Range
$\mathrm{Da}_1 = \frac{\tau_{\text{residence}}}{\tau_{\text{reaction}}}$	~0.5–5
$\mathrm{Da}_2 = \frac{\tau_{\text{diffusion}}}{\tau_{\text{reaction}}}$	~30–500
$\mathrm{Pe} = \frac{\tau_{\text{diffusion}}}{\tau_{\text{residence}}}$	~55–130

$$k_S = 2.4 \times 10^5 \exp\left(\frac{-1.08 \times 10^4}{T}\right) \tag{15}$$

The reaction rate has units of mole/m^2s where the area is the catalyst surface area. Molecular diffusion coefficients for propane and oxygen diffusion through air can be obtained from the Fuller correlation (Eq. (5)) [7].

Using estimates of these various time scales, nondimensional parameters can be calculated and used to determine the governing physical phenomena. These parameters and their approximate values for a catalytic microcombustor are summarized below in Table 2. From this simple time-scale analysis, it is clear that diffusion of reactants to the surface is a controlling parameter. The diffusion-based Damköhler number indicates that the surface reaction rate is much faster than the rate of diffusion to the surface. The Peclet number indicates that reactants can flow through the device without coming into contact with the active catalytic surface.

If a tubular plug flow reactor is assumed, the Peclet number can be estimated and shown to be a strong function of geometry. For a given set of flow conditions (pressure, temperature, and mass flow rate) Peclet number can be calculated for a range of diameters (or pore sizes). In this case, the gas velocity through the tube and the length of the tube are estimated based on the actual microcombustor. Figure 16 shows this parameter for $P=2$ atm, $T=1000$ K, and a mass flow rate=0.3 g/s for both propane and oxygen. For the diameters (or pore sizes) of interest the Peclet number is larger than unity. It is also important to note that propane diffuses more slowly than oxygen. This results in a larger Peclet number and indicates that propane diffusion to the active surface is the governing phenomenon.

5.3 One-Dimensional Isothermal Plug Flow Reactor Model. The equations developed here have been derived from a control volume analysis of a fluid element in a plug flow reactor. These equations coupled with the isothermal assumption yield trends in fuel conversion and bulk gas temperature rise through the reactor as a function of flow conditions and geometry.

The Peclet number analysis indicated that the diffusion of propane is the governing phenomenon; therefore, only the mass transport and consumption of the fuel species is taken into account in all subsequent derivations. Homogeneous gas-phase reactions will be neglected and the catalytic reaction mechanism shown in Eqs. (14) and (15) will be utilized for all further analyses.

A steady-state gas-phase mole balance across the control volume results in

$$C_b v \frac{dY_{f,b}}{dz} + a_v k_m C_b (Y_{f,b} - Y_{f,S}) = 0 \tag{16}$$

The surface area-to-volume ratio can be written in terms of porosity and foam fiber thickness as

$$a_v = \frac{4(1-\alpha)}{w} \tag{17}$$

A mole balance performed at the catalyst surface yields

$$k_m C_b (Y_{f,b} - Y_{f,S}) = (-R_f)_S (1-\alpha) \tag{18}$$

while an energy balance across the fluid element provides the final equation

$$-\rho C_p v \frac{dT_b}{dz} + a_v h (T_S - T_b) = 0 \tag{19}$$

Analytical solutions to these equations can be found or an appropriate numerical method can be applied to solve the system.

Correlations for gases in packed bed reactors have been used to approximate the heat and mass transfer coefficients in porous substrates. These transport coefficients are given in terms of nondimensional j factors, j_D for mass transfer, and j_H for heat transfer

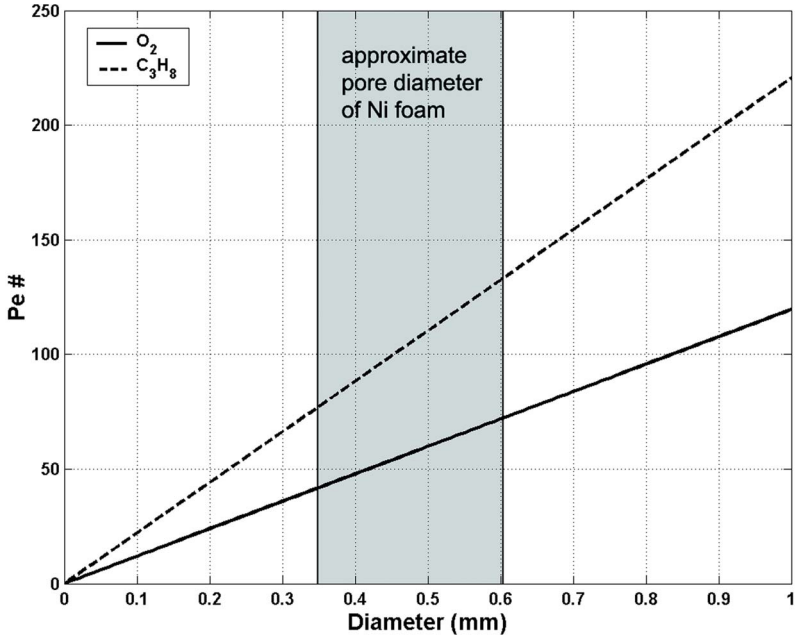

Fig. 16 Peclet number versus diameter

Table 3 Typical boundary and flow conditions for reactor inlet in 1D isothermal plug flow model

Parameter	Value
T_h	500 K
T_S	1000 K
$Y_{\text{fuel},b}$ (from ϕ)	0.04 (ϕ=1.0)
$Y_{\text{fuel},S}$	0.00
Pressure	2 atm
Mass flow	0.3 g/s

$$j_D = \frac{k_m}{v}\text{Sc}^{2/3} \tag{20}$$

$$j_H = \frac{h}{C_p \rho v}\text{Pr}^{2/3} \tag{21}$$

These j factors can be estimated using the following correlations [7]:

$$j_D = j_H = 0.91\ \text{Re}_j^{-0.51} S_f \quad \text{Re}_j < 50 \tag{22}$$

$$j_D = j_H = 0.91\ \text{Re}_j^{-0.41} S_f \quad \text{Re}_j > 50 \tag{23}$$

S_f is the shape factor and for this analysis a value of 0.79 was used (shape factor for ring-type structures). The Reynolds number used here can be found from

$$\text{Re} = \frac{\rho v w}{6(1-\alpha)\mu S_f} \tag{24}$$

The boundary conditions required to run the model include the inlet bulk gas temperature, the inlet bulk gas fuel mole fraction (obtained from equivalence ratio), and the inlet surface mole fraction. The catalyst surface temperature also must be specified and due to the isothermal condition is constant throughout the reactor. A typical set of boundary and flow conditions is shown in Table 3.

Figures 17 and 18 show temperature and fuel concentration profiles, respectively. The conditions listed above in Table 3 were used to generate these results along with a substrate porosity of 95% and an average foam fiber thickness of 90 μm.

Figure 19 shows a comparison of the model results to that obtained in the experiments for both the 95% and 88.5% porous substrates. Fuel conversion is the parameter being compared. The approximate geometries of the substrate materials were used as well as the measured pressure and mass flow rates from the experiment. The model replicates the trends shown in the experiments. These trends include a relatively constant fuel conversion over a broad mass flow range and the lower porosity material resulting in higher conversions and exit gas temperatures. However, the model does not predict overall levels well. Likely reasons for this are variations in the substrate geometry and the platinum coverage as well as flow leakage around the foam material.

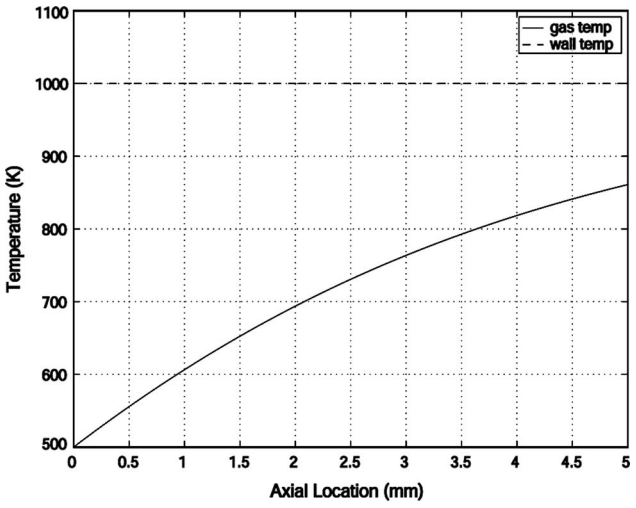

Fig. 17 Axial temperature profile in porous media plug flow reactor

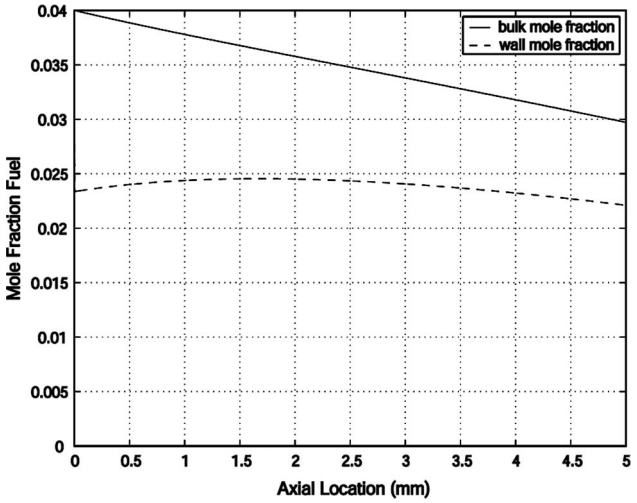

Fig. 18 Axial fuel concentration profile in porous media plug flow reactor

A model sensitivity study was performed and indicated that a variation of 20% in surface area-to-volume ratio results in a ~10% change in fuel conversion. The sensitivity to leakage flow around the foam material can also be estimated. The conversion for a reduced flow rate can be mass averaged with an unreacted leakage flow to simulate this scenario. Results indicate that fuel conversion changes by ~7% with each 20% increment in leakage. Leakages around the catalyst are expected to be ~20%; however, an actual measurement is not possible.

With this model, the effect of key design variables such as porosity and surface area can be further examined. For constant flow conditions, the model can produce fuel conversion profiles for various porosity and surface area materials. Figure 20 shows trends in fuel conversion for increasing surface area-to-volume ratios using the conditions listed in Table 3. The profiles indicate that higher surface area-to-volume ratios (usually a result of lower porosity for a constant fiber thickness) will significantly improve fuel conversion.

The 1D isothermal plug flow model can also be used to visualize a catalytic microcombustor's operating space. Figure 21 shows lines of constant power density on a plot of total pressure loss through the device versus catalyst temperature for an equivalence ratio of unity. The total pressure loss is estimated by adding the pressure loss through the substrate material as predicted by the Ergun equation to an estimate of the pressure loss due to the silicon structure [3]. The maximum power density is obtained from the exit gas temperature predicted by the model. Figure 21 indicates that at higher pressure loss (higher surface area-to-volume ratio) and higher catalyst temperatures, combustor performance improves. It is also clear that by relaxing the pressure loss constraint and utilizing a catalyst, which can survive at higher temperatures, the available operating space will broaden. The current microengine constraint of <5% total pressure loss is indicated by the black line and gray shaded area. The shaded area above a 1400 K catalyst temperature represents an approximate failure temperature for the catalyst layer.

The catalytic microcombustor operating space can be viewed more generally by plotting nondimensional parameters. Figure 22 shows lines of constant combustor efficiency on a chart with Pe-

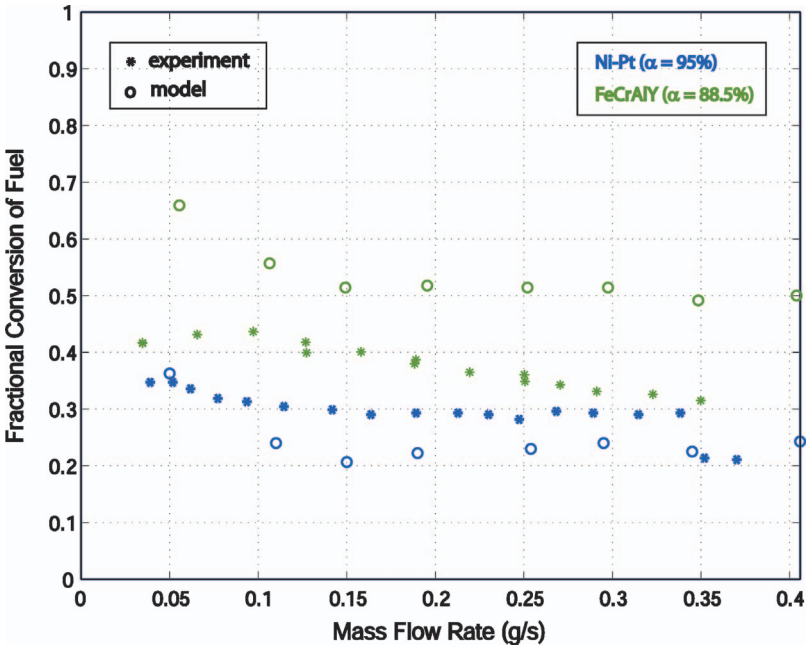

Fig. 19 Comparison of model to experiment

clet number versus thermal efficiency. As Peclet number decreases, combustor efficiency increases due to the time available for diffusion of the reactant species to the active surface. However, as heat is lost from the system (lower thermal efficiency), the overall efficiency decreases.

6 Design Recommendations

Design recommendations for catalytic microcombustion systems are listed below. These recommendations are based on the experimental results presented in Sec. 4, the low-order modeling in Sec. 5, and a materials characterization study described in Refs. [9]:

1. High power density catalytic microcombustors are diffusion controlled. A designer should seek to approach the high-temperature reaction controlled regime to maximize performance. This can be achieved by implementing the following:
   (a) Utilize the most thermally durable catalytic materials to achieve high-temperature operation.
   (b) Utilize the highest surface area-to-volume ratio substrate material available that does not violate the system pressure loss constraint.
   (c) Relax the total pressure loss constraint as far as the thermodynamic cycle will permit.
2. Searching for a more active catalytic material is not required unless:
   (a) The ignition transient is of concern.

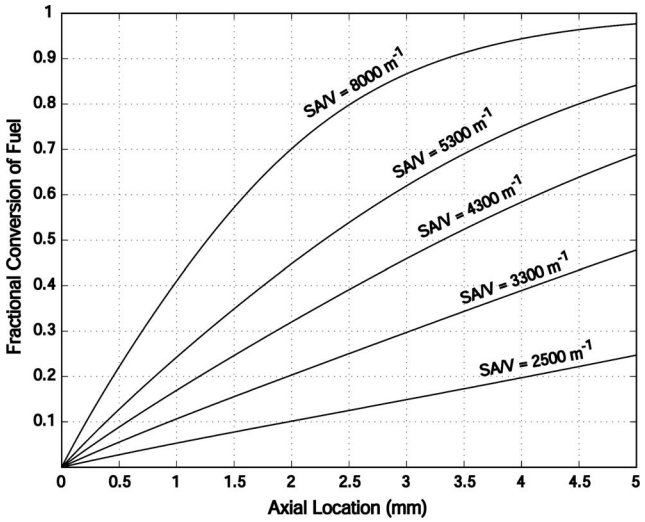

Fig. 20 Fuel conversion profiles for various surface area-to-volume ratios

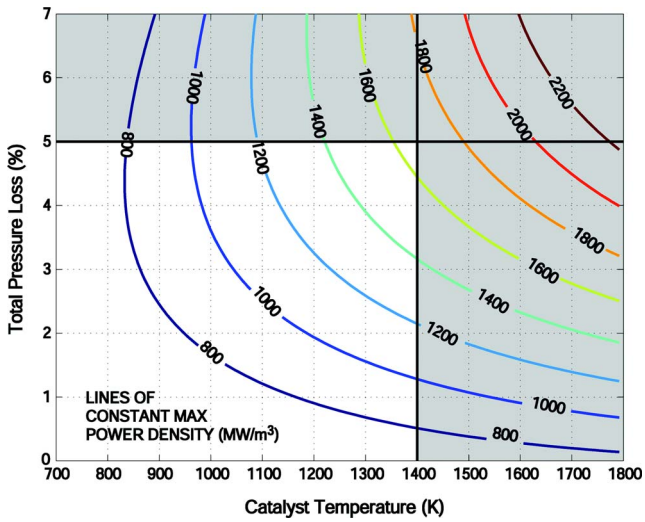

Fig. 21 Operating space for catalytic microcombustor; lines of constant power density

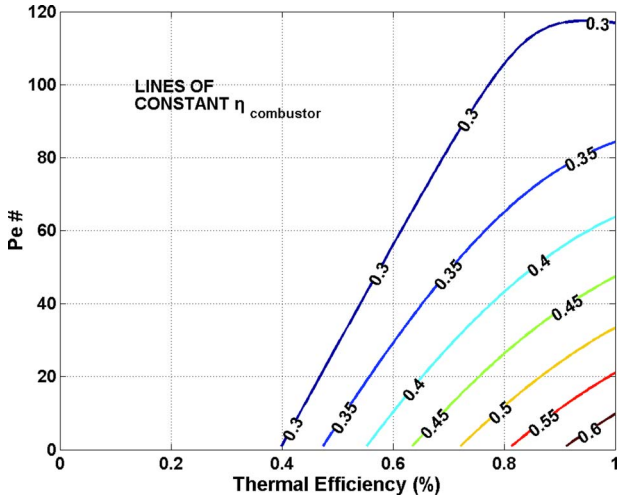

Fig. 22 Nondimensional operating space; Peclet number versus thermal efficiency

(b) The overall design lies in the reaction-controlled regime.

3. Although thermal management was not a problem in the devices tested here due to poor thermal contact of the catalyst to the silicon, leakage paths around the catalyst material, and the recirculation jacket, a more intimately contacted catalyst material operating at higher temperatures will likely suffer from significant thermal losses. A materials solution, such as a thermal barrier combined with a concept similar to the recirculation jacket, may mitigate these losses.
4. Because of high-temperature processing and operation, substrate materials for noble metal catalysts should be resistant to solid diffusion or include a diffusion barrier layer.
5. Catalytic materials which are less likely to agglomerate at high temperatures should be used.
6. A robust fabrication and assembly process that does not result in leakage paths around the catalyst material should be considered when designing the device.

7 Summary and Future Work

Because of the poor performance of gas-phase microcombustors with hydrocarbon fuels, a strategy of heterogeneous surface catalysis was pursued. This offered the potential to increase hydrocarbon microcombustor power density by directly increasing reaction rates. A catalytic six-wafer device compatible with the microengine geometry was developed.

This combustor consisted of filling the combustion chamber with a foam material coated with platinum as the active catalytic surface. Several catalyst substrate materials with varying porosity and surface area were tested. The combustors were ignited via preheating of the entire chip and flowing a hydrogen-air mixture through the device. After catalytic ignition of the hydrogen-air mixture, operation was converted to propane-air autothermal combustion.

The 95% porous foam devices achieved exit gas temperatures in excess of 850 K and efficiencies of ~30% with propane. Although the efficiency and gas temperatures were low, this combustor operated at high mass flow rates compared to previous gas-phase combustors. Mass flow rates over 0.35 g/s were achieved and power density was a 7.5-fold increase over propane-air gas-phase operation. The devices with 88.5% porous FeCrAlY foam achieved exit gas temperatures approaching 1100 K and efficiencies near 40%. The power density of this device was an 8.5-fold increase over the comparable gas-phase microcombustor.

Low-order modeling including a pressure loss correlation, timescale analyses, and a 1D isothermal plug flow reactor model indicated that high power density operation is diffusion controlled and the relatively lower porosity and higher surface area-to-volume ratio of the FeCrAlY foam substrate was responsible for improved performance.

Based on the results of this work, future research may include the following:

Improved Ignition Schemes. Although the ignition procedure described in Sec. 4.1 was effective for these bench-top catalytic microcombustor experiments, a more robust and self-contained system would be optimal for a practical device. A simple and effective means of achieving catalytic ignition of hydrocarbons over noble metal catalysts is to resistively heat the catalyst material itself [20,21]. By bringing the catalyst temperature up to the ignition temperature required for propane-air mixtures, the external preheating and hydrogen ignition procedure could be eliminated. In order to accomplish this in a device such as the six-wafer microcombustors presented here, there would need to be significant fabrication changes. This would involve incorporating multilevel electrical interconnects into the device and contacting them to the metal catalyst material. These interconnects would extend to the chip's surface where they could be connected to a power source for the resistive heating.

Hybrid Microcombustors. The catalytic microcombustors were successful in significantly increasing power density and mass flow range for hydrocarbon-fueled devices. However, the exit gas temperatures achieved were significantly lower than that required for the microengine thermodynamic cycle. Attaining these temperatures in a catalytic device of this kind is unlikely because the catalyst wall temperatures required would be high enough to cause significant agglomeration of the catalyst layer. In addition, to accomplish this in a relatively small volume the total pressure loss would be significantly greater than the 5% constraint imposed by the engine cycle. Although the gas-phase devices were capable of achieving high exit gas temperatures and efficiencies with hydrogen-air mixtures, their mass flow rate capability was significantly less than the engine design flow rate of 0.35 g/s and was even worse with hydrocarbon fuels.

As a result, a strategy for achieving both high temperature and high mass flow rate operation in a minimum volume may be to combine the two devices into a hybrid microcombustor similar to that proposed and developed by Dalla Betta et al. for large-scale, low NO_x applications [22,23].

For this type of device, the entrance region of the combustion chamber would consist of a porous substrate or microchannel-type geometry coated with a catalyst layer. The first stage would ignite the fuel-air mixture and bring it to some midrange temperature (~1000 K) with minimal total pressure loss. A second stage of open volume for homogeneous combustion would follow. The exit conditions of the catalytic section would serve as the inlet to the gas-phase section, which would burn the remaining fuel-air mixture. The combustion in the second stage would proceed quickly due to the already high inlet gas temperature ultimately achieving the 1600 K exit gas temperature in a minimum total volume.

Liquid Fuels. One final subject of potential future work is to include the use of liquid fuels, such as kerosene and JP8 in microcombustor development. These types of fuels are the most commonly used logistics fuels. The catalytic microcombustors described in this paper may be a first step toward achieving high power density operation with logistics fuels.

The use of these liquid fuels constitutes a significant development challenge. Some development issues may include:

1. liquid fuel injection and droplet atomization
2. condensation of the fuel upstream of the combustion chamber
3. evaporation of droplets and fuel-air mixing after atomization

4. diffusion of the larger hydrocarbon molecules to a catalyst surface
5. ignition procedures/methods
6. reaction rates of heavy hydrocarbons on catalysts
7. coking/fouling of catalyst surface

Acknowledgment

This work was conducted as part of the MIT Microengine Project and the authors are grateful to Professor A. Epstein for his leadership of this program. The entire microengine team, especially N. Miki, L. Ho, and X. Zhang, should also be acknowledged. The support of the technical and administrative staff at the MIT Gas Turbine Laboratory, particularly, V. Dubrowski, J. Costa, J. LeTendre, S. Parker, J. Finn, M. McDavvitt, and L. Martinez, is greatly appreciated. V. Sciortino and J. Peterson at Ionic Fusion Corporation are thanked for their innovative film deposition technique, G. Simpson at Vetrofuse Inc. and Mike Anzalone at Thunderline-Z Inc. for assistance in packaging. This work was supported by the US Army Research Laboratory under the Collaborative Technology Alliance agreement number DAAD19-01-2-0010.

Nomenclature

A = Arrhenius pre-exponential factor
a, b = Arrhenius exponents
a_v = surface area-to-volume ratio
d_h = hydraulic diameter
C_b = molar concentration
C_p = constant pressure specific heat
D = diffusion coefficient
Da_1 = residence time-based Damköhler number
Da_2 = diffusion-based Damköhler number
E'' = heat loss
E = heat generated
E_a = activation energy
h = enthalpy or heat transfer coefficient
j_D = j factor for mass transport
j_H = j factor for heat transfer
k_m = mass transport coefficient
k = reaction rate constant
l = length scale
LHV = lower heating value
M = molecular weight
$\dot{m}$ = mass flow
P = pressure
Pe = Peclet number
Pr = Prandtl number
$\dot{Q}_{\mathrm{loss}}$ = heat loss from combustor
R = gas constant
$(-R)$ = reaction rate
Re = Reynolds number
Sc = Schmidt number
S_f = shape factor
T = temperature
V = volume
v = velocity or diffusion volume
w = thickness
Y = mole fraction
z = axial location
η_c = overall combustor efficiency
η_{chemical} = chemical efficiency
η_{thermal} = thermal efficiency
ρ = fluid density
$\tau_{\mathrm{diffusion}}$ = diffusion time
τ_{reaction} = reaction time
$\tau_{\mathrm{residence}}$ = residence time

Subscripts

A, B = species
a = air
b = bulk
f = fuel
s = surface
0 = initial condition
1 = combustor inlet
2 = combustor exit

References

[1] Epstein, A. H., Senturia, S. D., Al-Midani, O., Anathasuresh, G., Ayon, A. A., Breuer, K., Chen, K.-S., Ehrich, F. F., Esteve, E., Frechette, L., Gauba, G., Ghodssi, R., Groshenry, C., Jacobsen, S. A., Kerrebrock, J. L., Lang, J. H., Lin, C-C., London, A. P., Lopata, J., Mehra, A., Mur Mirandi, J. O., Nagle, S., Orr, D. J., Piekos, E., Schmidt, M. A., Shirley, G., Spearing, S. M., Tan, C. S., Tzeng, Y-S., and Waitz, I. A., 1997, "Micro-Heat Engines, Gas Turbines, and Rocket Engines," 28th AIAA Fluid Dynamics Conference.

[2] Groshenry, C., 1995, "Preliminary Study of a Micro-Gas Turbine Engine," S.M. thesis, Massachusetts Institute of Technology, Cambridge, MA.

[3] Mehra, A., 2000, "Development of a High Power Density Combustion System for a Silicon Micro Gas Turbine Engine," Ph.D. thesis, Massachusetts Institute of Technology, Cambridge, MA.

[4] Mehra, A., Zhang, X., Ayon, A. A., Waitz, I. A., Schmidt, M. A., and Spadaccini, C. M., 2000, "A 6-Wafer Combustion System for a Silicon Micro Gas Turbine Engine," J. Microelectromech. Syst., **9**, pp. 517–527.

[5] Spadaccini, C. M., Mehra, A., Lee, J., Zhang, X., Lukachko, S., and Waitz, I. A., 2003, "High Power Density Silicon Combustion Systems for Micro Gas Turbine Engines," ASME J. Eng. Gas Turbines Power, **125**, pp. 709–719.

[6] Waitz, I. A., Gauba, G., and Tzeng, Y-S., 1998, "Combustors for Micro Gas Turbine Engines," ASME J. Fluids Eng., **20**, pp. 109–117.

[7] Hayes, R. E., and Kolaczkowski, S. T., 1997, *Introduction to Catalytic Combustion*, Gordon and Breach, Canada.

[8] Mehra, A., and Waitz, I. A., 1998, "Development of a Hydrogen Combustor for a Microfabricated Gas Turbine Engine," Solid-State Sensor and Actuator Workshop at Hilton Head.

[9] Spadaccini, C. M., 2004, "Combustion Systems for Power-MEMS Applications," Ph.D. thesis, Department of Aeronautics and Astronautics, Massachusetts Institute of Technology, Cambridge, MA.

[10] Fernandez-Pello, A. C., Pisano, A. P., Fu, K., Walther, D., Knobloch, A., Martinez, F., Senesky, M., Jones, D., Stoldt, C., and Heppner, J., 2002, "MEMS Rotary Engine Power System," *Power MEMS 2002: International Workshop on Power MEMS*, Tsukuba, Japan, Tech. Dig. - Int. Electron Devices Meet., pp. 28–31.

[11] Arana, L. R., 2003, "High-Temperature Microfluidic Systems for Thermally-Efficient Fuel Processing," Ph.D. thesis, Department of Chemical Engineering, Massachusetts Institute of Technology, Cambridge, MA.

[12] Schaevitz, S. B., 2000, "A MEMS Thermoelectric Generator," S.M. thesis, Department of Electrical Engineering and Computer Science, Massachusetts Institute of Technology, Cambridge, MA.

[13] Maruta, K., Takeda, K., Sitzki, L., Borer, K., Ronney, P. D., Wussow, S., and Deutschmann, 2001, "Catalytic Combustion in Microchannels for MEMS Power Generation," The Third Asia-Pacific Conference on Combustion, Seoul, June.

[14] Hatfield, J. M., and Peterson, R. B., 2001, "A Catalytically Sustained Microcombustor Burning Propane," 2001 IMECE, ASME, New York, November.

[15] Spadaccini, C. M., Zhang, X., Cadou, C. P., Miki, N., and Waitz, I. A., 2003, "Preliminary Development of a Hydrocarbon-Fueled Catalytic Microcombustor," Sens. Actuators, A, **103**, pp. 219–224.

[16] Ionic Fusion Corporation, 2003, corporate literature, Longmont, CO.

[17] Harrison, T., 2000, "Packaging of the MIT Microengine," S.M. thesis, Massachusetts Institute of Technology, Cambridge, MA.

[18] London, A. P., 2000, "Development and Test of a Microfabricated Bipropellant Rocket Engine," Ph.D. thesis, Department of Aeronautics and Astronautics, Massachusetts Institute of Technology, Cambridge, MA.

[19] Peck, J., 2003, "Development of a Catalytic Combustion System for the MIT Micro Gas Turbine Engine," S.M. thesis, Department of Aeronautics and Astronautics, Massachusetts Institute of Technology, Cambridge, MA.

[20] Williams, W. R., Stenzel, M. T., Song, X., and Schmidt, L. D., 1991, "Bifurcation Behavior in Homogeneous-Heterogeneous Combustion: I. Experimental Results Over Platinum," Combust. Flame, **84**, pp. 277–291.

[21] Goralski, C. T., Jr., and Schmidt, L. D., 1996, "Lean Catalytic Combustion of Alkanes at Short Contact Times," Catal. Lett., **42**, pp. 15–20.

[22] Dalla Betta, R. A., Schlatter, J. C., Yee, D. K., Loffler, D. G., and Shoji, T., 1995, "Catalytic Combustion Technology to Achieve Ultra Low NO_x Emissions: Catalyst Design and Performance Characteristics," Catal. Today, **26**, pp. 329–335.

[23] Dalla Betta, R. A., Schlatter, J. C., Nickolas, S. G., Razdan, and Smith, D. A., 1995, "Application of Catalytic Combustion Technology to Industrial Gas Turbines for Ultra-Low NO_x Emissions," ASME Paper No. 95-GT-65.

A Comparison of Single and Multiphase Jets in a Crossflow Using Large Eddy Simulations

Mirko Salewski[1]
e-mail: mirko.salewski@vok.lth.se

Dragan Stankovic

Laszlo Fuchs

Division of Fluid Mechanics,
Department of Heat and Power Engineering,
Lund Institute of Technology,
P.O. Box 118,
22100 Lund, Sweden

*Large eddy simulations (LES) are performed for single and multiphase jets in crossflow (JICF). The multiphase JICF are compared to the single-phase case for the same momentum and mass flow ratios but with droplets of different sizes. Multiphase JICF have stronger counterrotating vortex pairs (CVPs) than a corresponding single-phase JICF. Moreover, their trajectories are higher and their induced wakes weaker. The smaller the Stokes number of the droplets, the more the solution approaches the solution for single-phase flow. The computed results show the formation of a CVP and horseshoe vortices, which are convected downstream. LES also reveals the intermittent formation of upright wake vortices from the horseshoe vortices on the ground toward the CVP. The dispersion of polydisperse spray droplets is computed using the stochastic parcel method. Atomization and droplet breakup are modeled by a combination of the breakup model by Reitz and the Taylor analogy breakup model (see Caraeni, D., Bergström, C., and Fuchs, L., 2000, Flow, Turbul. Combust., **65**(2), pp. 223–244). Evaporation and droplet collision are also modeled. The flow solver uses two-way coupling. Averages of the velocity and gaseous fuel mass fraction are computed. The single-phase JICF is validated against experimental data obtained by PIV. Additionally, the PDFs and frequency spectra are presented.* [DOI: 10.1115/1.2180810]

Introduction

The design of gas turbine engines is governed by ever tightening requirements regarding thermodynamic efficiency and reduction of emissions. Although high thermodynamic efficiency tends to decrease the absolute amount of emissions per unit power, it also demands high inlet pressures and temperatures that, in turn, bring about faster formation of NO_x, especially thermal NO_x. Lean premixed prevaporized (LPP) combustion is a promising low-NO_x concept for gas turbine combustion. Liquid fuel is injected and, thereafter, breaks up, disperses, vaporizes, and mixes with air. The spray jet in crossflow (JICF) is advantageous as a fuel injection system since atomization offers the opportunity to disintegrate the liquid fuel jet to fine droplets while the momentum ratio, the injection angle, or swirl can be used to tailor various mixture fraction profiles.

Several unsteady coherent structures in the turbulent flow field of a JICF are reported: the counterrotating vortex pair (CVP), horseshoe vortices, wake vortices, and several vortices in the jet shear layer [1,2]. Unsteady coherent structures may lead to formation of pockets with variable mixture fraction. Mixture fraction variation may trigger combustion instability and may lead to the formation of hot spots with excessive production of thermal NO_x. The unsteady coherent structures pose an inherent modeling difficulty because their frequencies lie in the inertial subrange of the turbulence spectrum. Because of these coherent structures, large eddy simulation (LES) is a suitable tool to investigate such flows.

Figures 1–3 are snapshots of the coherent vortices in the flow field from various perspectives, visualized with the λ_2 method [3]. The most dominant vortices constitute the unsteady counterrotating vortex pair (CVP). The side view in Fig. 2 illustrates the trajectory of the CVP, whereas the front view in Fig. 3 captures that the CVP is a pair of vortices. The unsteady horseshoe vortices are visible in Fig. 1. The two branches are convected downstream from the injection point, close to the lower wall. Figure 2 visualizes the upright tornadolike wake vortices. Their formation is debated in the literature, e.g., [1,2,4–6]. Streamline visualizations in [2] suggest that the upright wake vortices form as lifted branches of the horseshoe vortices. The λ_2-visualization in Fig. 1 supports this view as the upright wake vortices connect the horseshoe vortices and the CVP.

Single-phase JICF are the topic of numerous studies. Experimental approaches include hot wire anemometry [1,5,7], smoke visualization [1], dye visualization [5], hydrogen bubble visualization [6], particle image velocimetry (PIV), and laser-induced fluorescence (LIF) [8,9]. Numerical simulations of the turbulent flow field provide additional insight. Some are performed with Reynolds-averaged Navier-Stokes (RANS)-based closures [10,11] and, recently, with LES-based closures [2,12,13]. Alternatively, potential flow fields are investigated in combination with vortex methods [14].

Multiphase JICF are not as well understood due to open questions associated with multiphase flow phenomena, especially breakup of the liquid jet [15]. Modeling liquid-jet breakup is addressed in [16,17]. Turbulence is modeled in the RANS framework in these studies. LES turbulence models are applied in [18]. Analytic models for dispersion of spray JICF are developed in [19]. Experimental techniques include shadowgraphy [15] and phase Doppler anemometry (PDA) [20,21].

Previous studies focus on spray penetration and trajectories, liquid volume flux distributions, and droplet sizes. The influences on some of these parameters are established for various momentum flux ratios [20]; various liquids, nozzle sizes and crossflow Mach numbers [15]; various pressures [21]; and various injection angles [22].

This study is concerned with a comparison between multiphase and single-phase JICF. It is shown that in the downstream field, the continuous phase flow fields correspond if the Stokes number is small. If the Stokes number is larger, the momentum transfer to the liquid phase is delayed and the droplets penetrate farther into the main (cross)flow.

[1]To whom all correspondence should be addressed.

Contributed by the International Gas Turbine Institute (IGTI) of ASME for publication in the JOURNAL OF ENGINEERING FOR GAS TURBINES AND POWER. Manuscript received August 25, 2005; final manuscript received September 28, 2005. Review conducted by K. C. Hall. Paper presented at the ASME Turbo Expo 2005: Land, Sea, and Air, Reno, NV, June 6–9, 2005, Paper No. GT2005-68150.

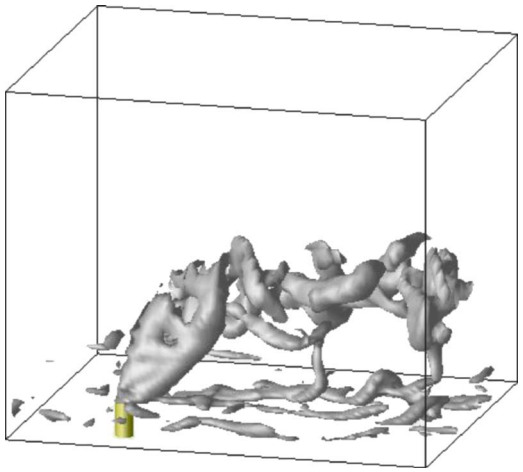

Fig. 1 λ_2 vortex visualization [3] of the CVP, the horseshoe vortices, and two upright tornadolike wake vortices, diagonal view

The experimental setup and the flow conditions are described first. Then governing equations and numerical methods are presented. The ability of the flow solver to predict a JICF flow field accurately is demonstrated in a single-phase JICF case where the computed results are compared to PIV data. Grid accuracy is established for single and multiphase flow. Characteristic frequencies of the flow field are implied to influence the time-dependent mixture fraction. PDFs of velocity and mixture fraction are presented. Finally, the flow field is compared to a corresponding spray JICF.

Case Description and Experimental Setup

The setup of the experiment is pictured in Fig. 4. The dimensions of the channel are $0.1\times0.1\times5$ m. Both jet and crossflow are gravity driven from an upper tank with constant water level. The flow rates are controlled independently and measured with rotameters. A perforated plate at the channel entrance and a grid one channel width downstream kill secondary motion and ensure fast development of turbulent flow. The jet injection point lies 3.3 m from the entrance and 1.7 m from the exit. The ratio of the channel width and the diameter of the round nozzle is 20. All length scales are nondimensionalized with the nozzle diameter (D=0.005 m). The volume flow rate in the channel is set to 1 l/s,

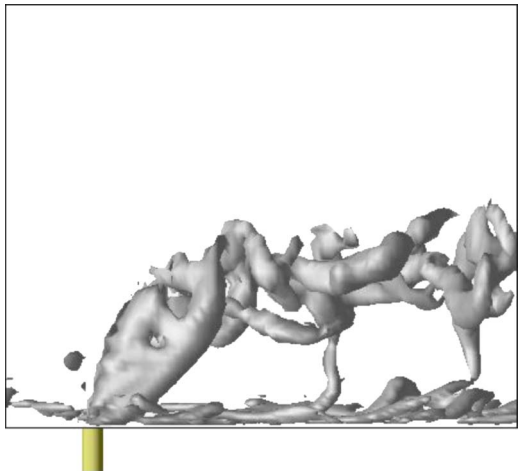

Fig. 2 λ_2 vortex visualization [3] of the CVP and two tornadolike wake vortices, side view

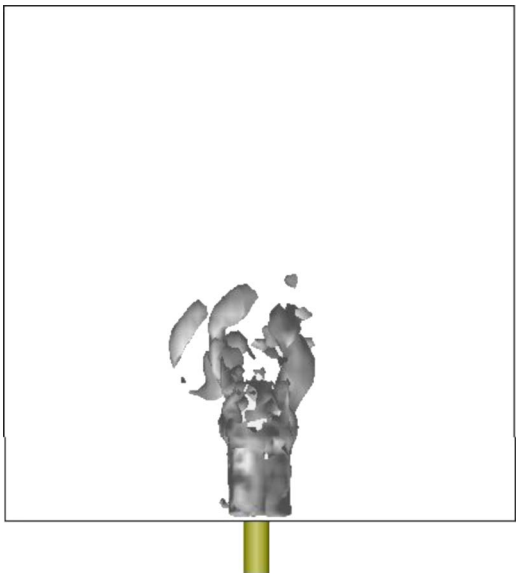

Fig. 3 λ_2 vortex visualization [3] of the CVP, front view

which gives a bulk flow velocity of 0.1 m/s and a Reynolds number of 10,000. The velocity ratio $V_{\text{jet}}/V_{\text{crossflow}}$ is 5. The PIV camera (LA Vision Flowmaster 3S) registers the vertical symmetry plane of the channel, which is illuminated by a Nd:YAG PIV Laser (Newave Research Gemini). Errors of the measurements stem from the errors introduced by the flowmeters, positioning of the laser sheet, scaling of the camera, and minimal displacement captured by the camera [23]. The overall error is estimated to be $<9\%$.

Governing Equations and Numerical Methods

The continuous phase is described in an Eulerian framework, whereas a Lagrangian description is selected for the dispersed phase. Two-way coupling between the phases is applied for momentum and mixture fraction transport.

Continuous Phase. The nondimensional continuity (Eq. (1)), momentum (Eq. (2)), and mixture fraction (Eq. (3)) transport equations for incompressible flow of Newtonian fluids with constant diffusivities are described in Eulerian framework

$$\frac{\partial u_j}{\partial x_j} = 0 \tag{1}$$

$$\frac{\partial u_i}{\partial t} + u_j\frac{\partial u_i}{\partial x_j} = -\frac{\partial p}{\partial x_i} + \frac{1}{\text{Re}}\frac{\partial^2 u_i}{\partial x_j^2} + \dot{F}_{s,i} \tag{2}$$

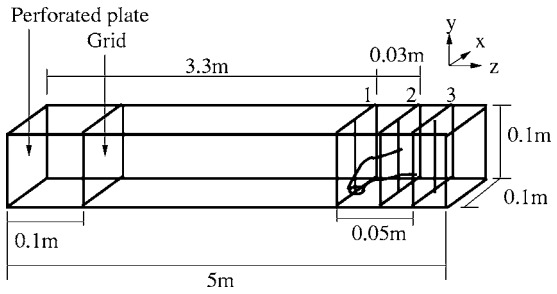

Fig. 4 Geometry (not to scale) with lines along which data is extracted: 6D~0.03 m, 10D~0.05 m

$$\frac{\partial Z}{\partial t} + u_j \frac{\partial Z}{\partial x_j} = \frac{1}{\mathrm{ReSc}} \frac{\partial^2 Z}{\partial x_j \partial x_j} + \dot{Z}_s \tag{3}$$

$\dot{F}_{s,i}$, $\dot{Z}_s$ are source terms for momentum and mixture fraction, respectively. The source terms provide for the coupling from the liquid phase to the gas phase. The mass source term is neglected.

A finite difference formulation is applied on a Cartesian, staggered, stretched grid. The convective terms are discretized with a fifth-order accurate weighted essentially non-oscillatory (WENO) scheme [24], the diffusive terms with a fourth-order central difference scheme. The flow solver uses an explicit third-order Runge-Kutta scheme. Large-scale turbulence is resolved within the LES framework. No explicit models for subgrid scale turbulence and subgrid scale mixing are applied.

Dispersed Phase. The dispersed phase is described by a probability density function (PDF), or the corresponding droplet distribution function f

$$f(\vec{x}_d, \vec{v}_d, r_d, T_d, y, \dot{y}) d\vec{x} d\vec{v} dr dT dy d\dot{y} \tag{4}$$

The droplet distribution function describes the number of droplets per unit volume at a position between $\vec{x}_d$ and $\vec{x}_d + d\vec{x}_d$, which have a velocity between $\vec{v}_d$ and $\vec{v}_d + d\vec{v}_d$, a temperature between T_d and $T_d + dT_d$, and a radius between r_d and $r_d + dr_d$ with distortion parameters between y and $y+dy$ and $\dot{y}$ and $\dot{y}+d\dot{y}$. As not all individual droplets can be tracked due to excessive computational load, droplets are represented by computational parcels, which consist of a number of droplets with identical properties (stochastic parcel method) [25].

The nondimensional source terms for the continuous phase are given by the rates of change of momentum and mass of all parcels

$$\dot{F}_{s,i} = -\frac{L}{\rho_g U^2} \int f \rho_l \left(\frac{4}{3} \pi r_p^3 \frac{dv_{p,i}}{dt} + 4 \pi r_p^2 \frac{dr_p}{dt} v_{p,i} \right) d\vec{v} dr dT_p dy d\dot{y} \tag{5}$$

$$\dot{Z}_s = -\frac{L}{\rho_g U} \int f \rho_l 4 \pi r_p^2 \frac{dr_p}{dt} d\vec{v} dr dT dy d\dot{y} \tag{6}$$

L and U are the crossflow length and velocity scales; ρ_g and ρ_l are densities of gas and liquid phase, respectively. The parcel trajectories are computed in a Lagrangian framework. The instantaneous parcel positions $\vec{x}_p$ are obtained by integration of the parcel velocities $\vec{v}_p$, which, in turn, are obtained from integration of the parcel accelerations $\vec{a}_p$,

$$\vec{v}_p = \frac{d\vec{x}_p}{dt} \tag{7}$$

$$\vec{a}_p = \frac{d\vec{v}_p}{dt} \tag{8}$$

The instantaneous parcel accelerations are given by Newton's second law, assuming the mass flux due to evaporation is uniformly distributed. All forces but aerodynamic drag are neglected. For spherical droplets, Newton's second law becomes

$$\frac{d\vec{v}_p}{dt} = -\frac{3}{8} \frac{\rho_g}{\rho_l} \frac{1}{r_p} C_d |\vec{v}_p - \vec{u}_g| (\vec{v}_p - \vec{u}_g) \tag{9}$$

C_d is the drag coefficient. $|\vec{v}_p - \vec{u}_g|$ is the relative speed, where $\vec{v}_p$ and $\vec{u}_g$ are velocity vectors of the parcels and the gas, respectively. C_d is modeled as

$$C_d = \begin{cases} \dfrac{24}{\mathrm{Re}_d} \left(1 + \dfrac{1}{6} \mathrm{Re}_d^{2/3} \right) & \text{for } \mathrm{Re}_d \leqslant 1000 \\ 0.424 & \text{for } \mathrm{Re}_d \geqslant 1000 \end{cases} \tag{10}$$

The droplet Reynolds number Re_d is defined as

$$\mathrm{Re}_d = \frac{|\vec{v}_p - \vec{u}_g| 2 r_p}{\nu_g} \tag{11}$$

A time scale inherent to Eq. (9) is the momentum response time τ_v [26]

$$\tau_v = \frac{\rho_l}{\rho_g} \frac{2 r_p^2}{9 \nu_g} \tag{12}$$

ν_g is the viscosity of the gaseous phase. The ratio of the momentum response time scale and a typical flow time scale τ_f is the Stokes number

$$\mathrm{St} = \frac{\tau_v}{\tau_f} \tag{13}$$

The trajectories of droplets with $\mathrm{St} \gg 1$ are marginally affected by the local flow conditions. In this case, the momentum exchange between the phases is slow. Contrarily, droplets with $\mathrm{St} \ll 1$ respond quickly and the droplets closely follow the fluid particles. From this point of view, the continuous phase flow field of a multiphase JICF may be comparable to the flow field of a single-phase JICF, if only the Stokes number is small enough.

Evaporation. Evaporation is calculated considering single, spherical, monocomponent droplets with homogeneous temperature and constant density [25]. It is assumed that no gas can be solved in the droplets or condense. Species and energy balances can be integrated over a control volume from the droplet surface to a boundary far away, if the problem is reduced to Stephan convection. The boundary conditions far away are given by the continuous phase. The boundary conditions close to the surface require two additional assumptions. First, the temperature is assumed to be continuous over the interface. Second, the partial pressure of fuel vapor is assumed to be equal to the vapor pressure at the droplet temperature. Under this assumption, Raoult's law is used to find the boundary condition for the fuel mass fraction. The fluxes are then corrected to include forced convection using the empirical Ranz-Marshall correlation.

Droplet Breakup. The aerodynamic Weber number We_p is the ratio of aerodynamic forces and surfaces tension forces σ and is therefore a characteristic parameter for droplet breakup

$$\mathrm{We}_p = \frac{\rho_g (\vec{v}_p - \vec{u}_g)^2 r_p}{\sigma} \tag{14}$$

Depending on the values of droplet Weber and Reynolds numbers, different regimes of droplet breakup can be delineated. In the present breakup model, bag breakup and stripping breakup are taken into account. While in the bag breakup regime droplets are distorted and break up, in the stripping breakup regime small droplets are sheared-off parent droplets. The two breakup regimes are taken into account using a combination of the Taylor analogy breakup model and the breakup model by Reitz (see [18]).

Droplet Collision. Droplet collisions control the spray propagation in dense regions where the collision time scales are smaller than the momentum relaxation time scales. After two droplets collide, they can shatter, bounce, or coalesce, depending on the ratio of surface tension to excess inertia. In the present model, coalescence and elastic bouncing are taken into account [25].

Boundary Conditions. The channel has dimensions of $(x,y,z) = (2,2,12)$ length units. The transverse jet is injected at (1,0,10) length units. At the upper and lower walls no-slip boundary conditions are applied; in the lateral direction, periodic boundary conditions are applied. The channel is divided into two parts. The first half is six length units long and has periodic boundary conditions in main flow direction. This first half of the channel is

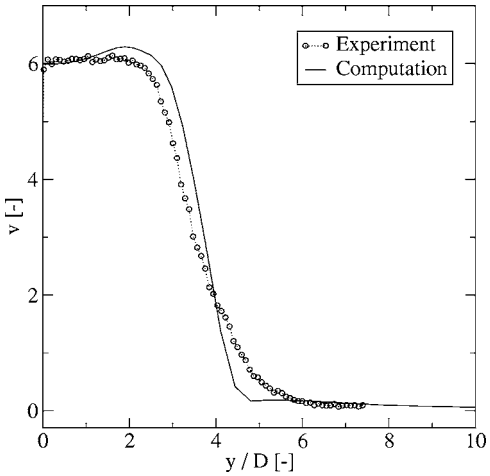

Fig. 5 Mean vertical velocity profile along prolongation of the nozzle axis

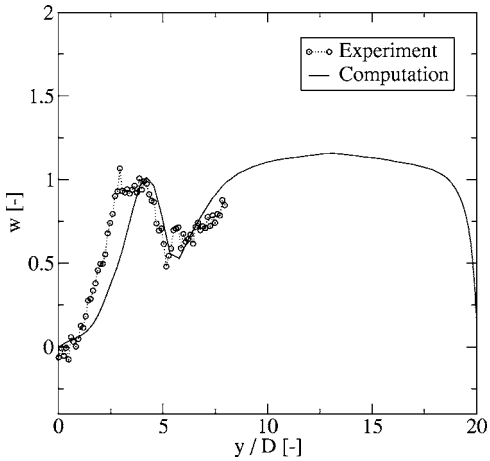

Fig. 6 Mean streamwise velocity profile along prolongation of the nozzle axis

used to compute a fully developed channel flow as inflow boundary condition for the second half of the channel. The outflow of the second half of the channel has a flux conserving zero-gradient boundary condition. The mixture fraction has a zero-gradient boundary condition. In the case of single-phase flow, the inflow of the jet has constant axial (flat) velocity profile. This profile is represented in the LES context by filtering it with a Gaussian function. In case of multiphase flow, the initial parcel position and velocity are set as explained below. The droplets bounce elastically at the walls, have periodic conditions in lateral direction, and are eliminated at the outlet.

Results

Comparison With Experiments for Single-Phase Flow. A single-phase JICF computation is compared to PIV measurements along vertical lines in the plane of symmetry. Figure 5 shows a comparison of measured and computed mean profiles of the vertical velocity (v component) along the jet nozzle axis. These profiles show the length of the potential core of the jet as is evident from the sharp drop in jet velocity at about $3D$. The radius of the nozzle in the computation is set 10% larger than in the experiment. This is necessary to obtain the same length for the potential cores in experiments and computation. Experimental data are only available up to $8D$ above the nozzle to ensure adequate spatial resolution in the PIV experiments.

In Fig. 6, the mean streamwise velocity (w) profiles along the same line as in Fig. 5 are presented. The high-speed region at the outer part (top) of the jet, is evident at around $3-4D$ above the nozzle. The low streamwise velocity region at around $5D$ is consistent with the PIV measurements. It coincides with the region of high jet-trajectory curvature where the momentum exchange between the jet, and the main flow is largest. Thereby, the main flow is slowed down. Qualitatively, the high-speed and low-speed regions are also found in LES of JICF with a velocity ratio of 3.3 [2].

The computed vertical velocity profile along a vertical line at $z=6D$ downstream (line 2 in Fig. 4) of the nozzle is in good qualitative agreement with the measurement but has too high dissipation (see Fig. 7). This is expected due to the length-scale ratio of 20 between the channel height and the nozzle diameter: The nozzle is not resolved enough for a more accurate near-field computation.

The corresponding streamwise velocity profiles are presented in Fig. 8. Although qualitative agreement is good, the local minimum at $8D$ is too low. This means that the strength of the wake tends to be overpredicted in the computations.

Grid Accuracy for Single and Multiphase Flow. The grid accuracy is established for a case with velocity ratio $V_{\text{jet}}/V_{\text{crossflow}}=0.8$. The three grids have 1.9, 3.4, and 3.8 million cells, corresponding to 64, 72, and 80 cells on the channel width. Computed mean streamwise velocity profiles in the downstream field for these three grids are compared in Fig. 9. The correspond-

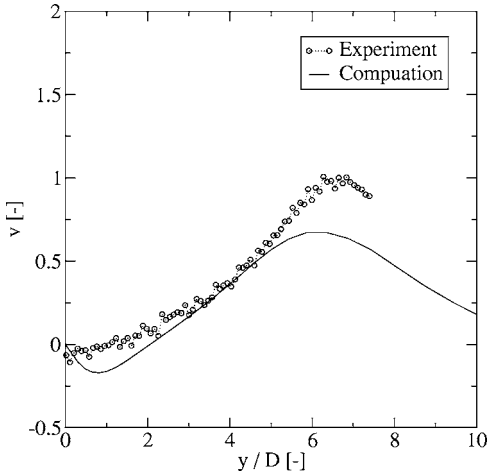

Fig. 7 Mean vertical velocity profile at $z=6D$

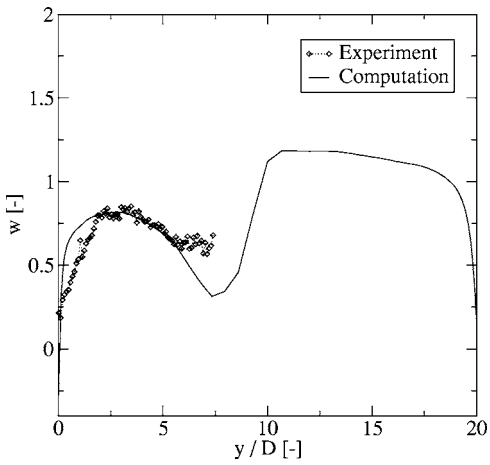

Fig. 8 Mean streamwise velocity profile at $z=6D$

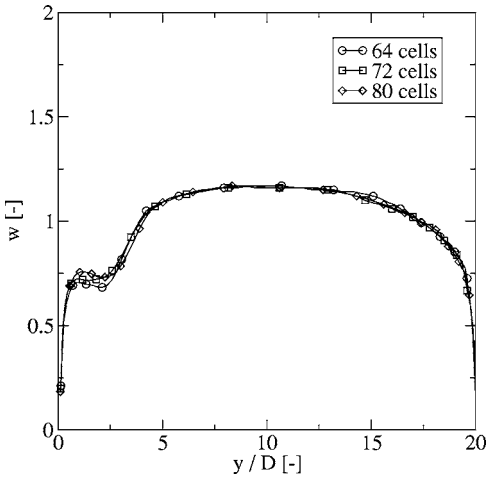

Fig. 9 Grid accuracy for the single-phase flow case

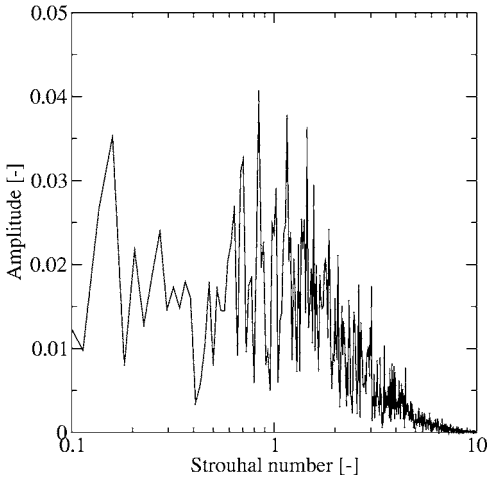

Fig. 11 Spectrum of the vertical velocity

ing numerical accuracy for a multiphase flow case is shown in Fig. 10. For both cases, the results lie within less than 10% for the three grids, and within 5% for the two finest grids. For the finest grid, $y^+ \sim 3$.

Unsteady Coherent Structures. The unsteady CVP, horseshoe vortices, and intermittent, upright, tornadolike wake vortices are visualized with the λ_2 method [3] in Figs. 1–3.

Unsteady coherent structures can be identified in the frequency spectra. Figures 11–13 show such spectra for a point in the centerplane in the wake 10 dia downstream of the nozzle at a height of 5 dia. A characteristic frequency of the present case is at a Strouhal number of 1.3. This characteristic frequency appears in the streamwise velocity (Fig. 12) and in the mixture fraction (Fig. 13), and as a minor peak in the vertical velocity (Fig. 11). This suggests a correlation between characteristic frequencies in mixture fraction and velocities. It is therefore likely that unsteady coherent structures are a main cause for the appearance of fuel- or air-rich pockets.

It is hard to simply characterize the different modes of the unsteadiness, since lateral, longitudinal, and transverse modes are present simultaneously, as is evident in flow animations. It does not seem possible to clearly identify particular peaks in the spectra with those modes as they all seem to have similar frequencies.

Figure 14 shows the PDF of the vertical velocity at the same point as the frequency spectra. The PDF is skewed, which means in this case that the right tail of the PDF extends longer than the left tail. In RANS framework, PDFs are assumed to be characterized by the mean value and the standard deviation only, and skewed PDFs or PDFs with bumps or plateaus cannot be predicted. The ability to predict skewed PDFs is an advantage of the time-consuming LES computations. Furthermore, unsteady coherent structures may be identified in PDFs as bumps, i.e., an in-

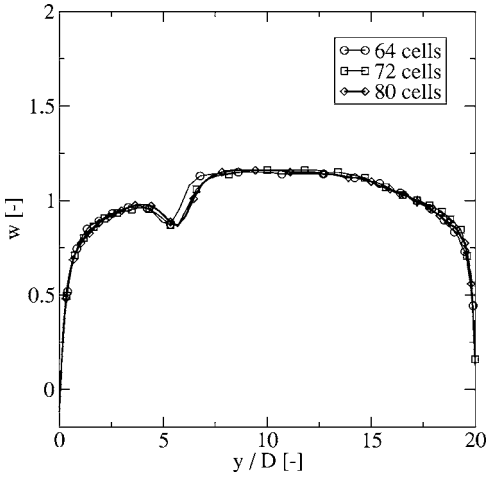

Fig. 10 Grid accuracy for the multiphase flow case

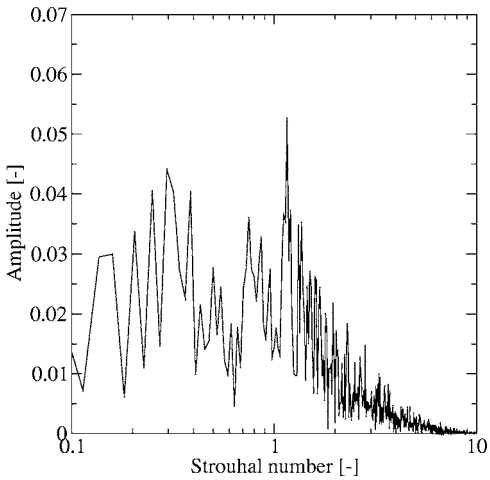

Fig. 12 Spectrum of the streamwise velocity

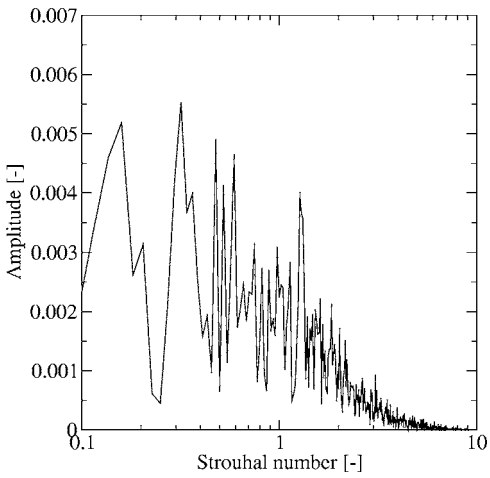

Fig. 13 Spectrum of the mixture fraction

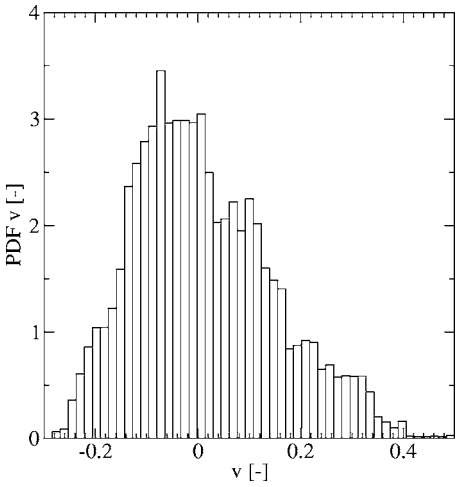

Fig. 14 PDF of the vertical velocity

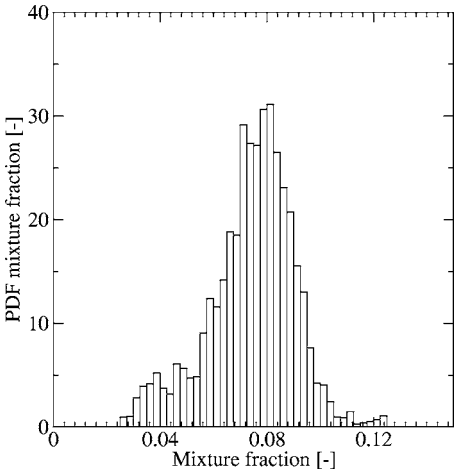

Fig. 16 PDF of the mixture fraction

creased probability density for a range of events to occur compared to the neighboring events. In the PDFs of the present case, there is a plateau in the streamwise velocity PDF between 0.9 and 1 (see Fig. 15). As the fuel mass flow rate is constant over time, an increased probability of fast streamwise velocities corresponds to an increased probability of fuel-lean pockets. Such increased probability can be observed in the PDF of the mixture fraction plotted in Fig. 16 at a mixture fraction of around 0.04; the left tail is significantly higher than the right tail.

Downstream-Field Comparison of Single and Multiphase JICF. The ability to simulate (using LES) the near-field of a single-phase JICF is demonstrated in previous sections. In this section, a comparison of the single-phase and multiphase JICF, in the downstream field, is conducted numerically. The near field of a spray JICF is different from the single-phase JICF due to multiphase flow phenomena; the momentum is not injected into the continuous phase right at the nozzle but is transferred from the dispersed phase to the continuous phase along the droplet trajectories while the droplets slow down. Since the droplets disperse and follow individual, different trajectories, the momentum injection into the continuous phase has a volumetric distribution. However, in the downstream field, it is less important how the transverse momentum is injected into the crossflow. Downstream, the effects of the momentum of the injected droplets are small and, hence, the final results are expected to resemble the single-phase flow case.

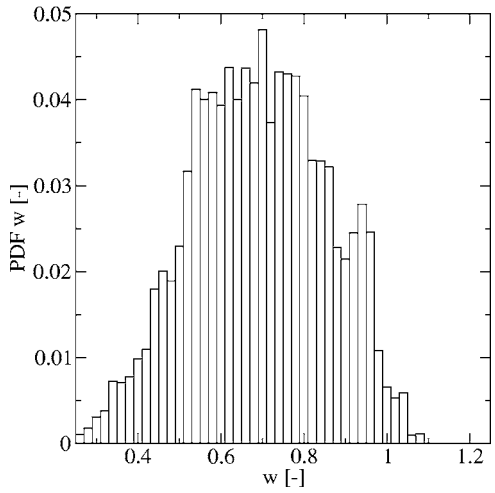

Fig. 15 PDF of the streamwise velocity

The downstream-field comparison is done for identical mass flow and momentum flow ratios for both the single-phase and multiphase JICF. Because of the density ratio of 100 between the liquid phase and the gas phase at elevated pressure, it is impossible to have the same momentum and mass flux ratios as in the single-phase JICF. However, momentum and mass flow ratios can be retained. The mass flows of the crossflow and the jet are kept as in the single-phase JICF. The channel flow bulk velocity is therefore set to 10 m/s (100 times larger as before). The velocity ratio $V_{\text{jet}}/V_{\text{crossflow}}$ is 5, corresponding to the single-phase case. This gives the liquid injection velocity of 50 m/s. Continuity requires the nozzle radius to be one-tenth of the nozzle radius in the single-phase case. The momentum flux ratio and the mass flux ratio are therefore 100 times larger in the multiphase flow case compared to the single-phase flow case while the momentum and mass flow ratios are the same. The scaling difference due to the nozzle diameter difference is thought to vanish in the downstream field.

The crossflow medium is air at 600 K. This high temperature is typical for gas turbine applications as it ensures the fast evaporation of the fuel; in the downstream-field plane, most fuel is in gaseous form. The fuel is octane at 298 K. The cone angle of the injection nozzle is 15 deg. The surface tension is 0.022 N/m. The droplets are polydisperse and are set to initially have a χ^2 distribution. Three different Sauter mean diameters are investigated: 1 μm, 10 μm, and 100 μm, corresponding to Stokes numbers of 0.0006, 0.06, and 6, respectively.

Figures 17 and 18 compare the vertical and streamwise velocity profiles of the single-phase flow case to multiphase flow cases in the downstream field. The injection droplet sizes are varied as mentioned above. The data are saved along a vertical line in the centerplane 10 dia downstream for the single-phase flow case (line 3 in Fig. 4). As the diameter for the multiphase flow case is ten times smaller, this location corresponds to 100 dia downstream in the multiphase flow case.

The single-phase JICF has the weakest CVP. Its trajectory is flattest and the wake is most pronounced. The multiphase flow cases have stronger CVPs. They follow higher trajectories and produce weaker wakes. The strength of the wake is evident in Fig. 18 as the lowest local minimum. The streamwise velocity of the single-phase case drops down to $w \sim 0.5$ at $y \sim 0.7$ whereas the velocities in the multiphase cases drop to $w \sim 0.7$–0.8 at $y \sim 1$. The strength of the CVP can be estimated from the maximum vertical velocities between the CVP (see Fig. 17). The single-phase flow has an upward velocity of $v \sim 0.3$, whereas the multi-

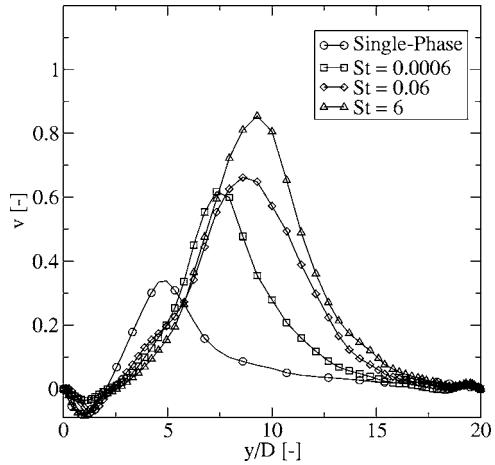

Fig. 17 Downstream-field comparison of vertical velocity profiles between single-phase and multiphase flow with various Stokes numbers

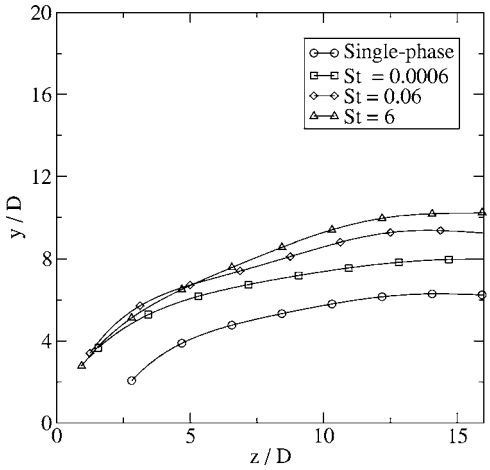

Fig. 19 Comparison of CVP trajectories for single-phase and multiphase flow with various Stokes numbers

phase flow cases have upward velocities of $v \sim 0.6-0.9$. The multiphase cases induce a stronger CVP. The height of the CVP can be defined as the y coordinate of the local maximum in the vertical velocity profiles, for example. The CVP trajectory obtained with this definition is plotted in Fig. 19. It is clear that all multiphase JICF cases have higher CVP trajectories than the single-phase case. Moreover, the lower the Stokes number is, the more the trajectory approaches trajectory of the single-phase flow case.

The multiphase flow differs from the single-phase flow in two respects: (i) the lack of communication within the liquid phase due to absence of diffusion and (ii) spatially smeared injection of the transverse momentum. In the single-phase case, the momentum is injected right at the nozzle. Contrarily, in the multiphase flow case, the momentum is slowly injected into the continuous phase while the droplets slow down. In the single-phase case, the momentum is therefore subject to diffusion right from the nozzle, whereas in the multiphase flow case, the momentum in the dispersed phase does not diffuse (aside from droplet collisions). The higher diffusion of the single-phase JICF causes the jet trajectory to be flatter and the CVP to be less pronounced. The flatter jet trajectory causes the wake to be more pronounced.

The rate of momentum transfer depends on the Stokes number of the droplets. The Stokes number is proportional to the square of the droplet diameter. Small droplets dispose of their excess momentum fast, whereas larger droplets slowly transfer their excess momentum along their trajectory. This is more intuitively explained by the elephant effect, i.e., the decreasing area-to-mass ratio with increasing size of the droplets: Aerodynamic forces scale with the droplet area, whereas inertial forces scale with the droplet volume. This means that smaller droplets have larger aerodynamic forces per unit mass, slow down faster, and therefore transfer their excess momentum to the continuous phase faster. Moreover, the faster response of small droplets to the turbulent flow enhances their lateral dispersion. High lateral dispersion of droplets has a similar effect on the strength and trajectory of the CVP as diffusion: The CVP is weaker and has a flatter trajectory.

In a case with evaporation, the rate of momentum transfer also depends on the ratio between the evaporation time and the momentum response time. The elephant effect is also evident in the faster evaporation of small droplets (D^2-law). As small droplets evaporate faster, they also transfer their momentum faster.

The case with the smallest droplets is closest to the single-phase flow case due to all three points. Figures 17–19 show this; the trajectory is flattest and the CVP weakest for the smallest droplets ($\mathrm{St} \sim 0.0006$). In this case, the momentum is injected closest to the nozzle and the single-phase flow case is approached most.

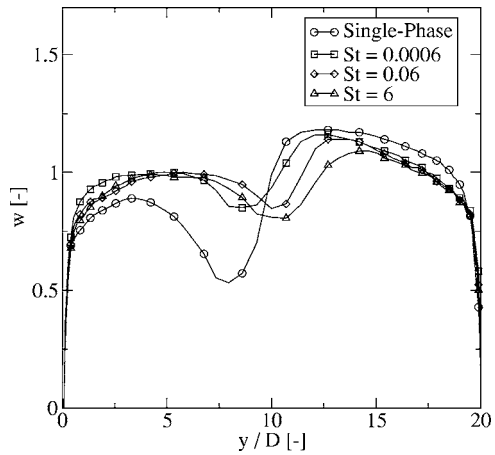

Fig. 18 Downstream-field comparison of streamwise velocity profiles between single-phase and multiphase flow with various Stokes numbers

Conclusions

For single-phase JICF, LES computations show the unsteady CVP and horseshoe vortices, and intermittent upright tornadolike wake vortices. The latter extend from the CVP to the horseshoe vortices, which supports the view that wake vortices are lifted branches of the horseshoe vortices.

The LES are in qualitative agreement with measured PIV data. Unsteady coherent structures with Strouhal numbers of order 1.3 can enhance inhomogeneities in fuel-air mixing. Characteristic frequencies found in the streamwise velocity correspond to frequencies in the mixture fraction. The PDF of the vertical velocities at a point in the wake is skewed. A bump in the PDF of streamwise velocity at fast velocities is postulated to be correlated with a bump in the PDF of mixture fraction on the lean side; peaks in streamwise velocities are associated with fuel-lean pockets.

A multiphase JICF can be compared to a single-phase JICF in the downstream field. The trajectory of a single-phase JICF is found to be lower than the trajectory of a corresponding multiphase JICF. As a consequence, the wake is more pronounced. The CVP is found to be weaker for the single-phase JICF. The two cases are most similar if the injected droplets are small. Increasing droplet sizes yield higher jet trajectories and more pronounced CVPs.

Acknowledgment

The project was supported by the Swedish Energy Agency (STEM). Computational resources were provided by LUNARC computing center at Lund University.

References

[1] Fric, T., and Roshko, A., 1994, "Vortical Structure in the Wake of a Transverse Jet," J. Fluid Mech., **279**, pp. 1–47.
[2] Yuan, L., Street, R., and Ferziger, J., 1999, "Large-Eddy Simulation of a Round Jet in Crossflow," J. Fluid Mech., **379**, pp. 71–104.
[3] Joeng, J., and Hussain, F., 1995, "On the Identification of a Vortex," J. Fluid Mech., **285**, pp. 69–94.
[4] Smith, S., and Mungal, M., 1998, "Mixing, Structure and Scaling of the Jet in Crossflow," J. Fluid Mech., **357**, pp. 83–122.
[5] Kelso, R., Lim, T., and Perry, A., 1996, "An Experimental Study of Round Jets in Cross-Flow," J. Fluid Mech., **306**, pp. 111–144.
[6] Kelso, R., and Smits, A., 1995, "Horseshoe Vortex Systems Resulting from the Interaction Between a Laminar Boundary Layer and a Transverse Jet," Phys. Fluids, **7**(1), pp. 153–158.
[7] Andreopoulos, J., and Rodi, W., 1984, "Experimental Investigation of Jets in Crossflow," J. Fluid Mech., **138**, pp. 93–127.
[8] Haven, B., and Kurosaka, M., 1997, "Kidney and Anti-Kidney Vortices in Crossflow Jets," J. Fluid Mech., **352**, pp. 27–64.
[9] Hasselbrink, E., and Mungal, M., 2001, "Tranverse Jets and Jet Flames. Part 2. Velocity and OH Field Imaging," J. Fluid Mech., **443**, pp. 27–68.
[10] Sykes, R., Lewellen, W., and Parker, S., 1986, "On the Vorticity Dynamics of a Turbulent Jet in a Crossflow," J. Fluid Mech., **168**, pp. 393–413.
[11] Alvarez, J., Jones, W., and Seoud, R., 1993, "Predictions of Momentum and Scalar Fields in a Jet in Cross-Flow Using First and Second Order Turbulence Closures," *Comp. and Exp. Assessment of Jets in Cross Flow*, AGARD, CP-534, pp. 21-1–24-10.
[12] Schlüter, J., and Schönfeld, T., 2000, "LES of Jets in Cross Flow and Its Application to a Gas Turbine Burner," Flow, Turbul. Combust., **65**, pp. 177–203.
[13] Priere, C., Gicquel, L., Kaufmann, P., Krebs, W., and Poinsot, T., 2004, "Large Eddy Simulation Predictions of Mixing Enhancement for Jets in Cross-Flows," ASME J. Turbomach., **5**(005), pp. 1–24.
[14] Cortelezzi, L., and Karagozian, A., 2001, "On the Formation of the Counter-Rotating Vortex Pair in Transverse Jets," J. Fluid Mech., **446**, pp. 347–373.
[15] Wu, P.-K., Kirkendall, K., Fuller, R., and Nejad, A., 1997, "Breakup Processes of Liquid Jets in Subsonic Crossflows," J. Propul. Power, **13**(1), pp. 64–73.
[16] Rachner, M., Becker, J., Hassa, C., and Doerr, T., 2002, "Modelling of the Atomization of a Plain Liquid Fuel Jet in Crossflow at Gas Turbine Conditions," Aerosol Sci. Technol., **6**, pp. 495–506.
[17] Madabhushi, R., 2003, "A Model for Numerical Simulation of Breakup of a Liquid Jet in Crossflow," Atomization Sprays, **13**, pp. 413–324.
[18] Caraeni, D., Bergström, C., and Fuchs, L., 2000, "Modeling of Liquid Fuel Injection, Evaporation and Mixing in a Gas Turbine Burner Using Large Eddy Simulation," Flow, Turbul. Combust., **65**, pp. 223–244.
[19] Ghosh, S., and Hunt, J., 1998, "Spray Jets in a Cross-Flow," J. Fluid Mech., **365**, pp. 109–136.
[20] Wu, P.-K., Kirkendall, K., Fuller, R., and Nejad, A., 1998, "Spray Structures of Liquid Jets Atomized in Subsonic Cross-Flows," J. Propul. Power, **14**(2), pp. 173–182.
[21] Leong, M., McDonnell, V., and Samuelsen, G., 2001, "Effect of Ambient Pressure on an Airblast Spray Injected into a Crossflow," J. Propul. Power, **17**(5), pp. 1076–1084.
[22] Fuller, R., Wu, P.-K., Kirkendall, K., and Nejad, A., 2000, "Effects of Injection Angle on Atomization of Liquid in Transverse Airflow," AIAA J., **38**(1), pp. 64–72.
[23] Westerweel, J., 2000, "Theoretical Analysis of the Measurement Precision in Particle Image Velocimetry," Exp. Fluids, **29**(7), pp. S003–S012.
[24] Jiang, G.-S., and Shu, C.-W., 1996, "Efficient Implementation of Weighted ENO Schemes," J. Comput. Phys., **126**, pp. 202–228.
[25] Amsden, A., O'Rourke, P., and Butler, T., 1989, "KIVA-II: A Computer Program for Chemically Reactive Flows With Sprays," Los Alamos National Laboratory, Tech. Rep. No. LA-11560-MS.
[26] Crowe, C., Sommerfeld, M., and Tsuji, Y., 1997, *Multiphase Flows With Droplets and Particles*, CRC Press, Boca Raton, FL.

T. Tinga
National Aerospace Laboratory NLR,
Anthony Fokkerweg 2,
1059 CM,
Amsterdam, The Netherlands
e-mail: tinga@nlr.nl

J. F. van Kampen

B. de Jager

J. B. W. Kok

Thermal Engineering,
Twente University,
P. O. Box 217,
7500 AE Enschede,
The Netherlands

Gas Turbine Combustor Liner Life Assessment Using a Combined Fluid/Structural Approach

A life assessment was performed on a fighter jet engine annular combustor liner, using a combined fluid/structural approach. Computational fluid dynamics analyses were performed to obtain the thermal loading of the combustor liner and finite element analyses were done to calculate the temperature and stress/strain distribution in the liner during several operating conditions. A method was developed to analyze a complete flight with limited computational effort. Finally, the creep and fatigue life for a measured flight were calculated and the results were compared to field experience data. The absolute number of cycles to crack initiation appeared hard to predict, but the location and direction of cracking could be correlated well with field data. [DOI: 10.1115/1.2360603]

1 Introduction

To improve gas turbine efficiency the operating temperatures have steadily increased. This makes greater demands on the structural integrity of the gas turbine components, especially the turbine blades and vanes and the combustor liner. The ability to perform a reliable life assessment is crucial for both gas turbine component design and maintenance. Damage as is shown for a combustor liner in Fig. 1 must be detected and repaired before it gets problematic. Therefore, reliable determination of inspection intervals is very important. To achieve this a vast amount of research has been done on predicting the time dependent thermomechanical loading of gas turbine components and performing life assessments.

The majority of the work published so far is devoted to turbine blades, since the high rotational speeds make these components the most severely loaded gas turbine components. The scope of the published work ranges from relatively simple engineering approaches [1,2] towards integrated multidisciplinary approaches combining computational fluid dynamics (CFD) and finite element (FE) codes to perform life assessments [3]. Surprisingly, much less work has been done on assessing the life of combustor liners.

The literature on combustors is mainly focused on fluid dynamics and combustion process optimization aiming at reducing emissions or optimizing the turbine inlet temperature profile [4–9]. The amount of published work on the prediction of liner thermal loading is very limited. Lai [10] did some work in this field and used a computational fluid dynamics analysis to predict the location of hot spots on a combustor liner. Also, the amount of publications on the coupling between the fluid and structural disciplines and on combustor life assessment is very limited. One of the few contributions in this field is the paper by Kiewel [11] that treats the life assessment of a ring combustor. In this work a measured temperature distribution at a single operating condition was used instead of a CFD calculated thermal loading history.

In the present work the integrated methods used for turbine blades were extended towards combustor liners. Mainly two developments were made to achieve this. First, a connection was established between several disciplines to be able to perform an integrated life assessment. Second, a method was developed to analyze a complete measured aircraft flight.

In the next section the different constituents of this multidisciplinary approach are described. Then Sec. 3 describes the method developed to analyze a real flight. In Sec. 4 the results are presented and finally Sec. 5 contains the conclusions.

2 Multidisciplinary Approach

Based on the output of an engine performance simulation program a CFD analysis was performed to simulate the combustion process and to calculate the liner thermal loading. Then a finite element analysis was used to predict the liner temperature and stress distribution, which were used as input for a life assessment. This section describes the details of the individual constituents of this integrated approach and their interfaces.

The engine system performance simulation program GSP [12] was used to calculate the input parameters for the CFD analyses. Measured engine and flight data, like power setting, altitude, and speed, were used to simulate a real flight. GSP provided gas temperatures, pressures, and mass flows at combustor entry and exit, which were used as boundary conditions in the CFD analyses. Note that GSP is a zero-dimensional program, which means that only cross-sectional averages at the various engine stations are calculated for the gas properties. The loading of the combustor liner is due to large temperature gradients in the metal, caused by the combined action of the combustion process and the fluid dynamics of both the hot gas and the numerous cooling flows. It is therefore inevitable to perform a detailed fluid dynamics analysis, despite the associated computational effort.

The CFD model describes the behavior of the gas volume inside the combustor liner, whereas the FE model describes the behavior of the structure (i.e., the liner) surrounding the gas. Since the loading of the structure is governed by the thermal and fluid dynamical behavior of the gas, it is very important that the geometry of the CFD and FE models matches at the interface through which they are coupled. Therefore, the models were constructed from the same geometric model. This geometric model was constructed from technical drawings and handbooks, taking into account details like the location and dimension of dilution and boroscope holes. The combustor liner is shown in Fig. 2 and the resulting CFD and FE models in Fig. 3.

As a result of the periodic flow field in the annular combustor, only 1/16th section of the total combustor had to be modeled.

Submitted to ASME for publication in the JOURNAL OF ENGINEERING FOR GAS TURBINES AND POWER. Manuscript received January 5, 2006; final manuscript received June 28, 2006. Review conducted by D. R. Ballal.

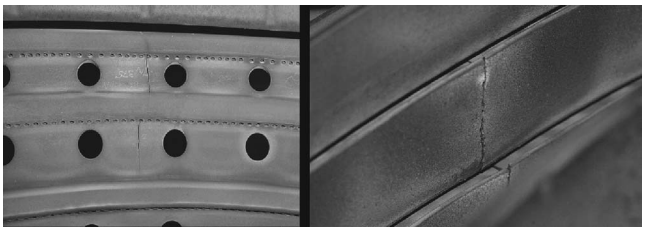

Fig. 1 Cracks in inner and outer liner of combustor

This is indicated by the dotted line in Fig. 2. Only the distribution of the boroscope holes is not periodic as these holes are not present in all sections (only four). Since the effect of the holes on the flow behavior inside the liner was believed to be significant, a boroscope hole was modeled in the 1/16th section (see Fig. 3).

2.1 Computational Fluid Dynamics Model. A fluid-dynamical analysis of the combustor was performed using the commercial CFD code ANSYS CFX 5.7. This code uses an unstructured solver, which facilitates the meshing of the relatively difficult geometry of the combustor (see Fig. 3). The geometry was meshed with mainly triangular mesh elements. The total number of elements assembling the geometry is 1.4 million.

In this section, the models that were used in the CFD analysis are described. Moreover, the translation step from the GSP data to boundary conditions for the CFD model is treated.

2.1.1 Model Description. For all cases considered in this paper, the flow in the combustor is turbulent. To predict the effects of turbulence on flow, combustion and heat transfer, the standard available *k*-epsilon turbulence model was used. At all inlet boundaries, a turbulence intensity of 10% of the mean inlet velocities was assumed, corresponding to intense turbulence.

Combustion was accounted for by a single-step combustion model which uses an effective Arrhenius law for the reaction rate. The fuel was considered to be fully vaporized, i.e., no liquid phase is included in the simulation. The aero gas turbine hydrocarbon fuel JP10 was used, for which the Arrhenius constants were fitted from a computational singular perturbation method based reduced version of a detailed chemical reaction scheme (see De Jager et al. [13] and the Appendix). From laminar flame data the reaction rate as a function of temperature is known. In order to establish the activation energy constant in an Arrhenius-type relation for the global conversion of JP10 into combustion products, a Gaussian fit can be applied to this data. The Gaussian fit to the activation energy and the pre-exponential factor is given by:

$$S_\eta = 261\,0e^{-(T-1938/358.2)}[\mathrm{kg/m^3/s}] \tag{1}$$

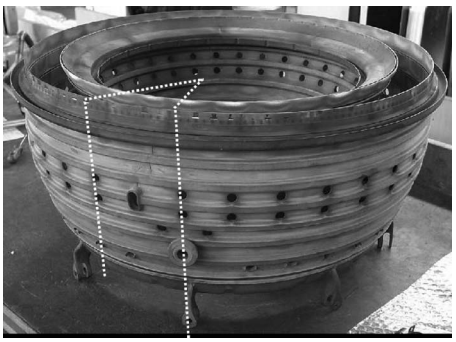

Fig. 2 Combustor liner with 1/16th section that is modeled indicated by dotted line

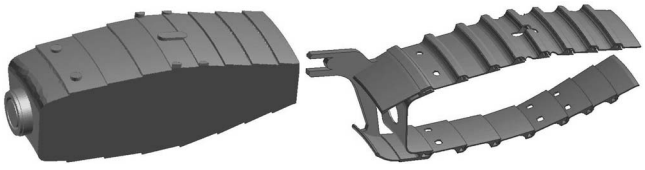

Fig. 3 Geometry of CFD (left) and FE models (right)

These laminar fitted global rate constants are used in the turbulent combustion calculation by use of a probability density function weighting over the mass fraction of fuel. This is represented in Eq. (2):

$$\tilde{S}_\eta = \int S_\eta P(y_f)dy_f[\mathrm{kg/m^3/s}] \tag{2}$$

In this compact combustor, turbulence intensity is not too high in the combustion zone. For that reason and for simplicity the pair distribution function for the fuel mass fraction is assumed to be a delta function. This way Eq. (2) can be used directly in a simple finite rate combustion simulation. This approach is used in many flamelet based combustion models [14].

The flame in the combustor is stabilized by a recirculation zone of hot gases. This recirculation zone is the result of the swirling inlet flow. The axial swirler vanes of the burner were not included in the model. However, from the geometry of the actual axial swirler vanes, a 45 deg angle between the tangential and axial velocity was estimated. The swirlers of the burners in the annular combustor are co-rotating, which justifies the use of periodic boundary conditions at the radial planes bounding the model.

The influence of the combustor walls on the flow was modeled with a wall function [14]. The walls itself were modeled as non-adiabatic walls. At the cooling air side of the walls (outside the computational domain), a heat transfer coefficient was imposed. This heat transfer coefficient was calculated from the Nusselt correlation of Dittus-Boelter. The input for this correlation followed from the geometry of the cooling passage and the total amount of air flowing past the inner and outer liner (see Fig. 4). These mass flows were determined by an analysis of the air distribution over the combustor, which is treated in the next section. The different mass flows yielded different heat transfer coefficients for inner and outer liner, ranging from 140 to 1400 $\mathrm{W/m^2\,K}$, depending on the engine operating condition considered. To obtain the heat flux to the cooling air, the temperature of the cooling air was also required, which was assumed to be constant. Since the residence time of the air in the cooling passage is in the order of a few milliseconds, the cooling air has only a small temperature increase

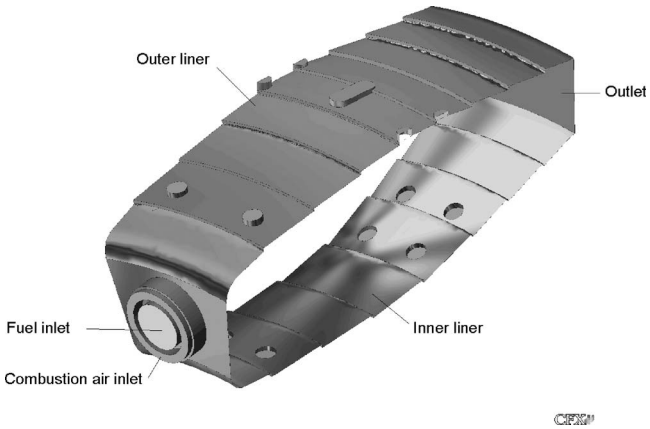

Fig. 4 Inlets and outlet in CFD geometry

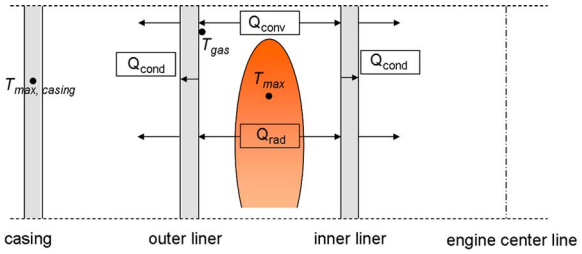

Fig. 5 Schematic representation of heat flows in combustor cross section

while flowing past the liner.

Besides convective heat transfer, radiation was accounted for as well. The fluid was considered optically transparent, implying that only radiation from the fluid to the walls was included in the analysis. Additionally, the radiative heat loss from the liner to the casing was modeled. For this purpose, a constant temperature was assumed for the casing: 100 K below the cooling air temperature.

2.1.2 Boundary Conditions. The GSP generated input data had to be transformed to mass flows at each inlet of the CFD model. These inlets comprise: the annular air swirler inlet of the burner, seven film cooling inlets in the inner liner, eight film cooling inlets in the outer liner, three pairs of dilution holes in the inner liner, three pairs of dilution holes in the outer liner, and the boroscope hole in the outer liner (see Fig. 4).

The pre-vaporized fuel was supplied at the center of the burner mouth. The film cooling holes, with a 1.5 mm diameter, are located in rows along the steps of the liner. For convenient modeling, the holes in each row were merged into a single slit-formed inlet. The distribution of the air flow through the burner and through the ensemble of the liner holes was determined by use of Bernoulli's law, assuming a global pressure difference over the liner. Furthermore, the distribution of the air over each individual air inlet hole was derived as proportional to the area of each inlet. This approach was allowed as the flow is by approximation, prior to combustion, isothermal, incompressible, and inviscous.

2.2 Finite Element Model. The finite element analysis was performed using the commercial FE code MSC.Marc 2001. In the geometry as shown in Fig. 3 a finite element mesh was created with isoparametric eight-node hexagonal elements. Typically ten elements were used in circumferential direction and two elements across the liner wall thickness, resulting in a total number of 11,646 elements and 18,285 nodes.

The model was first used for a thermal analysis to calculate the temperature distribution in the liner, using the CFD results as input. Then a structural analysis was performed to calculate the stress and strain distribution. The loads and boundary conditions that were used in these analyses are described in the next subsections.

2.2.1 Thermal Analysis. During the combustion process heat is transferred from the flame to the liner walls by convection and radiation. At the same time, cooling at the other side of the liner causes heat transfer from the liner wall to the cooling gas. This causes a temperature gradient across the wall thickness. These processes have to be covered by the thermal analysis, using the CFD results as input. This was done in the following manner (see also Fig. 5):

- Prescribing the CFD calculated wall adjacent gas temperature and heat transfer coefficient at the inner wall of the liner (convective boundary condition, Q_{conv})

$$Q_{\text{conv}} = h(T_{\text{gas}} - T_{\text{wall}}) \tag{3}$$

- Prescribing a radiative heat input at the inner wall using the CFD calculated maximum gas temperature (T_{max}) inside the liner. The radiative heat input is defined as

$$Q_{\text{rad}} = \sigma_{SB}\varepsilon^{*}(T_{\text{max}}^{4} - T_{\text{wall}}^{4}) \tag{4}$$

where σ_{SB} is the Stefan-Boltzmann constant and ε^{*} is the emissivity of the wall. For a metal surface the value of ε^{*} is about 0.75. However, a ceramic thermal barrier coating (TBC) was applied to the liner wall, reducing the emissivity to 0.35 [15].

- Prescribing a wall adjacent gas temperature equal to the combustor inlet temperature and a heat transfer coefficient, obtained from the Nusselt correlation of Dittus-Boelter, at the outer wall of the liner (convective boundary condition, Q_{conv}).
- Prescribing a radiative heat input at the outer wall using the casing temperature as T_{max}. It was assumed that the casing temperature is 100 K below the cooling gas temperature due to casing cooling from the outside.

Given these boundary conditions, the liner temperature distribution can be calculated.

Before the CFD calculated temperature field could be applied as a boundary condition, it had to be transferred from the CFD grid to the FE mesh. The pre-processing program MSC.Patran was used to transform the spatial fields for the CFD calculated temperature (T) and heat transfer coefficient (h) distribution to a convective FE nodal boundary condition.

The temperature drop across the TBC in the current application was approximated to be about 5 deg in a steady-state condition. Since the effect is very limited, this aspect of the TBC was not taken into account in the analysis. The effect of a reduced emissivity has a larger influence on the thermal behavior and was therefore included in the model as was described before.

2.2.2 Structural Analysis. Since only 1/16th part of the liner was modeled, periodic boundary conditions were applied at the edges of the model to account for the constraints applied by the omitted part of the structure. Therefore, displacements in circumferential direction were constrained at both end faces. Furthermore, the rigid body motion was constrained by fixing one point of the model (on the lug near the attachment to the diffuser casing) in all three directions. Finally, at the downstream end, both the inner and outer liner are fixed to the casing with metallic guides. These guides are sliding in axial direction and also provide some freedom to move in radial direction. Furthermore, the guides are somewhat flexible, which means that after the offsets in radial and axial direction have been reached due to deformation of the liners, they are still not rigidly fixed in space. Since it was expected that the liner deformations would not exceed the offsets of the guides, no boundary conditions were applied in this region.

The temperature distribution as calculated in the thermal analysis was used as loading for the structural model. Due to differences in thermal expansion thermal stresses develop and the material deforms elasto-plastically.

2.3 Life Assessment. Creep and low cycle fatigue (LCF) are the two potential failure mechanisms for a combustor liner. For both mechanisms a lifing method was defined, as will be described in this section. Also, the interaction between the mechanisms is discussed.

The creep strain accumulation was calculated during the FE analysis. The creep strain rate depended on stress σ (in Pa) and temperature T (in K) in the following way

$$\dot{\varepsilon}_{cr} = 3.48 \cdot 10^{-20} e^{4.02.10^{-8}\sigma} e^{0.0211T} \tag{5}$$

FE analysis of one flight provides the creep strain accumulation during that flight. However, analyzing the complete service life of a combustor in this way is computationally not feasible. Therefore, a method was defined to determine creep life based on a FE

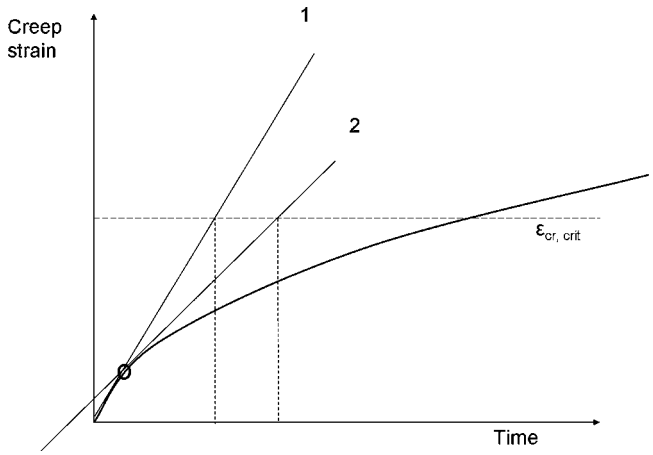

Fig. 6 Creep strain extrapolation using the average strain rate (1) and the tangent strain rate (2)

calculation of limited duration (Δt).

The most straightforward method is extrapolation of the damage after one flight (using the *average* creep rate) towards the critical amount of creep damage, also known as Robinson's rule [16]:

$$t_{cr} = \frac{\varepsilon_{cr,\text{critical}}}{\varepsilon_{cr,\Delta t}}\Delta t = \frac{\varepsilon_{cr,\text{critical}}}{\dot{\varepsilon}_{cr,\text{aver}}} \tag{6}$$

where $\varepsilon_{\text{cr,critical}}$ is the creep strain that is associated with the end of life.

However, it is well known that creep is not a linear process. The first reason is the non-linear shape of the creep curve and the second reason is the occurrence of stress relaxation. This makes that the creep strain rate is initially very high but then decreases to a constant value, as is illustrated in Fig. 6. If a FE creep analysis is performed for one flight, only a small part of the creep curve is covered and the constant creep rate is not reached. Extrapolation with the *average* creep rate towards the critical creep strain then yields a (very) conservative estimate of the creep life (see line 1 in Fig. 6). Therefore, the *tangent* creep rate at the end of the time period ($\dot{\varepsilon}_{cr,\Delta t}$) was used for the extrapolation (line 2 in Fig. 6), which yields a less conservative life assessment:

$$t_{cr} = \frac{\varepsilon_{cr,\text{critical}}}{\dot{\varepsilon}_{cr,\Delta t}} \tag{7}$$

The value of $\varepsilon_{\text{cr,critical}}$ is typically 2% creep strain. Note that this value is lower than the creep strain at rupture. However, creep rupture does not occur in this situation, since at creep strains of 2% other failure mechanisms, like coating spallation or grain boundary oxidation, become active and are the life limiting mechanisms.

For the low cycle fatigue (LCF) life analysis the cyclic loading of the construction is required. The fatigue life of a component is a combination of crack initiation and crack propagation. Normally the initiation life is calculated with a Manson-Coffin-type model and the crack propagation is predicted with a fracture mechanics-type analysis. However, such a detailed crack analysis is beyond the scope of this work and therefore a total life analysis is performed, in which the LCF life is defined as the number of cycles to a certain crack length. It is generally accepted that the initiation of cracks is best correlated with the *maximum shear* strain, whereas the propagation of cracks is governed by the *maximum principal* strain component. Since the maximum principal strain also provides information about the direction of crack propagation, this quantity was selected to calculate the LCF life distribution in the combustor. Further, for LCF conditions the load cycles contain both elastic and plastic deformation, which means that the LCF life is related to the total strain range ($\Delta\varepsilon_{\text{tot}} = \Delta\varepsilon_{el} + \Delta\varepsilon_{pl}$). The relation between total strain range ($\Delta\varepsilon_{\text{tot}}$ in %) and LCF life (N_{LCF}) for the liner material Hastelloy-X was obtained from Seeley et al. [17] and the functional relation used in the FE analysis is given by

$$N_{\text{LCF}} = \left(\frac{\Delta\varepsilon_{\text{tot}}}{21.253}\right)^{-2.36} \tag{8}$$

which represents the 870°C curve.

Finally, it is possible to combine the creep and fatigue damage to obtain the total creep and fatigue life of the combustor. However, it is very difficult to obtain the proper interaction between the two failure mechanisms. The simplest method is to combine the two mechanisms linearly, which is known as the Miner-Robinson rule:

$$\frac{1}{N_{\text{tot}}} = \frac{1}{N_{\text{LCF}}} + \frac{1}{N_{cr}} \tag{9}$$

Table 1 Details of characteristic operating conditions

Condition	1	2	3	4	5
$TT3$[K]	750	380	1000	750	750
W_f/W_{air}	0.0257	0.0257	0.0257	0.0033	0.0118

3 Analysis of a Complete Flight

The integrated approach described in the previous section can be used to analyze the liner loading and life consumption for a single operating condition. However, a real flight is a sequence of a large number of different operating conditions. Analyzing all conditions separately is computationally not feasible. Therefore, a method was developed to efficiently analyze a complete flight. In this section the method is described and the accuracy is demonstrated.

3.1 Method Description. The basic idea of the method is that detailed CFD analyses were performed for a limited number of characteristic conditions and that for any other condition thermal input properties were obtained by interpolating between these conditions. The time scale of the processes in the combustor fluid domain (~ milliseconds) is very different from the time scale of the overall engine transients (~ seconds). The transient behavior of the engine (e.g., fast or slow accelerations) is captured by GSP and translated into time sequences of the quantities that characterize the combustion process (fuel and airflow). Since the sampling rate of these quantities is in the order of seconds, it is appropriate to consider a transient mission analysis as a number of consecutive quasi-steady-state CFD analyses. Therefore, there is no need to do transient CFD analyses.

Appropriate quantities for interpolation, interpolation functions, and characteristic conditions had to be defined. Therefore, a large number of measured flights were analyzed with the gas turbine simulation program GSP. Air inlet temperature ($TT3$) and fuel/air ratio (W_f/W_{air}) proved to be the only two quantities required to fully characterize the combustor operating condition. Also the operating ranges of these parameters were established in this way, resulting in the definition of five characteristic operating conditions as indicated in Table 1. CFD analyses were performed for these five conditions and the results were stored in a database.

Interpolation functions were selected for the quantities required to define the boundary conditions in the FE analysis: wall adjacent gas temperature, inside heat transfer coefficient, maximum gas temperature, and outside heat transfer coefficient. GSP analyses showed that the gas temperature rise in the combustor was almost directly proportional to the fuel/air ratio, but the proportionality

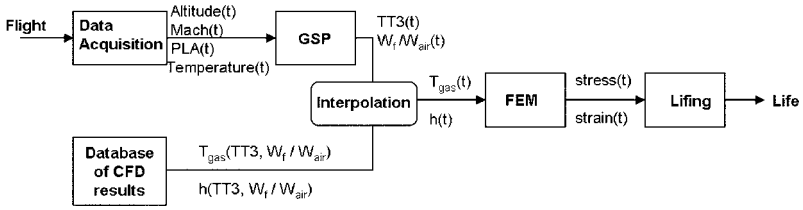

Fig. 7 Schematic representation of mission analysis method

constant depended on the initial gas temperature value. Therefore, the following linear interpolation function was adopted for the wall adjacent gas temperature:

$$T_{\text{gas}} = bTT3 + a\frac{W_f}{W_{\text{air}}} \Leftrightarrow \frac{T_{\text{gas}}}{TT3} = b + a\frac{W_f}{W_{\text{air}}TT3} \tag{10}$$

The heat transfer coefficient is largely determined by the amount of turbulence in the flow, which is strongly related to the mass flow. Therefore, the following linear interpolation function was adopted for the heat transfer coefficient:

$$h = c + dW_{\text{air}} \tag{11}$$

The interpolation functions for the maximum temperature in the combustor (used for radiative heat input) and the outside heat transfer coefficient were defined as

$$T_{\max} = 925 + TT3 + 22{,}946\frac{W_f}{W_{\text{air}}} \tag{12}$$

$$h_{\text{outside}} = 22.6 \cdot W_{\text{air}} \tag{13}$$

The parameters a, b, c and d in Eqs. (10) and (11) were determined for every node on the liner inner surface by fitting the functions to the five result cases that were available in the database of CFD results. This was done by using a least squares fitting method. The parameters were stored in a file, which was used during the transient FE analyses. The functions in Eqs. (12) and (13) are valid for the entire combustor model and therefore do not require fitting for all nodes.

The method to perform a transient analysis of a complete flight is shown schematically in Fig. 7 and can be summarized as follows.

- A number of CFD analyses were performed for five characteristic engine operating conditions that span the operating range, see Table 1.
- The calculated wall adjacent temperature distribution and heat transfer coefficient distribution for these conditions were transformed to FE boundary conditions and stored in a database.
- A recorded flight is analyzed with GSP as a transient analysis. GSP calculates the time sequence of the input variables $TT3$ and W_f/W_{air}.
- A transient thermal FE analysis is performed in which the time-dependent boundary conditions are calculated by **interpolating** (for every node at the liner inner surface) between the conditions in the CFD database, based on the given values of $TT3$ and fuel/air ratio.
- A transient structural FE analysis is performed in which the calculated time-dependent temperature distribution is imposed as loading.
- A life assessment is performed based on the FE calculated stress and temperature sequences.

3.2 Method Validation. In addition to the five CFD analyses for the conditions given in Table 1, one extra CFD analysis was performed to validate the interpolation method. The condition of this analysis, referred to as condition 6, represents the engine design point characterized by $TT3=817.6$ K and $W_f/W_{\text{air}}=0.0322$. This yields a fuel/air ratio of 0.0322 and a condition that is quite different from any of the other conditions in Table 1.

The first validation was done by comparing the CFD calculated T_{gas} and h with the interpolated T_{gas} and h. The result for every node on the liner inner surface is shown in Fig. 8. This shows that for the gas temperature the average of the complete set of points is on the 1-to-1 line and the deviation from the calculated value is typically less than 10%. For the heat transfer coefficient the correlation is even better.

Another validation of the method is shown in Fig. 9, where the calculated liner temperature distribution based on the CFD calculated and interpolated T_{gas} and h are compared. The distribution is very similar and also the global temperature values are very comparable. Only at the hot spots the interpolated temperature was in

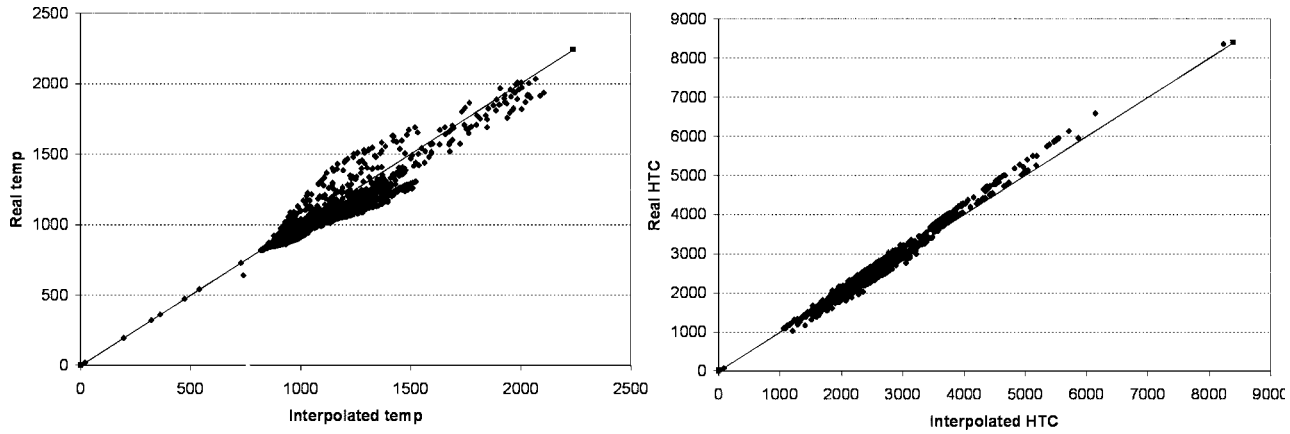

Fig. 8 Comparison of CFD calculated and interpolated T_{gas} and h

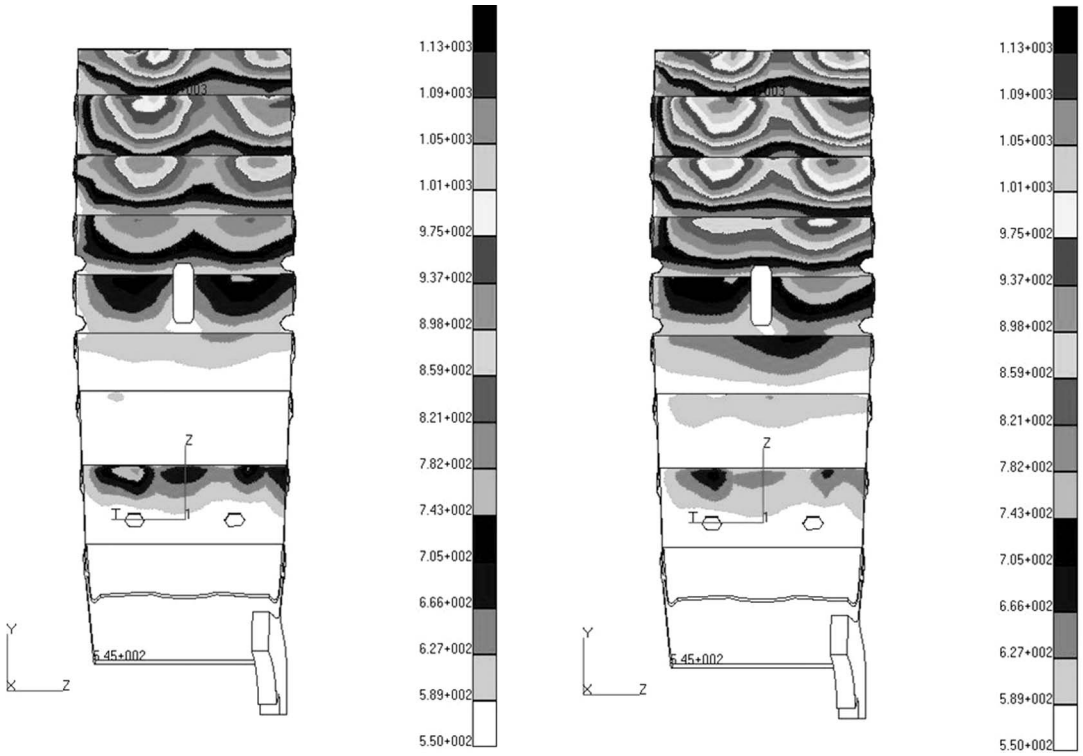

Fig. 9 Comparison of results based on real (left) and interpolated temperature distribution on outer liner

this case about 150° higher. This is a considerable deviation, but it is only for a small number of local spots. That may imply that at those spots the stresses relax quickly and that the effect on life consumption is small. However, the exact influence of these temperature deviations on life consumption was not determined. Furthermore, the condition used for validation is a severe condition which is quite different from the conditions used for interpolation. Therefore, for other conditions that occur during a mission the deviations may be smaller.

These two validation cases show that the method developed reduced the computational effort for a mission analysis enormously and still retained a very acceptable accuracy level. If a higher accuracy is required, the number of CFD analyses can be extended, which improves the interpolation method. However, the consequence will be a more time-consuming and more costly analysis.

4 Results

The integrated approach as described in Secs. 2 and 3 was used to analyze a real flight and perform a combustor liner life assessment. The variation of power lever angle (PLA) and flight altitude for the selected flight are shown in Fig. 10. The analysis results are shown in this section, starting with the flow properties predicted by the CFD analysis for a selected condition. Then the predicted temperature and stress distribution are shown and the results of the life assessment are presented. Finally, the results were compared to the damage observed in practice to validate the approach.

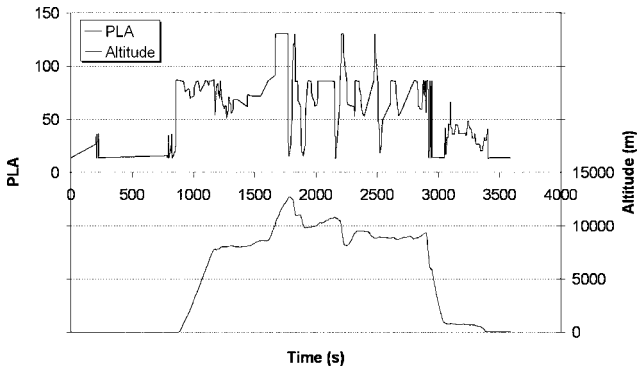

Fig. 10 Variation of power setting (PLA) and flight altitude during analyzed mission

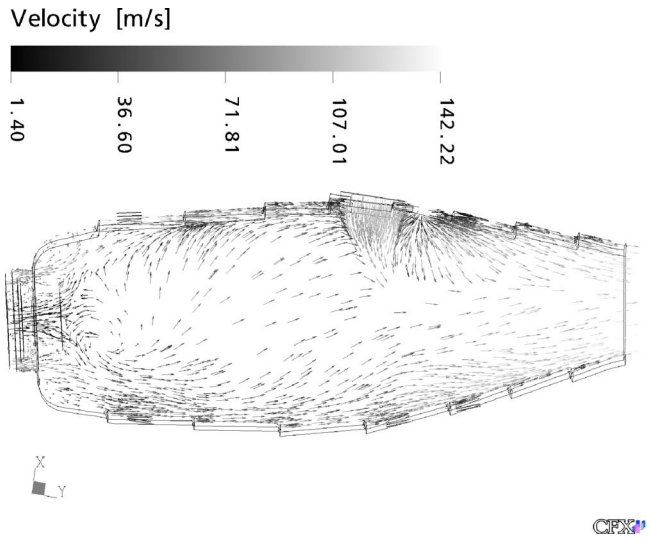

Fig. 11 Vector plot of the velocity field in a radial plane of the combustor

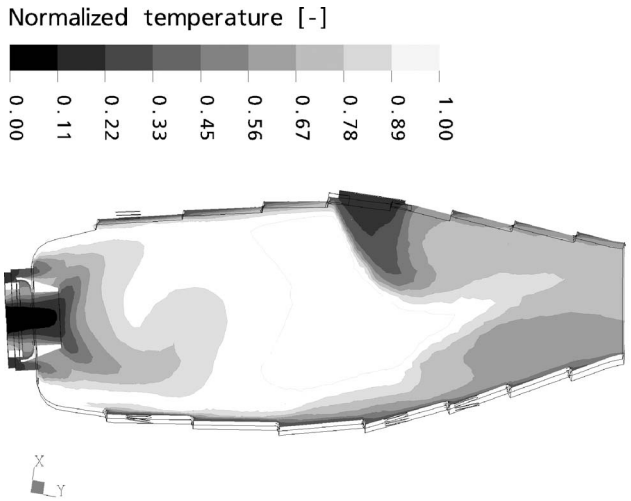

Fig. 12 Contour plot of the temperature field in a radial plane of the combustor at condition 1

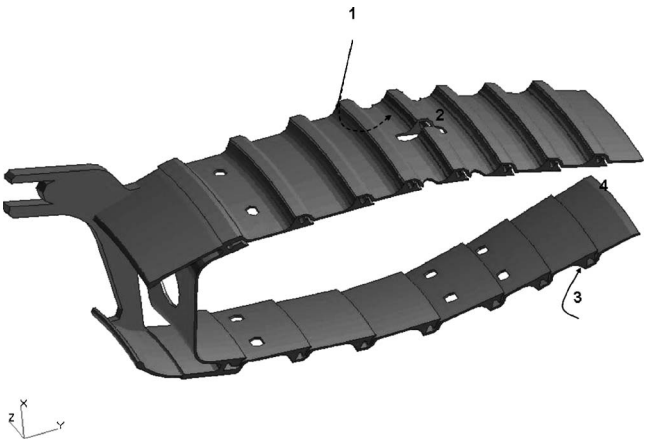

Fig. 14 Location of nodes used for plotting the temperature and stress history

4.1 Flow Properties. Figure 11 shows a vector plot of the flow field in a radial cross section of the burner for the first of the characteristic operating conditions (condition 1, see Table 1). As a result of the swirling inlet flow, a recirculation zone is established, providing flame stabilization. This recirculation zone is noticed by reversing flow near the burner outlet. Additionally, since the cross section is made in the plane of the boroscope hole, the effect of the cooling air flowing through this hole is clearly seen.

A contour plot of the scaled temperature field at the same operating condition is displayed in Fig. 12. The cooling air that is introduced by the boroscope hole is clearly influencing the temperature field. Moreover, due to the applied film cooling, the fluid near the wall remains relatively cool. The maximum temperature is found at approximately halfway the length of the combustor.

4.2 Thermal and Structural Results. The temperature distribution in the liner walls at operating condition 6 is shown in Fig. 13(*a*). This shows that the thermal loading of the liner is maximum at the downstream end of the inner liner. Figure 13(*b*) shows the tangential stress distribution in the liner walls. As with the temperature, the extreme values were found at the downstream ends of inner and outer liner.

The time variation of temperature and stress during the complete flight for the four locations indicated in Fig. 14 is shown in Fig. 15. This shows that significant variations in temperature and stress occur during the flight. For locations on the inside of the liners, stresses were mainly compressive, whereas locations on the outside were in a tensile stress state. However, the situation can be completely opposite at fast transients, as is observed just after 2000 s. Also, the average stress level decreased during the flight, which is caused by stress relaxation due to creep.

4.3 Life Assessment. The temperature and stress history were used to perform a life assessment on the combustor liner. Both the creep life and low cycle fatigue life were calculated applying the methods described in Sec. 2.3. The calculated distribution of creep and LCF life are shown in Fig. 16, indicating the critical locations on the liners. This plot shows that the creep life is minimal at the final louvers of both inner and outer liner with a minimum value of only 4 h. This calculated life is much too low and is probably a result of an overestimated temperature in the liner. Since the creep mechanism is extremely sensitive to the temperature, a small deviation in temperature leads to significant changes in creep life. This problem in predicting the creep life is a result of the lack of accuracy in the prediction of absolute values that will be addressed in the next subsection.

The minimum calculated fatigue life is around 1900 flights at some very small areas, mainly at the final louvers of the inner and outer liner. The majority of the structure has a fatigue life well above 10,000 flights.

4.4 Model Validation. To gain insight into predictive capability, the model had to be validated, especially because a large number of assumptions and approximations were made in the CFD, FE, and lifing analyses. Ideally, the model should have been validated and tuned to experimental data after each step in the sequence. For example, detailed information about the temperature distribution in the liner at a specific operating condition would give the possibility to tune the values of the outside heat transfer coefficients to obtain a good correlation with the available data. However, experimental data to do so was not available. Ac-

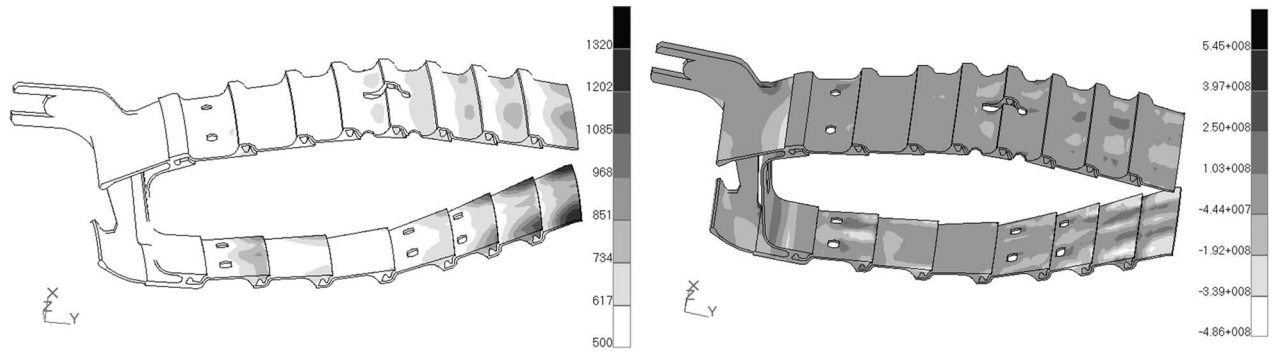

Fig. 13 (*a*) Temperature (in °C) and (*b*) tangential stress (in Pa) distribution at operating condition 6

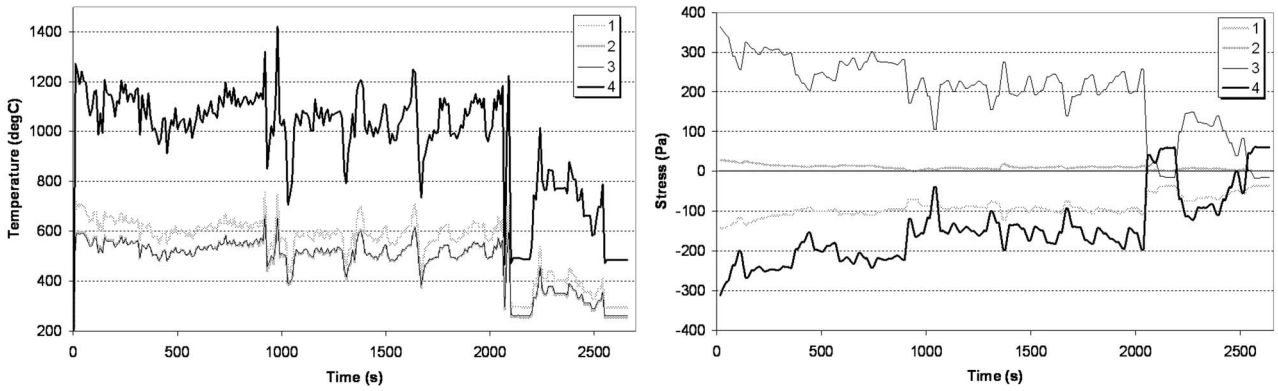

Fig. 15 Temperature and tangential stress variation on liner during a mission for the locations shown in Fig. 14

tually, the only way to validate the model was to compare the calculated life to the values observed in practice. This means that in the very complex chain of CFD—FE thermal—FE structural—life assessment analyses no intermediate check of the model was possible. It is quite likely that some assumption somewhere in one of the analyses leads to a deviation in results.

The results of the life assessment were compared to the damage observed in practice as shown in Fig. 1. The location of the cracks is expected to coincide with the location of lowest calculated fatigue life. As can be seen in Fig. 16, the lowest fatigue life was calculated at the final three louvers of the inner and outer liner. Furthermore, the creep damage on the final three louvers of the inner liner is significantly higher than on those of the outer liner. Since creep is believed to enhance crack initiation, it may be concluded that cracks will start to propagate at the final three louvers of the inner liner. This correlates well with the observation in practice that cracks occur at the inner liner on the 4th to 9th louvers.

The direction of crack growth is related to the orientation of the stress tensor in the material. In other words, cracks propagate mainly in a direction perpendicular to the maximum principal stress. Comparison of the different components of the calculated stress distribution in the louvers showed that the circumferential stress was the largest stress component and also best resembled the max principal stress distribution, as is shown in Fig. 17. This means that cracks will propagate in axial direction, as was observed in practice.

Finally, the number of cycles or flights to produce a fatigue crack could be checked. This showed that the order of magnitude of the calculated life corresponded to the real life, but the absolute prediction is not very accurate.

The only proper way to improve the predictive capability of the model is validation of intermediate results with experimental data. Although the prediction of absolute values for combustor life at certain operating conditions is hard, the current method is very appropriate to perform comparative life assessments. In that case, a wrong assumption somewhere in the model has a similar effect for every condition that is analyzed, which reduces the inaccuracy of the *comparison* considerably. Examples of such analyses are comparison of different mission types in terms of life consumption or the effect of increased firing temperature (due to compressor or turbine deterioration) on life consumption.

5 Conclusions

The following conclusions can be drawn from this work:

- The results of a CFD analysis were successfully linked to a FE model, which gave the possibility of calculating the thermal loading of the combustor for an arbitrary operating condition.
- An efficient method was developed to analyze a complete measured flight. A compromise between accuracy and computational effort must be found for each application.
- Although the actual number of cycles to crack formation could not be predicted accurately, the location of the cracks and the direction of crack growth correlated well to the observations in practice.
- The developed models and tools can be applied to perform comparative life assessment, e.g., for different mission types.

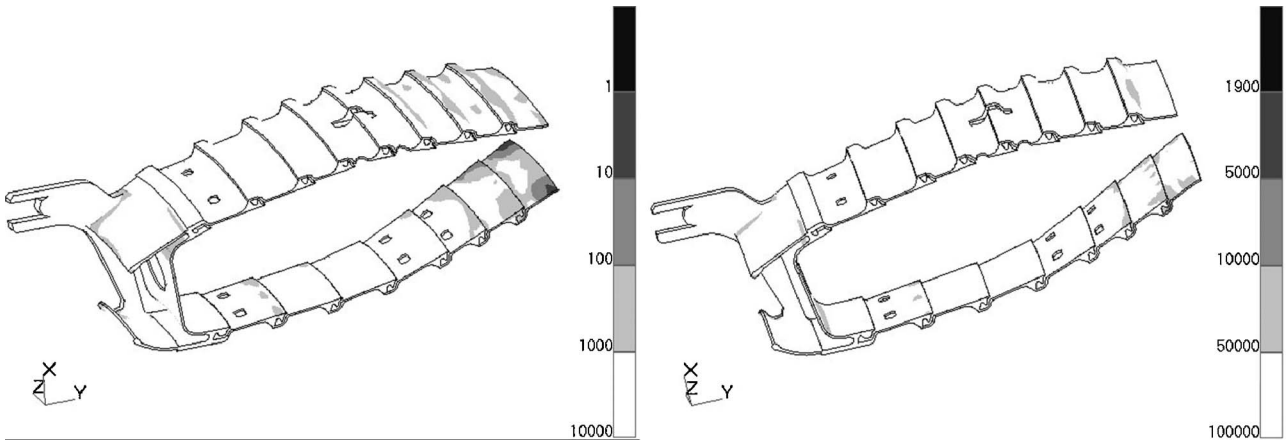

Fig. 16 Creep life (in hours) and fatigue life (in number of flights) distribution in the liner

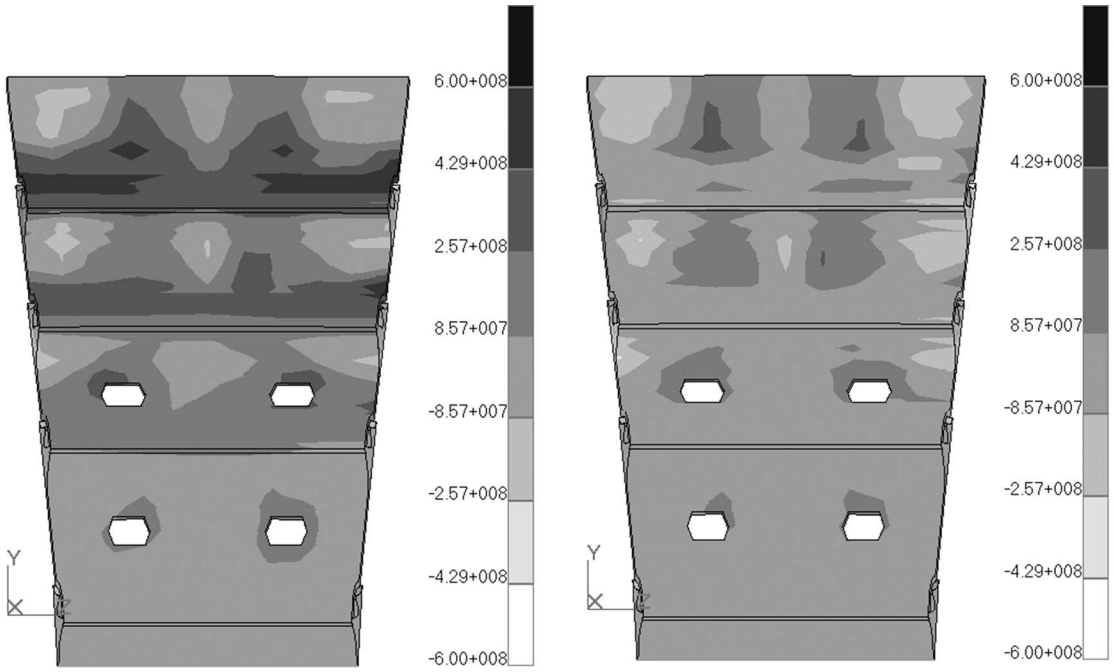

Fig. 17 Distribution of (*a*) circumferential and (*b*) max. principal stress on the final louvers of the inner liner

Appendix: JP10 Jet Fuel Chemistry

JP10 is a hydrocarbon fuel that is used in aero gas turbines. The molecule consists of 10 C atoms and 16 H atoms and its systematical name is Tricyclo[5.2.10]decane. Stoichiometric oxidation is given by the reaction

$$C_{10}H_{16} + 14O_2 \rightarrow 8H_2O + 10CO_2$$

Williams et al. [18–20] provided a mechanism for the oxidation of JP10 that consists of 42 species and 201 reactions. The basis of this mechanism is the San Diego Combustion mechanism. Added to this mechanism is a mechanism for the combustion of JP10. This addition consists of the breakup of the JP10 molecule into smaller hydrocarbons like butadiene, etc.

Laminar premixed 1D flame calculations at atmospheric and

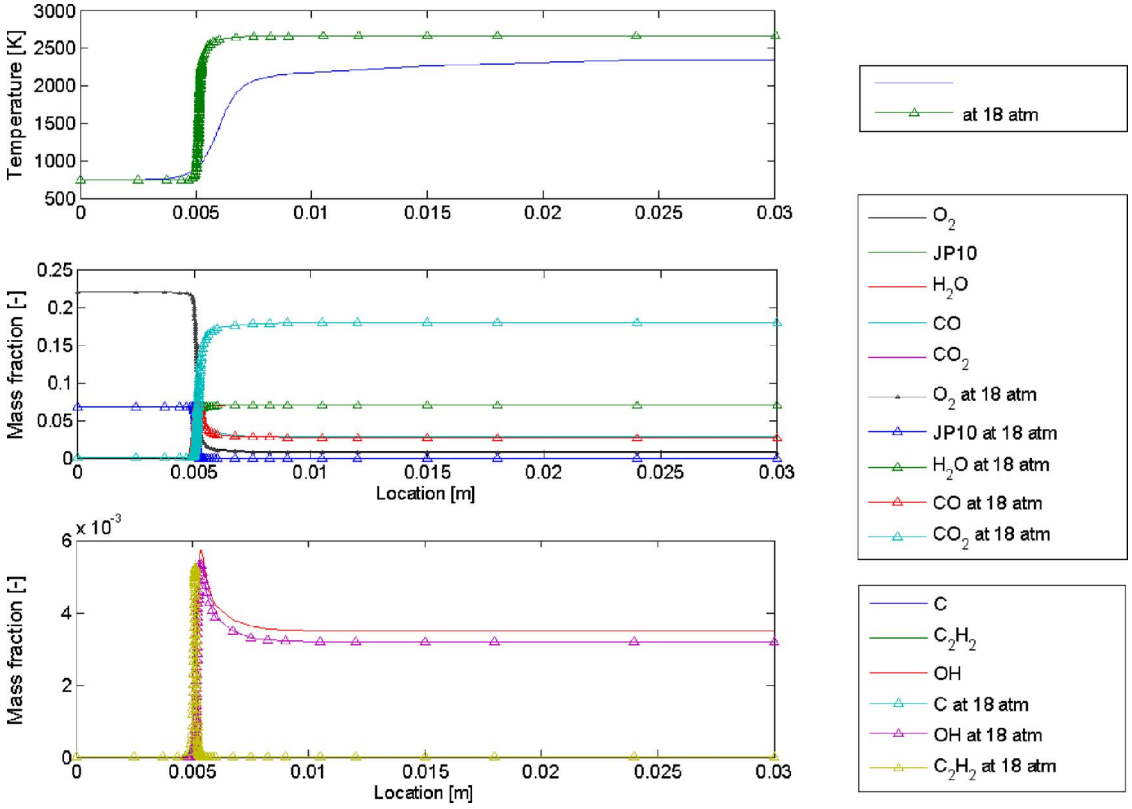

Fig. 18 The temperature and species profiles for a premixed flame at a pressure of 1 and 18 atm

Table 2 Non-steady-state species

CO	CO_2	O_2	H_2O	N_2	AR

elevated pressure yielded insight into the chemical reactions that dominate the oxidation behavior of JP10. The laminar flame calculations were analyzed using the computation singular perturbation (CSP) [21] technique, in order to select dominant species that govern the conversion of JP10 into products. This CSP analysis can give a global reaction rate as a function of the species in the mechanism or temperature.

Laminar Flames. Insight into global rates can be obtained by simulating a laminar premixed flame. In this report the results of a stoichiometric flame at 1 and 18 atm are shown. Figure 18 shows that the mechanism is behaving differently at atmospheric and high pressure. The temperature profile of the laminar flame at atmospheric pressure has a less steep descent than the temperature profile at 18 atm. The concentration of intermediate species and combustion products is not changing very much with the different pressures.

CSP Reduction. CSP analysis was carried out using the results from the laminar flame. A theoretical background of this method can be found in papers by Mastorakos et al. [21,22]. This analysis yields the species in Table 2 to be dominant in reaction rate determination, if the mechanism is to be projected on one global step. The global step that is constructed by CSP is given by the following reaction:

$$CO_2 \rightarrow CO + O_2$$

The results from CSP are similar to reduction of methane combustion as is reported by Mastorakos et al. [22]. An explanation for this is that both methane and JP10 are hydrocarbons and glo-

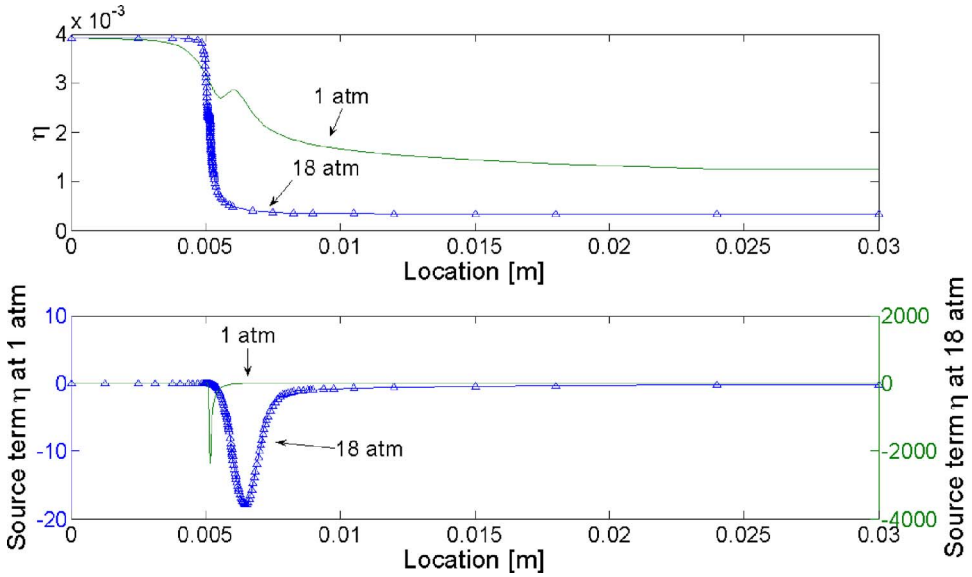

Fig. 19 Composed species concentration and source term (reaction rate)

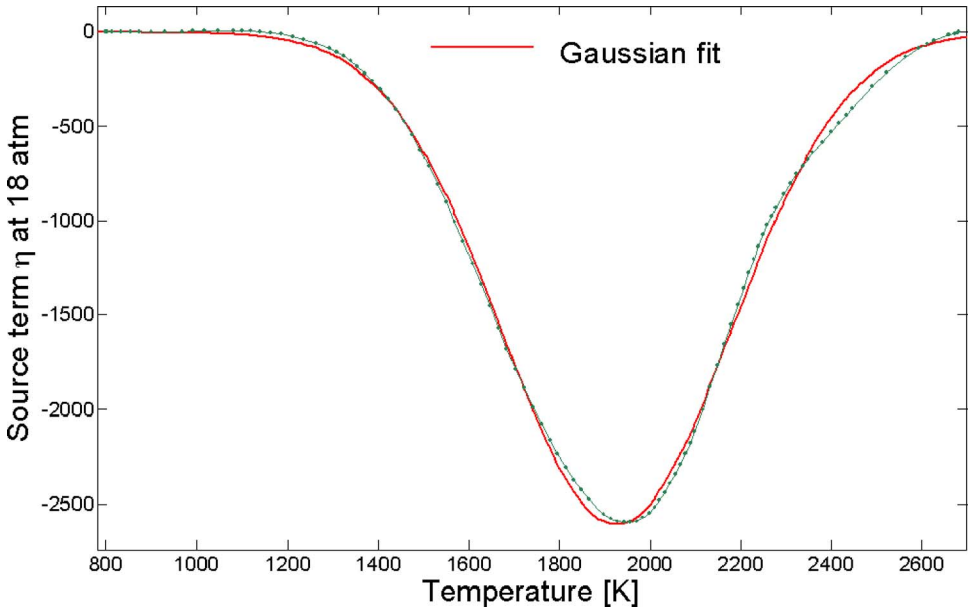

Fig. 20 CSP source term (reaction rate) fitted with Gaussian function

bally the same type of CH bond needs to be broken. Other types of CH bonds are also present in the JP10 mechanism, but they do not seem to affect the global step. The global step is not a physical step, it can rather be seen as an overall reaction that yields from element and mass conservation, but with *virtual* species.

Rate Fitting and Turbulent Simulations. Using the CSP analysis it is possible to construct a global reaction rate that represents the overall oxidation process composed of steady state relations. This composed reaction rate is accompanied by a composed species η that represents the thermo-chemical state of the mixture. In Fig. 19 this CSP analysis is projected on the laminar flame results from the previous section. It is seen that for atmospheric and high pressure there is a significant difference in the concentration profile of η. At high pressure the composed species behaves as a fuel molecule: a high initial concentration and during ignition a high consumption rate of the composed species. The shape of this profile is similar to the JP10 concentration profiles in Fig. 18. For atmospheric pressure, the composed species concentration profile is not showing much resemblance with a fuel molecule.

For turbulent combustion simulations the composed species and global rate can be used as a single step mechanism. This gives the advantage that only one extra transport equation is needed. From the laminar flame data at 18 atm the reaction rate as a function of temperature is known. In order to establish an Arrhenius-like relation for the global conversion of JP10 into combustion product, a Gaussian fit can be applied to this data (see Fig. 20). The Gaussian function is given by

$$S_\eta = 2610e^{-(T-1938/358.2)}\ [\mathrm{kg/m^3/s}] \qquad \text{(A1)}$$

This fitted rate can be used in a simple finite rate combustion simulation.

References

[1] Walls, D. P., and de Laneuville, R. E., 1997, "Damage Tolerance Based Life Prediction in Gas Turbine Engine Blades Under Vibratory High Cycle Fatigue," ASME J. Eng. Gas Turbines Power, **119**, pp. 143–146.

[2] Harrison, G. F., and Tranter, P. H., 1995, "Modelling of Thermomechanical Fatigue in Aero Engine Turbine Blades," Proceedings of the 81st Meeting of the AGARD Structures and Materials Panel on Thermal Mechanical Fatigue of Aircraft Engine Materials, Oct. 2–4, Banff, Canada, pp. 1–12.

[3] Tinga, T., Visser, W. P. J., de Wolf, W. B., and Broomhead, M. B. J., 2000, "Integrated Life Analysis Tool for Gas Turbine Components," ASME Paper No. 2000-GT-646, NLR-TP-2000-049.

[4] Scott Crocker, D., Nickolaus, D., and Smith, C. E., 1998, "CFD Modeling of a Gas Turbine Combustor From Compressor Exit to Turbine Inlet," ASME Paper No. 98-GT-184.

[5] Sivaramakrishna, G., Muthuveerappan, N., Venkataraman, S., and Sampathkumaran, T. K., 2001, "CFD Modeling of the Aero Gas Turbine Combustor," ASME Paper No. 2001-GT-0063.

[6] Malecki, R. E., and Rhie, C. M., 2001, "Application of an Advanced CFD-Based Analysis System to the PW6000 Combustor to Optimize Exit Temperature Distribution—Part I: Description and Validation of the Analysis Tool," ASME Paper No. 2001-GT-0062.

[7] McQuirk, J. J., and Spencer, A., 2000, "Coupled and Uncoupled CFD Prediction of the Characteristics of Jets From Combustor Air Admission Ports," ASME Paper No. 2000-GT-125.

[8] Snyder, T. S., Stewart, J. F., Stoner, M. D., and McKinney, R. G., 2001, "Application of an Advanced CFD-Based Analysis System to the PW6000 Combustor to Optimize Exit Temperature Distribution—Part II: Comparison of Predictions to Full Annular Rig Test Data," ASME Paper No. 2001-GT-0064.

[9] Fuller, E. J., and Smith, C. E., 1993, "Integrated CFD Modeling of Gas Turbine Combustor," AIAA Paper No. 93–2196.

[10] Lai, M. K., 1997, "CFD Analysis of Liquid Spray Combustion in a Gas Turbine Combustor," ASME Paper No. 97-GT-309.

[11] Kiewel, H., Aktaa, J., and Munz, D., 2002, "Advances in the Inelastic Failure Analysis of Combustor Structures," in: *High Intensity Combustors—Steady Isobaric Combustion*, Final Report of the Collaborative Research Centre, 167, S. Wittig and O. Vohringer, eds., Wiley-VCH, Weinheim.

[12] Visser, W. P. J., and Broomhead, M. J., 2000, "GSP—A Generic Object-Oriented Gas Turbine Simulation Environment," ASME Paper No. 2000-GT-002, NLR-TP-2000–267, www.gspteam.com.

[13] De Jager, B., Kok, J. B. W., and Van der Meer, Th. H., 2004, "Development of Reduced Chemistry With CSP for Application in Turbulent n-Heptane flames," *Proceedings of the European Congress on Computational Methods in Applied Sciences and Engineering (ECCOMAS)*, P. Neittaanmäki, T. Rossi, K. Majava, and O. Pironneau eds., W. Rodi, and P. Le Quéré assoc. eds., Jyväskylä, Finland, July 24–28, pp. 1–13.

[14] Peters, N., 1998, "Laminar Flamelet Concepts in Turbulent Combustion," *Proceedings of the International Symposium on Combustion*, Munich, pp. 1231–1250.

[15] Wittig, S., and Vohringer, O., 2002, "High Intensity Combustors—Steady Isobaric Combustion," Final Report of the Collaborative Research Centre, 167, S. Wittig and O. Vohringer, eds., Wiley-VCH, Weinheim, pp. 1–463.

[16] Robinson, E. L., 1952, "Effect of Temperature Variation on the Long-Time Rupture Strength of Steels," Trans. ASME, **74**(5), pp. 777–781.

[17] Seeley, R. R., and Ishwar, V. R., 1999, "Fatigue in Modern Nickel-base Alloys for Gas Turbine Applications," *Proc. Conf. Life Assessment of Hot Section Gas Turbine Components*, Oct. 5–7, Edinburgh, UK, pp. 61–82.

[18] Williams, F. A., 2003, Technical Report, http://maemail.ucsd.edu/combustion/cermech/.

[19] Rupley, F. M., Kee, R. J., and Miller, J. A., 1989, "Chemkin II: A FORTRAN Chemical Kinetics Package for the Analysis of Gas Phase Chemical Kinetics," Sandia Report No. SAND 89-8009.

[20] Varatharajan, B., Li, S. C., and Williams, F. A., 2001, "The Chemistry of JP10 Ignition," AIAA J., **39**(12), pp. 2351–2356.

[21] Goussis, D. A., and Lam, S. H., 1994, "The CSP Method for Simplifying Kinetics," Int. J. Chem. Kinet., **26**, pp. 461–486.

[22] Mastorakos, E., Massias, A., Diamantis, D., and Goussis, D. A., 1999, "An Algorithm for the Construction of Global Reduced Mechanisms With CSP Data," Combust. Flame, **117**, pp. 685–708.

Enhanced External Aerodynamic Performance of a Generic Combustor Using An Integrated OGV/Prediffuser Design Technique

A. Duncan Walker
e-mail: a.d.walker@lboro.ac.uk

Jon F. Carrotte

James J. McGuirk

Dept. of Aero. and Auto. Engineering,
Loughborough University Loughborough,
LE11 3TU, United Kingdom

In this paper we use experimental measurements to characterize the extent that improved the external aerodynamic performance (reduced total pressure loss, increased flow quality) of a gas-turbine combustion system may be achieved by adopting an integrated OGV/prediffuser technique. Two OGV/prediffuser combinations were tested. The first is a datum design corresponding to a conventional design approach, where the OGV and prediffuser are essentially designed in isolation. The second is an "integrated" design where the OGV blade shape has been modified, following recommendations of earlier CFD work (Final Report No. TT03R01, 2003), to produce a secondary flow/wake structure that allows the prediffuser to operate at a higher area ratio without boundary layer separation. This is demonstrated to increase static pressure recovery and reduce dump losses. Experimental measurements are presented on a fully annular rig. Several traverse planes are used to gather five-hole probe data that allow the flow structure through the OGV, at the inlet and exit of the prediffuser, and in the inner/outer annulus supply ducts to be examined. Both overall performance measures (loss coefficients) and measures of flow uniformity and quality are used to demonstrate that the integrated design is superior. [DOI: 10.1115/1.2364008]

Introduction

Gas turbine combustion systems require careful design of their external aerodynamic arrangements. These form the interface between the airflow supplied by the compression system and its distribution over the various feed paths to combustor components (fuel injector, dilution ports, cooling films), or downstream turbine components (e.g., Nozzle Guide Vane (NGV) cooling). The airflow distribution has to be accomplished at minimum total pressure loss to avoid associated Specific Fuel Consumption (SFC) penalties. The optimum configuration/layout of combustor external aerodynamics needs to be reviewed, since legislation for the emission of pollutants from aerogas turbines is dictating a significant change to the architecture of future combustor systems. Lean combustion is essential for the achievement of the envisaged NO_x reduction targets. This requires excess air in the primary combustion zone, leading to much larger air fractions than typical for conventional (annular) combustors entering the forward part of the flame tube. Hence, lean combustion impacts the airflow into the combustion system in several ways:

- Lean fuel injection modules are significantly larger than traditional airspray counterparts, thus necessitating a deeper flame tube. This will adversely affect the loss due to increased turning within the dump region.
- If lean fuel injection modules are to be operated satisfactorily, the airflow feed quality (e.g., uniformity of pressure profile over the injector inlet area) may need to be controlled much more closely than in traditional systems.
- Flow distribution within the combustor is significantly altered because the majority of the compressor efflux now passes directly through the injector, with only a small amount of flow passing down the annuli.
- The cooling flow itself must be reduced in order to provide sufficient air for lean combustion, requiring new cooling technologies to be developed. The air feed to these new cooling arrangements must be of appropriate quality, but is often taken from the low total pressure air near the diffuser walls, necessitating possible external aerodynamic changes.

Existing design rules for the external aerodynamic layout of conventional combustion systems may not therefore be easily extrapolated to lean low emission combustors.

This is particularly true for the prediffuser, which in a conventional system is required to provide an exit profile with a radially and circumferentially uniform distribution with maximum static pressure recovery but minimum total pressure loss. For future combustors, a nonuniform flow, varying for example circumferentially with the location of the fuel injectors, may be appropriate. Nevertheless, feed to the individual fuel injectors must still be of high quality with low loss and uniform distribution in order to ensure homogeneous mixing of the air and fuel. Further, the feed annulus flows around the flame tube will be made up predominantly of prediffuser boundary layer flow, which, already of poor quality, will have to turn and flow around a flame tube of increasing depth. The aerodynamic quality of this air is also critical, since the cooling systems must strive to maintain acceptable temperatures, despite the reduced supply of cooling air.

Additionally, changes in combustor geometry and flow distribution will affect the operation and performance of the prediffuser itself. The circumferential variation in downstream blockage and the likely desirable distribution of bulk pitch angle at exit will undoubtedly result in different optimum configurations of prediffuser area ratio and geometry than has been typical to date. Thus,

Contributed by the International Gas Turbine Institute (IGTI) of ASME for publication in the JOURNAL OF ENGINEERING FOR GAS TURBINES AND POWER. Paper presented at the ASME Turbo Expo 2006, Barcelona, Spain, May 8 – 11 2006, Paper No. GT2006-90184. Manuscript received October 1, 2005; final manuscript received February 1, 2006. IGTI Review Chair: R. S. Abhari.

for lean module combustion to be successful, it is argued that it is important that the design of the combustion system is a fully integrated concept with each component being optimized to allow the effect of, and the effect on, upstream and downstream components to be considered. In this paper we present recent work carried out to study how this may be achieved for the compressor OGV/prediffuser interaction.

The prediffuser/dump diffuser design concept has become established as the standard design philosophy over the last 20 years (Klein [1]). It is well known, however, that the performance of annular prediffusers is sensitive to the inlet conditions presented to them (Stevens et al. [2]; Klein [3]). Similarly, the introduction of load-bearing radial struts into the prediffuser can have beneficial effects (swirl level reduction, more uniform and stable annulus flow feed to flame tube features), but also performance reducing effects (extra pressure loss and poorer feed quality to burners in line with struts), so that careful aerodynamic design is needed (Barker et al. [4]). The importance of compressor exit conditions [Outlet Guide Vane (OGV) wake structure and turbulence field] on combustor annular diffuser performance has led to several studies to capture the characteristics of the flow entering the prediffuser in great detail (Zierer [5], Carrotte et al. [6], and Ma and Jiang [7]). It is observed, for example, that diffusers in turbomachinery environments achieve a considerably higher pressure recovery than with classical "clean" ducted flow inlet conditions ([1,5]) due to the increased turbulent mixing associated with compressor exit flow fields. OGV exit flow structure is fairly complex, with regions of relatively high loss located near the junction of OGV blade suction surface and inner/outer casings, thin wakes, and significant secondary flows [6]. This implies that diffuser performance will only be maximized when the diffuser and turbomachinery are aerodynamically matched.

This has been comprehensively examined recently by Barker and Carrotte ([8,9]). By examining diffusers of various area ratios downstream of an engine representative OGV row behind a single stage compressor, it was possible to determine that increases in loss associated with OGV wake mixing in the diffuser adverse pressure gradient field were mainly associated with the low energy flow adjacent to the casings. The data also confirmed that the diffuser pressure rise was enhanced by the OGV blade wake mixing process, leading to pressure increase beyond that which the casing wall boundary layer could sustain if simple axisymmetric inlet conditions had been present. Finally, a detailed analysis of the stream tube evolution within the diffuser indicated regions where the secondary flow convected high energy flow toward the diffuser endwalls, simultaneously removing low energy boundary layer fluid. The fluid element streakline paths were predominantly associated with the diffuser inlet conditions provided by the upstream OGV blade. These results confirmed that the secondary flow field generated at the OGV exit is significant in controlling endwall boundary layer growth and delaying flow separation in the diffuser. This implies that a flow control approach to OGV/prediffuser design could be adopted to optimize aerodynamic matching and allow, for example, maximum prediffuser area ratio to be achieved while retaining acceptable and stable flow quality within the diffuser for interactions with components farther downstream.

Diffuser/combustor flow interaction has been a longstanding area of interest in CFD studies of combustor external aerodynamics (Karki et al. [10]; Koutmos and McGuirk [11]). However, emphasis to date has focused on an analysis of a *prescribed* diffuser/combustor annulus geometry in terms of the resulting pressure loss and quality of air feed to injector, flame tube ports, etc. An alternative philosophy would be to use an optimization approach to find, for example, the best OGV/prediffuser arrangement that would lead to the overall best performance.

The idea of integrated consideration and optimization of components in gas-turbine turbomachinery is receiving much attention currently. Shahpar [12], for example, has outlined the development and application of a design system for automatic optimization used within a Rolls Royce (SOPHY), and has provided examples of industrial engine exhaust diffuser and bypass exhaust nozzle optimization. Schlüter et al. [13] have recently proposed a method for the simultaneous solution of a complete compressor/combustor/turbine flow, also including both RANS and LES CFD flow solvers. It is currently difficult to imagine such an approach being used for optimization purposes since overall compute times are long and optimization methods typically involve tens or hundreds of CFD solutions. However, the optimization of strongly coupled components such as the OGV row and downstream prediffuser certainly merit further study. To this end, Barker et al. [14], as part of an EU project entitled "LOPOCOTEP" (LOw POllutant COmbustor TEchnology Programme) conducted a detailed experimental and computational study comparing the performance of a conventional OGV/diffuser design (i.e., essentially designed on an isolated component basis with the OGV design ignoring the flow field within the diffuser, and vice versa), with an integrated optimized OGV design (IOGV) obtained from numerical predictions, which took account of the strong interaction between the components. This work demonstrated how the OGV geometry could be modified (e.g., via blade lean, sweep, etc.) to manipulate the secondary flow emerging from the OGV passage such as to create beneficial effects in the diffuser flow and allow increased area ratio and a gain in the overall system performance. The experimental part of this work provided inlet condition data (both mean and turbulence components) for CFD predictions of the OGV row and prediffuser and also validation data to assess the extent that the improved performance inferred by the CFD was achieved in practice.

The success reported in [14] has directly led to the present work. The experimental data gathered in [14] was restricted to the OGV/prediffuser itself; it was not possible to conduct measurements in the dump region or assess the overall system performance in terms of pressure loss improvements to the annulus regions surrounding the combustor. Accordingly, an experimental program was set in place (as part of a further EU project entitled "INTELLECT" (INTEgrated Lean Low Emission CombusTor)). This allowed a complete dataset to be gathered, for the same compressor rotor and dump region geometry, both for a conventional OGV/prediffuser design (referred to here as the "Datum" design) and for the optimized integrated OGV/prediffuser design recommended by [14] (referred to here as the "LOPOCOTEP" design). Detailed flow structure measurements from the rotor exit through to inner and outer annulus ducts surrounding a generic combustor flame tube were undertaken. This enabled OGV performance, prediffuser performance, and dump performance all to be assessed. The advantage of using a fairly simple and generic flame tube shape and providing measurements from rotor inlet through to annulus ducts means that the dataset is suitable for the validation of computational methods that capture both turbomachinery stage and combustor flow processes, such as reported in [13]. The dataset also allows a full and comprehensive assessment of the advantages of adopting an integrated approach for combustor external aerodynamics.

Experimental Facility and Instrumentation

Experimental Facility. All experimental data were obtained on a low speed isothermal test facility operating at nominally atmospheric conditions (Figs. 1 and 2). Air is drawn into a large inlet plenum above the vertically mounted facility, before passing through an inlet flare and honeycomb flow straightener. The air is then accelerated over a bell-mouth intake section prior to passing into the test section that comprises a single stage axial compressor with Inlet Guide Vanes (IGVs), an OGV/prediffuser assembly, and a downstream generic combustion system (Fig. 3). The mean radius of the IGV, rotor, and OGV rows is 375 mm with a passage height of 36.6 mm (hinlet). The IGV row consists of 80 vanes preceding a rotor operated at a fixed nondimensional mass flow

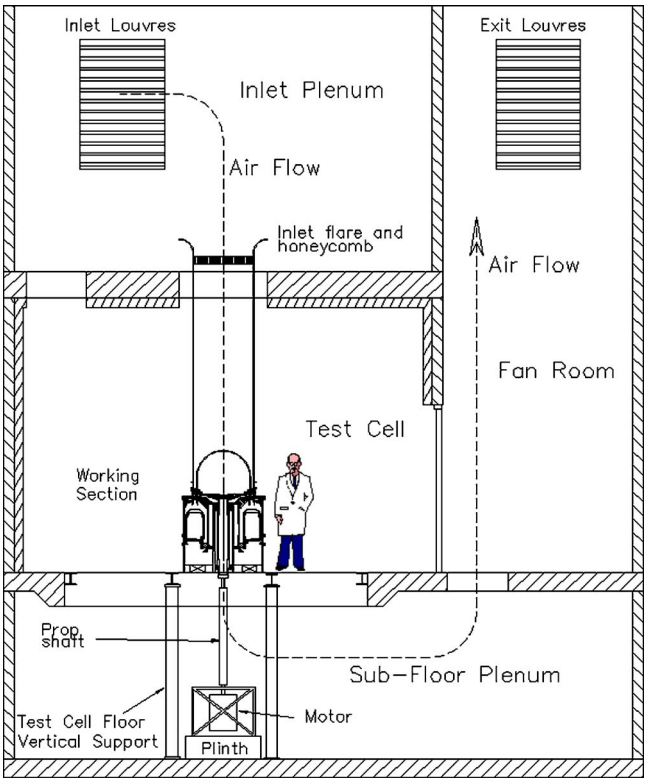

Fig. 1 Experimental facility—Test cell schematic

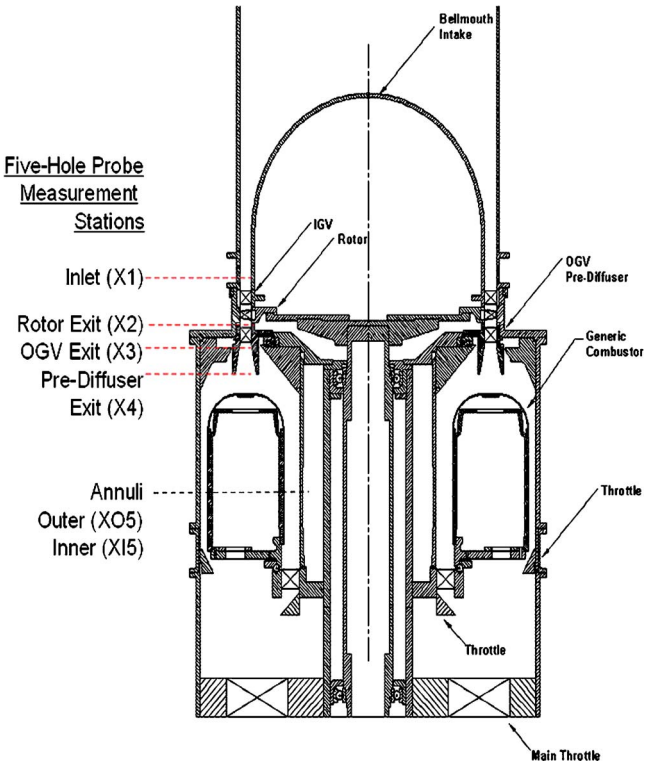

Fig. 3 Test section showing traverse plane locations

condition ($\dot{m}\sqrt{(\mathrm{RT})}/\mathrm{AP}$) and speed [$N\pi D/\sqrt{(\gamma \mathrm{RT})}$] corresponding to a flow coefficient (V_a/U) of $\phi=0.403$ and a mass flow of approximately 4 kg s^{-1}. This results in an axial velocity through the blade rows of approximately 40 m/s (Mach No. 0.12) and an OGV Reynolds number of approximately 1.6×105. The OGV is presented with approximately 450 of swirl by the rotor. After the flow passes through the OGV/prediffuser assembly its distribution to the feed annuli and combustor cowl ports (simulated fuel injector flow) is controlled by a system of downstream throttles, while a further throttle within the exhaust system ensures that the compressor is maintained on the desired operating point.

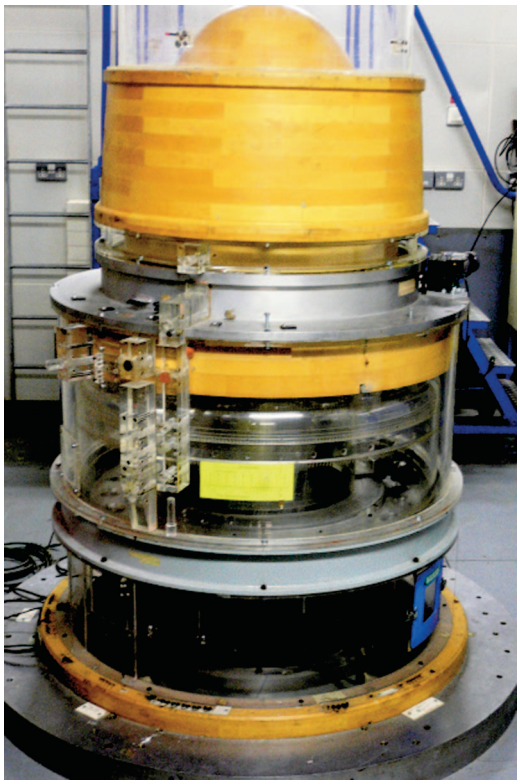

Fig. 2 Experimental facility—Test section photograph

OGV/Prediffuser Geometries.

Datum OGV/Prediffuser. The OGV row for this configuration consists of 160 vanes (note this is 2 per IGV) each of 39 mm chord, with a thickness to chord ratio of 6% and a constant blade section from hub to tip; in addition, the blade section was 2D, i.e., at any radius it was positioned in the same axial and circumferential location along the whole span. The prediffuser is a simple design having an area ratio of 1.6 and a nondimensional length (L/hinlet) of 2.23. Although designed using conventional design rules, if considered in isolation from the OGV row and downstream combustor, the datum prediffuser has a slightly larger area ratio than would be recommended using the design criteria as described in Howard et al. [15], whose experiments were conducted with axisymmetric thin boundary layers at the annular diffuser inlet. According to Howard et al. [15], for a nondimensional length of 2.23, the stall line corresponds to an area ratio of 1.58. However, Barker et al. [14] demonstrated that downstream of a single stage axial compressor the datum prediffuser, in fact, remains within a stable flow regime, which highlights the importance of diffuser inlet conditions.

Integrated (LOPOCOTEP) OGV/Prediffuser. The OGV row for this configuration also contains 160 vanes, however, as recommended in [14], OGV blade geometry changes were introduced. Based on the same chord and basic blade profile as the Datum vane and using computational techniques, Barker et al. [14] manually optimized the blade by moving (at each radial position across the span) the section axially (sweep) or circumferentially (lean)

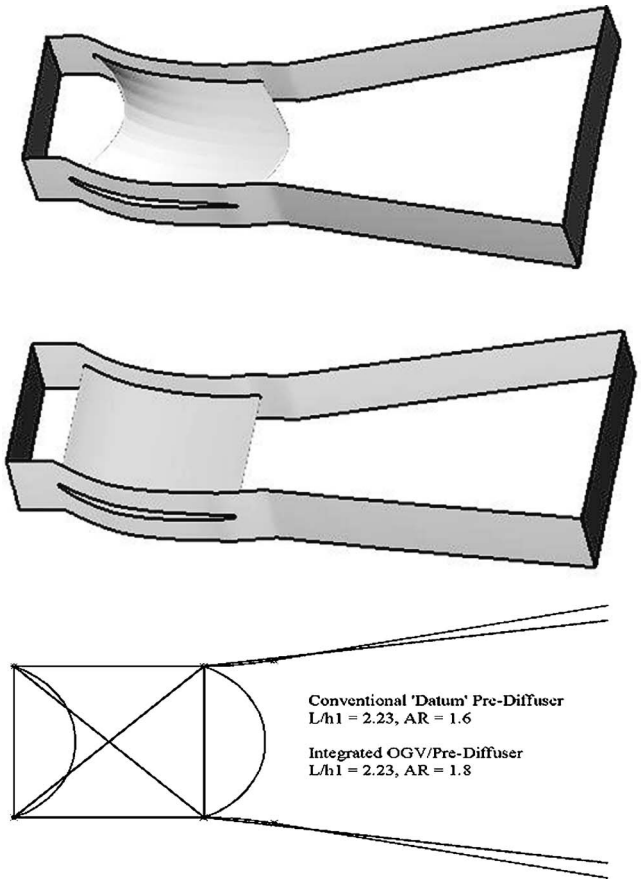

Fig. 4 Datum (top), integrated (middle) geometries, and cross-section comparison (bottom)

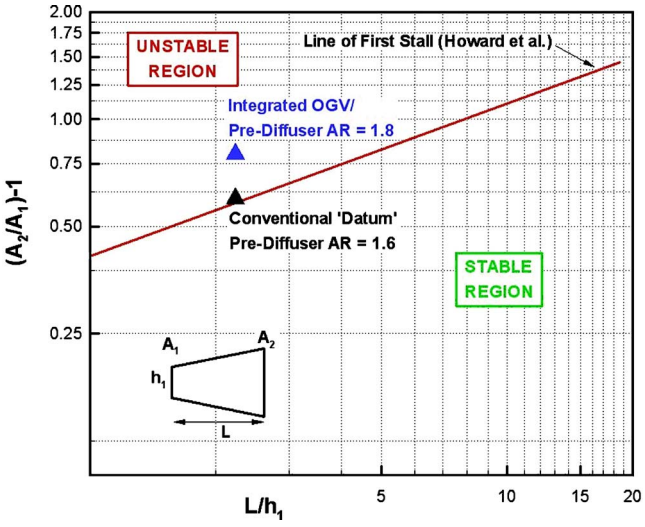

Fig. 5 Datum and integrated geometries on diffuser chart

relative to the hub location. This changes the aerodynamic loading along the span. In addition, a small change to the trailing edge camber of some sections was introduced to reduce the residual swirl level at exit from the OGV row. The resultant spanwise velocity components were observed to help reduce blade loading toward the hub and the tip and encourage higher momentum fluid transport toward the walls, thus off-loading the end wall boundary layers at the prediffuser inlet. Hence, although still a simple design, the LOPOCOTEP Integrated OGV/prediffuser was able to perform satisfactorily at an overall area ratio of 1.8. At the same nondimensional length of 2.23, this should undoubtedly have resulted in separation according to Howard et al. [15]. Figure 4 illustrates the geometry differences between the two designs in illustrative format and also contrasts the diffuser area ratios. Figure 5 plots the two diffusers on a nondimensional length/area ratio chart, showing the stall line implied by the Howard et al. [15] data. As already mentioned, even the Datum prediffuser operates satisfactorily, even though it is just above the "clean" inlet stall line, and the prediffuser for the LOPOCOTEP IOGV design is well above this stall line.

Generic Flame Tube Geometry. The flame tube geometry downstream of the prediffuser exit has been intentionally made simple for the present tests. While still presenting a realistic level of blockage, the combustor has been simplified such that it contains a typical dump region geometry, a fully annular flame tube of appropriate radial depth and inner/outer annulus flow heights, but a clean outer surface with no attempts made to include dilution ports or cooling film features. The only porosity in the flame tube is a series of 20 round holes to represent the path of air passing into the fuel injector (no burner arm or other features are used; see Fig. 6). Lean flow combustors often do not feature air admission ports in the annuli and are also likely to incorporate new cooling technologies. Hence removal/omission of these features seems logical at this stage. Figure 6 shows a close-up of the flame tube and dump region. The nondimensional distance from the OGV exit to the flame tube was maintained at 3.63 hinlet. The 20 round holes in the cowl have an effective area (radius ~20 mm), which allows in the present tests approximately 30% of the prediffuser efflux to enter the cowl. Here 30% is typical of conventional combustors for fuel injector plus head cooling mass flow, rather than the much higher cowl mass flow of lean burn fuel injector designs. The intention here is, in this first step, to investigate the benefits of the IOGV approach for a conventional system and then, in future measurements, to quantify the performance benefits for a higher cowl mass flow system. This step-by-step approach was necessary since the optimum IOGV design will certainly be influenced by the cowl mass flow and the LOPOCOTEP design adopted here was determined using 30% cowl flow. The remaining mass flow is evenly split between inner and outer annuli.

Instrumentation. The aerodynamic performance of each system was assessed using suitably calibrated miniature five-hole

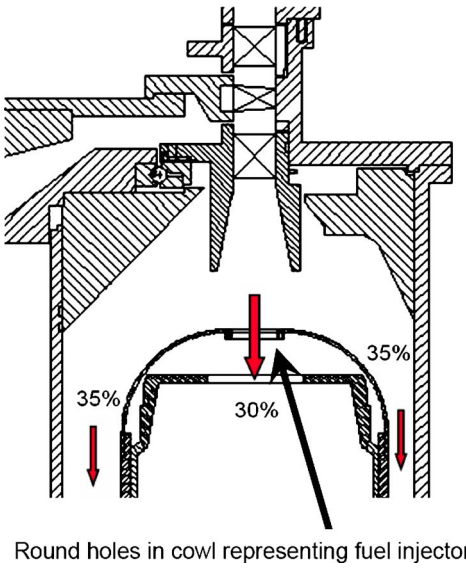

Fig. 6 Flame tube configuration and mass flow split

probes of overall diameter 1.5 mm, as described by Wray and Carrotte [16]. The probes were employed in the non-nulled mode to determine the local flow vector and total and static pressures. As indicated in Fig. 3, five-hole probe area traverses were conducted at rig inlet (X1), rotor exit (X2), OGV exit (X3), prediffuser exit (X4), and within the inner (XI5) and outer (XO5) feed annuli. The number of measurement points per area traverse plane was 820 (41 circumferential x 20 radial). Pressures were recorded using Furness FCO44 pressure transducers and corrected to ICAO standard day conditions (i.e., 101325 Pa and 288.15 K). The probes were traversed in the radial direction using a stepper motor powered linear guide attached to the external casings of the test section. Circumferential traversing was achieved by either rotation of the casing about the test section or rotation of the IGV, OGV, and flame tube using a dc motor. Operation of the test rig, positioning of the instrumentation, and digitization of all pressure signals was PC controlled. Further details of the mechanical arrangements of the rig and traversing systems are fully described in [16].

Data Reduction and Errors. The overall aerodynamic performance was quantified in terms of total pressure loss and static pressure recovery coefficients derived from the five-hole probe area traverse data. Thus, at any measurement plane the air mass flow rate and local bulk average velocity are defined as:

$$\dot{m} = \int \rho U \, dA = \rho \bar{U} A$$

For the experiments described here, the resulting mass flow balance on area traverse planes was generally within ±1% of the measured total air mass flow entering the test facility [measured via a single five-hole probe traverse at inlet to the IGV row (X1)]. Spatially averaged values of total and static pressure at each plane were derived using the mass-weighted technique described by Klein [15]:

$$\tilde{P} = \frac{1}{\dot{m}} \int P \, d\dot{m} = \frac{1}{\rho \bar{U} A} \int P \rho U \, dA$$

$$\tilde{P} = \tilde{p} + \alpha \frac{1}{2} \rho \bar{U}^2, \quad \alpha = \frac{1}{A} \int \left(\frac{U}{\bar{U}} \right)^3 dA$$

$$\lambda_{A-B} = \frac{\tilde{P}_A - \tilde{P}_B}{\tilde{P}_A - \tilde{p}_A}, \quad Cp_{A-B} = \frac{\tilde{p}_B - \tilde{p}_A}{\tilde{P}_A - \tilde{p}_A}$$

For spatially non-uniform incompressible flow which is in a predominantly axial direction it follows that:

Where the kinetic energy flux coefficient, α, represents the ratio of the mass weighted mean kinetic energy of the non-uniform flow to that of a uniform flow through the same passage area with the same mass flow rate. Changes in the spatially averaged pressures between measurement planes A and B are expressed in terms of the mass-weighted total pressure loss (λ) and static pressure rise (Cp) coefficients as follows:

The mass-weighted total pressures derived at each of the traverse planes shown in Fig. 3 were repeatable to within ±1 mm H_2O, a variation that amounts to less than ±0.5% of the dynamic pressure recorded at OGV exit. Thus, the repeatability of the derived total pressure loss and static pressure rise coefficients relating to overall performance was better than ±0.005 of the values presented here.

RESULTS AND DISCUSSION

Preliminary Rig Commissioning Measurements. As mentioned previously, the present measurements, conducted as part of the INTELLECT project, are following on from an earlier study conducted during the LOPOCOTEP project. In between these studies the experimental facility has been considerably modified; it was considered wise therefore to conduct a preliminary rig recommissioning test to make sure earlier data could be reproduced. With the inlet section (IGVs and rotor), compressor OGV/prediffuser assembly, and operating conditions in common, it was important to ensure that the flow field, particularly the boundary layer growth at the rotor inlet and exit, were consistent with previous work. Figure 7 illustrates a single radial traverse for mean axial velocity taken at rotor inlet (X1) and shows excellent agreement between previous and current builds for both Datum and IOGV configurations studied in the present investigation. It is clear that the effects of geometry modifications downstream have not penetrated upstream past the rotor. The inlet flow to the rotor is maintained as one with small boundary layer growth on the inner (12% h) and outer (16% h) casing walls, with a flat core. At the rotor exit (X2) the measurement sector corresponds to one OGV space and circumferentially averaged profiles of axial velocity and total pressure (Fig. 8) again show good agreement with previous data. The data shown are for the IOGV geometry only, but it is important to note that, within experimental error, results at X2 are comparable between Datum and IOGV designs. In other words the changes to the OGV and prediffuser geometry have also not influenced the static pressure field at rotor exit, which might

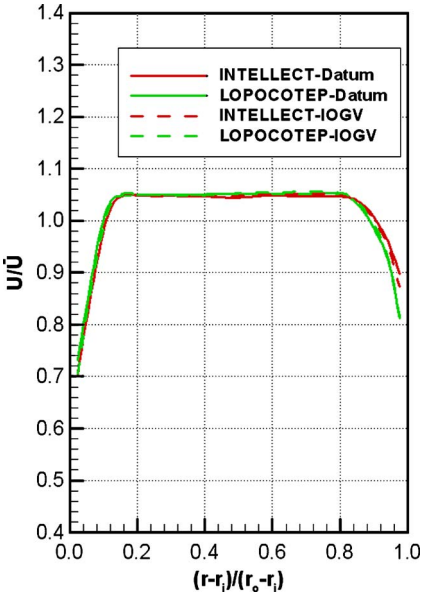

Fig. 7 Axial velocity profile at rotor inlet (X1)

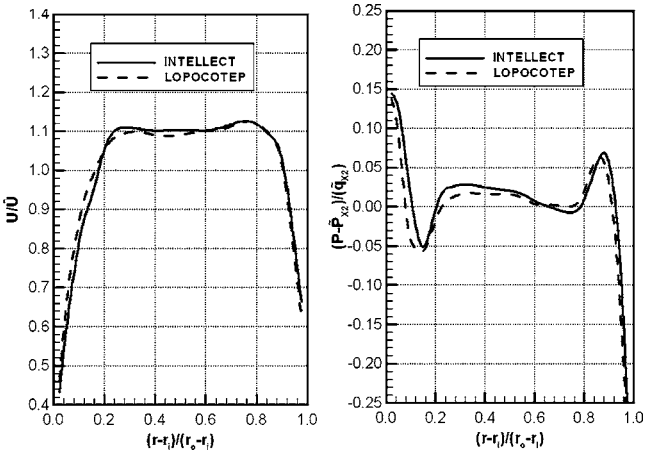

Fig. 8 Axial velocity and total pressure profiles (IOGV) at rotor exit (X2)

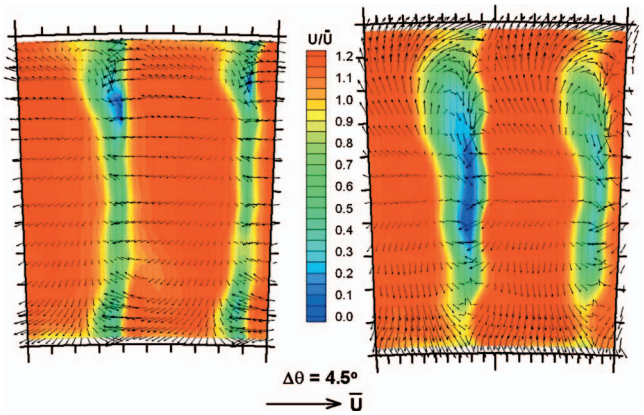

Fig. 9 OGV exit (X3) axial velocity contours and secondary flow vectors: Datum (left); IOGV (right)

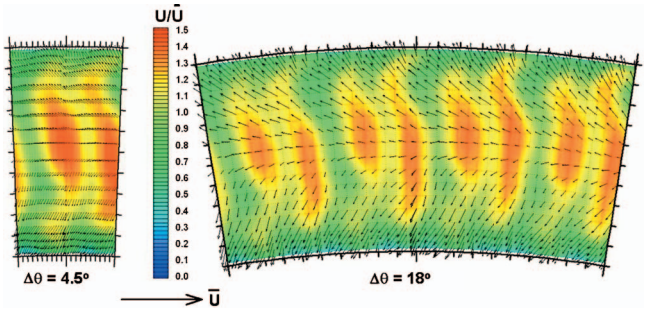

Fig. 10 Axial velocity contours and secondary flow vectors at pre-diffuser exit (X4) datum design 2 OGV sector (left); 8 OGV sector (right)

have led to a change in the work profile along the span of the rotor. Any interaction effects between the rotor and the different OGV/prediffuser systems have been minimized. It can be seen that at the rotor trailing edge the boundary layer growth is now ~25% of passage height and there is clear evidence of the work profile of the rotor and of a rotor tip vortex loss process in the total pressure profile.

OGV Exit (X3). The above data were considered adequate proof that the test facility had been successfully recommissioned. Attention was now turned to measurements that quantified both aerodynamic performance and allowed a comparison between Datum and IOGV designs. The first plane to be studied was OGV exit (X3). Axial velocity contours and secondary velocity vectors at station X3 are presented in Fig. 9, plotted over a two OGV measurement sector for both OGV/prediffuser configurations. The secondary velocity vectors plotted in Fig. 9 and elsewhere later represent simply the local ratio of radial to circumferential velocity components. A 2-OGV passage sector was chosen as the ratio of IGVs to OGVs could still be identified in neighboring OGV wakes at X3; see Fig. 9. For the Datum blade the wakes are relatively thin and contain two regions of low momentum near the hub and at two-thirds blade height, the latter associated with the rotor tip vortex. The secondary flow pattern of the Datum blade shows a small amount of residual swirl remains, with the radial flow being predominantly inward. The blade geometry of the IOGV design has clearly manipulated the wake structure in the vicinity of the endwalls. The secondary flow is directed by the blade toward each end wall and has already at X3 had the effect of energizing the endwall boundary layers; the wakes are, however, noticeably thicker near midpassage height. Table 1 summarizes the performance parameters for the OGV row; the IOGV design incurs a slightly higher loss as it is performing more work by imparting an increased radial component on the flow, and has thicker wakes.

Prediffuser Exit (X4). Velocity contours and secondary flow vectors at the prediffuser exit (X4) for the Datum and IOGV designs are presented next. Sector data were again initially collected over 2 OGV passages, to capture the IGV/OGV interaction mentioned previously, which can still be identified at the prediffuser exit (see Fig. 10 for the Datum geometry). In future experiments, when the injector mass flow will be increased, the prediffuser exit flow field may exhibit stronger evidence of the circumferential variation in downstream blockage. Under these circumstances it will be necessary to conduct measurements over a complete injector sector (eight OGV passages) in order to capture the circumferentially repeating pattern. To examine the acceptability of maintaining the number of measurement points at 820, an area traverse over an 8 OGV sector was conducted, and this is also shown in Fig. 10. It can be seen that the essential flow features at the prediffuser exit are still captured well by the lower spatial resolution of the complete injector sector, and hence this sector size was used in all further measurements. The prediffuser exit comparison in Fig. 11 demonstrates the differences in the development of the OGV wake structure and secondary flow field caused by the IOGV design. This design produces thinner high velocity zones, and a more endwall directed secondary flow with lower levels of residual swirl. As a consequence, the inner endwall boundary layer, in particular, is in better condition, even though the area ratio is 12.5% larger. This overall effect at the prediffuser exit is more apparent in the circumferentially averaged profiles shown in Fig. 12. Circumferential averaging was conducted by averaging data over all measured points at the same radius across either an OGV blade sector or a combustor sector. The averaging was done on an area basis for velocity and pitch angle, but a mass-weighted basis for pressure (pitch angle was defined locally via the ratio of radial to axial components and then area-weighted circumferentially averaged). For the Datum design the axial velocity profile is characterized by relatively thick boundary layers (~20% of the prediffuser exit height) and a noticeable peak at approximately midpassage height. Although this type of profile may feed the injector satisfactorily, the feed to the annuli will be comprised of the poor quality boundary layer flow that will, in turn, compromise the quality of the air delivered to the annuli. For the IOGV design, not only is the flow fully attached for a loading that would traditionally separate, but a high proportion of the flow has migrated outboard, resulting in much thinner and healthier boundary layers (now only approximately 10% of the prediffuser exit height). In addition, the flow pitch angles near the endwalls have increased by 30%, so that the flow is already starting to turn more toward

Table 1 OGV pressure loss and Cp coefficients

Geometry	$\lambda_{X2\text{-}X3}$	$Cp_{X2\text{-}X3}$
Datum	0.12	0.38
IOGV	0.14	0.38

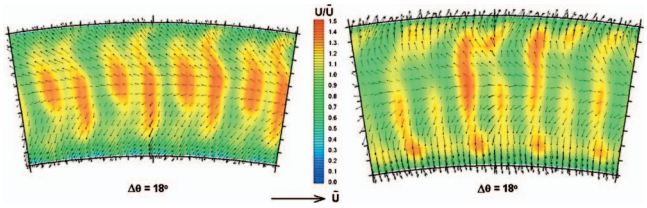

Fig. 11 Axial velocity contours and secondary flow vectors at prediffuser exit (X4) datum design (left); integrated design (right)

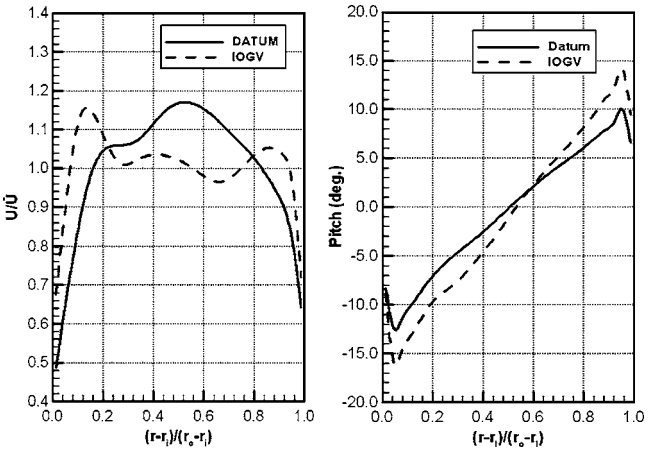

Fig. 12 Axial velocity and pitch angle profiles at X4

the feed annulus at the diffuser exit. This and the lower bulk average velocity due to the higher area ratio of the IOGV prediffuser all contribute positively to reducing dump and turning losses in the downstream region.

In terms of performance at the prediffuser exit, Table 2 presents the mass-weighted total pressure loss and static pressure recovery coefficients. These are quoted with respect to both rotor exit (X2) and OGV exit (X3), allowing a comparison of the combined OGV/prediffuser performance or just the prediffuser in isolation. In both cases the IOGV design incurs a higher overall loss that the Datum. However, the majority of the additional loss occurs within the blade row, with the prediffuser itself incurring only a small rise in loss due to increased secondary flow mixing. Further, Table 2 shows that with its increased prediffuser area ratio the IOGV prediffuser is able to produce a notable increase ($\sim$18%) in static pressure recovery. This, in conjunction with an enhanced exit profile, means that this design should result in improved flow distribution and lower losses in the downstream combustor.

Inner (XI5) and Outer (XO5) Annuli. The final aerodynamic aspect examined in this study was the feed quality to the annuli and whether the enhanced prediffuser exit profile and static pressure recovery coefficient of the IOGV design provided any overall system benefit. The interest in placing emphasis on these aspects is that improved annulus feed quality and reduced system loss are likely to be a prime concern of the deeper flame tube designs implied by lean module injectors.

Differences in the annulus flow fields are best revealed by an examination of circumferentially averaged profiles (Fig. 13). The axial velocity profiles are essentially the same for both designs; however, Fig. 13 shows that the pitch and yaw angles of the flow in both inner and outer annuli are different. This is not unexpected as, with reference to Fig. 11, the near endwall flow at prediffuser exit differs noticeably between the two designs, and it is this flow that passes into the annuli. The stream tubes feeding the annuli undergo diffusion between prediffuser exit and annulus entry, which will have a tendency to amplify the differences. Additionally, the fact that the flow is moving to a different radius means that the conservation of angular momentum will cause any swirl present at the prediffuser exit to increase in the inner annulus and decrease in the outer. Figure 13 shows that both pitch and yaw

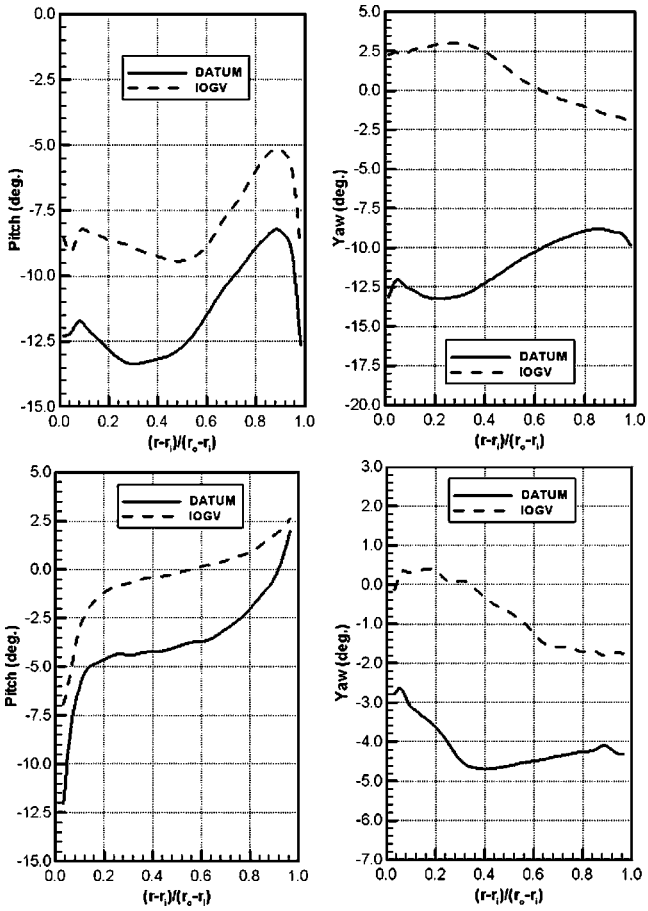

Fig. 13 Circumferentially averaged pitch and yaw angles in annuli: inner (XI5) top; outer (XO5) bottom

angles are reduced in the IOGV design, particularly the latter in the inner annulus, hence improving feed quality to any flame tube features. The final system performance data are presented in Tables 3 and 4.

It is clearly demonstrated that, considering the overall flow path from rotor to annulus flow, the loss to both annuli is significantly reduced. For example, with respect to the OGV exit (X3) the loss coefficient is reduced by 37% and 50% to the inner and outer feed annuli, respectively. Even taking the increased OGV blade loss into account, the system loss (X2-X5) has been reduced by 10% (inner) and 20% (outer), and the two annuli regions are much better balanced. The change in loss for the combined OGV + prediffuser + dump system through to the feed annuli clearly illustrates the benefits to the whole system of the integrated approach, even just one that considers only the OGV/prediffuser assembly. It is worth noting that the effect on the isolated OGV

Table 3 Inner Annulus Coefficients: λ and Cp

Geometry	$\lambda_{X2\text{-}XI5}$	$\lambda_{X3\text{-}XI5}$	$Cp_{X2\text{-}XI5}$	$Cp_{X3\text{-}XI5}$
Datum	0.246	0.252	0.678	0.593
IOGV	0.224	0.159	0.713	0.708

Table 2 Pressure loss λ and pressure recovery Cp

Geometry	$\lambda_{X2\text{-}X4}$	$\lambda_{X3\text{-}X4}$	$Cp_{X2\text{-}X4}$	$Cp_{X3\text{-}X4}$
Datum	0.15	0.055	0.66	0.55
IOGV	0.18	0.062	0.69	0.65

Table 4 Outer annulus coefficients: λ and Cp

Geometry	$\lambda_{X2\text{-}XO5}$	$\lambda_{X3\text{-}XO5}$	$Cp_{X2\text{-}XO5}$	$Cp_{X3\text{-}XO5}$
Datum	0.277	0.317	0.654	0.544
IOGV	0.221	0.152	0.791	0.722

performance of the lean/sweep blade changes means that such modifications would probably not be considered within a conventional design approach, since these lead to increased loss across the OGV, with the potential benefits to the downstream flow not being considered during the OGV design process. However, in an integrated approach, it is the overall performance that is considered, and in this case, the experimental data show that the increased OGV loss is acceptable because the overall loss (from OGV inlet to combustor feed annuli) has been reduced.

Summary and Conclusions

The present paper has focused attention on the possibility of improving the performance of one particular component of combustor external aerodynamics, namely the prediffuser/dump diffuser combination, by adopting an integrated OGV/diffuser design approach. While various other diffuser alternatives have been suggested in the past (e.g., a fully faired system [17] or a hybrid bled diffuser system [18]), emphasis has been placed here on improving the prediffuser/dump diffuser concept. A fully faired system offers the potential for a significant reduction in loss, but this is acknowledged to be at the expense of system stability. Bled diffusers offer the potential for operation at higher area ratios within a given overall axial length, but their use is limited by the increased complexity of the bleed, and the need to use the bled air efficiently within the engine cycle. Hence, the better stability and simplicity of the prediffuser/dump diffuser concept is still to be preferred and methods for improving its aerodynamic performance are of significant interest.

A detailed experimental study has been presented that has investigated the improvement in combustor external aerodynamics achieved using by an integrated design approach for the OGV/prediffuser components. Following suggestions made in [14], an alternative and integrated OGV/prediffuser design was investigated and compared to a traditional design. Experimental data showed that improvements in both feed quality to the annulus regions and overall pressure loss reductions could be achieved using the integrated approach. The main improvements were as follows: an increased diffuser area ratio from 1.6 to 1.8, static pressure recovery increased by 5% with respect to rotor exit, loss to inner/outer annuli reduced by 10% and 20%. The integrated approach is therefore considered worthy of future investigation and development, particularly its use in optimizing the external aerodynamic arrangements of future low emissions combustors.

Acknowledgment

The authors wish to acknowledge the financial support of the European Commission (Contract No. FP6-AST3-CT-2003-502961, Project No. INTELLECT_DM). The authors would also like to express their appreciation to L. Monk, W. Niven, and A. Fardoe for their help in the construction of the test facility. The helpful technical support provided by A. Barker is also gratefully acknowledged.

Nomenclature

A = passage area
AR = area ratio of prediffuser
c = outlet guide vane chord
Cp = static pressure rise coefficient
h = annulus passage height
L = diffuser length
$\dot{m}$ = mass flow rate
N = rotor speed
P, p = local total or static pressure
R = gas constant for air (perfect gas law)
R_n = nondimensional radius $[(r-r_i)/(r_o-r_i)]$
r = radius relative to rig centerline
r_i, r_o = inner casing, outer casing radius
s = blade pitch
T, t = total or static temperature
U = rotor midpassage blade speed
V_a = rotor midpassage axial velocity
x = axial distance
α = kinetic energy flux coefficient
ϕ = flow coefficient (V_a/U)
ρ = air density
λ = total pressure loss coefficient

Subscripts

Inlet = prediffuser inlet
X1 = rotor inlet traverse plane
X2 = rotor exit/OGV inlet traverse plane
X3 = OGV exit traverse plane
X4 = prediffuser exit traverse plane
XI5 = inner annulus traverse plane
XO5 = outer annulus traverse plane

Superscripts

$-$ = area weighted spatially averaged value
$\sim$ = mass weighted spatially averaged value

References

[1] Klein, A., 1995, "Characteristics of Combustor Diffusers," Prog. Aerosp. Sci., **31**, pp. 171–271.
[2] Stevens, S. J., Harasgama, S. P., and Wray, A. P., 1984, "The Influence of Blade Wakes on Combustor Shortened Pre-diffusers," J. Aircr., **21**, pp. 641–648.
[3] Klein, A., 1988, "The Relation Between Losses and Entry Flow Conditions in Short Dump Diffusers for Combustors," Z. Flugwiss. Weltraumforsch., (12), pp. 286–292.
[4] Barker, A. G., Carrotte, J. F., and Frodsham, C. W., 1997, "The Effect on Combustor Diffuser Performance of Structural OGV/Pre-Diffuser Systems," ASME Paper No. 97-GT-304.
[5] Zierer, T., 1993, "Experimental Investigation of the Flow in Diffusers Behind an Axial Flow Compressor," ASME Paper No. 93-GT-347.
[6] Carrotte, J. F., Young, K. F., and Stevens, S. J., 1995, "Measurements of the Flowfield Within a Compressor Outlet Guide Vane Passage," ASME J. Turbomach., **117**, pp. 29–37.
[7] Ma, H., and Jiang, H., 2000, "Three-Dimensional Turbulent Flowfield Downstream of a Single Stage Axial Compressor Rotor," ASME Paper No. 2000-GT-499.
[8] Barker, A. G., and Carrotte, J. F., 2001, "The Influence of Compressor Exit Conditions on Combustor Annular Diffusers - Part I: Diffuser Performance," J. Propul. Power, **17**, pp. 678–686.
[9] Barker, A. G., and Carrotte, J. F., 2001, "The Influence of Compressor Exit Conditions on Combustor Annular Diffusers - Part II: Flow Redistribution Within the Diffuser," J. Propul. Power, **17**, pp. 687–694.
[10] Karki, K. C., Oechsle, V. L., and Mongia, H. C., 1990, "A Computational Procedure for Diffuser-Combustor Flow Interaction Analysis," ASME Paper No. 90-GT-35.
[11] Koutmos, P., and McGuirk, J. J., 1989, "Numerical Calculations of the Flow in Annular Combustor Dump Diffuser Geometries," Proc. Inst. Mech. Eng., Part C: J. Mech. Eng. Sci., **203**, pp. 319–331.
[12] Shahpar, S., 2005, "SOPHY: An Integrated CFD Based automatic Design Optimisation System," Paper No. ISABE-2005-1086.
[13] Schlüter, J., Wu, X., Pitsch, M., Kim, S., and Alonso, S., 2005, "Integrated Simulations of a Compressor Combustor Turbine Assembly of a Gas Turbine Engine," ASME Paper No. GT2005-68-204.
[14] Barker, A. G., Carrotte, J. F., Luff, J., and McGuirk, J. J., 2003, "Design of an Integrated OGV/Diffuser System," Final Report No. TT03R01, for EU FP5 project, GRD1-2000-25062: "LOPOCOTEP."
[15] Howard, J. H. G., Henseler, H. J., and Thornton-Trump, A. B., 1967, "Performance and Flow Regimes for Annular Diffusers," ASME Paper No. 67-WA/FE-21.
[16] Wray, A. P., and Carrotte, J. F., 1993, "The Development of a Large Annular Facility for Testing Gas Turbine Combustor Diffuser Systems," AIAA Paper No. AIAA-93-2546.
[17] Carrotte, J. F., Denman, P. A., Wray, A. P., and Fry, P., 1994, "Detailed Performance Comparison of a dump and a Short Faired Combustor Diffuser System," Trans. ASME: J. Eng. Gas Turbines Power, **116**, pp. 517–526.
[18] Walker, A. D., Denman, P. A., and McGuirk, J. J., 2004, "Experimental and Computational Study of Hybrid Diffusers for Gas Turbine Combustors," Trans. ASME: J. Eng. Gas Turbines Power, **126**, pp. 717–725.

Fuzzy Logic Estimation Applied to Newton Methods for Gas Turbines

Dan Martis
Rolls-Royce Canada, 9545 Cote-de-Liesse,
Dorval, Quebec H9P 1A5, Canada
e-mail: dan.martis@rolls-royce.com

This method, based on fuzzy logic principles, is intended to find the most likely solution of an over-determined system, in specific conditions. The method addresses typical problems encountered in gas turbine performance analysis and, more specifically, to the alignment of a synthesis model with measured data. Generally speaking, the relatively low accuracy of measurements introduces a random noise around the true value of a performance parameter and distorts any deterministic solution of a square matrix-based linear system. The fuzzy logic estimator is able to get very close to the real solution by using additional (pseudo-redundant) parameters and by building the most likely solution based on each of the measurement accuracies. The accuracy—or "quality"—of a measurement is encapsulated within an extra dimension which is defined as fuzzy and which encompasses the whole range of values, between 0 (false) and 1 (true). The value of the method is shown in two examples. The first simulates compressor fouling, the other deals with actual engine test data following a hardware modification. Both examples experience noisy measurements. The method is stable and effective even at high level of noise. The results are within the close vicinity of the expected levels (within 0.2% accuracy) and the accuracy is about ten times lower than the noise level. [DOI: 10.1115/1.2360597]

Introduction

Understanding changes in engine performance has been a continuous and major concern for all gas turbine manufacturers. The reasons are multiple: hardware development, engine recoverable (fouling) and nonrecoverable deterioration, engine component malfunction, etc. The armory of monitoring and detection methods is impressive; Li [1] reviews and compares the most effective methodologies. A succinct list would include chronologically: linear/non-linear gas path analysis, linear estimators (mainly least squares derivatives [2,3]), non-linear methods [4], and artificial intelligence based methods such as neural networks [5], expert systems [6], genetic algorithm [7], and fuzzy logic [8,9].

Investigation methods used for model to engine performance alignment or fault detection during the product development phase usually benefit from a much better instrumentation level than in-service engines. Therefore, methods like Kalman filter derivatives (least squares based methods) are generally able to accurately predict multiple component functional changes if the number of measured parameters is greater than the number of total changes. However, such methods can encounter difficulties as highlighted in the literature [1,3,8], such as considerable numerical linear algebra due to matrix processing and the "smearing" effect when isolating a single fault. There are methods to reduce the smearing effect such as "fault concentrator" technique—Provost [2]—or the use of automated "fingerprint charts" when the estimate residual becomes significant—Doel [3]. Fuzzy logic based methods are more frequently used for in-service engine health monitoring. These methods are fast and effective for single fault detection and are able to work with the lower level of instrumentation typical of production engines. Usually the fuzzy sets are rule (model) based but case-based fuzzy sets can be added if necessary. The methods have been extended to address pairs of faults—Ganguli [8] and Marinai [9].

Another advantage of these methods is their flexibility. According to McCarthy and Hayes and other researchers [10–12], the uncertainty concept required for fault detection transcends classical probability definition. Therefore, fuzzy logic methods include a rich collection of inference engines and defuzzyfication methods and can easily handle complex uncertainty/noise distributions. Nonlinearity is addressed implicitly: fingerprint charts are calculated with the model, not derived from exchange rate factors (partial derivatives).

On the other hand, it is evident that by adding more component failures, the number of combinations becomes cumbersome and the decision process takes longer. This issue, combined with the limited number of parameter measurements, might increase the uncertainty level of the output set and impact the detection accuracy. The novel method presented in this paper is intended to address both gas path analysis and model-to-engine alignment [13,14]. This method combines the advantages of the two concepts described above:

— multiple fault detection by the use of redundant measurements
— the fuzzy logic key steps, redefined in such a way as to address and optimize the linearized gas path analysis and to conserve its uncertainty concept

Nonlinearity may be addressed by distorting the model using the initial solution, recalculating the partial derivatives, and then finding a revised fuzzy logic estimator (FLE) solution using the updated partials. In practice, this iteration converges rapidly, often in two steps. A non-linear model is solved using a Newton-type iterative process. The secant method with Broyden update is one of most effective methods of this class.

Gas Path Analysis

The alignment of an engine performance model to the actual data measured at the test bed or site is based on gas path analysis, built upon the parameter deltas between the modeled and measured parameters.

The measurement deltas δ_{p_j} $(j=1,\ldots,m)$ represent the components of the vector $\delta\mathbf{p}$ of differences between a parameter reading and its value calculated by the model at the engine running conditions.

A typical engine performance model calculates all thermodynamic and derived parameters of an engine for given:

Contributed by the International Gas Turbine Institute (IGTI) of ASME for publication in the JOURNAL OF ENGINEERING FOR GAS TURBINES AND POWER. Manuscript received October 1, 2003; final manuscript received March 1, 2004. IGTI Review Chair: A. J. Strazisar. Paper presented at the International Gas Turbine and Aeroengine Congress and Exhibition, Vienna, Austria, June 13–17, 2004, Paper No. GT2004-53978.

— functional characteristics of each component;
— installation conditions;
— engine rating.

The performance model includes a series of component functional characteristics, which define the vector $\boldsymbol{x_0}$. When the model is aligned with a different hardware, the vector $\boldsymbol{x_0}$ undergoes distortions, which correspond to various engine module changes (e.g., compressor and turbine efficiencies, flow capacities or pressure ratios, air system bleeds, the pressure drop across the combustor, etc.). As a result, a new vector $\boldsymbol{x}$, which represents the new hardware, is calculated. A new engine model, including the new hardware definition $\boldsymbol{x}$, can then be used to generate updated thermodynamic parameters.

The functional distortions δx_i are the components of a vector $\delta \boldsymbol{x}$ of differences between new and old components of vector $\boldsymbol{x}$:

$$\delta x_i = x_i - x_{0i} \tag{1}$$

where $i=1\ldots n$.

Usually, not all of the components are changed during the model realignment; n is defined as being the total number of relevant distortions ($\delta x_i \neq 0$).

The scope of our work is to derive the best estimate of the engine functional distortions δx_i based on the parameter deltas δp_j between the engine and the model.

From the synthesis model, partial derivatives can be derived at given running conditions; the derivatives describe the exchange rates between the functional distortion of a component x_i and the parameter p_j variation:

$$w_{ij} = \partial p_j / \partial x_i \tag{2}$$

where w_{ij} are elements of Jacobian matrix of derivatives $\boldsymbol{W}(\boldsymbol{x})$.

For a linear deterministic gas path analysis, $n=m$ which means the matrix $\boldsymbol{W}(\boldsymbol{x})$ is square, nonsingular and the system below has a unique solution:

$$\boldsymbol{W} * \delta \boldsymbol{x} = \delta \boldsymbol{p} \tag{3}$$

or

$$w_{1j}\delta x_1 + w_{2j}\delta x_2 + \ \ldots \ + w_{nj}\delta x_n = \delta p_j \tag{3'}$$

where $i,j=1\ldots n$.

For a non-linear gas path analysis, the functional distortion vector $\delta \boldsymbol{x}$ is calculated at each iteration step k and then the model provides the Jacobian for the new step $k+1$. The process ends when

$$\delta \boldsymbol{x}^{(k+1)} - \delta \boldsymbol{x}^{(k)} \leqslant \varepsilon_{\boldsymbol{0}} \tag{4}$$

where the error vector $\varepsilon_{\boldsymbol{0}}$ is given.

Such methods are very sensitive to measurement errors and component fault uncertainties. Therefore, more advanced estimation methods have been created (see Introduction) in order to mitigate these effects. The method presented here is part of this category of optimizers.

Introducing Fuzzy Logic

Having considered a deterministic analysis method for gas turbines as presented above, consider instead a rectangular matrix $\boldsymbol{W}(\boldsymbol{x})$, with $m>n$. This describes an overdetermined linear system at each iteration. Formally, the extra equations are redundant and normally such a system does not have a solution. Although this is true, in this application all the equations are based on measurements of the same physical phenomenon. This ultimately means that, even without a crisp, classical solution, a class of solutions can be defined that do not satisfy all of the system's equations but are located within the vicinity of the exact solutions of all the combinations of square systems.

Now, the issue is how to find this vicinity by processing the information altogether and thereby improving the accuracy of the estimated solution. Acting this way, any distortions due to low measurement accuracy can be progressively reduced by introducing additional equations, based on new measured parameters.

In summary, at each iteration step, the unique solution of a determined system is replaced by the most probable solution of an overdetermined system. The fuzzy logic estimator—presented in this paper—is able to convert the additional information into an increased accuracy of solution.

The overdetermined system derived from system (5) has n unknowns δx_i, which correspond to the functional distortions and m linear equations (where $m>n$), which correspond to the measured parameters. The system can be written then:

$$w_{1j}\delta x_1 + w_{2j}\delta x_2 + \ \ldots \ + w_{nj}\delta x_n = \delta p_j \tag{5}$$

where

$$\begin{matrix} i = 1, \ldots, n \\ j = 1, \ldots, m \end{matrix} \qquad m > n$$

Compared to the parameter's delta δp_j, the assumed accuracy of partial derivatives (calculated by the synthesis model) is quite high. This hypothesis is true for most of the models used in turbomachinery.

As a consequence, δp_j can be considered with good approximation as the only term in the Eqs. (5) affected by the measurement or uncertainty noise.

In order to measure this noise and the quality of measurement, the fuzzy numbers and eventually fuzzy logic [15,16] are introduced, as opposed to Boolean logic, which operates with crisp (YES/NO) notions. Why fuzzy logic and not statistics?

First, as stated in the Introduction [10], fuzzy logic is more flexible than classical statistics, allowing a multitude of rules for the same process—see sections on *Composition* and *Defuzzyfication*.

Second, using statistics, one must norm all the density functions, which are worked with by applying classical mathematical rules, which in most of the cases is not useful and sometimes even impossible (see *Inference*).

Fuzzy logic is more related to the quality than to the absolute quantity. What is of a real interest in our exercise is the relative value, compared to the others, within a certain vicinity. In this respect fuzzy logic is closely related to the human language and the way of thinking [15,16].

Previously, fuzzy logic has been adopted for the benefit of control systems in order to handle "partially true" decisions. Upon closer inspection, the principles of this logic can be applied to a wider range of applications. This is one of them.

In principle, an extra dimension ($n+1$th) is added—the fuzzy dimension—which encapsulates the quality of measurement and takes any value between 0 (FALSE) and 1 (TRUE). Instead of crisp values, the fuzzy numbers, equations, and domains (subsets) can be used, eventually working out a value, which is the most probable solution of the system.

Although the purpose of the analysis is different from current applications [8–10], the general four steps of the Fuzzy Expert System can *formally* be applied, with severe changes to the scope. The four steps are: *fuzzyfication*, *inference*, *composition*, *defuzzyfication*. Their new definitions are presented in the following sections.

Fuzzyfication

Introduces an extra dimension (*fuzzy*), *which encapsulates the quality of measurement*, *i.e.*, *it replaces the crisp value of a parameter delta* δp_j *with a probability distribution around it*.

The accuracy of δp_j will be expressed as a fuzzy number. Such a number, assigned to the parameter delta, allows us to incorporate all the noise around the given reading as a probability distribution.

By definition, the distribution will be limited to the maximum probability of the domain; therefore, the value of truth will always

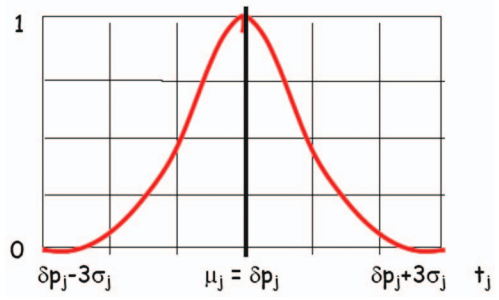

Fig. 1 Normal distribution applied to measurement p_j

be between 0 and 1 with a maximum of 1, in order to be consistent with the Boolean logic. This convention allows us to assign the value 1 to the maximum value of fuzzy domain after each process step and to re-scale the degree of truth in a simple way.

Subsequently, the value 1 must be understood as a local maximum value of truth, not as an absolute value. We apply a normal distribution to δp_j which is considered the only *fuzzy variable* in the Eq. (4)—see Fig. 1.

$$\rho(t_j, \mu_j, \sigma_j) = \exp\left[-\frac{(t_j - \mu_j)^2}{2\sigma_j^2}\right] \tag{6}$$

where

t_j is the parameter's local axis,
σ_j is the standard deviation,
$\mu_j = \delta p_j$ is the mean value which equals the nominal value itself.

The same judgment can be made for any other distribution: trapezoidal, rectangular, triangular, etc. The steps will apply in a similar way.

Inference

Introduces the fuzzy term δp_j into each equation of the system, creating a partially true subset, around each equation.

In other words, what is calculated is a non-zero *probability vicinity* described by Eq. (7) around each crisp surface (hyperplane) defined by the equations of system (4). Figure 2 displays a particular case of Eq. (7) for a 2D space (two unknown variables); the additional fuzzy dimension introduces a domain of partial truth around each Eq. (5)—in 2D case, a crisp line. Figure 3 shows the same example in 2D, as a scalar field.

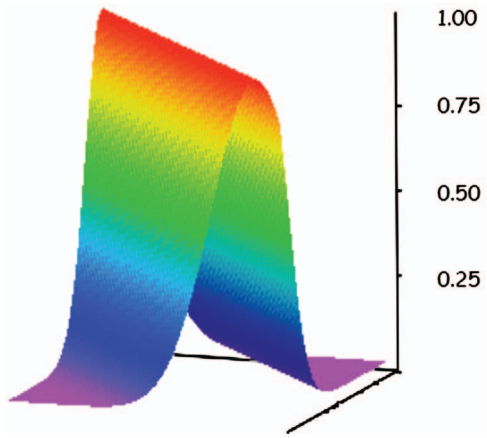

Fig. 2 Input fuzzy domain—normal distribution

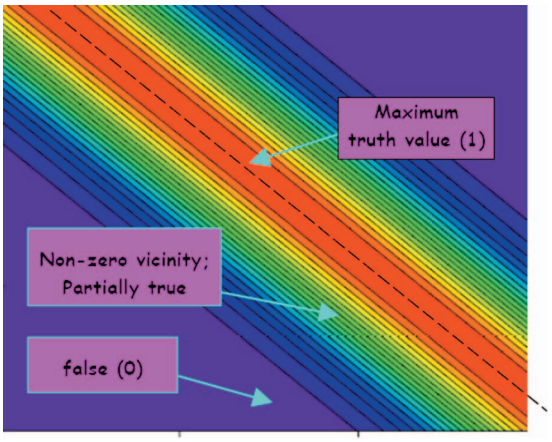

Fig. 3 Input fuzzy domain—normal distribution; scalar representation

$$\rho_j(T_j, \mu_j, \sigma_j) = \exp\left[-\frac{(T_j - \mu_j)^2}{2\sigma_j^2}\right] = \exp\left[-\frac{(\sum w_{ij}x_i - \delta p_j)^2}{2\sigma_j^2}\right] \tag{7}$$

where

$$T_j = \sum_i^n w_{ij}x_i; \quad \mu_j = \delta p_j$$

Composition

Calculates the resultant fuzzy domain in terms of possible solutions, assuming that the common domain is defined by the intersection of the probabilities (vicinities) attached to each equation of the system.

Assuming all the events are reciprocally independent, the intersection of those events leads to multiplication of their probabilities, as shown in the Eq. (8):

$$\Pr(E_1 \cap E_2 \cap \ \ldots \ \cap E_m) = \Pr(E_1) * \Pr(E_2) * \ \ldots \ * \Pr(E_m) \tag{8}$$

where E_j is the event corresponding to the domain defined by ρ_j.

Figure 4 depicts intuitively the intersection of events for a system where $m=3$ and $n=2$. Each line has an accuracy band around it. The solution of the events intersection exists only within the common domain (triangle) defined by the intersection of the three accuracy bands. Outside of the common domain, the probability can be considered negligible.

The fuzzy domain D which includes all the possible solutions, according to the universe of our discourse, is bordered by the

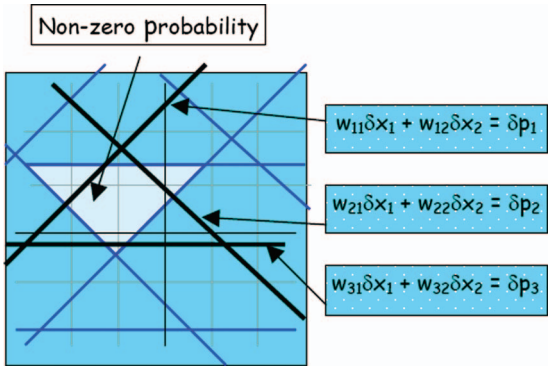

Fig. 4 Intersection of uncertainty domains

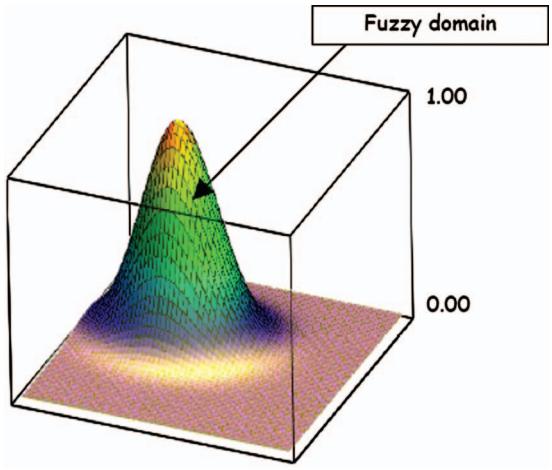

Fig. 5 Output fuzzy domain—normal distribution

surface $\psi(\delta\mathbf{x})$; this surface is described by the product of *probability vicinities* and is displayed in Fig. 5:

$$\psi(\delta\mathbf{x}) = \prod_{j=1}^{m} \rho_j(\delta\mathbf{x}) \tag{9}$$

where $\delta\mathbf{x}$ is the vector of the component functional distortions, our unknown variable.

In these examples, only normal distribution has been used; as mentioned above, any other combination of distributions can be utilized, customizing the noise pattern for each specific measurement or derived parameter.

As mentioned in the section *Introduction of Fuzzy Logic*, the *composition* can use other rules which lead to slightly different results. Another example rule could be: *the resultant degree of truth is the local minimum of truth level, among all subsets* ρ_j *defined by Eq.* (7), *where* $j=1,\ldots,m$. This latter rule is more sensitive to the noise distribution of each of the domains intersected and is less smooth than the product composition. It is recommended to use it when the distribution around measurements includes a significant amount of uncertainty. Alternative composition rules may be applied, however.

Defuzzyfication

Calculates a crisp/unique solution, defined as the most probable within the resultant fuzzy domain, according to one of the defuzzyfication rules.

Among the numerous methods, the *centroid* is the most consistent *defuzzyfication* method in our case since it corresponds to the mean of the distribution defined by the fuzzy domain and represents the first statistical momentum [17]. The coordinates c_i of the mass center of domain D are defined below:

$$c_i = \frac{\int_D \delta x_i \psi(\delta x) d\omega}{\int_D \psi(\delta x) d\omega}, \quad i = 1,2,\ldots,n \tag{10}$$

Figure 6 shows the *centroid* location for a normal distribution. For reasons of domain symmetry, the maximum value of truth in the normal distribution case is identical to the *mass center* (*centroid*).

As mentioned before, there are other *defuzzyfication* rules which can be applied; one of them, the *MAXimum*, has the advantage of simplicity but it is not always useful; i.e., when working with different types of distribution, this property may be invalid as can be seen in Figs. 7 and 8. In this particular case (intersection of three trapezoidal distributions), a maximum value does not even exist, being replaced by a plateau.

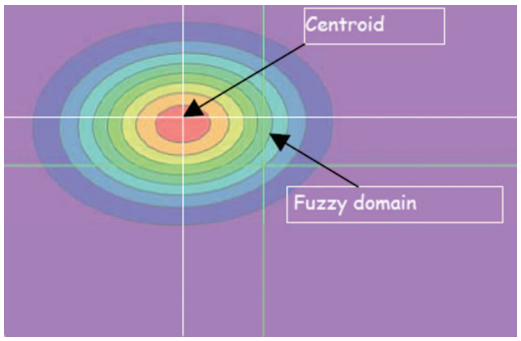

Fig. 6 Output fuzzy domain—normal distribution; scalar representation

Given the arguments above, the *centroid* method can be considered the most appropriate for gas turbines modeling.

Fuzzy logic estimator includes *least squares estimator* class as a particular case. The least squares estimators class can be derived when using normal distributions, the product composition rule, and the *MAXimum* as *defuzzyfication* method.

Justification: Eq. (7) is written for the particular case of a normal distribution. By introducing it into the product-type composition (Eq. (9)) and calculating the maximum probable value, the solution becomes:

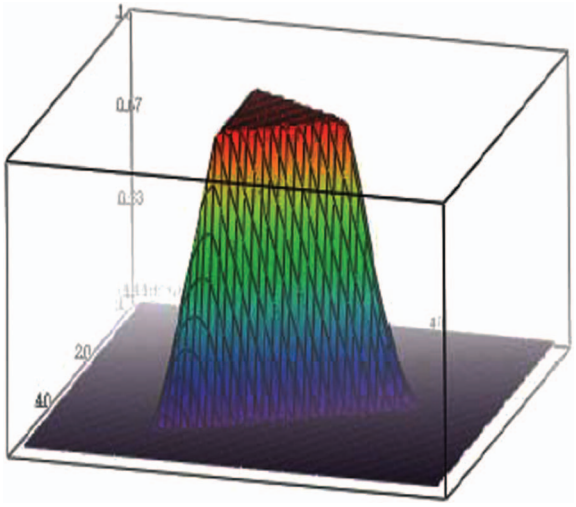

Fig. 7 Output fuzzy domain—trapezoidal distribution

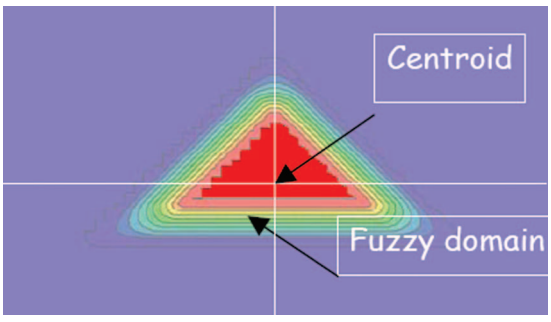

Fig. 8 Output fuzzy domain—trapezoidal distribution; scalar representation

$$\delta \mathbf{x_0} = MAX\left\{ \prod_{j=1}^{m} \exp\left[-\frac{(\sum w_{ij}x_i - \delta p_j)^2}{2\sigma_j^2} \right] \right\} \tag{11}$$

For this particular case, the maximum of a normal domain—Eq. (11)—is reached when the negative exponent reaches a minimum absolute value. This is equivalent to locating the minimum of the following function: The quadratic form (positively defined) from the exponent

$$\delta \mathbf{x_0} = MIN\left(\sum_{j=1}^{m} \frac{(\sum w_{ij}x_i - \delta p_j)^2}{2\sigma_j^2} \right) \tag{12}$$

or

$$\delta \mathbf{x_0} = MIN\left(\sum_{j=1}^{m} \frac{d_j^2}{2\Omega_j^2} \right) \tag{12'}$$

where

d_j represents the distance between the solution and the parameter measurement p_j
Ω–standard deviation of normal distribution of measurement p_j

Equation (12′) describes the general form of the least squares method: the condition of minimum distance between the solution and all the measurements defined as planes in an n-dimensional space. The equation also includes the weighting introduced by the normal distribution attached to each measurement. Consequently, the least squares solution may be considered a particular case of FLE solution.

The FLE thus allows the use of complex distributions, with various *composition* and *defuzzyfication* methods to identify the optimum solution. The user can choose the most appropriate approach for each particular case.

Compressor Fouling Estimate

The example below simulates compressor fouling, for a twin-spool gas generator, within a power generation plant. The fouling process and its effects on the engine components have been investigated in [18,19].

The main input conditions for our analysis are:

- simulation of compressors fouling; their characteristics are affected; for simplicity, an average distortion is considered for both compressors; this way a two variable case can be investigated, without altering the general principles;
- seeded compressors efficiency distortion of 1% (dce $=-1\%$)
- seeded compressors flow capacity distortion of 1% (dcw $=-1\%$)
- the readings are affected by a normally distributed noise due to instrumentation inaccuracy, other sources of deterioration, variation of installation conditions, etc.
- the accuracy distribution around the signal is seeded as well and encompasses a typical 2σ production instrumentation expanded by 30%–50% in order to simulate additional noise;

The engine performance has been compared at standard conditions and constant power turbine entry temperature (T44), before and after the deterioration. The parameters and stations nomenclature follow the practice recommended by [20]. The following parameters were selected:

- PW output power
- NI intermediate pressure spool rotational speed
- NH high pressure spool rotational speed
- P30 combustor inlet pressure

Table 1 Parameter deltas and noise bands

	DELTAS δp_j	2*SIGMA NOISE
dpw [%]	**–5.71**	**1.00**
dni [%]	**–0.52**	**0.25**
dnh [%]	**–0.02**	**0.25**
Dp30 [%]	**–4.24**	**0.80**
dwf [%]	**–3.89**	**0.50**

- WF fuel flow

The parameter deltas are displayed in Table 1, which also shows the 2σ band affecting each measurement; the seeded random noise value for each measurement (parameter delta) is included in the corresponding noise band.

The generic linear system (5) applied to this compressor's fouling problem gives the following ideal system (13), with two unknown variables (compressors average efficiency and flow capacity distortion) and five equations; the noise is not yet introduced:

$$\begin{cases} \textbf{dpw}: & \textbf{4.72dce + 0.99dcw = – 5.71} \\ \textbf{dni}: & \textbf{0.80dce – 0.28dcw = – 0.52} \\ \textbf{dnh}: & \textbf{0.45dce – 0.43dcw = – 0.02} \\ \textbf{dp30}: & \textbf{3.20dce + 1.03dcw = – 4.24} \\ \textbf{dwf}: & \textbf{3.08dce + 0.81dcw = – 3.89} \end{cases} \tag{13}$$

IDEAL $\delta \mathbf{p_j}$

For ideal δp_j, the overdetermined system produces a unique solution $(-1,-1)$; the equations define lines in (dce, dcw) plane—Fig. 9.

However, due to the noise which affects the parameter deltas—see Table 1, last column—the equations are distorted and the solution lost. Figure 10 gives an idea of how the seeded random noise can distort the system (13).

As mentioned earlier, a deterministic (square-matrix based) solution is no longer satisfactory; each intersection defines a noise-disturbed solution and none of them is sufficiently accurate. Even more seriously, there is no criterion for choosing the best of the many possible solutions.

Now, the fuzzy logic estimation process can be studied—how the fuzzy solution migrates progressively toward the ideal solution by adding extra equations (additional parameter deltas) to the system. Figure 11 shows the sequence of solutions, marked with squares; the sequence starts with a deterministic solution (two equations) and then continues with fuzzy solutions based on centroid method Eq. (10), by adding progressively extra information to the fuzzy domain expressed by Eq. (9).

The error function calculated for component distortions has the following expression:

$$\varepsilon_n(\delta x_E) = \left(\sum_{i}^{n} (\delta x_{Ei} - \delta x_{Ni})^2 \right)^{1/2} \tag{14}$$

where

δx_{Ei} is the estimated solution of the system with noise,
δx_{Ni} is the nominal solution (without noise).

The error function level reduces progressively from 1.6%—for one of the deterministic solutions, down to less than 0.2%—for the fuzzy solution of the five measured parameters (Fig. 12).

The deterministic solution is not unique and varies with the equations selected. However, the fuzzy solution is always within the close vicinity of the ideal solution and, in our example, better

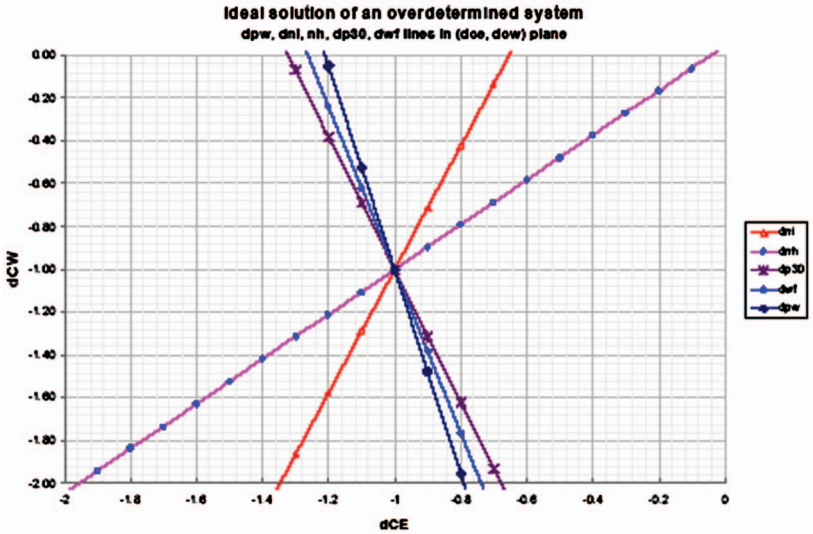

Fig. 9 The solution of system (13)—no noise

than any of them. The fuzzy solution is stable and consistent for it takes information from all measurements (final solution −0.85, −0.88 in this case).

Table 2 summarizes the differences between a deterministic solution (column 2) and a fuzzy solution based on 5 measurements (column 3). Although the deterministic solution zeroes two parameter deltas (shaded area), it ends up with big residual differences for the other parameter deltas and is far from identifying the ideal component distortion. The fuzzy solution minimizes all residual deltas and gets close to the ideal solution.

Comparison With Least Squares Method

An interesting result is obtained if the least squares method is applied to the same compressor fouling investigation and the noise distribution is quasinormal. The basic solution of least squares is given by the following equation:

$$\delta \mathbf{x}_0 = [(\mathbf{W}^T * \mathbf{W})^{-1}] * \mathbf{W}^T * \delta \mathbf{p} \tag{15}$$

and the solution is:

$$\Delta \mathrm{CE} = -0.96\%$$

$$\Delta \mathrm{CW} = -1.28\%$$

The FLE rules utilized are the *product composition* and the *centroid defuzzyfication*.

The error function (14) gives a bigger value (0.28%), compared to 0.19% in FLE case.

Another aspect of interest is the stability of the error as the parameter noise increases. The response of the two methods at higher noise levels is useful for assessing their stability and robustness. For instance, power measurement is quite noisy ($2\sigma = 1\%$). Figure 13 shows the error of the two methods at various power measurement noise levels, within $\pm\sigma$ range.

The FLE method is more stable for a large interval of measurement noise. This is due to the fact that FLE has introduced a more specific domain of uncertainty around the power measurement.

On a more general note, FLE is able to handle complicated noise distributions such as rectangular, asymmetric, or irregularly shaped. By using various techniques of composition and ranking the solutions in terms of likelihood, the method can provide a cluster of solutions which can be further refined. This allows an

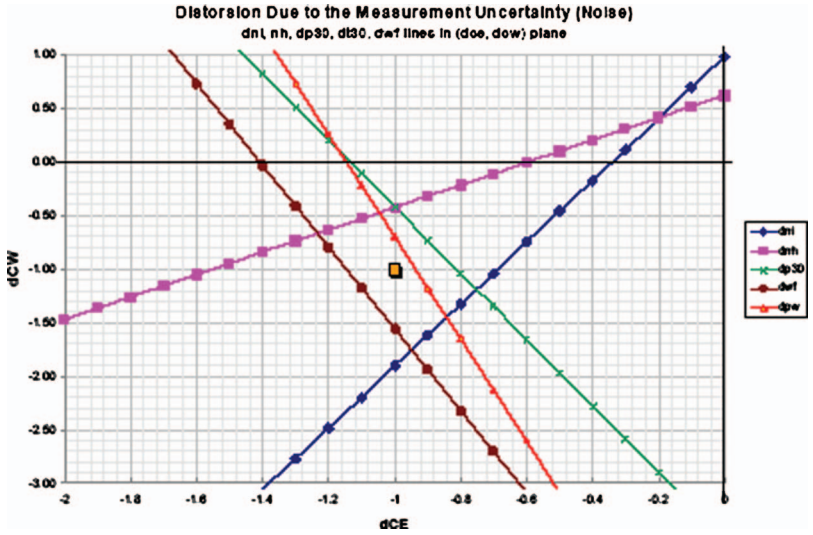

Fig. 10 System (13) with seeded noise

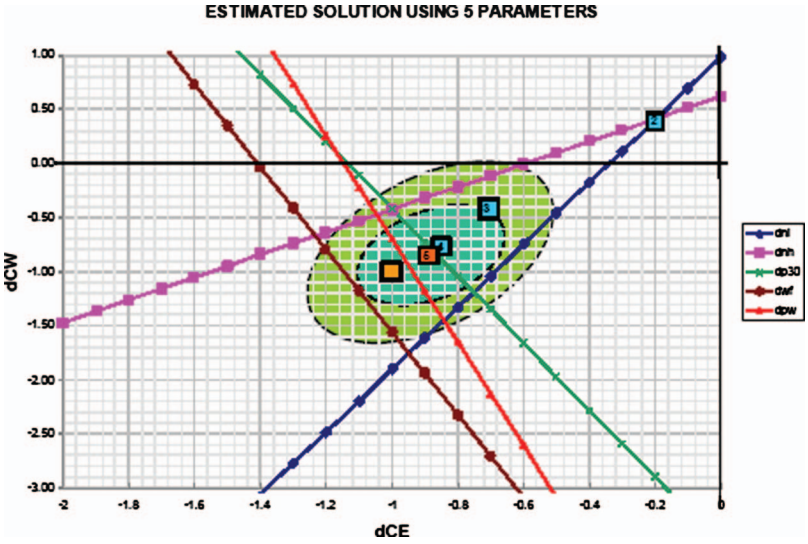

Fig. 11 The fuzzy solution migration toward ideal solution

engineer to apply his or her experience and judgment in choosing the optimum solution. Such an application is presented succinctly in the next section.

Example of Performance Change Estimate Made at High Level of Noise

A significant result was obtained when this method was applied to a predictive model to engine data, in which there was a large scatter of engine test results.

In this example, the engine hardware changes were related to the combustor and the combustor casing. Changes were therefore expected in:

- combustor pressure drop
- T44 position error (due to temperature profile change)
- core engine air system (two different sources of cooling air)
- efficiency of the electric load—as part of the installation uncertainty

Due to the big scatter of data, the first investigation based on a deterministic solution gave inconclusive results (+/−2% uncertainty band in overall performance). The higher uncertainty was mainly due to instrumentation corrections, modules replacement, and installation conditions variance.

A further investigation used the FLE and included the following measurements:

- power (electric output from generator)
- fuel flow
- LP turbine entry temperature
- HP spool speed
- IP spool speed
- pressure at the combustor inlet
- temperature at the combustor inlet
- inlet air mass flow

A good part of the measurements have been assigned non-Gaussian distributions with extended uncertainty due to:

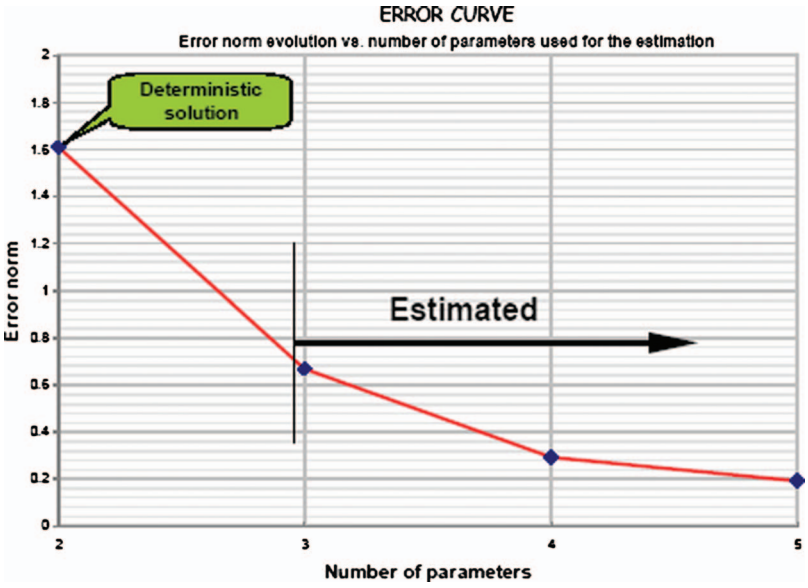

Fig. 12 Error function level versus number of measured parameters

Table 2 Comparison between fuzzy and deterministic solutions

Parameter delta	Resid_2 [%]	Resid_5 [%]
ΔP30	4.90	0.71
ΔNI	0.00	0.05
ΔNH	0.00	−0.01
ΔPower	3.44	0.55
ΔWF	3.78	0.49
ΔCW (ideal=−1%)	0.40	−0.85
ΔCE (ideal=−1%)	−0.20	−0.88

— changes in geometry of the new hardware located in the proximity of transducers
— variance of old engine module characteristics introduced by the fact that the comparison was performed between different engine builds with a significant period of time between them.

Fuzzy rules used: product composition and centroid defuzzyfication.

The FLE investigation comprised three steps:

— The first step assessed the domain of most likely variance for all the module changes and generator efficiency and selected the most relevant sets based on judgment/experience (0.5% fault level step)
— The second step refined the search and found the most likely scenario (0.1% step)
— The third step investigated the stability of the solution at increased noise, distorted distribution, and spurious measurements.

Combustor rig tests confirmed the results within 0.3% accuracy. The estimate of air system distortion was within 0.2% accuracy, according to the investigation carried out after the engine test. The results have shown that even though the distortion levels were lower than the noise, the fuzzy solution showed a very good accuracy. Additionally, the detection sensitivity was proven to be robust.

Conclusions

Fuzzy logic estimation is fast and stable. The results are consistent and robust even at high level of noise. The method can be used on a regular basis for model to engine alignment; further development of the method can address component fault detection or engine trending investigation as part of an *engine health monitoring* system.

Fuzzy logic estimator includes the *least squares estimator* class as a particular case. The least squares estimators can be derived if the *product composition rule* is used together with the *MAXimum defuzzyfication method*.

Typically, the fuzzy logic applications are based on a predefined discrete collection of fuzzy sets and disseminate the most convenient one according to the inference engine used.

The fuzzy logic estimator creates the most likely fuzzy set based on linear exchange rate factors.

The level of error ε_0 that controls the Newton iterative process needs to be correlated with the noise level affecting the readings. Therefore, there is little benefit in using a small error when dealing with high level of noise.

As well, the user can decide whether to use multiple iteration process, after considering the model nonlinearity, the magnitude of distortion, and the noise level.

The method is versatile. It can be used for any areas of analysis with large data uncertainty.

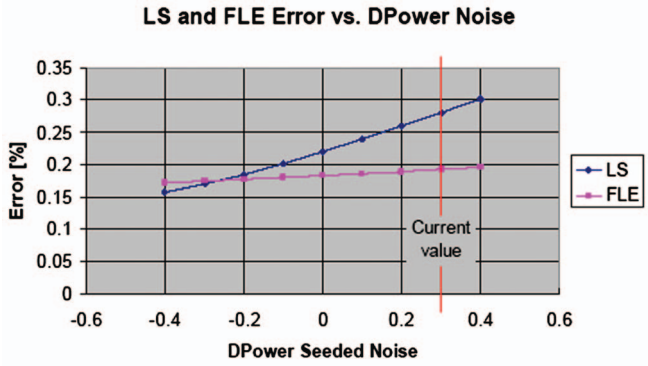

Fig. 13 Comparison of FLE and least squares error stability with increasing measurement noise

Acknowledgment

The author would like to thank Chris Barkey, Steve Richards, Vic Szewczyk, and Richard Tunstall at Rolls-Royce Canada, Industrial Engineering Business, for their continuous support and Phil Walsh, Steve Brown, John Martin and Barry Curnock, at Rolls-Royce UK, for their technical support and useful advice. The author also wishes to thank Professor Pericles Pilidis at Cranfield University for his continuous technical and moral support. The author is grateful to Professor Corneliu Berbente and Lecturer Paul Cocarlan at Polytechnic University in Bucharest for their active support.

Nomenclature

c_i = centroid coordinates of output fuzzy domain
dce = delta compressor efficiency
dcw = delta compressor flow function
dni = delta IP spool speed
dnh = delta HP spool speed
dp30 = delta combustor inlet pressure
dpw = delta shaft power
dwf = delta fuel flow
D = output fuzzy domain (after composition)
E_j = event associated to input fuzzy domain
m = number of measurements
n = number of component faults
p_j = parameter measurement
$\Pr(E)$ = probability of event E
t_j = parameter's local axis
$\boldsymbol{W}(\boldsymbol{x})$ = Jacobian matrix of the system
w_{ij} = element of $\boldsymbol{W}(\boldsymbol{x})$
$\boldsymbol{x}$ = vector of components functionality
x_i = component of $\boldsymbol{x}$
$\delta\boldsymbol{p}$ = vector of delta measurements
δp_j = component of $\delta\boldsymbol{p}$
$\delta\boldsymbol{x}$ = vector of component functionality changes
δx_i = component of $\delta\boldsymbol{x}$
δx_{Ei} = estimated solution with noise
δx_{Ni} = nominal solution (without noise)
ε_0 = error vector
$\varepsilon_n(\,)$ = error function
ψ = surface function of fuzzy domain D
ρ_j = input fuzzy set (domain) associated with measurement j
σ_j = standard deviation for normal distribution associated with measurement j
$d\omega$ = volume element of output fuzzy domain

Subscripts

0 = initial status or known value of a parameter
i = component fault indices

j = parameter measurement indices

Superscripts

k = iteration step
-1 = matrix inversion
T = matrix transpose

References

[1] Li, I. Y., 2002, "Performance-Analysis-Based Gas Turbine Diagnostics: A Review," Proc. Inst. Mech. Eng., Part A, **216**(5), pp. 363–377.
[2] Provost, M. J., 1995, "The Use of Optimal Estimation Techniques in the Analysis of Gas Turbines," Ph.D. thesis, Cranfield University, England.
[3] Doel, D. L., 1994, "TEMPER—A Gas Path Analysis Tool for Commercial Jet Engines," ASME J. Eng. Gas Turbines Power, **116**, pp. 82–89.
[4] Stamatis, A., Mathioudakis, K., and Papailiou, K. D., 1990, "Adaptive Simulation of Gas Turbines Performance," ASME J. Eng. Gas Turbines Power, **112**, pp. 168–175.
[5] Volponi, A. J., DePold, H., Ganguli, R., and Daguang, C., 2003, "The Use of Kalman Filter and Neural Network Methodologies in Gas Turbine Performance Diagnostics: A Comparative Study," ASME J. Eng. Gas Turbines Power, **125**, pp. 917–924.
[6] DePold, H. R., and Gass, F. D., 1999, "The Application of Expert Systems and Neural Networks to Gas Turbine Prognostics and Diagnostics," ASME J. Eng. Gas Turbines Power, **121**, pp. 607–612.
[7] Zedda, M., and Sing, R., 1999, "Gas Turbine Engine and Sensor Fault Diagnosis Using Optimization Techniques," AIAA Paper No. 99-2530.
[8] Ganguli, R., 2001, "Application of Fuzzy Logic for Fault Isolation of Jet Engines," ASME Paper No. 2001-GT-0013.
[9] Marinai, L., Singh, R., Curnock, B., and Probert, D., 2003, "Fuzzy-Logic-Based Diagnostic Process for Turbofan Engines," ISABE, Cleveland, Aug. 31–Sept. 5.
[10] Jackson, P., 1999, *Introduction to Expert Systems*, 3rd ed., Addison-Wesley, Longman, Boston.
[11] Ross, T. J., 1995, *Fuzzy Logic With Engineering Application*, McGraw–Hill, New York.
[12] Kosko, B., 1997, *Fuzzy Engineering*, Prentice-Hall, Englewood Cliffs, NJ.
[13] Martis, D., 2003, "Fuzzy Logic Estimator for Minimizing Signal Measurement Inaccuracy Effects in a Signal Processing System," US Patent No. 6,662,140 B2.
[14] Martis, D., 2000, "Fuzzy Logic Estimator Used in Gas Turbine Performance Analysis," Ph.D. thesis, Politechnic University Bucharest, Romania.
[15] Zadeh, L., 1973, "Outline of a New Approach to the Analysis of Complex Systems," IEEE Trans. Syst. Man Cybern., **3**.
[16] Bezdek, J. C., 1993, "Fuzzy Models – What Are They and Why?" IEEE Trans. Fuzzy Syst., **1**(1), pp. 1–6.
[17] Aleksandrov, A. D., Kolmogorov, A. N., and Lavrentiev, M. A., 1999, *Mathematics, Its Content, Methods and Meaning*, Dover, New York.
[18] Thames, J. M., Stegmaier, J. W., and Ford, Jr., J. J., 1989, "On-Line Compressor Washing Practices and Benefits," ASME Paper No. 89-65-91.
[19] Scheper, G. W., Mayoral, A. J., and Hipp, E. J., 1978, "Maintaining Gas Turbine Compressors for High Efficiency," Power Eng. J., Aug., pp. 54–57.
[20] SAE, 1974, "Gas Turbine Engine Performance Station Identification and Nomenclature, Aerospace Recommended Practice," Paper No. ARP 755A, Society of Automotive Engineers, Warrandale, PA.

Prediction of Engine Performance Under Compressor Inlet Flow Distortion Using Streamline Curvature

Vassilios Pachidis
e-mail: v.pachidis@cranfield.ac.uk

Pericles Pilidis
e-mail: p.pilidis@cranfield.ac.uk

School of Engineering,
Department of Power and Propulsion,
Gas Turbine Engineering Group,
Cranfield University,
Cranfield, Bedfordshire MK43 0AL, UK

Ioannis Templalexis
Section of Thermodynamics, Power, and Propulsion,
Hellenic Air Force Academy,
Dekeleia Air Base, Greece
e-mail: templalexis@hafa.gr

Theodosios Korakianitis
Department of Engineering,
Queen Mary University of London,
Mile End Road,
London E1 4NS, UK
e-mail: t.alexander@qmul.ac.uk

Petros Kotsiopoulos
Section of Thermodynamics, Power, and Propulsion,
Hellenic Air Force Academy,
Dekeleia Air Base, Greece
e-mail: kotsiopoulos@hafa.gr

Traditionally, engine performance has been simulated based on nondimensional maps for compressors and turbines. Component characteristic maps assume by default a given state of inlet conditions that cannot be easily altered in order to simulate two- or three-dimensional flow phenomena. Inlet flow distortion, for example, is usually simulated by applying empirical correction factors and modifiers to default component characteristics. Alternatively, the parallel compressor theory may be applied. The accuracy of the above methods has been rather questionable over the years since they are unable to capture in sufficient fidelity component-level, complex physical processes and analyze them in the context of the whole engine performance. The technique described in this paper integrates a zero-dimensional (nondimensional) gas turbine modelling and performance simulation system and a two-dimensional, streamline curvature compressor software. The two-dimensional compressor software can fully define the characteristics of any compressor at several operating conditions and is subsequently used in the zero-dimensional cycle analysis to provide a more accurate, physics-based estimate of compressor performance under clean and distorted inlet conditions, replacing the default compressor maps. The high-fidelity, two-dimensional compressor component communicates with the lower fidelity cycle via a fully automatic and iterative process for the determination of the correct operating point. This manuscript firstly gives a brief overview of the development, validation, and integration of the two-dimensional, streamline curvature compressor software with the low-fidelity cycle code. It also discusses the relative changes in the performance of a two-stage, experimental compressor with different types of radial pressure distortion obtained by running the two-dimensional streamline curvature compressor software independently. Moreover, the performance of a notional engine model, utilizing the coupled, two-dimensional compressor, under distorted conditions is discussed in detail and compared against the engine performance under clean conditions. In the cases examined, the analysis carried out by this study demonstrated relative changes in the simulated engine performance larger than 1%. This analysis proves the potential of the simulation strategy presented in this paper to investigate relevant physical processes occurring in an engine component in more detail, and to assess the effects of various isolated flow phenomena on overall engine performance in a timely and affordable manner. Moreover, in contrast to commercial computational fluid dynamics tools, this simulation strategy allows in-house empiricism and expertise to be incorporated in the flow-field calculations in the form of deviation and loss models. [DOI: 10.1115/1.2363414]

Introduction

Conventional, low-fidelity gas turbine performance simulation tools can offer a good prediction of the performance of a whole engine but are incapable of analyzing the performance of individual engine components in detail, or capturing complex physical phenomena, i.e., inlet flow distortion. On the other hand, CFD tools can predict the performance of individual engine components satisfactorily, under various operating conditions, but do not offer whole engine performance prediction. In the simulation of a complete gas turbine system, the presence of upstream and downstream engine components (compressor, bypass duct, etc.) affects the flow through a given component, therefore, the "presence" of the remaining engine components must be brought in the simulation to account for intercomponent effects.

Contributed by the International Gas Turbine Institute (IGTI) of ASME for publication in the JOURNAL OF ENGINEERING FOR GAS TURBINES AND POWER. Manuscript received October 1, 2005; final manuscript received February 1, 2006. IGTI Review Chair: R. S. Abhari. Paper presented at the ASME Turbo Expo 2006, Barcelona, Spain, May 8–11 2006, Paper No. GT2006-90806.

Several research efforts using 2D and 3D CFD component models, integrated with low-fidelity engine simulation software, have been reported in the past. Pachidis et al. [1,2] discussed the partial and full integration of a 3D CFD turbofan intake model with PYTHIA, the low-fidelity cycle analysis software developed at Cranfield University in the UK. Turner et al. [3] demonstrated a multi-fidelity simulation by NASA and GE of a turbofan engine with CFD component characteristics zoomed into "partial" performance maps for a 0D cycle simulation. Reed and Afjeh have also published on CFD numerical zooming techniques, in the context of the NPSS program [4–6]. In July 1997, Reed and Afjeh [7] published a paper on a comparative study of high- and low-fidelity fan models for turbofan engine system simulation. Smith [8] reported a collaborative research effort between NASA and GE on fan and compressor high-fidelity zooming.

By modelling the entire geometry of a propulsion system at the highest level of resolution (3D) using CFD, all the information necessary to assess engine life, reliability, and performance could probably be collected. Three issues, however, prevent this from being a practical solution. First, for a complete 3D system simu-

lation, the amount and level of detailed information needed as boundary and initial conditions would be extremely difficult to obtain. Second, the computational time and cost will be extremely high for effective and practical use in an industrial or academic research environment. Finally, commercially available CFD tools do not allow in-house empiricism and expertise to be incorporated in the flow-field solution in the form of deviation and loss models, and, in those cases where CFD results differ from experiments, there is really little one can do in order to identify the source of the inaccuracy. Given the current computational and financial resources, a faster method of combining different levels of analysis seems to be necessary. For the time being, however, "high fidelity simulation" and "faster simulation" are two contradictory concepts.

Streamline curvature methods have continued to receive refinements over the years and are still considered by industry as "state-of-the-art software," capable of providing an accurate, quick, and inexpensive solution compared to the full, three-dimensional, CFD methods. Although Wu [9] provided the basis for a hub-to-shroud flow field calculation, the term "streamline curvature" (SLC) became generally associated with through-flow analysis in 1967 following the work of Novak [10] and Jansen and Moffatt [11]. Between 1960 and 1990 a substantial number of computer codes for axial-flow turbomachine flow field analysis were developed using streamline curvature methods such as those of Denton [12], Jennions and Stow [13,14], and Barbosa [15].

Although streamline curvature methods have been around since the early 1950s, they have been mainly focused on simulating the flow field inside isolated components. There is actually little evidence in literature on the integration of streamline curvature component models with zero-dimensional cycle analysis, for high-fidelity studies in the context of the whole engine performance.

Simulation Strategy

This study focuses on a simulation strategy that allows the performance characteristics of a gas turbine engine component, resolved from a detailed, two-dimensional, streamline curvature analysis, to be integrated into an engine system analysis performed at a lower level of detail. This study has the potential to (i) investigate relevant physical processes occurring in an engine component in more detail and (ii) assess the effects of various isolated flow phenomena on overall engine performance in a timely and affordable manner. The method described in this paper follows the same overall principles of a "fully integrated" zooming strategy as described by Pachidis et al. [2].

This is a rather automatic and fully integrated approach to "high-fidelity" analysis with the two-dimensional, streamline curvature component model being directly linked to the 0D engine model, instead of the 0D component representation. During a DP calculation, the two-dimensional component is called at run-time in order to establish the component performance at the selected operating conditions and power setting. Averaged component performance characteristics are then returned back to the low-fidelity cycle analysis for the determination of the overall engine performance. Upstream component boundary conditions are determined by the user, in two dimensions, according to the needs of the particular study, or are determined from the outlet conditions of an upstream 2D component. During OD calculations, the two-dimensional component is called at run-time several times, in an iterative manner, until continuity of mass flow and power balance is satisfied throughout the engine.

The same process can be repeated for all engine operating conditions and power settings. Generation of a component characteristic map is not required. The high fidelity component can fully define the characteristic of the engine component at several operating conditions and can be used to provide a more accurate, physics-based estimate of the component's performance and, hence, engine performance, replacing the default maps within the 0D cycle model. This technique has the potential to become quasi-three-dimensional and can be applied to all engine components.

Simulation Tools

The study utilized two different simulation software: (i) a new, in-house 2D SLC Compressor Software, specifically developed for the purposes of this investigation, and (ii) the 0D gas turbine modelling and performance simulation system, developed at Cranfield University in the UK, called PYTHIA. The basic capability that the 2D SLC Compressor Software was initially developed to handle is outlined below:

- Facilitate steady-state, multi-stage compressor performance analysis in 2D, at both subsonic and transonic regimes
- Handle any type of standard or user-defined blade profile and compressor geometry
- Handle standard and user-defined models for secondary losses, shock losses, Reynolds, deviation, incidence, boundary layer blockage, tip clearance losses, etc.
- Identify conditions for surge and choking and handle nonuniform inlet flow conditions
- Calculate the overall compressor map and provide a converged solution at any given operating point within minutes

The 2D SLC Compressor Software was developed to provide great flexibility, in the sense that it can be used as a performance prediction tool for compressors of a known design or as a development tool to assess the changes in performance of a known compressor after implementing small geometry changes. Moreover, it can be used as a design tool to verify and refine the outcome of a preliminary compressor design analysis. Finally, the software can be used to create a 2D compressor model that can be integrated into a conventional 0D engine cycle code for the investigation of the influence of nonuniform flow profiles on whole engine performance.

The PYTHIA scheme has been developed by the Gas Turbine Engineering Group at Cranfield University [16]. Based on Cranfield's previous "generation" engine simulation software, called TURBOMATCH [17], it has been specifically developed to be a fully modular, object-oriented, engine cycle simulator that can perform steady-state design, off-design, and degraded performance analysis of civil aero, industrial, and military engines. PYTHIA is also a versatile engine diagnostics tool. A PYTHIA engine model is assembled from a collection of interconnected elements and controlled by an appropriate numerical solver. By means of engine component icons and via an engine component toolbar, various preprogrammed routines can be called up to simulate the action of the different components of the engine, resulting finally in output of engine thrust or power, fuel consumption, s.f.c., etc, together with details of individual component performance and of the gas properties at various stations within the engine.

Typically, a PYTHIA engine model uses performance maps for turbines and compressors to obtain a balanced, steady-state engine condition. In this particular case, the 2D SLC compressor model was integrated with PYTHIA and called at run-time as a Dynamic Link Library (.dll) component, completely replacing the default nondimensional compressor map.

2D SLC Compressor Software

All streamline curvature software is based on an inviscid through-flow analysis method, in which viscosity effects are taken into account by means of empirical models and correlations. A complete account of the development of the 2D SLC Compressor Software together with a full description of the various empirical deviation and loss models used in the code can be found in [18]. The scope of this chapter is to give the reader a brief flavor of the basics of the streamline curvature method adopted by this work.

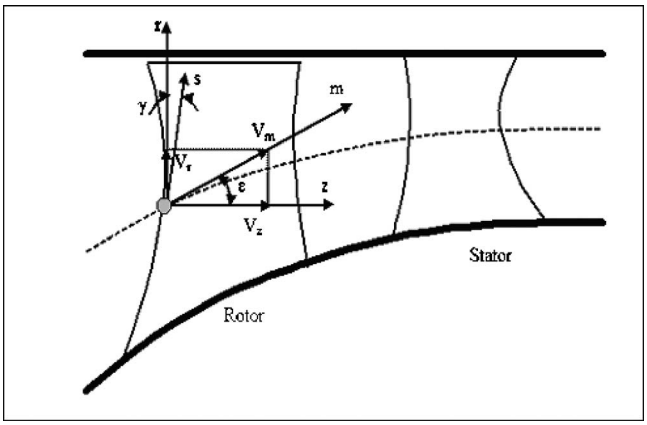

Fig. 1 Coordinate system

The flow within the compressor is considered as axisymmetric, compressible, and inviscid. For this specific type of flow the law of conservation of angular momentum has the following form in vector quantities (blade forces F are neglected in this case):

$$-\frac{1}{\rho}\nabla P = \frac{D\boldsymbol{W}}{Dt} + \boldsymbol{\omega}\times\boldsymbol{\omega}\times\boldsymbol{r} + 2\boldsymbol{\omega}\times\boldsymbol{W} + \boldsymbol{F} \tag{1}$$

Resolving each term of the above equation into cylindrical coordinates (z, r, w—axial, radial, tangential, Fig. 1), the following four expressions are derived:

i. The pressure forces:

$$-\frac{1}{\rho}\nabla\boldsymbol{P} = \left(-\frac{1}{\rho}\frac{\partial P}{\partial r}\right)\boldsymbol{e_r} + \left(-\frac{1}{r\rho}\frac{\partial P}{\partial w}\right)\boldsymbol{e_w} + \left(-\frac{1}{\rho}\frac{\partial P}{\partial z}\right)\boldsymbol{e_z} \tag{2}$$

ii. The material derivative of the relative velocity in steady state conditions ($\partial\boldsymbol{W}/\partial t \approx 0$):

$$\frac{D\boldsymbol{W}}{Dt} = (\boldsymbol{W}\cdot\nabla)\cdot\boldsymbol{W} + \frac{\partial\boldsymbol{W}}{\partial t}$$

$$\Leftrightarrow \frac{D\boldsymbol{W}}{Dt} = \left(W_r\frac{\partial\boldsymbol{W}}{\partial r}\right)\cdot\boldsymbol{e_r} + \left(\frac{W_w}{r}\frac{\partial\boldsymbol{W}}{\partial w}\right)\cdot\boldsymbol{e_w} + \left(W_z\frac{\partial\boldsymbol{W}}{\partial z}\right)\cdot\boldsymbol{e_z}$$

$$\Leftrightarrow \begin{cases} \dfrac{DW_r}{Dt} = W_r\dfrac{\partial W_r}{\partial r} + \dfrac{W_w}{r}\dfrac{\partial W_r}{\partial w} + W_z\dfrac{\partial W_r}{\partial z} \\ \dfrac{DW_w}{Dt} = W_r\dfrac{\partial W_w}{\partial r} + \dfrac{W_w}{r}\dfrac{\partial W_w}{\partial w} + W_z\dfrac{\partial W_w}{\partial z} \\ \dfrac{DW_z}{Dt} = W_r\dfrac{\partial W_z}{\partial r} + \dfrac{W_w}{r}\dfrac{\partial W_z}{\partial w} + W_z\dfrac{\partial W_z}{\partial z} \end{cases} \tag{3}$$

iii. The centripetal acceleration:

$$\boldsymbol{\omega}\times\boldsymbol{\omega}\times\boldsymbol{r} = (\boldsymbol{\omega}\cdot\boldsymbol{r})\cdot\boldsymbol{\omega} - (\boldsymbol{\omega}\cdot\boldsymbol{\omega})\cdot\boldsymbol{r} = -(\omega^2 r)\boldsymbol{e_r} + \boldsymbol{e_w} + \boldsymbol{e_z} \tag{4}$$

where the terms $\boldsymbol{e_w}$ and $\boldsymbol{e_z}$ are neglected (≈ 0).

iv. The coriollis acceleration:

$$2\boldsymbol{\omega}\times\boldsymbol{W} = (-2\omega W_w)\boldsymbol{e_r} + (2\omega W_r)\mathbf{e_w} + \boldsymbol{e_z} \tag{5}$$

where the term $\boldsymbol{e_z}$ is neglected (≈ 0). Solving a system of equations, it can be shown that the gradient of the meridional velocity in the s direction is given by the full radial equilibrium equation as shown below:

Table 1 Two-stage fan design overall parameters (NASA TP 1493)

Pressure ratio	2.399
Temperature ratio	1.334
Isentropic efficiency	0.849
Mass flow (kg/s)	33.248
rpm	16042.800
Inlet hub-tip ratio	0.375
First rotor tip speed (m/s)	428.896
Second rotor tip speed (m/s)	405.341

$$\frac{\partial V_m^2}{\partial s} = V_m^2 2\cos^2\alpha\left[\frac{\cos(\varepsilon+\gamma)}{R_c} - \frac{\tan\alpha(\partial\alpha/\partial s)}{\cos^2\alpha} + \sin(\varepsilon+\gamma)\left(-\frac{1}{\cos(\varepsilon+\gamma)}\frac{\partial\varepsilon}{\partial s} + \frac{\tan(\varepsilon+\gamma)}{R_c} - \frac{\partial(\ln(r\rho))}{\partial m}\right)\right] + 2\cos^2\alpha\left(\frac{\partial I}{\partial s} - 2\cos\gamma\omega(V_w - U) - T\frac{\partial S}{\partial s}\right) \tag{6}$$

Equation (6) basically describes the gradient of meridional velocity from hub to tip but not its average magnitude. A further constraint is required to determine the level of meridional velocity, which can be provided by integrating the meridional velocity profile across the compressor annulus to check for continuity of mass flow. At each stream tube the mass flow rate is generally given by:

$$\dot{m}_j = \int_A \bar{\rho}_j\bar{V}_{m,j}\,dA \tag{7}$$

Equation (7) can be numerically solved as:

$$\dot{m}_j = \frac{\pi}{2}\left[\rho_{j+1}V_{m,j+1}\cos(\varepsilon_{j+1}+\gamma_{j+1}) + \rho_j V_{m,j}\cos(\varepsilon_j+\gamma_j)\right] \times\left(\frac{r_{j+1}^2 - r_j^2}{\cos[(\gamma_{j+1}+\gamma_j)/2]}\right) \tag{8}$$

The radial equilibrium equation (6) and the equation of mass flow Eq. (8) are solved iteratively. A first guess for the shape of streamlines, and distribution of meridional velocity from hub to tip is made. After calculating velocity triangles, entropy along streamlines, and enthalpy, Eq. (6) is solved to establish the rate of change of meridional velocity from hub to tip. Integrating the meridional velocity profile establishes the compressor mass flow, which is then compared to the overall (actual) mass flow. Based on the mass flow difference, the overall level of meridional velocity is readjusted accordingly and a new iteration takes place. During this process the streamtube mass flow is used to determine the new positions of the streamlines at the intersections with the blade edges, to be used in the new iteration.

SLC Software Validation

The SLC Compressor Software was validated against published experimental data for both clean-inlet and distorted conditions. A 2D model of a two-stage fan was constructed according to the detailed geometric data published in NASA Technical Paper No. 1493 by Urasek et al. [19]. The overall design performance of the two-stage fan is given in Table 1.

The performance of the SLC two-stage compressor model under uniform inlet conditions was compared against the measured performance data provided in the aforementioned report. Figures 2 and 3 present the comparison between the measured and simulated compressor performance for the first stage.

The analysis showed that there was a very good qualitative and quantitative agreement between the simulated and experimental data, especially in the case of the pressure ratio versus corrected

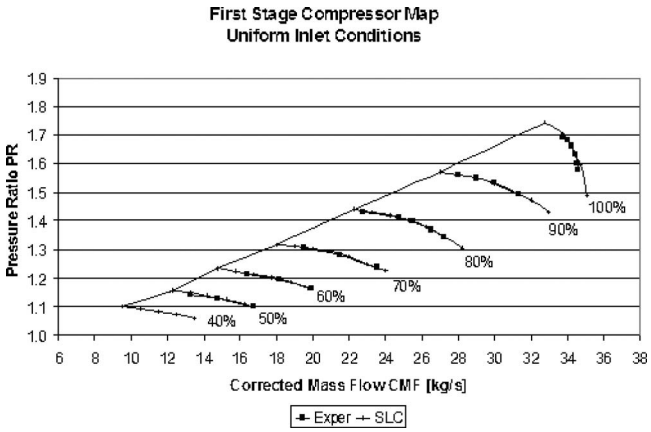

Fig. 2 Uniform inlet conditions comparison with experimental results—pressure ratio versus corrected mass flow

mass flow speed lines. Isentropic efficiency versus corrected mass flow speed lines were in a good qualitative agreement as well, although the overall shape of the lines did not exactly match the experimental readings. It must be stated that no particular effort was made to achieve a better agreement between simulated and experimental data by trying different combinations of the loss models provided in the SLC Compressor Software. It was decided that the initial agreement was more than sufficient in order to allow the subsequent qualitative trend analysis to take place.

For the software validation under distorted conditions, NASA Technical Paper No. 1294 by Schmidt and Ruggeri [20] was used as a reference. This paper discusses in detail the performance of a single-stage fan with and without inlet radial distortion. The design overall parameters of the single-stage fan discussed in NASA TP No. 1294 are very similar to the first stage of the NASA TP No. 1493 two-stage compressor. Table 2 lists the overall design parameters of the two stages.

The performance of the SLC compressor model, and especially the performance of the first stage, was qualitatively compared against the measured data in NASA TP 1294 for hub and tip radial pressure distortions. The analysis showed similar qualitative trends for the same kind of radial pressure distortion and extend, given in NASA TP No. 1294 by the radial Pressure Distortion Index (PDI_{radial}) as:

$$\mathrm{PDI}_{\mathrm{radial}} = \frac{P_{o,\max} - P_{o,\min}}{P_{o,\max}} \tag{9}$$

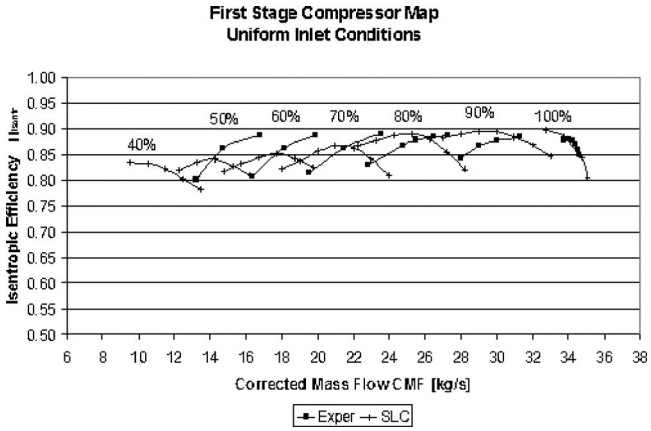

Fig. 3 Uniform inlet conditions comparison with experimental results—isentropic efficiency versus corrected mass flow

Table 2 Stage comparison between NASA TP 1493 and 1294 fans

Stage Parameter	NASA TP1493	NASA TP1294
Pressure ratio	1.590	1.574
Temperature ratio	1.167	1.170
Isentropic efficiency	0.848	0.816
Mass flow (kg/s)	33.248	29.484
rpm	16042.800	16100.000
Tip speed (m/s)	428.896	424.601

Figures 4 and 5 illustrate the effect on stage performance of a total pressure deficit at the tip of 20%, as predicted by the SLC. The trends on the map are in a very good agreement with experimental data for a PDI_{radial} of approximately 0.189.

More analytically, the SLC analysis predicted accurately the reduction in surge margin associated with radial pressure distortion at the tip, and the slight shift of the speed lines to the right, especially at intermediate speeds. The speed line movement to the right reduced towards higher speeds and actually reversed close to 100% design speed. Generally, the radial pressure distortion reduced the mass flow in the distorted region and caused a redistribution of flow parameters at the inlet with the total pressure and axial velocity being lower than in the case of a clean inlet. Incidence angle increased in the affected regions and reduced in the unaffected ones, increasing and reducing blade loading, respectively.

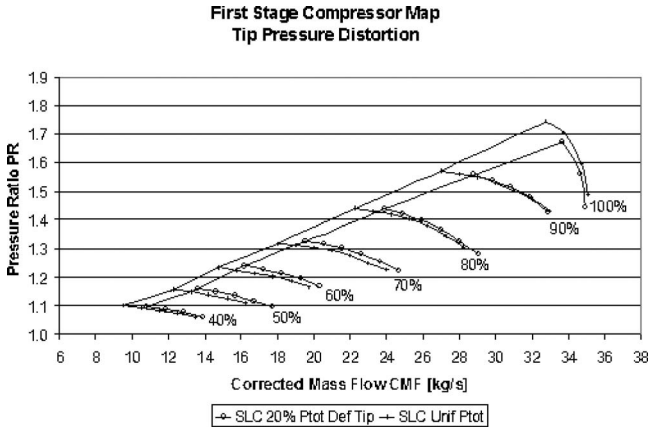

Fig. 4 Tip pressure distortion effect—pressure ratio versus corrected mass flow

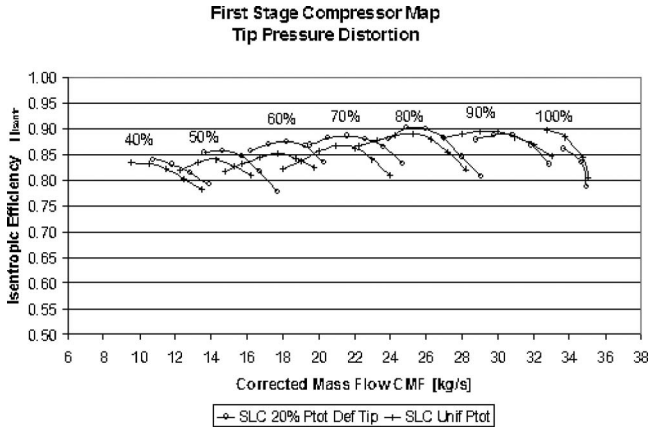

Fig. 5 Tip pressure distortion effect—isentropic efficiency versus corrected mass flow

Table 3 Notional engine design performance parameters

W (kg/s)	33.24
OPR	3.56
TET (K)	1000.00
BPR	0.714
GT (N)	10,103.30
SFC (mg/N s)	26.029

The higher blade loading in the distorted region produced a total pressure and temperature ratio greater than the clean-inlet value, which justifies the slight increase in efficiency throughout the operating range as shown above. However, in the distorted region the inlet total pressure was lower than the clean value and the higher pressure ratio only resulted in exit total pressures more or less equal to the clean-inlet value. In the undistorted flow region the exit total pressure was less than the average due to the blade operating unloaded, at a lower work input and total pressure ratio. Therefore, over the entire blade span the average total pressure level was lower than the corresponding clean case and the overall pressure ratio lower as well. Despite the reduction in pressure ratio, a small increase in the corrected mass flow is responsible for the speed lines appearing slightly sifted to the right at medium speeds.

Case Study: Effect of Radial Pressure Profiles on Fan and Engine Performance

This case study looked into the effect of two particular radial pressure profiles on fan performance and subsequently on engine performance by fully integrating the 2D SLC Compressor Software with the 0D cycle analysis. The two radial pressure profiles were constructed by reducing and increasing respectively the rotor inlet total pressure at the hub by 30%, compared to the mass-averaged value, which remained the same and equal to the clean-inlet value in both cases. In other words, the pressure towards the tip was allowed to increase or reduce accordingly so that the same mass-averaged value of inlet total pressure was maintained. The objective of this study was to analyze the pure effect of the different pressure profiles on the performance of the blading by keeping the overall mass flow through the compressor annulus and inlet total pressure the same.

Moreover, for the purposes of this investigation a notional engine model was built based on the configuration of an existing two-shaft, LBR, mixed-exhaust, military turbofan, scaled down in terms of OPR, mass flow, and TET. The engine model was constructed in PYTHIA and the first stage of the validated two-stage fan was coupled to the software to represent the LP fan of the engine. Only the first stage was used in the engine simulation in order to reduce the amount of convergence time required, particularly in off-design calculations. The overall design performance of the notional engine is illustrated in Table 3.

Figures 6 and 7 illustrate the effect of the two radial pressure profiles on fan performance. The design point of the engine fan was selected at a mass flow of 33.24 kg/s. It can be observed that the 30% total pressure deficit at the hub (with an associated increase of total pressure at the tip) pushes the speed lines to slightly higher pressure ratios, efficiencies, and nondimensional mass flows, but reduces, however, the surge margin of the fan considerably. The exactly opposite pressure profile demonstrates opposite effects as it would be expected. The complete compressor maps have been produced for the three cases studied (clean inlet, 30% deficit, and 30% surplus) by running the 2D fan model independently and only for demonstration purposes. They played no part in the engine performance simulation other than establishing the equilibrium running line on the map and calculating the actual surge margin.

The shift of the engine running line under the different fan inlet pressure profiles is also illustrated in Fig. 6. The 30% total pressure deficit at the hub causes the fan to run at higher pressure ratios and closer to surge. The 30% total pressure surplus at the hub seems to be causing the opposite effect but at reduced efficiencies. The effect of the two different distortion profiles on the movement of the running line appears more pronounced close to design point and seems to reduce towards lower corrected speeds.

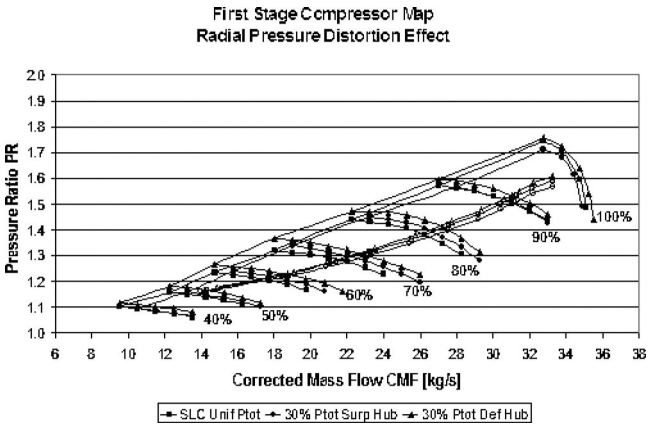

Fig. 6 Radial pressure distortion effect on first stage compressor map—pressure ratio versus corrected mass flow

Figures 8–11 illustrate the effect of distortion on overall engine performance. Similarly to the running line, the effect on engine performance parameters is stronger towards the design point and

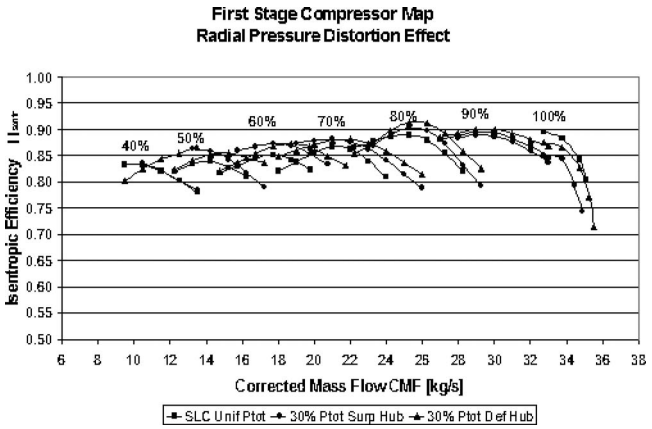

Fig. 7 Radial pressure distortion effect on first stage compressor map—isentropic efficiency versus corrected mass flow

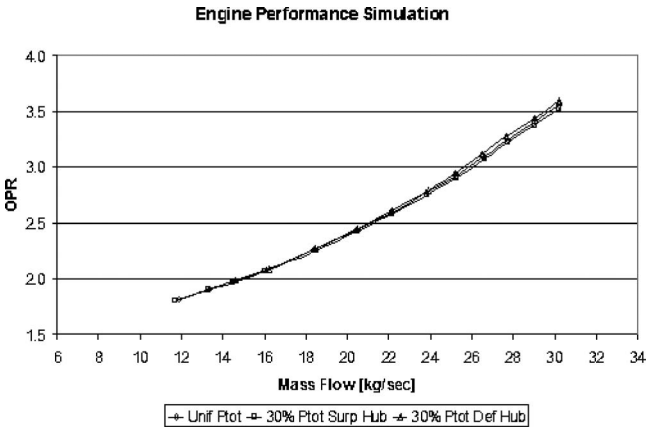

Fig. 8 Radial pressure distortion effect on engine performance—overall pressure ratio versus mass flow

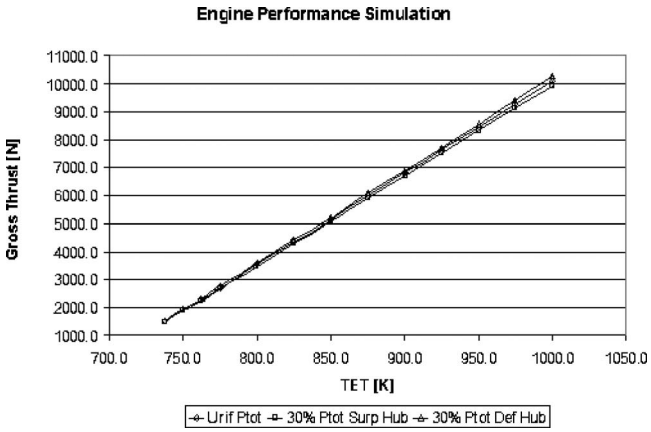

Fig. 9 Radial pressure distortion effect on engine performance—gross thrust versus turbine entry temperature

reduces towards lower speeds. As a direct consequence of the fan pressure ratio change close to design point, the engine OPR drops by 0.99%, in the case of a 30% total pressure surplus at the hub and increases by 1.02% in the case of the total pressure deficit at the hub. The difference in OPR at very low mass flows is negligible. Gross thrust also drops in the first case by 1.6% and increases in the second by 1.71%. The difference in gross thrust compared to the clean case is reduced in both cases to almost half

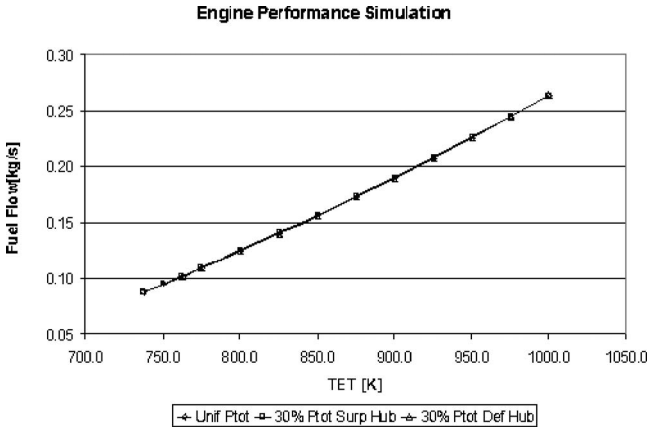

Fig. 10 Radial pressure distortion effect on engine performance—fuel flow versus turbine entry temperature

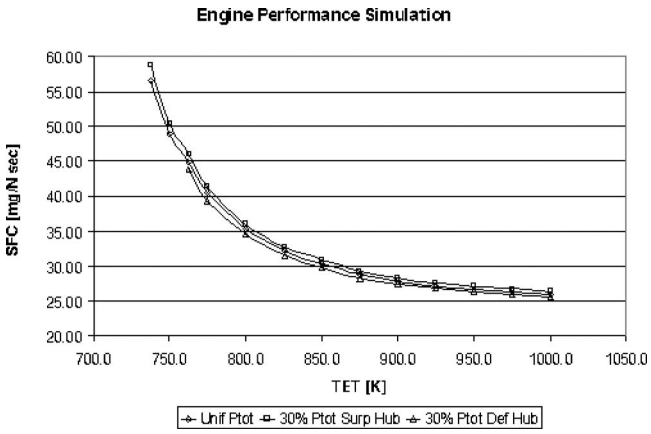

Fig. 11 Radial pressure distortion effect on engine performance—SFC versus turbine entry temperature

the design point percentages at low TET values (750 K). Fuel flow remains largely unaffected throughout the engine operating range. SFC, however, displays an almost constant difference with the clean case values at both design and off-design, increasing by 1.58% in the first case and reducing by 1.64% in the second.

Repeating the process for different distortion profiles and engine operating conditions establishes the "full" engine performance using the fully integrated approach. At this stage, however, it was outside the scope and requirements of the investigation to repeat the same methodology for a larger number of different cases.

The high-fidelity compressor model fully defined the performance characteristics of that particular fan geometry, at the simulated operating conditions, and was then used to provide a more accurate, physics-based estimate of the fan's performance and, hence, engine performance, replacing the default compressor maps within the PYTHIA cycle model.

Conclusions

This work demonstrated the potentials of the "fully integrated" approach by using a 2D Streamline Curvature compressor model, directly coupled to a 0D engine performance simulation software. This technique is a fully automated one, can be applied to all engine components, and does not require the generation of a component characteristic map.

This paper discussed in detail the development of the 2D SLC Compressor Software and its validation against experimental data under both clean and distorted conditions. The SLC model was based on the geometry and performance of a NASA experimental compressor and was used in the 0D cycle analysis to provide a more accurate, physics-based estimate of compressor performance and, hence, engine performance, under clean and nonuniform inlet conditions.

A detailed comparison between the simulated, baseline engine performance and the one obtained by using the SLC-coupled approach was also presented in this paper. Gross thrust, OPR fuel flow, and SFC were compared for two different distortion cases. Engine performance results presented in this report are to be taken only qualitatively, because of the notional nature of the engine model used. However, in the cases examined, the analysis carried out by this study, demonstrated relative changes in the simulated engine performance larger than 1%.

The above analysis proves the potential of the simulation strategy presented in this paper to investigate relevant physical processes occurring in an engine component in more detail, and to assess the effects of various isolated flow phenomena on overall engine performance in a timely and affordable manner. Moreover, in contrast to commercial CFD tools, it allows in-house empiricism and expertise to be incorporated in the flow-field calculations in the form of deviation and loss models.

Nomenclature

Abbreviations

BPR = bypass ratio
CFD = computational fluid dynamics
CMF = corrected mass flow
GT = gross thrust
OPR = overall pressure ratio
PR = pressure ratio
SLC = streamline curvature
SFC = specific fuel consumption
TET = turbine entry temperature
0D = zero-dimensional or nondimensional
2D = two-dimensional
3D = three-dimensional

Greek Symbols

α = absolute air angle

β = relative air angle
γ = sweep angle
ε = streamline slope
η = efficiency
ρ = density
ω = rotational speed

Latin Symbols

F = blade forces
I = rothalpy
j = number of node or streamline
P = pressure
r = radius
R_c = streamline curvature
S = entropy
s = direction along blade LE
T = temperature
t = time
U = blade speed
W = relative velocity, mass flow
V = absolute velocity

Subscripts

1 = inlet plane
2 = outlet plane
isentr = isentropic
o = total conditions
m = meridional
r = radial
z = axial

Superscript

- = mean value

References

[1] Pachidis, V., Pilidis, P., Guindeuil, G., Kalfas, A., and Templalexis, I., 2005, "A Partially Integrated Approach to Component Zooming Using Computational Fluid Dynamics," ASME Paper No. GT2005-68457.

[2] Pachidis, V., Pilidis, P., Talhouarn, F., Kalfas, A., and Templalexis, I., 2005, "A Fully Integrated Approach to Component Zooming Using Computational Fluid Dynamics," ASME Paper No. GT2005-68458.

[3] Turner, M. G., Reed, J. A., Ryder, R., and Veres, J. P., 2004, "Multi-fidelity Simulation of a Turbofan Engine With Results Zoomed Into Mini-maps for a Zero-d Cycle Simulation," ASME Paper No. GT2004-53956.

[4] Reed, J. A., and Afjeh, A. A., 1994, "Development of an Interactive Graphical Propulsion System Simulator," 30th AIAA/ASIVIEISAE/ASEE Joint Propulsion Conference, University of Toledo, AIAA Paper No. 94-3216, June.

[5] Reed, J. A., and Afjeh, A. A., 1994, "Distributed and Parallel Programming in Support of Zooming in Numerical Propulsion System Simulation," NASA Proceeding of Symposium on Applications of Parallel and Distributed Computing, Columbus, OH, April.

[6] Reed, J. A., and Afjeh, A. A., 1995, "An Interactive Graphical System for Engine Component Zooming in a Numerical Propulsion System Simulation," University of Toledo, 33rd Aerospace Sciences Meeting and Exhibit, A1AA Paper No. 95-0118, January.

[7] Reed, J. A., and Afjeh, A. A., 1997, "A Comparative Study of High and Low Fidelity Fan Models for Turbofan Engine System Simulation," *Proceedings of the IASTED International Conference on Applied Modelling and Simulation*, Banff, Canada, July.

[8] Smith, L. H., 1994, "NASA/GE Fan and Compressor Research Accomplishments," ASME J. Turbomach., **116**(4), pp. 554–568.

[9] Wu, C., H., 1952, "A General Through-Flow Theory of Three-Dimensional Flow in Subsonic and Supersonic Turbomachines of Axial-, Radial-, and Mixed-Flow Types," NASA Report No. TN2604.

[10] Novak, R. A., 1967, "Streamline Curvature Computing Procedures for Fluid-Flow Problems," ASME J. Eng. Power, **89**, pp. 478–490.

[11] Jansen, W., and Moffatt, W. C., 1967, "The Off-Design Analysis of Axial Flow Compressors," ASME J. Eng. Power, **89**, pp. 453–462.

[12] Denton, J. D., 1978, "Throughflow Calculations for Transonic Axial Flow Turbines," ASME J. Eng. Power, **100**, pp. 212–218.

[13] Jennions, I. K., and Stow, P., 1985, "The Quasi-Three-Dimensional Turbomachinery Blade Design System, Part I: Throughflow Analysis, Part II: Computerized System," Trans. ASME: J. Eng. Gas Turbines Power, **107**, pp. 308–316.

[14] Jennions, I. K., and Stow, P., 1986, "The Importance of Circumferential Non-uniformities in a Passage Averaged Quasi-Three-Dimensional Turbomachinery Design System," Trans. ASME: J. Eng. Gas Turbines Power **108**, pp. 240–245.

[15] Barbosa, J. R., 1987, "A Streamline Curvature Computer Program for Axial Compressor Performance Prediction," Ph.D thesis, Vol. 1, Cranfield Institute of Technology, School of Mechanical Engineering.

[16] Pachidis, V., 2004, "Gas Turbine Simulation – PYTHIA Workshop Guide," Part I and II, Cranfield University, Department of Power, Propulsion and Aerospace Engineering, ASME/IGTI Aero Engine Life Management Conference, London, March.

[17] Palmer, J. R., 1990, "The TURBOMATCH Scheme For Aero/Industrial Gas Turbine Engine Design Point/Off Design Performance Calculation," SME, Thermal Power Group, Cranfield University.

[18] Pachidis, V., 2006, "Gas Turbine Advanced Performance Simulation," Ph.D thesis, Cranfield University, School of Engineering, January.

[19] Urasek, D. C., Gorell, W. T., and Cunnan, W. S., 1979, "Performance of Two-Stage Fan Having Low-Aspect-Ratio, First Stage Rotor Blading," NASA Technical Paper No. 1493.

[20] Schmidt, J. F., and Ruggeri, R. S., 1978, "Performance With and Without Inlet Radial Distortion of a Transonic Fan Stage Designed for Reduced Loading in the Tip Region," NASA Technical Paper No. 1294, August.

Basic Limitations on the Performance of Stirling Engines

P. C. T. de Boer
Graduate School Professor of Mechanical and Aerospace Engineering
Mem.ASME
Cornell University,
Upson Hall,
Ithaca, NY 14853

The performance of Stirling engines is subject to limitations resulting from power dissipation in the regenerator. The dissipation is caused by pressure gradients in the regenerator required to generate flow. Without this flow the power output would be zero. Hence the dissipation is an essential element of the operation of the engine. Using linearized theory, the pressure in the compression and expansion spaces is found as a function of the ratio of piston amplitudes and piston phase difference. The regenerator is taken to be thermally perfect. All variations are taken to be sinusoidal in time. Expressions are derived for the dimensionless power output and the thermal efficiency at a given amplitude of the compression piston. Upper bounds on the power output and the efficiency are found as function of frequency and of regenerator void volume. Special attention is given to the case of piston amplitude ratio equal to 1. [DOI: 10.1115/1.2204629]

1 Introduction

The Stirling engine has an illustrious history. An excellent description of this history is included in the book by Hargreaves [1]. The present paragraph is based on information given in this book. The Stirling engine was invented by the Reverend Robert Stirling, who in 1816 obtained a patent called "Improvements for diminishing the consumption of fuel, and in particular an engine capable of being applied to the moving (of) machinery." A crucial part of the invention was the use of a regenerator. Stirling pointed out that the engine in principle could work without the regenerator, and used the name "economizer," instead. Stirling and his brother James went on to build several of these "hot air" engines. It is reported that in 1843 a Stirling engine had achieved an efficiency of 18%, which was better than the efficiency of most steam engines. One of Stirling's engines was in operation at the Dundee Foundry from 1843 until 1847. The Foundry then reverted to steam because "the bottoms of the air vessels of the Stirling engine could not be made to withstand the heat to which they were exposed." Among the many others who built engines of the Stirling type in the 19th century were Sir George Cayley, John Ericson, Laubereau, Lehmann, Stenberg, A. K. Rider, and D. W. van Rennes. The Stirling engine never became a serious competitor to steam engines. By the end of the century, the only Stirling-type air engines still being manufactured were small ones used for special applications. A revival of sorts occurred in the 20th century, when the Philips Company of the Netherlands wanted to develop markets for radio sets in remote areas that were without a supply of electricity. The use of batteries in these areas was quite expensive. A small power unit of the Stirling-engine type would satisfy the perceived need, at least in principle. This resulted in a large development program aimed at many diverse applications, the details of which are described in [1]. Use was made of many ingenious inventions, such as the rhombic drive, the swash-plate drive, the rollsock seal, the use of pressurized helium instead of atmospheric air, and the four-cylinder double-acting engine. The most recent large program involving Stirling engines took place in the 1970s, when the Philips Company teamed up with the Ford Motor Company to build and test a Stirling-Torino automobile as well as a Philips-DAF Stirling bus. A Stirling engine mounted in a Ford Pinto was tested in a concurrent program between Ford and United Stirling of Sweden. The Ford Motor Company concluded that there are three major stumbling blocks to the use of Stirling engines in automobiles: the design of the heating system, the control of power, and the failures of roll-sock seals. Ford ended its efforts in the development of the Stirling engine in 1987.

There still remains optimism in various circles about a future large scale implementation of Stirling engines. They may have a role to play in connection with environmental pollution, and with the diminishing availability of high grade fossil fuels. Because the combustion process of the Stirling engine is external, it can use a multitude of fuels, and can be controlled precisely to minimize harmful emissions. It can also use solar power as its source of heat. Coupling a solar Stirling engine with a generator might lead to electric power generation with an efficiency higher than that of solar cells. Another frequently cited advantage of Stirling engines is their quiet operation resulting from the lack of valves closing and opening at high frequency.

An early theoretical analysis of the Stirling engine is that by Schmidt [2]. Schmidt neglected the pressure gradients in the regenerator. He took the heat transfer processes in the compression and expansion spaces to be isothermal. Because his model represents a reversible heat engine cycle, it has the Carnot efficiency. The analysis was generalized by Finkelstein [3], who allowed for irreversible heat exchange with the walls of the compression and expansion spaces. The solution of the Finkelstein model is accomplished numerically, using nodal analysis. The Schmidt and Finkelstein models have served as the basis for modern analyses of the Stirling engine. These modern analyses make extensive use of numerical computations and account for many additional phenomena of importance. Detailed accounts of modern developments are presented in [4–12].

The performance of Stirling engines depends on the characteristics of the regenerator. The theory describing regenerator performance is quite involved [13–15]. It must take account of the rate of heat transfer between matrix and gas, of the variations in temperature, pressure and velocity of the gas, and of the variations in temperature of the matrix. All variations depend on both space and time. Because of this complexity, the full equations governing regenerator performance can only be solved numerically. In order to establish general characteristics of regenerator behavior, it is desirable to have solutions in closed form. This requires making simplifying assumptions. Many authors have used the so-called harmonic approximation. It is the basis of acoustic theory, and consists of linearizing the equations and taking the variations to be sinusoidal in time (see, e.g., [16–23] and references cited therein). Of particular interest for the present paper are results reported by de Waele et al. [21] and Mayzus et al. [22,23]. They assumed the thermal capacity of the matrix to be large compared with that of the gas. Starting from the full equations of fluid dynamics and using various simplifying assumptions, they showed that the equa-

Submitted to ASME for publication in the JOURNAL OF ENGINEERING FOR GAS TURBINES AND POWER. Manuscript received January 26, 2006; final manuscript received January 31, 2006. Review conducted by L. S. Langston.

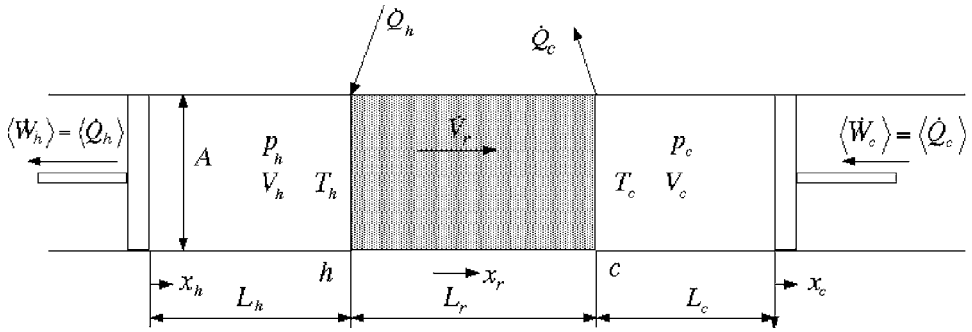

Fig. 1 Sketch of model used for Stirling engine. The high-temperature space is the expansion space, the low-temperature one is the compression space. L_r is the effective length of the void volume of the regenerator.

tion governing the pressure in the regenerator can be reduced to a modified Bessel equation. The solution of this equation yields all required properties in terms of Bessel functions.

In a recent paper [24], it was pointed out that power dissipation in the regenerator results in basic limitations on the performance of Stirling engines, and of all heat engines making use of the regenerative principle. This power dissipation is inherent in the principle of operation of such engines. Without the pressure differences leading to the dissipation, there would be no flow through the regenerator, and the engine would produce no power. The treatment was based on the harmonic approximation, and the volume of the gaseous phase of the regenerator (the "void volume") was assumed to be negligible. It was shown that optimization of the power output leads to a less than optimum thermal efficiency. There is a trade-off between power output and efficiency: higher efficiencies can be achieved at lower power outputs.

The present paper is an extension of the work described in [24]. The analysis is based on a model consisting of a regenerator connected to an expansion space and a compression space. Account is taken of the motion of the pistons, and of the influence of the void volume of the regenerator. The regenerator is assumed to be thermally perfect. The basic equations are given in dimensionless form (Sec. 2). Following the work of [21–23] and [25], the equation for the pressure in a regenerator with nonzero void volume is solved for the case of a linear temperature distribution (Appendix A). Expressions for the piston powers are derived as function of piston amplitude ratio and piston phase difference (Sec. 3). Knowledge of these powers yields the power output and the thermal efficiency. The power output is expressed as the product of a dimensional factor containing the amplitude of the piston on the compression side, and a dimensionless factor. The dimensional factor is taken to be a given constant. The dimensionless power output is optimized with respect to piston amplitude ratio and piston phase difference (Sec. 4 and Appendix B). The corresponding values of the thermal efficiency are determined. Analytical results are derived for optimum power output and corresponding efficiency in the limit of zero frequency (Appendix C). These results provide upper bounds on performance as function of regenerator void volume and ratio of temperatures across the regenerator. Results are also presented for optimized thermal efficiency and corresponding power output. Section 5 describes conclusions about upper bounds that can be drawn from the results obtained.

2 Basic Equations

The model used for the Stirling engine consists of a regenerator with pistons on each side (see Fig. 1). The temperatures at the ends of the regenerator are assumed to be maintained at T_h and T_c, respectively. The corresponding rates of heat flow in and out of these ends are $\dot{Q}_h$ and $\dot{Q}_c$. The model is one-dimensional; i.e., all radial variations are neglected. The regenerator is taken to be thermally perfect: its thermal capacity is assumed to be infinitely large, local temperature differences between regenerator and gas are assumed to be zero, and axial conduction in the regenerator is neglected. The conductance of the regenerator is taken to be finite, and account is taken of dissipation resulting from friction in the regenerator. All other loss mechanisms are neglected, including friction of the pistons and heat losses to the walls. The flow in the high- and low-temperature spaces is assumed to be isentropic and subsonic (Mach number $\ll 1$). The fluid is taken to be an ideal gas with a constant ratio of specific heats. For the sake of conciseness, the analysis is carried out using complex notation. All physical quantities are represented by the real parts of their corresponding complex expressions. Quantities are counted positive in the direction of the arrows shown in Fig. 1. Following earlier work [17–25], the equations are linearized. This permits finding closed form solutions that can be used to optimize power output or efficiency. In turn, this provides upper bounds on performance. The pressures in the expansion and compression spaces are represented by

$$p_h = \Delta p_h e^{i(\omega t+\delta_h)} + p_o \quad (\Delta p_h \ll p_o) \tag{1}$$

$$p_c = \Delta p_c e^{i(\omega t+\delta_c)} + p_o \quad (\Delta p_c \ll p_o) \tag{2}$$

The unperturbed pressure p_o is constant throughout the two spaces and the regenerator. Similarly, the positions of the pistons are given by the first-order quantities

$$x_h = \Delta x_h e^{i(\omega t+\phi_h)} \quad (\Delta x_h \ll L_h) \tag{3}$$

$$x_c = \Delta x_c e^{i(\omega t+\phi_c)} \quad (\Delta x_c \ll L_c) \tag{4}$$

The pressure variations in the expansion and compression spaces follow from the linearized isentropic relations

$$\frac{dp_h}{dt} = \frac{\gamma p_o}{V_h}\left[-\dot{V}_r(x_r=0) + A\frac{dx_h}{dt}\right] \tag{5}$$

$$\frac{dp_c}{dt} = \frac{\gamma p_o}{V_c}\left[\dot{V}_r(x_r=L_r) - A\frac{dx_c}{dt}\right] \tag{6}$$

The volume flow rate in the regenerator is taken to be proportional to the local pressure gradient

$$\dot{V}_r = -C_{xr}\frac{\partial p_r}{\partial x_r} \quad \text{(regenerator flow rate equation)} \tag{7}$$

The linearized continuity equation for flow in the regenerator can be written

$$\frac{A_r\rho_o}{k_r p_o}\frac{\partial p_r}{\partial t} + \frac{\partial(\rho_o \dot{V}_r)}{\partial x_r} = 0 \tag{8}$$

The assumption that the regenerator is thermally perfect implies that the polytropic constant $k_r=1$. The unperturbed density in the

regenerator follows from the ideal gas equation $\rho_o = p_o/(RT_o)$. The unperturbed temperature T_o is taken to be a given function of x_r (see Appendix A), and to be independent of time. Substituting Eq. (7) in Eq. (8) yields the equation governing the pressure distribution in the regenerator

$$\frac{1}{\rho_o}\frac{\partial}{\partial x_r}\rho_o\frac{\partial p_r}{\partial x_r} = \frac{A_r}{p_o C_{xr}}\frac{\partial p_r}{dt} \quad \text{(regenerator equation)} \tag{9}$$

The foregoing equations are cast in dimensionless form by setting

$$\xi = \frac{x_r}{L_r}, \quad \tau = \omega t, \quad \pi_h = \frac{\Delta p_h}{\Delta p_c}, \quad \delta = \delta_h - \delta_c,$$

$$\pi_r(\xi,\tau) = \frac{p_r(x,t) - p_o}{\Delta p_c e^{i\delta_c}}, \quad \alpha = \frac{p_o C_{xr}}{A_r L_r^2 \omega}, \quad \dot{\vartheta}_r = \frac{1}{A_r L_r \omega}\frac{p_o}{\Delta p_c e^{i\delta_c}}\dot{V}_r, \tag{10}$$

$$F = \frac{\omega V_c L_r}{\gamma p_o C_{xr}}, \quad K_{cr} = \frac{\gamma A_r L_r}{V_c}, \quad K_{hr} = \frac{\gamma A_r L_r}{V_h}, \quad K_{ch} = \frac{V_h}{V_c}$$

These dimensionless groups represent the following: ξ=distance along the regenerator, τ=time, π_h=ratio of pressure amplitudes in the expansion and compression spaces, δ=phase difference of pressures in the expansion and compression spaces, $\pi_r(\xi,\tau)$ =pressure in the regenerator, α=diffusion constant of the regenerator, $\dot{\vartheta}_r$=flow rate in the regenerator, F=frequency based on compression space volume and regenerator conductance, K_{cr} =effective ratio of regenerator void volume to compression space volume, K_{hr}=effective ratio of regenerator void volume to expansion space volume, K_{ch}=ratio of compression space volume to expansion space volume. For future reference, it is noted that $\alpha = 1/(K_{cr}F)$.

Application of Eqs. (10) to Eqs. (5)–(7) and (9) results in the following set of dimensionless equations

$$\frac{\gamma p_o A \Delta x_h e^{i\phi_h}}{V_h \Delta p_h e^{i\delta_h}} = 1 - i\frac{K_{hr}}{\pi_h e^{i\delta}}\dot{\vartheta}_{r,\xi=0}e^{-i\tau} \quad \text{(expansion space equation)} \tag{11}$$

$$\frac{\gamma p_o A \Delta x_c e^{i\phi_c}}{V_c \Delta p_c e^{i\delta_c}} = -1 - iK_{cr}\dot{\vartheta}_{r,\xi=1}e^{-i\tau} \quad \text{(compression space equation)} \tag{12}$$

$$\dot{\vartheta}_r = -\alpha\frac{\partial \pi_r}{\partial \xi} \quad \text{(regenerator flow rate equation)} \tag{13}$$

$$\frac{1}{\rho_o}\frac{\partial}{\partial \xi}\rho_o\frac{\partial \pi_r}{\partial \xi} = \frac{1}{\alpha}\frac{\partial \pi_r}{\partial \tau} \quad \text{(regenerator equation)} \tag{14}$$

The regenerator equation can only be solved if the temperature distribution $T_o(\xi)$ along the regenerator is known. In principle, $T_o(\xi)$ follows from the energy equation of the matrix. For the present simplified case this equation is left out of account, and the distribution needs to be assumed. Analytic solutions are available for the case of a linear temperature distribution, as well as for an exponential one [21–23,25]. The results for the two cases are quite similar. This indicates that the exact form of the temperature distribution is not of great importance. Here, the linear distribution is chosen. Its solution is reproduced in Appendix A, and yields

$$\dot{\vartheta}_{r,\xi=0} = \alpha(C_1 + C_2\pi_h e^{i\delta})e^{i\tau} \tag{15}$$

$$\dot{\vartheta}_{r,\xi=1} = \alpha(C_3 + C_4\pi_h e^{i\delta})e^{i\tau} \tag{16}$$

The parameters C_1, C_2, C_3, and C_4 are complex functions of the temperature ratio T_h/T_c and α. Their definitions are given in Appendix A. Substituting Eq. (15) in Eq. (11) yields

$$\frac{\Delta x_h e^{i\phi_h}}{\Delta p_h e^{i\delta_h}} = \frac{V_h}{\gamma p_o A}\left[1 - iK_{hr}\alpha\left(\frac{C_1}{\pi_h e^{i\delta}} + C_2\right)\right] \tag{17}$$

Similarly, substituting Eq. (16) in Eq. (12) yields

$$\frac{\Delta x_c e^{i\phi_c}}{\Delta p_c e^{i\delta_c}} = \frac{V_c}{\gamma p_o A}[-1 - iK_{cr}\alpha(C_3 + C_4\pi_h e^{i\delta})] \tag{18}$$

Taking the ratio of Eqs. (17) and (18) provides the ratio of piston amplitudes $\chi \equiv \Delta x_h/\Delta x_c$ and the piston phase difference $\phi \equiv \phi_h - \phi_c$ in terms of $\pi_h e^{i\delta}$

$$\frac{\Delta x_h e^{i\phi_h}}{\Delta x_c e^{i\phi_c}} \equiv \chi e^{i\phi} = \frac{K_{ch}\pi_h e^{i\delta} - iK_{cr}\alpha(C_1 + C_2\pi_h e^{i\delta})}{-1 - iK_{cr}\alpha(C_3 + C_4\pi_h e^{i\delta})} \tag{19}$$

Conversely, $\pi_h e^{i\phi}$ is given in terms of the piston parameters χ and ϕ by

$$\pi_h e^{i\delta} = \frac{\chi e^{i\phi}(F + iC_3) - iC_1}{-i\chi e^{i\phi}C_4 - FK_{ch} + iC_2} \tag{20}$$

3 Power and Thermal Efficiency

The rate of work obtained from the expansion piston is given by

$$\langle \dot{\tilde{W}}_h \rangle = -\langle (p_h - p_o) A dx_h/dt \rangle = -\langle (p_h - p_o)\dot{V}_r(x_r = 0) \rangle \tag{21}$$

Here, each factor in the expressions between brackets is the real part of its complex representation. The second equality follows from multiplying both sides of Eq. (5) by $\mathrm{Re}(p_h - p_o)$ and integrating over a cycle. Working out the right-hand side of Eq. (21) results in

$$\langle \dot{\tilde{W}}_h \rangle = -\left\langle \Delta p_h \cos(\tau + \delta_h)\frac{C_{xr}}{L_r\alpha}\,\mathrm{Re}(\Delta p_c e^{i\delta_c}\dot{\vartheta}_{r,\xi=0}) \right\rangle$$

$$= -\frac{1}{2}\frac{C_{xr}}{L_r}(\Delta p_h)^2\,\mathrm{Re}\left(\frac{C_1}{\pi_h e^{i\delta}} + C_2\right) \tag{22}$$

Similarly, the rate of work delivered to the compression piston is

$$\langle \dot{\tilde{W}}_c \rangle = -\left\langle \Delta p_c \cos(\tau + \delta_c)\frac{C_{xr}}{L_r\alpha}\,\mathrm{Re}(\Delta p_c e^{i\delta_c}\dot{\vartheta}_{r,\xi=1}) \right\rangle$$

$$= -\frac{1}{2}\frac{C_{xr}}{L_r}(\Delta p_c)^2\,\mathrm{Re}(C_3 + C_4\pi_h e^{i\delta}) \tag{23}$$

The net power obtained thus is

$$\langle \dot{\tilde{P}} \rangle = \langle \dot{\tilde{W}}_h \rangle - \langle \dot{\tilde{W}}_c \rangle = \frac{1}{2}\frac{C_{xr}}{L_r}\left(\frac{\Delta x_c \gamma p_o A}{V_c}\right)^2 P \tag{24}$$

where the dimensionless power output P is given by

$$P = \frac{F}{a^2 + b^2}(K_{ch}\pi_h^2 c - b) \tag{25}$$

$$a = -1 + K_{cr}\alpha\,\mathrm{Im}(C_3 + C_4\pi_h e^{i\delta}) \tag{26}$$

$$b = -K_{cr}\alpha\,\mathrm{Re}(C_3 + C_4\pi_h e^{i\delta}) \tag{27}$$

$$c = -K_{hr}\alpha\,\mathrm{Im}\left(\frac{C_1}{\pi_h e^{i\delta}} + C_2\right) \tag{28}$$

The thermal efficiency is given by

$$\eta \equiv 1 - \langle \dot{\tilde{W}}_c \rangle / \langle \dot{\tilde{W}}_h \rangle = 1 - \frac{b}{K_{ch}\pi_h^2 c} \tag{29}$$

4 Maximum Power and Maximum Efficiency

Equations (25) and (29) in combination with Eq. (20) can be used to find the power output P and the efficiency η as function of the ratio of piston amplitudes $\chi \equiv \Delta x_h/\Delta x_c$ for given piston phase

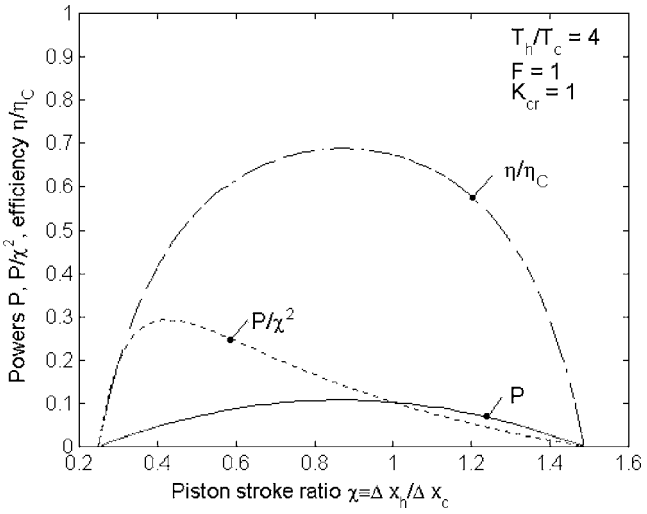

Fig. 2 Nondimensional power outputs P, P/χ^2 and thermal efficiency η/η_C as function of piston amplitude ratio $\chi \equiv \delta x_h/\delta x_c$ for the case $T_h/T_c=4$, $F=1$, $K_{cr}=1$. ϕ was chosen to optimize P.

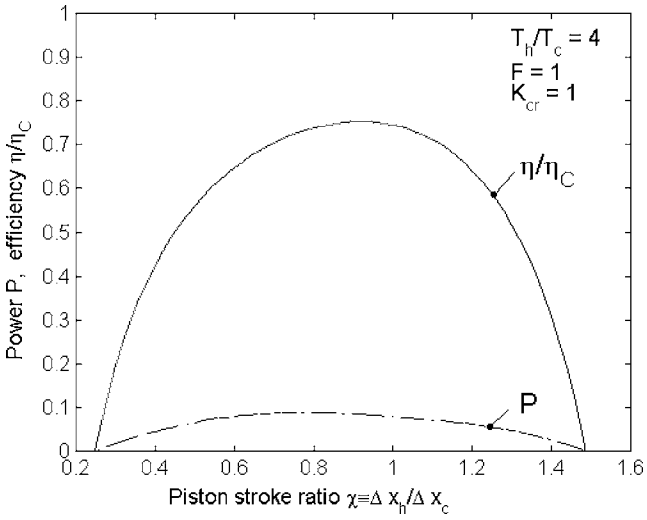

Fig. 3 Nondimensional power output P and thermal efficiency η/η_C as function of piston amplitude ratio $\chi \equiv \delta x_h/\delta x_c$ for the case $T_h/T_c=4$, $F=1$, $K_{cr}=1$. ϕ was chosen to optimize η/η_C.

difference $\phi \equiv \phi_h - \phi_c$. A typical result is shown in Fig. 2. In obtaining this figure, ϕ was chosen so as to optimize P (solid line). The optimization was accomplished by numerically solving Eq. (B6). The temperature ratio T_h/T_c was chosen equal to 4 as a representative value. In these and all following results, K_{ch} was taken equal to 1. Figure 2 shows that in this particular case, maximum dimensionless power output and maximum efficiency both occur at $\chi \equiv \Delta x_h/\Delta x_c$ near 1. The maximum efficiency in this case is about 0.7.

The dimensionless power output P corresponds to the case of given amplitude Δx_c of the compression piston (see Eq. (24)). An alternative way of defining dimensionless power output would be to take Δx_h rather than Δx_c to be the given constraint. This means replacing Δx_c in the dimensional part of Eq. (24) by Δx_h. The dimensional part then is increased by the factor χ^2, the dimensionless part is divided by the same factor, thus leaving the physical power output unchanged. The curve for P/χ^2 is included in Fig. 2. It has a maximum of about 0.3 at $\chi \equiv \Delta x_h/\Delta x_c \approx 0.4$. This maximum is attained by increasing Δx_c by a factor of about 2.5 while keeping Δx_h constant. The value of η/η_c corresponding to this maximum is only about 0.45. On the other hand, if both Δx_c and Δx_h are increased by a factor of about 2.5 (keeping $\chi \approx 1$), the maximum physical power output increases by a factor of about 2.5^2. Under this scenario, the efficiency η/η_c remains at about 0.7. This example illustrates that the constraint of given Δx_c leads to more desirable outcomes than does the one of given Δx_h. Therefore, only the former constraint is considered in the remainder of the paper.[1]

Results obtained when ϕ is chosen so as to optimize η/η_C instead of P are shown in Fig. 3. They are obtained by numerically solving Eq. (B14) instead of Eq. (B6). The results are seen to be similar to those of Fig. 2. The curve for η/η_c in Fig. 3 is only slightly higher than the corresponding curve in Fig. 2, and the curve for P is only slightly lower than that in Fig. 2.

Figures 2 and 3 represent the special case $F=1$ and $K_{cr}=1$. In order to investigate the influence of these parameters on performance, the maximum value of the power output was obtained by optimizing P given by Eq. (25) with respect to both χ and ϕ. This involved the numerical solution of two equations with χ and ϕ as the two unknowns (Eqs. (B6) and (B11)). Results for $P_{\max}$ at $T_h/T_c=4$ are plotted in Fig. 4 as function of F for various values of K_{cr}. Also shown are the corresponding values of the efficiency η^*/η_C (superscript "*" denotes quantities that correspond to optimized power output $P_{\max}$). The limiting value of $P_{\max}$ at $F=0$, $K_{cr}=0$ is given by $(T_h/T_c-1)^2/[2(T_h/T_c)(T_h/T_c+1)]$, which equals 9/40 at $T_h/T_c=4$ (Eq. (C24)). The value of $P_{\max}$ at $F=0$ decreases significantly as K_{cr} increases. The limiting value of the efficiency η^*/η_C at $T_h/T_c=4$ equals $1/(1+T_c/T_h)=4/5$ for all values of K_{cr} (Eq. (C25)). For $K_{cr}>0$, all curves decrease as frequency increases. The decreases are faster for larger values of K_{cr}. The physical explanation for this effect is that larger K_{cr} and larger F lead to less effective transmission of pressure waves across the regenerator.

The limiting values at $F=0$ constitute upper bounds on performance as function of K_{cr}. Expressions for these bounds are derived in Appendix C, and results are shown in Fig. 5. Both power

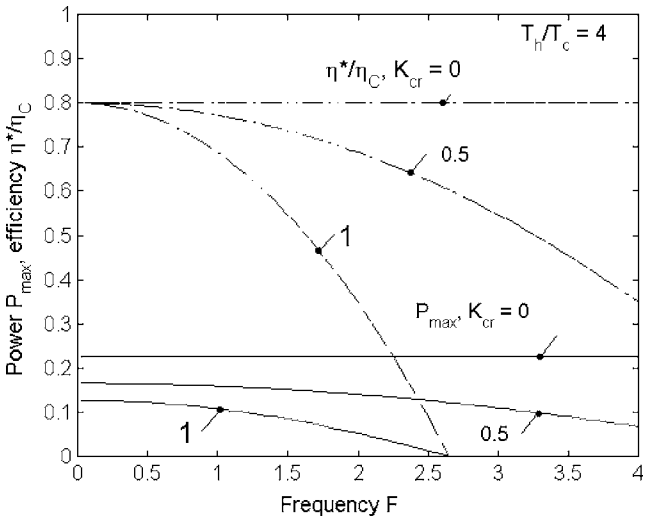

Fig. 4 Nondimensional power output P_{max} and corresponding thermal efficiency η^*/η_C as function of frequency F, at several values of regenerator void volume K_{cr}

[1] In [24], the amplitude of the pressure on the expansion side was taken to be given. The efficiency corresponding to maximum nondimensional power output then was shown to be half of the Carnot efficiency. If, instead, the amplitude of the pressure on the compression side is taken to be given, the efficiency corresponding to maximum nondimensional power output is considerably higher. This is analogous to the present situation with respect to taking either Δx_h or Δx_c to be given.

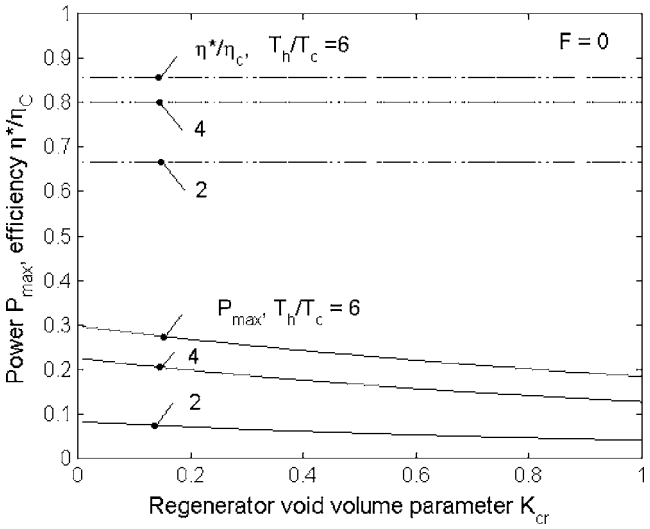

Fig. 5 Upper bounds for power output P_{max} and corresponding thermal efficiency η^*/η_C as function of regenerator void volume parameter K_{cr}

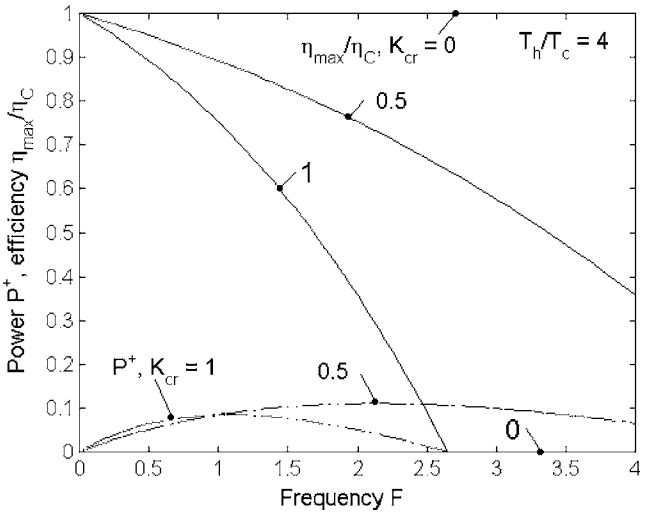

Fig. 7 Thermal efficiency η_{max}/η_C and corresponding power output P^+ as function of frequency F, at several values of relative regenerator void volume K_{cr}

output and thermal efficiency increase with temperature ratio. The increases in power output are seen to be quite pronounced.

Curves for χ^* and ϕ^* corresponding to optimized power output P_{max} are shown in Fig. 6. The value of ϕ^* equals $-\pi/2$ at $F=0$, and gradually decreases as F increases. The values of χ^* are slightly less than 1 over most of the frequency range. However, as F goes to zero, χ^* goes to ∞.

Figures 4–6 represent results obtained by optimizing P with respect to χ and ϕ. The corresponding values of efficiency η are below their possible maximum values η_{max}. Results for η_{mac} were obtained by optimizing η given by Eq. (29) with respect to both χ and ϕ. This involved solving Eqs. (B14) and (B17) for χ and ϕ. Curves for the resulting η_{max} at $T_h/T_c=4$ are plotted in Fig. 7. Also shown are the corresponding values P^+ of the power output (superscript "+" denotes quantities corresponding to optimized efficiency η_{max}). At $K_{cr}=0$, $\eta_{max}/\eta_C=1$ and $P^+=0$ for all frequencies F. Comparison with Fig. 4 shows that optimizing efficiency η rather than power output P leads to somewhat higher values of efficiency, but to considerably lower values of power output at low frequencies.

A geometry of practical interest is that in which the ratio χ of piston amplitudes equals 1. Values for P and η at $\chi=1$ as function of frequency F are shown in Fig. 8. The value of ϕ at each F was chosen so as to optimize P. This involved solving Eq. (B6) with $\chi=1$. For each nonzero value of K_{cr}, there is only a limited range of frequencies over which power output and efficiency are positive. Within this range, the power output has a maximum, while the efficiency always decreases as frequency increases. At low frequencies, the power output approaches zero as a result of the restriction $\chi=1$ (compare Fig. 6). As in Fig. 4, both power output and efficiency decrease markedly as K_{cr} increases.

All of the previous results are based on the realistic case of finite regenerator conductivity C_{xr}/L_r. In the limit of infinite regenerator conductivity, the dimensionless frequency F becomes zero, while the product $FC_{xr}/L_r=\omega V_c/(\gamma p_o)$ remains finite. In this case the power output of Eq. (24) can be rewritten as

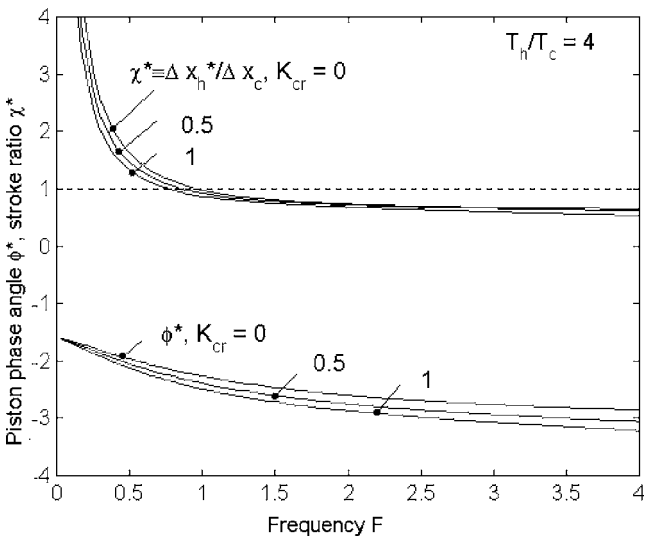

Fig. 6 Piston amplitude ratio χ^* and phase difference ϕ^* as function of frequency F, at $P=P_{max}$

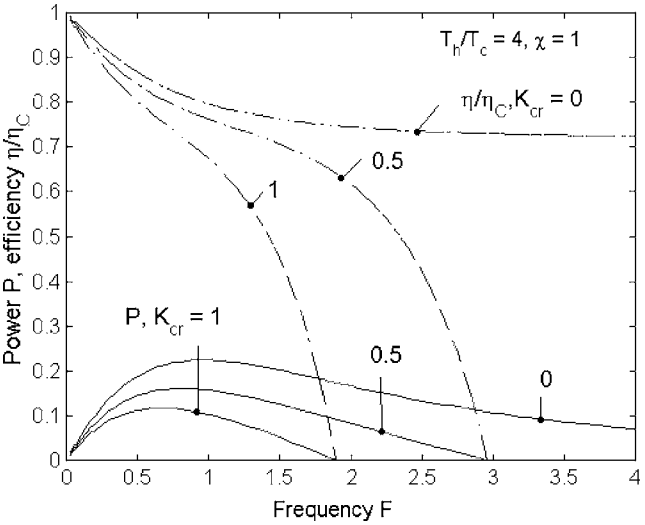

Fig. 8 Thermal efficiency η/η_C and power output P as function of frequency F, at piston amplitude ratio $\chi=1$, for several values of relative regenerator void volume K_{cr}

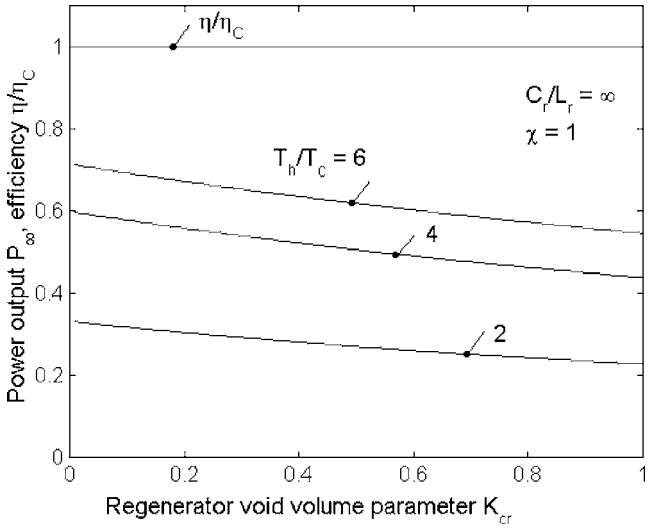

Fig. 9 Power output P_∞ and thermal efficiency η/η_C as function of K_{cr}, at infinite regenerator conductivity C_{xr}/L_r and piston amplitude ratio $\chi=1$

$$\langle \dot{\tilde{P}} \rangle = \frac{1}{2}\frac{\omega V_c}{\gamma p_o}\left(\frac{\Delta x_c \gamma p_o A}{V_c}\right)^2 P_\infty \tag{30}$$

where the dimensionless power output P_∞ is given by

$$P_\infty = \frac{(K_{ch}\pi_h^2 c - b)}{a^2 + b^2} \tag{31}$$

The latter quantity is plotted in Fig. 9 as function of the regenerator void volume parameter K_{cr}, for $\chi=1$ and various values of the temperature ratio T_h/T_c. The value of ϕ at each K_{cr} was chosen so as to optimize P_∞. Also plotted is the corresponding value of η/η_c, which equals 1 in the limit of infinite regenerator conductivity. This illustrates that the losses in efficiency found previously are due to friction inside the regenerator.

As stated in Sec. 1, the regenerator was taken to be thermally perfect. In this idealized case, there still are losses due to irreversible heat transfer at the regenerator ends. However, these "interface losses" are of second order, and hence do not manifest themselves in a linearized theory [20,26].

5 Conclusions

The performance of a Stirling engine was analyzed taking account of dissipation in the regenerator, while neglecting all other losses. The power output was expressed as the product of a dimensional factor and a nondimensional factor P. The dimensional factor contains the amplitude Δx_c of the compression piston, which was considered a given constraint. Both the nondimensional power output P and the thermal efficiency η depend on the piston amplitude ratio χ and the piston phase difference ϕ. This dependence is illustrated in Figs. 2 and 3 for the particular case of frequency $F=1$, regenerator void volume parameter $K_{cr}=1$, and regenerator temperature ratio $T_h/T_c=4$. The difference between the two figures is that ϕ is chosen to optimize P in Fig. 2, and to optimize η in Fig. 3. There is little difference between the two figures. Both P and η achieve their maximum values at $\chi \approx 1$in this particular case. Curves for the maximum possible values of P as function of F for various values of K_{cr} are given in Fig. 4. The value of $P_{\max}$ at $K_{cr}=0$ is given by $(T_h/T_c-1)^2/[2(T_h/T_c)(T_h/T_c+1)]$, which equals 9/40 for $T_h/T_c=4$. Increases of K_{cr} cause significant decreases in $P_{\max}$. These decreases are most pronounced at higher frequencies F. There is no positive power output beyond certain values of F. Figure 4 also shows curves for the corresponding values of thermal efficiency η^*/η_C. At $K_{cr}=0$, $\eta^*/\eta_C = 1/(1+T_c/T_h)$. This result equals 4/5 for $T_h/T_c=4$, and is independent of frequency F. For $K_{cr}>0$, the values of η^*/η_C decrease with increasing F. The decreases are more pronounced at larger values of K_{cr}. It follows that the results at $F=0$ represent upper bounds for the power output. Expressions for these upper bounds as function of K_{cr} and T_h/T_c were derived using the perturbation analysis presented in Appendix C (see Eq. (C24)). Results are shown Fig. 5. The bounds increase strongly with increasing T_h/T_c, and decrease slowly with increasing K_{cr}. Also shown in Fig. 5 are corresponding curves for the efficiency η^*/η_C. The latter also increase with T_h/T_c, but they are independent of K_{cr}.

The values of the ratio of piston amplitudes $\chi^* \equiv \Delta x_h^*/\Delta x_c$ and the piston phase difference $\phi^* \equiv \phi_h^* - \phi_c$ corresponding to the maximum power outputs of Fig. 4 are shown in Fig. 6. The value of χ^* is slightly below 1 over most of the frequency range, but goes to infinity as F approaches 0. This means that the upper bounds for power output shown in Fig. 5 require an infinitely large ratio of piston amplitudes, and hence are out of reach in any practical sense.

Results analogous to Fig. 4 but with optimized η instead of optimized P are shown in Fig. 7. As frequency F goes to zero, the efficiency $\eta_{\max}/\eta_C$ goes to its ideal value of 1, and the power output P^* goes to zero. The curves for $\eta_{\max}/\eta_C$ are somewhat higher than the corresponding ones in Fig. 4. The curves for P^* in Fig. 7 are considerably below the corresponding one for $P_{\max}$ in Fig. 4.

Figure 8 shows η/η_C and P for the case $T_h/T_c=4$ with piston amplitude ratio $\chi=1$. In computing these results, the value of ϕ was chosen so as to optimize P. In the limit of zero frequency, the power output P equals zero and the efficiency η/η_C equals 1. For each value of K_{cr}, there is a value of frequency F at which the power output is maximum. The values of η/η_C at this frequency are on the order of 0.8.

All of the results obtained are based on the realistic case of finite regenerator conductance C_{xr}/L_r. In the limit $C_{xr}/L_r \to \infty$, the formulation of the problem needs to be reconsidered. In this limit, the thermal efficiency equals the Carnot efficiency. This illustrates that the losses in efficiency found for finite C_{xr}/L_r are due to friction in the regenerator.

The results obtained represent upper bounds on power output and efficiency. The bounds apply to all heat engines using a regenerator. Taking account of these bounds can provide a standard of comparison in assessing the performance such heat engines.

Left out of account here are nonlinear effects, as well as losses associated with heat transfer over finite temperature differences in the regenerator. These losses will cause decreases in performance beyond those described here. Their inclusion is not within the scope of the present paper.

Nomenclature

A = cross-sectional area (m^2)
a,b,c = see Eqs. (26)–(28)
a_i,b_i,c_i = $i=1$–6; see Appendix C
C_{xr} = conductance with respect to pressure gradient (m^5s/kg)
C_i = $i=1$–4, complex functions of T_h/T_c and α; Appendix A and B
F = dimensionless frequency; Eq. (10)
K_{ch} = $V_h/(V_c)$
K_{cr} = $\gamma A L_r/(V_c)$
K_{hr} = $\gamma A L_r/(V_h)$
k = polytropic constant
L = distance (m)
P = nondimensional power
$\dot{\tilde{P}}$ = power (W)
p_o = average pressure (Pa)

p = pressure (Pa)
$\dot{Q}$ = rate of heat flow (W)
T = temperature (K)
t = time (s)
V = volume (m^3)
$\dot{V}$ = volume flow rate (m^3/s)
$\dot{\tilde{W}}$ = rate of work done (W)
X = dimensionless pressure distribution in regenerator; Eq. (A1)
x_r = axial coordinate in regenerator (m)
x, y, x = see Eq. (C16)
$\langle\rangle$ = denotes average over a cycle

Greek Symbols

α = dimensionless diffusivity; equals $1/(K_{cr}F)$
γ = ratio of specific heats; equals 5/3 for a noble gas
Δ = denotes amplitude of first order quantity
δ = pressure phase difference, $\delta_h - \delta_c$
δ_h, δ_c = phase angles of pressures; Eqs. (1) and (2)
η = thermal efficiency
η_C = Carnot thermal efficiency, $1 - T_c/T_h$
$\dot{\vartheta}$ = dimensionless flow rate; Eq. (10)
λ = $-\xi + T_h/\Delta T$
ξ = dimensionless axial coordinate; Eq. (10)
π_h = ratio of pressure amplitudes, $\Delta p_h/\Delta p_c$
π_r = dimensionless pressure in regenerator; Eq. (10)
ρ = density (kg/m^3)
τ = ωt, nondimensional time
ϕ = piston phase difference, $\phi_h - \phi_c$
ϕ_h, ϕ_c = phase angles of pistons; Eqs. (3) and (4)
χ = ratio of piston amplitudes, $\Delta x_h/\Delta x_c$
ω = angular frequency (s^{-1})

Subscripts

C = Carnot
c = cold; compression space
h = hot; expansion space
max = maximum
o = unperturbed
r = regenerator

Superscripts

$\sim$ = denotes dimensional quantity
$*$ = denotes quantities corresponding to $P_{\max}$
$+$ = denotes quantities corresponding to $\eta_{\max}$

Appendix A: Results for Regenerator

Upon setting

$$\pi_r(\xi,\tau) = X(\xi)e^{i\tau} \tag{A1}$$

the spatial part of the Eq. (14) becomes

$$\frac{d^2X}{d\xi^2} + \frac{1}{\rho_o}\frac{d\rho_o}{d\xi}\frac{dX}{d\xi} = \frac{i}{\alpha}X \tag{A2}$$

For a linear temperature distribution in the regenerator

$$T_o(\xi) = T_h - \Delta T\xi \tag{A3}$$

where $\Delta T \equiv T_h - T_c$. Use of the ideal gas equation $\rho_o = p_o/(RT_o)$ (where p_o is a constant) then provides

$$\frac{1}{\rho_o}\frac{d\rho_o}{d\xi} = \frac{1}{-\xi + T_h/\Delta T} \tag{A4}$$

The regenerator pressure $p_r(x_r = L_r, \tau)$ at the cold side must equal the compression chamber pressure $p_c(\tau)$. This provides the boundary condition $X(\xi=1)=1$. Similarly, $p_r(x_r=0,\tau)$ must equal the expansion chamber pressure $p_h(\tau)$, which provides the second boundary condition $X(\xi=0)=\pi_h e^{i\delta}$. The solution of Eq. (A2) under these boundary conditions is

$$X(\xi) = C_+\zeta_+H_1^{(1)}(\zeta_+) + C_-\zeta_-H_1^{(1)}(\zeta_-) \tag{A5}$$

where

$$\zeta_\pm \equiv \pm\left(-\xi + \frac{T_h}{\Delta T}\right)\frac{e^{-i\pi/4}}{\sqrt{\alpha}} \tag{A6}$$

$$C_+ = (B_{1h} - B_{1c}\pi_h e^{i\delta})/D, \quad C_- = (A_{1c}\pi_h e^{i\delta} - A_{1h})/D \tag{A7}$$

$$D = A_{1c}B_{1h} - A_{1h}B_{1c} \tag{A8}$$

$$A_{1c} = \zeta_c H_1^{(1)}(\zeta_c), \quad B_{1c} = -\zeta_c H_1^{(1)}(-\zeta_c) \tag{A9}$$

$$A_{1h} = \zeta_h H_1^{(1)}(\zeta_h), \quad B_{1h} = -\zeta_h H_1^{(1)}(-\zeta_h) \tag{A10}$$

$$\zeta_c = (T_c/\Delta T)e^{-i\pi/4}/\sqrt{\alpha}, \quad \zeta_h = (T_h/\Delta T)e^{-i\pi/4}\sqrt{\alpha} \tag{A11}$$

$H_1^{(1)}$ is the first Hankel function of first order. The two terms in Eq. (A5) represent pressure waves originating at the two ends of the regenerator, respectively. The amplitudes of these waves decay in an exponential fashion.

Using Eqs. (13), (A1), and (A5), it is found that

$$\dot{\vartheta}_r = -\alpha\frac{dX}{d\xi}e^{i\tau} = \sqrt{\alpha}e^{i(\tau-\pi/4)}[C_+\zeta_+H_0^{(1)}(\zeta_+) - C_-\zeta_-H_0^{(1)}(\zeta_-)] \tag{A12}$$

where $H_0^{(1)}$ is the first Hankel function of zero order, and where use was made of the relation

$$\frac{d}{dz}[zH_1^{(1)}(z)] = zH_0^{(1)}(z)$$

([27], Section 3.60, Eq. (9)). It follows from Eq. (A12) that the dimensionless flow rates at the two sides of the regenerator are given by

$$\dot{\vartheta}_{r,\xi=0} = \alpha(C_1 + C_2\pi_h e^{i\delta})e^{i\tau}, \quad \dot{\vartheta}_{r,\xi=1} = \alpha(C_3 + C_4\pi_h e^{i\delta})e^{i\tau} \tag{A13}$$

where

$$C_1 = (A_{oh}B_{1h} - A_{1h}B_{oh})/D, \quad C_2 = (-A_{oh}B_{1c} + A_{1c}B_{oh})/D \tag{A14}$$

$$C_3 = (A_{oc}B_{1h} - A_{1h}B_{oc})/D, \quad C_4 = (-A_{oc}B_{1c} + A_{1c}B_{oc})/D \tag{A15}$$

$$A_{oc} = \frac{e^{-i\pi/4}}{\sqrt{\alpha}}\zeta_c H_0^{(1)}(\zeta_c), \quad B_{oc} = \frac{e^{-i\pi/4}}{\sqrt{\alpha}}\zeta_c H_0^{(1)}(-\zeta_c) \tag{A16}$$

$$A_{oh} = \frac{e^{-i\pi/4}}{\sqrt{\alpha}}\zeta_h H_0^{(1)}(\zeta_h), \quad B_{oh} = \frac{e^{-i\pi/4}}{\sqrt{\alpha}}\zeta_h H_0^{(1)}(-\zeta_h) \tag{A17}$$

The quantities C_1, C_2, C_3, and C_4 all are known once the values of T_h/T_c, K_{cr}, and F have been specified.

Equivalent results for these quantities are available for the case of an exponential temperature distribution in the regenerator [25]. The performance characteristics for the linear and exponential temperature distributions are quite similar [22,25].

Appendix B: Optimization Procedures

In optimizing P and η with respect to χ and ϕ, it is convenient to write

$$\pi_h e^{i\delta} = \frac{A + iB}{C + iD} \tag{B1}$$

It follows from Eq. (20) that

$$A(\chi,\phi) = \chi\cos\phi[F - \mathrm{Im}(C_3)] - \chi\sin\phi\,\mathrm{Re}(C_3) + \mathrm{Im}(C_1) \tag{B2}$$

$$B(\chi,\phi) = \chi\cos\phi\,\mathrm{Re}(C_3) + \chi\sin\phi[F - \mathrm{Im}(C_3)] - \mathrm{Re}(C_1) \tag{B3}$$

$$C(\chi,\phi) = \chi\cos\phi\,\mathrm{Im}(C_4) + \chi\sin\phi\,\mathrm{Re}(C_4) - FK_{ch} - \mathrm{Im}(C_2) \tag{B4}$$

$$D(\chi,\phi) = -\chi\cos\phi\,\mathrm{Re}(C_4) + \chi\sin\phi\,\mathrm{Im}(C_4) + \mathrm{Re}(C_2) \tag{B5}$$

Optimization of $P(\chi,\phi)$ given by Eqs. (25)–(28) and (20) with respect to ϕ for given χ requires finding ϕ by solving the equation

$$\left.\frac{\partial P(\chi,\phi)}{\partial\phi}\right|_\chi = \left.\frac{\partial P}{\partial\pi_h}\right|_\delta \left.\frac{\partial\pi_h}{\partial\phi}\right|_\chi + \left.\frac{\partial P}{\partial\delta}\right|_{\pi_h} \left.\frac{\partial\delta}{\partial\phi}\right|_\chi = 0 \tag{B6}$$

where

$$\left.\frac{\partial P}{\partial\pi_h}\right|_\delta = \frac{1}{(a^2+b^2)^2}\{(a^2+b^2)[\mathrm{Re}(C_1e^{-i\delta}) + 2FK_{ch}\pi_h c] + (a^2 - b^2 + 2K_{ch}\pi_h^2 bc)\,\mathrm{Re}(C_4e^{i\delta}) - 2a(K_{ch}\pi_h^2 c - b)\,\mathrm{Im}(C_4e^{i\delta})\} \tag{B7}$$

$$\left.\frac{\partial P}{\partial\delta}\right|_{\pi_h} = \frac{\pi_h}{(a^2+b^2)^2}[-(a^2+b^2)\mathrm{Im}(C_1e^{-i\delta}) - 2a(K_{ch}\pi_h^2 c - b)\,\mathrm{Re}(C_4e^{i\delta}) + (-a^2+b^2-2K_{ch}\pi_h^2 bc)\mathrm{Im}(C_4e^{i\delta})], \tag{B8}$$

$$\left.\frac{\partial\pi_h}{\partial\phi}\right|_\chi = \frac{1}{(C^2+D^2)^2\pi_h}\left[(C^2+D^2)\left(A\frac{\partial A}{\partial\phi} + B\frac{\partial B}{\partial\phi}\right) - (A^2+B^2)\times\left(C\frac{\partial C}{\partial\phi} + D\frac{\partial D}{\partial\phi}\right)\right] \tag{B9}$$

$$\left.\frac{\partial\delta}{\partial\phi}\right|_\chi = -\frac{B}{A^2+B^2}\frac{\partial A}{\partial\phi} + \frac{A}{A^2+B^2}\frac{\partial B}{\partial\phi} + \frac{D}{C^2+D^2}\frac{\partial C}{\partial\phi} - \frac{C}{C^2+D^2}\frac{\partial D}{\partial\phi} \tag{B10}$$

After ϕ has been found for the specified value of χ, all quantities of interest follow directly.

Similarly, optimization of $P(\chi,\phi)$ with respect to χ for given ϕ requires solving the equation

$$\left.\frac{\partial P(\chi,\phi)}{\partial\chi}\right|_\phi = \left.\frac{\partial P}{\partial\pi_h}\right|_\delta \left.\frac{\partial\pi_h}{\partial\chi}\right|_\phi + \left.\frac{\partial P}{\partial\delta}\right|_{\pi_h} \left.\frac{\partial\delta}{\partial\chi}\right|_\phi = 0 \tag{B11}$$

where

$$\left.\frac{\partial\pi_h}{\partial\chi}\right|_\phi = \frac{1}{(C^2+D^2)^2\pi_h}\left[(C^2+D^2)\left(A\frac{\partial A}{\partial\chi} + B\frac{\partial B}{\partial\chi}\right) - (A^2+B^2)\times\left(C\frac{\partial C}{\partial\chi} + D\frac{\partial D}{\partial\chi}\right)\right] \tag{B12}$$

$$\left.\frac{\partial\delta}{\partial\chi}\right|_\phi = -\frac{B}{A^2+B^2}\frac{\partial A}{\partial\chi} + \frac{A}{A^2+B^2}\frac{\partial B}{\partial\chi} + \frac{D}{C^2+D^2}\frac{\partial C}{\partial\chi} - \frac{C}{C^2+D^2}\frac{\partial D}{\partial\chi} \tag{B13}$$

Optimization of $\eta(\chi,\phi)$ given by Eqs. (29) and (20) with respect to ϕ for given χ requires finding ϕ by solving

$$\left.\frac{\partial\eta(\chi,\phi)}{\partial\phi}\right|_\chi = \left.\frac{\partial\eta}{\partial\pi_h}\right|_\delta \left.\frac{\partial\pi_h}{\partial\phi}\right|_\chi + \left.\frac{\partial\eta}{\partial\delta}\right|_{\pi_h} \left.\frac{\partial\delta}{\partial\phi}\right|_\chi = 0 \tag{B14}$$

where

$$\left.\frac{\partial\eta}{\partial\pi_h}\right|_\delta = \frac{1}{K_{ch}F\pi_h^2}\left[\frac{2bF}{c\pi_h} + \frac{1}{c}\,\mathrm{Re}(C_4e^{i\delta}) + \frac{b}{K_{ch}c^2\pi_h^2}\,\mathrm{Re}(C_1e^{-i\delta})\right] \tag{B15}$$

$$\left.\frac{\partial\eta}{\partial\delta}\right|_{\pi_h} = -\frac{1}{K_{ch}F\pi_h^2c^2}\left[c\pi_h\,\mathrm{Im}(C_4e^{i\delta}) + \frac{b}{K_{ch}\pi_h}\,\mathrm{Im}(C_1e^{-i\delta})\right] \tag{B16}$$

Finally, optimization of $\eta(\chi,\phi)$ with respect to χ for given ϕ requires finding χ by solving

$$\left.\frac{\partial\eta(\chi,\phi)}{\partial\chi}\right|_\phi = \left.\frac{\partial\eta}{\partial\pi_h}\right|_\delta \left.\frac{\partial\pi_h}{\partial\chi}\right|_\phi + \left.\frac{\partial\eta}{\partial\delta}\right|_{\pi_h} \left.\frac{\partial\delta}{\partial\chi}\right|_\phi = 0 \tag{B17}$$

Appendix C: Results for C_1, C_2, C_3 and C_4 in the Limit of Zero Frequency

The limit $F=0$ corresponds to $\alpha=\infty$. In order to derive analytic results in this limit, Eq. (A4)) is substituted in Eq. (A2), and the result is rewritten as

$$\frac{d^2X}{d\lambda^2} - \frac{1}{\lambda}\frac{dX}{d\lambda} = \frac{i}{\alpha}X \tag{C1}$$

where $\lambda \equiv -\xi + T_h/\Delta T$. To second order in $1/\alpha$, the solution of this equation under the boundary conditions $X(\lambda = T_h/\Delta T) = \pi_h e^{i\delta}$, $X(\lambda = T_c/\Delta T) = 1$ is

$$X(\lambda) = a_0 + a_2\lambda^2 + i\alpha^{-1}[b_0 + b_2\lambda^2 + b_{2\ell}\lambda^2\ln(\lambda) + b_4\lambda^4] + \alpha^{-2}[c_0 + c_2\lambda^2 + c_{2\ell}\lambda^2\ln(\lambda) + c_4\lambda^4 + c_{4\ell}\lambda^4\ln(\lambda) + c_6\lambda^6] \tag{C2}$$

where

$$a_0 = \frac{(T_h/T_c)^2 - \pi_h e^{i\delta}}{(T_h/T_c)^2 - 1}, \quad a_2 = \frac{1 - a_0}{(T_c/\Delta T)^2}, \quad b_4 = \frac{a_2}{8}, \quad b_{2\ell} = \frac{a_0}{2}$$

$$b_2 = -\frac{1}{(T_h/\Delta T)^2 - (T_c/\Delta T)^2}\left\{b_{2\ell}\left[\left(\frac{T_h}{\Delta T}\right)^2\ln\left(\frac{T_h}{\Delta T}\right) - \left(\frac{T_c}{\Delta T}\right)^2\ln\left(\frac{T_c}{\Delta T}\right)\right] + b_4\left[\left(\frac{T_h}{\Delta T}\right)^4 - \left(\frac{T_c}{\Delta T}\right)^4\right]\right\}$$

$$b_0 = -b_2\left(\frac{T_h}{\Delta T}\right)^2 - b_{2\ell}\left(\frac{T_h}{\Delta T}\right)^2\ln\left(\frac{T_h}{\Delta T}\right) - b_4\left(\frac{T_h}{\Delta T}\right)^4$$

$$c_6 = -\frac{b_4}{24}, \quad c_{4\ell} = -\frac{b_{2\ell}}{8}, \quad c_4 = -\frac{b_2}{8} - \frac{3c_{4\ell}}{4}, \quad c_{2\ell} = -\frac{b_0}{2}$$

$$c_2 = -\frac{1}{(T_h/\Delta T)^2 - (T_c/\Delta T)^2}\left\{c_{2\ell}\left[\left(\frac{T_h}{\Delta T}\right)^2\ln\left(\frac{T_h}{\Delta T}\right) - \left(\frac{T_c}{\Delta T}\right)^2\ln\left(\frac{T_c}{\Delta T}\right)\right] + c_4\left[\left(\frac{T_h}{\Delta T}\right)^4 - \left(\frac{T_c}{\Delta T}\right)^4\right] + c_{4\ell}\left[\left(\frac{T_h}{\Delta T}\right)^4\ln\left(\frac{T_h}{\Delta T}\right) - \left(\frac{T_c}{\Delta T}\right)^4\ln\left(\frac{T_c}{\Delta T}\right)\right] + c_6\left[\left(\frac{T_h}{\Delta T}\right)^6 - \left(\frac{T_c}{\Delta T}\right)^6\right]\right\}$$

$$c_0 = -c_2\left(\frac{T_h}{\Delta T}\right)^2 - c_{2\ell}\left(\frac{T_h}{\Delta T}\right)^2 \ln\left(\frac{T_h}{\Delta T}\right) - c_4\left(\frac{T_h}{\Delta T}\right)^4 - c_{4\ell}\left(\frac{T_h}{\Delta T}\right)^4 \ln\left(\frac{T_h}{\Delta T}\right) - c_6\left(\frac{T_h}{\Delta T}\right)^6 \tag{C3}$$

It follows from Eqs. (A13) that

$$C_1 + C_2\pi_h e^{i\delta} = dX/d\lambda\big|_{\lambda=T_h/\Delta T}, \quad C_3 + C_4\pi_h e^{i\delta} = dX/d\lambda\big|_{\lambda=T_c/\Delta T} \tag{C4}$$

Upon defining

$$C_j = C_{j0} + \alpha^{-1}C_{j1} + \alpha^{-2}C_{j2} + \cdots \quad (j=1,2,3,4) \tag{C5}$$

equating coefficients of terms without and with $\pi_h e^{i\delta}$ yields

$$C_{10} = \left(2a_2\frac{T_h}{\Delta T}\right)_{\pi_h e^{i\delta}=0} = \frac{-2T_h/T_c}{T_h/T_c+1}$$

$$C_{20} = \left(2a_2\frac{T_h}{\Delta T}\right)_{\pi_h e^{i\delta}=1} - C_{10} = \frac{2T_h/T_c}{T_h/T_c+1} \tag{C6}$$

$$C_{30} = \left(2a_2\frac{T_c}{\Delta T}\right)_{\pi_h e^{i\delta}=0} = \frac{-2}{T_h/T_c+1}$$

$$C_{40} = \left(2a_2\frac{T_c}{\Delta T}\right)_{\pi_h e^{i\delta}=1} - C_{30} = \frac{2}{T_h/T_c+1} \tag{C7}$$

$$C_{11} = \left\{2b_2\frac{T_h}{\Delta T} + b_{2\ell}\left[2\frac{T_h}{\Delta T}\ln\left(\frac{T_h}{\Delta T}\right) + \frac{T_h}{\Delta T}\right] + 4b_4\left(\frac{T_h}{\Delta T}\right)^3\right\}_{\pi_h e^{i\delta}=0} \tag{C8}$$

$$C_{21} = \left\{2b_2\frac{T_h}{\Delta T} + b_{2\ell}\left[2\frac{T_h}{\Delta T}\ln\left(\frac{T_h}{\Delta T}\right) + \frac{T_h}{\Delta T}\right] + 4b_4\left(\frac{T_h}{\Delta T}\right)^3\right\}_{\pi_h e^{i\delta}=1} - C_{11} \tag{C9}$$

$$C_{31} = \left\{2b_2\frac{T_c}{\Delta T} + b_{2\ell}\left[2\frac{T_c}{\Delta T}\ln\left(\frac{T_c}{\Delta T}\right) + \frac{T_c}{\Delta T}\right] + 4b_4\left(\frac{T_c}{\Delta T}\right)^3\right\}_{\pi_h e^{i\delta}=0} \tag{C10}$$

$$C_{41} = \left\{2b_2\frac{T_c}{\Delta T} + b_{2\ell}\left[2\frac{T_c}{\Delta T}\ln\left(\frac{T_c}{\Delta T}\right) + \frac{T_c}{\Delta T}\right] + 4b_4\left(\frac{T_c}{\Delta T}\right)^3\right\}_{\pi_h e^{i\delta}=1} - C_{31} \tag{C11}$$

$$C_{12} = \left\{2c_2\frac{T_h}{\Delta T} + c_{2\ell}\left[2\frac{T_h}{\Delta T}\ln\left(\frac{T_h}{\Delta T}\right) + \frac{T_h}{\Delta T}\right] + 4c_4\left(\frac{T_h}{\Delta T}\right)^3 + c_{4\ell}\left[4\left(\frac{T_h}{\Delta T}\right)^3\ln\left(\frac{T_h}{\Delta T}\right) + \left(\frac{T_h}{\Delta T}\right)^3\right] + 6c_6\left(\frac{T_h}{\Delta T}\right)^5\right\}_{\pi_h e^{i\delta}=0} \tag{C12}$$

$$C_{22} = \left\{2c_2\frac{T_h}{\Delta T} + c_{2\ell}\left[2\frac{T_h}{\Delta T}\ln\left(\frac{T_h}{\Delta T}\right) + \frac{T_h}{\Delta T}\right] + 4c_4\left(\frac{T_h}{\Delta T}\right)^3 + c_{4\ell}\left[4\left(\frac{Th}{\Delta T}\right)^3\ln\left(\frac{T_h}{\Delta T}\right) + \left(\frac{T_h}{\Delta T}\right)^3\right] + 6c_6\left(\frac{T_h}{\Delta T}\right)^5\right\}_{\pi_h e^{i\delta}=1} - C_{12} \tag{C13}$$

$$C_{32} = \left\{2c_2\frac{T_c}{\Delta T} + c_{2\ell}\left[2\frac{T_c}{\Delta T}\ln\left(\frac{T_c}{\Delta T}\right) + \frac{T_c}{\Delta T}\right] + 4c_4\left(\frac{T_c}{\Delta T}\right)^3 + c_{4\ell}\left[4\left(\frac{T_c}{\Delta T}\right)^3\ln\left(\frac{T_c}{\Delta T}\right) + \left(\frac{T_c}{\Delta T}\right)^3\right] + 6c_6\left(\frac{T_c}{\Delta T}\right)^5\right\}_{\pi_h e^{i\delta}=0} \tag{C14}$$

$$C_{42} = \left\{2c_2\frac{T_c}{\Delta T} + c_{2\ell}\left[2\frac{T_c}{\Delta T}\ln\left(\frac{T_c}{\Delta T}\right) + \frac{T_c}{\Delta T}\right] + 4c_4\left(\frac{T_c}{\Delta T}\right)^3 + c_{4\ell}\left[4\left(\frac{T_c}{\Delta T}\right)^3\ln\left(\frac{T_c}{\Delta T}\right) + \left(\frac{T_c}{\Delta T}\right)^3\right] + 6c_6\left(\frac{T_c}{\Delta T}\right)^5\right\}_{\pi_h e^{i\delta}=1} - C_{32} \tag{C15}$$

Because $\alpha = 1/(K_{cr}F)$, the preceding results are valid also in the limit $K_{cr}=0$ for any value of F.

The remainder of this appendix concerns the case $F=0$ for arbitrary K_{cr}. In order to optimize P given by Eq. (25) at $F=0$, we set

$$\pi_h = 1 + x/\alpha^2 + \text{h.o.}, \quad \delta = y/\alpha + z/\alpha^2 + \text{h.o.} \tag{C16}$$

(this choice is guided by numerical results). The factor between parentheses in Eq. (25) then becomes $(K_{cr}/\alpha)(N_0+N_1x)+\text{h.o.}$, where

$$N_0 = -y^2 - y(C_{11}+C_{41}) - C_{12} - C_{22} + C_{32} + C_{42}$$

$$N_1 = -2(T_h/T_c-1)/(T_h/T_c+1). \tag{C17}$$

The quantities a and b become

$$a = -1 + K_{cr}\left(\frac{2}{T_h/T_c+1}y + C_{31} + C_{41}\right) + \frac{1}{\alpha}C_{40}z + \text{h.o.} \tag{C18}$$

$$b = -\frac{1}{\alpha}K_{cr}\left[\frac{2}{T_h/T_c+1}\left(x - \frac{y^2}{2}\right) - yC_{41} + C_{42}\right] + \text{h.o.} \tag{C19}$$

Nonzero values of P in the limit $\alpha=\infty$ require $a=0$ to lowest order, and hence

$$y = \left(\frac{1}{K_{cr}} - C_{31} - C_{41}\right)\frac{T_h/T_c+1}{2} \tag{C20}$$

Optimization of P furthermore requires $z=0$. This leads to $a=0+O(1/\alpha^2)$, $b=(1/\alpha)(D_0+D_1x)$, where

$$D_0 = -K_{cr}\left(-\frac{1}{T_h/T_c+1}y^2 - yC_{41} + C_{32} + C_{42}\right)$$

$$D_1 = -K_{cr}\frac{2}{T_h/T_c+1} \tag{C21}$$

It follows that in the limit $\alpha=\infty$ for all K_{cr}

$$P = (N_0 + N_1x)/(D_0 + D_1x)^2 \tag{C22}$$

Optimization with respect to x yields

$$P_{\max} = \frac{N_1^2}{4D_1(N_1D_0 - N_0D_1)} \quad (F=0, \text{ all } K_{cr}) \tag{C23}$$

at $x^* = D_0/D_1 - 2N_0/N_1$. In the limit of zero regenerator void volume, this result reduces to

$$P_{\max} = (T_h/T_c-1)^2/[2(T_h/T_c)(T_h/T_c+1)] \quad (F=0, K_{cr}=0) \tag{C24}$$

Substituting the results obtained for x, y, and z in Eq. (29) for the thermal efficiency leads to $\eta^* = (1-T_c/T_h)/(1+T_c/T_h)$, and hence to

$$\eta^*/\eta_C = 1/(1+T_c/T_h) \quad (F=0, \text{ all } K_{cr}) \tag{C25}$$

References

[1] Hargreaves, C. M., 1991, *The Philips Stirling Engine*, Elsevier Science Publishers, Amsterdam.

[2] Schmidt, G., 1871, "Theorie der Lehrmanschen Calorischen Maschine," Z. Ver. Dtsch. Ing., **15**(1), pp. 1–12; 1871, "Theorie der Lehrmanschen Calorischen Maschine," Z. Ver. Dtsch. Ing., **15**(2), pp. 97–112.

[3] Finkelstein, T., 1960, "Generalized Thermodynamic Analysis of Stirling Engines," SAE paper 118 B. See also [10], Appendix VIII.

[4] Reader, G. T., and Hooper, C., 1983, *Stirling Engines, E. & F.N.Spon*, London, Appendix A.

[5] Walker, G., 1980, *Stirling Engines*, Clarendon, Oxford.

[6] Organ, A. J., 1997, *The Regenerator and the Stirling Engine*, Mechanical Engineering Publications Limited, London.

[7] Urieli, I., and Berchowitz, D. M., 1984, *Stirling Cycle Analysis*, Adam Hilger Ltd., Bristol.

[8] Walker, G., and Senft, J. R., 1985, *Free Piston Stirling Engines*, Springer-Verlag, Berlin.

[9] West, C. D., 1986, *Principles and Applications of Stirling Engines*, Van Nostrand Reinhold, New York.

[10] Organ, A. J., 1992, *Thermodynamics and Gas Dynamics of the Stirling Cycle Machine*, Cambridge University Press, Cambridge, UK.

[11] Senft, J. R., 1993, *Ringborn Stirling Engines*, Oxford University Press, Oxford.

[12] Finkelstein, T., and Organ, A. J., 2001, *Air Engines, the History, Science and Reality of the Perfect Engine*, ASME, New York.

[13] Hausen, H., 1983, *Heat Transfer in Counterflow, Parallel Flow and Cross Flow*, MacGraw-Hill, New York.

[14] Schmidt, F. W., and Willmott, A. J., 1981, *Thermal Energy Storage and Regeneration*, Hemisphere, Washington, DC.

[15] Ackermann, R. A., 1997, *Cryogenic Regenerative Heat Exchangers*, Plenum, New York.

[16] Swift, G. W., 1988, "Thermoacoustic Engines," Cryogenics, **84**(4), pp. 1145–1179.

[17] Xiao, J. H., 1992, "Thermoacoustic Theory for Cyclic Flow Regenerators. Part I: Fundamentals," Cryogenics, **32**(10), pp. 895–901.

[18] Xiao, J. H., 1995, "Thermoacoustic Heat Transport and Energy Transformation. Part I: Formulation of the Problem," Cryogenics, **35**(1), pp. 15–19.

[19] Roach, P. R., Kashani, A., and Lee, J. M., 1996, "Theoretical Analysis of a Pulse Tube Regenerator," *Advances in Cryogenic Engineering*, Vol. 41, P. Kittel, ed., Plenum, New York, pp. 1357–1363.

[20] Bauwens, L., 1998, "Interface Loss in the Small Amplitude Orifice Pulse Tube Model," *Advances in Cryogenic Engineering* 43B, P. Kittel, ed., Plenum, New York, pp. 1933–1940.

[21] de Waele, A. T. A. M., Hooijkaas, H. W. G., Steijaart, P. P., and Benschop, A. A. J., 1998, "Regenerator Dynamics in the Harmonic Approximation," Cryogenics, **38**(4), pp. 995–1006.

[22] Mayzus, P., Fang, L., Deng, X., and Bauwens, L., 2002, "Pressure Gradients in Oscillating Flows in Regenerators—Analysis and Application to Pulse-Tube Refrigerators," AIP Conf. Proc., **613**, pp. 969–976.

[23] Mayzus, P., Fang, L., Deng, X., Fauvel, O. R., and Bauwens, L., 2002, "Pressure gradients in the Regenerator and Overall Pulse-Tube and Refrigerator Performance," AIAA J., **40**(9), pp. 1897–1906.

[24] de Boer, P. C. T., 2003, "Maximum Attainable Performance of Stirling Engines and Refrigerators," ASME J. Heat Transfer, **125**(5), pp. 911–915.

[25] de Boer, P. C. T., 2003, "Characteristics of the Double Inlet Pulse Tube," Cryogenics, **43**, pp. 379–391.

[26] de Boer, P. C. T., 2002, "Maximum Attainable Performance of Pulse Tube Refrigerators," Cryogenics **42**, pp. 123–125.

[27] Watson, G. N., 1966, *A Treatise on the Theory of Bessel Functions*, Cambridge University Press, Cambridge, UK.

A Study of On-Line and Off-Line Turbine Washing to Optimize the Operation of a Gas Turbine

Meherwan P. Boyce
Fellow ASME
The Boyce Consultancy Group, LLC,
2121 Kirby Drive,
Houston, TX 77019

Francisco Gonzalez
Enterprise Products Company,
10207 FM 1942,
Mont Belvieu, TX 77580

This paper highlights the procedure followed in order to establish an effective on-line and off line water wash program on a fleet of 36 small industrial turbines. To determine the efficacy of water washing, a program of tests under controlled conditions was organized. With proper condition monitoring techniques, a set of tests were developed in order to identify the proper water wash frequency and the dissolving agent used to water wash. The goal of the water wash program is to maximize turbine power, and efficiency, while minimizing maintenance labor, and material. The gas turbine compressor isentropic efficiency, the overall heat rate, and the overall thermal efficiency were used to compare the tests and evaluate the performance of different water wash frequencies and solvents. 8760 points defined each test as the data were taken over a 1 yr *time period, at a* 1 h *interval.* [DOI: 10.1115/1.2181180]

Introduction

The new gas turbines are the corner stone of the rise of the combined cycle as the power source of the new millennium. The new gas turbines have a very high pressure ratio, a high firing temperature, and in some case a reheat burner in the gas turbine. The gas turbines have also new dry low NOx combustors. The combination of all these components has dramatically increased the thermal efficiency of the gas turbine. The gas turbine since the early 1960s has gone from efficiencies as low 15–17% to efficiencies around 45%. This has been due to the pressure ratio increase from around 7:1 to as high as 30:1, and an increase in the firing temperature from about 1500°F (815°C) to about 2500°F (1371°C). With these changes we have also seen the efficiency of the major components in the gas turbine increase dramatically. The gas turbine compressor efficiency increased from around 78% to 87%; the combustor efficiency from about 94% to 98%, and the turbine expander efficiency from about 84% to 92%.

The higher-pressure-ratio compressors are subject to fouling, and can result in surge problems or blade excitation problems, which lead to blade failure. The effect of compressor fouling is also very important on the overall performance of the gas turbine since it uses nearly 60% of the work generated by the gas turbine. The effect of fouling of the compressor, which reduces the compressor efficiency, leads to a reduction in the overall efficiency [1–3].

The cleaning of these blades by on line water washing is a very important operational requirement. The practice of using abrasive cleaning by injecting walnut shells, rice or spent catalyst is being suspended in most new and old plants. Where used, it must be carefully evaluated; rice, for instance, is a very poor abrasive since it shatters and tends to get into seals, bearings, and into the lubrication system. Walnut shells should never be used since they tend to collect inside the heat recovery steam generator (HRSG) system and in some cases have been known to catch on fire. Abrasive cleaning is replaced with on-line water wash.

In many plants, on-line water wash procedures have contributed literally hundreds of thousands of dollars to the bottom line.

Contributed by the International Gas Turbine Institute (IGTI) of ASME for publication in the JOURNAL OF ENGINEERING FOR GAS TURBINES AND POWER. Manuscript received August 25, 2005; final manuscript received September 28, 2005. IGTI Review Chair: K. C. Hall. Paper presented at the ASME Turbo Expo 2005: Land, Sea, and Air, Reno, NV, June J, 2005–June 9, 2005, Paper No. GT2005–69126.

General Characteristics of Gas Turbines

The increase in compressor pressure ratio decreases the operating range of the compressor. The operating range of the compressor stretches from the surge line at the low flow end of the compressor speed line to the choke point at the high flow end. As seen in Fig. 1, the lower-pressure speed line has a larger operational range than the higher pressure speed line. Therefore, the higher-pressure-ratio compressors are more susceptible to fouling, and can result in surge problems or blade excitation problems, which can lead to blade failures.

The drop in pressure ratio at the turbine inlet due to filter fouling, amounts to a substantial loss in the turbine overall efficiency, and the power produced. An increase in the pressure drop of about 25 mm WC amounts to a drop of about 0.3% reduction in power. Table 1 shows the approximate changes that would occur for changes in ambient conditions; the fouling of the inlet filtration system and the increase in back pressure on the gas turbine in a combined cycle mode. These modes were selected because these are the most common changes that occur on a system in the field. It must be remembered that these are just approximations and will vary for individual power plants.

Figure 2 shows the effect of compressor fouling on overall cycle efficiency. The effect of fouling of the compressor, which reduces the compressor efficiency, leads to a reduction in the overall efficiency. The higher the pressure ratio of the compressor, the greater the reduction in the overall thermal efficiency of the turbine as can be seen in Fig. 2.

On-line water washing is a very important operational requirement. On-line water washing is not the answer to all compressor fouling problems since after each wash the full power is not regained; therefore, a time comes when the unit needs to be cleaned off-line, as seen in Fig. 3.

The time for off-line cleaning must be determined by calculating the loss of income in power as well as the cost of labor to do so and equate it against the extra energy costs. In the trade-off between performance and availability one must consider the fact that the reduction in power should also be treated as equivalent forced outage hours, thus reducing the plant availability.

The availability of a power plant is the percent of time the plant is available to generate power in any given period at its acceptance load. The acceptance load or the net established capacity would be the net power generating capacity of the power plant at design or reference conditions established as result of the performance tests conducted for acceptance of the plant. The actual

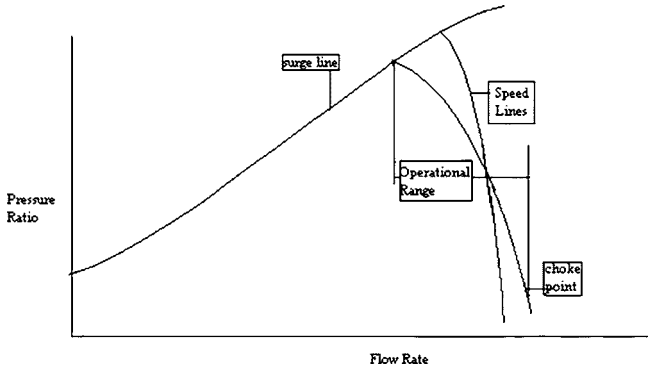

Fig. 1 Compressor performance map

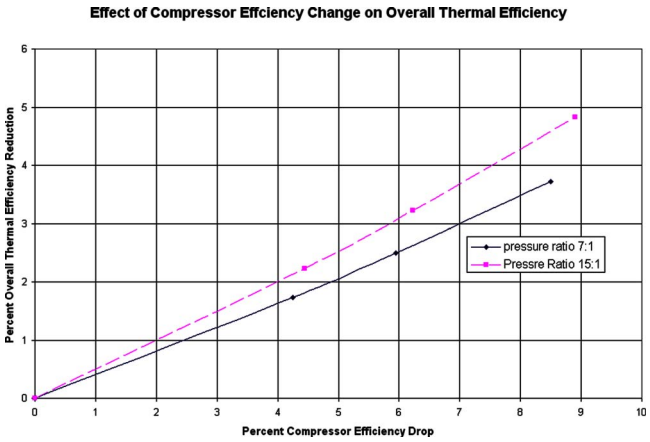

Fig. 2 Effect of compressor efficiency drop on the overall thermal efficiency reduction

power produced by the plant should be corrected to the design or reference conditions and is the actual net available capacity of the power plant. Thus, it is necessary to calculate the effective forced outage hours, which are based on the maximum load the plant can produce in a given time interval when the plant is unable to produce the power required of it. The effective forced outage hours is based on the following relationship:

$$\mathrm{EFH} = \mathrm{HO}x\frac{(\mathrm{MW}_d - \mathrm{MW}_a)}{\mathrm{MW}_d} \tag{1}$$

The availability of a plant can now be calculated by the following relationship, which takes into account the stoppage due to both forced and planned outages, as well as the forced effective outage hours:

$$A = \frac{(\mathrm{PT} - \mathrm{PM} - \mathrm{FO} - \mathrm{EFH})}{\mathrm{PT}} \tag{2}$$

The reliability of the plant is the percentage of time between planned overhauls and is defined as:

$$R = \frac{(\mathrm{PT} - \mathrm{FO} - \mathrm{EFH})}{\mathrm{PT}} \tag{3}$$

Availability and reliability have a very major impact on the plant economy. Reliability is essential in that when the power is needed it must be there. When the power is not available it must be generated or purchased and can be very costly in the operation of a plant. Planned outages are scheduled for nonpeak periods. Peak periods is when the majority of the income is generated as usually there are various tiers of pricing depending on the demand. Many power purchase agreements have clauses that contain capacity payments, thus making plant availability critical in the economics of the plant.

Table 1 Effect of various parameters on the output and heat rate

Parameters	Parameter Change	Power Output	Heat Rate Change
Ambient Temperature	10°C	−6.5%	2%
Ambient Pressure	10 mbar	0.9%	0.9%
Ambient Relative Humidity	10%	−0.0002%	0.0005%
Pressure Drop in Filter	25 mm WC	−0.5%	0.3%
Increase in Gas Turbine Back Pressure	25 mm WC	−0.25%	0.08%

Reliability of a plant depends on many parameters, such as the type of fuel, the preventive maintenance programs, the operating mode, the control systems, and the firing temperatures.

Axial Flow Gas Turbine Compressor Performance. The turbine compressor efficiency and pressure ratio are closely monitored to ensure that the turbine compressor is not fouling. Based on these computations the turbine compressor on-line water wash was evaluated. The gas turbine axial compressor work amounts to between 60% and 65% of the total work produced by the gas turbine.

The overall compressor work is calculated using the following relationship:

$$W_c = m(H_{2a} - H_1) = mc_{\mathrm{pavg}}T_1\left[\left(\frac{P_2}{P_1}\right)^{(\gamma-1/\gamma)} - 1\right]/\eta_{\mathrm{ad}} \tag{4}$$

The work per stage is calculated assuming the energy per stage is equal, this has been found to be a better assumption than assuming the pressure ratios per stage to be equal. It is necessary to know this if there is an interstage bleed of the air for cooling or other reasons.

$$W_{\mathrm{stg}} = \frac{W_c}{N_{\mathrm{stg}}} \tag{5}$$

It is of great importance that the unit operates as close to its point of maximum efficiency without operating in an unstable flow region. The benefits of having a performance evaluation at any given time outweigh the expense for obtaining this type of

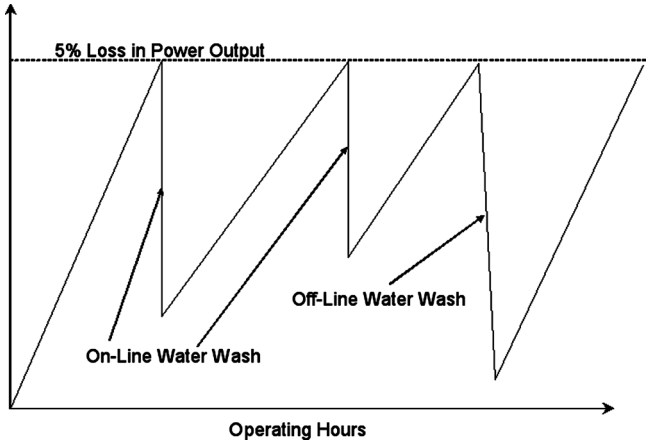

Fig. 3 Effect of compressor water wash on power output

analysis. Some of the benefits include longer operating intervals between overhauls, reduction in operating expenses, and greater operating equipment knowledge.

The work of the compressor under ideal conditions occurs at constant entropy. The actual work occurs with an increase in entropy; thus, the adiabatic efficiency can be written in terms of the total changes in enthalpy:

$$\eta_{\text{ad}} = \frac{\text{Isentropic Work}}{\text{Actual Work}} = \frac{(H_{2TI} - H_{IT})}{(H_{2a} - H_{1T})} \tag{6}$$

where

H_{2TI} = total enthalpy of the gas at isentropic exit conditions

H_{2a} = Total enthalpy of the gas at actual exit conditions

H_1 = total enthalpy of the gas at inlet conditions

For a calorically perfect gas, Eq. (6) can be written as:

$$\eta_{\text{ad}} = \frac{\left[\left(\frac{P_2}{P_1}\right)^{(\gamma-1/\gamma)} - 1\right]}{\left[\frac{T_{2a}}{T_1} - 1\right]} \tag{7}$$

The actual process between the inlet and outlet being a polytropic process, allows Eq. (7) to be re-written as follows:

$$\eta_{\text{ad}} = \frac{\left[(P_2/P_1)^{(\gamma-1/\gamma)} - 1\right]}{\left[\left(\frac{P_2}{P_1}\right)^{(n-1/n)} - 1\right]} \tag{8}$$

The polytropic efficiency is a concept of efficiency used in the process industry as a basis of compressor evaluation. It is often referred to small stage or infinitesimal stage efficiency.

Assuming that

$$P_2 = P_1 + \Delta P$$

and

$$\left(\frac{P_2}{P_1}\right)^{\left(\frac{n-1}{n}\right)} = \left(1 + \frac{\Delta P}{P_1}\right)^{(n-1/n)} \tag{9}$$

further assuming that

$$\frac{\Delta P}{P_1} \ll 1$$

then expanding Eq. (9) using a Taylor series expansion and neglecting second-order terms and substituting it into Eq. (8), the following relationship is obtained:

$$\eta_p = \frac{\frac{\gamma - 1}{\gamma}}{\frac{n - 1}{n}} \tag{10}$$

Overall Turbine Efficiency. The overall thermal efficiency of the gas turbine in a simple cycle (varies between 25% and 47% depending on the turbine) is computed to determine deterioration of the turbine:

$$\eta_{\text{th}} = \frac{\text{Power Output}}{\text{Heat Input}}$$

$$\eta_{\text{th}} = \frac{\frac{W_{\text{pc}}}{\eta_{\text{mt}}}}{m_f \text{LHV}} 100 \tag{11}$$

Heat rate of the turbine. The heat rate can now be easily computed as

$$\text{HR} = \frac{2544.4}{\frac{\eta_{\text{th}}}{100}} \tag{12}$$

where

HR = Heat rate (BTU/hp − h)

Compressor Water Wash. On-line and off-line compressor washing is a very important part of gas turbine operations. Two approaches to compressor cleaning are abrasion and solvent cleaning. The use of abrasive cleaning has diminished due to erosion problems, liquid washing is now primarily being used. The new high-pressure compressors are very susceptible to dirt on the blades, which can not only lead to a reduction in performance, but can also lead to compressor surge. Washing efficacy is site specific due to the different environmental conditions at each plant. There are many excellent techniques and systems for water washing. Operators must often determine the best approach for their gas turbines. This includes what solvents if any should be used, and the frequencies of wash. This is a complex technical-economic problem also depending on the service that the gas turbines are in and the plant surroundings.

Off-line water washing (with or without detergents) cleans by water impact and by removing the water-soluble salts. It is important that the water used should be demineralized water. The detergent/water ratio is also another important parameter. Water washing using a water-soap mixture is an efficient method of cleaning. This cleaning is most effective when carried out in several steps, which involve the application of a soap and water solution, followed by several rinse cycles. Each rinse cycle involves the acceleration of the machine to approximately 20–50% of the starting speed, after which the machine is allowed to coast to a stop. A soaking period follows during which the soapy water solution may work on dissolving the salt.

A fraction of airborne salt always passes through the filter. The method recommended for determining whether or not the foulants have a substantial salt base, is to soap wash the turbine and collect the water from all drainage ports available. Dissolved salts in the water can then be analyzed.

Online washing is widely used as a means to control fouling by keeping the problem from developing. The effect of water cleaning is usually not very effective after the first few stages. Techniques and wash systems have evolved to a point where this can be done effectively and safely. Washing can be accomplished by using water, water-based solvents, petroleum-based solvents, or surfactants. The solvents work by dissolving the contaminants, while surfactants work by chemically reacting with the foulants. Water-based solvents are effective against salt, but fare poorly against oily deposits. Petroleum-based solvents do not effectively remove salty deposits. With solvents, there is a chance of foulants being redeposited in the latter compressor stages.

Even with good filtration, salt can collect in the compressor section. During the collection process of both salt and other foulants, an equilibrium condition is quickly reached, after which re-ingestion of large particles occurs. This re-ingestion has to be prevented by the removal of salt from the compressor prior to saturation. The rate at which saturation occurs is highly dependent on filter quality. In general, salts can safely pass through the turbine when gas and metal temperatures are less than 1000°F. Aggressive attacks will occur if the temperatures are much higher. During cleaning, the actual instantaneous rates of salt passage are very high together with greatly increased particle size.

Plant Equipment. Enterprise Products Mont Belvieu Plant operates 36 gas turbines. The gas turbines are used to compress process gases in heat pump, refrigeration process and power generation. Twenty-eight of the turbines are used in mechanical drives, and eight of the turbines are used in power generation. All of the turbines are used in a hot oil combine cycle that helps

recover the energy in the waste heat. Most of the gas turbines are in the 4000 hp range, but the largest turbine is a 15,000 hp Mars turbine driving a process gas axial compressor. Thirty-three of the 36 gas turbines are equipped with on-line water wash capability.

Gas Turbine Configuration. The turbines used for all of the online water wash test were Solar T4702S *Centaur*® generators. All of the turbines are configured identically, and all of the turbines have about the same amount of operating hours. These generator turbines are equipped with an inlet air prefilter with primary filters made by Donaldson filters. The filter is configured with cylindrical/conical filter synthetic media. The filtration system is a Huff- and -Puff filter system. The filter efficiency is 99.5 on particles of 1–3 μm. The average pressure drop across the filters is 2.4 in. H_2O. The *Centaur*® engines coupled to a speed reducer gearbox and to a generator are capable of producing 3 MW. The turbine exhaust is routed to a heat recovery unit that heats up a hot oil media that is used for process purposes. The typical exhaust gas temperature is around 950°F (510°C) before the hot oil coils and 200°F (93°C) after the coils.

Performance Deterioration of a Gas Turbine. A gas turbine engine requires frequent cleaning to maintain an efficient operation. Performance degradation in a gas turbine can be categorized as recoverable and nonrecoverable. Recoverable performance is the deterioration in a gas turbine performance that can be recovered by engine cleaning, otherwise known as an on-line and off-line water wash. Nonrecoverable degradation is the performance deterioration of a gas turbine caused by internal engine component wear. The only way to recover the nonrecoverable degradation is by performing a shop inspection and engine overhaul.

The rate at which a gas turbine deteriorates is affected primarily by the amount of contaminants that enter the turbine through the inlet air filters, ducts, water from evaporative coolers, fuel, and the frequency as well as the thoroughness of engine water washing. At times there exist unusual site conditions that accelerate the gas turbine degradation. Unusual airborne contaminants from process mists, smoke, and oil, and chemical releases, dust storms, sugar cane burning smoke, and other sources have been documented to accelerate engine degradation. It is for these reasons that a site-specific test program should be conducted in order to optimize the effectiveness of a turbine water wash program. Deterioration in turbine performance is indicated by one or more of the following conditions:

- slower engine acceleration
- engine compressor surge or stall
- lower power output
- loss of engine compressor discharge pressure
- increase in compressor discharge temperature

Figure 4 is a typical nonrecoverable power and heat rate degradation curve as a function of equivalent engine operating hours (EOH). With an increase in equivalent engine operating hours there is a sharp drop in delivered horsepower and an increase in the turbine heat rate during the first 5000 equivalent operating hours. These losses are nonrecoverable in most cases, and would require the turbine to be returned to the shop, and new components would be needed.

Different Wash Systems. There are primarily three different types of wash systems: an on-line wash system, off-line crank wash system, and manual hand-held crank wash system. These cleaning systems are designed primarily to maintain the engine compressor at its maximum efficiency. The effectiveness of a system will greatly depend on their proper use. In order to evaluate the effectiveness of these systems it is strongly recommend to link the use of these systems to engine performance parameters.

For the most part, the on-line wash system is intended as a supplement to the off-line crank wash system and not as a substitute. In general, it is extremely important to implement a turbine

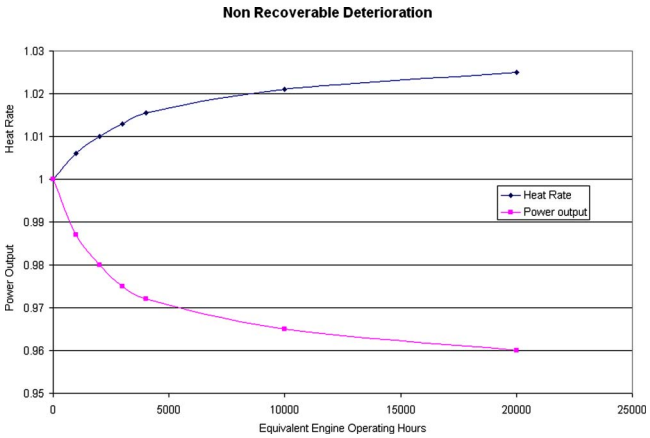

Fig. 4 Nonrecoverable losses in a gas turbine as a function of equivalent operating hours

crank wash program in order to recover most of the recoverable performance deterioration. At times when turbine crank washes are put off due to operating constraints, there may be a need to manually clean the turbine compressor blades, as a large buildup of dirt will be on the blades. In order to manually clean the compressor blades, the turbine compressor case has to be inspected and hand scrubbed in the field. Testing has revealed that an additional five efficiency points were recovered in a Mars turbine when an off-line water wash was performed.

On-Line Wash Cleaning System. The online wash cleaning system is used while the turbine operating parameters are stable. The system can be used without disturbing the operational unit; thus, it does not matter if the turbine is operating at part or full load. Cleaning the turbine compressor with the online wash system should be a routine, and scheduled maintenance function. The on-line water wash system is based on injecting atomized cleaning fluid, thus avoiding any problems that could be associated with abrasive cleaning methods that could erode blades, and damage component coatings.

All of the gas turbines were equipped with an on-line water wash system, as shown in Fig. 5.

The typical on-line wash system consists of a wash ring located outside of the turbine inlet air plenum as seen in Fig. 6. The wash ring has several pigtails that are connected to the eight atomizing type nozzles, as seen in Fig. 7.

The wash nozzles are rated to discharge 0.24 gpm of wash fluid at 100 psig. The wash fluid is stored in a 26 gallon SS holding tank. The tank is equipped with a pressure connection used to

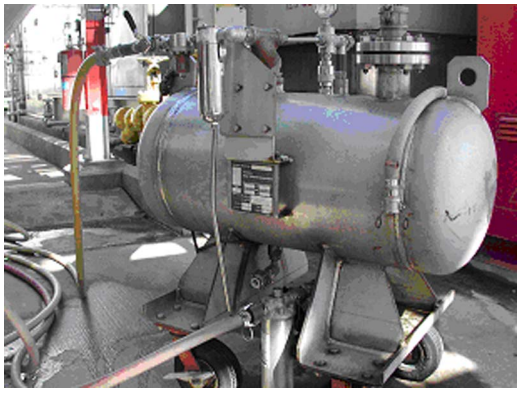

Fig. 5 Water wash system

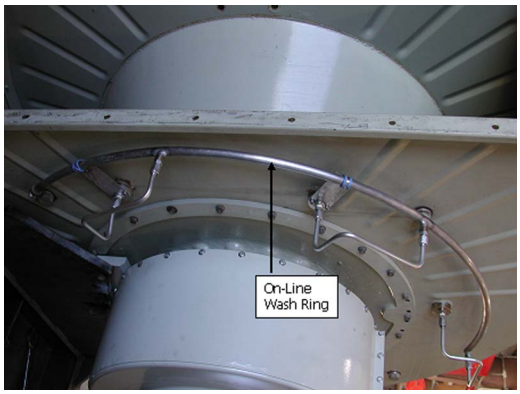

Fig. 6 Gas turbine plenum showing the on-line water ring on the outside of the plenum

pressure up the tank in order to inject the wash fluid into the wash ring through stainless steel piping. The system is portable and, is moved from turbine to turbine.

Off-Line Crank Wash Cleaning System. The off-line crank wash system is used while the turbine is out of service. The off-line wash is performed when the turbine is manually cranked by the engine starter with the fuel and ignition system de-activated. This type of wash is more effective in recovering the performance degradation that the turbine experiences. Before performing this procedure most of the low drain piping, igniter, torch, pilot gas, etc., is removed in order to avoid liquid pockets in the turbine fuel igniter piping. The effectiveness of this cleaning method is enhanced by the use of different wash fluids. Manufactures recommend different water and solvent base wash fluids, and field technicians have exhausted many different combinations of relatively available household agents.

Our turbines are configured with a crank wash ring with nozzles that do not atomize the water. The wash fluid is mixed and stored in a 26 gallon SS holding tank. The tank is equipped with a pressure connection and outlet connection. Plant air is used to force the mixed fluid into the turbine inlet air plenum through the stainless steel piping and valves.

Fig. 7 Inside view of air plenum showing the off-line water wash ring and the on-line water wash nozzles

Table 2 Water specifications

Water Specification	
Sodium and fluorine	<1.9 ppmw
Chlorine	<40 ppmw
Lead	<0.7 ppmw
Vanadium	<0.35 ppmw
Iron, tin, silicon, Aluminum, copper, manganese, phosphorus, calcium, and magnesium	<3.8 ppmw
Dissolved Solids	<5 ppmw
*p*H	6–9

A preferred method used to perform a crank wash is through the use of a hand-held wash wand. Several of the turbine inlet air inspection covers have to be removed in order to obtain access in to the compressor inlet. A hand-held wand is rotated around the inlet turbine screen in order to spray the compressor air inlet evenly.

Hand scrubbing the compressor blades is another method of recovering the performance of an engine compressor. A routine off-line crank wash is performed before the compressor case is open for inspection and cleaning. This is a very labor-intensive method that helps recover an additional level of performance. Not all gas turbines compressor blades can be accessed in the field, and the economic incentives have to be evaluated before this method is undertaken. Currently, we perform this type of cleaning on a Solar Mars 15000 *SoLoNo*$_x$™ turbine that has to operate 11 to 12 months continuously without any shutdowns while minimizing power loss. The expected engine compressor polytropic efficiency improvement is about 0.5 to 1 efficiency point. In an engine that has to run for 11 months without a crank wash, the extra efficiency point is an added boost in fuel savings and additional power delivered.

Wash Fluids

Water Specification for On-Line and Off-Line Water Wash. Water quality for both on-line and off-line water washes must be stringent, so as to ensure that impurities are not introduced. Table 2 gives a detailed specification of the quality of the water required to complete a successful water wash.

Testing the quality of the water is critically essential before performing a routine on-line water wash. A common problem with demineralized water sources is the occasional fluid channeling in the catalyst beds. A demineralized water-polishing skid after the demineralized water is recommended for the turbine water wash in order to ensure good water quality. Since the water wash of each turbine is a batch mode, the polishing skid is designed for small batch rates thus water consistency is maintained. Effectiveness of every on-line water wash has greatly improved by incorporating a testing of the water quality. A detailed analysis of the water for every water wash would be time consuming and expensive, an alternative would be to use a hand held conductivity /total dissolved solids/ *p*H meter. The meter readings should indicate a water conductivity of <0.5 μmhos/cm, total dissolved solids of <1.0 ppmw and *p*H between 7 and 9.

On-Line and Off-Line Water Wash Fluids. Many solvents are used for turbine on-line and off-line water washing. Water base, solvent base, industrial cleaners, and demineralized water are just a few of the different types of agents used to clean gas turbine engine compressors.

There are several types of water base agents used for compres-

sor cleaning. The most popular water base solvents contain low metal content, and are derived from highly active natural oils and surfactants. The water base agents are environmentally safe and contain no solvents that are capable of dissolving and removing engine deposits that accumulate with time. Other industrial agents such as *Mr. Clean*™ have been known to work well in combination with water base agents and solvent base agents. Most turbine manufactures offer to the users an approved list of soaps that can be used with their turbines. It is extremely important not to use an agent that the OEM does not approve or has not reviewed.

Many different types of solvent base agents are also used for on-line and off-line turbine washes. Most solvents are derived from hydrocarbon base stocks, and contain very little metals. Most of these solvents are not fully considered environmental friendly, but with the proper procedures these agents can be used in a safe manner. These solvents are used predominantly during off-line crank washes.

By far the most common agent used for water washing is demineralized water. Demineralized water systems are very effective if the filtration system effectively filters out the majority of airborne particles and oily substances.

On-Line Water Wash Procedure. Before implementing a water wash procedure, the procedure should be discussed with the turbine manufacture and soap vendor supplier. Their expertise in the subject in hand will contribute to your success with the program in mind.

Obtain 25 gallons of demineralized water. Have water sampled to meet the specifications required. If a water wash agent is used, mix the fluids in the tank per the soap vendor's specifications. The water quantity required depends on the recommended soap to water ratio and the size of the gas turbine.

Water washes are done with the turbine operating at steady state conditions, and ambient temperatures above 40°F. Special procedures must be applied if ambient temperatures are below 40°F.

Connect the outlet of the water wash cart to the turbine water wash piping. Connect the air hose supply to the tank air inlet valve, adjust the air pressure from your supply header to obtain 85 to 100 psig.

Open the tank water wash fluid outlet valve and the turbine water wash inlet valve, which is connected to the water wash manifold. The wash fluid will be forced into the turbine by the air pressure in the tank. Observe turbine performance, the compressor discharge pressure will rise and firing temperature will drop when the water is injected. Power will increase, but will not affect process variables. The turbine will have adequate power to maintain its set points.

- Observe the time it takes to ingest the 25 gallons of fluid.
- If the time to ingest the fluid increases with time, then the injection nozzles, are getting plugged.
- When the wash fluid ends, the turbine operation will continue with out any problems.
- If a wash solvent is used, follow this same procedure with a water only rinse.

Off-Line Crank Wash Procedure. Shut down the turbine and allow sufficient time for the turbine to cool below 150°F (66°C). This is extremely important if solvent base agents will be used for cleaning. Disconnect the lower case drain plug and igniter torch tubing, remove all low point tubing components such as the gas line to the fuel manifold, and install caps to all of the open lines.

Remove the Turbine Inlet Inspection Covers. Fill a hand-held pump sprayer with the appropriate crank wash solution, water or solvent base agent with its appropriate water mixture. Initiate manual crank mode on the turbine engine. Spray the crank wash solution into turbine inlet air bell mouth. Continue this process until the wash solution is almost finished. Shut down the manual crank mode and continue to spray the solution during the engine coast down. Let the solution sit in the turbine for 10–15 min.

Fig. 8 Three Centaur-solar gas turbines

Introduce 10 gallons of demineralized water into the crank wash water tank. Start manual crank mode, and inject the water into the crank wash manifold. For better results use the hand-held injection wand. Care must be taken to make sure foreign objects are not sucked into the turbine air inlet, and that the protective foreign object screens are in place before starting this procedure.

Inject a recommended detergent during turbine's crank mode and during coast down. Let the solution sit for about 10–15 min. Fill the injection cart with 20–30 gallons of demineralized water. Start manual turbine crank mode and inject water into turbine inlet bell mouth. You can either use the hand injection wand or use the water injection ring.

Continue to inject demineralized water until you obtain a clean water stream out of the turbine drains.

Axial Compressor Instrumentation. In order to properly assess the performance of the wash procedure, the compressor horsepower, fuel flow, inlet temperature and pressure, and engine compressor pressure and temperature, the axial flow compressors were instrumented so that detailed data can be obtained. The axial flow compressor can and does foul so that it is important to monitor its performance to ensure that its operation is in a stable region and operating close to its design point.

The pressure measurements are static measurements, whereas the temperature measurements are total, since static temperatures cannot be measured in any practical manner. With the instrumentation available, the performance deterioration on any given day can be computed. This instrumentation has been extremely helpful in identifying the associated problems with the axial compressor deterioration. The following is a list of the instrumentation on this axial compressor.

In order to perform a thorough engine performance evaluation the following parameters should be measured:

- compressor suction static pressure
- compressor suction total temperature
- compressor discharge static pressure
- compressor discharge total temperature
- gas producer speed
- barometer pressure
- firing temperature
- exhaust pressure and temperature.

Tests

Five tests were conducted on three identical gas turbine generator sets sitting next to each other, as seen in Fig. 8. These tests were conducted to determine the proper solvents to use, and the frequency of the washes that affect the performance. The tests were conducted on these gas turbines being operated as baseline turbines over a period of a year of turbine operation. Thus, each turbine was operated for over 8600 h.

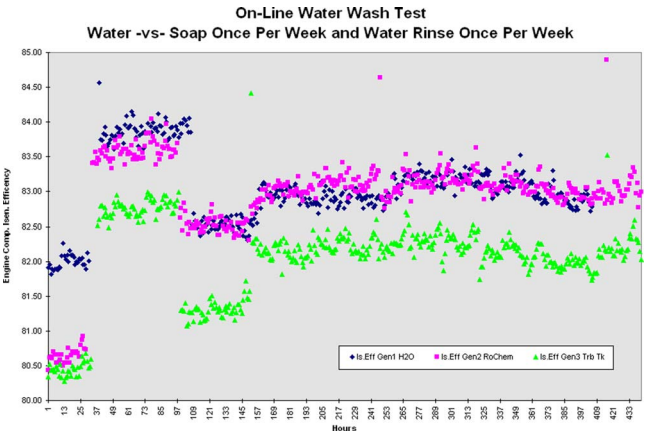

Fig. 9 Results of tests of demineralized water and different soap vendors

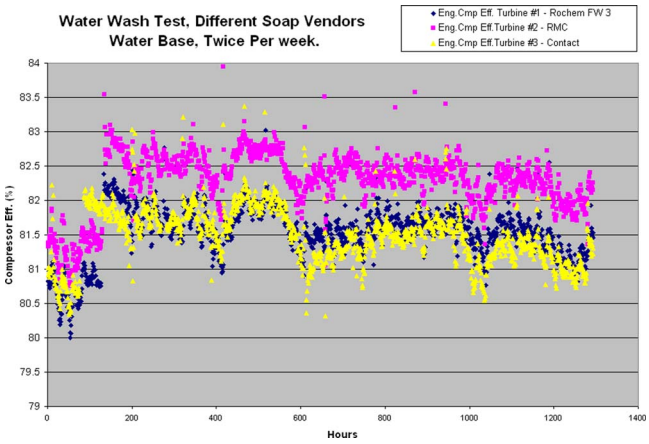

Fig. 11 Results of tests of different water base solvents

Test One: Demineralized Water and Different Soap Vendors. Figure 9 shows the results of a water wash only, and soap washes, from two different soap vendors once a week on three identical gas turbines located next to each other. In this figure, the crank wash was performed after 45 h of operation. After 90 h of operation the water quality was not being monitored and the turbines were washed erroneously with water which did not meet the specification given in Table 2. A large drop in compressor performance was noted, indicating the fouling of the compressor by contaminants in the water. The turbines were then washed once again using water meeting the specifications as per Table 2, and with a water-soap solution using a soap from two different vendors. After 155 h, the turbine performance improved on all three units. As can be seen, the wash with water alone was just as good as soap solutions.

Test Two: Demineralized Water, Water Base Soap, and Solvent Base Soap. The object of this test was to determine which soap was better, solvent base or water base soap. Demineralized water was used as a third agent. In Fig. 10, notice the vertical gap between the water and the soap solutions in the earlier part of the test. As time went on the vertical gap between the soaps and water was reduced to almost nothing, indicating that the solvents were more effective during the first week, but after some time the efficacy of the solvents diminished to the point where they were no more effective than plain demineralized water.

Test Three: Different Water Base Solvents. The object of this test was to determine if a different vendor had a better water base soap. Each vendor claims that their soap has a different chemistry and different philosophy in how the soap cleans the compressor blades. Only water base soaps were used as they are more environmentally friendly. The tests were based on using the solvents twice a week followed by a demineralized water rinse. Figure 11 shows the results of these tests and indicates that all of the soaps had exactly the same results.

Test Four: Different Frequencies With Demineralized Water and Water Base Solvents. The object of this test was to determine the optimum frequency to perform the on-line water wash tests. The tests consisted of a daily demineralized water wash on one gas turbine, and demineralized water wash twice per week on another gas turbine. The third gas turbine was washed daily with demineralized water mixed with a water base solvent. The demineralized water and soap mixture was used daily on these tests, since twice per week tests had already been conducted on the same water and soap mixture. Figure 12 shows that the demineralized water and soap every day have the same results, the water twice per week has a flatter slope. This indicates that over a period of time, water twice a week is most effective.

Test Five: Long-Term Degradation Effects. The object of this test was to determine the degradation in compressor efficiency and total turbine heat rate with and without on-line water wash. The second objective of this test was to quantify the effects of operating a gas turbine for extended number of hours without a crank wash. This test was conducted over approximately 4000 h of operation (6 months). Turbine 2 was washed twice a week with clean demineralized water, while Turbine 3 was not washed at all.

At the beginning of this test, both turbines were crank washed with the manufacturer-recommended of-line cleaning agent. The

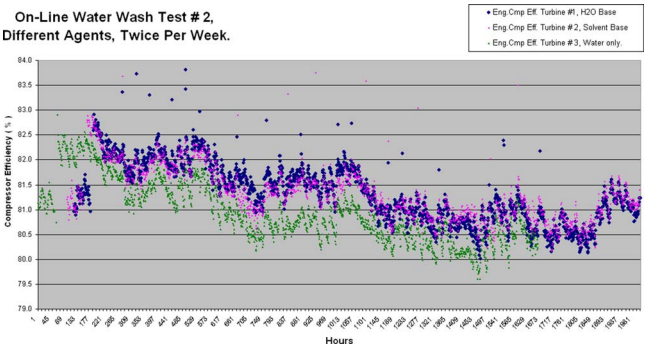

Fig. 10 Results of test of demineralized water, water base soap, and solvent base soap

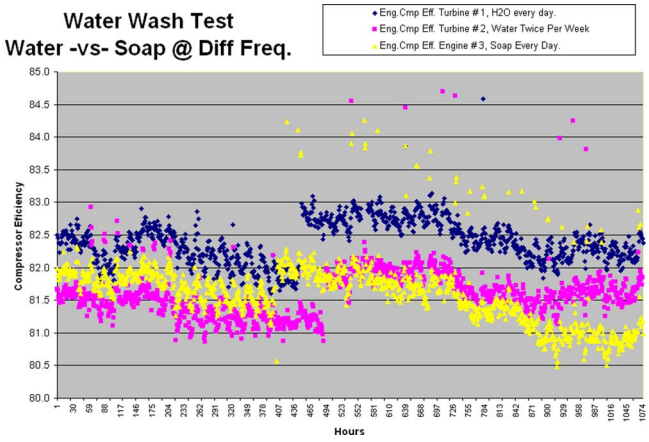

Fig. 12 Result of tests of different frequencies with demineralized water and water base solvents

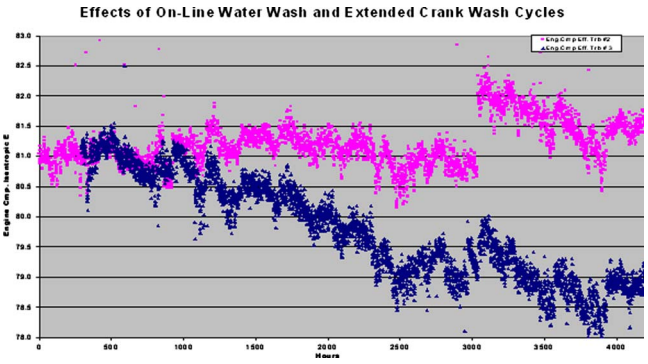

Fig. 13 Degradation of turbine compressor efficiency

isentropic axial flow compressor efficiency of both turbines were calculated to be approximately 81% at the beginning of the test. At the end of 3000 h, turbine 2, in addition to being washed on-line twice a week, was also crank washed. Figure 13 shows the results of this test. At 3000 h, turbine 2 had a compressor efficiency of about 80.8% a reduction of only 0.2%, while turbine 3 had a compressor efficiency of 79.0%, a reduction of 2.5%. Turbine 2 was then crank washed again, this time, however, with a new cleaning agent. Using a new cleaning agent, the turbine efficiency was restored to 82%, about 1% higher than after the original crank wash. This, in our opinion, was due to the use of a different cleaning agent (Mr. Clean™). The use of effective cleaning agents is very important to the success of the cleaning cycle. The test was continued for a further 1000 h; at the end of that period the turbine compressor efficiency of turbine 2 was measured to be 81.5% and turbine 3 to be 78.5%, a reduction after 4000 h of about 3.7%.

The effect on the turbine heat rate was also measured. Figures 14 and 15 show the increase in the heat rate of both turbines over the 4000 operating hours. Figure 14 shows that the heat rate and overall thermal efficiency remains relatively constant in turbine 2 which has been water washed. Figure 15 shows that the heat rate is increased by 2.7% and the overall thermal efficiency decreased by 2.7%. It should be remembered here that all of the heat rate increase or the decrease in overall thermal efficiency can not be attributed to the compressor wash. The compressor efficiency loss contributes about 60% to the overall thermal efficiency loss.

In order to calculate the heat rate, and overall thermal efficiency, several key measurements had to be obtained, such as horsepower, fuel flow, and fuel composition. In many cases it can be difficult to calculate the delivered horsepower in mechanical drive packages, as compared to power production units. At the same time, additional accurate instrumentation is required to measure the fuel flow and fuel quality. In contrast, the engine compressor efficiency can be calculated with very simple measurements such as inlet and exit engine compressor pressures and temperatures. By obtaining the engine compressor efficiency one can also quantify the results of an effective on-line and off-line water wash program, as seen in Fig. 13.

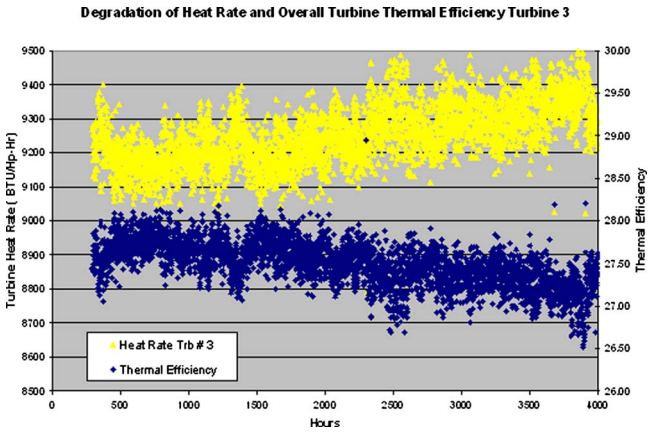

Fig. 14 Degradation of heat rate and overall turbine thermal efficiency, turbine 2

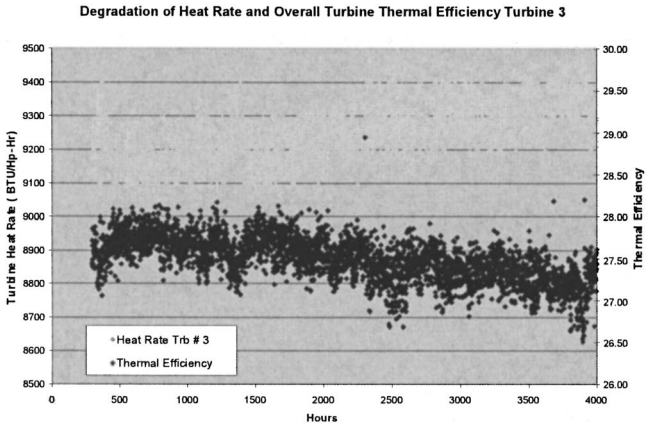

Fig. 15 Degradation of heat rate and overall turbine thermal efficiency, turbine 3

Cost Analysis

The average fuel consumption for the turbines used in these tests is approximately 36 MMBtu/h. The fuel used was pipeline quality natural gas available in the U.S. Gulf Coast Region with a LHV/HHV of 1010/1100 BTU/cu.ft. The lower heating value of the gas is one in which the H_2O in the products has not condensed. The lower heating value is equal to the higher heating value minus the latent heat of the condensed water vapor. Most gas contracts are based on HHV, while the efficiencies and heat rate calculations are based on LHV.

It is not uncommon to find users that perform crank washes based on power loss, and not on overall thermal efficiency loss, nor loss of compressor efficiency, which is rarely measured. Power loss in a simple cycle gas turbine is caused by many factors, such as an increase in pressure drop in the air filtration system, compressor fouling, fuel heating value changes, combustor fouling, turbine expander fouling, and increase in turbine back pressure. A 3–4% compressor efficiency loss, causes the thermal efficiency to be reduced by 1.8–2.4%.

A 3% savings in fuel, reduces the cost of operating one of the turbines tested, over a 1 yr time period, with an availability of 96%, based on a cost of $7/MMBtu of natural gas: $64,901. Therefore, in the fleet of 36 turbines, which compose this site, the savings totals $2,288,756 per year.

An on-line effective water wash program should consider fuel savings as well as cost of materials and labor required, plus any lost production costs. A typical on-line water wash can be done in an hour by one person. Since each turbine application is different, the cost associated with lost production is left for the user to compare, to the fuel savings associated with an off-line water wash program.

Conclusions

The proper combination of on-line water wash and crank wash will vary from location to location. By monitoring the performance and performing several water wash tests, any site can determine the best water wash combination. The result of the tests indicated that under most operating conditions, the demineralized

water wash done twice weekly is as effective as water-soap mixtures. The following are some tips that should be followed by operators during water washes:

1. Good air filtration is the key to prevent engine compressor fouling.
2. The water used should be demineralized. The use of nondemineralized water would harm the turbine.
3. In the tests performed the soaps did not outperform the demineralized water.
4. All water-solvent washes should be followed by a water rinse.
5. After numerous water washes, the compressor performance will deteriorate and an off-line crank wash will be necessary.
6. Off-line crank wash should be done whenever compressor performance diminishes by 3–4%.
7. It is imprudent to let foulants buildup before commencing a water wash regime, since the foulants will be washed down stream causing blockages in the last stages.
8. Low carbon stainless steel should be used for tanks, nozzles, and manifolds, to reduce corrosion problems.
9. Spray nozzles should be placed where proper misting of the water would occur, and to minimize the downstream disturbance of the flow. Care should be taken that a nozzle would not vibrate loose and enter the flow passage.

Nomenclature

A = availability
c_p = specific heat at constant pressure
c_v = specific heat at constant volume
EFH = equivalent forced outage hours
FO = forced outage hours
H = enthalpy
HO = hours of operation at reduced load.
HHV = higher heating value
LHV = lower heating value
m = mass flow of air
m_f = mass flow of fuel
MW_d = Desired output corrected to the design or reference conditions. This must be equal to or less than the plant load measured and corrected to the design or reference conditions at the acceptance test.
MW_a = actual maximum acceptance test produced and corrected to the design or reference conditions
n = polytropic exponent
N_{stg} = number of stages
P = pressure
PT = time period (8760 h/yr)
PM = planned maintenance hours
R = reliability
T = temperature
W_c = work compressor
W_{pc} = work at generator
W_{stg} = compressor work per stage

Greek Symbols

γ = adiabatic polytropic exponent (c_p/c_v)
η_{ad} = compressor adiabatic efficiency
η_{mt} = mechanical efficiency
η_p = compressor polytropic efficiency
η_{th} = overall total efficiency

References

[1] Boyce, M. P., and Latcovich, J. A., 2002, "Condition Monitoring and Its Effect on the Life of New Advanced Gas Turbines," Gas Turbine Users Association Conference, Houston, TX, April 21–25.
[2] Boyce, M. P., 2003, *Gas Turbine Engineering Handbook*, 2nd Ed., Butterworth-Heinemann, Boston.
[3] Boyce, M. P., 2003, *Handbook for Cogeneration and Combined Cycle Power Plants*, ASME, New York.

CO_2 Sequestration From IGCC Power Plants by Means of Metallic Membranes

Paolo Chiesa
Dipartimento di Energetica,
Politecnico di Milano,
P.zza Leonardo da Vinci, 32,
20133 Milan, Italy
e-mail: paolo.chiesa@polimi.it

Thomas G. Kreutz
Princeton Environmental Institute,
Princeton University,
25 Guyot Hall,
Princeton, NJ, 08544 USA
e-mail: kreutz@princeton.edu

Giovanni G. Lozza
Dipartimento di Energetica,
Politecnico di Milano,
P.zza Leonardo da Vinci, 32,
20133 Milan, Italy
e-mail: giovanni.lozza@polimi.it

This paper investigates novel IGCC plants that employ hydrogen separation membranes in order to capture carbon dioxide for long-term storage. The thermodynamic performance of these membrane-based plants are compared with similar IGCCs that capture CO_2 *using conventional (i.e., solvent absorption) technology. The basic plant configuration employs an entrained-flow, oxygen-blown coal gasifier with quench cooling, followed by an adiabatic water gas shift (WGS) reactor that converts most of CO contained in the syngas into* CO_2 *and* H_2*. The syngas then enters a WGS membrane reactor where the syngas undergoes further shifting; simultaneously,* H_2 *in the syngas permeates through the hydrogen-selective, dense metal membrane into a counter-current nitrogen "sweep" flow. The permeated* H_2*, diluted by* N_2*, constitutes a decarbonized fuel for the combined cycle power plant whose exhaust is* CO_2 *free. Exiting the membrane reactor is a hot, high pressure "raffinate" stream composed primarily of* CO_2 *and steam, but also containing "fuel species" such as* H_2S*, unconverted CO, and unpermeated* H_2*. Two different schemes (oxygen catalytic combustion and cryogenic separation) have been investigated to both exploit the heating value of the fuel species and produce a* CO_2*-rich stream for long term storage. Our calculations indicate that, when* 85 vol % *of the* H_2+CO *in the original syngas is extracted as* H_2 *by the membrane reactor, the membrane-based IGCC systems are more efficient by* ~1.7 *percentage points than the reference IGCC with* CO_2 *capture based on commercially ready technology.* [DOI: 10.1115/1.2181184]

Introduction

Despite the concerns about rising concentrations of greenhouse gases in the atmosphere, fossil fuels are likely to remain the main source of primary energy for a long time. An option to mitigate the negative effects of using fossil fuel in power plants is capturing CO_2 before it is emitted and storing it over an indefinite period. Generally speaking, CO_2 capture in a power cycle can be accomplished in one of three basic ways:

(1) "Postcombustion decarbonization," where CO_2 is separated (often by solvent scrubbing) from the exhaust gas,
(2) "Oxy-fuel combustion," where the fuel (diluted with recycled CO_2) is burned in oxygen instead of air in order to produce a CO_2-rich flow as exhausts,
(3) "Precombustion decarbonization," where synthesis gas is water-gas shifted to mostly H_2 and CO_2, and then split into two separate streams: one that is CO_2 rich (to be compressed and stored), and one that is H_2 rich (to be used as decarbonized fuel).

Limiting the investigation to plants belonging to the third group, this paper compares the performance of a novel class of plants, where in fuel decarbonization is achieved through a novel hydrogen separation membrane technology, with those of reference plants based on commercially ready technology. All plants considered employ an oxygen-blown, slurry-fed, entrained-flow coal gasifier and a large, heavy-duty gas turbine. Our interest in coal as a feedstock is motivated by multiple considerations: (i) it is abundant—more than a 2000 y supply at current consumption rates[1]; (ii) it has wide geographic distribution; and (iii) its prices are relatively low and nonvolatile.

A reference plant based on commercially ready technology for capturing CO_2 from IGCC plants is conceptually represented in Fig. 1 [2]. An oxygen-blown coal gasifier produces a synthesis gas whose primary constituents are CO, CO_2, H_2, and H_2O. The relative concentrations of these species alter significantly as the syngas passes through a sulfur-tolerant water-gas shift reactor (WGSR) in which the exothermic shift reaction ($CO+H_2O \rightarrow CO_2+H_2+41.15$ kJ/mole) relocates the heating value from CO to H_2, i.e., from a carbon-bearing to a carbon-free fuel. Large fractions of the H_2S and CO_2 (exceeding 99% and 90%, respectively) are separated from the syngas through a solvent absorption process, and then dried and compressed to a supercritical fluid for pipeline transport and long-term storage, most likely in deep geologic formations. The remaining syngas (mainly hydrogen, with traces of inert gases and unconverted components) is used as clean, low-carbon fuel in a rather conventional combined cycle power plant. An air separation unit (ASU) completes the system, providing oxygen to the coal gasification process and nitrogen to the gas turbine unit as a fuel diluent in order to moderate the flame temperature and reduce NO_x emissions. Although this entire precombustion decarbonization scheme has never been realized in an operational plant, we refer to this system as "conventional" because it is based on commercial technologies commonly used in both the electric utility and chemical process industries. Such a plant has been studied in depth by numerous research groups, and its technical feasibility is widely recognized [3–6].

Contributed by the International Gas Turbine Institute (IGTI) of ASME for publication in the JOURNAL OF ENGINEERING FOR GAS TURBINES AND POWER. Manuscript received August 30, 2005; final manuscript received September 6, 2005. IGTI Review Chair: K. C. Hall. Paper presented at the ASME Turbo Expo 2005: Land, Sea, and Air, Reno, NV, June 6–9, 2005, Paper No. GT200568023.

[1]According to Rogner et al. [1], reserves of coal (known resources that can be recovered with current technology and today's prices) are about 20,700 EJ, whereas resources (which include additional coal in the ground at sufficiently high concentration that it is estimated to be recoverable in the future with some combination of better technology and higher prices) are ~199,700 EJ. Global coal consumption was 92 EJ in 1998.

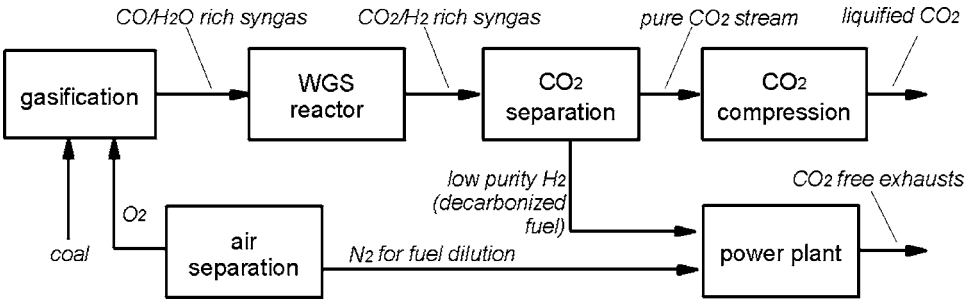

Fig. 1 Conceptual scheme of a low CO_2 emission IGCC plant based on commercially ready technology

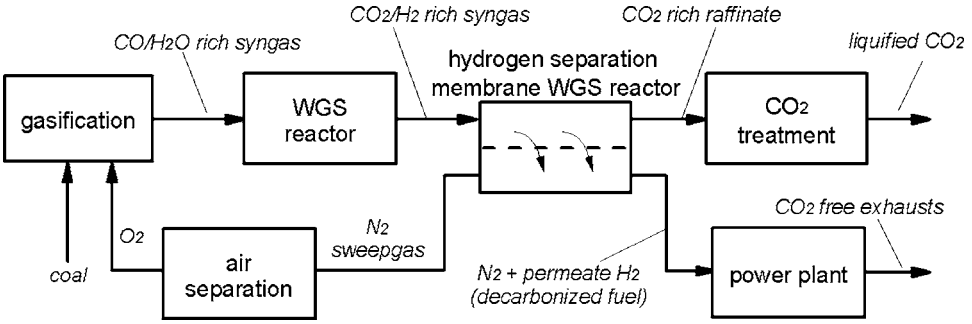

Fig. 2 Conceptual scheme of a low CO_2 emission IGCC plant based on a hydrogen separation membrane reactor (HSMR)

An alternative plant design investigated in this paper is shown in Fig. 2. The shifted syngas exiting the WGSR enters the "raffinate" side of a hydrogen separation membrane reactor (HSMR) in which a sulfur-tolerant, thin-film, dense Pd/Cu membrane allows the selective permeation of hydrogen to the "permeate" side. The raffinate side of the reactor contains a sulfur-tolerant water-gas shift reaction catalyst and thus, as H_2 partial pressure in the raffinate gas decreases, more H_2 is produced by the shift reaction, further improving the conversion of CO to H_2. On the permeate side, pure nitrogen from the ASU acts as a "sweep gas" to keep the H_2 partial pressure low (increasing the driving force for H_2 permeation and thereby reducing the required membrane surface area) while the total pressure remains high enough to feed the gas turbine without the need for fuel compression. Diluting the fuel gas with N_2 is not a drawback because such dilution is required in order to suppress NO_x formation in the gas turbine combustor. The high-pressure raffinate stream, consisting primarily of CO_2 and water, carries all the remaining carbon, sulfur, and minor impurities present in the input syngas. Conceptually, CO_2 is separated from the raffinate stream via cooling (and condensation), and subsequent dehydration of the humidified CO_2; details are discussed below. This plant design shares some basic concept with that employed in our previous research [2,7], in which the HSMR raffinate stream was combusted in O_2 and then expanded through a turbine expander to generate electric power. The turbine exhaust (primarily H_2O and CO_2) is cooled and condensed (and optionally desulfurized), leaving a CO_2-rich stream that is dehydrated and compressed to 150 bar for pipeline transport and geologic storage.

Table 1 Legend of the acronyms for plant configurations considered in this paper

Configuration	CV	CP	MO	MC
CO_2 Capture	No	Pure CO_2	SO_2 co-capture	H_2S co-capture
CO_2 Separation method	···	Physical absorption	···	···
Hydrogen Separation Membrane	No	No	Yes	Yes
Treatment of the Raffinate Stream	···	···	O_2 combustion	inconden sable gas separation

Description of the Plant Configurations

In this work, we focus only on configurations based on gasification with quench cooling. Activity is in progress to extend the analysis to syngas cooling and alternative arrangements aimed at exploiting potential advantages that are particular to HSMR-based plants; plant economics will also be explored. The various plants considered here are listed in Table 1; each is identified by a unique label, where

- the first letter specifies if the plant is based on "conventional" technology (letter "C") or if it employs a membrane reactor (letter "M"),
- for the "conventional" configurations, the second letter denotes the fate of the CO_2: vented to the atmosphere ("V"), captured as a pure stream ("P")[2]. For membrane-based plants, the second letter indicates the method of separating CO_2 from the H_2-rich HSMR raffinate stream: either oxy-combustion ("O") or cryogenic purification ("C"),

Figure 3 is a detailed process layout of the reference plant with

[2]As an alternative to the usual approach where H_2S and CO_2 are removed from the syngas in different steps, "co-capture" is realized when H_2S and CO_2 are captured, dried, compressed, transported and stored *together* in the same reservoir. It has been shown [7] that "co-capture" can provide some economic benefits with respect to the separate removal of CO_2 and H_2S. The co-capture and co-storage of H_2S and CO_2 is a process sometimes carried out at natural gas fields to clean the gas before delivery to the pipeline [8].

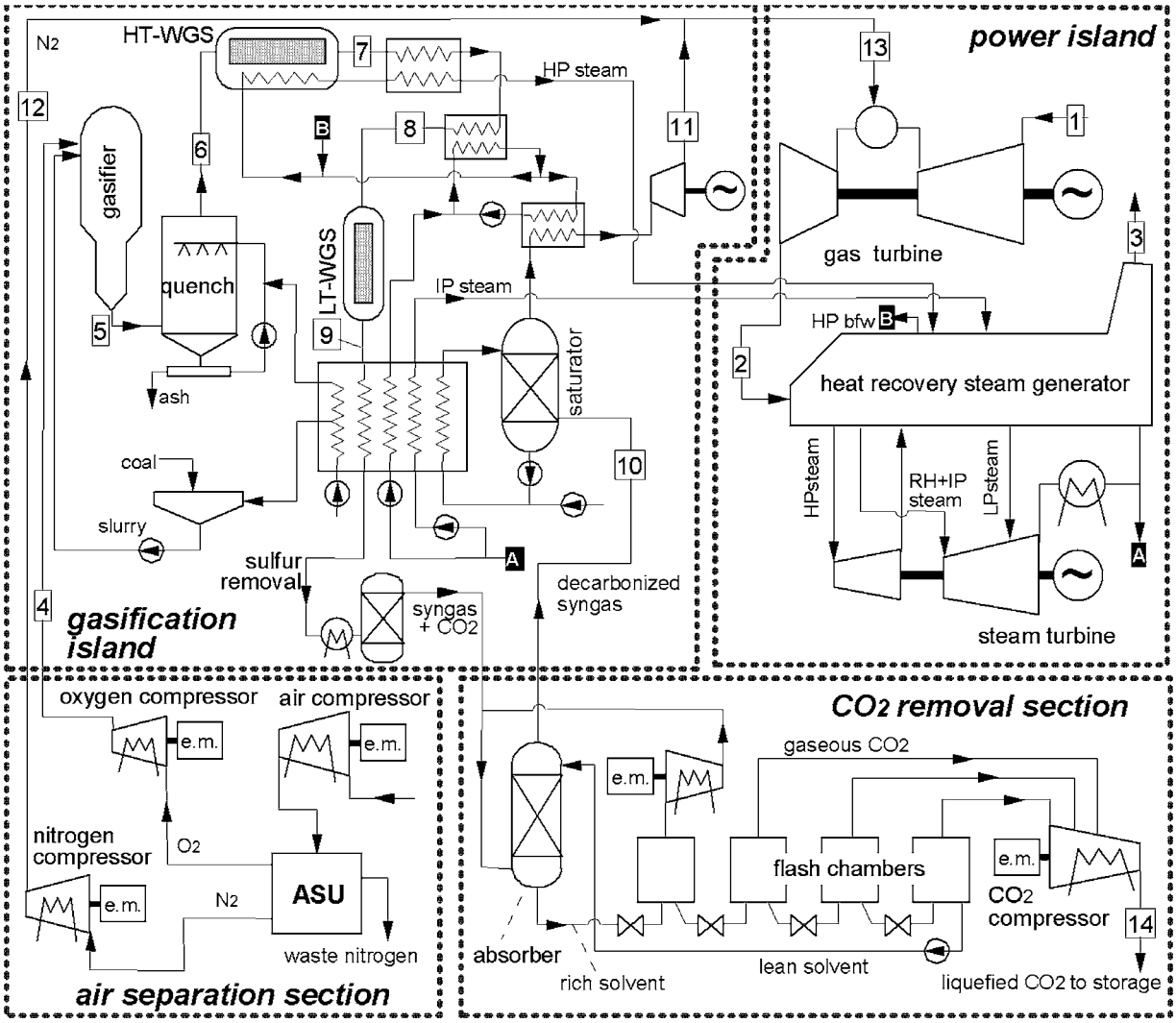

Fig. 3 Detailed scheme of the CP plant configuration

pure CO_2 capture, labeled CP. Coal is fed to an entrained-flow, oxygen-blown, slurry-fed gasifier whose characteristics reproduce the Texaco (now GE Energy) gasification technology. The raw syngas produced in the gasifier is then "quenched" (i.e., cooled) by direct contact with a large water stream, saturated with water and scrubbed. The stream then enters the sulfur-tolerant high-temperature WGSR, where its temperature increases (to ~400°C) due to the exothermic reaction. Heat released at this temperature is used to generate a high-pressure (HP) saturated steam. The syngas flow is then cooled by heating up feedwater for the HP boiler and, by means of an intermediate loop, by warming the gas turbine fuel. After condensed water is removed, the syngas is further shifted in the low-temperature (~200°C) WGSR, increasing the overall CO conversion efficiency to 98.7%. Low-temperature heat recovery (including condensation of the excess water) is performed by a network of heat exchangers, producing: (i) intermediate pressure (15 bar) steam, (ii) warm water for slurry and quench make-up, and (iii) hot water for syngas saturation. The syngas then undergoes the acid gas removal by means of physical absorption using Selexol® solvent. For the sake of simplicity, in Fig. 3 the H_2S and CO_2 absorption systems are represented as separate processes; in the reality, they are connected in a more complicated fashion to limit CO_2 absorption (and subsequent venting to the atmosphere) in the H_2S removal system. In the pure CO_2 capture system, captured H_2S is converted to elemental sulfur in a Claus plant, with a SCOT unit to process its offgas; CO_2 absorbed in the Selexol® is released in a series of flash drums and then compressed to a final pressure of 150 bar. In a slightly altered plant design, termed "H_2S-CO_2 co-sequestration," H_2S and CO_2 are captured and stored *together*. This option is motivated by a simpler and less expensive acid gas removal unit—for example, the Claus and SCOT units can be eliminated entirely (yet the thermal balance of the plant is virtually unchanged).

In plant CP, the decarbonized syngas is composed primarily (>90%) of H_2, the remainder being unconverted CO, unabsorbed CO_2, and traces of CH_4, N_2, and water. The syngas is warmed and humidified in a saturator, heated, expanded (to recover mechanical energy) to the pressure needed by the gas turbine, and eventually mixed with compressed nitrogen coming from the ASU. In our calculations, the amount of nitrogen is determined by the requirement of a stoichiometric flame temperature lower than 2300 K, a level sufficient to achieve low NO_x emissions (15–35 ppmvd at 15% O_2) in diffusive burners [9]. The decarbonized, diluted fuel is used by a rather conventional combined cycle, based on an heavy-duty gas turbine with the characteristics of a Siemens V94.3A, i.e., with a pressure ratio of 17 and a turbine inlet temperature of 1350°C, and adapted to operate on hydrogen fuel as described in [10]. Plant CV (a standard IGCC without CO_2 capture) is very

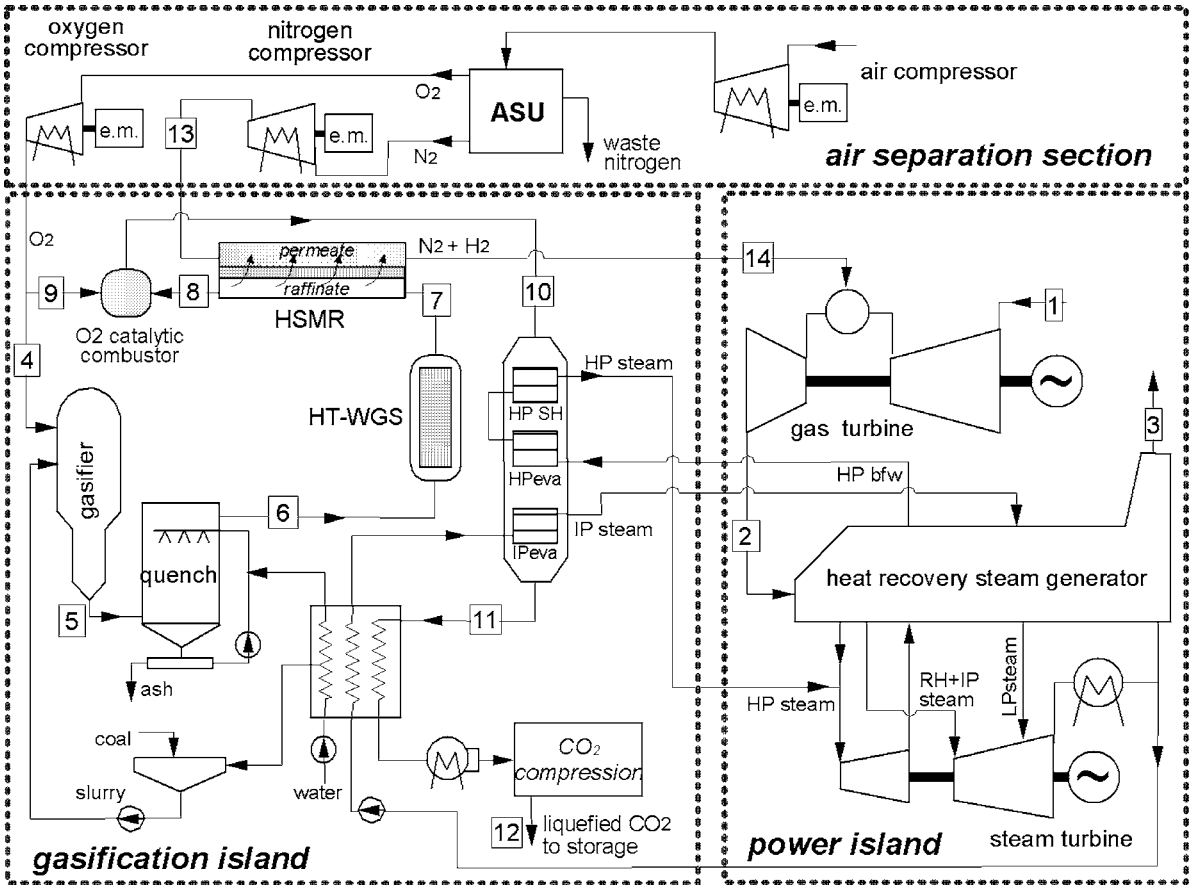

Fig. 4 Detailed scheme of the MO plant configuration

similar to plant CP, except for the absence of the two-stage WGSR and the CO_2 removal section; high-pressure steam cannot be produced from syngas heat recovery.

Detailed plant layouts for membrane-based plants MO and MC are shown in Figs. 4 and 5. In both plants, the syngas exiting the high-temperature WGSR enters the raffinate side of the HSMR, in which the water-gas shift reaction advances, aided by the continuous permeation of H_2 through the membrane. Using nitrogen as a sweep gas in a counter-current arrangement (Fig. 6) results in a high H_2 separation efficiency that minimizes the required surface area of the (relatively costly, Pd-based) membrane; in addition, the N_2 sweep gas keeps the permeate side pressure high enough to feed the gas turbine without further compression of the fuel gas. At about 450°C, the fuel gas is much hotter than is typically handled by gas turbine fuel systems (250–300°C is common in IGCCs); fuel gas cooling (producing steam) might be required in a practical design, but it is not implemented here.

Processing the HMSR raffinate stream to extract the CO_2 is a somewhat complex endeavor. The raffinate is composed mostly of CO_2 and H_2O, but also contains valuable fuel gases (unconverted CO, nonpermeated H_2 and traces of CH_4) as well as H_2S and N_2. The heating value of the raffinate ultimately depends on the gas separation efficiency of the membrane (or "hydrogen recovery factor," HRF, described below), which is a plant design parameter. In plant MO, the energy in the raffinate is recovered by burning it with oxygen in a catalytic combustor, producing a moderately hot (~900°C) stream of CO_2, H_2O, SO_2, and noncondensable gases (N_2 and excess O_2). A catalyst is required because of the very low heating value of the fuel. Heat is recovered from the oxidized stream by usual means (production of multi-pressure steam and warm water; see Fig. 4) and, after water condensation, high-pressure CO_2 (at a pressure equal to the gasification pressure minus the head losses) is available for dehydration and final compression. Associated with this scheme are two unresolved technological issues: (i) the development of the catalytic combustor, for which little experience exists for these particular operating conditions or even for power plants in general, and (ii) since the condensate comes from a stream that includes SO_2 and O_2, it will be very acidic. As a result, more complex designs and expensive materials will be required to limit corrosion problems in the heat exchangers and piping. In addition, the condensate might require the addition of a base such as limestone, re-introducing material and water balance issues more typical of FGD processes rather than of IGCCs[3].

Using an alternative membrane-based configuration, plant MC (see Fig. 5), is designed specifically to avoid these concerns altogether. In MC, the *uncombusted* HSMR raffinate is first cooled to ambient temperature, leaving sulfur in the form of H_2S. As a result, the aqueous condensate, although still acidic, is not particularly aggressive, having roughly same *p*H as condensate streams found in the syngas cooling process of typical quench-cooled IGCCs. During condensation, only liquid water (and gases dissolved in it) is removed; otherwise, the composition of raffinate stream is unchanged from that found at the HSMR exit. The cooled raffinate then undergoes a cryogenic separation process, described below in detail, in which CO_2 (the main component) and H_2S are first liquefied by cooling to −53°C and then separated by gravity from the uncondensed gas. The two output streams of this process are: (i) gaseous CO_2 and H_2S (at a pressure lower than that of the

[3]Alternative processes might be considered as a means to solve these issues; for instance, a modification of the WSA-SNOX system proposed by Haldor-Topsøe [11], producing H_2SO_4 as the final sulfurated compound. A detailed study of this problem is beyond the scope of this paper.

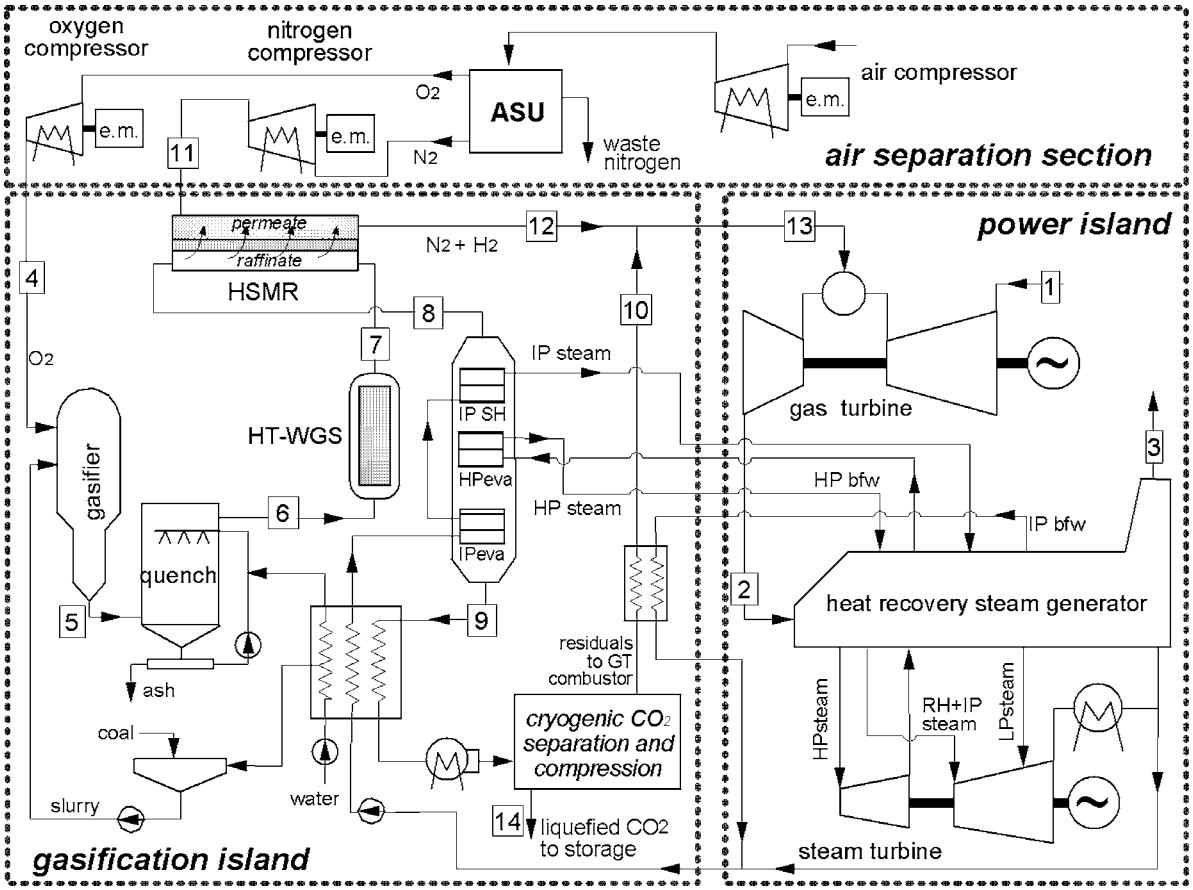

Fig. 5 Detailed scheme of the MC plant configuration

raffinate) which are compressed and liquefied for storage, and (ii) a stream of incondensable species (H_2, CO, CH_4, N_2, and some CO_2) to be used as additional fuel for the gas turbine, at the cost of emitting some CO_2.

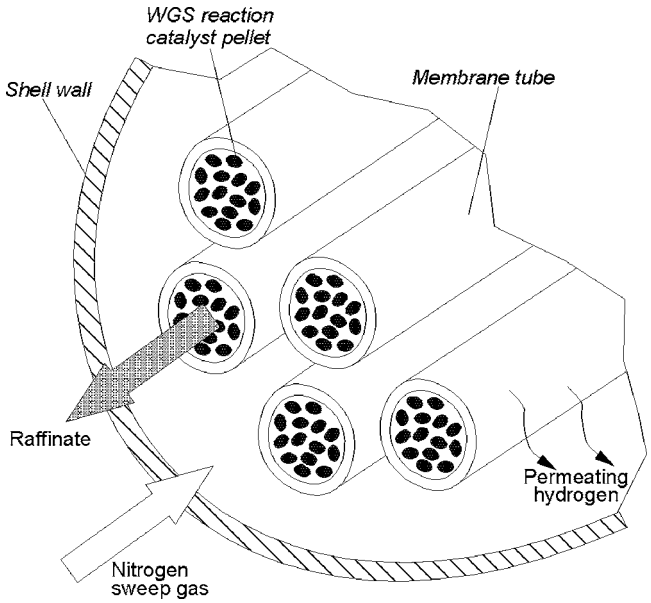

Fig. 6 HSMR shell-and-tube arrangement

Metallic Membranes for Gas Separation

In contrast with the conventional technology plants, where decarbonized fuel is produced by removing CO_2 from the shifted syngas, in membrane-based plants, the decarbonized fuel (derived from coal or natural gas) consists of pure hydrogen that has been extracted from the syngas via permeation through a membrane within a HSMR [12–16].

In the plant described here, continuous extraction of hydrogen shifts the WGS equilibrium, thus promoting the conversion of $CO+H_2O$ to CO_2+H_2, a process that effectively separates the carbon in the syngas (carried by CO_2) from its chemical enthalpy (carried by H_2). Hydrogen separation carried out in the HSMR also allows for a CO conversion efficiency that would require a much lower operating temperature in a conventional WGS reactor; said another way, higher temperatures (and thus faster reaction kinetics and a smaller reactor) are possible for a given (target) conversion efficiency.

The HSMR is modeled here as a series of H_2-permeable tubes filled with WGS catalyst, arranged in the shell-and-tube configuration of Fig. 6. Hydrogen is separated by means of a palladium-based membrane made of a dense metal film supported by a porous ceramic or metallic tube (Fig. 7).

In these membranes, H_2 transport occurs in a series of different stages, including: (i) dissociative adsorption of hydrogen on the syngas (or "raffinate") side of the membrane surface, (ii) diffusion of protons through the metal lattice, (iii) proton recombination to hydrogen molecules on the "permeate" side surface, and (iv) desorption of H_2 into the sweep gas. The consequences of the trans-

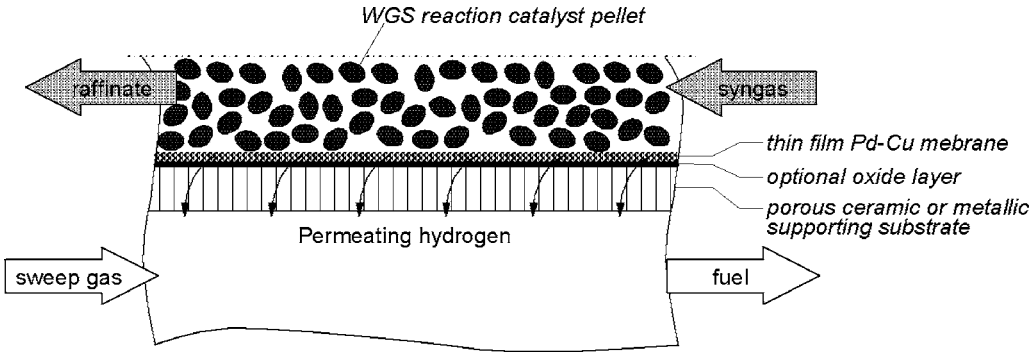

Fig. 7 Detail of the membrane reactor assembly. The oxide layer between Pd–Cu film and support is sometimes used in experimental membranes to limit molecular interdiffusion that dramatically reduces performance at high temperatures.

port mechanism are that, excluding leakages, H_2 selectivity is infinite (i.e., H_2 is separated at 100% purity) and the rate of permeation (Φ) is given by the expression

$$\Phi = \frac{\mathrm{Pe}}{t}(p_R^{0.5} - p_P^{0.5})$$

where Pe is H_2 permeability through the separating film material, t is the film thickness (while the ratio Pe/t is referred to as permeance), and p_R and p_P are, respectively, the partial pressures of H_2 on the raffinate and permeate sides of the membrane. The value assumed here for the exponent of pressure (0.5) implies that the hydrogen flux is controlled by the H atom diffusion rate through the dense metal layer, while the adsorption/dissociation and re-association/desorption steps are at equilibrium, a hypothesis experimentally verified in case of thick membranes.

Because of its high H_2 permeability and ability to catalyze H_2 dissociation/recombination, palladium is a common element in dense metal H_2 separation membranes. Unfortunately, traces of H_2S in the syngas fed to the membrane reactor prevent the use of most palladium alloys, which are poisoned or deactivated by H_2S concentrations as low as a few ppmv. However, experimental investigations indicate that Pd–Cu alloys, which can (under certain conditions) maintain their permeance in the presence of relevant H_2S concentrations, represent a possible candidate for processing coal gasifier syngas. The Pd-40Cu alloy (40% by weight in copper) has received particular attention because the bcc alloy phase formed below 600°C, allows permeability comparable to pure palladium [17].

Supported composite thin film Pd-40Cu membranes have been tested over a wide range of temperatures, with H_2S concentrations as high as 0.1% in H_2. A selected list of data is shown in Table 2. Edlund [18] tested a 50 μm thick Pd-40Cu membrane at 500°C (with a feed stream containing 1000 ppm H_2S in H_2 at 100 psig total pressure, and permeate at ambient pressure) for over 350 h, measuring a stable flux of 11.5 SCFH/ft^2 (corresponding to a H_2 permeance of 7.6×10^{-5} mol m^{-2} s^{-1} Pa$^{-0.5}$). Morreale [19] tested three different Pd–Cu alloys (80%, 60%, and 53% Pd by weight) and concluded that sulfur contamination does not affect the permeance within the fcc stability region, while the permeance of bcc phase is reduced by as much as two orders of magnitude when exposed to H_2S. At the operating temperature of the membrane reactor (450–500°C), the Pd-40Cu alloy presents a bcc-fcc mixed phase; from the shown data, it is unclear if exposure to 1000 ppm H_2S will significantly reduce the hydrogen permeability.

With regard to tests on sulfur-free feed streams, Howard et al. [20] report from the literature permeabilities in the range 2.32×10^{-9}–2.75×10^{-8} mol m^{-1} s^{-1} Pa$^{-0.5}$ in the temperature range 450–500°C for Pd–Cu alloys of different compositions. Their tests for a 100 μm thick membrane Pd-40Cu show a H_2 permeance of 6×10^{-5} mol m^{-2} s^{-1} Pa$^{-0.5}$. Roa et al. [21] assembled a very thin film (1.5 μm thickness) of Pd-40Cu alloy on an asymmetric support for which measured, in a test operated at 450°C, a H_2 flux of 0.81 mol m^{-2} s^{-1} under a pressure difference of 190 kPa (permeance of 3.46×10^{-3} mol m^{-2} s^{-1} Pa$^{-0.5}$) with a selectivity over N_2 equal to 90. In conclusion, we adopt a H_2 permeance of 1.83×10^{-4} mol m^{-2} s^{-1} Pa$^{-0.5}$ (the same value assumed by the authors in a previous paper [13] which, assuming the permeability estimated by Edlund [22] for 1000 ppm H_2S concentration, can be achieved by a ~20 μm thick membrane. Note that the concentration of H_2S in the syngas of IGCC plants considered here (fueled by bituminous Illinois #6 coal) exceeds this value by a factor of 5. Data at higher H_2S levels are unavailable (although Edlund claims that the Pd-40Cu alloy is not permanently poisoned by exposure to 10% H_2S streams). Note that the membrane permeance has almost *no* effect on the thermodynamic performance of the plant; rather, it controls the membrane surface area required to achieve the specified extent of H_2 extraction from the syngas, or the "hydrogen recovery factor" (HRF), defined as the mole ratio of permeated H_2 to H_2+CO in the entering syngas. Since the cost of the Pd–Cu membrane dominates the cost of the HSMR, its surface area affects the final cost of electricity.

At the comparatively high temperatures (~450°C) found in the HSMR, the WGS reaction kinetics are sufficiently rapid that most of the reaction and heat release occurs within the first ~20% of the reactor length, before a significant fraction of the H_2 can permeate through the membrane. For this reason, we choose to "split

Table 2 Performance of Pd-40Cu membranes from experimental data collected in the literature

Reference	Edlund [18]	Morreale et al. [19]	Morreale et al. [19]	Howard et al. [20]	Roa et al. [21]
Temperature, °C	500	441	441	450	450
Thickness, μm	50	100	100	100	1.5
H_2S vol. concentration, %	0.1	0.1	0.0	0.0	0.0
Permeance, mol m^{-2} s^{-1} Pa$^{-0.5}$	7.61×10^{-5}	4.00×10^{-6}	1.80×10^{-5}	6.00×10^{-5}	3.46×10^{-3}
Permeability, mol m^{-1} s^{-1} Pa$^{-0.5}$	3.80×10^{-9}	4.00×10^{-10}	1.80×10^{-9}	6.00×10^{-9}	5.18×10^{-9}

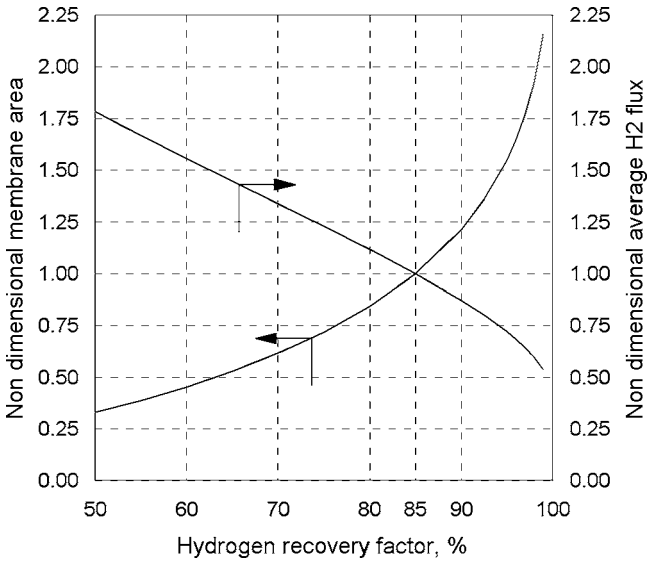

Fig. 8 Average H_2 flux and resulting membrane area as a function of the HRF for the HSMR of the MC plant, reported as a ratio with respect to the 85% HRF case

off" this section of the HSMR as a separate upstream adiabatic WGS reactor, (the "HT-WGS" reactor that appears in all membrane-based plants). This arrangement increases the hydrogen concentration in the HSMR feed stream, thereby reducing the membrane surface area; in addition, it shields the relatively delicate membrane reactor from large temperature gradients, frequent catalyst changes, and trace contaminants in the syngas.

A further reduction in membrane surface area is obtained by using an inert sweep gas in the permeate stream, arranged in a counter-current configuration. The sweep gas reduces the hydrogen partial pressure on the permeate side, which increases the driving force across (and thus the average H_2 flux through) the membrane. In plants devoted uniquely to electricity production (i.e., where the purity of the H_2 product is not important), there do not appear to be any drawbacks in using nitrogen as a sweep gas. A substantial flow of nitrogen is already available from the ASU at virtually no cost, and nitrogen is an effective diluent for H_2-rich gas turbine fuels necessary to moderate the flame temperature in order to limit NO_x production [23]. Therefore, in all membrane-based plants, we feed to the permeate side of the HSMR the full nitrogen flow from the ASU[4].

The membrane surface area required to achieve any given value of HRF is calculated by means of a one-dimensional, steady state model of the HSMR [24,25], with ideal gas behavior and infinite H_2 selectivity (i.e., 100% H_2 purity). The model assumes infinitely fast WGS reaction kinetics, so that chemical equilibrium is reached in each segment of the reactor. In general, the overall efficiency of the plant is found to increase monotonically with increasing HRF (with all other relevant parameters fixed) because the HSMR serves as a syngas "enthalpy splitter" that routes the pure H_2 permeate to the gas turbine topping cycle, and the raffinate to the less efficient steam turbine bottoming cycle. Unfortunately, attempting to increase plant efficiency via high HRF values, e.g., above ~80–90%, carries with it a significant cost. As shown in Fig. 8 (for case MC), increasing HRF leads to a near-linear decrease in the average H_2 flux through the membrane in the range of HRF between 50% and 85%. For HRF values higher than 85% the average H_2 flux drops faster so that the required membrane surface area (inversely proportional to the average H_2 flux)—and relative HSMR cost—increase precipitously. Varying the HRF from 50 to 99%, the combined effects of increasing the H_2 permeated and reducing the average flux lead to expand by almost an order of magnitude the membrane surface. As might be anticipated, such variations in HRF also dramatically alter the overall thermal balance of the plant. For any given plant, the optimal HRF value is determined by minimizing the cost of electricity (see, for example, De Lorenzo et al. [25]). Since this endeavor requires an economic analysis of the whole plant—an activity that is not undertaken here—we employ a fixed value of HRF=85% for all membrane-based plant calculations.

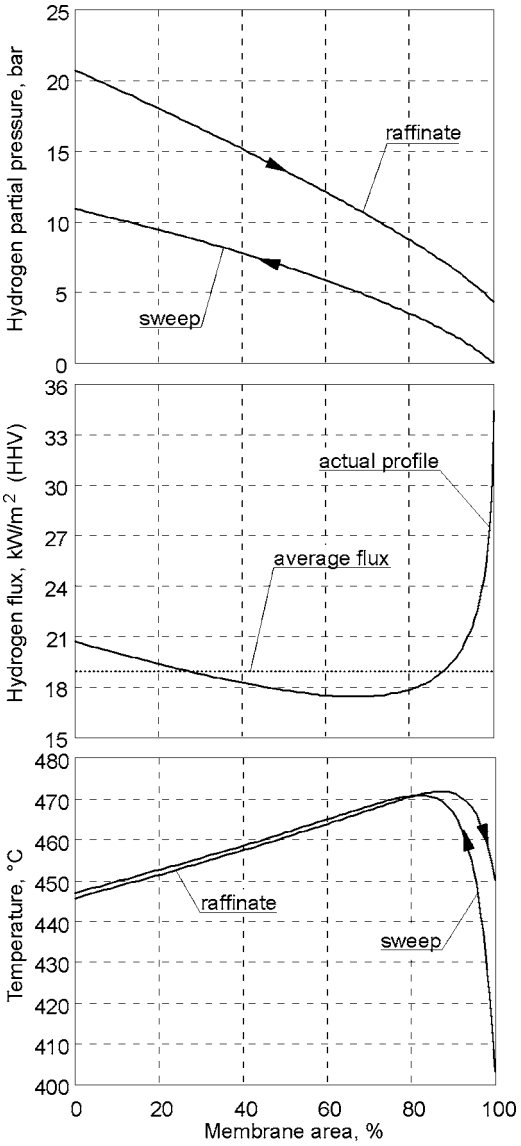

Fig. 9 —Operating condition of the hydrogen separation membrane water gas shift reactor placed in the MC plant (HRF=85%)

Figure 9 provides a detailed view of the operation of the HSMR in plant MC (at HRF=85%). In the top diagram, the hydrogen partial pressure profiles are shown as a function of the cumulative membrane area (or, equivalently, length along the reactor); note that zero corresponds to the raffinate inlet/permeate outlet end of the HSMR. Feed gas enters the HSMR at 65.2 bar with an equilibrium composition; given a H_2 concentration of 31.9 vol % the H_2 partial pressure is 20.8 bar. With the assumed HRF of 85%, the raffinate stream exits the reactor with a H_2 mole fraction of

[4]The ASU is sized to produce the oxygen required for coal gasification and, in MO configuration, to feed the catalytic combustor. Aside from the N_2 used to regenerate the filters, the pure nitrogen flow available for use as "sweep gas" is about three times the mass flow of oxygen.

6.7% and a partial pressure of 4.3 bar. At this point, the difference in hydrogen partial pressure between the streams reaches a minimum, but the permeation driving force $p_R^{0.5}-p_P^{0.5}$ reaches a *maximum* (as shown in the following diagram) because p_P is zero. Counter-current nitrogen sweep gas, entering the HSMR at the end where the raffinate stream exits, dilutes the permeated hydrogen and reduces its partial pressure, so that the permeate stream exits the reactor with a N_2/H_2 mole ratio of 1.34; given a total pressure of 25.6 bar (needed to feed the fuel in the gas turbine combustor), the H_2 partial pressure is 10.9 bar.

In the middle diagram, the H_2 flux through the membrane (proportional to $p_R^{0.5}-p_P^{0.5}$) is shown as a function of the cumulative membrane surface area. The countercurrent arrangement allows maintaining the H_2 flux rather uniform through the reactor length (the minimum H_2 flux is only 8.2% less than the reactor average), a key factor to reduce the total membrane surface for high HRF values.

Finally, temperature profiles through the HSMR are given in the bottom diagram. While the reactor is assumed to be globally adiabatic, heat transfer between raffinate and permeate streams is explicitly considered. Since reliable heat transfer coefficients are unavailable for this specific case, a preliminary guess of 100 W/m^2 K has been assumed based on estimates given in [26] for a membrane steam re-former. As evidenced by the temperature "crossover" shown in the figure, heat generation and transfer are complicated in the HSMR. On the left side of the diagram, the syngas enters the raffinate side of the reactor at a temperature slightly below that of the exiting permeate/sweep stream. Heat is generated in the WGS reactor, raising the temperature of the raffinate. At the same time, H_2 is lost through the membrane (lowering the heat capacity of the raffinate stream), *cooling down* the hotter permeate/sweep stream.

Third, heat is conducted through the membrane from the sweep to raffinate streams. Despite the varying heat capacities of both streams, their temperature profiles are observed to parallel each other through ~70% of the reactor, behavior similar to that found in a simple counter-current heat exchanger. At ~80% of the length of the reactor, the heat capacities are sufficiently altered that the temperature profiles cross. Working now from the right-hand side of the figure, the sweep gas enters the HSMR 50°C below the temperature of the exiting raffinate; heat transfer rates are highest in this section of the reactor. As it traverses the reactor, it receives both hot H_2 molecules (increasing its heat capacity) and heat, through the membrane from the hotter raffinate stream; thus, it is heated as the raffinate is cooled.

The observed temperature "crossover" is caused by the sensible enthalpy exchanged between the streams via the permeation of hot H_2 through the membrane. Heat is transferred (for both H_2 permeation and conduction across the membrane wall) from permeate to the raffinate stream at the left of the crossover point. At the right-hand side, the heat flux reverses. Given the low temperature difference along most of reactor length, the average conduction heat flux across the membrane is small (on average less than 280 W/m^2). The overall net heat transferred via conduction across the wall is only 3.2 MW (from raffinate to permeate) and therefore even substantial changes in the heat transfer coefficient do not significantly modify the heat balance of this component.

CO_2 Cryogenic Separation

In plant MC, the raffinate stream exiting the HSMR is cooled (for heat recovery) down to the ambient temperature. Since no combustion takes place, the sulfur is present in the mixture as H_2S, and corrosion problems during the cooling are comparable to those encountered in a standard IGCC. Due to the assumed 85% HRF, the cold syngas contains gases (mainly H_2 and CO) having a considerable heating value. To recover these fuel gases, we use a cryogenic process (considered by Davison et al. to be the most appropriate technique to purify CO_2 streams with high CO_2 concentration), where the CO_2 temperature is made sufficiently low that CO_2 is liquified and can be separated from the other species by gravity.

Table 3 Percentage molar flow of the streams at the borders of the cryogenic separation plant (Fig. 10)

	Input (1)	Fuel (7)	Flow to storage (17)
Ar	1.45	1.14	0.31
CH_4	0.06	0.04	0.01
CO	1.21	1.07	0.14
CO_2	79.02	5.04	73.97
H_2	15.46	14.97	0.48
H_2S	1.65	0.08	1.58
N_2	1.16	1.02	0.13
Total	100.00	23.37	76.63

The raffinate stream to be processed (second column of Table 3) contains a substantial amount of H_2S as a result of the high sulfur content of the Illinois #6 coal feedstock. Since the CO_2 is more volatile than H_2S (i.e., saturation temperature of H_2S is higher than that of CO_2 at all pressures), H_2S also liquefies along with CO_2 as the temperature of the gas mixture is reduced. Where CO_2 and H_2S co-storage is possible, a single process allows for simultaneous separation of H_2S and CO_2. If pure CO_2 storage is required, H_2S can be removed by physical or chemical absorption prior to CO_2 separation, and subsequently converted to elemental sulfur in a Claus/SCOT plant. Alternatively, H_2S could be separated by distillation of the chilled CO_2-H_2S liquid mixture inside the cryogenic plant. The performance of plant MC is presented only for the co-sequestration option. If an H_2S absorption process is added, the efficiency and power output will be slightly reduced because a small steam flow is bled from steam turbine to provide heat to the stripper re-boiler.

The CO_2 purification scheme adopted here is shown in detail in Fig. 10; it follows the method proposed by Wilkinson et al. [27] for purifying the CO_2-rich stream at the stack of an oxygen combustion boiler. It is based on a two-step flash separation that reduces the compression power required to overcome the pressure losses introduced by the process. In the adopted configuration, the CO_2-rich stream is first dehydrated with a circulating triethylene glycol desiccant and/or molecular sieve (also employed in the ASU) and, before entering the cold box, expanded from 60 to 33 bar, a pressure low enough for an effective separation between the liquid and gaseous phases (point 1 in Fig. 10). The stream is then cooled and partially condensed in the multiflow heat exchanger, HE1. The temperature at the hot side outlet of HE1 (point 2) is an important parameter in operating the process. Lowering this temperature reduces the mass flow rate sent to knockout drum 2 and hence the mass flow rate of the second-stage condensate circulated to (and the power required for) the low-pressure (LP) compressor. On the other hand, lowering the temperature of point 2 increases the heat duty of heat exchanger HE1, requiring a higher pressure drop in the throttling valve TV1 to keep a given minimum temperature difference inside HE1; this lowers the pressure of the combined condensate (point 16) entering the main compressor, increasing its duty. In order to strike a compromise between these opposing effects, the temperature of point 2 has been set to −25°C, a value that minimizes the overall compression power. Note that the extent to which incondensable gases can be recovered is almost independent of the temperature of point 2.

The liquid at point 13 (primarily CO_2 and H_2S) separated in the first knockout drum is throttled through valve TV1 and introduced to the cold side of heat exchanger HE1, in which it is heated and evaporated. The pressure drop in TV1 (14.3 bar) is set to ensure a 2 K minimum approach inside HE1 (see Fig. 11). Since the separation efficiency increases monotonically with decreasing temperature, the vapor fraction exiting the first knockout drum (point

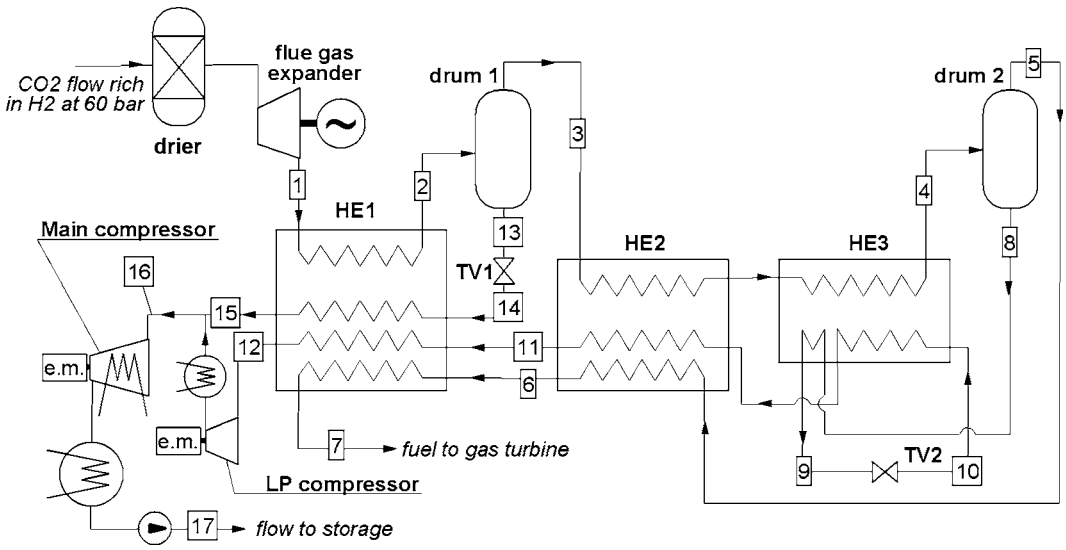

Fig. 10 Detailed scheme of the cryogenic process adopted in the MC configuration to separate the incondensable gases from the CO_2 stream. For individual stream properties (see Table 4).

3) is further cooled down to −53 °C through the exchangers HE2 and HE3 (point 4). This value has been selected to ensure that the temperature of the stream entering the cold side of HE3 (point 10) remains slightly above (+0.6 K) the CO_2 freezing point. The pressure drop introduced by the throttling valve TV2 (25.5 bar) and the particular arrangement of HE3 have again been selected to insure a 2 K temperature difference within HE3. The liquid streams separated in the drums and evaporated in the heat exchangers (points 12 and 15) are finally compressed in an intercooled compression train up to 100 bar and then pumped in liquid phase to 150 bar for long range transportation.

The vapor fraction exiting drum 2 (point 5), which contains 96.9% of the original hydrogen in the input stream, is heated up in HE2 and HE1 and combined with the primary H_2 fuel stream for the gas turbine. According to our calculations, carried out using Aspen Plus commercial software, 4.7% of the H_2S contained in the input stream is not separated by this cryogenic process, and would result in a significant sulfur emission at the stack if it is not removed before combustion. These sulfur emissions could be reduced to the ultra-low levels typical of IGCC technology by means of a chemical absorption process that, due to the low amount of the H_2S and the to high pressure of the feed stream, should be a relatively low-cost component.

In plant MC, the thermodynamic properties of the most significant points in the cryogenic separation process are listed in Table 4; the last two columns in Table 3 indicate the degree of separation achieved. A 93.6% CO_2 separation efficiency is attained, with a small power penalty of about 0.016 kW h per each kg of the flow sent to storage. This value includes the compression power needed to raise the pressure of the outlet flow to that of the inlet flow (~60 bar); i.e., the difference between the power required by the system of Fig. 10 and that of a simple compression of the inlet flow from 60 to 150 bar.

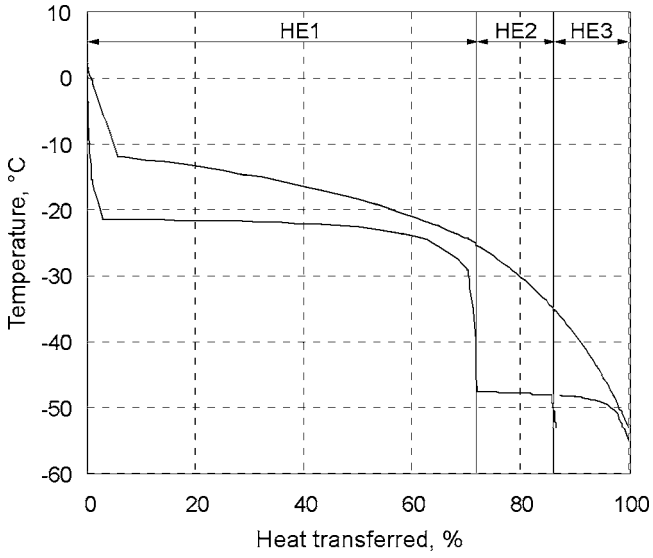

Fig. 11 Aggregate temperature-heat duty diagram for the heat exchangers included in the cryogenic process of Fig. 10

Calculation Method

Heat and material balances have been estimated by a computer code originally developed to assess the performance of gas/steam cycles for power production [28–30] and later extended to handle gasification of coal and essentially all the processes encountered

Table 4 Properties of selected streams in the cryogenic separation scheme (Fig. 10)

Point	Temperature, °C	Pressure, bar	Percentage Mass Flow Rate	Liquid Fraction
1	2.3	33.0	1.0000	0.0000
2	−25.0	33.0	1.0000	0.5645
3	−25.0	33.0	0.3350	0.0000
4	−53.0	33.0	0.3350	0.4633
5	−53.0	33.0	0.0975	0.0000
6	−40.3	33.0	0.0975	0.0000
7	0.3	33.0	0.0975	0.0000
8	−53.0	33.0	0.2376	1.0000
9	−50.0	33.0	0.2376	1.0000
10	−56.0	7.5	0.2376	0.9511
11	−40.3	7.5	0.2376	0.0000
12	−15.5	7.5	0.2376	0.0000
13	−25.0	33.0	0.6650	1.0000
14	−29.3	18.7	0.6650	0.9601
15	−15.5	18.7	0.6650	0.0000
16	−2.4	18.7	0.9025	0.0000
17	34.1	150.0	0.9025	1.0000

Table 5 Main assumptions adopted to generate the results presented in the paper

Coal Handling, Gasifier, and ASU	
Coal used: Illinois #6 (ultimate analysis: C: 61.27%, H: 4.69%, O: 8.83%, N: 1.1%, S: 3.41%, Moisture: 12%, Ash: 8.7%) HHV 26.143 MJ/kg, LHV 24.826 MJ/kg	
Water/solids ratio in slurry	0.50
Gasification pressure, bar	70
Syngas temperature at gasifier exit, °C	1327
Heat losses in gasifier, % of input LHV	0.5
Carbon conversion, %	99.2
ASU power consumption, kW h_{el}/kg_{PURE} O_2	0.261
O_2 purity, vol.%	95
Pressure of O_2 and N_2 delivered by ASU, bar	1.05
Pressure of O_2 to gasifier and catalytic combustor, bar	84
Temperature of O_2 to gasifier and combustor, °C	207.4
Pressure of N_2 to gas turbine combustor/air pressure	1.2
Electric power for auxiliaries, % of input coal LHV	1
Heat Exchangers	
Pressure loss, %	2
Minimum ΔT for gas-liquid heat transfer, °C	10
Pinch point ΔT for evaporators, °C	8
Heat losses, % of heat transferred	0.7
CO_2 Compressor	
Final delivery pressure, bar	150
Compressor isentropic efficiency, %	82
High pressure pump efficiency, %	75
Temperature at intercooler exit, °C	35
Power Cycle	
Steam evaporation pressures, bar	166, 36, 15, 4
Steam temperature at admission, °C	565
Condensation pressure, bar	0.04
HRSG gas side pressure losses, kPa	3
Pinch point ΔT, °C	8
Minimum ΔT in SH and RH, °C	25
Power for heat rejection, % of heat discharged	1
Gas turbine auxiliaries, % of gross output	0.35
Electric generator efficiency, %	98.7

Table 6 Comparison between performances quoted by the manufacturer and predictions from the model used for thermal balances for the natural gas-fired version of the Siemens V94.3A gas turbine. Exhaust mass flow rate: 600 kg/s; Pressure ratio: 17; Turbine inlet temperature: 1350°C; Compressor inlet Δp: 1 kPa; Turbine exhaust Δp: 1 kPa (simple cycle), 3 kPa (combined cycle). The input parameter used to reproduce the manufacturer's data have been adopted for all IGCC calculations.

Predictions	Siemens[a]	Our model
Simple cycle data		
Net electric power, MW	260.0	259.3
Turbine outlet temperature, °C	584	583
Net efficiency (LHV),%	38.20	38.17
Combined cycle data		
Net electric power, MW	390.0	388.3
Net efficiency (LHV),%	57.30	57.19

[a]Siemens web site, www.pg.siemens.com, May 2003.

in advanced power plants [31,32]. As mentioned before, performance of the HSMR and the cryogenic CO_2 separator have been simulated by means of additional software packages (custom MatLab code and Aspen Plus, respectively). The results of these ancillary models were incorporated into the overall mass and heat balance through an iterative procedure.

Table 5 summarizes the main assumptions, representative of state-of-the-art IGCC technology, adopted to generate the results presented here. The syngas streams exiting the gasifier and shift reactors are assumed to be in chemical equilibrium at the specified exit temperatures; their compositions are calculated accordingly. In a real gasifier, departures from equilibrium at the gasifier outlet may occur, depending on the reactivity of coal, the design of the gasification chamber, and the residence time within it; however, as long as the carbon conversion is properly accounted for, the impact of these variables on heat/mass balances has been found to be quite small [33]. At the outlet of the WGS reactors, the approach to equilibrium depends on the activity of the shift catalysts, which slowly decreases in time; our assumption of full equilibrium is believed to be satisfactory for most of the catalyst life.

The correlations and assumptions used in the power section of the model have been calibrated to reproduce the performance of advanced gas turbines [30] and of commercial combined cycles. For example, published information about the performance of the Siemens V94.3A gas turbine (a modeled version of which we employ here) is compared with the results of our computational model in Table 6. In particular, the gas turbine calculation procedure is structured to automatically take into account changes in the compositions of the fuel and/or the working fluid; for instance, cooling flows are varied according to different heat transfer properties. However, the adaptability of a gas turbine unit developed for natural gas to operate with different fuels (including dilution) must be properly considered in the calculations. A lower fuel heating value fuel yields a higher gas flow rate through the combustor and turbine, typically requiring: (1) a larger turbine nozzle section, (2) increased pressure ahead of the turbine (usually requiring additional compressor stages), or (3) reduced air flow through the compressor. To avoid modifying the gas turbine, we adopt the third approach.

By closing the compressor variable guide vanes (VGVs), the reduced air flow enables gas turbine operation at its design pressure ratio (equal to 17) and design turbine nozzle area. The turbine inlet temperature is kept unchanged at 1350°C after verification of the blade cooling requirements[5]. Provided that a sufficient stall margin exists to operate the compressor at constant pressure ratio and lower mass flow rate, this strategy does not affect the cycle efficiency[6], but it is important for the power output and therefore for the cost evaluation.

Results and Discussion

Table 7 summarizes the performance of the four plants previously described. Column CV reports the performance of an IGCC without CO_2 capture. Tables 8 to 10 give the temperature, pressure, mass, mole flow rate, and composition of the most significant streams in each plant (Figs. 3–5). Our discussion on comparative plant performance focuses on four issues: (1) CO_2 capture efficiency, (2) overall plant efficiency, (3) the tradeoffs inherent in choosing the N_2 flow rate, and (4) technological hurdles.

CO_2 Capture Efficiency. Of the three plants that capture CO_2, MO has the lowest specific CO_2 emissions (zero, in fact) because its gas turbine is fed only with pure hydrogen. Since the H_2 selectivity of the membrane is assumed to be infinite, the gas turbine fuel and exhaust flows are completely carbon free. Except for the unconverted carbon from the gasifier and scrubber (assumed to be

[5]Fueling a gas turbine with diluted hydrogen increases the water concentration in combustion products and leads to a higher heat transfer to the turbine blades compared to natural gas operation. Two options are possible: (i) lowering the firing temperature, (ii) increasing the coolant flow. For conceptual simplicity we preferred the second option that also yields the best achievable performance.

[6]Cycle efficiency is not affected provided that the compressor efficiency does not change as the VGVs close, as is assumed in this paper. This is a simplification, but is sufficiently accurate, to the authors' knowledge, within the limited range of VGV positions considered here (80% to 100% airflow).

Table 7 Performance of the plants considered in the paper

	CV	CP	MO	MC
Mol steam/C to WGSR	···	2.390	2.462	2.459
Gas turbine airflow, kg/s	536.0	553.9	495.1	532.8
Gas turbine power, MW	294.3	293.7	315.5	300.2
Steam turbine power, MW	178.6	179.3	266.3	181.0
Syngas expander, MW	9.5	9.8	0.0	0.0
ASU consumption, MW	−26.3	−28.5	−41.4	−27.6
O_2 compressor, MW	−16.8	−18.2	−26.4	−17.6
N_2 compressor, MW	−33.3	−28.5	−68.4	−45.5
Auxiliaries, MW	−15.9	−17.2	−20.2	−16.1
CO_2 capture & compr., MW	···	−28.6	−3.8	−7.8
Net power output, MW	390.1	361.9	421.5	366.6
LHV fuel input, MW	908.2	983.7	1098.1	949.4
Plant efficiency, %, LHV	42.95	36.79	38.38	38.61
Carbon removed, %	0.00	92.02	100.00	92.15
CO_2 emissions, kg/kW h	0.752	0.070	0.000	0.066
Stoichiometric flame temp, K	2300.0	2300.0	2130	2265
Membrane area, m^2	···	···	33202	34337

0.8% of the input), all carbon is contained in the CO_2-rich stream sent to geologic storage. In plant MC, the efficiency of cryogenic carbon separation is only 92.3%; the remaining gases are routed to the gas turbine (in order to recover the heating value of the H_2 and CO remaining in the CO_2-depleted raffinate), whose exhaust is vented to the atmosphere. Note that the CO_2 capture efficiency in plant MC depends on CO conversion in the HSMR (which in turn depends on HRF). At HRF=85%, the specific CO_2 emissions of MC (66 g/kW h) is comparable to that of the conventional technology reference plant, CP (70 g/kW h).

Overall Plant Efficiency. Among the three CO_2 capture plants, the two membrane-based plants have overall efficiencies that are higher (by ~1.7 percentage points) than reference plant CP. MC is the most efficient design (38.6% LHV), more efficient than CP because of its low power requirements for CO_2 capture and compression (7.8 versus 28.6 MW). Although plant MO uses even less power (3.8 MW) for CO_2 capture and compression, its efficiency (38.4% LHV) is not quite as high as MC because of its radically different power balance. In MC, the heating value of the raffinate stream is exploited in the gas turbine topping cycle, whereas in MO it is used to generate steam for the steam turbine bottoming cycle (note that the 266 MW steam turbine output in MO is much higher than MCs 181 MW). The difference in efficiency between the two plants would be even higher were it not for the non-negligible heating value of H_2S (24.2 MW_{th}, or 2.1% of the input coal LHV) which is burned to generate power in plant MO, instead of being discarded in the other plants (i.e., the difference would be higher if a low sulfur coal is used).

Nitrogen Flow: The Tradeoff Between Plant Efficiency, HSMR Cost, and NO_x emissions. The efficiencies of both membrane plants are affected by our practice of compressing *all* N_2 available from the ASU and routing it to the HSMR, a design that minimizes the membrane surface area, the HSMR cost, and NO_x emissions. The flow of N_2 in plant MC is larger than in CP, as reflected in their relative power requirements for N_2 compression (45.5 versus 28.5 MW). In plant MO, whose ASU is larger than in the other plants (because O_2 is used for raffinate combustion as well as gasification), the N_2 flow is greater still (compression power=68.4 MW). Adding compressed N_2 to the gas turbine (GT) combustor as a diluent effectively replaces a similar quantity of compressed air from the GT compressor, reducing its power needs and thus increasing the net GT output power. However, this gain is typically more than offset by the power required for N_2 compression. For example, the GT in MC generates 7 MW more than in CP, but the larger N_2 compressor requires an extra 17 MW. The practice of substituting N_2 for air as the turbine working fluid has two drawbacks: (1) N_2 injected as a diluent in the gas turbine combustor experiences a significant (~20%) pressure drop and therefore requires more compression work than the main air flow, and (2) the GT compressor efficiency is higher than that of the N_2 compressor. Another obstacle to the high N_2 flow rate in plant MO is that reducing the air flow to the GT compressor by closing the inlet guide vanes (while keeping the design pressure ratio) may drive the compressor beyond its surge margin. For such high N_2 flow rates, alternative solutions (e.g., larger turbine nozzle area) may be required.

Despite the loss in plant efficiency, the increased N_2 flow yields some advantages, although they are small. With a 50% increase in the flow of N_2, the membrane surface area required in MO is slightly (3.2%) lower than MC, although the latter membrane separates 16% more hydrogen (2.638 versus 2.275 mole/s). MO's increased N_2 flow also leads to a reduced stoichiometric flame temperature in the GT combustor (2130 K, compared to 2265 K in MC and 2300 K in CP) and therefore lower NO_x emissions are expected.

One way to explore these tradeoffs is to reduce the N_2 flow in MO to that used in MC (i.e., a N_2:H_2 mole ratio of 1.34). This boosts the plant efficiency by 0.32 percentage points to 38.7%, but raises the stoichiometric flame temperature to 2243 K, and increases the required membrane surface area by 20%. Given the many competing tradeoffs, it is clear that the optimal N_2 flow rate can be determined only in the context of a complete economic analysis designed to minimize the cost of electricity.

Technical Hurdles. Designing novel power cycles is an exercise in balancing potential thermodynamic and economic advantages against the difficult technological challenges they imply. It is worth recapitulating some of the technical obstacles the occur in membrane-based plants MC and MO. Despite many small scale experiments with membrane reactors, the HSMR envisioned here is presently just an abstraction. The real device would be very large (with almost a football field of surface area, ~34,000 m^2), expensive and probably relatively delicate. It remains to be demonstrated that such a unit can withstand attack by a chemically aggressive (and, compositionally, quite variable) coal synthesis gas at high temperature and pressure over the life of the plant. Plant MO employs a catalytic combustor to burn a low-BTU syngas containing H_2S, and a condensing heat exchanger that operates at high pressure with an extremely acidic aqueous condensate. It is not clear whether or not such devices can be economically built and maintained. The cryogenic plant system in MC plant, even if not including "exotic" components, is rather innovative and complicated; it requires large heat transfer surfaces made of costly materials (high quality stainless steel) with a significant cost impact. In both membrane plants, the H_2+N_2 permeate stream exits the HSMR over 400°C and is directly injected into the GT combustor; this temperature is notably higher than that encountered in current IGCC plants[7]. CO_2+H_2S cosequestration raises a host of regulatory, technical, geological, and safety-related issues that are under active investigation. Finally, the whole idea of large scale CO_2 capture and storage for the purpose of mitigating global climate change is a work in progress. Studies such as this illuminate but a small portion of this complex problem.

Conclusions

The membrane-based plants were expected to have the following advantages over the commercially ready reference plant: (1) superior efficiency, (2) higher CO_2 capture efficiency, and (3) a reduction in plant capital cost. To quantify these advantages, aiming to understand their potential in the power production industry,

[7]The efficiency loss caused by fuel cooling to 300°C (a value compatible with the IGCC standards) can be estimated in 0.3 percentage points when heat is recovered to generate HP steam.

we calculated the thermodynamic performance of low CO_2 emission IGCC cycles based on H_2 separation membranes. These cycles present slightly higher thermodynamic and CO_2 removal efficiencies than comparable plants based on the conventional gas separation technology (CO_2 absorption by means of solvents). The potential efficiency improvement here evaluated is 1.6–1.8 percentage point, but further improvement should be possible by adopting more efficient syngas cooling technology. In fact, when using syngas coolers rather than quench, the HSMR solutions are expected to show their best potential, not requiring large water quantities to promote the shift reaction (we intend to investigate this aspect in a future paper). A better CO_2 capture is actually achieved, especially for the configuration with catalytic combustion with 100% removal.

The economic aspects will be investigated in a subsequent paper, but on a very rough basis it can be said that the investment cost of MC plant will be convenient, compared to a conventional (CP) plant, if the sum of the costs of membrane reactor and cryogenic system is lower than the cost of the CO_2-H_2S separation/compression system (including absorption and regeneration), the other components being shared by both the plants. The same applies to the MO plant, considering the costs of membrane reactor and catalytic combustor. However, the overall cost of the CO_2 -H_2S separation/compression section only accounts for about 15% of the total investment cost of the CP plant [7], substantial capital cost savings do not appear achievable by means of HSMR, also considering that an expensive material as palladium is required for the membrane reactor.

In conclusion, it is authors' opinion that HSMR may represent an advancement in the state-of-the-art of CO_2 capture in power plants, deserving more research and development actions to overcome the substantial technical hurdles that remain, but the enhancement allowed by this technology is limited to few percentage points in terms of plant performance and cost.

References

[1] Rogner, H. H., et al., 2000, "Energy Resources," World Energy Assessment: Energy the Challenge of Sustainability, Study Sponsored Jointly by the U.N. Development Programme, the U.N. Department of Social and Economic Affairs, and the World Energy Council. Bureau for Development Policy, United Nations Development Programme, New York, Table 5.7, p. 149.

[2] Chiesa, P., Consonni, S., Kreutz, T., and Williams, R., 2004, "Co-production of Hydrogen, Electricity and CO_2 From Coal With Commercially Ready Technology. Part A: Performance and Emissions," Int. J. Hydrogen Energy, **30**(7), pp. 747–767.

[3] Shelton, W. W., and Lyons, J. L., 2000, "Texaco Gasifier IGCC Base Cases," DOE/NETL Process Engineering Division, PED-IGCC-98-001, June, revision, http://www.netl.doe.gov/coal/gasification/system/texac3y.pdf (accessed 10-28-04).

[4] Domenichini, R., 2003, "Gasification Power Generation Study," IEA Greenhouse Gas R&D Programme.

[5] Holt, N., Booras, G., and Todd, D., 2003, "A Summary of Recent IGCC Studies of CO_2 Capture for Sequestration," *Proc. of 2003 Gasification Technologies Conference*, San Francisco, October.

[6] Shilling, N., 2003, "Gas Turbines for Low CO_2 Power Production," Conference on Cycles for Low Carbon Dioxide, Cranfield University, Cranfield, UK, March.

[7] Kreutz, T., Williams, R., Consonni, S., and Chiesa, P., 2005, "Co-production of Hydrogen, Electricity and CO_2 From Coal With Commercially Ready Technology. Part B: Economic Analysis," Int. J. Hydrogen Energy, **30**(7), pp. 769–784.

[8] Bachu, S., and Gunter, W. D., 2003, "Acid Gas Injection in the Alberta Basin, Canada: A CO_2 Storage Experience," *Proc. of the 7th International Conference on Greenhouse Gas Control Technologies*, Vancouver, Canada, September.

[9] Lozza, G., and Chiesa, P., 2001, "Low CO_2 Emission Combined Cycles with Natural Gas Reforming, Including NO_x Suppression," ASME Paper No. 2001-GT-561.

[10] Lozza, G., and Chiesa, P., 2002, "CO_2 Sequestration Techniques for IGCC and Natural Gas Power Plants: A Comparative Estimation of Their Thermodynamic and Economic Performance," *Proc. of CCT2002* (International Conference on Clean Coal Technologies for our Future), Chia Laguna, CA, Italy, October.

[11] Laursen, J. K., 1999, "Sulfur Removal by the WSA Process," available at Haldor Topsøe website: http://www.haldortopsoe.com/site.nsf/vALLWEBDOCID/KVOOPGFB7/$file/Env-WSAdownl422pdf.pdf (accessed on 10-19-04).

[12] Paglieri, S. N., and Birdsell, S. A., 2002, "Composite Membranes for Coal Gas Reforming," 16th Annual Conference on Fossil Energy Materials, April, available at the NELT website: http://www.netl.doe.gov/publications/proceedings/02/materials/paglieri.pdf (accessed on 10-19-04).

[13] Kreutz, T. G., Williams, R. H., Socolow, R. H., Chiesa, P., and Lozza, G., 2002, "Production of Hydrogen and Electricity From Coal With CO_2 Capture," *Proc. of the 6th International Conference on Greenhouse Gas Control Technologies*, Kyoto, Japan, October.

[14] Rao, A. D., Samuelsen, G. S., Robson, F. L., and Geisbrecht, R. A., 2004, "Coal-Based Power Plant System Configurations for the 21st Century," ASME Paper GT2004-53105.

[15] Jordal, K., Bredesen, R., Kvamsdal, H. M., and Bolland, O., 2004, "Integration of H_2-Separating Membrane Technology in Gas Turbine Processes for CO_2 Capture," Energy, **29**, pp. 1269–1278.

[16] Bredesen, R., Jordal, K., and Bolland, O., 2004, "High-Temperature Membranes in Power Generation With CO_2 Capture," Atmos. Technol., **43**, pp. 1129–1158.

[17] Roa, F., Way, J. D., McCormick, R. L., and Paglieri, S. N., 2003, "Preparation and Characterization of Pd–Cu Composite Membranes for Hydrogen Separation," Chem. Eng. J., **93**, pp. 11–22.

[18] Edlund, D., 1996, "A Membrane Reactor for H2S Decomposition," Proc. of Advanced Coal-Fired Power Systems "96 Review Meeting, Morgantown, WV, July; available at the NELT website: http://www.netl.doe.gov/publications/proceedings/96/96ps/ps_pdf/96pspb14.pdf (accessed 19-10-04).

[19] Morreale, B. D., Ciocco, M. V., Howard, B. H., Killmeyer, R. P., Cugini, A. V., and Enick, R. M., 2004, "Effect of Hydrogen-Sulfide on the Hydrogen Permeance of Palladium-Copper Alloys at Elevated Temperatures," J. Membr. Sci., **241**, pp. 219–224.

[20] Howard, B. H., Killmeyer, R. P., Rothenberger, K. S., Cugini, A. V., Morreale, B. D., Enick, R. M., and Bustamante, F., 2004, "Hydrogen Permeance of Palladium-Copper Alloy Membranes Over a Wide Range of Temperatures and Pressures," J. Membr. Sci., **241**, pp. 207–218.

[21] Roa, F., Block, M. J., and Way, J. D., 2002, "The Influence of Alloy Composition on the H_2 Flux of Composite Pd–Cu Membranes," Desalination, **147**, pp. 411–416.

[22] Edlund, D. L., and Henry, M. H., 1995, "A Catalytic Membrane Reactor for Facilitating the Water-Gas-Shift Reaction at High Temperatures," Phase II Final Report to the U.S. DOE, Contract No. DE-FG03–91-ER81229, Nov. 30.

[23] Chiesa, P., Lozza, G., and Mazzocchi, L., 2003, "Using Hydrogen as Gas Turbine Fuel," ASME Paper No. 2003-GT-38205.

[24] Viganó, F., 2002, "Performance Evaluation of Hydrogen Separation Membrane Reactors for Water Gas Shift" (in Italian) thesis, Politecnico di Milano, Italy.

[25] De Lorenzo, L., Kreutz, T., Chiesa, P., and Williams, R., 2005, "Carbon-Free Hydrogen and Electricity From Coal: Options for Syngas Cooling in Systems Using a Hydrogen Separation Membrane Reactor," ASME Paper No. GT2005-68572.

[26] Marigliano, G., Barbieri, G., and Drioli, E., 2001, "Effect of Energy Transport on a Palladium-Based Membrane Reactor for Methane Steam Reforming Process," Catal. Today, **67**, pp. 85–99.

[27] Wilkinson, M. B., Boden, J. C., Panesar, R. S., and Allam, R. J., 2001, "CO_2 Capture via Oxyfuel Firing: Optimisation of a Retrofit Design Concept for a Refinery Power Station Boiler" 1st National Conference on Carbon Sequestration, Washington DC, May 15–17.

[28] Lozza, G., 1990, "Bottoming Steam Cycles for Combined Gas Steam Power Plants: A Theoretical Estimation of Steam Turbine Performance and Cycle Analysis," *Proc. of 1990 ASME Cogen Turbo*, New Orleans, ASME, New York, pp. 83–92.

[29] Consonni, S., 1992, "Performance Prediction of Gas/Steam Cycles for Power Generation," Ph.D. thesis, Princeton University, Princeton, NJ.

[30] Chiesa, P., and Macchi, E., 2002, "A Thermodynamic Analysis of Different Options to Break 60% Electric Efficiency in Combined Cycle Power Plants," ASME Paper GT-2002–30663.

[31] Chiesa, P., Consonni, S., and Lozza, G., 1998, "A Comparative Analysis of IGCCs With CO_2 Sequestration," 4th International Conference on Greenhouse Gas Control Technologies, Interlaken, Switzerland, August.

[32] Campanari, S., and Macchi, E., 1998, "Thermodynamic Analysis of Advanced Power Cycles Based Upon Solid Oxide Fuel Cells, Gas Turbines and Rankine Cycles," ASME Paper No. 98-GT-585.

[33] Chiesa, P., 1995, "Thermodynamic Analysis of Humid Air Gas Turbine Cycles (HAT) Integrated With Coal Gasification Processes," Ph.D. thesis, Politecnico di Milano, Italy.

High-Pressure Turbine Deposition in Land-Based Gas Turbines From Various Synfuels

Jeffrey P. Bons
Jared Crosby
James E. Wammack
Brook I. Bentley

Department of Mechanical Engineering,
Brigham Young University,
Provo, UT 84602

Thomas H. Fletcher
Department of Chemical Engineering,
Brigham Young University,
Provo, UT 84602

Ash deposits from four candidate power turbine synfuels were studied in an accelerated deposition test facility. The facility matches the gas temperature and velocity of modern first-stage high-pressure turbine vanes. A natural gas combustor was seeded with finely ground fuel ash particulate from four different fuels: straw, sawdust, coal, and petroleum coke. The entrained ash particles were accelerated to a combustor exit flow Mach number of 0.31 before impinging on a thermal barrier coating (TBC) target coupon at 1150°C. *Postexposure analyses included surface topography, scanning electron microscopy, and x-ray spectroscopy. Due to significant differences in the chemical composition of the various fuel ash samples, deposit thickness and structure vary considerably for each fuel. Biomass products (e.g., sawdust and straw) are significantly less prone to deposition than coal and petcoke for the same particle loading conditions. In a test simulating one turbine operating year at a moderate particulate loading of 0.02 parts per million by weight, deposit thickness from coal and petcoke ash exceeded 1 and* 2 mm, *respectively. These large deposits from coal and petcoke were found to detach readily from the turbine material with thermal cycling and handling. The smaller biomass deposit samples showed greater tenacity in adhering to the TBC surface. In all cases, corrosive elements (e.g., Na, K, V, Cl, S) were found to penetrate the TBC layer during the accelerated deposition test. Implications for the power generation goal of fuel flexibility are discussed.* [DOI: 10.1115/1.2181181]

Introduction

Due to current economic and political pressures, alternate fuels such as coal, petcoke, and biomass are being considered to produce substitute syngas fuels to replace natural gas in power turbines. Given the present volatility in natural gas markets and the uncertainty regarding projected fuel availability over the 20–30 yr design lifetime of newly commissioned power plants, coal and petroleum derivative fuels are already being used at a handful of gas turbine power plants worldwide. In addition, intermediate goals of the DOE Future Gen and DOE Turbine Program focus on coal syngas as a turbine fuel in an effort to reduce dependency on foreign supplies of natural gas. At the same time, environmental concerns have led to government mandated biomass utilization in boilers in some European countries. Biomass turbine power plants are of particular interest since they would potentially provide a CO_2 emission benefit without expensive CO_2 capture and sequestration. Thus, the stage is set for broader integration of alternate fuels in gas turbine power plants.

Despite the greatest precaution in filtration and cleanup systems, small levels of unwanted contaminants are introduced into the hot section of gas turbines. At the high mass flow rates typical of large utility engines, even trace amounts of particulate can accumulate to significant quantities. For example, a particulate concentration of 0.1 parts per million by weight (ppmw) will produce 2 tons of ingested material in a large utility power plant during an 8000 h operating year. These contaminants may either pass through the engine with no effect, or attack the surfaces of the engine through erosion, corrosion, or deposition. The adverse effects of these three degradation mechanisms are well documented in the literature. Erosion reduces engine performance by opening up tip clearances and altering blade contours. For example, Ghenaiet et al. [1] reported a 6–10% loss in adiabatic efficiency for 6 h of sand ingestion in an axial fan. Deposition poses the opposite problem by clogging critical bleeds and reducing blade flow passages. Wenglarz [2] proposed a model for estimating the loss in turbine power that occurs when the choked mass flow limit is reduced due to deposit buildup at the nozzle guide vane passage throat. Kim et al. [3] documented the disastrous results of film-cooling holes being plugged by massive ingestion from simulated volcanic ash in aircraft gas turbines. Deposition can also accelerate material corrosion by bringing significant concentrations of corrosive elements in direct (molten) contact with the turbine material system. Both erosion and deposition are also known to increase levels of surface roughness, which produces corresponding increases in heat transfer (up to 50%) and skin friction (up to 300%) [4]. Finally, all three degradation mechanisms (including corrosion) reduce part life and increase the risk of run-time failure.

The prevailing mode of surface degradation for a given combination of airborne contaminants is a function of the specific turbine operating environment. Two of the important determining factors are the gas (and particle) temperature and the turbine surface temperature. The gas temperature determines the physical state of the particles (e.g., solid, molten, or vapor). This in turn influences whether the particles rebound from the surface (potentially causing erosion upon impact) or instead tend to deposit. Previous turbine tests with coal-derived fuels by Wenglarz and Fox [5,6] show a dramatic increase in deposition rate as the gas temperature is raised above the particulate melting point. In their study, coated turbine superalloy specimens were subjected to 2–5 h of deposition from three coal-water fuel (CWF) formulations. The coal had been cleaned to simulate ash levels ($\sim$1%) that would be considered acceptable for use in a gas turbine. The ash consisted primarily of Fe, Si, Al, and Ca with $<$2% concentrations of K, Na, P, Ti, and Mn. The fuel was burned in a low-emission subscale turbine combustor at realistic flow rates (e.g.,

Contributed by the International Gas Turbine Institute (IGTI) of ASME for publication in the JOURNAL OF ENGINEERING FOR GAS TURBINES AND POWER. Manuscript received August 30, 2005; final manuscript received September 6, 2005. IGTI Review Chair: K. C. Hall. Paper presented at the ASME Turbo Expo 2005: Land, Sea, and Air, Reno, NV, June 6–9, 2005, Paper No. GT2005-68479.

impact velocities ~180 m/s) and gas temperatures (1100°C). With the turbine specimens located at two different streamwise locations downstream of the combustor exit, the influence of gas temperature on deposition rate could be studied. It was noted that the upstream specimens (operating at gas temperatures ~1100°C) experienced one to two orders of magnitude higher deposition rates compared to the downstream specimens (operating at gas temperatures ~980°C). High-temperature deposits were primarily Fe, Al, and Si, while the lower temperature deposits had a disproportionately high concentration of Na. This corresponded with the lower softening temperature of Na compared to Al and Si. In addition, the lower temperature deposit spalled off with test shutdown, while the higher temperature deposits adhered to the surface more tenaciously. Compared to a previous series of tests with lower ash content (0.025%) residual fuel oil, the deposit levels with coal-water fuels were two to three orders of magnitude larger for the same operating temperature [7].

Wenglarz and Fox [5] also explored the possibility of subcooling the upstream turbine specimens and found a factor of 2.5 reduction in deposits for a 200°C drop in metal surface temperature. Lower deposit formation in areas of reduced surface temperature was also noted by Bons et al. [8] in their study of serviced turbine hardware. Cooled turbine vanes which exhibited large (1–2 mm thick) marine deposits over their entire surface were noticeably free of deposits in the film-cooling flow path where surface temperatures are significantly lower. This effect created substantial troughs or "furrows" which extended for more than 10 hole diameters downstream of the cooling-hole exit. These results confirm the important role of gas and surface temperature in determining deposition rates from ash-bearing fuels.

For biomass fuels, Patnaik et al. [9] conducted flame tunnel tests on MCrAlY (oxidation-resistant coating) and TBC material systems using a wood pulp liquid fuel suspension. Specimen temperatures of 850°C and 650°C were attained to simulate conditions in a gas turbine, though gas velocities were not representative. The study focused on the corrosive influence of alkali elements in the high-ash content biomass fuel. These elements can not be washed out with standard scrubbing techniques. Ash deposits of up to 2 mm in thickness were observed after 50 h of exposure to the high-temperature biomass flame. The actual deposition rate may have been significantly larger than this given evidence of deposit flaking and renewal during the test duration. The deposits consisted primarily of K and Ca, with smaller concentrations of Ni, Si, Cu, Cr, and S. Subsequent 1000 h corrosion tests at constant temperature yielded evidence of Type I hot corrosion despite low levels of sulfur present in the deposit. Significant coating degradation and removal was noted due to repeated fusing and flaking off of deposits during the flame exposure test.

In a related study, Wright et al. [10] reviewed the composition of typical biomass fuels (grass-based and wood-based) and assessed the relative degradation threat posed to gas turbines by these renewable fuels compared to coal. Wood and grass-based biomass fuels both have higher levels of corrosive alkali metals such as K and Na than coal. Of the two classifications studied, grass-based fuels were identified as having the potential to be most troublesome due to higher levels of S and Cl. Similar to Patnaik et al. [9], this study by Wright et al. concluded that biomass cleanup to remove alkali is more problematic than coal due to the high moisture content.

Considering these well-documented findings, power plant operators and manufacturers interested in promoting fuel flexibility in gas turbines would do well to consider issues related to deposition from higher ash content fuels. This is particularly critical in light of recent advances in turbine material systems which now routinely allow turbine inlet temperatures in excess of 1400°C. At these elevated temperatures, more stages of a gas turbine encounter gas (and particles) at temperatures in excess of particle melting temperature, and are thus more susceptible to deposition. Moreover, modern G- and H-class turbines rely heavily on innovative cooling strategies which may influence deposition patterns in the flow path. Finally, advanced material systems (EB-PVD and APS TBCs) have been designed and validated during a period when natural gas is the gas turbine fuel of choice. As such, the impact of depositing contaminants on TBCs may present unforeseen viability issues for existing high-performance turbines. Clearly, new research is needed to evaluate the impact of alternate fuels in this complex operating environment.

The objective of the present study is to provide a comparative analysis of various fuel alternatives at engine representative conditions. This is done using the recently commissioned Turbine Accelerated Deposition Facility (TADF) described in detail by Jensen et al. [11]. The design premise of this test facility is that deposition in gas turbines is governed by essentially three critical parameters: gas (particle) temperature, gas (particle) impact velocity, and particle loading. Gas temperature insures that the particles are in the correct physical state (solid, molten liquid, or vapor) when they arrive at the turbine surface, particle velocity governs the primary delivery mode of inertial impaction, and particle loading is the net particle loading experienced by the turbine over a given period of time. The latter of these three simulation parameters is potentially the most controversial since it implies that 4000 h of deposition exposure on a real gas turbine can be simulated with a 4 h accelerated laboratory test as long as the net particle throughput is matched. Thus, by increasing the particle concentration in the combustor gas (parts per million by weight, or ppmw) by three orders of magnitude from that found in a typical operating turbine, the test duration can be reduced by the same three orders of magnitude to preserve the same particle loading [ppmw h]. The validation of this hypothesis was the subject of a previous paper by Jensen et al. [11]. Heat transfer characteristics of deposits generated in the accelerated deposition facility were compared with deposits on in-service hardware. It was found that for all of the critical features affecting convective heat transfer (i.e., deposit surface roughness) and conduction heat transfer (i.e., deposit thickness, structure, and elemental constituents), the accelerated test produced comparable results to longer duration exposure.

Using this accelerated facility, the influence of different operating parameters on deposition can be rapidly evaluated in a comprehensive test matrix. For example, a previous study considered the effect of gas temperature and impingement angle on deposit formation from airborne particles typical of dust-laden operating environments [11]. The present study addresses the effect of different fuels at constant operating conditions.

Ash Preparation and Characterization

To avoid the considerable capital expense and complexity associated with simulating combustor operation with different fuel formulations (e.g., fluidized bed, gas cleanup system, etc.), the Turbine Accelerated Deposition Facility (TADF) employs a natural gas combustor seeded with ash particles. Thus, it is critical to insure that the ash particles are of the same size, state, and composition that might be expected to impact on turbine surfaces after reasonable gas cleanup.

The four ash samples used in this study were collected from various sources. Coal and petcoke samples were obtained externally, while the biomass samples were prepared locally using facilities in BYU's Advanced Combustion Engineering Research Center. Subbituminous coal fly ash was obtained from an operating power plant, while the petcoke ash is boiler slag obtained from a combined cycle gas turbine power plant operating with a blend of 55% petcoke and 45% coal. Straw ash was produced in a two-step process. First, raw material was partially burned to eliminate volatiles. Second, the partially burned ash was placed in a programmable furnace and cycled through a standard ashing process. This same two step process was repeated to generate sawdust ash. A standard kitchen wheat grinder set on the finest setting was used to grind the ash particles to the size needed for testing.

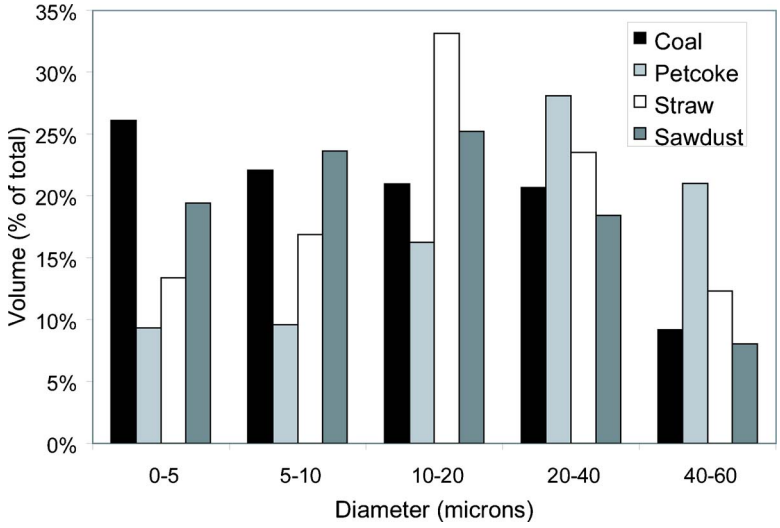

Fig. 1 Ash particle size distribution from Coulter Counter measurement

Since the objective of the study was to simulate ash that could be entrained by the flow leading to the turbine, the particles must be small enough to navigate the various gas cleanup systems. Filtration systems in modern gas turbine powerplants are designed to remove all particles with diameters greater than 10 μm and a majority of particles larger than 1 μm. Measurements of particle size distributions from properly functioning advanced filtration systems indicate mass mean diameters of order 1 μm, even for hot gas clean-up. With inadequate or degraded filtration, these levels can be exceeded. Thus the target mass mean particle diameter for this study was less than 10 μm. After grinding, the size of each ash sample was determined using a laser-based Coulter Counter. The ash was suspended in distilled water and dispersed through the Coulter Counter feed system with the use of a sonicator and/or small amounts of liquid detergent. When illuminated by the laser beam, the particles scatter light in patterns according to their size. This scattered light was detected using photodetectors and converted to the particle distributions shown in Fig. 1; mass mean diameters are presented in Table 1. With the exception of the petcoke sample, the mass mean diameters are all between 10 μm and 20 μm, with a significant portion of each sample under 10 μm. Thus, the majority of particles in this study are larger than those found with properly functioning gas cleanup. Larger particles (>1 μm) are deposited by inertial impaction while smaller particles (<1 μm) are generally deposited by turbulent diffusion and thermophoresis. Thus, the results of this study are appropriate for deposition dominated by inertial impaction. Nearly all of the particles are less than 40 μm in diameter, which was determined to be the maximum diameter that would attain full velocity and thermal equilibrium with the hot gases in the combustor exit nozzle of the TADF [11]. Thus, the particles are expected to be at the proper gas temperature before impact.

Following the Coulter Counter measurement, ash samples were placed inside a FEIXL30 environmental scanning electron microscope to obtain qualitative validation of the particle size and shape. Figure 2 shows typical ESEM images from two of the ash samples. The coal ash particles appeared mostly spherical in shape while the straw ash particles were more uniform in size but more irregular in shape. The petcoke ash (not shown) was similar to the straw in shape though not in size. Finally, the sawdust ash particles (not shown) were highly irregular, with indistinct boundaries between clumps and edges that appeared fibrous. The bulk density of each ash sample was measured in a graduated cylinder, and the apparent density (mass per particle exterior volume) was calculated using an estimated packing factor of 0.5 (see Table 1).

X-ray spectroscopy was used to determine the composition of the four types of ash while they were in the ESEM. An EDAX Phoenix Spectrometer with super ultrathin window was used to obtain elements down to an atomic number of carbon. The elemental compositions of the four types of ash, as determined by the x-ray analysis, are given in Table 1. Values of 0.0 indicate levels below the background noise level of the spectrometer. An independent elemental analysis was conducted on the four ash samples by ALS Chemex using inductively coupled plasma atomic emission spectroscopy (ICP-AES). The results identified the same elements as the x-ray spectrometer in approximately the same weight percentages, though the ICP-AES analysis of the bulk ash showed 15–20% greater silicon content compared to the x-ray measurements which were spot measurements. In addition, the ICP-AES is unable to measure vanadium.

Table 1 Ash particle summary statistics: size, density, and average elemental composition

	Coal	Petcoke	Straw	Sawdust
Mass Mean Diameter (μm)	13.3	33.0	17.6	19.7
Median Diameter (μm)	10.6	28.5	15.1	11.8
Bulk Density (g/cc)	0.99	1.45	0.84	0.48
Apparent Density (g/cc)	1.98	2.90	1.68	0.96
Element	Weight %	Weight %	Weight %	Weight %
Na	6.9	4.3	1.7	5.9
Mg	3.6	2.2	2.54	12.4
Al	17.8	14.5	1.8	5.1
Si	47.4	38.3	48.4	11.6
P	1.6	0.0	3.4	2.2
S	1.8	1.0	3.0	1.3
Cl	0.0	0.0	2.8	0.0
K	2.6	2.5	23.4	10.7
Ca	8.7	7.5	7.8	42.9
Ti	1.6	0.8	0.0	1.3
V	0.0	3.4	0.0	0.0
Cr	0.0	0.0	0.0	0.0
Mn	0.0	0.0	0.0	4.5
Fe	6.4	22.9	5.0	1.0
Ni	0.0	0.9	0.0	0.0

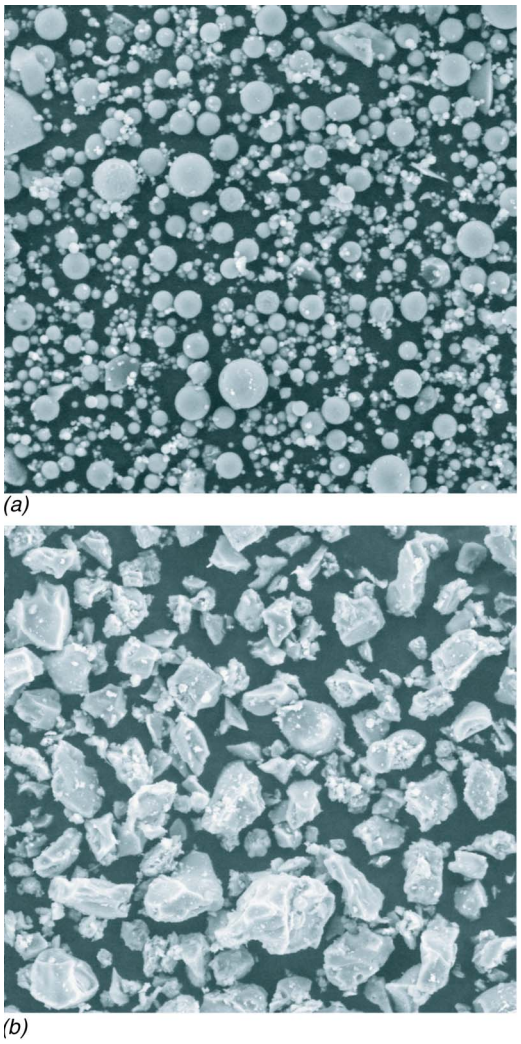

Fig. 2 ESEM images of (*a*) coal and (*b*) straw ash after processing. Images are approximately 150 μm×150 μm.

Of particular note in Table 1 are the high levels of S and Cl in straw (as noted by Wright et al. [10]) and the vanadium found in petcoke (added during petroleum processing). Petcoke also shows particularly high levels of iron oxide. Calcium and magnesium are especially prevalent in the sawdust ash, while sodium is indicated in all of the samples, though at a lower level in straw ash. The potassium levels in biomass are also significantly higher than coal and petcoke, as noted earlier.

Experimental Test Conditions

A detailed description of the Turbine Accelerated Deposition Facility (Fig. 3) is provided by Jensen et al. [11]; only a brief summary of the essential features is given here. High pressure air is fed into the base of the combustor, where it is properly dispersed and straightened to provide uniform flow to the burner with no swirl. Natural gas is fed into the combustor through four symmetrically placed copper tubes. A small amount of air is premixed with the natural gas. This partial premixing drastically reduces soot formation in the facility, but for safety considerations the amount of air added is kept small to avoid the flammability limit. A fraction of the high pressure air is also directed through the particle feed system where the ash particulate is injected into the center of the combustor. The particle feed system consists of a glass bulb that has two inlets and one exit. The primary air enters through the top and the particulate is steadily injected through a

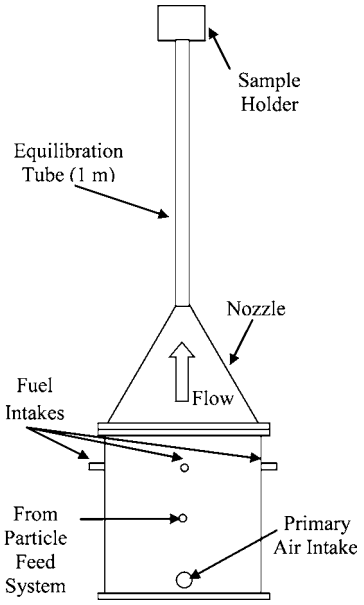

Fig. 3 Schematic of Turbine Accelerated Deposition Facility (TADF) at BYU

side inlet by a glass syringe driven by an electric motor. The particulate-carrying flow exits from the bottom of the bulb to the combustor. Test conditions are monitored using mass flow and temperature sensors. Air flow is measured by a choked flow orifice plate. The natural gas mass flow rate is determined using a rotameter and a pressure gauge in the line. The uncertainty in the mass flow was ±4% for the nominal flow rate (0.011 kg/s).

After combustion the flow enters a 20 deg cone axisymmetric nozzle with a 370:1 inlet to exit area ratio. This is followed by a 1 m long pipe where entrained particles less than 40 μm in size reach 95% of the flow velocity and temperature before impacting the test specimen. The flow exits this equilibration pipe as a turbulent jet and impinges on the target coupon located 2–3 jet diameters from the pipe exit (Fig. 3). Jet exit temperatures were measured using two Super OMEGACLAD K-type thermocouple probes positioned just upstream of the turbine blade sample. Overall error in temperature measurements is less than 15°C at the operating temperature of 1150°C.

Particle feeding commenced after the facility was brought to steady-state operating conditions, which were maintained throughout the duration of each test. The steady-state conditions at the combustor exit were approximately 1150°C with a 200 m/s exit velocity (Mach number of 0.31), matching the typical inlet Mach number range (0.2–0.4) for a first-stage turbine blade row. As mentioned earlier, the operating principle of the accelerated deposition facility is to match the net loading of particulate, measured in ppmw hr. Table 2 contains the test duration and ppmw h loading data. The majority of testing was conducted at a nominal value of 140 ppmw h, while two additional tests were performed at significantly higher loadings. As a reference, the 140 ppmw h loading level would be equivalent to 1 operating year (8000 h) at a relatively low particulate concentration of 0.02 ppmw.

Circular turbine blade samples, approximately 2.41 cm in diameter and 0.45 cm thick, were obtained from a turbine blade coating manufacturer. The samples were representative of a high-performance turbine material system: a cobalt-based super-alloy substrate approximately 0.3 cm thick, an MCrAlY oxidation resistant coating approximately 125 μm thick, and an APS yttrium stabilized zirconium (YSZ) TBC layer approximately 0.75 mm thick. All tests were run with the samples at a 45 deg impingement angle. No cooling was applied to the specimen, so that the

Table 2 Particle loading test conditions

Ash Type	Test Time (h)	Particle Concentration (ppmw)	Net Particle Loading (ppmwh)	Net Deposit Weight (mg)	Deposition rate (mg/cm^2h)	Net Particle Capture Efficiency (%)
Coal	3	55	165	1.1	72	17%
Petcoke	2	70	140	Not measured	N/A	N/A
Straw	2	77	154	<0.1	N/A	N/A
Sawdust	3	37	111	0.2	13	5%
Coal	4	150	600	2.9	143	12%
Petcoke	3	165	495	1.15	76	6%

system operates approximately isothermally at the gas temperature. Temperature gradients through the TBC thickness that exist in practice are therefore not simulated.

After completing the tests, each sample was weighed and compared to its preburn weight. The samples were then placed on a Hommel profilometer to measure the surface topography and roughness of the deposits. Multiple steps were required to prepare the sample for analysis in the ESEM. Each sample was potted in epoxy to preserve the deposit. Using a water-cooled, diamond-tipped saw, each sample was cut in half perpendicular to the flow direction. The cut sample was then encased in bakelite and polished. Finally, because deposit layers and TBC are not electrically conductive, the sample was coated with a fine layer of carbon to prevent charge buildup from distorting the ESEM images.

Results and Discussion

After cross-sectioning each specimen, the average deposit thickness was determined from a series of point measurements made every 3 mm along the cut section. This average thickness data are plotted versus net particle loading (ppmw h) in Fig. 4. Since the cross section was deliberately taken through the peak thickness of the deposit, this measurement is a linear average and does not represent an average for the entire specimen surface area. From the limited coal and petcoke data it appears that the deposit thickness varies linearly with net particle loading (as denoted by the lines from the origin).

Using the pretest and post-test weight measurements, the net specimen weight gain during exposure was assessed (Table 2). Dividing this deposit weight by the exposed coupon surface area and the test duration yielded deposition rate measurements of 143 mg/cm^2 h and 76 mg/cm^2 h for the highest particle loading coal and petcoke cases, respectively (Table 2). This coal deposition rate is comparable to those witnessed in the coal water fuel study of Wenglarz and Fox [5] where deposition rates from 200–400 mg/cm^2 h were recorded at comparable gas temperatures. The petcoke deposit is a factor of 4 less dense than the coal deposit. It has twice the average thickness but only half the weight. This is indicative of the porous nature of the petcoke deposit as will be seen in the ESEM images below. This finding is particularly surprising since the petcoke ash apparent density is roughly 50% higher than that for coal ash (Table 1). One final deposition metric that is tabulated in Table 2 is the net particle capture efficiency (mg/h of deposit divided by mg/hr of particulate in the flow). Coal has the highest capture efficiency (17%), which drops to 12% as particle loading (ppmw) is increased. The petcoke and biomass net capture efficiencies are less than half of the lowest value calculated for coal.

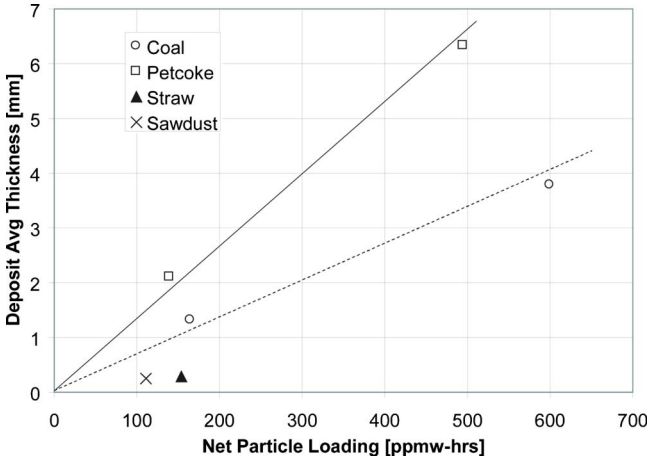

Fig. 4 Average deposit thickness vs. net particle loading for 4 fuels

The coal deposit was brownish in color with a surface that was rutted and broken. The majority of the coal deposit separated from the coupon after the specimen cooled down and was removed from the holder. This left a thin (~100 μm) layer of deposit residue on the TBC. When the deposit separated from the surface, thin sheets of deposit were also dislocated from the main body of the deposit. These interface layers resembled thin sheets of mica, and later X-ray analysis indicated higher concentrations of silicon and lower concentrations of iron and aluminum relative to the bulk of the deposit. The interface sheets also registered small (~5%) but significantly elevated concentrations of potassium, phosphorus, and titanium compared to the main deposit.

The petcoke deposit behaved similarly to the coal deposit by separating from the coupon after test shutdown and subsequent handling. The deposit had a purplish/red color and a surface texture similar to lava rock. The dark brown sawdust deposit was considerably thinner but adhered more tenaciously than the coal or petcoke deposits. This greater adherence may be caused by its small average thickness (0.25 mm), since the residual interface stresses induced by differing coefficients of thermal expansion in the deposit and TBC decrease as the deposit becomes a thin sheet. Finally, the straw deposit had a glasslike, greenish-white surface that appeared relatively uniform in thickness. It was by far the most tenacious, with no obvious post-test dislocation from the TBC.

Surface topologies from three of the deposit samples are shown in Fig. 5. The straw (Fig. 5(*a*)) and coal residual (Fig. 5(*c*)) surface maps represent a large fraction (8×22 mm) of the exposed coupon surface while the coal deposit surface map (Fig. 5(*b*)) was taken from a small 3 mm×3 mm separated piece of deposit. All three maps are shown with the surface curvature removed so that the surface roughness is highlighted. The straw deposit surface (Fig. 5(*a*)) is more irregular than the coal deposit surface (Fig. 5(*b*)). Centerline-averaged roughness (Ra) values are 40 μm and 28 μm for the straw and coal deposits, respectively. In addition, the straw deposit roughness is steeper than the coal (average forward-facing surface angle of 23 deg versus 15 deg for the coal), so that the effect of the roughness on the flow is more

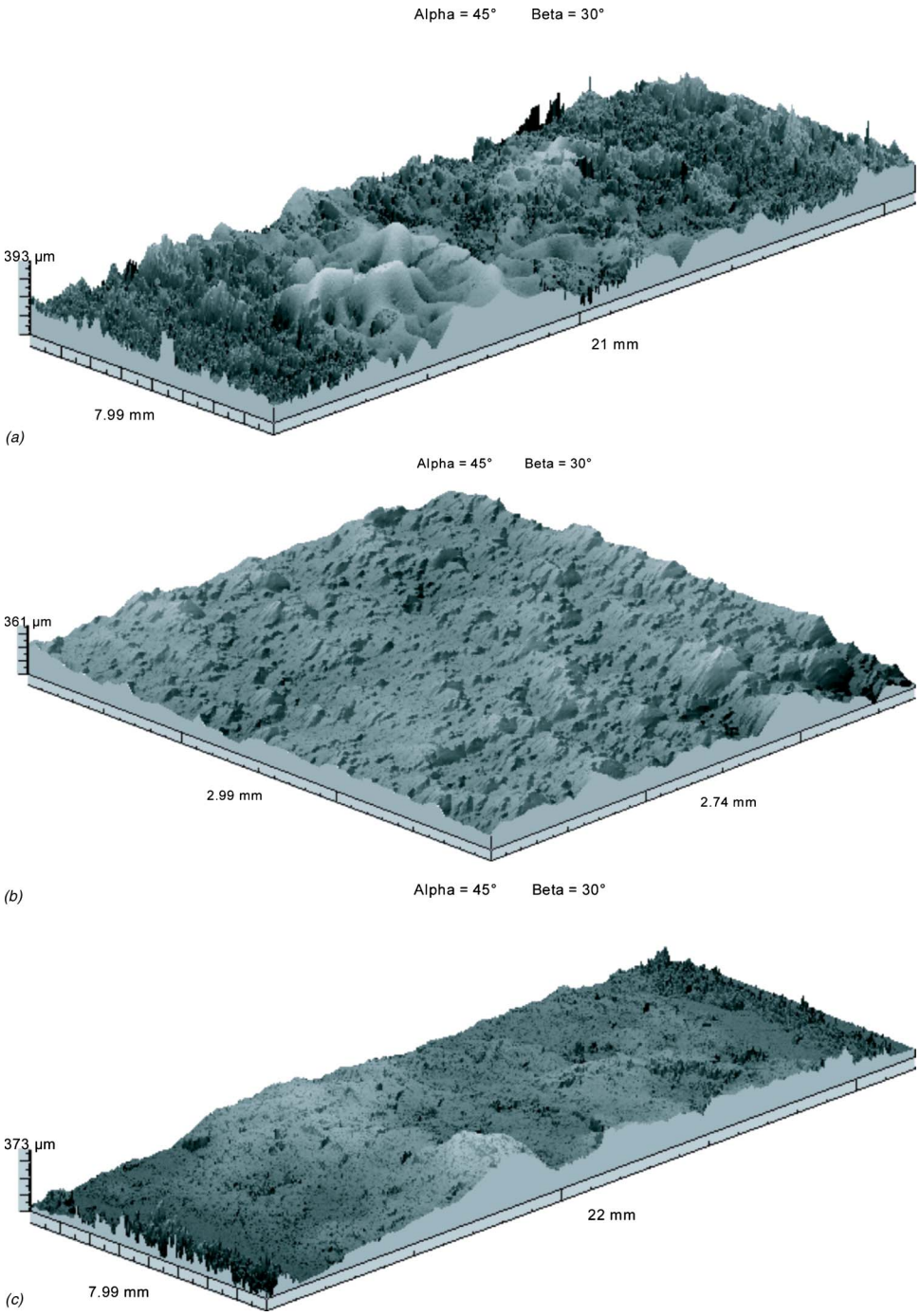

Fig. 5 Surface topographies of 3 different deposits from Hommel profilometer measurements. (*a*) 8 mm×21 mm section of straw deposit surface—peak height ~400 μm (*b*) 3 mm×3 mm section of coal deposit surface—peak elevation ~600 μm (*c*) 8 mm×22 mm section of residual coal deposit after deposit separated—peak ~350 μm.

pronounced. Comparing these values to data acquired by Bons [4] for a large turbine vane operating with $Re_c \sim 1 \times 10^6$, these roughness values correspond to estimated increases in convective heat transfer coefficient ranging from 15% to 20% and increases in skin friction from 70% to 140% (for the coal and straw surfaces, respectively). After the coal deposit separated from the TBC surface, the residual deposit on the specimen has a roughness signature comparable to the straw deposit (Fig. 5(*c*)). Thus, if in practice large coal and petcoke deposits are removed by thermal cycling of the gas turbine, the detrimental influence on turbine efficiency due to the residual deposit could actually increase.

Scanning electron microscope cross-sectional images of the four different fuel deposits reveal significant differences in the deposit structure as well. A previous TADF study with airborne dust particles showed layering in the deposit, with structures predominantly oriented parallel to the surface [11]. By comparison, the fuel deposits in this study are fairly isotropic in structure and composition. Figure 6(*a*) is an ESEM cross-sectional image of the coal deposit. Note the large (±100 μm) amplitude surface height variations observed previously in the topology of Fig. 5(*c*). The coal deposit is riddled with 30–80 μm diameter inclusions. Fur-

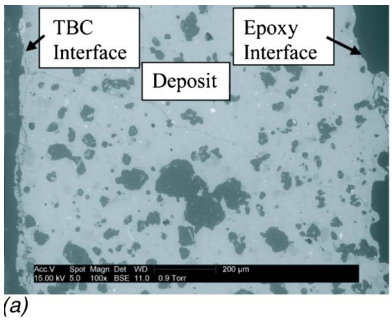

(a)

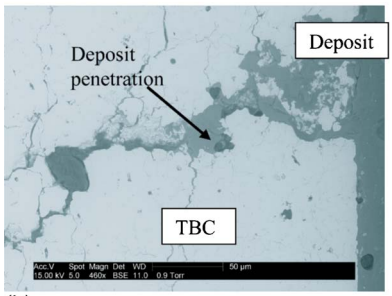

(b)

Fig. 6 ESEM cross-section of coal surface deposit and coal/TBC interface. (*a*) Coal surface deposit structure (*b*) Coal deposit penetration into TBC.

ther interrogation using x-ray spectroscopy indicated that while the majority are solid (metal) particles that were trapped in the molten deposit at temperature, some are porous cavities. The second coal ESEM image (Fig. 6(*b*)) was taken at high magnification near the deposit/TBC interface. At this location, a crack in the TBC has been penetrated by the coal deposit.

The petcoke deposit (Fig. 7) exhibits much larger inclusions (100–300 μm diameter) with strandlike structures lining the cavity walls. This high porosity accounts for the low density of the petcoke deposit compared to the coal deposit, as noted earlier. The isotropic matrix surrounding the inclusions registers over 60% silicon content while the strands have a composition similar to the ash. Thus, the strands may be evidence of larger petcoke ash particles that were captured by the molten glass (silicon) matrix, thus greatly augmenting the deposit thickness. The sawdust deposit (not shown) exhibited a much more homogeneous character with significantly fewer and smaller (10–30 μm diameter) inclusions. The straw deposit (Fig. 8) is most like the airborne dust deposits mentioned earlier [11], with structures running parallel to the TBC surface. The darkened region in Fig. 8 is an elongated cavity formed during the deposition test. This deposit is the most "glass-

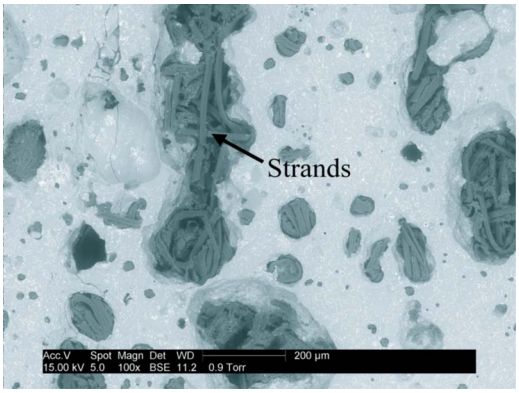

Fig. 7 ESEM cross-section of petcoke deposit inclusions

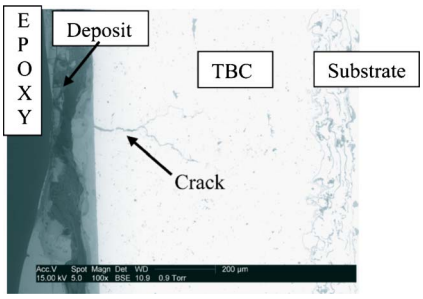

Fig. 8 ESEM cross-section of straw deposit

like" and appears to have formed in sheets along the surface. A deposit-filled TBC crack is indicated in this figure as well.

While mounted in the ESEM, the deposits were interrogated using x-ray spectroscopy. The ESEM registers regions of different structure with distinctively different hues (e.g., the inclusions in Figs. 6–8). Some of these regions exhibited significantly different elemental composition as well. In all cases, at least three measurements were made in each region of the deposit. The composition values in Table 3 are area-weighted averages of the various measurements. Thus, if the inclusions in Fig. 6(*a*) represented 20% of the cross-sectional area of the deposit, they were averaged with a 20% weighting. Values of 0.0 indicate levels below the background noise level of the spectrometer. As has been found in previous data from actual aircraft turbine deposits [11,12], elemental concentrations showed no demonstrable trend with thickness.

In general, the relative concentration of elements detected in the deposits (Table 3) are similar to those detected in the ash (Table 1). A side-by-side comparison of these data can be used to determine if there are specific preferences for deposition at the given operating conditions (Fig. 9). For example, the petcoke and sawdust deposits show significant increases in the concentration of Si in the deposit (relative to the ash) at the expense of Fe (in the case of petcoke) and Ca, K, Mg (in the case of sawdust). Since silicon is noncorrosive and essentially insulates the TBC surface, this trend is favorable for blade life. On the other hand, sharp increases in Na, P, and Cl (e.g., the straw deposit) are undesirable for blade life.

Perhaps even more worrisome for the health of the turbine blade material system is the observed penetration of deposit materials into cracks in the TBC (Figs. 6(*b*) and 8). These vertical segmentation cracks are deliberately formed in the APS TBC to improve erosion and thermal shock resistance. It is possible that these fissures present paths for premature contamination of the TBC. Though the observed deposits in the TBC cracks could possibly have been caused by contamination during specimen pro-

Table 3 Average elemental composition of deposits (values are in wt %)

Element	Coal	Petcoke	Straw	Sawdust
Na	5.8	3.5	4.4	5.6
Mg	4.1	1.8	2.6	7.7
Al	18.9	12.5	3.2	7.8
Si	45.3	55.0	42.6	31.8
P	1.84	0.0	6.6	0.9
S	0.9	0.0	2.0	0.9
Cl	0.0	0.0	6.7	0.0
K	2.0	1.9	15.9	4.6
Ca	11.6	6.8	7.6	34.3
Ti	1.8	1.1	3.6	0.8
V	0.0	2.2	0.0	0.0
Cr	0.0	0.3	1.2	0.0
Mn	0.0	0.0	0.0	1.8
Fe	7.8	14.5	0.0	3.8
Ni	0.0	0.5	0.0	0.0

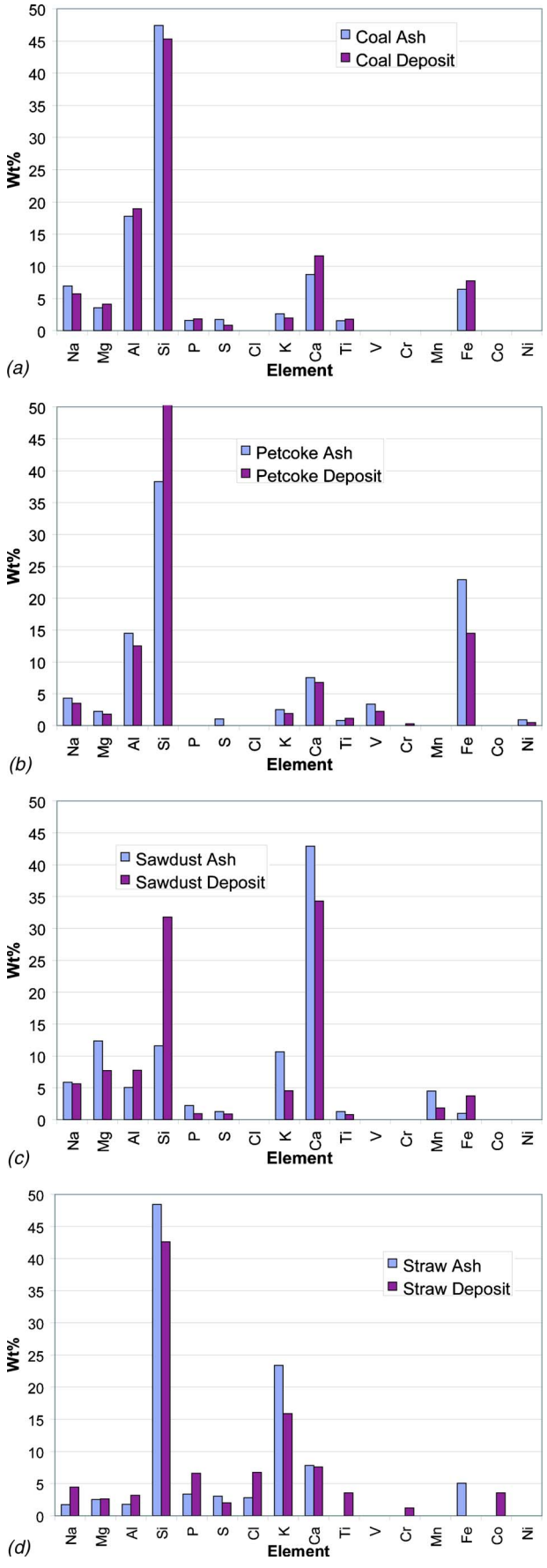

Fig. 9 Comparison of element weight percent for fuel ash vs. deposit: (*a*) coal (*b*) petoke (*c*) sawdust (*d*) straw

cessing, this is considered unlikely since upon inspection with the spectrometer the penetrating deposit exhibited a unique elemental composition as compared with the surface deposits. Further study is necessary to more rigorously examine these internal deposits and determine whether this deposit penetration leads to accelerated corrosion in the base metal alloy. The deposits could also induce TBC spallation during thermal cycling due to the mismatch in coefficients of thermal expansion between the ceramic TBC and the metal deposit (similar to CMAS attack in aircraft and land-based turbines (where CMAS represents the four most common depositing oxides: calcium, magnesium, aluminum, and silicon)). Likewise, the combustion of herbaceous biomass materials, such as straws and grasses, often leads to unmanageable deposition problems in boilers. In particular, the amounts of sodium, potassium, chlorine, and sulfur in the biomass play major roles in deposition and corrosion. Potassium salts (KCl and K_2SO_4) are low melting compounds that can bind fly ash particles together and enhance the amount of deposition. There is evidence that KCl in deposits, in the absence of sulfur species, seems to initiate corrosion of superheater tubes in biomass-fired boilers [13–15]. The penetration of potassium and sodium into the ceramic thermal barrier coating of gas turbine surfaces is therefore important for understanding both deposition and corrosion tendencies.

Conclusions

Deposits from four alternative synfuels for the gas turbine were studied in an accelerated test facility at a gas temperature and velocity representative of first-stage high-pressure turbines. Net particle loading in the accelerated testing facility is representative of operating industrial turbines though the particle size distribution was larger (mass mean diameter 10–20 μm) than typically found after proper filtration. Thus, the study focuses on inertial impaction as the deposition mode. Based on the results presented in this study, the following conclusions are offered:

(1) For the same net particulate loading in the gas stream, coal and petroleum coke (petcoke) produced order of magnitude larger deposits than biomass fuels. This is not proposed as a universal finding since deposition is a strong function of specific fuel type and gas temperature.
(2) Though the data sample was limited, deposit thickness appears to increase linearly with particle loading for the case of petcoke and coal. Capture efficiencies ranged from 12–17% for coal to 5% and 6% for sawdust and petcoke, respectively. ESEM images indicate that a molten layer of silicon on the target material may be responsible for high particle capture rates in petcoke.
(3) Large (>2 mm thick) coal and petcoke deposits separate from the turbine surface following test shutdown and handling while thinner biomass deposits are more tenacious.
(4) Evidence of deposit penetration into cracks in the TBC was found in all four specimens.

Acknowledgment

Various individuals provided invaluable support to this research effort. The authors would particularly like to thank the assistance provided by Arun Mehta from Pacificorp for the coal flyash samples, Walt Steimel of Premcor, Harold Stocker of Cinergy, and Tampa Electric Company for assistance in locating petcoke samples, and Dr. Larry Baxter (BYU) for the biomass samples. Dr. Tom Taylor of Praxair Surface Technologies generously donated coupon specimens without which the study would not have been possible. Thanks also to Daniel Fletcher for performing particle size analysis and other helpful tasks. Michael Standing's expert assistance with the ESEM and x-ray spectrometer measurements was invaluable. Discussions with Richard Wenglarz of SCIES were helpful in establishing test matrices and framing results. This work was partially sponsored by the U.S. Department of Energy—National Energy Technology Laboratory through a

cooperative agreement with the South Carolina Institute for Energy Studies at Clemson University. The views expressed in this article are those of the authors and do not reflect the official policy or position of the Department of Energy or U.S. Government.

Nomenclature

APS = air plasma sprayed
EB-PVD = electron beam-plasma vapor deposition
ESEM = environmental scanning electron microscope
TBC = thermal barrier coating

References

[1] Ghenaiet, A., Elder, R. L., and Tan, S. C., 2001, "Particles and Trajectories Through an Axial Fan and Performance Degradation due to Sand Ingestion," ASME Paper No. 2001-GT-497.
[2] Wenglarz, R. A., 1992, "An Approach for Evaluation of Gas Turbine Deposition," ASME J. Eng. Gas Turbines Power, **114**, pp. 230–234.
[3] Kim, J., Dunn, M. G., Baran, A. J. et al., 1993, "Deposition of Volcanic Materials in the Hot Sections of Two Gas Turbine Engines," ASME J. Eng. Gas Turbines Power, **115**, pp. 641–651.
[4] Bons, J. P., 2002, "St and C_f Augmentation for Real Turbine Roughness With Elevated Freestream Turbulence," J. Turbomach., **124**, pp. 632–644.
[5] Wenglarz, R. A., and Fox, R. G., Jr., 1990, "Physical Aspects of Deposition From Coal-Water Fuels Under Gas Turbine Conditions," ASME J. Eng. Gas Turbines Power, pp. 9–14.
[6] Wenglarz, R. A., and Fox, R. G., Jr., 1990, "Chemical Aspects of Deposition/Corrosion From Coal-Water Fuels Under Gas Turbine Conditions," ASME J. Eng. Gas Turbines Power, pp. 1–8.
[7] Sherlock, T. P., and Wenglarz, R. A., 1983, "Combustion-Turbine Design Guidelines Based on Deposition-Corrosion Considerations," Residual Fuel Oil Studies, EPRI Report AP-2739, Vol. 1.
[8] Bons, J. P., Taylor, R., McClain, S., and Rivir, R. B., 2001, "The Many Faces of Turbine Surface Roughness," J. Turbomach., **123**(4), pp. 739–748.
[9] Patnaik, P. C., Adams, C., Fuleki, D., and Thamburaj, R., 1998, "Elevated Temperature Exposure of Gas Turbine Materials to a Bio-fuel Combustion Environment," ASME Paper No. 98-GT-164.
[10] Wright, I. G., Leyens, C., and Pint, B. A., 2000, "An Analysis of the Potential for Deposition, Erosion, or Corrosion in Gas Turbines Fueled by the Products of Biomass Gasification or Combustion," ASME Paper No. 2000-GT-0019.
[11] Jensen, J. W., Squire, S. W., Bons, J. P., and Fletcher, T. H., 2004, "Simulated Land-Based Turbine Deposits Generated in an Accelerated Deposition Facility," ASME Paper No. GT2004-53324.
[12] Borom, Marcus P., Johnson, Curtis A., and Peluso, Louis A., 1996, "Role of Environmental Deposits and Operating Surface Temperature in Spallation of Air Plasma Sprayed Thermal Barrier Coatings," Surf. Coat. Technol., **86–87**, pp. 116–126.
[13] Wall, T. F., Bhattacharya, S. P., Baxter, L. L., Richards, G., and Harb, J. N., 1995, "The Character of Ash Deposits and the Thermal Performance of Furnaces," Fuel Process. Technol., **44**, p. 143–153.
[14] Hein, K. R. G., Heinzel, T., Kicherer, A., and Spliethoff, H., 1996, "Deposit Formation During the Co-combustion of Coal Biomass Blends," *Applications of Advanced Technology to Ash-Related Problems in Boilers*, L. Baxter and R. DeSollar, eds., Waterville Valley, NH, July 16–21, 1995, pp. 97–116.
[15] Lokare, S., Dunaway, D., Rogers, D., Anderson, M., Baxter, L., and Tree, D., 2004, "Effects of Fuel Ash Composition on Corrosion Deposits," Conference on Science in Thermal and Chemical Biomass Conversion, Victoria, British Columbia, Canada, August 30–September 2, 2004.

A. El-Shafei
S. H. Tawfick
M. S. Raafat
G. M. Aziz

Faculty of Engineering,
Department of Mechanical Design and Production,
Cairo University,
Giza 12316, Egypt

Some Experiments on Oil Whirl and Oil Whip

The oil whirl and oil whip phenomena have been well known since the early twentieth century. However, there is a lot of confusion on the parameters that affect the onset of instability. In this study, we investigate the onset of instability on a flexible rotor mounted on two plain cylindrical journal bearings. The rotor is run through the first critical speed, the instability, and the second critical speed. Tests are conducted at various unbalance levels, pressures, and misalignment conditions on the coupling. It is shown that, by far, the misalignment of the coupling is the parameter that is most effective on the onset of instability. In particular angular misalignment resulted in the smoothest rotor response. [DOI: 10.1115/1.2181185]

Introduction

Ever since the 1925 paper of Newkirk and Taylor [1], the phenomena of oil whirl and oil whip have attracted the attention of many researchers. Although extensive work on oil whirl and oil whip spanning three quarters of a century has been exerted, yet this subject is still of current interest [2,3]. Actually, Kirk [2] recently explained that this interest lies essentially in answering the following two questions: "Are there any possibilities that the rotor system can transgress the threshold speed? Can the rotor system operate above this threshold speed?" [2]. These two questions are also the motivation for this work presented herein, in addition to the need to understand the parameters that influence the onset of instability.

Perhaps the interest in studying the stability of fixed geometry fluid film bearing lies in its historical significance. They allowed the development of rotating machines in the nineteenth century. Actually a review paper on the theory of lubrication [4] suggests that the fluid film bearing is probably the single most important element in the recent technological development, only comparable in its significance to the effect of electricity. Early fluid film bearings were designed to carry the loads, and were hailed as low-friction devices possibly capable of continuously carrying the machine [5]. However, with the increased speed of rotating machines in the twentieth century, it became evident [1] that the journal bearing itself can cause the problems of oil whirl and oil whip. This has caused many researchers to investigate, experimentally and theoretically, the phenomena of oil whirl and oil whip. Robertson [6] provided an early calculation, which showed that the rotor is always unstable. Hagg [7] investigated the stability of rotating machines on oil film journal bearings and found that the upper limit of the whirling frequency is one-half the rotating speed.

However, it was not until the 1950s when a coherent theory of oil whip started to evolve. Poritsky [8] showed that the instability occurs only at speeds exceeding twice the first critical speed. Newkirk and Lewis [9,10] reported experimental cases in which the rotating speed reached five or six times the first critical speed before the instability occurred, while Pinkus [11,12] reported cases in which whipping disappeared and resumed again, and cases of stable and unstable states separated by regions of transient whip. Actually, the Newkirk and Pinkus experiments were contradictory in many senses; even on the effect of temperature. Newkirk and Lewis [9] reported that hotter oil provides a greater range of stable operation, while the Pinkus [12] experiments showed that cooler oil provides a greater range of stable operation. In an excellent paper, Hori [13] provided a theory of oil whip, trying to explain the gap between Newkirk and Pinkus.

In the 1960s and 1970s, significant work on alternative fluid film bearing designs to control the instability were conducted [14]. Moreover, significant efforts went into calculating linearized bearing coefficients [15] and in predicting rotordynamic response [16].

In the eighties, renewed interest in the journal bearing instability was triggered by the work of Muszynska [17]. She performed extensive testing on journal bearing supported rotors [18]. Moreover, she illustrated the presence of second mode whirl [19]. In the eighties as well, major advances in understanding the nonlinear dynamics of journal bearings through bifurcation analysis [20] and Hopf bifurcation [21] were made.

The interest in journal bearing instability continued both theoretically and experimentally into the nineties. Elrod and Vijayaraghan [22,23] provided a stability analysis of journal bearings incorporating the effects of cavity flow. Crandall [24,25] studied the stability of a Jeffcott rotor on cylindrical fluid film bearings. He obtained the global locus of Hopf bifurcations where the configuration loses its stability, and also the global locus of saddle nodes of periodic orbits that mark the boundary of the region in which stable limit cycles exist. Horattas et al. [26] showed experimentally that multiple Hopf bifurcation points and multiple hysteresis loops can exist, while the Deepak and Noah [27] experiments showed the existence of a supercritical and a subcritical bifurcation regime. Moreover, their experiments have shown that an unbalanced mass reduced the stability threshold speed.

The interest in journal bearing stability spilled over into the new century. Guo and Kirk provided the instability boundary for rotor-hydrodynamic bearing systems [2,3], while Inayat-Hussain [28] applied the continuation method to whirl instability in journal bearings.

The study presented in this paper is designed to investigate experimentally the onset of oil whirl and whip in journal bearings. The experiments are designed to replicate the conflicting work of Newkirk and Lewis [9] and Pinkus [12], using modern measurement tools. Thus, the experiments were made to investigate the onset of instability of a flexible rotor on journal bearings, focusing on the effects of unbalance, supply pressure and misalignment on the onset of instability. In particular, the authors of this paper believe that the experimental investigation of misalignment of the driver and driven shafts and its effect on journal bearings are novel. In the literature, no investigation has been reported for the effects of angular misalignment on the onset of instability in journal bearings.

Contributed by the International Gas Turbine Institute (IGTI) of ASME for publication in the JOURNAL OF ENGINEERING FOR GAS TURBINES AND POWER. Manuscript received October 1, 2003; final manuscript received March 1, 2004. IGTI Review Chair: A. J. Strazisar. Paper presented at the International Gas Turbine and Aeroengine Congress and Exhibition, Vienna, Austria, June 13–17, 2004, Paper No. GT2004-53644.

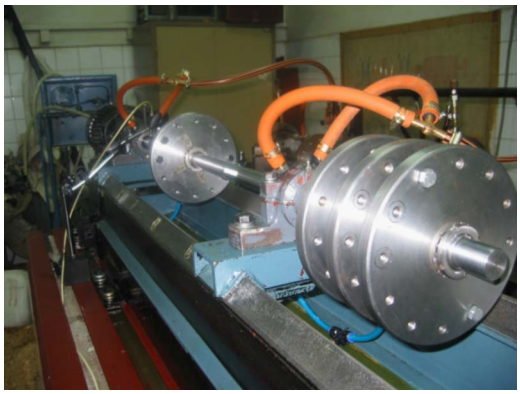

Fig. 1 Test rig

The Test Rig

The test rig (Fig. 1) on which the experiments were conducted consists of a rotor-bearing assembly. The rotor is a 1 in. diameter chrome-coated stainless steel of 1.2 m length, 7800 kg/m^3 density, and 210 GPa modulus of elasticity. Four disks are fixed on the shaft as shown in Fig. 2, each disk is 170 mm outer diameter, 15 mm thickness, and 2.6 kg weight. Twelve 8 mm diameter holes are drilled in each disk on a 140 mm diameter circle in order to allow for balancing masses fixation. Each disk is mounted on the shaft using tapered seating and is fixed in its position by means of a lock-nut. This rotor configuration was selected in an overhung shape, in order to cross two critical speeds in a relatively low speed range and to allow for large modal activity at the bearings. Essentially, a disk in the rotor midspan and another overhung disk would have been sufficient for these purposes, however, this would have resulted in a relatively large overhung disk. In order to overcome this problem, the overhung disk is replaced by three smaller disks, all the same size. This has an additional benefit since it is possible to move the disks around to obtain alternative rotor configurations.

A rotordynamic computer model of the test rig (Fig. 3) was developed using a commercial software package [29]. Gyroscopic effects and speed-dependent bearing characteristics were included. The calculated critical speeds were at 1680 rpm and 4171 rpm, and the mode shapes are shown in Fig. 3. One can notice that the nondrive side bearing has a significantly larger modal activity, particularly at the second mode. A linear stability analysis indicated that instability occurs at a speed of 3150 rpm. Figure 3(*b*) shows all the rotor natural frequencies at different speeds in the Campbell diagram format.

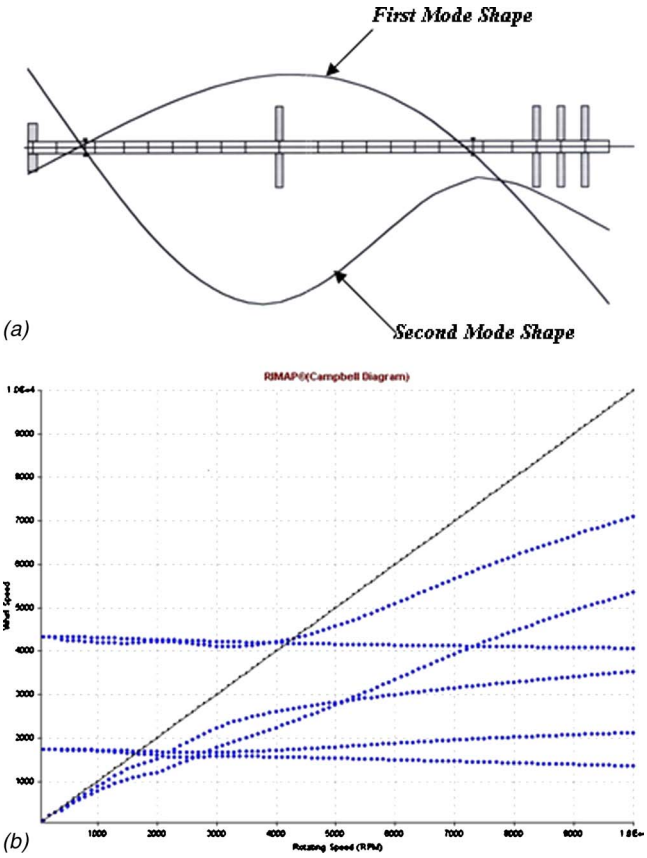

Fig. 3 (*a*) Default rotor data. (*b*) Rotor Campbell diagram.

It should be noted that the rotor critical speeds, natural frequencies, and mode shapes constitute a complete modal model and can be used to extrapolate the experimental results to other generic rotor systems.

The shaft is driven by a three-phase electric motor of 2.2 kW power through a Fenaflex flexible coupling, which has a maximum permissible radial "parallel" misalignment capacity of

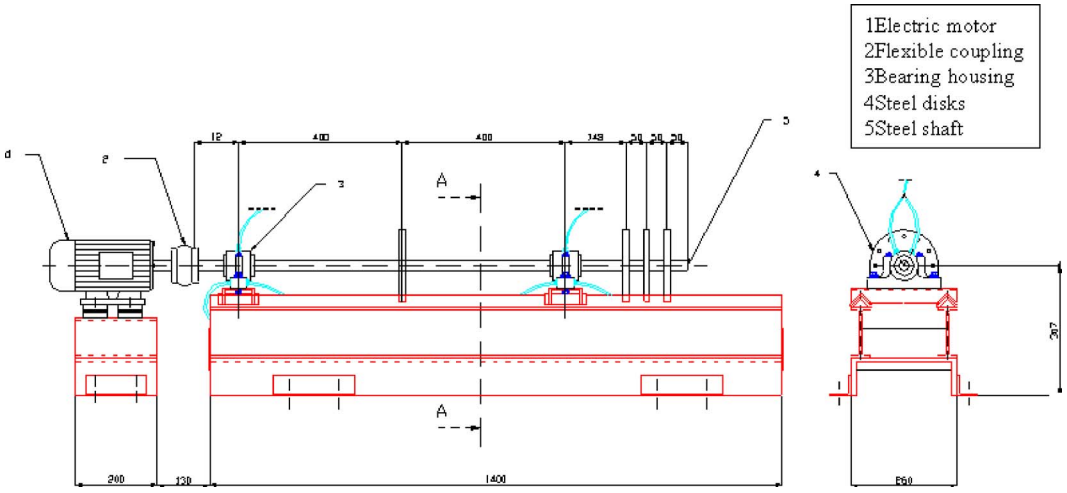

Fig. 2 Schematic of test rig

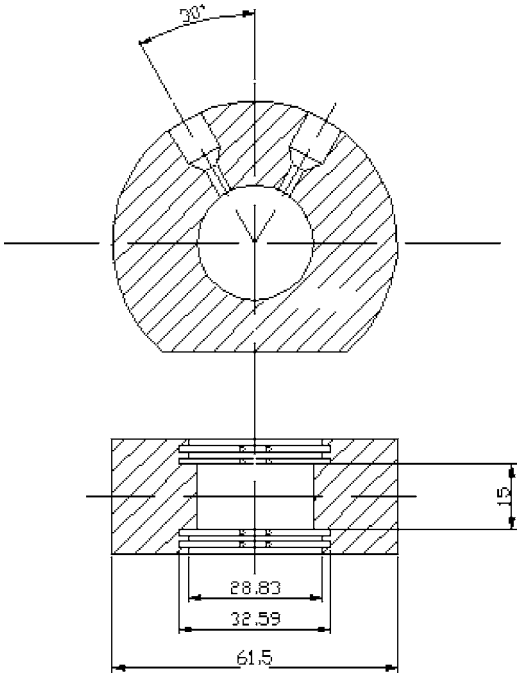

Fig. 4 Plain journal bearing

1.3 mm, as well as 4 deg maximum permissible angular misalignment capacity. Speed was controlled using a frequency inverter FUJI electric FVR-E11 2.2 kW, 400 Hz output.

The bearing material is SAE 64 Phosphor bronze which is considered as a typical copper alloy cast bearing material [30], which has a hardness of 63 BH, tensile strength 240 MPa, and a maximum operating temperature of 230°C.

The bearings have 62 mm outer diameter, 25.4 mm inner diameter, 35 μm diametral clearance, 15 mm effective length; thus, L/D is equal to 0.6. Four circumferential grooves were turned on the two sides of the effective bearing length, thus causing a two-stage pressure drop for the oil side flow. Oil inlets were drilled at 30 deg from the vertical direction with a 3 mm diameter.

Four oil drain holes were drilled in the middle of each circumferential groove. Snap rings and washer assembly on both sides of the drive-side bearing were used to constrain axial movement of the rotor (see Fig. 4).

Oil is supplied to the bearing through a Sperry Vickers pump. The hydraulic circuit is shown in Fig. 5, where the supply line pressure was monitored by a Hotlinger type PE 200/20 bar digital pressure gauge. The pressure is controlled in the supply line via the throttle valves connecting to the drain, in parallel to the relief valve.

Measurement System

Measurement of the vibration signal at each bearing was carried out by 2 proximity probes, 90 deg apart, located at ~5 cm from the center of the bearing. The probes were separated by an axial distance of ~2 cm to avoid interference between their magnetic fields. The proximity probes are Bently-Nevada, series 7200, 5 mm.

A Schenck photoelectric probe, model P84, is used to measure the rotational speed of the shaft, as well as to establish the phase reference. The photoelectric probe is monitoring a reflective tape fixed on the shaft, and acts as a phase reference.

Signals from the proximity probes and the photoelectric probe are simultaneously fed to a Bently Nevada digital vector filter (DVF-3), a Brüel and Kjaer spectrum analyzer model 2515, and a 20 MHz analog oscilloscope, BK Precision model 2522A (see Fig. 6).

The DVF-3 is a two channel tracking filter. The x and y probes on one bearing and the phase reference were fed to the DVF-3. The other bearing data were fed to the DVF-3 through a switch,

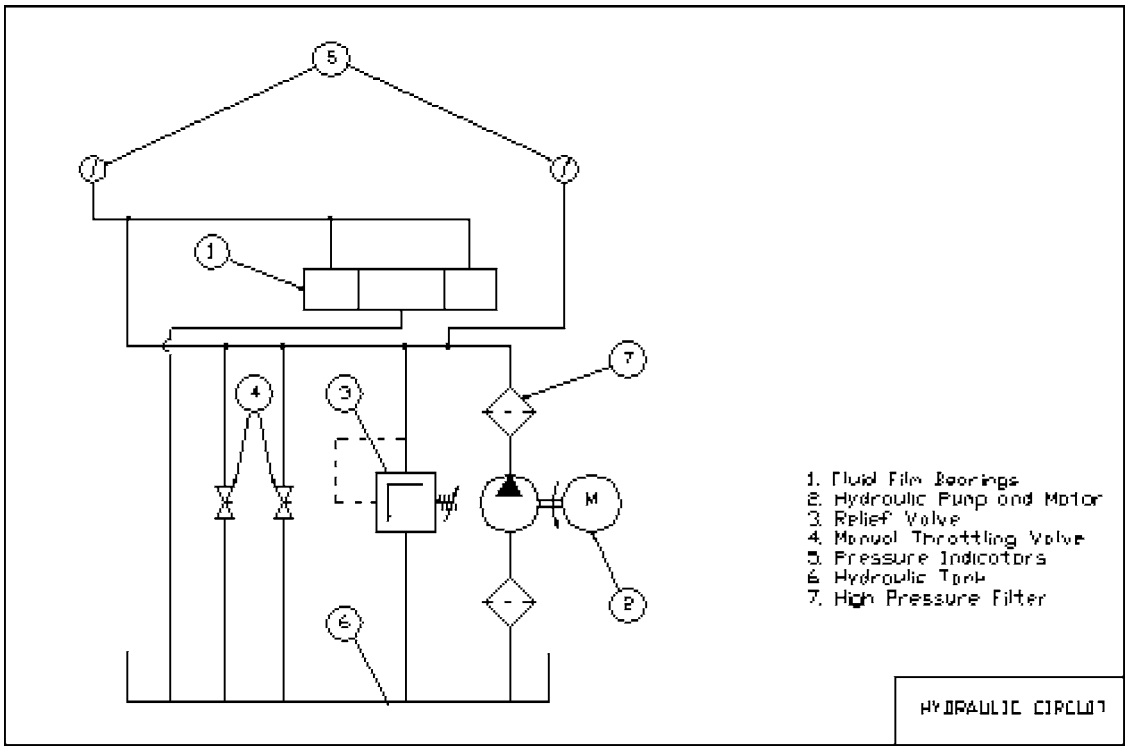

Fig. 5 Fluid supply circuit

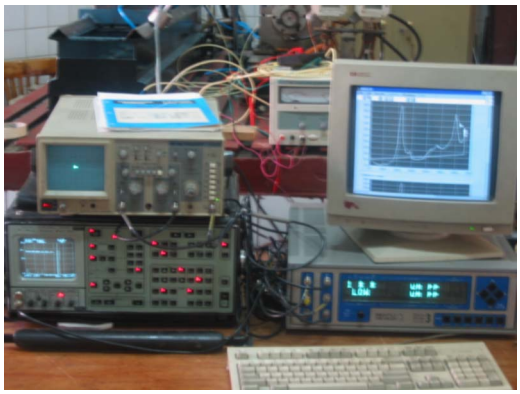

Fig. 6 Measurement system

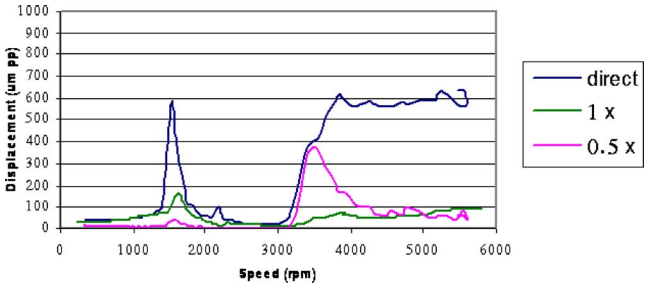

Fig. 7 Tracking data, case 1

but the test had to be repeated. Transient data were obtained by the DVF-3. The 2515 is a single-channel spectrum analyzer, and one of the probe signals was fed to the analyzer. Spectral as well as time wave-form data were obtained from the 2515. The oscilloscope was used to view orbital data, one bearing at a time.

Orbits were captured from the oscilloscope's display by means of a Canon PowerShot S30 digital camera, then downloaded through a USB connection to the computer. The computer used is a Pentium® III, 550 MHz with 128 MB RAM and 8 GB hard disk. It is equipped with a National Instruments GPIB card model PC II/IIA, in agreement with the IEEE 488.2 standards. The card was used to interface both the spectrum analyzer and the DVF-3. Data from the spectrum analyzer were downloaded, stored, and plotted by means of the Brüel and Kjaer "WT—9324" software.

Test Procedure

The tests conducted herein were essentially run-up/coast-down tests. The rotor is run up slowly to the desired speed and is left to coast down on its own. Several precautions are necessary in these tests. The first concerns safety. It is easy for the person conducting the test to become fascinated with the experimental results and become excited and forget that these are instability tests and thus are inherently dangerous. Four safety procedures were in action. The first was continuous instructions on the perils of an accident and the dangers of conducting the tests, thus increasing the safety awareness of the experimenters. Second, the experimenters were assigned particular areas in the lab, such that even if an accident occurred, they will be safe. Third, specific instructions were given on not venturing into new territory with respect to speeds, unbalance, or otherwise, without first discussing the experiments and getting approval. Fourth, the test rig was located in an isolated area, in order to minimize the possibility of secondary damage in case of an accident.

Regarding the technical precautions, the prime concern was the uncontrolled variables in the test rig. For example, the oil temperature was not controlled in this test rig. To maintain constant temperature during testing, the test rig was usually operated for at least 1 h with the rotor running at a moderate speed, thus ensuring that the oil was heated by operation before conducting the experiments.

To maintain the accuracy of proximity probes used to measure the vibration, a regapping procedure was employed to maintain the gap voltage in its linear range each time the tests were conducted.

Before starting the experiments, the rotor was first adequately balanced at the first and second critical speeds. This was a little bit difficult due to the unusual rotor configuration chosen, where three disks are overhung, and only one disk is located between the bearings. However, adequate balancing for both of the first and second modes was achieved, as shown in Fig. 7, and this balance condition was maintained throughout the experiments, except where an unbalance was purposefully introduced.

Before starting the experiments, the coupling connecting the drive motor to the test rig was aligned by the reverse indicator method to a parallel tolerance of 0.1 mm and an angular tolerance of 0.08 deg. Again, these alignment tolerances were maintained throughout the experiments, except where an angular or offset misalignment was purposefully introduced.

For all of the cases considered, the following was the testing procedure. The rotor was run up slowly, crossing the first critical speed, the region of high subsynchronous vibration, the second critical speed (if possible), and sometimes even higher if the vibration level was tolerable. The rotor was then left to coast down under its own inertia. During the run-up and the coast-down, filtered data were collected, these included the usual 1× data (in Bodé plot format), 0.5× (with a 120 rpm filter bandwidth), and sometimes 2× filtered data. The filtered data were usually taken on a coast-down. Direct unfiltered data were also collected.

In addition, spectra of measured data were collected, usually at selected speeds on the run-up in order to have a controlled speed and allow time for the spectral measurement. An orbital picture was usually taken off the oscilloscope with the digital camera, under the same conditions.

Parametric testing was conducted, including the investigation of the effects of misalignment, unbalance, and supply pressure. The reference test was conducted at a supply pressure of 4 bar, with the alignment and balance condition as described above. Under these conditions, the tests were also conducted at 2, 6, and 8 bar supply pressures. With the supply pressure at 4 bar, an unbalance of 2.7 gm at a radius of 7 cm was then introduced at the center disk. That is a total unbalance of 189 gm mm, at an angle of 180 deg away from the phase reference. With this unbalance, the tests were conducted at the supply pressures of 2, 4, 6, and 8 bar as above. The unbalance was then removed from the center disk, the same unbalance was introduced on the overhung disk, and the tests were conducted at all four supply pressures as indicated above.

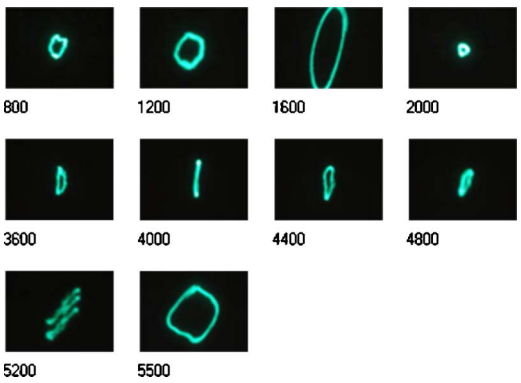

Fig. 8 Orbital data, case 1 (speeds in rpm)

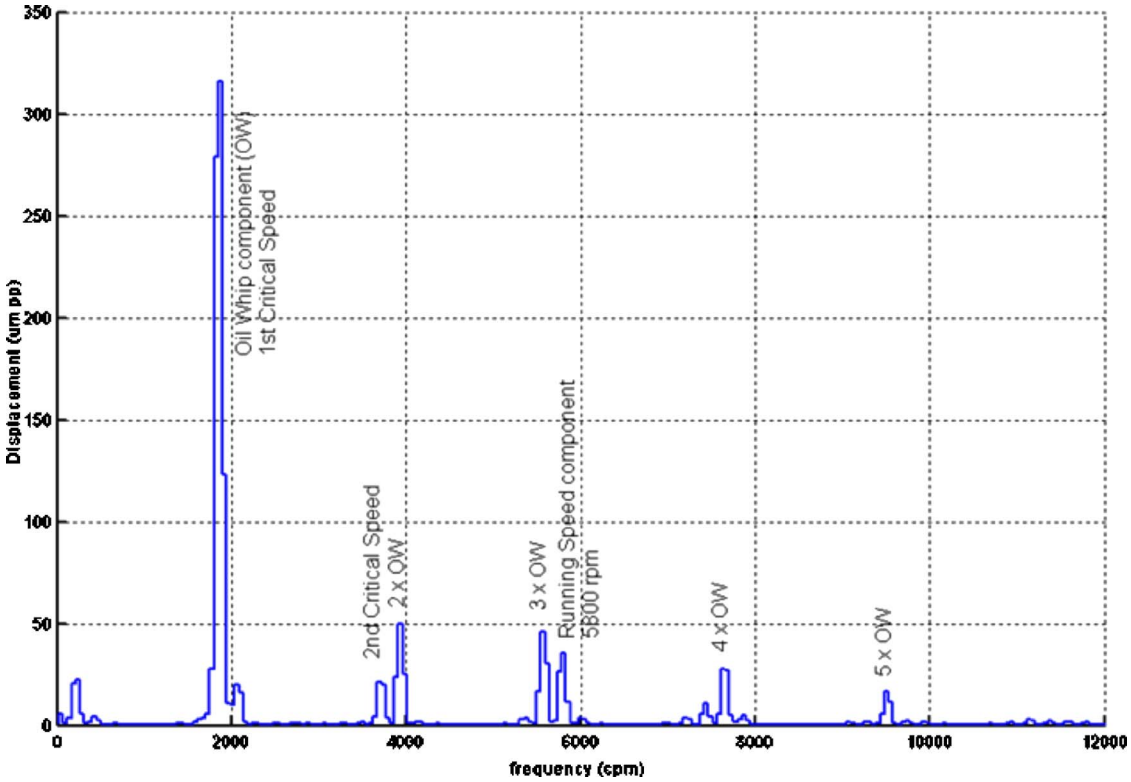

Fig. 9 Spectral data (speed 5800 rpm), case 1

In all these tests, the run-up and coast-down data, including spectra, oscilloscope pictures, and filtered data were all collected and analyzed, as described above.

The next set of data was conducted by introducing a 1.85 mm offset misalignment at the coupling and the tests were conducted while varying the supply pressure and varying the unbalance condition, as described above for the first set with no misalignment.

The last set of data was conducted by correcting the offset misalignment to within the specified tolerance, and introducing an angular misalignment of 1 deg at the coupling. The tests were also conducted while varying the supply pressure and the unbalance condition, as described above. This completes the test matrix for the investigation.

Data

Due to the huge amount of data collected in the test matrix, and the many formats available for presentation, the most difficult part in presenting the results was the selection of condensed data in an appropriate format that would make the conclusion clear.

Before venturing into presenting the data and explaining the results, it is appropriate to reiterate the known definitions of oil whirl and oil whip [17]. Oil whirl is a form of instability (less severe) that occurs at little less than half the running speed (0.49× in this case), which leads to the more violent oil whip when the oil whirl frequency coincides with the first critical speed [17]. The main difference lies in the fact that oil whirl is speed dependent (0.49× in this case), while oil whip locks up at the first critical speed even though the rotor speed is increasing [17]. Thus, tracking the 0.49× component will show only the oil whirl, as well as tracking the 1× component will show only the usual Bodé plot with evidence of critical speeds. Plotting of the direct (unfiltered) vibration with speed will illustrate the total vibration activity measured at that location. Instead of presenting waterfall plots, which are usually [18] used to present such experimental results, where

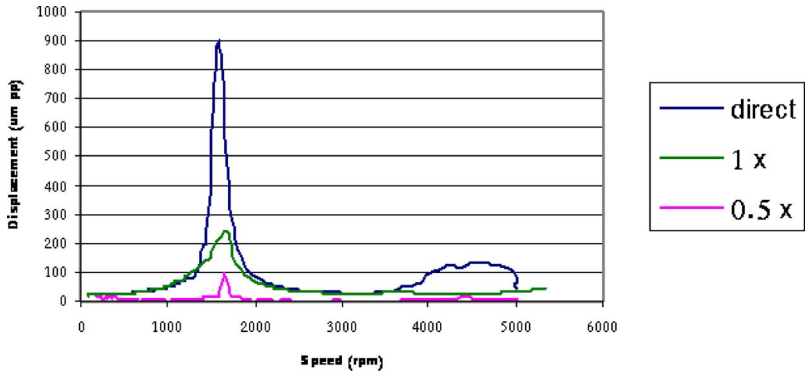

Fig. 10 Tracking data, nondrive side bearing

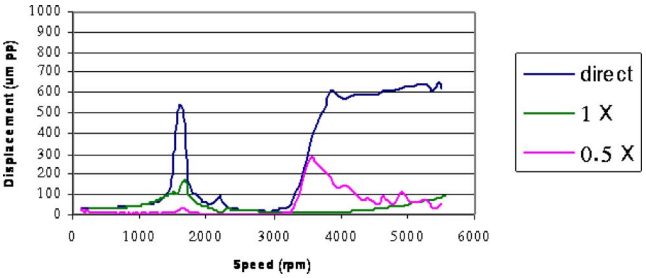

Fig. 11 Tracking data, case 2

it is sometimes difficult to extract information, presenting the results in this Bodé format, tracking different components, was chosen.

Capabilities of the measurement system were exploited, in which the DVF-3 can provide the 1× filtered data (showing the critical speed activity), 0.5× filtered (showing the oil whirl activity), as well as the direct unfiltered vibration with the speed change. A large filter bandwidth (120 cpm) for the 0.5× filtered data was chosen since the oil whirl in the test rig occurred at 0.49×. Thus, filter bandwidth should be enough to capture all oil whirl activity. The direct unfiltered data contains all the spectral information. An increase in the direct vibration data that cannot be explained by either the 1× or 0.5× vibration is an indication of some other phenomena. Since the DVF-3 cannot track a particular speed component (the first critical for oil whip), we used the direct unfiltered data as an indication of oil whip. Thus, if the direct unfiltered data increased with no corresponding increase of the 0.5× or 1× components, then this is an indication of oil whip. This was confirmed by spectral plots, where the main vibration component while the rotor was operating at a high speed, was at the first critical speed and its multiples. An exception occurred while crossing the first critical speed (see, for example, Fig. 7). Since this is transient data, and the first mode is lightly damped, the 1× vibration levels increased sharply, but actually the DVF-3 could not capture all the 1× activity in the filtered 1× display during fast critical speed crossing. However, the direct measurement does not have this shortcoming. Thus, only at the first critical speed, the high direct vibration is actually all 1×. This is clearly seen in the orbit shapes around the critical speed (see, for example, Fig. 8).

Although numerous tests were conducted, only seven cases of the measured data from the test matrix will be presented. In each case, tracking data as well as shaft orbits on the drive-side bearing are presented. In addition, sometimes spectral data that illustrate a point or tracking data for the nondrive side bearing are selectively presented.

Case 1. The first case to be considered is the case of a well balanced and aligned rotor, with the oil supplied at a pressure of 4 bar. Tracking data for the horizontal (x) probe are shown in Fig. 7, while shaft orbits are shown in Fig. 8. It can be seen that the first critical speed occurs at 1638 rpm, while the measured second critical speed is split 3920 rpm at the horizontal (x) probe, and 4095 rpm at the vertical (y) probe. The onset of instability (increase of 0.5× component) was at 3164 rpm. One can notice that the 0.5× component decreases at about 4400 rpm, while the direct vibration is still high, indicating the persistence of oil whip. This can be seen in the spectral plot of Fig. 9. The tracking data of the nondrive-side bearing are shown in Fig. 10. This figure indicates that the nondrive side had a delayed and benign instability. The onset of instability on the nondrive-side bearing was at 3794 rpm. This is probably due to the bearing overload by the large overhung.

Case 2. Case 2 is similar to case 1, but with the supply pressure at 8 bar. Tracking data are shown in Fig. 11, while the orbits are shown in Fig. 12. One can also notice that the onset of instability here occurs at 3306 rpm. Thus, the supply pressure has a slight beneficial effect.

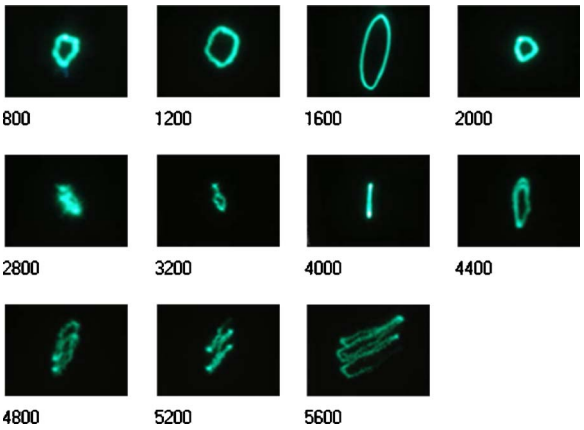

Fig. 12 Orbital data, case 2 (speeds in rpm)

Case 3. Case 3 is also similar to case 1, but with unbalance at the middle disk. Figure 13, shows the tracking data, while Fig. 14 shows the orbit data. The unbalance resulted in the excitation of the second critical, but somewhat reduced the oil whirl and extenuated the effect of oil whip. The onset of instability was at 3134 rpm.

Case 4. Case 4 is similar to case 1, with an unbalance weight at the overhung disk. Figure 15 shows tracking data, while Fig. 16 shows the orbital data. The onset of instability was at 3236 rpm.

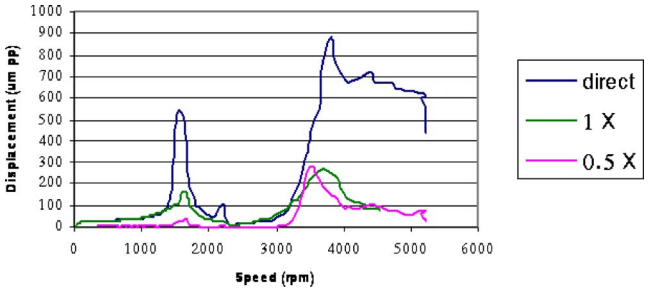

Fig. 13 Tracking data, case 3

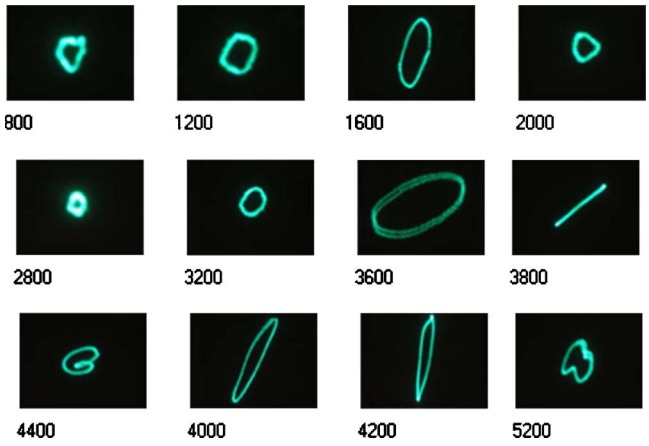

Fig. 14 Orbital data, case 3 (speeds in rpm)

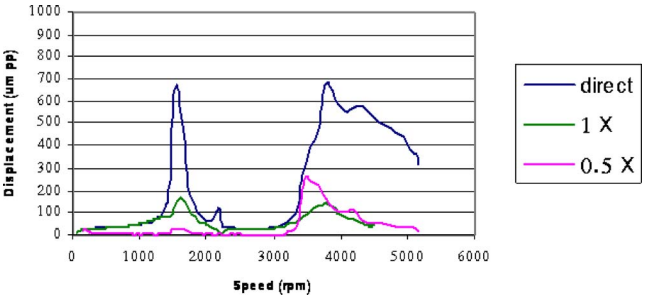

Fig. 15 Tracking data, case 4

Again here the unbalance excited the second mode, but somewhat reduced the effect of oil whirl. The oil whip was initially extenuated but its effect is decreasing with speed.

Case 5. Case 5 is similar to case 1, but with offset misalignment. Figure 17 shows the tracking data, while Fig. 18 shows rotor orbits. The onset of instability was delayed to 3885 rpm. The oil whirl component was obviously benign, but the oil whip became dominant at higher speeds.

Case 6. Case 6 is similar to case 1, but with angular misalignment. Figure 19 shows tracking data, while Fig. 20 shows orbital data. This is the most interesting case. With angular misalignment, the drive-side bearing has only benign subharmonic vibration. The rotor has its smoothest behavior in this case. However, the nondrive-side bearing (Fig. 21) went into oil whip at 4474 rpm, which is a considerably delayed onset of instability.

Case 7. Case 7 is similar to case 1, but with combined angular misalignment and unbalance at the middle disk. The tracking data are shown in Fig. 22, and the orbital data are shown in Fig. 23. Here, the beneficial effect of the angular misalignment was overcome by the unbalance, and the onset of instability was at 3236 rpm. The unbalance excited the second critical speed and maintained an oil whip condition at high speeds.

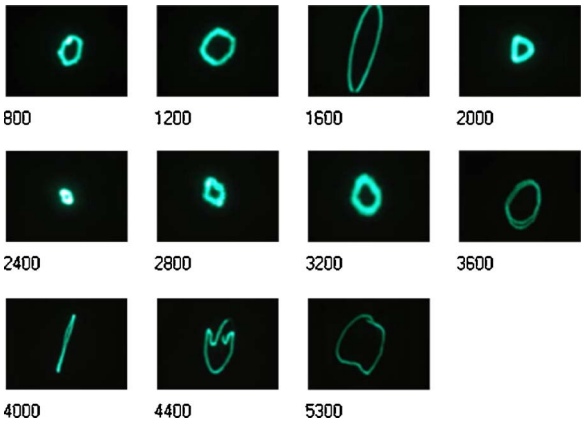

Fig. 16 Orbital data, case 4 (speeds in rpm)

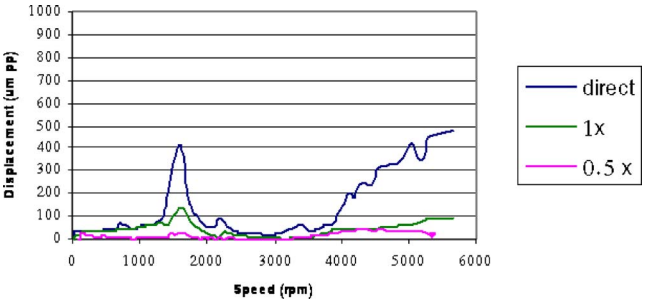

Fig. 17 Tracking data, case 5

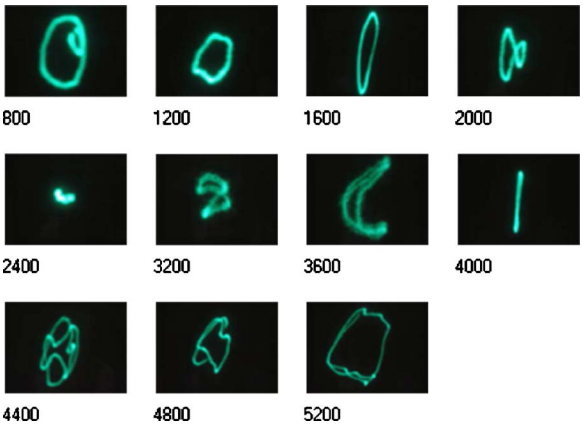

Fig. 18 Orbital data, case 5

Waterfall Spectra

In order to illustrate the measurements in the usual waterfall plots, where spectra are plotted in a three-dimensional plot for various speeds, Figs. 24 and 25 are presented. This is the format used by many researchers in studying oil whirl and oil whip (see, for example, [17–19]), and it aids in understanding the tracking data presented earlier. In particular, the waterfall plots clearly show that the cause of the increase of the direct vibration, when both the 1× and 0.5× are small, is due to oil whip, and not to any other malfunction.

Figure 24 illustrates the waterfall plot for Case 5, with offset misalignment. It corresponds to the tracking data of Fig. 17. It can

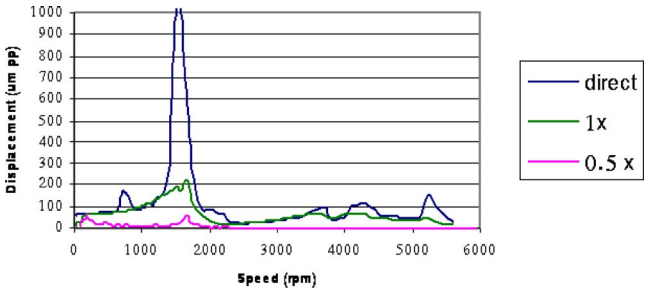

Fig. 19 Tracking data, case 6

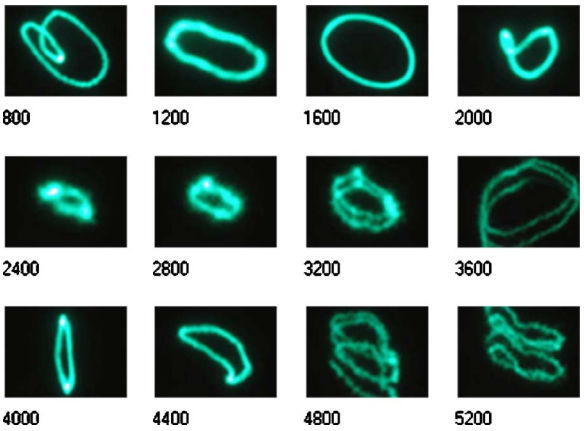

Fig. 20 Orbital data, case 6 (speeds in rpm)

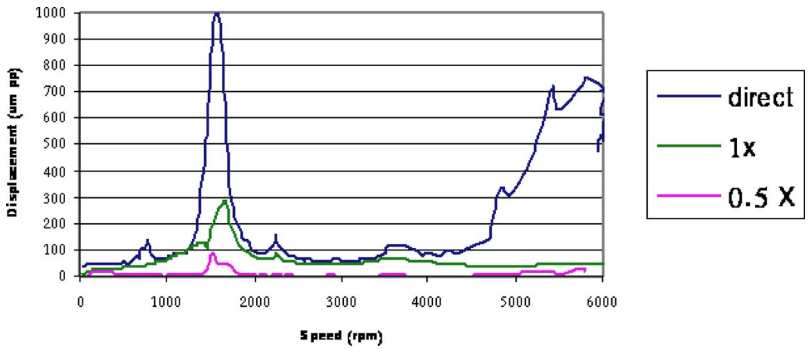

Fig. 21 Tracking data, nondrive side bearing, case 6

be seen from Fig. 24 that the spectra at low speeds contain essentially 1× and 2× vibration, which is to be expected for the offset misalignment case. As the speed increases, it can be seen that the 1× component increases at the first critical speed of approximately 1680 rpm and at the second critical speed of approximately 4170 rpm, while the 2× component excites the second critical speed, and barely excites the first critical, since the spectral measurement was started at about 800 rpm. It is noted that due to the capabilities of the measurement system, adequate resolution in speed are not available, since the spectra are captured by the B&K 2515 spectrum analyzer at particular speeds and stored for later processing in the waterfall plots. Thus, the waterfall plots should be viewed as visualization and general indications plots, while the actual data extraction for determining the instability should be interpreted from the tracking data.

Further analysis of Fig. 24 at higher speeds, beyond the stability limit, illustrate that the spectra are dominated by the spectral component of the first critical speed, 1680 cpm, which locks at this frequency with the increase in speed, a well-known characteristic of oil whip [17]. Again, due to inadequate resolution in speed, the actual onset of instability is determined from the tracking data (Fig. 17).

Figure 25 illustrates the waterfall plot for case 6, with angular misalignment, for the drive side bearing. This figure corresponds to the tracking data of Fig. 19. It can be clearly seen that, for the drive side bearing, no instability occurs: only 1× and 2× vibration appear.

Discussion

The systematic experiments presented herein, clearly show the effect of supply pressure, unbalance of middle disk, unbalance of overhung disk, offset misalignment, and angular misalignment. These experiments clearly separate the effect of each of these conditions on bearing instability independently of each other. This separation should be exploited further.

The journal bearing instability is usually explained by the cross-coupled stiffness effect in the journal bearing. It is well known that loading the bearings [31] can improve stability characteristics of the rotor-bearing system. Bearing loading affects the stiffness characteristics of the bearing, thus increasing the threshold of instability. Bearing loading is usually taken to mean an increase in the bearing static eccentricity. This fact has led many investigators to consider offset misalignment as a means of loading bearings. As an example, the work of Kato, Matsuoka, and Hori [32] illustrates experimentally the favorable effect of offset misalignment on the journal bearing instability. Actually, in practice, this has become a common procedure to load bearings and improve stability. As an example, most vertical pump manufacturers use the middle of three bearings to load the bearings and increase the stability threshold.

The bearing loading through static eccentricity is quite similar to the effect of offset misalignment (see case 5). The separation of angular misalignment (case 6) from the offset misalignment in the presented experiments actually provides insight on their respective behavior. Actually, the presented experimental results clearly show that angular misalignment is much more effective than offset (or parallel) misalignment in improving the stability characteristics.

As an illustration of the difference in the behavior of the rotor system under offset and angular misalignment consider the effect on the nondrive-side bearing. For offset misalignment, Fig. 17 shows the tracking data for the drive-side bearing (instability at 3885 rpm), which is very similar to the measurements on the nondrive-side bearing (not shown). However, for angular misalignment, Fig. 19 shows the tracking data of the drive-side bearing (with no instability), and Fig. 21 shows the tracking data of the nondrive-side bearing (with instability at 4474 rpm). This shows that the bearing loading on both bearings is similar in the offset misalignment case, while the nature of the bearing loading is different between the drive side and the nondrive-side in the angular misalignment case. This is because the angular misalign-

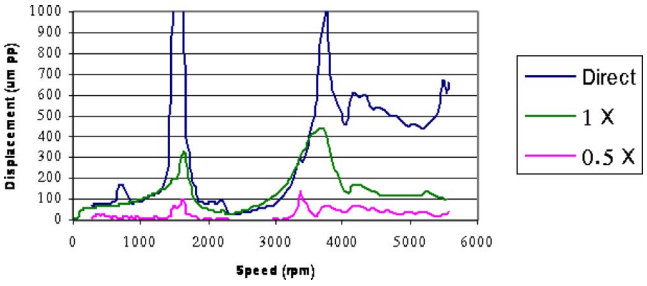

Fig. 22 Tracking data, case 7

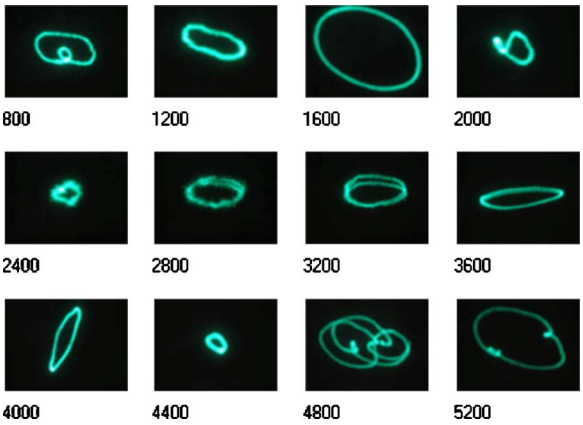

Fig. 23 Orbital data, case 7 (speeds in rpm)

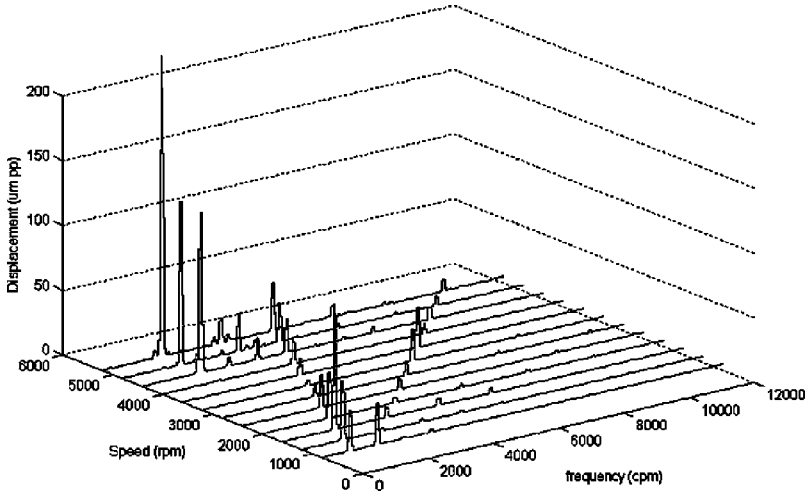

Fig. 24 Waterfall plot, case 5

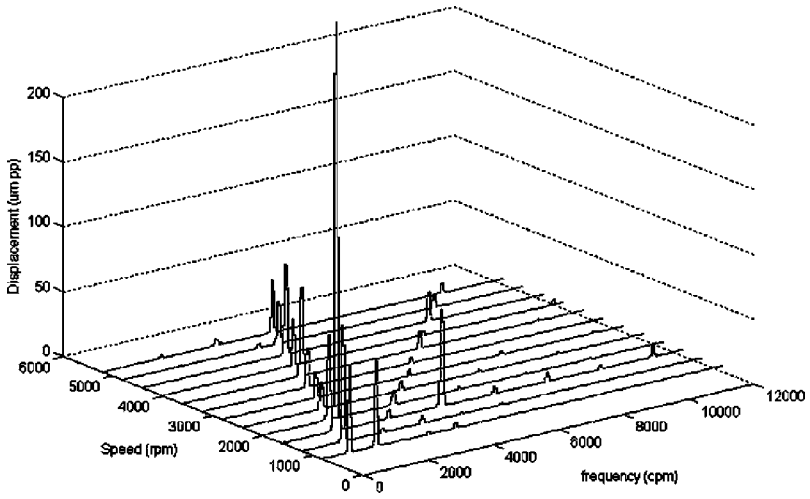

Fig. 25 Waterfall plot, case 6

ment is introduced at the coupling, thus, the rotor is skewed differently on the drive side bearing than on the nondrive-side bearing. The difference between offset and angular misalignment is clearly illustrated in Fig. 26.

The authors searched the literature for the effect of angular misalignment on onset of instability in journal bearings. This included searching the wealth of information on the Bently Nevada website [33]. Unfortunately, the literature does not cover this important topic. The only paper that the authors found that is related to the subject is the excellent work of Yu and Adams [34]. They do consider a 4×4 stiffness model for bearings in the case of radial and angular misalignment. This is in contrast to the usual 2×2 stiffness model. They consider not only the x and y motions, but also the angular motions in two perpendicular directions. Unfortunately, this bearing model is not extended to investigate the stability of the bearing under these conditions. The stability analysis using 4×4 stiffness matrices should be quite interesting as a further investigation to the current work.

Conclusion

In this paper, a structured test program for the study of oil whirl and oil whip in plain journal bearings is presented. The test matrix

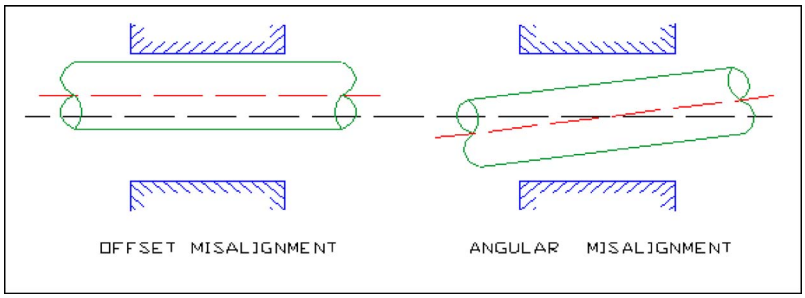

Fig. 26 Offset and angular misalignment

presented cases of the variation of supply pressure, unbalance of middle disk, unbalance of overhung disk, offset misalignment, and angular misalignment. The onset of instability was measured in each case. A simple method for determining oil whirl and oil whip from tracking data was presented.

The most important conclusion from these tests is that angular misalignment delayed significantly the onset of instability. This conclusion needs to be digested further; however, it has been consistent and repeatable.

References

[1] Newkirk, B. L., and Taylor, H. D., 1925, "Shaft Whipping Due to Oil Action in Journal Bearings," Gen. Electr. Rev., **28**, pp. 559–568.

[2] Guo, Z., and Kirk, R. G., 2003, "Instability Boundary for Rotor-Hydrodynamic Bearing Systems," ASME J. Vibr. Acoust., **125**(4), pp. 417–422.

[3] Guo, Z., and Kirk, R. G., 2003, "Instability Boundary for Rotor-Hydrodynamic Bearing Systems, Part 2: Rotor With External Flexible Damped Support," ASME J. Vibr. Acoust., **125**(4), pp. 423–426.

[4] Fuller, D. D., 1983, "On the Contribution of Beauchomp Tower to Current World Technology," Symposium on Fluid Film Lubrication, A Century of Progress: ASLE/ASME Lubrication Conference, Hartford, CT.

[5] Fuller, D. D., 1984, *Theory and Practice of Lubrication for Engineers*, 2nd ed., John Wiley & Sons, New York.

[6] Robertson, D., 1933, "Whirling of a Journal in a Sleeve Bearing," Philos. Mag., **715**, pp. 113–130.

[7] Hagg, A. C., 1946, "The Influence of Oil-Film Journal Bearings on the Stability of Rotating Machines," ASME J. Appl. Mech., **68**, pp. A211–A220.

[8] Poritsky, H., 1953, "Contribution to the Theory of Oil Whip," Trans. ASME, **75**, pp. 1153–1161.

[9] Newkirk, B. L., and Lewis, J. F., 1956, "Oil Film Whirl-An Investigation on Disturbances Due to Oil Films in Journal Bearings," Trans. ASME, **78**, pp. 21–27.

[10] Newkirk, B. L., 1956, "Varieties of Shaft Disturbances Due to Fluid Films in Journal Bearings," Trans. ASME, **78**, pp. 985–988.

[11] Pinkus, O., 1953, "Note on Oil Whip," ASME J. Appl. Mech., **20**, pp. 450–451.

[12] Pinkus, O., 1956, "Experimental Investigation of Resonant Whip," Trans. ASME, **78**, pp. 975–983.

[13] Hori, Y., 1959, "A Theory of Oil Whip," ASME J. Appl. Mech., **26**, pp. 189–198.

[14] Rieger, N. F., Poritsky, H., Lund, J. W. et al., 1965–1968, "Rotor-Bearing Dynamics Design Technology," 1–9, Wright-Patterson AFB, Aero Propulsion Reports.

[15] Lund, J. W., and Thomsen, K. K., 1978, "A Calculation Method and Data for the Dynamic Coefficients of Oil-Lubricated Journal Bearings," Topics in Fluid Film Bearing and Rotor Bearing System Design and Optimization, ASME Design Engineering Conference Publication, pp. 1–28.

[16] Lund, J. W., 1974, "Stability and Damped Critical Speeds of Flexible Rotor in Fluid Film Bearings," Trans. ASME, **96**, pp. 509–517.

[17] Muszynska, A., 1986, "Whirl and Whip-Rotor/Bearing Stability Problems," J. Sound Vib., **110**(3), pp. 443–462.

[18] Muszynska, A., 1986, "Fluid-related Rotor/Bearing/Seal Instability Problems," Bently Rotor Dynamics Research Corporation Report.

[19] Muszynska, A., 1988, "Multi-Mode Whirl and Whip in Rotor/Bearing Systems," 2nd International Symposium on Transport Phenomena, Dynamics, and Design of Rotating Machinery, Honolulu, Hawaii, April 4–6.

[20] Myers, C. J., 1984, "Bifurcation Theory Applied to Oil Whirl in Plain Cylindrical Journal Bearings," ASME J. Appl. Mech., **51**, pp. 244–250.

[21] Hollis, P., and Taylor, D. L., 1986, "Hopf Bifurcation to Limit Cycles in Fluid Film Bearings," ASME J. Tribol., **108**, pp. 184–189.

[22] Elrod, H. G., and Vijayaraghan, D., 1994, "A Stability Analysis for Liquid-Lubricated Bearings Incorporating the Effects of Cavity Flow, Part I: Classical One-Dimensional Journal Bearing," ASME J. Tribol., **116**, pp. 330–336.

[23] Elrod, H. G., and Vijayaraghan, D., 1994, "A Stability Analysis for Liquid-Lubricated Bearings Incorporating the Effects of Cavity Flow, Part II: Journal Bearings with Central Groove," ASME J. Tribol., **117**, pp. 365–367.

[24] Crandall, S. H., 1995, "The Instability Mechanism Responsible for Oil Whirl and Oil Whip," Proc. 4th Greek National Congress on Mechanics, Democritus University of Thrace, Xanthi, pp. 659–672.

[25] Crandall, S. H., 1996, "Velocity Linearization of the Dynamic Response of Fluid-Film Bearings," Proc. EUROMECH-2nd European Nonlinear Oscillation Conference, Prague, September 9–13.

[26] Horattas, G. A., Adams, M. L., Abdel Magied, M.F. et al., 1997, "Experimental Investigation of Dynamic Nonlinearities in Rotating Machinery," Proc. ASME DETC 97, Sacramento, CA, Sept. 14–17.

[27] Deepak, S. T., and Noah, S. T., 1998, "Experimental Verification of Subcritical Whirl Bifurcation of a Rotor Supported on a Fluid Film Bearing," ASME J. Tribol., **120**, pp. 605–609.

[28] Inayat-Hussain, J. I., 2003, "Continuation Method Applied to Whirl Instability in Journal Bearings," Proc. 11th World Congress in Mechanism and Machine Science, August 18–21, Tianjin, China.

[29] RIMAP *User Guide*, 2002, Version 1.3, RITEC, Cairo, Egypt.

[30] Booser, E. R., 1970, "Plain Bearing Material," Mach. Des., **42**(15), pp. 14–20.

[31] Muszunska, A., and Bently, D. E., 1989, "Fluid Generated Instabilities of Rotors," ORBIT, **10**(1), pp. 6–14.

[32] Kato, T., Matsuoka, H., and Hori, Y., 1993, "Seismic Response of Linearly Stable, Misaligned Multirotor System," Tribol. Trans., **36**(2), pp. 311–315.

[33] www.bently.com

[34] Yu, H., and Adams, M. L., 1989, "The Linear Model for Rotor-Dynamic Properties of Journal Bearings and Seals with combined Radial and Misalignment Motions," J. Sound Vib., **131**(3), pp. 367–378.

Advancements in the Structural Stiffness and Damping of a Large Compliant Foil Journal Bearing: An Experimental Study

Mohsen Salehi
e-mail: Salehim@asme.org

Hooshang Heshmat
Fellow ASME

James F. Walton II

Mohawk Innovative Technology, Inc.,
Albany, NY 12205

This paper presents the results of an experimental investigation into the dynamic structural stiffness and damping characteristics of a 21.6-cm (8.5 in.)-diameter compliant surface foil journal bearing. The goal of this development was to achieve high levels of damping without the use of oil, as is used in squeeze film dampers, while maintaining a nearly constant dynamic stiffness over a range of frequencies and amplitudes of motion. In the experimental work described herein, a full compliant foil bearing was designed, fabricated, and tested. The test facility included a non-rotating journal located inside the bearing. The journal was connected to an electrodynamic shaker so that dynamic forces simulating expected operating conditions could be applied to the structurally compliant bump foil elements. Excitation test frequencies to a maximum of 400 Hz at amplitudes of motion between 25.4 and 102 μm were applied to the damper assembly. During testing, both compressive preload and unidirectional static loads of up to 1335 and 445 N, respectively, were applied to the damper assembly. The experimental data from these tests were analyzed using both a single degree of freedom model and an energy method. These methods of data analysis are reviewed here and results are compared. Excellent agreement in results obtained from the two methods was achieved. Equivalent viscous damping coefficients as high as 1050 N. s/cm (600 lbf. s/in) were obtained at low frequencies. Dynamic stiffness was shown to be fairly constant with frequency.
[DOI: 10.1115/1.2360598]

Introduction

Air lubricated compliant foil bearings (CFBs) have demonstrated excellent promise for various applications such as aircraft air cycle machines, turbochargers, gas turbine engines, and other high speed turbomachines. Since advanced turbomachinery operating conditions are projected to become more severe, oil-free rotor support systems that can be designed to meet a wide variety of stiffness and damping requirements at elevated temperatures are desired. The compliant structural elements of high temperature CFBs, being made of a nickel based superalloy, are very attractive for use in extreme ambient conditions, such as high temperature and high speed. The compliant bump foil configuration used in CFB construction, as shown in Fig. 1, consists of two main parts, a smooth top foil, which constitutes the bearing surface, and multiple flexible corrugated bump foil strips which provide both compliancy and frictional damping. The bump foil segments are welded or otherwise pinned at or near one end of the strip while the other end(s) remain free. The top smooth foil that is laid on top of the bump foil strip segments is free at one end and welded or pinned to the bearing/damper housing at the other end.

When used as a hydrodynamic CFB, load capacity, stiffness, and damping characteristics are the result of two predominant mechanisms. One is via the foils, which provide both local and global stiffness and damping, and the other through its hydrodynamic action resulting from the fluid film pressures generated between the journal surface and top foil. With proper matching of the compliant structural stiffness to the hydrodynamic film pressures, the desired system stiffness, damping, and load capacity can be achieved. It has been shown that, in addition to structural stiffness, the friction between the bump foil and both the top foil and housing provides additional system stiffness and damping [1–4] (see Fig. 2). The stiffness of a compliant foil bearing is nonlinear, arising from the combination of frictional and structural stiffness. The authors are investigating the behavior of each individual stiffness component; however, the relationship between the two is addressed to some extent in references cited. Due to geometry of the bump foils, when under applied load with increasing amplitude of motion, the restoring force (force at the contact) increases based on equilibrium of the body force diagram. However, at a fixed frequency with increasing amplitude of motion, we have found that the effect of frictional forces decreases. Figure 2 shows a double layer bump foil configuration, where the first layer is active at amplitudes of motion >0 and less than a pre-designed value. At this initial small amplitude condition, the second layer is not active. Beyond the pre-established motion level, both layers are active and therefore the total stiffness increases. This effect will be shown in the results section, where the stiffness versus displacement is shown for various designs.

Regardless of whether the bump foil elements are intended for hydrodynamic compliant foil bearing application or for use in a structural bearing damper, their design must include a wide array of factors. For example, besides the bump foil geometry, tribomaterial and preload, frequency of vibration, amplitude of motion at the interface, and various deterministic parameters such as static friction coefficient between the elements affect the magnitude of the structural stiffness and damping that can be attained. Determination of frictional forces continues to be one of the most challenging aspects of research in tribology. For most dynamical systems, this coefficient is a vital parameter for determination of system stiffness and damping coefficients. The complexity originates mainly from dependency of frictional parameters on many

Contributed by the International Gas Turbine Institute (IGTI) of ASME for publication in the JOURNAL OF ENGINEERING FOR GAS TURBINES AND POWER. Manuscript received October 1, 2003; final manuscript received March 1, 2004. IGTI Review Chair: A. J. Stazisar. Paper presented at the International Gas Turbine and Aeroengine Congress and Exhibition, Vienna, Austria, June 13–17, 2004, Paper No. GT2004-53860.

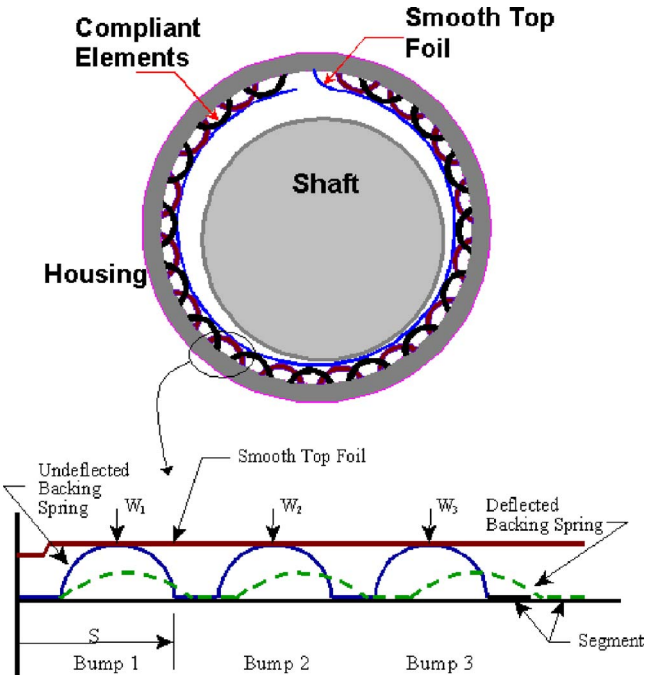

Fig. 1 Compliant foil bearing generation 4 components and mechanism of bump foil deflection

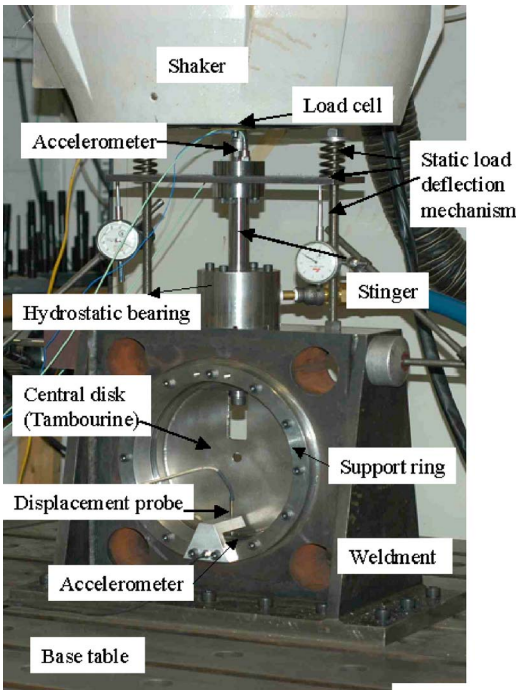

Fig. 3 Experimental test rig

factors, such as environment, surface condition and operating conditions (i.e., load, frequency, and amplitude of motion). Mathematical models and approaches, such as perturbation and linearization, which attempt to describe the behavior of a system with dry friction, are not generally successful due to high nonlinearity, especially in the vicinity of equilibrium point. The outcomes of experimental studies also show that the results are affected by time, humidity, interface properties, and history of motion [5–7].

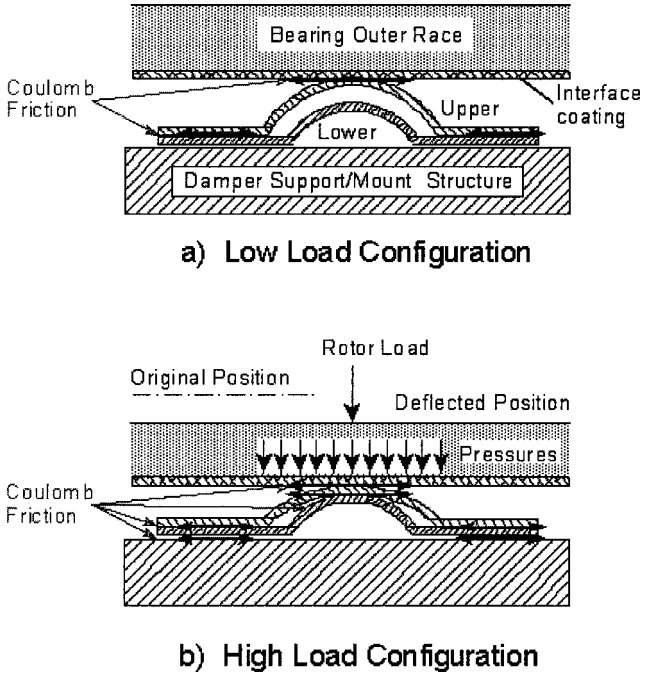

Fig. 2 Friction due to micro to meso scale motion between bump foil and top foil and housing surfaces

Experimental Test Rig

An experimental test rig was designed and fabricated in order to conduct dynamic tests on a complete compliant bump foil bearing damper ring assembly. The experimental test rig, shown in Fig. 3, included the following main components:

(a) Electrodynamic Shaker, with controller and stinger assembly to transfer motion to the bearing damper assembly through an inner ring and disk
(b) Large base plate on which the test rig assembly was mounted
(c) Weldment housing, inside which the compliant test elements were mounted
(d) Inner ring/disk assembly with stinger attachment
(e) Hydrostatic bearing for stinger alignment
(f) Bump foil test assembly
(g) Static load deflection assembly

The shaker motion was transmitted to the inner ring/disk assembly via a solid stainless steel stinger. Each component is briefly described below.

Shaker. In order to ensure that desired motions could be applied to the foil bearing damper assembly at up to 400 Hz, a high capacity electrodynamic shaker was chosen. In addition to having to apply high frequency and amplitude motion to the test damper, it was also desired to have the ability to apply a known static load to the assembly such as might be experienced under gravity load or in aircraft applications under maneuver conditions. As such, a built-in air load support with a maximum payload capacity of 100 kg (220 lb) and full relative displacement was included in the shaker capabilities. Detailed specifications of the shaker are given below:

Peak force—sine wave: 4100 N (922 lbf)
Frequency range: 5–5000 Hz
Maximum acceleration: 951 m/s2 (97 g)
Maximum velocity: 1.0 m/s (39.4 in./s)
Maximum displacement: 25 mm (0.984 in.)
Resonant frequency: 3150 Hz

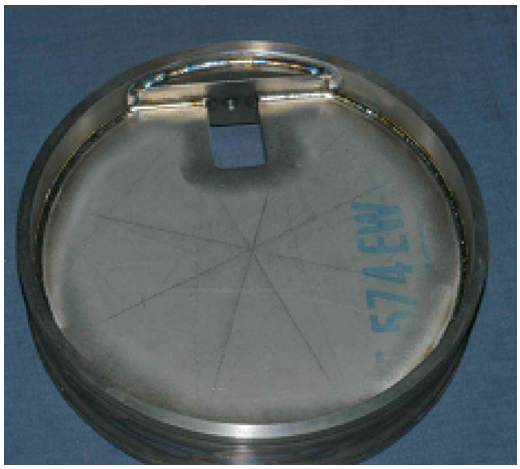

Fig. 4 Central disk with plate stiffener and top dead center hole for stinger connection

Weldment (Foil Bearing Housing). The weldment, made of hard rolled steel, was used for holding the compliant foil bearing damper assembly. The weldment hardware, shown in Fig. 3, has overall dimensions of 51*25*38 (L*W*H) cm and was secured to the base table via 16 high strength screws. A passage hole was made at the top dead center of the weldment, which allowed for connection of the stinger to the central disk, as well as accommodating the reciprocating motion of the stinger.

In order to increase the accuracy of the displacement measurement during the dynamic tests, any detrimental movement by the foil bearing housing had to be minimized. In particular, it was essential that the test system be free of resonances within the desired frequency test range as much as possible. Therefore, a finite element model of the test setup was established and used in determining the natural frequencies of the weldment structure. The finite element analysis (FEA) results included the deformation of the damper holder structure at its natural frequencies. The first two mode shapes at 680 and 1050 Hz, respectively, for the foil bearing housing were found to be above the maximum expected test frequency.

Central Disk/Stinger. The central disk/tambourine (along with the stinger) served as an interface assembly piece providing a connection to the shaker so that the desired motions could be imposed upon the compliant bump foils. The central disk hardware, shown in Fig. 4, was made of Ti -6Al 4V and was comprised of a 203-mm-diam, 50-mm-wide outer ring, and a 6.35-mm-thick (0.25 in.) solid flat stiffener plate centered axially inside the ring.

A hole was drilled into the inner ring; a small segment of the stiffener plate was removed; and a small connector block was installed to permit installation of the stinger.

The central disk was made of Ti 6Al 4V to keep moving mass low since the shaker capacity was limited to 4003 N (900 lbs) and maximum amplitude of motion over the widest frequency range was desired. Additionally, the material had to be stiff enough that, at high frequencies and high amplitude of motion, the deformations of the inner ring/disk assembly would remain small.

A FEA was conducted to identify the natural frequencies of the inner ring/disk and stinger assembly. In this FEA model, the boundary condition included elements that contain both stiffness and damping to be representative of the bump foil damper during dynamic testing. The central disk/stinger natural frequencies and mode shapes resulting from the FEA are presented in Fig. 5. Since the operation frequency was chosen in the range of 0–400 Hz, note that mode shapes one and two (214.4 and 310.8 Hz) are within the range of operation. It was decided that if the resonant

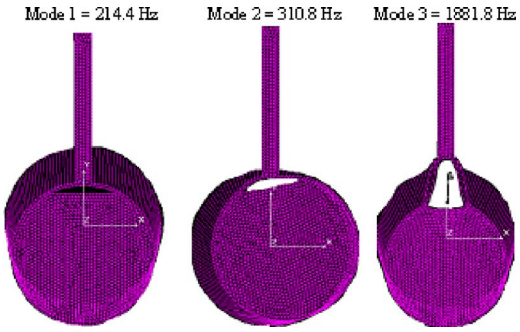

Fig. 5 The natural frequencies and mode shapes for the central disk /stinger assembly

frequencies were causing large error in data reduction, an additional stiffener would be fabricated and initial impact tests would be conducted to identify the resonant frequencies.

The stinger was a solid rod made of PH13-8 Mo with a 25.4 mm diameter and 23.038 cm length. Both ends of the stinger had inside threaded holes for connection to the inner ring/disk assembly and shaker.

Stinger Hydrostatic Guide Bearing. In order to minimize undesired off axis motions being introduced, due to potential misalignment between the stinger and the surface of the passage hole at the top dead center of the weldment, an air bearing was used to guide the stinger motion. The air bearing, as shown in Fig. 3, was made of 1010 steel, designed with a diametral clearance of 0.05 mm, and used shop air with a maximum pressure of 150 psi. The air bearing housing was mounted on top of the weldment and aligned with the center of the hole on the top of the weldment.

Bump Foil Assembly. An intermediate ring, made of 17-4 PH, was placed between the weldment and the central disk. The intermediate ring was kept inside the weldment via interference fit. A hole was made at the top of the ring to allow the shaker stinger rod to pass through and be connected to the central disk assembly. The compliant bump foil assembly was mounted between this intermediate ring and the central disk. The ring had an overall outside diameter of 22.25 cm, inner diameter of 21.488 cm and axial length of 5.473 cm. Two support/clamp rings were installed on both sides of the weldment for final axial adjustment of the central disk inside the disk/stinger assembly. After the adjustment of the central disk inside the weldment, the rings were then removed.

The bump foils were designed using an existing compliant bump foil structural stiffness and damping program [2,3]. Parameters such as foil thickness, bump height, pitch, length, and material (including interface friction coefficient), were varied in order to achieve the desired stiffness and damping values. Based on the desired stiffness value and maximum expected motion, the compliant bumps were made of 0.152-mm-thick Inconel foil. Figure 6 shows an unwrapped section of the full compliant foil journal bearing damper subassembly.

Static Load Deflection Mechanism. In order to conduct a static load deflection test on the full damper once installed in the

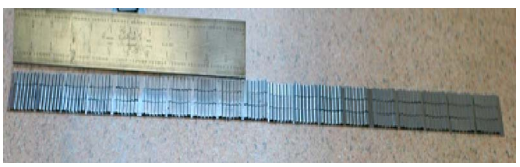

Fig. 6 A section of the hardware for compliant bump foil assembly

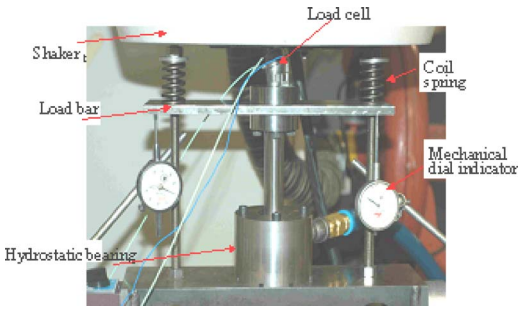

Fig. 7 Static load deflection mechanism for full damper

weldment, a mechanism as shown in Fig. 7 was designed and fabricated. This mechanism used two precision coil springs and a bar to apply a known load to the inner ring/disk assembly. The displacement of the bump foil assembly, due to the applied external load, was measured using two high precision mechanical indicators (precision as high as 50 μm). Additionally, in various tests, an eddy current displacement sensor was used to measure inner ring motion to verify the readings taken with the dial indicators.

Previous testing of a smaller 150-mm-diameter compliant foil damper assembly was completed using a computer controlled and automated load deflection tester as shown in Fig. 8.

This rig was comprised of a stationary outer base, an inner hydrostatically levitated slide table with a post sized to accommodate the 150-mm-diameter damper assembly; a strain gauge load cell, an eddy current displacement sensor, a counter weight and an air cylinder to affect the desired range of motion. While this automated tester was not configured for the 216-mm-diameter damper, data from the 150 mm damper assemblies were useful in validating the static load deflections of the 216-mm-diameter damper taken when installed in the dynamic test rig weldment.

Measurement and Instrumentation

The instrumentation for the dynamic test rig included the following:

(a) Load cell connected to the shaker
(b) Accelerometer mounted on the inner ring/disk assembly
(c) Displacement probes
(d) Oscilloscope for observing the signals
(e) Shaker control
(f) PC based data acquisition and reduction system

The input dynamic forces were measured using a Kistler Model XYZ piezoelectric load cell with a maximum force range of 34,918 N (7850 lbf). The load cell was mounted directly to the shaker armature table with the stinger attached to the exposed end of the force cell. The output of the load cell was directed to a matched and calibrated charge amplifier and subsequently to the

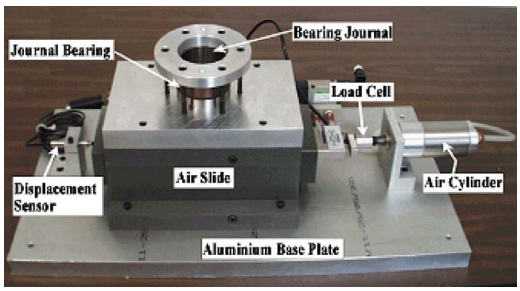

Fig. 8 Computer automated foil bearing and damper load deflection test rig

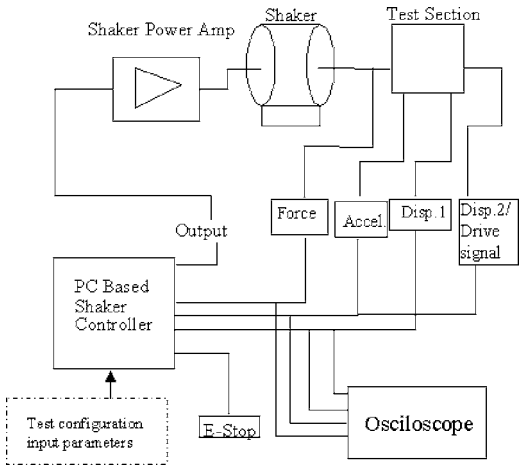

Fig. 9 The shaker control circuit

shaker controller and data acquisition system. A Piezotronics piezoelectric accelerometer was mounted near the shaker on the end of the stinger attached to the force transducer. This accelerometer was used to ensure that the desired input acceleration control was obtained.

Measurement of the inner central disk motion was accomplished using a Kistler eddy current probe. To ensure planar sinusoidal motion of the inner ring at the point farthest from the stinger input, displacement sensors were mounted on both sides of the inner ring at bottom dead center at an axial spacing of 50 mm apart. During checkout of the hardware test setup, a second series of similar displacement sensors were installed near top dead center to ensure that the motion observed at bottom dead center was accurate and that the inner ring/disk assembly was not distorting during test. A Tektronix digital oscilloscope was used to monitor the input and response signals. The scope has four channels, which were used for displacement, load, acceleration, and input signal to the shaker. The scope output signals could be saved on a floppy disk for further processing.

The shaker controller permitted direct control over test conditions. Tests could be performed under constant input displacement or acceleration, as well as variable displacement, velocity, or acceleration over specified frequency ranges. The shaker control circuit is shown in Fig. 9.

To ensure that the prescribed test parameters were obtained, the controller output drive signal was compared to the measured shaker and test hardware displacements, accelerations, and forces. The test results presented here were conducted at constant amplitude of motion within the frequency range of 0–400 Hz. In all of the dynamic tests, the amplitude of motion was kept constant during the whole frequency range. All the tests were conducted under a sinusoidal excitation from the shaker. In all of the tests, the drive signal was used as a reference signal for correction of the phase angle with frequency for measurements such as force and displacement.

Data Analysis

The output signals from the shaker were in the form of a complex number. Each signal then could be presented mathematically as:

$$X_{\text{com}} = X_{\text{rel}} + iX_{\text{img}} \tag{1}$$

The magnitude and phase angle are presented as:

$$|X_o| = [X_{re}{}^2 + X_{\text{img}}{}^2]^{0.5} \tag{2}$$

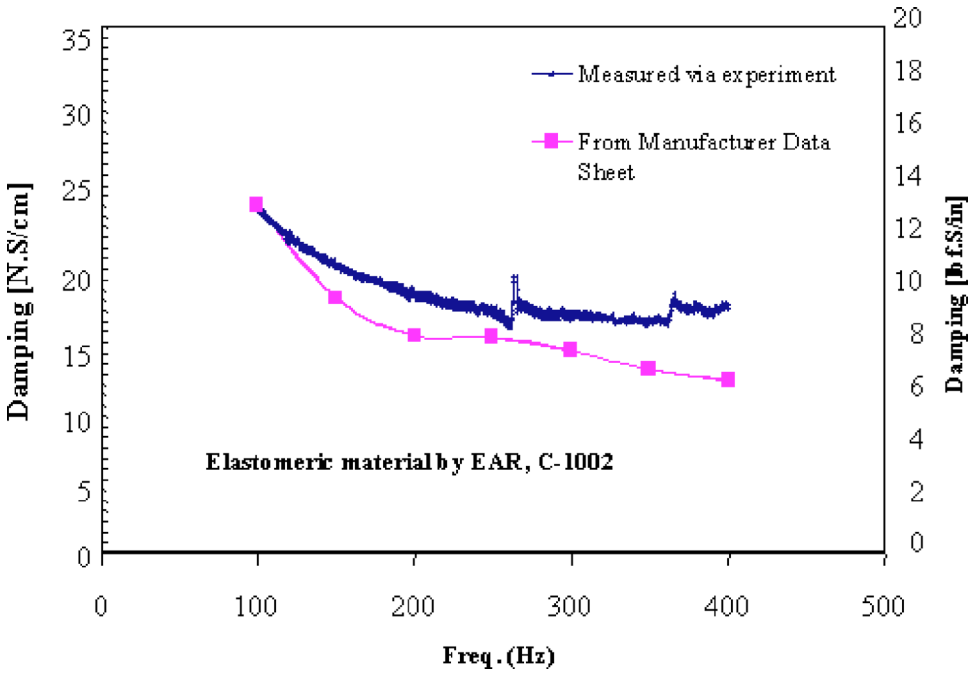

Fig. 10 Damping values from manufacturer compared with experimental values

$$\varphi_X = \tan^{-1}\left\{\frac{X_{\text{img}}}{X_{re}}\right\} \tag{3}$$

The single degree of freedom equation of motion can be presented as:

$$m\ddot{x} + C\dot{x} + kx = F_o \sin(\omega t) \tag{4}$$

From the above equation, the stiffness and damping could be presented as a complex number combined in the following parameter:

$$\frac{F_{\text{com}}}{X_{\text{com}}} = K + i\omega C \tag{5}$$

where F, X, K, T, and C represent the force, displacement, stiffness, angular velocity, and damping, respectively. In calculation of the force, the inertial term is calculated separately and then accounted for calculation of stiffness and damping.

For some tests, an alternative method known as the energy method was used to verify the results from the above method. In this method, the energy dissipated per cycle is calculated and from this energy, the damping value is obtained. With this method, when the force signal is plotted versus the displacement signal, an ellipse is generated. The area enclosed by this ellipse is an estimation of the energy stored. This ellipse is known as "Hysteresis Loop."

The energy stored per each cycle can be obtained from the following equation:

$$\Delta E = \oint F_d \,.\, dx = \mu F_n \int_0^{2\pi/\omega} \dot{X} \,.\, \text{sgn}(\dot{X}) dt \tag{6}$$

where E represents the energy. Alternatively the dissipated energy can be associated with the damping value through the following equation:

$$\Delta E = \int_0^{2\pi/\omega} C\dot{X} dt = \pi C \omega X_o^{\ 2} \tag{7}$$

From the above equation the damping value can be obtained. More detail on the analysis of damper and effects of various parameters can be seen in [1].

Test Results and Discussions

In order to qualify the test rig for use and to gauge the level of accuracy in data reduction and signal outputs from the instrumentation, it was decided to measure the damping values for EAR, C-1002 elastomeric damper specimen and compare the data from the manufacturer with shaker output for damping. Prior to testing, the following parameters were held as close as possible to those applied by the manufacturer:

(a) Temperature of the test
(b) Loading condition, merely shear loading with a predetermined compression on the elastomer piece
(c) Size of the elastomer piece so that the geometrical similitude is best maintained.

For this test, elastomer pieces were installed on both sides of the flat plate in the central disk with approximately 10% compression. This setup was used to maintain shear motion when the shaker was activated. Each elastomer piece was $25.4^{*}25.4^{*}6.35$ ($L^{*}W^{*}H$) mm. The damping values for the elastomer were calculated over a frequency range of 100–400 HZ. The comparison of the damping values for the elastomer is shown in Fig. 10. A comparison was also made between the loss factor ($\ni$) for the elastomeric material and that of the compliant foil damper for test at 25°C. The results are shown in Table 1.

It is interesting to note that the loss factor of the elastomeric materials, in general, decreases drastically with increasing frequency and a slight temperature, while our study indicated that after a threshold frequency of approximately 500 Hz (for this

Table 1 Comparison of loss factor

Frequency (Hz)	Γ (Elastomeric material)	Γ (Compliant bump foil)
100	1	8
200	1	3.8
300	1	1.6
400	0.9	0.97
500	0.8	0.9*

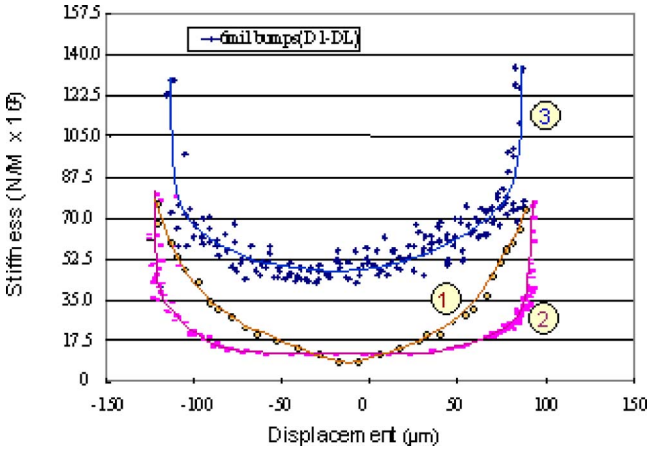

Fig. 11 150-mm-diam bump foil damper static stiffness versus displacement

work), the damping of the compliant bump foil assembly asymptotically approaches a lower limit and stays constant and is minimally affected by temperature up to 250°C.

This threshold frequency depends on the bump foil configuration and boundary conditions, such as static load and preload. The effect of temperature also has substantially less influence on the performance of the compliant bump foil than elastomers since the thermo-physical properties of most metals are constant within a large range of temperature.

In parallel with the dynamic rig qualification testing, a subscale 150-mm-diam bump foil bearing damper was fabricated as a means of evaluating and fine tuning the bump foil static stiffness prior to assembly of the full scale 216-mm-diam bearing damper. As seen in Fig. 11, the static stiffness as a function of displacement (as measured with the automated load deflection rig) varied from approximately 875.8 KN/m (5000 lb/in.) to 7.8 MN/m (45,000 lb/in.) with almost no constant stiffness region. Since a nearly constant stiffness was desired over a 0.25 mm displacement range, the design was altered and the results of which are shown as curve 2 in Fig. 11. Having achieved a wide constant stiffness range, it was next desired to demonstrate an increased stiffness value as seen in curve 3 of Fig. 11. This optimized sub-scale configuration was then used in all subsequent full scale testing. For all the results presented here, except the results for energy method, the optimized foil bearing design was used.

For this design, the bump foil specification, such as thickness, pitch, and material, was maintained the same. Presentation of the results for the performance of the compliant foil bearing starts with a test conducted for evaluation of the structural stiffness. The structural stiffness was obtained via the static loading mechanism explained earlier. Displacement of the central disk was measured for every increment of load (about 25 N). For each test, both values for loading and unloading were measured. The result for the stiffness is shown in Fig. 12. In general, for compliant bump foils, a non-linear relationship between the displacement and load exists. However, in this work, efforts were made to decrease this nonlinearity via an optimized combination of bump foil characteristics, such as height, length, pitch, and thickness. As shown, the stiffness value starts with a minimum value of 40,000 kN/cm and within a total displacement of 150 μm in each direction, a maximum of 300 kN/cm is obtained.

The dynamic structural stiffness of the full size foil bearing is shown in Fig. 13. The stiffness is shown for a highly preloaded condition with large amplitude of motion. Considering the nonlinear characteristics of the compliant bump foil, small variation in magnitude of stiffness resulted.

The results for damping tests start with Fig. 14, where the compliant foil bearing was subjected to sinusoidal amplitudes of 51 μm, interference preload of 1335 N, and various unidirectional static loads. The results for all cases show that the damping values decrease with increasing frequency in a semiexponential format. The effect of static load on the damping characteristics of the compliant bump foils can be seen by examination of three plots. As shown, with increasing static load from 255 to 445 N, the damping values decreased. The relative reduction in damping over the tested frequency range is between 30 % and 40%. However, when increasing static load from 0 to 225 N, the damping values increased.

The relative increase in damping value over the range of fre-

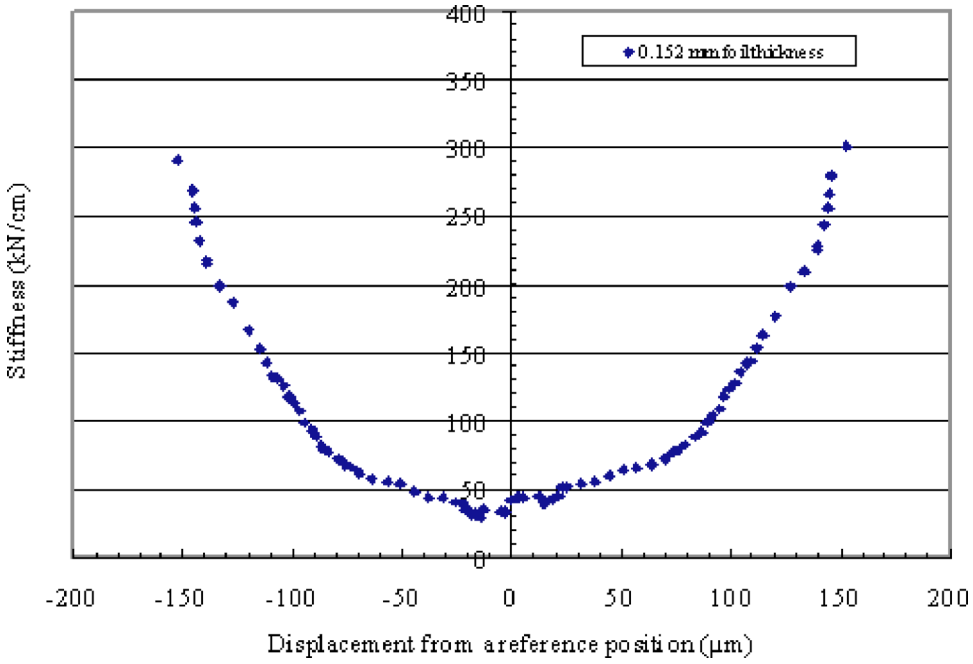

Fig. 12 Structural stiffness of 216 mm compliant foil bearing versus displacement

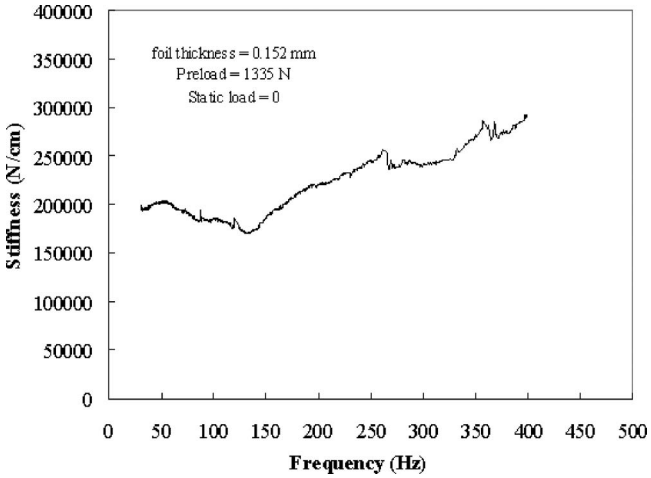

Fig. 13 Dynamic structural stiffness of full size compliant foil bearing (*Xo*, max=101 μm)

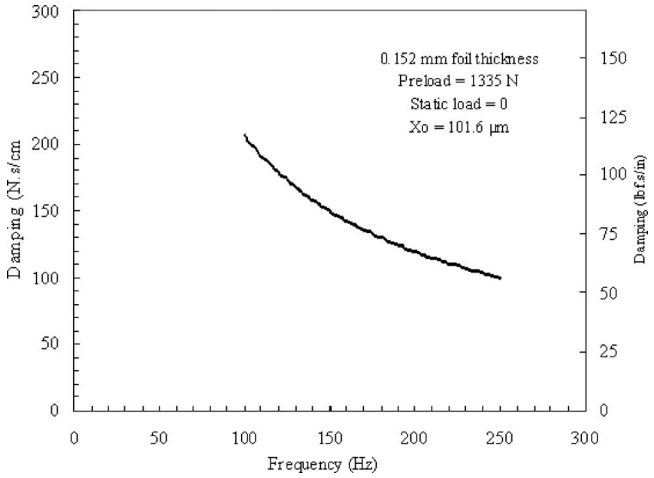

Fig. 15 Damping values for high amplitude of motion

quency tests was 16–25%. The results of many tests conducted showed that, for all cases, an increase in static load up to a specific threshold value, damping increased. However, at static loads above this threshold damping decreased. This variation can be associated with the fact that with an increase in the static load the friction between the compliant bump foil and the foil bearing housing increases and therefore the damping values also increase. At high static load, the loaded compliant bump foils (bottom portion) result in higher damping; however, for the unloaded bump foils (e.g., the top half portion), the damping values decrease, thus the overall damping value is decreased. For damping values as in the frequency range of 30–300 Hz, a maximum and a minimum value of 820 and 140 kN/cm were, respectively, obtained.

The damping values for large amplitude of motion (*Xo* =101.6 μm) are shown in Fig. 15. As discussed analytically in [1], the coefficient of friction decreases due to increase of relative velocity between the two bodies, resulting in decreasing the damping values. Compared with Fig. 13, the results show that the damping value for a frequency of 30 Hz has decreased by 350%.

The damping values presented so far were all calculated based on the single degree of freedom model. In an attempt to verify the validity of the model and its accuracy, the damping values were calculated from the energy method as described in Eqs. (6) and (7). For each test and at each frequency and amplitude of motion, the plot of force versus displacement (or hysteresis plot), was used for calculation of energy dissipated. A hysteresis plot for a selected test is shown in Fig. 16. In this plot, the horizontal and vertical axes represent the displacement and force, respectively. The black color ellipse represents the experimental values and the green continuous ellipse is the curve fitted plot.

The area inscribed by the ellipse represents the energy loss due to frictional damping.

The damping values calculated by the two methods are compared in Fig. 17. As shown, a good agreement between the two methods was obtained. This indicates that, for many applications, a good approximation of the damping values can be obtained via the hystersis plot.

Conclusions

The results of an experimental study for structural stiffness and damping values of a 21.6-cm-diam compliant foil bearing were presented and discussed. The results obtained were comparable with results obtained for a smaller size bearing. The stiffness and damping values for a frequency range of 0–400 Hz, and amplitude of motion between 0 and 102 μm, a static load of 0–445 N, and a preload from 0 to 1335 N were presented. The results show that damping values increased with static load up to a threshold after which increasing the static load decreased the damping values. The damping values decreased with increasing frequency in

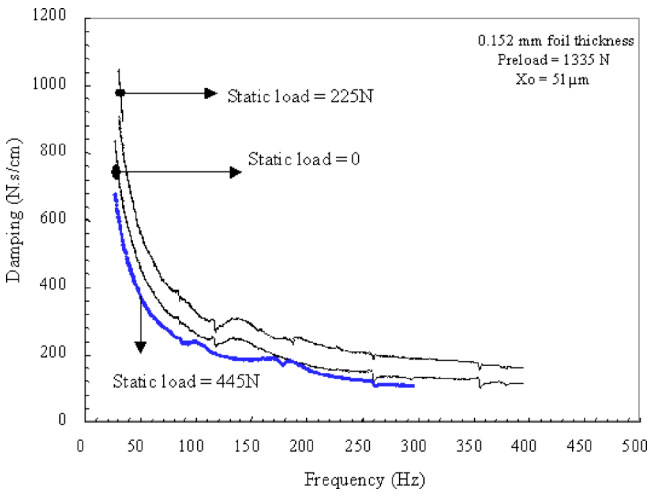

Fig. 14 Damping values for bump foil with various preloads

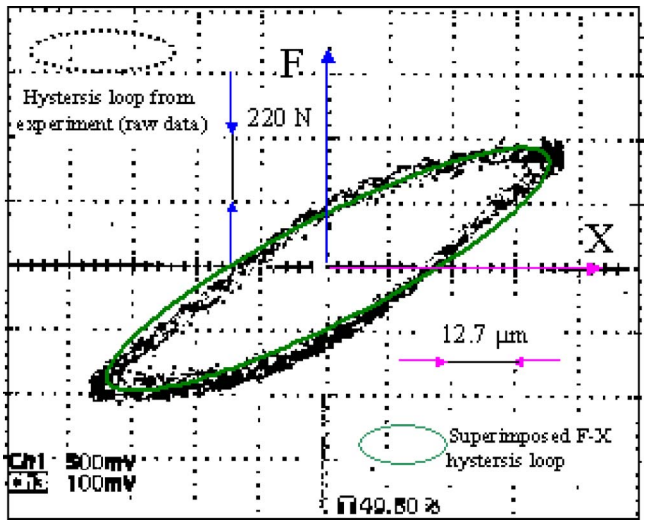

Fig. 16 Energy dissipation in a cycle

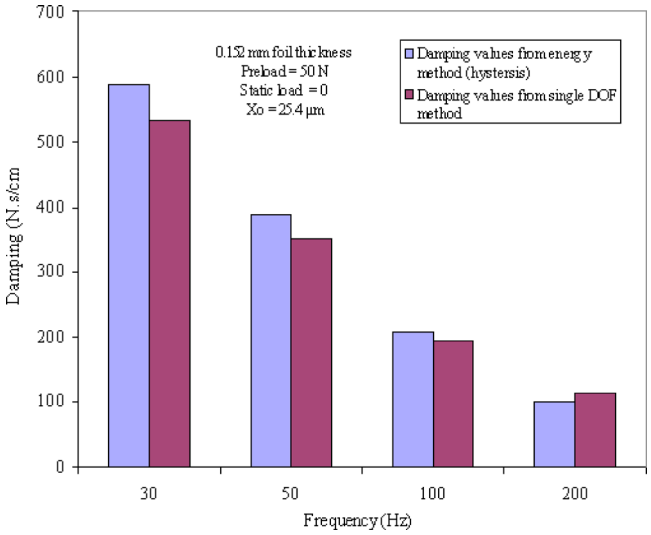

Fig. 17 Comparison of damping values resulting from two different methods

all tested conditions; a semiexponential decay could be seen. The damping values calculated from two methods, single degree of freedom and energy methods, were compared and a good agreement between the two methods was obtained.

Dynamic stiffness varied slightly with increases in frequency. Statically, it was shown that with variation in the design, dramatic changes in stiffness are possible, including expanding the range over which stiffness remains constant. Achieving this constant stiffness and high levels of damping given the nonlinearity of the compliant bump characteristics shows the viability of this concept for wide ranging applications.

Finally, the results presented show clearly that the bump foil damper is capable of providing stiffness and damping levels consistent with oil squeeze film dampers. Additional investigations into the effects of preload/materials are warranted.

Acknowledgment

The Allison Advanced Development Company and the U.S. Air Force Aero-Propulsion/Power Directorate Laboratory, and WPAFB provided support for this work. The authors would like to thank Dr. Wright and Dr. Nelson Forster for their support and sustained interest in tribology. The assistance of Mes John Lawler and Michael J. Tomaszewski in testing and hardware design is greatly appreciated.

Nomenclature

C = damping
E = energy, work
e = eccentricity
f = frequency
F = force
K = stiffness
m = mass
t = time
X, x = displacement, coordinate axis
Xo = amplitude of motion
y = coordinate axis
w = load, width
$:$ = coefficient of friction
T = angular velocity ($2\ \pi f$)
$\ni$ = loss factor

References

[1] Salehi, M., Heshmat, H., and Walton, J., 2003, "The Frictional Damping Characterization of Compliant Bump Foils," ASME J. Tribol., **125**(4), pp. 804–813.
[2] Ku, C. P. R., and Heshmat, H., 1992, "Compliant Foil Bearing Structural Stiffness Analysis Part I: Theoretical Model Including Strip and Variable Bump Foil Geometry," ASME J. Tribol., **113**(2), pp. 364–369.
[3] Ku, C. P. R., and Heshmat, H., 1994a, "Structural Stiffness and Coulomb Damping in Compliant Foil Journal Bearings: Theoretical Considerations," STLE Tribol. Trans., **37**(3), pp. 525–533.
[4] Ku, C. P. R., and Heshmat, H., 1994b, "Structural Stiffness and Coulomb Damping in Compliant Foil Journal Bearings: Parametric Studies," STLE Tribol. Trans., **37**(1), pp. 255–262.
[5] Godet, M., 1987, "Modeling of Friction and Wear Phenomena," *Tribology Series 15*, Elsevier Science, Amsterdam, pp. 12–35.
[6] Heshmat, H., 1989, "The Effect of Dynamic Loads in Tribometers: Analysis and Experiments," *Sixteenth Leeds and Lyon Symposium on Tribology (Tribology Series 17)*, D. Dowson, C. M. Taylor, M. Godet, and Y. Berthier, eds., Elsevier, Amsterdam, Paper No. XXII, pp. 465–473.
[7] Ferri, A. A., 1995, "Frictional Damping and Isolation Systems," J. Sound Vib., **117**, pp. 196–206.

Onome Scott-Emuakpor

M.-H. Herman Shen[1]
e-mail: shen.1@osu.edu

Department of Mechanical Engineering,
The Ohio State University,
Columbus, OH 43210

Tommy George

Charles J. Cross

Jeffrey Calcaterra

Air Force Research Laboratory,
Wright-Patterson AFB, OH 45433

Development of an Improved High Cycle Fatigue Criterion

An integrated computational-experimental approach for prediction of total fatigue life applied to a uniaxial stress state is developed. The approach consists of the following elements: (1) development of a vibration based fatigue testing procedure to achieve low cost bending fatigue experiments and (2) development of a life prediction and estimation implementation scheme for calculating effective fatigue cycles. A series of fully reversed bending fatigue tests were carried out using a vibration-based testing procedure to investigate the effects of bending stress on fatigue limit. The results indicate that the fatigue limit for 6061-T6 aluminum is approximately 20% higher than the respective limit in fully reversed tension-compression (axial). To validate the experimental observations and further evaluate the possibility of prediction of fatigue life, an improved high cycle fatigue criterion has been developed, which allows one to systematically determine the fatigue life based on the amount of energy loss per fatigue cycle. A comparison between the prediction and the experimental results was conducted and shows that the criterion is capable of providing accurate fatigue life prediction. [DOI: 10.1115/1.2360599]

1 Introduction

Structural components subjected to high frequency vibrations, such as those used in rotating parts of gas turbine engines, are usually required to be designed using a lifetime failure-free criterion for a very large number of cycles, or an endurance limit. Design tools, such as the Goodman diagram and the modified Goodman diagram are often used, which are usually constructed using uniaxial fatigue data. The Goodman diagram is a plot of alternating stress (half of the cyclic stress range) versus mean stress and represents the fatigue strength of a given material for a given number of cycles. However, the uniaxial data might be insufficient for assessing high cycle fatigue limit stresses in components that are subjected to multiaxial stresses over a wide range of loading frequencies. In turbine blades, for example, fatigue failure often occurs under high order bending or combined bending and twist modes that produce short wavelength stress states at very high frequencies. Unfortunately, the capability of conducting biaxial fatigue tests, especially under bending, is adversely affected by the high cost of test method development and low frequency limitations of existing equipment. In turn, the development of a basic understanding of the effects of frequency, biaxial stress state, and stress gradient in bending on the high cycle fatigue strength of complex geometries has been hampered. Hence, current U.S. Air Force high cycle fatigue (HCF) research efforts to develop new design methodologies for HCF under realistic stress states have been significantly hindered due to lack of ability to obtain sufficient fatigue data for a meaningful fatigue strength assessment of actual components.

Furthermore, uniaxial fatigue tests on conventional test machines require long time periods to achieve a large number of cycles approaching the endurance limit. Even a servohydraulic test machine operating at 40 Hz requires approximately 6.9 h to accumulate 10^6 cycles for a point on an *S-N* curve. Additionally, for each value of mean stress or stress ratio, several data points are needed in order to interpolate the value of stress at the desired life (10^6 in this example) to get a point on the Goodman diagram. Therefore, significant amounts of time are required to characterize the uniaxial fatigue properties of a material.

To address these concerns, a novel vibration-based testing concept [1] was developed by the authors for assessing fatigue strength for materials under representative stress states found in real engine hardware. The idea is to subject a base-excited plate specimen at high frequency resonant modes to achieve high cycle fatigue. The performance of the vibration-based fatigue testing technique for achieving various stress ratios was demonstrated in [2] with experimental results from 6061-T6 aluminum plate specimens. These results had been used to construct a significant portion of the important Goodman diagram for fatigue design. Furthermore, the authors [3] generalized the technique to accommodate the failures subjected to biaxial stress states, and applied it to a variety of materials. A geometrical design procedure that incorporates a finite element analysis process with a mathematical programming search algorithm was used to characterize the shape of the specimens for ensuring the required biaxial stress patterns.

The authors' previous studies [1–3] clearly showed that it is possible: (1) to accomplish fatigue testing in only a few hours compared to the tens of hours required of typical fatigue test machines, (2) to generate both uniaxial and biaxial fatigue data through proper specimen topological design, and (3) to identify the presence of fatigue crack in the test specimen while it is still in the initiation stage. Further development and modifications to this technique is in progress which will allow generation of multiaxial fatigue data at various stress ratios as well as estimation/prediction of fatigue life via energy approaches.

In this study, the objective is to explore the feasibility of using the vibration-based fatigue testing procedure for accomplishing fatigue life assessment under tension-compression (axial) and bending. To validate the experimental observations and further evaluate the possibility of prediction of fatigue life, an improved high cycle fatigue criterion is proposed, which allows one to systematically determine the fatigue life based on the amount of energy loss per fatigue cycle. A comparison between the prediction and the experimental results was conducted and shows that the criterion is capable of providing accurate fatigue life prediction.

2 Experiemental Procedures

To assess the fatigue life or fatigue limit of materials, a stress versus cycle plot, so-called *S-N* curve, was created to display the

[1]To whom correspondence should be addressed.

Contributed by the International Gas Turbine Institute (IGTI) of ASME for publication in the JOURNAL OF ENGINEERING FOR GAS TURBINES AND POWER. Paper presented at the International Gas Turbine and Aeroengine Congress and Exhibition, Vienna, Austria, June 13–17, 2004, Paper No. 2004-GT-53851. Manuscript received October 1, 2003; final manuscript received March 1, 2004. IGTI Review Chair: A. J. Strazisar.

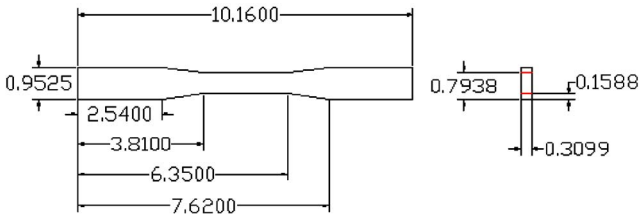

Fig. 1 Dimensions (cm) of the ASTM fatigue dog-bone specimen

relationship between the number of cycles to failure and the alternating fatigue stress for aluminum 6061-T6 specimens under axial (tension-compression) and bending stress states.

2.1 *S-N* Curve Construction: Tension/Compression. Axial (tension-compression) loading data was acquired first from the ASTM standard fatigue dog-bone (coupon) specimen in Fig. 1. To assure accuracy in the cross-sectional area, the specimen was cut from a 3.1 mm sheet of aluminum using a water jet procedure. This procedure provided a maximum variance of 2% for a specimen with a 19.7 mm^2 cross-sectional area.

All the tests were conducted at the room temperature using a MTS Systems Corporation servo hydraulic load frame [4]. The dog-bone specimen is held in place with hydraulic grips (Fig. 2) and a cyclic axial force, at a frequency of about 40 Hz, is applied. The fatigue limit strength in the tests is determined as the stress for the number of total cycles at which complete failure occurs. Thirty dog-bone tests were completed and the data is acquired using a TestStar II control system [4].

The results of the tension-compression fatigue tests were summarized as a plot of stress versus number of cycles that can be seen on the *S-N* plot in Fig. 3. In order to reduce the effect due to the machine instability at different frequencies, all the tests were conducted at 40 Hz.

2.2 *S-N* Curve Construction: Bending. Bending fatigue data was acquired from the uniaxial fatigue specimen in Fig. 4 [1]. The specimen is 114.3×165.1 mm with a clamp area of 50.8×165.1 mm and was sheared from the same 3.1 mm thick sheet of aluminum 6061-T6 as the dog-bone specimens.

Bending tests were conducted with an Unholtz Dickie 6000 lb electrodynamic shaker (Fig. 5) located in the Turbine Engine Fatigue Facility (TEFF) of the Air Force Research Laboratory (AFRL) in the Propulsion Directorate at Wright-Patterson Air Force Base. As shown in Fig. 5, the test specimen is mounted cantilevered to the shaker head. A forced vibration is then conducted on the specimen at two-stripe mode (frequency range: 1200–1600 Hz). The Vibratory displacement of the plate during two-stripe mode, analyzed with the finite element software ABAQUS, is shown in Fig. 6 [11]. The test specimen is sufficient for acquiring bending data due to the behavior at the free edge being similar to a free-free bending analysis.

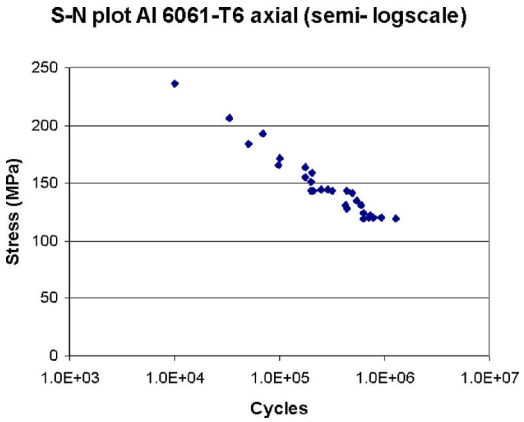

Fig. 3 *S-N* data tension/compression

The measurement instruments used consist of accelerometers, a laser-vibrometer for measuring the velocity or displacement of a point on the specimen, and strain gages. The finite element (FEM) study, from Fig. 6, was conducted before the tests to locate the instrumentation on the plate specimens and to determine the frequency at which the two-stripe mode occurred [1].

Due to strain gauges experiencing internal failure at cycles fewer than the total at the anticipated fatigue limit, the fatigue tests were conducted using the laser vibrometer for measurement. This provides the only nonintrusive technique of the available instrumentation as well as an accelerometer for monitoring the shaker input force. However, the velocity signal from the laser

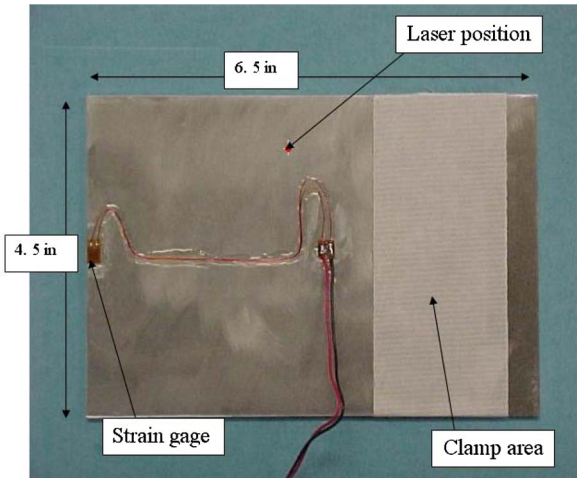

Fig. 4 Bending fatigue specimen

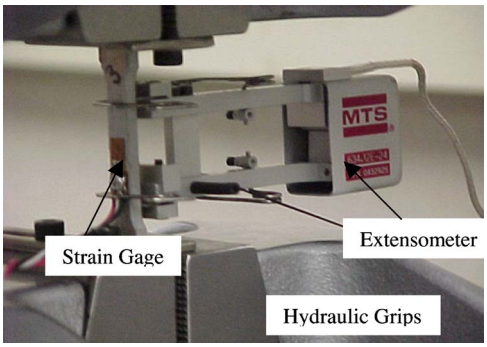

Fig. 2 MTS clamping and measurement devices

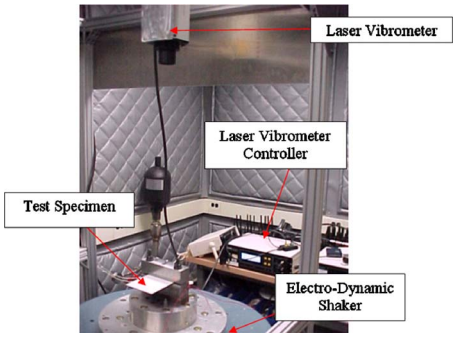

Fig. 5 Vibration-based fatigue experiment setup

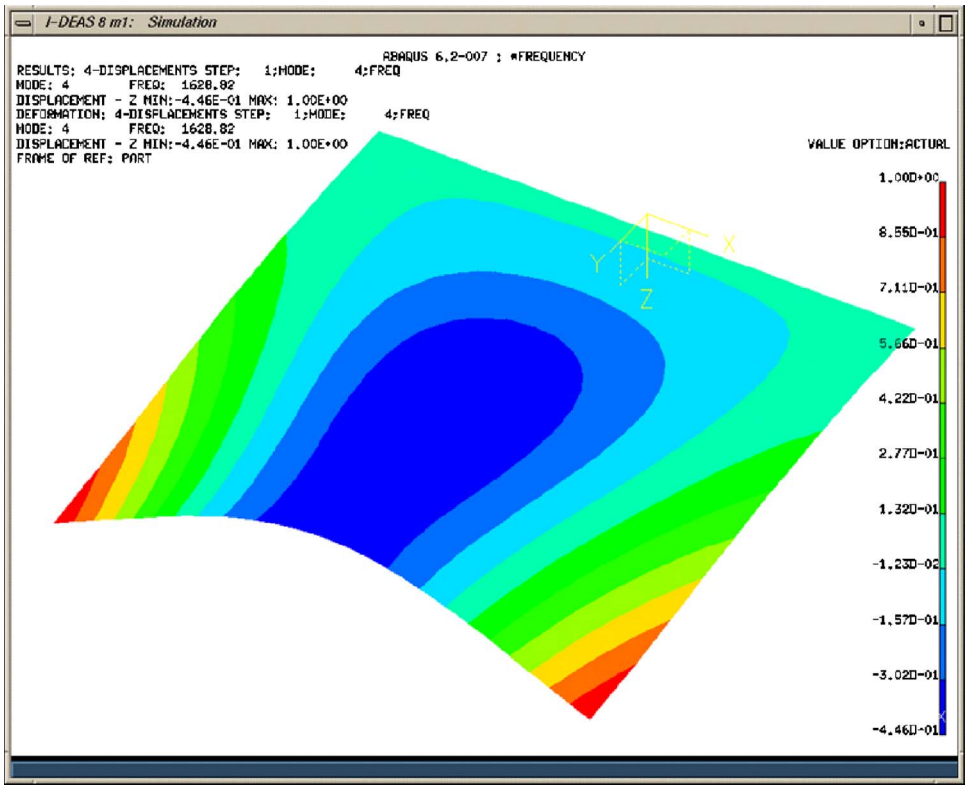

Fig. 6 FEM two-stripe mode shape of the plate specimen

must first be calibrated to the corresponding strain in the fatigue region of the plate. This was achieved by running a calibration test with the plate specimen instrumented with a strain gage placed in the expected maximum strain region or the fatigue region, the midpoint at the free edge of the plate.

During the calibration process, data were taken from both the strain gage and from the laser vibrometer while the specimen was in resonance at various shaker power settings, or in other words, for various strain levels in the specimen which allows for the construction of a strain-laser calibration curve. Once a relationship between the strain in the fatigue region and the velocity/displacement at the laser position is established, which is approximately linear as shown in Fig. 7, a fatigue test may be conducted. It is important to note that the linear comparison between strain and velocity is not the same for all tests. Minimal changes in the natural frequency of a test specimen, which are caused by slight changes in the clamping fixture and precision of the specimen's geometry, can alter the slope between velocity and strain data. Therefore, the calibration must be done for each bending fatigue test.

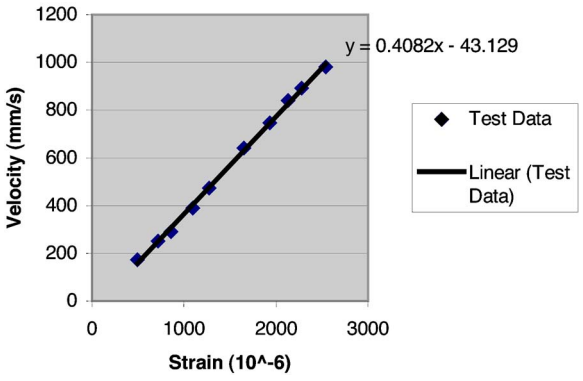

Fig. 7 Laser-strain gage correlation

All the bending fatigue tests were conducted in accordance with the step-test method developed by Maxwell and Nicholas [5]. This step-test technique uses a single specimen to generate a fatigue limit from multiple incremental loading steps. Each step corresponds to the number of cycles considered to be necessary to reach the fatigue limit. In the bending fatigue tests, the fatigue limit was assigned a life in the range between 10^4 and 2×10^6 cycles. The step-test method has been utilized in our previous studies [1,2] and shown to produce fatigue limit stresses that are consistent with those obtained using conventional *S-N* test results [3]. The fatigue limit stress is determined using the following equation:

$$\sigma_A = \sigma_{\text{pr}} + \frac{N_f}{N_t}(\sigma_f - \sigma_{\text{pr}}) \tag{1}$$

where σ_A is the (max) alternating stress, σ_{pr} is the (max) stress level of the step prior to failure, N_f is the number of cycles to failure in the final step, σ_f is the (max) stress level of the final (failure) step, and N_t is the number of cycles of each complete step. The test is begun at a stress level below that of the anticipated fatigue crack initiation stress at the number of cycles of interest for the particular test specimen material. After completing the specified number of cycles in a step without failure, the stress level is increased incrementally for the next step. The procedure is repeated until failure occurs. Then, using the above equation, the fatigue limit stress of the material at the desired number of cycles can be determined.

The fatigue limit strength in typical tension/compression tests, presented in Fig. 3, was determined as the stress at which complete failure occurs at the required number of cycles. Total life,

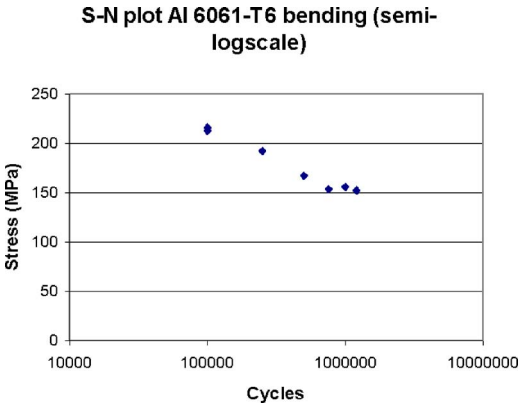

Fig. 8 *S-N* data: bending

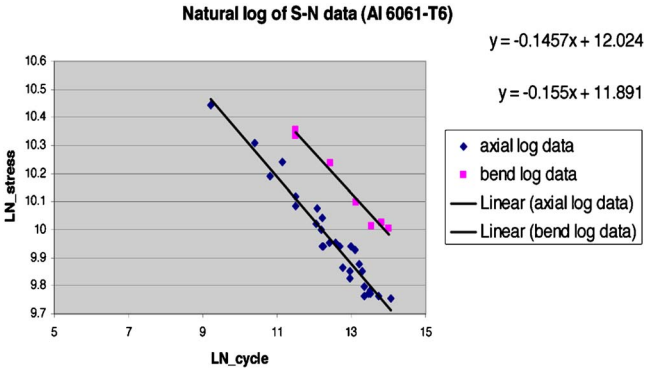

Fig. 9 *S-N* curve: tension/compression, in linear-log scale

where the fatigue crack propagates through the specimen and failure occurs, was not distinguished from crack nucleation or crack initiation life. Computations have shown that the fatigue crack propagation life is only a small fraction of total life when testing at stress levels near the HCF limit defined at 10^6 cycles. In the case of vibration-based bending fatigue testing under resonance conditions, however, there does not exist a definitive phenomenon such as abrupt failure. Therefore, in all bending tests the fatigue limit is defined at the instance corresponding to a sudden change in the dynamic response of the plate associated with the initial stage of fatigue crack development. The development of a crack in the specimen changes its stiffness and hence its resonant frequency. The initiation or development of the fatigue crack in the plate specimens was observed by the onset of a rapid decrease in the measured velocity for a given shaker driving frequency and amplitude and it is at this point that the fatigue limit stress was determined. This technique was developed and has been verified in our previous studies [1–3].

3 Results and Discussion

Seven plates have been fatigued at the two-stripe mode with natural frequency around 1600 Hz. Recall that, typical tension-compression fatigue tests on a MTS tensile test machine operate at 40 Hz, requiring approximately 70 h to accumulate 10^7 cycles for each step during the step-test. Therefore, significant amounts of time can be saved to characterize the bending fatigue properties via the vibration-based fatigue testing procedure [1,2].

Bending fatigue data from all seven tests are given in Fig. 8 in the form of a linear-logarithmic *S-N* curve. The range of number of cycles to failure is 10^5–1.2×10^6. The data in Fig. 8 show a very small amount of scatter and expect a clear comparison with those tension-compression (axial) fatigue in Fig. 3 via a linear regression analysis.

The linear regression analysis was conducted to determine the slope of the lines from which values of A, B, and m were obtained (see Table 1) for use in Eq. (2).

$$\sigma = A(N+B)^{-m} + \sigma_e \tag{2}$$

In order to accommodate the cyclic range of the axial fatigue data, no bending test has been conducted for longer than 1.2 million cycles. Not having data at higher cycles prevents an assumption to be made for the value of the endurance limit σ_e.

Table 1 Parameter data for linear regressive analysis

Procedure	A (MPa)	B (Cycles)	m
Axial	1029.3	1890	0.155
Bending	1132.5	14189	0.1457

Therefore, this value has been set to zero to assure that the experimental curve is accurate with respect to the data collected. Values of A, B, and m have been calculated by using the axial and bending fatigue data in Figs. 3 and 8, respectively. These values were summarized in Table 1 and are in good agreement with the fatigue data when plotted (see Fig. 9) in accordance with Eq. (2).

It is interesting to observe that, the results in Fig. 9 show that the bending fatigue limit of 6061-T6 aluminum is significantly higher than the respective limit in fully reversed tension-compression (axial). To substantiate the effect of bending on fatigue limits, more evidence was obtained through comparison of the *S-N* curves presented in Fig. 10. This comparison clearly indicates that the fatigue limit for 6061-T6 aluminum in fully reversed bending is approximately 20% higher than the respective limit in fully reversed tension-compression.

It is important to note that, the 20% difference between the fatigue limits is observed for all the fatigue tests that correspond to various number of failure cycles. The higher bending fatigue limit is therefore exclusively due to the gradient effect of the normal stress. In a tension/compression specimen, as shown in Fig. 11, the distribution of the normal stress along the thickness of the specimen is constant, therefore the stress gradient is zero. In the case of bending, the normal stress decreases from the surface to the neutral axis thus creating a stress gradient. Based on this observation, intuitively, it is natural to assume that at the same number of cycles, the alternating fatigue stress level of a bending specimen must be higher than that of a tension/compression specimen to compensate for not having the maximum normal stress constant through the thickness. On the other hand, under the same stress level, the number of cycles to failure for a bending specimen is expected to be higher.

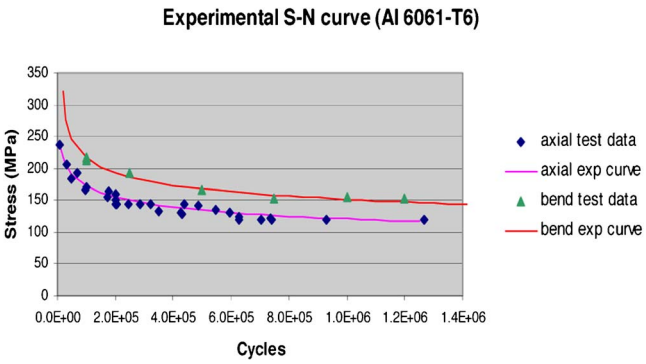

Fig. 10 *S-N* curves: tension/compression, bending

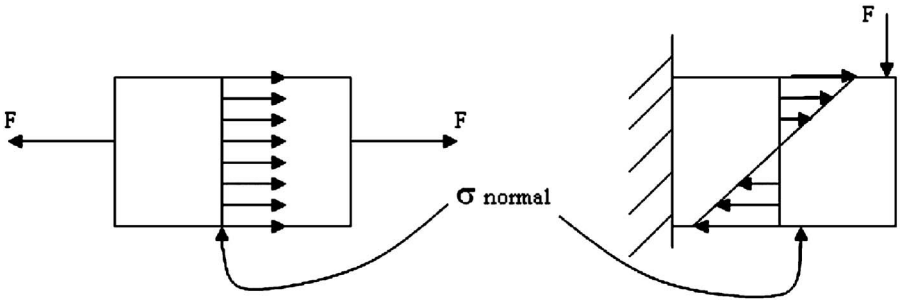

Fig. 11 Stress distributions of axial and bending

4 An Energy Based High Cycle Fatigue Criterion

It is believed that the gradient influence to the different fatigue limits could be explained on the basis of a framework integrating energy theories and probabilistic approaches. This problem is quite significant and complex which will be dealt with in our future studies. In this work, in order to lay down a solid theoretical and experimental foundation for the follow-up research, an improved high cycle fatigue criterion has been developed. The criterion allows one to systematically determine the fatigue life based on the amount of energy loss per fatigue cycle.

4.1 Analytical Stress-Strain Representation. Previously stated in the Introduction, it has been suggested that the strain energy required to fracture a material monotonically is the same as the strain energy accumulated during a cyclic fatigue procedure [6,7]. Even though the strain energy dissipation in a material under the respective loading processes can be affected by factors other than the stress level, stress is still observed as the dominating factor. Based on this observation, the representation of strain in both the monotonic and cyclic procedures is based, solely, with respect to the corresponding stress level [8–10]. This representation is shown as Eq. (3), where σ is the corresponding stress level, E is Young's modulus σ_o is a defined constant, and ε_o is a curve fit constant [12]. This equation is obviously an ideal state, which will not be assumed when dealing with materials experiencing a severe case of the endurance limit phenomenon. Also, this representation will not be assumed during monotonic analysis after the necking phenomenon. Despite the behavior of these occurrences, Eq. (3) will be the benchmark representation for further understanding of these materials with more complex *S-N* behavior,

$$\varepsilon = \frac{\sigma}{E} + \varepsilon_o \sinh\left(\frac{\sigma}{\sigma_o}\right) \tag{3}$$

Results from both the low cycle and the monotonic fracture procedures of aluminum 6061-T6 can be seen on Figs. 12 and 13, respectively. The data in each figure are plotted as engineering stress and strain. The use of engineering stress-strain representation for cyclic and monotonic results is not satisfactory. Though it can be argued that the data in Fig. 12 are acceptable for curve fitting with Eq. (3) (based on the limited plastic deformation during the process), it also is not acceptable for curve fitting purposes.

In order to develop an accurate analytical representation of monotonic stress versus strain, Fig. 13 had to be converted to true stress and strain values. The conversion of engineering data to true data was conducted with basic conservation of volume laws described in Ref. [12]. The results of the conversion of the monotonic analysis to true stress-strain data are displayed in Fig. 14. This figure shows a vacancy in stress-strain results between the necking and fracture stress. Though the stress-strain result on this figure from zero-load to necking can be accurately represented by Eq. (3), the true stress-strain relationship between necking and fracture is assumed to be linear due to the absence of experimental data. Therefore, Eq. (4) is used to represent the linear stress-strain relationship in the region between necking and fracture, where β_1 is the slope of the function and β_o is the intercept constant,

$$\sigma = \beta_1 \varepsilon + \beta_o \tag{4}$$

For the monotonic case, there are two unknown parameters from Eq. (3): ε_o and σ_o. The parameter σ_o is defined based on the following equation [7]:

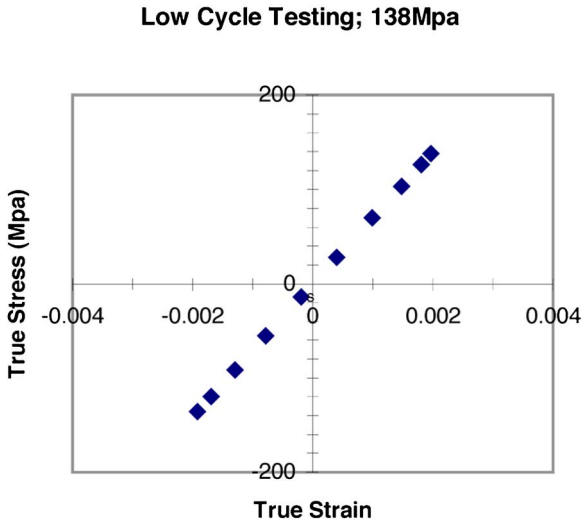

Fig. 12 Cyclic stress-strain experimental data for aluminum 6061-T6

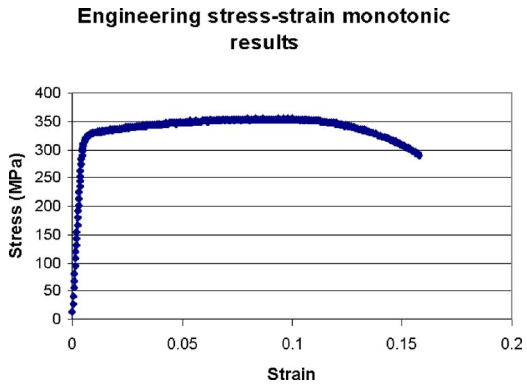

Fig. 13 Monotonic stress-strain experimental data for aluminum 6061-T6

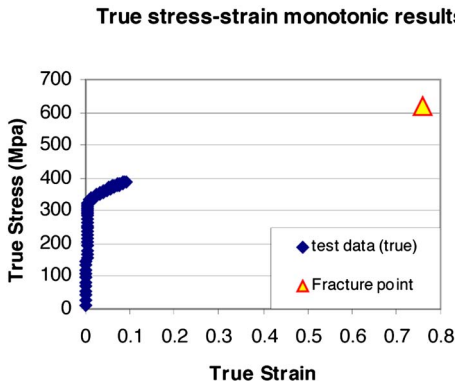

Fig. 14 Monotonic true stress-strain experimental data for aluminum 6061-T6

$$\sigma_o = \frac{\sigma_n - \sigma_y}{\ln(\varepsilon_n/0.002)} \tag{5}$$

where σ_n is the necking stress, ε_n is the necking strain, and σ_y is the yielding stress. As for ε_o, this is a curve fit parameter that is adjusted until the plot of Eq. (3) is sufficiently fit to the experimental results. The fit is deemed sufficient when the plot of Eq. (3) visibly fits over the test data, as well as when the strain difference at the necking point is less than 1%. After sufficiently fitting Eq. (3) over the experimental results and determining the linear necking relation between two points (necking and fracture), the following constants in Table 2 were determined for Eqs. (3) and (4), thus fully developing an analytical representation of the true stress-strain relation for the monotonic fracture (Fig. 15).

Based on the extremely small plastic deformation during cyclic loading, visual validation of the strain equation to experimental

Table 2 Curve fit results for monotonic stress-strain approximation

E (MPa)=	6.89E+04
ε_o=	3.89E−11
ε_n=	0.092106
σ_o (MPa)=	17
σ_y (MPa)=	323
σ_n (MPa)=	389
β_1 (MPa)=	347
β_o (MPa)=	357

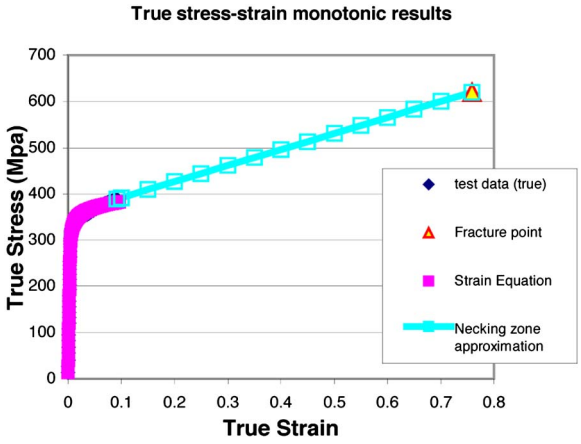

Fig. 15 Monotonic true stress-strain test data and strain equation approximation for aluminum 6061-T6

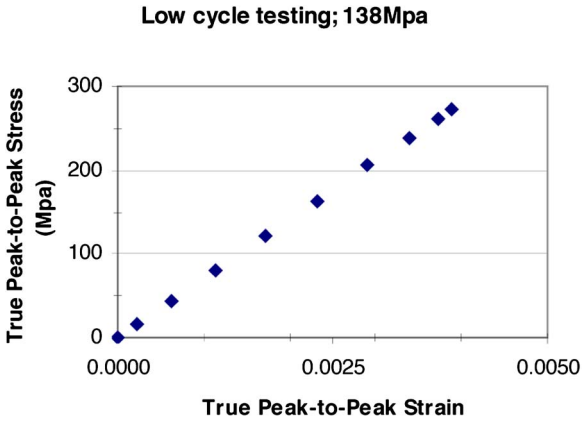

Fig. 16 Cyclic peak-to-peak stress-strain experimental data for aluminum 6061-T6

results does not provide a thorough method for curve fitting. Due to this minimal plastic deformation, the curve fit of the strain equation for cyclic loading is determined by a statistical procedure. Before this statistical procedure takes place, the experimental cyclic results are put into generalized axes. In the generalized coordinate system, minimum stress and strain values are viewed as the origin. Therefore, the experimental data are going from zero values to peak-to-peak values, as displayed in Fig. 16 and Table 3. The advantage of the axes modification is that it simplifies the cyclic stress-strain loop approximation by requiring only two identical equations for construction, as opposed to the four unique equations required for the conventional axes.

To prevent future complications when determining the fatigue life calculation method, the strain equation variables used in Eq. (3) for the monotonic strain approximation are changed for the cyclic analysis. Though they provide the same purpose as the monotonic strain parameter, the parameters changed for the cyclic equation (Eq. (6)) go as follows: σ_{pp} is twice the alternating stress value (σ), σ_o is changed to σ_c, and ε_o is written as $1/C$. However, unlike the monotonic analysis, the constant inside the hyperbolic sine (σ_c) is adjusted along with the outside coefficient, which in this case is $1/C$,

$$\varepsilon = \frac{\sigma_{PP}}{E} + \frac{1}{C}\sinh\left(\frac{\sigma_{PP}}{\sigma_c}\right) \tag{6}$$

For comparison between the generalized data in Table 2 and Eq. (6), a MATLAB program was generated to find the best fit between the two. The core of the optimization tool used in the MATLAB program is the observance of the standard deviation of the percent difference between Eq. (3) and the generalized data from Table 3. The optimization program is essentially a two-loop code that operates as follows: In loop one, the C value that provides the mini-

Table 3 Generalized (peak-to-peak) stress-strain cyclic data from Fig. 16

Pos σ (MPa)	Pos ε
0.00	0
16.2	0.0002228
43.8	0.000622
80.0	0.0011345
121.6	0.0017181
163.7	0.0023181
205.1	0.0029094
239.1	0.0033955
262.1	0.0037223
273.3	0.0038857

Table 4 Computational results for cyclic stress-strain curve fit

σ (MPa)	C	σ_c (MPa)	Standard deviation
137.8	3.33E+07	37.906	1.3071
206.8	2.00E+07	55.136	0.9978
234.3	5.00E+07	55.136	1.0554

mum standard deviation at a specific σ_c value is determined. In loop two, out of an array of σ_c values with corresponding optimal C values, the σ_c value with the minimum standard deviation is determined. Based on this optimization code, curve fit results were acquired from three experimental cyclic testing results at three different alternating stress levels. These results are displayed in Table 4. The important result category to observe in Table 4 is the minimum standard deviation from the three low cycle tests conducted. Viewing this category, it clearly shows that the test conducted at 206.8 MPa provides the smallest standard deviation between the three results. The importance of this information will be addressed during the fatigue life calculation analysis discussed in the following subsection.

4.2 Fatigue Life Calculation Analysis. The prediction of fatigue life via energy analysis comes from an approach, as suggested earlier, which states that the strain energy required to fracture a material monotonically is the same as the strain energy accumulated during a cyclic fatigue procedure [3,7]. Based on this suggestion, the following equation holds true:

$$W_f = NW_c \tag{7}$$

where W_f is the total strain energy from a monotonic fracture, W_c is the strain energy of one cycle from a fatigue process, and N is the number of cycles to failure in the fatigue process corresponding to the test that developed W_c. In this equation, W_c and W_f can be viewed as strain energy density, due to the uniform stress distribution of axially loaded specimens. The strain energy density is determined for monotonic and cyclic analysis as follows: the area underneath the approximated curve of Fig. 15, and the area within the loop developed by Eq. (6), respectively. From the calculation of the strain energy density for monotonic and cyclic analysis and the use of Eq. (7), a sufficient calculation scheme for predicting fatigue life was developed and is represented by Eq. (8),

$$N = C\frac{\sigma_n\left(\varepsilon_n - \frac{\sigma_n}{2E}\right) + \varepsilon_o\sigma_o\left[\cosh\left(\frac{\sigma_n}{\sigma_o}\right) - 1\right] + \frac{\beta_1}{2}(\varepsilon_f^2 - \varepsilon_n^2) + \beta_o(\varepsilon_f - \varepsilon_n)}{2\sigma_c\left\{\frac{\sigma}{\sigma_c}\sinh\left(\frac{2\sigma}{\sigma_c}\right) - \left[\cosh\left(\frac{2\sigma}{\sigma_c}\right) - 1\right]\right\}} \tag{8}$$

Using Eq. (8) and the values from Tables 2 and 4, the following fatigue life values were estimated for the three corresponding alternating stress levels in Table 4. These estimations were compared with experimental data in Fig. 17. From the comparison, the results show that the cyclic experimental analysis at 30 ksi provide the best fatigue life estimation. This optimal fatigue life estimation shows correlation to the minimum standard deviation acquired from the optimization MATLAB code, which is displayed in Table 4. Therefore based on the strain equation values in Table 4 and the optimal estimation results in Fig. 17, the C and σ_c variables for 30 ksi were used to construct an entire accelerated S-N curve. This S-N curve, which is predicted based on C and σ_c from the 30 ksi analysis, is compared with experimental results in Fig. 18. This comparison shows highly sufficient agreement and validates the use of one cyclic experimental point at a specified loading stress for prediction of S-N behavior over a large fatigue life range.

5 Conclusions

The vibration-based fatigue testing procedure is capable of producing bending fatigue data at greatly reduced savings in both time and cost. This testing procedure can be further extended, through proper specimen topological design [1] and a yielding process [3], to generate fatigue data at various stress ratios, so that assessment of material fatigue properties can be achieved at

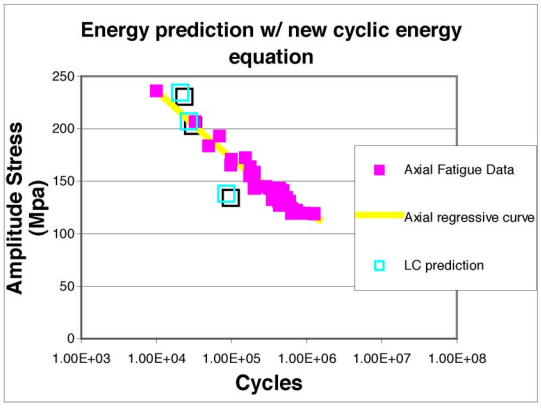

Fig. 17 Tension/compression fatigue comparison

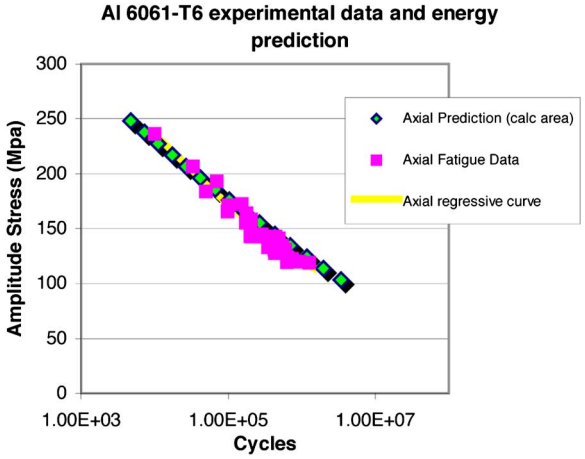

Fig. 18 Tension/compression fatigue comparison

greatly reduced savings in both time and cost [2]. The resulting fatigue data from 6061-T6 aluminum under fully reversed bending and axial stresses have been used to construct *S-N* curves for comparison. A significantly higher fatigue limit in bending was observed. Finally, an improved energy-based criterion was developed for fatigue life prediction. The comparison between the life prediction and the experimental results clearly indicates that the criterion provides reasonable life estimations.

Acknowledgment

The Air Force Research Labs, specifically the Materials Lab and the TEFF Lab, and Universal Technology Corporation for their financial support, facility and equipment access, and encouragement of this research.

References

[1] George, T., Seidt, J., Shen, M.-H. H., Cross, C., and Nicholas, T., 2004, "Development of A Novel Vibration-Based Fatigue Testing Methodology," Int. J. Fatigue, **26**(5), pp. 477–486.

[2] George, T., Shen, M.-H. H., Cross, C., and Nicholas, T., 2006, "A New Multiaxial Fatigue Testing Method for Variable-Amplitude Loading and Stress Ratio," ASME J. Eng. Gas Turbines Power, **128**, pp. 857–864.

[3] George, T., Shen, M.-H. H., Scott-Emuakpor, O., Nicholas, T., Cross, C., and Calcaterra, J., 2005 "Goodman Diagram via Vibration-Based Fatigue Testing," J. Eng. Mater. Technol., **127**, pp. 58–64.

[4] MTS Systems website, http://www.mts.com/menusystem

[5] Maxwell, D. C., and Nicholas, T., 1998, "A Rapid Method for Generation of a Haigh Diagram for High Cycle Fatigue," Fatigue and Fracture Mechanics: 29th *ASTM STP* 1321.

[6] Feltner, C. F., and Morrow, J. D., 1961, "Microplastic Strain Hysteresis Energy as A Criterion for Fatigue Fracture," J. Basic Eng., **83**, pp. 15–22.

[7] Stowell, E., 1966, "A Study of the Energy Criterion for Fatigue," Nucl. Eng. Des., **3**, pp. 32–40.

[8] Skelton, R., 1991, "Energy Criterion for High Temperature Low Cycle Fatigue Failure," Mater. Sci. Technol., **7**, pp. 427–439.

[9] Skelton, R., 1993, "Cyclic Hardening, Softening and Crack Growth During High Temperature Fatigue," Mater. Sci. Technol., **9**, pp. 1001–1008.

[10] Martin, D. E., 1961, "An Energy Criterion for Low-Cycle Fatigue," J. Basic Eng., **83**, pp. 565–571.

[11] ABAQUS website, http://www.abaqus.com

[12] Kalpakjian, S., 1995, *Manufacturing Engineering and Technology*, Addison-Wesley, Reading, MA.

Operation of a Mesoscopic Gas Turbine Simulator at Speeds in Excess of 700,000 rpm on Foil Bearings

Mohsen Salehi
e-mail: salehim@asme.org

Hooshang Heshmat

James F. Walton II

Michael Tomaszewski

Mohawk Innovative Technology, Inc.,
Albany, NY 12205

A small mesoscopic gas turbine engine (MGTE) simulator was tested at speeds over 700,000 rpm. The MGTE was operated with specially designed miniature compliant foil journal and thrust air bearings. The operation of the simulator rotor and foil bearing system is a precursor to development of turbine powered micro-aerial vehicles and mesoscopic power generators. The foil bearings use a new fabrication technology in which each bearing is split. This feature permits the use of these bearings in highly advanced engines where single piece ceramic rotors may be required. The simulator weighed 56 g (including the 9 g rotor) and included two non-aerodynamic wheels to simulate the compressor and turbine wheels. Each compliant foil journal bearing had a diameter of 6 mm and was located equidistant from each end of the rotor. Experimental work included operation of the simulator at speeds above 700,000 rpm and at several different orientations including having the spin axis vertical. Results of the rotor bearing system dynamics are presented along with experimentally measured natural frequencies at many operating speeds. Good correlation between measurement and analysis is observed indicating the scalability of the analysis tools and hardware used. The rotor was very stable and well controlled throughout all testing conducted. Based on this successful testing it is expected that the goal of operating the rotor at speeds exceeding 1 million rpm will be achieved. [DOI: 10.1115/1.2360600]

Introduction

Mesoscopic sized power generating and propulsion systems are currently attracting attention due to their high output energy efficiency. Mesoscale machines (i.e., "sugar cube to fist sized" and typically weighing 50 g or less) offer a unique opportunity to meet a wide array of power and propulsion needs efficiently, reliably, and inexpensively. Among the power sources using chemical fuels, the gas turbine generator is known to have the highest power to weight ratio [1]. Significant additional commercial applications are also expected in support of miniature fuel cells, diesel engines, and other propulsion and power generating machinery. An analysis of a gas turbine-fuel cell hybrid microgeneration system has shown power efficiency of over 65% in the best possible case [2,3]. Such a hybrid system would be based on a micro-gas turbine (μGT) and a solid oxide fuel cell and is expected to achieve much higher efficiency than a traditional μGT. With progress in manufacturing techniques, it is expected that the cost of these mesoscopic scale machines will be reduced drastically, making the application of these devices more attractive [4]. However, many issues need to be addressed, including compressor, combustor and turbine efficiency, component fabrication, and scaling. In addition to these, the long overlooked rotor-bearing system integration issues are essential to the ultimate operation of such systems. For example, the reduced size of mesoscopic scale machines impacts internal clearances, balancing, manufacturing tolerances, damping, and thermal management. To address the engine system development issues that will make these mesoscopic turbo machines a reality with high performance, reliability, and long term storability, MiTi® has developed and demonstrated the supporting oil-free bearing technologies [5–11].

The importance of oil-free compliant foil bearings to mesoscopic gas turbine engines is evident in their inherently low power loss as compared to rolling element bearings. A series of preliminary cycle analyses, the results of which are shown schematically in Fig. 1, highlight the benefits of using foil bearings. Using the power loss for each bearing (see Fig. 2) as a function of speed, the available mesoscopic engine shaft output power was evaluated. For a given operating speed of 870,000 rpm, the inlet air temperature was varied while holding compressor, combustor, and turbine efficiencies constant. As seen in Fig. 1, even at the lowest inlet temperature of 15°C, which results in the highest available output power, the ball bearing power loss would prevent full speed operation. In this first idealized case, the combined power needed to drive the compressor and overcome the ball bearing power loss exceeds turbine output power by 4 W. Conversely, the foil bearing supported system, with its substantially lower power loss, would make it possible to provide up to 144 W of electrical generating power. The situation only gets worse for the rolling element case as the air inlet temperature increases. The cycle analysis with increased inlet air temperatures also points out the need for system thermal management to limit the heat soak back from the turbine to the compressor during operation.

Due to the close proximity of all components and the limited available pathways to remove heat, it is essential that materials with low thermal conductivity be used and that parasitic heat losses be minimized in these machines. For example, with higher physical temperatures of the compressor itself, additional turbine power is needed to maintain the compression ratio and mass flow rate. The extraction of additional work from the turbine reduces the available shaft output power to drive a generator. Thus, from this simple analysis, it is concluded that the feasibility of developing efficient mesoscopic power and propulsion turbine engines

Contributed by the International Gas Turbine Institute (IGTI) of ASME for publication in the JOURNAL OF ENGINEERING FOR GAS TURBINE AND POWER. Manuscript received October 1, 2003; final manuscript received March 1, 2004. IGTI Review Chair: A. J. Strazisar. Paper presented at the International Gas Turbine and Aeroengine Congress and Exhibition, Vienna, Austria, June 13–17, 2004, Paper Nos. 2004-GT-53509 and 2004-GT-53870.

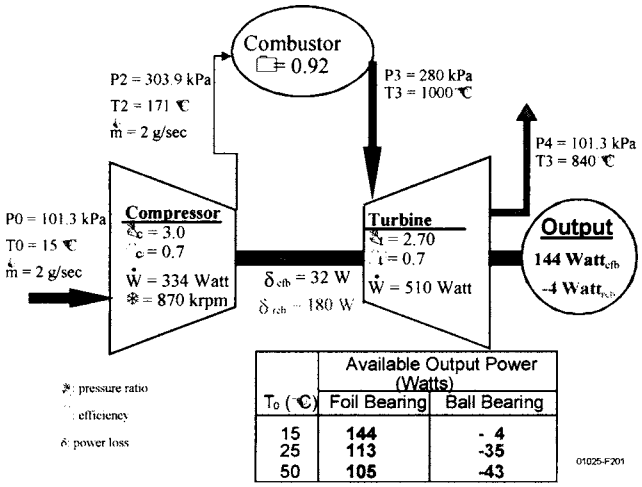

T_0 (°C)	Available Output Power (Watts) Foil Bearing	Ball Bearing
15	144	- 4
25	113	-35
50	105	-43

Fig. 1 Microturbine cycle analysis results

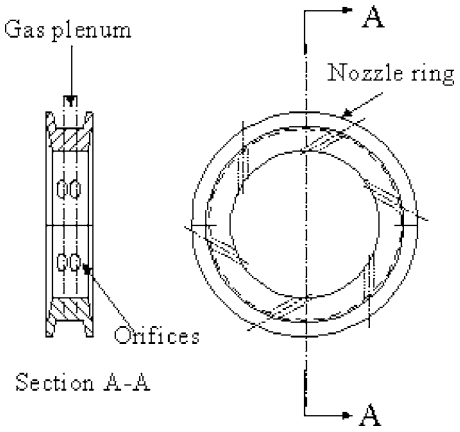

Fig. 4 Schematic of the nozzle box

will require the use of ceramic rotors with their low thermal conductivity and foil bearings with their low power loss.

Having identified the need for ceramic rotors and foil bearings, one must then consider manufacturing related and cost issues, especially for mesoscopic sized rotor and bearing systems. For example, typical clearance ratios (clearance/diameter) in gas bearings range from 0.0001 to 0.001, which for a 6-mm-diam shaft would mean that the bearing diametral clearance would be between 0.6 and 6 μm. Centrifugal growth of a ceramic shaft at 1 million rpm would be approximately 0.4 μm, consuming from 15% to over 60% of the available bearing clearance if a rigid pad gas bearing design were used. With the addition of thermal growth, which for ceramics would be on the order of 1.5 μm for a shaft-to-bearing differential temperature as small as 75°C, bear-

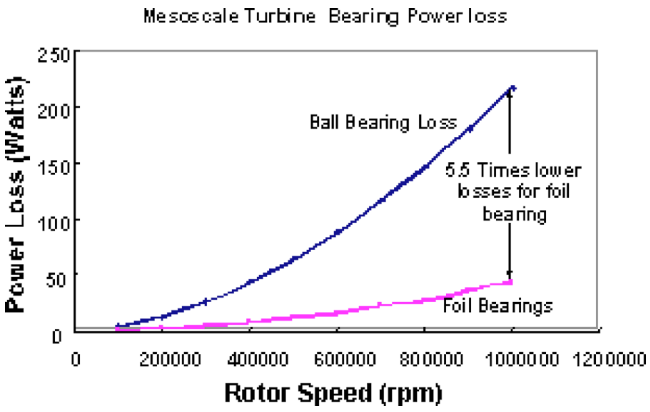

Fig. 2 Comparison of foil and ball bearing power loss versus speed

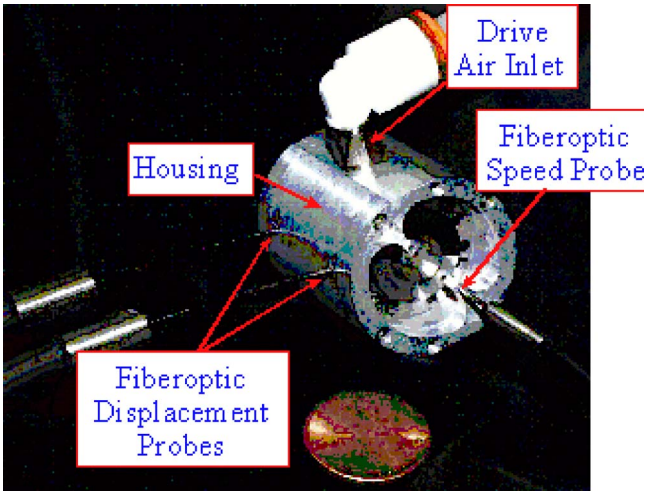

Fig. 3 Assembled and instrumented mesoscopic simulator

Fig. 5 The rotor hardware with mesoscale turbine

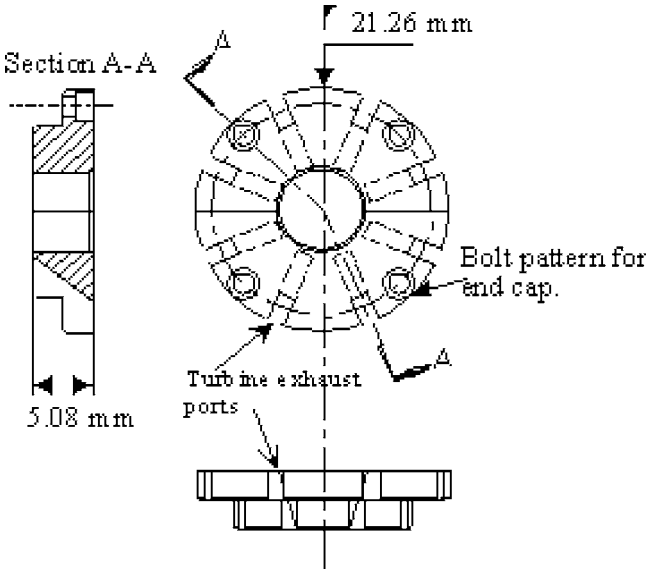

Fig. 6 Schematic of the split bearing shell

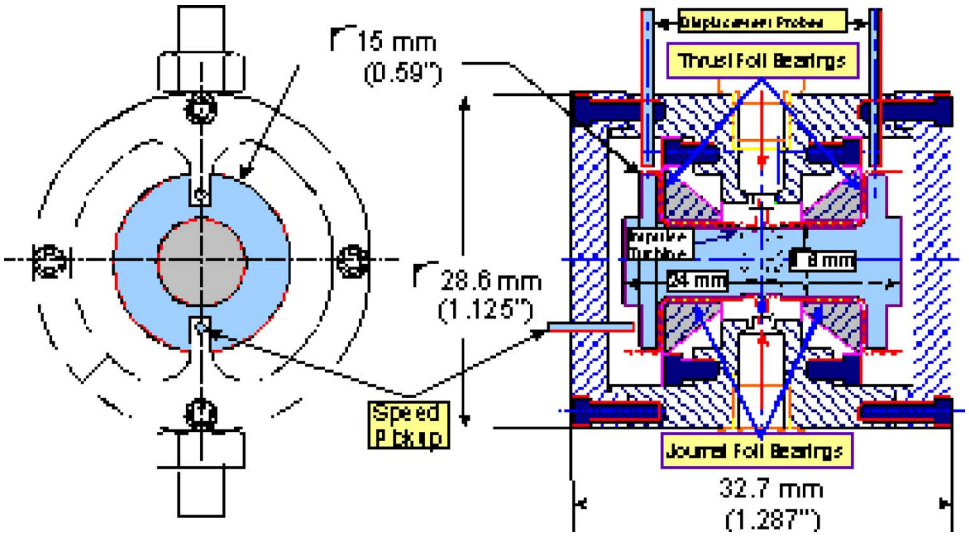

Fig. 7 Cross section of dynamic simulator

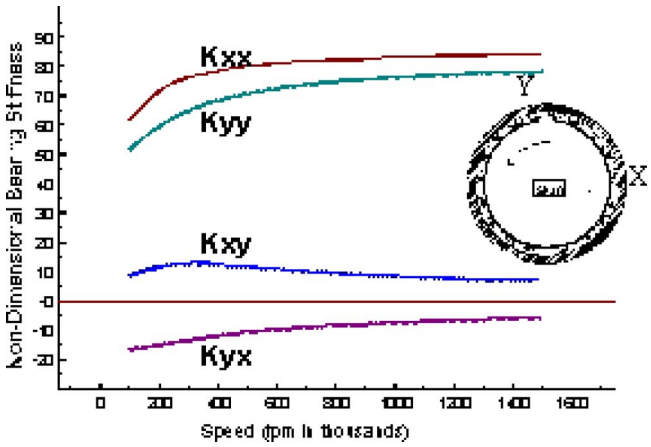

Fig. 8 Stiffness coefficients as a function of speed

ing clearance could be totally eliminated with certain gas bearing designs. The compliant foil bearing design, however, inherently accommodates such growth.

Besides shaft growth and manufacturing processes, balancing of the rotating group must also be considered, both from manufacturing and operating points of view. Balance specifications according to ISO 1940/1 and ANSI S2.19 for gas turbine and turbogenerator class rotors would dictate that the balance limit for a 9 g rotor should be 2.286×10^{-4} g cm when operating a 700,000 rpm and 2.54×10^{-5} g cm when operating at one million rpm. At this balance level, the expected rotor vibration would be approximately 2.8 μm when operating at 700,000 rpm. Given that a bearing clearance of less than 6 μm would be likely, the combined rotor growth of 2 μm and rotor displacement of 2.8 μm would make operation of the rotor system unlikely without a unique bearing system. Further, achieving such stringent balance levels would be nearly impossible with a multi-piece rotor assembly. It is also well known that joining and structural integrity are two issues that must be addressed when using ceramics. Thus, when combined with the need for low cost, the only real logical manufacturing method is to make the rotating group as a single piece. The single piece rotor design choice dictates that split bearings should be used in order for assembly to be possible.

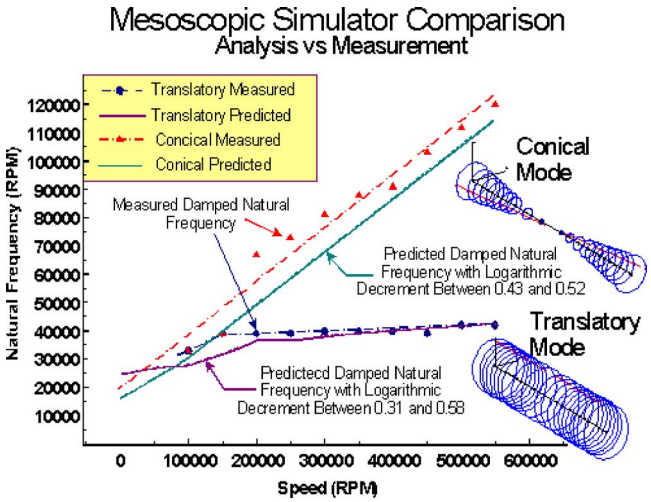

Fig. 9 Whirl speed map showing mode shapes and both predicted and measured natural frequencies as a function of spin speed

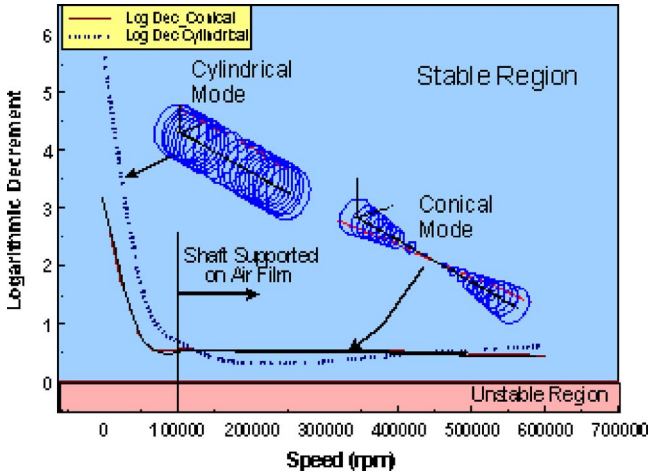

Fig. 10 Stability map—logarithmic decrement versus rotor speed for the two rigid body natural frequencies

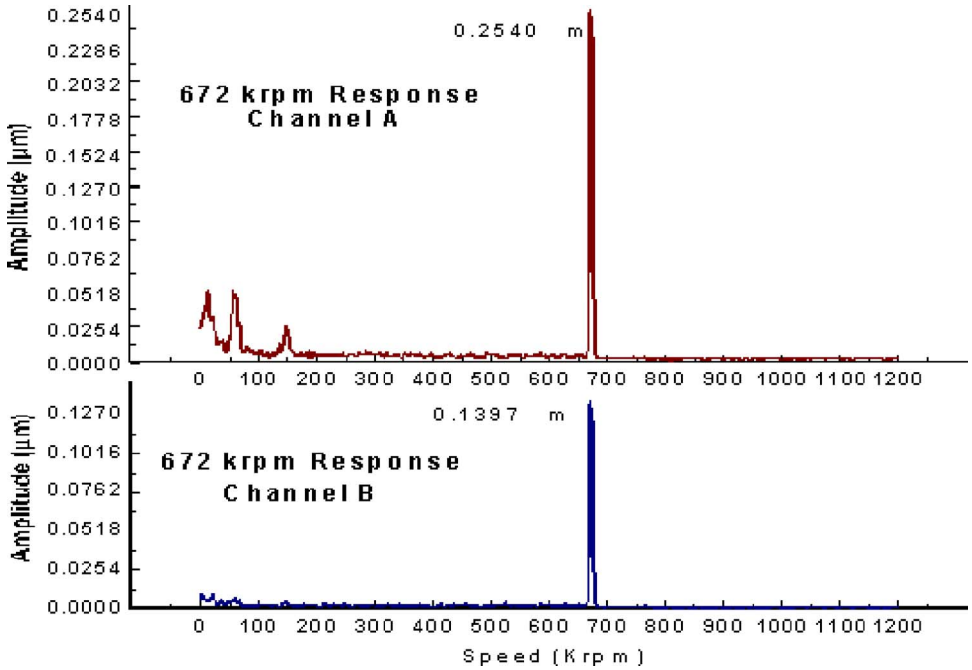

Fig. 11 Rotor frequency spectrum for horizontal position at 675,000 rpm

Simulator Design and Test Method

Since bearings have been identified as one of the key limiting factors in the operation of high speed mesoscopic machines, it was felt that machine feasibility would best be demonstrated through rotor-bearing system simulator testing. As such, a mesoscopic scale rotor-bearing system dynamic simulator was designed, built and tested to demonstrate rotor-bearing system stability, design analysis scalability, and the potential of successfully operating and manufacturing split compliant foil bearings. In this section of the paper, details of the experimental setup (simulator), rotordynamic analysis, and experimental results are explained.

Turbine Simulator Test Rig. The mesoscopic turbine simulator consists of an impulse turbine driven single piece rotor supported by two compliant foil journal bearings. Two compliant foil thrust bearings were used to maintain rotor axial position. Compliant foil air bearings were selected for this demonstration because of their ability to operate at almost unrestricted speeds, low power loss, as discussed above, and ability to operate at temperatures above 650°C (1200°F) for extended durations. The use of a proprietary high temperature, high durability coating was also selected to permit thousands of machine start/stop cycles without degradation. The newly developed split journal and thrust designs were also used.

The simulator housing included a split bearing shell, a turbine nozzle box, end caps, and provisions for fiber optic displacement sensors and speed pickup. Total simulator weight was 56 g, including the 9 g solid rotor. The simulator housing was made of

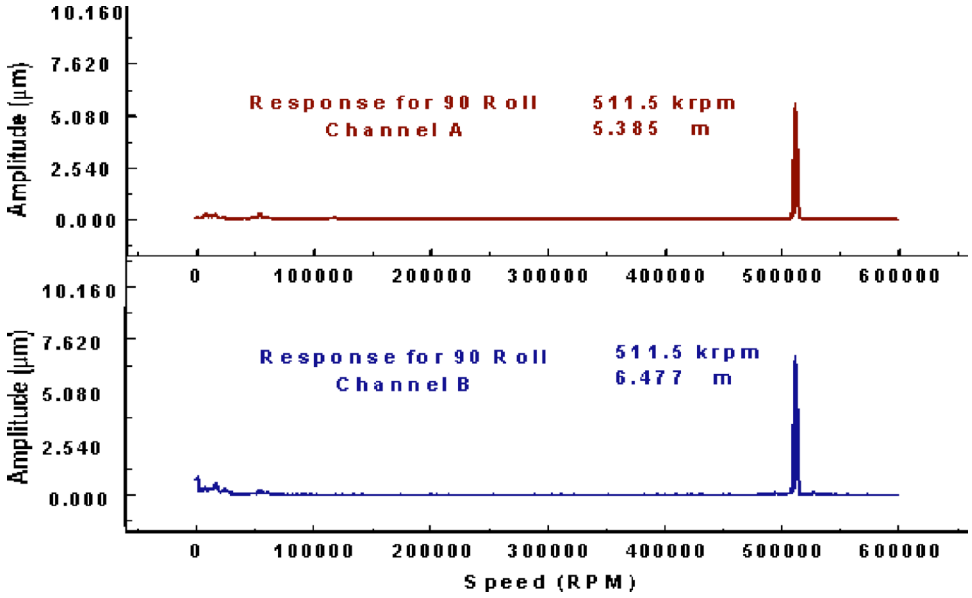

Fig. 12 Spectrum for 90 deg roll about spin axis

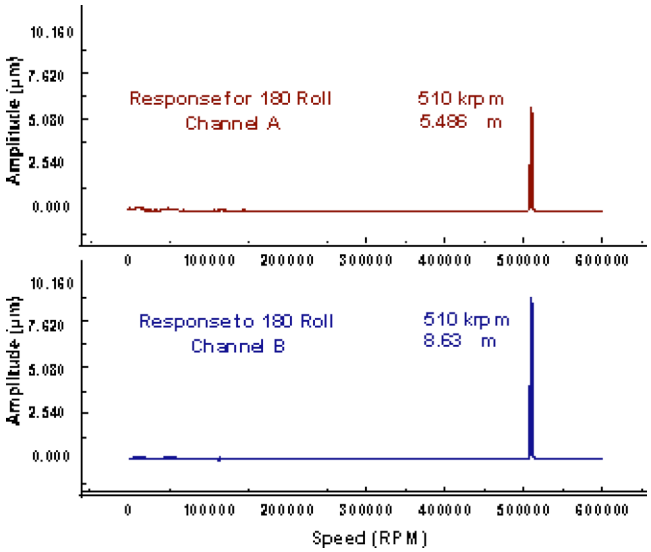

Fig. 13 Spectrum for 180 deg roll about spin axis

aluminum with an overall length and diameter of 32.7 and 28.6 mm, respectively. The simulator hardware in its assembled state is shown in Fig. 3.

Two end caps with embedded holes were used on both ends of the simulator housing to secure the split housings and provide a location for the optical speed pick up and/or an axial displacement probe if desired and, finally, for directing the impulse turbine exhaust to the outside. The simulator shell or housing included holes for the impulse turbine drive air and optical displacement probes. The simulator housing and interior components, such as the bearing shells and nozzle box, were made of two halves. The drive turbine nozzle box featured a ring with an inside diameter (i.d.) of 7.518 mm and outside diameter (o.d.) of 11.43 mm, on whose circumference 12 holes in six equally spaced circumferential positions were installed. The schematic of the nozzle box is shown in Fig. 4. The rotor shown in Fig. 5 was made of PH13-8 Mo, had an overall length of 24 mm, and featured two 15-mm-diam, 1.664-mm-long wheels at each end of the rotor. These 15-mm-diam wheels were used to simulate the mass and inertia properties of the expected turbine and compressor stages. The main diameter of the center shaft section of the rotor was 6 mm, which established the foil journal bearing diameter. The impulse turbine pockets used to drive the rotor were machined in the center of the single piece rotor.

The PH13-8 Mo bearing shells each had an overall o.d. and length of 21.26 and 5.08 mm, respectively, as shown schematically in Fig. 6 to accommodate the smooth top foil and supporting compliant bump foil assembly.

The simulator was equipped with two displacement probes and one speed pickup probe. The optical displacement probes were positioned to record displacements of each of the two end simulator wheels.

The speed pickup probe was installed on one of the end caps pointing at the axial face of one of the two wheels. The simulator cross section with position of the probes is shown in Fig. 7.

It should be noted that while the current test setup directed all air through the foil bearings, in an engine application only a small portion of the total flow would be used for bearing thermal management. The amount of airflow that passes through the compliant foil bearing is typically very small though not measured for these tests. This air is mainly used to reduce the heat distortion (thermal stresses) effects. In the analysis presented in Fig. 1, the calculated losses are due to hydrodynamic effects (at the required operating condition) only. The effect of destabilizing force of inlet air was

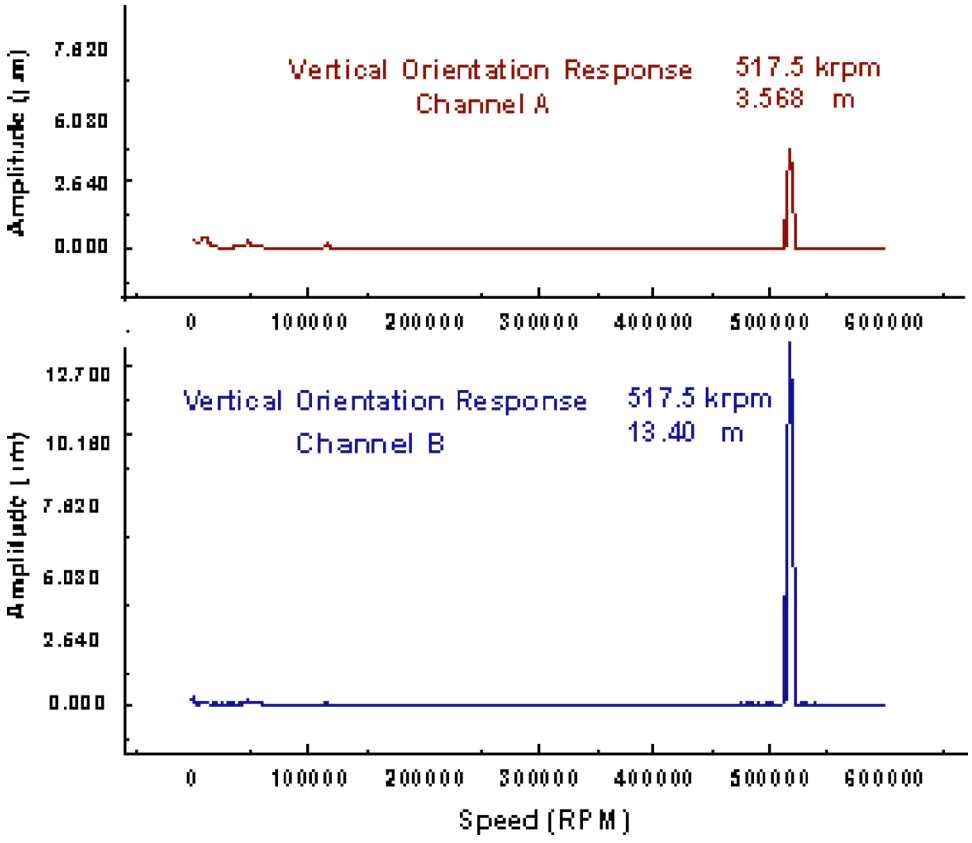

Fig. 14 Spectrum for vertical operation

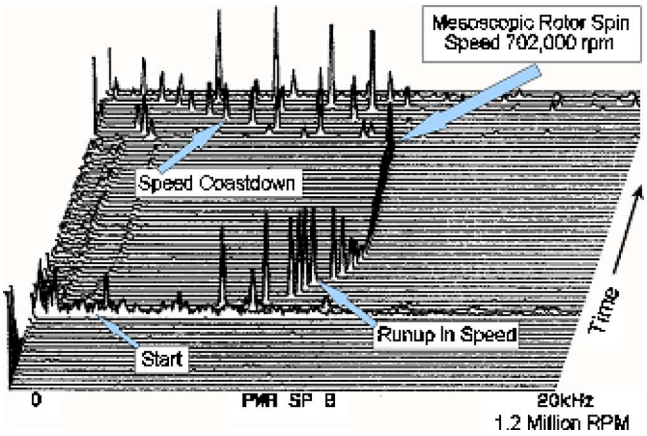

Fig. 15 Waterfall frequency spectrum showing operation above 700,000 rpm, from startup to shutdown

not considered. The authors relied on signature of the system parameters such as vibration and displacement for diagnostic purposes. The aerodynamic forces mainly affected the rotor turbine blades since a small amount of gas passes through the bearings due to small clearance.

Bearing System Design and Analysis

During this effort, rotordynamic and bearing analyses were completed to ensure scalability of the mesoscale components. The 6-mm-diam compliant bearings were designed to provide the stiffness characteristics (non-dimensional values) shown in Fig. 8. The bearings were designed via iterative procedures. First, the bearings were designed, analyzed, and scaled to the current size to establish the dynamic characteristics. Second, the bearings were used in rotor analysis to ensure the rotor system stability. Detailed technical background on integration of structural and fluid film dynamic elements, frictional damping and scaling in foil bearings are presented in [5–16]. Stiffness coefficients for small displacement from the bearing equilibrium position $(e,2)$ can be obtained from the following general equation:

$$K = \frac{\partial F}{\partial e}\sin(\theta) + \frac{1}{e}\frac{\partial F}{\partial \theta}\cos(\theta) \tag{1}$$

where k, F, e and 2 are stiffness, load, eccentricity and load angle, respectively.

For bearing loss calculations, the governing hydrodynamic and structural equations for compressible flow and compliant surface are solved simultaneously. From the results of the analysis, parameters such as film thickness, pressure profile, stiffness and damping, power loss and flow rate are obtained. The calculation procedure is given in [8–12]. It is important in these calculations to account for effect of pressure and temperature on thermophysical properties (e.g., viscosity) of the working gas. With regard to bearing loss and assumption of the continuity, the authors ensure the satisfaction of the continuity equation in each step of the solution. Then, the results of the stiffness and damping are used for rotordynamic analysis. The rotordynamic analysis results, such as critical speed, mode shapes, and stability, are then compared with the experimental results to validate our design procedure and analysis.

It should be noted that the authors did not attempt to address the detail and complete interaction of the air at blade tips in this work. However, in loss calculation, the bearing and aerodynamic losses (such as Windage losses) are accounted for. The approximate Knudsen number in the bearings is 0.035. The split foil thrust bearings have an o.d. of 15 mm and an i.d. of 8 mm.

The results of the rotordynamic analysis are presented in Figs. 9 and 10. Figure 9 shows both the predicted and measured rigid body natural frequencies when operating at speeds up to 550,000 rpm. As seen, even with the small-scale rotor and foil journal bearings, correlation between the measured and predicted natural frequencies is quite good. The logarithmic decrements reported in Fig. 9 are those predicted for the two rigid body modes when operating at the corresponding spin speeds. Figure 10 shows that rotor system stability is expected over the entire operating speed range, as noted by the positive logarithmic decrements for all speeds.

Test Results

In this section the results of tests with the simulator are shown. The simulator was tested at various speeds and rotor axis orientations through rolling or rotation of the simulator while it was spinning. These tests identify the performance of the bearing in maintaining a stable rotor system while transient dynamic conditions are imposed on the rotor system. The rotor frequency spectrum for various speeds and various orientations is presented to show both the synchronous and sub-synchronous vibration content. Presentation of results starts with the rotor vibration spectrum at 672,000 rpm. Figure 11 shows the frequency spectrum obtained from two fiber optic displacement sensors with the rotor in the preferred horizontal position. As shown, a very small rotor displacement in the order of 0.25 μm (0.00001 in.) at the spin speed is observed.

Figures 12 and 13 show rotor spectrum with the rotor remaining horizontal but the housing rolled or rotated about the spin axis 90 deg and 180 deg from its preferred orientation. Figure 14 shows the vibration spectrum when the rotor spin axis is rotated to the vertical orientation. The increase in rotor orbits when operating with the vertical spin axis is expected due to the reduced bearing stiffness experienced during unloaded operation [17].

Finally, Fig. 15 shows the operation of the mesoscopic turbine simulator rotor at a speed above 700,000 rpm. When operating at this speed, the rotor synchronous and subsynchronous responses are both well controlled and low.

Acknowledgment

This work was supported by MiTi®, as an internal research and development program. The authors would like to thank MiTi® for supporting this project. Special thanks are reserved for David Slezak for his fabrication of the mesoscale foil bearings and Romano Sandomenico for machining critical parts used in the testing.

References

[1] Isomura, K., et al., 2002, "Development of Microturbocharger and Microcombustor For a Three-Dimensional Gas Turbine At Microscale," ASME Paper No. GT-2002–30580.
[2] Mohawk Innovative Technology Inc. (MiTi®) Development Newsletter, 2003, "Mesoscopic Turbojet Simulator Tested at Speeds Above 700,000 rpm on Air Foil Bearings," **17**, pp. 1–4.
[3] Uechi, H., Kimijima, S., and Kasagi, N., 2001, "Cycle Analysis of Gas Turbine-Fuel Cell Hybrid Micro Generation System," ASME Paper No. JPGC2001/PWR-19171.
[4] Kang, S., Stampfl, J., Cooper, A., and Prinz, F., 2001, "Application of the Mold SDM Process to the Fabrication of Ceramic Parts for a Mircro Gas Turbine Engine," publication of Rapid Prototyping Laboratory, Stanford University, Stanford, CA.
[5] Ku, C. P. R., and Heshmat, H., 1994, "Structural Stiffness and Coulomb Damping in Compliant Foil Journal Bearings: Theoretical Considerations," Tribol. Trans., **37**(3), pp. 525–533.
[6] Ku, C. P. R., and Heshmat, H., 1994, "Structural Stiffness and Coulomb Damping in Compliant Foil Journal Bearings: Parametric Studies," STLE Tribol. Trans., **37**(1), pp. 255–262.
[7] Salehi, M., Heshmat, H., and Walton, J., 2003, "The Frictional Damping Characterization of Compliant Bump Foils," ASME J. Tribol., **125**(4), pp. 804–813.
[8] Heshmat, H., and Ku, C. P. R., 1994, "Structural Damping of Self-Acting Compliant Foil Journal Bearings," ASME J. Tribol., **116**(1), pp. 76–82.
[9] Heshmat, C. A., Xu, D., and Heshmat, H., 2000, "Analysis of Gas Lubricated Foil Thrust Bearings Using Coupled Finite Element and Finite Difference Methods," ASME J. Tribol., **122**, pp. 199–204.

[10] Heshmat, H., Walowit, J., and Pinkus, O., 1983, "Analysis of Gas-Lubricated Compliant Thrust Bearings," ASME J. Lubr. Technol., **105**(4), pp. 638–646.
[11] Heshmat, H., Walowit, J., and Pinkus, O., 1983, "Analysis of Gas-Lubricated Compliant Journal Bearings," ASME J. Lubr. Technol., **105**(4), pp. 647–655.
[12] Heshmat, H., 1999, "The Integration of Structural and Fluid Film Dynamic Elements in Foil Bearings—Part I: Past Approaches to the Problem," ASME Paper No. DETC/VIB 8271.
[13] Heshmat, H., 1999, "Operation of Foil Bearings Beyond the Bending Critical Mode," Trans. ASME, J. Tribol., **122**, pp. 192–198.
[14] Heshmat, H., 1993, "Role of Compliant Foil Bearings in Advancement and Development of High-Speed Turbomachinery," publication of ASME Pumping Machinery, P. Cooper, ed., ASME, New York, FED **154**, pp. 359–377.
[15] Heshmat, H., 1994, "Advancements In the Performance of Aerodynamic Foil Journal Bearings: High Speed and Load Capability," ASME J. Tribol., **116**(2), pp. 287–295.
[16] Heshmat, H., Chen, H. M., and Walton, J. F., 2000, "On the Performance of Hybrid Foil-Magnetic Bearings," ASME J. Eng. Gas Turbines Power, **122**, pp. 73–81.
[17] Walton, J. F., and Heshmat, H., 1999, "Application of Foil Bearings to Turbomachinery Including Vertical Operation," ASME Paper No. 99-GT-391.

Effects of Bearing Stiffness Anisotropy on Hydrostatic Micro Gas Journal Bearing Dynamic Behavior

L. X. Liu

Z. S. Spakovszky

Gas Turbine Laboratory,
Department of Aeronautics and Astronautics,
Massachusetts Institute of Technology,
Cambridge, MA 02139

The high-speed microhydrostatic gas journal bearings used in the high-power density MIT microengines are of very low aspect ratio with an L/D of less than 0.1 and are running at surface speeds of order 500 m/s. *These ultra-short high-speed bearings exhibit whirl instability limits and a dynamic behavior much different from conventional hydrostatic gas bearings. The design space for stable high-speed operation is confined to a narrow region and involves singular behavior (Spakovszky and Liu, 2005, "Scaling Laws for Ultra-Short Hydrostatic Gas Journal Bearings," ASME J. Vibr. Acoust., **127**(3), pp. 254–261). This together with the limits on achievable fabrication tolerance, which can be achieved in the silicon chip manufacturing technology, severely affects bearing operability and limits the maximum achievable speeds of the microturbomachinery. This paper introduces a novel variation of the axial-flow hydrostatic micro gas journal bearing concept, which yields anisotropy in bearing stiffness. By departing from axial symmetry and introducing biaxial symmetry in hydrostatic stiffness, the bearing's top speed is increased and fabrication tolerance requirements are substantially relieved making more feasible extended stable high-speed bearing operation. The objectives of this work are: (i) to characterize the underlying physical mechanisms and the dynamic behavior of this novel bearing concept and (ii) to report on the design, implementation, and test of this new microbearing technology. The technical approach involves the combination of numerical simulations, experiment, and simple, first-principles-based modeling of the gas bearing flow field and the rotordynamics. A simple description of the whirl instability threshold with stiffness anisotropy is derived explaining the instability mechanisms and linking the governing parameters to the whirl ratio and stability limit. An existing analytical hydrostatic gas bearing model is extended and modified to guide the bearing design with stiffness anisotropy. Numerical simulations of the full nonlinear governing equations are conducted to validate the theory and the novel bearing concept. Experimental results obtained from a microbearing test device are presented and show good agreement between the theory and the measurements. The theoretical increase in achievable bearing top speed and the relief in fabrication tolerance requirements due to stiffness anisotropy are quantified and important design implications and guidelines for micro gas journal bearings are discussed.* [DOI: 10.1115/1.2180813]

Introduction

Gas-lubricated bearings are used in high-speed rotating machinery predominantly due to their ultra-low frictional characteristics, the freedom from temperature limitations, and long maintenance-free life. One of the most severe difficulties encountered with gas bearings is their tendency to be unstable or to produce self-excited whirl instabilities of the rotordynamic system in which they are components. A generalized class of rotordynamic whirl instabilities may be characterized by a driving force, which is generated due to cross-coupled stiffness; that is, a force that is proportional to the rotor deflection and rotor speed but that acts in the direction normal to the deflection. In gas bearings, this cross-coupled stiffness is caused by film forces, induced by the pumping action of the rotor rotation, and are commonly referred to as hydrodynamic forces. The dynamic behavior of gas bearings and the characterization of the bearing forces have been investigated extensively, both experimentally and analytically. Larson and Richardson [1] report an experimental study of whirl instability in pressurized gas bearings and discuss the observed trends using a simple, qualitative stability criterion.

On the micro-scale, gas journal bearings have become a prominent design choice for supporting the rotors of high-speed microturbomachinery used in power MEMS (micro-electro-mechanical systems). For example, the MIT microengines use gas journal bearings that are located at the outer periphery of the rotors and designed to operate at rotational speeds of order 2×10^6 rpm in order to reach turbomachinery tip speeds of 500 m/s. A detailed discussion of the evolution of the MIT microdevice design and their bearings can be found in Piekos et al. [2], Ehrich and Jacobson [3], and more recently in Epstein [4] and in Fréchette et al. [5].

The current MIT microdevices are designed with axial-flow hydrostatic gas journal bearings, which are very short compared to their relatively large bearing diameters; the bearing L/D is typically <0.1, which is at least one order of magnitude smaller than in conventional gas bearings. A detailed discussion of the design, the bearing modeling and analysis, and the experimental testing of these bearings is given in Liu et al. [6]. One marked difference between the ultra-short high-speed gas bearing and its large-scale, long-bearing counterpart is that the former exhibits very different

Contributed by the International Gas Turbine Institute (IGTI) of ASME for publication in the JOURNAL OF ENGINEERING FOR GAS TURBINES AND POWER. Manuscript received October 1, 2003; final manuscript received March 1, 2004. Review conducted by K. C. Hall. Paper presented at the ASME Turbo Expo 2005: Land, Sea, and Air, Reno, NV, June 6–9, 2005, Paper No. GT2005-68199.

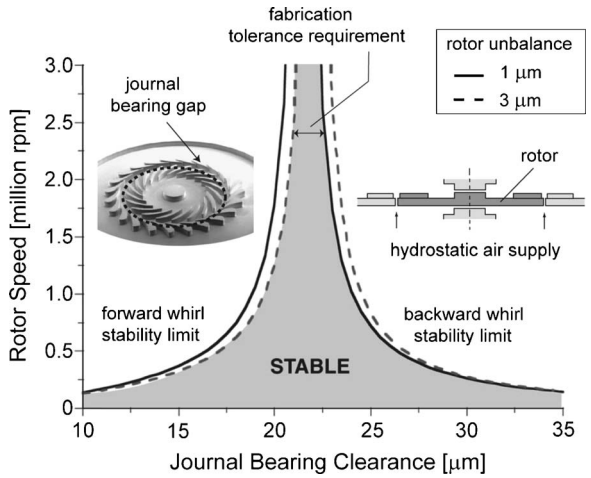

Fig. 1 Singular behavior of whirl instability limit for ultra-short hydrostatic micro-gas journal bearings at different levels of rotor unbalance (SEM photo by [8])

rotordynamic characteristics and whirl instability behavior. These bearings resemble short annular seals, where the bearing inlet pressure loss governs the hydrostatic direct stiffness, known as the Lomakin effect [7].

In addition to the hydrostatic effects, the bearing also experiences whirl-inducing forces. The net cross-coupled force generated in the short bearing gap is due to two effects that act in opposite directions: hydrodynamic pumping and viscous drag due to rotor rotation. Unlike in conventional, large-scale long bearings, the viscous drag effect is not negligible compared to the hydrodynamic pumping effect. For certain bearing geometries the two forces cancel and the net cross-coupled force vanishes. This implies very high rotor speeds at the whirl instability limit. Furthermore, the stable bearing design space is confined to a narrow region and involves singular behavior as depicted in Fig. 1. A detailed derivation of the scaling laws for ultrashort gas journal bearings and the definition of this whirl instability criterion can be found in Spakovszky and Liu [9].

Apart from dynamic instabilities, the main challenges and limitations encountered with microscale gas bearings are the manufacturing constraints and fabrication tolerances and uncertainties. The MIT microdevices are fabricated on silicon wafers using deep-reactive-ion-etching (DRIE). Two of the limitations of this manufacturing technology are the maximum etch depth and minimum cutting width, which are strongly influenced by the complexity and arrangement of the features on the wafer. The MIT microdevices typically consist of five to six wafers that are bonded together, each of which is of relatively complex geometry. For example, the bearing clearance is typically a 350 μm deep and 20 μm wide circular trench that is cut at a radius of 2 mm. For such a bearing etch, the fabrication uncertainty can be as much as $1-2$ μm in bearing clearance and $10-20$ μm in bearing length. Given the high-speed bearing design requirements depicted in Fig. 1, the bearing clearance must be 21.5 μm in order to achieve a stable design speed of 2.4×10^6 rpm. The misalignment of the geometric center of the ring of turbomachinery blades and the center of the journal bearing as well as the etch nonuniformity in forming the side of the disk at the base of the blades yield a rotor unbalance of typically 2 μm (expressed as displacement of the rotor's center of gravity from its rotational centerline). Returning to Fig. 1, the allowable tolerance on the bearing clearance then becomes ±0.5 μm.This tolerance on the bearing clearance design specification is clearly below the fabrication capabilities and limits the maximum achievable rotor speed to roughly half the design speed.

Symmetry—Enemy of Stability. A possible modification to plain cylindrical bearings to improve their stability range is to introduce multiple lobes or pads. In conventional, large-scale gas bearings, this can improve the dynamic performance by creating a preload (the dimensional difference in clearance between the lobe and the bearing), which provides direct stiffness at the bearing-centered operating condition. For higher speeds and light loads, multiple-lobe bearings are known to offer a slightly more stable behavior than plain cylindrical journal bearings as reported by Fuller [10] and Garner et al. [11]. Lobed journal bearings were also investigated as a possible means to improve microbearing dynamic behavior. Piekos [12] reports numerical simulations of multi-lobed hydrodynamic gas journal bearings for the MIT microengine and concludes that, for the very short micro bearings, a lobed configuration deteriorates the stability. More recently Kim et al. [13] discuss the modeling of micro gas journal bearings with a stepped casing. The authors conclude that plain gas journal bearings are more stable than the stepped gas journal bearings and report that implementing axial grooves in addition to the steps, or reducing the number of steps, improves the bearing stability.

It was suggested by Smith [14] that when there is considerable lack of symmetry in the bearing support stiffness, the transition speed from stable to unstable operation is very high compared to critical speeds, even if there is no stationary damping. The asymmetry in support stiffness, commonly referred to as anisotropic support stiffness, was further investigated by Gunter and Trumper [15] to mitigate hysteretic whirl. More recently Ehrich [16] analyzed the stability limit of a Jeffcott rotor model for a representative range of values of support stiffness anisotropy and of system damping ratio. Ehrich showed that anisotropy is effective in suppression of instability for lightly damped systems but less so for systems with higher damping.

The novel micro gas journal bearing configuration presented in this paper is based on the idea of bearing stiffness anisotropy. The concept is to break symmetry in hydrostatic direct stiffness without much affecting the hydrodynamic cross-coupled stiffness. This is in contrast to the lobed bearings reported by Piekos [12], where both direct and cross-coupled stiffness are affected by the nonuniform geometry and the stability limit is deteriorated.

In essence, the direct consequence of the concept introduced in this paper is the elimination of the singular behavior of the whirl instability limit through asymmetry in hydrostatic stiffness. This extends the geometric design space for stable operation and yields a higher whirl instability limit and a major relief in the fabrication tolerance requirements, enabling an increased bearing top-speed. The impact of bearing stiffness anisotropy on the stable design space is shown in Fig. 2 in comparison to a micro-gas bearing with symmetric hydrostatic stiffness. The latter is hereafter called isotropic bearing stiffness, implying that the bearing stiffness is independent of the direction of rotor displacement.

Scope of the Paper. The details of the bearing configuration to achieve anisotropy in hydrostatic stiffness and the impact on bearing dynamic behavior is the subject of this paper and will be discussed at length. The major goals of the paper are to investigate the physical mechanisms at play, to quantify the benefits of such a bearing configuration, and to delineate performance and design implications. More specifically, the objectives are to

- introduce the concept of bearing stiffness anisotropy and implement this concept in axial-flow hydrostatic micro gas bearings
- predict the dynamic behavior (critical frequencies, damping ratio, etc.) and whirl instability limit of this bearing concept
- characterize the underlying physical mechanisms and the dynamic behavior of this bearing concept
- quantify the increase in bearing top speed and the relief in fabrication tolerance requirements due to stiffness anisotropy

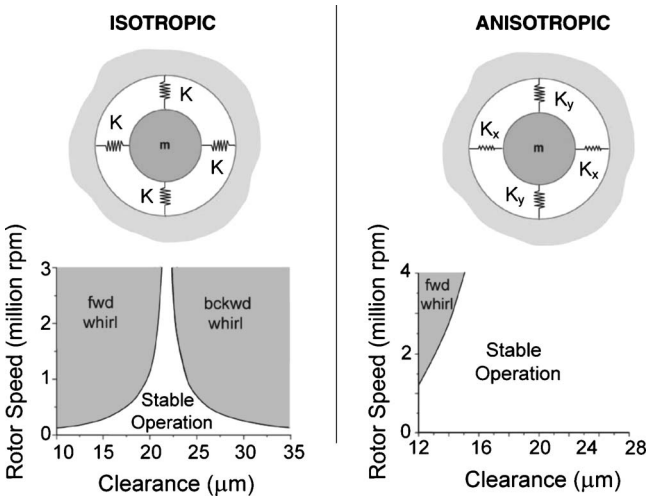

Fig. 2 Elimination of singular behavior of whirl instability limit and extension of geometric design space for stable high-speed operation using bearing stiffness anisotropy in ultra-short hydrostatic micro gas journal bearings

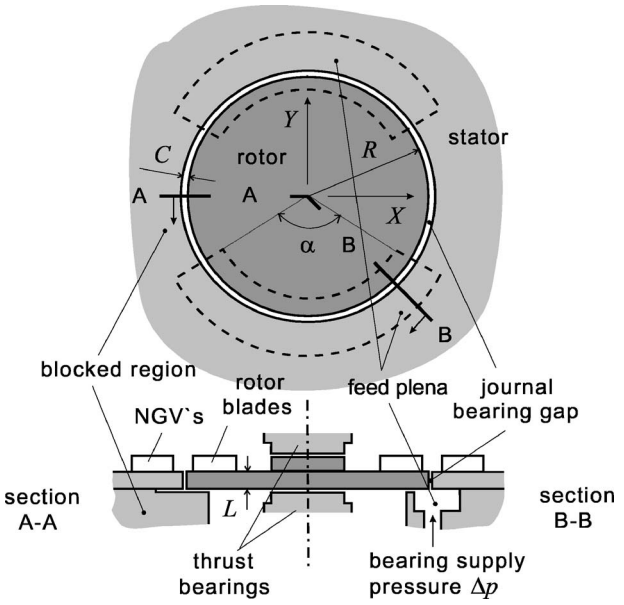

Fig. 3 Hydrostatic micro-gas bearing configuration with stiffness anisotropy (dimensions are not to scale)

- assess and quantify the effects of bearing side-load on anisotropic bearing dynamic behavior
- delineate design guidelines and implications for gas bearings with stiffness anisotropy.

The technical approach involves the combination of numerical simulations, experiment, and simple, first-principles-based modeling of the gas bearing flow field and the rotor dynamics.

The paper is organized as follows. First, the novel bearing design configuration is defined. Next, an existing analytical hydrostatic gas bearing model [6,9] is extended and modified for stiffness anisotropy. A simple description of the whirl instability threshold with stiffness anisotropy is derived explaining the instability mechanisms and linking the governing parameters to the whirl ratio. Then, the increase in achievable bearing top-speed and the relief in fabrication tolerance requirements due to stiffness anisotropy are quantified. Numerical simulations of the full nonlinear governing equations are conducted to validate the theory and the novel bearing concept. Next, the effect of bearing side-load on the dynamic behavior is investigated. Experimental results obtained from a microbearing test device are presented and compared to the predicted bearing dynamic behavior. Finally, important design implications and guidelines for micro gas journal bearings are discussed and the conclusions are summarized.

Gas Bearing Stiffness Anisotropy

The hydrostatic gas journal bearings of the MIT microdevices are designed as axially fed bearings. The journal bearing air is fed from the aft side of the rotor and flows through the journal bearing gap in the axial direction, as shown in Fig. 1. The ultra-short journal bearing essentially acts like a short annular seal and generates hydrostatic stiffness due to the Lomakin effect. These micro gas bearings yield a damping ratio of two orders of magnitude smaller but a whirl ratio (the ratio of rotor speed at instability onset to the critical speed) of one order of magnitude larger compared to their long-bearing counterparts. For a given L/D, this occurs only for a narrow range of bearing clearance to radius ratio C/R, which constitutes the singular behavior discussed earlier (for more details, see [9]).

The goal is to break the symmetry in hydrostatic stiffness without a substantial increase in the hydrodynamic cross-coupled stiffness that gives rise to whirl instability. Since the bearing feed pressure, and hence the flow rate, govern the hydrostatic stiffness,[1] anisotropy can be introduced by reducing or increasing the amount of flow through a circumferential sector of the bearing gap. The simplest configuration is to block the flow through two circumferential sectors, as depicted in Fig. 3. The two remaining circumferential sectors are fed with pressurized air from plena located on the aft side of the rotor. Since the axial clearance gap between the rotor and the static structure in the blocked region is small and yields very high flow resistance, the hydrostatic pressure buildup is limited and the hydrostatic stiffness is thus reduced in these locations. As a consequence, the hydrostatic stiffness in the X and Y directions are different and anisotropy in journal bearing stiffness is introduced. Note that the journal and rotor geometries are still circular and axisymmetric, and that asymmetry is introduced only in the hydrostatic feed air system (without the blocked feed regions the journal bearing is axisymmetric and the hydrostatic stiffness is isotropic).

Anisotropic Gas Bearing Theory. The dynamic behavior and whirl instability limit of the micro-gas journal bearing with stiffness anisotropy are analyzed using a previously developed modeling framework [6]. The analytical model consists of two parts, a fluid dynamic model for axial-flow gas journal bearings and a rotordynamic model for micro-bearings. The fluid dynamic model is modified to account for the flow blockage in the blocked sectors, which affects the pressure field acting on the rotor. Integration of the pressure field and viscous stress field on the rotor yields the hydrostatic force F^{hs}, the hydrodynamic force F^{hd}, and the damping force F^{dp}, which, in a stationary coordinate system, govern the motion of the rotor according to

$$\begin{aligned} m\ddot{x} &= F_x^{hs} + F_x^{hd} + F_x^{dp} + m\Omega^2 a\cos(\Omega t) \\ m\ddot{y} &= F_y^{hs} + F_y^{hd} + F_y^{dp} + m\Omega^2 a\sin(\Omega t) \end{aligned} \tag{1}$$

The excursions of the geometric center of the rotor in the X and the Y direction are denoted by x and y, respectively, and the last term denotes the harmonic forcing at rotor frequency Ω due to rotor unbalance a. For low unbalance, the motion can be viewed linear by and Eq. (1) becomes

[1]The scaling law for hydrostatic stiffness is $(K^{hs})/(p_oC) \propto (L/D)(C/R)^{-2}(\Delta p/p_o)$. For a derivation, see [9].

$$m\ddot{x} + K_{xx}x + K_{xy}y + C_x\dot{x} = O(x^2) + O(y^2)$$
$$m\ddot{y} + K_{yy}y + K_{yx}x + C_y\dot{y} = O(x^2) + O(y^2) \quad (2)$$

where K_{xx}, K_{yy}, C_x, and C_y are the direct-coupled hydrostatic stiffness and damping coefficients in the X and Y direction, respectively. K_{xy} and K_{yx} denote the cross-coupled hydrodynamic stiffness coefficients. Note that for an *isotropic* bearing configuration the bearing coefficients become in the limit of small eccentricity (see [9] for details):

$$K_{xx} = K_{yy} = K^{hs} \approx 8\frac{RL}{C} \cdot \Delta p \quad (3)$$

$$K_{xy} = -K_{yx} = K^{hd} \approx \pi\frac{\mu RL}{C}\left(\frac{L^2}{2C^2} - \frac{R}{C}\right)\Omega \quad (4)$$

$$C_x = C_y = C^{\text{sys}} \approx \pi\frac{\mu RL^3}{C^3} \quad (5)$$

Returning to the anisotropic bearing configuration, the dynamics of the linearized equations of motion Eq. (2) can be solved in the frequency domain using the Laplace transform $\mathcal{L}: z(t) \rightarrow Z(s)$. The characteristic equation for the rotordynamic behavior of the anisotropic journal bearing then yields

$$m^2s^4 + m(C_x + C_y)s^3 + m[(K_{xx} + K_{yy}) + C_xC_y]s^2 + (K_{xx}C_y + K_{yy}C_x)s + K_{xx}K_{yy} - K_{xy}K_{yx} = 0 \quad (6)$$

where $s = j\Omega_N$ is the Laplace variable and Ω_N is the natural frequency of the oscillation. The hydrodynamic stiffness is proportional to the rotor frequency Ω such that one can write $K^{hd} = k^{hd}\Omega$ and similarly $K_{xy} = k_{xy}\Omega$, and so forth. Setting the real and imaginary parts of Eq. (6) to zero yields

$$\Omega_N^2 = \frac{K_{xx}C_y + K_{yy}C_x}{m(C_x + C_y)} \quad (7)$$

and, using the rotor frequency at whirl instability onset $\Omega = \Omega_w$,

$$\Omega_w^2 = -\frac{C_xC_y}{k_{xy}k_{yx}}\left[\Omega_N^2 + \frac{(K_{xx} - K_{yy})^2}{(C_x + C_y)^2}\right] \quad (8)$$

Equation (7) determines the natural frequency Ω_N of the rotor system, and Eq. (8) defines the whirl instability limit Ω_w. Note that, generally, k_{xy} and k_{yx} are of opposite signs[2] such that the right-hand side of Eq. (8) is positive and Ω_w has a real root.

Similar to the case of isotropic bearing stiffness, as discussed in Spakovszky and Liu [9], the whirl instability limit depends on the ratio of the damping coefficients to the cross-coupled hydrodynamic stiffness. In fact, in the isotropic limit (Eqs. (3)–(5)), the above equations reduce to the classic whirl ratio result for isotropic bearing configurations

$$\mathfrak{R} = \frac{\Omega_w}{\Omega_N} = \frac{C^{\text{sys}}}{k^{hd}} \quad (9)$$

The key difference between the isotropic and anisotropic bearing cases is the additional term on the right-hand side of Eq. (8), $(K_{xx} - K_{yy})^2/(C_x + C_y)^2$, which depends on the difference or asymmetry of the direct-coupled hydrostatic stiffness in the two orthogonal directions X and Y. This term carries the dynamic effect of anisotropy and constitutes the main mechanism that enhances the stability margin and increases bearing top speed. For the micro-gas bearing systems considered, the magnitude of this term is, generally, two orders of magnitude larger than the first term, which is related to the isotropic bearing case.

[2]It can be shown that if k_{xy} and k_{yx} were of the same sign, the resulting root occurs at even higher frequency and shows a different dynamic behavior that does not constitute whirl instability.

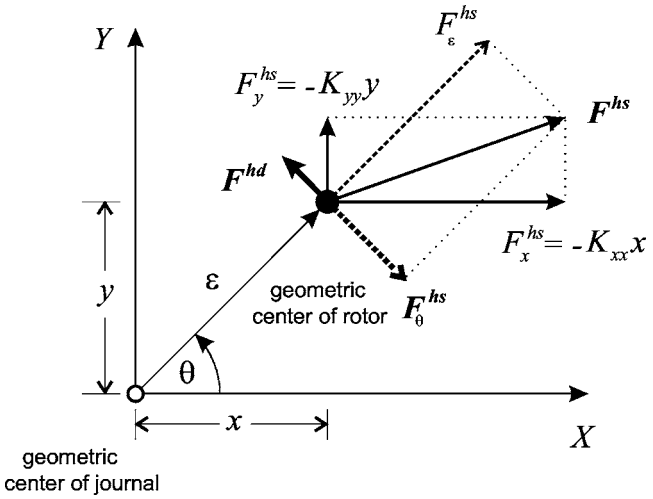

Fig. 4 Hydrostatic and hydrodynamic bearing forces for a bearing configuration with anisotropy in hydrostatic stiffness

Physical Mechanism and Implications. To investigate the mechanisms underlying the improved stability margin due to hydrostatic stiffness anisotropy, the following simplifications can be made. Since the second term on the right-hand side of Eq. (8) is much larger than the first, the latter can be neglected. Furthermore, the asymmetric bearing system can be simplified by considering anisotropy only in the hydrostatic stiffness while keeping the hydrodynamic stiffness and damping coefficients isotropic. Equation (8) then reduces to

$$\Omega_w = \frac{|K_{xx} - K_{yy}|}{|2k^{hd}|} \quad (10)$$

This illustrates that the bearing design should encompass as large a difference in hydrostatic stiffness between the two orthogonal directions $|K_{xx} - K_{yy}|$ as possible while keeping the cross-coupled hydrodynamic stiffness coefficient k^{hd} as low as possible. This can be achieved by varying the hydrostatic feed air over parts of the circumference, as outlined in Fig. 3.

The physical mechanism behind the enhanced stability margin and increased rotor speed at whirl instability onset is demonstrated next. Figure 4 depicts the hydrostatic and hydrodynamic forces acting on the rotor for an anisotropic bearing configuration. Because of anisotropy in hydrostatic stiffness, $K_{xx} \neq K_{yy}$ as shown above, the hydrostatic force F^{hs} has a nonzero component in the tangential direction θ. The hydrodynamic force $F^{hd} = k^{hd}\Omega\varepsilon$ acts in the direction perpendicular to the rotor deflection, and the total destabilizing force in the θ direction then becomes

$$F_\theta = \left(k^{hd}\Omega - \frac{K_{xx} - K_{yy}}{2}\sin(2\theta)\right)\varepsilon \quad (11)$$

Nondimensionalization of the above by the hydrodynamic force allows one to express the total destabilizing force as a function of whirl ratio and natural frequency

$$\frac{F_\theta}{F^{hd}} = 1 - \frac{K_{xx} - K_{yy}}{2k^{hd}\Omega}\sin(2\theta) = 1 - \frac{\mathfrak{R}}{\left(\frac{\Omega}{\Omega_N}\right)}\sin(2\theta) \quad (12)$$

For ultra-short hydrostatic micro-gas journal bearings, the whirl ratio $\mathfrak{R}$ is much larger than one [9]. For anisotropic bearing configurations, the whirl ratio becomes even larger (by one to two orders of magnitude) such that at the rotational speeds of interest (millions of revolutions per minute), the circumferential variation

in the total destabilizing force becomes sinusoidal. The net destabilizing force over the full circumference then essentially vanishes, and as a consequence, the whirl instability limit is shifted to very high rotational speeds. Put another way, introducing an asymmetry in hydrostatic stiffness yields a sinusoidally varying force component in the tangential direction, which, for ultrashort hydrostatic gas journal bearings, is much larger in magnitude than the cross-coupled hydrodynamic force. On a net basis, the whirl-inducing tangential force component vanishes and the stable operating range is extended to very high rotational speeds.

For rotor speeds near the limit of whirl instability $\Omega \approx \Omega_w$, the magnitude of the sinusoidal variation in tangential force is of order one and the net whirl inducing force becomes positive. This suggests that, for anisotropic bearing configurations at whirl instability onset, the rotor tends to forward whirl only. This is in contrast to isotropic bearing configurations where both forward and backward whirl tendency is observed as depicted in Fig. 2.

In summary, although cross-coupled hydrodynamic effects always induce destabilizing forces (a criterion to minimize this force was derived in [9]), the whirl-inducing forces can be balanced by asymmetry or anisotropy in direct-coupled hydrostatic stiffness.

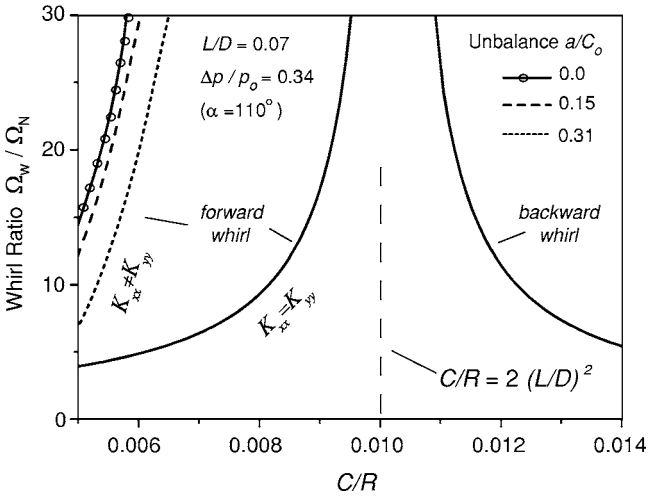

Fig. 5 Whirl ratio for isotropic and anisotropic bearing configurations as a function of *C*/*R* and different levels of unbalance *a*/*C*$_o$. Anisotropic case: numerical solution result (solid line) compared to simple analytical solution (circles).

Assessment of Stability Improvement due to Bearing Anisotropy

The analysis above assumed that the rotor unbalance is negligible and allowed a linearized treatment of the equations of motion around the equilibrium point $x=y=0$ as indicated in Eq. (2). Generally, there is a certain amount of unbalance of the rotor due to geometric nonuniformities and etch depth variations such that the center of mass will be offset from the geometric center of the rotor. At supercritical speeds, the rotor will spin around the center of mass and, as a consequence, the fluid forces in the journal gap will vary with time as the rotor precesses in the journal. In addition, if the journal bearing supply pressures of the two feed plena are different, the rotor will experience a side-load and the journal bearing clearance will decrease on one side, introducing nonlinear behavior of the bearing fluid forces at larger eccentricities.

Since both rotor unbalance and rotor side-load introduce nonlinear effects and thus affect the whirl instability limit, the full nonlinear set Eq. (1) must be solved. A numerical solution scheme was set up to directly solve the nonlinear unsteady equations of motion. As such, for a selected rotational speed and bearing pressure supply and a fixed level of rotor unbalance and side-load, the nonlinear hydrostatic, hydrodynamic, and damping forces are calculated for every time step according to the rotor position and velocity. The time trend of the orbit of the center of the rotor is then analyzed and permits the determination of whether the system is dynamically stable or unstable at the given rotor speed and selected bearing supply pressure.

Figure 5 depicts the whirl ratio $\Re$ as a function of clearance to radius ratio C/R for a fixed $L/D = 0.07$, a fixed bearing supply pressure $\Delta p/p_o=0.34$, and for different levels of rotor unbalance a marked by the solid, dashed, and dotted lines. The rotor unbalance is nondimensionalized by the nominal bearing clearance $C_o = 13\ \mu$m, and calculations are conducted for both an anisotropic ($K_{xx} \neq K_{yy}$) and an isotropic ($K_{xx}=K_{yy}$) bearing configuration. In the anisotropic case the bearing pressure in the two supply plena, each covering 110 deg of the circumference, are at all times kept the same to avoid rotor side-load.

The results indicate that, even with significant amounts of rotor unbalance, the whirl ratios are much higher compared to the isotropic case. Furthermore, the singular behavior in whirl instability limit[3] vanishes in the anisotropic case (forward whirl tendency branch only) such that the journal bearing top speed is increased and the stringent tolerance requirements are relieved.

In addition to the numerical simulations, the simplified, linearized analysis for bearing anisotropy is carried out for the same bearing conditions assuming zero rotor unbalance. The analytical results for the whirl instability limit are plotted as circles in Fig. 5. The results show that the analytical solution compares well to the numerical simulation for zero rotor unbalance (solid line) and thus validates the simplified approach for low rotor unbalance.

Furthermore, the simulation results suggest that the optimum circumferential extent of the bearing feed plena for a maximum extension of stable operating range is in the vicinity of $\alpha = 110$ deg. Figure 6 compares the isotropic bearing performance to the one of an optimized anisotropic bearing design. Both cases have the same geometric bearing characteristics $R=2.1$ mm, $C = 13\ \mu$m, and $L=300\ \mu$m. The effect of hydrostatic stiffness anisotropy greatly enhances the stable operating range (i.e., at a bearing supply pressure of $\Delta p=5$ psig, the bearing top-speed of

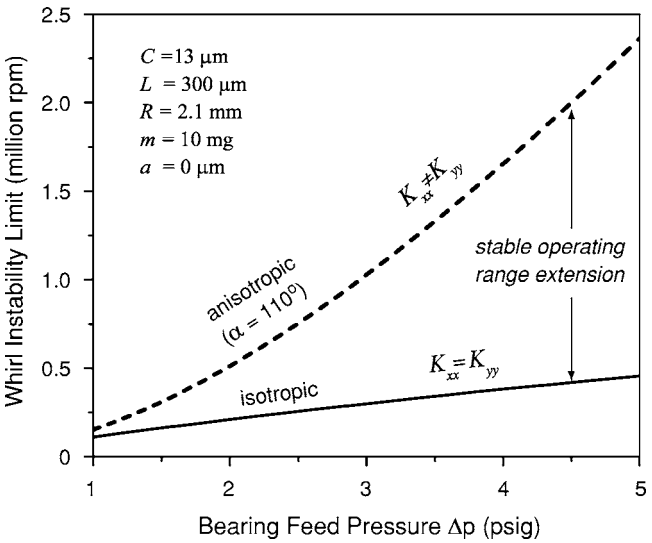

Fig. 6 Stable operating range extension using bearing stiffness anisotropy

[3]The vertical dashed line indicates the simple whirl instability criterion for isotropic bearing configurations, $C/R=2(L/D)^2$, established in [9].

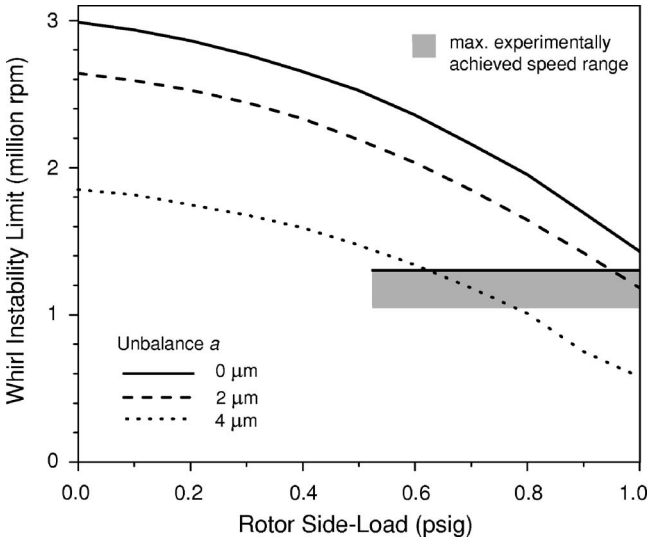

Fig. 7 Effect of rotor side-load on whirl instability limit of an anisotropic bearing configuration

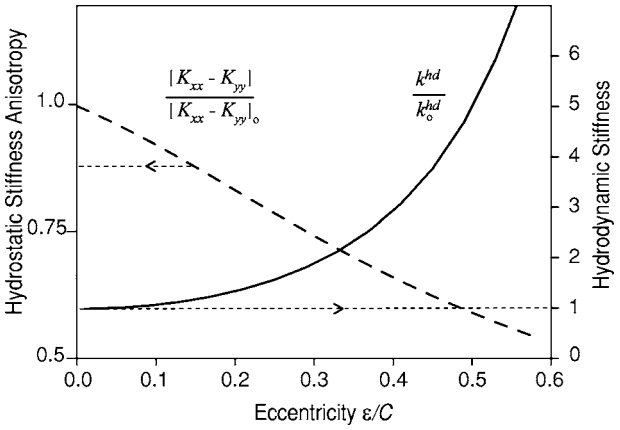

Fig. 8 Effect of eccentricity due to rotor side-load on hydrostatic stiffness anisotropy $|K_{xx}-K_{yy}|$ and hydrodynamic stiffness k^{hd}

500,000 rpm in the isotropic case is increased to a maximum stable rotor speed of 2.4×10^6 rpm using the anisotropic bearing configuration sketched in Fig. 3).

Effect of Rotor Side-Load on Bearing Dynamic Behavior

The mechanical design of the simplest anisotropic bearing configuration consists of two separate bearing air supply plena and feed systems. This design inherently offers the possibility to impose a side-load on the rotor by feeding the two plena at different supply pressures. As a consequence, the rotor will be shifted to one side and the dynamic behavior will be altered due to the increased eccentricity. The effect of rotor side-load on the whirl instability limit is assessed next using the numerical solution of the nonlinear, unsteady equations of motions.

In Fig. 7, the limit rotor speed at whirl instability onset is shown as a function of rotor side-load (the difference in supply pressure between the two opposite feed plena) for three levels of rotor unbalance (marked by the solid, dashed, and dotted lines). The results reveal that the effect of rotor side-load dramatically decreases the bearing top speed. This behavior and the underlying mechanisms are investigated next.

As mentioned earlier, the asymmetry in feed pressure between the two bearing air supply plena pushes the rotor toward the lower supply pressure side and, thus, the equilibrium point of the rotor is no longer at the center of the journal. For higher rotor side-loads, the eccentricity of the rotor relative to the journal will increase and the hydrodynamic pumping effect will yield a larger hydrodynamic force. The hydrodynamic force can be written as [6]

$$F^{hd} = \frac{\pi}{2}\mu\frac{RL^3}{C^2}\Omega\frac{\varepsilon}{(1-\varepsilon^2)^{1.5}} - 2\pi\mu\frac{R^2L}{C}\Omega\frac{1-\sqrt{1-\varepsilon^2}}{\varepsilon\sqrt{1-\varepsilon^2}} \quad (13)$$

Thus, the hydrodynamic stiffness $K^{hd}=\partial F^{hd}/\partial\varepsilon$ will nonlinearly increase with eccentricity. The rotor speed corrected hydrodynamic stiffness $k^{hd}=K^{hd}/\Omega$ is nondimensionalized by its value at zero eccentricity and plotted in Fig. 8 as the solid line.

Since, on time average, an increased eccentricity yields a reduced flow resistance through the bearing gap, the level of anisotropy in hydrostatic stiffness $|K_{xx}-K_{yy}|$ will decrease with rotor side-load in contrast to the increase in hydrodynamic stiffness. This decrease in stiffness anisotropy with eccentricity is plotted as the dashed line in Fig. 8. To first order, the rotor speed at whirl instability onset is the ratio of hydrostatic stiffness anisotropy to the hydrodynamic stiffness as given in Eq. (10), and therefore, the whirl instability limit must decrease nonlinearly with eccentricity. This behavior and the effect of rotor side-load on bearing top speed is clearly captured in Fig. 7. It is important to note that the level of anisotropy in hydrostatic stiffness $|K_{xx}-K_{yy}|$ and the magnitude of hydrodynamic stiffness k^{hd} constitute two competing effects in the dynamic behavior of the gas bearing system: the former stabilizes, while the latter destabilizes the system. Rotor side-load detrimentally impacts both effects in the light of whirl instability.

Experimental Validation of Anisotropic Gas Bearing Theory

Experiments were conducted in the MIT micro-bearing devices, and the hydrostatic gas-journal bearing configuration with stiffness anisotropy was tested. It has to be pointed out that it is difficult and not very practical to experimentally determine the rotor speed at whirl instability onset for the following reasons: (i) a failure at high-speed destroys the device and the experiment cannot be repeated on the same device, (ii) the number of microfabricated devices is limited and can involve significant variations between different devices, and (iii) a device can fail due to other phenomena that are not related to whirl instability (i.e., thrust bearing resonance, thrust balance issues, and effects of conical modes; these effects are investigated in [17]). Thus, an alternate approach is suggested to validate the theory of hydrostatic stiffness anisotropy and its impact on the whirl instability limit. Since the micro-bearing design with stiffness anisotropy yields different stiffness in the two orthogonal directions, the rotordynamic system will exhibit two distinct natural frequencies associated with the two orthogonal directions. The natural frequencies of the micro-device can be measured using fiber-optic sensors and pressure transducers, and can be determined using system identification schemes as discussed in [6].

Thus, the experimentally determined natural frequencies of the microdevices are compared to the model predictions using anisotropic gas bearing theory. The experimentally measured first and second natural frequencies of a microdevice are plotted in Fig. 9 as open circles and solid squares. The model prediction of the natural frequencies for this device are also plotted and marked as the dashed and solid lines, respectively. The results show that the experimentally measured natural frequencies match the predictions well. It can thus be conjectured that the anisotropy in bearing stiffness was successfully implemented in the bearing design and that the theory is partially validated.

In addition, multiple sets of microdevices were tested at high-speed. To date, the maximum achieved speed ranges between 1.1

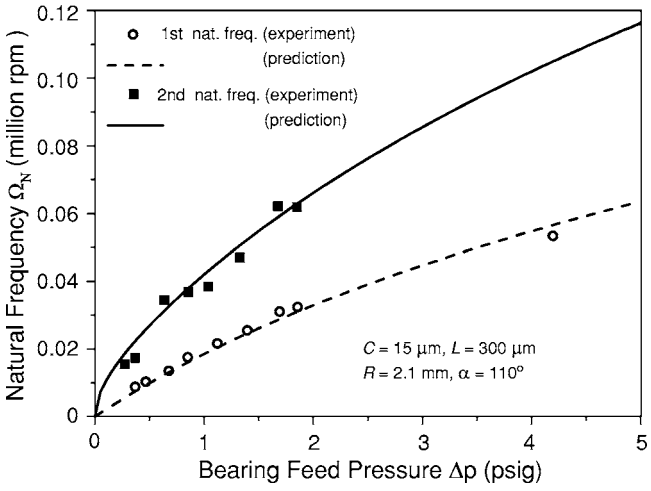

Fig. 9 Experimental verification of natural frequencies in an anisotropic bearing configuration. Measurements are marked by symbols (data by [18]), and the predictions using anisotropic gas bearing theory are marked by lines

and 1.3×10^6 rpm, at bearing pressure settings of $\Delta p=5$ psig. According to the predictions for zero unbalance and no rotor side-load given in Fig. 6, the devices should have been able to reach a rotor top speed of order 2×10^6 rpm. Considering effects of rotor unbalance and side-load, the bearing top speed is reduced as discussed in Fig. 7. In reality, an average device will have a rotor unbalance of 2 μm. In addition, it is very likely that there is a rotor side-load because of imperfections and asymmetries in the air feed system and piping to the plena inside and outside the test device. It is estimated from measurements that the pressure difference between the two bearing feed plena is of the order of 1 psig. Referring to Fig. 7, the maximum predicted speed for an unbalance of ~2 μm and a rotor side-load of ~1 psig is in the vicinity of 1.2×10^6 rpm. This is near the experimentally determined maximum bearing speed range for devices with bearing anisotropy (marked by the shaded area).

Design Implications and Guidelines

Given the insight gained from the anisotropic gas bearing theory and the experimental results, the following bearing design implications are established:

1. In order to improve the dynamic behavior and to increase the whirl ratio, the difference in hydrostatic stiffness in the two orthogonal directions (anisotropy) should be maximized. This can be achieved (while maintaining adequate levels of average stiffness) by supplying hydrostatic feed air at different pressures over parts of the journal circumference.
2. The optimum circumferential extent over which bearing air is supplied should be determined to maximize the effect of hydrostatic stiffness anisotropy. In general, each of the two feed plena at the higher supply pressure should cover about one-third (that is, $\sim$110 deg) of the circumference.
3. In addition, the hydrodynamic stiffness of the journal bearing should be minimized. For a given bearing L/D, this can be done using the criteria established for isotropic bearing configurations by adjusting the clearance to radius ratio according to $C/R\approx2(L/D)^2$.
4. The mechanical design of the bearing air supply system and piping should be kept bisymmetric, and the pressure losses in the opposite feed systems should be matched to avoid any rotor side-load.
5. In general, as for any rotordynamic design, rotor unbalance should be kept low. However, anisotropic bearing designs enable a relief in fabrication tolerance requirements and a relaxation in rotor balancing constraints compared to their isotropic counterparts.

Summary and Conclusions

A novel axial-flow hydrostatic micro gas bearing concept was introduced that yields anisotropy in bearing stiffness. By breaking symmetry in hydrostatic stiffness, the bearing design increases bearing top speed and relieves fabrication tolerance requirements. This enables stable high-speed bearing operation and extends the bearing operating range.

Anisotropy in hydrostatic stiffness is achieved by blocking the bearing supply air over two circumferential sectors located opposite to each other. The two remaining circumferential sectors are fed with pressurized air from plena located on the aft side of the rotor. As a consequence, a difference in hydrostatic stiffness in the two orthogonal directions is introduced without substantially altering the cross-coupled hydrodynamic stiffness.

The anisotropic bearing configuration was investigated using a combination of numerical simulations, experiment, and simple, first-principles-based modeling of the gas bearing flow field and the rotordynamics. A simple description of the whirl instability threshold with stiffness anisotropy was derived explaining the instability mechanisms and linking the governing parameters to the whirl instability limit. The rotor speed at whirl instability onset is governed by the difference in hydrostatic stiffness in the two orthogonal directions (anisotropy) and the cross-coupled hydrodynamic stiffness. Although cross-coupled hydrodynamic forces always destabilize the system, the asymmetry in hydrostatic force due to anisotropy can balance the whirl inducing force. This enables a significantly increased whirl instability limit and, thus, higher bearing top speed. Furthermore, the fabrication tolerance requirements are relieved due to the altered gas bearing dynamic behavior.

An existing analytical hydrostatic gas bearing model [6] was extended and modified to account for stiffness anisotropy. Numerical simulations of the full nonlinear governing equations were conducted to validate the theory and to assess the performance of the novel bearing concept. The results show that the stable operating range can be extended and the bearing top speed can be increased by about a factor of 5 compared to an isotropic bearing configuration.

The effects of rotor unbalance and side-load in anisotropic bearing systems were investigated. It was found that both effects can decrease the whirl instability limit to lower speeds. Rotor unbalance alone has less of an effect, and the bearing dynamic behavior is robust to fabrication uncertainties. Rotor side-load detrimentally impacts both the difference in hydrostatic stiffness and the hydrodynamic stiffness such that the rotor speed at whirl instability onset is reduced.

Experimental results obtained from micro-bearing test devices were presented and the measured natural frequencies in the presence of bearing anisotropy showed good agreement with the model predictions. At the time of this paper, bearing top speeds between 1.1 and 1.3×10^6 rpm were achieved experimentally, which is corroborated by the theory limiting the stable operating range to the order of 1.2×10^6 rpm due to the effects of rotor unbalance and side-load.

Finally, using the anisotropic gas bearing theory and experimental results, design implications and guidelines for micro gas journal bearings with stiffness anisotropy were established.

Acknowledgment

The authors would like to thank Dr. F. Ehrich for the very useful comments and insightful discussions, Dr. S. Jacobson and C. J. Teo for testing the microbearing devices, and Dr. H. Li for his invaluable help and insight on microfabrication issues. This research was sponsored by DARPA and the U.S. Army Research Laboratory under the Collaborative Technology Alliance Program.

Nomenclature

a = rotor unbalance
α = circumferential extent of feed plena
C = journal bearing clearance, damping coefficient
D = bearing diameter
ε = eccentricity
F = fluid force on rotor
K_{xx} = direct-coupled hydrostatic stiffness coefficient
K_{xy} = cross-coupled hydrodynamic stiffness coefficient
k = rotor-speed-corrected stiffness coefficient K/Ω
L = bearing length
m = rotor mass
μ = viscosity
Ω, Ω_N = rotor frequency, natural frequency
Ω_w = rotor frequency at whirl instability onset
$\Delta p, p_o$ = bearing supply pressure, ambient pressure
$R, \Re$ = bearing radius, whirl ratio Ω_w/Ω_N
$s=j\Omega$ = Laplace variable
θ = circumferential angle
x, y = rotor deflections in X and Y directions
X, Y = stationary coordinate system
$\{\}^{hs}, \{\}^{hd}$ = hydrostatic, hydrodynamic
$\{\}^{dp}, \{\}^{\mathrm{sys}}$ = damping, system damping
$\{\}_o$ = nominal

References

[1] Larson, R., and Richardson, H., 1962, "A Preliminary Study of Whirl Instability for Pressurized Gas Bearings," ASME J. Basic Eng., **84**, pp. 511–520.
[2] Piekos, E., Orr, D., Jacobson, S., Ehrich, F., and Breuer, K., 1997, "Design and Analysis of Microfabricated High Speed Gas Journal Bearings," 28th *AIAA Fluid Dynamics Conference*, Snowmass Village, CO, AIAA Paper No. 97-1966.
[3] Ehrich, F., and Jacobson, S., 2003, "Development of High-Speed Gas Bearings for High-Power-Density Micro-Devices," ASME J. Eng. Gas Turbines Power, **125**, pp. 141–148.
[4] Epstein, A., 2004, "Micro-Engines-Scholar Lecture," ASME J. Turbomach., **5**(2), pp. 204–211.
[5] Fréchette, L., Jacobson, S., Breuer, K., Ehrich, F., Ghodssi, R., Khanna, R., Wong, C., Zhang, X., Schmidt, M., and Epstein, A., 2005, "High-Speed Microfabricated Silicon Turbomachinery and Fluid Film Bearings," J. Microelectromech. Syst., **14**(1), pp. 141–152.
[6] Liu, L., Teo, C., Epstein, A., and Spakovszky, Z., 2005, "Hydrostatic Gas Journal Bearings for Micro-Turbomachinery," ASME J. Vibr. Acoust., **127**(2), pp. 157–164.
[7] Lomakin, A., 1958, "Calculation of Critical Number of Revolutions and the Conditions Necessary for Dynamic Stability of Rotors in High-Pressure Hydraulic Machines When Taking into Account Forces Originating in Sealings," *Power and Mechanical Engineering* (in Russian).
[8] Lin, C., 1999, "Development of a Microfabricated Turbine-Driven Air Bearing Rig," Ph.D. thesis, Department of Aeronautics and Astronautics, MIT, Cambridge, MA.
[9] Spakovszky, Z., and Liu, L., 2005, "Scaling Laws for Ultra-Short Hydrostatic Gas Journal Bearings," ASME J. Vibr. Acoust., **127**(3), pp. 254–261.
[10] Fuller, D., 1969, "A Review of the State-of-the-Art for the Design of Self-Acting Gas-Lubricated Bearings," ASME J. Lubr. Technol., **91**(1), pp. 1–16.
[11] Garner, D., Lee, C., and Martin, F., 1980, "Stability of Profile Bore Bearings: Influence of Bearing Type Selection," Tribol. Int., **13**(5), pp. 204–210.
[12] Piekos, E., 2000, "Numerical Simulation of Gas-Lubricated Journal Bearings for Microfabricated Machines," Ph.D. thesis, Department of Aeronautics and Astronautics, MIT, Cambridge, MA.
[13] Kim, D., Lee, S., Bryant, M., and Ling, F., 2004, "Hydrodynamic Performance of Gas Microbearings," ASME J. Tribol., **126**, pp. 711–718.
[14] Smith, D., 1933, "Motion of a Rotor Carried by a Flexible Shaft in Flexible Bearings," Proc. R. Soc. London, Ser. A, **142**(864), pp. 92–118.
[15] Gunter, E., and Trumper, P., 1969, "The Influence of Internal Friction on the Stability of High Speed Rotors With Anisotropic Supports," ASME J. Eng. Ind., Nov., pp. 1105–1113.
[16] Ehrich, F., 1989, "The Role of Bearing Support Stiffness Anisotropy in Suppression of Rotordynamic Instability," *ASME DTC–12th Biennial Conference on Mechanical Vibration and Noise*, September, Montreal.
[17] Teo, C., and Spakovszky, Z., 2005, "Modeling and Experimental Investigation of Micro Hydrostatic Gas Thrust Bearings for Micro-Turbomachines," ASME Paper No. GT-2005-68222.
[18] Teo, C.-J., 2006, "MEMS Turbomachinery Rotordynamics: Modeling, Design and Testing," Ph.D. thesis, Department of Aeronautics and Astronautics, MIT, Cambridge, MA.

A Bulk Flow Model for Off-Centered Honeycomb Gas Seals

Thomas Soulas
Research Assistant

Luis San Andres
Mast-Childs Tribology Professor

Mechanical Engineering Department,
Texas A&M University,
College Station, TX 77843-3123

*A computational analysis for prediction of the static and dynamic forced performance of gas honeycomb seals at off-centered rotor conditions follows. The bulk-flow analysis, similar to the two-control volume flow model of Kleynhans and Childs (1997, "The Acoustic Influence of Cell Depth on the Rotordynamic Characteristics of Smooth-Rotor/Honeycomb-Stator Annular Gas Seals," ASME J. Eng. Gas Turbines Power, **119**, pp. 949–957), is brought without loss of generality into a single-control volume model, thus simplifying the computational process. The formulation accommodates the honeycomb effective cell depth, and existing software for annular pressure seals and is easily upgraded for damper seal analysis. An analytical perturbation method for derivation of zeroth- and first-order flow fields renders the seal equilibrium response and frequency-dependent dynamic force impedances, respectively. Numerical predictions for a centered straight-bore honeycomb gas seal shows good agreement with experimentally identified impedances, hence validating the model and confirming the paramount influence of excitation frequency on the rotordynamic force coefficients of honeycomb seals. The effect of rotor eccentricity on the static and dynamic forced response of a smooth annular seal and a honeycomb seal is evaluated for characteristic pressure differentials and rotor speeds. Leakage for the two seal types increases slightly as the rotor eccentricity increases. Rotor off-centering has a pronounced nonlinear effect on the predicted (and experimentally verified) dynamic force coefficients for smooth seals. However, in honeycomb gas seals, even large rotor center excursions do not sensibly affect the effective local film thickness, maintaining the flow azimuthal symmetry. The current model and predictions thus increase confidence in honeycomb seal design, operating performance, and reliability in actual applications.* [DOI: 10.1115/1.2227031]

Introduction

Interstage seals and balance piston seals are of importance in the rotordynamics of high performance turbomachinery. Field practice and laboratory experimentation show that annular damping gas seals (roughened stator/smooth rotor) offer more effective damping and reduced leakage than smooth-surface seals or labyrinth seals. Von Pragenau [1] first proposed to reduce cross-coupled forces with deliberately roughened stator surfaces and discussed the advantages of damping seals over smooth-surface annular and labyrinth seals. The superior rotordynamic performance of damping gas seals with low-cross coupled forces is derived from the reduction of circumferential flow and properly tuned fluid compressibility effects. The engineered seal design offers either high direct stiffness or high damping force coefficients at rotor frequencies of interest, such as, when traversing critical speeds. Thus, honeycomb stator/smooth rotor annular seals are currently employed to eliminate or reduce potential instabilities in centrifugal compressors and steam turbines.

Childs, Elrod, and Hale [2] present test results for leakage and rotordynamic coefficients for seven honeycomb seals. The rotordynamic coefficients show a considerable sensitivity to changes in honeycomb cell dimensions. Comparisons to labyrinth and smooth annular seals show the honeycomb seals to have the lowest leakages and improved rotordynamic stability, in particular for conditions of positive inlet fluid preswirl. Ha and Childs [3] measured tester friction factors in a flat plate for honeycomb surfaces and found optimum geometries as a function of cell width to depth and clearance to cell width ratios. Dawson, Childs, and Holt [4], and Dawson and Childs [5] present measurements of leakage and frequency dependent force impedances for smooth and honeycomb straight-bore and convergent tapered-bore annular gas seals. In general, the honeycomb seals demonstrate superior leakage control, substantially more direct stiffness, notably less destabilizing cross-coupled stiffness, and relatively less damping than smooth straight-bore annular seals. Most importantly, experimentally derived honeycomb seal impedance coefficients are strongly influenced by frequency, as opposed to those found in smooth surface annular seals.

Despite the favorable field experience with honeycomb seals, past efforts to develop accurate predictive analyses proved unsuccessful, mainly because of the inadequacy of the usual frequency-independent models for the seal reaction forces. Kleynhans and Childs [6] first forwarded a two-control-volume bulk-flow analysis for honeycomb seals and used the Blasius' friction factor coefficients to introduce the concept of effective cell depth, and predicted frequency-dependent stiffness and damping coefficients at the rotor centered position. The analysis, verified by extensive experimental evidence, was comprised of a conventional flow-through control volume coupled to a radial-flow only control volume representing the honeycomb cell, as illustrated in Fig. 1.

The deep control volume representing a honeycomb cell drops the effective acoustic velocity of the gas passing through the seal into the frequency range of interest for rotordynamics. At the rotor centered position, the Kleynhans and Childs' analysis introduced a general transfer function model of the form

$$-\begin{Bmatrix} F_X(j\omega) \\ F_Y(j\omega) \end{Bmatrix} = \begin{bmatrix} D(j\omega) & E(j\omega) \\ -E(j\omega) & D(j\omega) \end{bmatrix} \begin{Bmatrix} X(j\omega) \\ Y(j\omega) \end{Bmatrix} \tag{1}$$

where $D(j\omega)$ and $E(j\omega)$ are direct and cross-coupled impedance functions, respectively. Correspondingly, frequency-dependent

Contributed by the International Gas Turbine Institute (IGTI) of ASME for publication in the JOURNAL OF ENGINEERING FOR GAS TURBINES AND POWER. Manuscript received October 1, 2001; final manuscript received March 1, 2002. Review conducted by E. Benvenuiti. Paper presented at the International Gas Turbine and Aeroengine Congress and Exhibition, Amsterdam, June 3–6, 2002, Paper No. GT2002-30286.

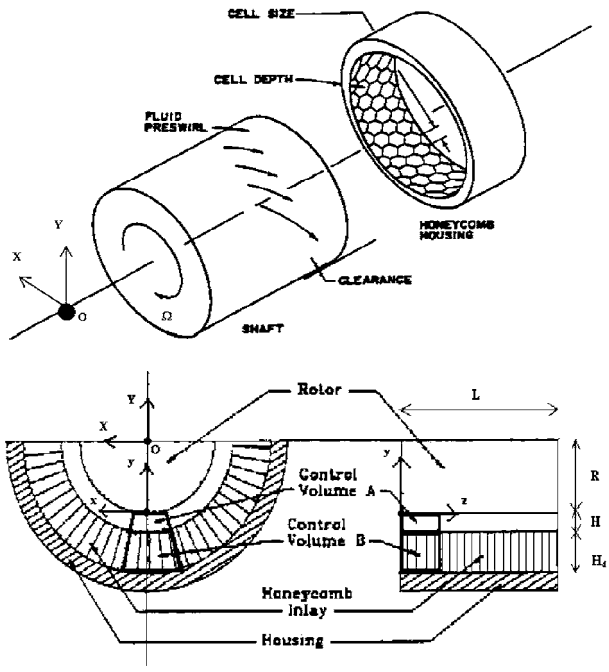

Fig. 1 Honeycomb annular seal and rotating shaft—Two control volume model

stiffness and damping coefficients are derived from the impedances real and imaginary components, i.e.,

$$D(j\omega) = K(\omega) + j\omega \cdot C(\omega) \tag{2}$$

and

$$E(j\omega) = k(\omega) + j\omega \cdot c(\omega) \tag{3}$$

Predictions from Kleynhans and Childs bulk-flow analysis agree well with measurements of leakage and dynamic impedances in centered honeycomb gas seals [4–7], and demonstrate the large effect of fluid compressibility and cell-depth and -volume on the generation of frequency-dependent dynamic force coefficients.

Presently, experimental and predictive computational efforts intend to extend and demonstrate the effectiveness of damping seals for off-centered rotor operation. Li, Kushner, and DeChoudhury [8] first show experimentally that leakage and effective force coefficients could be sensitive to the honeycomb seal eccentricity. The test results are derived from simple imbalance response measurements and used rudimentary identification techniques with no specified repeatability or uncertainty.

The current paper presents a computational analysis for prediction of the static and dynamic forced performance of gas honeycomb seals at eccentric rotor conditions. The bulk-flow analysis, similar to the two-control volume flow model of Kleynhans and Childs [6], is brought without loss of generality into a single-control volume model, thus simplifying the computational process. An analytical perturbation method for small amplitude rotor excursions about an off-centered position renders zeroth-order and first-order flow fields, which determine the seal leakage and frequency-dependent force impedances, respectively. The isothermal bulk-flow transport equations with Moody's friction factors are solved numerically using an efficient CFD algorithm.

Analysis

Figure 1 depicts the geometry of a honeycomb seal. The flow is confined to the annular region between an inner rotating shaft and a honeycomb stator. Large turbulence levels due to high axial pressure drops and high rotor speeds characterize the fluid flow across the seal. Furthermore, due to fluid inertia, pressure drops occur at the seal entrance and exit planes. The analysis regards the fluid as barotropic (isothermal ideal gas), and for simplicity, neglects energy transport considerations.

The Basic Equations. Kleynhans [7] models the gas bulk-flow using two control volumes, one for the flow through the annular region with small clearance (H), and a second one which connects the main flow to the deep honeycomb cell through a radial velocity (V). The governing bulk-flow equations are as follows:

Continuity and momentum transport for annular gap flow (control volume A)

$$\frac{\partial}{\partial t}(\rho H) + \frac{\partial}{\partial x}(\rho UH) + \frac{\partial}{\partial z}(\rho WH) + \rho V = 0 \tag{4}$$

$$-H\frac{\partial P}{\partial z} = \tau_z + \rho WV + \frac{\partial}{\partial t}(\rho WH) + \frac{\partial}{\partial x}(\rho UWH) + \frac{\partial}{\partial z}(\rho W^2 H) \tag{5}$$

$$-H\frac{\partial P}{\partial x} = \tau_x + \rho UV + \frac{\partial}{\partial t}(\rho UH) + \frac{\partial}{\partial x}(\rho U^2 H) + \frac{\partial}{\partial z}(\rho UWH) \tag{6}$$

Continuity equation for honeycomb cell flow (control volume B)

$$\rho V = H_d \frac{\partial \rho}{\partial t} \tag{7}$$

No momentum exchange is considered within the cell volume. In turbulent flows, the wall shear stress differences (τ_z and τ_x) are expressed in terms of the mean flow components through turbulence shear parameters (see Nomenclature).

Note that the effective honeycomb cell depth ($H_d \gg H$) is constant. Substituting (7) into Eqs. (4)–(6) eliminates the radial velocity (V), and renders the following single set of simpler bulk-flow equations:

$$\frac{\partial}{\partial t}[\rho(H + H_d)] + \frac{\partial}{\partial x}(\rho UH) + \frac{\partial}{\partial z}(\rho WH) = 0 \tag{8}$$

$$-H\frac{\partial P}{\partial z} = \frac{\mu}{H}(k_z W) + \left[\frac{\partial}{\partial t}(\rho WH) + W\frac{\partial}{\partial t}(\rho H_d) + \frac{\partial}{\partial x}(\rho UWH) + \frac{\partial}{\partial z}(\rho W^2 H)\right] \tag{9}$$

$$-H\frac{\partial P}{\partial x} = \frac{\mu}{H}\left(k_x U - k_r \frac{R\Omega}{2}\right) + \left[\frac{\partial}{\partial t}(\rho UH) + U\frac{\partial}{\partial t}(\rho H_d) + \frac{\partial}{\partial x}(\rho U^2 H) + \frac{\partial}{\partial z}(\rho UWH)\right] \tag{10}$$

The turbulent shear parameters (k_z, k_x, k_r) are local functions of the friction factors (f_r and f_s) relative to the rotor and stator surfaces. Presently, Moody's friction factor formulas are used for simplicity, albeit other relationships, such as Blasius', could be easily implemented.

Note that Eqs. (8)–(10) are similar to those forwarded for variable fluid properties annular seals [9], except that the effective honeycomb cell depth (H_d) introduces additional temporal variations affecting the dynamics of the bulk flow. The equations show that the honeycomb cell depth has an effect only for a compressible fluid.

Presently, the fluid properties are general functions of the local pressure and a mean temperature (T^*) uniform within the flow region, i.e.,

$$\rho = \rho(P, T^*);\ \mu = \mu(P, T^*) \tag{11}$$

The boundary conditions for the bulk-flow velocity and pressure fields on the closure of the flow region are:

(a) The pressure and velocity fields are continuous and single-valued in the circumferential direction (x).

(b) The local acceleration of fluid from relatively stagnant conditions at the upstream seal region to a high velocity at the seal inlet causes a sudden pressure drop, and modeled by a simple Bernoulli equation,

$$P_i = P|_{z=0} = P_S + \frac{\rho}{2}(1+\xi)\, W^2|_{z=0} \tag{12}$$

(c) Additionally, depending on upstream conditions, the entrance circumferential velocity into the seal is

$$U|_{z=0} = \beta R\Omega \tag{13}$$

where β is a preswirl factor.

(d) At the seal exit plane, $z=L$, an end restriction coefficient models additional pressure losses [10]:

$$P_e = P|_{z=L} = P_D + \frac{\rho}{2} C_S\, W^2|_{z=L} \tag{14}$$

Perturbation Analysis, Dimensionless Equations, Leakage, and Dynamic Force Coefficients. At steady-state conditions, the rotor center coordinates are (e_{X0}, e_{Y0}) relative to the seal stator center. Superimposed on this static equilibrium position, the rotor describes closed motions of frequency (ω) and small amplitudes, (Δe_X) and (Δe_Y). The film thickness (H) is given by the real part of

$$H = H_0 + e^{j\omega t}(\Delta e_X \cos\theta + \Delta e_Y \sin\theta) = h \cdot c^*;$$

$$H_0 = c^* + e_{X0}\cos\theta + e_{Y0}\sin\theta \tag{15}$$

For small amplitude rotor motions, velocity, and pressure fields, as well as fluid properties and shear coefficients are expressed as the sum of a zeroth-order and first-order complex fields, describing the equilibrium condition and the perturbed motions, i.e.

$$\phi = \phi_0 + e^{j\omega t}(\Delta e_X \phi_X + \Delta e_Y \phi_Y) \tag{16}$$

with $\phi = \{P, U, W, k_x, k_z, \ldots\}$.

Substitution of the flow variables (16) into the governing Eqs. (8)–(10) and boundary conditions (12)–(14) yields the differential equations for the zeroth- and first-order flow fields. The zeroth-order equations are identical to the ones derived by San Andrés [9]. That is, the honeycomb cell depth (H_d) does not affect directly the equilibrium flow equations, although it largely influences the friction factors. The Appendix lists the first-order flow equations accounting for the effective honeycomb cell depth (H_d).

San Andrés [9] details the finite volume CFD method implemented to solve the nonlinear partial differential equations governing the flow. The procedure follows the scheme advanced by Launder and Leschziner [11] with the SIMPLE Consistent algorithm of Van Doormal and Raithby [12] to accelerate convergence. The algorithm does account for fluid density corrections to insure fast and accurate solutions at arbitrary excitation frequencies.

The zeroth-order solution determines the steady-state pressure and velocity fields. The seal mass flow rate or leakage (Q) is

$$Q = \frac{\rho^* c^{*3} \Delta P}{\mu^*} \int_0^{2\pi} (\bar{\rho} w h)_0|_{\bar{z}=L/R} d\bar{x} \tag{17}$$

The perturbation analysis renders the seal static and dynamic reaction forces as

$$-\begin{Bmatrix} F_X(j\omega) \\ F_Y(j\omega) \end{Bmatrix} = -\begin{Bmatrix} F_{X0} \\ F_{Y0} \end{Bmatrix} + \begin{bmatrix} D(j\omega) & E(j\omega) \\ G(j\omega) & F(j\omega) \end{bmatrix} \begin{Bmatrix} X(j\omega) \\ Y(j\omega) \end{Bmatrix} \tag{18}$$

where integration of the complex first-order pressure fields over the rotor surface gives the direct (D,F) and cross-coupled (E,G) force impedances,

$$D = \Delta P \frac{R^2}{c^*} \int_0^{L/R} \int_0^{2\pi} p_X h_X d\bar{x}\, d\bar{z} \quad E = \Delta P \frac{R^2}{c^*} \int_0^{L/R} \int_0^{2\pi} p_Y h_X d\bar{x}\, d\bar{z}$$

$$F = \Delta P \frac{R^2}{c^*} \int_0^{L/R} \int_0^{2\pi} p_Y h_Y d\bar{x}\, d\bar{z} \quad G = \Delta P \frac{R^2}{c^*} \int_0^{L/R} \int_0^{2\pi} p_X h_Y d\bar{x}\, d\bar{z} \tag{19}$$

with $h_X = \cos\theta$ and $h_Y = \sin\theta$. The real part of the first-order pressure fields gives rise to the dynamic stiffness coefficients, while its imaginary part renders the damping coefficients, i.e.

$$D(j\omega) = K_{XX}(\omega) + j\omega \cdot C_{XX}(\omega) \quad E(j\omega) = K_{XY}(\omega) + j\omega \cdot C_{XY}(\omega)$$

$$F(j\omega) = K_{YY}(\omega) + j\omega \cdot C_{YY}(\omega) \quad G(j\omega) = K_{YX}(\omega) + j\omega \cdot C_{YX}(\omega) \tag{20}$$

Note that for concentric rotor position $(e_{X0} = e_{Y0} = 0)$, $D = F$ and $E = -G$.

Table 1 Test straight-bore honeycomb seal: geometry and operating conditions. Fluid: Air.

Parameter	Magnitude
Diameter, D	114.3 mm
Length, L	85.7 mm
Radial clearance, c^*	0.19 mm
Effective cell depth, H_d	2.20 mm
Rotor speed	15,200 rpm (medium)
Supply pressure, P_S	12.1×10^5 Pa (medium)
Discharge pressure, P_D	6.05×10^5 Pa (50% pressure ratio, P_D/P_S)
Inlet Temperature, T^*	302.4 K
Gas supply density, ρ_S	13.94 kg/m^3
Gas discharge density, ρ_D	6.97 kg/m^3
Gas viscosity, μ	18.57×10^{-6} N s/m^2
Relative surface roughness, $\bar{r}$	Rotor: 0.001 (smooth) Stator: 0.4 (honeycomb)
Moody's friction parameters	$a_M = 0.001375$, $b_M = 5 \times 10^5$ $e_M = 0.333$
Entrance loss coefficient	$\xi = 0$
Exit discharge seal coefficient	$C_S = 0$
Inlet preswirl ratio	$\beta = 0$

Comparison of Current Model Predictions to Experimental Data for Centered Rotor Condition. To test the validity of the analysis, comparisons follow with experimental data reported by Dawson and Childs [5] and predictions using Kleynhans' model [6]. Table 1 lists the geometry parameters and operating conditions for a straight-bore honeycomb gas (air) seal [medium-speed (MS), medium-pressure (MP), 50% pressure ratio]. The seal clearance is 0.19 mm, and the honeycomb cell depth and width are 3.1 mm and 0.79 mm, respectively, resulting into an effective cell depth (H_d) of 2.2 mm. The ratio of the total honeycomb cell volume to the seal surface area defines the effective depth.

In general, the leakage flow rate predictions conform well to the measured leakage rates. Both Kleynhans model[1] and the present one overpredict the measured seal leakage flow rate by 10% maximum.

As per the evaluation of the frequency-dependent rotordynamic coefficients, Fig. 2 shows the measured and predicted real and imaginary parts of the direct (D) and cross-coupled (E) impedances versus excitation frequency. Note that the uncertainty of the dynamic impedances measurements is about 0.15 MN/m [4,5].

Experimental values and predictions show the large influence of the excitation frequency on the rotordynamic coefficients. Both models give good qualitative trends for the dynamic force impedances with respect to the excitation frequency over the range con-

[1]The empirical values for the Blasius' rotor and stator friction coefficient parameters used in Kleynhans' model are $n_r = 0.0586$, $m_r = -0.2170$, $n_s = 0.0785$, and $m_s = -0.1101$ respectively.

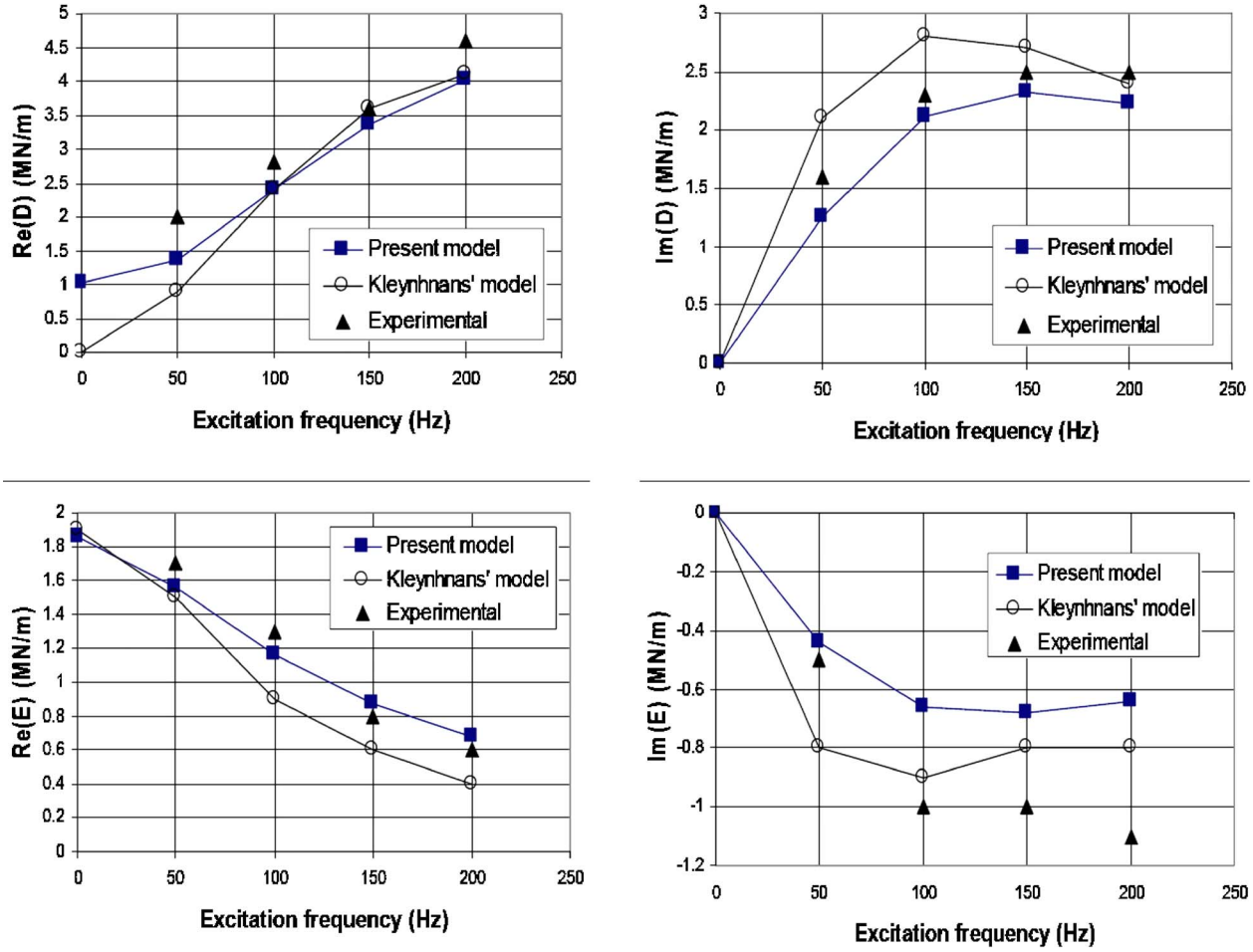

Fig. 2 Measured and predicted (real and imaginary parts) dynamic impedances (*D*) and (*E*) for a honeycomb seal versus excitation frequency. Medium speed/medium pressure (P_D/P_S=0.50), rotor centered condition (ε=0).

sidered. The real part of the direct impedance (D) increases rapidly with frequency, while the real part of the cross-coupled impedance (E) appears to decrease linearly. Both models predict maximum and minimum values for the imaginary parts of the direct (D) and cross-coupled (E) impedances, respectively. The present analysis provides slightly better quantitative correlations with the experimental data than Kleynhan's model. On average, the relative difference between the current predictions and the experimental values is 15% for the real part of the direct (D) impedance, 10% for the real part of the cross-coupled (E) impedance, and 10% for the imaginary part of the direct (D) impedance. Comparisons to other test operating conditions given in [5] lead to similar conclusions, and not shown here for brevity.

Effect of Rotor Eccentricity on the Dynamic Forced Performance of Honeycomb Gas Seals. The prior analysis [5,6] predicts honeycomb seal performance at a rotor centered position. The present analysis allows prediction of the static and dynamic forced performance of gas honeycomb seals at off-centered rotor conditions, including shaft misalignment and dynamic moment coefficients (not reported for brevity). In the absence of published experimental data[2] for off-centered honeycomb gas seals, numerical predictions to determine the effect of rotor eccentricity on the forced response of honeycomb gas seals follow.

Table 1 lists the characteristics of the straight-bore smooth rotor/honeycomb stator seal considered. Table 2 details the operating conditions for which predictions ensue. The notation MSMP corresponds to a medium rotor speed and medium supply pressure configuration, for example.

Comparisons of leakage and frequency-dependent dynamic

Table 2 Operating conditions for honeycomb seal at 50% pressure ratio (P_D/P_S=0.50)

	Configuration	Rotor speed (rpm)	Synchronous frequency (Hz)
LS	Low Speed	10,200	170
MS	Medium Speed	15,200	253
HS	High Speed	20,200	337
	Configuration	Supply pressure (bar)	Discharge pressure (bar)
LP	Low Pressure	6.9	3.45
MP	Medium Pressure	12.1	6.05
H P	High Pressure	17.2	8.60
	Configuration	Supply density (kg/m^3)	Discharge density (kg/m^3)
LP	Low Pressure	8.0	4.0
MP	Medium Pressure	13.9	7.0
HP	High Pressure	19.8	9.9

[2]Weatherwax [15] presents honeycomb seal test results for increasing rotor eccentricities with comparisons to predictions from the present model.

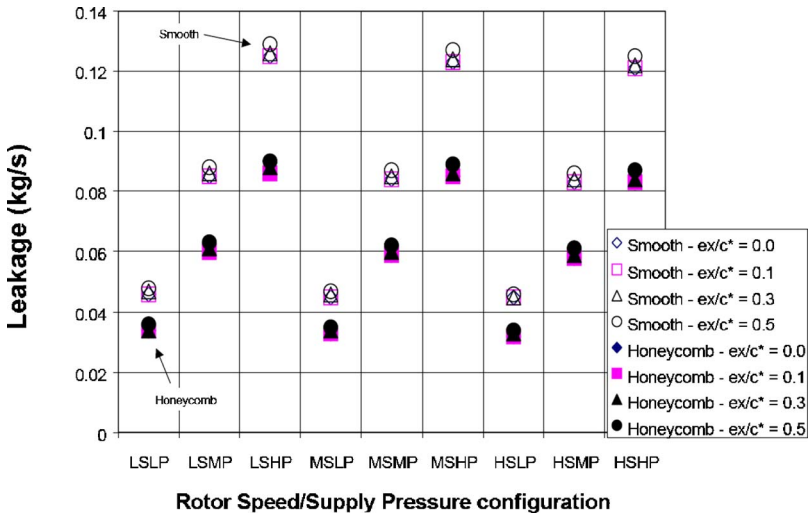

Fig. 3 Leakage (Q) predictions versus rotor speed/supply pressure for smooth and honeycomb gas seals (P_D/P_S=0.50), rotor eccentricity ratio (e_X/c^*) increases

force coefficients are made for predictions to a similar smooth rotor/smooth stator seal configuration (identical radial clearance, length and diameter, and operating conditions). Predictions follow for eccentricity ratios $\varepsilon_{X0}=\varepsilon=0.0$, 0.1, 0.3, and 0.5, while $\varepsilon_{Y0}=0.0$. Percentile variations refer to parameters evaluated at the centered condition ($\varepsilon=0$).

Leakage. Figure 3 shows evidence of one of the advantages of honeycomb seals over smooth seals, namely smaller leakages. The reduction in flow rate is due to the higher relative roughness of the honeycomb stator surface. For both smooth and honeycomb seals the leakage increases slightly when increasing the eccentricity ratio (5% difference for an eccentricity ratio of 0.5). Yang, San Andrés, and Childs [13] predict the same trend for smooth annular gas seals, and compare well with test data for water annular seals [14].

Dynamic Direct Stiffness Coefficients. Figure 4 illustrates the influence of excitation frequency, for increasing rotor eccentricities, on the dynamic direct stiffness coefficient $K_{XX}=\mathrm{Re}(D)$ of both seals. The effect is more pronounced for the honeycomb seal. For different operating conditions, the impact of eccentricity on the direct stiffness is reduced as the excitation frequency increases. Further predictions not presented for brevity, show that except for the low pressure condition, rotor eccentricity does not have a large influence on the direct stiffness coefficients (K_{XX}) and (K_{YY}), for both seals (15% difference at $\varepsilon=0.5$ for the honeycomb seal). Note that at high frequencies, honeycomb seals render larger direct stiffnesses. Rotor eccentricity sensibly affects the smooth seal direct stiffness coefficients for the medium and high pressure cases (maximum 75% difference for 50% eccentricity ratio in the HSHP configuration at 700 Hz). However, current bulk flow models usually tend to underpredict the effect of rotor eccentricity on (liquid) smooth seal forced performance [14].

Figure 5 presents both direct stiffness coefficients (K_{XX} and K_{YY}) versus excitation frequency at an eccentricity ratio (ε) of 50% for the LSLP configuration. The predictions show again that for honeycomb seals, unlike in smooth seals, the influence of rotor eccentricity is small.

Dynamic Cross-Coupled Stiffness Coefficients. Off-centered honeycomb seal cross-coupled stiffness coefficients [$K_{XY}=\mathrm{Re}(E)$ and $K_{YX}=\mathrm{Re}(G)$] depend sensibly on the excitation frequency, as illustrated in Fig. 6 for K_{XY}. Similar trends follow for K_{YX}. However, except at very low frequencies, the higher the eccentricity ratio, the smaller the cross-coupled stiffness coefficient (20% difference for $\varepsilon=0.5$). However, note that for the smooth seal, the cross-coupled stiffness increases rapidly with frequency (40%

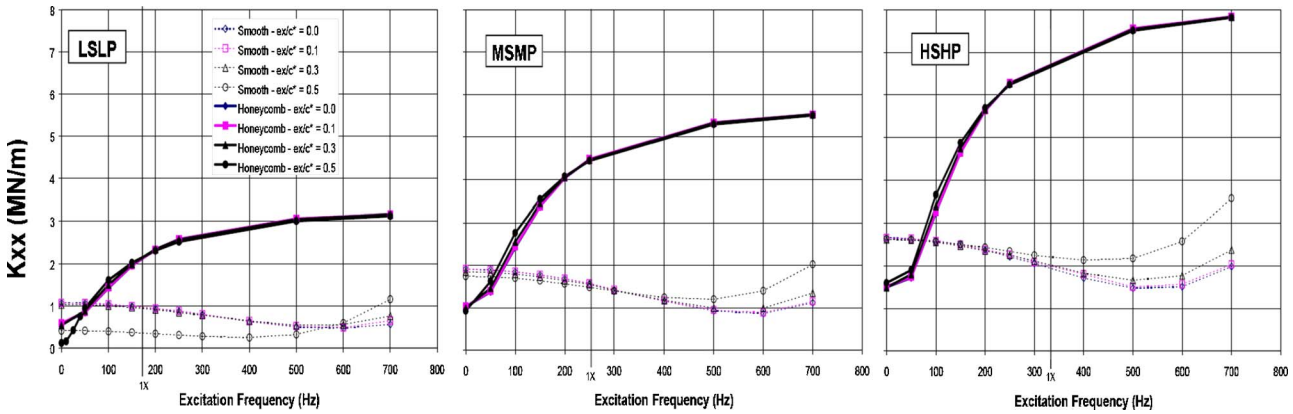

Fig. 4 Dynamic direct stiffness coefficient $K_{XX}=\mathrm{Re}(D)$ versus excitation frequency for smooth and honeycomb seals (P_D/P_S=0.50) as a function of rotor eccentricity (e_X/c^*)—LSLP, MSMP, and HSHP configurations

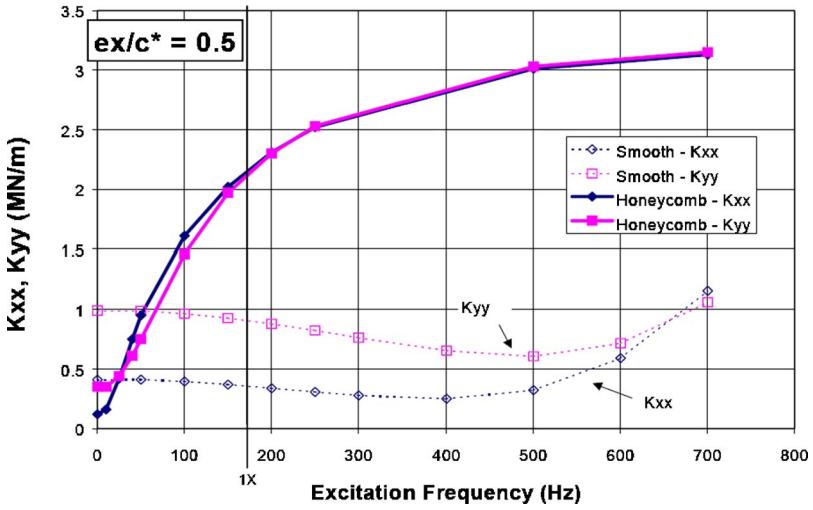

Fig. 5 Dynamic direct stiffness coefficients K_{XX}=Re(D) and K_{YY}=Re(F) versus excitation frequency for smooth and honeycomb seals (P_D/P_S=0.50), eccentricity ratio e_X/c^*=0.5—LSLP configuration

larger for 50% eccentricity ratio). Figure 6 also emphasizes the main advantage of honeycomb seals over smooth seals, i.e., reduced cross-coupled effects and better stability characteristics.

Figure 7 presents the cross-coupled stiffness coefficients ($K_{XY}, -K_{YX}$) versus frequency at eccentricity ratio (ε) equal to 0.5 for the LSLP configuration. The predictions show the honeycomb seal coefficient asymmetry to decrease as the excitation frequency increases. The larger smooth seal cross-coupled stiffness coefficients are apparent over the whole frequency range.

Dynamic Direct Damping Coefficients. For the honeycomb seal, rotor eccentricity does not have a noteworthy influence on the coefficients, ωC_{XX}=Im(D) and ωC_{YY}=Im(F), as shown in Fig. 8 for ωC_{XX}, with at most a 10% difference for an eccentricity ratio of 0.5. On the other hand, for the smooth seal, a 50% rotor eccentricity increases by 20% the magnitude of the direct damping coefficients. Also note that the honeycomb seal renders less direct damping than the smooth seal, whose direct damping coefficient (C_{XX}) is nearly constant over the frequency range displayed (i.e., linear variation of ωC_{XX} with respect to ω). The other direct damping coefficient (ωC_{YY}) shows similar features.

Figure 9 presents both direct coefficients ($\omega C_{XX}, \omega C_{YY}$) versus excitation frequency (ε=0.5) for the LSLP configuration. The predictions for the smooth seal show the characteristic asymmetry, which is less important for the honeycomb seals. The dynamic cross-coupled coefficients ($\omega C_{XY}, \omega C_{YX}$) are usually small, even for large frequencies (up to 700 Hz), and do not affect the seal dynamic forced performance. Effective stiffness and damping coefficients defined as

$$K_{X\,\mathrm{eff}} = \mathrm{Re}(D) + \mathrm{Im}(E) = K_{XX} + \omega C_{XY};$$

$$K_{Y\,\mathrm{eff}} = \mathrm{Re}(F) - \mathrm{Im}(G) = K_{YY} - \omega C_{YX} \tag{21}$$

and

$$C_{X\,\mathrm{eff}} = [\mathrm{Im}(D) - \mathrm{Re}(E)]/\omega = C_{XX} - K_{XY}/\omega;$$

$$C_{Y\,\mathrm{eff}} = [\mathrm{Im}(F) + \mathrm{Re}(G)]/\omega = C_{YY} + K_{YX}/\omega \tag{22}$$

are useful for comparing the rotordynamic performance of the two seals. Figures 10 and 11 show the effective stiffness ($K_{X\mathrm{eff}}$) and damping ($C_{X\mathrm{eff}}$) coefficients for both seals versus excitation frequency and increasing rotor eccentricities. Note that rotor off centering largely affects the smooth seal coefficients, with a reduction in stiffness and an increase in damping at high frequencies. Conversely, the honeycomb seals show the characteristic "hardening" effect at large frequencies, with a characteristic "break" frequency [5] for maximum effective damping.

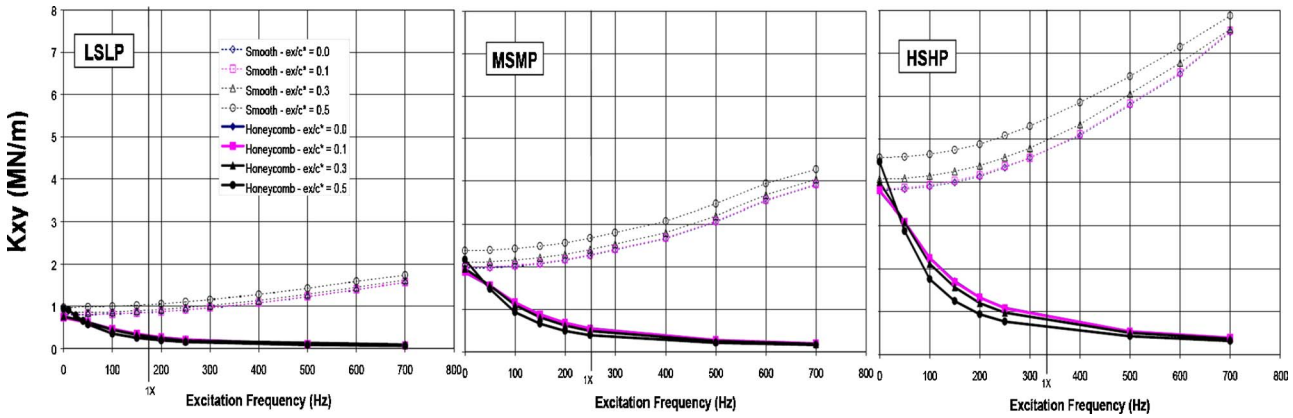

Fig. 6 Dynamic cross-coupled stiffness coefficient K_{XY}=Re(E) versus excitation frequency for smooth and honeycomb seals (P_D/P_S=0.50) as a function of rotor eccentricity (e_X/c^*)—LSLP, MSMP, and HSHP configurations

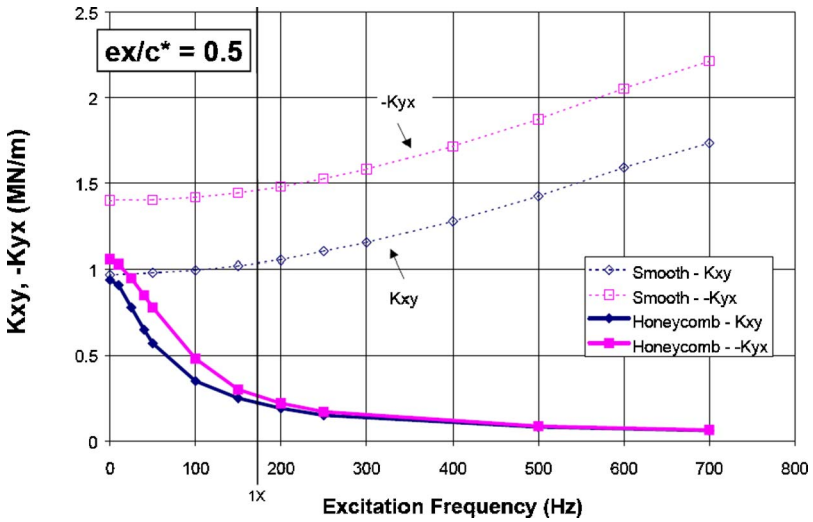

Fig. 7 Dynamic cross-coupled stiffness coefficients K_{XY}=Re(E) and $-K_{YX}$=−Re(G) versus excitation frequency for smooth and honeycomb seals, (P_D/P_S=0.50) and eccentricity ratio e_X/c^*=0.5—LSLP configuration

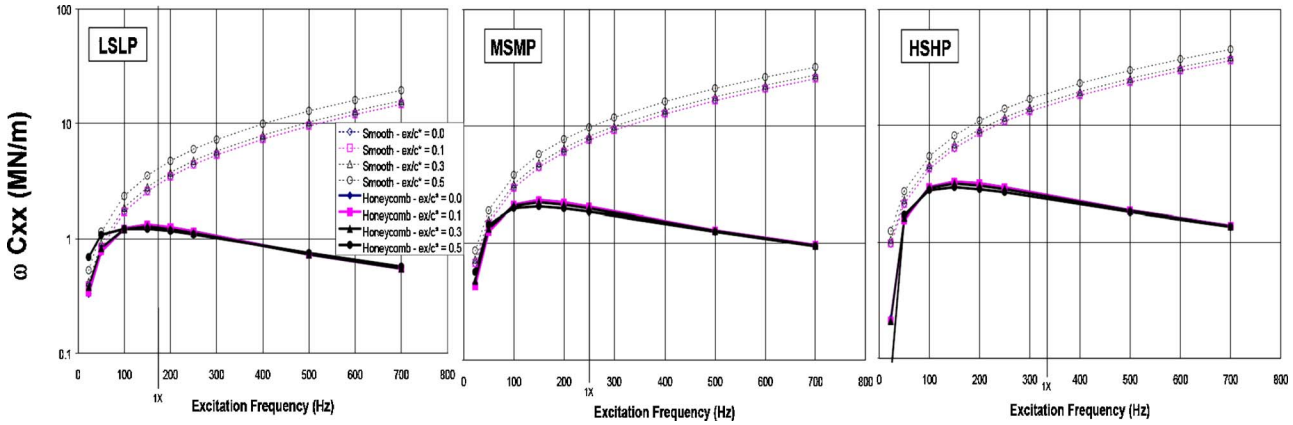

Fig. 8 Coefficient ωC_{XX}=Im(D) versus excitation frequency for smooth and honeycomb seals (P_D/P_S=0.50) as a function of rotor eccentricity (e_X/c^*)—LSLP, MSMP, and HSHP configurations

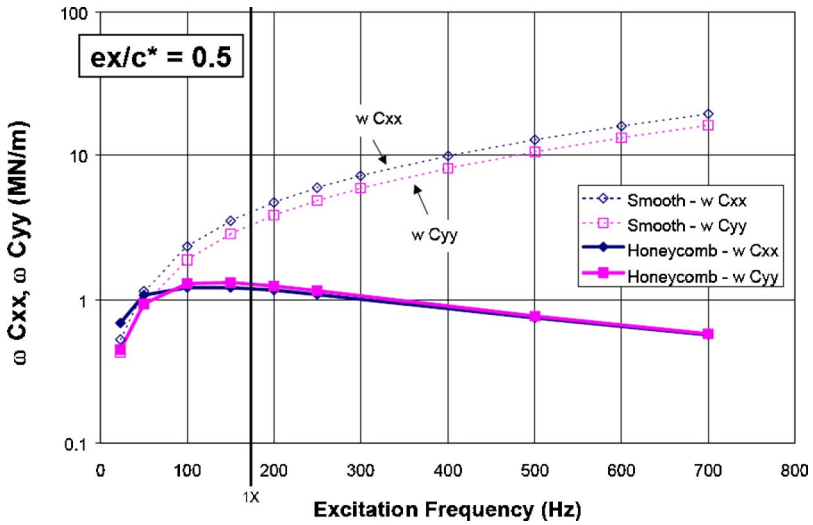

Fig. 9 Coefficients ωC_{XX}=Im(D) and ωC_{YY}=Im(F) versus excitation frequency for smooth and honeycomb seals, (P_D/P_S=0.50) and eccentricity ratio e_X/c^*=0.5—LSLP configuration

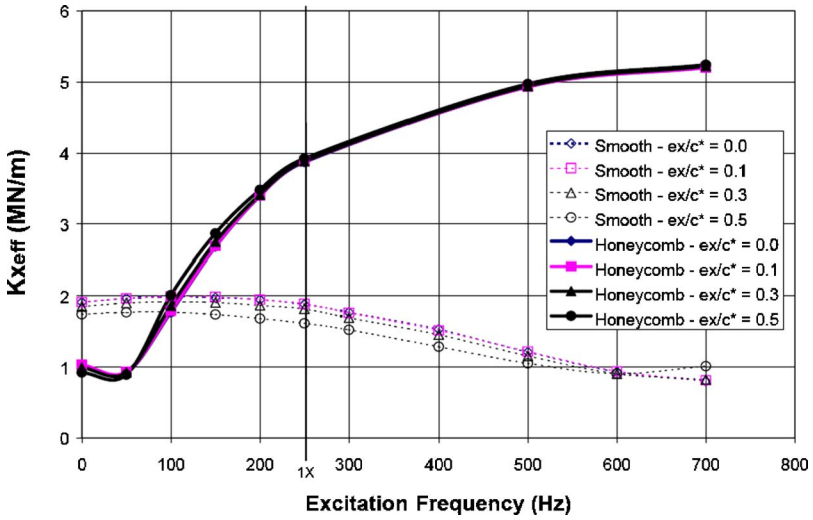

Fig. 10 Effective stiffness coefficient (K_{Xeff}) versus excitation frequency for smooth and honeycomb seals (P_D/P_S=0.50) as a function of rotor eccentricity (e_X/c^*). MSMP configuration

Conclusions

The analysis advances a bulk-flow model to predict the static and dynamic frequency-dependent forced performance characteristics of gas honeycomb seals at off-center rotor positions. The single control volume formulation includes the honeycomb effective cell depth on the perturbed (first-order) flow equations, which are otherwise similar to existing computational bulk-flow models for annular pressure seals.

Numerical predictions for a centered straight-bore test honeycomb gas seals (3.1 mm cell depth and 0.79 mm cell width) show good agreement with experimental results, thus validating the model and confirming the influence of excitation frequency on the rotordynamic coefficients of honeycomb seals.

As for the effect of rotor eccentricity on the performance of honeycomb gas seals, comparisons are made with predictions for a similar smooth surface seal under the same operating conditions. Leakage for the two seals increases as the rotor eccentricity increases (5% difference for an eccentricity ratio of 0.5). The influence of rotor eccentricity on the dynamic force coefficients of the honeycomb seal depends on the excitation frequency, though it appears to be rather mild. That is, the honeycomb seal impedances do not differ greatly as the rotor static excursion increases; the dynamic direct and cross-coupled stiffness and direct damping coefficients vary by up to 15%, 20% and 10%, respectively, for an eccentricity ratio of 0.5. However, rotor eccentricity does have a pronounced effect on the predicted (and experimentally verified) dynamic force coefficients for smooth seals (the direct and cross-coupled stiffness and direct damping coefficients vary by 75%, 40%, and 20%, respectively, for a 50% eccentricity ratio).

The minimal influence of rotor eccentricity on the dynamic force coefficients of honeycomb seals is due to the honeycomb cell depth, which is several times the seal radial clearance. Hence, even large rotor eccentricities do not sensibly affect the effective local film thickness and maintain the flow circumferential symmetry. Thus, rotor eccentricity does not greatly affect the dynamic force coefficients in a honeycomb seal. Recent experiments [15] confirm the current computational predictions. The present analysis could also be applied to round-hole pattern damping seals since the effective cell depth concept comprises the hole-depth and hole-density on the seal surface.

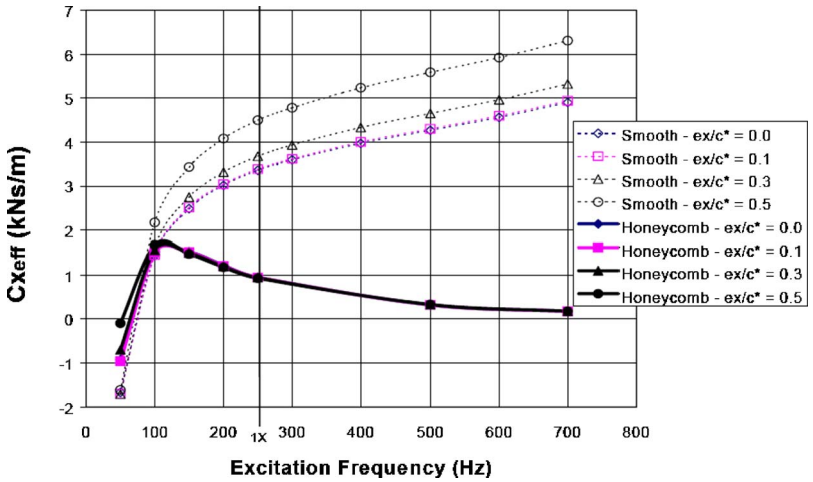

Fig. 11 Effective damping coefficient (C_{Xeff}) versus excitation frequency for smooth and honeycomb seals (P_D/P_S=0.50) as a function of rotor eccentricity (e_X/c^*). MSMP configuration

Acknowledgment

Thanks to Professor Dara Childs for his encouragement to advance the analysis and engineering practice of honeycomb gas seals.

Nomenclature

a_M, b_M, e_M = coefficients in Moody's friction factor formula
C, C_{XX}, C_{YY} = direct damping coefficients (N s/m)
C_S = end seal discharge coefficient
c, C_{XY}, C_{YX} = cross-coupled damping coefficients (N s/m)
c^* = typical seal radial clearance (m)
D, F = direct force impedances (N/m)
E, G = cross-coupled force impedances (N/m)
e_X, e_Y = rotor eccentricity components (m)
F_X, F_Y = seal reaction force components (N)
f_r = Moody's friction factor at rotor$=a_M[1+(10^4.r_r/H+b_M/\mathrm{Re}_r)^{e_M}]$
f_s = Moody's friction factor at stator$=a_M[1+(10^4.r_s/H+b_M/\mathrm{Re}_s)^{e_M}]$
H = seal film thickness (m)
h = dimensionless seal film thickness$=H/c^*$
H_d = effective honeycomb cell depth (m)
h_d = dimensionless honeycomb cell depth$=H_d/c^*$
j = imaginary unit ($j^2=-1$)
K, K_{XX}, K_{YY} = direct stiffness coefficients (N/m)
k, K_{XY}, K_{YX} = cross-coupled stiffness coefficients (N/m)
k_r, k_s = turbulent shear parameter at rotor and stator surfaces$=f_r.\mathrm{Re}_r, f_s.\mathrm{Re}_s$
k_x, k_z = circumferential and axial flow shear parameters$=(k_r+k_s)/2$
L = seal axial length (m)
P = pressure (Pa), $p=(P-P_D)/\Delta P$
P_D, P_S = discharge and supply pressures (Pa)
Q = seal leakage or flowrate (kg/s)
R = rotor (journal) radius (m)
r_r, r_s = mean surface roughness at rotor and stator (m)
$\bar{r}_r$, $\bar{r}_s$ = relative surface roughness at rotor and stator. $\bar{r}_r=r_r/H$, $\bar{r}_s=r_s/H$
Re_P^* = characteristic Reynolds number$=(\rho^*.c^{*3}.\Delta P)/(\mu^{*2}.R)c^*/R$
Re_r, Re_s = Reynolds numbers relative to rotor and stator surfaces$=(\rho/\mu)H[(U-R\Omega)^2+W^2]^{1/2}$, $(\rho/\mu)H[U^2+W^2]^{1/2}$
T^* = supply gas temperature (K)
t = time (s)
U = circumferential bulk-flow velocity (m/s) $u=(U.\mu^*.R)/(c^{*2}.\Delta P)$
V = radial bulk-flow velocity from annular gap to honeycomb cell (m/s)
W = axial bulk-flow velocity (m/s), $w=(W.\mu^*.R)/(c^{*2}.\Delta P)$
X, Y = Cartesian coordinate system (m)
x, y, z = circumferential, radial, and axial coordinates in plane of flow (m)
β = inlet velocity preswirl factor
ΔP = pressure differential$=P_S-P_D$ (Pa)
ε_X, ε_Y = dimensionless rotor eccentricities. $(e_X,e_Y)/c^*$
μ = gas viscosity (N s/m^2)
ξ = empirical entrance loss coefficient
ρ = gas density (kg/m^3)
τ_z = axial wall shear stress function$=\mu k_z W/H$ (N/m^2)
τ_x = circumferential wall shear stress difference function$=\mu(k_x U-k_r R\Omega/2)/H$ (N/m^2)
τ = dimensionless time$=\omega t$
Ω = rotor speed (rad/s)
ω = excitation frequency (rad/s)

Subscripts and Superscripts

0 = zeroth-order fields
α = first-order fields, X, Y directions
e = seal exit plane
i = seal inlet plane
eff = effective coefficients
$*$ = characteristic value at supply condition

Appendix: First-Order Governing Bulk-Flow Equations

The first-order bulk-flow continuity, axial and circumferential momentum transport equations for honeycomb seal analysis are, in dimensionless form:

$$\frac{\partial}{\partial \bar{x}}(\bar{\rho}_0 h_0 u_\alpha + \bar{\rho}_0 u_0 h_\alpha + u_0 h_0 \bar{\rho}_\alpha) + \frac{\partial}{\partial \bar{z}}(\bar{\rho}_0 h_0 w_\alpha + \bar{\rho}_0 w_0 h_\alpha + w_0 h_0 \bar{\rho}_\alpha) = -j\sigma[\bar{\rho}_0 h_\alpha + (h_0 + h_d)\bar{\rho}_\alpha] \tag{A1}$$

$$-h_0 \frac{\partial p_\alpha}{\partial \bar{z}} = j\bar{\rho}_0 h_0 \,\mathrm{Re}_S\, w_\alpha + \gamma_{zx} u_\alpha + \gamma_{zz} w_\alpha + \gamma_{zc} h_\alpha + \gamma_{z\mu}\bar{\mu}_\alpha + (\gamma_{z\rho} + j\,\mathrm{Re}_S\, w_0 h_d)\bar{\rho}_\alpha + \mathrm{Re}_P^*\left\{ \frac{\partial}{\partial \bar{x}}(\bar{\rho}_0 h_0 u_0 w_\alpha) + \frac{\partial}{\partial \bar{z}}(\bar{\rho}_0 h_0 w_0 w_\alpha) + \bar{\rho}_0 h_0 \left[u_\alpha \frac{\partial w_0}{\partial \bar{x}} + w_\alpha \frac{\partial w_0}{\partial \bar{z}} \right] \right\} \tag{A2}$$

$$-h_0 \frac{\partial p_\alpha}{\partial \bar{x}} = j\bar{\rho}_0 h_0 \,\mathrm{Re}_S\, u_\alpha + \gamma_{xx} u_\alpha + \gamma_{xz} w_\alpha + \gamma_{xc} h_\alpha + \gamma_{x\mu}\bar{\mu}_\alpha + (\gamma_{x\rho} + j\,\mathrm{Re}_S\, u_0 h_d)\bar{\rho}_\alpha + \mathrm{Re}_P^*\left\{ \frac{\partial}{\partial \bar{x}}(\bar{\rho}_0 h_0 u_0 u_\alpha) + \frac{\partial}{\partial \bar{z}}(\bar{\rho}_0 h_0 w_0 u_\alpha) + \bar{\rho}_0 h_0 \left[u_\alpha \frac{\partial u_0}{\partial \bar{x}} + w_\alpha \frac{\partial u_0}{\partial \bar{z}} \right] \right\} \tag{A3}$$

where $\sigma=(\mu^*\cdot\omega\cdot R^2)/(c^*\cdot\Delta P)$ and $\mathrm{Re}_S=(\rho^*\cdot\omega\cdot c^{*2})/\mu^*$ represent a characteristic frequency number and squeeze film Reynolds number, respectively. The coefficients ($\gamma_{\Phi\Psi}$) arise from the perturbation of the shear stress factors (k_x, k_z, and k_r). San Andrés [9] gives explicit formulas. For a barotropic fluid (ideal gas =isothermal),

$$\bar{\rho}_\alpha = \left(\frac{\partial \bar{\rho}}{\partial p}\right)_0 p_\alpha \quad \bar{\mu}_\alpha = \left(\frac{\partial \bar{\mu}}{\partial p}\right)_0 p_\alpha \tag{A4}$$

The first-order entrance and exit pressures and inlet circumferential velocity are

$$p_{i\alpha} = 1 - (1+\xi)\mathrm{Re}_P^* \left(\bar{\rho}_0 w_0 w_\alpha + \frac{w_0^2}{2}\bar{\rho}_\alpha \right)\Big|_{\bar{z}=0} \tag{A5}$$

$$p_{e\alpha} = C_S \,\mathrm{Re}_P^* \left(\bar{\rho}_0 w_0 w_\alpha + \frac{w_0^2}{2}\bar{\rho}_\alpha \right)\Big|_{\bar{z}=L/R} \tag{A6}$$

$$u_\alpha|_{\bar{z}=0} = 0 \tag{A7}$$

References

[1] Von Pragenau, G. L., 1982, "Damping Seals for Turbomachinery," Technical Report No. TP-1987, NASA Marshall Space Flight Center, AL.
[2] Childs, D., Elrod, D., and Hale, K., 1989, "Annular Honeycomb Seals: Test Results for Leakage and Rotordynamic Coefficients; Comparisons to Labyrinth and Smooth Configurations," ASME J. Tribol., **111**, pp. 293–301.
[3] Ha, T. W., and Childs, D. W., 1992, "Friction-Factor Data for Flat-Plate Tests of Smooth and Honeycomb Surfaces," ASME J. Tribol., **114**, pp. 722–730.
[4] Dawson, M., Childs, D., and Holt, C., 2001, "Measurements Versus Predictions for the Dynamic Impedance of Annular Gas Seals: Part I—Test Facility and Apparatus," ASME Paper No. 2001-GT-0237.

[5] Dawson, M., and Childs, D., 2001, "Measurements Versus Predictions for the Dynamic Impedance of Annular Gas Seals: Part II—Smooth and Honeycomb Geometries," ASME Paper No. 2001-GT-0238.
[6] Kleynhans, G., and Childs, D., 1997, "The Acoustic Influence of Cell Depth on the Rotordynamic Characteristics of Smooth-Rotor/Honeycomb-Stator Annular Gas Seals," ASME J. Eng. Gas Turbines Power, **119**, pp. 949–957.
[7] Kleynhans, G. F., 1996, "A Two-Control-Volume Bulk-Flow Rotordynamic Analysis for Smooth-Rotor/Honeycomb-Stator Gas Annular Seals," Ph.D. thesis, Texas A&M University, College Station, TX.
[8] Li, J., Kushner, F., and DeChoudhury, P., 2000, "Gas Damper Seal Test Results, Theoretical Correlation, and Applications in Design of High-Pressure Compressors," in Proceedings of the 29th Turbomachinery Symposium, Houston, Texas, pp. 55–64.
[9] San Andrés, L. A., 1991, "Analysis of Variable Fluid Properties, Turbulent Annular Seals," ASME J. Tribol., **113**, pp. 694–702.
[10] San Andrés, L. A., 1992, "Analysis of Hydrostatic Journal Bearings With End Seals," ASME J. Tribol., **114**, pp. 802–811.
[11] Launder, B. E., and Leschziner, M., 1978, "Flow in Finite Width Thrust Bearings Including Inertial Effects, I—Laminar Flow, II—Turbulent Flow," ASME J. Lubr. Technol., **100**, pp. 330–345.
[12] Van Doormal, J. P., and Raithby, G. D., 1984, "Enhancements of the SIMPLE Method for Predicting Incompressible Fluid Flows," Numer. Heat Transfer, **7**, pp. 147–163.
[13] Yang, Z., San Andrés, L., and Childs, D. W., 1994, "Dynamic Force Performance of Annular Gas Seals at Off-Center Conditions," STLE Tribol. Trans., **37**, pp. 33–42.
[14] Marquette, O. R., Childs, D. W., and San Andrés, L., 1997, "Eccentricity Effects on the Rotordynamic Coefficients of Plain Annular Seals: Theory Versus Experiment," ASME J. Tribol., **113**, pp. 694–702.
[15] Weatherwax, M., 2001, "A Study of the Effects of Eccentricity on Honeycomb Annular Gas Seals," M.S. thesis, Texas A&M University, College Station, TX.

A Bulk-Flow Model of Angled Injection Lomakin Bearings

Luis San Andrés
Mast-Childs Tribology Professor
e-mail: lsanandres@mengr.tamu.edu

Thomas Soulas
Research Assistant

Mechanical Engineering Department,
Texas A&M University,
College Station, TX, 77843-3123

Patrice Fayolle
Snecma Moteurs—DMF,
Unités de Conception Turbomachines—FLTTR,
Forêt de Vernon—BP 802,
27208 Vernon Cedex, France

This paper introduces a bulk-flow model for prediction of the static and dynamic force coefficients of angled injection Lomakin bearings. The analysis accounts for the flow interaction between the injection orifices, the supply circumferential groove, and the thin film lands. A one control-volume model in the groove is coupled to a bulk-flow model within the film lands of the bearing. Bernoulli-type relationships provide closure at the flow interfaces. Flow turbulence is accounted for with shear stress parameters and Moody's friction factors. The flow equations are solved numerically using a robust computational method. Comparisons between predictions and experimental results for a tangential-against-rotation injection water Lomakin bearing show that novel model well predicts the leakage and direct stiffness and damping coefficients. Computed cross-coupled stiffness coefficients follow the experimental trends for increasing rotor speeds and supply pressures, but quantitative agreement remains poor. A parameter investigation shows evidence of the effects of the groove and land geometries on the Lomakin bearing flowrate and force coefficients. The orifice injection angle does not influence the bearing static performance, although it largely affects its stability characteristics through the evolution of the cross-coupled stiffnesses. The predictions confirm the promising stabilizing effect of the tangential-against-rotation injection configuration. Two design parameters, comprised of the feed orifices area and groove geometry, define the static and dynamic performance of Lomakin bearing. The analysis also shows that the film land clearance and length have a larger impact on the Lomakin bearing rotordynamic behavior than its groove depth and length. [DOI: 10.1115/1.2227032]

Introduction

Current trends in high performance turbomachinery drive towards higher operational speeds and pressures to increase their power. In particular, in cryogenic turbopumps, externally pressurized fluid film bearings and seals will be used for primary space-power applications due to their long-life time, low friction and wear, significant load capacity, and large direct stiffness and damping coefficients [1]. In theory, fluid film bearings, unlike rolling element bearings, have no diameter × rotational speed (DN) limit, and hence allow rotating machinery to operate at higher speeds with better efficiency and reduced overall weight and size.

Lomakin bearings, as shown in Fig. 1, are fluid film bearings comprising two annular film lands in parallel and separated by a circumferential feeding groove. Radial or angled injection holes supply the bearing with the working fluid. Characterized by its design simplicity, the Lomakin bearing is a promising alternative to a hydrostatic journal bearing in cryogenic turbopumps. Indeed (proprietary) experimental measurements on a tangential-against-rotation injection Lomakin bearing demonstrate its stabilizing rotordynamic characteristics with small or even negative whirl frequency ratios due to its large direct damping and reduced cross-coupled stiffness coefficients [2]. However, Lomakin bearings typically generate lower direct stiffnesses than hydrostatic pocket bearings. Note that a modern cryogenic turbopump could be easily retrofitted with Lomakin bearings and, unlike with hydrostatic bearings, would not require special filtering systems to avoid orifice clogging.

A brief review of the main components of a Lomakin bearing follows to provide a sense of the current state of art. In addition to maintaining a pressure differential and control leakage between stages in turbomachinery, annular seals can produce significant forces on its rotor. Fully developed turbulent flow develops in pump seals because of the large clearances and pressure differentials. The combined effect of an inlet pressure loss and the axial-pressure gradient within the seal lands accounts for the large direct (centering) stiffnesses, even without rotor spinning. Lomakin [3] first demonstrated this effect, and since then, numerous applications and analysis for adequate seal design have followed.

As related to rotordynamics, analysis of bearings and seals forwards the forces acting on the rotor as a consequence of shaft motion. About a rotor centered position, the seal reaction force components (F_X, F_Y) due to lateral shaft motions (X, Y) are [4]:

$$-\begin{Bmatrix} F_X \\ F_Y \end{Bmatrix} = \begin{bmatrix} K_{XX} & K_{XY} \\ K_{YX} & K_{YY} \end{bmatrix} \begin{Bmatrix} X \\ Y \end{Bmatrix} + \begin{bmatrix} C_{XX} & C_{XY} \\ C_{YX} & C_{YY} \end{bmatrix} \begin{Bmatrix} \dot{X} \\ \dot{Y} \end{Bmatrix} + \begin{bmatrix} M_{XX} & M_{XY} \\ M_{YX} & M_{YY} \end{bmatrix} \begin{Bmatrix} \ddot{X} \\ \ddot{Y} \end{Bmatrix} \tag{1}$$

where $(K, C, M)_{XX,YY}$ are direct stiffness, damping, and inertia force coefficients, and $(K, C, M)_{XY,YX}$ are cross-coupled coefficients, respectively. From a rotordynamics viewpoint, the design of bearings and seals strives to minimize the cross-coupled stiffnesses (K_{XY}, K_{YX}), maximize the direct damping (C_{XX}, C_{YY}), and provide relatively large direct stiffness coefficients (K_{XX}, K_{YY}).

Von Pragenau [5] discusses the advantages of "damping seals" over smooth seals, labyrinth seals, hydrostatic bearings, and ball bearings, in particular for cryogenic turbopump applications. The damping seal consists of a rough surface stator (akin to round hole pattern) and a smooth journal. Numerous experimental programs and field applications have verified Von Pragenau predictions, i.e., damping seals show superior dynamic performance with reduced swirl flow, low cross-coupled forces, high direct stiffness and damping force coefficients, and low leakage [6].

Seals with angled fluid injection against rotor rotation have

Contributed by the International Gas Turbine Institute (IGTI) of ASME for publication in the JOURNAL OF ENGINEERING FOR GAS TURBINES AND POWER. Manuscript received October 1, 2001; final manuscript received March 1, 2002. Review conducted by E. Benvenuiti. Paper presented at the International Gas Turbine and Aeroengine Congress and Exhibition, Amsterdam June 3–6, 2002, Paper No. GT2002-30287.

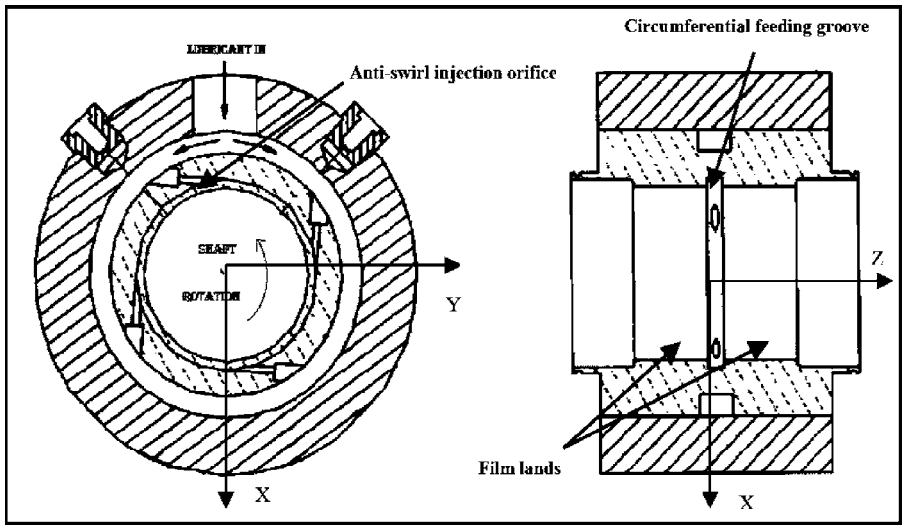

Fig. 1 Angled injection Lomakin bearing and coordinate system

been used to eliminate subsynchronous vibration in industrial compressors. Fluid injected at an angle breaks up the circumferential swirl flow or may even change the circumferential bulk-flow direction within the seal leading to the enhancement of its rotordynamic performance [7]. It is well known that fluid swirl brakes just before entry to annular seals (mainly balance piston seals) may eliminate or reverse the destabilizing cross-coupling forces [8]. San Andrés and Childs [9] also introduce angled injection for improving the rotordynamic performance in hybrid journal bearings. Measurements by Franchek and Childs [10] on water hydrostatic/hydrodynamic bearings with angled orifice injection demonstrate improved rotordynamic performance with virtual elimination of cross-coupled stiffness coefficients and null or even negative whirl frequency ratios. Kim and Lee [11] present experimental force coefficients and leakage for annular seals implementing an ad hoc antiswirl self-injection. The test results yield a significant improvement in whirl frequency ratios as compared to smooth and damper seals.

Deep circumferential feed grooves not only provide a uniform axial flow into the thin film lands of a bearing or seal, but could also contribute significantly to its rotordynamic force performance. Large dynamic pressures (and fluid film forces) can be generated in squeeze film dampers with a central feed groove [12]. Experimental measurements and analysis attest to the importance of fluid inertia and the interaction between the flow in the thin film lands and the fluid volume "trapped" in the groove.

Prediction of performance in Lomakin bearings needs to account for the flow interaction between the injection orifices, the supply circumferential groove, and the film lands. Presently, a novel bulk-flow model for estimation of the rotordynamic force coefficients and leakage of Lomakin bearings follows. The influence of the holes and the groove is considered with a sound physical model based on rational assumptions and simplifications, and coupled with an existing bulk-flow computational program for annular seals presented in [13]. Numerical predictions are compared to existing experimental flow rate and force coefficients for a tangential-against-rotation injection Lomakin water bearing [2]. The influence of orifice and groove geometry on the Lomakin bearing performance is also investigated.

Analysis

Figure 2 shows the configuration of the angled injection orifices and groove in a Lomakin bearing. The fluid is supplied by an external source through equally spaced holes into the large volume of the central groove, pushing axial flow through the adjacent thin film lands. The flow region is bounded between a stationary bearing housing and an inner rotating shaft. The rotor is centered and the overall configuration is axially symmetric (identical land lengths, and without rotor misalignment).

Most analyses for pump seals use "bulk-flow" models for the fluid flow within the seal. A bulk-flow velocity represents the average (across the clearance) velocity component. Wall shear stress differences, from stator and rotor, are modeled with friction factors depending on the local Reynolds numbers and surface conditions [14]. Childs [4,15] uses Blasius' friction factor formula, while Nelson [16] and San Andrés [13,17] use Moody-type factors which account for local surface roughness effects.

The present isothermal bulk-flow model assumes fully developed turbulent flow in the film lands and in the feeding groove. Material properties of cryogenic liquids used in the space industry depend strongly on their absolute pressure and temperature, but cryogens have very low viscosity, and thus, temperature effects

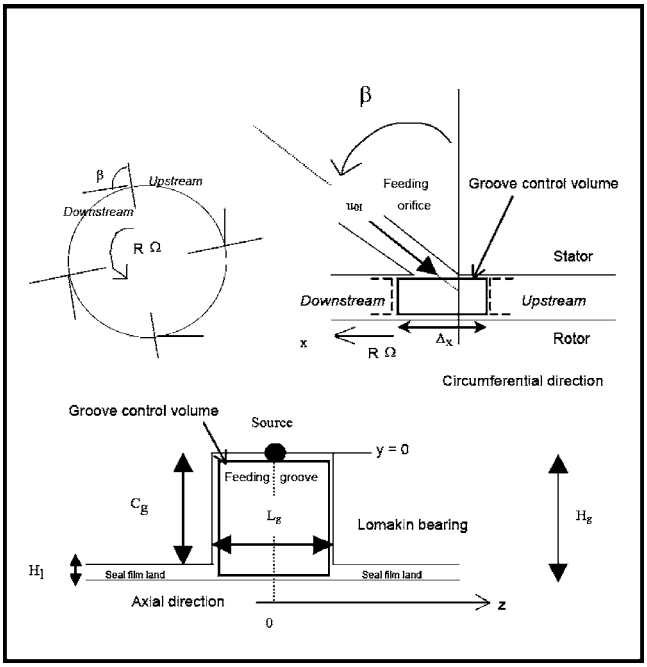

Fig. 2 Location and geometry of the feed orifices, groove, and film lands

due to shear drag and extrusion power losses are of minor importance [1]. On the other hand, the effect of pressure on the liquid properties and ultimate bearing performance is important since the applications show high-pressure differentials. Therefore, the analysis regards the fluid as barotropic and neglects energy transport considerations without loss of generality [18].

The Governing Flow Equations in the Film Lands. Continuity and momentum transport equations govern the bulk flow of a barotropic fluid within the thin film lands of the bearing, i.e. [13]

$$\frac{\partial(\rho_l U_l H_l)}{\partial x} + \frac{\partial(\rho_l W_l H_l)}{\partial z} + \frac{\partial(\rho_l H_l)}{\partial t} = 0 \tag{2}$$

$$-H_l \frac{\partial P_l}{\partial x} = \frac{\mu_l}{H_l}\left(k_{xl} U_l - k_{Rl}\frac{R\Omega}{2}\right) + \left\{\frac{\partial(\rho_l H_l U_l)}{\partial t} + \frac{\partial(\rho_l H_l U_l^2)}{\partial x} + \frac{\partial(\rho_l H_l W_l U_l)}{\partial z}\right\} \tag{3}$$

$$-H_l \frac{\partial P_l}{\partial z} = \frac{\mu_l}{H_l}(k_{zl} W_l) + \left\{\frac{\partial(\rho_l H_l W_l)}{\partial t} + \frac{\partial(\rho_l H_l U_l W_l)}{\partial x} + \frac{\partial(\rho_l H_l W_l^2)}{\partial z}\right\} \tag{4}$$

Refer to the Nomenclature for appropriate definitions. The turbulent shear parameters (k_{xl}, k_{zl}, k_{Rl}) are local functions of the friction factors (f_{Rl} and f_{Sl}) relative to the rotor and stator surfaces, respectively. The pressure and velocity fields are continuous and single valued in the circumferential direction (x).

The Governing Flow Equations in the Groove. The flow in the groove is extraordinarily complex since it combines (and mixes) radial or angled fluid injection, swirl velocity due to rotor motion, and sharp turns forcing axial flow through the film lands. Presently, a groove bulk-flow velocity (U_g) represents the overall flow across its depth and width (radial and axial), and the pressure within the groove (P_g) is considered uniform on account of its relatively short axial length. From the general flow equations, bulk-flow continuity and circumferential momentum transport equations in a control volume within the feed groove result as

$$L_g \frac{\partial(\rho_g H_g)}{\partial t} + H_g L_g \frac{\partial(\rho_g U_g)}{\partial x} + 2\rho_g W_l H_l - \delta_{OI}\rho_g u_{OI} A_O/\Delta x = 0 \tag{5}$$

$$-H_g \frac{\partial P_g}{\partial x} L_g = \frac{\mu_g}{2H_g}[k_{Sg} U_g d_g + k_{Rg}(U_g - R\Omega)L_g - \delta_{OI} k_O U_{OI} A_{Oc}/\Delta x] + \left[\frac{\partial(\rho_g H_g U_g)}{\partial t} L_g + 2\rho_g U_l W_l H_l - \delta_{OI}\rho_g u_{OI} U_{OI} A_O/\Delta x\right] \tag{6}$$

where Δx is the circumferential extent of the control volume (Δx is small but still larger than an orifice diameter). Above, $\delta_{OI}=1$ in a control volume containing an injection orifice, otherwise $\delta_{OI}=0$. The effective orifice area $A_O = C_{do}\cdot\pi\cdot d_o^2/4$ includes the (empirical) discharge coefficient (C_{do}). The orifice injection velocity (u_{OI}) has circumferential and radial components $U_{OI} = -u_{OI}\cdot\sin(\beta)$, and $V_{OI} = u_{OI}\cdot\cos(\beta)$, where β is the injection angle.

Due to the axial symmetry of the Lomakin bearing, the circumferential velocities at the entrances of the two film lands are identical, while the axial velocities are equal in magnitude but opposite in direction. Moreover, the constant groove depth (C_g) is typically an order of magnitude larger than the film thickness (H_l), and consequently, geometrical variations of H_l with respect to x (or θ) are assumed not to affect the film thickness (H_g) in the groove. An order of magnitude analysis considering the geometric characteristics of the orifices/groove/film land configuration also shows that fluid inertia effects *within* the groove are negligible, and consequently, omitted from further analysis [19].

Within the groove, the shear stress parameters (k) are functions of the local Reynolds numbers and the Moody's friction factors at the respective surfaces. Following [20], the expression for the circumferential direction groove shear stress (k_{xg}) includes the side surfaces of the groove wetted by fluid. The characteristic length (d_g) equals ($L_g + 2C_g$).

Orifice Flow Equation and Boundary Conditions at the Groove-Film Lands Interface. At the orifices discharge planes in the groove, following [9]:

$$P_{gOI}(t) = P_S - \rho_{gOI}(t)\cdot\frac{u_{OI}^2(t)}{2} \tag{7}$$

where P_{gOI} and ρ_{gOI} are the orifice pressure and density, and P_S is the supply pressure. The local acceleration of fluid from the groove into a high axial velocity at the film land inlet (z_i) causes a sudden pressure drop, and modeled by a simple Bernoulli equation,

$$P_l(\theta, z_i, t) = P_g(\theta, t) + \frac{\rho_l(\theta, z_i, t)}{2}(1+\xi)W_l^2(\theta, z_i, t) \tag{8}$$

Flow continuity establishes

$$U_l(\theta, z_i, t) = U_g(\theta, t) \tag{9}$$

i.e., the equivalence of circumferential bulk-flow velocities at the groove and inlet to the film lands. At the film land exit plane (z_e), an end restriction coefficient (C_S) simulates additional pressure losses [21]:

$$P_l(\theta, z_e, t) = P_D + \frac{\rho_l(\theta, z_e, t)}{2} C_S W_l^2(\theta, z_e, t) \tag{10}$$

Perturbation Analysis. Consider rotor motions of frequency (ω) and small amplitudes, (Δe_X and Δe_Y), about the centered equilibrium position. The film thickness (H) is given by the real part of

$$H = H_0 + e^{j\omega t}(\Delta e_X \cos\theta + \Delta e_Y \sin\theta) = h\cdot c^*$$
$$H_0 = c^* + e_{X0}\cos\theta + e_{Y0}\sin\theta \tag{11}$$

where $j=\sqrt{-1}$, and H_0 is the film thickness at the static equilibrium position. For small amplitude rotor motions, velocity and pressure fields, as well as fluid properties and shear coefficients are expressed as the sum of a zeroth-order and first-order complex fields, describing the equilibrium condition and the perturbed motions, i.e.,

$$\phi = \phi_0 + e^{j\omega t}(\Delta e_X \phi_X + \Delta e_Y \phi_Y) \tag{12}$$

with $\phi = \{P, U, W, k_x, k_z, \ldots\}$.

Substitution of the flow variables into the film lands governing equations yields equations of continuity and momentum for the zeroth- and first-order flow fields. Reference [13] details the analysis. The Appendix gives the first-order flow equations in the groove and boundary conditions at the interfaces with the film lands. In the groove, periodicity conditions from orifice to orifice are adopted for the zeroth-order fields in the circumferential direction

The Numerical Solution Procedure. A control-volume finite difference scheme is devised to solve the coupled, nonlinear partial differential equations of mass and momentum transport in the groove and film lands. The procedure, based on Launder and Leschziner [22] and Van Doormal and Raithby [23] schemes, is detailed in [1,13] for solution of the bulk-flow equations in variable fluid properties, turbulent flow bearings and seals. The flow field is represented by a series of discrete nodal velocities and pressures on staggered grids. The velocity nodes are located at points lying

at interfaces midway between the nodes where the pressure is determined. The iterative convergence procedure not only satisfies local residuals in mass and momentum transport, but also fulfills the overall balance of flow through the orifices equating the discharge flow at the bearing exit planes.

Note that for concentric rotor operation the zeroth-order flow field in the groove is periodic from orifice to orifice. In the iterative procedure, the flow mass constraint equating the exit flow through the bearing discharge planes to the sum of the flows through the injection orifices is used to update the orifice pressure, Eq. (7). For the first-order flow field, periodicity from orifice to orifice is no longer valid; and hence, the equations are solved along the bearing circumference, using the flow balance applicable to each control volume containing an injection orifice, in order to update the first-order orifice pressure [19]. Presently, the model is restricted to the prediction of centered bearing operation. The numerical procedure could be easily adapted to include rotor eccentric position, although its applicability to a practical situation may be somewhat limited.

Lomakin Bearing Flowrate and Rotordynamic Coefficients. The zeroth-order solution determines the steady-state pressure and circumferential velocity as well as axial leakage or flow rate. The bearing flow rate (Q) is

$$Q = 2 \cdot \int_0^{2\pi R} (\rho W H)_{l0}\big|_{z_e} dx \tag{13}$$

The Lomakin bearing dynamic force coefficients (dynamic stiffness and damping) follow from integration of the complex first-order pressure fields over the rotor surface (groove and two lands). The force coefficients for the groove and film lands are ($\alpha, \gamma = X, Y$):

$$K_{g\alpha\gamma} - \omega^2 \cdot M_{g\alpha\gamma} + j \cdot \omega \cdot C_{g\alpha\gamma} = \frac{L_g}{C^*} \cdot \int_0^{2\pi R} P_{g\gamma} \cdot h_{l\alpha} \cdot dx \tag{14}$$

and

$$K_{l\alpha\gamma} - \omega^2 \cdot M_{l\alpha\gamma} + j \cdot \omega \cdot C_{l\alpha\gamma} = \frac{1}{C^*} \cdot \int_0^{L_f} \int_0^{2\pi R} P_{l\gamma} \cdot h_{l\alpha} \cdot dx \cdot dz \tag{15}$$

respectively. Thus, the bearing force coefficients become

$$K_{\alpha\gamma} = K_{g\alpha\gamma} + 2 \cdot K_{l\alpha\gamma}$$

$$C_{\alpha\gamma} = C_{g\alpha\gamma} + 2 \cdot C_{l\alpha\gamma}$$

$$M_{\alpha\gamma} = M_{g\alpha\gamma} + 2 \cdot M_{l\alpha\gamma} \tag{16}$$

where $h_{lX} = \cos\theta$ and $h_{lX} = \sin\theta$. For concentric rotor position, $K_{YY} = K_{XX}$, $K_{YX} = -K_{XY}$, $C_{YY} = C_{XX}$, $C_{XX} = -C_{XY}$, $M_{YY} = M_{XX}$, and $M_{YX} = -M_{XY}$.

Comparison of Predictions to Experimental Results. Proprietary test measurements [2] for the flow rate and dynamic force coefficients of a tangential-against-rotation injection water Lomakin bearing are compared to numerical predictions based on the model. Note that for an incompressible fluid, the rotordynamic coefficients are independent of the excitation frequency.

Table 1 presents the test Lomakin bearing geometric characteristics and operating conditions. As an example, in the following, MSMP represents a result for a Medium rotor speed and medium supply pressure condition. Figures 3–10 depict dimensionless results only. Predictions obtained for the nominal MSMP configuration are the referential values. Reference [2] reports experimental uncertainties, with respect to the reference values, of 3% for direct stiffnesses, 4% for cross-coupled stiffnesses, 1% for direct dampings, 20% for the direct inertia coefficients, and less than 1% for flow rates [2].

Table 1 Test Lomakin bearing: geometry and operating conditions. Fluid: water. From Fayolle, Phillips, and Childs [2].

Parameter	Magnitude
Diameter, D	76.46 mm
Film land length, L_f	34.29 mm
Film land radial clearance, C^*	0.100 mm
Groove length and depth, $L_g \times C_g$	7.62 mm × 3.81 mm
Number of injection orifices, n	4
Injection orifice diameter, d_o	3.175 mm
Injection angle, β	+85 deg
Rotor speed	LS 10,200 rpm
	MS 17,400 rpm
	HS 24,600 rpm
Supply pressure, P_S	LP 41.4 bar
	MP 55.3 bar
	HP 69.1 bar
Discharge pressure, P_D	1.013 bar
Inlet temperature, T^*	328 K
Fluid density, ρ	984.5 kg/m^3
Fluid viscosity, μ	0.5×10^{-3} N s/m^2
Relative surface roughness, r	0.0033
Moody's friction parameters	$a_M = 0.001375$, $b_M = 5 \times 10^5$
	$e_M = 0.333$
Orifice discharge coefficient	C_{do} [a]
Entrance loss coefficient, ξ	0.1
Exit loss coefficient, C_S	0

[a]Matching numerical and measured flow rates at theMSMP configuration determined the coefficient C_{do}.

Mass Flowrate. Figure 3 compares predictions and measurements of flow rate or leakage (Q) for the Lomakin bearing. Numerical results show good agreement with experimental data (1%–7% difference). Bearing flow rate increases as the supply pressure rises, while rotor speed tends to slightly reduce the flow rate. The current model slightly overpredicts (underpredicts) leakage at low (high) rotor speeds.

Direct Stiffness Coefficient (K_{XX}). Figure 4 depicts measurements and predictions for direct stiffness as the rotor speed and feed pressure increase. The direct stiffness increases linearly with feed pressure, and it is enhanced by rotor speed. Predictions show a 15% difference in average when compared to the experimental results. The model overpredicts the direct stiffness coefficient at low speeds. Furthermore, at the low pressure, while the experiments show that (K_{XX}) remains constant from the medium to high speed condition, the current model predicts a noticeable reduction. In general, the model predicts a larger effect of supply pressure than the experimental values exhibit.

Cross-Coupled Stiffness Coefficient (K_{XY}). Figure 5 depicts the major benefit of the angled-injection Lomakin bearing, namely its ability to generate large (negative) cross-coupled stiffness coefficients for most operating conditions. Increasing rotor speed reduces the effect, yet the stabilizing effect of the antiswirl orifice feed is apparent. Predictions from the model exhibit the correct trends with respect to rotor speed and supply pressure (K_{XY} decreases when the supply pressure increases). However, the present model still largely underpredicts the large (negative) experimentally derived cross-coupled stiffness coefficient. The large test values are an indicative of extremely high circumferential velocities opposing the rotor speed (ΩR). Clearly, the bulk-flow model is not able to predict with accuracy the appropriate inlet circumferential speed into the film lands.

Direct Damping Coefficient (C_{XX}). Figure 6 depicts measure-

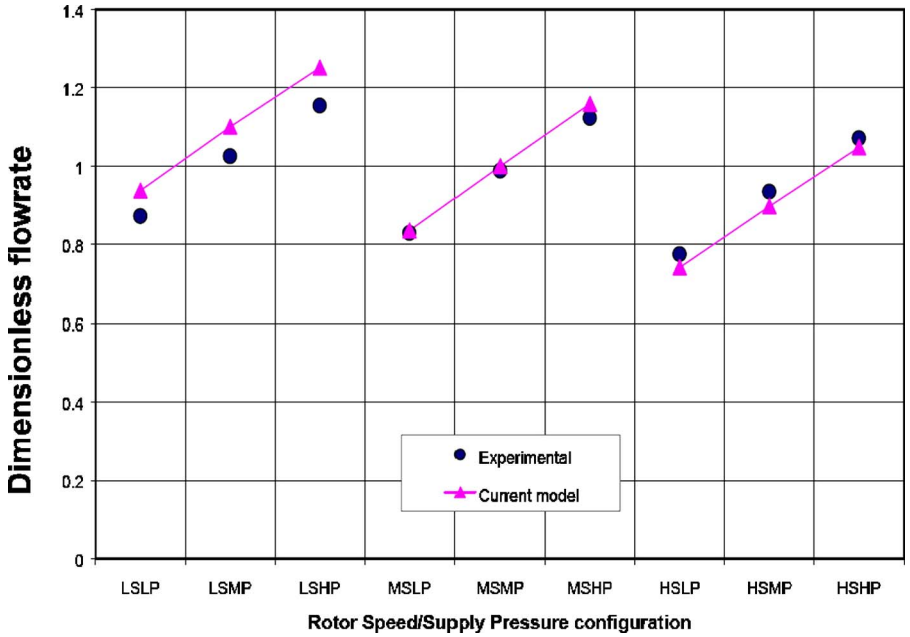

Fig. 3 Dimensionless flowrate (Q) versus rotor speed and supply pressure conditions—tests and predictions (reference value: MSMP numerical)

ments and predictions for direct damping as the rotor speed and feed pressure increase. Predictions are in good agreement with the experimental results (5% difference in average). C_{XX} increases for increasing feed pressures and rotor speeds. It is worth noting that a large portion of the damping arises from the fluid flow within the groove.

Direct Added-Mass Coefficient (M_{XX}). Figure 7 presents predictions and experimental estimations for the direct added mass coefficient. Large discrepancies are evident; however, the experimental uncertainty on this parameter is typically large as well. Predictions indicate that the inertia coefficient (M_{XX}) increases rapidly with rotor speed (larger frequencies), and decreases as the feed pressure rises.

Further predictions [19], not presented here for brevity, show that the current model provides a noticeable improvement when compared to results from a simpler model, i.e., two annular seals in parallel and without accounting for the feeding groove and the injection orifices. In this simpler model, besides the need for selecting (empirically) the groove pressure, a large negative preswirl ratio (~ -5) must be used to predict cross-coupled stiffness coefficients in agreement with the experimental values.

Influence of Geometry on the Performance of Lomakin Bearings. The current model becomes an effective design tool to optimize the performance characteristics of Lomakin bearings. To

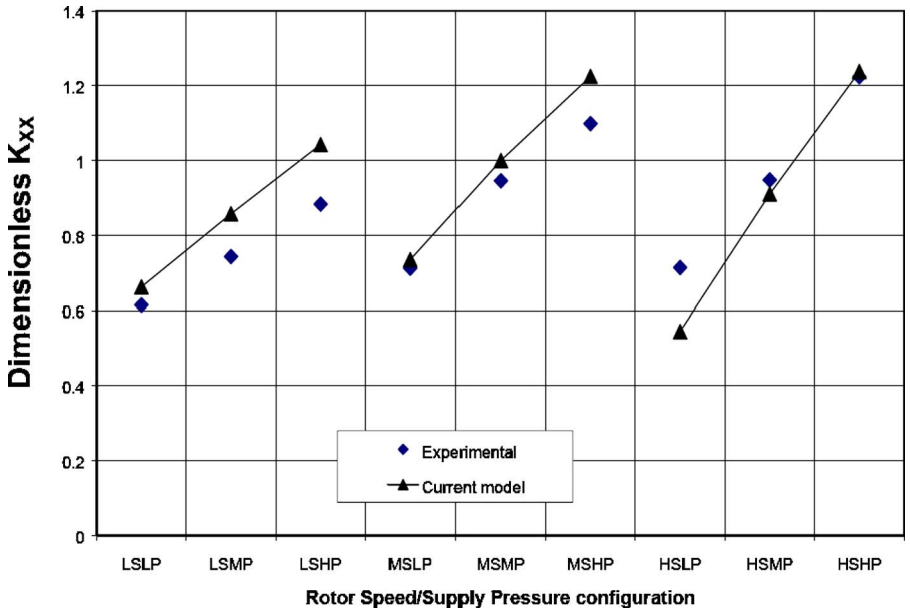

Fig. 4 Dimensionless direct stiffness coefficients $K_{XX}=K_{YY}$ versus rotor and supply pressure conditions—tests and predictions (reference value: MSMP numerical)

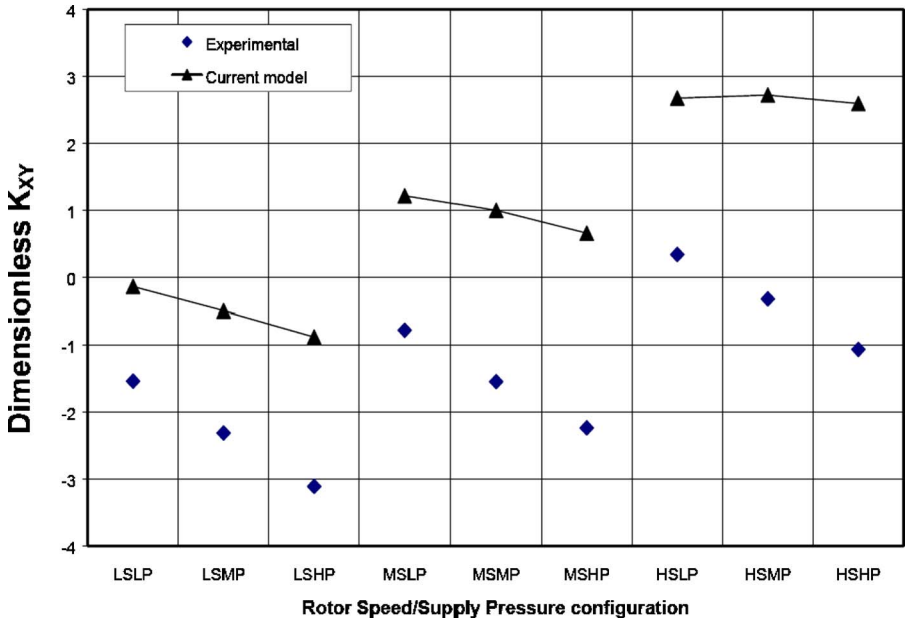

Fig. 5 Dimensionless cross-coupled stiffness coefficients $K_{XY}=-K_{YX}$ versus rotor speed and supply pressure conditions—tests and predictions (reference value: MSMP numerical)

this end, a parametric study demonstrates the effects of orifices (number, size, and angled disposition), and groove and film land geometry on the bearing flow rate and rotordynamic performance.

In general, the film clearance (C^*) and axial length (L_f) have a much larger effect on the Lomakin bearing performance than its groove depth (C_g) and length (L_g). The cross-coupled stiffness (K_{XY}) and direct damping (C_{XX}) coefficients sensibly increase, while the direct stiffness coefficient (K_{XX}) presents a maximum when the film clearance decreases and the axial length increases. Optimum direct stiffness is attained for about a 50% pressure drop at the inlet plane into the film lands.

The orifice injection angle (β) is the main design parameter with regard to the prediction of circumferential velocity in the groove, and consequently the determination of the cross-coupled stiffness coefficient and the whirl frequency ratio, i.e., WFR $=K_{XY}/(C_{XX}\cdot\Omega)$. Figure 8 illustrates, for the MSMP condition, a linear decrease of cross-coupled stiffness (K_{XY}) as the injection angle (β) varies from tangential with-rotation to against-rotation ($\beta=0$ denotes radial injection). For best rotordynamic stability, the tangential-against-rotation injection configuration is recommended. In general, the injection angle does not greatly affect the average groove pressure, and thus bearing flow rate, direct stiffness, and damping coefficients remain relatively unchanged [19].

The design of a Lomakin bearing requires appropriate selection of the total orifices area ($A_{on}=n\cdot\pi\cdot d_o^2/4$), the groove transversal

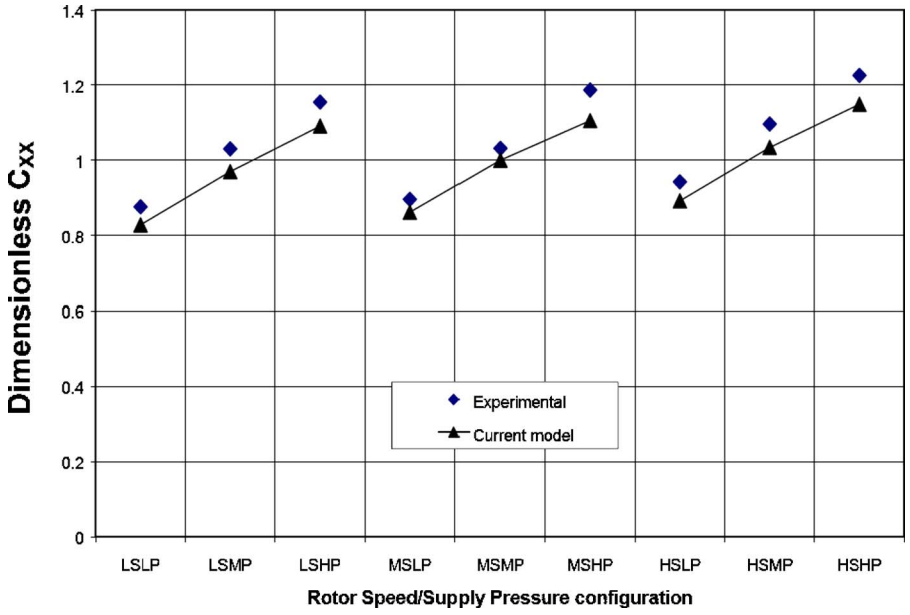

Fig. 6 Dimensionless direct damping coefficients $C_{XX}=C_{YY}$ versus rotor speed and supply pressure conditions—tests and predictions (reference value: MSMP numerical)

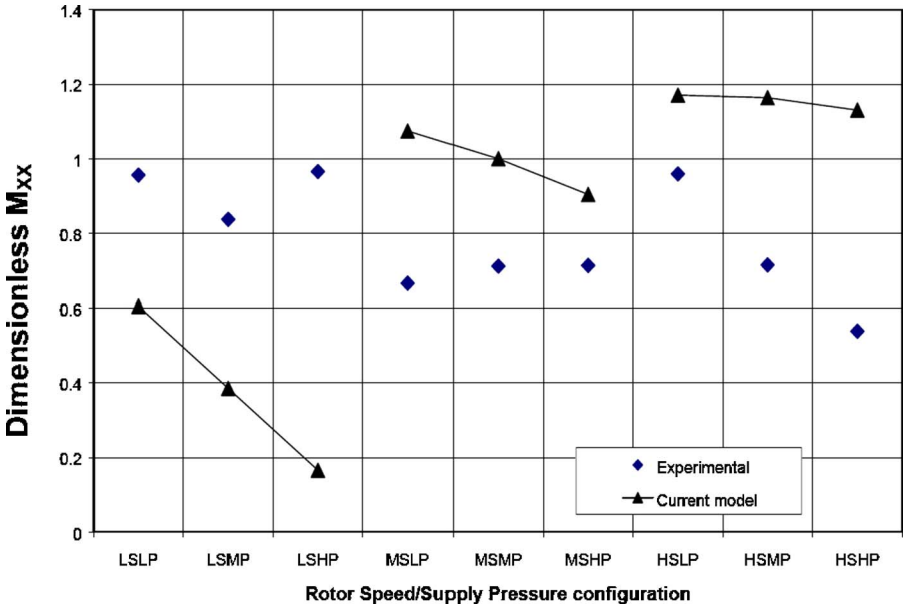

Fig. 7 Dimensionless direct added-mass coefficient $M_{XX}=M_{YY}$ versus rotor speed and supply pressure conditions—tests and predictions (reference value: MSMP numerical)

area ($A_g=L_g\cdot C_g$), and the groove length/depth ratio (L_g/C_g). The parametric analysis reveals two dimensionless parameters, (G_D) and (G_C), which uniquely determine the effects of the orifice arrangement (number and size) and groove geometry (depth and width), on the performance of Lomakin bearings [19]. The parameters are defined as:

$$G_D=\frac{A_{on}/(R\cdot C^*)}{(A_g/(R\cdot C^*))^{1/4}}=\frac{n\cdot(\pi\cdot d_o^2/4)/(R\cdot C^*)}{(L_g\cdot C_g/(R\cdot C^*))^{1/4}} \tag{17}$$

$$G_C=\frac{A_{on}}{R\cdot C^*}\cdot\left(\frac{L_g/R}{C_g/C^*}\right)^{1/4}=\frac{n\cdot(\pi\cdot d_o^2/4)}{R\cdot C^*}\cdot\left(\frac{L_g/R}{C_g/C^*}\right)^{1/4} \tag{18}$$

As an example, Fig. 9 shows the direct stiffness coefficient (K_{XX}) versus G_D for instances when the total orifice area (A_{on}) or the groove area (A_g) vary independently. The direct stiffness as well as the other direct force coefficients (C,M), the flow rate, and the average groove-pressure increase as G_D increases, i.e., as the number and diameter of the orifices increases and/or the groove area decreases. A performance parameter (Φ) follows (approximately) the relationship $\Phi_{\mathrm{MAX}}\cdot(1-e^{-\delta_\Phi\cdot G_D})$. The (MAX) index denotes the largest (Φ) value and δ_Φ is a growth rate determined from the analysis. In Fig. 9, the nominal references the test bearing in [2].

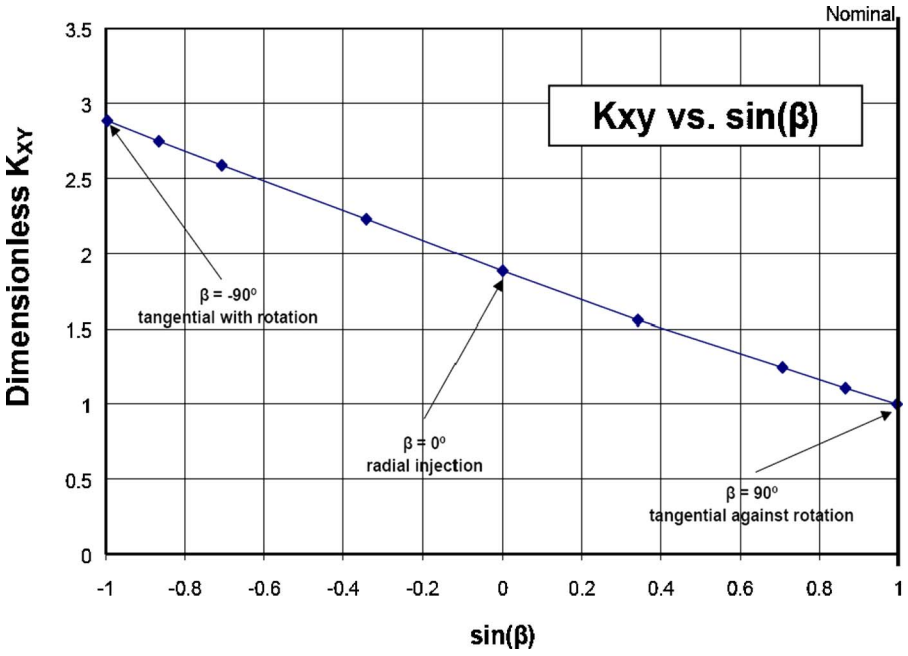

Fig. 8 Variation of dimensionless $K_{XY}=-K_{XY}$ versus injection angle β—MSMP configuration (reference value: MSMP numerical)

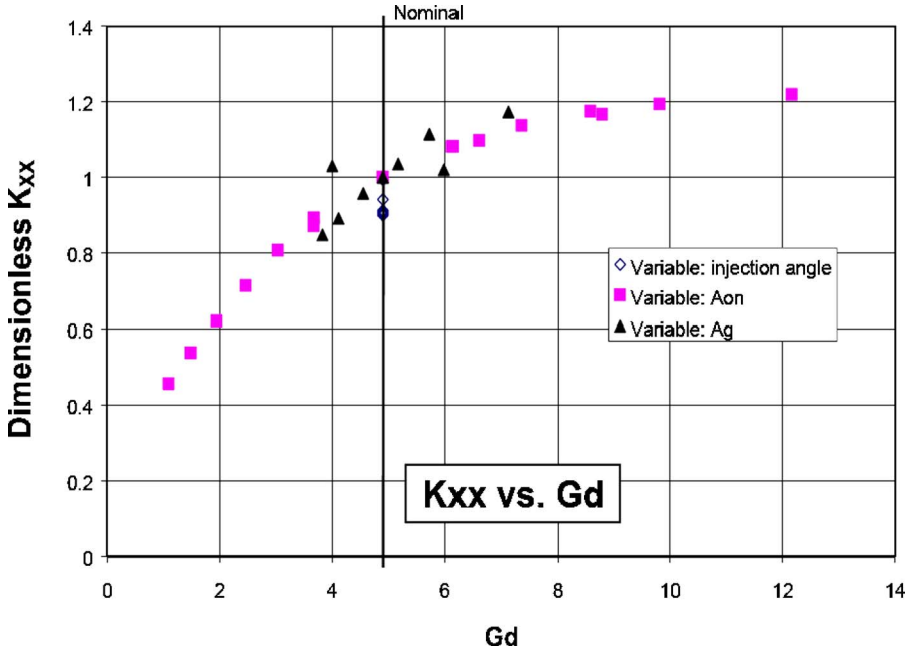

Fig. 9 Variation of direct stiffness $K_{XX}=K_{YY}$ versus G_D parameter. Total orifice area (A_{on}) and groove area (A_g) change. MSMP configuration (reference value: MSMP numerical)

Figure 10 depicts the cross-coupled stiffness (K_{XY}) versus G_C for independent variations of the total feed orifice area (A_{on}) and groove ratio (L_g/C_g). For $G_C>2$, the cross-coupled stiffness and WFR increase linearly, irrespective of the A_{on} or (L_g/C_g) magnitudes. Most importantly, as A_{on} varies and for $G_C<2$, K_{XY} and WFR, as well as the circumferential velocity in the groove, attain a minimum at the condition for best (against-rotation) effect from the feed orifices and groove (short and deep).

Conclusions

Lomakin bearings are a simple alternative to hydrostatic bearings in modern cryogenic turbopumps. An all-fluid film bearing technology will certainly reduce turbopump size and cost while extending its useful life. Favorable experimental results obtained from a water lubricated Lomakin bearing [2] urged the present computational analysis to predict the bearing dynamic forced per-

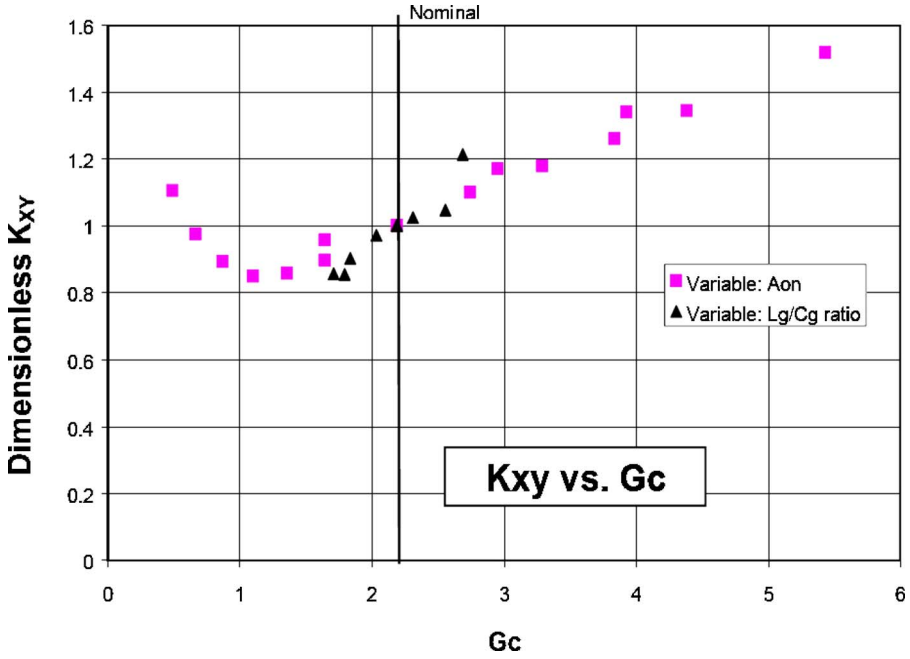

Fig. 10 Variation of cross-coupled stiffness $K_{XY}=-K_{YX}$ versus G_C parameter. Total orifice area (A_{on}) and groove length/depth ratio (L_g/C_g) change. MSMP configuration (reference value: MSMP numerical).

formance. The bulk-flow model couples the fluid motion in the thin film lands to a simple model in the groove describing the circumferential flow and momentum exchange with angled injection orifices. Zeroth- and first-order bulk-flow equations describe the steady flow and the perturbed flow fields, respectively, for a centered bearing with small amplitude rotor motions about an equilibrium position. An efficient CFD algorithm solves the nonlinear flow equations and renders the bearing flow rate and rotordynamic force coefficients.

Predictions for flow rate and rotordynamic force coefficients are compared to experimental results from a tangential-against-rotation injection Lomakin bearing tested in water. Predictions agree well with test results for various supply pressures and rotor speeds, ranging from 41 to 69 bars and 10.2 to 24.6 krpm, respectively. The bearing flow rate, direct stiffness, and damping coefficients increase, while the cross-coupled stiffness coefficient decreases, or becomes even negative, as the supply pressure rises. The flow rate and direct damping coefficient show minute variations for increasing rotor speeds, while the direct stiffness appears to be invariant at the largest rotor speeds.[1] The experimental cross-coupled stiffness is mostly negative for all speeds, showing evidence for the major benefit of a Lomakin bearing, namely to promote rotor stability. This stabilizing effect becomes less pronounced as the rotor speed increases.

The bulk-flow model correctly predicts the leakage and the direct stiffness and damping coefficients but largely underpredicts the (negative) cross-coupled stiffness. The discrepancies are attributed to the inaccurate prediction of the circumferential flow velocity entering the bearing film lands. Presently, the circumferential momentum from the orifice injection dissipates within the vicinity of the feed orifices. However, the flow mechanics in the groove and the jet mixing with the circumferential flow are more complex than the model asserts. It appears that the flow area where the injection act produces large inlet circumferential velocities, is not well modeled at present.

A parametric study reveals important design considerations for appropriate selection of the orifice size and number, and groove axial extent and depth. The injection angle does not influence the bearing flow rate and direct force coefficients, although it largely affects the bearing stability characteristics through the evolution of the cross-coupled stiffnesses. The predictions confirm the promising stabilizing effect of the tangential-against-rotation injection configuration. The total feed orifice area and the groove transversal area are important to establish desired flow rates and direct stiffness, damping and added-mass coefficients. The groove length/depth ratio affects the cross-coupled stiffness coefficient and the whirl frequency ratio. Two typical numbers, comprised of the orifice and groove areas, define the static and dynamic performance of Lomakin bearings for the characterization of the direct and cross-coupled effects, respectively.

Acknowledgment

The support of Snecma Moteurs (France) and the Turbomachinery Laboratory (Texas A&M University) is gratefully acknowledged.

Nomenclature

A_O, A_{Oc} = effective orifice area, $=\frac{1}{4}\, C_{do}\cdot\pi\cdot d_o^2$, $=A_O/\cos\beta(\mathrm{m}^2)$
a_M, b_M, e_M = coefficients in Moody's friction factor formula
C^*, C_g = typical film clearance and groove depth (m)
C_{do}, C_S = orifice and exit plane discharge coefficients
$C_{\alpha\gamma}$ = damping coefficients (N s/m), $\alpha, \gamma = X, Y$
D = stator diameter (m)
d_g = groove characteristic length $= L_g + 2C_g$ (m)
d_o = orifice diameter (m)
$f_{R,S}$ = Moody's friction factor at rotor and stator $= a_M[1 + (10^4 . r_{R,S} + b_M/\mathrm{Re}_{R,S})^{e_M}]$
G_D, G_C = groove-orifice design parameters, Eqs. (17) and (18)
H = radial clearance (m), $h = H/C^*$
$K_{\alpha\gamma}$ = stiffness coefficients (N/m), $\alpha, \gamma = X, Y$
$k_{O,R,S}$ = shear flow parameter at orifice, rotor and stator interfaces $= (f\cdot \mathrm{Re})_{O,R,S}$
k_{xg} = groove circumferential shear flow parameter $= (k_R + (d_g/L_g)\cdot k_S)/2$
k_{xl}, k_z = land circumferential and axial shear flow parameters $= (k_R + k_S)/2$
L_f, L_g = film land and groove axial lengths (m)
$M_{\alpha\gamma}$ = inertia coefficients (kg), $\alpha, \gamma = X, Y$
n = number of injection orifices
P = dimensional pressure (Pa), $p = (P - P_D)/\Delta P$
P_D, P_S = discharge and supply pressures (Pa)
Q = bearing mass flowrate (kg/s)
R = rotor (journal) radius $= D/2$ (m)
$\mathrm{Re}_{O,R,S}$ = Reynolds numbers relative to orifice, rotor and stator interfaces $= (\rho_g/\mu_g)H_g|U_g - U_{OI}|$, $(\rho/\mu)H[(U - R\Omega)^2 + W^2]^{1/2}$, $(\rho/\mu)H[U^2 + W^2]^{1/2}$
r_R, r_S = mean surface relative roughness at rotor and stator
T^* = fluid temperature (K)
t = time (s)
U = circumferential bulk-flow velocity (m/s), $u = (U . \mu^* . R)/(C^{*2} . \Delta P)$
U_{OI}, V_{OI} = orifice circumferential and radial velocities $= -u_{OI}\cdot\sin\beta$, $u_{OI}\cdot\cos\beta$ (m/s)
u_{OI} = fluid velocity through injection orifice (m/s)
W = axial bulk-flow velocity (m/s), $w = (W\cdot\mu^*\cdot R)/(C^{*2}\cdot\Delta P)$
X, Y, Z = Cartesian coordinate system (m)
x, y, z = circumferential, radial, and axial coordinates in plane of flow (m)
β = orifice injection angle (rad)
ΔP = pressure differential $= P_S - P_D$ (Pa)
μ = fluid viscosity (N s/m^2)
ξ = empirical film land entrance loss coefficient
θ = angular coordinate $= x/R$ (rad)
ρ = fluid density (kg/m^3)
Ω = rotor speed (rad/s)
ω = excitation frequency (rad/s)

Subscripts

0 = zeroth-order fields
α, γ = first-order fields, X, Y directions
g, l, R, O, S = groove, land, rotor, orifice, stator

Superscripts

$-$ = dimensionless fields
* = characteristic value at supply condition

Appendix: First-Order Flow Equations in the Groove

The first-order continuity and circumferential momentum transport equations in the groove are, in dimensionless form

$$h_g \frac{L_g}{R}\frac{\partial(\bar{\rho}_{g0}u_{g\alpha} + \bar{\rho}_{g\alpha}u_{g0})}{\partial\bar{x}} + 2(\bar{\rho}_{g0}w_{l0}h_{l\alpha} + \bar{\rho}_{g0}w_{l\alpha}h_{l0} + \bar{\rho}_{g\alpha}w_{l0}h_{l0})$$
$$= -j\sigma\frac{L_g}{R}(h_g\bar{\rho}_{g\alpha} + h_{l\alpha}\bar{\rho}_{g0}) + \delta_{OI}\frac{A_O}{RC^*\Delta\bar{x}}(\bar{\rho}_{g\alpha}\bar{u}_{OI0} + \bar{\rho}_{g0}\bar{u}_{OI\alpha}) \quad \text{(A1)}$$

[1] The groove pressure approaches the supply pressure value as the rotor speed increases.

$$-h_g\frac{L_g}{C^*}\frac{\partial p_{g\alpha}}{\partial \bar{x}} = j\,\mathrm{Re}_{Sq}\frac{L_g}{C^*}(\bar{\rho}_{g0}h_g u_{g\alpha}+\bar{\rho}_{g0}h_{l\alpha}u_{g0}+\bar{\rho}_{g\alpha}h_g u_{g0}) + 2\,\mathrm{Re}_P(\bar{\rho}_{g0}w_{l0}u_{l0}h_{l\alpha}+\bar{\rho}_{g0}w_{l0}u_{l\alpha}h_{l0}+\bar{\rho}_{g0}w_{l\alpha}u_{l0}h_{l0} + \bar{\rho}_{g\alpha}w_{l0}u_{l0}h_{l0}) - \delta_{OI}\,\mathrm{Re}_P\frac{A_O}{RC^*\Delta\bar{x}}(\bar{\rho}_{g0}\bar{u}_{OI0}\bar{U}_{OI\alpha} + \bar{\rho}_{g0}\bar{u}_{OI\alpha}\bar{U}_{OI0}+\bar{\rho}_{g\alpha}\bar{u}_{OI0}\bar{U}_{OI0}) + \mathrm{Re}_P(\gamma_U u_{g\alpha}+\gamma_\rho\bar{\rho}_{g\alpha} + \gamma_\mu\bar{\mu}_{g\alpha}+\gamma_{U_{OI}}\bar{U}_{OI\alpha}) \tag{A2}$$

where $\mathrm{Re}_P=(\rho^* C^{*3}\Delta P)/(\mu^{*2}R)$, $\mathrm{Re}_P^*=\mathrm{Re}_P\cdot C^*/R$, are characteristic Reynolds numbers due to pressure flow, and $\mathrm{Re}_{Sq}=(\rho^*\omega C^{*2})/\mu^*$ and $\sigma=(\mu^*\omega R^2)/(C^{*2}\cdot\Delta P)$ correspond to a squeeze film Reynolds number and an excitation frequency number, respectively.

The perturbed shear coefficients for the first-order solution in the groove are given by [$j=S$ (stator), R (rotor) or O (orifice)]

$$\gamma_U=\frac{1}{2h_g}\left\{\frac{d_g}{C^*}(k_{S0}\bar{\mu}_0+u_{g0}\bar{\mu}_0 k_{SU})+\frac{L_g}{C^*}[k_{R0}\bar{\mu}_0+(u_{g0}-\Lambda)\bar{\mu}_0 k_{RU}] - \delta_{OI}\frac{A_{Oc}}{RC^*\Delta\bar{x}}\bar{U}_{OI0}\bar{\mu}_0 k_{OU}\right\} \tag{A3}$$

$$k_{jU}=\frac{k_{j0}}{u_{j0}}\left(1-\frac{e_M b_M}{\mathrm{Re}_{j0}\left[10^4 r_j+\dfrac{b_M}{\mathrm{Re}_{j0}}\right]}\right) \tag{A4}$$

$$u_{S0}=u_{g0}\quad u_{R0}=u_{g0}-\Lambda\quad u_{O0}=u_{g0}-\bar{U}_{OI0} \tag{A5}$$

where $\Lambda=(\mu^*\cdot\Omega\cdot R^2)/(C^{*2}\cdot\Delta P)$ is a rotor speed parameter and $r_O=0$,

$$\gamma_\rho=\frac{1}{2h_g}\left\{\frac{d_g}{C^*}u_{g0}\bar{\mu}_0 k_{S\rho}+\frac{L_g}{C^*}(u_{g0}-\Lambda)\bar{\mu}_0 k_{R\rho} - \delta_{OI}\frac{A_{Oc}}{RC^*\Delta\bar{x}}\bar{U}_{OI0}\bar{\mu}_0 k_{O\rho}\right\} \tag{A6}$$

$$k_{j\rho}=\frac{k_{j0}}{\bar{\rho}_0}\left(1-\frac{e_M b_M}{\mathrm{Re}_{j0}\cdot\left[10^4\cdot r_j+\dfrac{b_M}{\mathrm{Re}_{j0}}\right]}\right) \tag{A7}$$

$$\gamma_\mu=\frac{1}{2h_g}\left\{\frac{d_g}{C^*}(k_{S0}u_{g0}+u_{g0}\bar{\mu}_0 k_{S\mu})+\frac{L_g}{C^*}[k_{R0}(u_{g0}-\Lambda)+(u_{g0} - \Lambda)\cdot\bar{\mu}_0 k_{R\mu}]-\delta_{OI}\frac{A_{Oc}}{RC^*\Delta\bar{x}}\bar{U}_{OI0}(k_{O0}+\bar{\mu}_0 k_{O\mu})\right\} \tag{A8}$$

$$k_{j\mu}=-\frac{k_{j0}}{\bar{\mu}_0}\left(1-\frac{e_M b_M}{\mathrm{Re}_{j0}\left[10^4 r_j+\dfrac{b_M}{\mathrm{Re}_{j0}}\right]}\right) \tag{A9}$$

$$\gamma_{UOI}=-\delta_{OI}\frac{1}{2h_g}\frac{A_{Oc}}{RC^*\Delta\bar{x}}(k_{O0}\bar{\mu}_0+\bar{U}_{OI0}\bar{\mu}_0 k_{OUOI}) \tag{A10}$$

$$k_{OUOI}=-\frac{k_{O0}}{u_{g0}-\bar{U}_{OI0}}\left(1-\frac{e_M b_M}{\mathrm{Re}_{O0}\left[\dfrac{b_M}{\mathrm{Re}_{O0}}\right]}\right) \tag{A11}$$

The first-order boundary condition at the orifices discharge planes in the groove is, in dimensionless form:

$$p_{gOI\alpha}=-\mathrm{Re}_P^*\,\bar{u}_{OI0}\left(\bar{\rho}_{gOI0}\bar{u}_{OI\alpha}+\bar{\rho}_{gOI\alpha}\frac{\bar{u}_{OI0}}{2}\right) \tag{A12}$$

The first-order film land entrance and exit pressures and inlet circumferential velocity are given in dimensionless form as

$$p_{l\alpha}\big|_{\bar{z}_i}=p_{g\alpha}-(1+\xi)\cdot\mathrm{Re}_P^*\cdot\left[\bar{\rho}_{l0}\cdot w_{l0}\cdot w_{l\alpha}+\frac{w_{l0}^2}{2}\cdot\bar{\rho}_{l\alpha}\right]\Bigg|_{\bar{z}_i} \tag{A13}$$

$$p_{l\alpha}\big|_{\bar{z}_e}=C_S\cdot\mathrm{Re}_P^*\cdot\left[\bar{\rho}_{l0}\cdot w_{l0}\cdot w_{l\alpha}+\frac{w_{l0}^2}{2}\cdot\bar{\rho}_{l\alpha}\right]\Bigg|_{\bar{z}_e} \tag{A14}$$

$$u_{l\alpha}\big|_{\bar{z}_i}=u_{g\alpha} \tag{A15}$$

Flow periodicity follows for the whole groove circumference. Note that periodicity from one orifice to the next only holds for the equilibrium (zeroth-order) solution.

References

[1] San Andrés, L., 1995, "Thermodynamic Analysis of Fluid Film Bearings for Cryogenic Applications," AIAA J., **11**(5), pp. 964–972.

[2] Fayolle, P. G., Phillips, S. G., and Childs, D. W., 1997, "Experimental Rotordynamic Coefficient Results for a 0.100-mm Clearance Tangential-Against-Rotation Injection Lomakin Bearing," Technical Report No. TAMU 0710, Texas A&M University, College Station, TX.

[3] Lomakin, A., 1958, "Calculation of Critical Speed and Securing of the Dynamic Stability of Rotors in High-Pressure Hydraulic Machines With Reference to Forces Arising in Seal Gaps," Energomashinostroenie, **4**(4), pp. 1–5.

[4] Childs, D. W., 1983, "Finite-Length Solutions for Rotordynamic Coefficients of Turbulent Annular Seals," ASME J. Lubr. Technol., **105**, pp. 437–445.

[5] Von Pragenau, G. L., 1992, "From Labyrinth Seals to Damping Seals/Bearings," *Fourth International Symposium on Transport Phenomena and Dynamics of Rotating Machinery*, Honolulu, HI, Vol. A, pp. 277–285.

[6] Childs, D., and Vance, J., 1994, "Annular Seals as Tools to Control Rotordynamic Response of Future Gas Turbine Engines," 30th AIAA/ASME/SAE/ASEE Joint Propulsion Conference, Indianapolis, IN, Vol. AIAA 94–2804, pp. 1–9.

[7] Martzinkovsky, V. A., 1993, "The Lomakin Effect and Its Applications in Pumps and Sealings," in *Proceedings of the Rotating Machinery Conference and Exposition*, Somerset, NJ, Vol. 2, pp. 1–59.

[8] Black, H. F., Allaire, P. E., and Barrett, L. E., 1981, "Inlet Flow Swirl in Short Turbulent Annular Seal Dynamics," Ninth International Conference on Fluid Sealing, BHRA Fluid Engineering, Leeuwenhorst, Netherlands, pp. 1–14.

[9] San Andrés, L., and Childs, D., 1997, "Angled Injection—Hydrostatic Bearings, Analysis and Comparison to Test Results," ASME J. Tribol., **119**(1), pp. 179–187.

[10] Franchek, N., and Childs, D., 1994, "Experimental Test Results for Four High-Speed, High Pressure, Orifice-Compensated Hybrid Bearings," ASME J. Tribol., **116**(2), pp. 285–290.

[11] Kim, C. H., and Lee, Y. B., 1994, "Test Results for Rotordynamic Coefficients of Anti-Swirl Self-Injection Seals," ASME J. Tribol., **116**, pp. 508–513.

[12] Arauz, G. L., and San Andrés, L., 1996, "Experimental Study on the Effect of a Circumferential Feeding Groove on the Dynamic Force Response of a Sealed Squeeze Film Damper," ASME J. Tribol., **118**, pp. 900–905.

[13] San Andrés, L. A., 1991, "Analysis of Variable Fluid Properties, Turbulent Annular Seals," ASME J. Tribol., **113**, pp. 694–702.

[14] Hirs, G. G., 1973, "A Bulk-Flow Theory for Turbulence in Lubricant Films," ASME J. Lubr. Technol., **95**(2), pp. 137–146.

[15] Childs, D. W., 1983, "Dynamic Analysis of Turbulent Annular Seals Based On Hirs' Lubrication Equation," ASME J. Lubr. Technol., **105**, pp. 429–436.

[16] Nelson, C. C., 1985, "Rotordynamic Coefficients for Compressible Flow in Tapered Annular Seals," ASME J. Tribol., **107**, pp. 318–325.

[17] San Andrés, L., 1993, "Dynamic Force and Moment Coefficients for Short Length Annular Seals," ASME J. Tribol., **115**, pp. 61–70.

[18] Childs, D. W., 1993, *Turbomachinery Rotordynamics*, Wiley, New York, Chap. 5.

[19] Soulas, T., 2001, "A Bulk-Flow Model of Angled Injection Lomakin Bearings," M.S. thesis, Texas A&M University, College Station, TX.

[20] Li, J., San Andrés, L., and Vance, J., 1999, "Bulk Flow Analysis of Multiple-Pocket Gas Damper Seals," ASME J. Eng. Gas Turbines Power, **121**(2), pp. 355–362.

[21] Childs, D., 1989, "Fluid Structure Interaction Forces at Pump-Impeller-Shroud Surfaces for Rotordynamic Calculations," ASME J. Vib., Acoust., Stress, Reliab. Des., **111**, pp. 216–225.

[22] Launder, B. E., and Leschziner, M., 1978, "Flow in Finite Width Thrust Bearings Including Inertial Effects, I-Laminar Flow, II-Turbulent Flow," ASME J. Lubr. Technol., **100**, pp. 330–345.

[23] Van Doormal, J. P., and Raithby, G. D., 1984, "Enhancements of the Simple Method for Predicting Incompressible Fluid Flows," Numer. Heat Transfer, **7**, pp. 147–163.

Field Methods for Identification of Bearing Support Parameters—Part I: Identification From Transient Rotor Dynamic Response due to Impacts

Oscar C. De Santiago
Dresser-Rand Company,
Olean, NY 14760
e-mail: desantiago@dresser-rand.com

Luis San Andrés
Mast-Childs Tribology Professor
Texas A&M University,
College Station, TX 77843-3123
e-mail: lsanandres@mengr.tamu.edu

A simple procedure, with the potential as a field resource, for identification of a bearing support parameter from recorded transient rotor responses due to impact loads follows. The method is applied to a test rotor supported on a pair of mechanically complex bearing supports, each comprising a tilting pad bearing in series with an integral squeeze film damper. Identification of frequency dependent bearing force coefficients is good at a rotor speed of 2000 rpm. Stiffness coefficients are best identified in the low frequency range (below 25 Hz) while damping coefficients are best identified in the vicinity of the first natural frequency (48 Hz) of the rotor bearing system. The procedure shows that using multiple-impact frequency averaged rotor responses reduces the variability in the identified parameters. The identification of frequency-dependent force coefficients at a constant rotor speed is useful to assess rotor-bearing system stability.
[DOI: 10.1115/1.2227033]

Introduction

Experimental identification of fluid film bearing parameters is essential for adequate interpretation of rotating machinery performance and necessary to validate predictions from computational fluid film bearing models. Parameter identification in the field with current customary instrumentation is also promising for condition monitoring and troubleshooting, and in the near future for self-adapting rotor-bearing control systems. The use of combined (in series) bearing supports to control vibration limits and force transmissibility increases the complexity of the identification procedures since the equivalent bearing parameters become speed and frequency dependent.

The force coefficients (stiffness and damping) of fluid film bearings are important in rotor-bearing system analysis since they largely determine the rotor dynamic synchronous response and stability. Numerous efforts have established reliable techniques to accurately identify fluid film bearing coefficients under controlled experimental conditions mainly for verification of thin film fluid flow models. Presently, however, there is also the need for proven identification techniques that allow assessing the validity of predicted bearing force coefficients in their working environment.

The current trend for larger power to weight ratios in rotating machinery demands high speeds and operation well within flexible rotor modes, and thus this condition poses new challenges in terms of dynamic stability control. Modern turbomachinery uses additional sources of damping (such as damper seals) and softer bearing supports to achieve satisfactory stability margins and accurate control and position of critical speeds. A bearing configuration nowadays in use refers to the integration of a tilting pad journal bearing (TPJB) in series with a squeeze film damper (SFD) due to its inherent stability and low force transmissibility. Currently, there is the need to verify the combined bearing dynamic force coefficients in machines that are already operating in the field and which commonly feature this type of support, such as process gas compressors and land based gas turbines.

The objective of this paper is to forward useful procedures for in situ bearing parameter identification. The key feature of the proposed methods is the requirement of minimal external equipment, little or no changes to existing hardware, and the use of measuring instruments commonly found in the field for machine protection and monitoring.

Brief Review of Parameter Identification Methods

The discussion on bearing parameter identification methods focuses on their aptness for implementation in the field. The general problem of bearing parameter identification requires measurements (or estimates) of the bearing reaction force and rotor displacements (response) due to controlled external load excitations. Dynamic loads applied on the rotor or bearing housing (harmonic, pseudorandom, or impulsive forces) allow estimation of the bearing impedance functions in the frequency domain by direct measurement of the applied load magnitude and the corresponding rotor response. One of the most common test rigs for identification of bearing parameters is one in which a (nearly) rigid shaft rotates with no whirl allowed and supported on precision ball or roller bearings [1]. The test bearing, installed at the rotor mid span, is softly supported and free to whirl. Special mechanisms apply static loads in any direction desired. Hydraulic or electromagnetic shakers attached to the test bearing outer shell exert loads in two orthogonal directions. This configuration allows us to conveniently vary the force field applied to the bearing, and to control the eccentricity and amplitude of the bearing response. Independent adjustment of the shaker frequency also allows studying the frequency dependence of bearing force coefficients [2,3]. Despite its merits as a tool for accurate parameter identification leading to verification of predictive bearing models, this excitation method requires elaborate experimental setup and expensive controls not suitable for field implementation.

One of the simplest excitation methods to generate an (apparent) excitation load is to insert calibrated imbalance masses to the

Contributed by the International Gas Turbine Institute (IGTI) of ASME for publication in the JOURNAL OF ENGINEERING FOR GAS TURBINES AND POWER. Manuscript received October 1, 2002; final manuscript received March 1, 2003. Assoc. Editor: H. R. Simmons. Paper presented at the International Gas Turbine and Aeroengine Congress and Exhibition, Atlanta, GA June 16–19, 2003, Paper No. 2003-GT-38583.

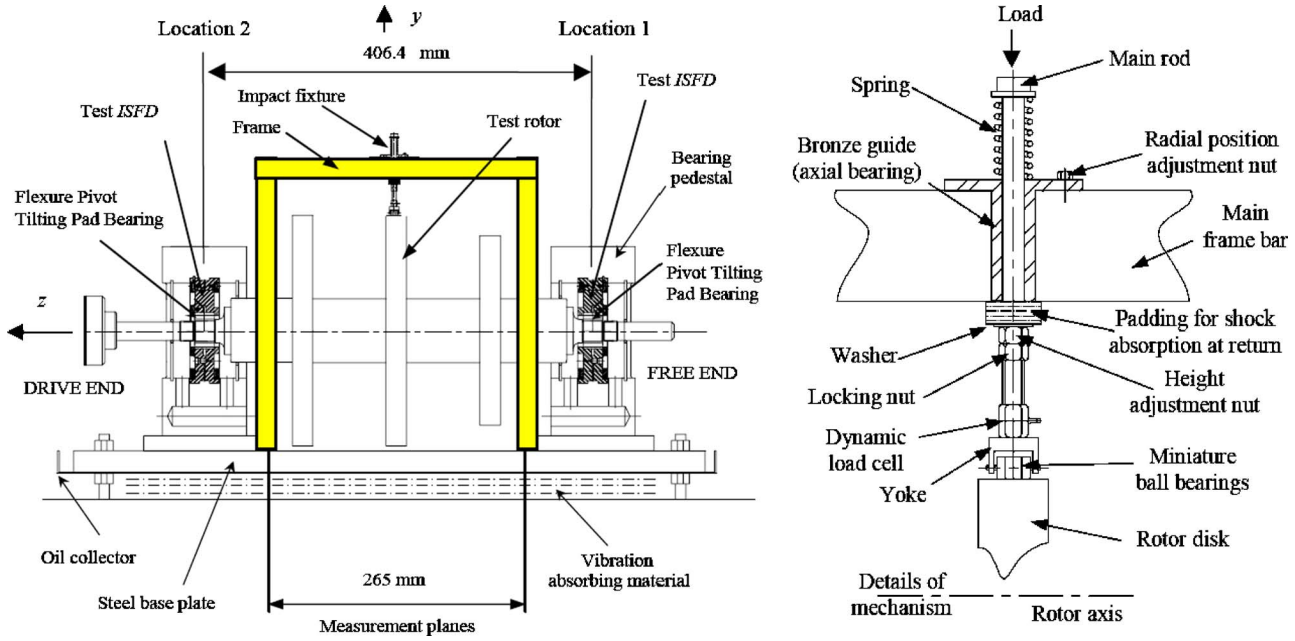

Fig. 1 Test apparatus used for bearing parameter identification and special fixture used to deliver impacts

rotor, so that the centrifugal force excites the rotor-bearing system. In general, the resulting identification equations generated by imbalance excitations tend to be ill-conditioned, and most experimental identifications show considerable scatter of results [4]. However, despite the limitations, this method is appealing for in situ identification of bearing parameters due to the minimal requirements of external excitation systems and easiness of implementation in the field.

Another method for bearing excitation consists of applying periodic or random loads by means of shakers. This method requires vast instrumentation and a more elaborate signal processing procedure that includes generation of the excitation signals and calculation of power spectral densities if noise from the bearing fluid flow occurs in the same range as the frequencies of interest [5]. These factors limit its applicability as a suitable procedure for ready implementation in the field.

Transient loading of rotor-bearing systems (from impact loads, for example) is yet another option for bearing parameter identification. This method has the advantage of exciting a broad range of frequencies in a single experiment, considerably reducing the experimental effort and identification time. Besides, repetition of the experiment is extremely simple, allowing for economical averaging and variability studies. Furthermore, this method does not require as expensive instrumentation and preparation effort as the procedures discussed above. Nicholas et al. [6] suggest the use of frequency response functions obtained by impacts applied to the housing of turbomachines as a means to improve predictions of rotor response. Marscher [7] uses impact tests to identify natural frequencies and damping ratios of rotor-bearing systems that have large noise to signal ratios using a particular time window. Nordmann and Shollhorn [8] identify eight bearing parameters (four stiffness and four damping coefficients) in a symmetric rotor supported on identical journal bearings using impact excitations directly applied to the rotating shaft. The authors regard the bearing parameters as constant over a frequency range and use curve fitting of the frequency response (mobility) function amplitudes determined from the Fourier transform of the measured displacements and force. The method renders excellent correlation with theoretical predictions in the range of Sommerfeld numbers (0.75–2.3) for cylindrical journal bearings.

Diaz and San Andrés [9,10] discuss in more detail the frequency domain and the time domain based identification methods applied to bearing and seal elements in rotating machinery. A companion paper [11] presents the application of the imbalance response method for identification of force coefficients with application to the rotor-bearing configuration presented herein.

Test Rig and Bearing Supports

Figure 1 depicts the test rig for rotordynamic measurements and application of impact loads. The apparatus consists of a three-disk (rigid) rotor supported on a pair of identical bearings housed in bearing pedestals resting on a thick steel plate. The plate is attached to a concrete table isolated from the laboratory floor by a bottom steel plate and elastomeric material. De Santiago and San Andrés [12] fully describe the test rig and lubrication system used for measurements of rotor response to imbalance and verification of squeeze film damper characteristics. The rotor has the size and inertia properties similar to those found in small aircraft gas turbines. Figure 1 includes the major rig dimensions and Table 1 presents a summary of the rotor inertia properties.

Table 1 Test rotor geometry characteristics and inertia properties

Mass (including half of flexible coupling) (m)		45.3 kg (99.8 lb.)
Rotor transverse moment of inertia (I_T)		0.704 kg m^2 (2406 lb in.^{2})
Rotor total polar inertia (I_P)		0.299 kg m^2 (1022 lb in.^{2})
Shaft main diameter		76.2 mm (3.00 in.)
Total rotor length		673 mm (26.50 in.)
Bearing span		406 mm (16.0 in.)
Rotor cg location from drive end		285 mm (11.2 in.)
Distances from cg to bearing locations (l_1,l_2)	217 mm (8.54 in.)	189 mm (7.44 in.)
Distances from cg to planes of impact excitation (d_1,d_2)	0 mm	0 mm
Distances from cg to location of displacement sensors (s_1,s_2)	146 mm (5.75 in.)	119 mm (4.69 in.)

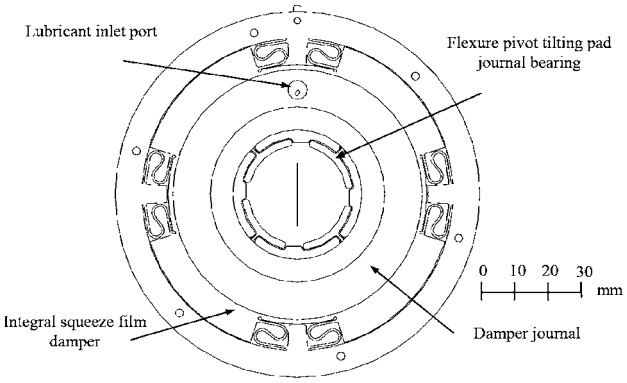

ISFD outer diameter = 126 mm (4.61 in), land radius = 48.26 mm (1.9 in)
FPJB nom. diam – 30.15 mm (1.19 in), axial length – 22.86 mm (0.9 in)

Fig. 2 Combined integral damper and flexure pivot bearing used for parameter identification

Currently, the test rig features a support bearing consisting of a flexible pivot tilting pad journal bearing (FPJB) in series with a squeeze film damper of the integral type. Figure 2 shows a schematic of the combined bearing support, and Table 2 presents the components main dimensions, including measured clearances and lubricant properties. The test damper consists of two (outer and inner) rings connected with four pairs of S-shaped structural springs machined with the EDM process. After the static load is applied (rotor weight), a small clearance of 229 microns (~9 mils) separates the two rings and forms the damper land where the lubricant film generates the viscous dissipation forces. The damper land is thus sectioned by the springs into four pads with an arc extent of 52 deg. Lubricant enters the film lands through four radial holes located around the damper outer ring, and a groove machined on the outer face of the ring forms a plenum for lubricant supply once the damper seats in its housing. The damper inner ring (also called damper journal) accommodates the tilting pad bearing and provides a lateral orifice for independent bearing lubricant supply. An inner groove machined on the damper inner ring also forms a plenum from where the lubricant enters the bearing radially at feed port locations between the pads. The test bearing has four pads (70 deg in extent) flexibly attached to an outer ring through integrally machined thin elastic beams (pivots). In the experiments, the bearings are installed in the (gravity) load between pad configurations.

Table 2 Integral squeeze film damper and flexure pivot tilting pad bearing main dimensions[a]

Squeeze film damper	4 pads (52 deg)
Damper land radius	48.26 mm (1.900 in.)
Land clearance (centered)	0.229 mm (9 mils)
Damper axial length	23.00 mm (0.910 in.)
Flexure pivot TPJB	4 pads (70 deg)
Nominal diameter	30.15 mm (1.187 in.)
Axial length	22.9 mm (0.902 in.)
Radial clearance	0.076 mm (3 mils)
Pad preload[b] /pivot offset	0.405/0.5
Pad rotational stiffness	40 N m/rad (354 lb. in./rad)
Static load between pads	
Drive end bearing	247.3 N (55.5 lb.)
Free end bearing	198.2 N (44.5 lb.)

[a]Lubricant: ISO VG10 oil, average inlet viscosity (μ): 15.76 cP at 24.4 °C (76 °F).
[b]Dimensionless.

In the current experiments, an ad hoc fixture delivers impact loads to the rotor middle disk while the rotor spins. The impact force is transmitted through a tandem arrangement of (four) miniature ball bearings whose axis is aligned with the rotor main axis, as shown in detail in Fig. 1. This arrangement of multiple bearings is needed in order to share the impact load and to prevent failure of the rolling elements. A medium-hardness rubber hammer impacts an aluminum rod which slides in a bronze guide supported on a metallic structure attached to the test rig base plate. A coil spring returns the rod assembly to the initial position and an elastomeric material overdampens the assembly motion. The aluminum rod transmits the load through a calibrated load cell that measures the total applied load to the rotor. The opposite end of the load cell features a special yoke mechanism upon which the miniature bearings are installed. In all experiments, special care is taken to ensure that the axes of the impact mechanism aligns with the corresponding radial directions (x,y) and perpendicular to the rotor axis of rotation. The resting position of the ball bearings is no more than 0.5 mm from the rotor disk surface to minimize inertia effects and undesirable signal noise arising from bouncing after the shock. After installation of the impact delivery fixture on the test rig, a detailed calibration of all mechanical components and the instrumentation followed.

The main rig instrumentation consists of two pairs of eddy current displacement transducers located on the inboard side of the bearing housings that measure the rotor motion in the two orthogonal directions (x,y). An optical tachometer provides a reference signal to the acquisition system for further signal filtering and to a digital display of rotor speed. Two piezoelectric load cells in the impactor mechanism provide time signals of the applied loads on the rotor. The data acquisition system consists of a high speed, simultaneous multichannel unit interfaced to a PC. Driver software developed includes pretriggering to ensure that the impact force signal is completely acquired within the time record of an experiment.

Identification Procedure

The identification method in [8] is readily adapted for estimation of frequency dependent force coefficients in complex bearing supports, as is the case for the series FPJB-SFD tested. The recorded critical speeds of the rotor-bearing system [12] equal 2900 rpm and 6100 rpm, corresponding to (rigid rotor) cylindrical and conical motions, respectively. The first rotor elastic mode is estimated at 12,000 cpm from a transfer matrix model, and well above the maximum frequency of interest (~70 Hz). Thus, the motion of the test rotor on the bearing supports (series FPJB-SFD) is modeled as a four-degree of freedom system including the cylindrical and conical modes of vibration excited in the frequency range of interest. Figure 1 depicts the coordinate system notation used in the analysis. In the frequency domain, the equations of motion for a perfectly balanced rotor and bearing support system reduce to the algebraic form

$$-\omega^2\mathbf{M}\mathbf{q}_o + j\omega\Omega\mathbf{G}\mathbf{q}_o + j\omega\mathbf{C}\mathbf{q}_o + \mathbf{K}\mathbf{q}_o = \mathbf{E}_o \tag{1}$$

where $\mathbf{M}$, and $\mathbf{G}$ are the (4×4) inertia and gyroscopic moments matrices, and $\mathbf{C}$ and $\mathbf{K}$ are the (speed and frequency dependent) bearing support damping and stiffness matrices. The Appendix lists the terms in these matrices. Ω is the rotor speed and ω is a selected excitation frequency. The response vector $\mathbf{q}_o = [x_1, x_2, y_1, y_2]^T$ contains the complex amplitudes of motion (x,y) at the bearing locations (1,2). Prior to the transformation into the frequency domain, $\mathbf{E}(t)$ is the transient rotor excitation (impact load) given by the generalized vector:

$$\mathbf{E}(t) = \begin{bmatrix} \sum_i F_{ix} \\ \sum_i d_i F_{ix} \\ \sum_i F_{iy} \\ \sum_i d_i F_{iy} \end{bmatrix} = \begin{bmatrix} F_{1x} + F_{2x} + \cdots \\ d_1 F_{1x} + d_2 F_{2x} + \cdots \\ F_{1y} + F_{2y} + \cdots \\ d_1 F_{1y} + d_2 F_{2y} + \cdots \end{bmatrix} \tag{2}$$

where $F_{1x}(t), F_{2x}, \ldots, F_{1y}, F_{2y}, \ldots$ are the excitation forces (impacts) applied at the ith location along the rotor and at a distance d_i from the rotor center of mass. Note that Eq. (1) holds at any constant rotor speed Ω and at any particular frequency ω. At the rotor speed Ω, the steady state response is of the form $\mathbf{q} = \mathbf{q}_o e^{j\Omega t}$. This response at $\omega = \Omega$ defines the synchronous rotor response solely due to the impact excitation. In practice, an adequate procedure must filter out the remnant imbalance and synchronous noise components (due say to shaft eccentricity) for satisfactory identification of synchronous force coefficients at this frequency.

From Eq. (1), the bearing support reaction forces are expressed as the product of a response matrix $\mathbf{Q}$ and a vector of (stiffness and damping) parameters $\mathbf{P}$, and decomposed along the x and y directions, as

$$\mathbf{Q}^x \mathbf{P}^x = [\mathbf{E}_o + [\omega^2 \mathbf{M} - j\omega\Omega \mathbf{G}]\mathbf{q}_o]^x = \mathbf{E}_T^x \tag{3a}$$

$$\mathbf{Q}^y \mathbf{P}^y = [\mathbf{E}_o + [\omega^2 \mathbf{M} - j\omega\Omega \mathbf{G}]\mathbf{q}_o]^y = \mathbf{E}_T^y \tag{3b}$$

where

$$\mathbf{Q}^x = \begin{bmatrix} \mathbf{q}_o^T \\ \mathbf{q}_o^T \mathbf{l} \end{bmatrix}_{2\times 4}$$

$$\mathbf{P}^x = [Z_{xx1}, Z_{xx2}, Z_{xy1}, Z_{xy2}]^T \tag{4}$$

with $\mathbf{l}$ as a diagonal matrix with components $\bar{\mathbf{l}} = [l_1, l_2, l_1, l_2]^T$. Z_{ij} are the complex bearing impedance functions defined as $\{K_{ij} + j\omega C_{ij}\}_{ij=x,y}$. Similar relationships hold for $\mathbf{Q}^y$ and $\mathbf{P}^y$. The subindices 1 and 2 correspond to the bearing supports on the free and drive end sides of the rotor, respectively.

Vibration data generated by two impacts A and B producing linearly independent responses can be stacked and Eqs. (3) render $\mathbf{P}^x$ and $\mathbf{P}^y$ from

$$\mathbf{P}^x = \bar{\mathbf{Q}}^{x^{-1}} \bar{\mathbf{E}}_T^x \tag{5a}$$

$$\mathbf{P}^y = \bar{\mathbf{Q}}^{y^{-1}} \bar{\mathbf{E}}_T^y \tag{5b}$$

where matrix $\bar{\mathbf{Q}}^{x,y}$ and vector $\bar{\mathbf{E}}_T^{x,y}$ result from stacking data from the two tests. Each of the identification Eqs. (5) represent four complex equations with four unknown impedances along each direction (x,y), thus rendering a total of eight stiffness and eight damping coefficients. The conditions for linear independence of Eqs. (5) depend on the axial location and on the direction of the applied load. These conditions can be stated from the definition of the excitation vector in Eq. (2). Recall that $F_{i(x,y)}(t)$ represent impact loads applied along directions x, y on the rotor. Consider the case of a single impact applied at a time. The excitation in test B is linearly independent from the one applied in test A by simply shifting the excitation location along the rotor, even if the impact is applied in the same direction, i.e.

$$\mathbf{E}_A(t) = \begin{bmatrix} F_{1x} \\ d_1 F_{1x} \\ 0 \\ 0 \end{bmatrix}$$

$$\mathbf{E}_B(t) = \begin{bmatrix} F_{1x} \\ d_2 F_{1x} \\ 0 \\ 0 \end{bmatrix} \tag{6}$$

$\mathbf{E}_B$ is linearly independent from $\mathbf{E}_A$ if $d_1 \neq d_2$. Applying impacts first in one direction and then in an orthogonal direction also yields linearly independent excitation vectors, even if the axial location of the impacts is the same. Impact loads may be applied at the rotor center of gravity ($d_1 = 0$) or away from it. Assuming the bearings supports' coefficients to be identical[1] reduces the number of impedances to 4, and full identification is possible with only one impact excitation. In all cases, several consecutive impacts at the same rotor speed provide redundant data for error minimization.

Most times, measurements of the rotor response are not taken at the bearing locations. In this case, a simple geometrical transformation using the rigid rotor consideration allows the use of recorded rotor responses $x, y|_{s1}$, $x, y|_{s2}$ at locations s_1 and s_2 away from the rotor center of gravity (cg).

Experiments and Discussion of Results

This section presents the results of bearing support force coefficients identified at a rotor speed of 2000 rpm. Impacts were delivered at the rotor middle disk coinciding with its cg and the transient response measured at two axial locations. The test procedure included five repetitions of the impact excitation along each direction (x, y, horizontal and vertical). Extensive tests showed a linear rotor response with respect to the applied load amplitude. Thus, an averaging process in the frequency domain was performed to each group of five measurements (x,y) after a run out (synchronous speed) filter was applied to each recorded time response.

Figure 3 shows a typical time trace of the recorded rotor responses at the drive end, horizontal (x_2) location before and after filtering of the shaft run out motion. The filter subtracts the shaft run out from the recorded dynamic signal in a point-by-point procedure from left to right and from right to left in the time window. Notice from Fig. 3 that a pretrigger of about 40 ms is used in the acquisition, thus allowing us to capture a full period of shaft run out for filtering. Figure 3(b) shows the filtered signal in the frequency domain and compared with a frequency-domain-based filter. The use of time filtering is preferred in this case because frequency-based filters require a more elaborate synchronized acquisition of a full shaft run out time record. In contrast, time filtering requires only a short pretrigger time for acquisition.

Presently, rotor transient motions in a direction orthogonal to that of an impact are very small and due only to cross-coupled force effects, which are known to be small for the test bearing support elements. The transient responses in the main direction of impact die out rapidly within the recorded time elapsing a few periods of synchronous rotor motion. Typical magnitudes of rotor transient motion after the release of the load are in the order of 25 microns ($\sim$1 mil) 0-pk for the first peak. The time decay of the peak amplitudes denotes viscous damping with some amount of Coulomb damping, probably from the structural components of the bearing. Note that the fundamental period of rotor motion is about 20 ms (48 Hz), i.e. approximately 16 times longer than the duration of a typical impact load. Reference [13] shows a detailed explanation of the measurements and identification procedure.

Figure 4 shows the identified (a) direct and (b) cross-coupled stiffness and damping coefficients for the two bearing supports at a rotor speed of 2000 cpm (33.3 Hz). The results presented are for a total of five averaged impacts. The figure also presents predic-

[1]This condition assumes identical bearing supports, similar lubricant operating conditions and equal static load.

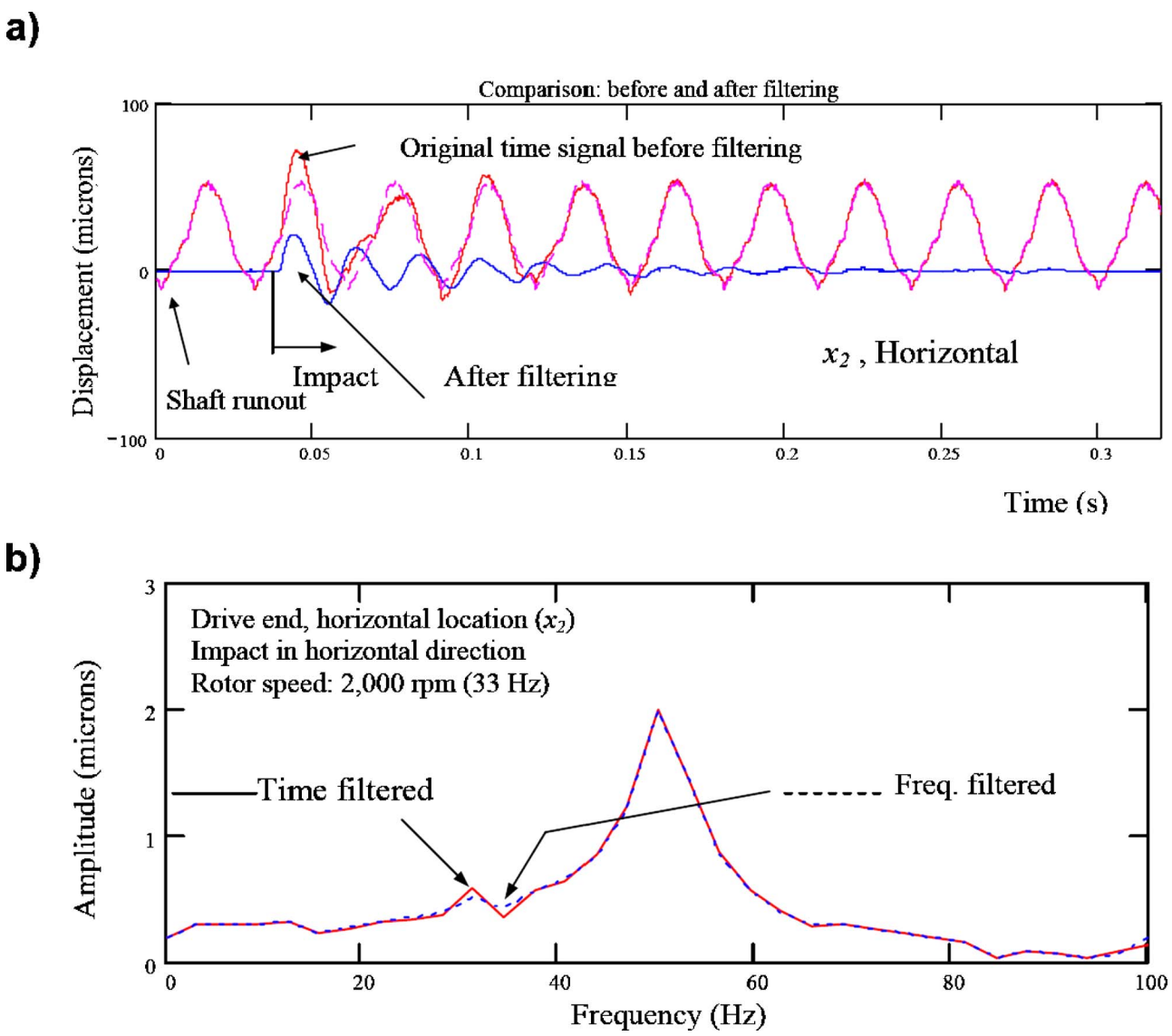

Fig. 3 Digital vibration signal filtering. (*a*) Original time record and time-based filtered signal; (*b*) DFT of filtered signal and comparison with a frequency-based synchronized filter.

tions, to be discussed later. The estimated bearing support force coefficients represent equivalent values for the FPJB in series with a SFD. Stiffness coefficients are very similar for the two bearing supports and along the two directions (x,y). The vertical direct stiffness (K_{yy}) of the drive end support (subindex 2) is slightly larger than the vertical stiffness of the free end throughout the frequency range, as a result of the larger load supported by the bearing at the drive end. Stiffness coefficients remain nearly invariant up to a frequency of 40 Hz (~1.2 times the synchronous rotor speed frequency) and then decrease sharply until 60 Hz, above the rotor-bearing system's first natural frequency (48 Hz). At this frequency (60 Hz), there is a clear distinction between the stiffness of the drive end and free end bearing supports, the drive end bearing presenting a larger stiffness (approximately 70% larger). Also at this frequency of 60 Hz, the equivalent direct stiffnesses in the vertical and horizontal directions are practically identical.

Figure 4 also depicts the identified bearing support damping coefficients in the main directions (x,y). Experimental identification of damping coefficients at low frequencies is not accurate due to the smallness of the damping forces developed. Damping coefficients around the synchronous frequency do not present a definite trend and appear more sensitive to small variations in the rotor response than the stiffness coefficients. The identified direct damping coefficients remain nearly invariant in the range of 37–53 Hz; and then show a sharp increase at higher frequencies, in particular the damping coefficients of the free end bearing (C_{yy}). In general, identified direct damping coefficients in the vertical direction are larger than those along the horizontal direction.

The values of identified cross-coupled stiffness and damping coefficients remain small for the entire range of frequencies, as displayed in Fig. 4. Note the differences in the scales for the depiction of direct and cross-coupled stiffness coefficients. Cross-coupled damping coefficients are virtually null with some perturbations at the running speed. Cross-coupled stiffness coefficients remain bounded, with magnitudes at most 20% of the direct stiffnesses. Furthermore, cross-coupled stiffness coefficients have the same sign over the entire frequency range considered.

Predictions for the equivalent bearing support coefficients involve estimation of the equivalent impedances from the integral squeeze film damper and tilting pad bearing elements. Based on earlier measurements with this type of mechanical element [12], the damper structural stiffness and damping coefficients equal 3.4 MN/m and 950 N s/m, respectively, constants over the range

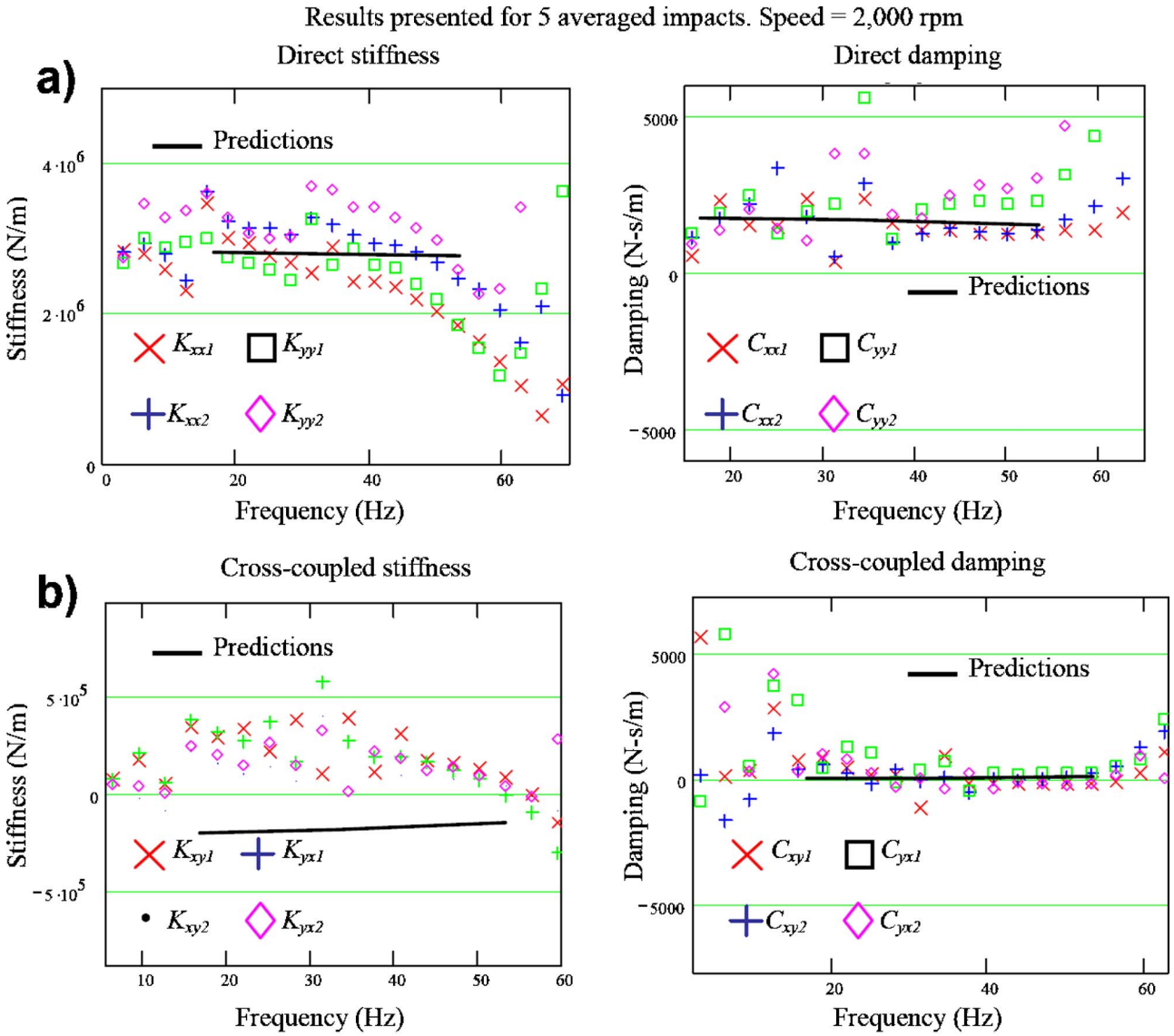

Fig. 4 Identified frequency-dependent bearing force coefficients and comparison with predicted parameters for the combined ISFD-FPJB bearing support. (*a*) Direct force coefficients; (*b*) cross-coupled force coefficients.

of frequencies tested. On the other hand, tilting pad bearing force coefficients are well known to be frequency dependent. Reference [14] details the bearing flow model used for prediction of flexure pivot tilting pad bearing force coefficients. The predicted combined support stiffness and damping coefficients include the damper journal attachment mass (~1.2 kg) and show a modest dependency on the frequency of rotor excitation. This small change of the (analytical) equivalent stiffness with respect to frequency is due to the large amounts of predicted damping from the tilting pad bearing. The experimentally derived parameters demonstrate that predictions resemble closely the direct stiffnesses and slightly overpredict the direct damping coefficients. Predicted cross-coupled damping coefficients are also nearly null, whereas cross-coupled stiffnesses are of the same magnitude but opposite in sign as those derived from the tests and identification procedure.

Note that the direct stiffness identified at low frequencies corresponds with the damper structural stiffness (3.4 MN/m). The sharp decrease in identified stiffness coefficients as frequency increases suggests that inertial effects from other components not considered in the rotordynamic model are present in the measured response, probably as a result of a test rig steel base plate resonance. It is also possible that the SFD and FPJB show much stronger frequency effects than previously known.

Effect of Response Averaging on Parameter Identification From Impact Response Measurements. The high quality of the instrumentation used in the experiments warrants a small uncertainty in the magnitude of the identified coefficients (maximum values of uncertainty amount to less than ±3%) as derived for a single experiment [13]. However, averaging of multiple test frequency responses offers a way to estimate the "true" values of the support force coefficients. Two impacts along each of the directions (x, y) suffice to identify the support parameters, for example. Multiple impacts (with their associated responses) increase rapidly the number of data pairs available for estimation of the force coefficients. Note that repeated delivered impacts are not strictly identical nor the measured rotor responses.

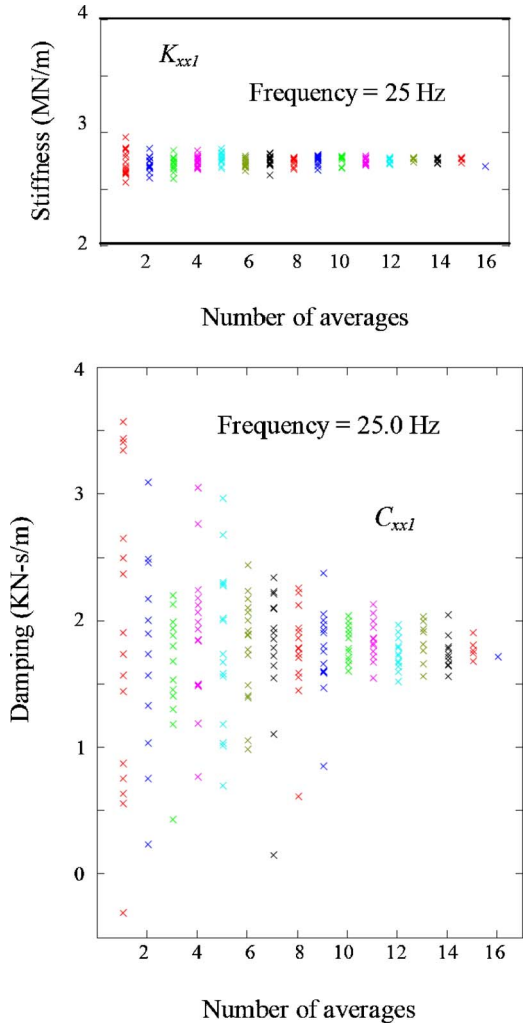

Fig. 5 Identified direct stiffness and damping coefficients as a function of the number of (impact) paired responses used. Operating condition: rotor speed=20,000.

In the experiments, the rotor is impacted several times along both directions (x,y); and thus, each time there is a larger number of paired responses that the identification procedure can use to identify the system parameters. Figure 5 depicts the effects of multiple frequency response averaging on the direct stiffness and damping coefficients at a particular frequency (25 Hz) for the free end bearing support. In the figure, the horizontal axis shows the number of data pairs used in the identification, 16 being the maximum. The results shown make patent the beneficial effect of increasing the number of impact pair responses to estimate actual parameters. For example, increasing the number of pairs in the averaging beyond 9 pairs does little to improve the direct stiffness (K_{xxl}) variability range. Thus, three impacts along each direction may suffice for a satisfactory identification of bearing stiffness coefficients.

Figure 5 also shows the identified direct damping coefficient (C_{xxl}) as a function of the number of averages used in the identification. The damping coefficient shows large variability scattering, spread in a range of up to two times its mean value. However, the trend is clear, i.e., increasing the number of averages does bring the identification process to converge towards the mean (true) value. For the frequency shown, 16 impacts are necessary to provide a reliable value of damping. The cross-coupled stiffness coefficients, not shown for brevity, have a similar trend to that of the direct damping coefficients, but with less variability with respect to the number of averages. In this case, 10 averages suffice to converge to a unique value.

In order to validate the identified bearing parameters, the rigid rotor model of Eq. (1) is used to predict the rotor response at the locations of measurement under known experimental excitations. Figure 6 shows the measured (symbols) and predicted (lines) rotor responses resulting from an impact. The predictions shown are based on (*a*) the estimated bearing support parameters and (*b*) the analytically derived bearing support force coefficients. The experimental response shown was not used in the identification procedure, and thus represents a truly independent record. The predicted rotor displacements (from identified parameters) in the directions of impact follow closely the experimental responses (amplitude and phase), thus indicating that the identified coefficients accurately represent the bearing support characteristics.

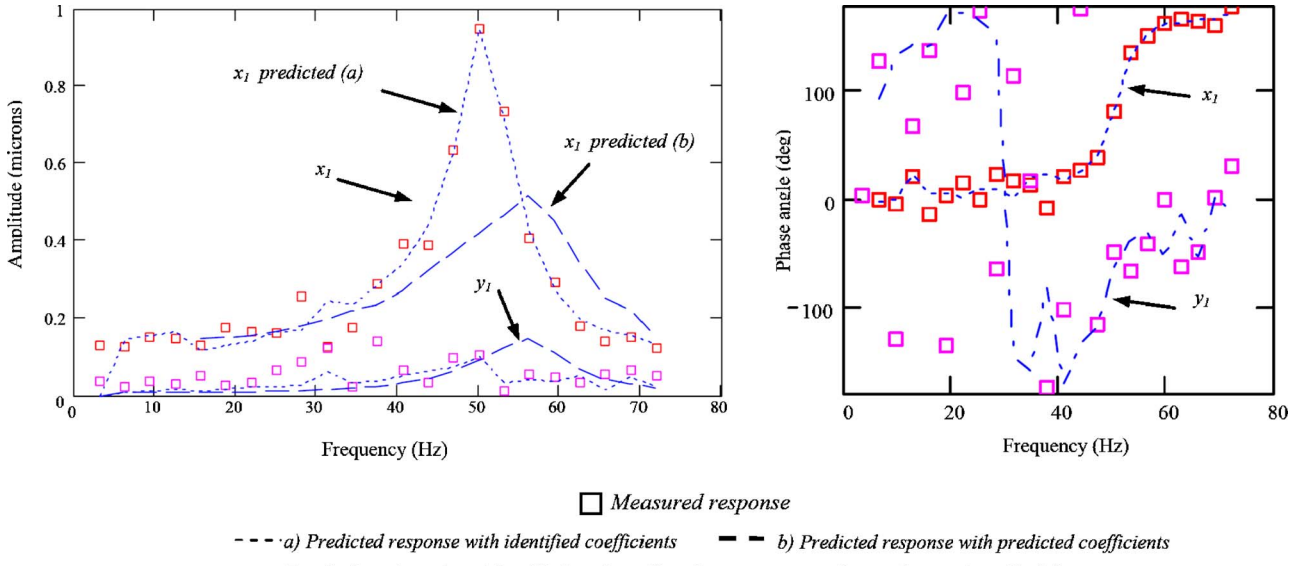

Fig. 6 Comparison of measured and predicted rotor forced response at bearing locations. Impact in horizontal direction.

Conclusions

The paper details a procedure (along with experimental validation) for identification of rotordynamic force coefficients of a series bearing support (FPJB-SFD). Identification of frequency-dependent bearing force coefficients at constant rotor speed requires measurements of the rotor responses to impact loads delivered along two orthogonal directions and/or in two characteristic axial planes.

Identification from impact excitations of the FPJB-SFD series support indicates that the equivalent damping force coefficients are not strong functions of the frequency of excitation. On the other hand, identified equivalent direct stiffness coefficients seem to be affected by other rig component dynamics that reduce the stiffness values at frequencies above the first natural frequency of the rotor-bearing system (48 Hz). In general, predicted (analytical) bearing force coefficients show good agreement with the experimentally derived coefficients within the frequency range of identification.

The identification procedure developed is limited to the case of nearly rigid rotors. Presently, the method is being extended towards its implementation with flexible rotors. Another important limitation of the experimental procedure described is that a special mechanical arrangement must be devised to deliver the impact loads. A viable alternative is to impact the machine casing instead of the rotating structure. In this case, an appropriate model of the support structure is necessary.

Acknowledgment

The authors thank the support of the Turbomachinery Research Consortium of Texas A&M University. The help of Mr. Fernando Romero, undergraduate student, in performing the experiments is also appreciated.

Nomenclature

- $\mathbf{C}$ = rotor-bearing system damping matrix
- C = bearing damping force coefficient (N s/m)
- d = distance from impact plane to rotor CG (m)
- $\mathbf{E}$ = transient rotor excitation vector
- F = force (N)
- $\mathbf{G}$ = gyroscopic moments matrix
- I_T = rotor total transverse moment of inertia ($\mathrm{kg\,m^2}$)
- I_P = rotor total polar moment of inertia ($\mathrm{kg\,m^2}$)
- j = $\sqrt{-1}$ Imaginary unit
- $\mathbf{K}$ = rotor-bearing system stiffness matrix
- K = bearing stiffness force coefficient (N/m)
- L = bearing span, $L=l_1+l_2$ (m)
- L_b, L_d = bearing and damper elements axial length (m)
- l = distance of bearing location to rotor CG (m)
- $\mathbf{M}$ = system mass matrix
- M = total rotor mass (kg)
- $\mathbf{P}$ = vector of system parameters
- $\mathbf{q}$ = rotor response vector
- $\mathbf{Q}$ = matrix of responses for parameter identification
- s = distance from sensor location to rotor CG (m)
- t = time (s)
- (x,y) = coordinates of rotor motion (m)
- Z = bearing impedance $[Z=(K+j\omega C)]$ (N/m)
- Ω = frequency of rotor speed (rad/s)
- ω = frequency of excitation (rad/s)

Appendix: Model Matrices Definition

The test rotor is modeled as a four degree of freedom system. The matrices in Eq. (1) are defined as

$$\mathbf{M}=\frac{1}{L}\begin{bmatrix} Ml_2 & Ml_1 & 0 & 0 \\ -I_T & I_T & 0 & 0 \\ 0 & 0 & Ml_2 & Ml_1 \\ 0 & 0 & I_T & -I_T \end{bmatrix}$$

$$\mathbf{G}=\frac{1}{L}\begin{bmatrix} 0 & 0 & 0 & 0 \\ 0 & 0 & -I_P & I_P \\ 0 & 0 & 0 & 0 \\ -I_P & I_P & 0 & 0 \end{bmatrix}$$

$$\mathbf{K}=\begin{bmatrix} K_{xx1} & K_{xx2} & K_{xy1} & K_{xy2} \\ -K_{xx1}l_1 & K_{xx2}l_2 & -K_{xy1}l_1 & K_{xy2}l_2 \\ K_{yx1} & K_{yx2} & K_{yy1} & K_{yy2} \\ K_{yx1}l_1 & -K_{yx2}l_2 & K_{yy1}l_1 & -K_{yy2}l_2 \end{bmatrix}$$

$$\mathbf{C}=\begin{bmatrix} C_{xx1} & C_{xx2} & C_{xy1} & C_{xy2} \\ -C_{xx1}l_1 & C_{xx2}l_2 & -C_{xy1}l_1 & C_{xy2}l_2 \\ C_{yx1} & C_{yx2} & C_{yy1} & C_{yy2} \\ C_{yx1}l_1 & -C_{yx2}l_2 & C_{yy1}l_1 & -C_{yy2}l_2 \end{bmatrix}$$

References

[1] Someya, O. J., 1988, *Journal Bearing Data Book*, Springer-Verlag, Berlin, Chap. 5.

[2] Ha, H. C., and Yang, S. H., 1998, "Excitation Frequency Effects on the Stiffness and Damping Coefficients of a Five-Pad Tilting Pad Journal Bearing," ASME Paper No. 98-TRIB-44.

[3] Pettinato, B. C., Flack, R. D., and Barrett, L. E., 2001, "Effects of Excitation Frequency and Orbit Magnitude on the Dynamic Characteristics of a Highly Preloaded Three-Lobe Journal Bearing," Tribol. Trans., **44**, pp. 575–582.

[4] Goodwin, M. J., 1991, "Experimental Techniques for Bearing Impedance Measurement," ASME J. Eng. Ind., **113**, pp. 335–342.

[5] Rouvas, C., and Childs, D. W., 1993, "A Parameter Identification Method for the Rotordynamic Coefficients of a High Reynolds Number Hydrostatic Bearing," ASME J. Vibr. Acoust., **115**, pp. 264–270.

[6] Nicholas, J. C., Whalen, J. K., and Franklin, S. D., 1986, "Improving Critical Speed Calculations Using Flexible Bearing Support FRF Compliance Data," *Proceedings of the 15th Turbomachinery Symposium*, Houston, TX, ASME, New York, pp. 69–78.

[7] Marsher, W. D., 1999, "Modal Testing of Rotating Machinery While It Is Operating," Sound Vib., **33**, pp. 29–32.

[8] Nordmann, R., and Shollhorn, K., 1980, "Identification of Stiffness and Damping Coefficients of Journal Bearings by Means of the Impact Method," *Proceedings of the International Conference on Vibration in Rotating Machinery* (ISROMAC), IMechE, Cambridge, England, pp. 231–238.

[9] Diaz, S., and San Andrés, L., 1999, "A Method for Identification of Bearing Force Coefficients and Its Application to a Squeeze Film Damper With a Bubbly Lubricant," STLE Tribol. Trans., **42**, pp. 739–746.

[10] Diaz, S., and San Andrés, L., 2000, "Orbit-Based Identification of Damping Coefficients on Off-Centered Squeeze Film Dampers Including Support Flexibility," ASME Paper No. 2000-GT-0394.

[11] De Santiago, O., and San Andrés, L., 2003, "Field Methods for Identification of Bearing Support Parameters. Part II-Identification From Rotor Dynamic Response Due to Imbalances," ASME Paper No. GT-2003-38585.

[12] San Andrés, L., and De Santiago, O., 2003, "Imbalance Response of a Rotor Supported on Flexure Pivot Tilting Pad Journal Bearings in Series With Integral Squeeze Film Dampers," ASME J. Eng. Gas Turbines Power, **115**, pp. 1026–1032.

[13] De Santiago, O., 2002, "Identification of Bearing Supports' Force Coefficients From Rotor Responses Due To Imbalances and Impact Loads," Ph.D. dissertation, Texas A&M University, College Station, TX.

[14] San Andrés, L., 1996, "Turbulent Flow, Flexure-Pivot Hybrid Bearing for Cryogenic Applications," ASME J. Tribol., **118**, pp. 190–200.

Field Methods for Identification of Bearing Support Parameters—Part II: Identification From Rotor Dynamic Response due to Imbalances

Oscar C. De Santiago
Dresser-Rand Company,
Olean, NY 14760
e-mail: desantiago@dresser-rand.com

Luis San Andrés
Mast-Childs Tribology Professor
Texas A&M University,
College Station, TX 77843-3123
e-mail: lsanandres@mengr.tamu.edu

This paper describes a procedure suitable for field implementation that allows identification of synchronous bearing support parameters (force coefficients) from recorded rotor responses to imbalance. The experimental validation is conducted on a test rotor supported on two dissimilar bearing supports, both mechanically complex, each comprising a hydrodynamic film bearing in series with a squeeze film damper and elastic support structure. The identification procedure requires a minimum of two different imbalance distributions for identification of force coefficients from the two bearing supports. Presently, the test rotor responses show minimal cross-coupling effects, as also predicted by analysis, and the identification procedure disregards cross-coupled force coefficients thereby reducing its sensitivity to small variations in the measured response. The procedure renders satisfactory force coefficients in the speed range between 1500 and 3500 rpm*, enclosing the rotor-bearing system first critical speed. The identified direct force coefficients are in accordance with those derived from the impact load excitations presented in a companion paper.* [DOI: 10.1115/1.2227034]

Introduction

The identification of bearing parameters is traditionally confined to laboratory environments, which rarely present the same operating characteristics as in actual practice. Methods to identify in situ bearing force coefficients are available, although their application is limited due to their excessive complexity (mechanical and analytical). However, state of the art instrumentation, readily available in high performance machinery, enables the application of simpler methods that rely on customary measurements of rotor vibration response.

The design of turbomachinery relies on the accurate prediction of rotor response to imbalance. Synchronous bearing support force coefficients are largely responsible for the response characteristics of turbo rotors; and frequently, are the source of discrepancies between predicted and measured responses. Furthermore, the use of mechanically complex supports to better address the increasingly stringent vibration limits and stability margins (i.e., series damper-bearings) calls for the development of suitable identification methods to verify in the field predicted bearing support synchronous force coefficients.

The general problem of bearing parameter identification requires measurements (or estimates) of the bearing force (excitation) and rotor displacements (response). There are currently numerous methods advanced for bearing parameter identification. Excitation sources that allow estimation of the bearing impedance functions include harmonic forces, pseudorandom periodic excitation, rotor imbalance, and transient impulse loads (impacts), among others. A companion paper [1] presents the application of impact loads to identify frequency-dependent bearing force coefficients at a constant running speed.

One of the simplest excitation methods to generate an (apparent) excitation load is to apply calibrated imbalances to the rotating shaft, so that the centrifugal force excites the system. Many identification methods, most applied in the laboratory, restrict their attention to point mass (rigid) rotors and identical bearing supports [2–5]. However, actual rotating machinery often features bearing supports that are different on each end of a rotor. Furthermore, most turbo rotors are not symmetrical, and the bearings on both ends carry different static loads. In overhung rotors, the load differences can be dramatic. Thus, bearing force coefficients differ largely between the drive and free ends of a rotor (even in the case of identical bearings). Thus, it is necessary to extend the previous methods by including the effect of rotor dynamics if in situ identification is to become viable (without means to measure transmitted forces through the bearings). The resulting model then includes the rotor mass moment of inertia properties as well as gyroscopic effects. Then, the extended set of equations of motion provides enough information to derive estimates for the eight force coefficients (stiffness and damping) for each support bearing at a single speed or excitation frequency.

In general, the system of equations generated by imbalance excitations tends to be ill-conditioned, and most experimental identifications show considerable scatter of results [6]. However, in spite of the known limitations, this method continues to appeal as an in situ identification procedure since it does not require external load excitation and is ready for implementation in instrumented rotor bearing systems (vibration sensor conditioned). Lee and Hong [7] estimate speed-dependent synchronous bearing coefficients of two different bearings supporting a rigid rotor by separating the forward and backward whirl frequency responses resultant of the gyroscopic moments. However, this cumbersome procedure is not necessary since the measured vibration already contains both whirl components, and the noted distinction is perfunctory. The procedure in [7] fails to identify force coefficients from isotropic bearings since the identification matrix becomes singular. Tieu and Qiu [8] also identify 16 synchronous coeffi-

Contributed by the International Gas Turbine Institute (IGTI) of ASME for publication in the JOURNAL OF ENGINEERING FOR GAS TURBINES AND POWER. Manuscript received October 1, 2002; final manuscript received March 1, 2003. Assoc. Editor H. R. Simmons. Paper presented at the International Gas Turbine and Aeroengine Congress and Exhibition, Atlanta, GA June 16–19, 2003, Paper No. 2003-GT-38585.

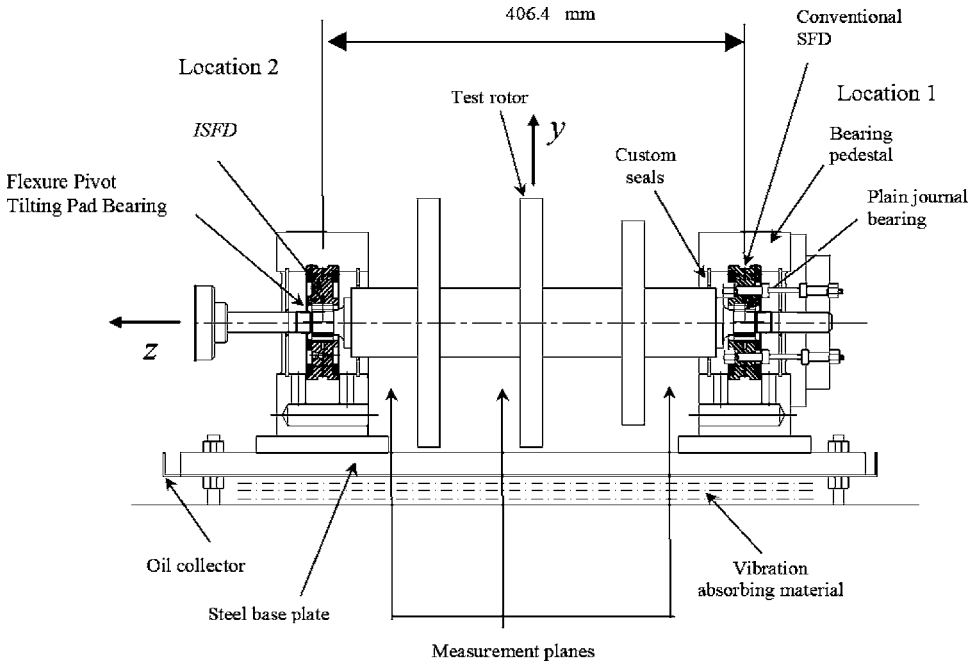

Fig. 1 Test rig for measurements of imbalance response of rotor supported on hydrodynamic bearings and squeeze film dampers

cients of two bearings supporting a rigid rotor from two or more imbalance response measurements. The authors utilize unfiltered responses and forward a numerical procedure to minimize noise influence. The experimental results show good correlation with theoretical predictions of force coefficients for a cylindrical journal bearing. Note that the procedure could have used filtered synchronous responses and avoided entirely the issue of high frequency noise.

The key features of a successful method for ready field implementation are minimal external equipment, little or no changes to existing hardware, and the use of measuring instruments commonly used in machine protection and monitoring. Recognize that, in modern turbomachinery, more stringent vibration limits promote the use of flexible supports (combined or series bearings) which offer advantages of reduced force transmissibility and control in critical speed positioning. However, flexible supports increase the complexity of the identification procedures since the equivalent bearing parameters become speed and frequency dependent. Presently, the objective is to further extend and validate the methods in [7,8] to identify parameters for two dissimilar mechanically complex bearing supports.

Experimental Facility and Test Bearings

The bearing configuration for testing the identification procedure is the combined support hydrodynamic fluid film bearing and squeeze-film damper (SFD). Reference [9] describes in detail the test rig, lubrication system and instrumentation. Figure 1 shows the test rig and mayor bearing support components. The drive end support features a Flexure Pivot Tilting Pad Bearing (FPJB) in series with an integral SFD, while the free end support comprises a plain cylindrical hydrodynamic bearing in series with a conventional cylindrical SFD and an elastic structural support emulating a squirrel cage.

Figure 2(*a*) shows a schematic view of the FPJB-ISFD bearing support, and Table 1 summarizes the rotor dimensions and characteristics of the support components. This novel support has advantages of compactness, integral construction and lightweight. Most importantly, it offers increased rotordynamic stability, control of critical speed positioning, and reduced force transmissibility [9].

The cylindrical bearing at the free end has the same nominal diameter as the tilting pad bearing and an even radial clearance of 0.051 mm (2 mils). Figure 2(*b*) shows this support at the free end and Table 1 summarizes its main characteristics. The SFD is identical in dimensions as the integral damper (radius, land length, and

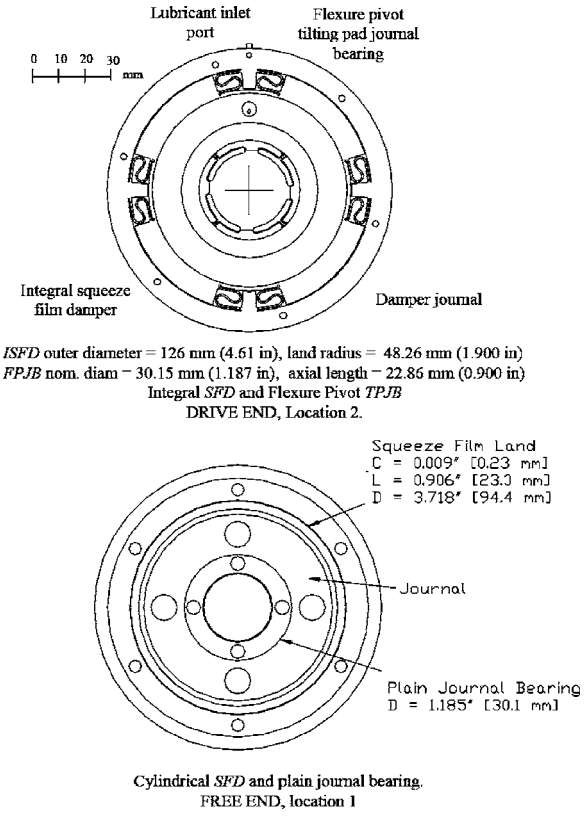

Fig. 2 Series supports composed of squeeze film damper and fluid film bearing used for equivalent parameter identification

Table 1 Summary of rotor inertia properties and complex test bearings geometry[a]

Rotor total mass (including half of flexible coupling) (M)	45.3 kg (99.8 lb.)	
Rotor total transverse moment of inertia	0.704 kg m^2 (2406 lb. in.^{2})	
Rotor total polar inertia	0.299 kg m^2 (1022 lb. in.^{2})	
Shaft main diameter	76.2 mm (3.00 in.)	
Total rotor length	673.1 mm (26.50 in.)	
Bearing span	406.4 mm (16.0 in.)	
Rotor cg location from left end	285.0 mm (11.2 in.)	
Radii of imbalance (r_1, r_2)	95.3 mm (3.75 in.)	114 mm (4.5 in.)
Distances from cg to bearing locations (l_1, l_2)	217 mm (8.54 in.)	189 mm (7.44 in.)
Distances from cg to planes of imbalance excitation (d_1, d_2)	102 mm (4.01 in.)	67 mm (2.54 in.)
Distances from cg to location of proximity probes (s_1, s_2)	146 mm (5.75 in.)	119 mm (4.69 in.)
Squeeze film damper		
Damper land radius	48.26 mm (1.900 in.)	
Land radial clearance (centered)	0.229 mm (9 mils)	
Damper axial length	23.00 mm (0.910 in.)	
Drive end:	Integral type, 4 pads, arc extent: 52 deg	
Free end:	Fully cylindrical	
Fluid film bearings		
Drive end	Type: FPJB, 4 pads (70 deg)	
Bearing nominal diameter	30.15 mm (1.187 in.)	
Bearing axial length	22.9 mm (0.902 in.)	
Bearing radial clearance	0.076 mm (3 mils)	
Pad preload[b]/ pivot offset stiffness	.0405/0.5	
Pad rotation	40 N m/rad (354 lb. in./rad)	
Free end:	Type: plain cylindrical	
Bearing radial clearance	0.051 mm (2 mils)	
Static load on bearings		
Drive end bearing (between pads)	247.3 N (55.5 lb.)	
Free end bearing	198.2 N (44.5 lb.)	

[a]Lubricant ISO VG 10 oil, average viscosity (μ) 15.76 cP at 24.4°C (76°F).
[b]Dimensionless.

radial clearance), but the land extends over the full circumference of the damper. A squirrel-cage type centering spring provides radial stiffness to the damper in the free end.

The test rotor features equally-spaced threaded holes in each one of the three disks where calibrated imbalance masses can be attached at radii of 114.3 mm (4.50 in.) for the two largest disks and 95.25 mm (3.75 in.) for the smaller disk. The data acquisition system allows recording and filtering of synchronous vibration vectors, as well as compensation for shaft run out at low speeds. This feature is particularly important in the current experiments since only the synchronous response is needed for identification of bearing force coefficients.

Description of Identification Procedure

A four-degree of freedom system models the dynamics of the test rotor and support bearings [1]. The rotor is regarded as rigid since its first bending critical speed is at around 12 krpm, well above the maximum speed of the measurements [9,1]. The equations of motion for the rotor bearing system are

$$\mathbf{M}\ddot{\mathbf{q}} + \mathbf{C}\dot{\mathbf{q}} + \Omega\mathbf{G}\dot{\mathbf{q}} + \mathbf{K}\mathbf{q} = \mathbf{F}_o\, e^{j\Omega t} \tag{1}$$

where $\mathbf{M}$, $\mathbf{C}$, and $\mathbf{K}$ are the (4×4) inertia, damping and stiffness matrices and $\mathbf{G}$ is the gyroscopic moments matrix given in the Appendix of the companion paper [1]. Ω is the rotor speed, $j = \sqrt{-1}$, and t is time. $\mathbf{F}=\mathbf{F}_o\, e^{j\Omega t}$ is the "excitation" force vector derived from the imbalance masses attached at two axial planes on the rotor. The response vector ($\mathbf{q}$) in Eq. (1) is $\mathbf{q}=\mathbf{q}_o\, e^{j\Omega t}$, with $\mathbf{q}_o=[x_1, x_2, y_1, y_2]^T$, containing the complex amplitude of vibration at the bearing locations (1, 2) and in two orthogonal directions (x, y) corresponding to the speed Ω.

The generalized imbalance vector ($\mathbf{F}_o$) in (1) is given by

$$\mathbf{F}_o = \begin{bmatrix} f_1 + f_2 \\ -j(f_1 + f_2) \\ -f_1 d_1 + f_2 d_2 \\ -j(f_1 d_1 - f_2 d_2) \end{bmatrix} \Omega^2 \tag{2}$$

where the imbalance functions f_1 and f_2 are $f_1=m_1 r_1\, e^{-j\phi_1}$ and $f_2=m_2 r_2\, e^{-j\phi_2}$ with m_1 and m_2 as the imbalance masses attached at

radii r_1 and r_2 and at circumferential locations ϕ_1 and ϕ_2, respectively. These angles are physically measured from the key-phasor mark on the rotor, and taken as positive in a direction opposite to its rotation. The key-phasor mark provides also a reference for measurement of the phase angle of rotor response. In Eq. (2) the subindices (1, 2) represent different axial planes on the rotor. The excitation forces in (2) cannot be measured but only estimated from the known imbalance distribution. Incidentally, the amplitude of the "excitation" force is proportional to the power 2 of rotor speed, and thus it is small in magnitude at low rotor speeds. Note that imbalance inherently renders a phase angle of 90 deg between the "excitations" along the (x) and (y) directions.

At steady state, Eq. (1) becomes

$$j\Omega\mathbf{C}\mathbf{q}_o + \mathbf{K}\mathbf{q}_o = \mathbf{F}_o + [\Omega^2\mathbf{M} - j\Omega^2\mathbf{G}]\mathbf{q}_o \tag{3}$$

where the left-hand side contains the bearing support reaction forces and moments in terms of the unknown damping and stiffness force coefficients. In the procedure, these forces and moments are expressed as the product of a response matrix $\mathbf{Q}$, and a vector of bearing support (stiffness and damping) parameters (impedances) $\mathbf{P}$, i.e., along the x and y directions,

$$\mathbf{Q}^x\mathbf{P}^x = [\mathbf{F}_o + [\Omega^2\mathbf{M} - j\Omega^2\mathbf{G}]\mathbf{q}_o]^x = \mathbf{F}_T^x \tag{4a}$$

$$\mathbf{Q}^y\mathbf{P}^y = [\mathbf{F}_o + [\Omega^2\mathbf{M} - j\Omega^2\mathbf{G}]\mathbf{q}_o]^y = \mathbf{F}_T^y \tag{4b}$$

where

$$\mathbf{Q}^x = \begin{bmatrix} \mathbf{q}_o^T \\ \mathbf{q}_o^T\mathbf{l} \end{bmatrix}_{2x4}$$

$$\mathbf{P}^x = [Z_{xx1}, Z_{xx2}, Z_{xy1}, Z_{xy2}]^T \tag{5}$$

with $\mathbf{l}$ as a diagonal matrix with components $\bar{\mathbf{l}}=[l_1, l_2, l_1, l_2]^T$. Z_{ij} are the complex bearing impedance functions defined as $\{K_{ij} + j\Omega C_{ij}\}_{ij=x,y}$. Similar relationships hold for $\mathbf{Q}^y$ and $\mathbf{P}^y$. The subindices 1 and 2 correspond to the bearing supports on the free and drive end sides of the rotor, respectively. The impedance functions represent the equivalent action of the fluid film bearing and squeeze film dampers operating in series. The method does not aim to characterize fully each of the bearing components, but rather its combined action on the rotor response.

Stacking two linearly independent imbalance responses (A, B) at a particular rotor speed Ω, renders the identification equations

$$\mathbf{P}^x = \bar{\mathbf{Q}}^{x^{-1}}\bar{\mathbf{F}}_T^x \tag{6a}$$

$$\mathbf{P}^y = \bar{\mathbf{Q}}^{y^{-1}}\bar{\mathbf{F}}_T^y \tag{6b}$$

where $\bar{\mathbf{Q}}^{x,y}$ and $\bar{\mathbf{F}}_T^{x,y}$ are the response matrix and impedance vector containing data from the two tests. The condition for linear independence of the row vectors in the response matrix $\bar{\mathbf{Q}}^{x,y}$ is obtained from the solution of (3) for the response vector $\mathbf{q}_o$,

$$\mathbf{q}_o = [-\Omega^2\mathbf{M} + j\Omega^2\mathbf{G} + j\Omega\mathbf{C} + \mathbf{K}]^{-1}\mathbf{F}_o \tag{7}$$

Equation (7) merely establish a linear transformation, and thus two linearly independent (l.i.) excitations $\mathbf{F}_{o\mathbf{A}}$ and $\mathbf{F}_{o\mathbf{B}}$ generate linearly independent responses $\mathbf{q}_{o\mathbf{A}}$ and $\mathbf{q}_{o\mathbf{B}}$. The conditions for linearly independent excitations can be stated from the definition of the excitation vector $\mathbf{F}_o$ (Eq. (2)). The excitation in test B is linearly independent from that of test A by shifting the location and/or magnitude of the imbalance masses (m_1, m_2) at the two imbalance locations and such that the resultant vector $\mathbf{F}_{o\mathbf{B}}$ is not a (complex) multiple of the original vector $\mathbf{F}_{o\mathbf{A}}$.

Note that "excitations" in only one imbalance plane cannot render linearly independent excitation vectors since the force vector $\mathbf{F}_{o\mathbf{B}}$ can always be expressed as a multiple of $\mathbf{F}_{o\mathbf{A}}$. Thus, two imbalance planes are mandatory for identification of all sixteen bearing parameters. Further analysis shows that force coefficients from perfectly isotropic bearings will cause numerical singularities during the inversion of the response matrices $\bar{\mathbf{Q}}^{x,y}$. The stated procedure is not able to identify the force coefficients in this case. However, assuming identical bearings on each end (for example, when the bearings carry the same static load) or neglecting cross-coupled force coefficients (if they are known to be small) reduces the number of unknowns and simplifies the experimental requirements. These two last cases are of practical interest since most fluid film bearings render anisotropic stiffness and damping force coefficients (i.e., $K_{xx} \neq K_{yy}$, etc.).

If measurements of the rotor response are not taken at the bearing locations l_1 and l_2, a geometry transformation allows the use of imbalance responses x_{p1}, x_{p2} at locations s_1 and s_2 away from the rotor center of gravity.

Numerical experiments [10] (not shown here for brevity) demonstrate that the identification method based on measurements of the rotor transient response is less sensitive to noise than the identification from rotor imbalance responses. In general, identification of bearing parameters from imbalance responses is least sensitive to noise at the system critical speeds because the amplitudes of rotor motion are the largest, and thus the signal (response) to noise ratio is a maximum. It is important to note that using two axial planes for rotor excitation allows identification of all the force coefficients from two bearings supporting the rotor.

Results of Identification for the System With Null Cross-Coupling Forces

This section describes the experimental identification of bearing parameters from the measured imbalance response. The combined hydrodynamic bearing-squeeze film damper supports have speed-dependent force coefficients. Predictions show that the equivalent force coefficients representing the combined action of the fluid film bearings and dampers change more as a function of rotor speed than as a function of the excitation frequency.

As demonstrated by the identification of frequency-dependent force coefficients in the companion paper [1], equivalent cross-coupled force coefficients of the FPJB-ISFD support are about one order of magnitude smaller than the force coefficients in the principal directions. Furthermore, measurements of rotor response to imbalance with the hydrodynamic journal bearing and cylindrical damper support show no trace of subsynchronous rotor vibration. Thus, a reasonable assumption in this case is that the cross-coupled forces are small, and the identification procedure thus ignores the cross-coupled coefficients to provide satisfactory identification of coefficients along the principal directions. The identification procedure requires only small changes for the case of negligible cross-coupling force coefficients. Ultimately, only one imbalance response is required for the identification since the number of parameters is reduced by half.

Figure 3 shows the synchronous test rotor responses at the bearing locations due to the imbalance condition presented in Table 2. Imbalance masses are attached in two axial planes at the same angular position and thus can be lumped into a single plane for analysis purposes. At the system natural frequency, imbalance forces are comparable in magnitude with the impact forces delivered in the previous experiments with impulse excitations, see [1]. At higher frequencies, the forces developed by the imbalance are much larger than those from impact excitations. The data acquisition system records rotor displacements at speed increments of 50 rpm. Notice that the identification Eqs. (5) allow full estimation of coefficients at each individual speed, thus rendering the speed-dependent synchronous bearing parameters.

Figure 3 depicts the rotor responses compensated for slow roll and remnant imbalance vectors. The rotor response shows resonance peaks between 2800 and 3100 rpm at the displacement sensor locations. Note that the amplitudes of motion while crossing a critical speed at the drive end bearing (x_2, y_2) are larger than the amplitudes at the free end (x_1, y_1). Figure 3 also shows the phase

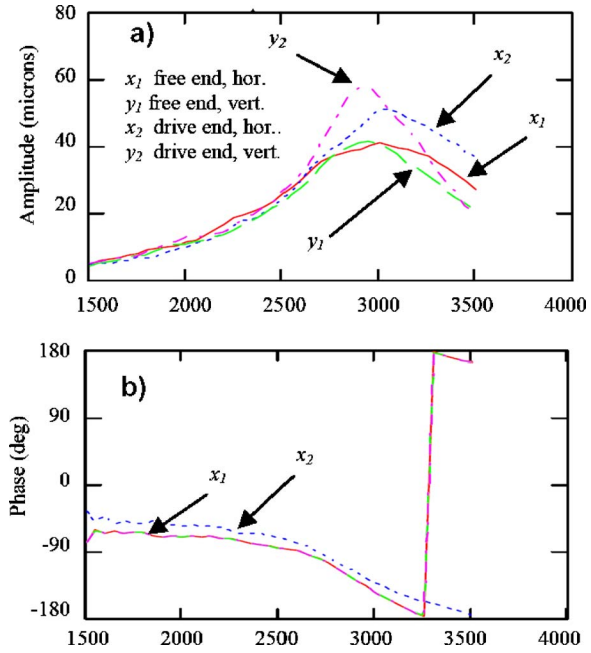

Fig. 3 Rotordynamic response of test rotor to calibrated imbalances. (*a*) Synchronous response amplitudes; (*b*) phase angle of response.

angles of response in the horizontal direction at both rotor axial locations, with a clear shift occurring between 2600 and 3200 rpm.

Figure 4 shows the identified (synchronous) equivalent bearing force coefficients along with predictions as a function of the rotor speed. The figure also includes predictions, discussed later. The equivalent denomination denotes the combined action of the hydrodynamic bearing in series with its corresponding squeeze film damper. Equivalent stiffness coefficients remain almost constant for speeds up to 3000 rpm, and then show a sharp decrease. This drift is very similar to the trend presented by frequency-dependent force coefficients identified above 40 Hz (2400 cpm) and associated with a table resonance [1]. Notice that the magnitudes of stiffness at location 1 (free end) are slightly lower than the magnitudes at location 2 (drive end), due to the difference of the SFD elastic support used. The identification procedure verifies that, at low rotor speeds, the direct stiffnesses correspond to the structural stiffnesses of the squeeze film dampers.

Identified equivalent synchronous damping coefficients decrease steadily as the rotor speed increases in most of the identification speed range. Also, damping coefficients at location 1 (free end) are larger than the damping coefficients at location 2 (drive end). This is a direct result of the cylindrical damper that provides larger damping forces to the free end bearing, as evidenced by the smaller magnitude of response at this location (see Fig. 3). Notice that the identified equivalent damping coefficients at lower speeds show larger variations because rotor displacements are also small and, consequently, damping forces are also small. The best range for identification of damping coefficients is clearly around the critical speeds where amplitudes of rotor motion are largest, and damping is most effective.

Table 2 Imbalance distribution of test rotor for experimental identification of series-support equivalent synchronous force coefficients[a]

	Drive end disk[b]	Free end disk[c]
Unbalance	3.2 gr at 30 deg	3.3 gr at 30 deg

[a]Positive angles on rotor are measured opposite to the direction of rotation and from rotating reference (i.e., keyway in rotor or reflective pick-up mark).
[b]Drive end disk: radius r_2=0.114 m, distance from rotor CG d_2=0.067 m.
[c]Free end disk: radius r_1=0.095 m, distance from rotor CG d_1=0.102 m.

De Santiago [10] shows that the identification method is very sensitive to noise introduced in the phase angle of response. Measurements of the phase angle are more consistent around the critical speed, as a result of the larger rotor motions. This fact is important because it reveals that the method has a limitation in the low speed range for identification of damping force coefficients (as in the identification of frequency-dependent force coefficients, see [1]).

Analytical predictions for the force coefficients from the hydrodynamic bearings (plain and tilting pad) along with their corresponding squeeze film damper force coefficients and structural stiffness are combined to render predictions for the equivalent force coefficients of the complex bearing support. A computational program [11] provides the tilting pad bearing synchronous speed[1] reduced force coefficients. Earlier measurements with this type of mechanical element FPJB-ISFD [9] show that the damper structural stiffness and damping coefficients equal 3.4 MN/m and 950 N s/m, respectively. On the other hand, the cylindrical damper has similar stiffness values but predicted damping coefficients of 2000 N s/m. Predictions of equivalent force coefficients are in general close to the values of the (experimentally) identified parameters. Stiffness coefficients are slightly overpredicted (probably due to the contribution of the table flexibility) while equivalent damping coefficients are underpredicted. Note that due to the fact that the parameters are identified at each speed, predicted rotor responses using Eq. (7) are identical to the test responses at the measurement locations.

Closure

The paper details a procedure for identification of bearing support parameters in rotor-bearing systems as derived from measurements of the rotor response to known mass imbalances. The method renders synchronous stiffness and damping force coefficients best representing the rotor-bearing support system at a given speed. Experiments validating the procedure are conducted on a test rotor supported on two mechanically complex bearing supports. One support combines a tilting pad bearing in series with an integral multiple pad film damper, and the other is a plain journal bearing in series with a conventional cylindrical squeeze film damper. Both dampers have centering elastic structures.

Test synchronous rotor responses show minimal cross-coupling effects, as also predicted by computational analysis. The identification procedure then avoids the identification of cross-coupled force coefficients to minimize false cross-correlations causing ill-conditioning of the identification matrix and delivering unrealistic parameter estimates [10]. Identified equivalent direct stiffness and damping coefficients for each of the bearing supports agree well with predictions obtained from the combined action of the fluid film bearings and dampers in series. In general, equivalent force coefficients decrease as the rotor speed increases, in a range that includes the system critical speeds (1500–3500 rpm). The test derived bearing support stiffnesses also reveal an important reduction, as in the case of identification from impact excitations, at frequencies above the first critical speed, ~3000 rpm.

The identification procedures described here and in the companion [1] are suitable for use in the field, although special mechanical arrangements must be devised for the case of transient rotor responses. On the other hand, using imbalances to generate rotor responses requires accurate measurement of the phase angle, most uncertain at low shaft speeds. Furthermore, this last procedure is inherently more sensitive to small variations in the mea-

[1]Tilting pad bearings show frequency dependent force coefficients. Presently, the force coefficients are obtained at a frequency coinciding with rotor speed, i.e., synchronous.

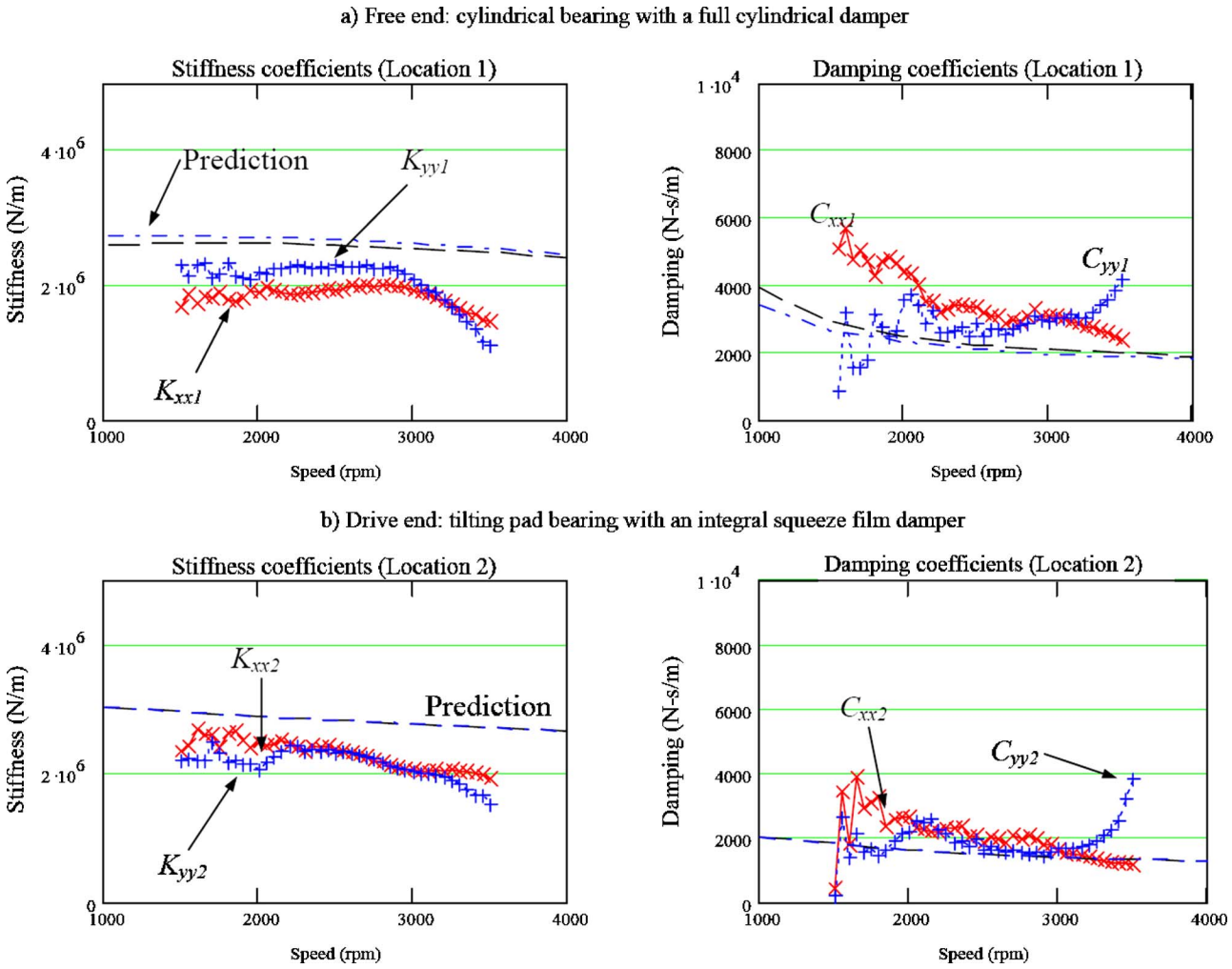

Fig. 4 Equivalent, synchronous force coefficients of test series damper-bearing support identified from imbalance response measurements. (*a*) Support: plain journal bearing and cylindrical SFD. (*b*) Tilting pad bearing and integral SFD. Identification reliable on speed range 2–3 krpm.

sured response (particularly variations in the phase angle of response) than the identification from transient responses [10]. The present identification methods are limited to the case of nearly rigid rotors. Extensions to flexible rotor bearing systems are under development.

Nomenclature

- $\mathbf{C}$ = rotor-bearing system damping matrix
- C = bearing damping force coefficient (N s/m)
- d = distance from imbalance plane to rotor CG (m)
- $\mathbf{F}$ = rotor excitation vector from imbalance (N)
- f = Imbalance function ($f=mre^{-j\phi}$)
- $\mathbf{G}$ = gyroscopic moments matrix
- j = $\sqrt{-1}$ imaginary unit
- $\mathbf{K}$ = rotor-bearing system stiffness matrix
- K = bearing stiffness force coefficient (N/m)
- l = distance of bearing location to rotor CG (m)
- $\mathbf{M}$ = system mass matrix
- m = imbalance mass (kg)
- M = total rotor mass (kg)
- $\mathbf{P}$ = vector of bearing parameters (impedances, N/m)
- $\mathbf{q}$ = rotor response vector
- $\mathbf{Q}$ = matrix of responses for parameter identification
- r = radius of disk where imbalance is attached (m)
- s = location of displacement probes from rotor CG (m)
- t = time (s)
- (x,y) = coordinates of rotor motion (m)
- Z = bearing impedance [$Z=(K+j\omega C)$] (N/m)
- Ω = frequency of rotor speed (rad/s)
- ϕ = angular location of imbalance mass (rad)

Acknowledgment

The authors gratefully acknowledge the support of the Turbomachinery Research Consortium of Texas A&M University.

References

[1] De Santiago, O., and San Andrés, L., 2003, "Field Methods For Identification of Bearing Support Parameters. Part I—Identification From Transient Rotor Dynamic Response Due to Impacts," ASME Paper No. GT-2003-38583.

[2] Woodcock, J. S., and Holmes, R., 1970, "Determination and Application of the Dynamic Properties of a Turbo-Rotor Bearing Oil Film," Proc. Inst. Mech. Eng., **184**, pp. 223–231.

[3] Sahinkaya, M. N., and Burrows, C. R., 1984, "Estimation of Linearized Oil Film Parameters From the Out-of-Balance Response," Proc. Inst. Mech. Eng., **198c**, pp. 131–135.

[4] Goodwin, M. J., 1981, "Variable Impedance Bearings for Large Rotating Machinery," Ph.D. thesis, Aston University, UK.

[5] Diaz, S., and San Andrés, L., 2000, "Orbit-Based Identification of Damping Coefficients for a Rotor Mounted on Off-Centered Squeeze Film Dampers and Including Support Flexibility," ASME Paper No. GT-2000-394.
[6] Goodwin, M. J., 1991, "Experimental Techniques for Bearing Impedance Measurement," ASME J. Eng. Ind., **113**, pp. 335–342.
[7] Lee, C. W., and Hong, S. W., 1989, "Identification of Bearing Dynamic Coefficients by Imbalance Response Measurements," Proc. Inst. Mech. Eng., Part C: J. Mech. Eng. Sci., **203**, pp. 93–101.
[8] Tieu, A. K., and Qiu, Z. L., 1994, "Identification of Sixteen Dynamic Coefficients of Two Journal Bearings From Experimental Imbalance Responses," Wear, **177**, pp. 63–69.
[9] San Andrés, L., and De Santiago, O., 2003, "Imbalance Response of a Rotor Supported on Flexure Pivot Tilting Pad Journal Bearings in Series With Integral Squeeze Film Dampers," ASME J. Eng. Gas Turbines Power, **115**, pp. 1026–1032.
[10] De Santiago, O., 2002, "Identification of Bearing Supports' Force Coefficients From Rotor Responses Due to Imbalances and Impact Loads," Ph.D. dissertation, Texas A&M University, College Station, TX.
[11] San Andrés, L., 1996, "Turbulent Flow, Flexure-Pivot Hybrid Bearing for Cryogenic Applications," ASME J. Tribol., **118**, pp. 190–200.

A Study of the Effects of Inlet Preswirl on the Dynamic Coefficients of a Straight-Bore Honeycomb Gas Damper Seal

Tony B. Sprowl
Lockheed Martin Aeronautics Company,
Fort Worth, TX

Dara W. Childs
Leland T. Jordan Professor of Mechanical Engineering,
Turbomachinery Laboratory,
Texas A&M University,
College Station, TX 77843

Honeycomb seals are frequently used as replacements for labyrinth seals in high-pressure centrifugal compressors to enhance rotordynamic stability. A concern exists that this enhanced stability will be lost if the honeycomb cavities become clogged. Static and dynamic tests were conducted on a honeycomb and a smooth seal (representing the honeycomb seal with completely clogged cells) at the same constant clearances using air with a supply pressure of 70 bars. The test matrix included three speeds, three pressure ratios, and three inlet preswirl conditions. The results show increased leakage, decreased synchronous stiffness, and decreased dynamic stability for the smooth seal with preswirled flow. The results strongly support the use of swirl brakes at the entrance of a honeycomb seal if clogging is a concern. Comparisons between test results and predictions from a two-control-volume theory by Kleynhans and Childs showed excellent agreement in general. [DOI: 10.1115/1.2227416]

Introduction

Honeycomb (HC) seals for compressors use a HC stator with a smooth rotor, as shown in Fig. 1. This is in contrast to typical gas turbine applications with a tooth-on-rotor labyrinth operating against an abradable HC surface. HC seals are typically used for the balance-piston seal in "straight-through" type compressors, and for the division-wall seal in "back-to-back" type designs. These seals typically handle a large pressure differential and have large L/D ratios. In these applications, leakage flow approaching these seals tends to have high circumferential velocity, or preswirl.

HC seals were originally used in compressors in the 1960s as a replacement for aluminum labyrinth seals that were being consumed by process fluids The first example of their potential for improving rotordynamics arose with the high-pressure oxygen turbopump on the Space Shuttle main engine [1]. For the turbine interstage seal of the high pressure oxygen turbopump, replacing the original tooth-on-rotor labyrinth with a HC seal (including a swirl brake) eliminated synchronous and subsynchronous vibration problems. Numerous case studies have been presented in which unstable injection compressors have been stabilized by replacing a labyrinth seal with a HC seal, e.g., Ref. [2].

In some applications of HC seals, a concern has been raised regarding particles within the product gas depositing in the HC cells, eventually filling them. This can—in the limit—produce a nearly smooth inner surface within the seal. The first question of interest this paper addresses is: *How would filling the cells impact performance* (*leakage*) *and rotordynamic coefficients?* The present results answer that question by providing test results for both a HC seal and a smooth seal. A second question of interest is: *How well does the two-control-volume model of Kleynhans and Childs predict the static and dynamic behavior of smooth and HC seals?* The work presented here was developed to answer these questions.

The next section will introduce the rotordynamic models used for the reaction forces developed by smooth and HC seals with subsequent material describing the test procedures and results.

Contributed by the International Gas Turbine Institute (IGTI) of ASME for publication in the JOURNAL OF ENGINEERING FOR GAS TURBINES AND POWER. Manuscript received October 1, 2003; final manuscript received March 1, 2004. IGTI Review Chair: A. J. Strazisar. Paper presented at the International Gas Turbine and Aeroengine Congress and Exhibition, Vienna, Austria, June 13–17, 2004, Paper No. GT2004-53328.

Small-Motion Model for Annular Gas Seals

For small motion, the force-reaction model for a *smooth* seal can be stated,

$$-\begin{Bmatrix} F_x \\ F_y \end{Bmatrix} = \begin{bmatrix} K & k \\ -k & K \end{bmatrix} \begin{Bmatrix} \Delta x \\ \Delta y \end{Bmatrix} + \begin{bmatrix} C & c \\ -c & C \end{bmatrix} \begin{Bmatrix} \Delta \dot{x} \\ \Delta \dot{y} \end{Bmatrix} + M \begin{Bmatrix} \Delta \ddot{x} \\ \Delta \ddot{y} \end{Bmatrix} \tag{1}$$

Assuming circular centered orbits with radius A, and precession frequency Ω, the reaction force on the rotor can be stated:

$$F_r = [(K - M\Omega^2) + c\Omega]A \tag{2}$$

$$F_\theta = (k - C\Omega)A \tag{3}$$

These equations can be used to define the effective stiffness and damping of the seal:

$$K_{\text{eff}} = (K - M\Omega^2) + c\Omega \tag{4}$$

$$C_{\text{eff}} = C - k/\Omega \tag{5}$$

As demonstrated by Kleynhans and Childs [3], Childs two-control-volume model for HC seals [4] predicts strongly frequency-dependent rotordynamic coefficients, requiring the following force-reaction model,

$$-\begin{Bmatrix} F_x(s) \\ F_y s(s) \end{Bmatrix} = \begin{bmatrix} D & E \\ -E & D \end{bmatrix} \begin{Bmatrix} \Delta x(s) \\ \Delta y(s) \end{Bmatrix}, \tag{6}$$

where s is the Laplace-domain variable. Equation (6) can be expressed in terms of the following frequency-dependent rotordynamic coefficients

$$-\begin{Bmatrix} F_x \\ F_y \end{Bmatrix} = \begin{bmatrix} K(\Omega) & k(\Omega) \\ -k(\Omega) & K(\Omega) \end{bmatrix} \begin{Bmatrix} \Delta x \\ \Delta y \end{Bmatrix} + \begin{bmatrix} C(\Omega) & c(\Omega) \\ -c(\Omega) & C(\Omega) \end{bmatrix} \times \begin{Bmatrix} \Delta \dot{x} \\ \Delta \dot{y} \end{Bmatrix}, \tag{7}$$

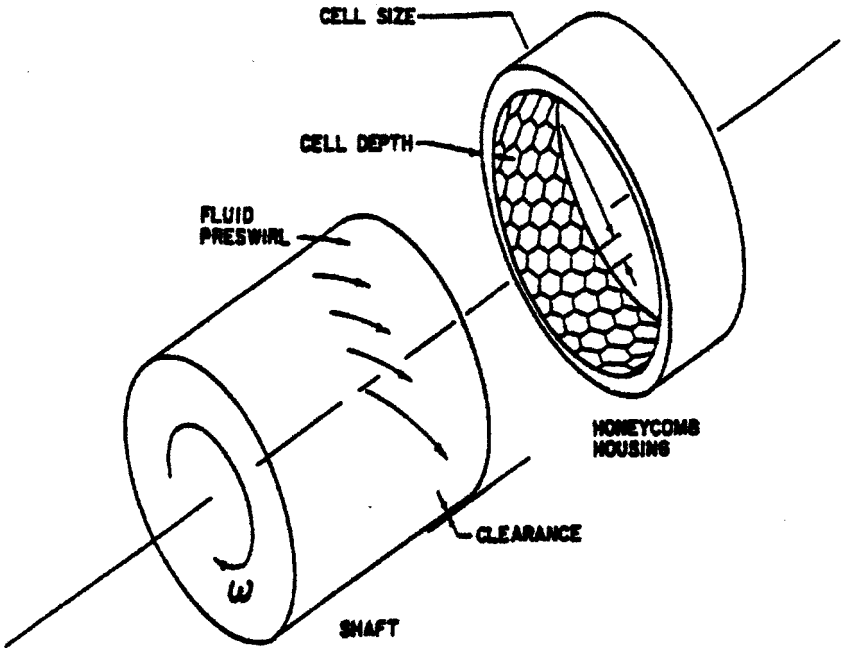

Fig. 1 Honeycomb annular seal

The frequency dependency of $K(\Omega)$ incorporates and eliminates the mass coefficient in Eq. (7). From Eqs. (6) and (7),

$$\boldsymbol{D} = K(\Omega) + j\Omega C(\Omega) \tag{8}$$

$$\boldsymbol{E} = k(\Omega) + j\Omega c(\Omega) \tag{9}$$

Finally, the effective stiffness and damping can be defined in a similar manner as for the smooth seal using the seal impedances as

$$K_{\text{eff}} = K(\Omega) + \Omega c(\Omega) \tag{10}$$

$$C_{\text{eff}} = C(\Omega) - K(\Omega)/\Omega \tag{11}$$

Test Objectives

Dawson et al. [5] presented test results for smooth and HC seals with supply pressures up to 17 bars. However, their test assembly used radial inlet flow upstream of the test seals with no intentional preswirl of the gas. Additionally, this preswirl, or circumferential velocity, of the gas entering the seals was not measured. An expected consequence of a transition from a HC surface to a smooth surface is an increase of leakage and (due to conservation of moment of momentum) an increase in circumferential velocity at the seal inlet. Hence, tests for HC or smooth seals need to include a range of test points for accurately measured fluid preswirl at the seal inlet. As explained below, the present test results achieve these goals. In addition, these tests were conducted with a higher supply pressure of 70 bars to more accurately reflect conditions in actual field applications.

Test Apparatus

The gas seal test stand was discussed by Dawson et al. [6], and a side view is provided in Fig. 2. The rotor is supported by two hydrostatic bearings that provide very high stiffness in comparison to that developed by the seals. The test stator is excited and supported by two hydraulic shakers. The shakers are oriented orthogonally to one another, representing the X and Y directions and are also both oriented 45 deg from the vertical. The shakers are mounted on two large I-beam supports and excite the stator with a pseudo-random waveform to obtain the rotordynamic coefficients of the seals. The stator is suspended between the stiff bearing housings by six turn-buckle style screws (three on each side) pulled tightly in tension between the stator and bearing housings. Fine adjustment of these turn-buckles gives precise control of the pitch and yaw of the stator in relation to the rotor. Hence, the turn-buckles, commonly referred to as "pitch stabilizers," cause the stator to remain parallel with, and nominally centered (axially) about, the rotor during excitation.

Supply air is fed into the center of the stator. The three preswirl rings illustrated in Fig. 3 provide varying levels of preswirl. The first ring set injects air radially to create a near zero "low preswirl" case. The two remaining preswirl rings inject air at 60 deg from the radial. The highest preswirl is obtained by injection through smaller diameter holes that increase fluid velocity. Fluid preswirl values are calculated by using a pitot tube connected to an electronic transducer to measure the static and dynamic pressure differential.

Returning to Fig. 2, a labyrinth seal is provided downstream of each test seal in the stator to provide backpressure control. Between the test seal exit and the labyrinth backpressure seal, a vent line running to a manual valve is provided to control the pressure in this space. Hence, the pressure ratio across the test seal can be controlled (within limits) independently from the supply pressure. Also a swirl brake is provided at the inlet to the labyrinth backpressure seal to minimize destabilizing forces.

Test Matrix

Both the HC and smooth seal have an inner diameter of ~114.7 mm and a length/diameter ratio of 0.75. Also, each seal has a radial clearance of 0.203 mm. The targeted test matrix for each seal consists of tests for the following 27 different operating conditions:

- three shaft speeds: 10,200, 15,200, and 20,200 rpm;
- three backpressures: 15%, 35%, and 50% of inlet pressure (70.0 bar-a) to the seal; and
- three inlet preswirl magnitudes: 0%, 30%, and 60% of the surface velocity of the rotor at 15,200 rpm.

For each test condition, the stator is simultaneously excited with an ensemble of frequencies from 20 to 300 Hz. The targeted inlet

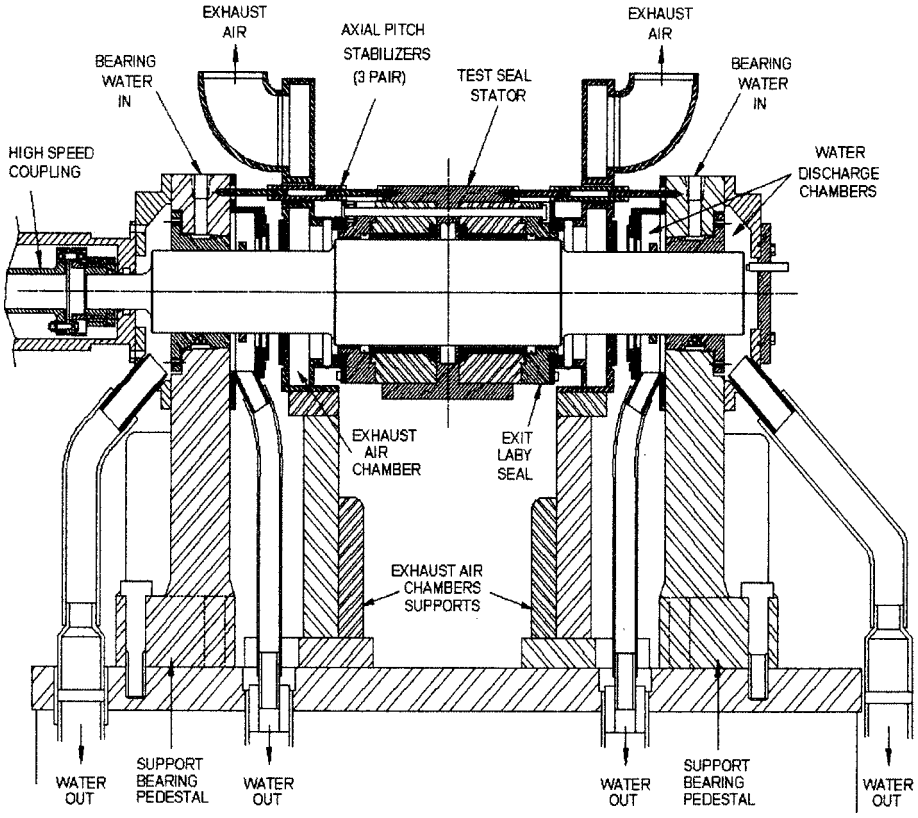

Fig. 2 Annular gas seal test stand

pressure was 70 bars; in some cases it had to be reduced to lower the magnitude of the cross-coupled stiffness and prevent instabilities of the stator.

A "tare" measurement is made for the test assembly with the test seals removed and a supply pressure that gives the correct backpressure at the vent location (upstream of the labyrinth backpressure seals). The dynamic stiffness coefficients for these tests are subtracted from the results for the complete assembly to isolate coefficients for the test seals.

Experimental Results

This section gives experimental results for the dynamic coefficients of the seals tested. The following subsection "Honeycomb Seal" below discusses the effects of preswirl on the effective stiffness K_{eff}^*, cross-coupled stiffness k^*, and effective damping C_{eff}^*. The next subsection, "Honeycomb Versus Smooth Seal," compares the same dynamic coefficients for both seal types at varying levels of preswirl.

As noted above, the target inlet pressure of 70 bar-a was not obtainable for the entire test matrix of each seal, especially for the smooth seal. To aid in comparisons, measured stiffness coefficients were nondimensionalized as follows:

$$K_{\text{eff}}^* = \frac{K \cdot C_r}{F_o} = K_{\text{eff}}\left(\frac{C_r}{\Delta P \cdot D_{in} \cdot L}\right) \tag{12}$$

The same approach was used to normalize the damping coefficients; hence, the normalized damping coefficient C_{eff}^* has units of seconds. This approach has worked well for smooth and HC seals in previous work.

Honeycomb Seal. A total of 27 test cases were conducted using the 0.79 mm (1/32 in.) cell-width HC seal. Only 4 of the 27 test cases had inlet pressures below the target pressure of 70 bar-a because of stator instability. Three of these four tests arose when using the "high" inlet preswirl ring. Note that all of the following figures show the preswirl ratio in the figure legends. This number is the ratio of inlet airflow circumferential velocity to rotor surface

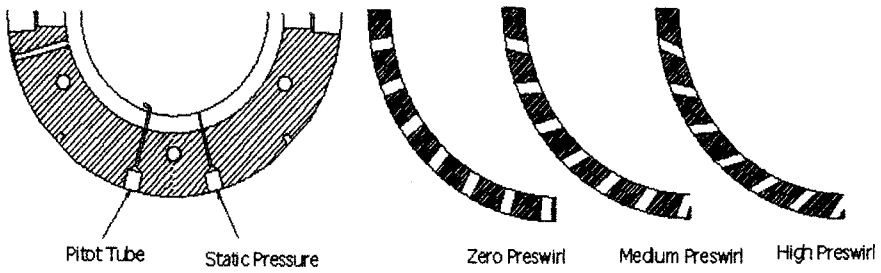

Fig. 3 Pitot tube location and preswirl rings

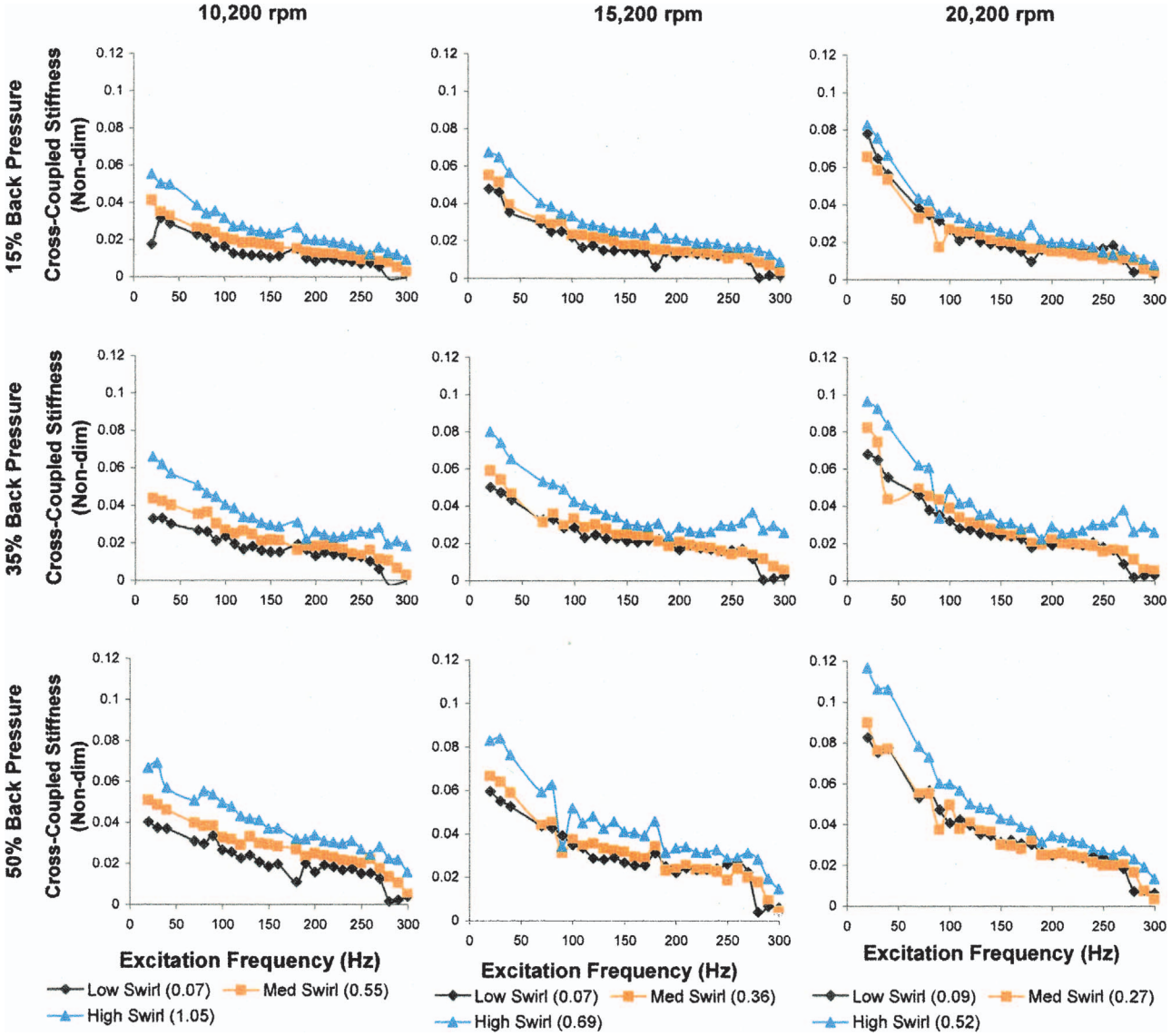

Fig. 4 k^* **versus excitation frequency for the HC seal at three levels of preswirl**

velocity.

Figure 4 illustrates k^* for the test matrix. When looking at Fig. 4 and the remaining test results, note that the 50% pressure ratio is most applicable to the balance piston and division wall seals of injection compressors. Figure 4 shows a sensitivity of k^* to increasing inlet preswirl. This outcome is most apparent at the 10,200-rpm test speed, where there is an average 37% increase when preswirl is increased from low to medium and a 50% increase when preswirl is increased from medium to high. As rotor speed is increased, results for low and medium preswirl begin to converge. At 20,200-rpm, high preswirl shows an average increase of about 38% versus medium preswirl. In the low excitation frequency range, k^* shows a slight decrease in magnitude as backpressure is decreased.

The results for k^* support the use of swirl brakes to reduce preswirl for HC seals. They also explain observed experiences for which "shunt injection" was used to eliminate a compressor instability that included a HC balance-piston seal. With shunt injection, part of the discharge gas is diverted and reinjected within the balance-piston seal and close to its inlet. Both shunt injection and swirl brakes primarily act to reduce the circumferential velocity within the seal.

Figure 5 presents test results for the effective direct stiffness $K_{\text{eff}}{}^*$ as defined in Eq. (9). These results show that $K_{\text{eff}}{}^*$ is generally insensitive to changes in preswirl. However, the high inlet preswirl does show the lowest values in most cases, especially below 200 Hz. Comparing 15% backpressure to 50% backpressure, there is a consistent drop of the peak magnitude of $K_{\text{eff}}{}^*$ by about 45% for all levels of preswirl. Note that $K_{\text{eff}}{}^*$ can have negative values at low frequencies, particularly at the lower pressure ratios.

The effective-damping coefficient C_{eff} combines the stabilizing influence of the direct damping coefficient C and the destabilizing influence of the cross-coupled stiffness coefficient k and is useful in evaluating the stabilizing performance of seals. Figure 6 presents test results for $C_{\text{eff}}{}^*$. The negative values at lower frequencies arise due to k. The frequency at which $C_{\text{eff}}{}^*$ changes sign is called the "cross-over" frequency, and this parameter has a significant impact on rotordynamics. If the system's first natural frequency is above the cross-over frequency, the seal is stabilizing. If it is below, the seal is destabilizing. Increasing preswirl increases the cross-over frequency, increasing the low frequency range for which the seal would be destabilizing. Again, swirl brakes or shunt injection that reduce the preswirl tend to increase the precession-frequency range over which a HC seal is stabilizing.

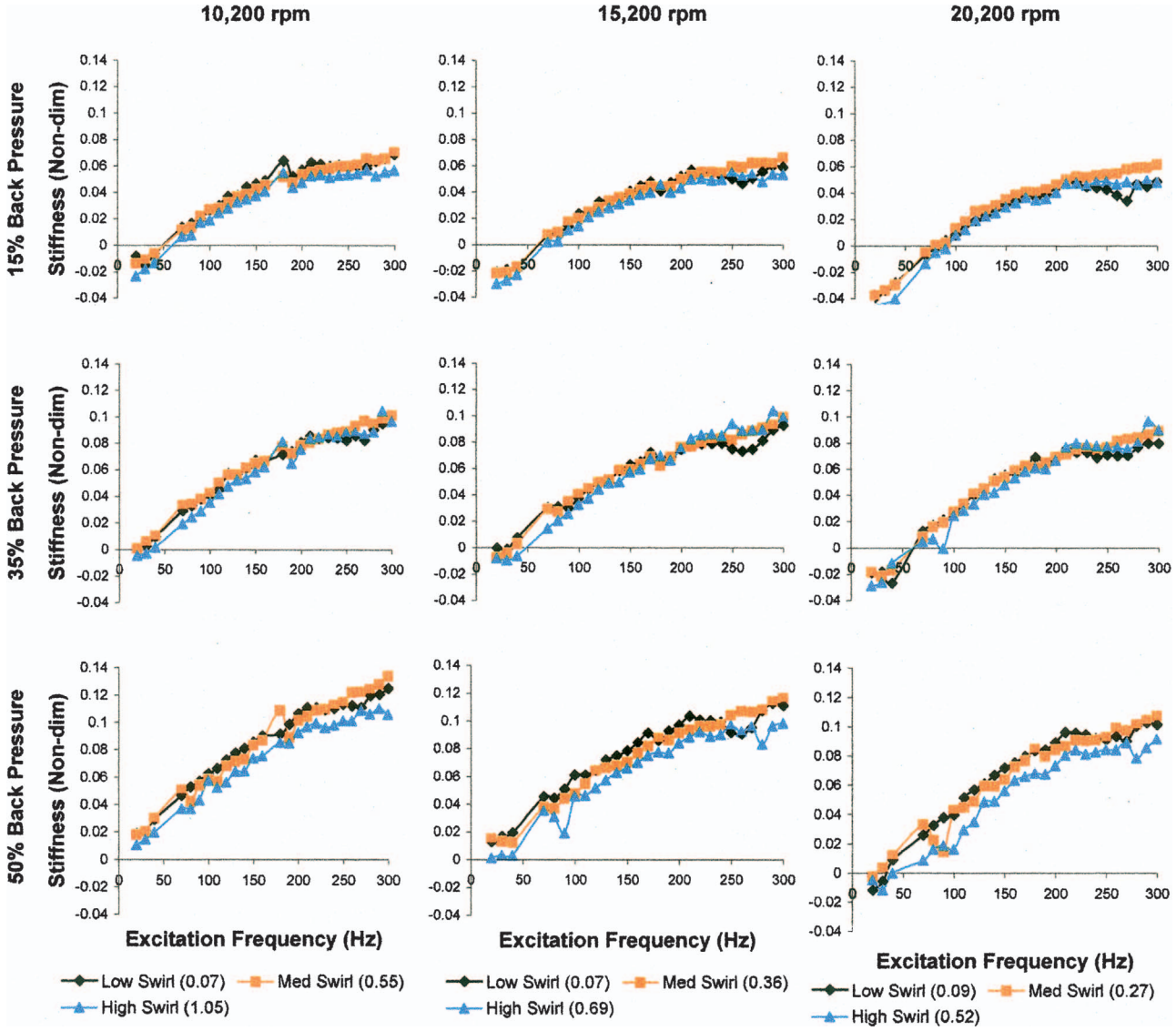

Fig. 5 K_{eff}^{*} **versus excitation frequency for the HC seal at three levels of preswirl**

Note that the peak effective damping is increased by reducing the preswirl. Reducing the preswirl is most effective at the lowest rotor speed [7,8].

Honeycomb Versus Smooth Seal Performance. Only higher preswirl ratio conditions (>0.4) data will be presented, representative of applications without swirl brakes or shunt injection. Because of higher leakage, the smooth seal has a much higher preswirl ratio than the HC seal, netting about 65% more preswirl for the medium preswirl ring. Hence, results for the smooth seal using the medium preswirl ring will be compared to results for the HC seal using the high preswirl inlet ring, since there is only about a 15% difference in the measured preswirl ratio for these two setups. Tests using the high inlet preswirl ring for the smooth seal could not be conducted because of stator instabilities. Also, because of the high leakage rate of the smooth seal, the 15% backpressure case could not be achieved due to choking. Therefore, only the 35% and 50% backpressure cases are compared.

Figure 7 demonstrates k^{*} for the smooth seal with medium preswirl and the HC seal at high preswirl. Results for the smooth-seal are less frequency dependent than the HC seal and are also much larger. For the 200 to 300 Hz range, k^{*} averages about 600% (7.0×) higher than the HC seal.

Figure 8 compares K_{eff}^{*} results for the two seals. The smooth seal has larger K_{eff}^{*} at low frequencies, producing a greater "static" stiffness. At higher frequencies, the HC seal has substantially higher effective stiffness, by about 50% for the 35% pressure ratio and about 31% for 50% backpressure. Balance piston and division-wall seals for compressors can have stiffness values at the running-speed frequencies that are comparable to the bearings' stiffness. In several applications, replacing a labyrinth with a HC has produced a substantial increase in a compressor's critical speed. Hence, a stiffness reduction at higher frequencies due to cell clogging may produce a reduction in critical speeds.

Figure 9 presents C_{eff}^{*} for the two seals under similar, higher preswirl test conditions. The cross-over frequency for the HC seal is at about 50 to 70 Hz, but at about 140 Hz for the smooth seal. These results show a potential dramatic loss in stability for clogged cells arising from an increase in k, reemphasizing the desirability of providing a swirl brake for a HC seal.

Predictions Versus Measurements

The measured dynamic coefficients illustrated and discussed for the HC seal in the previous section are now compared to predictions from a computer program developed by Kleynhans and

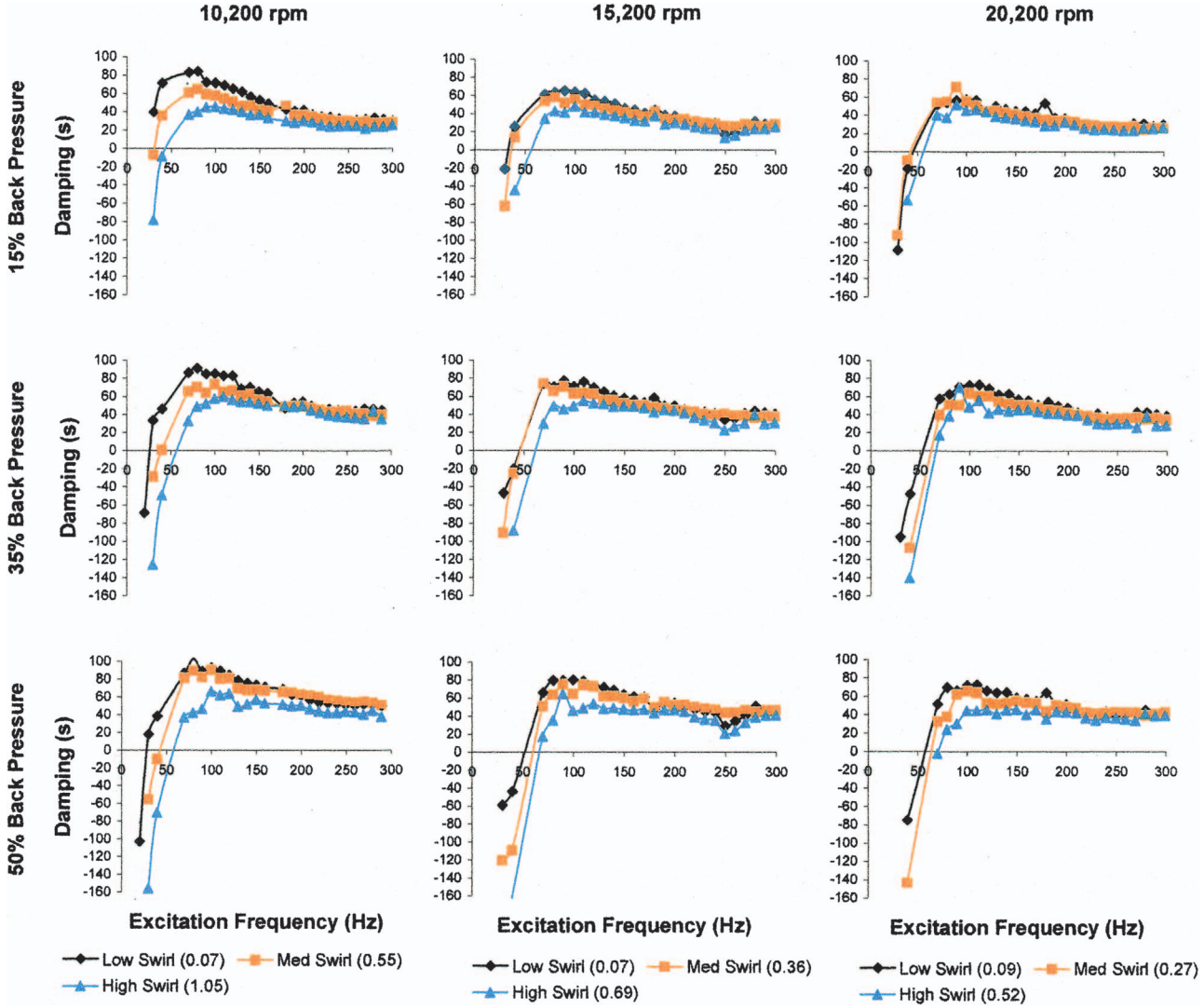

Fig. 6 C_{eff}^{*} **versus excitation frequency for the HC seal at three levels of preswirl**

Childs [3] that produces solutions for Childs' two-control-volume model. The code produces predictions for leakage flowrate and dynamic coefficients for HC, hole-pattern, and smooth seals. The friction factor coefficients used for the HC surfaces are based on experimental flat-plate tests presented by Ha and Childs [7]. Measured supply and discharge pressures and temperatures, and inlet preswirl ratios are used in calculations.

Dynamic Coefficients. For brevity, only the 50% backpressure-condition results are presented since this pressure ratio is most representative of conditions in real compressors. The experimental results shown in prior figures are based on 32 independent tests with averaging in the frequency domain. Error bars shown in the remaining figures are based on ten repeated tests (each containing 32 tests) and show one standard deviation of each data point. On average, the largest error bars show a standard deviation variance of approximately ±6%, ±5.5%, and ±6.5% about the mean value for k^*, K_{eff}^*, and C_{eff}^*, respectively. The standard deviation of each point is largely independent of inlet preswirl except for k^* for which the error bars are actually smaller at higher preswirl values.

As shown in Fig. 10, predictions generally agree well with measurements for k^*. For low preswirl, the model underpredicts k^* modestly, i.e., the seals are more destabilizing than predicted. For high preswirl, the model modestly overpredicts k^* at 10,500 rpm, slightly overpredicts at 15,200 rpm, and closely predicts the measured results at 20,200 rpm.

Figure 11 compares measurements and predictions for K^*, showing generally good agreement, with better predictions for the low preswirl results than the high preswirl. For the high preswirl case, K^* is underpredicted by about 32% up to at least 280 Hz.

Finally, Fig. 12 shows predictions and measurements for effective damping C_{eff}^*. The model generally does a good job in predicting the frequency dependency, doing a better job for the low preswirl than the high preswirl. The seal is more stable than predicted for the high preswirl, having a lower crossover frequency and higher peak values than predicted.

D'Souza and Childs [8] examined changes in the friction-factor model showing only modest improvements in predictions for several friction-factor models and a range of Blasius friction-factor coefficients. The Blasius coefficients used here are based on flat-plate test results and gave the best overall agreement.

Discussion and Conclusions

Test results show that the HC seal has little change in effective stiffness, K_{eff}^*, due to a change in preswirl. However, the cross-coupled stiffness increases briskly with preswirl. At 10,200 rpm with a 50% pressure ratio, k^* increased roughly 50% from the low (0.07) to high (1.05) preswirl ratio. The increase in k^* causes a

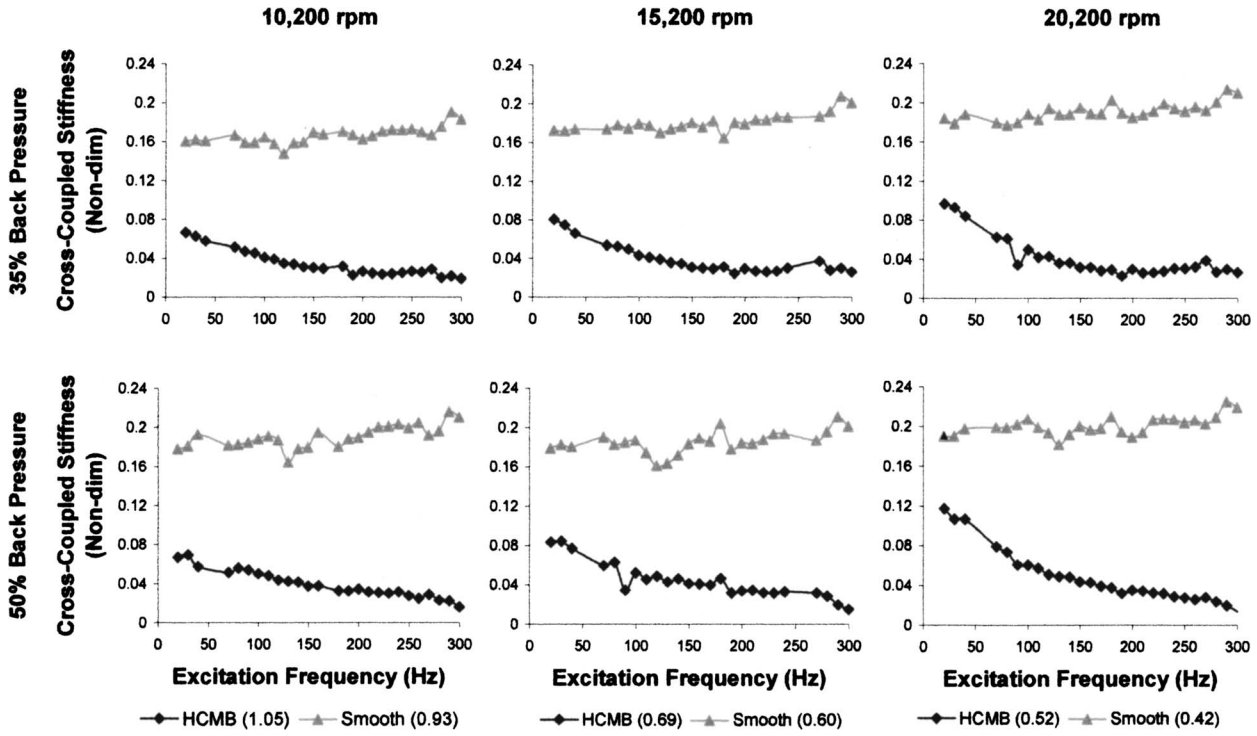

Fig. 7 k^* **for the HC seal at high preswirl and the smooth seals at medium preswirl**

reduction in the magnitude of $C_{\text{eff}}{}^*$ and an increase in the cross-over frequency at which $C_{\text{eff}}{}^*$ shifts from positive to negative. These results support the use of swirl brakes for a HC seal irrespective of concerns for cell clogging.

Direct comparison of the dynamic coefficients for the HC and smooth seal were made to understand how the HC seal might behave if its cells became clogged and caused it to approach the behavior of a smooth seal. First, there is a potential reduction in $K_{\text{eff}}{}^*$ of up to 50%, which could cause a problem if the HC seal is being used to keep a rotor critical speed placed above the operating speed. For comparable inlet preswirl conditions, the cross-coupled stiffness k^* is much higher for a smooth seal than a HC

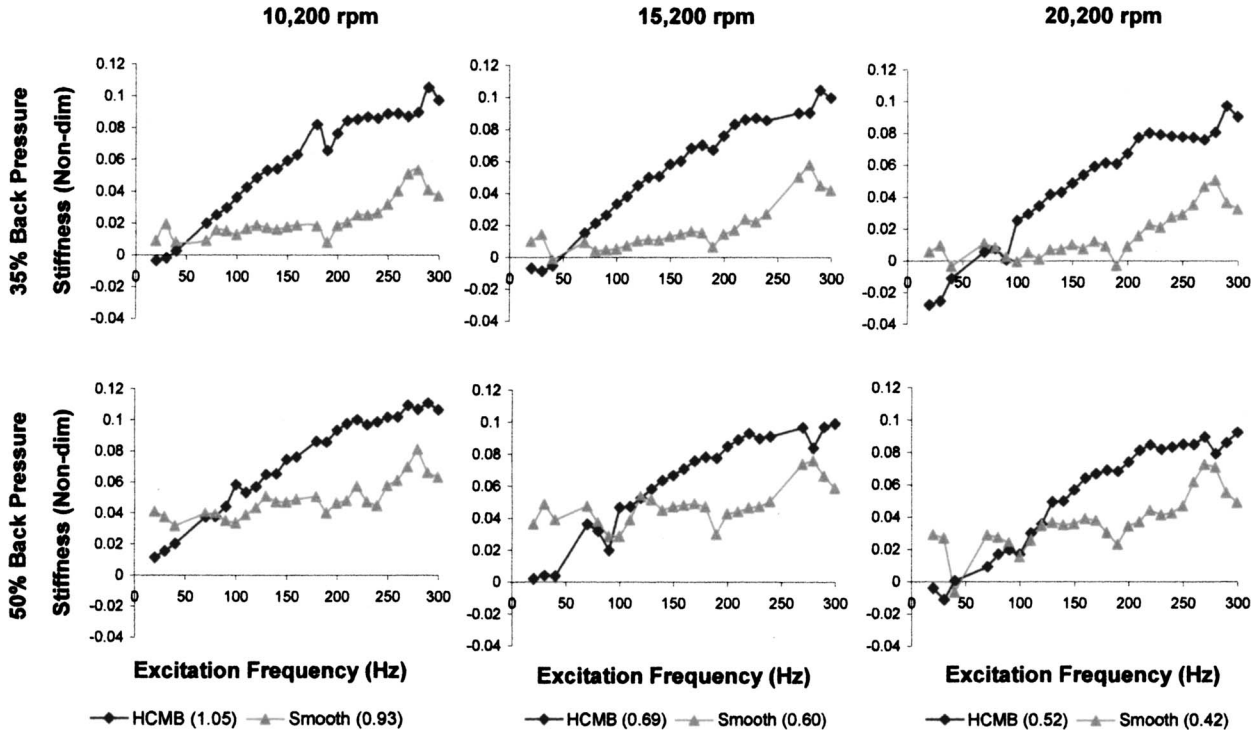

Fig. 8 $K_{\text{eff}}{}^*$ **for HC at high preswirl and a smooth seal at medium preswirl**

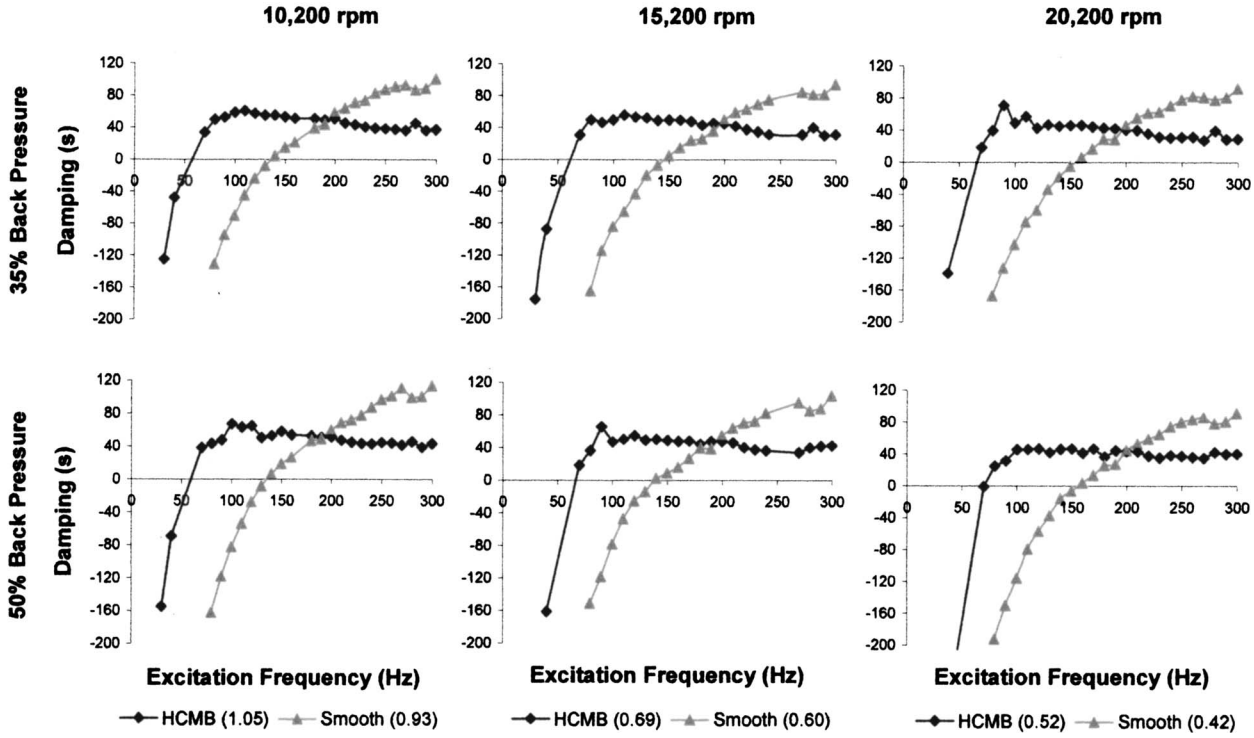

Fig. 9 C_{eff}^{*} for HC at high preswirl and the smooth seals at medium preswirl

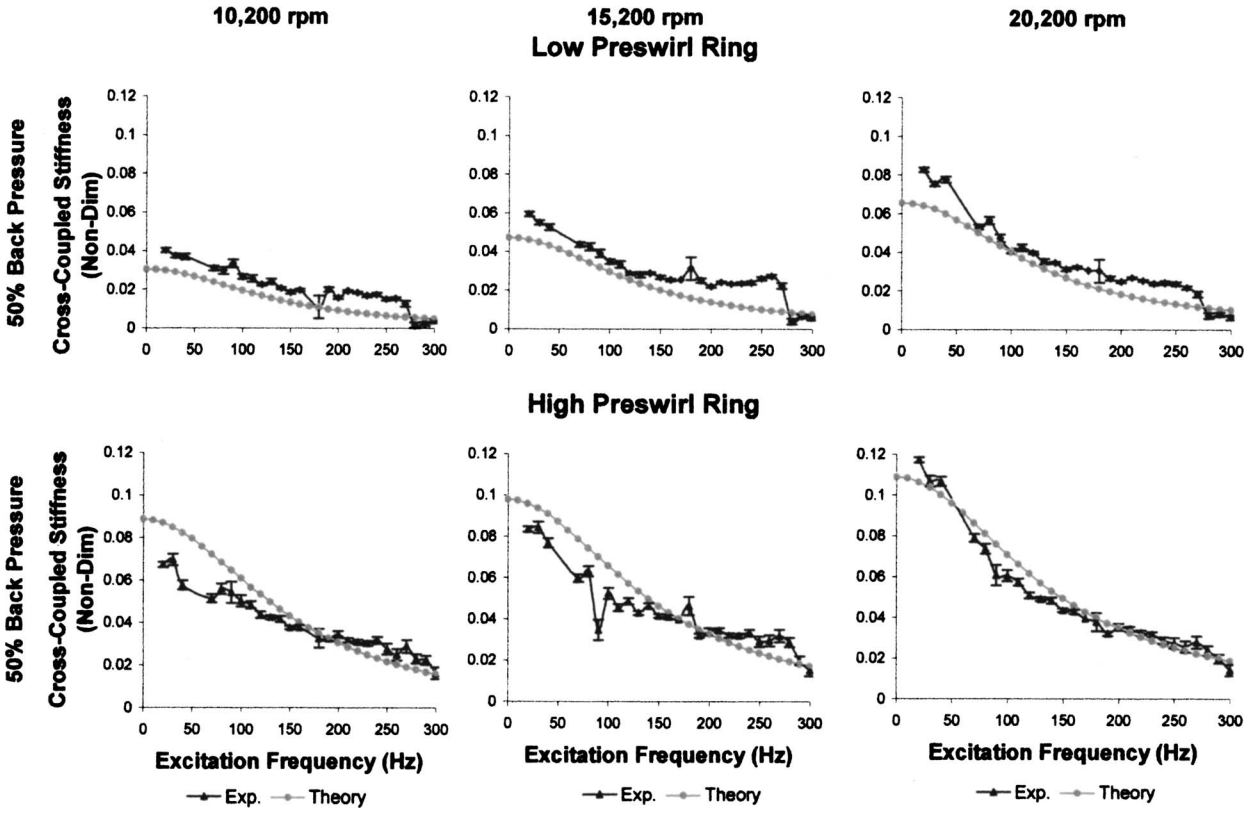

Fig. 10 Experimental and theoretical k^{*} versus excitation frequency for low/high preswirl (50% backpressure)

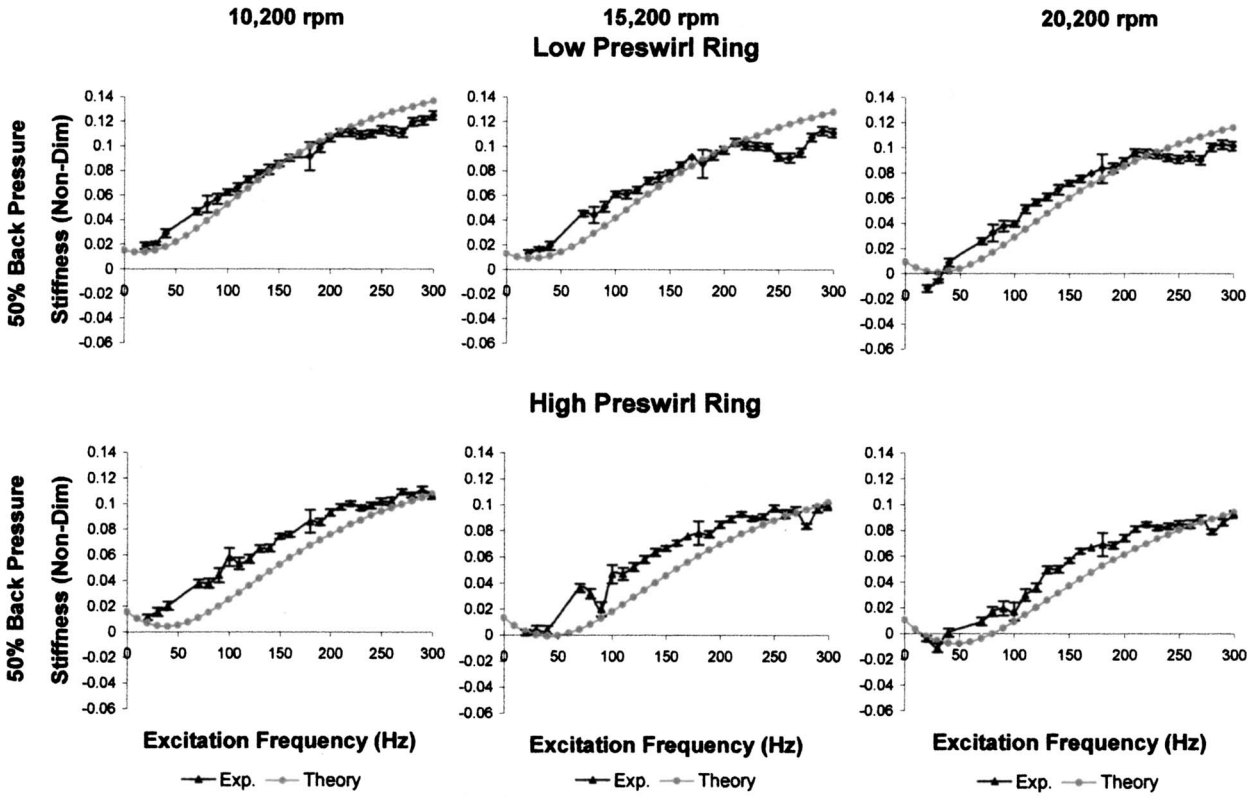

Fig. 11 HC tests and theoretical K^* versus excitation frequency for low/high preswirl (50% backpressure)

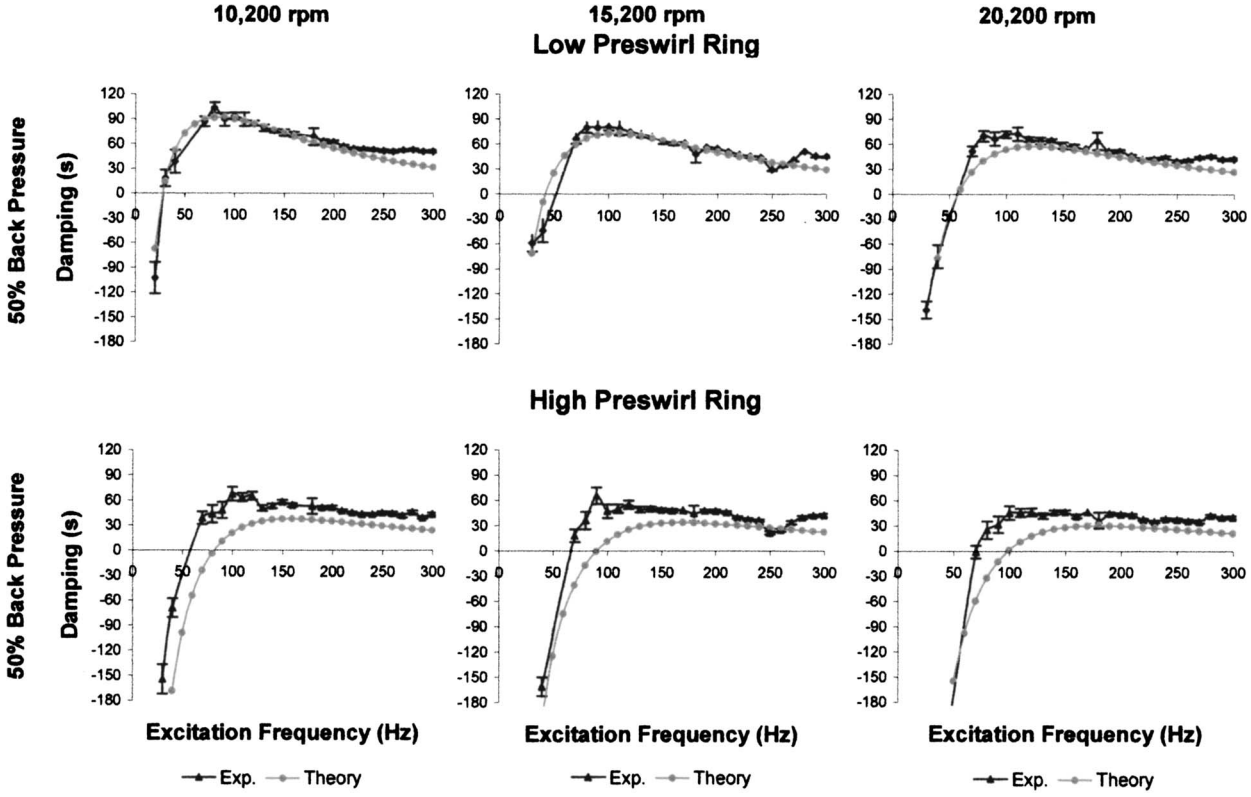

Fig. 12 HC C_{eff}^* predictions versus measurements for low/high preswirl (50% backpressure)

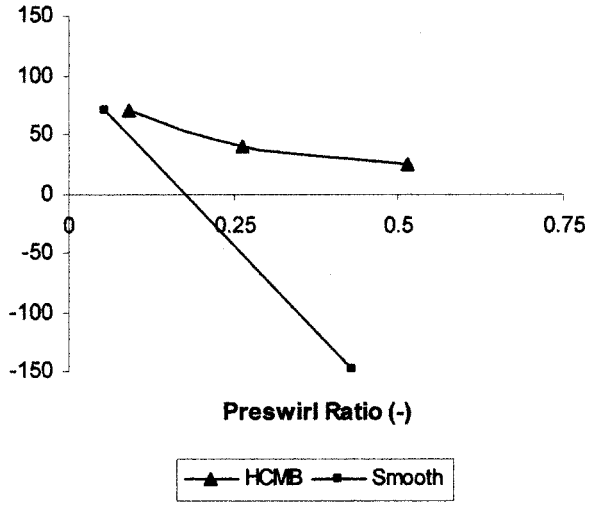

Fig. 13 C^*_{eff} versus preswirl ratio for the smooth and HC seals at 80 Hz excitation frequency, 20,200 rpm, and 50% pressure ratio

seal. As a consequence, $C_{\text{eff}}{}^*$ values are lower for smooth seals, and the cross-over frequency increases from 70 to 140 Hz (smooth) at the higher preswirl values (>0.4). These results strongly support the inclusion of swirl brakes for a HC seal if there is any concern in regard to cell clogging.

The two-control-volume theory model by Kleynhans and Childs [3] with Ha's [7] friction-factor coefficients does a good job in predicting the frequency-dependent experimental data for the HC seal. The theory seems to modestly overpredict increases in k^* as preswirl is increased. Thus, values for $C_{\text{eff}}{}^*$ are typically underpredicted (conservative predictions) for higher levels of preswirl.

Figure 13 shows C^*_{eff} versus preswirl for the present smooth and HC seals at 80 Hz. The test conditions are 50% pressure ratio and 20,200 rpm. At reduced preswirl—corresponding to an effective swirl brake—similar effective damping values are obtained. Moore and Soulas [9] conclusively validated this result. They tested a compressor at full speed and full pressure, alternately using: (i) a smooth seal and (ii) a hole-pattern-roughened stator seal. The same effective swirl brake was used with both seals. An external shaker was used to measure the compressor's frequency-response characteristics, producing log-decrement results. The compressor's log decrement was the same for both seals, but the smooth seal leaked roughly 50% more.

In conclusion, experimental results show that a swirl brake should be used at the inlet of a HC seal whether there is a concern for cell clogging or not to enhance the seal's stability characteristics. A swirl brake is particularly needed if the holes become clogged. Theory-versus-experiment results show that predictions for stability parameters k^* and $C_{\text{eff}}{}^*$ are typically conservative and trustworthy. Predictions for K_{eff} might be improved with better measured friction-factor coefficients.

Nomenclature

A = precession amplitude (L)
C, c = direct and cross-coupled damping coefficients (FT/L)
C^*, c^* = nondimensional direct and cross-coupled damping coefficients (t)
C_{eff} = effective damping coefficient, defined in Eq. (11) (FT/L)
$C_{\text{eff}}{}^*$ = nondimensional effective damping coefficient (t)
C_r = radial clearance between stator and rotor (L)
D = direct impedance (F/L)
D_{in} = seal inner diameter (L)
E = cross-coupled impedance (F/L)
F_x, F_y = seal reaction forces (F)
F_r, F_θ = radial and tangential seal reaction forces (F)
j = $\sqrt{-1}$
I_R, I_θ = radial and tangential impedance (F/L)
K, k = direct and cross-coupled stiffness coefficients (F/L)
K^*, k^* = nondimensional direct and cross-coupled stiffness coefficients
K_{eff} = effective stiffness coefficient, defined in Eq. (10) (F/L)
$K_{\text{eff}}{}^*$ = nondimensional effective stiffness coefficient
L = axial length of the seal (L)
M = inertia coefficient (M)
x, y = relative displacement between stator and rotor (L)
$\dot{x}$, $\dot{y}$ = relative velocity between stator and rotor (L/T)
$\ddot{x}$, $\ddot{y}$ = relative acceleration between stator and rotor (L/T^2)
ΔP = pressure drop across the length of the seal (F/L^2)
ω = rotor rotational frequency (1/T)
Ω = rotor precession frequency (1/T)
HC = honeycomb

References

[1] Childs, D., and Moyer, D., 1985, "Vibration Characteristics of the HPOTP (High Pressure Oxygen Turbopump) of the SSME (Space Shuttle Main Engine)," ASME J. Eng. Gas Turbines Power, **107**(1), pp. 152–159.
[2] Zeidan, F., Perez, R., and Stephenson, E., 1993, "The Use of Honeycomb Seals in Stabilizing Two Centrifugal Compressors," *Proceedings of the 22nd Turbomachinery Symposium*, Turbomachinery Laboratory, Texas A&M University, September 14-16, ASME, New York, pp. 3–15.
[3] Kleynhans, G., and Childs, D., 1997, "The Acoustic Influence of Cell Depth on the Rotordynamic Characteristics of Smooth Rotor/Honeycomb Stator Annular Gas Seals," ASME J. Eng. Gas Turbines Power, **119**, pp. 949–957.
[4] Ha, T.-W., and Childs, D., 1994, "Annular Honeycomb-Stator Turbulent Gas Seal Analysis Using A New Friction-Factor Model Based on Flat Plate Tests," ASME J. Tribol., **116**, pp. 352–360.
[5] Dawson, M., Childs, D., Holt, C., and Phillips, S., 2002, "Theory Versus Experiments for the Dynamic Impedances of Annular Gas Seals: Part 2—Smooth and Honeycomb Seals," ASME J. Eng. Gas Turbines Power, **124**, pp. 963–970.
[6] Dawson, M., Childs, D., Holt, C., and Phillips, S., 2002, "Theory Versus Experiments for the Dynamic Impedances of Annular Gas Seals: Part 1—Test Facility and Apparatus," ASME J. Eng. Gas Turbines Power, **124**, pp. 958–963.
[7] Ha, T., and Childs, D., 1992, "Friction-Factor Data for Flat-Plate Tests of Smooth and Honeycomb Surfaces," ASME J. Tribol., **114**, pp. 722–729.
[8] D'Souza, R., and Childs, D., 2002, "A Comparison of Rotordynamic-Coefficient Predictions of Annular Honeycomb Gas Seals Using Different Friction-Factor Models," ASME J. Tribol., **124**, pp. 524–529.
[9] Moore, J., and Soulas, T., 2003, "Damper Seal Comparison in a High-Pressure Re-Injection Centrifugal Compressor During Full-Load, Full-Pressure Factory Testing, Using Direct Rotordynamic Stability Measurement," Paper No. DETC2003/Vib-48458.

Effects of Multi-Injection Mode on Diesel Homogeneous Charge Compression Ignition Combustion

Wanhua Su
e-mail: whsu@tju.edu.cn

Bin Liu
e-mail: lbin79583@gmail.com

Hui Wang
e-mail: whblank@sohu.com

Haozhong Huang
e-mail: hhz421@tom.com

State Key Laboratory of Engines,
Tianjin University,
92 Weijin Road,
Tianjin 300072, China

Early injection, well before top dead center (TDC), has perhaps been the most commonly investigated approach to obtain homogeneous charge compression ignition (HCCI) combustion in a direct-injection (DI) diesel engine. However, wall wetting due to overpenetration of the fuel spray can lead to unacceptable amounts of unburned fuel and removal of lubrication oil. Another difficulty of diesel HCCI combustion is the control of combustion phasing. In order to overcome these difficulties, a multipulse fuel injection technology has been developed for the purpose of organizing diesel HCCI combustion, by which the injection width, injection number, and the dwell time between two neighboring pulse injections can be flexibly regulated. In present paper, the effects of a series of multipulse injection modes realized based on the prejudgment of combustion requirement, on engine emissions, thermal efficiency, and cycle fuel energy distribution of diesel HCCI combustion are studied. The designed injection modes include so-called even mode, hump mode, and progressive increase mode, and each mode with five and six pulses, respectively. Engine test was conducted with these modes. The experimental results show that diesel HCCI combustion is extremely sensitive to multipulse injection modes and that thermal efficiency can be improved with carefully modulated ones. There are many modes that can reach near zero NO_x *and smoke emissions, but it is significant to be aware that multipulse injection mode must be carefully designed for higher thermal efficiency.*
[DOI: 10.1115/1.2204977]

Introduction

Diesel-fueled HCCI has been studied for its potential of simultaneously reducing NO_x and particulate matter (PM) emissions while providing high efficiency from the mid 1990s. According to the methods of fueling, diesel HCCI comprises three main categories [1,2]: port injection [3–5], early in-cylinder injection [2,6–13], and late in-cylinder injection [14,15]. Some of the above-proposed injection strategies are in application, which enable diesel-fueled engine to realize HCCI combustion in limited operation conditions [12,14,15], successfully controlling combustion phasing and reducing NO_x and PM emissions simultaneously. But there still exists obstacles in organization of diesel HCCI combustion due to diesel fuel properties, which need to be understood further and to develop the art of combustion state control.

For diesel-fueled HCCI engines, high compression ratio is of benefit to enhance auto-ignition at light load, and direct in-cylinder fuel injection can be used to control combustion timing. However, the low-temperature chemical properties of diesel fuel tend to cause a rapid auto-ignition once compression temperature exceeds a threshold, bringing out problems of combustion phasing control. The low volatility of diesel fuel together with its propensity of high fuel cetane number makes it extremely difficult to organize HCCI combustion in wider operation conditions. In addition, most of proposed diesel HCCI engines are equipped with only one fuel-handling system with high fuel injection pressure, which tends to cause wall wetting, resulting in increased unburned-hydrocarbon (UHC) emission and degradation of lubrication oil. A fuel injection technology for these engines that can help homogeneous mixture formation without fuel wall impact is in an active demand.

A previous work done by the authors has presented a new HCCI combustion technology [16–18], which operates the engine with HCCI combustion at low loads, combined HCCI combustion, and lean diffusion combustion at medium and high loads. The combined combustion process is basically organized by the multipulse fuel injection strategy. Recently, it was reported that the multiinjection strategy was applied successfully in passenger car size common rail DI diesel engines in HCCI mode, in order to achieve thorough mixing of air and fuel and to avoid wall wetting. Helmantel and Denbratt [19] carried out a study on HCCI combustion with a single cylinder test engine configured as a Volvo NED5 common rail direct injection diesel engine. The fuel was injected in a series of five short injections at the injection timing of −90 deg of crank angle after top dead center (deg CA ATDC). For the purpose of reducing the droplet size and fuel penetration and thus improving the air/fuel mixing, the injector was fitted with a special ten-hole nozzle with an included angle of 60 deg. The diameter of the nozzle orifice was 0.111 mm. Cooled exhaust gas recirculation (EGR) and lower compression ratio were adopted to control combustion timing and rate of heat release. With these methods the NO_x and soot emissions were reduced by 98% and 95%, respectively, compared to those of conventional diesel operation, while the UHC and CO emissions increased dramatically. Ralf Buchwald et al. [20] studied the multi-injection HCCI on a direct-injection passenger-car Diesel engine equipped with a turbocharger and a common rail injection system. To avoid cylinder wall wetting, the fuel was injected in several portions (multiple injections) in order to reduce the penetration depth of fuel sprays. By experimental study, the optimized parameters of injection strategy were determined as follows: the injection nozzle angle was 156 deg; the injection number was 5; the common rail pressure was 75 MPa; and the injection timing was −54 deg CA ATDC. Compared to the test results with those of engine operation of European III (EU III) mode and minimum brake specific fuel consumption (BSFC) mode, HCCI mode resulted in dramati-

Contributed by the Internal Combustion Engine Division of ASME for publication in the JOURNAL OF ENGINEERING FOR GAS TURBINES AND POWER. Manuscript received January 17, 2005; final manuscript received March 24, 2006. Review conducted by D. Assanis.

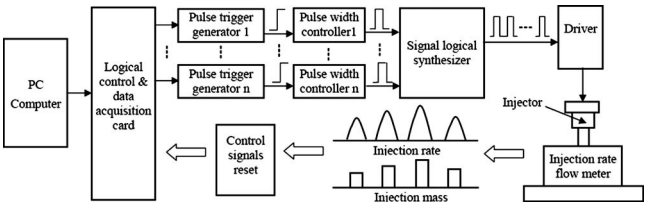

Fig. 1 Schematic of injection mode modulation system

cally decrease in NO_x and soot emissions; however, the UHC and CO emissions were 3 and 8.5 times than that of EU III mode, respectively.

Our recent report on multipulse fuel strategy further confirmed that near zero engine emissions of NO_x and PM were achieved in a certain operation range by multipulse injection control [21,22]. But it was found by thermal balance analysis of combustion process that combustion efficiency of the compound combustion mode dropped down by about 3%, compared to that of a conventional DI diesel engine, due to uncompleted combustion and increased heat loss attributed to advanced combustion phase [20]. Therefore, the mechanism of mixing process needs to be deeply investigated, including the effects of multipulse injection parameters on spray atomization, evaporation, and mixing, so that the injection mode for low engine emissions and potential high thermal efficiency in wider engine operation conditions can be precisely designed. The authors also found by a computer simulation [18] that the multipulse injection timing was of paramount interests since it determined in-cylinder conditions of pressure and temperature, and then their effects on evaporation and mixing. For earlier injection cases, the pulse width showed a strong impact on evaporation and mixing rate. Long width lead to overpenetration of fuel sprays, which would result in severe wall wetting. Hence, the short pulse width should be employed for earlier pulse injections. The dwell time was also an important factor, and short dwell time would result in less stratification of the fuel for later injection cases. Naturally, it was important to match and optimize the above three injection parameters, and then the engine could operate in a well-premixed mode [18]. However, the effects of multipulse injection parameters were not investigated by engine test.

In this paper, a series of multipulse injection modes with different injection parameters, such as pulse number, pulse width, and dwell time, are systematically designed and successfully modulated, and their effects on engine emissions, thermal efficiency, and cycle fuel energy distribution of diesel HCCI combustion on a test engine at various injection timings are studied. It is found that diesel HCCI combustion is very sensitive to the multipulse injection mode (injection rate pattern), and with a carefully modulated one, the thermal efficiency can be potentially improved.

Injection Mode Modulation

The modulation of multipulse injection mode is realized through changing the pulse width and dwell time between two neighboring pulse injections of control signal of the FIRCRI common rail system, as shown in Fig. 1. The system is a PC computer-based data acquisition and multipulse injection control system. By the standard data bus of the PC computer, the computer resources of hardware and software can be fully employed for the purpose of synthesis of driving signals for a designed injection mode. Two programmable logical GAL chips are incorporated in the signal logical synthesizer, which simplifies creation and management of pulse width and dwell time of control signals, and with which up to 10 pulses can be flexibly controlled.

A series of typical injection modes of five- and six-pulse injections were successfully modulated in this paper and were named even mode (EM), hump mode (HM), and progressive increase

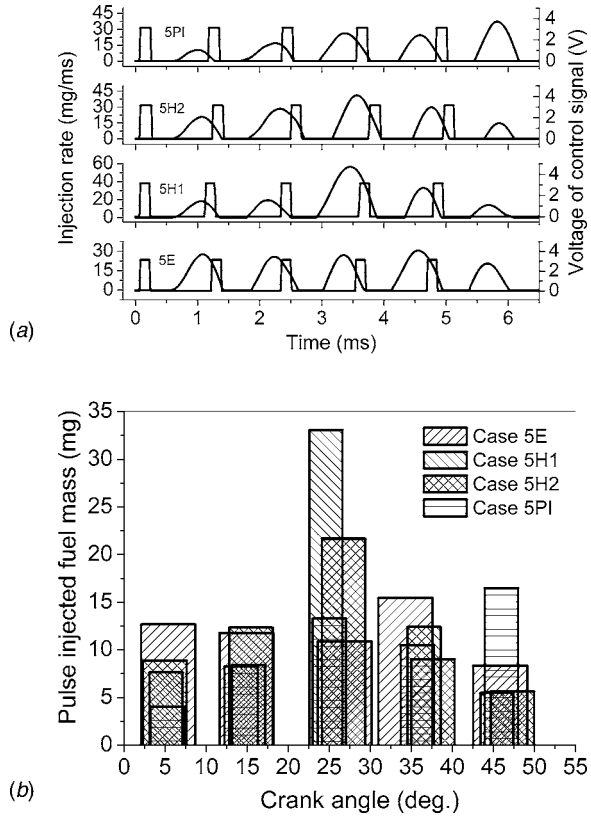

Fig. 2 Injection mode modulations for five-pulse injection modes: (a) injection rate and corresponding control signal; and (b) pulse fuel mass distribution of various injection modes

mode (PIM), respectively. As shown in Fig. 2, the name of each mode contains two numbers and one or two alphabets. The beginning number (4 or 5) denotes pulse injection number, the end number (1 or 2) is the ordinal for a certain mode, and the alphabets (E,H or PI) between the two numbers stand for even mode, hump mode, and progressive increase mode, respectively. Table 1 gives detail of the measured results of pulse-injection duration, dwell time, individual pulse fuel mass and its deviation, total cycle fuel mass and its deviation, and so on. The mass deviations for each pulse injection and for total injection of 120 working processes are expressed by

$$P_{fdj} = \sqrt{\frac{\sum_{i=1}^{n} (m_{pij} - \bar{m}_{pj})^2}{n}} \tag{1}$$

$$T_{fd} = \sqrt{\frac{\sum_{i=1}^{n} (m_{ti} - \bar{m}_{t})^2}{n}} \tag{2}$$

where n is the number of working process, P_{fdj} is the jth pulse fuel mass deviation, T_{fd} is total fuel mass deviation, m_{pij} is the jth pulse fuel mass of the ith working process, $\bar{m}_{pj}$ is the mean jth pulse fuel mass of n working processes, m_{ti} is the total fuel mass of the ith working process, and $\bar{m}_t$ is the mean total fuel mass of n working processes. Figures 2(a) and 3(a) show two groups of these modulated injection rates and their corresponding control signals according to their pulse number, and Figs. 2(b) and 3(b) show their pulse fuel mass distributions with crank angle. The total injection durations for these five- or six-pulse injection modes are nearly the same, respectively, as shown in Figs. 2(a)

Table 1 Test engine mode and engine condition

CASE NO.	Pulse width of injection / Dwell time (ms)						Pulse injected fuel mass (mg) / Pulse mass deviation (%)						Total fuel mass (mg)/ Fuel mass deviation (%)	Equivalence ratio ϕ
	I	II	III	IV	V	VI	I	II	III	IV	V	VI		
5E	0.832	0.752	0.672	0.832	0.656		12.67	11.78	10.87	15.46	8.358		59.13/8.24	0.3404
	0.464	0.4	0.432	0.416			6.661	18.22	23.9	44.97	80.72			
5H1	0.768	0.72	0.976	0.592	0.704		7.636	8.406	33.06	12.40	5.476		66.98/5.65	0.3869
	0.432	0.4	0.448	0.464			13.32	24.66	7.63	23.38	74.94			
5H2	0.816	0.864	0.848	0.544	0.56		8.867	12.33	21.67	9.006	5.630		57.51/19.77	0.3323
	0.432	0.448	0.496	0.56			26.95	30.12	23.81	34.48	70.28			
5PI	0.672	0.88	0.832	0.704	0.72		4.028	8.248	13.28	10.49	16.48		52.53/20.24	0.3035
	0.4	0.4	0.448	0.512			25.25	51.89	34.23	52.38	29.50			
6E	0.864	0.672	0.784	0.736	0.72	0.832	14.26	9.964	13.80	15.86	7.004	18.81	79.69/11.91	0.4541
	0.464	0.432	0.384	0.464	0.416		5.014	12.54	18.56	28.04	84.45	58.47		
6H1	0.72	0.848	0.656	0.768	0.736	0.64	5.196	16.07	13.06	13.11	9.53	6.859	63.83/15.90	0.3650
	0.432	0.448	0.448	0.432	0.416		21.12	34.70	27.54	46.10	58.57	66.88		
6PI	0.768	0.704	0.704	0.656	0.832	0.752	8.108	7.740	12.03	6.506	18.43	17.19	69.99/18.19	0.4036
	0.448	0.368	0.448	0.4	0.432		19.35	31.49	25.48	59.77	36.48	42.29		
6H2	0.688	0.944	0.656	0.816	0.528	0.544	3.724	13.06	8.410	17.74	8.644	5.449	57.03/22.95	0.3295
	0.4	0.464	0.512	0.528	0.56		32.11	38.72	57.34	51.93	68.39	86.85		

and 3(*a*), so the time sequence for 5PI and 6H1 at different injection timing are given in Figs. 4 and 5 to discuss those for five- and six-pulse injection modes, respectively.

Experimental Setup

The experimental setup is just the same as our previous work [16–18]. The test engine, as shown in Fig. 6, is a heavy-duty inline six-cylinder truck engine, and its detail specifications are shown in Table 2. In this study, the engine is modified so that the first cylinder is used as the test cylinder and the other five cylinders are used as a motor to drive it. The test cylinder is equipped with a FIRCRI common rail fuel injection system [23], a separate air supply system, and a separate exhaust system. In the FIRCRI common rail fuel injection system, the nozzle included angle is 150 deg, the orifice number is 7 and its diameter is 0.23 mm, as shown in Table 2. The air supply system comprises an air com-

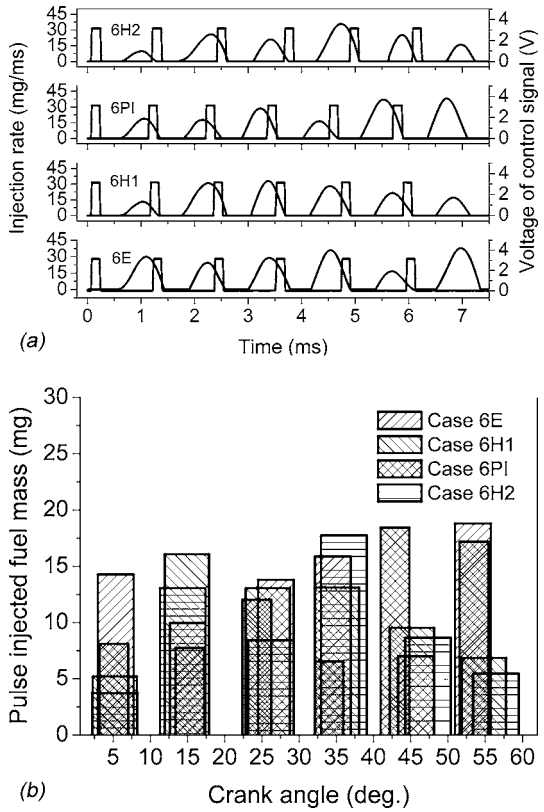

Fig. 3 Injection mode modulations for six-pulse injection modes: (a) injection rate and corresponding control signal; and (b) pulse fuel mass distribution of various injection modes

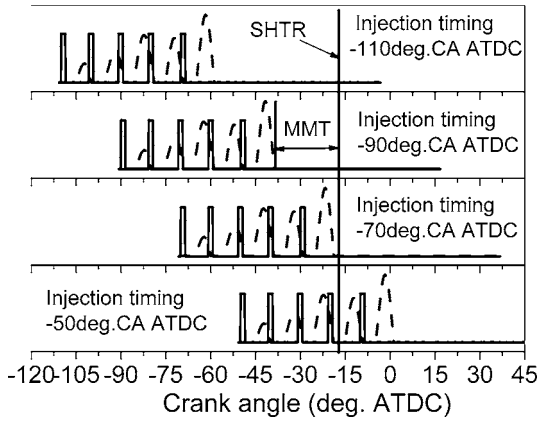

Fig. 4 Injection time sequence for 5PI at different injection timing

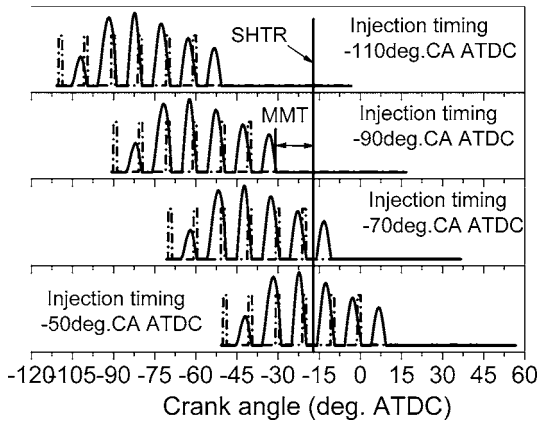

Fig. 5 Injection time sequence for 6H1 at different injection timing

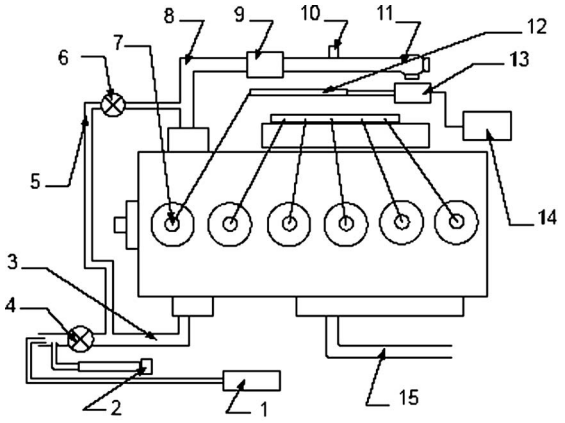

Fig. 6 Schematic of experimental setup

pressor, a surge tank, an intake air filter, and a pressure control valve. A gate valve in the exhaust pipe of the first cylinder is used to control the exhaust back pressure, which is normally caused by a turbocharger. The engine test for all cases is kept at 1400 rpm, 80 MPa rail pressure, 309 K intake temperature, and 0.132 MPa intake pressure. In order to focus on the study on effects of injection mode on HCCI combustion, in the present work, the technology of exhaust gas recirculation (EGR) is not used in this engine test, even though an EGR pipe and its control system are equipped on the test cylinder.

Results of Engine Tests

Emissions and Power Output. Figures 7–10 show NO_x emissions, smoke emission, CO emission, and the specific indicated mean effective pressure (IMEP) for five- and six-pulse injection modes at various injection timing, respectively. In this paper, knock combustion points are marked in the figure of specific IMEP using "knock points," and the specific IMEP is given to evaluate the work ability of per unit fuel mass furthermore, which is defined as

$$\mathrm{IMEP}_s = \frac{\mathrm{IMEP}}{m_f} \tag{3}$$

where IMEP_s is the specific IMEP (in kilopascal per milligram), IMEP is the measured IMEP (in kilopascal), and m_f is cycle fuel mass (in milligrams).

In the injection timing interval of −90 to −110 deg CA ATDC, extra low NO_x emissions of 0.1–0.6 g/(kW h) can be obtained by

Table 2 Specifications of the test engine

Bore (mm)	126
Stroke (mm)	130
Compression ratio	15
Swirl ratio	1.8
Fuel system	FIRCRI common rail injector
Injection pressure (MPa)	80
Orifice number × diameter (mm)	7 × 0.23
Injection mode	Multipulse injection
Combustion chamber	BUMP

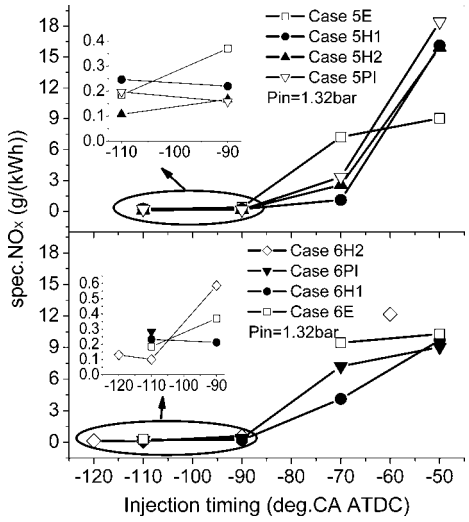

Fig. 7 Effects of various five- and six-pulse injection modes on NO_x emissions at different injection timing

all these five- and six-pulse injection modes. At injection timing of −70 deg CA ATDC, NO_x emissions of 5E reach to 7.4 g/(kW h) but those of the other three five-pulse injection modes are all lower than 3.25 g/(kW h). 6PI has NO_x emissions of 9 g/(kW h), while those of the other three six-pulse injection modes are all above 3 g/(kW h). As injection timing retarded to −50 deg CA ATDC, shown in Fig. 7, NO_x emissions of all these modes increase dramatically. NO_x emissions of 5E are the lowest among five-pulse injection modes, while the smallest value of the other three five-pulse injection modes is 15 g/(kW h). For six-pulse injection modes, their NO_x emissions are all about 8 g/(kW h).

Smoke emissions for all these injection modes at various injection timings are lower than 0.5BSU, and are almost the same except for 5H1 at injection timing of −110 deg CA ATDC, which has the largest value of 1.0BSU. This may be caused by a large quantity of unburned fuel droplets, since its third pulse fuel mass of 33.06 mg is far greater than that of the other five-pulse injection modes (as shown in Fig. 2(*b*)), resulting in long spray penetration and severe wall wetting.

CO emissions for all these injection modes decrease with re-

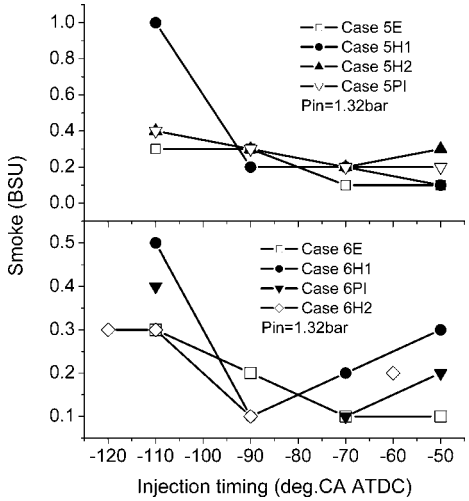

Fig. 8 Effects of various five- and six-pulse injection modes on smoke emission at different injection timing

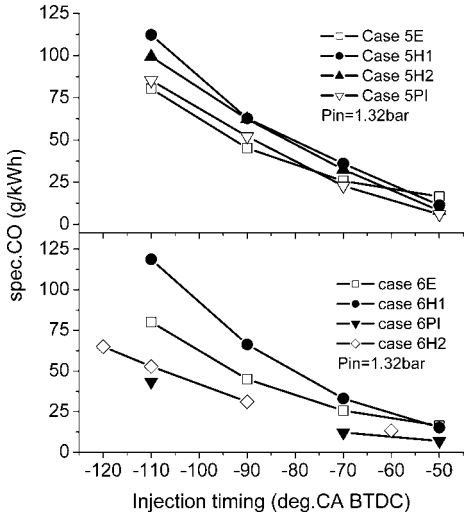

Fig. 9 Effects of various five- and six-pulse injection modes on CO emission at different injection timing

tarded injection timing. Among five-pulse injection modes, 5PI has relatively the lowest CO emission, while 6PI has the lowest one among six-pulse injection modes. CO emission is the product of incomplete combustion of CO. In this paper, it is found that CO emission and unburned fuel droplets are the main heat loss of fuel energy, as shown in Figs. 11 and 12, which will be discussed in detail in the next section.

Correspondingly, the specific IMEP for all these injection modes increase with retarded injection timing. 6H2 has the highest specific IMEP at all injection timings among six-pulse injection modes and so does 5PI among five-pulse injection modes. It is probably due to the fact that at retarded injection timing, higher in-cylinder pressure shortens penetration of fuel jets and enhances mixing of fuel and air, resulting in decreased heat loss of unburned fuel droplets as shown in Figs. 11 and 12, which will also be discussed in detail in the next section.

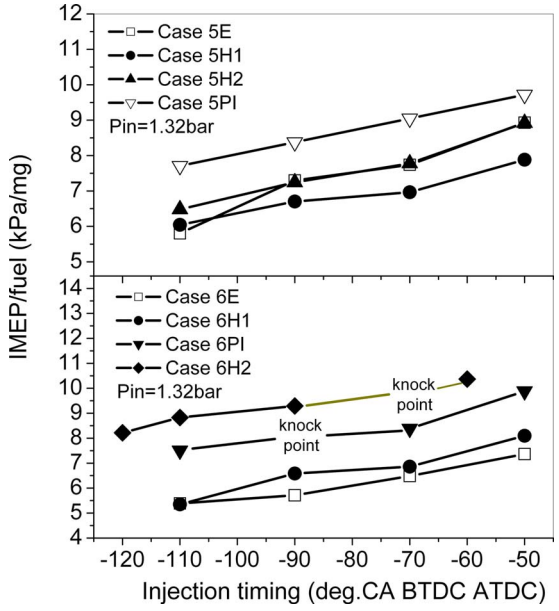

Fig. 10 Effects of various five- and six-pulse injection modes on specific IMEP at different injection timing

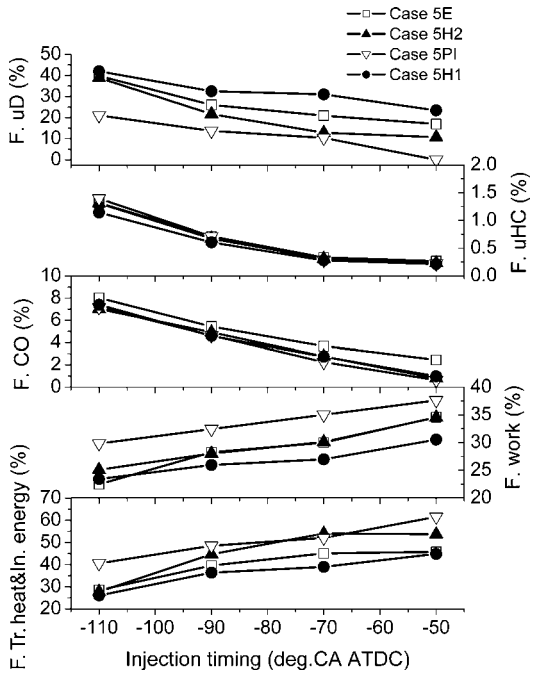

Fig. 11 Energy distribution of cycle fuel mass for five-pulse injection modes

Measured Energy Distribution for Various Injection Modes. According to energy balance law, cycle fuel mass energy finally changes into the following four parts: energy loss of cycle unburned fuel droplets, energy loss of cycle UHC emission, energy loss of cycle CO emission and heat release of fuel combustion, and the last one includes engine cycle indicated work, heat loss due to heat transfer and the changed internal energy of cycle charge, which can be expressed as a balance formula

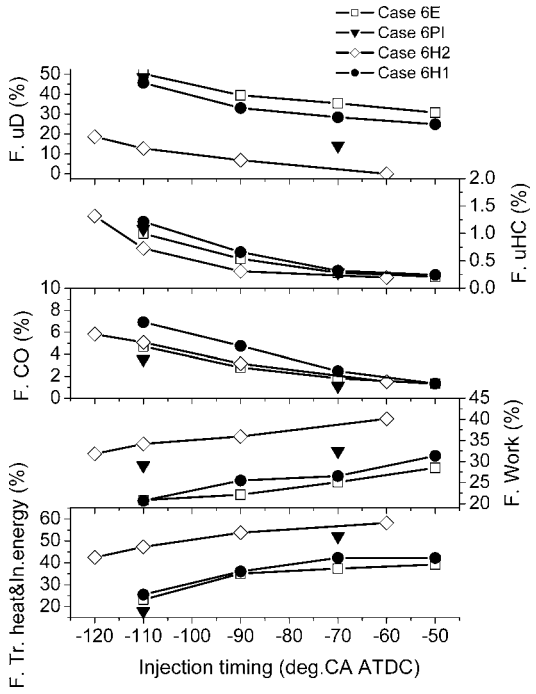

Fig. 12 Energy distribution of cycle fuel mass for six-pulse injection modes

$$m_f \cdot H_u = m_{uD} \cdot H_u + m_{\mathrm{UHC}} \cdot H_u + m_{\mathrm{CO}} \cdot (h_{\mathrm{CO_2}} - h_{\mathrm{CO}}) + W_i + Q_{the} \tag{4}$$

where m_f is the cycle fuel mass (in milligrams); H_u is the low heat value of diesel fuel (in Joules per milligram); m_{uD} is the mass of cycle unburned fuel droplets (in milligrams); m_{UHC} is the mass of cycle UHC emission, mg; m_{CO} is the mass of cycle CO emission (in milligrams); $h_{\mathrm{CO_2}}$ is the enthalpy of CO_2 (in Joules per milligrams); h_{CO} is the enthalpy of CO (in Joules per milligram); W_i is engine cycle indicated work (in Joules); Q_{the} includes cycle heat transfer loss and the change of internal energy of cycle cylinder charge (in Joules). In this paper, the energy loss fraction of UHC and CO emissions, the fraction of indicated work are denoted as F.UHC, F.CO, and F.Work respectively; and the fraction of Q_{the} and heat loss fraction of unburned fuel droplets are denoted as F.Qthe and F.UD, respectively. Obviously, the fraction of indicated work F.Work is the representative of indicated thermal efficiency.

Looking at Figs. 11 and 12, CO emission and unburned fuel droplets are the main loss of cycle fuel energy, in comparison to heat loss due to cycle unburned hydrocarbon. It is well known that the heat loss of unburned fuel droplets, including those sticking on the cylinder liner and those distributing in cooler areas of the cylinder volume, such as the piston tolerance volume and the piston crevice, is the most severe heat loss if the combustion is not precisely organized by early in-cylinder fuel injection strategy, because of two influence factors of lower in-cylinder pressure, temperature, and lower volatility of diesel fuel. This kind of heat loss usually does not result in severe emission of UHC, but in smoke emission (see Fig. 8). F.UHC, F.CO, and F.UD of all these injection modes decrease with retarded injection timing, while F.Work and F.Qthe are greatly improved.

As also can be seen in Figs. 11 and 12, F.UD values of five-pulse injection modes decline with retarded injection timing and stand in the line of 5H1 > 5E > 5H2 > 5PI for all injection timings, while for six-pulse injection modes, it is 6E > 6H1 > 6PI > 6H2. The curve trend of F.UD value at different injection timing for five-pulse injection modes correlates closely with their pulse fuel mass distribution, when looking at Table 1, where the sum of the first two pulse injections fuel mass for five-pulse injection modes stands in the line of 5E > 5H2 > 5H1 > 5PI. It behaves just the same as their F.UD values do, except for the two modes of 5H2 and 5E. It can be explained by the over large fuel mass of the third pulse injection of 5H1. For the same argument, the first three pulse-injections fuel mass sum for six-pulse injection modes stands in the line of 6E > 6H1 > 6PI > 6H2, which is also the same sequence as their F.UD values. So it comes to the conclusion that the pulse fuel mass at earlier injection stage should be as small as necessary for eliminating wall wetting and overly large fuel mass for any individual pulse injection should be avoided for the same purpose.

Combustion Analysis. In order to carry out combustion analysis, typical parameters of combustion process are deduced from measured in-cylinder pressure data. For a further understanding of the combustion phenomenon of early in-cylinder multipulse injection, some simulation results of chemical kinetics is also cited in this section.

Figures 13–15 show the calculated rate of heat release (ROHR) and the cumulated heat release (CHR), which is normalized by the total energy of cycle fuel, based on the measured in-cylinder pressure data at three typical injection timings of −110, −90, and −50 deg CA ATDC for five- and six-pulse injection modes, respectively (The latest injection timing for 6H2 is −60 deg CA ATDC). As shown in these figures, the low-temperature reaction of in-cylinder fuel always starts at about −25 deg CA ATDC for all test cases and the corresponding in-cylinder temperature is about 800 K. It is consistent with the simulation results calculated by the state key lab engines (SKLE) chemical kinetic model [24].

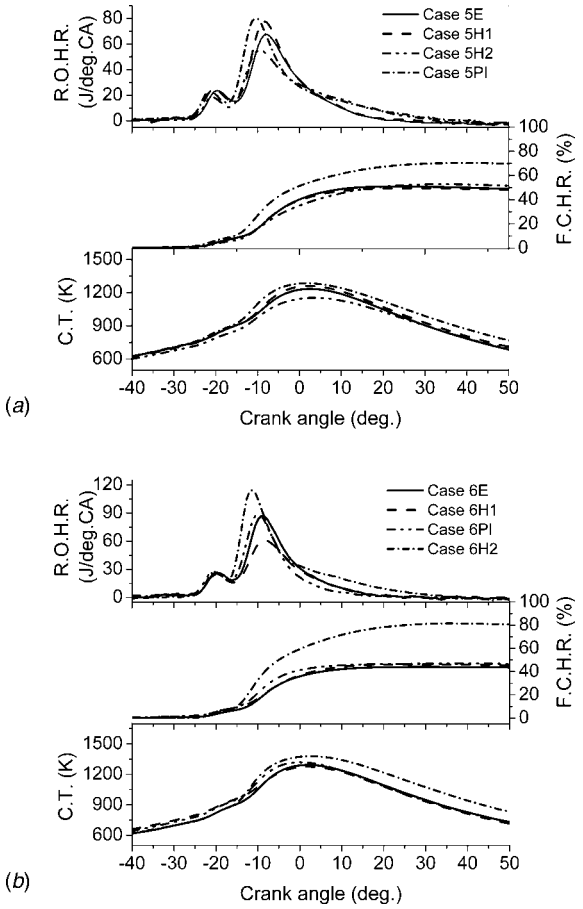

Fig. 13 ROHR, CHR, and mean cylinder temperature for various five- and six-pulse injection modes at injection timing of −110 deg CA ATDC: (a) modes of five-pulse injection; and (b) modes of six-pulse injection

However, it is clearly seen from these figures that the ROHR and the CHR curves during the low-temperature reaction vary with different injection timing and mode. At earlier injection timings, such as −110 and −90 deg CA ATDC, lower ROHR and less CHR appear than do at later injection timings. It causes delayed high-temperature reaction, leading to low peaks of ROHR with tardy rising rates. When looking at the curves of ROHR, the different curve trend yield different total released fraction of cycle fuel energy, which correlates very well with energy distribution, including F.Work and F.UD shown in Figs. 11 and 12. For the mode with the higher value of unburned fuel droplets F.UD, its ROHR for low- and high-temperature reaction becomes lower, and vice versa.

At later injection timing such as −50 deg CA ATDC, in Fig. 15, especially for modes of 5PI and 6H2, higher ROHR and more released total energy CHR appear. From the view points of fuel wall impingement and thermal efficiency, very precise regulation of fuel system parameters is necessary for homogeneous mixture preparation in HCCI combustion, including injection mode modulation, injection timing selection and also injector nozzle configuration design.

Figure 16 shows the combustion durations θ_d for these multipulse injection modes derived from their ROHR data, which is defined as

$$\theta_d = \theta_{90} - \theta_{10} \tag{5}$$

where θ_{90} is the crank angle when 90% of total released heat of a test case is released (in degrees CA); θ_{10} is the crank angle when 10% of total released heat of a test case is released (in degrees

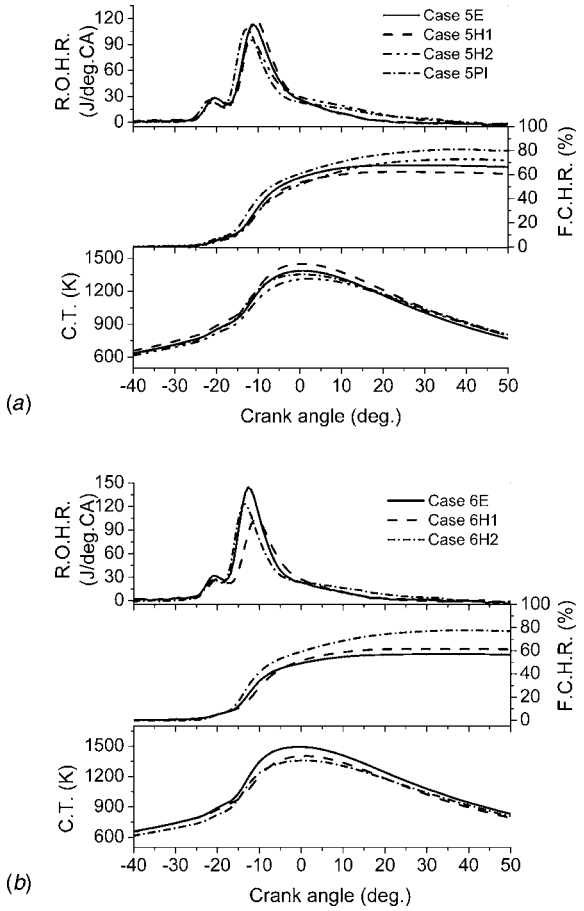

Fig. 14 ROHR, CHR, and mean cylinder temperature for various five- and six-pulse injection modes at injection timing of −90 deg CA ATDC: (a) modes of five-pulse injection; and (b) modes of six-pulse injection

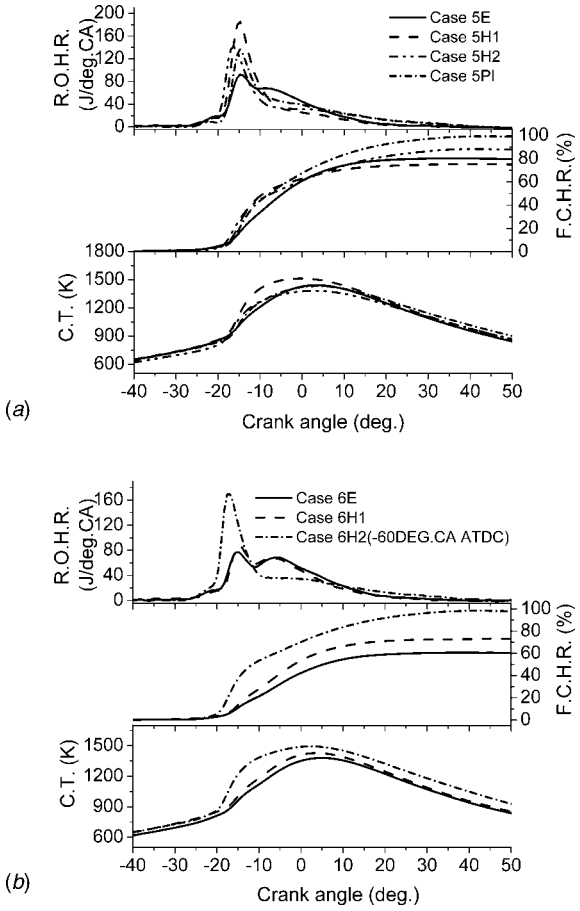

Fig. 15 ROHR, CHR, and mean cylinder temperature for various five- and six-pulse injection modes at injection timing of −50 deg CA ATDC: (a) modes of five-pulse injection; and (b) modes of six-pulse injection

CA). Compared combustion durations θ_d for these injection modes in Fig. 16 with their corresponding energy distribution in Figs. 11 and 12, it is clear to see that θ_d for a certain mode also correlates closely with its F.Work and F.UD. The longer the θ_d, the higher the F.Work and the less the F.UD, but the longest θ_d here is shorter than that of conventional diesel combustion. Therefore, lower ROHR companied with shorter θ_d is the consequence that less fuel completes mixing process and takes part in combustion, resulting in higher F.UD. Although the NO_x emissions are pretty low with many injection modes at earlier injection timings of −110 and −90 deg CA ATDC, only those with no heat loss of F.UD and high thermal efficiency are the target of injection mode control.

On the other hand, it is confirmed from analysis of combustion duration and ROHR that the premixed combustion process organized by multipulse injection is not a flash explosion of high-temperature reaction but a typically finite rate reaction process. Looking at Figs. 13 and 14, when at injection timing of −110 and −90 deg CA ATDC respectively, there are long tails of ROHR curves after the heat release peak of premixed combustion for various modes, which keep for about 40 degs CA. In order to understand the mechanism of tail combustion, a newly developed *n*-heptane reduced chemical kinetic model for diesel HCCI combustion was employed to study the effects of engine operating conditions, including fuel/air equivalence ratio ϕ, intake pressure and temperature, compression ratio, engine speed, and so on, on the formation and transformation rates of CO into CO_2.

Figure 17 shows a calculated result based on the model under the precondition of 325 K intake temperature, 1.2 bar intake pressure, 1400 rpm engine speed and 14.4 compression ratio. It can be seen that CO formation starts at various time, corresponding to various fuel/air equivalence ratio ϕ, but it may be really caused by the difference of temperature in various in-cylinder fuel concen-

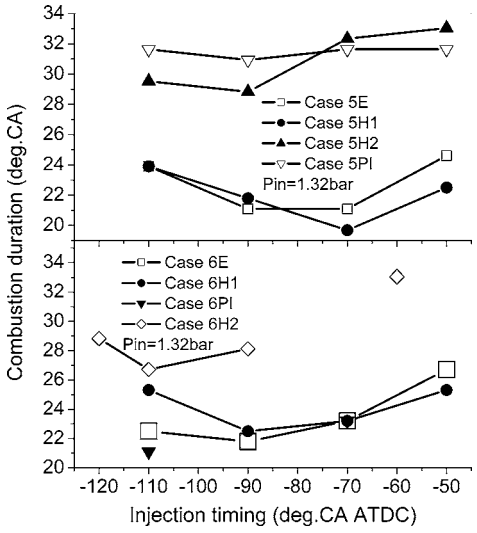

Fig. 16 Combustion durations for various five- and six-pulse injection modes at different injection timing

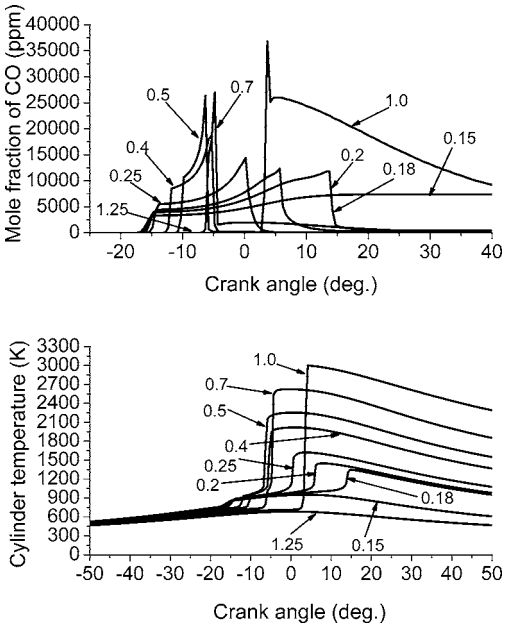

Fig. 17 Effects of equivalent ratio on mole fraction of CO and in-cylinder temperature (T_0=325 K, P_0=1.2 bar, ε=14.4, engine speed: 1400 r/min)

tration regions, which is due to different fuel evaporation heat and charge specific heat. A clear evidence is that the start of CO formation when ϕ=1 is delayed for about 15 degs CA compared to that of when ϕ=0.15. For ϕ=1.25, CO formation actually does not occur because of the lower compression temperature than the activation temperature at which the in-cylinder low-temperature reaction begins. However, it is interesting to find that the transformation rate of CO into CO_2 depends strongly on fuel/air equivalence ratio ϕ, as shown in Fig. 17. When ϕ=0.15, the transformation of CO into CO_2 does not occur, so the already generated CO due to low-temperature reaction certainly becomes the source of CO emission. In these test cases, the fuel in cooler and overmixing zones may form such very lean mixture, leading to substantive heat loss of CO. The transformation time of CO advances as ϕ increases from ϕ=0.18. When ϕ=0.7, the highest transformation rate is observed. For ϕ=1, CO_2 dissociation delays the transformation rate of CO into CO_2 due to a very high combustion temperature of about 2800 K, as shown in Fig. 17.

In the present study, the premixed charge is prepared by a series of multipulse injection modes at a certain injection time sequence. Therefore, the in-cylinder mixture is actually stratified in both fuel/air equivalence ratio and temperature. Thus, the long tails of ROHR curves appearing in Figs. 13 and 14 at earlier injection timings of −110 and −90 deg CA ATDC can be explained by the fact of the low transformation rate of CO into CO_2 in local lean and cooler regions due to charge stratification.

Looking at the curves of ROHR in Fig. 15 for five- and six-pulse injection modes at injection timing of −50 deg CA ATDC, there also exist long tails after the heat release peaks of premixed combustion for almost all these modes, with features of diffusion combustion, which are different from those at earlier injection timings of −110 and −90 deg CA ATDC. For instance, on the ROHR curve of 6E, a diffusion combustion heat release peak after the premixed combustion heat release peak is clearly observed, which causes NO_x emissions to increase rapidly, as shown in Fig. 7. As mentioned above, the low-temperature reaction for all these modes starts at about −25 deg CA ATDC and the high-temperature reaction for all these modes starts at about −17 deg CA ATDC. Therefore, only the last pulse injection ends before −17 deg CA ATDC can fuel injection and combustion be separated, and it even ends closely before −17 deg CA ATDC, the diffusion combustion may be avoided if flash mixing is realized. In this study, however, it is shown that a certain mixing time is necessary to separate fuel mixing and combustion for the purpose of low NO_x emissions. From Figs. 7, 11, and 12, it can be found that the injection timing of −90 deg CA ATDC for all the test cases is close to the optimum injection timing from the view points of NO_x emissions and thermal efficiency compromise. Thus, in Figs. 4 and 5, where we show the injection time sequence for five- and six-pulse injection modes at various injection timings, the minimum mixing time (MMT) between the end of the last pulse injection and the start of high temperature reaction (SHTR) should be in the range of 12.5–22.5 degs CA. The lowest value of 12.5 degs CA belongs to hump mode with six-pulse injection, and the highest one belongs to progressive increase mode with five-pulse injection.

Summary

1. The effects of multipulse injection modes on engine emissions and thermal efficiency were investigated by engine test with various modulated multipulse injection rate patterns. It is confirmed that early in-cylinder injection diesel HCCI combustion is very sensitive to multipulse injection modes as well as injection timing, because they effect the pulse fuel distribution, the fuel jet behavior of atomization, evaporation, mixing, and finally, the energy distribution of cycle fuel mass, which is interrelated closely with engine thermal efficiency. Many injection modes are able to achieve extra low NO_x emissions, but only those carefully modulated can meet the requirement of low emissions of NO_x and PM and thermal efficiency high enough, with which wall wetting and unburned fuel droplets loss can be eliminated.
2. For the purpose of higher thermal efficiency and extra low NO_x and PM emissions, the optimum injection start timing is around −90 deg CA ATDC. Further retarding of injection would increase NO_x emissions dramatically due to diffusion combustion, and on the contrary, would result in increase of wall wetting and unburned fuel droplets loss.
3. For the same purpose, there must be a so-called minimum mixing time interval between the end of the multipulse injection and the start of combustion, which falls in the range of 12.5–22.5 degs CA in this study. The largest value belongs to the progressive increase mode (PI) with five-pulse injection and the lowest value belongs to the hump mode with six-pulse injection. The latter obtains a little better engine performance.

Acknowledgment

The research is supported by the National Natural Science Foundation of China through its key project funding, and by the Ministry of Science and Technology through its 973 National Key Project on HCCI Combustion Engines and Fuels.

References

[1] Stanglmaier, R. H., and Roberts, C. E., 1999, "Homogenous Charge Compression Ignition (HCCI): Benefits, Compromises, and Future Engine Applications," SAE Paper No. 1999-01-3682.
[2] Zhao, F., Asmus, T. W., Assanis, D. N., Dec, J. E., Eng, J. A., and Najt, P. M., 2002, *Homogenous Charge Compression Ignition (HCCI) Engines: Key Research and Development Issues*, Society of Automotive Engineers, Warrendale, PA.
[3] Ryan, T. W., III, and Callahan, T. J., 1996, "Homogeneous Charge Compression Ignition of Diesel Fuel," SAE Paper No. 961160.
[4] Gray, A. W., III, and Ryan, T. W., III, 1997, "Homogeneous Charge Compress Auto-ignition (HCCI) of Diesel/Fuel," SAE Paper No. 971676.
[5] Midlam-Mohler, S., 2004, "Diesel HCCI With External Mixture Preparation," 10th Diesel Engine Emissions Reduction (DDER) Workshop, Aug. 29–Sept. 2.
[6] Nakagome, K., Shimazaki, N., Niimura, K., and Kobayashi, S., 1997, "Com-

bustion and Emission Characteristics of Premixed Lean Diesel Combustion Engine," SAE Paper No. 970898.
[7] Hashizume, T., Miyamoto, T., Akagawa, H., and Tsujimura, K., 1998, "Combustion and Emission Characteristics of Multiple Stage Diesel Combustion," SAE Paper No. 980505.
[8] Akagawa, H., Miyamoto, T., Harada, A., Sasaki, S., Shimazaki, N., Hashizume, T., and Tsujimura, K., 1999, "Approaches to Solve Problems of the Premixed Lean Diesel Combustion," SAE Paper No. 1999-01-0183.
[9] Nishijima, Y., Asaumi, Y., and Aoyagi, Y., 2001, "Premixed Lean Diesel Combustion (PREDIC) Using Impingement Spray System," SAE Paper No. 2001-01-1892.
[10] Yokota, H., Kodo, Y., Nakajima, H., Kakegawa, T., and Suzuki, T., 1997, "A New Concept for Low Emission Diesel Combustion," SAE Paper No. 970891.
[11] Iwabuchi, Y., Kawai, K., Shoji, T., and Takeda, Y., 1999, "Trial of New Concept Diesel Combustion System—Premixed Compression-Ignition Combustion," SAE Paper No. 1999-01-0185.
[12] Yanagihara, H., Sato, Y., and Mizuta, J., 1997, "A Study of DI Diesel Combustion Under Uniform Higher-Dispersed Mixture Formation," JSAE Rev., **18**(1997), pp. 247–254.
[13] Walter, B., and Gatellier, B., 2002, "Development of the High Power NADI Concept Using Dual Mode Diesel Combustion to Achieve Zero NO_x and Particulate Emissions," SAE Paper No. 2002-01-1744.
[14] Kimura, S., Aoki, O., Ogawa, H., Muranaka, S., and Enomoto, Y., 1999, "New Combustion Concept for Ultra-Clean and High-Efficiency Small DI Diesel Engines," SAE Paper No. 1999-01-3681.
[15] Aiyoshizawa, E., Hasegawa, M., Kawashima, J.-I., and Muranaka, S., 2000, "Combustion Characteristics of a Small DI Diesel Engine," JSAE Rev., **21**(2000), pp. 241–243.
[16] Su, W., Lin, T., and Pei, Y., 2003, "A Compound Technology for HCCI Combustion in a DI Diesel Engine Based on the Multi-Pulse Injection and the BUMP Combustion Chamber," SAE Paper No. 2003-01-0741.
[17] Su, W., Lin, T.. Zhao, H., and Pei, Y., 2005, "Research and Development of an Advanced Combustion System for the Direct Injection Diesel Engine," Proc. Inst. Mech. Eng., Part D (J. Automob. Eng.) **219**, pp. 241–252.
[18] Su, W., Zhang, X., Lin, T., Pei, Y., and Zhao, H., 2004, "Study of Pulse Spray, Heat Release, Emissions and Efficiencies in A Compound Diesel HCCI Combustion Engine," ASME Paper No. ICEF2004-927.
[19] Helmantel, A., and Denbratt, I., 2004, "HCCI Operation of a Passenger Car Common Rail DI Diesel Engine With Early Injection of Conventional Diesel Fuel," SAE Paper No. 2004-01-0935.
[20] Buchwald, R., Brauer, M., Blechstein, A., Sommer, A., and Kahrstedt, J., 2004, "Adaption of Injection System Parameters to Homogeneous Diesel Combustion," SAE Paper No. 2004-01-0936.
[21] Su, W., Wang, H., and Liu, B., 2005, "Injection Mode Modulation for HCCI Diesel Combustion," SAE Paper No. 2005-01-0117.
[22] Wang, H., Su, W., and Liu, B., 2005, "Study of Characteristics of Premixed Diesel Combustion and Emissions Based on Modulated Multi-Pulse Injection Modes," Trans. CSICE, **23**(4), pp. 289–296 (in Chinese).
[23] Su, W., Wang, Y., Lin, T., Xie, H., Pei, Y., Li, S., Cheng, G., and Wang, X., 2001, "A Study of Effects of Design Parameters on Transient Response and Injection Rate Shaping for a Common Rail Injector System," SAE Paper No. 2001-01-3506.
[24] Su, W., and Huang, H., 2005, "Development and Calibration of a Reduced Chemical Kinetic Model of *n*-Heptane for HCCI Engine Combustion," Fuel, **84**, pp. 1029–1040.

Hoon Cho
Dohoy Jung
Zoran S. Filipi
Dennis N. Assanis

Mechanical Engineering,
The University of Michigan,
Ann Arbor, MI 48109

John Vanderslice
Ford Motor Company,
Dearborn, MI 48124

Walter Bryzik
U.S. Army Tank-Automotive Research,
Development & Engineering Center,
Warren, MI 48397

Application of Controllable Electric Coolant Pump for Fuel Economy and Cooling Performance Improvement

The engine cooling system for a typical class 3 pickup truck with a medium duty diesel engine was modeled with a commercial code, GT-Cool, in order to explore the benefit of a controllable electric pump on the cooling performance and the pump operation. As the first step, the cooling system model with a conventional mechanical coolant pump was validated with experimental data. After the model validation, the mechanical pump submodel was replaced with the electric pump submodel, and then the potential benefit of the electric pump on fuel economy was investigated with the simulation. Based on coolant flow analysis, a modified thermostat hysteresis was proposed to reduce the recirculating flow and the electric pump effort. It was also demonstrated that the radiator size could be reduced without any cooling performance penalty by replacing the mechanical pump with the electric pump. The predicted results indicate that the cooling system with the electric pump can dramatically reduce the pump power consumption during the FTP 74 driving schedule and that the radiator can be downsized by more than 27% of the original size, under the grade load condition. [DOI: 10.1115/1.2227035]

Introduction

The need for higher fuel economy and performance has stimulated the introduction of advanced mechatronics technology to automobile systems, and a significant portion of vehicle components has been replaced with actively controllable electronic components. However, the basic design of automotive cooling systems with passively controlled components has remained essentially unchanged over a very long period of time [1]. For instance, a mechanical coolant pump is driven by the engine and the pump speed is in proportion to the engine speed. Accordingly, the coolant flow rate is determined by the engine speed, which is not an optimal control in most cases. Hence, a conventional engine-driven coolant pump could cause unnecessary parasitic losses. For this reason, an actively controllable electric coolant pump has been introduced to allow control of the coolant flow rate regardless of engine speed and enable a subsequent reduction of the parasitic losses.

Another potential benefit of the electric coolant pump is the possibility for radiator downsizing. Cooling systems are usually designed for extremely severe conditions. Since the mechanical coolant pump speed and coolant flow rate are governed only by the engine speed, the design points of the cooling components in conventional cooling systems are based on low coolant flow ranges at high loads and hot ambient temperatures. Therefore, a cooling system designed to prevent system failure at occasional extreme conditions is inevitably overdesigned for the majority of normal, mild driving conditions. However, the pump speed and the coolant flow rate in a cooling system with an electric coolant pump can be controlled, depending on the coolant temperature, regardless of the engine speed, which indicates flexibility in selecting the operating point.

Research results on advanced cooling systems have been published over the last several years, with a primary focus on control schemes based on simulation studies. Xu et al. [2,3] developed, simulated, and tested a control scheme for various cooling components of a heavy duty diesel engine cooling system. In their work, a computer controlled fan clutch, variable speed coolant pump, and a modified thermostat were introduced to the control scheme. Melzer et al. [4] proposed the potential of a demand-responsive cooling system and specified the requirements and they built a conceptual advanced cooling system to demonstrate the fuel economy benefit of the system experimentally. Hnatczuk et al. [5] introduced servo-motor driven coolant pumps in order to improve thermal efficiency, reduce engine parasitic losses, and control the engine temperature or emissions. Cortona et al. [6] developed a thermal behavior model of a cooling circuit and a control method for an electric pump and valve. A servo motor driven valve and pump were installed into the cooling system to regulate the coolant flow with an engine control unit by Wagner et al. [7,8]. In their work, the coolant flow rig tests were performed to study these dual actuators. They used an electric heater, not a real engine, to simulate the heat rejection from the engine.

Previous investigations were aimed at the development of a cooling system model and control scheme for electric pumps and valves. However, they were conducted to validate model with rig tests or research engine tests for the simulated simple engine condition, and not necessarily focused on demonstrating the improvement of fuel economy for vehicle driving schedules. Moreover, the radiator downsizing, which can be another benefit of the electric pump, has rarely been studied in previous researches.

Thus, the objective of this work is to conduct simulation studies in order to evaluate the impact of a controllable electric pump on the cooling performance and pump operation for the vehicle driving schedule. The possibility of radiator downsizing with an electric pump is also investigated. At first, the conventional cooling system model for a V6 diesel engine vehicle was configured using a commercial code, GT-Cool, and then it was validated with experimental data. The cooling system model was modified to implement the electric pump into this system. Next, the reduction of the electric pump power consumption was investigated. Finally, a simulation under the grade load condition was conducted to evaluate the possibility of radiator downsizing with a controllable electric pump.

Contributed by the Internal Combustion Engine Division of ASME for publication in the JOURNAL OF ENGINEERING FOR GAS TURBINES AND POWER. Manuscript received March 31, 2005; final manuscript received January 9, 2006. Review conducted by J. Cowart.

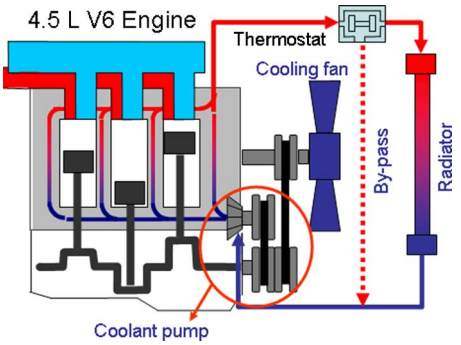

Fig. 1 Schematic diagram of V6, 4.5 l diesel engine with its cooling system

Table 1 Specifications of a V6, 4.5 l diesel engine

Engine type	Diesel, 4-cycle
Configuration	V6
Bore and stroke	95 mm×105 mm
Compression ratio	18.5: 1
Aspiration	Turbocharger, intercooler
Combustion System	Direct Injection
Max. power	200 hp@2750 rpm
Max. torque	440 lb-ft@1850 rpm

Modeling. A V6, 4.5 l diesel engine with its cooling system was used to configure the cooling system model shown in Fig. 1. Table 1 shows the specifications of the engine.

The cooling system model was built with the commercial code, GT-Cool from Gamma Technologies. GT-Cool is based on one-dimensional fluid dynamics, representing the flow and heat transfer in the pipe and the other components of a cooling system, and it is a module-based code that provides flexible model configuration capability.

The complete V6 diesel engine cooling system model is presented in Fig. 2. Various modules in the GT-Cool library were configured in order to simulate the cooling components. The components and modeling approaches for the V6 diesel engine and each cooling component are as follows:

Engine. The engine was modeled with a look-up table type module. The engine heat rejection rate and BSFC data as a function of engine speed and load (BMEP) were provided by a user input file. In this work, the engine performance maps were obtained from the engine dynamometer test. In order to simulate the driving schedule, engine operating points, including engine speed and load, were specified as a function of time by another user input file.

Engine Block. The lumped thermal mass method was used to calculate the heat transfer to the environment. In this model, the engine block was assumed to have a uniform wall temperature that was calculated from the balance of heat rejection by the engine, heat transfer to the coolant, and heat transfer to the ambient air.

Coolant Pump. Pump performance maps were used in order to calculate the pump power consumption. The map data of mechanical and electric pumps were provided by International Truck and Engine Co. and Engineered Machined Products, Inc. (EMP), respectively. Pump performance maps consist of pressure rise, flow rate, pump speeds, and efficiencies. Based on these map data, the pump power consumption was calculated using the following equation:

$$P = \eta \cdot Q \cdot \Delta P \tag{1}$$

where P=pump power consumption (kW), η=pump efficiency, Q=volumetric flow rate (m^3/s), ΔP=pressure rise across the pump (kPa)

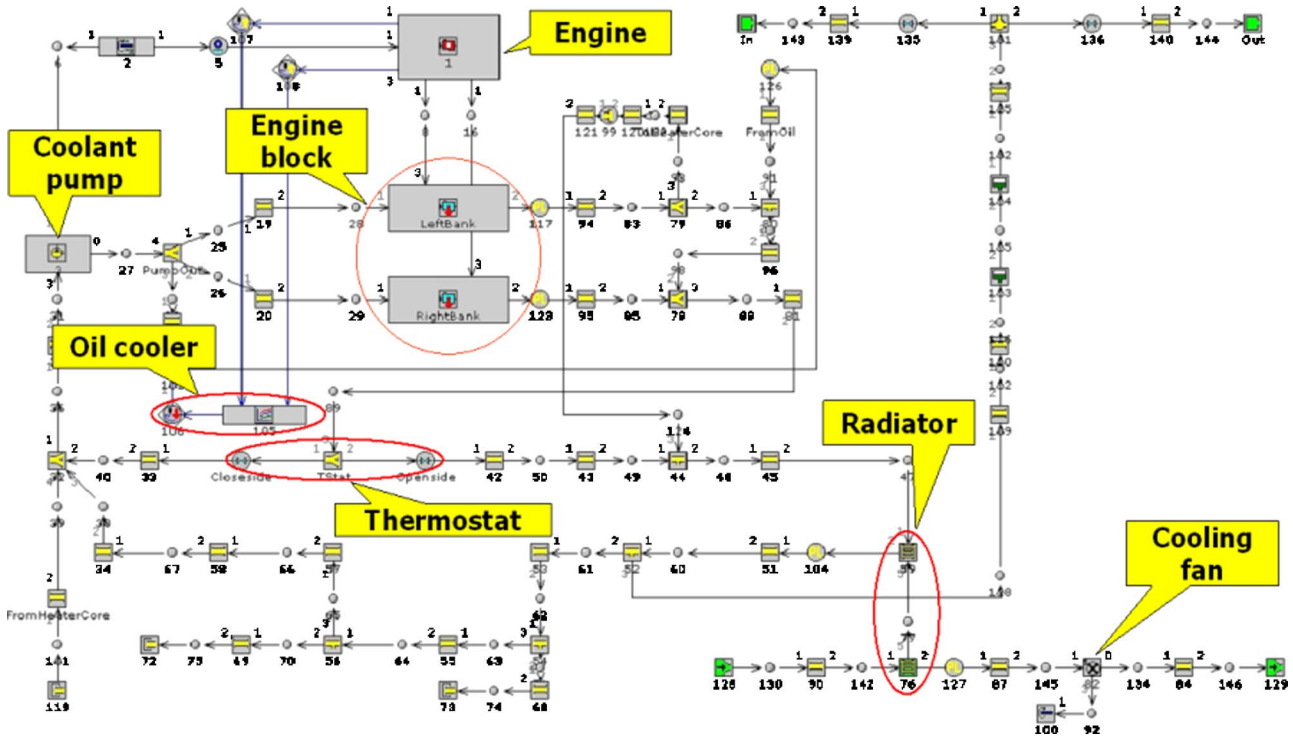

Fig. 2 Complete conventional cooling system model

Table 2 Coefficient of Nusselt correlation

Water side	a	1.1714
	b	0.2289
Air side	a	0.0277
	b	0.9711

Oil Cooler. The heat addition model was used to simulate an oil cooler, which means that the heat from the oil is added directly to the coolant. The heat addition rate from the oil cooler to the coolant depends on engine speed and load. The heat addition rate at the full load condition was measured at each engine speed, and the heat addition rate at the part load condition was calculated by interpolating the full load data.

Radiator. Two modules, as shown in Fig. 2, were used to model the heat exchange between two fluid circuits, i.e., coolant and air. The heat transfer coefficients were calculated from the separate Nusselt number's,

$$\mathrm{Nu} = a\,\mathrm{Re}^{b}\,\mathrm{Pr}^{1/3} \tag{2}$$

where

$$\mathrm{Nu} = \left(\frac{hL}{k}\right)$$

$$\mathrm{Re} = \left(\frac{\rho UL}{\mu}\right)$$

$$\mathrm{Pr} = \left(\frac{\mu C_P}{k}\right)$$

The constants a and b were extracted from steady-state experimental performance data and the values are listed in Table 2. The specifications of the radiator are summarized in Table 3.

Model Validation

Experimental data of the V6, 4.5 l diesel engine with a conventional mechanical pump provided by Ford Motor Co. was used to validate the cooling system model. The heat rejection rate from the engine block to the coolant was measured, which was used as the input data for the engine model. The steady state experiments were conducted in order to specify the heat transfer coefficient of the radiator. The coolant temperature was measured at three points, before and after the thermostat and radiator exit.

The experimental condition for validation was the FTP 74 vehicle driving cycle, which is shown in Fig. 3. The cooling fan was operated at a constant speed of 3000 rpm. Figure 4 shows the comparison of predicted and measured coolant temperatures during the FTP 74 driving cycle. As shown in this figure, the predicted coolant temperature is very well matched with experimental data. This result indicates that this cooling system model is capable of simulating coolant temperature behavior during a transient engine condition and evaluating the cooling system performance.

Figure 5 shows the predicted coolant mass flow rate to the pump and radiator. As can be seen in this graph, the coolant flow to the pump inlet is much higher than to the radiator. Under normal driving conditions at moderate ambient temperatures, which are represented by the FTP 74 driving cycle, most of the coolant recirculates inside the engine and the coolant flow to the radiator is limited by the thermostat to prevent overcooling, until the engine coolant temperature becomes higher than the thermostat opening temperature. This is because the cooling system is usually designed to prevent overheating at extremely severe conditions. This phenomenon indicates that a majority of the power consumed by the pump is wasted on recirculating the coolant instead of cooling the engine. Hence, a new cooling device, such as a controllable electric pump, has a significant potential to save the excess power consumption of the coolant pump.

Table 3 Specifications of the radiator

Height of radiator (mm)	434
Width of radiator (mm)	810
No. of radiator tube rows	56
Radiator tube depth (mm)	25.91
Radiator fin thickness (mm)	0.1016
Radiator fin height (mm)	9.15

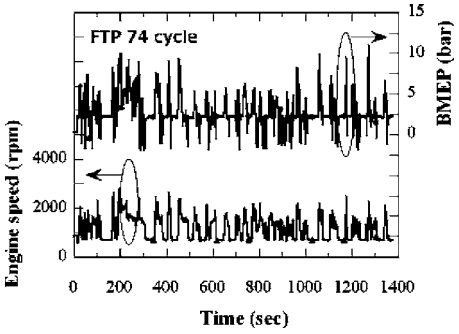

Fig. 3 Engine transient duty cycle corresponding to the Federal Urban Vehicle Schedule

Electric Coolant Pump

The application of the electric coolant pump enables the reduction of power consumption by optimizing coolant flow control. In addition, an electric coolant pump has a higher efficiency than a mechanical pump. One of the reasons for this is that a mechanical

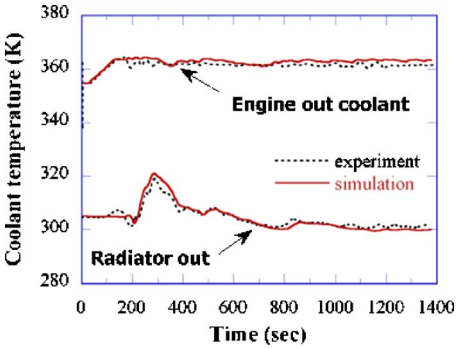

Fig. 4 Comparison of temperature predictions and measurements during the FTP 74 driving cycle

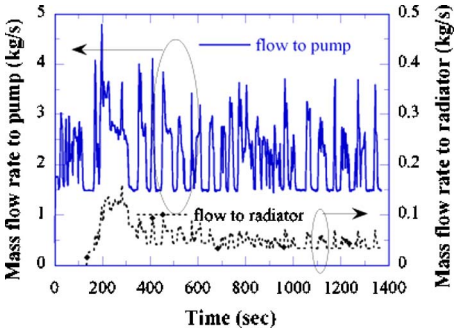

Fig. 5 Predicted coolant mass flow rates during the FTP 74 driving cycle

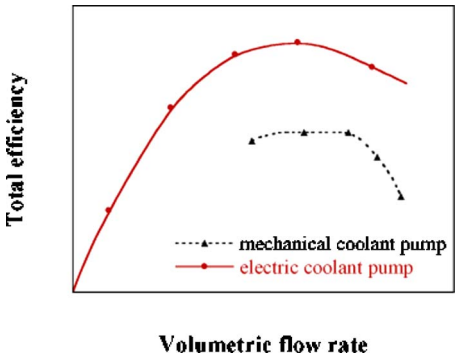

Fig. 6 Comparison of mechanical and electric coolant pump efficiencies

pump receives driving power through belts or gears. Its configuration with a drive shaft and auxiliary elements reduces hydraulic efficiency. However, an electric pump is directly driven by an electric servo-motor, which can eliminate external elements, such as the belt pulley, and offer more flexibility in the pump configuration design in order to enhance the hydraulic efficiency [9].

The electric pump characteristics data were used to investigate the effect of an electric pump on power saving. Figure 6 shows the comparison of the total efficiency between mechanical and electric pumps plotted using the same scale. The overall efficiency of the electric pump is much higher than that of the mechanical pump over the complete flow range. The cooling system model was modified to simulate an electric pump.

Figure 7 shows the FTP 74 driving cycle simulation result using an EMP electric coolant pump. The minimum pump speed was set at 200 rpm to facilitate a more stable speed control and avoid potential, local hot spots. The engine-out coolant temperature from the experimental data was used as a target temperature for PID control in order to compare the pump power consumption between two cases under the same condition. The simulation result shows good agreement with the target signal. Up to 200 s, the coolant temperature gradually increased, which is the warm-up period, and then it converged to about 365 K.

The coolant mass flow rates to the electric coolant pump and the radiator during the FTP 74 driving cycle are presented in Fig. 8. The coolant mass flow toward the mechanical pump was changed in proportion to the engine speed regardless of the coolant temperature, as shown in Fig. 5, which is the reason for the unnecessary parasitic losses. In cases of the electric pump, the coolant mass flow was maintained at the initial rate as determined by the initial pump speed during the warm-up period, and then the coolant mass flow gradually increased to match the target signal. However, the coolant mass flow by the electric pump increased to

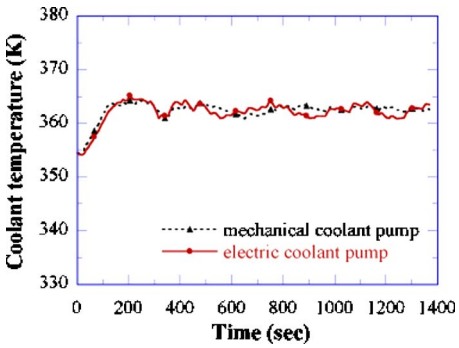

Fig. 7 Comparison of coolant temperature at the exit of engine block between mechanical and electric pumps during the FTP 74 driving cycle

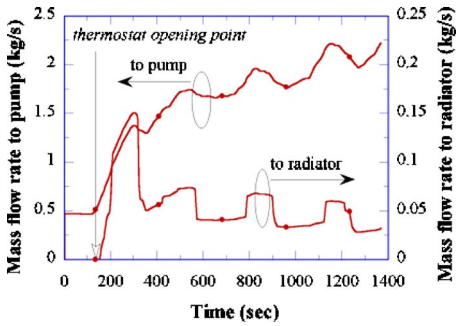

Fig. 8 Predicted coolant mass flow rates with the electric coolant pump during the FTP 74 driving cycle

match the target signal in spite of the convergence of the engine-out coolant temperature as shown in Fig. 7. This was caused by conventional thermostat characteristics. The FTP 74 driving cycle consists of various part load conditions, which are mild for the cooling system. Hence, the conventional thermostat lift is varied within the small range. Because of the small thermostat lift, most of the coolant flow cannot go through the radiator but recirculates inside the engine, as can be seen in Fig. 8, and the radiator is not effectively used to cool down the engine. For this reason, the PID controller increases the pump speed, and consequently, the coolant mass flow is increased to cool down the engine. As a result, even though the coolant flow was controlled to match the target signal by the PID controller with the electric pump, most of the coolant still recirculated inside the engine, which indicates a significantly untapped possibility for power saving.

After the thermostat is opened, the coolant flow is divided into two directions, which are the recirculating flow and the flow to the radiator. In other words, the coolant flow to pump is the sum of the recirculating flow and the coolant flow to the radiator. Hence, if the radiator is effectively used to cool down the engine by modifying the thermostat hysteresis, the recirculating coolant flow could be reduced and additional power saving can be achieved. The effect of the thermostat hysteresis on the coolant flow rate to the pump was investigated during the FTP 74 driving cycle. The opening/closing temperatures of the thermostat were modified without any change of the hysteresis curve shape, as can be seen in Fig. 9. In Fig. 10, the coolant mass flow to the pump was predicted with the modified thermostat hysteresis which was reduced by 1, 3, and 5 °C. The coolant mass flow to the pump decreased until the thermostat hysteresis was moved down by 5 °C, and in that case the initial coolant flow was maintained unchanged during the FTP 74 driving cycle. Therefore, the thermostat hysteresis has to be modified in order to reduce the electric pump effort.

Figure 11 shows the effect of the thermostat hysteresis on the engine wall temperature with the electric pump operating. Even

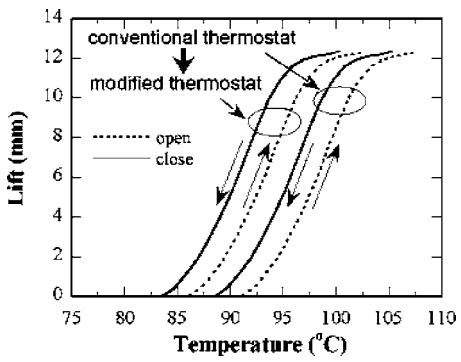

Fig. 9 Modification of thermostat hysteresis

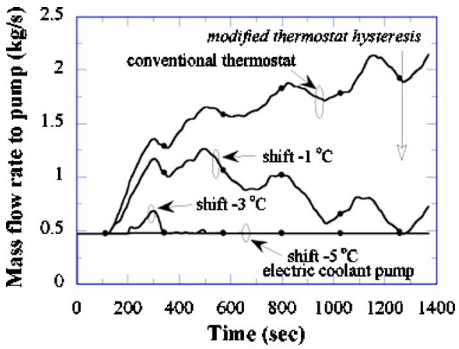

Fig. 10 Predicted coolant mass flow rates toward the electric coolant pump inlet with the modified thermostat hysteresis

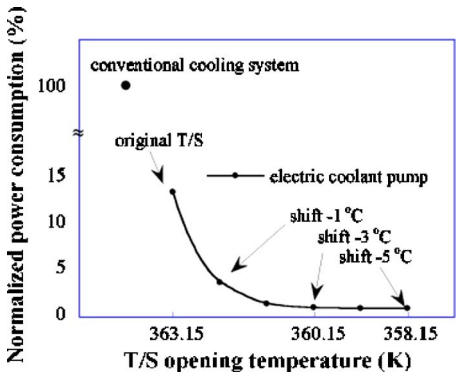

Fig. 12 Comparison of coolant pump power consumption during the FTP 74 driving cycle

though the thermostat was opened at a lower temperature than the original thermostat, the engine block wall temperature rarely fell because the heat transfer to the coolant was lower with the smaller coolant mass flow. This result indicates that the initial coolant flow rate is enough to cool down the engine with the modified thermostat.

Figure 12 shows the pump power consumption during the FTP 74 driving cycle. Compared with the mechanical pump, more than 86% of the power was saved by using the electric pump with the original thermostat, due to the higher efficiency of the electric pump, and more than 99% of the power was saved using the modified thermostat hysteresis. In order to utilize the electric pump for reducing the power consumption, the minimum pump speed, which was set at 200 rpm, should be carefully determined. Otherwise, an insufficient coolant flow rate due to a low minimum pump speed setting for the electric pump could cause local hot spots on the engine block or head. Therefore, the minimum pump speed or coolant flow rate has to be investigated in order to prevent hot spots in the application of the electric pump.

Radiator Downsizing

Radiator downsizing is another important benefit in the development of a cooling system with an electric pump. As mentioned early, a mechanical pump circulates coolant through the water jacket and radiator while the pump speed and coolant flow rates are determined only by the engine speed. Hence, the design points of radiator size are based on a low coolant flow range at a high load and hot ambient temperature in order to prevent overheating. However, the electric coolant pump is operated independent of the engine speed. For this reason, it is expected that a cooling system with an electric pump gives the possibility for radiator downsizing.

The possibility of radiator downsizing was evaluated using this cooling system model. The conditions for the simulation study of radiator down-sizing are summarized in Table 4. The vehicle condition for the cooling test procedure was selected from a published piece of research [10]. The vehicle was driven under a grade load condition (7% grade at 72 km/h for 30 min) at a high ambient temperature. In order to find the corresponding engine condition, Vehicle and Engine SIMulation (VESIM), which was developed by researchers in the Automotive Research Center at the University of Michigan, was used [11]. The driveline and vehicle dynamic model were configured for a typical pickup truck with a gross vehicle weight of 3150 kg (Class 3 vehicle), and the engine performance map from a dynamometer test was used in VESIM. The corresponding engine speed was 2194 rpm at a 73% load. It was assumed that the radiator inlet air temperature was 65 °C, taking into account high ambient temperature and air-conditioner operation. The radiator inlet velocity was estimated with a correlation developed from experimental results, which determined the effect of a vehicle speed on the radiator inlet velocity [12]. The coolant flow rate was determined by the pump speed in proportion to engine speed in a conventional cooling system. However, the electric pump was operated at its maximum speed. It was assumed that a downsized radiator has the same performance as the original radiator, which means that it has the same heat rejection rate per area as the original. The initial coolant temperature was set at 90 °C to simulate a grade load test after a fully warmed up vehicle condition

The size of the radiator should be designed such that the vehicle can avoid overheating under the extreme conditions described above. In order to determine if the radiator size can be reduced with the electric pump, the maximum cooling capacity of the cooling system with a mechanical pump was evaluated first. Then, the cooling capacity of the system with the electric pump was

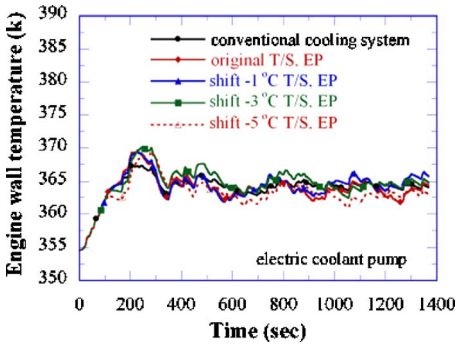

Fig. 11 The effect of thermostat hysteresis on the engine wall temperature

Table 4 Condition for simulation study of radiator downsizing

Vehicle condition	72 km/h, going up 7% grade Driving time: 30 min Ref. 10 Corresponding engine condition: 2194 rpm, 73% load
Radiator inlet temperature	65 °C
Radiator inlet air velocity	Function of vehicle speed: based on experimental data Ref. 12
Initial coolant temperature	90 °C
Pump speed	Electric pump: max. speed Mechanical pump: in proportion to engine speed
Radiator performance	Same heat rejection rate per area, only scaled down

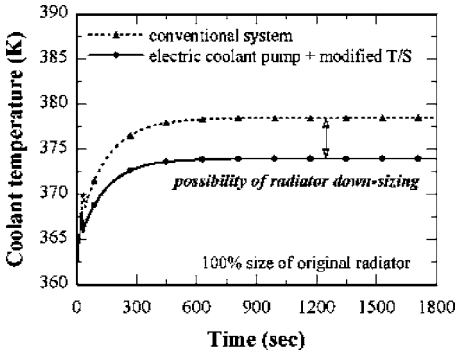

Fig. 13 Investigation of cooling capacity of each cooling system with original size radiator

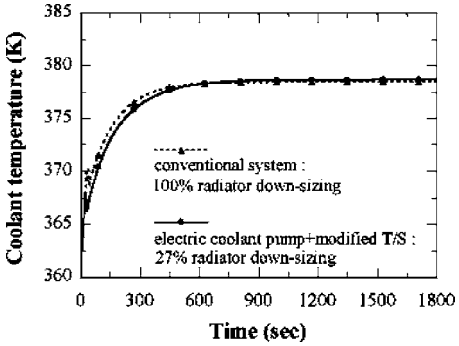

Fig. 14 Evaluation of the possibility of radiator downsizing

investigated. The performance difference between the two systems indicated the potential for down-sizing, as discussed in detail in the remainder of this section.

The cooling capacity of each cooling system was investigated under a grade load condition. Figure 13 shows the coolant temperature trace with the original size radiator. The coolant temperature reached up to 378 K in the case of the conventional cooling system. However, the maximum coolant temperature attained with the electric pump system was lower than the conventional pump case. This result shows that a cooling system with an electric pump could operate with a down-sized radiator and still satisfy the cooling performance comparable to a conventional system.

Consequently, the radiator size was scaled-down until the maximum coolant temperature matched the conventional case, which is shown in Fig. 14. This led to the reduction of the radiator size by 27% with the electric pump. It is possible to make an engine compartment more compact and reduce the weight by downsizing the radiator and consequently, enable an additional fuel economy improvement.

Conclusion

A cooling system model for a typical class 3 pickup truck with a medium duty diesel engine was configured with a commercial code, GT-Cool. The simulation results were compared with experimental data in order to validate the cooling system model, and then the reduction of the pump power consumption was investigated under realistic driving conditions. Finally, a simulation under a grade load condition was conducted to evaluate the possibility of radiator down-sizing with an electric pump. The main conclusions of this research are summarized as follows:

(1) Compared to a mechanical coolant pump, power consumption can be reduced by more than 87% during the FTP 74 driving cycle with an electric pump. The benefit is the result of both the ability to control the pump speed and the increased efficiency of the electric pump.
(2) Thermostat hysteresis has to be modified in order to take full advantage of the electric pump operation.
(3) The cooling system with the electric pump enables the reduction of a radiator size by more than 27% of the original size. The benefit stems from the ability to increase the pump speed to its maximum value, independent of the engine speed.

Acknowledgment

This work was financially supported by the U.S. Army TACOM through a Dual Use Science and Technology Program on Simulation Based Design and Demonstration of Next Generation Advanced Diesel Technology. Additional funding was provided by the Post-doctorial Fellowship Program of the Korea Science and Engineering Foundation (KOSEF). The authors also gratefully acknowledge Ford Motor Company for providing the experimental data, as well as International Truck and Engine Corporation and Engineered Machined Products, Inc. for providing technical information about their products.

References

[1] Visnic, B., 2001, "Thermostat, Thy Days are Numbered," Wards AutoWorld, **37**(6), pp. 53–54.
[2] Xu, Z., Johnson, J. H., and Chiang, E. C., 1984, "A Simulation Study of a Computer Controlled Cooling System for a Diesel Powered Truck," SAE Paper No. 841711.
[3] Xu, Z., Johnson, J. H., and Chiang, E. C., 1984, "The Design and Testing of a Computer Controlled Cooling System for a Diesel Powered Truck," SAE Paper No. 841712.
[4] Melzer, F., Hesse, U., Rocklage, G., and Schmitt, M., 1999, "Thermomanagment," SAE Paper No. 1999-01-0238.
[5] Hnatczuk, W., Lasecki, M. P., Bishop, J., and Goodell, J., 2000, "Parasitic Loss Reduction for 21st Century Trucks," SAE Paper No. 2000-01-3423.
[6] Cortona, E., and Onder, C. H., 2000, "Engine Thermal Management With Electric Cooling pump," SAE Paper No. 2000-01-0965.
[7] Wagner, J. R., Paradis, L., Marotta, E. E., and Dawson, D., 2002, "Enhanced Automotive Engine Cooling systems—A Mechatronics Approach," Int. J. Veh. Des., **28**(1/2/3), pp. 214–240.
[8] Wagner, J. R., Srinivasan, V., Dawson, D. M., and Marotta, E. E., 2003, "Smart Thermostat and Coolant Pump Control for Engine Thermal Management Systems," SAE Paper No. 2003-01-0272.
[9] Allen, D. J., and Lasecki, M. P., 2001, "Thermal Management Evolution and Controlled Coolant Flow," SAE Paper No. 2001-01-1732.
[10] Winnard, D., Venkateswaran, G., and Barry, R. E., 1995, "Underhood Thermal Management by Controlling Air Flow," SAE Paper No. 951013.
[11] Assanis, D. N., Bryzik, W., Chalhoub, N., Filipi, Z., Henein, N., Jung, D., Liu, X., Louca, L., Moskwa, J., Munns, S., Overholt, J., Papalambros, P., Riley, S., Rubin, Z., Sendar, P., Stein, J., and Zhang, G., 1999, "Integration and Use of Diesel Engine, Drive-line and Vehicle Dynamics Models for Heavy Duty Truck Simulation," SAE Paper No. 1999-01-0970.
[12] Ngy Srun, A. P., 1999, "A Simple Engine Cooling System Simulation Model," SAE Paper No. 1999-01-0237.

Modeling Diesel Spray Flame Liftoff, Sooting Tendency, and NO_x Emissions Using Detailed Chemistry With Phenomenological Soot Model

Song-Charng Kong[1]
e-mail: kong@iastate.edu

Yong Sun

Rolf D. Rietz[2]

Engine Research Center,
University of Wisconsin,
1500 Engineering Drive,
Madison, WI 53706

A detailed chemistry-based CFD model was developed to simulate the diesel spray combustion and emission process. A reaction mechanism of n-heptane is coupled with a reduced NO_x mechanism to simulate diesel fuel oxidation and NO_x formation. The soot emission process is simulated by a phenomenological soot model that uses a competing formation and oxidation rate formulation. The model is applied to predict the diesel spray lift-off length and its sooting tendency under high temperature and pressure conditions with good agreement with experiments of Sandia. Various nozzle diameters and chamber conditions were investigated. The model successfully predicts that the sooting tendency is reduced as the nozzle diameter is reduced and/or the initial chamber gas temperature is decreased, as observed by the experiments. The model is also applied to simulate diesel engine combustion under premixed charge compression ignition (PCCI) conditions. Trends of heat release rate, NO_x, and soot emissions with respect to EGR levels and start-of-injection timings are also well predicted. Both experiments and models reveal that soot emissions peak when the start of injection (SOI) occurs close to TDC. The model indicates that low soot emission at early SOI is due to better oxidation while low soot emission at late SOI is due to less formation. Since NO_x emissions decrease monotonically with injection retardation, a late injection scheme can be utilized for simultaneous soot and NO_x reduction for the engine conditions investigated in this study. [DOI: 10.1115/1.2181596]

1 Introduction

A better understanding of the diesel spray combustion process is crucial to help design low emission diesel engines. This is important because diesel engine manufacturers are facing stringent emission regulations. Motivated by the need to better understand the soot and NO_x formation processes in diesel sprays, researchers have made direct optical measurements in both engines [1–5] and high-temperature, high-pressure combustion chambers [6–8]. These investigations have provided new insights into diesel spray combustion and emission formation processes and have also helped numerical model development [9–12].

Experimental data have been used to construct a conceptual diesel spray combustion image that depicts the flame structure and soot and NO_x distributions [1]. It has been shown that the details of the flame structure are crucial to the soot formation process during the mixing-controlled combustion phase [7,8]. The lifted flame consists of a diffusion flame at the periphery of the fuel jet (where NO_x is formed) and a rich reaction zone located downstream of the lift-off length in the central region of the fuel jet (where soot is formed). The lift-off length determines the time for fuel-air mixing prior to ignition and entering the reacting zone, and thus will affect the sooting tendency of diesel fuel jet.

As a complement to optical soot and NO diagnostics, predictive numerical models can also help understand the diesel spray combustion process and provide insights to the details of flame structure. Development and applications of engine CFD models have become increasingly important and effective in analyzing the complex diesel combustion process [9–12]. The use of detailed chemistry is also essential to better predict fuel oxidation and emission formation, especially for the low-temperature HCCI combustion process which is of much interest [11,12].

This study develops a numerical model that uses detailed chemical kinetics to simulate the diesel lift-off flame and its combustion and emission formation. The model is validated using experimental combustion and emission data from a combustion vessel and from a heavy-duty diesel engine under various operating conditions.

2 Model Formulation

2.1 Engine CFD Code. The CFD code is a version of KIVA-3V [13] with improvements in various physical and chemistry models developed at the Engine Research Center, University of Wisconsin—Madison. The major model improvements include the spray atomization, drop-wall impingement, wall heat transfer, piston-ring crevice flow, and soot formation and oxidation models [14,15]. The RNG k-ϵ turbulence model was used for in-cylinder flow simulations using the standard values for turbulence parameters as those derived originally [16].

Since detailed reaction mechanisms for *n*-heptane were used to simulate diesel fuel chemistry, the CHEMKIN chemistry solver [17] was integrated into KIVA-3V for solving the chemistry during multi-dimensional engine simulations. The chemistry and flow solutions were then coupled. Details of the model can be found in the original literature in which various PCCI engines have been

[1]Currently at the Department of Mechanical Engineering, Iowa State University, Ames, IA 50011.

[2]To whom correspondence should be addressed.

Contributed by the Internal Combustion Engine Division of ASME for publication in the JOURNAL OF ENGINEERING FOR GAS TURBINES AND POWER. Manuscript received May 16, 2005; final manuscript received December 15, 2005. Review conducted by M. Wooldridge.

simulated, including premixed and direct-injection conditions [11,12]. It should be noted that the chemistry and flow turbulence are already coupled using the present model via diffusion transport, and a subgrid scale turbulence-chemistry interaction model is not used in this study. The turbulence affects the combustion by property transport, wall heat flux, etc.

2.2 Fuel Oxidation Chemistry. A skeletal reaction mechanism for *n*-heptane [18] was used to simulate diesel fuel chemistry due to their similar ignition characteristics and cetane number. This mechanism is obtained from a larger mechanism [19] using an interactive reduction scheme that utilizes SENKIN, XSENKPLOT, and genetic algorithm optimization. The resulting mechanism retains the main features of the detailed mechanism and includes reactions of polycyclic aromatic hydrocarbons. The mechanism was validated using constant-volume ignition delay data in a shock tube and also from engine combustion experiments.

In the present study, the physical properties of the fuel use those of tetradecane (C14H30), based on which the spray atomization model was developed [15]. However, due to the availability of the reaction mechanism and the similar cetane number (56 for *n*-heptane), the reaction chemistry of *n*-heptane is used to simulate that of diesel fuel.

2.3 Reduced NO Reaction Mechanism. A new NO mechanism was obtained by reducing the Gas Research Institute (GRI) NO mechanism [20], which contains an additional 22 species and 101 reactions pertaining to the formation of nitric oxides, in addition to the fuel oxidation mechanism. The GRI NO mechanism was first integrated with the fuel oxidation mechanism to be used in the SENKIN simulations. Both constant volume ignition delay and zero-dimensional HCCI engine combustion simulations were performed using SENKIN. The SENKIN solution files were then analyzed by XSENKPLOT to help construct the reduced NO mechanism. The choices of the resulting species and reactions are based on their flux values, which are an indication of the relative importance in the reaction pathway. The resulting NO mechanism contains only four additional species (N, NO, NO_2, N_2O) and nine reactions that describe the formation of nitric oxides as listed below. All the rate constants remain the same as in the original GRI NO mechanism [20]. Note that the sum of NO and NO_2 in this study is compared with the engine-out NO_x emissions measurements in this study.

The original GRI NO mechanism includes both thermal and prompt NO. As a result of mechanism reduction, it was found that the prompt mechanism reaction (such as $CH+N_2$) is not significant under the present conditions studied partly due to the lack of fuel-bound nitrogen.

$$N + NO \Leftrightarrow N_2 + O \tag{1}$$

$$N + O_2 \Leftrightarrow NO + O \tag{2}$$

$$N_2O + O \Leftrightarrow 2NO \tag{3}$$

$$N_2O + OH \Leftrightarrow N_2 + HO_2 \tag{4}$$

$$N_2O + m \Leftrightarrow N_2 + O + m \tag{5}$$

$$HO_2 + NO \Leftrightarrow NO_2 + OH \tag{6}$$

$$NO + O + m \Leftrightarrow NO_2 + m \tag{7}$$

$$NO_2 + O \Leftrightarrow NO + O_2 \tag{8}$$

$$NO_2 + H \Leftrightarrow NO + OH \tag{9}$$

2.4 Phenomenological Soot Model. Soot emissions are predicted using a phenomenological soot model [14] that was incorporated into the KIVA/CHEMKIN code. Two competing processes are considered in this model, namely soot formation and oxidation. The rate of change of soot mass $\dot{M}_s$ within a computational cell is determined from the soot formation rate $\dot{M}_{sf}$ and soot oxidation rate $\dot{M}_{so}$.

$$\frac{dM_s}{dt} = \frac{dM_{sf}}{dt} - \frac{dM_{so}}{dt} \tag{10}$$

The formation rate uses an Arrhenius expression and the oxidation rate is based on a carbon oxidation model, described as

$$\frac{dM_{sf}}{dt} = A_{sf} M_{C_2H_2} P^n \exp\left(-\frac{E_{sf}}{RT}\right) \tag{11}$$

$$\frac{dM_{so}}{dt} = \frac{6Mw_c}{\rho_s D_s} M_s R_{\text{Total}}. \tag{12}$$

The original formation rate calculation used a characteristic-time combustion model in which only seven major combustion species were considered [14], and fuel was used as the soot inception species in Eq. (11). However, when a detailed reaction mechanism is used for combustion simulation, fuel is depleted quickly to form intermediate hydrocarbon species once reactions start. Thus, it is no longer useful to use fuel as the inception species for soot formation. Therefore, based on the previous literature and available species in the reaction mechanism used in this study, it was decided to use acetylene (C_2H_2) as the inception species for soot formation, i.e., $M_{C_2H_2}$ in Eq. (11). This is because acetylene is the most relevant species pertaining to soot formation in hydrocarbon fuels. The preexponential constant Asf was adjusted accordingly for the present implementation and also to account for the fuel effects. On the other hand, the soot oxidation rate is determined by the Nagle-Strickland-Constable model that considers carbon oxidation by two reaction pathways whose rates depend on surface chemistry of two different reactive sites, as in the original model [14].

In the present model, Esf=12,500 cal/mol, Asf=150, soot density ρ_s=2 g/cm^3, and Ds=2.5E-6 cm. In the calculation, acetylene is consumed to form soot particles, which, in turn, will be converted to CO, CO_2, and HC as a result of oxidation.

3 Experiments

3.1 Sandia Combustion Chamber. Experiments conducted in an optically accessible, constant-volume combustion chamber under simulated quiescent diesel engine conditions were used for model validations [7,8]. The vessel has a cubical combustion chamber, 108 mm on a side. The fuel injector is centrally mounted in one side of the chamber. Optical access is provided by sapphire windows that permit line-of-sight and orthogonal optical access to the injected fuel jet.

The high-temperature and high-pressure environments are created by burning a specified premixed mixture before the start of fuel injection. Optical diagnostics of diesel spray combustion are performed under ambient conditions similar to those in typical diesel engines at the time of injection. A wide range of pressure, temperature, and density conditions were considered in the Sandia experiments and some of the cases were used to validate the present KIVA/CHEMKIN/soot model.

The flame lift-off experiments are valuable for model validations because they were under well-controlled environments and well characterized. Low-temperature combustion characteristics of the flame lift-off experiments can be related to those in diesel engines. The fuel injectors and ambient conditions that result in low emissions can be utilized to help achieve low emissions in diesel engines [7,8].

3.2 Caterpillar Diesel Engine. Engine experiments performed on a Caterpillar heavy-duty diesel engine were also used for model validations [21]. The engine is a single-cylinder engine

Table 1 Caterpillar 3410E engine specifications [21]

Bore × Stroke	137.2 mm × 165.1 mm
Compression ratio	16.1:1
Displacement	2.44 L
Connecting rod length	261.6 mm
Squish height	1.57 mm
Combustion chamber geometry	In-piston Mexican hat with sharp-edged crater
Piston	Articulated
Charge mixture motion	Quiescent
Maximum injection pressure	190 MPa
Number of nozzle holes	6
Nozzle hole diameter	0.214 mm
Included spray angle	145 deg
Injection rate shape	Rising
Experimental conditions for model validation	
Case group	SOI (ATDC)
A (8% EGR)	−20, −15, −10, −5, 0, +5
B (27% EGR)	−20, −15, −10,−5, 0, +5
C (40% EGR)	−20, −15, −10, −5, 0, +5

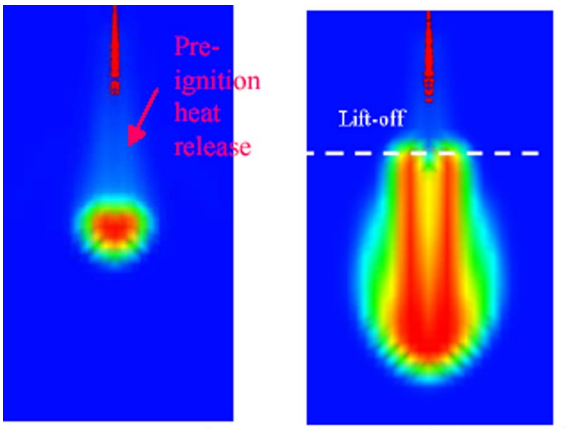

Fig. 1 Sample images of the predicted fuel spray and gas temperature distributions for d_{nozz}=100 μm, T_{amb}=900 K, P_{amb}=138 MPa, ρ_{amb}=14.8 kg/m^3. Color scale: 900 to 2600 K.

whose specifications are listed in Table 1. The gaseous emissions recorded in the experiments include NO_x, intake CO_2, exhaust CO_2, carbon monoxide, and hydrocarbons. The particulate was measured using a full dilution tunnel and an AVL DPL 439 particulate analyzer. The EGR level was varied by changing the exhaust back pressure. The intake and exhaust pressures were controlled by two Omega PID controllers, and the intake air flow rates were measured using critical flow orifices.

Experimental data obtained using a high-pressure injector [21] were simulated by the model. The engine operating conditions were optimized to achieve low NO_x and particulate emissions and fuel consumption. The parameters that were varied included start-of-injection timing and EGR. The fuel injector was a production style Caterpillar electronic unit injector (EUI). The experimental results indicated that low emissions could be achieved by optimizing the operating conditions to allow an optimal time interval between the end of fuel injection and the start of combustion. This is to allow a longer time for better mixing to produce a more homogeneous mixture. The experimental conditions used for model validation are also listed in Table 1 and include three EGR levels.

4 Results

4.1 Sandia Combustion Chamber. Experimental results of the Sandia combustion chamber [7,8] were used to validate the present models. The baseline experimental conditions for model validations are listed in Table 2.

The computations used a 0.5 deg sector mesh with 2 mm grid size in both radial and axial directions. The computational domain was 12.6 cm in diameter and 10 cm in height such that the total volume is the same as that of the combustion chamber in the experiment. Uniform chamber temperature, pressure, and species concentration based on experimental data were assumed initially without considering combustion radicals.

Table 2 Experimental conditions for model validations

Fuel	#2 Diesel
Injection system	Common-rail
Injection profile	Top-hat
Injector orifice diameter	50, 100, 180 μm
Orifice pressure drop	138 MPa
Discharge coefficient	0.80, 0.80, 0.77
Fuel temperature	436 K
Ambient temperature	850–1300 K
Ambient density	7.3, 14.8, 30.0 kg/m^3
O_2 concentration	21%

A typical image of predicted fuel spray and gas temperature distributions of a free diesel lift-off flame is shown in Fig. 1. The injector is located at the top of the image. It can be seen that the liquid fuel undergoes atomization, vaporization, and mixing with entrained air before the lift-off location and then enters the reaction zones. Put into the context of a transient injection process, chemical reactions take place once the fuel is injected and mixed with air, and lead to autoignition at a certain location as seen in Fig. 1(*a*). Note that in Fig. 1(*a*), the light colors seen between the spray tip and the ignition location indicate a continuous temperature rise as a result of preignition chemical reactions. The ignition location is approximately where the steady-state flame is stabilized in most cases, i.e., the lift-off location. The lift-off length is thus determined by both fluid mechanics and chemical kinetics that take place during the fuel/air mixing process prior to the lift-off location.

It is believed that chemical reactions prior to the lift-off location play an important role such that the flame is stabilized due to successive ignition events of the incoming fuel-air mixture. For example, it has been demonstrated that after the flame is established, if the chemical reactions before the lift-off location are suddenly deactivated, the flame is blown downstream and extinguished. It is noted that the high gas velocity of the injected diesel fuel jet would require an unreasonably high turbulent flame speed to balance the incoming reactive mixture in order to stabilize a free standing diesel flame. Nonetheless, more research is needed to study the physics of diesel flame lift-off under engine conditions.

4.1.1 Spatial Soot Distributions. Planar laser-induced incandescence (PLII) images of soot along a thin plane of the fuel jet were compared with model predictions, as shown in Fig. 2. The injector orifice is located at the far left center of each image, with fuel being injected to the right. The flame lift-off length was determined from the OH chemiluminescence images in the experiments [7,8]. It is defined as the axial distance between the orifice and the location where the OH chemiluminescence intensity is approximately 50% of that just downstream of the initial rapid rise in the OH chemiluminescence. The cross-sectional average equivalence ratio at the flame lift-off length was estimated and is given on the left of the PLII images.

The present simulated soot mass fraction distributions are given in Fig. 2(*b*) to compare with the PLII images. The predicted lift-off length was determined from the contour of OH species using a

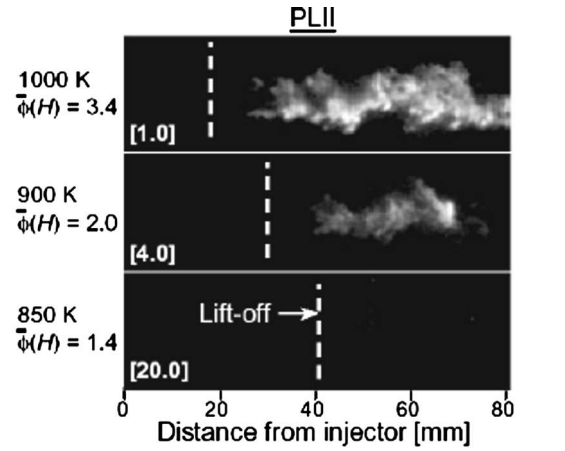

(a) Experimental lift-off length and PLII images

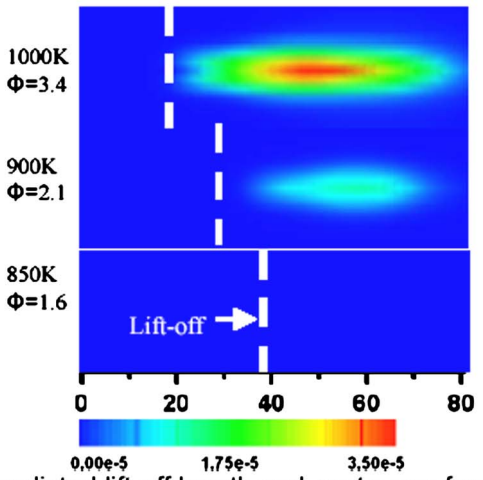

(b) Predicted lift-off length and soot mass fraction

Fig. 2 Comparisons between PLII images and predicted soot mass fractions at the central plane of the fuel jet at 3.2 ms ASI. The equivalence ratios were estimated at the lift-off length. Relative PLII camera gain is given in brackets. d_{nozz}=100 μm, P_{inj}=138 MPa, ρ_{amb}=14.8 kg/m^3.

similar method as in the experiments. The predicted equivalence ratio at the lift-off length is also given on the left of the images. The color scale of the predicted soot mass fraction is also shown in Fig. 2.

It can be seen that the predicted soot distributions agree extremely well with the experiments. Both experiments and simulations show that as the ambient gas temperature decreases, lift-off length increases, soot concentration decreases, and the equivalence ratio at the lift-off length also decreases. The conditions with ambient temperatures 1000 and 900 K are found to be sooting cases while no soot production is observed for the 850 K case, as revealed by both the experiments and simulations. In the simulations, the two sooting cases are found to have a soot mass fraction of the order of 1.0E−5 while the predicted maximum soot mass fraction is only about 1.0E−8 for the 850 K case. Other comparisons between model results and experimental images suggest that a soot mass fraction of 1.0E−5 can be used as the criterion to specify sooting and nonsooting conditions in the simulations. This criterion is used later in this paper to determine the sooting limit of injectors with different orifice diameters.

The temporal evolution of a typical injection and combustion event is illustrated in Fig. 3. Time after start of injection (ASI) for each image is given on the left. The distance from the injector is shown at the bottom. The dashed vertical line shows the lift-off

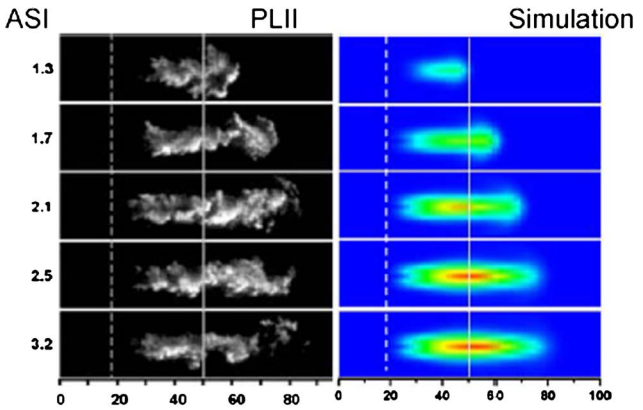

Fig. 3 Time sequence (ASI in ms) of PLII images and predicted soot mass fraction contours. The lift-off length and x=50 mm positions are shown on the images with vertical dashed and solid lines, respectively. d_{nozz}=100 μm, P_{inj}=138 MPa, T_{amb}=1000 K, ρ_{amb}=14.8 kg/m^3.

length (18.3 mm) and the solid line shows the x=50 mm position, which was found in the experiments to have the peak soot emissions at 3.2 ms ASI.

It can be seen from the figure that the evolution of the soot emissions predicted by the model agrees well with the experimental results, especially after 2.0 ms. It was found that the model predicts a slightly longer ignition delay which can explain the lower soot formation at the early stages, e.g., at 1.3 ms ASI. Numerical results indicate that soot does not appear upstream of the lift-off length, which is consistent with the conclusion drawn from the experiments [8].

4.1.2 Axial Soot Distributions. The axial distributions of soot along the centerline of the fuel jet were also compared. Figure 4 shows comparisons of measured time-averaged *KL* factors and predicted soot mass fraction at 3.2 ms ASI. The *KL* factor is an indication of optical thickness derived from laser-extinction soot measurements [8]. The *KL* factor is proportional to the mass of soot along the line of sight of the extinction measurement, so it can be compared with the predicted soot mass that is integrated

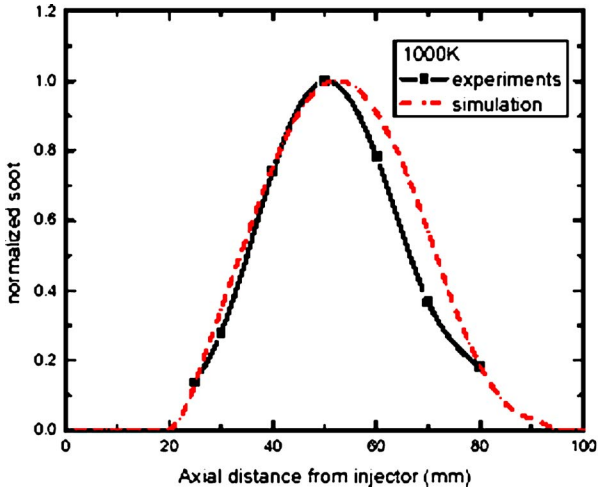

Fig. 4 Comparisons of measured time-averaged *KL* factors and predicted soot mass along the central axis of the fuel jet for the same conditions as in Fig. 3. Both measured and predicted data were normalized to allow qualitative comparison. Results were acquired at 3.2 ms ASI for d_{nozz}=100 μm, T_{amb}=1000 K, P_{inj}=138 MPa, ρ_{amb}=14.8 kg/m^3.

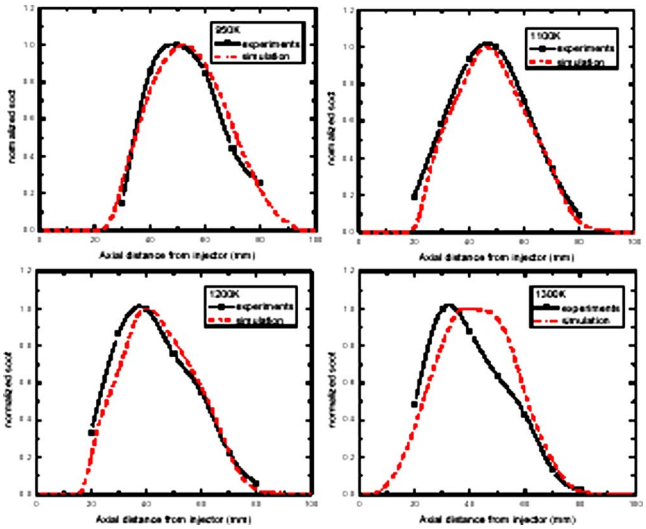

Fig. 5 Comparisons of measured time-averaged *KL* factors and predicted soot mass for various ambient temperatures 950, 1100, 1200, and 1300 K. Both measured and predicted data were normalized to allow qualitative comparison. Results were acquired at 3.2 ms ASI for d_{nozz}=100 μm, P_{inj}=138 MPa, ρ_{amb} =14.8 kg/m^3.

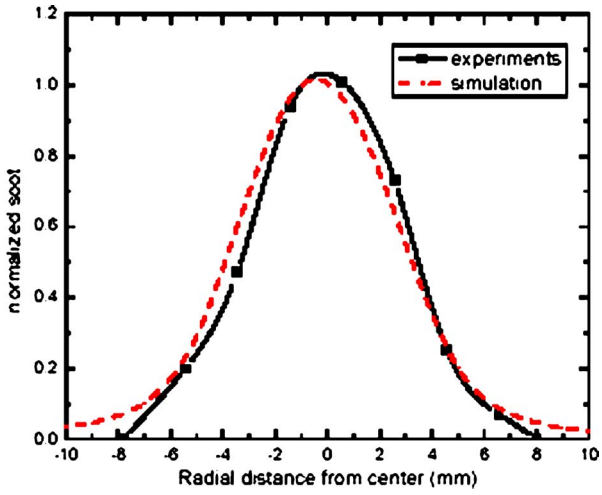

Fig. 6 Comparisons of measured time-averaged *KL* factors and predicted soot mass as a function of radial distance from the jet centerline at an axial distance of 50 mm from the orifice (vertical solid line in Fig. 3). Both measured and predicted data were normalized to allow qualitative comparison. Results were acquired at 3.2 ms ASI for the same conditions as in Fig. 3.

along the same line.

Optical thickness data were acquired at multiple axial locations along the centerline of the fuel jet at a certain time after start of injection. Due to the different nature of the *KL* factor from measurements and the integrated soot mass from the simulations, only qualitative comparisons can be made to assess the model performance. Thus, both measured *KL* factors and predicted soot mass are normalized to allow qualitative comparisons, as shown in Fig. 4.

Comparisons of the normalized curves show good agreement in the general trend of the soot distribution along the jet central axis. Although the positions of the peak value of soot emissions differ slightly between the simulation and experiments (50 mm in experiments and ~55 mm in simulation), the agreement in the shape of the curves indicates that the transient features of soot formation and oxidation processes are captured by the present model.

Comparisons between the measured *KL* factors and predicted soot mass along the central axis at 3.2 ms ASI were also presented in Fig. 5 for other ambient gas temperature conditions of 950, 1100, 1200, and 1300 K. It can be seen that the predicted axial soot distributions agree with measurements very well. It can be seen that as the ambient temperature increases, the peak of the soot curve moves upstream toward the fuel jet. The early soot formation is consistent with the observation that lift-off length decreases at high ambient temperatures as in Fig. 2.

4.1.3 Radial Soot Distribution. The measured radial soot distribution 50 mm downstream of the injector (location indicated by the vertical solid lines in Fig. 3) was also compared with simulations in Fig. 6. Optical thickness data were acquired at multiple radial locations 50 mm from the injector at 3.2 ms ASI for the same conditions as in Fig. 3. Note that a 3-D cubic mesh with 2 mm grid size was used for the calculation such that it would be easier to integrate the soot mass in the radial direction. As before, both measured *KL* factors and predicted soot mass were normalized to allow qualitative comparisons. Figure 6 also indicates that the simulation results match the experiments very well even for such a small length scale (note that the length scale is 20 mm in the radial direction while it is 100 mm for the axial direction).

4.1.4 Sooting Tendency of Diesel Spray. The ultimate goal of the numerical model is to predict the sooting tendency of a diesel injector under different operating conditions. Figure 7 shows comparisons of the measured and predicted sooting tendency of diesel injectors with different orifice diameters in an ambient density-temperature domain. To the left of each curve are the nonsooting regimes and to the right are sooting regimes. In the experiments, the sooting limit is determined by the visibility of soot in the PLII images. In the simulations, the maximum soot mass fraction of 1.0E−5 is used as the criterion, as discussed earlier.

To determine the sooting limit in the simulation, cases of different temperatures with a 25 K interval were simulated at a fixed ambient density. For example, nonsooting and sooting cases are marked with open and closed symbols, respectively, as shown in Fig. 7. The average temperature between adjacent nonsooting and sooting cases is regarded as the sooting limit for a specific injector at the corresponding ambient density condition.

As can be seen in Fig. 7, although there are discrepancies between the exact locations of the measured and predicted sooting curves, especially for the small orifice (50 μm) injector, the trends are well predicted. As ambient density and temperature increase,

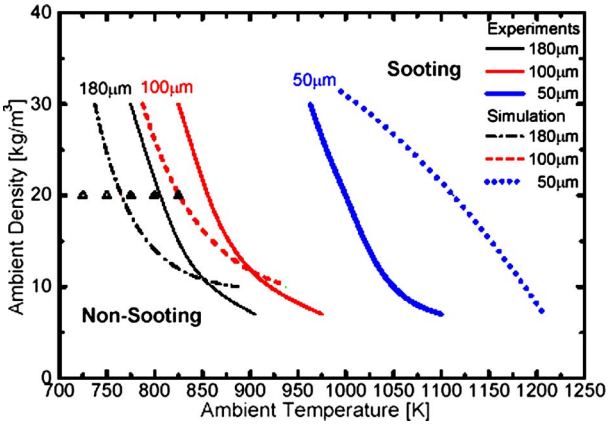

Fig. 7 Measured (solid lines) and predicted (dashed) sooting and nonsooting regimes as a function of ambient gas temperature and density for P_{inj}=138 MPa. For the conditions of each curve, nonsooting combustion occurs to the left and sooting combustion to the right of each curve.

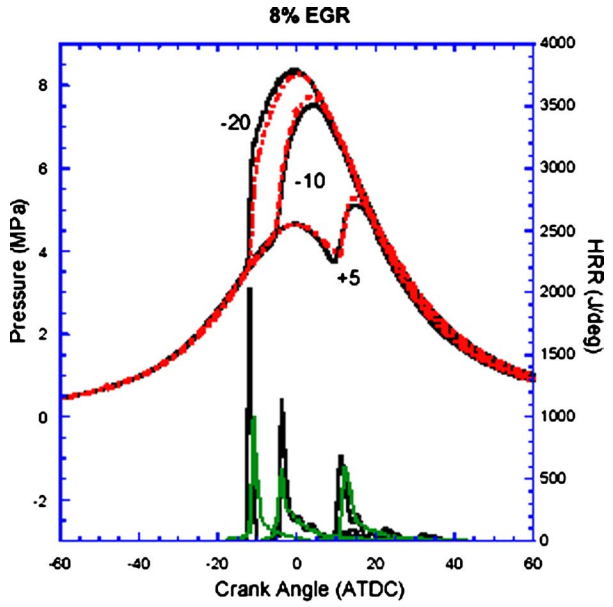

Fig. 8 Comparisons of measured (solid line) and predicted (dotted) cylinder pressure and heat release rate data for 8% EGR cases (SOI=−20, −10, and +5ATDC)

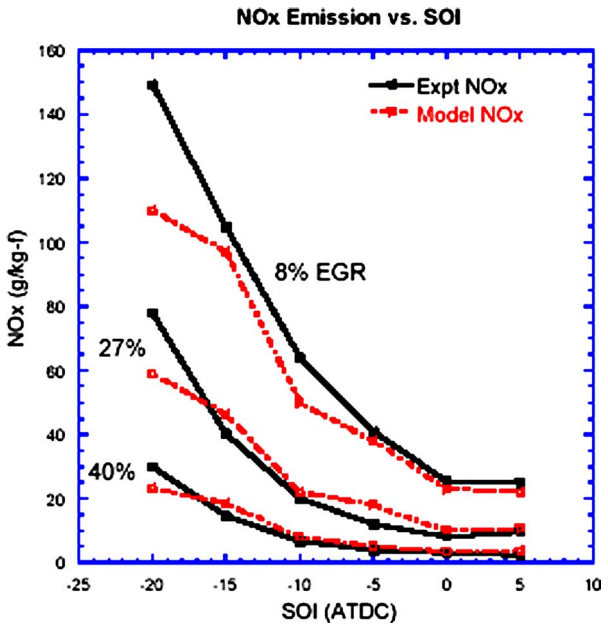

Fig. 10 Measured and predicted engine-out NO_x emissions for cases listed in Table 1

or as orifice diameter increases, the sooting tendency increases. The discrepancy between measurements and predictions for the small orifice is probably due to the significant difference in the spray atomization and mixing processes between orifices with a conventional size and a small size which may not be well captured by the present spray model.

4.2 Caterpillar Diesel Engine. The present models were further applied to simulate combustion and emission processes in a heavy-duty diesel engine. Figures 8 and 9 show the measured and computed cylinder pressure and heat release rate data for selected cases. The model is seen to perform well over a wide range of engine conditions. The heat release rate data do not exhibit the distinct premixed and diffusion burn characteristics of conventional diesel engines. The highly premixed burned features of the present PCCI experiments are captured well by the model.

The predicted soot and NO_x (i.e., sum of NO and NO_2) emissions were also compared with the measurements, as shown in Figs. 10 and 11. It can be seen that the overall trends of soot and NO_x are captured with respect to the start-of-injection timing. Discrepancies in soot emissions at early injection timings may be due to the details of the spray/wall interactions. It is of interest to note that engine-out soot emissions reach a peak value when fuel is injected near top-dead-center. The present model also predicts correctly the soot reduction seen at further retarded injection timing (e.g., SOI=+5ATDC) for all different EGR levels.

The numerical model can explain the soot emission reduction

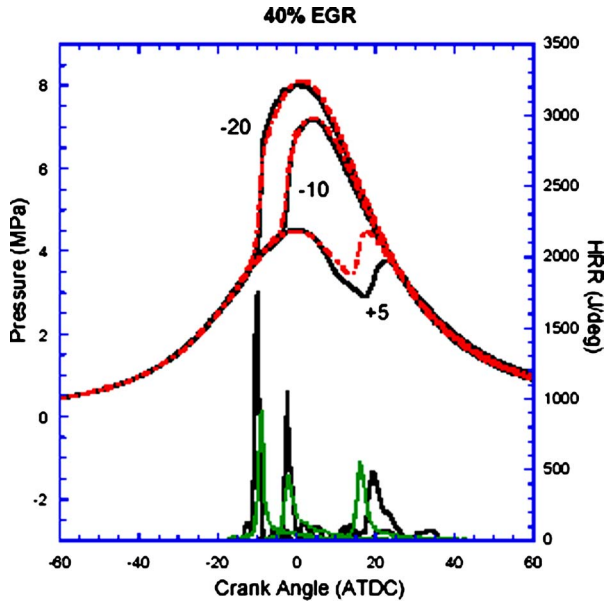

Fig. 9 Comparisons of measured (solid line) and predicted (dotted) cylinder pressure and heat release rate data for 40% EGR cases (SOI=−20, −10, and +5ATDC)

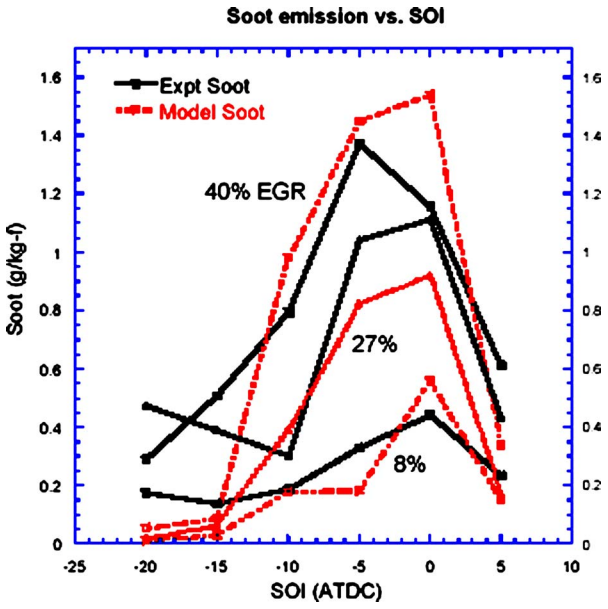

Fig. 11 Measured and predicted engine-out soot emissions for cases listed in Table 1

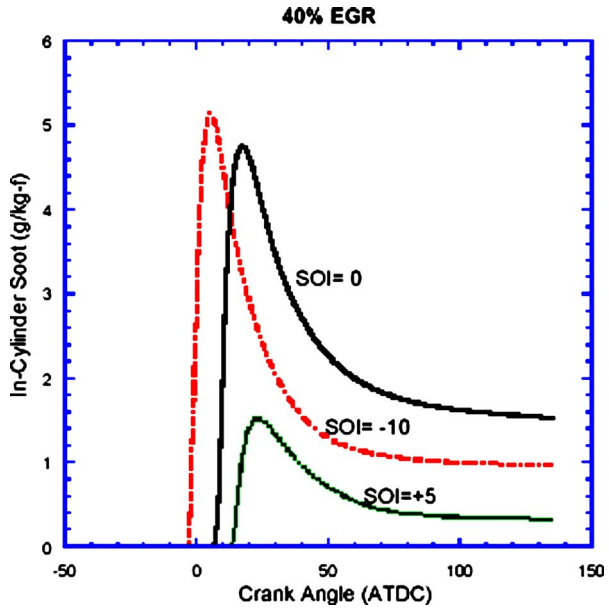

Fig. 12 In-cylinder soot mass histories for 40% EGR cases at three different injection timings. Values at exhaust valve opening (130 ATDC) are shown in Fig. 11.

seen as the injection is further retarded past TDC. This reduction is not seen in the conventional diesel combustion soot-NO_x tradeoff with respect to injection timing. Figure 12 shows the total in-cylinder soot mass evolutions for three different injection timings, i.e., SOI=−10, 0, +5ATDC. The model results indicate that the lower exhaust soot emissions for SOI=−10ATDC are due to a better oxidation process as compared to that of SOI=0ATDC. On the other hand, a lower soot emission for SOI=5ATDC is because less soot is formed in the cylinder as a result of the low-temperature combustion (as also can be seen from the low cylinder pressure in Figs. 8 and 9 for SOI=5ATDC). The above low-temperature combustion characteristics are consistent with results in HSDI diesel engines [22] as well, and can be further facilitated to achieve low-emission diesel PCCI operation.

5 Conclusions

A numerical model has been developed to simulate diesel fuel jet combustion in a combustion vessel and in a heavy-duty diesel engine. The model uses a skeletal reaction mechanism to describe the fuel oxidation and NO_x formation processes and a phenomenological model to simulate soot formation and oxidation.

The model successfully predicts the lift-off length of a free diesel diffusion flame under various ambient conditions. The model results indicate that chemical reactions prior to the lift-off location are important for the stabilization of the lift-off flame. The simulations also agree with the measurements in predicting the sooting tendency of diesel fuel jets increases as the ambient gas density, temperature, or orifice diameter increases.

Experiments conducted in a heavy-duty diesel engine under PCCI-like conditions were also modeled. The predicted heat release rate data, NO_x, and soot emissions agreed well with the measurements. The model results indicate that low soot emissions can be obtained at late injection timings (i.e., SOI past TDC) by suppressing the total soot formation as a result of low-temperature combustion. Since NO_x emissions decrease monotonically as injection is retarded, such a late injection scheme can be utilized for simultaneous soot and NO_x reduction for future low-emission diesel PCCI engines.

Acknowledgment

The authors acknowledge the financial support by the DOE/Sandia National Labs and Caterpillar, Inc. Experimental data provided by Dr. L. Pickett and Dr. D. Siebers (Sandia) and Adam Klingbeil and Jim von der Ehe (University of Wisconsin—Madison) for the model validation are greatly appreciated.

References

[1] Dec, J. E., 1997, "A Conceptual Model of DI Diesel Combustion Based on Laser Sheet Imaging," SAE Paper No. 970873.
[2] Dec, J. E., and Canaan, R. E., 1998, "PLIF Imaging of NO Formation in a DI Diesel Engine," SAE Paper No. 980147.
[3] Zhao, H., and Ladommatos, N., 1998, "Optical Diagnostics for Soot and Temperature Measurement in Diesel Engines," Prog. Energy Combust. Sci., **24**, pp. 221–255.
[4] Dec, J. E., and Tree, D. R., 2001, "Diffusion Flame/Wall Interactions in a Heavy-Duty Diesel Engine," SAE Paper No. 2001-01-1295.
[5] Musculus, M. P., Dec, J. E., and Tree, D. R., 2002, "Effects of Fuel Parameters and Diffusion Flame Lift-Off on Soot Formation in a Heavy-Duty DI Diesel Engine," SAE Paper No. 2002-01-0889.
[6] Bruneaux, G., Verhoeven, D., and Baritaud, T., 1999, "High-Pressure Diesel Spray and Combustion Visualization in a Transparent Model Diesel Engine," SAE Paper No. 1999-01-3648.
[7] Pickett, L. M., and Siebers, D. L., 2004, "Non-Sooting, Low Flame Temperature Mixing-Controlled DI Diesel Combustion," SAE Paper No. 2004-01-1399.
[8] Pickett, L. M., and Siebers, D. L., 2004, "Soot in Diesel Fuel Jets: Effects of Ambient Temperature, Ambient Density, and Injection Pressure," Combust. Flame, **138**, pp. 114–135.
[9] Hergart, C., Barths, H., and Peters, N., 1999, "Modeling the Combustion in a Small-Bore Diesel Engine Using a Method Based on Representative Interactive Flamelets," SAE Paper No. 1999-01-3550.
[10] Tao, F., Golovitchev, V. I., and Chomiak, J., 2004, "A Phenomenological Model for the Prediction of Soot Formation in Diesel Spray Combustion," Combust. Flame, **136**, pp. 270–282.
[11] Kong, S. C., and Reitz, R. D., 2002, "Application of Detailed Chemistry and CFD for Predicting Direct Injection HCCI Engine Combustion and Emissions," Proc. Combust. Inst., **29**, pp. 663–669.
[12] Kong, S. C., Patel, A., Yin, Q., and Reitz, R. D., 2003, "Numerical Modeling of Diesel Engine Combustion and Emissions Under HCCI-Like Conditions With High EGR Levels," SAE Paper No. 2003-01-1087.
[13] Amsden, A. A., 1997, "KIVA-3V: A Block-Structured KIVA Program for Engines with Vertical or Canted Valves," LA-13313-MS.
[14] Han, Z., Uludogan, A., Hampson, G. J., and Reitz, R. D., 1996, "Mechanism of Soot and NO_x Emission Reduction Using Multiple-Injection in a Diesel Engine," SAE Paper No. 960633.
[15] Patterson, M. A., and Reitz, R. D., 1998, "Modeling the Effects of Fuel Spray Characteristics on Diesel Engine Combustion and Emissions," SAE Paper No. 980131.
[16] Han, Z., and Reitz, R. D., 1995, "Turbulence Modeling of Internal Combustion Engines Using RNG k-ϵ Models," Combust. Sci. Technol., **106**, pp. 267–295.
[17] Kee, R. J., Rupley, F. M., and Miller, J. A., 1989, "CHEMKIN-II: A FORTRAN Chemical Kinetics Package for the Analyses of Gas Phase Chemical Kinetics," Sandia Report, SAND 89-8009.
[18] Patel, A., Kong, S.-C., and Reitz, R. D., 2004, "Development and Validation of a Reduced Reaction Mechanism for HCCI Engine Simulations," SAE Paper No. 2004-01-0558.
[19] Golovitchev, V. I., 2000, http://www.tfd.chalmers.se/~valeri/MECH.html, Chalmers Univ of Tech, Goteborg, Sweden.
[20] Smith, G. P., Golden, D. M., Frenklach, M., Moriarty, N. W., Eiteneer, B., Goldenberg, M., Bowman, C. T., Hanson, R. K., Song, S., Gardiner, W. C., Lissianski, V. V., and Qin, Z., 2000, http://www.me.berkeley.edu/gri-mech/.
[21] Klingbeil, A. E., 2002, "Particulate and NO_x Reduction in a Heavy-Duty Diesel Engine Using High Levels of Exhaust Gas Recirculation and Very Early and Very Late Injection," M.S. thesis, University of Wisconsin—Madison.
[22] Miles, P. C., Choi, D., Pickett, L. M., Singh, I. P., Henein, N., RempelEwert, B. A., Yun, H., and Reitz, R. D., 2004, "Rate-Limiting Processes in Late-Injection, Low-Temperature Diesel Combustion Regimes," *Proc. THIESEL 2004 Conference*, pp. 429–447.

Comparisons of Diesel PCCI Combustion Simulations Using a Representative Interactive Flamelet Model and Direct Integration of CFD With Detailed Chemistry

Song-Charng Kong[1]
e-mail: kong@iastate.edu

Hoojoong Kim

Rolf D. Reitz[2]

Engine Research Center,
University of Wisconsin,
1500 Engineering Drive,
Madison, WI 53706

Yongmo Kim
Department of Mechanical Engineering,
Hanyang University,
Seoul, Korea

Diesel engine simulation results using two different combustion models are presented in this study, namely the representative interactive flamelet (RIF) model and the direct integration of computational fluid dynamics and CHEMKIN. Both models have been implemented into an improved version of the KIVA code. The KIVA/RIF model uses a single flamelet approach and also considers the effects of vaporization on turbulence-chemistry interactions. The KIVA/CHEMKIN model uses a direct integration approach that solves for the chemical reactions in each computational cell. The above two models are applied to simulate combustion and emissions in diesel engines with comparable results. Detailed comparisons of predicted heat release data and in-cylinder flows also indicate that both models predict very similar combustion characteristics. This is likely due to the fact that after ignition, combustion rates are mixing controlled rather than chemistry controlled under the diesel conditions studied. [DOI: 10.1115/1.2181597]

Introduction

The use of multidimensional computer models for engine combustion analysis has become popular due to the increasing accuracy of the physical and chemistry submodels that describe the engine in-cylinder processes. Modeling diesel engine combustion is especially challenging due to the complex interactions between the engine flow, fuel spray, chemical reaction, and emission formation processes. The development of a predictive combustion model has been the objective of researchers so that the model can be used as a design tool.

A single-step approach was first used to simulate the diesel combustion energy release by assuming that the species conversion rate is controlled by a characteristic turbulent mixing time [1]. To better simulate the different phases of diesel combustion, an improved model was developed that used the Shell hydrocarbon "knock" model for the low temperature autoignition, a characteristic-time model for the high temperature combustion, and phenomenological soot and NO_x models for emission formation [2]. A pacs distribution function (PDF)-time-scale model was further introduced to account for the chemistry-controlled premixed burn and mixing-controlled diffusion combustion [3]. The above models only consider the major combustion species that are sufficient to accurately predict the equilibrium thermodynamic temperature.

The time-scale concept has been extended to formulate a progress variable approach that uses representative progress variables to describe the different combustion phases and to account for more complex chemistry [4]. Various alternative approaches have also been proposed for diesel combustion modeling, such as the intrinsic low dimensional manifold (ILDM) method [5] and the coherent flamelet model [6].

Due to the need to introduce more complex chemistry while accounting for the effects of turbulence, the representative interactive flamelet (RIF) model was introduced for diesel combustion modeling [7]. The flamelet concept views a turbulent flame as an ensemble of flamelet structures representing the instantaneous flame surface that is corrugated by the turbulent flow field [8]. The model can account for turbulence-chemistry interactions and allows consideration of detailed chemistry. Hence, autoignition, combustion, and pollutant formation do not need to be modeled separately, but are included as part of the comprehensive chemical mechanism. The flamelet model concept has been further improved to account the spatial inhomogeneity of the scalar dissipation rate [9], and implemented with more features for various applications [10–12]. Effects of vaporization on turbulence-chemistry interaction have also been incorporated [13].

An alternative method to introduce complex chemistry for engine combustion modeling is to integrate the chemistry solver into the computational fluid dynamics (CFD) code directly. For example, the CHEMKIN code has been incorporated into the KIVA engine code for diesel combustion simulations [14–16]. This approach is particularly suited for diesel premixed charge compression ignition (PCCI) modeling due to the short combustion duration and the need to predict ignition accurately. The model simulates the overall ignition, combustion, and emission processes by using a comprehensive reaction mechanism. To enhance the computational efficiency, a data retrieval methodology has also been developed to reduce the computer time in obtaining chemistry solutions [17].

Despite the fact that both the RIF model and the direct integration method both use complex chemistry for the combustion simulation, the bases of the two methods differ significantly. The direct integration method solves for the chemistry in every computational cell while the RIF model solves for the chemistry in a

[1]Currently at the Department of Mechanical Engineering, Iowa State University, Ames, IA 50011.

[2]To whom correspondence should be addressed.

Contributed by the Internal Combustion Division of ASME for publication in the JOURNAL OF ENGINEERING FOR GAS TURBINES AND POWER. Manuscript received May 16, 2005; final manuscript received January 24, 2006. Review conducted by M. Wooldridge.

generalized mixture fraction space, and then the solutions are used to calculate the reacting scalars (e.g., mean species density and temperature) onto every grid point through an assumed PDF. Both methods have demonstrated success in diesel combustion simulations, but they are usually based on different CFD codes under different engine conditions. It is thus of great interest to compare the results of both models when they are implemented into the same CFD code and applied to the identical engine conditions, as will be presented in this study.

Model Formulation

Engine CFD Code. The CFD code is a version of the KIVA-3V code [18] with improvements in various physical and chemistry models developed at the Engine Research Center, University of Wisconsin-Madison. The major model improvements include the spray atomization, drop-wall impingement, wall heat transfer and piston-ring crevice flow models [19,20]. The RNG k-ε turbulence model was used for the in-cylinder flow simulations.

Chemical Reaction Mechanisms. A skeletal reaction mechanism for n-heptane (30 species and 65 reactions) [16] was used to simulate diesel fuel chemistry due to the similarity in cetane number (56 for n-heptane) and ignition characteristics. On the other hand, the physical properties of the diesel fuel were based on those of tetradecane. The skeletal mechanism retains the main features of detailed mechanisms and includes reactions of polycyclic aromatic hydrocarbons. The mechanism was validated using constant-volume ignition delay data and engine combustion experiments using diesel fuel.

NO_x emissions are simulated by a reduced NO mechanism that is derived from the GRI NO mechanism [21]. Consequently, four additional species (N, NO, NO_2, N_2O) and nine reactions are added to the above n-heptane chemistry [22]. On the other hand, soot emissions are modeled differently in the two methods, as will be described in the following.

KIVA/CHEMKIN Model. Since the reaction mechanism for n-heptane were used to simulate the diesel fuel chemistry, the CHEMKIN chemistry solver [23] was integrated into the KIVA-3V code for solving the chemistry during multidimensional engine simulations. The chemistry and flow solutions were then coupled. It should be noted that the convection and diffusion transport between different computational cells are modeled by the RNG k-ε turbulence model and a subgrid scale turbulence-chemistry interaction model is not used in this study.

The interpreter of CHEMKIN is first executed to generate a binary linking file that contains all the reaction and species information as an input to KIVA. An interface program was developed such that CHEMKIN is used as the chemistry subroutine in KIVA. Basically the reaction mechanism is solved for every computational cell at each time step. Species and thermodynamic conditions are passed to the CHEMKIN solver to obtain the full chemistry solutions.

The reactive mixture in each grid cell is treated as a closed system in which the rate of change of each individual species is

$$\frac{dY_k}{dt} = v\dot{\omega}_k W_k \tag{1}$$

where v is the specific volume, Y_k is the mass fraction, $\dot{\omega}_k$ is the production rate, and W_k is the molecular weight of species k. By using the ideal gas mixture assumption, the energy equation can be obtained under constant volume conditions as

$$c_v \frac{dT}{dt} + v\sum_{k=1}^{K} e_k \dot{\omega}_k W_k = 0 \tag{2}$$

where c_v is the mean specific heat of the mixture, T is temperature, and e_k is the internal energy of species k. This formulation is consistent with the KIVA formulation that solves the internal energy equation, and the volume of the computational cell is not updated until the final rezoning phase. During the chemistry solution, the CFD time step is taken as the integration time in the chemistry solver (DVODE) to obtain new mixture conditions.

Despite the fact that both the species production rate and energy equations are solved by the DVODE solver, only the new species concentration is passed to the interface program which, in turn, calculates the change in specific internal energy of each computational cell. The new gas phase temperature obtained from the chemistry solver is not immediately updated in the CFD code. This strategy is also consistent with the KIVA formulation that retains the change in specific internal energy and updates the gas temperature at the end of each computational timestep.

Experience shows that the DVODE utility is relatively stable since it uses a fully implicit scheme and performs internal iterations within the CFD time step. The maximum number of iterations within DVODE can be increased and/or the CFD time step can be decreased if necessary. An alternative semi-implicit chemistry solver has also been developed to enhance the computational efficiency [24].

Soot emissions are predicted by a phenomenological soot model that uses competing formation and oxidation rates. The formation is described by the Hiroyasu soot formation model while the oxidation is predicted by the Nagle-Strickland-Constable oxidation model [19]. In the model, acetylene (C_2H_2) is used as the soot formation species since it is an important precursor species. The soot model is not part of the reaction mechanism and the soot formation/oxidation is calculated following the major combustion and NO chemistry. The present soot model has been validated and can predict the sooting tendency of diesel sprays under constant volume conditions [22].

KIVA/RIF Model. The RIF model was also implemented into the same KIVA code. The flamelet concept is based on the assumption that all reacting scalars are uniquely related to the mixture fraction variable Z that describes the local fuel-to-air ratio for nonpremixed combustion, such as in diesel engines. The local flamelet structure is described by the flamelet equations for species and enthalpy assuming unity Lewis number [7]

$$\frac{\partial Y_k}{\partial t} = \frac{\chi}{2}\left(\frac{\partial^2 Y_k}{\partial Z^2}\right) + \frac{\dot{\omega}_k}{\rho} \tag{3}$$

$$c_p \frac{\partial T}{\partial t} = \frac{\chi}{2}\frac{\partial^2 h}{\partial Z^2} - \sum_{k=1}^{N} h_k\left(\frac{\chi}{2}\frac{\partial^2 Y_k}{\partial Z^2} + \frac{\dot{\omega}_k}{\rho}\right) - \frac{\partial P}{\partial t} \tag{4}$$

where χ is the scalar dissipation rate and Z is the mixture fraction. The CFD code provides the necessary parameters to the flamelet code for solving the flamelet equations, and the species mass fractions obtained from the flamelet code are passed onto the CFD code. The transient effects of the turbulent flow on chemistry are accounted for through appropriate modeling of the scalar dissipation rate. The turbulent mean values of the reactive scalars can be evaluated once the conditional scalar dissipation rate and the PDF of mixture fraction are known.

The instantaneous distribution of scalar dissipation rate within a flamelet is assumed to be

$$\langle \chi | Z \rangle (Z) = \chi_{st} f(Z) = \chi_{st} \frac{Z^2}{Z_{st}^2} \frac{\ln Z}{\ln Z_{st}} \tag{5}$$

where Z_{st} is the stoichiometric mixture fraction. The mean scalar dissipation rate conditioned on stoichiometric mixture fraction becomes

$$\langle \chi_{st} \rangle \equiv \int_0^\infty \chi'_{st} \tilde{P}(\chi'_{st}) d\chi'_{st} = \frac{c_\chi \frac{\tilde{\varepsilon}}{\tilde{k}} \widetilde{Z''^2}}{\int_0^1 f(Z') \tilde{P}(Z') dZ'} \tag{6}$$

Note that k/ε is the turbulent mixing timescale obtained from the k-ε turbulence model. This is the same time scale as that used in the simpler and more intuitive characteristic-time combustion model of Kong et al. [2].

The transient flamelet solutions do not need to be calculated for all computational cells. In the original single flamelet approach [7], the entire domain was represented by one flamelet. Hence, the conditional scalar dissipation rate is defined as a domain averaged value rather than being spatially resolved. The domain average of the scalar dissipation rate conditioned on stoichiometric mixture is [9]

$$\widehat{\langle \chi_{st} \rangle} = \frac{\int_V \langle \chi_{st} \rangle^{3/2} \bar{\rho} \tilde{P}(Z_{st}) dV'}{\int_V \langle \chi_{st} \rangle^{1/2} \bar{\rho} \tilde{P}(Z_{st}) dV'} \tag{7}$$

In this case, there is effectively a single global turbulence timescale that represents an average of k/ε over the entire domain.

Since the local flame structures are represented by a conserved scalar, two additional transport equations for the local mean mixture fraction $\tilde{Z}$ and its variance $\widetilde{Z''^2}$ have to be solved in the CFD code to define the local mean species composition.

Turbulent combustion models originally developed for gaseous flames have been applied to simulate spray combustion processes without considering the effects of vaporization on small-scale turbulent mixing and turbulent combustion. In order to account for the effects of vaporization, the present study adopts the model proposed by Demoulin and Borghi [25]. A transport equation of mixture fraction variance is derived by using a PDF transport equation for mixture fraction. The equations for the mean mixture fraction and its variance coupled with vaporization effects written as

$$\frac{\partial}{\partial t}(\bar{\rho}\tilde{Z}) + \frac{\partial}{\partial x_j}(\bar{\rho}\tilde{u}_j\tilde{Z}) = \frac{\partial}{\partial x_j}\left(\frac{\mu_t}{\sigma_Z}\frac{\partial \tilde{Z}}{\partial x_j}\right) + \bar{\rho}\tilde{\omega}_v \tag{8}$$

$$\frac{\partial}{\partial t}(\bar{\rho}\widetilde{Z''^2}) + \frac{\partial}{\partial x_j}(\bar{\rho}\tilde{u}_j\widetilde{Z''^2}) = \frac{\partial}{\partial x_j}\left(\frac{\mu_t}{\sigma_{Z''^2}}\frac{\partial \widetilde{Z''^2}}{\partial x_j}\right) + \frac{2\mu_t}{\sigma_{Z''^2}}\frac{\partial^2 \tilde{Z}}{\partial x_j^2} - \bar{\rho}\tilde{\chi} + 2(\widetilde{\bar{\rho}Z\omega_v} - \bar{\rho}\tilde{Z}\tilde{\omega}_v) + \bar{\rho}\tilde{Z}^2\tilde{\omega}_v - \widetilde{\bar{\rho}Z^2\omega_v} \tag{9}$$

The last four additional source terms appearing in Eq. (9) account for the effects of vaporization on mixture fraction variance through the vaporization rate ω_v. These new correlations take into account the fluctuation of equivalence ratio due to vaporization but are in an unclosed form. By assuming that the spray vaporization takes places only at liquid surfaces, Demoulin and Borghi [25] proposed a model for these correlations

$$\widetilde{\bar{\rho}Z\omega_v} \approx \widetilde{\bar{\rho}Z_s\omega_v} = \sum_p Z_s^p \frac{\dot{m}_p}{V} \tag{10}$$

$$\widetilde{\bar{\rho}Z^2\omega_v} \approx \widetilde{\bar{\rho}Z_s^2\omega_v} = \sum_p (Z_s^p)^2 \frac{\dot{m}_p}{V} \tag{11}$$

where the subscript s denotes the value at the liquid surface, p is the index for fuel spray particle, and $\dot{m}_p$ is the rate of change of particle mass. These additional source terms mainly contribute to the production of mixture fraction fluctuations. In spray combustion processes, these terms increase the scalar dissipation rate and the ignition delay time, as well as modifying the small-scale mixing rates and the spray structure.

Another important effect due to vaporization is related to the fact that the upper limit of the mixture fraction is not unity in spray combustion processes. Therefore, the upper limit (Z_{ini}) of the mixture has to be determined. By utilizing a conditional PDF of Z_{ini} and a mixture fraction equation, Demoulin and Borghi [25] derived the following balance equation:

$$\frac{\partial}{\partial t}(\bar{\rho}\tilde{Z}\bar{Z}_{ini}) + \frac{\partial}{\partial x_j}(\bar{\rho}\tilde{u}_j\tilde{Z}\bar{Z}_{ini}) = \frac{\partial}{\partial x_j}\left(\frac{\mu_t}{\sigma_Z}\frac{\partial \tilde{Z}\bar{Z}_{ini}}{\partial x_j}\right) + \bar{\rho}\int_0^1 Z_{ini}\tilde{\omega}_{v|Z_{ini}} dZ_{ini} \tag{12}$$

For a given position, therefore, the allowable space for mixture fraction Z has to be automatically adjusted from 0 to $\bar{Z}_{ini}$. In the present study, the β-PDF $\tilde{P}(Z;\vec{x},t)$ is employed and its shape is renormalized from the three constraints:

$$1 = \int_0^{\bar{Z}_{ini}} \tilde{P}(Z) dZ, \quad \tilde{Z} = \int_0^{\bar{Z}_{ini}} Z\tilde{P}(Z) dZ$$

$$\widetilde{Z''^2} = \int_0^{\bar{Z}_{ini}} (Z - \tilde{Z})^2 \tilde{P}(Z) dZ \tag{13}$$

This modified upper limit of mixture fraction also influences the ignition delay and the spray combustion processes. A decrease in the upper limit of mixture fraction increases the probability of combustion in a given mixture fraction. Note that the solutions of the transport equation of mixture fraction only affect the shape of β-PDF at each computational cell. The procedure of renormalization follows the constraints give by Eq. (13) and changes only the β-PDF at each time step at each cell. The mean value of a scalar is not species density but species mass fraction since the mean value is determined by PDF weighing procedure. To achieve mass conservation, the cell density remains constant and the density of each species is determined by multiplication of cell density and updated mass fraction. The multiplication of cell density, enthalpy, and change of mass fraction becomes one of the source terms in energy equation. This procedure is consistent with that used in the KIVA code.

A soot formation model [26] was also implemented into the present KIVA/RIF code. Two additional transport equations for the volume fraction and number density of soot are solved. The Favre-averaged transport equation of soot number density ($\phi_n = n/\rho N_a$) and soot volume fraction ($\phi_v = \rho_{soot} f_v/\rho$) are

$$\frac{\partial \bar{\rho}\tilde{\phi}_i}{\partial t} + \frac{\partial \bar{\rho}\tilde{u}_j\tilde{\phi}_i}{\partial x_j} = \frac{\partial}{\partial x_j}\left(\frac{\mu_e}{\mathrm{Pr}_t}\frac{\partial \tilde{\phi}_i}{\partial x_j}\right) + \overline{S_{\phi_i}} \tag{14}$$

The source term for number density equation is

$$\overline{S_{\phi_n}} = \bar{\alpha} - \overline{\beta\rho^2}(\tilde{\phi}_n)^2 \tag{15}$$

where α and β are nucleation and coagulation rates, respectively. The source term for the soot volume fraction equation is

$$\overline{S_{\phi_v}} = N_a^{1/3}\overline{\gamma\rho}(\tilde{\phi}_n)^{1/3}(\tilde{\phi}_v)^{2/3} + \bar{\delta} \tag{16}$$

where γ is the surface growth rate and $\bar{\delta}$ represents the impact of nucleation on soot volume fraction. The following Arrhenius rate expressions have been proposed for the rate constants [26]:

$$\alpha = 6 \times 10^6 \rho^2 T^{1/2}[X_f]\exp(-46100/T)$$

$$\beta = 2.25 \times 10^{15} T^{1/2}$$

$$\gamma = 6.3 \times 10^{-14} \rho T^{1/2}[X_f]\exp(-12600/T)$$

Table 1 Caterpillar 3401 engine specifications

Bore × Stroke	137.2 mm × 165.1 mm
Compression ratio	16.1:1
Displacement	2.44 l
Connecting rod length	261.6 mm
Squish height	1.57 mm
Combustion chamber geometry	In-piston mexican hat with sharp edged crater
Piston	Articulated
Charge mixture motion	Quiescent
Injector	HEUI
Maximum injection pressure	190 ° MPa
Number of nozzle holes	6
Nozzle hole diameter	0.214 mm
Included spray angle	145 deg
Injection rate shape	Rising
Experimental conditions for model validations	
Case group	SOI (ATDC)
A (8% EGR)	−20, −15, −10, −5, 0, +5
B (27% EGR)	−20, −15, −10, −5, 0, +5
C (40% EGR)	−20, −15, −10, −5, 0, +5

$$\bar{\delta} = 144\alpha \tag{17}$$

where T is the gas temperature and X_f is the molar fraction of the soot precursor, which is assumed to be acetylene in this study.

In the present RIF-based approach, the laminar flamelet data obtained from the flamelet code are used to express the source terms in the transport equations of soot volume fraction and number density as a function of the mixture fraction Z. By convoluting these source terms with the assumed PDF, the mixture fraction averaged source terms are obtained.

Experiments

Engine experiments performed on a caterpillar heavy-duty diesel engine [27] were used for model validations. The engine is a single-cylinder engine with the specifications listed in Table 1. The gaseous emissions recorded in the experiments include NO_x, intake CO_2, exhaust CO_2, carbon monoxide, and hydrocarbons. The particulate was measured using a full dilution tunnel and an AVL DPL 439 particulate analyzer. The (EGR) level was varied by changing the exhaust back pressure.

Results

The experiments used the caterpillar stock electronic unit injector (EUI). The experiments were part of the optimization study performed to explore PCCI characteristics by a genetic algorithm [27]. Both the KIVA/CHEMKIN and KIVA/RIF models were applied to simulate the cases listed in Table 1 with various EGR levels from 8% to 40% and injection timings.

A 60-deg sector mesh was used for 3D simulations. The average grid size is approximately 2 mm and the number of computational cells is approximately 6000 at (BDC). The present mesh resolution is considered to be adequate for the engine flow turbulence modeling [30]. In addition, the cylindrical mesh is finer near the injector for fuel spray simulations. Simulations started from intake valve closure with swirl ratio of 1. The initial conditions were obtained from the 1D code simulations that also consider the EGR level [15]. Wall temperature boundary conditions use 433 K for the cylinder wall, 523 K for the cylinder head, and 553 for the piston surface.

Figures 1 and 2 show comparisons of measured and computed cylinder pressure and heat release rate data for selected cases. Both models are seen to perform very well over a wide range of engine conditions. The heat release rate data does not exhibit the distinct premixed and diffusion burn regimes typically seen in conventional diesel engines. The highly premixed burned feature of the present PCCI experiments is captured by both models.

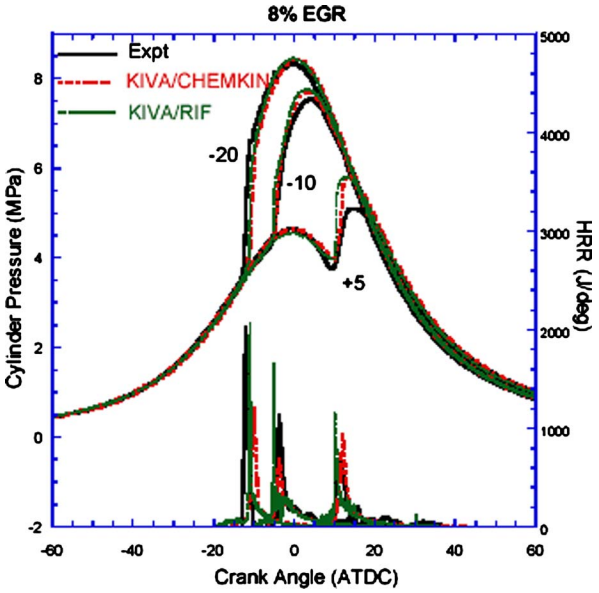

Fig. 1 Comparisons of measured (solid line), KIVA/CHEMKIN (thick dotted line), and KIVA/RIF (thin dotted line) cylinder pressure and heat release rate data for 8% EGR cases (SOI=−20, −10, and +5 ATDC)

In the present KIVA/RIF model, a single flamelet approach is used to simulate the in-cylinder combustion. The temporal evolution of the flamelet with respect to mixture fraction during ignition is shown in Fig. 3 for 40% EGR, SOI=−20 ATDC. As the combustion process proceeds, ignition of the flamelet occurs and later reaches a high temperature. It can be seen that the ignition occurs at mixture fractions that are on the rich side of stoichiometry, which is approximately equal to 0.05 in the case shown considering the presence of EGR. The temporal evolutions of fuel and

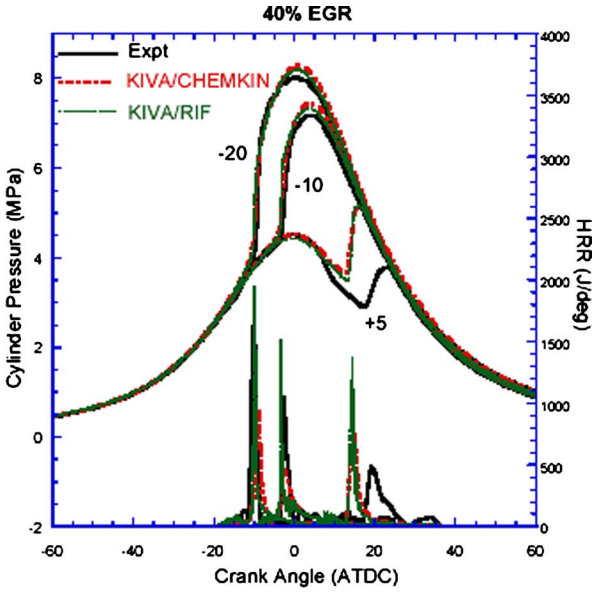

Fig. 2 Comparisons of measured (solid line), KIVA/CHEMKIN (thick dotted line), and KIVA/RIF (thin dotted line) cylinder pressure and heat release rate data for 40% EGR cases (SOI=−20, −10, and +5 ATDC)

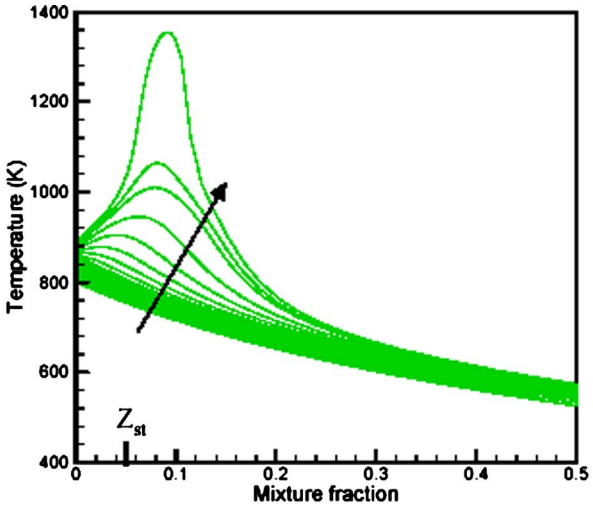

Fig. 3 Temporal evolution of the flamelet using KIVA/RIF during ignition (40% EGR, SOI=−20 ATDC)

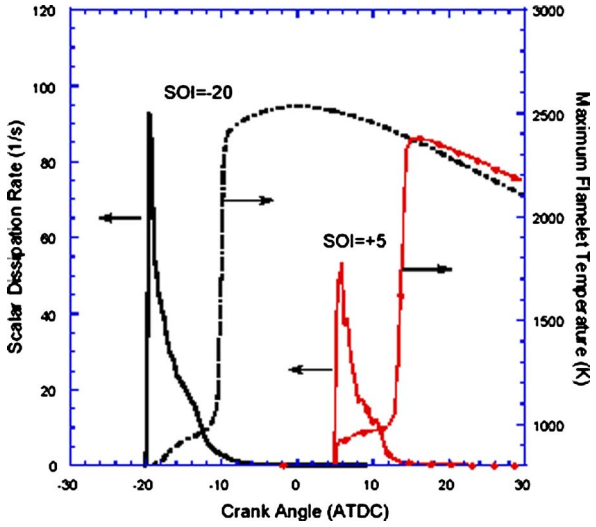

Fig. 5 History of mean scalar dissipation rate and maximum flamelet temperature predicted by KIVA/RIF for 40% EGR, SOI =−20, and 5 ATDC cases

oxygen with respect to mixture fraction are also shown in Fig. 4 that indicates the consumption of fuel and oxygen during the combustion process.

The temporal evolutions of the mean scalar dissipation rates and maximum flamelet temperatures are shown in Fig. 5 for EGR=40%, SOI=−20 and 5 ATDC cases. The rapid increase in the scalar dissipation rate is due to the increase in turbulent intensity generated by the high velocity of the fuel jet. As the fuel injection ends, the scalar dissipation rate continues to decrease, and the diffusive loss becomes small so that heat and radicals produced by chemical reactions can build up and lead to ignition.

The predicted soot and NO_x (i.e., sum of NO and NO_2) emissions were also compared with the measurements, as shown in Figs. 6–8. It can be seen that the overall trend of engine-out soot and NO_x are captured with respect to the start-of-injection timing. It is of interest to note that soot emissions reach a peak value when fuel is injected near top-dead center. Note that different soot models are used in KIVA/CHEMKIN and KIVA/RIF codes, as described earlier. However, both soot models start from the same precursor species (C_2H_2). Soot emissions predicted by KIVA/CHEMKIN agree somewhat better with the measurements. Nevertheless, both models predict correctly the soot reduction that is seen at further retarded injection timings (e.g., SOI=+5 ATDC) for all different EGR levels.

Comparisons of the predicted in-cylinder NO_x history for two selected cases (40% EGR, SOI=−20 and +5 ATDC) indicate that both models predict similar NO_x formation characteristics, e.g., the NO_x chemistry freezes at a certain point during piston expansion, as shown in Fig. 9. For these two selected cases, a similar level of NO_x emissions predicted by the two models is consistent with the fact that both models predict similar combustion temperatures, as shown in Fig. 10.

The present numerical models can be used to explain the soot emission reduction as the injection is further retarded past TDC which differs from the conventional diesel soot-NO_x trade-off with respect to the injection timing. Figure 11 shows the total in-cylinder soot mass evolutions for two different injection timings, SOI=−10 and +5 ATDC. The model results indicate that a relatively large amount of soot is formed in the cylinder for SOI

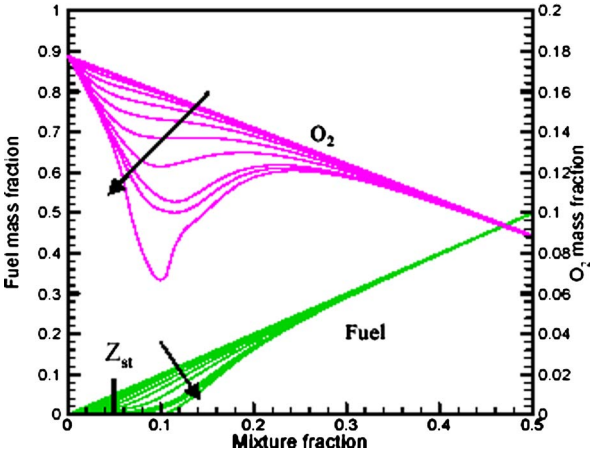

Fig. 4 Temporal evolutions of O_2 and fuel mass fraction with respect to mixture fraction using KIVA/RIF during ignition (40% EGR, SOI=−20 ATDC)

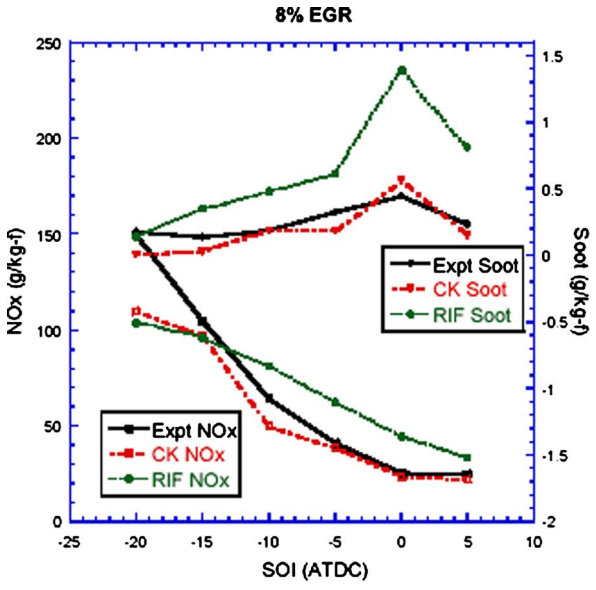

Fig. 6 Measured and predicted emissions for 8% EGR cases

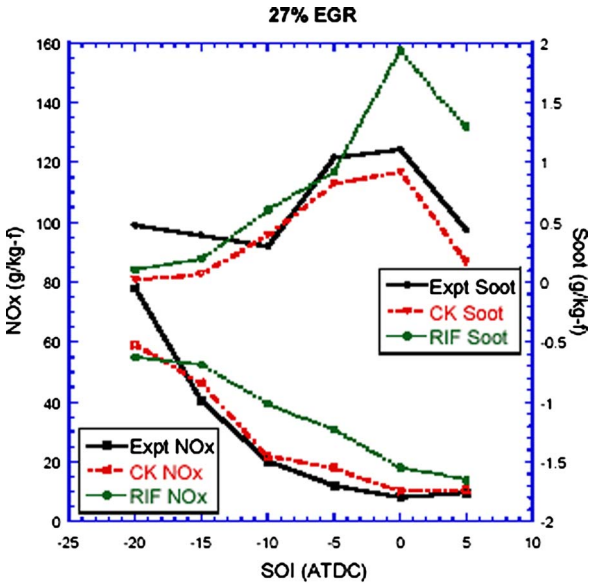

Fig. 7 Measured and predicted emissions for 27% EGR cases

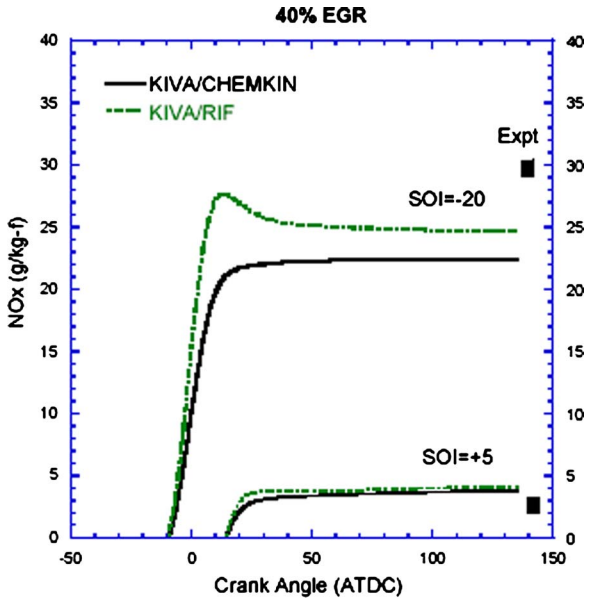

Fig. 9 Predicted in-cylinder NO_x history using two models compared with engine exhaust data (solid squares) for 40% EGR cases with SOI=−20 and +5 ATDC

=−10 ATDC but the soot oxidation process is very active due to high in-cylinder gas temperatures. On the other hand, a relatively small amount of soot is formed in the cylinder for SOI=5 ATDC such that the exhaust soot emissions are low. The low soot emission at such a retarded injection timing is due to low temperature combustion (as can be seen from low cylinder pressure in Fig. 2). The above low temperature combustion characteristics can be further optimized to achieve low emission diesel PCCI operations.

As can be seen from the emission prediction comparisons, both the KIVA/CHEMKIN and KIVA/RIF models predict the trends correctly, only the magnitudes are somewhat different. It is thus of interest to further investigate the in-cylinder details predicted by the two models.

The fuel spray and vapor distributions in the cylinder are shown in Fig. 12 for 40% EGR, SOI=+5 ATDC. Note that the mixture conditions are the same before ignition occurs since the same turbulence and spray models are used in both KIVA/CHEMKIN and KIVA/RIF. It can be seen that nearly all the liquid fuel has vaporized prior to the onset of combustion. The models predict that the fuel spray impinges on the piston surface and a counter-clockwise flow motion is generated that pushes the mixture to the squish region where ignition takes place, as can be seen from the temperature contours in Fig. 13. The predicted in-cylinder temperature fields of KIVA/CHEMKIN and KIVA/RIF are very similar, as can be seen by comparing Figs. 13 and 14. Combustion takes place mostly in the squish region and at the outer edge of the bowl.

Soot contours predicted by KIVA/CHEMKIN are shown in Fig. 15. Soot is initially formed near the piston bowl edge under the cylinder head and then is moved following the counter-clockwise flow motion slightly to the left. As the piston further expands, the soot cloud is stretched and oxidized by the surrounding air. It is

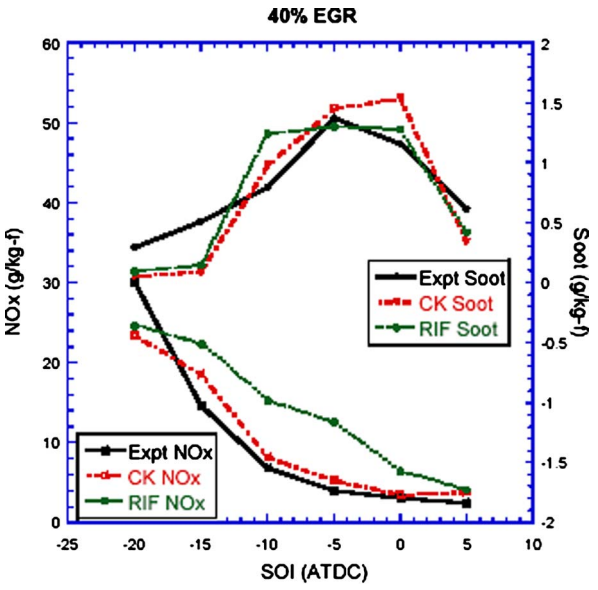

Fig. 8 Measured and predicted emissions for 40% EGR cases

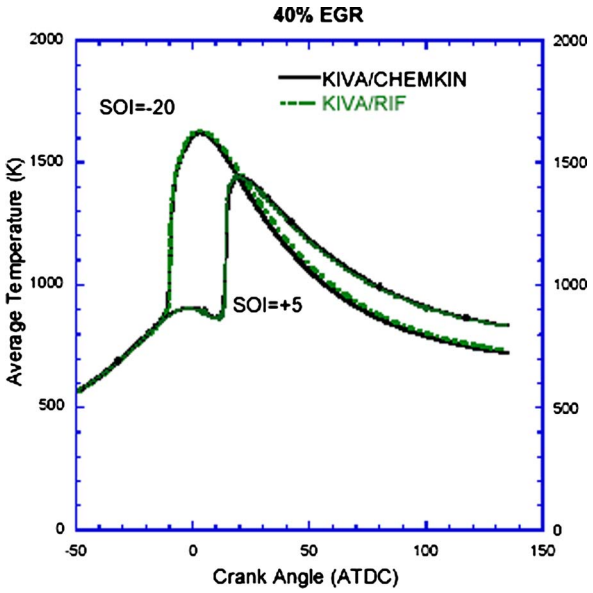

Fig. 10 Predicted in-cylinder average gas temperature for 40% EGR cases with SOI=−20 and +5 ATDC (same conditions as in Fig. 8)

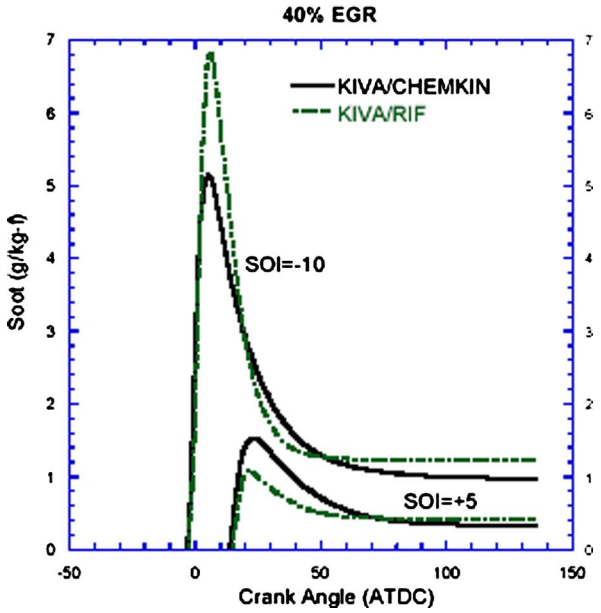

Fig. 11 In-cylinder soot mass histories for 40% EGR cases at two different injection timings

interesting that the KIVA/RIF model also predicts very similar soot distribution results as the KIVA/CHEMKIN model, as seen in Fig. 16.

The present KIVA/CHEMKIN model solves for the chemical reactions in each computational cell based on the local mixture and thermodynamic conditions. The effects of turbulent flow on combustion are modeled by the RNG k-ε turbulence model via mixing and property transport at the resolution level of the computational grid. No subgrid scale turbulence-chemistry interaction model [16] was used in this study. On the other hand, the KIVA/RIF model uses the laminar flamelet assumptions, and attempts to resolve the structure of a representative flamelet. The model relates the flamelet solutions to obtain thermodynamic properties in the physical domain. The effects of turbulence on chemistry are accounted for by the use of the scalar dissipation that serves to diffuse species in subgrid scales. However, as shown in the present study, both KIVA/CHEMKIN and KIVA/RIF codes give very similar combustion and emission predictions.

The fact that both modeling approaches gave similar results suggests that, after ignition, the effective combustion rates are

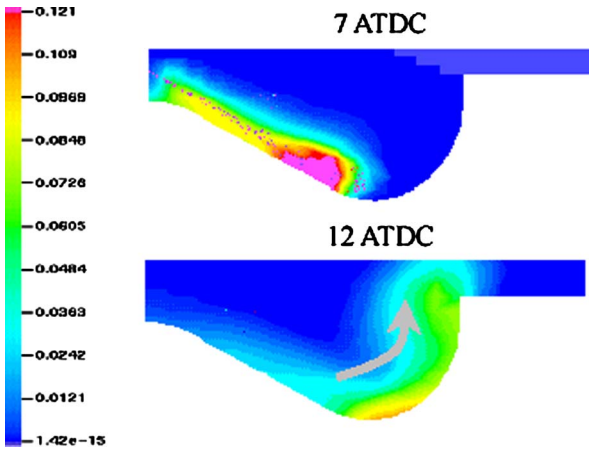

Fig. 12 Distribution of liquid drops and fuel vapor prior to ignition (40% EGR, SOI=+5 ATDC). Arrow indicates the flow pattern generated by the fuel injection and reverse squish flow.

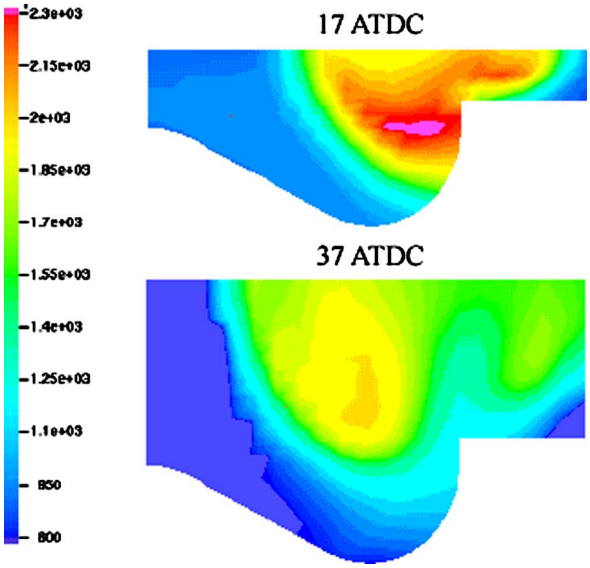

Fig. 13 Temperature contours predicted by KIVA/CHEMKIN (40% EGR, SOI=+5 ATDC)

determined not by the chemical source terms, but instead, by mixing rates, which are the same in both codes. Of course, ignition is predicted similarly because the same chemical mechanism is used in both cases. The controlling role of mixing was also suggested by Pickett and Siebers [28] in their study of the sooting tendency of diesel fuel jets, in which the heat release rate is generally limited by the rate of mixing of fuel with the surrounding air. The direct integration approach of KIVA/CHEMKIN is more intuitive and straightforward. Note that the accuracy of both models depend strongly on the fidelity of the chemical reaction mechanism.

The computer times used in the two different approaches were also compared. In the present KIVA/CHEMKIN code, chemistry is solved for each computational cell (approximately 2000 cells during the main combustion stage). In the KIVA/RIF code, chemistry is solved for at 50 discretized points in mixture fraction space (see Figs. 3 and 4), i.e., chemistry is solved for 50 different mixture fractions per CFD time step. However, transport equa-

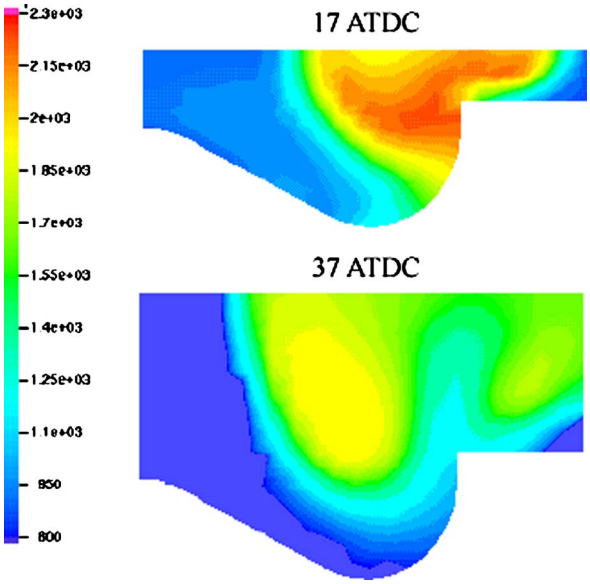

Fig. 14 Temperature contours predicted by KIVA/RIF (40% EGR, SOI=+5 ATDC) using the same color scale as in Fig. 13

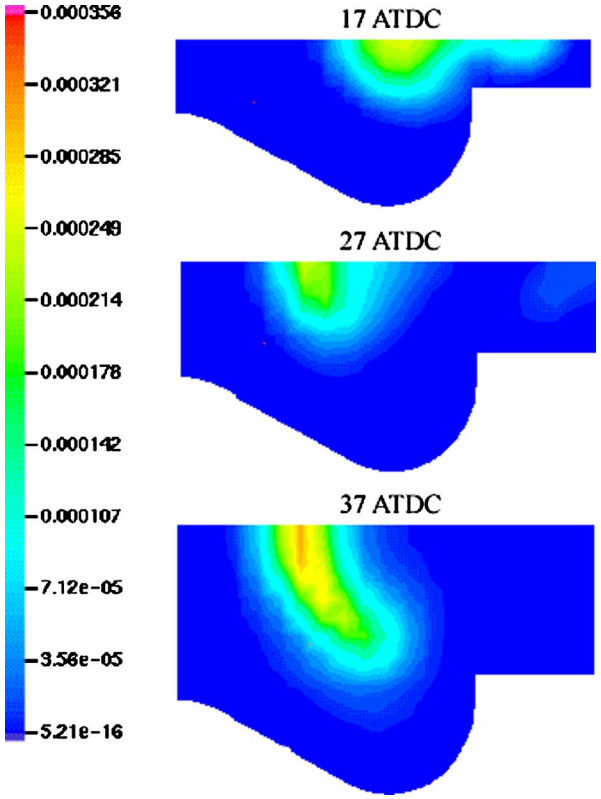

Fig. 15 Soot mass fraction contours predicted by KIVA/CHEMKIN (40% EGR, SOI=+5 ATDC)

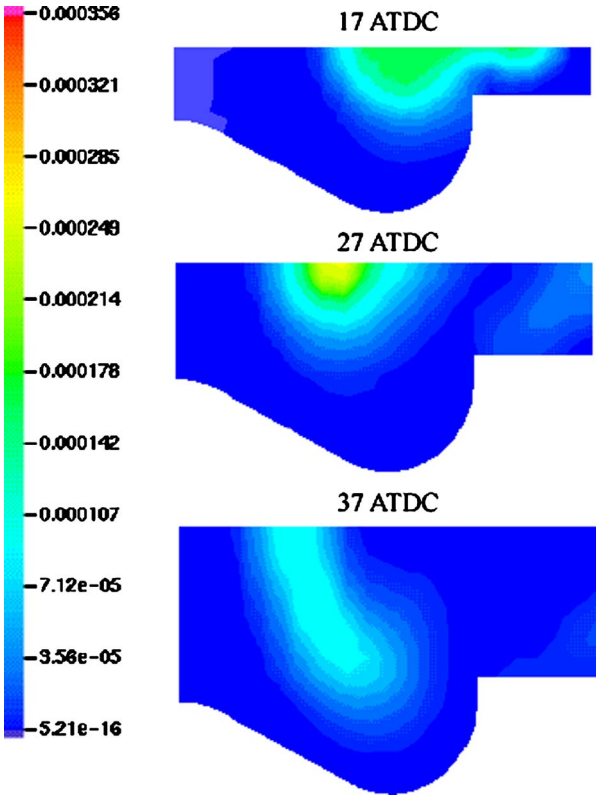

Fig. 16 Soot contours predicted by KIVA/RIF (40% EGR, SOI =+5 ATDC) using the same color scale as in Fig. 15

tions for the mixture fraction and its variance are also solved, together with additional PDF equations to couple the flamelet solutions to the CFD code. Moreover, transport equations for the soot number density and volume fraction also needed to be solved. It is of interest to note that the CPU time using KIVA/RIF is approximately 20% of that using KIVA/CHEMKIN for a typical simulation from intake valve closure to exhaust valve open, e.g., 20 CPU hours on a Pentium-4 PC for KIVA/CHEMIN.

As expected, the computer time for KIVA/CHEMKIN depends on the number of computational cells. Computational efficiency can be improved by using parallel computing, as done by Ali et al. [29] or by using a data retrieval method that obtains chemistry solutions from a dynamically built library, as done by Zhang et al. [17]. In the KIVA/RIF model, the computer time depends on the number of discretization points in mixture fracture space and the number of representative flamelets. Thus, it may offer the potential of better computational efficiency in simulating combustion in a domain with a large number of computational cells.

Conclusions

Diesel engine combustion and emissions were simulated using two different models, namely, the KIVA/CHEMKIN and KIVA/RIF models. Despite the fact that both models used different concepts for combustion modeling, the simulation results show that both models predict very similar combustion and emission characteristics.

The predicted cylinder pressure and heat release rate data were nearly identical using the two models. The present KIVA/RIF model predicts slightly higher in-cylinder gas temperatures that result in higher NO_x emissions. However, the trends of NO_x emissions with respect to EGR levels and SOI timings are captured.

The trends of soot emissions with respect to EGR levels and SOI timings were also captured by the two models despite the fact that different soot models were used. Both models also predicted the benefits of late injection (past TDC) to soot emissions as a result of low temperature combustion.

The fact that both combustion modeling approaches give similar results suggests that, after ignition occurs, heat release rates and local gas temperatures are mainly controlled by turbulent diffusion rates, i.e., mixing-controlled combustion, under the engine conditions studied here.

Acknowledgment

The authors acknowledge the financial support by DOE/Sandia National Labs, DOE HCCI Consortium Project Contract No. DE-FC04-02AL67612, and Caterpillar, Inc. The financial support by the Korean Science and Engineering Foundation for H. Kim and Y. Kim is also greatly appreciated.

Nomenclature

C_p = specific heat at constant pressure
C_v = specific heat at constant volume
e = internal energy
h = enthalpy
K = total number of species
k = turbulent kinetic energy
m_p = mass production rate for p-th spray particle
N_a = Avogadro's number
P = probability density function
Pr = Prandtl number
S = source term in soot model
T = temperature
u = velocity
V = cell volume
v = specific volume
W = molecular weight
Y = mass fraction of chemical species
Z = mixture fraction

Z_{ini} = upper limit of mixture fraction

Greek Symbols

α = nucleation rate
β = coagulation rate
γ = surface growth rate
χ = scalar dissipation rate
ε = dissipation of turbulent kinetic energy
μ_e = effective viscosity
ρ = density
ω = production rate of chemical species
ω_v = production rate of chemical species

Subscripts

j = spatial component
k = k-th chemical species
p = spray particle
s = liquid surface
st = stoichiometric

Symbols

$\langle\rangle$ = PDF averaged
$\tilde{}$ = Favre averaged
$\bar{}$ = Reynolds averaged

References

[1] Magnussen, B. F., and Hjertager, B. H., 1976, "On Mathematical Modeling of Turbulent Combustion with Special Emphasis on Soot Formation and Combustion," Proc. Combust. Inst., **16**, pp. 719–729.

[2] Kong, S. C., Han, Z. W., and Reitz, R. D., 1995, "The Development and Application of a Diesel Ignition and Combustion Model for Multidimensional Engine Simulations," SAE Paper No. 950278, J. Eng., **104**, pp. 502–518.

[3] Rao, S., and Rutland, C. J., 2002, "A Flamelet Time Scale Model for Non-Premixed Combustion Including Unsteady Effects," Combust. Flame, **133**, pp. 189–191.

[4] Steiner, R., Bauer, C., Kruger, C., Otto, F., and Maas, U., 2004, "3D Simulation of DI-Diesel Combustion Applying a Progress Variable Approach Accounting for Complex Chemistry," SAE Paper No 2004-01-0106.

[5] Correa, C., Niemann, H., Schramm, B., and Warnatz, J., 2000, "Use of ILDM Reduced Chemistry in Direct Injection Diesel Engines," *THIESEL 2000 Conference*, Valencia, Spain, pp. 163–170.

[6] Beard, P., Colin, O., and Miche, M., 2003, "Improved Modeling of DI Diesel Engines Using Subgrid Descriptions of Spray and Combustion," SAE Paper No. 2003-01-0008.

[7] Pitsch, H., Barths, H., and Peters, N., 1996, "Three Dimensional Modeling of NO_x and Soot Formation in DI-Diesel Engines Using Detailed Chemistry Based on the Interactive Flamelet Approach," SAE Paper No. 962057.

[8] Peters, N., 1984, "Laminar Diffusion Flamelet Models in a Non-Premixed Turbulent Combustion," Prog. Energy Combust. Sci., **10**, pp. 319–339.

[9] Barths, H., Antoni, C., and Peters, N., 1998, "Three-Dimensional Simulation of Pollutant Formation in a DI Diesel Engine Using Multiple Interactive Flamelets," SAE Paper No. 982459.

[10] Hasse, C., Bikas, G., and Peters, N., 2000, "Modeling DI-Diesel Combustion Using the Eulerian Particle Flamelet Model (EPFM)," SAE Paper No. 2000-01-2934.

[11] Hasse, C., and Peters, N., 2004, "A Two Mixture Fraction Flamelet Model Applied to Split Injections in a DI Diesel Engine," Proc. Combust. Inst., **30**, pp. 2755–2762.

[12] Hergart, C., Barths, H., and Peters, N., 1999, "Modeling the Combustion in a Small-Bore Diesel Engine Using a Method Based on Representative Interactive Flamelets," SAE Paper No. 1999-01-3550.

[13] Kim, H., Heo, N., Kim, Y., Lee, J.-H., and Lee, J. K., 2004, "Numerical Study of Combustion Processes and Pollutant Formation in HSDI Diesel Engines," SAE Paper No. 2004-01-0126.

[14] Kong, S.-C., and Reitz, R. D., 2002, "Application of Detailed Chemistry and CFD for Predicting Direct Injection HCCI Engine Combustion and Emissions," Proc. Combust. Inst., **29**, pp. 663–669.

[15] Kong, S. C., Patel, A., Yin, Q., and Reitz, R. D., 2003, "Numerical Modeling of Diesel Engine Combustion and Emissions Under HCCI-Like Conditions with High EGR Levels," SAE Paper No. 2003-01-1087.

[16] Patel, A., Kong, S.-C., and Reitz, R. D., 2004, "Development and Validation of a Reduced Reaction Mechanism for HCCI Engine Simulations," SAE Paper No. 2004-01-0558.

[17] Zhang, Y. Z., Kung, E. H., and Haworth, D. C., 2004, "A PDF Method for Multidimensional Modeling of HCCI Engine Combustion: Effects of Turbulence/Chemistry Interactions on Ignition Timing and Emissions," Proc. Combust. Inst., **30**, pp. 2763–2772.

[18] Amsden, A. A., 1997, "KIVA-3V: A Block-Structured KIVA Program for Engines With Vertical or Canted Valves," LA-13313-MS.

[19] Han, Z., Uludogan, A., Hampson, G. J., and Reitz, R. D., 1996, "Mechanism of Soot and NO_x Emission Reduction Using Multiple-Injection in a Diesel Engine," SAE Paper No. 960633.

[20] Patterson, M. A., and Reitz, R. D., 1998, "Modeling the Effects of Fuel Spray Characteristics on Diesel Engine Combustion and Emissions," SAE Paper No. 980131.

[21] Smith, G. P., Golden, D. M., Frenklach, M., Moriarty, N. W., Eiteneer, B., Goldenberg, M., Bowman, C. T., Hanson, R. K., Song, S., Gardiner, W. C., Lissianski, V. V., and Qin, Z., 2000, http://www.me.berkeley.edu/gri_mech/

[22] Kong, S. C., Sun, Y., and Reitz, R. D., 2005, "Modeling Diesel Spray Flame Lift-Off, Sooting Tendency and NO_x Emissions Using Detailed Chemistry With Phenomenological Soot Model," ASME Paper No. ICES2005-1009.

[23] Kee, R. J., Rupley, F. M., and Miller, J. A., 1989, "CHEMKIN-II: A FORTRAN Chemical Kinetics Package for the Analyses of Gas Phase Chemical Kinetics," Sandia Report, SAND 89-8009.

[24] Liang, L., Juung, C., Kong, S. C., and Reitz, R. D., 2005, "Development of a Semi-Implicit Solver for Detailed Chemistry Simulations," ASME Paper No. ICES2005-1005.

[25] Demoulin, F. X., and Borghi, R., 2000, "Presumed PDF Modeling of Turbulent Spray Combustion," Combust. Sci. Technol., **158**, pp. 249–271.

[26] Moss, J. B., Stewart, C. D., and Young, K. J., 1995, "Modeling Soot Formation and Burnout in a High Temperature Laminar Diffusion Flame Burning Under Oxygen Enriched Conditions," Combust. Flame, **101**, pp. 491–500.

[27] Klingbeil, A. E., 2002, "Particulate and NO_x Reduction in a Heavy-Duty Diesel Engine Using High Levels of Exhaust Gas Recirculation and Very Early and Very Late Injection," MS thesis, University of Wisconsin-Madison.

[28] Pickett, L. M., and Siebers, D. L., 2004, "Non-Sooting, Low Flame Temperature Mixing-Controlled DI Diesel Combustion," SAE Paper No. 2004-01-1399.

[29] Ali, A., Cazzoli, G., Kong, S. C., Reitz, R. D., and Montgomery, C., 2003, "Improvement in Computational Efficiency for HCCI Engine Modeling by Using Reduced Mechanisms and Parallel Computing," *Proc. Third Joint Meeting, Combust. Inst.*

[30] Han, Z., and Reitz, R. D., 1995, "Turbulence Modeling of Internal Combustion Engines Using RNG k-ε Models," Combust. Sci. Technol., **106**, pp. 267–295.

Sensitivity Analysis of NO_x Formation Kinetics in Pilot-Ignited Natural Gas Engines

Huateng Yang
Department of Mechanical Engineering,
The University of Alabama,
Tuscaloosa, AL 35487

S. R. Krishnan
Energy Systems Division,
Argonne National Laboratory,
Argonne, IL 60439

K. K. Srinivasan
Department of Mechanical Engineering,
Mississippi State University,
Starkville, MS 39762

K. C. Midkiff
Department of Mechanical Engineering,
The University of Alabama,
Tuscaloosa, AL 35487
e-mail: cmidkiff@eng.ua.edu

A sensitivity analysis of NO_x formation in pilot-ignited natural gas dual fuel engines is performed based on a phenomenological combustion model. The NO_x formation mechanism employed in this study incorporates a super-extended Zel'dovich mechanism (up to 43 reactions). The sensitivity analysis compares the contribution of each major reaction to NO_x formation, and identifies the rate-controlling NO_x formation reactions in different high-temperature regions—the burning pilot spray, the premixed flame associated with the gaseous fuel-air mixture, and the burned combustion products. The formation rates for reactions involving NO_x are also investigated to reveal the primary NO_x formation paths. Results show two main NO_x formation paths both in the pilot spray (also called the packets zone) and the burned zone. The rate-limiting reactions for the packets zone are $O+N_2=NO+N$ and $N_2+HO_2=NO+HNO$. Rate-limiting reactions for the burned zone are $N_2O+M=N_2+O+M$ and $N_2+HO_2=NO+HNO$. Since the aforementioned reactions significantly influence the net NO_x prediction, it is important that the corresponding reaction rates be determined accurately. Finally, because the quasi-steady-state assumption is commonly used for certain species in NO_x modeling, a transient relative error is estimated to evaluate the validity of the assumption. The relative error in NO_x prediction with and without the use of the steady-state assumption is small, of the order of 2%. This work also confirms that sensitivity analysis can provide valuable insight into the possible NO_x formation pathways in engines and improve the ability of current prediction tools to obtain more reliable predictions. [DOI: 10.1115/1.2360601]

Introduction

NO_x emissions from engines are an important source of air pollution. Reduction of engine-out NO_x emissions has been an impetus for both engine design improvement and the search for alternative fuels. The low pilot ignited natural gas engine is a promising step towards this goal. In the application at the University of Alabama, natural gas is introduced into the intake manifold and mixes with air to form homogeneous mixtures that are inducted into the cylinder and ignited later in the compression stroke by a very small amount of diesel (2–3% on an energy basis) [1]. Since most of the combustion occurs in a lean natural gas-air mixture, particulate emissions are expected to be minimal. Recent experimental research employing diesel pilots at advanced injection timings (50–60 crank angles before top dead center (BTDC)) [2,3] have shown that NO_x emissions can be reduced significantly to approximately 0.2 g/kWh with a fuel conversion efficiency of 41.3%, which is comparable to base line diesel operation.

At advanced injection timings (around 55–60 deg BTDC), the very small amount of pilot diesel fuel has enough time to evaporate, diffuse and mix with the surrounding natural gas and air. The combustion is expected be similar to lean premixed combustion with relatively low local temperature because of lean local equivalence ratio. As a result, NO_x emissions that scale with local temperatures exponentially are expected to be low. These results have been independently confirmed by Tomita et al. [4].

The NO_x formation mechanism for such locally lean combustion is different from traditional diesel combustion or spark ignited engine combustion, where the extended Zel'dovich mechanism dominates the NO_x formation. A literature review shows that for such combustion, while the extended Zel'dovich mechanism can give the correct NO_x formation trend, it underpredicts NO_x formation substantially. For instance, Dodge [5] shows that for lean burn natural gas engines, especially in the 0.61–0.75 equivalence ratio range, the extended Zel'dovich thermal NO mechanism greatly underpredicts the NO_x emissions. Hampson et al. [6] simulated a heavy-duty diesel engine converted to burn gaseous fuel and found that the predicted NO_x trends showed good agreement with measured results, but that the actual values were substantially underpredicted. Other researchers [7,8] have arrived at similar conclusions. The fact that the extended Zel'dovich mechanism underpredicts NO_x even with a satisfactory combustion model indicates that there are important missing reactions in the NO_x formation scheme. Based on previous investigations, Bowman [9] concludes that N_2O, NH and NO_2 play a significant role in the formation of NO_x. Tomeczek and Gradon [10] illustrated the role of nitrous oxide in the flame temperature range using the so-called extended thermal mechanism that includes the Malte and Pratt [11] N_2O mechanism. Mellor [12] suggested that the extended Zel'dovich mechanism alone may not be sufficient to describe the underlying NO kinetics for lean combustion since NO formation could assume importance in high pressure premixed or diffusion flames through an N_2O mechanism.

A systematic approach to analyze reaction mechanisms to locate the dominant reactions or rate-limiting reactions may be achieved through sensitivity analysis. Sensitivity analysis is an important tool in analyzing reaction mechanisms, and has long been in use. A good review on this topic by Turányi [13] defines sensitivity analysis as an investigation of the effect of parameter changes on the solution of mathematical models. Several schemes

Contributed by the Internal Combustion Engine Division of ASME for publication in the JOURNAL OF ENGINEERING FOR GAS TURBINES AND POWER. Manuscript received by the ICE Division May 23, 2005; final manuscript received May 31, 2006. Review conducted by M. Wooldridge.

to implement sensitivity analyses include the brute-force method [14], in which each reaction rate constant is changed one at a time and the outputs before and after the change are compared by the calculation of sensitivity coefficients. While this approach requires no extra programming, it is extremely tedious. More elegant approaches are the direct method [15], the Green's function method [16], and the polynomial approximation method [17], among others.

The suspicion that reactions other than those of the extended Zel'dovich mechanism may also assume importance in pilot ignited natural gas engines necessitates the application of sensitivity analysis on the NO_x reaction mechanisms. This paper presents such work done by the authors in the context of simulation.

Sensitivity analysis of a NO_x reaction mechanism requires both a combustion model and a NO_x reaction mechanism. First, a combustion model must be able to predict the in-cylinder temperature and equivalence ratio history accurately. Second, a NO_x mechanism must be chosen to calculate the net NO_x formed. Depending on the extent of details incorporated, combustion models can range from zero-dimensional, phenomenological models to multidimensional models with detailed chemical kinetics. The combustion model used in this paper is a phenomenological model developed by Krishnan et al. [18]. Great progress in developing accurate NO_x formation mechanisms has been achieved in the last several decades, e.g., the detailed NO_x formation mechanisms proposed by Miller and Bowman [19], GRI_Mech [20], Glaborg et al. [21], and Zabetta et al. [22]. Nevertheless, none of these mechanisms are universal, since reaction rate data still need to be obtained experimentally for novel applications. Also, most of these schemes are so detailed (usually several hundred reactions and over 40 species) that the solution process is computationally intensive and time consuming. Consequently, these highly detailed reaction schemes are primarily used to model simplified combustion systems, such as partially stirred or plug flow reactors [23] among others. It is challenging to implement such schemes in multiple-zone, complex engine combustion models that will provide results with acceptable run times. In this paper, a set of reactions intermediate in complexity between the extended Zel'dovich mechanism and detailed reaction schemes, called a "super-extended Zel'dovich mechanism," [24] is chosen to model the NO_x formation and is subjected to sensitivity analysis.

Model Description

The phenomenological combustion model developed by Krishnan et al. [18] to model pilot-ignited natural gas combustion is used as the basic supporting combustion model for the present work. Figure 1 shows the phenomenological sketch of the zones used in this combustion zone. In essence, the combustion model is a multi-zone model in which four zones are considered: the unburned zone containing a mixture of unburned natural gas and air, the pilot fuel zones (or packets) that account for diesel and natural gas combustion in the vicinity of the pilot diesel spray, the flame zone that models premixed natural gas combustion by means of turbulent flame propagation, and the burned zone containing combustion products. The pilot fuel zones are typically assumed to have about 100 packets. The onset of ignition is calculated using the Shell auto-ignition model. An Arrhenius-type reaction rate is used to describe combustion in the packets. Flame propagation in the flame zone is modeled with an eddy entrainment approach [25]. Further details of the combustion model may be obtained from Ref. [20]. The NO formation is calculated from the packets zone, flame zone, and burned zone separately. It should be noted that the NO in the burned zone includes the NO transferred from the packets zone and the flame zone. Thus the final NO present in the burned zone is identical to the total net NO formed in the engine cylinder.

The NO_x model uses a super-extended Zel'dovich mechanism [24,26], which is a group of empirically important NO formation reactions. Because the three-equation extended Zel'dovich mechanism typically tends to underpredict NO compared to experimental results [5], the super-extended Zel'dovich mechanism is used here in consideration of its more detailed description of the NO_x formation process. The super-extended Zel'dovich mechanism used here has been reported previously [27] by the authors. The mechanism can predict the NO_x emissions closer to the experiment results with an approximately 25% increase of NO compared to the extended Zel'dovich mechanism alone. The NO_x prediction model is modified to accommodate for the sensitivity analysis of the NO_x reaction mechanisms. The essential features of the model are summarized below:

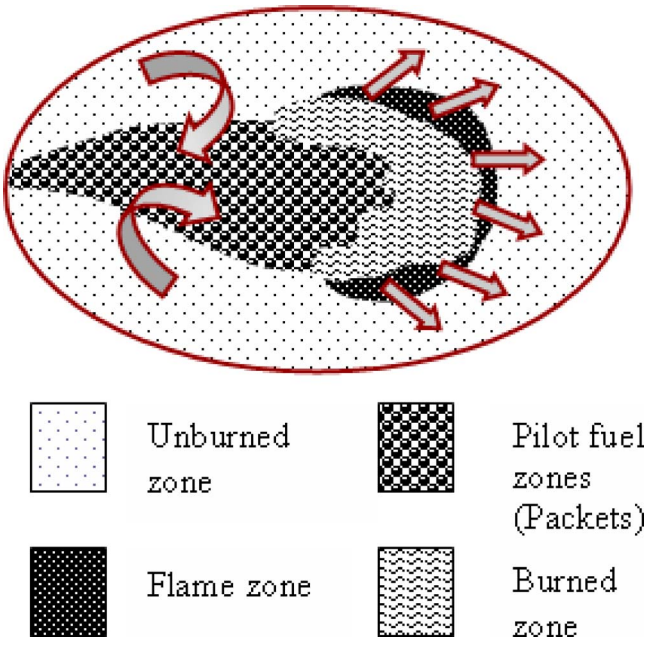

Fig. 1 Conceptual schematic of zone evolution (Krishnan et al. [20])

(1) A total of 43 reactions and 21 species are considered.
(2) The reaction rates for each of them are taken from Ref. [24] and are listed in the Appendix.
(3) The combustion and NO_x formation processes are assumed to be decoupled, which means that all of the NO_x is formed from the combustion products only.
(4) The species NO, N, N_2O, NO_2, NH, and HNO are all kinetically controlled.
(5) All other species are assumed to be at chemical equilibrium.
(6) From the available forward reaction rates, reverse reaction rates are calculated using the following relationships:

$$K_r = K_f / K_c \tag{1}$$

$$K_c = K_p \left(\frac{P_{\text{atm}}}{RT} \right)^{\sum_{k=1}^{K} \upsilon_k} \tag{2}$$

$$K_p = \exp\left(\frac{\Delta S^0}{R} - \frac{\Delta H^0}{RT} \right) \tag{3}$$

$$\frac{\Delta S^0}{R} = \sum_{k=1}^{K} \upsilon_k \frac{S_k^0}{R} \tag{4}$$

$$\frac{\Delta H^0}{RT} = \sum_{k=1}^{K} v_k \frac{H_k^0}{RT} \tag{5}$$

where K is the species index for each reaction, K_f, K_r, K_c, K_p are forward reaction rate, backward reaction rate, equilibrium constant based on concentration, equilibrium constant based on at constant pressure, respectively. Values of S^0/R and H^0/RT for species are obtained from Ref. [28]. There are a total of six ordinary differential equations governing the six kinetically controlled species, N, N_2O, NO_2, NH, HNO, and NO, to be solved. The coefficients of these equations change with time and all equations are "stiff."

The super-extended Zel'dovich mechanism is a group of "empirically important" NO_x formation reactions [24,26]. The term empirically important means that the reactions may not be elementary. However, they are treated like elementary reactions that follow the law of mass action. Also, since the reaction rate is expressed as $K_f = AT^{\beta} \exp(-E_0/T)$, three parameters need to be determined: the pre-exponential factor A, the temperature exponent β, and the activation energy E_0. All have uncertainty and there are several different reaction rate formulations even for the same reaction due to the limited understanding of the actual mechanism(s). In this paper β and E_0 are assumed to be "certain" and the actual uncertainties in both are "lumped" together with the uncertainty in the pre-exponential factor A. Performing sensitivity analyses with the pre-exponential factor A as the sensitivity parameter, the sensitivity coefficients for each reaction can be calculated. The reactions yielding high sensitivity coefficients are expected to play more important roles in NO_x formation. Therefore, to predict NO_x accurately, the pre-exponential factors of reactions with high sensitivity coefficients must be known accurately.

The numerical sensitivity analysis method can be described as follows. For an initial value problem which can be described by the following equation,

$$f(t,u,v,u',p) = 0 \tag{6}$$

if some variables are governed by algebraic equations rather than differential equations, then they can be described by

$$g(t,u,v,p) = 0 \tag{7}$$

In order to perform sensitivity analysis based on parameter p, Eqs. (6) and (7) need to differentiated with respect to p; this yields

$$\frac{\partial f}{\partial u} s_u + \frac{\partial f}{\partial v} s_v + \frac{\partial f}{\partial u'} s_u' + \frac{\partial f}{\partial p} = 0 \tag{8}$$

$$\frac{\partial g}{\partial u} s_u + \frac{\partial g}{\partial v} s_v + \frac{\partial g}{\partial p} = 0 \tag{9}$$

Equations (6) and (7) are differential and algebraic equations, respectively, while Eqs. (8) and (9) are sensitivity differential equations for Eqs. (6) and (7), respectively, obtained by differentiating Eqs. (6) and (7) with respect to the sensitivity parameter p. The quantities t, u, v are representative of time, a state variable, and an algebraic variable. S_u and S_v are sensitivity variables for the state and algebraic variables, respectively, defined as:

$$s_u = \frac{\partial u}{\partial p} \tag{10}$$

$$s_v = \frac{\partial v}{\partial p} \tag{11}$$

Note that the algebraic variables are essentially the same as the state variables, i.e., species concentrations in the present case. If some species are assumed to be at quasi-steady state, then the variables representing their concentrations become algebraic variables instead of state variables that must be obtained by solving differential equations. Such algebraic variables are represented in the algebraic equation, Eq. (7). Specifically, in this application, the concentration of NO is a state variable, while the concentrations of N, N_2O, NO_2, NH, and HNO are either state variables or algebraic variables depending whether the quasi-steady-state assumption is applied or not. Also, more often than not, normalized sensitivity variables are used since they are more meaningful for widely different orders of magnitude of the sensitivity parameters (pre-exponential factors here). The normalized forms of Eqs. (10) and (11) are:

$$s_u^{\text{norm}} = \frac{\partial u}{u} \Big/ \frac{\partial p}{p} = \frac{\partial \ln u}{\partial \ln p} \tag{12}$$

$$s_v^{\text{norm}} = \frac{\partial v}{u} \Big/ \frac{\partial p}{p} = \frac{\partial \ln v}{\partial \ln p} \tag{13}$$

In this paper, a differential-algebraic equations solver, DASPK 3.0, developed by Li and Petzold [29] is used to solve the equations using the direct method [15]. As part of the sensitivity analyses, the quasi-steady-state assumption (QSSA), which is often used in NO_x modeling, is examined.

Usually species such as N, N_2O, NO_2, NH, and HNO are considered to be at quasi-steady state, which greatly simplifies the calculations. This assumption will be examined later in this paper. Note that if this assumption is used, the five ordinary differential equations related to these five species become algebraic equations. To solve the resulting set of differential equations and mixed (differential and algebraic) equations, the DASPK 3.0 software is used. This software uses the backward differentiation formula method of variable step size and variable order to rewrite the nonlinear equations, and then solves them using a modified Newton's method. Further details on these methods are available in Ref. [29]. Since the Jacobian matrix is required in the solution procedure, the user has the choice of manually providing it as input, which is tedious and sometimes difficult to calculate, or of using the automatic numerical differencing evaluation provided in the software. The latter option often results in a singular Jacobian matrix when the system is stiff. So in this work, the automatic differentiation software, ADIFOR 2.0 [30], is used to perform the differentiation whenever finite differencing is required.

Results

The total predicted NO formation curves in the cylinder from the extended Zel'dovich mechanism (EZM) and super-extended Zel'dovich mechanism (SEZM) compared with experimental results are shown in Fig. 2. The EZM consists of the first three reactions listed in the Appendix, while the SEZM consists of all the 43 reactions listed in the Appendix, including thermal NO_x mechanism, N_2O mechanism, and HNO mechanism, etc. The experimental results were measured from the exhaust gas with a chemiluminiscent detector and shown by a triangle in Fig. 2. A good agreement is evident between the super-extended Zel'dovich mechanism prediction and the experimental results. The SEZM gives about 6% error compared to experimental results while the EZM gives around 60% prediction error. This shows that the SEZM can predict the NO_x formation satisfactorily. The focus of the remainder of this paper will be on the sensitivity aspects of the NO_x model.

Part 1: Investigation of the Quasi-Steady-State Assumption. The quasi-steady-state assumption (QSSA) [31] is often used in NO_x modeling to simplify the calculations. In this section the validity of QSSA for species such as N, N_2O, NO_2, NH, and HNO will be examined. First, the entire system of equations is solved without this assumption, i.e., NO, N, N_2O, NO_2, NH, and HNO concentrations are all calculated by integration of the governing nonlinear ordinary differential equations. Then the instantaneous relative errors obtained when employing the QSSA are calculated. The procedure used to calculate the QSSA error is as follows:

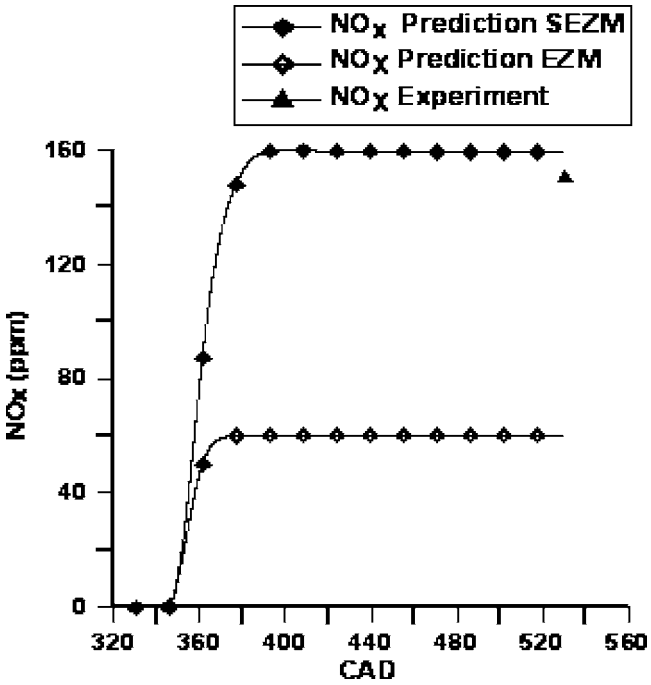

Fig. 2 Crank resolved NO_x prediction (EZM and SEZM) versus experimental NO_x measurement at an injection timing of 30 BTDC

$$\dot{\omega} = \dot{C} - \dot{D} \tag{14}$$

$$e = \frac{\dot{\omega}}{\dot{D}} \times 100\,\% = \left(\frac{\dot{C}}{\dot{D}} - 1\right) \times 100\% \tag{15}$$

where $\dot{\omega}$ is the net formation rate of any species, $\dot{C}$ is the formation rate of that species, $\dot{D}$ is the destruction rate of that species, and e is the instantaneous percentage QSSA error at a given crank angle. If the QSSA assumption is valid, e is small, i.e., the formation rate will be of the same order as the destruction rate.

It should be pointed out that the QSSA used here is based on the "full steady-state relationship" instead of the "truncated steady-state relationship" [31]. The full steady-state relationship is based on all reactions involving the QSSA species considered. Because five species are assumed to be at steady state, their concentrations are coupled by five non-linear equations. Solving the non-linear equations is usually not an easy task. In the present work, DASPK 3.0 is used to solve these equations by iteration. On the other hand, the truncated steady-state relationship involves decoupling the nonlinear equations to simplify the solution procedure. This may either be done by truncating the coupled terms if those terms are small compared to other terms or by using a partial equilibrium relationship to isolate the coupling between some species. A truncated steady-state relationship is not always obtainable and its feasibility depends on the specific application. But once obtained, it will greatly simplify the calculations by turning the nonlinear equations into linear equations. In any case, the fully steady-state relationship remains the more accurate choice between the two because it represents the complete physics.

There are four zones considered in the combustion model, so the validity of QSSA will be examined for each zone except the unburned zone, which does not yield any NO_x. Figure 3 shows the instantaneous QSSA error for the packet zone. Of the 123 total packets used in the combustion model, only the first packet introduced into the cylinder at the beginning of fuel injection will be considered here, as a representative case. From Fig. 3 it can be seen that except for the first few time steps, in which the QSSA error is high, the QSSA error is minimal for the remainder of the calculation time steps. The reason for the invalidity of QSSA for the initial few time steps may be explained as follows. Initially, there is no N, N_2O, NO_2, NH, or HNO in the packet, i.e., their concentrations are zero. For the first few time steps, their concentrations remain low. Thus, their destruction rates are smaller than their formation rates (if the concentration of one species is zero, then its destruction rate must be zero from the law of mass action). From Eq. (15) the QSSA error must be large if destruction rate is much smaller than the formation rate. For example, if the QSSA error is 40%, then the formation rate is 1.4 times the destruction rate for a given species. Note that as time elapses, the QSSA error may become negative because the destruction rate exceeds the formation rate. But from Fig. 3, after the first few time steps, whether QSSA error is positive or negative, the absolute value is very small (close to zero). So, in fact, the formation rate is about the same as the destruction rate, which is the basis of the QSSA. Similar results were also obtained for other packets and this justifies the use of QSSA for the packet zone.

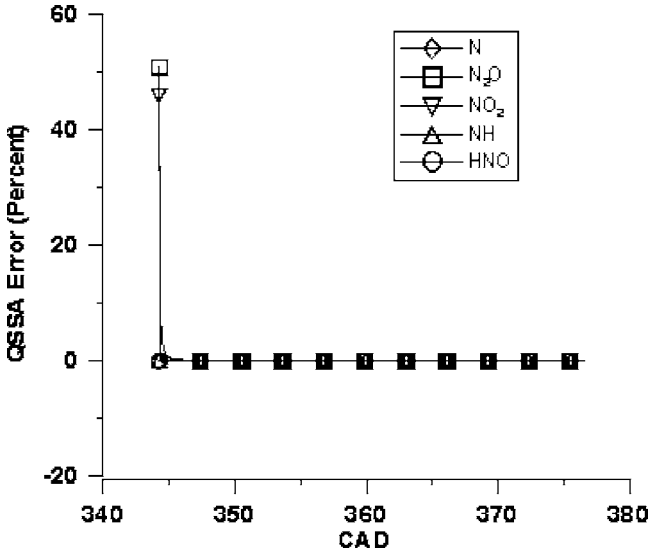

Fig. 3 QSSA error for five species and temperature (TP (1,1)) for packet (1,1) versus crank angle

Figure 4 shows the QSSA error for N, N_2O, NO_2, NH, and

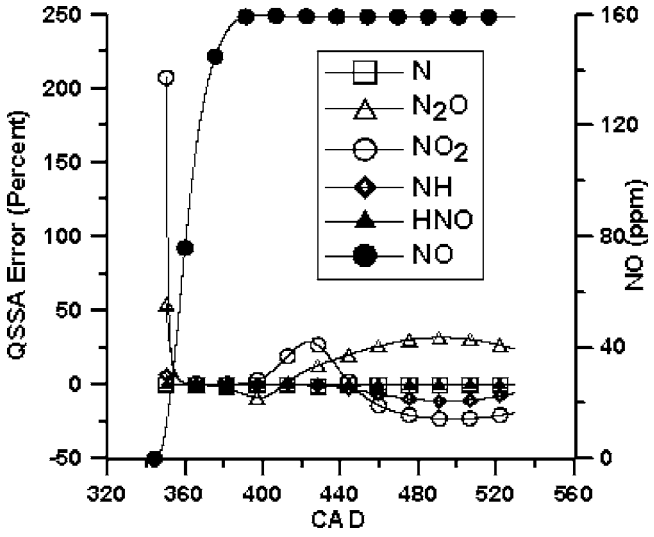

Fig. 4 QSSA error for five species for the burned zone and total engine NO prediction versus crank angle

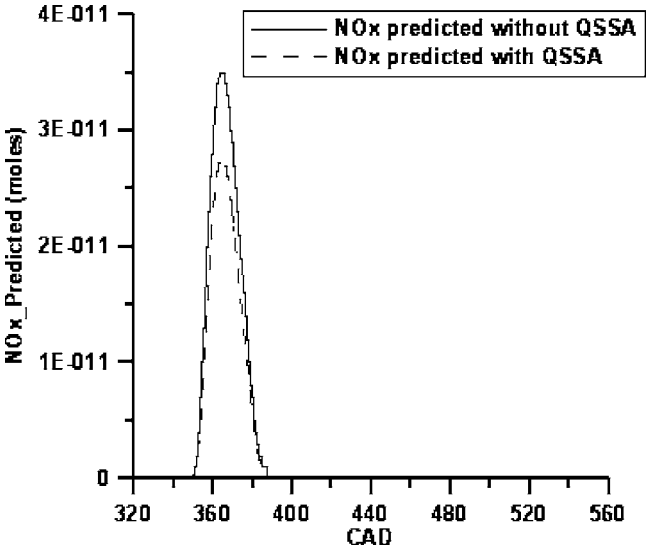

Fig. 5 Comparison of instantaneous NO_x predicted from the flame zone with and without QSSA

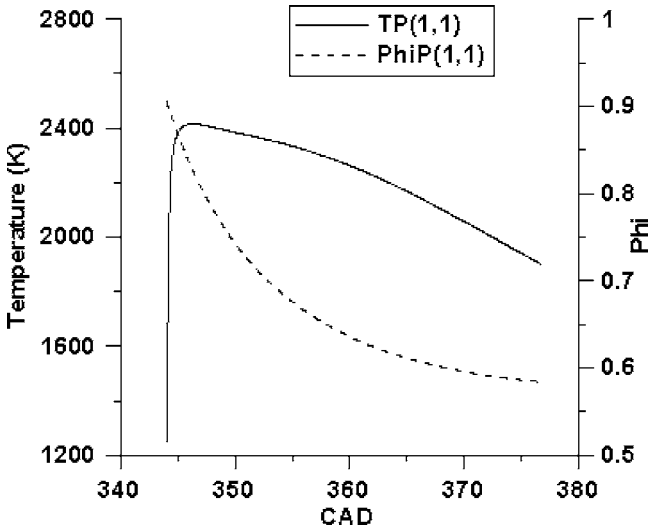

Fig. 6 Temperature and equivalence ratio history of the first injected packet in the packets zone

HNO for the burned zone and the total predicted NO for the engine. The QSSA error for the burned zone appears significant for much of the calculation period. After 400 deg crank angle (CAD) the QSSA error worsens considerably for NO_2 and N_2O, with either formation rate much greater than destruction rate or vice versa. At 350 CAD and earlier, the formation rate is much greater than the destruction rate for the same reason mentioned for the packets zone but the effect is more pronounced than for the packets because of the lower temperature of the burned zone. It appears that the QSSA leads to considerable inaccuracy for the burned zone. However, if the total predicted NO curve shown in Fig. 4 together with the QSSA error curves is examined, it shows that for the greater part of the NO formation period, starting from around 345 CAD to about 400 CAD where NO freezes, the QSSA error is small. In this period the QSSA may be used without expecting large associated errors. This observation will be discussed further below.

Similarly, for the flame zone, the QSSA is valid for species N, NH, and HNO as in the burned zone, i.e., QSSA is valid for most of the time interval of NO formation. However, for N_2O and NO_2, the QSSA error again behaves differently indicating that QSSA for N_2O and NO_2 is not valid. This can be verified from Fig. 5 where instantaneous NO predicted from the flame zone with and without QSSA are compared. The instantaneous NO with prediction without the QSSA is higher than with QSSA as much as 30%. However, as will be seen, this difference of NO prediction from the flame zone will not affect the total NO prediction from the cylinder.

The invalidity of QSSA in the flame zone is caused not by the species or the reactions, but by the fuel-lean nature of the flame zone itself. As shown in Figs. 6–8, the equivalence and ratio and temperature history of both flame zone and burned zone are significantly less than that of the packet zone. It is noted that the equivalence ratio of the flame zone is constant because of the homogeneous mixture of natural gas and air. For the burned zone, the equivalence ratio is constant before the dumping of packets; then increases as dumping occurs and finally remains constant again after dumping. First, the lean combustion in the flame zone leads to relatively lower flame temperatures (compared to the packets) and therefore, lower NO formation rates. In addition, the flame zone continuously experiences entrainment of fresh natural gas-air mixture and expulsion of burned products from the previous time step to the burned zone. This method of treating the flame zone mass transfers dictates that the combustion products stay in the flame zone for only one combustion time step. As mentioned earlier, it is assumed that combustion and NO formation are decoupled, and only the NO from combustion products is calculated. Since the combustion is lean and the combustion products stay in the flame zone for a very short time, the concentration of species such as N_2O and NO_2 remain very low, which means their formation rates are always greater than their destruction rates. In other words, these species are transferred to the burned zone before their concentrations become high enough to cause the destruction rates to increase to the magnitude of the formation rates. Consequently, the QSSA is not valid for the flame zone. It is worth noting that the QSSA is still applicable to the species N, NH, and HNO; this shows that they are more reactive and more amenable to the QSSA than are N_2O and NO_2.

Having examined the validity of the QSSA for the three zones, the NO predictions with and without using the QSSA can now be compared. Figure 9 shows such a comparison. The difference between the NO predicted in both cases (with and without QSSA) is only about three ppm ($\sim 2\%$). For clarification, NO formed from the packets zone and flame zone feeding into the burned zone are

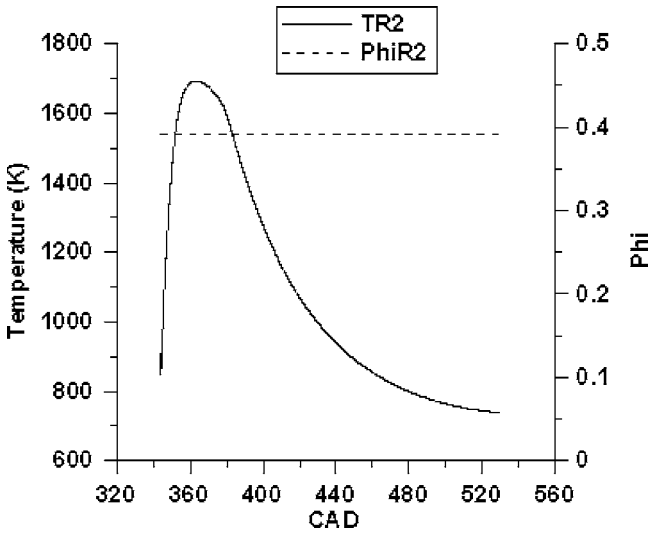

Fig. 7 Temperature and equivalence ratio history of flame zone

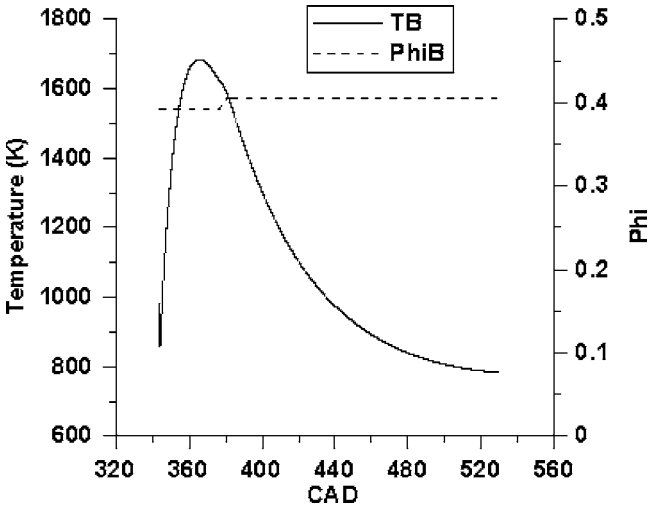

Fig. 8 Temperature and equivalence ratio history of burned zone

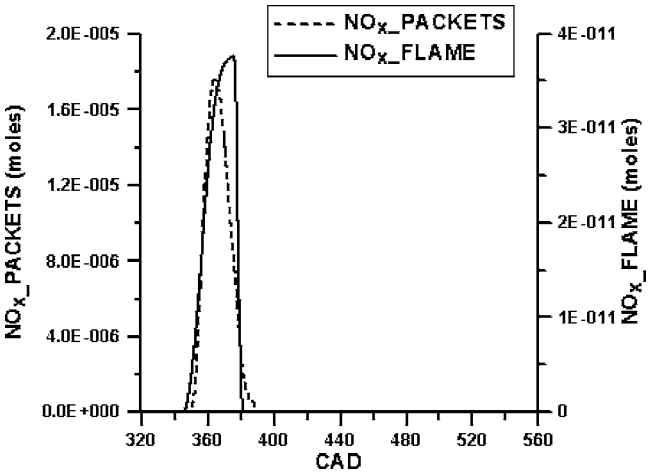

Fig. 10 Comparison of NO_x formed from packets zone and flame zone

also plotted. The obvious question that arises is "*Why is the net* NO *prediction almost invariant although the QSSA is clearly not valid for the flame zone?"* This is because, as discussed above, the combustion in the flame zone is lean. As a result, the flame temperatures are lower than packet temperatures. Therefore, very little of the total NO formed comes from the flame zone. Moreover, the residence time of the combustion products in the flame zone is very small. Consequently, the net NO formed, which is obtained by numerically integrating the NO formation rate over the short residence time, is also small. Clearly, these results indicate that the invalidity of the QSSA in the flame zone does not significantly affect the overall NO prediction.

To corroborate the preceding argument, the instantaneous NO present in the packets zone is compared to that present in the flame zone in Fig. 10. Both plots dropping to zero are the result of dumping completely burned packets and flame zones to the burned zone. It is noted that at their peak value almost one million times more NO is formed in the packets zone than in the flame zone. Evidently, such a small amount of NO formed in the flame zone will have no effect on the total NO prediction. In fact, even the three ppm NO prediction differences in Fig. 9 result from the fact that the QSSA is not completely valid for the burned zone over the entire calculation period.

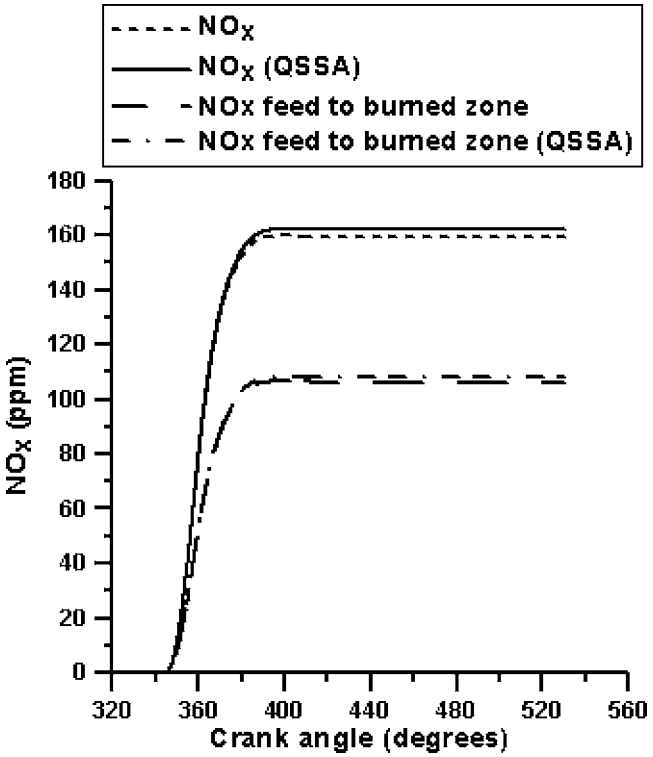

Fig. 9 Comparison of NO_x prediction with and without QSSA

Part 2: Sensitivity Analysis of NO_x Formation Reactions. In this section, results from the sensitivity analysis of the NO mechanism are discussed. To ensure maximum possible accuracy, the sensitivity analysis is done without using the QSSA for N, N_2O, NO_2, NH, and HNO, i.e., all of these species are calculated from kinetics, similar to the NO calculation. Also, since little NO is formed in the flame zone, the flame zone is excluded from the sensitivity analysis. The results are shown as normalized sensitivity coefficients and only the important reactions (identified by large sensitivity coefficients) are shown. Results from both the packets zone and the burned zone are discussed.

Figure 11 shows the sensitivity coefficients for the first injected packet (a representative of the packets zone) at 360 CAD. At this instant, Reactions 1, 2, 3, 4, 10, 17, and 21 (see the Appendix) all have relatively significant sensitivity coefficients. Among these, Reactions 1, 2, 3 constitute the extended-Zel'dovich mechanism with Reaction 1 having higher sensitivity coefficients than Reactions 2 or 3. This conforms to the current understanding of the

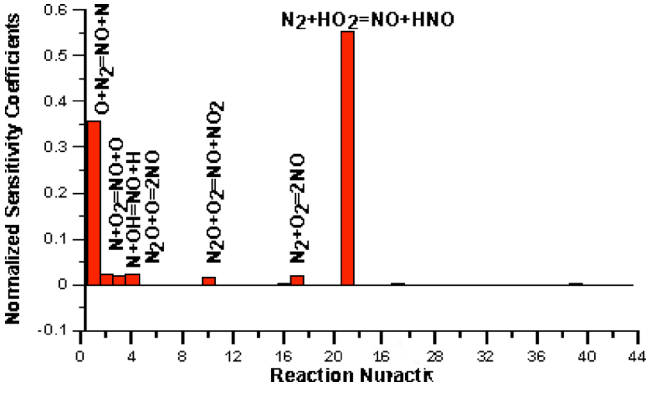

Fig. 11 Normalized sensitivity coefficients of important reactions for the first injected packet at 360 crank angle degrees

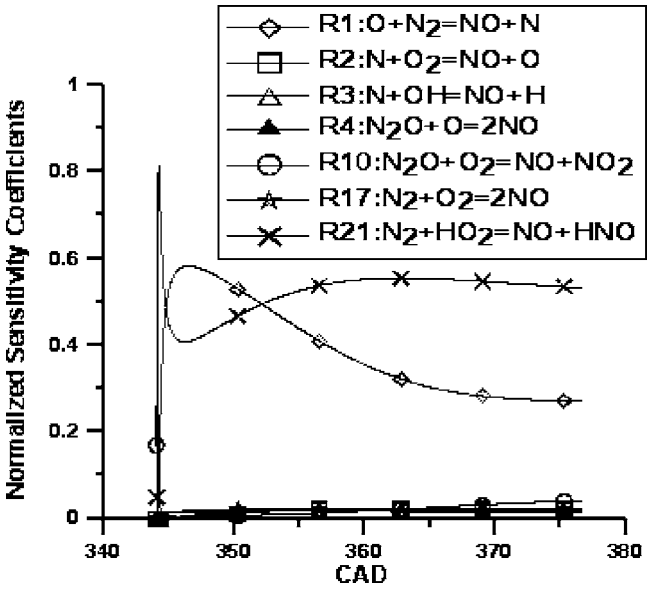

Fig. 12 Normalized sensitivity coefficients of important reactions for the first injected packet versus crank angle

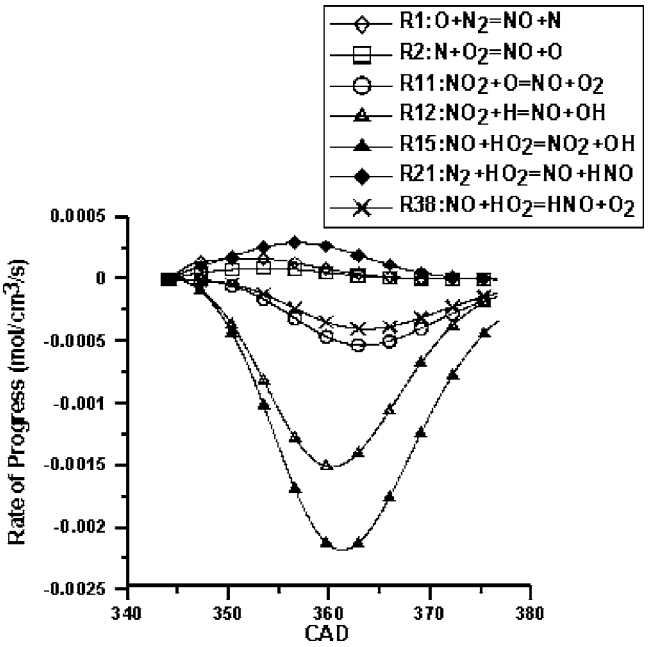

Fig. 13 Rate of progress of important reactions for the first injected packet versus crank angle

extended-Zel'dovich mechanism or "thermal mechanism," i.e., Reaction 1 is the rate-limiting step among the three reactions. Reaction 4 is one of the reactions of the "Malte and Pratt N_2O mechanism" [11]. It also has a significant sensitivity coefficient, indicating that significant amounts of NO are formed through this mechanism. Reaction 17 accounts for the NO formed directly from N_2 and O_2. This reaction will contribute to some of the NO formed at high temperatures. Reaction 21, which forms NO and HNO from N_2 and HO_2, has the highest sensitivity coefficient. The reaction rate of this reaction is given by Bahn [32] and the reaction is also used in Lange's NO_x model [33]. This reaction will affect the predicted NO considerably in view of its high sensitivity coefficient. Consequently, this reaction rate needs to be known as accurately as possible for accurate predictions using the current NO_x mechanism. This reaction rate is not given in any detailed NO_x formation mechanism since it is not an elementary reaction but is an empirical global reaction. Figure 12 shows the sensitivity coefficients of the important reactions as a function of crank angle. It shows that the most important reactions for the packets zone are Reactions 1 and 21.

Figures 11 and 12 provide a glimpse of the important reactions for the packet zone. To know how NO is formed from nitrogen, the rate of progress for each reaction should be examined. The rate of progress variable q_i for the ith reaction is given by the difference of the formation and destruction rates as

$$q_i = K_{fi}\prod_{k=1}^{K}[X_k]^{\upsilon'_{ki}} - K_{ri}\prod_{k=1}^{K}[X_k]^{\upsilon''_{ki}} \tag{16}$$

where $[X_k]$ is the molar concentration of the kth species present in the ith reaction and υ'_{ki} and υ''_{ki} are the stoichiometric coefficients of the species present in the reactants and products, respectively.

Figure 13 shows the rate of progress of important reactions. The main reactions with high rate of progress, Reactions 1, 2, 11, 12, 15, 21, and 38, are plotted versus crank angle. It may be noted that these reactions are not all exactly the same as those that have high sensitivity coefficients. This apparent discrepancy can be explained as follows. Sensitivity results give the most sensitive reactions with regard to the NO production, while Fig. 13 gives the reactions with high rate of progress, although not necessarily with high sensitivity coefficients. The reactions indicated by both results may be thought of as the rate-limiting reactions. In this sense, Reactions 1 and 21 are rate limiting for the packet zone. From Fig. 13, it can be seen that NO formation in the packets zone follows two main pathways, (i) and (ii)

$$\text{(i)}\quad O + N_2 = NO + N \tag{R1}$$

$$N + O_2 = NO + O \tag{R2}$$

In path (*i*), nitrogen is converted to NO through Reaction 1. The N formed in Reaction 1 will react with O_2 to form NO again. This is the standard Zel'dovich mechanism.

$$\text{(ii)}\quad N_2 + HO_2 = NO + HNO \tag{R21}$$

$$NO + HO_2 = HNO + O \tag{R38}$$

In path (ii), nitrogen reacts with HO_2 to form NO and HNO; HNO will react with O to form NO again. The rate of progress is negative in Reaction 38, indicating that NO is actually formed from Reaction 38 occurring in the reverse direction.

Path (i) is quite straightforward and has been reported by numerous researchers. Path (ii) involves NO formation through HNO species. As indicated above, both Reactions 21 and 38 are not elementary reactions but global reactions; there is no guarantee that the NO will be formed through the two reactions specifically. However, these two reactions do give us a hint that the NO will be formed through HNO species, which could be formed through species such as N_2O. In fact, Zabetta and Kilpinen [34] proposed an "N_2O extension mechanism," which is a set of five reactions in which N_2O is oxidized to NO via NH and HNO intermediates. This mechanism acts very much like path (ii) identified here and it is believed that Reactions 21 and 38 are global reactions, perhaps including the five reactions of the "N_2O extension mechanism."

Reactions 11, 12 and 15 in Fig. 13 are only involved in the conversion between NO and NO_2. NO_2 is formed from NO through Reactions 11 and 12 and is converted back to NO through Reaction 15. These three reactions form the basis of the NO_2 quasi-steady-state assumption.

Figure 14 shows the normalized sensitivity coefficients for the burned zone at 360 CAD. The burned zone is cooler than the packets zone, so a different set of important reactions is expected.

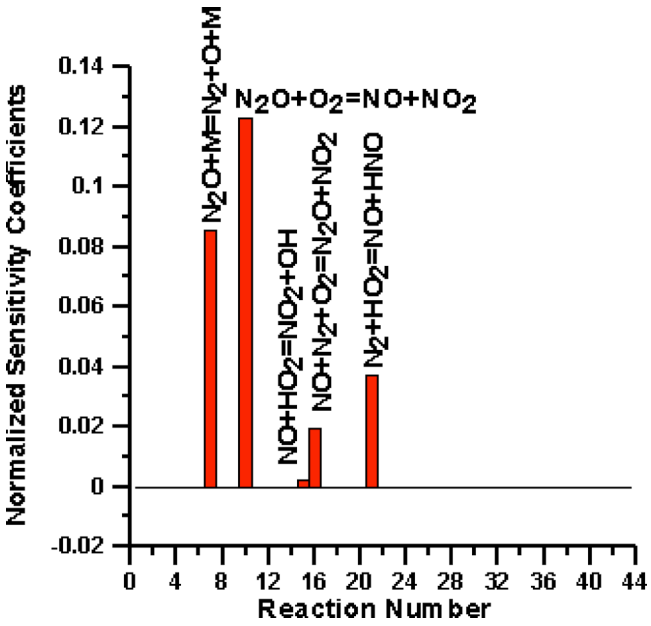

Fig. 14 Normalized sensitivity coefficients of important reactions for the burned zone at 360 crank angle

These include Reactions 7, 10, 15, 16 and 21. Reaction 7 between nitrogen and atomic oxygen forms nitrous oxide, which is important because N_2O is the source of the NO from the Malte and Pratt mechanism [11]. Reaction 10 has the largest coefficient, so its reaction rate determines the rate of conversion of N_2O to NO as well as the direction of Reaction 7. Since these are two competing reactions in the sense of N_2O dissociation, the N_2O formed from the reverse Reaction 7 will either be converted to NO via Reaction 10, or converted back to N_2 via Reaction 7. Reaction 21 is also important as it is for the packets zone. Reaction 15, 16 are reactions related to the NO-NO_2 conversion and so they are important since they decide whether the final NO_x will be in the form of NO or NO_2.

Figure 15 shows the normalized sensitivity coefficients for important reactions for the burned zone plotted against crank angle. Reaction 10 dominates the entire calculation period with the highest sensitivity coefficient. Interestingly, Reactions 1, 2, and 3,

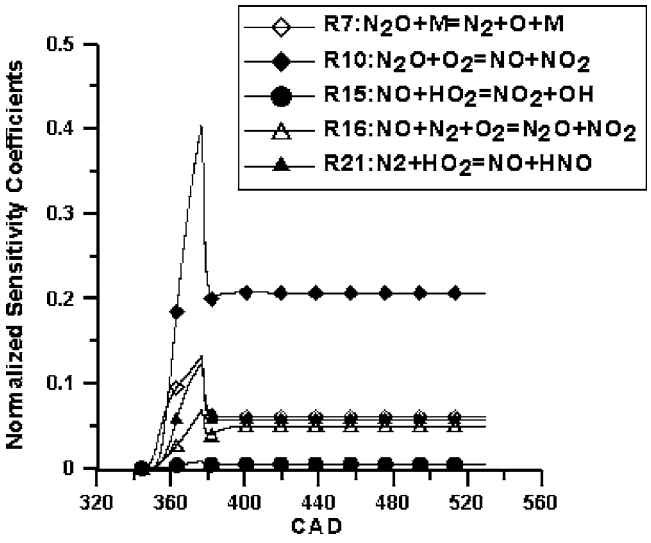

Fig. 15 Normalized sensitivity coefficients of important reactions for the burned zone versus crank angle

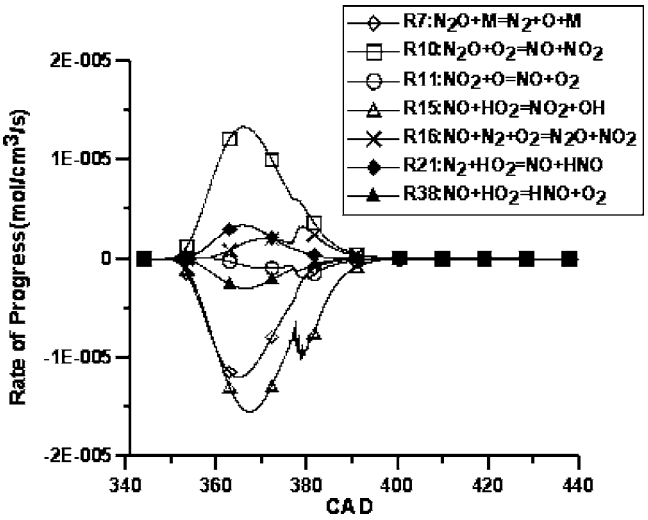

Fig. 16 Rate of progress of important reactions for the burned zone versus crank angle

which form the extended Zel'dovich mechanism, are no longer important for the burned zone. Because the burned zone temperature is lower than the packets zone temperature [18], the extended Zel'dovich mechanism, also called the "thermal mechanism" because of its temperature dependence, becomes less important.

Similar to the packets zone, the rate of progress of each reaction for the burned zone is examined to yield additional information about NO_x formation. Figure 16 shows that Reactions 7, 10, 11, 15, 16, 21 and 38 exhibit significant rates of progress. From Fig. 12 it can be concluded that there are two main NO formation paths, (i) and (ii), in the burned zone. The first path is:

$$\text{(i)}\quad N_2O + M = N_2 + O + M \qquad \text{(R7)}$$

$$N_2O + O2 = NO + NO_2 \qquad \text{(R10)}$$

For path (*i*), Fig. 16 shows that the formation rate of Reaction 7 is negative, which means N_2O is formed through Reaction 7. The formation rate of Reaction 10 is positive, so NO is formed via Reaction 10. The second path is:

$$\text{(ii)}\quad N_2 + HO_2 = NO + HNO \qquad \text{(R21)}$$

$$NO + HO_2 = HNO + O \qquad \text{(R38)}$$

For path (ii), the formation rate of Reaction 21 is positive, so NO and HNO are formed via Reaction 21. The negative rate of progress of Reaction 38 means HNO is converted back to NO.

The first path identified as important for the burned zone is also described by Zabetta and Kilpinen [34] as the "N_2O intermediate mechanism." In their results the N_2O is converted to NO along a different pathway as:

$$N_2O + O = NO + NO \qquad \text{(R4)}$$

Even though this is a different pathway to convert N_2O to NO as identified in Ref. [34], this discrepancy is attributed to the fact that Reaction 10 is not an elementary reaction and Reaction 4 is included in Reaction 10 implicitly. Also Zabetta and Kilpinen [34] pointed out the "N_2O intermediate mechanism" can only assume importance for fuel-lean mixtures. This could also be supported by the fact that the equivalence ratio of the burned zone is about 0.4, whereas the equivalence ratio for a typical packet, like Packet (1, 1) is between 0.88 and 1.1.

Reactions 11, 15, and 16 involve the inter-conversion of NO and NO_2. From the positive or negative value of each reaction's rate of progress, it can be seen that the NO_2 is formed from NO via Reactions 11 and 16, and is converted back to NO mainly via

Reaction 15. These three reactions (Reactions 11, 15 and 16) form the basis of the QSSA of NO_2 species for the burned zone. It was mentioned earlier that Reactions 11, 12 and 15 form the basis of the QSSA for the packets zone. The different sets of reactions required for the same QSSA for NO_2 species in different zones indicate that it is difficult to determine a truncated steady-state relationship suitable for all cases.

Conclusions

The NO_x formation in pilot-ignited natural gas engines was modeled using a super-extended Zel'dovich mechanism based upon a multi-zoned phenomenological combustion model. A sensitivity analysis was performed for the NO_x model in the different zones (packets or pilot fuel zone, flame zone, and burned zone) of the combustion model. The results obtained are summarized below:

1. The quasi-steady-states assumption (QSSA) is valid for the packets zone. It remains valid for most of the calculation time for the burned zone, but is not valid for the flame zone as it is currently treated.
2. Invoking the QSSA for the flame zone does not significantly affect NO_x predictions because very little NO is formed from the flame zone.
3. The primary NO formation paths for the packets zone are:

$$O + N_2 = NO + N \quad (R1)$$

$$N + O_2 = NO + O \quad (R2)$$

$$N_2 + HO_2 = NO + HNO \quad (R21)$$

$$NO + HO_2 = HNO + O \quad (R38)$$

4. The primary NO formation paths for the burned zone are:

$$N_2O + M = N_2 + O + M \quad (R7)$$

$$N_2O + O_2 = NO + NO_2 \quad (R10)$$

$$N_2 + HO_2 = NO + HNO \quad (R21)$$

$$NO + HO_2 = HNO + O \quad (R38)$$

5. The pre-exponential factors for Reactions 1, 7, 10, and 21 are the most sensitive parameters of the model; thus, they should be obtained as accurately as possible.
6. The most sensitive parameters for NO_x modeling are the temperature and local equivalence ratio of the cylinder. The absolute NO_x predictions were not the focus of this paper because the combustion model is still being developed. However, the results of this paper provide some indications of the other sensitive parameters.
7. Finally, it must be noted that the reactions considered in this paper are not all elementary reactions. The reactions rates obtained from published data also have some uncertainty. Therefore, a sensitivity analysis was done here to find the most sensitive parameters.

Acknowledgment

The authors wish to thank The Center for Advanced Vehicle Technologies at The University of Alabama, which receives partial funding from the U. S. Dept. of Transportation Federal Highway Administration under Grant No. DTFH61-99-X-00007, for funding this project.

Nomenclature

K_f = forward reaction rate
K_r = backward reaction rate
K_c = equilibrium constant based on concentrations
K_p = equilibrium constant based on partial pressure
P_{atm} = standard atmosphere pressure
ν_k = stoichoimetric coefficients
R = universal gas constant
T = temperature
S^0 = absolute entropy
H = absolute enthalpy
ΔS^0 = absolute entropy difference
ΔH^0 = absolute enthalpy difference
$[A]$ = concentrations of species A
t = time
u = state variable
v = algebraic variable
p = sensitivity parameter
s_u = state sensitivity variable
s_v = algebraic sensitivity variable
$\dot{\omega}$ = net formation rate
$\dot{C}$ = production rate
$\dot{D}$ = destruction rate
e = relative steady states assumption error
q = rate of progress of reaction

Appendix (from Ref. [9])

The following table shows the forward reaction rate for the reaction equations considered in the modified super-extended Zel'dovich mechanism. Rate coefficients are in the form of $K_f = AT^b \exp(-E_0/T)$, where units are moles, cubic centimeters, seconds, Kelvin.

	Reaction	A (cm^3/mole s)	b	E_0 (K)
1.	$N_2+O \leftrightarrow NO+N$	1.800E+14	0.0	38,370
2.	$N+O_2 \leftrightarrow NO+O$	1.800E+10	1.0	4680
3.	$N+OH \leftrightarrow NO+H$	7.100E+13	0.0	450
4.	$N_2O+O \leftrightarrow 2NO$	6.900E+13	0.0	13,400
5.	$N_2O+O \leftrightarrow N_2+O_2$	1.000E+14	0.0	14,100
6.	$N_2O+H \leftrightarrow N_2+OH$	7.587E+13	0.0	7600
7.	$N_2O+M \leftrightarrow N_2+O+M$	1.600E14	0.0	25,969
8.	$N_2O+N \leftrightarrow NO+N_2$	1.000E+13	0.0	10,000
9.	$N_2O+NO \leftrightarrow NO_2+N_2$	1.000E+14	0.0	25,000
10.	$N_2O+O_2 \leftrightarrow NO+NO_2$	6.000E+14	−1.5	4985
11.	$NO_2+O \leftrightarrow NO+O_2$	1.000E+13	0.0	300
12.	$NO_2+H \leftrightarrow NO+OH$	3.467E+14	0.0	740
13.	$NO_2+NO_2 \leftrightarrow 2NO+O_2$	1.995E+12	0.0	13,500
14.	$NO_2+N \leftrightarrow O+N_2O$	5.012E+12	0.0	0.0
15.	$NO+HO_2 \leftrightarrow NO_2+OH$	2.089E+12	0.0	−240
16.	$NO+N_2+O_2 \leftrightarrow N_2O+NO_2$	2.300E+14	0.0	18,000
17.	$N_2+O_2 \leftrightarrow 2NO$	2.730E+13	0.0	53,800
18.	$NO+O_2 \leftrightarrow N+O_3$	2.700E+14	−1.0	63,140
19.	$NO_2+O \leftrightarrow N+O_3$	3.700E+14	−0.5	40,280
20.	$NO+O_3 \leftrightarrow O+NO_3$	6.000E+14	−1.5	8000
21.	$N_2+HO_2 \leftrightarrow NO+HNO$	5.925E+10	0.5	21,550
22.	$N+OH \leftrightarrow NH+O$	1.290E+14	0.0	2165
23.	$N+H_2 \leftrightarrow NH+H$	1.320E+15	0.0	11,230
24.	$N+H_2O \leftrightarrow NH+OH$	3.590E+15	0.0	18,430
25.	$NH+OH \leftrightarrow NO+H_2$	1.600E+12	0.56	755
26.	$NH+O \leftrightarrow NO+H$	5.000E+11	0.5	0.0
27.	$NH+OH \leftrightarrow HNO+H$	6.440E+11	0.0	1460
28.	$NH+O_2 \leftrightarrow HNO+O$	4.380E+12	0.0	6546
29.	$HNO+M \leftrightarrow H+NO+M$	1.900E+16	0.0	25,179
30.	$HNO+OH \leftrightarrow NO+H_2O$	2.100E+12	0.5	0.0
31.	$HNO+H \leftrightarrow NO+H_2$	1.400E+13	0.0	1510
32.	$HNO+O \leftrightarrow NO+OH$	5.000E+11	0.5	0.0
33.	$NH+O \leftrightarrow N_2O+H$	2.240E+13	0.0	10,600
34.	$N_2O+NH \leftrightarrow N_2+HNO$	1.995E+12	0.0	3000
35.	$NO_2+NH \leftrightarrow HNO+NO$	1.000E+11	0.5	2000
36.	$N+H_2O \leftrightarrow NH+OH$	1.000E+13	0.0	1000
37.	$N+HO_2 \leftrightarrow NH+O_2$	1.000E+13	0.0	1000

	Reaction	A (cm^3/mole s)	b	E_0 (K)
38.	$NO+HO_2 \leftrightarrow HNO+O$	1.900E+11	0.0	1000
39.	$HNO+NO \leftrightarrow N_2O+OH$	6.140E+12	0.0	17,100
40.	$HNO+N \leftrightarrow NO+NH$	1.000E+13	0.0	1000
41.	$HNO+HNO \leftrightarrow 2NO+H_2$	2.000E+10	0.5	2230
42.	$NH+N \leftrightarrow N_2+H$	6.310E+11	0.5	0.0
43.	$NH+N_2 \leftrightarrow N+H+N_2$	3.160E+21	−2.0	42,000

(Enhanced third-body efficiencies: $H_2O=10.0$, $N_2=2.0$, $O_2=2.0$, $H_2=2.0$ [21])

References

[1] Krishnan, S. R., Srinivasan, K. K., Singh, S., Bell, S. R., Midkiff, K. C., Gong, W., Fiveland, S., and Willi, M., 2004, "Strategies of for Reduced NO_x Emissions in Pilot-Ignited Natural Gas Engines," ASME J. Eng. Gas Turbines Power, **126**(3), pp. 665–671.

[2] Srinivasan, K. K., Krishnan, S. R., Sing, S., Midkiff, K. C., Bell, S. R., , W., Fiveland, S., and Willi, M., 2003, "The Advanced Low Pilot Ignited Natural Gas Engine – A Low NO_x Alternative to The Diesel Engine," ASME Paper No. IJPGC2003-40098.

[3] Singh, S., Krishnan, S. R., Srinivasan, K. K., Midkiff, K. C., and Bell, S. R., 2004, "Effect of Pilot Injection Timing, Pilot Quantity and Intake Charge Conditions on Performance and Emissions for An Advanced Low-Pilot-Ignited Natural Gas Engine," Int. J. Eng. Res., **5**(4), pp. 329–348.

[4] Tomita, E., Kawahara, N., Piao, Z., and Yamaguchi, R., 2002, "Effect of EGR and Early Injection of Diesel Fuel on Combustion Characteristics and Exhaust Emissions in a Methane Dual Fuel Engine," SAE Paper No. 2002-01-2723.

[5] Dodge, L. G., Kubesh, J. T., Naegeli, D. W., and Cambell, P. F., 1998, "Modeling NO_x Emissions from Lean-Burn Natural Gas Engines," SAE Paper No. 981389.

[6] Hampson, G. J., Xin, J., Liu, Y., Han, Z., and Reitz, R. D., 1996, "Modeling of NO_x Emissions with Comparison to Exhaust Measurement for a Gas Fuel Converted Heavy-Duty Diesel Engine," SAE Paper No. 961967.

[7] Wang, G., Li, G., Liu, Y., Chen, L., Zhang, X., and Lu, J., 1999, "A Developed Model for Emissions Prediction of a DI Diesel Engine," SAE Paper No. 1999-01-0233.

[8] Pirouzpanah, V., and Kashani, B. O., 1999, "Prediction of Major Pollutants Emission in Direct-Injection Duel Fuel Diesel and Natural Gas Engines," SAE Paper No. 1999-01-0841.

[9] Bowman, C. T., 1975, "Kinetics of Pollutant Formation and Destruction in Combustion," Prog. Energy Combust. Sci., **1**, pp. 33–45.

[10] Tomeczek, J., and Gradon, B., 1997, "The Role of Nitrous Oxide in the Mechanism of Thermal Nitric Oxide Formation Within the Flame Temperature Range," Combust. Sci. Technol., **125**, pp. 159–180.

[11] Malte, P. C., and Pratt, D. T., 1975, "Measurement of Atomic Oxygen and Nitrogen Oxides in Jet Stirred Combustion Engines," *Fifteenth Symposium (International) on Combustion*, The Combustion Institute, Pittsburgh, pp. 543–55.

[12] Mellor, A. M., 1998, "Skeletal Mechanism for NO_x Chemistry in Diesel Engines," SAE Paper No. 981450.

[13] Turányi, T., 1990, "Sensitivity Analysis of Complex Kinetics Systems: Tools and Applications," J. Math. Chem., **5**, pp. 203–248.

[14] Olsson, J. O., and Andersson, L. L., 1987, "Sensitivity Analysis Based on an Efficient Brute-Force Method, Applied to an Experimental CH_4/O_2 Premixed Laminar Flame," Combust. Flame, **67**, pp. 99–109.

[15] Dunker, A. M., 1984, "The Decoupled Direct Method for Calculating Sensitivity Coefficients in Chemical Kinetics," J. Chem. Phys., **81**(5), pp. 2385–2393.

[16] Hwang, J. T., Dougherty, E. P., Rabitz, S., and Rabitz, H., 1978, "The Green's Function Method of Sensitivity Analysis in Chemical Kinetics," J. Chem. Phys., **69**(11), pp. 5180–5191.

[17] Hwang, J. T., 1983, "Sensitivity Analysis in Chemical Kinetics by the Method of Polynomial Approximations," Int. J. Chem. Kinet., **15**, pp. 959–987.

[18] Krishnan, S. R., 2005, "Experimental Investigations and Phenomenological Simulation of Combustion in a Low Pilot-Ignited Natural Gas Engine With a Focus on Advanced Injection Timings," Ph.D. dissertation, The University of Alabama, Tuscaloosa, AL.

[19] Miller, J. A., and Bowman, C. T., 1989, "Mechanism and Modeling of Nitrogen Chemistry in Combustion," Prog. Energy Combust. Sci., **15**, pp. 287–338.

[20] Smith, G. P., Golden, D. M., Frenklach, M., Moriarty, N. W., Eiteneer, B., Goldenberg, M. C., Bowman, T., Hanson, R., Song, S., Gardiner, W. C., Jr., Lissianski, V., and Qin, Z., http://www.me.berkeley.edu/grimech.

[21] Glaborg, P., Alzueta, M. U., Dam-Johansen, K., and Miller, J. A., 1998, "Kinetic Modeling of Hydrocarbon/Nitric Oxide Interactions in a Flow Reactor," Combust. Flame, **115**(1), 1–27.

[22] Coda Zabetta, E., Kilpinen, P., Hupa, M., Ståhl, K., Leppälahti, J., Cannon, M., and Nieminen, J., 2000, "Kinetics Modeling Study on the Potential of Staged Combustion in Gas Turbines for the Reduction of Nitrogen Oxide Emission from Biomass IGCC Plants," Energy Fuels, **14**, pp. 751–761.

[23] Lutz, A. E., Kee, R. J., and Miller, J. A., 1986, "Senkin: A Fortran Program for Predicting Homogeneous Gas Phase Chemical Kinetics with Sensitivity Analysis," Sandia National Laboratories Report No. SAND86-8209.

[24] Miller, R., Davis, G., Lavoie, G., Newman, C., and Gardner, T., 1998, "A Super-Extended Zel'dovich Mechanism for NO_x modeling and Engine Calibration," SAE Paper No. 980781.

[25] Tabaczynski, R. J., Ferguson, C. R., and Radhakrishnan, K., 1977, "A Turbulent Entrainment Model for Spark Ignition Engine Combustion," Trans. SAE, **86**, pp. 2414–2433.

[26] Miller, R., Russ, S., Weaver, C., Kaiser, E., Newman, C., Davis, G., and Lavoie, G., 1998, "Comparison of Analytically and Experimentally Obtained Residual Fractions and NO_x Emissions in Spark-Ignited Engines," SAE Paper No. 982562.

[27] Yang, H., Krishnan, S. R., Srinivasan, K. K., and Midkiff, K. C., 2003, "Modeling of NO_x Emissions Using a Super-Extended Zel'dovich Mechanism," ASME Paper No. ICEF2003-713.

[28] Gordon, S., and McBride, B. J., 1976, "Computer Program for Calculation of Complex Chemical Equilibrium Compositions, Rocket Performance, Incident and Reflected Shocks and Chapman-Jouguet Detonations," NASA Report No. SP-273.

[29] Li, S., and Petzold, L., "Design of New DASPK for Sensitivity Analysis," 1999, http://www.engineering.ucsb.edu/~cse.

[30] Bischof, C., Carle, A., Hovland, P., Khademi, P., and Mauer, A., 1998, "ADIFOR 2.0 Users' Guide," Technical Report CRPC-95516-S, http://www-unix.mcs.anl.gov/autodiff/ADIFOR.

[31] Wang, W., and Rogg, B., "Premixed Ethylene/Air and Ethane/Air Flames: Reduced Mechanisms Based on Inner Iteration," *Reduced Kinetic Mechanisms for Application in Combustion Systems*, Springer, Berlin, pp. 75–101.

[32] Bahn, G. S., 1968, *Reaction Rate Compilation for the H-O-N System*, Gordon and Breach, New York.

[33] Lange, H. B., Jr., 1972, "NO_x Formation in Premixed Combustion: a Kinetic Model and Experimental Data," *Air Pollution and Control* (AIChE Symposium Series 126), pp. 17–24.

[34] Zabetta, E. C., and Kilpinen, P., 2001, "Improved NO_x Submodel for In-Cylinder CFD Simulation of Low- and Medium-Speed Compression Ignition Engines," Energy Fuels, **15**, pp. 1425–1433.

Development of a Semi-implicit Solver for Detailed Chemistry in Internal Combustion Engine Simulations

Long Liang[1]
e-mail: lliang@wisc.edu

Song-Charng Kong[2]

Chulhwa Jung

Rolf D. Reitz

Engine Research Center,
University of Wisconsin-Madison,
1500 Engineering Drive,
Madison, WI 53706

An efficient semi-implicit numerical method is developed for solving the detailed chemical kinetic source terms in internal combustion (IC) engine simulations. The detailed chemistry system forms a group of coupled stiff ordinary differential equations (ODEs), which presents a very stringent time-step limitation when solved by standard explicit methods, and is computationally expensive when solved by iterative implicit methods. The present numerical solver uses a stiffly stable noniterative semi-implicit method. The formulation of numerical integration exploits the physical requirement that the species density and specific internal energy in the computational cells must be non-negative, so that the Lipschitz time-step constraint is not present and the computation time step can be orders of magnitude larger than that possible in standard explicit methods. The solver exploits the characteristics of the stiffness of the ODEs by using a sequential sort algorithm that ranks an approximation to the dominant eigenvalues of the system to achieve maximum accuracy. Subcycling within the chemistry solver routine is applied for each computational cell in engine simulations, where the subcycle time step is dynamically determined by monitoring the rate of change of concentration of key species, which have short characteristic time scales and are also important to the chemical heat release. The chemistry solver is applied in the KIVA-3V code to diesel engine simulations. Results are compared to those using the CHEMKIN package, which uses the VODE implicit solver. Good agreement was achieved for a wide range of engine operating conditions, and 40–70% CPU time savings were achieved by the present solver compared to the standard CHEMKIN. [DOI: 10.1115/1.2204979]

Introduction

Rapid development of computer technology has made it possible to implement more and more sophisticated mathematical models into computational fluid dynamics (CFD) codes for internal combustion (IC) engine combustion simulations. In recent years, attention is being given to models that include comprehensive elementary chemical kinetic mechanisms. This trend has stimulated research both on the development of chemical kinetic mechanisms and on the numerical methods of solving the detailed chemistry systems.

In this paper, we focus on the discussion of numerical issues associated with solving the detailed chemistry in combustion systems, which are essentially groups of nonlinearly coupled extremely stiff ordinary differential equations (ODEs). The presence of stiffness in the calculation can cause time-step restrictions in computations of combustion. Each chemical species evolves with its own characteristic time scale, and the numerical time step may be required to be comparable to the smallest of these time scales for reasons of stability and/or accuracy [1,2]. This problem has led many researchers to use implicit numerical methods in calculations of stiffly coupled chemical kinetic equations [3,4].

In the engine combustion simulation community, CHEMKIN is a very widely used package for including detailed chemical kinetics, where the chemical kinetic ODE sets are solved by the VODE implicit solver [3]. Kong and Reitz [5] incorporated CHEMKIN into the KIVA-3V code such that more detailed NO_x and soot emission models could be added, and unburned HC emissions could also be better predicted. However, the inclusion of detailed kinetics results in computer times that are much longer than using KIVA-3V with the standard simplified five-species/eight-reaction "shell" ignition model and the single turbulent time-scale combustion model of Kong et al. [6]. This makes the KIVA-CHEMKIN code too computationally expensive for practical engine simulations, and also makes it less suitable for engine optimization research using, for example, genetic algorithms [7].

The semi-implicit chemical kinetic equation solver implemented in the standard KIVA code can stably deal with simplified mechanisms made up of global reactions using normal hydrodynamic time steps [8]. However, when the number of reactions, is increased considerably, and especially when stiff elementary reactions, such as those of the H_2–O_2 system are added, a dramatic loss of accuracy can result, making the standard KIVA solver no longer suitable.

In this work, a stiffly stable, noniterative semi-implicit numerical solver was developed that is based on the basic numerical solution technique in standard KIVA. The new solver incorporates an algorithm that can handle the reactions present in the detailed chemical kinetic mechanisms used for engine combustion simulations, including third body reactions, pressure dependent reactions, etc. [9–11]. The new solver also adopts a sequential sort integration algorithm and a subcycling scheme that is based on the characteristics of the stiffness of the ODE system. Therefore, the new solver allows the use of numerical time steps that can be orders of magnitude larger than those possible with standard explicit methods, and significant CPU time savings have been achieved. The present engine simulation results show that the new

[1]Author to whom correspondence should be addressed.
[2]Current address: Department of Mechanical Engineering, Iowa State University, Ames, IA 50011.

Contributed by the Internal Combustion Engine Division of ASME for publication in the JOURNAL OF ENGINEERING FOR GAS TURBINES AND POWER. Manuscript received May 23, 2005; final manuscript received February 28, 2006. Review conducted by J. Cowart.

solver achieves the same order of accuracy as CHEMKIN in practical engineering combustion calculations.

Chemical Kinetics Formulation

The detailed chemistry in combustion simulations can be described by chemical kinetic mechanisms, which define the pathways and the associated reaction rates leading to the change of species concentrations. In the mechanisms the reversible (or irreversible) elementary reactions involving K chemical species can be represented in the general form [12]

$$\sum_{k=1}^{K} \nu'_{ki}\chi_k \Leftrightarrow \sum_{k=1}^{K} \nu''_{ki}\chi_k \quad (i=1,\ldots,I) \tag{1}$$

The production rate $\dot{\omega}_{ki}$ of the kth species in the ith reactions can be written as

$$\dot{\omega}_{ki} = \nu_{ki} q_i \quad (k=1,\ldots,K) \tag{2}$$

where

$$\nu_{ki} = \nu''_{ki} - \nu'_{ki} \tag{3}$$

$$q_i = k_{fi}\prod_{l=1}^{K}[X_l]^{\nu'_{li}} - k_{bi}\prod_{l=1}^{K}[X_l]^{\nu''_{li}} \quad (i=1,\ldots,I) \tag{4}$$

Equation (4) defines the rate-of-progress variable q_i for the ith elementary reaction. Note that the expressions for the production rate need to be modified in special cases considering third-body effects, or pressure-dependent effects.

The rate constants are given by the empirical Arrhenius form

$$k_{fi} = A_i T^{\beta_i} \exp\left(\frac{-E_i}{R_u T}\right) \tag{5}$$

with a corresponding expression for k_{bi}.

Substituting Eqs. (3) and (4) into Eq. (2), $\dot{\omega}_{ki}$ can be written as the difference of two absolutely non-negative parts, i.e.,

$$\dot{\omega}_{ki} = \left(\nu''_{ki}k_{fi}\prod_{l=1}^{K}[X_l]^{\nu'_{li}} + \nu'_{ki}k_{bi}\prod_{l=1}^{K}[X_l]^{\nu''_{li}}\right) - \left(\nu'_{ki}k_{fi}\prod_{l=1}^{K}[X_l]^{\nu'_{li}} + \nu''_{ki}k_{bi}\prod_{l=1}^{K}[X_l]^{\nu''_{li}}\right) \tag{6}$$

Rewriting Eq. (6) as

$$\dot{\omega}_k = \frac{d[X_k]}{dt} = f_k([X_l]) = f_k^+([X_l]) - f_k^-([X_l]) \tag{7}$$

where superscripts + and − in Eq. (7) refer to the strictly positive and negative contributions to the overall source term $f_k([X_l])$. Since Eq. (7) is the general formulation for every elementary reaction i, the subscript i is suppressed. Equation (7) is the form that was used in the numerical schemes studied by Reitz [1], and was also implemented in the standard KIVA-3V code for its reference species scheme [8].

The summation of $\dot{\omega}_{ki}$ for all of the elementary reactions yields the net rate of change of species density for the kth species and, correspondingly, the rate of change of specific internal energy of the fluid. In KIVA, detailed chemical kinetic mechanisms are solved as the chemical source terms in the species and energy transport equations, by this means are the chemical kinetics coupled with the hydrodynamic calculations [8].

Semi-Implicit Numerical Method

Two different finite difference semi-implicit schemes were developed for the integration of Eq. (7). The derivation of both schemes will be demonstrated using a first-order accurate formulation for simplicity, although up to third order accurate methods have been used in the study.

Scheme I. The first-order accurate finite difference equation representation for Eq. (7) is

$$\frac{X_k^{n+1} - X_k^n}{\Delta t} = F_k^+(X_l^n) - F_k^-(X_l^n) \tag{8}$$

Multiplying $F_k^-(X_l^n)$ in Eq. (8) by the ratio X_k^{n+1}/X_k^n, which is to first-order equal to unity, the new updated concentration of the kth species becomes

$$X_k^{n+1} = \frac{X_k^n + F_k^+(X_l^n)\Delta t}{1 + \dfrac{F_k^-(X_l^n)\Delta t}{X_k^n}} \tag{9}$$

It is readily seen that X_k^{n+1} in Eq. (9) is strictly non-negative no matter how large Δt becomes, which prevents the species density and, therefore, the specific internal energy from being driven negative.

Based on the updated expression for X_k^{n+1} in Eq. (9), the new production rate becomes

$$\frac{X_k^{n+1} - X_k^n}{\Delta t} = \frac{F_k^+(X_l^n) - F_k^-(X_l^n)}{1 + \dfrac{F_k^-(X_l^n)\Delta t}{X_k^n}} \tag{10}$$

Comparison of Eqs. (8) and (10) shows the denominator of Eq. (10) essentially acts as a damping term, which maintains the stability of the stiff ODE system. Under nonstiff situations, the second term in the denominator of Eq. (9) is orders of magnitude <1, and therefore is negligible. This first order accurate numerical scheme is exactly the same as that used by Reitz [1] and that used in standard KIVA [8].

By employing the same manipulation on the explicit second and third derivative terms in the Taylor series, the above scheme can be raised to higher orders. The first-to-third-order formulations are summarized as follows:

$$\frac{X_k^{n+1} - X_k^n}{\Delta t} = \alpha G_1^n + \beta G_2^{n-1} + \gamma G_3^{n-2} \tag{11}$$

$$G_1^n = F_k^+(X_l^n) - \left[\frac{F_k^-(X_l^n)}{X_k^n}\right] X_k^{n+1} \tag{11a}$$

$$G_2^{n-1} = F_k^-(X_l^{n-1}) - \left[\frac{F_k^+(X_l^{n-1})}{X_k^{n-1}}\right] X_k^{n+1} \tag{11b}$$

$$G_3^{n-2} = F_k^+(X_l^{n-2}) - \left[\frac{F_k^-(X_l^{n-2})}{X_k^{n-2}}\right] X_k^{n+1} \tag{11c}$$

where first order: $\alpha=1$, $\beta=0$, $\gamma=0$; second order: $\alpha=3/2$, $\beta=1/2$, $\gamma=0$; and third order: $\alpha=5/3$, $\beta=5/6$, $\gamma=1/6$.

Scheme II. Scheme I introduced a damping term into the production rate expressions by multiplying $F_k^-(X_l^n)$ in Eq. (8) by the ratio X_k^{n+1}/X_k^n to maintain the stability of the stiff ODE system. But, at the same time, an associated inaccuracy was also introduced because of this extra term. In scheme II, this inaccuracy is reduced by multiplying $F_k^-(X_l^n)$ by an additional term $(X_k^{n+1}/X_k^n)_{\text{predict}}$, which is the concentration ratio predicted by Eq. (9), i.e.,

$$\frac{X_k^{n+1} - X_k^n}{\Delta t} = F_k^+(X_l^n) - F_k^-(X_l^n)\frac{X_k^{n+1}}{X_k^n}\left(\frac{X_k^n}{X_k^{n+1}}\right)_{\text{predict}} \tag{12}$$

This manipulation does not destroy the non-negativity characteristics of the updated species densities, and the stiffly stable performance was maintained. The predicted production rate in this scheme then becomes

$$\frac{X_k^{n+1}-X_k^n}{\Delta t}=\frac{F_k^+(X_l^n)-F_k^-(X_l^n)}{1+\dfrac{1}{X_k^n}\dfrac{\{\Delta t[F_k^-(X_l^n)]\}^2}{X_k^n+\Delta t[F_k^+(X_l^n)+F_k^-(X_l^n)]}} \tag{13}$$

Compared to Eq. (10), the denominator of Eq. (13) has a different form, but its function as a damping term remains the same. However, the order of accuracy is increased.

For a second-order formulation, the same treatment can be applied, i.e., reducing the inaccuracy introduced by applying $(X_k^{n+1}/X_k^n)_{\text{predict}}$ to the first derivative term and applying $(X_k^{n+1}/X_k^n)_{\text{predict}}$ and $(X_k^n/X_k^{n-1})_{\text{predict}}$ to the explicit second derivative terms in the Taylor series. The second-order accurate expression of scheme II is then

$$X_k^{n+1}=\frac{X_k^n+\dfrac{3}{2}\Delta tF_k^+(X_l^n)+\dfrac{1}{2}\Delta tF_k^-(X_l^{n-1})}{1+\dfrac{3}{2}\dfrac{\Delta tF_k^-(X_l^n)\eta}{X_k^n}+\dfrac{1}{2}\dfrac{\Delta tF_k^+(X_l^{n-1})\eta\zeta}{X_k^{n-1}}} \tag{14}$$

where

$$\eta=\left(\frac{X_k^n}{X_k^{n+1}}\right)_{\text{predict}}=\frac{X_k^n+F_k^-(X_l^n)\Delta t}{X_k^n+F_k^+(X_l^n)\Delta t} \tag{15}$$

$$\zeta=\left(\frac{X_k^{n-1}}{X_k^n}\right)_{\text{predict}}=\frac{X_k^{n-1}+F_k^-(X_l^{n-1})\Delta t}{X_k^{n-1}+F_k^+(X_l^{n-1})\Delta t} \tag{16}$$

Reitz [1] has shown using a first-order accurate example that the Lipschitz timestep constraint no longer exists in scheme I, it can be shown that this statement is also true for scheme II. In both schemes, in case the species concentrations had zero initial values, the explicit formula (i.e., Eq. (8)) was applied.

Sequential Sort Integration Algorithm

In CHEMKIN, the ODEs are formulated with respect to every species by summing Eq. (2) for all reactions in the kinetic mechanism [3,12]. In the standard KIVA solver, the ODEs are formulated with respect to the production rate of a reference species in each reaction, where mass conservation is automatically guaranteed by the stoichiometric coefficients [8]. The standard KIVA chemistry solver can only deal efficiently with cases in which the numbers of reactions are small (normally the reactions are all global reactions).

The present solver followed the same approach of formulating the ODEs as used in the standard KIVA code, but improvement has been achieved by exploiting the characteristics of the stiffness of the ODE system, so that the new solver has the capability of achieving high numerical accuracy. In this algorithm, the sequence for the ODEs to be integrated was dynamically sorted by ranking the absolute values of the rate-of-progress variables q_i in Eq. (4), where the values of q_i were evaluated based on the species concentrations from the previous timestep, such that

$$|q_1(X_l^n)|\geq|q_2(X_l^n)|\geq\cdots\geq|q_j(X_l^n)|\geq\cdots\geq|q_J(X_l^n)| \tag{17}$$

where $j=1,\ldots,J$ and j represents the new index of the reactions for integration.

The rate-of-progress variables can be argued to be an approximation of the dominant eigenvalues of the ODE system, and the idea of index sorting is similar to that used in the Gauss-Seidel method for solving algebraic equations. By applying this sort algorithm to the integration, information associated with the reactions with the smallest chemistry time scales would be first taken into consideration in the calculation, by which the maximum overall accuracy could be achieved.

In the integration process, the reaction rates of reaction j are evaluated using the intermediate concentration values that have been updated due to kinetic reactions $<j$, but not reactions $\geq j$. This algorithm can thus be expressed as

$$X_k^{0,n+1}=\widetilde{X}_k^{J,n} \tag{18a}$$

$$\widetilde{X}_k^{1,n+1}=G_1(X_k^{0,n+1}) \tag{18b}$$

$$\cdots$$

$$\widetilde{X}_k^{j,n+1}=G_j(\widetilde{X}_k^{j-1,n+1}) \tag{18c}$$

$$\cdots$$

$$\widetilde{X}_k^{J,n+1}=G_J(\widetilde{X}_k^{J-1,n+1}) \tag{18d}$$

$$X_k^{0,n+2}=\widetilde{X}_k^{J,n+1} \tag{18e}$$

where the G's are general notations for the functions that govern the changes of species concentrations within every reaction, and the subscript represents the index of the reaction being calculated. The $\widetilde{X}$'s represent the intermediate concentrations of species, whose second superscript denotes the numerical time level, and the first superscript denotes the index of the reaction in which the concentrations were just updated, where 0 represents the initial species concentrations of time $n+1$, which were inherited from the previous chemical kinetic time step n.

Subcycling Scheme in Chemistry Routine

Although the present numerical method is stiffly stable, accuracy of the integration could still be sacrificed if too much damping is added. Therefore, the numerical timesteps for practical chemical kinetics calculations should be restricted.

The present solver utilized a time subcycling scheme within the chemistry solver routine. For every computational cell, the overall hydrodynamic timestep of the KIVA code was dynamically divided into n uniform subcycle time steps by monitoring the relative change in magnitude of concentration of key species, which have short characteristic time scales, and are also important to the chemical heat release. Then the chemistry calculation was implemented multiple times within a single hydrodynamic time step.

In the development of the ERC-reduced n-heptane mechanism, Patel et al. [10] showed that the ketone intermediate species is important for the cool flame heat release and the OH radical is crucial for the overall heat release during the ignition process, which represents the stiffest period of the whole combustion process. With these considerations, the magnitudes of relative change of concentration of the ketone species and the OH radical were used as criteria for determining the number of subcycles needed, viz.,

$$\frac{|X_{\text{OH}}^{n+1}-X_{\text{OH}}^n|}{X_{\text{OH}}^n}<C_{\text{sub}} \tag{19}$$

$$\frac{|X_{\text{ketone}}^{n+1}-X_{\text{ketone}}^n|}{X_{\text{ketone}}^n}<C_{\text{sub}} \tag{20}$$

where C_{sub} is an empirical constant. For the cool flame heat release phase (normally $T<1000$ K), both criteria were applied, whereas for the main heat release, only the OH radical was monitored because the ketone species was no longer important. In this solver, the default value of the number of subcycles is 1, and if either of the criteria were not satisfied, then the subcycle number increased by a factor of 3, and the computation was restarted from the beginning of the hydrodynamic time step.

The value of C_{sub} was picked by sensitivity analysis using ignition delay tests of homogeneous mixtures under constant volume and adiabatic conditions [10]. Figure 1 shows the results of stoichiometric mixture at $p=40$ bar using numerical scheme I and ERC-reduced n-heptane mechanism [10]. Results from KIVA-CHEMKIN code were used as the baseline. It is seen that smaller C_{sub} generally yields better matching with the baseline, but reduc-

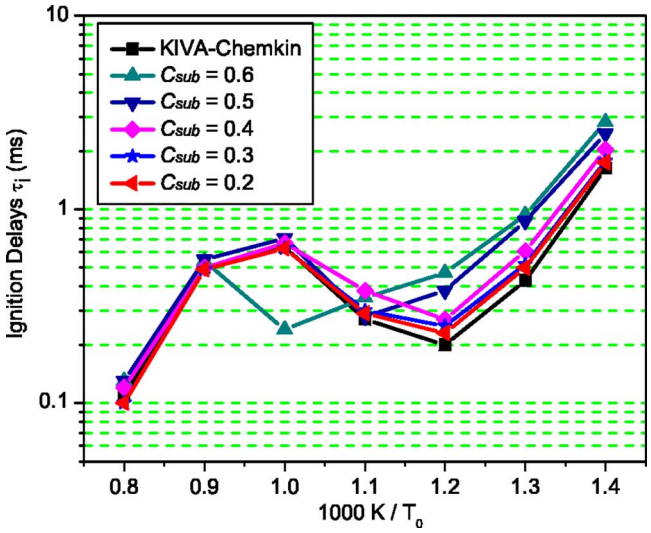

Fig. 1 Sensitivity analysis of C_{sub} by ignition delay tests (ERC mechanism + scheme I, Φ=1.0, p=40 bar)

ing C_{sub} also results in the increase of computation time due to more subcycles. Based on Fig. 1, 0.3 was taken as the optimal value of C_{sub} because smaller values did not improve the accuracy significantly but increased the computational time considerably. The same analysis was also carried out for numerical scheme II and MIT mechanism [11]. More efforts need to be done in future work for more mathematically strict criteria to make the subcycling scheme independent of chemical kinetic mechanisms.

Experiment and Simulation Environments

Although the present chemical kinetics solver is applicable to general IC engine combustion simulations, in the present work, it was coupled with the standard KIVA-3V code and applied to diesel engine simulations. The performance was tested by comparing the results with predictions from the KIVA/CHEMKIN code and against engine experimental data.

The specifications of the Caterpillar 3401E single-cylinder diesel engine used for the study are listed in Table 1. In the experiments, the parameters that were varied were the time of start-of-injection, the injection duration and the EGR rate. Six experimental conditions of Klingbeil [13] were chosen as the baseline cases for the comparisons to simulation results. Those cases covered both low (8%) and high (44%) EGR, early (−20 ATDC) and late (+5 ATDC) start-of-injection timings, as shown in Table 2. Thus the present solver was tested for predicting the chemical kinetic processes that govern the ignition delay time and heat release rates over a wide range of operating conditions.

In the simulations, two reduced n-heptane chemical kinetic mechanisms were exploited for simulating diesel engine combustion. The first is the ERC reduced n-heptane mechanism with 30 species (including acetylene for soot modeling) and 65 reactions [10], and the second is MIT reduced primary reference fuel (PRF)

Table 1 Caterpillar 3410E engine specifications [13]

Bore × stroke	137.2 mm×165.1 mm
Compression ratio	16.1:1
Displacement	2.44 L
Combustion chamber geometry	In-piston Mexican hat with sharp-edged crater
Maximum injection pressure	190 MPa
Number of nozzle holes	6
Nozzle hole diameter	0.214 mm
Included spray angle	130 deg

Table 2 Experimental conditions of selected cases

Case	SOI (ATDC)	EGR (%)
1	−20	44.0
2	−10	44.0
3	+5	44.0
4	−20	8.0
5	−10	8.0
6	+5	8.0

mechanism with 32 species and 55 reactions [11]. In the simulations using MIT mechanism, the fuel was set to be 100% n-heptane and the species and reactions for the iso-octane related chemistry were actually unused. The two mechanisms were chosen for the multi-dimensional engine simulations mainly because of their relative simplicity, so that the CPU time would be affordable for practical engine design or optimization simulations.

It is worth noting that the main difference between the two reduced mechanisms is that the MIT PRF mechanism contains several global reactions that convert big fuel molecules into CO, HO_2, and H_2O directly, without breaking up into medium-size molecules, i.e., C_6–C_2 level molecules. Those global reactions are followed by the CO oxidation and H_2-O_2 reactions. In contrast, the ERC reduced n-heptane mechanism keeps reactions involving medium-size molecules and was formed from the 40 species mechanism of Golovitchev [9]. Considering that the reaction rates of fuel molecule decomposition reactions are generally orders of magnitude faster than other reactions, the global reaction assumptions in the MIT mechanism are acceptable for engine simulations. However, the difference between the mechanisms has some effect on the necessary accuracy of the chemistry solver. Specifically, it was found that numerical scheme I worked very well with the ERC-reduced mechanism, but when applied to the MIT mechanism, it had difficulty in predicting ignition delay times for late injection, high EGR cases. The reason is that a small loss of computational accuracy results in misfire under these extreme conditions.

The difficulty for scheme I to work with the MIT mechanism motivated the further improvement of numerical accuracy which resulted in scheme II. Thus, performance of scheme I was demonstrated with simulations based on the ERC mechanism, while scheme II was applied with the MIT mechanism.

First-order accurate formulations of the numerical schemes were used for the simulations presented here. The higher formal order schemes allow larger subcycle timesteps to be applied. But additional computations showed the higher-order formulations did not have significant advantages over the first-order formulations in terms of the overall accuracy and CPU time. The first-order formulations were deemed accurate enough for practical engine simulations.

Discussion of Results

Pressure and Heat Release Rate. Figure 2 shows the computed in-cylinder pressures and heat release rates based on scheme I for the baseline cases compared to the simulation results from KIVA/CHEMKIN as well as the measured data. As mentioned above, the chemistry mechanism used was the ERC n-heptane mechanism.

For cases 1, 2, 4, and 5, the computed pressure and heat release rate traces from the semi-implicit solver and CHEMKIN generally match very well. Although the ignition time and peak pressure also match well between measured and calculated results, relatively large discrepancies are observed in the heat release rate, which may be partly due to the uncertainties in the chemical kinetic mechanisms and/or the spray model.

For late injection cases (SOI=+5 ATDC), discrepancies between the experimental data and the simulation results are more consid-

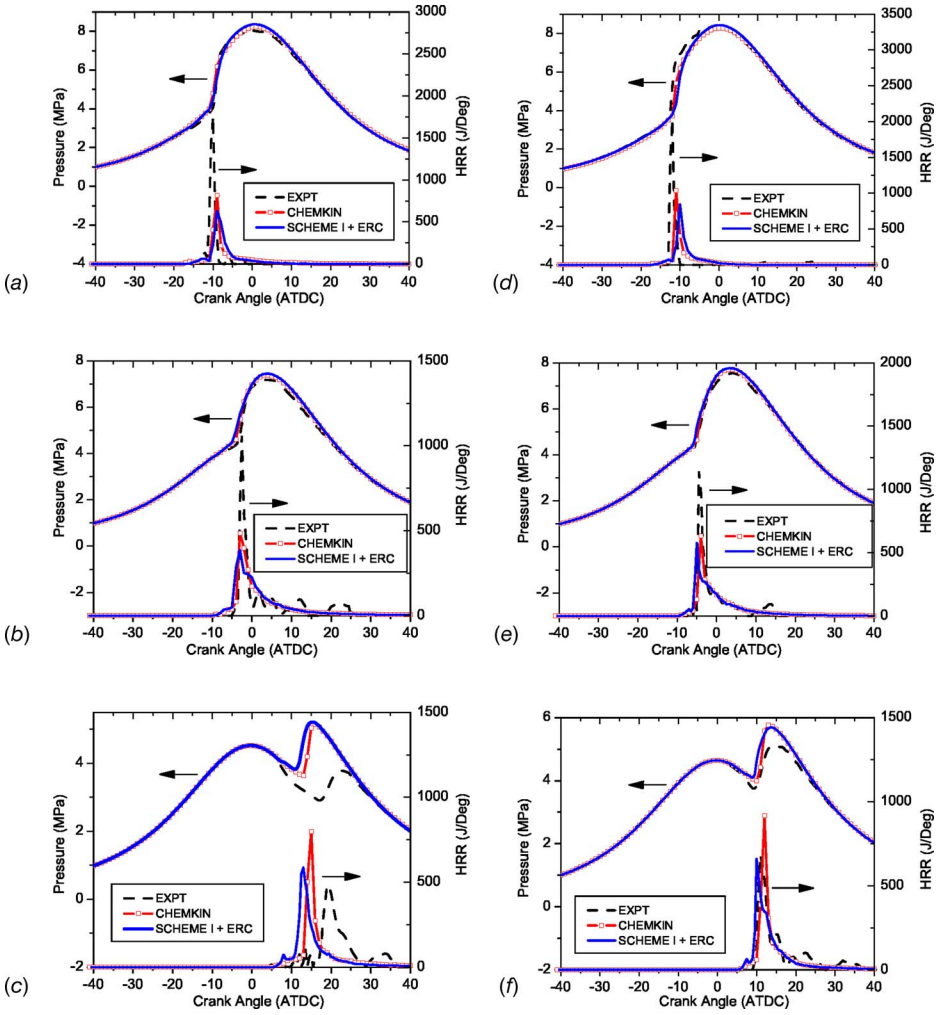

Fig. 2 Pressure and heat release rate comparisons based on the ERC reduced *n*-heptane mechanism: (*a*) case 1: SOI =–20 ATDC, 44% EGR, ERC mechanism, (*b*) case 2: SOI =–10 ATDC, 44% EGR, ERC mechanism, (*c*) case 3: SOI =+5 ATDC, 44% EGR, ERC mechanism, (*d*) case 4: SOI =–20 ATDC, 8% EGR, ERC mechanism, (*e*) case 5: SOI =–10 ATDC, 8% EGR, ERC mechanism, and (*f*) case 6: SOI =+5 ATDC, 8% EGR, ERC mechanism

erable, especially in the 44% EGR case, the simulated ignition occurs seven to eight crank angles in advance of the measured one. This is because those extreme operating conditions are very near the misfire limit of the engine. The contribution of uncertainties to the accuracy of the simulations is also relatively large due to the borderline conditions. But with regard to the comparison between the new solver and CHEMKIN, the new solver still gives acceptable results compared to those from CHEMKIN.

The simulation results based on scheme II and the MIT PRF mechanism are shown in Fig. 3. Good agreement between the pressure curves from the semi-implicit solver and those from CHEMKIN was achieved again, although relatively more obvious discrepancies can be observed in heat release rate. The improvement of scheme II over scheme I is readily observed by the good pressure matching in the late injection cases 3 and 6, where scheme I failed to predict any ignition when coupled with the MIT mechanism, as mentioned earlier. Based on similar ignition delay tests as shown in Fig. 1, the constant Csub in Eqs. (19) and (20) was set 0.5 in the simulation cases using MIT mechanism.

Figure 4 shows the calculated pressure curves using ERC mechanism and scheme II for cases 1–3, compared to the measured curves and the results from CHEMKIN. It is seen that scheme II gives the same order of accuracy compared to scheme I when applied to the ERC mechanism.

In-Cylinder Species Mass. The in-cylinder pressure and heat release histories are both governed by changes of mixture composition in the cylinder during the combustion process. Figure 5 shows the total in-cylinder mass histories of some of the key species using scheme I and the ERC mechanism, as compared to the CHEMKIN results.

The three cases shown with different SOI timings and EGR ratios all indicate that the in-cylinder total mass of O_2, CO_2, H_2O, CO, and OH match very well between the new solver and CHEMKIN. Although some discrepancies are observed for the mass of fuel and C_7ket_{12}, the trends and magnitudes are the same. Also, only after the magnitudes of the species become very small do the differences become appreciable (note the logarithmic scale). This shows that the present solver is able to capture the information of the most important species such as CO and OH in practical engine simulations.

CPU Time Comparisons. Figure 6 shows CPU time comparison between the present solver and CHEMKIN. The computational platform was a Linux workstation that uses a Pentium 4 CPU. For all cases, the initial hydrodynamic time steps were set to be 5 μs, and the simulations were initialized with specified conditions at intake valve closure (IVC), and ended at exhaust valve open (EVO).

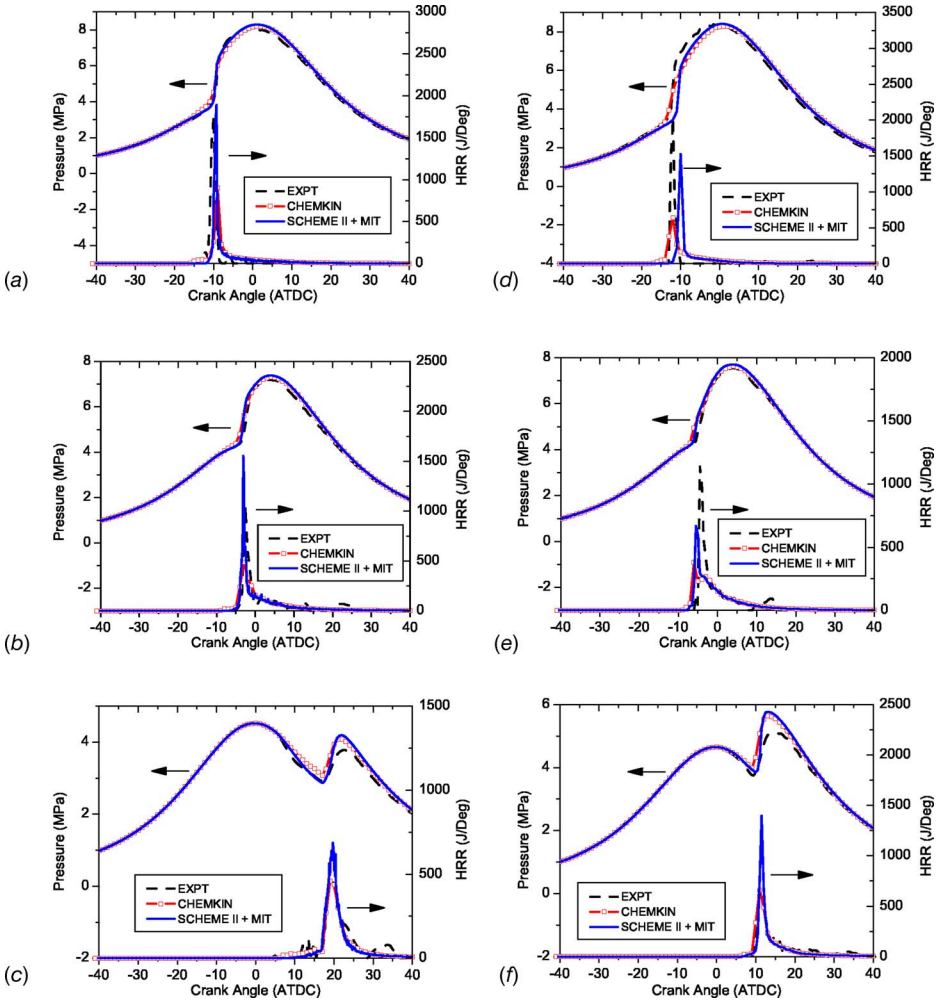

Fig. 3 Pressure and heat release rate comparisons based on the MIT reduced PRF mechanism: (*a*) case 1: SOI =−20 ATDC, 44% EGR, MIT mechanism, (*b*) case 2: SOI =−10 ATDC, 44% EGR, MIT mechanism, (*c*) case 3: SOI =+5 ATDC, 44% EGR, MIT mechanism, (*d*) case 4: SOI =−20 ATDC, 8% EGR, MIT mechanism, (*e*) case 5: SOI =−10 ATDC, 8% EGR, MIT mechanism, and (*f*) case 6: SOI =+5 ATDC, 8% EGR, MIT mechanism

Figure 6(*a*) shows results for the ERC mechanism and the semi-implicit solver using the first-order formulation of scheme I. Also shown in this figure is the CPU time for cases based on the standard "shell" ignition model and the CTC combustion model of Kong et al. [6] (i.e., no detailed chemistry). Generally, the CPU time for the detailed chemistry cases using CHEMKIN is roughly ten times longer than the cases without detailed chemistry, which makes the application of detailed chemistry to engine design or optimization work impractical. The present solver in general achieves 40–60 % CPU time savings compared to CHEMKIN, which makes it useful for introducing detailed chemistry in engineering calculations.

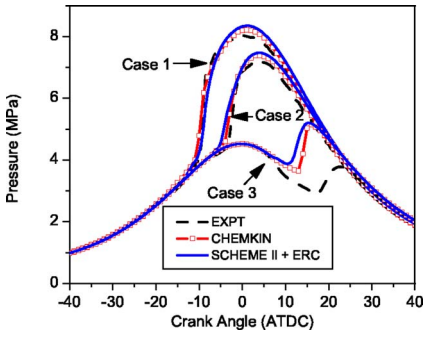

Fig. 4 Pressure trace comparisons based on the ERC mechanism and numerical scheme II

The results in Fig. 6(*b*) are based on the MIT mechanism and the semi-implicit solver (using scheme II). It should be noted that schemes I and II had similar CPU times for the same engine case. As seen, the present solver presented 50–70 % CPU time savings compared to CHEMKIN using the same detailed chemistry mechanism. Based on the present solver, the CPU time could be expected to be further reduced by applying other computer time-reduction strategies in future work, such as employing parallel computing and/or bypassing computational cells in which chemical reaction effects are essentially negligible.

Conclusions

Good agreement between the present numerical solver and those obtained from CHEMKIN has been achieved in terms of in-cylinder pressure and species mass traces for both high and low EGR ratios. However, discrepancies were observed in the comparisons of heat release rate, especially for late injection cases. The simulation results used a first-order accurate formulation of the numerical schemes. This indicates that a lower-order semi-

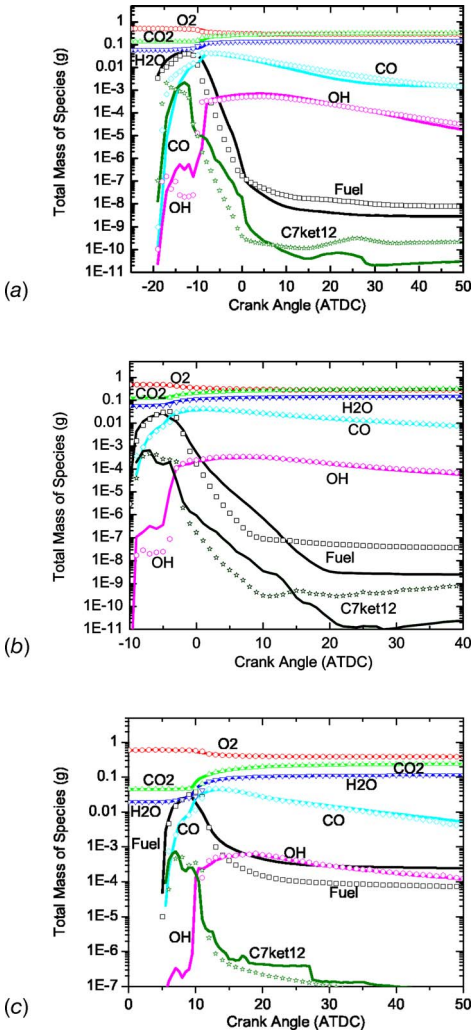

Fig. 5 In-cylinder total masses of species compared between the present solver (solid lines) and CHEMKIN (symbols): (*a*) SOI =−20 ATDC, 44% EGR, ERC mechanism, (*b*) SOI =−10 ATDC, 44% EGR, ERC mechanism, and (*c*) SOI =+5 ATDC, 8% EGR, ERC mechanism

implicit solver is sufficiently accurate for capturing the main thermal and chemical information in practical computations of engine combustion, and it is stiffly stable.

As would be expected, the numerical schemes in the present solver were found to be sensitive to the choice of the kinetics mechanism. The lower-accuracy scheme I yielded good results when coupled with ERC reduced *n*-heptane mechanism, but more accuracy was needed when coupled with the MIT PRF mechanism, especially for borderline misfire late injection cases. Scheme II worked well for both chemistry mechanisms. Although higher formal-order formulations of the present numerical schemes did not show significant advantage over the first-order formulation presented in this study, their potential for further improvement in terms of using larger timesteps, and enhancing prediction accuracy will be studied in the future.

The CPU time comparisons demonstrate that significant increases in computational efficiency have been gained with the use of the present semi-implicit chemistry solver compared to the standard CHEMKIN solver. The CPU time could be expected to be further saved by applying other strategies in the future.

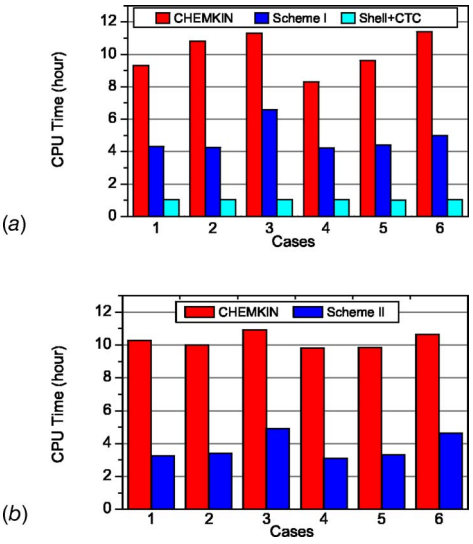

Fig. 6 CPU time comparisons: (*a*) scheme I, first-order formulation, ERC mechanism, and (*b*) scheme II, first-order formulation, MIT mechanism

Nomenclature

Acronyms

ATDC = after top dead center
CTC = characteristic time combustion (model)
EGR = exhaust gas recirculation
EVO = exhaust valve open
HRR = heat release rate
IC = internal combustion
IVC = intake valve closure
ODE = ordinary differential equation
PRF = primary reference fuel
SOI = start of injection

Arabic Symbols

A = pre-exponential constant
b = temperature exponent in Eq. (5)
C_{sub} = empirical constant in Eqs. (19) and (20)
f = production rate function
E = activation energy
F = numerical approximation to f
G = functions in Eqs. (11); general function in Eq. (18)
I = total number of reactions
j = index of integration sequence of the reactions, $1,\ldots,J$
J = total number of reactions, $J=I$
k = rate constant
K = total number of species
p = pressure
q = rate-of-progress variable
R_u = universal gas constant
t = time
T, T_0 = temperature
X = numerical approximation to $[X]$
$[X]$ = species concentration
$\tilde{X}$ = intermediate species concentration

Greek Symbols

α, β, γ = parameters in Eq. (11)
Δt = numerical time step
ζ, η = intermediate parameters in Eq. (14)–(16)
ν = stoichiometric coefficient

Φ = equivalence ratio
χ = chemical species symbol
ω = production rate

Subscripts

b = backward elementary reaction step
f = forward elementary reaction step
i = reaction index $1,\ldots,I$
k = species index $1,\ldots,K$
ketone = ketone species in the chemical kinetic mechanisms
l = running index for species $1,\ldots,K$
OH = OH radical in the chemical kinetic mechanisms predicted expression by the first-order accuracy numerical scheme (Eq. (9)) presented in this paper
$'$ = forward reaction
$''$ = backward reaction

Superscript

n = numerical time level

Acknowledgment

Ford Motor Company is acknowledged for the financial support of this project. The authors also thank Drs. Feng Tao and Youngchul Ra for helpful discussions.

References

[1] Reitz, R. D., 1980, "Computations of Laminar Flame Propagation Using an Explicit Numerical Method," *18th Symposium (International) on Combustion*, Combust. Inst., Pittsburgh, PA, pp. 433–442.
[2] Roberts, C. E., 1979, *Ordinary Differential Equations: A Computational Approach*, Prentice-Hall, Englewood Cliffs, NJ.
[3] Kee, R. J., Rupley, F. M., and Miller, J. A., 1989, "CHEMKIN-II: A FORTRAN Chemical Kinetics Package for the Analyses of Gas Phase Chemical Kinetics," Sandia Report, No. SAND 89-8009.
[4] Brown, P. N., Byrne, G. D., and Hindmarsh, A. C., 1989, "VODE, A Variable-Coefficient ODE Solver," SIAM (Soc. Ind. Appl. Math.) J. Sci. Stat. Comput., **10**, pp. 1038–1051.
[5] Kong, S.-C., and Reitz, R. D., 2002, "Application of Detailed Chemistry and CFD for Predicting Direct Injection HCCI Engine Combustion and Emissions," *Proc. Combust. Inst.*, Philadelphia, PA, Vol. 29, pp. 663–669.
[6] Kong, S.-C., Han, Z., and Reitz, R. D., 1995, "The Development and Application of a Diesel Ignition and Combustion Model for Multidimensional Engine Simulation," SAE Paper No. 950278.
[7] Senecal, P. K., and Reitz, R. D., 2000, "Simultaneous Reduction of Engine Emissions and Fuel Consumption Using Genetic Algorithms and Multi-Dimensional Spray and Combustion Modeling," SAE Paper No. 2000-01-1890.
[8] Amsden, A. A., O'Rourke, P. J., and Butler, T. D., 1989, "KIVA-II: A Computer Program for Chemically Reactive Flows with Sprays," Los Alamos National Labs, LA-11560-MS.
[9] Golovitchev, V. I., 2000, http://www.tfd.chalmers.se/~valeri/MECH.html, Chalmers Univ. of Tech, Gothenburg, Sweden.
[10] Patel, A., Kong, S.-C., and Reitz, R. D., 2004, "Development and Validation of a Reduced Reaction Mechanism for HCCI Engine Simulations," SAE Paper No. 2004-01-0558.
[11] Tanaka, S., Ayala, F., and Keck, J. C., 2003, "A Reduced Chemical Kinetic Model for HCCI Combustion of Primary Reference Fuels in a Rapid Compression Machine," Combust. Flame, **133**, pp. 467–481.
[12] Turns, S. R., 2000, *An Introduction to Combustion: Concepts and Applications*, McGraw-Hill, New York.
[13] Klingbeil, A. E., 2002, "Particulate and NO_x Reduction in a Heavy-Duty Diesel Engine Using High Levels of Exhaust Gas Recirculation and Very Early and Very Late Injection," MS thesis, University of Wisconsin-Madison.

An Experimental Investigation on the Effect of Post-Injection Strategies on Combustion and Emissions in the Low-Temperature Diesel Combustion Regime

Hanho Yun
Delphi Research Labs,
51786 Shelby Parkway,
Shelby Township, MI 48315

Rolf D. Reitz
University of Wisconsin—Madison,
1500 Engineering Drive,
Madison, WI 53706

In order to meet future emissions regulations, new combustion concepts are being developed. Among them, the development of low-temperature diesel combustion systems has received considerable attention. Low NO_x *emissions are achieved through minimization of peak temperatures during the combustion process. Concurrently, soot formation is inhibited due to a combination of low combustion temperatures and extensive fuel-air premixing. In this study, the effect of late-cycle mixing enhancement by post-injection strategies on combustion and engine-out emissions in the low-temperature (low soot and* NO_x *emissions) combustion regime was experimentally investigated. The baseline operating condition considered for low-temperature combustion was* 1500 rpm, 3 bar *IMEP with 50% EGR rate, and extension to high loads was considered by means of post injection. Post-injection strategies gave very favorable emission results in the low-temperature combustion regime at all loads tested in this study. Since post injection leads to late-cycle mixing improvement, further reductions in soot emissions were achieved without deteriorating the* NO_x *emissions. With smaller fuel injected amounts for the second pulse, better soot emissions were found. However, the determination of the dwell between the injections was found to be very important for the emissions.*
[DOI: 10.1115/1.2180812]

Introduction

Several different strategies have been successfully developed to attain the desired combustion characteristics. Among them, two different strategies, according to the timing of fuel injection, featuring "early" mixture formation (e.g., the homogeneous charge compression ignition (HCCI) concept [1,2]), and "late" mixture formation (e.g., the modulated kinetics (MK) concept [3,4]), have received much attention.

Early injection strategies, often called HCCI, have been widely studied as a combustion technology to avoid simultaneous NO_x and smoke formation regions. This combustion technology achieves low-combustion temperatures primarily by premixing the fuel and air to overall lean conditions, and thus reduces both NO_x and smoke emissions. A very long mixing period is required to form a lean and uniform mixture, and it is necessary to inject fuel at a fairly early time in the initial stages of the compression stroke.

Although early injection strategies have met with some success, difficulties remain with control of the combustion phasing and fuel wall impingement. In order to overcome these problems, methods such as suppression of the penetrating force of the spray using a special nozzle [5] or the narrow angle direct injection (NADI) technology [6] have been suggested, which require substantial hardware modification of engines. Additionally, to enhance the mixing process, changes in fuel injection equipment and combustion chamber geometries are often adopted. These changes can lead to less desirable performance at high loads, when conventional diesel combustion operating modes may be required.

On the contrary, late injection strategies have succeeded in achieving simultaneous low NO_x and soot emissions over a low-to-moderate speed and load range. This combustion concept has advantages compared to early injection strategies. The combustion phasing is determined by the fuel injection event and does not require any modification of current standard diesel fuel injection equipment or combustion chamber geometries. Therefore, the present research was focused on investigating this late-injection low-temperature combustion regime.

Many experimental and numerical investigations have demonstrated the capability of late-injection low-temperature combustion to reduce both NO_x and soot emissions, simultaneously. Kimura et al. [3,4] conducted experimental investigations of so-called MK combustion using a single-cylinder direct-injection (DI) diesel engine.

In the MK combustion concept, NO_x formation is maintained low by implementing high rates of cooled exhaust gas recirculation (EGR), late injection timings, and use of a low compression ratio. Each of these factors also extends the ignition delay, allowing a greater time for fuel-air premixing, which is thought to be the dominant factor suppressing soot formation. To ensure that all of the fuel has enough time to premix, the ignition delay should exceed the injection duration, which is an essential feature of MK combustion. To shorten the injection duration, high injection pressures are adopted. Furthermore, a high swirl ratio is employed to suppress the formation of unburned hydrocarbons and soluble organic fraction (SOF) of the particulate, although a small NO_x penalty is observed.

Contributed by the Internal Combustion Division of ASME for publication in the JOURNAL OF ENGINEERING FOR GAS TURBINES AND POWER. Manuscript received September 2, 2005; final manuscript received December 6, 2005. Review conducted by J. Cowart.

It is well known that NO_x is formed at high temperatures, while soot is formed at high equivalence ratios and in a specific temperature region. Thus, low-combustion temperature helps to reduce NO_x and soot emissions, simultaneously. Akihama et al. [7] developed so-called smokeless rich combustion and obtained near-zero NO_x and soot emissions under near stoichiometric and even rich operating conditions. They also proposed a quantitative $\phi-T$ map by performing zero-dimensional (0D) calculations using a detailed soot formation model. The main soot suppression mechanism in smokeless combustion is that the temperature reduced by large amounts of EGR is low enough to allow the combustion to avoid the soot formation region.

In another investigation, Ishiyama et al. [8] experimentally examined the mechanism of spray ignition of *n*-heptane using a constant-volume vessel in low-temperature combustion, as well as conventional diesel combustion. They observed negative temperature coefficient (NTC) behavior of ignition delays accompanying two-stage ignition at a low ambient pressure, while a monotonic temperature dependency was obtained with single-stage ignition at a higher ambient pressure. They found that the enhancement of fuel-air mixing with elevated injection pressure and a reduced nozzle orifice delays the appearance of the hot flame in the NTC condition.

Shimazaki et al. [9] also investigated the characteristics of premixed compression ignition (PCI) combustion with fuel injection timings near top dead center (TDC). They found that simultaneous reduction of NO_x, soot, and brake-specific fuel consumption (BSFC) is obtained using commercial diesel fuel with high ignitability, in combination with high EGR in order to achieve enough mixing time to reduce the amount of fuel-rich mixture. The mixture formation depends heavily on "high turbulent mixing rates," which were obtained by high injection pressures with small-hole nozzles and near-TDC injection. It was also pointed out low hydrocarbon (HC) emissions can be obtained through near-TDC injection due to a mixture that does not disperse into the squish region, which causes HC emissions.

Bianchi et al. [10] numerically investigated the possibility to extend the low-temperature combustion concept developed for low-load conditions [4,8] to medium-high load. They found that it is very difficult because the maximum allowable EGR rate diminishes and greater chemical energy is released due to the large amount of fuel injected. They concluded that improvements in mixture formation are of particular importance to reduce soot formation at medium load.

Recently, Miles et al. [11,12] found that the low-temperature combustion regime more closely resembles a standard, two-stage diesel combustion process—consisting of a rich premixed burn phase followed by mixing-limited combustion—rather than a fully premixed (homogeneous or otherwise) process. Therefore, methods to improve the late-cycle mixing rate in the low-temperature combustion regime would be very helpful to further reduce the soot emissions. Mixing enhancement by means of a second injection was chosen for this purpose in this research. The effect of injection timing, dwell, and the amount of fuel injected were investigated, and these results were compared to those of single injection.

Experimental Setup

The test engine used in this research is a single-cylinder version of a 2.4 L five-cylinder engine that is in production in Europe. The maximum power is 22 kW at 3800 rpm. The cylinder head, piston, and other important engine parts were manufactured at FIAT, and the block was a Hydra from Ricardo Research. The specifications of the engine are shown in Table 1 [13].

The engine features two intake ports, which generate different amounts of flow swirl. Hence, the operating swirl ratio can be adjusted by throttling the helical port between 1.8 and 3.3. Figure 1 shows the schematic of engine experimental setup layout including the intake and exhaust system [13].

Table 1 Engine specifications

Engine type	4 valve HSDI diesel
Bore × stroke	82.0 × 90.4 mm
Compression ratio	18.79:1
Displacement	477 cm^3
Chamber geometry	Reentrant bowl
Intake ports	1 helical(swirl) port,
Swirl ratio (at IVC)	1.83–3.30
Bowl diameter (mm)	46.0
Squish clearance volume	26.84 cm^3
IVO/IVC	10 deg BTDC/38 deg ABDC
EVO/EVC	38 deg BBDC/8.5 deg ATDC

Exhaust gas recirculation (EGR) is attained by a direct link between the exhaust and intake surge tanks. EGR rates are calculated as a volumetric percentage of intake air using the following equation:

$$\%\,\mathrm{EGR} = \frac{\%\,\mathrm{CO_2(intake)} - \%\,\mathrm{CO_2(ambient)}}{\%\,\mathrm{CO_2(exhaust)} - \%\,\mathrm{CO_2(ambient)}} \times 100$$

A heat exchanger is used to cool the recirculated exhaust gas. Thus, the temperature of the EGR was maintained at the temperature of the fresh intake air.

The common-rail injection system is capable of injecting the fuel at a range of injection pressures from 150 bar to 1350 bar, along with up to two injections per combustion event. The injector was an electrohydraulically controlled injector. The injection strategies, such as the injection pressure, timing, and quantity, could be set through a program provided with the injection system. The common-rail injection system specifications are summarized in Table 2. Instantaneous mass rate-of-injection (ROI) profiles and the corresponding fuel delivery quantities are obtained using the method developed by Bosch [14].

Cylinder pressure was acquired using a piezoelectric pressure transducer (Kistler, model 6125A) and a charge amplifier (Kistler, model 5010B). The data acquisition system is used to take cylinder pressure averaged over 100 cycles by 1/4 crank-angle degree increments. The in-cylinder pressure data along with other engine operating parameters are analyzed to obtain the apparent heat release rate, following the procedure given by Heywood [15] and employing a constant specific heat ratio of 1.33.

The emission data measured during the experiments are the gaseous emissions and soot emissions. The gaseous emissions including NO, NO_x, CO, HC, and exhaust CO_2 were measured with a Thermo Nicolet NEXUS 670, FT-IR emissions analyzer. Samples taken from the exhaust surge tank are run to the Fourier transform infrared (FTIR) analyzer by a heated line after passing through a heated soot filter. The sample is kept above 170°C to prevent emissions species from condensing. Intake CO_2 is assessed with a Horiba PIR-9000 infrared gas analyzer. Exhaust smoke levels are determined with a Bosch model RTT100 smoke opacimeter. The Bosch smoke opacimeter originally measures visual opacity and an absorption coefficient, and then the data is converted into mass concentration through the use of an internal conversion table. This mass concentration specifies the amount of soot with units of milligrams per cubic meter. It is presented as soot level in this work, after being converted into units of grams per kilowatt hour [13].

In order to investigate the effect of the post injection on the combustion and emissions, two different strategies could be applied. One is a fixed fueling test and the other is a fixed indicated mean effective pressure (IMEP) test. Initially, the fixed fueling procedure was selected in order to assess the best test method and to explore the effect of post injections.

As shown in Fig. 2, combustion and emissions formation can be controlled by four factors, including the start-of-injection (SOI) timing of the first pulse, the duration of the first pulse, the dwell between pulses, and the duration of the second pulse. The SOI

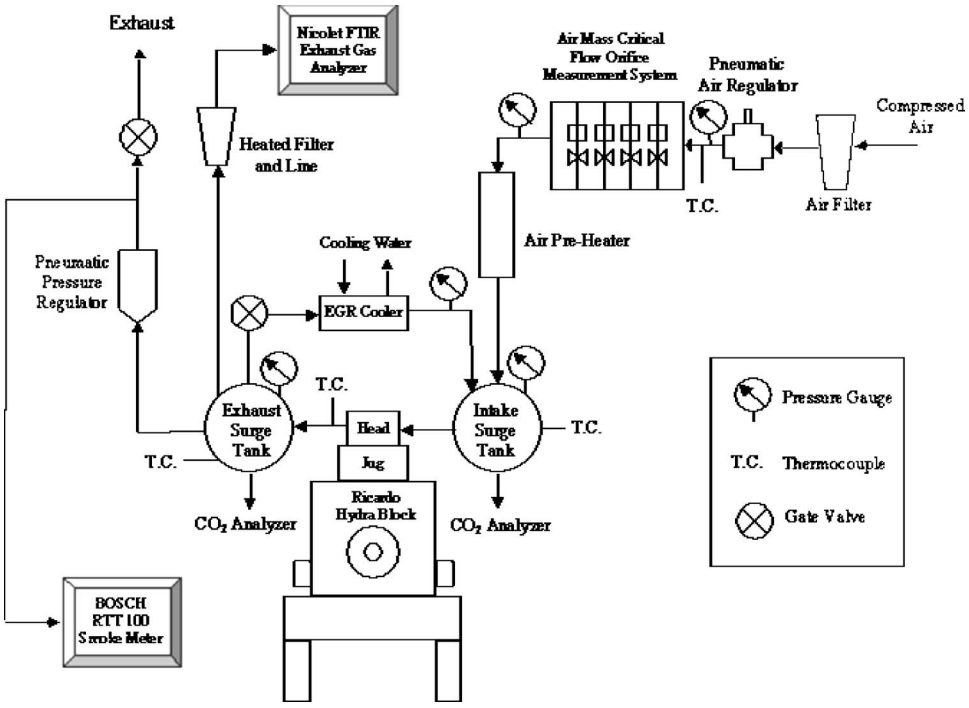

Fig. 1 Schematic of experimental engine setup

timing for the main or first injection was fixed to be the same as that of the single-injection condition (−7.5 deg ATDC). The duration of the main injection was chosen by the value (ETp =330 μs) required to achieve 3 bar IMEP with 2000 μs dwell. Then the dwell between injections was changed from 1000 μs to 3000 μs. Thus, the SOI timing for the second (post-) injection was varied. The duration of the post injection (ET) was also fixed with an energizing time of 150 μs. The total fuel mass per injection (main+post) and the associated IMEP variation for the fixed-injection energizing time (fixed fuel flow rate) test are shown in Fig. 3.

As can be seen, the actually delivered total fuel mass per injection is nonmonotonically changed with the dwell. In order to investigate further this phenomenon and find out the main reason for this, the rate-of-injection (ROI) profile was measured using the Bosch bench meter as a function of dwell time, and is illustrated in Fig. 4. The first pulse, which corresponds to the main injection event, has identical shape and area regardless of the dwell. However, the details of the second post-injection event show strong sensitivity to the dwell. Even though the same energizing time of the injector was used (ET=150 μs), the actual delivered fuel mass caused by the second injection is changed with varying dwell time. The high-pressure wave dynamics inside the injector and associated plumbing is the cause of this phenomenon.

Since different fueling rates can influence the emissions results, this complicates explanations of the effect of dwell between injections on combustion and emissions. Thus, the fixed IMEP test procedure was finally selected to examine the effect of post-injection strategies, including the dwell and the fuel distribution effects.

Table 2 Fuel injection system specifications

Injector type	Electrohydraulically controlled injector
Injection pressure	150–1350 bar
Nozzle type	Dual-guided VCO nozzle
Number of nozzle holes	6
Hole Diameter	160 μm
Hole L/D ratio	6.25
Included spray angle	145 deg

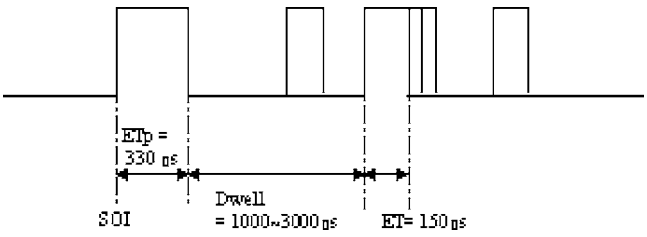

Fig. 2 Example control strategy for post injections for the fixed injection energizing time tests

Results and Discussion

The operating conditions for the present low-temperature combustion studies are shown in Table 3. Unless otherwise noted, the injection pressure used was 800 bar.

The effect of the amount of second injected fuel on the combustion and emissions was explored with fixed IMEP operating conditions. Three different amounts of second injected fuel were used in which the energizing time of the injector was 100 μs, 150 μs, and 200 μs, respectively. In order to maintain the fixed load condition, the duration (energizing time of the injector) of the main injection (ETp) was adjusted. Two different values, 1400 μs and 1600 μs, were used for dwell time between injections. Other engine operating conditions correspond to those shown in Table 3.

Figure 5 presents emissions results acquired in the test. As the amount of second injected fuel is increased, soot emissions increase, while the NO_x emissions remain relatively constant. The reason why soot emissions are closely related with the amount of second injected fuel may be that there is a trade-off between mixing rate and mixing time. As the amount of second injected fuel is increased, soot production from locally rich regions due to insufficient mixing time becomes much higher than the enhancement of mixing rate by the injection event. Compared to the result of the single injection, the smallest amount of second injected fuel reduced soot emissions by 50%.

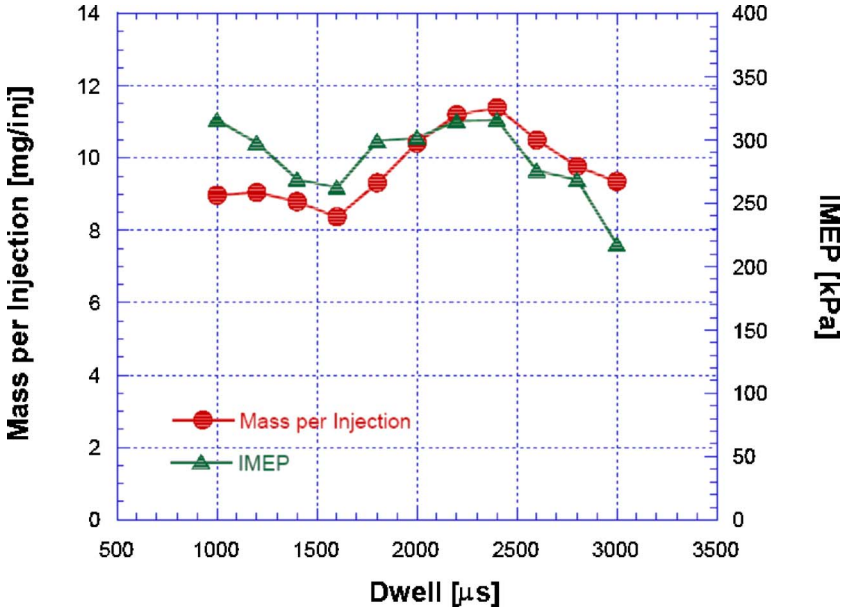

Fig. 3 Variations in total fuel mass per injection and the associated IMEP as a function of dwell with fixed energizing time for both injection pulses. (ET*p* =330 μs, ET=150 μs)

Effect of Dwell Between Injections. The effect of dwell was also investigated with fixed IMEP conditions. SOI timing of the main injection was adjusted to maintain the combustion phasing by matching the location of peak pressure (LPP) with that of the single injection. Also, the amount of first injected fuel (ET*p*) was varied to achieve the load condition (3 bar IMEP) with 800 bar injection pressure. The duration of the second injection was fixed with 100 μs energizing time based on the results obtained in Fig. 5. A dwell ranging between 400 μs and 3200 μs was chosen to explore the effect of dwell on combustion and emissions.

Changes in the apparent heat release rate (AHRR) obtained as the dwell was varied are shown in Fig. 6. The heavy dotted line indicates the heat release rate of the single injection. Note that even though the same duration is used for the second injection, the duration of the first injection had to be changed to achieve the desired load condition due to the injector wave dynamics. The location of the peak of the premixed burn was matched at around 10 CAD. All heat release rate curves show the typical character-

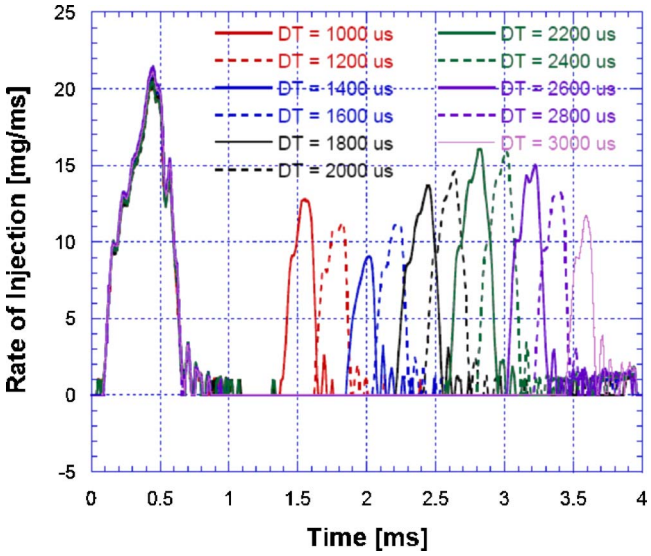

Fig. 4 Rate-of-injection profile with different dwell time (DT) at fixed energizing time (ET*p*=330 μs, ET=150 μs)

Table 3 Operating conditions

Speed (rpm)	1500
Load (bar IMEP)	3
EGR (%)	50
Injection pressure (bar)	800, 1100
Intake temperature (°C)	65
Intake pressure (kPa)	134
Swirl ratio	1.83

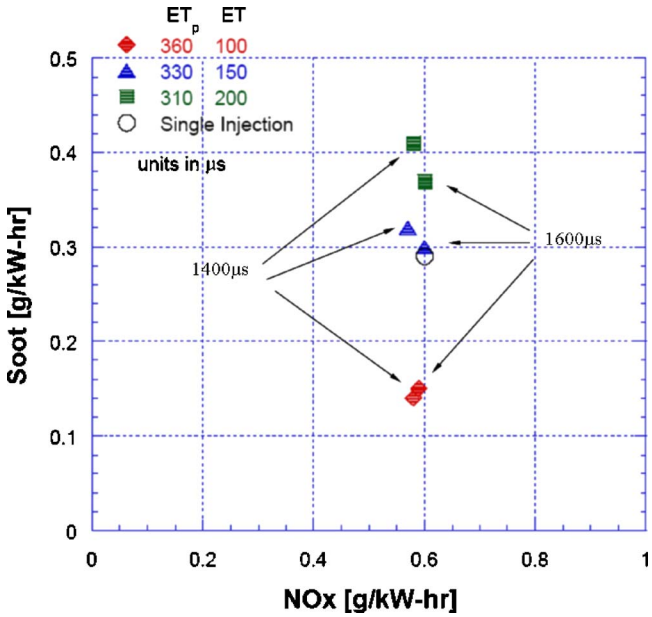

Fig. 5 NO_x-soot trade-off with different amount of second injected fuel with 1400 μs and 1600 μs dwell time, 3 bar IMEP (open circle, single injections)

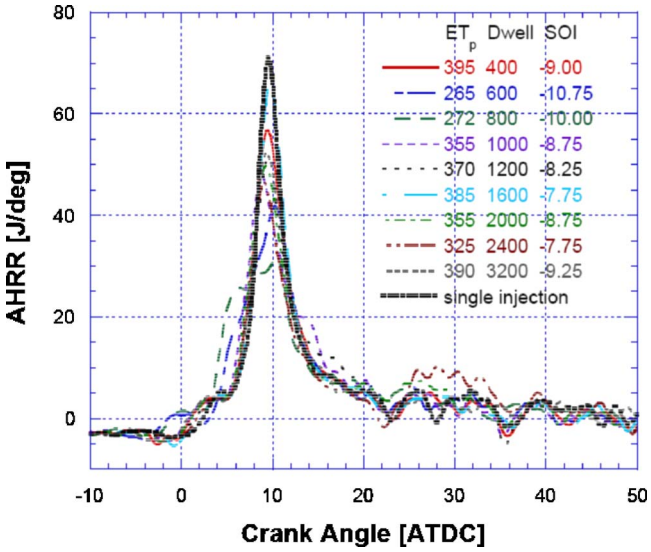

Fig. 6 Changes in AHRR with the dwell time between injections

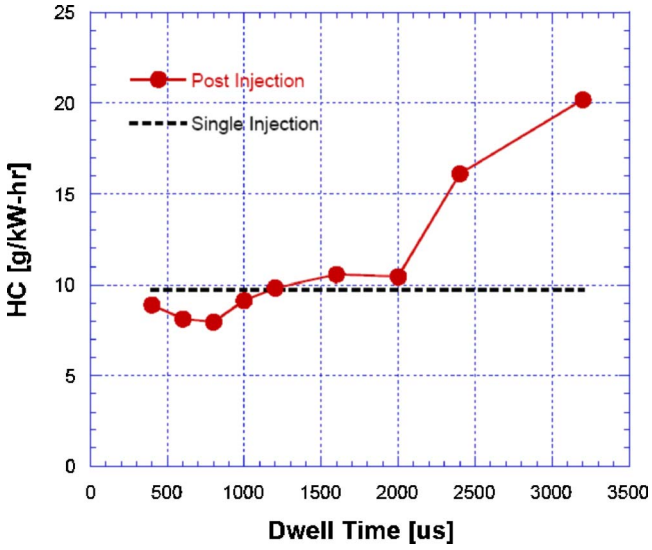

Fig. 8 Comparison results of HC emissions with single injection results

istics of the low-temperature combustion, which are a long ignition delay, and small low-temperature heat release (two-stage ignition) prior to the main premixed burn. It is also seen that, as the dwell is increased, the location that is influenced by the second injection during the combustion process is moved toward the expansion stroke.

Figure 7 shows the corresponding emissions results. Open symbols indicate the emissions results of single injections. The soot emissions show a strong correlation with the dwell; however, the NO_x emissions are only a little influenced by the dwell. Lower soot emissions than those obtained with the single injection were achieved through the post injection at specific dwell times. These specific dwell times correspond to times that avoid injection into an existing soot cloud [16]. This result is consistent with that of other recently published work [17]. It is thought that an additional mixing at the appropriate time during the late-cycle period causes the air motion from the post injection to play a significant role in reducing soot emissions. On the contrary, since temperature changes caused by the post injection are expected to be negligible due to the small injected fuel quantity, NO_x emissions show similar results to those of the single injection case. Thus, using a post injection, lower soot emission is obtained without deteriorating NO_x emissions.

The corresponding variations in HC emissions with increasing dwell are depicted in Fig. 8. The dotted line indicates the result of the single injection. HC emissions become higher than that of the single-injection case for dwells greater than 1600 μs. This suggests that the temperature in the cylinder during the expansion stroke is too low to burn all the injected fuel completely. Based on these results, it is seen that the shortest available dwell (400 μs) shows the best emissions results in all aspects.

High Load Low-Temperature Combustion. In the previous sections, the low-temperature combustion concept was applied to relatively low load cases (3 bar IMEP). It is interesting to investigate the possibility to extend the low-temperature concept to medium-high load conditions. The expected obstacles when the engine load is increased will be that the increase in the fuel amount and the less tolerated EGR rates may not allow low combustion temperatures.

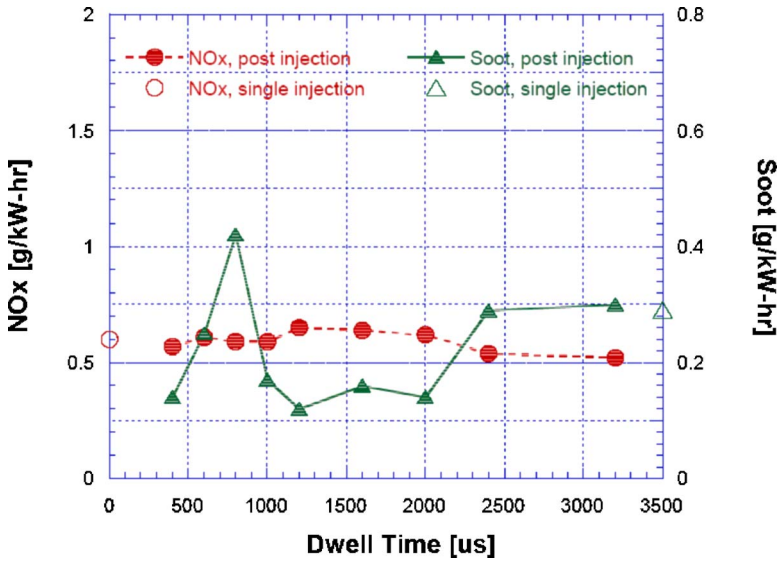

Fig. 7 Variations in NO_x and soot emissions as a function of dwell

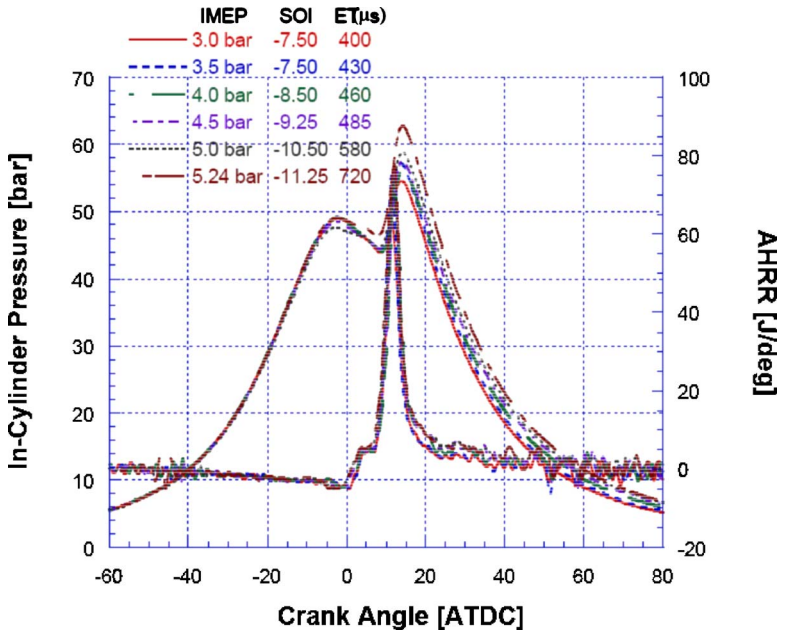

Fig. 9 Changes in the combustion characteristics with increasing load with single injections

First, the upper limit of allowable load was investigated using single injections in the low-temperature combustion regime. The engine operating conditions were the same as those previously investigated (see Table 3), but the total amount of fuel injected was increased. SOI timing was adjusted as shown in Fig. 9 to retain the same combustion phasing by matching the location of peak pressure.

As load is increased, the peak cylinder pressure is increased, but there is little influence on the heat release rate curve. The maximum load that could be obtained while maintaining the features of low-temperature combustion (long ignition delay, low soot, and NO_x emissions) was 5.24 bar IMEP. Above this load, complete combustion could not be achieved due to oxygen deficiency. Thus, even though the injected fuel was further increased, the power output was not increased any further.

NO_x and soot emissions acquired in the load swing test are shown in Fig. 10. Beyond the 4.5 bar IMEP condition, soot emissions increased rapidly because of insufficient mixing, and decreased oxygen availability for soot oxidation.

In addition to increased soot emissions, as shown in Fig. 11, CO emissions also increased sharply due to insufficient oxygen availability beyond the 4.5 bar IMEP load condition. Accordingly, the maximum practical load point was chosen at 4.5 bar IMEP.

Insufficient mixing due to lack of oxygen limits the application of low-temperature combustion at higher load. Therefore, means for enhancement of the mixing rate might extend the desirable load range and improve soot emissions. As shown previously, post-injection strategies proved to be helpful to enhance the mixing rate at the lower load condition. Thus, investigations were made to determine if these strategies could help extend the upper limit of the low-temperature combustion concept. In addition, the effect of mixing enhancement on emissions reduction, especially soot emissions, was examined.

The amount of first fuel injected (ET*p*) was increased to

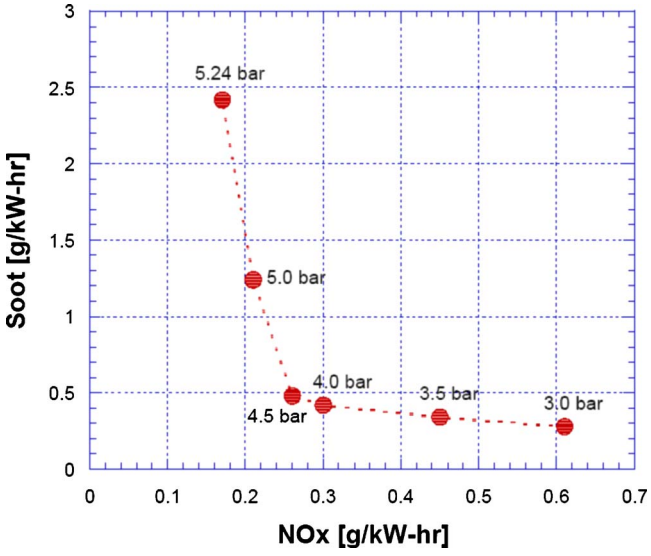

Fig. 10 Soot and NO_x emissions for the load tests of Fig. 10

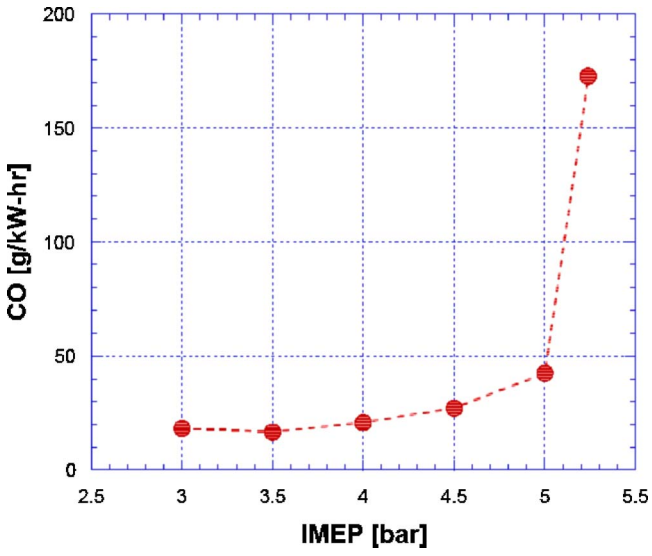

Fig. 11 Changes in CO emissions with increased load

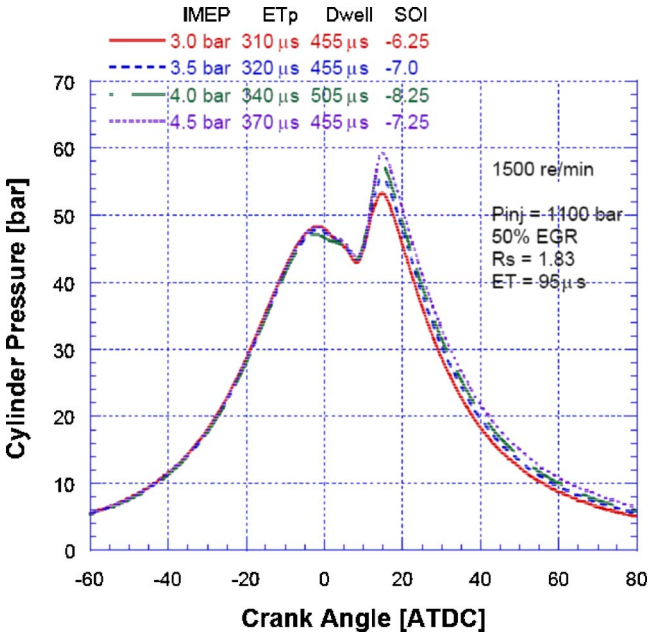

Fig. 12 Changes in cylinder pressure with increased load and post injections (injection pressure 1100 bar)

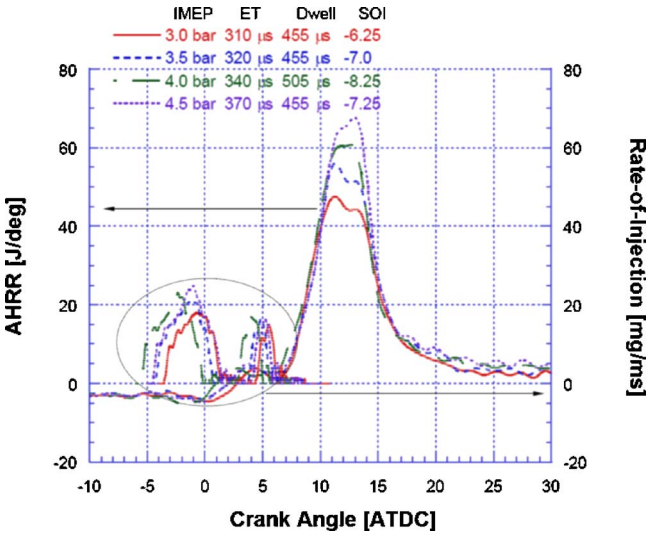

Fig. 14 AHRR and ROI profile obtained with post injections for the conditions of Fig. 13 (injection pressure 1100 bar)

achieve the load condition requested, as shown in Fig. 12. The dwell was also adjusted to find the best emissions results. The amount of second fuel injected was fixed with 95 μs energizing time, which was found to be the minimum possible for repeatable injection with the current injection system (at P_{inj}=1100 bar). The other operating conditions, such as swirl ratio and EGR rate, are the same as those shown in Table 3. As illustrated in Fig. 12, the location of peak pressure was matched to maintain the thermodynamic conditions inside the cylinder by adjusting the SOI timing for the main injection.

Despite the mixing enhancement due to the post injection, as in the previous single-injection results, the highest load that could be obtained while maintaining desirable operating conditions was 4.5 bar IMEP. However, some favorable gain was obtained on emissions, as shown in Fig. 13. As can be seen, a big reduction in soot emissions was achieved for all load conditions investigated using the post-injection strategy while NO_x emissions were held relatively constant.

On the other hand, Fig. 14 illustrates the corresponding apparent heat release and rate-of-injection profiles with increasing load. Regardless of load, the second injection occurred before the main premixed burn started. In addition to the ignition delay for the first injection, another relatively long ignition delay for the second injection was found, as can be seen by the existence of a second peak of the heat release rate in Fig. 14. This long ignition delay could reduce soot emissions by providing extra time for late-cycle mixing. Also the increase in turbulence intensity at late-cycle through the injection event might have an impact on soot reduction.

Finally, the combustion characteristics of single and post injections at 3 bar IMEP are plotted in Fig. 15. Prior to starting the main premixed burn, the two combustion cases have virtually identical cool flame portions of the early heat release rate and long ignition delays. Sufficient mixing time due to the long ignition delay and low combustion temperature (due to the large EGR rate)

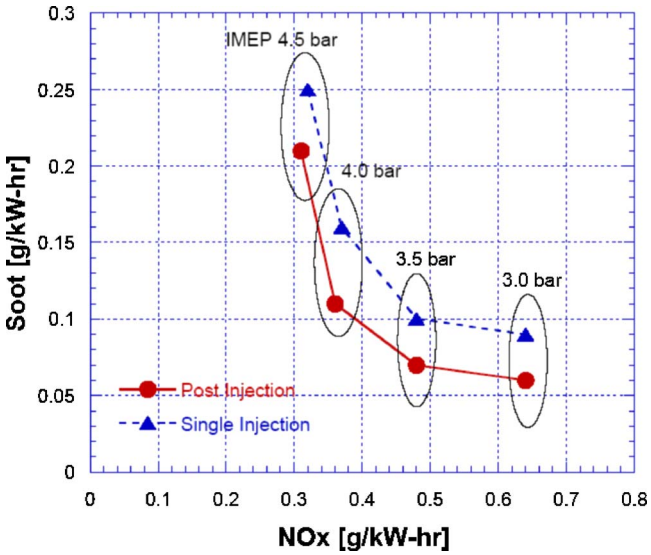

Fig. 13 Comparison of emissions between single and post injections for the conditions of Fig. 12 and Table 3 (injection pressure 1100 bar for both single and post injections)

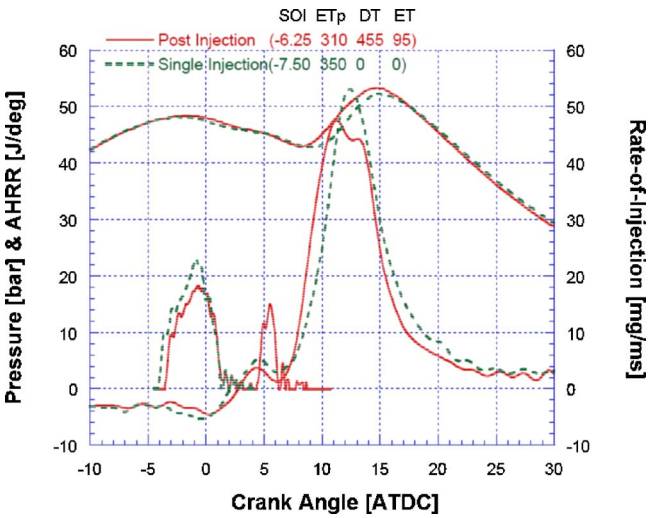

Fig. 15 Comparison of combustion characteristics and ROI profile between single and post injection with P_{inj}=1100 bar, *Rs*=1.83 at 3 bar IMEP

are the major reasons for the decreased engine-out emissions. Note, however, that a second long ignition delay is found in case of post injection associated with the second injection. This means that significant extra time is available for mixing for the second injection before its combustion occurs. This is an explanation for the fact that more soot reduction is achieved through improved late-cycle mixing with the post injection.

Conclusions

The effect of late-cycle mixing enhancement by post injections on combustion and engine-out emissions in the low-temperature combustion regime was experimentally investigated. The baseline operating condition considered for low-temperature combustion was chosen to be 1500 rpm, 3 bar IMEP with 50% EGR rate, and the effects of injection parameters (SOI timing, dwell, and fuel-injected amounts in each pulse) and the use of post injection to increase the allowable load were studied.

Post injections were shown to be useful to reduce soot emissions in low-temperature combustion regimes by facilitating late-cycle mixing. Since post injection leads to late-cycle mixing improvement, further reductions in soot emissions were achieved without deteriorating the NO_x emissions. With smaller amounts of second fuel injected, better soot emissions were obtained. However, the determination of the dwell between the injections was found to be very important for the emissions. The study showed that the combustion of each injected fuel pulse occurs in a distinct "premixed" combustion process. Low emissions and higher load operation can be achieved by optimizing the combustion phasing for each pulse.

Acknowledgment

The authors would like to thank the Department of Energy (DOE) and Sandia National Laboratories for their generous support. The authors would also like to thank Dr. Paul Miles and Dr. Dae Choi for their valuable technical expertise during the course of this work.

References

[1] Ryan, T. W. III, and Callahan, T. J., 1996, "Homogeneous-Charge Compression-Ignition (HCCI) Engines," SAE Paper No. 961160.

[2] Stanglmaier, R. H., and Roberts, C. E., 1999, "Homogeneous Charge Compression Ignition (HCCI): Benefits, Compromises and Future Engine Application," SAE Paper No. 1999–01–3682.

[3] Kimura, S., Aoki, O., Ogawa, H., Muranaka, and S., Enomoto, Y., 1999, "New Combustion Concept for Ultra-Clean and High Efficiency Small DI Diesel Engines," SAE Paper No. 1999–01–3681.

[4] Kimura, S., Aoki, O., Kitahara, Y., and Aiyoshizawa, E., 2001, "Ultra-Clean Combustion Technology Combining a Low-Temperature and Premixed Combustion Concept for Meeting Future Emission Standards," SAE Paper No. 2001–01–0200.

[5] Iwabuchi, Y., Kawai, K., Shoji, T., and Takeda, Y., 1999, "Trial of New Concept Diesel Combustion System—Premixed Compression-Ignited Combustion," SAE Paper No. 1999–01–0185.

[6] Walter, B., and Gatellier, B., 2002, "Development of the High Power NADI™ Concept Using Dual Mode Diesel Combustion to Achieve Zero NO_x and Particulate Emissions," SAE Paper No. 2002–01–1744.

[7] Akihama, K., Takatori, Y., Inagaki, K., Sasaki, S., and Dean, A. M., 2001, "Mechanism of the Smokeless Rich Diesel Combustion by Reducing Temperature," SAE Paper No. 2001–01–0655.

[8] Ishiyama, T., Shioji, M., Ihara, T., and Katsuura, A., 2003, "Modeling and Experiments on Ignition of Fuel Sprays Considering the Interaction Between Fuel-Air Mixing and Chemical Reactions," SAE Paper No. 2003–01–1071.

[9] Shimazaki, N., Tsurushima, T., and Nishimura, T., 2003, "Dual Mode Combustion Concept With Premixed Diesel Combustion by Direct Injection Near Top Dead Center," SAE Paper No. 2003–01–0742.

[10] Bianchi, G. M., Cazzoli, G., Pelloni, P., and Corcione, F. E., "Numerical Study Towards Smoke-Less and NO_x-Less HSDI Diesel Engine Combustion," SAE Paper No. 2002–01–1115.

[11] Miles, P. C., Choi, D., Pickett, L. M., Singh, I. P., Henein, N., RempelEwert, B. A., Yun, H., and Reitz, R. D., 2004, "Rate-Limiting Processes in Late-Injection, Low-Temperature Diesel Combustion Regimes," *THIESEL 2004 Conferences on Thermo- and Fluid Processes in Diesel Engines*, September, Valencia, Spain.

[12] Choi, D., Miles, P. C., Yun, H., Tao, F., and Reitz, R. D., 2004, "A Parametric Study of Low-Temperature, Late-Injection Combustion in a HSDI Diesel Engine," *Proceedings of COMODIA Conference*, Aug., Yokohama, Japan.

[13] Tennison, P., 1998, M.S. thesis, Dept. of Mechanical Engineering, University of Wisconsin-Madison.

[14] Bosch, W., 1966, "The Fuel Rate Indicator: A New Measuring Instrument for Display of the Characteristics of Individual Injection," SAE Paper No. 660749.

[15] Heywood, J. B., 1998, *Internal Combustion Engine Fundamentals*, McGraw-Hill, New York.

[16] Yun, H., Sun, Y., and Reitz, R. D., 2005, "An Experimental and Numerical Investigation on the Effect of Post Injection Strategies on Combustion and Emissions in the Low-Temperature Diesel Combustion Regime," ASME Paper No. ICES2005–1043.

[17] Kanda, T., Hakozaki, T., Uchimoto, T., Hatano, J., Kitayama, N., and Sono, H., 2005, "PCCI Operation With Early Injection of Conventional Diesel Fuel," SAE Paper No. 2005-01-0378.

On-Line Measurements of Engine Oil Aeration by X-Ray Absorption

Devon Manz

Wai K. Cheng

Sloan Automotive Laboratory,
Department of Mechanical Engineering,
Massachusetts Institute of Technology,
77 Massachusetts Avenue,
Cambridge, MA 02139

The oil aeration in a V-6 spark-ignition passenger car engine under motoring condition was measured by the X-ray absorption method in the speed range of 2000–6000 rpm. Measurements were made at different locations in the sump representing the state of the oil at (1) the pump inlet, (2) the head return, and (3) the timing chain return. The aeration of the block return was estimated from these measurements. At a fixed engine speed, the aeration (in % volume of air) of the head return and the chain return were about the same, and they were approximately twice the value found in the block return. This distribution did not change with engine speed. When weighted by the flow rate, however, the block return contributed to 55% of the aeration at the pump inlet; the total contribution of the head return and the chain return was 45% (36% from head return and 9% from chain return). Further aeration observations were made by comparing the cases with and without the oil sump windage tray in place. When the tray was removed, aeration at the pump inlet was found to increase by less than 30% for all speeds.
[DOI: 10.1115/1.2360604]

Introduction

The presence of air in the engine oil system can adversely affect the lubrication and hydraulic functions [1–5]; in some cases, severe aeration leads to hardware failures (e.g., loss of lubrication in the rotating components [4,5]). The degree of aeration is especially severe at high engine speeds because of the increased level of air ingestion into the oil, and because of the shorter residence time in the sump for the air bubbles to rise and escape from entering the oil pump inlet.

The solubility of air in the engine oil is governed by the Bunsen coefficient or Henry's constant (the two quantities are related; see Appendix A). The amount of air dissolved in the oil is proportional to the system pressure p. Thus if the aeration (defined as the ratio of the volume of free air to the total volume of air and oil) is high at the oil pump inlet, it will be substantially lower when the fluid is pressurized by the pump since more air will dissolve in the oil. However when the pressure is released, for example, in a rotating bearing due to the centrifugal force, air will be significantly desorbed and will have an adverse effect on the system performance. Therefore, it is of interest to inventory the flow of free air into the oil pump inlet.

Measurements of aeration level were either done by sampling the oil, letting the air separate out and measuring its volume [3,4], or by monitoring the density of the fluid consisting of the free air and oil together. For the latter, the density may be measured inertially, usually by using a Coriolis flow meter [6,7], or by X-ray absorption [8]. The density measurement methods are preferred because they can monitor the engine state in real time.

This paper describes the measurement of aeration in a passenger car engine motoring at high speed by X-ray absorption. The method was used to inventory the flow of free air in the sump pump inlet and in the return flows from the head and timing chain, respectively. Also aeration level comparisons were made for the engine operating with and without the windage tray. The purpose was to quantify the sources of free air that is fed to the sump pump.

Contributed by the Internal Combustion Engine Division of ASME for publication in the JOURNAL OF ENGINEERING FOR GAS TURBINES AND POWER. Manuscript received February 6, 2006; final manuscript received May 24, 2006. Review conducted by M. Wooldridge.

X-Ray Absorption Method

A commercially available X-ray absorption based apparatus (Air-X from DSI-Deltabeam [8]) was used to monitor aeration in an engine. The measurement principle was based on the fact that free air has a negligible X-ray absorption cross section compared to the engine oil. Thus if the aeration level is x, defined by

$$x = \frac{\text{Volume of free air}}{\text{Volume of free air} + \text{Volume of oil}} \tag{1}$$

where free air refers to the air with is trapped but not dissolved in the oil, then x is related to the measured X-ray intensities I by

$$x = \frac{\log(I/I_0)}{\log(I_1/I_0)} \tag{2}$$

Here, I_0 and I_1 are the intensities measured at $x=0$ (all oil) and $x=1$ (all air) in a calibration process (see the Nomenclature for symbol definitions).

Error Estimate. The error estimate for the aeration measurement may be obtained from Eq. (2) as

$$(\sigma_x)^2 = \left(\frac{\partial x}{\partial I}\sigma_x\right)^2 + \left(\frac{\partial x}{\partial I_0}\sigma_{I_0}\right)^2 + \left(\frac{\partial x}{\partial I_1}\sigma_{I_1}\right)^2 \tag{3}$$

The worst case (largest σ_x) is when $x=0$ (all oil). Then

$$(\sigma_x)^2 = \frac{2}{[\log(I_1/I_0)]^2}\left(\frac{\sigma_{I_0}}{I_0}\right)^2 \tag{4}$$

Since the detector counts X-ray photons, the signals are subject to shot noise, whence

$$\left(\frac{\sigma_{I_0}}{I_0}\right)^2 = \frac{1}{\dot{C}\tau} \tag{5}$$

where $\dot{C}\tau$ is the total count of photons received by the detector at $x=0$ at a counting rate of $\dot{C}$ in a time interval τ. Thus the error estimate for the aeration level x is

$$\sigma_x = \frac{1}{[\log(I_1/I_0)]}\sqrt{\frac{2}{\dot{C}\tau}} \tag{6}$$

The error in x is proportional to $(1/\tau)^{1/2}$. Hence there is a tradeoff

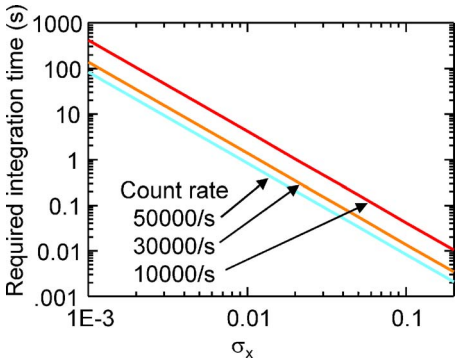

Fig. 1 Required integration time as a function of standard deviation in aeration measurement (σ_x) and count rates

between uncertainty and time resolution.

For the Air-X machine, $I_1/I_0 \approx 2$; the counting rate $\dot{C}$ from the Cadmium 109 X-ray source is of the order of 50,000 per s (the value is for a new source; the half-life of the source is 1.3 year). The tradeoff between accuracy and time resolution is shown in Fig. 1. For the results in this paper, τ was set at 5 s. Then σ_x is of the order of 1%.

Measurement Adjustments. There are two adjustments to be made to the measurements according to Eq. (2). First, the instrument may be calibrated by measuring I_0 at a different temperature than the in-use temperature. Then the thermal expansion of the oil density has to be taken into account. The instrument was used to measure the relative density of the oil as a function of temperature (Fig. 2), and these data were stored to be used for density correction. The Air-X apparatus software has build-in functions to do this correction.

The second adjustment is due to the fact that the sample is transferred from the engine at temperature T_1 and pressure p_1 to the instrument measurement section which is at a different temperature and pressure (T_2 and P_2). Thus the measured value of aeration, x_2, has to be converted to the value x_1 in the engine by accounting for the change in volume of free air and oil due to temperature and pressure changes, and the desorption/absorption of air from the oil. Details of the calculation are described in Appendix B.

Experimental Setup

A production Ford 3.0L V6 DOHC engine was used in this study. The setup has been described in a previous publication [9]; it is briefly described here for completeness. The engine was driven by a 75 hp motor with a 2.29 gear ratio chain drive so that

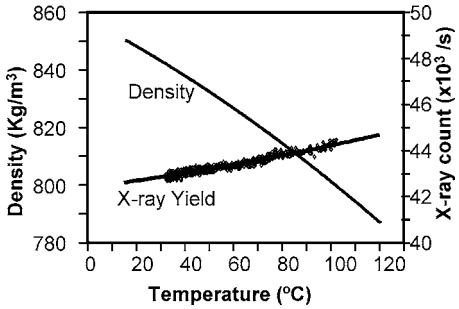

Fig. 2 Air-X sensor signal as a function of oil temperature and the inferred relative density; SAE 5W-20 oil. The density was pegged at the published value at 15.6°C (60°F).

Table 1 Properties of the lubrication oil used in this experiment from Ref. [10]

SAE grade	5W-20
API service	SJ/EC
Gravity	35 °API
Density, @ 15.5°C	851 kg/m^3
Flash point, COC	185°C
Kinematic viscosity at 40°C	4.9×10^{-5} m^2/s
Kinematic viscosity at 100°C	8.8×10^{-6} m^2/s
Viscosity index	161
HT/HS Viscosity @ 150°C	2.65 cP
Pour point	−45°C
Sulfated ash	0.94 wt. %
Total base number	7.5 TBN
ASTM color	4

a maximum speed of 8000 rpm was achievable. The engine was instrumented with thermocouples and pressure gauges to monitor steady state and transient conditions.

The engine was filled with 4 l of SAE 5W-20 oil. The oil properties are shown in Table 1. When the engine was not running, the oil level was 10 mm below the lowest point of the crank shaft counter weight trajectory. When the engine was operating, approximately 2.2 l of oil remained in the sump, while the rest occupied the various engine passageways.

The oil was externally heated or cooled to obtain a reasonable range of temperatures, but the temperature was not precisely controlled because the oil was also heated by the friction of the motoring process. Depending on the engine speed and the location of measurement, the oil temperature was in the range of 80–110°C.

The flow paths of the oil in the engine and in the sump are shown in Figs. 3 and 4. There were three head return paths (two for the right-head and one for the left-head) which drained directly into the sump. The oil form the cam chain and the pump relief returned at the front side of the engine. We will use the name "*block return*" to refer to the oil returned from the engine components in the block (the main and connecting rod bearings, and the blow-by); this flow was nominally collected on the windage tray and drained to the surface of the sump oil.

Oil Sampling. At first, we attempted to sample directly the oil from the head return by using a funnel to collect that oil and to feed it to the Air-X instrument. The measured aeration, however, depended very much on the sample flow rate (which was regulated by the pump of the instrument) because isokinetic sampling

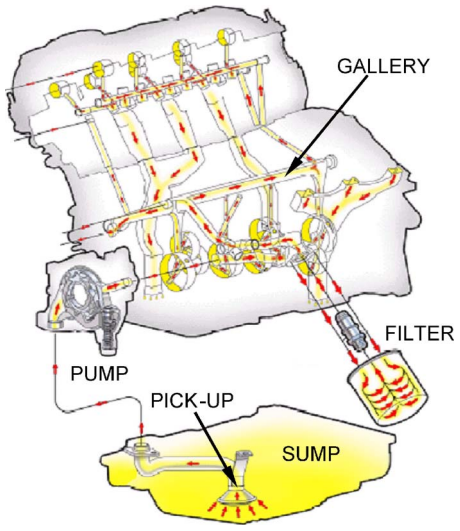

Fig. 3 Oil flow paths in the engine

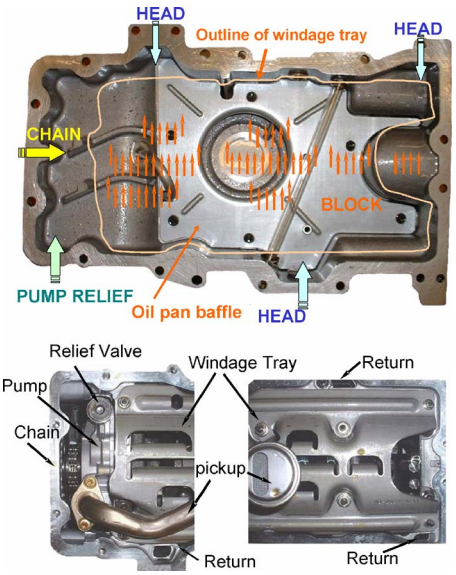

Fig. 4 Geometry of oil flow in the sump. Top figure: view from top of sump with windage tray removed. Bottom figure: view from the bottom of the sump towards the top of the engine.

condition was not achieved. The situation is illustrated in Fig. 5. When the oil flow collected by the funnel is faster than the sample flow rate (Fig. 5(*a*)), the fresh oil spills out of the funnel; the sampling draws in the oil which has been sitting in the funnel for some time, during which some of the air bubbles rise and escape. Therefore the instrument measures a lower aeration level. When the sample flow rate is faster than the collection rate (Fig. 5(*b*)), air is ingested by the sampling system; hence the instrument measures a higher aeration level.

The final sampling configuration is shown in Fig. 6. Oil was sampled from the oil pan at points close to where the various return oil flows entered the sump oil and at the entrance to the pump. (In principle, the oil pan acted as a large collecting funnel, but in this case, it was part of the engine instead of the sampling system so that the effects illustrated in Fig. 5 were not relevant.) The sample locations were at the:

1. Sump pump inlet
2. Head oil return path (referred to as head return)
3. Oil return from the cam chain chamber (referred to as the chain return).

The sampling rate was 1 l per min, which was less than 10% of the oil throughput rate at all the engine speeds in the experiments. The three sample lines were selected by a set of valves to direct

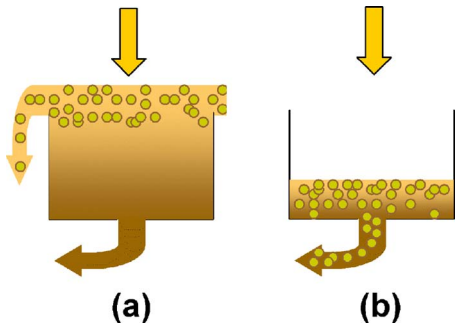

Fig. 5 Nonisokinetic sampling of oil flow. (a) Sampling rate smaller than the collection rate – spill over; (b) sampling rate faster than the collection rate – ingestion of air.

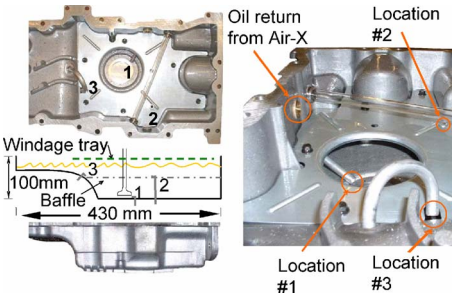

Fig. 6 Engine oil sampling points in the sump; the line drawing is to scale. The sampling locations were (1) sump pump inlet; (2) head return; (3) chain return. The glass view tube in the right picture was not used in this experiment.

the flow to the Air-X instrument. The line length from locations 1, 2, and 3 to the X-ray apparatus was 0.58, 0.89, and 0.53 m, respectively. The line inner diameters were 12 mm. The residence time of the oil in the line was 4–6 s. The temperature drop from the sump (at 80–110°C) to the instrument measurement section was approximately 4°C.

Aeration Measurements

Typical aeration data are shown in Fig. 7 for the three sampling locations. To flush out the sampling system, the first portion of the data were not used when the sampling line was switched. The steady state data scatter was of the order of 1 percentage point.

The continuous data for a speed change are shown in Fig. 8. It took approximately 50 s for the measured value to re-establish steady state. This time constant was a combination of the filling/emptying time of the sampling system and the adjustment time of the aeration level in the engine. When the speed was changed, typically a 50–100 s wait period ensured a steady state condition.

To investigate whether the aeration level was dependent on the previous state, the following four sets of data were taken with the procedure described above:

(i) baseline data in which the speed was changed from 2000 to 6000 rpm in 1000 rpm increments;
(ii) then the data was repeated with the engine speed changed in the order of 2000, 5000, 3000, 6000, and 4000 rpm;
(iii) the engine was shut down for 100 s after the second experiment, and (i) was repeated. The oil was given the chance to deaerate, while the temperature was only reduced modestly;

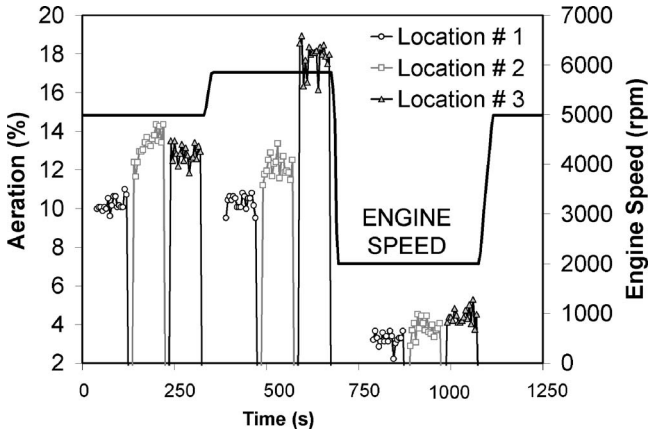

Fig. 7 Typical aeration data from the three locations shown in Fig. 6. Engine speed ranged from 2000 to 6000 rpm. Sample integration time of 5 s; 1 l/min sample flow.

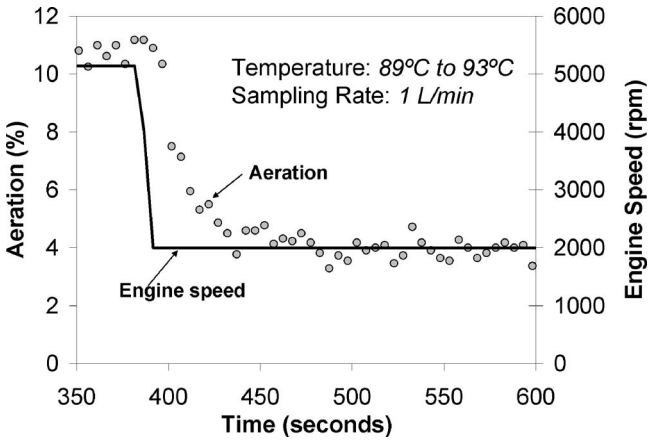

Fig. 8 Aeration measurement in a speed change. Measurement from sump pump inlet (location 1).

(iv) The data were taken after a 24 h waiting period during which the oil had completely deaerated and cooled to ambient temperature.

The results are shown in Fig. 9. The four procedures produced essentially the same results. (Some of the data points overlapped.) Thus the steady state aeration level is an equilibrium value which does not depend on prior conditions.

The data in Fig. 9 clearly show that the aeration increased with engine speed and that location 1, being further from the oil surface than location 3, had a lower aeration level. These observations are consistent with the explanation that air bubbles rise and escape from the sump oil; so aeration decreases as a function of depth and increases with higher engine speed (shorter residence time).

To decouple the speed effect and sump residence time effect on the aeration at the pump inlet, the total oil volume in the engine was changed. The premise was that the residence time should scale as the oil volume in the sump divided by the pump flow rate. The engine oil was drained and refilled with 4, 4.5, and 5 l of 5W-20 oil, respectively. When the engine was running, the amount of oil in the sump was at approximately 2.2, 2.7, and 3.2 l; thus there should be a significant change in the sump residence time at the same engine speed.

The aeration values at the pump inlet for the three different oil volumes are shown in Fig. 10. (Note that the pump relief valve kicked in at 3000 rpm; but that should not affect the results for comparing the aeration at the same rpm.) The aeration increased with speed; there was, however, no significant dependence on oil volume within the experimental uncertainty of ±1%. Further experimental results are therefore needed to clarify the role of air bubble rise and the sump residence time on aeration.

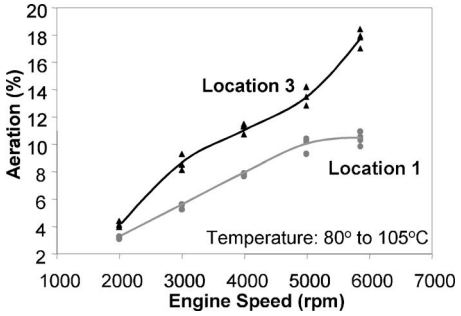

Fig. 9 Aeration at different engine speeds for locations 1 and 3 in Fig. 6. The four data points at each speed for each location correspond to the values obtained from the four procedures described in the text.

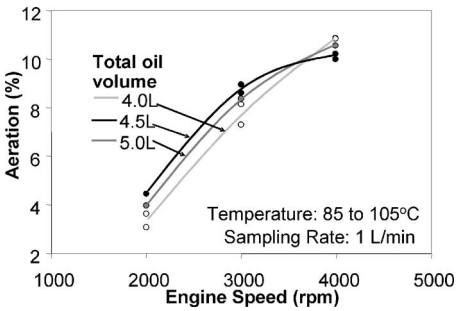

Fig. 10 Aeration at the sump pump inlet (location 1) for total engine oil volumes of 4.0, 4.5, and 5.0 l (corresponding to 2.2, 2.7, and 3.2 l of oil in the sump when engine was running)

Flow of Free Air in the Sump

Figure 11 shows the oil aeration as a function of engine speeds at the three locations shown in Fig. 6. Location 1 measured the oil at the pump inlet; location 2 measured the oil returned from the head; location 3 measured the oil returned from the chain. The oil flow through the engine was known (see Fig. 12): 12% delivered to each side of the head, 6% to the chain drive, and 70% to the main and connecting rod bearings. Since the flow at the sump pump inlet was equal to the sum of the flows returning from the head, the chain and the block, the aeration of the block return may

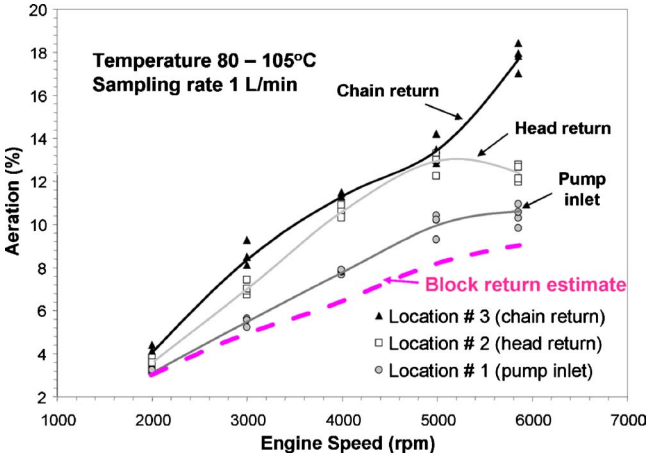

Fig. 11 Aeration measurements as a function of engine speed at different locations in the sump

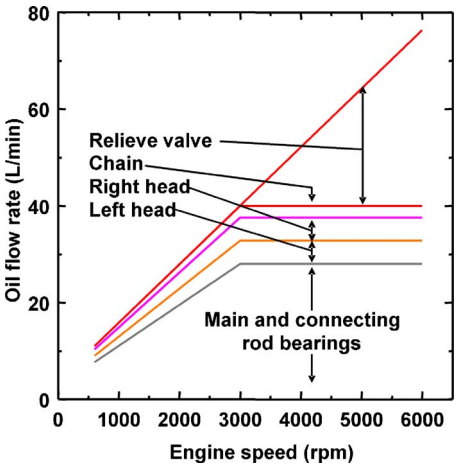

Fig. 12 Oil flow distribution in engine. Sump pump relief valve activated at 3000 rpm.

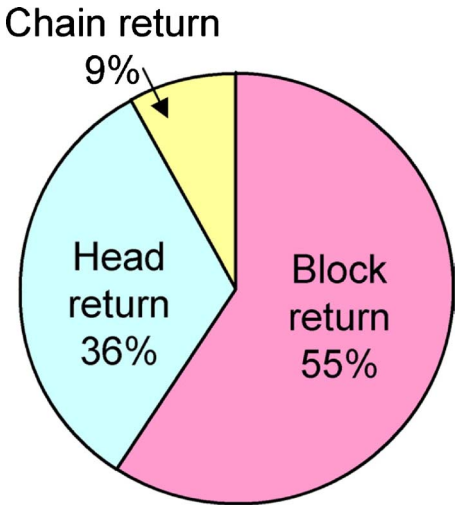

Fig. 13 Distribution of air transport from the returns

be estimated. In this estimate, the oil from the relief valve was assumed to be at the same aeration as the pump inlet since the entrained air that was absorbed when the oil was pressurized would be released when the pressure was relieved. Furthermore, the amount of deaeration was assumed to be small in the sump. This assumption was supported by the insensitivity of the aeration at the pump inlet to the oil volume (Fig. 10). Nevertheless, the resulting value for the block return aeration would be a lower estimate. Then,

$$x_b = \frac{(Q_i - Q_r)x_1 - Q_h x_2 - Q_c x_3}{Q_b} \tag{7}$$

where

x_b= aeration of the block return (i.e., oil return from engine components in the block)
x_1= aeration at the pump inlet (measured at location 1)
x_2= aeration of the head return oil (measured at location 2)
x_3= aeration of the chain return oil (measured at location 3)
Q_i= volume flow rate at the pump inlet
Q_r= relief valve flow rate (valve activated at 3000 rpm)
Q_h= head (both sides) flow rate
Q_c= chain drive flow rate

The estimated aeration, x_b, of the block return is shown as a dashed line in Fig. 11.

The data in Fig. 11 show that the aeration of the head return and the chain return oil were about the same; they were approximately twice the values found in the block return. This distribution did not change with the engine speed. When weighed by the flow rate, however, the block return contributed to 55% of the aeration at the pump inlet; the total contribution of the head return and chain return was 45% (36% from head return and 9% from chain return), see Fig. 13. (Since the oil flow from the relief valve was assumed to have the same aeration as the pump inlet, it was not considered as a primary source of aeration, and therefore not included in this accounting.) Thus both the block return and head return were major contributors to the flow of trapped air to the sump pump. The chain return contribution was much less because of the low volumetric flow rate.

Measurements Without Windage Tray

To assess the effect of the windage tray on aeration, measurements were made with the windage tray removed. The results are shown in Fig. 14. When the tray was removed, the aeration at the sump pump inlet increased by less than 30% for all speeds.

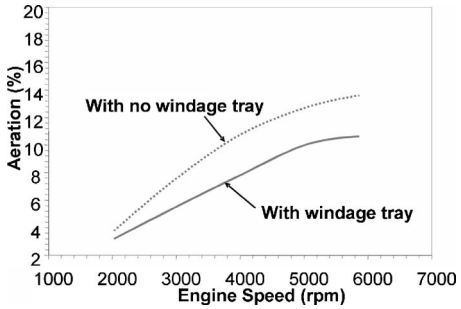

Fig. 14 Aeration at sump pump inlet as a function of engine speed, with and without windage tray in place

The windage tray blocks the majority of the oil drops in the crankcase from striking the oil in the sump. Only 20% of the windage tray area was open for venting (see Figs. 3 and 4). If the oil drops from the moving crank and the blow-by were a major source of aeration, a much bigger difference in aeration would be expected when the windage tray was removed.

To explain this observation, it was conjectured that a significant amount of aeration was produced by the droplets striking the oil layer on the windage tray. Therefore, the difference between the cases with and without the windage tray in place was only in the interaction of the oil drops from the crankcase with the oil layer on the tray and with the oil in the sump. Hence, a big difference was not found.

Conclusions

The oil aeration in a motoring V-6 spark-ignition passenger car engine was measured by X-ray absorption. The method was used to inventory the flow of free air to the sump pump inlet from the return oil flows. The following observations were made:

1. At a fixed engine speed, the aeration (as % volume of free air in the air/oil mixture) of the head return and the chain return were about the same, and they were approximately twice the value found in the block return. This distribution did not change with engine speed.
2. When weighted by the flow rate, however, the block return contributed to 55% of the aeration at the pump inlet and the head return contributed to 36%. The chain return contribution of 9% was much smaller because the volume flow rate was much less.
3. There were no significant changes in aeration at the sump pump inlet when the total engine oil volume was changed from 4 to 5 l, which corresponded to a sump oil volume of 2.2 and 3.2 l under running condition.
4. When the windage tray was removed, aeration at the pump inlet increased by less than 30% over all engine speeds.

The X-ray absorption method was found to be a very effective means of measuring oil aeration in an engine.

Acknowledgment

This work was supported by the Ford Motor Company under the Ford/MIT Alliance Program. Devon Manz was also partially supported by the Natural Sciences and Engineering Research Council of Canada (NSERC). Feng Shen, Ejakov Mikhail, Ben Ni, and John Pieprzak from Ford POEE initiated the project and provided the engine hardware and valuable inputs. We would also like to thank Bob Finchum and Bill Hall from the Ramsey Products Corporation for their donation of the silent chain drive for the motor. Setting up the X-ray absorption measurement apparatus was greatly facilitated by Benoit Deconninck and Thierry Delvigne, from DSI Deltabeam, and Ken Oxorn, from ANS Technologies.

Nomenclature

- ' = quantities dissolved in oil
- B = Bunsen coefficient
- $\dot{C}$ = X-ray counting rate at detector
- H = Henry's constant
- I = measured X-ray intensity
- I_0 = measured X-ray intensity at $x=0$
- I_1 = measured X-ray intensity at $x=1$
- N_0 = mole of oil
- N = mole of free air
- N' = mole of dissolved air
- p = absolute pressure
- p^* = reference pressure (1 bar)
- Q_i = volume flow rate at pump inlet
- Q_r = relief valve flow rate (valve activated at 3000 rpm)
- Q_h = head (both sides) flow rate
- Q_c = chain drive flow rate
- R = universal gas constant
- T = temperature
- T^* = reference temperature (293 K)
- V_{oil} = volume of oil
- V = volume of air
- V^* = volume of dissolved air when released to the reference condition of T^* and p^*
- x = aeration level; ratio of volume of free air to total volume of free air plus oil
- x_b = aeration of block return
- x_1 = aeration at pump inlet (measured at location 1)
- x_2 = aeration of head return oil (measured at location 2)
- x_3 = aeration of chain return oil (measured at location 3)
- ρ_0 = molar density of oil
- σ = standard deviation
- τ = integration time of the X-ray detector

Appendix A: Relationship Between Henry's Constant and Bunsen Coefficient

Henry's constant H and Bunsen coefficient B are two ways of assessing the solubility of air in a liquid. Consider N_0 mole of oil in thermodynamic equilibrium with air at absolute pressure p. Then the number of moles of dissolved air, N', is governed by the Henry's constant H,

$$p = H\frac{N'}{N_0 + N'} \tag{A1}$$

The Bunsen coefficient B is defined by the following:

$$V^* = BV_{\text{oil}}\frac{p}{p^*} \tag{A2}$$

where V_{oil} is the oil volume and V^* is the volume occupied by the dissolved air when it is released to a reference condition at p^* and T^* (1 bar and 293 K). Thus,

$$N' = \frac{p^*V^*}{RT^*} \tag{A3}$$

where R is the universal gas constant. Comparing Eqs. (A1)–(A3), the Bunsen coefficient and Henry's constant are related by

$$B = \frac{\rho_0 RT^*}{H - p} \tag{A4}$$

where ρ_0 is the molar density of the oil. For $N_0 \gg N'$ (equivalent to $H \gg p$), which is usually the case, Eq. (B4) simplifies to

$$B = \frac{\rho_0 RT^*}{H} \tag{A5}$$

Typical values for air dissolving in lubrication oil are $\rho_0 = 1.76$ kmol/m^3, $B=0.09$, $H=476$ bar.

Appendix B: Relationship Between Aeration Level at Sample Inlet and at Instrument Measurement Section

At the sample inlet, the instrument draws in N_1 mole of free air and N_1' mole of dissolved air which is contained in N_0 mole of oil at temperature T_1 and pressure p_1. The free air occupies a volume of V_1 given by

$$V_1 = \frac{N_1 RT_1}{p_1} \tag{B1}$$

where R is the universal gas constant. The aeration level x_1 at the inlet is given by

$$x_1 = \frac{V_1}{V_1 + N_0/\rho_{0,1}} \tag{B2}$$

where $\rho_{0,1}$ is the molar density of oil at the inlet condition. This sample (free air+oil+dissolved air) is transferred to the measurement section of the instrument which is at temperature T_2 and pressure p_2. Here the volume of free air is V_2. The aeration level x_2 at the measurement section is given by

$$x_2 = \frac{V_2}{V_2 + N_0/\rho_{0,2}} \tag{B3}$$

where $\rho_{0,2}$ is the molar density of oil at the measurement section.

To calculate x_1 from x_2, two physical effects have to be accounted for: (i) the change in gaseous and liquid volumes via the ideal gas law and coefficient of expansion of the oil; (ii) desorption/absorption of air by the oil. The calculation applies Henry's law (Eq. (A1), assuming that $N_0 \gg N'$) to relate the free and dissolved quantities of air, and notes that the total moles of free and dissolved air are conserved,

$$N_2 + N_2' = N_1 + N_1' \tag{B4}$$

After some algebra, x_1 is related to x_2 by

$$x_1 = \frac{\xi}{1 + \xi} \tag{B5}$$

where

$$\xi \equiv \left(\frac{p_2}{p_1}\frac{T_1}{T_2}\frac{\rho_{0,1}}{\rho_{0,2}}\right)\frac{x_2}{1 - x_2} + \frac{\rho_{0,1}RT_1}{H_1}\left(\frac{p_2}{p_1}\frac{H_1}{H_2} - 1\right) \tag{B6}$$

The subscripts 1 and 2 refer to the inlet and measurement section conditions, respectively. The first term in the ξ expression in Eq. (B6) represents the effect of changes in gaseous and liquid volumes. The second term represents the desorption/absorption effect. For T_2, P_2 is the same as T_1, P_1, and the expression reduces to $x_1 = x_2$.

References

[1] Ni, B., and Pieprzak, J., 2004, "Transportation and Transformation of Air Bubbles in Aerated Oil Through an Engine Lubrication System," SAE Paper No. 2004-01-2915.

[2] Nemoto, S., Kawata, K., Kuribayashi, T., Akiyama, K., Kawai, H., and Murakawa, H., 1997, "A Study of Engine Oil Aeration," JSAE Rev., **18**, pp.

271–276.
[3] Koch, F., Hardt, T., and Haubner, F., 2001, "Oil Aeration in Combustion Engines – Analysis and Optimization," SAE Paper No. 2001-01-1074.
[4] Choi, J. K., Min, B. S., and Han, D. C., 1993, "Effect of Oil Aeration Rate on the Minimum Oil Film Thickness and Reliability of Engine Bearing," SAE Paper No. 932785.
[5] Maassen, F., and Koch, F., and Pischinger, F., 1998, "Connecting Rod Bearing Operation with Aerated Lube Oil," SAE Paper No. 981404.
[6] Morgan, C., Cummings, J., Fewkes, R., and Jackson, J., 2004, "A New Method of Measuring Aeration and Deaeration of Fluids," SAE Paper No. 2004-01-2914.
[7] Sparks, D., Smith, R., Massoud-Ansari, S., and Najafi, N., "Coriolis Mass Flow, Density and Temperature Sensing with a Single Vaccum Sealed Mems Chip," http://www.memsissys.com/pdf/issystech17.pdf
[8] Deconninck, B., Delvigne, T., and Videx, G., 2003, "Air-X, an Innovative Device for On-line Oil Aeration Measurement in Running Engines," SAE Paper No. 2003-01-1995.
[9] Manz, D. L., Cowart, J. S., and Cheng, W. K., 2004, "High-Speed Video Observation of Engine Oil Aeration," SAE Paper No. 2004-01-2913.
[10] Motorcraft website: http://www.motorcraft.com

H.-J. Kretzschmar[1]
Department of Technical Thermodynamics,
Zittau/Goerlitz University of Applied Sciences,
P.O. Box 1455, D-02754 Zittau, Germany
e-mail: hj.kretzschmar@hs-zigr.de

J. R. Cooper
Department of Engineering,
Queen Mary University of London,
Mile End Road, London E1 4NS, UK

A. Dittmann
Department of Technical Thermodynamics,
Technical University of Dresden, Dresden
D-01062, Germany

D. G. Friend
Physical and Chemical Properties Division,
National Institute of Standards and Technology,
325 Broadway, Boulder, CO 80305

J. S. Gallagher
Physical and Chemical Properties Division,
National Institute of Standards and Technology,
100 Bureau Drive, Gaithersburg, MD 20899-8380

A. H. Harvey
Physical and Chemical Properties Division,
National Institute of Standards and Technology,
325 Broadway, MS 838.08 Boulder, CO 80305
e-mail: aharvey@boulder.nist.gov

K. Knobloch
Department of Technical Thermodynamics,
Zittau/Goerlitz University of Applied Sciences,
P.O. Box 1455, D-02754 Zittau, Germany

R. Mareš
Department of Thermodynamics,
University of West Bohemia, Univerzitni 8,
Plzeň CZ 306 14, Czech Republic

K. Miyagawa
4-12-11-628 Nishiogu,
Arakawa-ku Tokyo 116-0011, Japan

N. Okita
Thermal Plant Systems Project Department,
Toshiba Corporation, 1-1, Shibaura 1-chome
Minato-ku, Tokyo 105-8001, Japan

I. Stöcker
Department of Technical Thermodynamics,
Zittau/Goerlitz University of Applied Sciences,
P.O. Box 1455, D-02754 Zittau, Germany

W. Wagner
Lehrstuhl für Thermodynamik, Ruhr-Universität
Bochum, Bochum D-44780, Germany

I. Weber
Siemens AG, PG ER4,
Freyeslebenstr. 1,
D-91058 Erlangen,
Germany

Supplementary Backward Equations $T(p,h)$, $v(p,h)$, and $T(p,s)$, $v(p,s)$ for the Critical and Supercritical Regions (Region 3) of the Industrial Formulation IAPWS-IF97 for Water and Steam

In modeling advanced steam power cycles, thermodynamic properties as functions of pressure and enthalpy (p,h) or pressure and entropy (p,s) are required in the critical and supercritical regions (region 3 of IAPWS-IF97). With IAPWS-IF97, these calculations require cumbersome two-dimensional iteration of temperature T and specific volume v from (p,h) or (p,s). While these calculations in region 3 are not frequently required, the computing time can be significant. Therefore, the International Association for the Properties of Water and Steam (IAPWS) adopted backward equations for $T(p,h)$, $v(p,h)$, $T(p,s)$, and $v(p,s)$ in region 3, along with boundary equations for the saturation pressure as a function of enthalpy, $p_{3\mathrm{sat}}(h)$, and of entropy, $p_{3\mathrm{sat}}(s)$. Using the new equations, two-dimensional iteration can be avoided. The numerical consistency of temperature and specific volume obtained in this way is sufficient for most uses. This paper summarizes the need and the requirements for these equations and gives complete numerical information. In addition, numerical consistency and computational speed are discussed. [DOI: 10.1115/1.2181598]

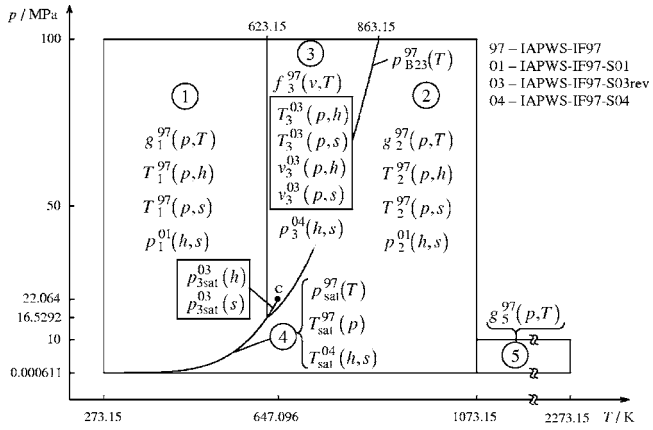

Fig. 1 Regions and equations of IAPWS-IF97, IAPWS-IF97-S01, IAPWS-IF97-S04, and the backward equations $T_3^{03}(p,h)$, $v_3^{03}(p,h)$, $T_3^{03}(p,s)$, and $v_3^{03}(p,s)$ and boundary equations $p_{3sat}^{03}(h)$ and $p_{3sat}^{03}(s)$ of this work

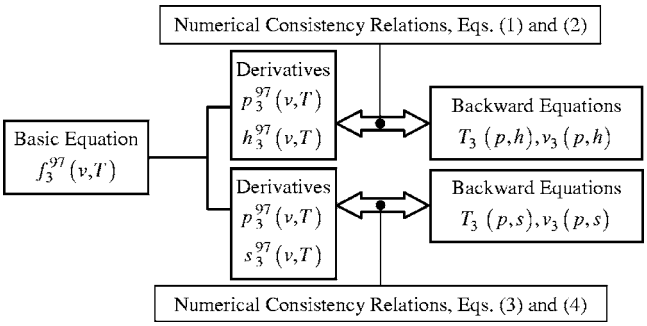

Fig. 2 Numerical consistency relations of the backward functions $T(p,h)$, $v(p,h)$, and $T(p,s)$, $v(p,s)$ with the IAPWS-IF97 basic equation $f_3^{97}(v,T)$

1 Introduction

In 1997, the International Association for the Properties of Water and Steam (IAPWS) adopted its formulation for industrial use for the thermodynamic properties of water and steam (IAPWS-IF97) [1,2]. IAPWS-IF97 contains fundamental equations and saturation equations; it also contains equations for the most often used backward functions $T(p,h)$ and $T(p,s)$ for the liquid region 1 and the vapor region 2; see Fig. 1.

In 2001, IAPWS-IF97 was supplemented by equations for the backward function $p(h,s)$ for regions 1 and 2 (see Fig. 1) [3,4]. This is referred to here as IAPWS-IF97-S01.

In modeling advanced steam power cycles, thermodynamic properties as functions of (p,h) or (p,s) are required in region 3. Performing these calculations with IAPWS-IF97 requires two-dimensional iteration using the functions $p(v,T)$, $h(v,T)$ or $p(v,T)$, $s(v,T)$ that can be explicitly derived from the region 3 fundamental equation $f(v,T)$. While these calculations in region 3 are not frequently required, the relatively large computing time can be significant. Therefore, in 2003 IAPWS adopted backward functions $T_3^{03}(p,h)$, $v_3^{03}(p,h)$ and $T_3^{03}(p,s)$, $v_3^{03}(p,s)$ (see Fig. 1). With temperature and specific volume calculated from the new backward equations, the other properties in region 3 can be calculated using the IAPWS-IF97 basic equation $f_3^{97}(v,T)$. Subsequently, equations for the saturation pressure as a function of enthalpy $p_{3sat}^{03}(h)$ and as a function of entropy $p_{3sat}^{03}(s)$ for the saturated-liquid and saturated-vapor boundaries of region 3 (see Fig. 1) were developed. Using these boundary equations, it can be determined directly whether a state point is in the single-phase or two-phase region. The boundary equations were adopted by IAPWS in 2004 and became part of the "Revised Supplementary Release on Backward Equations for the Functions $T(p,h)$, $v(p,h)$ and $T(p,s)$, $v(p,s)$ for Region 3 of the IAPWS Industrial Formulation 1997 for the Thermodynamic Properties of Water and Steam" [5], referred to here as IAPWS-IF97-S03rev. The purpose of this paper is to document IAPWS-IF97-S03rev.

Figure 1 also shows an additional supplementary release, referred to as IAPWS-IF97-S04, which was adopted in 2004 for efficient calculation of properties in region 3 as a function of the variables (h,s) [6]. The entire system of adopted and proposed supplementary backward equations to IAPWS-IF97 is summarized in [7].

2 Backward Equations $T(p,h)$, $v(p,h)$, $T(p,s)$, and $v(p,s)$ for Region 3

2.1 Consistency Requirements IAPWS-IF97 region 3 is covered by a basic equation for the Helmholtz free energy $f_3^{97}(v,T)$; see Fig. 2. Derived from this equation are the pressure p, specific enthalpy h, and specific entropy s as functions of specific volume v and temperature T. Equations for backward functions need to be numerically consistent with the basic equation. The consistency requirements for the backward functions $T(p,h)$, $v(p,h)$, $T(p,s)$, and $v(p,s)$ can be formulated as follows:

$$|\Delta T| = |T_3[p_3^{97}(v,T),h_3^{97}(v,T)] - T| \leq |\Delta T|_{tol} \tag{1}$$

$$\left|\frac{\Delta v}{v}\right| = \left|\frac{v_3[p_3^{97}(v,T),h_3^{97}(v,T)] - v}{v}\right| \leq \left|\frac{\Delta v}{v}\right|_{tol} \tag{2}$$

$$|\Delta T| = |T_3[p_3^{97}(v,T),s_3^{97}(v,T)] - T| \leq |\Delta T|_{tol} \tag{3}$$

$$\left|\frac{\Delta v}{v}\right| = \left|\frac{v_3[p_3^{97}(v,T),s_3^{97}(v,T)] - v}{v}\right| \leq \left|\frac{\Delta v}{v}\right|_{tol} \tag{4}$$

Equation (1) means that the difference between the temperature calculated from the backward equation $T_3(p,h)$ for given values of p and h and the temperature obtained by iteration from the IAPWS-IF97 basic equation for the same p and h must be smaller than the tolerance $|\Delta T|_{tol}$. For the specific volume, Eq. (2), the similarly defined relative difference must be smaller than the tolerance $|\Delta v/v|_{tol}$. Equations (3) and (4) give similar consistency requirements for the backward functions $T(p,s)$ and $v(p,s)$.

The tolerance for consistency of the backward functions $T(p,h)$ and $T(p,s)$ with the basic equation $f(v,T)$, $|\Delta T|_{tol}$=25 mK, was determined by IAPWS [8,9] in an international survey. $|\Delta T|_{tol}$ and other tolerances for this work are listed in Table 1.

The tolerance Δv_{tol} for consistency of the backward functions $v(p,h)$ and $v(p,s)$ can be estimated from the total differentials

Table 1 Numerical consistency values $|\Delta T|_{tol}$ of [8,9] required for $T(p,h)$ and $T(p,s)$, values $|\Delta h|_{tol}$, $|\Delta s|_{tol}$ of [11], and resulting tolerances $|\Delta v/v|_{tol}$ required for $v(p,h)$ and $v(p,s)$

$\lvert\Delta T\rvert_{tol}$	$\lvert\Delta h\rvert_{tol}$	$\lvert\Delta s\rvert_{tol}$	$\lvert\Delta v/v\rvert_{tol}$
25 mK	80 J kg^{-1}	0.1 J kg^{-1} K^{-1}	0.01%

[1]To whom correspondence should be addressed.

Submitted to ASME for publication in the JOURNAL OF ENGINEERING FOR GAS TURBINES AND POWER. Manuscript received March 17, 2005; final manuscript received January 10, 2006. Review conducted by L. Langston.

$$\Delta v_{\mathrm{tol}} = \left(\frac{\partial v}{\partial T}\right)_h \Delta T_{\mathrm{tol}} + \left(\frac{\partial v}{\partial h}\right)_T \Delta h_{\mathrm{tol}} \tag{5}$$

and

$$\Delta v_{\mathrm{tol}} = \left(\frac{\partial v}{\partial T}\right)_s \Delta T_{\mathrm{tol}} + \left(\frac{\partial v}{\partial s}\right)_T \Delta s_{\mathrm{tol}} \tag{6}$$

where the partial derivatives are calculated from the IAPWS-IF97 basic equation [10] and Δh_{tol} and Δs_{tol} were determined for IAPWS-IF97 from a survey of power companies and related industries [11]. In order to provide conservative uncertainties, only the mean value of the smallest of the four summands of Eqs. (5) and (6) was taken for determining Δv_{tol}. Table 1 shows the resulting tolerance $|\Delta v/v|_{\mathrm{tol}}=0.01\%$ for both $v(p,h)$ and $v(p,s)$.

2.2 Development of Equations. A major motivation for the development of IAPWS-IF97 and its supplementary backward equations was reducing computing time. Investigations during the development of IAPWS-IF97 showed that polynomials in the form of series of additions and multiplications are effective as basic terms [12]. Therefore the following general functional form was used:

$$\frac{Z(X,Y)}{Z^*} = \sum_i n_i \left(\frac{X}{X^*} + a\right)^{I_i} \left(\frac{Y}{Y^*} + b\right)^{J_i} \tag{7}$$

The final equations were found from Eq. (7) by an approximation algorithm [13–16]. The reducing parameters Z^*, X^*, and Y^* are maximum values of the corresponding property within the range of validity of the equation. The shifting parameters a and b were determined by nonlinear optimization. The exponents I_i, J_i, and coefficients n_i were determined from the structure optimization method of Wagner [17] and Setzmann and Wagner [18], which chooses the optimal terms from a bank of terms with various values of I_i and J_i. In the optimization process, the backward equations were fitted to T-v-p-h or T-v-p-s values, with p, h, and s calculated from the IAPWS-IF97 basic equation $f_3^{97}(v,T)$, for values of v and T distributed over the range of validity. The critical point was set as a constraint. The algorithm considers the computing time needed for the equation as a part of the optimization. Details of the fitting processes are given in [13,19].

2.3 Subregions. Region 3 is defined by $623.15\ \mathrm{K} \leqslant T \leqslant 863.15\ \mathrm{K}$ and $p_{\mathrm{B23}}^{97}(T) \leqslant p \leqslant 100\ \mathrm{MPa}$ (see Fig. 1), where p_{B23}^{97} represents the B23 equation of IAPWS-IF97. Investigations showed that it was not possible to meet the numerical consistency values of Table 1 with a simple equation for each function. The problem was solved by dividing region 3 into two subregions, 3a and 3b (see Fig. 3).

The boundary between subregions 3a and 3b approximates the critical isentrope $s=s_{\mathrm{c}}$. In order to decide the appropriate subregion for the functions $T_3(p,h)$ and $v_3(p,h)$, the boundary equation $h_{3\mathrm{ab}}(p)$, Eq. (8), is used; see Fig. 3. This equation is a third-degree polynomial in reduced pressure

$$\frac{h_{3\mathrm{ab}}(p)}{h^*} = \eta(\pi) = n_1 + n_2\pi + n_3\pi^2 + n_4\pi^3 \tag{8}$$

where $\eta=h/h^*$ and $\pi=p/p^*$ with $h^*=1\ \mathrm{kJ\,kg^{-1}}$ and $p^*=1\ \mathrm{MPa}$. The coefficients n_1 to n_4 are listed in Table 2. The function $h_{3\mathrm{ab}}(p)$ is valid from the critical point up to 100 MPa. The temperature at 100 MPa is 762.380873481 K. Equation (8) does not exactly describe the critical isentrope. The maximum specific entropy deviation is

$$|\Delta s_{3\mathrm{ab}}|_{\max} = |s_3^{97}[\overbrace{T_{\mathrm{it}}^{97}(p,h_{3\mathrm{ab}}(p))}, \overbrace{v_{\mathrm{it}}^{97}(p,h_{3\mathrm{ab}}(p))}] - s_{\mathrm{c}}|_{\max} = 0.00066\ \mathrm{kJ\,kg^{-1}\,K^{-1}}$$

where T_{it}^{97} and v_{it}^{97} are obtained by iteration using $p_3^{97}(v,T)$ and $s_3^{97}(v,T)$ derived from the IAPWS-IF97 basic equation for region 3. If the given specific enthalpy h is greater than $h_{3\mathrm{ab}}(p)$ calculated from the given pressure p, then the state point is located in subregion 3b, otherwise it is in subregion 3a (see Fig. 3).

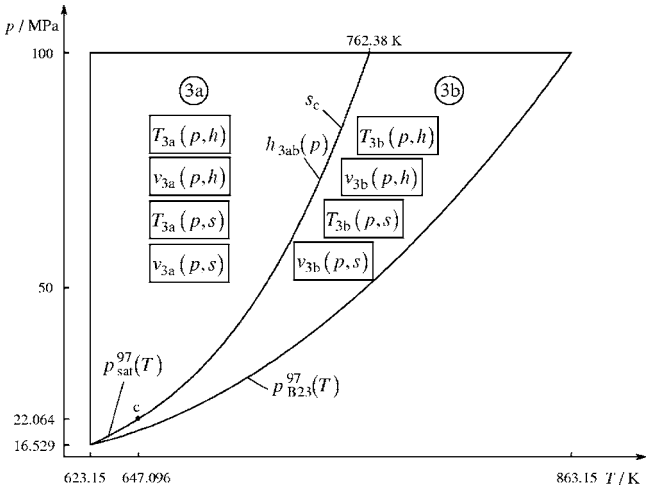

Fig. 3 Division of region 3 into subregions 3a and 3b for the backward equations $T_3(p,h)$, $v_3(p,h)$, $T_3(p,s)$, and $v_3(p,s)$

For the functions $T(p,s)$ and $v(p,s)$, input points can be tested directly to identify the subregion since entropy is an independent variable. If the given specific entropy s is less than or equal to

$$s_{\mathrm{c}} = 4.41202148223476\ \mathrm{kJ\,kg^{-1}\,K^{-1}}$$

then the point is located in subregion 3a; otherwise it is in subregion 3b. The critical specific entropy s_{c} is given with 15 digits to avoid numerical problems.

For computer-program verification, Eq. (8) gives the following p-h point: $p=25\ \mathrm{MPa}$, $h_{3\mathrm{ab}}(p)=2.095936454\times10^3\ \mathrm{kJ\,kg^{-1}}$.

2.4 Backward Equations $T(p,h)$ and $v(p,h)$

2.4.1 $T(p,h)$

2.4.1.1 Subregion 3a. The backward equation $T_{3\mathrm{a}}(p,h)$ has the dimensionless form

$$\frac{T_{3\mathrm{a}}(p,h)}{T^*} = \theta_{3\mathrm{a}}(\pi,\eta) = \sum_{i=1}^{31} n_i(\pi+0.240)^{I_i}(\eta-0.615)^{J_i} \tag{9}$$

where $\theta=T/T^*$, $\pi=p/p^*$, and $\eta=h/h^*$ with $T^*=760\ \mathrm{K}$, $p^*=100\ \mathrm{MPa}$, and $h^*=2300\ \mathrm{kJ\,kg^{-1}}$. The coefficients n_i and exponents I_i and J_i are listed in Table 3.

2.4.1.2 Subregion 3b. The backward equation $T_{3\mathrm{b}}(p,h)$ is

$$\frac{T_{3\mathrm{b}}(p,h)}{T^*} = \theta_{3\mathrm{b}}(\pi,\eta) = \sum_{i=1}^{33} n_i(\pi+0.298)^{I_i}(\eta-0.720)^{J_i} \tag{10}$$

where $\theta=T/T^*$, $\pi=p/p^*$, and $\eta=h/h^*$ with $T^*=860\ \mathrm{K}$, $p^*=100\ \mathrm{MPa}$, and $h^*=2800\ \mathrm{kJ\,kg^{-1}}$. The coefficients n_i and exponents I_i and J_i are listed in Table 4.

Table 2 Coefficients of Eq. (8)

i	n_i	i	n_i
1	$0.201464004206875\times10^4$	3	$-0.219921901054187\times10^{-1}$
2	$0.374696550136983\times10^1$	4	$0.875131686009950\times10^{-4}$

Table 3 Coefficients and exponents of Eq. (9)

i	I_i	J_i	n_i	i	I_i	J_i	n_i
1	−12	0	$-0.133645667811215\times10^{-6}$	17	−3	0	$-0.384460997596657\times10^{-5}$
2	−12	1	$0.455912656802978\times10^{-5}$	18	−2	1	$0.337423807911655\times10^{-2}$
3	−12	2	$-0.146294640700979\times10^{-4}$	19	−2	3	−0.551624873066791
4	−12	6	$0.639341312970080\times10^{-2}$	20	−2	4	0.729202277107470
5	−12	14	$0.372783927268847\times10^{3}$	21	−1	0	$-0.992522757376041\times10^{-2}$
6	−12	16	$-0.718654377460447\times10^{4}$	22	−1	2	−0.119308831407288
7	−12	20	$0.573494752103400\times10^{6}$	23	0	0	0.793929190615421
8	−12	22	$-0.267569329111439\times10^{7}$	24	0	1	0.454270731799386
9	−10	1	$-0.334066283302614\times10^{-4}$	25	1	1	0.209998591259910
10	−10	5	$-0.245479214069597\times10^{-1}$	26	3	0	$-0.642109823904738\times10^{-2}$
11	−10	12	$0.478087847764996\times10^{2}$	27	3	1	$-0.235155868604540\times10^{-1}$
12	−8	0	$0.764664131818904\times10^{-5}$	28	4	0	$0.252233108341612\times10^{-2}$
13	−8	2	$0.128350627676972\times10^{-2}$	29	4	3	$-0.764885133368119\times10^{-2}$
14	−8	4	$0.171219081377331\times10^{-1}$	30	10	4	$0.136176427574291\times10^{-1}$
15	−8	10	$-0.851007304583213\times10^{1}$	31	12	5	$-0.133027883575669\times10^{-1}$
16	−5	2	$-0.136513461629781\times10^{-1}$				

2.4.2 $v(p,h)$

2.4.2.1 Subregion 3a. The backward equation $v_{3a}(p,h)$ has the dimensionless form

$$\frac{v_{3a}(p,h)}{v^*} = \omega_{3a}(\pi,\eta) = \sum_{i=1}^{32} n_i(\pi+0.128)^{I_i}(\eta-0.727)^{J_i} \quad (11)$$

where $\omega=v/v^*$, $\pi=p/p^*$, and $\eta=h/h^*$ with $v^*=0.0028\ \mathrm{m^3\,kg^{-1}}$, $p^*=100$ MPa, and $h^*=2100\ \mathrm{kJ\,kg^{-1}}$. The coefficients n_i and exponents I_i and J_i are listed in Table 5.

2.4.2.2 Subregion 3b. The backward equation $v_{3b}(p,h)$ is

$$\frac{v_{3b}(p,h)}{v^*} = \omega_{3b}(\pi,\eta) = \sum_{i=1}^{30} n_i(\pi+0.0661)^{I_i}(\eta-0.720)^{J_i} \quad (12)$$

where $\omega=v/v^*$, $\pi=p/p^*$, and $\eta=h/h^*$ with $v^*=0.0088\ \mathrm{m^3\,kg^{-1}}$, $p^*=100$ MPa, and $h^*=2800\ \mathrm{kJ\,kg^{-1}}$. The coefficients n_i and exponents I_i and J_i are listed in Table 6.

2.4.3 Test Values. To assist in computer-program verification of Eqs. (9)–(12), Table 7 contains test values for calculated temperatures and specific volumes.

2.4.4 Consistency With IAPWS-IF97. The maximum and root-mean-square (RMS) differences between temperatures calculated from Eqs. (9) and (10) and from the IAPWS-IF97 basic equation $f_3^{97}(v,T)$ are listed in Table 8. Table 8 also contains the maximum and RMS relative deviations for specific volumes from Eqs. (11) and (12) compared to IAPWS-IF97. The maximum deviations for temperature and specific volume are less than the permissible values. The critical temperature and critical volume are reproduced exactly. The RMS value is given as

$$\Delta z_{\mathrm{RMS}} = \sqrt{\frac{1}{m}\sum_{i=1}^{m}(\Delta z_i)^2}$$

where Δz_i can be either the absolute or percentage difference between the corresponding quantities z and m is the number of Δz_i values (100 million points well distributed over the range of validity).

2.4.5 Consistency at the Subregion Boundary. The maximum difference between the backward equations $T_{3a}(p,h)$, Eq. (9), and $T_{3b}(p,h)$, Eq. (10), along the subregion boundary $h_{3ab}(p)$, Eq. (8), is 0.37 mK, which is smaller than the 25 mK numerical consistency specified for IAPWS-IF97. The maximum relative difference between the backward equations $v_{3a}(p,h)$, Eq. (11), and $v_{3b}(p,h)$, Eq. (12), along this boundary is 0.00015%, which is smaller than the 0.01% consistency requirement of Eqs. (11) and (12) with the IAPWS-IF97 basic equation.

Table 4 Coefficients and exponents of Eq. (10)

i	I_i	J_i	n_i	i	I_i	J_i	n_i
1	−12	0	$0.323254573644920\times10^{-4}$	18	−3	5	$-0.307622221350501\times10^{1}$
2	−12	1	$-0.127575556587181\times10^{-3}$	19	−2	0	$-0.574011959864879\times10^{-1}$
3	−10	0	$-0.475851877356068\times10^{-3}$	20	−2	4	$0.503471360939849\times10^{1}$
4	−10	1	$0.156183014181602\times10^{-2}$	21	−1	2	−0.925081888584834
5	−10	5	0.105724860113781	22	−1	4	$0.391733882917546\times10^{1}$
6	−10	10	$-0.858514221132534\times10^{2}$	23	−1	6	$-0.773146007130190\times10^{2}$
7	−10	12	$0.724140095480911\times10^{3}$	24	−1	10	$0.949308762098587\times10^{4}$
8	−8	0	$0.296475810273257\times10^{-2}$	25	−1	14	$-0.141043719679409\times10^{7}$
9	−8	1	$-0.592721983365988\times10^{-2}$	26	−1	16	$0.849166230819026\times10^{7}$
10	−8	2	$-0.126305422818666\times10^{-1}$	27	0	0	0.861095729446704
11	−8	4	−0.115716196364853	28	0	2	0.323346442811720
12	−8	10	$0.849000969739595\times10^{2}$	29	1	1	0.873281936020439
13	−6	0	$-0.108602260086615\times10^{-1}$	30	3	1	−0.436653048526683
14	−6	1	$0.154304475328851\times10^{-1}$	31	5	1	0.286596714529479
15	−6	2	$0.750455441524466\times10^{-1}$	32	6	1	−0.131778331276228
16	−4	0	$0.252520973612982\times10^{-1}$	33	8	1	$0.676682064330275\times10^{-2}$
17	−4	1	$-0.602507901232996\times10^{-1}$				

Table 5 Coefficients and exponents of Eq. (11)

i	I_i	J_i	n_i	i	I_i	J_i	n_i
1	−12	6	$0.529944062966028\times10^{-2}$	17	−2	16	$0.568366875815960\times10^{4}$
2	−12	8	−0.170099690234461	18	−1	0	$0.808169540124668\times10^{-2}$
3	−12	12	$0.111323814312927\times10^{2}$	19	−1	1	0.172416341519307
4	−12	18	$-0.217898123145125\times10^{4}$	20	−1	2	$0.104270175292927\times10^{1}$
5	−10	4	$-0.506061827980875\times10^{-3}$	21	−1	3	−0.297691372792847
6	−10	7	0.556495239685324	22	0	0	0.560394465163593
7	−10	10	$-0.943672726094016\times10^{1}$	23	0	1	0.275234661176914
8	−8	5	−0.297856807561527	24	1	0	−0.148347894866012
9	−8	12	$0.939353943717186\times10^{2}$	25	1	1	$-0.651142513478515\times10^{-1}$
10	−6	3	$0.192944939465981\times10^{-1}$	26	1	2	$-0.292468715386302\times10^{1}$
11	−6	4	0.421740664704763	27	2	0	$0.664876096952665\times10^{-1}$
12	−6	22	$-0.368914126282330\times10^{7}$	28	2	2	$0.352335014263844\times10^{1}$
13	−4	2	$-0.737566847600639\times10^{-2}$	29	3	0	$-0.146340792313332\times10^{-1}$
14	−4	3	−0.354753242424366	30	4	2	$-0.224503486668184\times10^{1}$
15	−3	7	$-0.199768169338727\times10^{1}$	31	5	2	$0.110533464706142\times10^{1}$
16	−2	3	$0.115456297059049\times10^{1}$	32	8	2	$-0.408757344495612\times10^{-1}$

2.5 Backward Equations $T(p,s)$ and $v(p,s)$

2.5.1 $T(p,s)$

2.5.1.1 Subregion 3a. The backward equation $T_{3a}(p,s)$ has the dimensionless form

$$\frac{T_{3a}(p,s)}{T^*}=\theta_{3a}(\pi,\sigma)=\sum_{i=1}^{33} n_i(\pi+0.240)^{I_i}(\sigma-0.703)^{J_i} \quad (13)$$

where $\theta=T/T^*$, $\pi=p/p^*$, and $\sigma=s/s^*$ with $T^*=760$ K, $p^*=100$ MPa, and $s^*=4.4$ kJ kg^{-1} K^{-1}. The coefficients n_i and exponents I_i and J_i are listed in Table 9.

2.5.1.2 Subregion 3b. The backward equation $T_{3b}(p,s)$ is

$$\frac{T_{3b}(p,s)}{T^*}=\theta_{3b}(\pi,\sigma)=\sum_{i=1}^{28} n_i(\pi+0.760)^{I_i}(\sigma-0.818)^{J_i} \quad (14)$$

where $\theta=T/T^*$, $\pi=p/p^*$, and $\sigma=s/s^*$ with $T^*=860$ K, $p^*=100$ MPa, and $s^*=5.3$ kJ kg^{-1} K^{-1}. The coefficients n_i and exponents I_i and J_i are listed in Table 10.

2.5.2 $v(p,s)$

2.5.2.1 Subregion 3a. The backward equation $v_{3a}(p,s)$ has the dimensionless form

Table 6 Coefficients and exponents of Eq. (12)

i	I_i	J_i	n_i	i	I_i	J_i	n_i
1	−12	0	$-0.225196934336318\times10^{-8}$	16	−4	6	$-0.321087965668917\times10^{1}$
2	−12	1	$0.140674363313486\times10^{-7}$	17	−4	10	$0.607567815637771\times10^{3}$
3	−8	0	$0.233784085280560\times10^{-5}$	18	−3	0	$0.557686450685932\times10^{-3}$
4	−8	1	$-0.331833715229001\times10^{-4}$	19	−3	2	0.187499040029550
5	−8	3	$0.107956778514318\times10^{-2}$	20	−2	1	$0.905368030448107\times10^{-2}$
6	−8	6	−0.271382067378863	21	−2	2	0.285417173048685
7	−8	7	$0.107202262490333\times10^{1}$	22	−1	0	$0.329924030996098\times10^{-1}$
8	−8	8	−0.853821329075382	23	−1	1	0.239897419685483
9	−6	0	$-0.215214194340526\times10^{-4}$	24	−1	4	$0.482754995951394\times10^{1}$
10	−6	1	$0.769656088222730\times10^{-3}$	25	−1	5	$-0.118035753702231\times10^{2}$
11	−6	2	$-0.431136580433864\times10^{-2}$	26	0	0	0.169490044091791
12	−6	5	0.453342167309331	27	1	0	$-0.179967222507787\times10^{-1}$
13	−6	6	−0.507749535873652	28	1	1	$0.371810116332674\times10^{-1}$
14	−6	10	$-0.100475154528389\times10^{3}$	29	2	2	$-0.536288335065096\times10^{-1}$
15	−4	3	−0.219201924648793	30	2	6	$0.160697101092520\times10^{1}$

Table 7 Test values for temperature and specific volume calculated from Eqs. (9)–(12) for selected pressures and enthalpies

Equation	p/MPa	h/kJ kg^{-1}	T/K	v/m^3 kg^{-1}
$T_{3a}(p,h)$, Eq. (9)	20	1700	6.293083892×10^{2}	1.749903962×10^{-3}
$v_{3a}(p,h)$, Eq. (11)	50	2000	6.905718338×10^{2}	1.908139035×10^{-3}
	100	2100	7.336163014×10^{2}	1.676229776×10^{-3}
$T_{3b}(p,h)$, Eq. (10)	20	2500	6.418418053×10^{2}	6.670547043×10^{-3}
$v_{3b}(p,h)$, Eq. (12)	50	2400	7.351848618×10^{2}	2.801244590×10^{-3}
	100	2700	8.420460876×10^{2}	2.404234998×10^{-3}

Table 8 Maximum and root-mean-square differences between temperature and specific volume calculated from Eqs. (9)–(12) and those from the IAPWS-IF97 basic equation $f_3^{97}(v,T)$ and related tolerances

Subregion	Equation	$\lvert\Delta T\rvert_{tol}$ (mK)	$\lvert\Delta T\rvert_{max}$ (mK)	$\lvert\Delta T\rvert_{RMS}$ (mK)
3a	(9)	25	23.6	10.5
3b	(10)	25	19.6	9.6
Subregion	Equation	$\lvert\Delta v/v\rvert_{tol}$ (%)	$\lvert\Delta v/v\rvert_{max}$ (%)	$\lvert\Delta v/v\rvert_{RMS}$ (%)
3a	(11)	0.01	0.0080	0.0032
3b	(12)	0.01	0.0095	0.0042

$$\frac{v_{3a}(p,s)}{v^*} = \omega_{3a}(\pi,\sigma) = \sum_{i=1}^{28} n_i(\pi+0.187)^{I_i}(\sigma-0.755)^{J_i} \quad (15)$$

where $\omega=v/v^*$, $\pi=p/p^*$, and $\sigma=s/s^*$ with $v^*=0.0028\ \mathrm{m^3\,kg^{-1}}$, $p^*=100$ MPa, and $s^*=4.4\ \mathrm{kJ\,kg^{-1}\,K^{-1}}$. The coefficients n_i and exponents I_i and J_i are listed in Table 11.

2.5.2.2 Subregion 3b. The backward equation $v_{3b}(p,s)$ is

$$\frac{v_{3b}(p,s)}{v^*} = \omega_{3b}(\pi,\sigma) = \sum_{i=1}^{31} n_i(\pi+0.298)^{I_i}(\sigma-0.816)^{J_i} \quad (16)$$

where $\omega=v/v^*$, $\pi=p/p^*$, and $\sigma=s/s^*$ with $v^*=0.0088\ \mathrm{m^3\,kg^{-1}}$, $p^*=100$ MPa, and $s^*=5.3\ \mathrm{kJ\,kg^{-1}\,K^{-1}}$. The coefficients n_i and exponents I_i and J_i are listed in Table 12.

2.5.3 Test Values. To assist in computer-program verification of Eqs. (13)–(16), Table 13 contains test values for calculated temperatures and specific volumes.

2.5.4 Consistency with IAPWS-IF97. The maximum and RMS differences between the temperatures calculated from Eqs. (13) and (14) and the IAPWS-IF97 basic equation $f_3^{97}(v,T)$ in comparison with the permissible differences are listed in Table 14. Table 14 also contains the maximum and RMS relative deviations for the specific volume of Eqs. (15) and (16) from IAPWS-IF97. The maximum deviations for temperature and specific volume are less than the permissible values. The critical temperature and critical volume are reproduced exactly.

2.5.5 Consistency at the Subregion Boundary. The maximum difference between the backward equations $T_{3a}(p,s)$, Eq. (13), and $T_{3b}(p,s)$, Eq. (14), along the subregion boundary s_c is 0.093 mK. The maximum relative specific volume difference between the backward equations $v_{3a}(p,s)$, Eq. (15), and $v_{3b}(p,s)$, Eq. (16),

Table 9 Coefficients and exponents of Eq. (13)

i	I_i	J_i	n_i	i	I_i	J_i	n_i
1	−12	28	$0.150042008263875\times10^{10}$	18	−4	10	$-0.368275545889071\times10^{3}$
2	−12	32	$-0.159397258480424\times10^{12}$	19	−4	36	$0.664768904779177\times10^{16}$
3	−10	4	$0.502181140217975\times10^{-3}$	20	−2	1	$0.449359251958880\times10^{-1}$
4	−10	10	$-0.672057767855466\times10^{2}$	21	−2	4	$-0.422897836099655\times10^{1}$
5	−10	12	$0.145058545404456\times10^{4}$	22	−1	1	−0.240614376434179
6	−10	14	$-0.823889534888890\times10^{4}$	23	−1	6	$-0.474341365254924\times10^{1}$
7	−8	5	−0.154852214233853	24	0	0	0.724093999126110
8	−8	7	$0.112305046746695\times10^{2}$	25	0	1	0.923874349695897
9	−8	8	$-0.297000213482822\times10^{2}$	26	0	4	$0.399043655281015\times10^{1}$
10	−8	28	$0.438565132635495\times10^{11}$	27	1	0	$0.384066651868009\times10^{-1}$
11	−6	2	$0.137837838635464\times10^{-2}$	28	2	0	$-0.359344365571848\times10^{-2}$
12	−6	6	$-0.297478527157462\times10^{1}$	29	2	3	−0.735196448821653
13	−6	32	$0.971777947349413\times10^{13}$	30	3	2	0.188367048396131
14	−5	0	$-0.571527767052398\times10^{-4}$	31	8	0	$0.141064266818704\times10^{-3}$
15	−5	14	$0.288307949778420\times10^{5}$	32	8	1	$-0.257418501496337\times10^{-2}$
16	−5	32	$-0.744428289262703\times10^{14}$	33	10	2	$0.123220024851555\times10^{-2}$
17	−4	6	$0.128017324848921\times10^{2}$				

Table 10 Coefficients and exponents of Eq. (14)

i	I_i	J_i	n_i	i	I_i	J_i	n_i
1	−12	1	0.527111701601660	15	−5	6	$0.880531517490555\times10^{3}$
2	−12	3	$-0.401317830052742\times10^{2}$	16	−4	12	$0.265015592794626\times10^{7}$
3	−12	4	$0.153020073134484\times10^{3}$	17	−3	1	−0.359287150025783
4	−12	7	$-0.224799398218827\times10^{4}$	18	−3	6	$-0.656991567673753\times10^{3}$
5	−8	0	−0.193993484669048	19	−2	2	$0.241768149185367\times10^{1}$
6	−8	1	$-0.140467557893768\times10^{1}$	20	0	0	0.856873461222588
7	−8	3	$0.426799878114024\times10^{2}$	21	2	1	0.655143675313458
8	−6	0	0.752810643416743	22	3	1	−0.213535213206406
9	−6	2	$0.226657238616417\times10^{2}$	23	4	0	$0.562974957606348\times10^{-2}$
10	−6	4	$-0.622873556909932\times10^{3}$	24	5	24	$-0.316955725450471\times10^{15}$
11	−5	0	−0.660823667935396	25	6	0	$-0.699997000152457\times10^{-3}$
12	−5	1	0.841267087271658	26	8	3	$0.119845803210767\times10^{-1}$
13	−5	2	$-0.253717501764397\times10^{2}$	27	12	1	$0.193848122022095\times10^{-4}$
14	−5	4	$0.485708963532948\times10^{3}$	28	14	2	$-0.215095749182309\times10^{-4}$

Table 11 Coefficients and exponents of Eq. (15)

i	I_i	J_i	n_i	i	I_i	J_i	n_i
1	−12	10	$0.795544074093975\times10^{2}$	15	−3	2	−0.118008384666987
2	−12	12	$-0.238261242984590\times10^{4}$	16	−3	4	$0.253798642355900\times10^{1}$
3	−12	14	$0.176813100617787\times10^{5}$	17	−2	3	0.965127704669424
4	−10	4	$-0.110524727080379\times10^{-2}$	18	−2	8	$-0.282172420532826\times10^{2}$
5	−10	8	$-0.153213833655326\times10^{2}$	19	−1	1	0.203224612353823
6	−10	10	$0.297544599376982\times10^{3}$	20	−1	2	$0.110648186063513\times10^{1}$
7	−10	20	$-0.350315206871242\times10^{8}$	21	0	0	0.526127948451280
8	−8	5	0.277513761062119	22	0	1	0.277000018736321
9	−8	6	−0.523964271036888	23	0	3	$0.108153340501132\times10^{1}$
10	−8	14	$-0.148011182995403\times10^{6}$	24	1	0	$-0.744127885357893\times10^{-1}$
11	−8	16	$0.160014899374266\times10^{7}$	25	2	0	$0.164094443541384\times10^{-1}$
12	−6	28	$0.170802322663427\times10^{13}$	26	4	2	$-0.680468275301065\times10^{-1}$
13	−5	1	$0.246866996006494\times10^{-3}$	27	5	2	$0.257988576101640\times10^{-1}$
14	−4	5	$0.165326084797980\times10^{1}$	28	6	0	$-0.145749861944416\times10^{-3}$

along this boundary is 0.00046%. In both cases, the maximum difference is much smaller than numerical differences with the IAPWS-IF97 equation.

2.6 Computing Time Relative to IAPWS-IF97. A major motivation for the development of these backward equations was reducing the computing time required to obtain T and v given (p,h) or (p,s). Using the equations developed here, the calculation is about 14 times faster than two-dimensional iteration of the IAPWS-IF97 basic equation with convergence tolerances set to the values shown in Table 1.

3 Equations $p_{\mathrm{sat}}(h)$ and $p_{\mathrm{sat}}(s)$ for Region 3

3.1 Determination of Region Boundaries From (p,h) and (p,s). The boundaries between region 3 and the liquid-vapor two-phase region 4 are the saturated liquid $(x=0)$ and saturated vapor $(x=1)$; see Figs. 4 and 5. To identify whether a state point is located in region 4 or in region 3, iterations using the IAPWS-IF97 basic equation $f_3^{97}(v,T)$ are required to calculate the enthalpy or entropy from a given pressure on the saturation curves of region 3. The equations $p_{3\mathrm{sat}}(h)$ and $p_{3\mathrm{sat}}(s)$ provided here make it

Table 12 Coefficients and exponents of Eq. (16)

i	I_i	J_i	n_i	i	I_i	J_i	n_i
1	−12	0	$0.591599780322238\times10^{-4}$	17	−4	2	$-0.121613320606788\times10^{2}$
2	−12	1	$-0.185465997137856\times10^{-2}$	18	−4	3	$0.167637540957944\times10^{1}$
3	−12	2	$0.104190510480013\times10^{-1}$	19	−3	1	$-0.744135838773463\times10^{1}$
4	−12	3	$0.598647302038590\times10^{-2}$	20	−2	0	$0.378168091437659\times10^{-1}$
5	−12	5	−0.771391189901699	21	−2	1	$0.401432203027688\times10^{1}$
6	−12	6	$0.172549765557036\times10^{1}$	22	−2	2	$0.160279837479185\times10^{2}$
7	−10	0	$-0.467076079846526\times10^{-3}$	23	−2	3	$0.317848779347728\times10^{1}$
8	−10	1	$0.134533823384439\times10^{-1}$	24	−2	4	$-0.358362310304853\times10^{1}$
9	−10	2	$-0.808094336805495\times10^{-1}$	25	−2	12	$-0.115995260446827\times10^{7}$
10	−10	4	0.508139374365767	26	0	0	0.199256573577909
11	−8	0	$0.128584643361683\times10^{-2}$	27	0	1	−0.122270624794624
12	−5	1	$-0.163899353915435\times10^{1}$	28	0	2	$-0.191449143716586\times10^{2}$
13	−5	2	$0.586938199318063\times10^{1}$	29	1	0	$-0.150448002905284\times10^{-1}$
14	−5	3	$-0.292466667918613\times10^{1}$	30	1	2	$0.146407900162154\times10^{2}$
15	−4	0	$-0.614076301499537\times10^{-2}$	31	2	2	$-0.327477787188230\times10^{1}$
16	−4	1	$0.576199014049172\times10^{1}$				

Table 13 Test values for temperature and specific volume calculated from Eqs. (13)–(16) for selected pressures and entropies

Equation	p/MPa	s/kJ kg^{-1} K^{-1}	T/K	v/m^3 kg^{-1}
$T_{3a}(p,s)$, Eq. (13)	20	3.8	6.282959869×10^{2}	1.733791463×10^{-3}
$v_{3a}(p,s)$, Eq. (15)	50	3.6	6.297158726×10^{2}	1.469680170×10^{-3}
	100	4.0	7.056880237×10^{2}	1.555893131×10^{-3}
$T_{3b}(p,s)$, Eq. (14)	20	5.0	6.401176443×10^{2}	6.262101987×10^{-3}
$v_{3b}(p,s)$, Eq. (16)	50	4.5	7.163687517×10^{2}	2.332634294×10^{-3}
	100	5.0	8.474332825×10^{2}	2.449610757×10^{-3}

Table 14 Maximum and root-mean-square differences between the temperature and specific volume calculated from Eqs. (13)–(16) and those from the IAPWS-IF97 basic equation $f_3^{97}(v,T)$ and related tolerances

Subregion	Equation	$\lvert\Delta T\rvert_{tol}$ (mK)	$\lvert\Delta T\rvert_{max}$ (mK)	$\lvert\Delta T\rvert_{RMS}$ (mK)
3a	(13)	25	24.8	11.2
3b	(14)	25	22.1	10.1
Subregion	Equation	$\lvert\Delta v/v\rvert_{tol}$ (%)	$\lvert\Delta v/v\rvert_{max}$ (%)	$\lvert\Delta v/v\rvert_{RMS}$ (%)
3a	(15)	0.01	0.0096	0.0052
3b	(16)	0.01	0.0077	0.0037

possible to determine without iteration whether the given point is in region 4 or region 3.

The boundary between regions 1 and 3 can be calculated directly from a given pressure p and from $T=623.15$ K using the IAPWS-IF97 basic equation $g_1^{97}(p,T)$. The boundary between regions 2 and 3 can be calculated directly from p and from the B23 equation $T=T_{B23}^{97}(p)$ of IAPWS-IF97 using the basic equation $g_2^{97}(p,T)$.

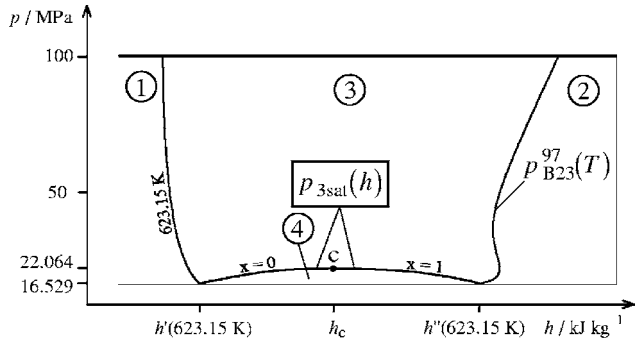

Fig. 4 IAPWS-IF97 region 3 and the boundary equation $p_{3sat}(h)$ in a p-h diagram

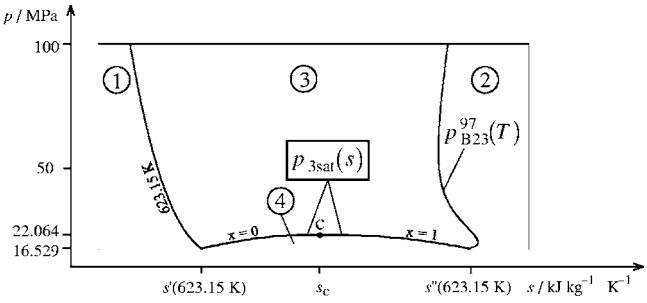

Fig. 5 IAPWS-IF97 region 3 and the boundary equation $p_{3sat}(s)$ in a p-s diagram

Table 16 Pressure values calculated from Eq. (17)

Equation	h/kJ kg^{-1}	p/MPa
$p_{3sat}(h)$, Eq. (17)	1700	1.724175718×10^{1}
	2000	2.193442957×10^{1}
	2400	2.018090839×10^{1}

3.2 Consistency Requirements. The required accuracy of the equations for the saturation boundaries of region 3 results from IAPWS requirements on backward functions. The backward functions $T(p,h)$, $v(p,h)$, $T(p,s)$, and $v(p,s)$ must fulfill their numerical consistency requirements when using $p_{3sat}(h)$ and $p_{3sat}(s)$ to determine the region for a given state point.

3.3 Boundary Equations $p_{sat}(h)$ and $p_{sat}(s)$

3.3.1 The Equations. $p_{3sat}(h)$ describes the saturated-liquid and saturated-vapor curves, including the critical point, in the enthalpy range (see Fig. 4):

$$h'(623.15\ \text{K}) \leqslant h \leqslant h''(623.15\ \text{K}),$$

$$\text{where } h'(623.15\ \text{K}) = 1.670858218\times10^{3}\ \text{kJ kg}^{-1}$$

$$\text{and } h''(623.15\ \text{K}) = 2.563592004\times10^{3}\ \text{kJ kg}^{-1}$$

$p_{3sat}(h)$ has the dimensionless form

$$\frac{p_{3sat}(h)}{p^*} = \pi(\eta) = \sum_{i=1}^{14} n_i(\eta-1.02)^{I_i}(\eta-0.608)^{J_i} \qquad (17)$$

where $\pi=p/p^*$ and $\eta=h/h^*$ with $p^*=22$ MPa and $h^*=2600$ kJ kg^{-1}. The coefficients n_i and exponents I_i and J_i are listed in Table 15.

If the given pressure p is greater than $p_{3sat}(h)$ calculated from the given enthalpy h, then the point is located in region 3, otherwise it is in region 4 (see Fig. 4). To assist in computer-program verification of Eq. (17), Table 16 contains test values for calculated pressures.

$p_{3sat}(s)$ describes the saturated-liquid and saturated-vapor curves, including the critical point, in the entropy range (see Fig. 5)

$$s'(623.15\ \text{K}) \leqslant s \leqslant s''(623.15\ \text{K}),$$

$$\text{where } s'(623.15\ \text{K}) = 3.778281340\ \text{kJ kg}^{-1}\ \text{K}^{-1}$$

$$\text{and } s''(623.15\ \text{K}) = 5.210887825\ \text{kJ kg}^{-1}\ \text{K}^{-1}$$

$p_{3sat}(s)$ has the dimensionless form

$$\frac{p_{3sat}(s)}{p^*} = \pi(\sigma) = \sum_{i=1}^{10} n_i(\sigma-1.03)^{I_i}(\sigma-0.699)^{J_i} \qquad (18)$$

where $\pi=p/p^*$ and $\sigma=s/s^*$ with $p^*=22$ MPa and $s^*=5.2$ kJ kg^{-1} K^{-1}. The coefficients n_i and exponents I_i and J_i are

Table 15 Coefficients and exponents of Eq. (17)

i	I_i	J_i	n_i	i	I_i	J_i	n_i
1	0	0	0.600073641753024	8	8	24	$0.252304969384128\times10^{18}$
2	1	1	$-0.936203654849857\times10^{1}$	9	14	16	$-0.389718771997719\times10^{19}$
3	1	3	$0.246590798594147\times10^{2}$	10	20	16	$-0.333775713645296\times10^{23}$
4	1	4	$-0.107014222858224\times10^{3}$	11	22	3	$0.356499469636328\times10^{11}$
5	1	36	$-0.915821315805768\times10^{14}$	12	24	18	$-0.148547544720641\times10^{27}$
6	5	3	$-0.862332011700662\times10^{4}$	13	28	8	$0.330611514838798\times10^{19}$
7	7	0	$-0.235837344740032\times10^{2}$	14	36	24	$0.813641294467829\times10^{38}$

Table 17 Coefficients and exponents of Eq. (18)

i	I_i	J_i	n_i	i	I_i	J_i	n_i
1	0	0	0.639767553612785	6	12	14	$-0.378829107169011\times10^{18}$
2	1	1	$-0.129727445396014\times10^{2}$	7	16	36	$-0.955586736431328\times10^{35}$
3	1	32	$-0.224595125848403\times10^{16}$	8	24	10	$0.187269814676188\times10^{24}$
4	4	7	$0.177466741801846\times10^{7}$	9	28	0	$0.119254746466473\times10^{12}$
5	12	4	$0.717079349571538\times10^{10}$	10	32	18	$0.110649277244882\times10^{37}$

listed in Table 17.

If the given pressure p is greater than $p_{3sat}(s)$ calculated from the given entropy s, then the point is located in region 3, otherwise it is in region 4 (see Fig. 5). To assist in computer-program verification of Eq. (18), Table 18 contains test values for calculated pressures.

3.3.2 Consistency With IAPWS-IF97 Saturation Equation. The maximum relative deviations between the calculated pressures $p_{3sat}(h)$, Eq. (17), and $p_{3sat}(s)$, Eq. (18), and the IAPWS-IF97 saturation equation $p_{sat}^{97}(T)$ are 0.00043% for Eq. (17) and 0.0033% for Eq. (18).

3.3.3 Consistency of Backward Equations With IAPWS-IF97 Along the Boundary Equations $p_{sat}(h)$ and $p_{sat}(s)$. The maximum temperature differences between the backward equations $T_{3a}(p,h)$, Eq. (9), and $T_{3b}(p,h)$, Eq. (10), and the IAPWS-IF97 basic equation $f_3^{97}(v,T)$ along the boundary given by $p_{3sat}(h)$, Eq. (17), are shown in Table 19. Table 19 also shows the maximum percentage differences of specific volume between the backward equations $v_{3a}(p,h)$, Eq. (11), and $v_{3b}(p,h)$, Eq. (12), and the IAPWS-IF97 basic equation along $p_{3sat}(h)$. The maximum differences are much smaller than the corresponding tolerances. Table 20 shows a similar comparison using the boundary equation $p_{3sat}(s)$, Eq. (18). Once again, the tolerances for consistency are easily met.

3.4 Computing Time Relative to IAPWS-IF97. The motivation for the development of $p_{3sat}(h)$, Eq. (17), and $p_{3sat}(s)$, Eq. (18), was reducing the computing time to determine the region for a given state point (p,h) or (p,s). With these boundary equations, this calculation is significantly faster than the iterative calculation that would otherwise be required.

Table 18 Pressure values calculated from Eq. (18)

Equation	s/kJ kg^{-1} K^{-1}	p/MPa
$p_{3sat}(s)$, Eq. (18)	3.8	1.687755057×10^{1}
	4.2	2.164451789×10^{1}
	5.2	1.668968482×10^{1}

Table 19 Maximum differences of temperature and specific volume calculated by Eqs. (9)–(12) from the IAPWS-IF97 basic equation $f_3^{97}(v,T)$ along the boundary equation $p_{3sat}(h)$, Eq. (17), and related tolerances

Subregion	Equation	$\lvert\Delta T\rvert_{tol}$ (mK)	$\lvert\Delta T\rvert_{max}$ (mK)
3a	(9)	25	0.47
3b	(10)	25	0.46
Subregion	Equation	$\lvert\Delta v/v\rvert_{tol}$ (%)	$\lvert\Delta v/v\rvert_{max}$ (%)
3a	(11)	0.01	0.00077
3b	(12)	0.01	0.0012

4 Application of Equations

The numerical consistency of the backward equations presented in Sec. 2 and of the boundary equations presented in Sec. 3 with the IAPWS-IF97 basic equation is sufficient for most applications in heat-cycle and boiler calculations. For users not satisfied with this consistency, these equations are recommended for generating starting points to reduce the time required for convergence of an iterative process.

These equations can only be used in the ranges of validity described in Secs. 2.3 and 3.3.1. They should not be used for determining thermodynamic derivatives. Derivatives can be determined from the IAPWS-IF97 fundamental equation $f_3^{97}(v,T)$ as described in [10]. The equations should also not be used in iterative calculations of other backward functions such as $p(h,s)$. Iteration should only be performed by using the fundamental equations of IAPWS-IF97.

In any case, depending on the application, a conscious decision is required whether to use the backward and boundary equations or to calculate the corresponding values by iteration from the basic equation of IAPWS-IF97.

5 Further Information

Further details of the numerical consistency mentioned in Secs. 2.4.4, 2.4.5, 2.5.4, 2.5.5, and 3.3.2 may be found in the dissertation of Knobloch [19]. Computer code for these equations may be obtained from the corresponding author (H.-J.K.), and links to sources for software implementing IAPWS property formulations may be found on the IAPWS website (www.iapws.org).

6 Summary

We have presented backward equations $T(p,h)$, $v(p,h)$, $T(p,s)$, and $v(p,s)$ and boundary equations $p_{sat}(h)$ and $p_{sat}(s)$ for water in IAPWS-IF97 region 3. The numerical consistencies of temperature and specific volume calculated from the backward equations with the IAPWS-IF97 basic equation $f_3^{97}(v,T)$ are sufficient for most applications in heat-cycle and boiler calculations. The new backward equations are about 14 times faster than the iterative calculation that would otherwise be needed.

The consistencies of the boundary equations $p_{sat}(h)$ and $p_{sat}(s)$ with the IAPWS-IF97 saturation equation $p_{sat}^{97}(T)$ are sufficient to

Table 20 Maximum differences of temperature and specific volume calculated by Eqs. (13)–(16) from the IAPWS-IF97 basic equation $f_3^{97}(v,T)$ along the boundary equation $p_{3sat}(s)$, Eq. (18), and related tolerances

Subregion	Equation	$\lvert\Delta T\rvert_{tol}$ (mK)	$\lvert\Delta T\rvert_{max}$ (mK)
3a	(13)	25	2.69
3b	(14)	25	2.12
Subregion	Equation	$\lvert\Delta v/v\rvert_{tol}$ (%)	$\lvert\Delta v/v\rvert_{max}$ (%)
3a	(15)	0.01	0.0034
3b	(16)	0.01	0.0020

determine the region given (p,h) or (p,s). The boundary equations are significantly faster than the iterative calculation that would otherwise be needed.

For applications where the demands on numerical consistency are extremely high, iteration using the IAPWS-IF97 equations may still be necessary. In these cases, the equations presented can be used to generate very accurate starting values.

Acknowledgment

The authors are indebted to other members of the IAPWS Working Groups "Industrial Requirements and Solutions" and "Thermophysical Properties of Water and Steam." We are grateful to all IAPWS colleagues who contributed to the project of the development of supplementary equations for IAPWS-IF97. Two of us (H.-J.K. and K.K.) are particularly grateful to the Saxony State Ministry of Science and Art for its financial support.

Nomenclature

f = specific Helmholtz free energy
g = specific Gibbs free energy
h = specific enthalpy
p = pressure
s = specific entropy
T = absolute temperature
v = specific volume
Δ = difference in any quantity
η = reduced enthalpy, $\eta=h/h^*$
θ = reduced temperature $\theta=T/T^*$
π = reduced pressure, $\pi=p/p^*$
ρ = density
σ = reduced entropy, $\sigma=s/s^*$
ω = reduced volume, $\omega=v/v^*$
n = coefficient
I, J = exponent
i, j = serial number

Superscripts

97 = quantity or equation of IAPWS-IF97
01 = equation of IAPWS-IF97-S01
03 = equation of IAPWS-IF97-S03rev
04 = equation of IAPWS-IF97-04
* = reducing quantity
$'$ = saturated liquid state
$''$ = saturated vapor state

Subscripts

1 = region 1
2 = region 2
3 = region 3
3a = subregion 3a
3b = subregion 3b
3ab = boundary between subregions 3a and 3b
4 = region 4
5 = region 5
B23 = boundary between regions 2 and 3
c = critical point
it = iterated quantity
max = maximum value of a quantity
RMS = root-mean-square value of a quantity
sat = saturation state
tol = tolerance value of a quantity

References

[1] International Association for the Properties of Water and Steam, 1997, "Release on the IAPWS Industrial Formulation 1997 for the Thermodynamic Properties of Water and Steam," IAPWS Release, IAPWS Secretariat, available at www.iapws.org

[2] Wagner, W., Cooper, J. R., Dittmann, A., Kijima, J., Kretzschmar, H.-J., Kruse, A., Mareš, R., Oguchi, K., Sato, H., Stöcker, I., Šifner, O., Tanishita, I., Trübenbach, J., and Willkommen, Th., 2000, "The IAPWS Industrial Formulation 1997 for the Thermodynamic Properties of Water and Steam," J. Eng. Gas Turbines Power, **122**, pp. 150–182.

[3] International Association for the Properties of Water and Steam, 2001, "Supplementary Release on Backward Equations for Pressure as a Function of Enthalpy and Entropy $p(h,s)$ to the IAPWS Industrial Formulation 1997 for the Thermodynamic Properties of Water and Steam," IAPWS Release, IAPWS Secretariat, available at www.iapws.org

[4] Kretzschmar, H.-J., Cooper, J. R., Dittmann, A., Friend, D. G., Gallagher, J. S., Knobloch, K., Mareš, R., Miyagawa, K., Stöcker, I., Trübenbach, J., Wagner, W., and Willkommen, Th., "Supplementary Backward Equations for Pressure as a Function of Enthalpy and Entropy $p(h,s)$ to the Industrial Formulation IAPWS-IF97 for Water and Steam," J. Eng. Gas Turbines Power, in press.

[5] International Association for the Properties of Water and Steam, 2004, "Revised Supplementary Release on Backward Equations for the Functions $T(p,h)$, $v(p,h)$ and $T(p,s)$, $v(p,s)$ for Region 3 of the IAPWS Industrial Formulation 1997 for the Thermodynamic Properties of Water and Steam," IAPWS Release, IAPWS Secretariat, available at www.iapws.org

[6] International Association for the Properties of Water and Steam, 2004, "Supplementary Release on Backward Equations $p(h,s)$ for Region 3, Equations as a Function of h and s for the Region Boundaries, and an Equation $T_{sat}(h,s)$ for Region 4 of the IAPWS Industrial Formulation 1997 for the Thermodynamic Properties of Water and Steam," IAPWS Release, IAPWS Secretariat, available at www.iapws.org

[7] Kretzschmar, H.-J., and Knobloch, K., 2005, "Supplementary Backward Equations for the Industrial Formulation IAPWS-IF97 of Water and Steam for Fast Calculations of Heat Cycles, Boilers, and Steam Turbines," in M. Nakahara et al., eds., *Water, Steam and Aqueous Solutions for Electric Power: Advances in Science and Technology*, *Proceedings of the 14th International Conference on the Properties of Water and Steam*, Maruzen Co., Ltd., Kyoto, Japan, pp. 34–45.

[8] Kretzschmar, H.-J., 2001, "Specifications for the Supplementary Backward Equations $T(p,h)$ and $T(p,s)$ in Region 3 of IAPWS-IF97," B. Dooley, ed., Minutes of the Meetings of the Executive Committee of the International Association for the Properties of Water and Steam, Gaithersburg 2001, IAPWS Secretariat, Palo Alto, CA, p. 6 and Attachment 7-Item #6.

[9] Rukes, B., 1994, "Specifications for Numerical Consistency," B. Dooley, ed., *Minutes of the Meetings of the Executive Committee of the International Association for the Properties of Water and Steam*, Orlando, 1994, IAPWS Secretariat, Palo Alto, CA, pp. 31–33.

[10] Kretzschmar, H.-J., Stöcker, I., Klinger, J., and Dittmann, A., 2000, "Calculation of Thermodynamic Derivatives for Water and Steam Using the New Industrial Formulation IAPWS-IF97," P. R. Tremaine et al., eds., *Steam, Water and Hydrothermal Systems: Physics and Chemistry Meeting the Needs of Industry*, *Proceedings of the 13th International Conference on the Properties of Water and Steam*, NRC Press, Ottawa, pp. 238–247.

[11] Rukes, B., and Wagner, W., 1991, "Final Set of Specifications for the New Industrial Formulation," B. Dooley, ed., *Minutes of the Meetings of the Executive Committee of the International Association for the Properties of Water and Steam*, Tokyo 1991, IAPWS Secretariat, Palo Alto, CA, pp. 78–82.

[12] Kruse, A., and Wagner, W., 1998, "Neue Zustandsgleichungen für industrielle Anwendungen im technisch relevanten Zustandsgebiet von Wasser (New Equations of State for Water for Industrial Use)," *Fortschr.-Ber. VDI, Reihe 6*, Nr. 393, VDI-Verlag, Düsseldorf.

[13] Trübenbach, J., 1999, "Ein Algorithmus zur Aufstellung rechenzeitoptimierter Gleichungen für thermodynamische Zustandsgrößen (An Algorithm for Developing Equations of State Optimized Regarding Their Computing Time Consumption)," *Fortschr.-Ber. VDI, Reihe 6*, Nr. 417, VDI-Verlag, Düsseldorf.

[14] Willkommen, Th., Kretzschmar, H.-J., and Dittmann, A., 1995, "An Algorithm for Setting up Numerically Consistent Forward and Backward Equations for Process Modelling," in H. J. White et al., eds., *Physical Chemistry of Aqueous Systems*, *Proceedings of the 12th International Conference on the Properties of Water and Steam*, Begell House, New York, pp. 194–201.

[15] Willkommen, Th., 1995, "Ein Algorithmus zur Aufstellung numerisch konsistenter Gleichungen für die in Prozessmodellierungen benötigten thermodynamischen Umkehrfunktionen (An Algorithm for Developing Numerically Consistent Backward Equations for Use in Process Modeling)," Dissertation, Faculty of Mechanical Engineering, Technical University of Dresden, Dresden.

[16] Kretzschmar, H.-J., 1990, "Zur Aufbereitung und Darbietung thermophysikalischer Stoffdaten für die Energietechnik (The Preparation and Processing of Thermophysical Properties for Power Engineering)," Habilitation, Faculty of Mechanical Engineering, Technical University of Dresden, Dresden.

[17] Wagner, W., 1974, "Eine mathematisch statistische Methode zum Aufstellen thermodynamischer Gleichungen—gezeigt am Beispiel der Dampfdruckkurve reiner fluider Stoffe (A Mathematical Statistical Method for Developing Equations of State—Demonstration With the Vapor Pressure Curves of Pure Fluids)," *Fortschr.-Ber. VDI, Reihe 3*, Nr. 39, VDI-Verlag, Düsseldorf.

[18] Setzmann, W., and Wagner, W., 1989, "A New Method for Optimizing the Structure of Thermodynamic Correlation Equations," Int. J. Thermophys., **10**, pp. 1103–1126.

[19] Knobloch, K., "Gleichungen für thermodynamische Umkehrfunktionen von Wasser und Wasserdampf im kritischen und überkritischen Zustandsgebiet für energietechnische Prozessberechnungen (Equations for Thermodynamic Backward Functions of Water in the Critical and Supercritical Regions for Power Cycle Calculations)," *Fortschr.-Ber. VDI, Reihe 6*, in preparation.